The Search for Superdeformation in Odd-Odd Praseodymium-132

Volume I

By

Christine Veronica Socha Hampton

A DISSERTATION

Submitted to
Michigan State University
in partial fulfillment of the requirements
for the Degree of

DOCTOR OF PHILOSOPHY

Department of Chemistry

1999

ABSTRACT

THE SEARCH FOR SUPERDEFORMATION IN ODD-ODD PRASEODYMIUM-132

By

Christine Veronica Socha Hampton

Results are presented from a fusion-evaporation experiment, conducted at the Holifield Heavy Ion Research facility at Oak Ridge National Laboratory. The reaction ^{100}Mo(^{37}Cl,γ)^{137}Pr* was studied using a beam energy of 160 MeV from the Tandem van deGraaf generator. Approximately 250×10^6 coincidence events with a three–fold or higher multiplicity in the 20 HPGe Compton Suppression Spectrometer γ-ray detector array were recorded for analysis. The objective of this work was to determine the rotational band structure of ^{132}Pr at high spin and to search for superdeformation in this nucleus. Superdeformed rotational bands (SD) have the properties of deformed prolate rotors (β= .35–.5) and appear to originate from highly deformed intruder orbitals such as the $i_{13/2}$ neutron orbital and have been attributed to quasiparticle alignments.

A double gating method was developed to better select the ^{132}Pr transitions. Events in coincidence with four major transitions (116, 130, 178, 283 keV) were scanned into a 2-D array; then selected energy gates were summed to represent each band. Spectra of interest were extracted from the 2D arrays and refined using a novel Fast Fourier Transform technique that we developed during the course of this work.

The coincidence spectra for ^{132}Pr, in general, confirm the three rotational bands

observed in a previous (low spin) study. The negative parity, prolate shaped $\pi h_{11/2} \otimes \nu g_{7/2}$ (band 1) and the triaxial $\pi h_{11/2} \otimes \nu h_{11/2}$ (band 2) have been extended by a few energy transitions. We have seen five additional energy transitions, extending the decay scheme of the doubly decoupled band based on a $\pi h_{11/2} \otimes \nu i_{13/2}$ orbital coupling.

Four regularly spaced, weakly populated rotational bands were observed in coincidence with low-lying transitions in the ground state structure of ^{132}Pr. The four bands have very similar rotational characteristics. The spacings of successive transitions is comparable to those observed in superdeformed bands in the region. Cranked Shell Model (CSM) and Total Routhian Surface (TRS) calculations using a Woods-Saxon potential suggest a small set of plausible structures.

Also, in the course of this work, we have developed an extremely sensitive search technique for superdeformed bands. Our initial objective was to construct a fast method that would locate the same peaks within a simple total projection of all the energies within the data set. The Segmented FFT technique works through a mathematical investigation of the peaks that are present in the total spectrum. Peaks will be located depending on the presence of their spectral harmonics. The important features of this technique are: 1) the extreme sensitivity allows SD bands to be located within a total energy projection spectrum, as well as a spectrum generated without background subtraction from the sum of energy gates on the band and 2) the method is extremely fast. Once the parameters and conditions have been optimized, the analysis is complete within minutes instead of weeks that other methods require. 3) The technique can be used to confirm the presence of a known SD band or to locate a potential SD band prior to setting gates on a data array. When using a template for a known band, the Segmented FFT routine can be a diagnostic tool that cannot be matched by any other search techniques.

A.M.D.G.

To Erick, Emily, and Zoe

with love

PREFACE

A most dramatic, historically important event occurred during the time of this research experiment. We drove to Oak Ridge, Tennessee for two weeks to do the experiment and on the way back we heard that the Berlin Wall was being torn down, making way for the most unprecedented strides in thinking that this Century has known. Minds were open and the stage was set for tremendous change: The people of the Soviet Union said no to communism. Israel and Palestine talked peace.... And, on a personal note, for me, freedom and scientific research were forever linked.

There are many people who deserve acknowledgment for this work. Foremost, for help during the experiment at HHIRF, Oak Ridge National Lab, and for advice about the analysis, I would like to express my gratitude to: Professor William C. McHarris, Reg Ronningen, Aracelys Rios, Wade Olivier (NSCL), Rahmat Aryaeinejad (EG & G Idaho), the Oak Ridge Nuclear Structure Group: Francis McGowan, Jim McNeil, I.Yang Lee, Mark Whitley, Shi Yong, Noah Johnson, Cyrus Backtash, J.D. Garrett, the Tandem Operators who provided days of a 160.00 MeV, $^{37}Cl^{+7}$ beam, and Franda Irving and the people who coordinate the Holifield Joint Institute for Heavy Ion Research facility that provided accommodations for the stay at Oak Ridge.

After the experiment, the actual day-to-day work was replete with tedium and trial-and-error repetition of the analyses until the results looked right. The data tapes were spinning so often that one of the post-docs suggested that the computer be renamed 'Hampton'. I found a source of consolation and inspiration in the following anonymous poem entitled 'dream big' that was published in *The State News* circa 1991. It was the lead-in to a computer advertisement section called 'The big paper about ideas, college and Macintosh' and was helpful on many more than one occasion.

If there were ever a time to dare,
to make a difference,
to embark on something worth doing,
it is now.
Not for any grand cause, necessarily —
but for something that tugs at your heart,
something that's your aspiration,
something that's your dream.
You owe it to yourself
to make your days here count.
Have fun.
Dig deep.
Stretch.
Dream big.
Know, though, that things worth doing
seldom come easy.
There will be good days.
And there will be bad days.
There will be times when you want to turn around,
pack it up,
and call it quits.
Those times tell you
that you are pushing yourself,
that you are not afraid to learn by trying.
Persist.
Because with an idea,
determination,
and the right tools,
you can do great things.
Let your instincts,
your intellect,
and your heart
guide you.
Trust.
Believe in the incredible power of the human mind.
Of doing something that makes a difference.
Of working hard.
Of laughing and hoping.
Of lazy afternoons.
Of lasting friends.
Of all the things that will cross your path this year.
The start of something new
brings the hope of something great.
Anything is possible.
And you will pass this way only once.
Do it right.

For help during those long, seemingly countless days of spinning tapes and generating data arrays, thanks go to: Bill Milner from the Oak Ridge computer group; the NSCL computer group: Richard Au, Ron Fox, Barbara Pollack, Lisa Besko, Lori and Cindi Ramon and Bill Paddock. We would like to express our appreciation to Karl Hauschild (LBNL) and the authors of Ref. [hau95] who provided the ^{133}Ce SD data to help with the development of the SD search technique. Also, we acknowledge those who sent data to test out our FFT signal enhancement techniques: Nada Jevtic (SRI), Thomas Semkow (Albany), Arlyn Antolak (Sandia), and K. Hauschild.

We would like to thank Henry Blosser, Sam Austin, and Konrad Gelbke, directors of the National Superconducting Cyclotron Lab for the extended use of the facilities. Also, we would like to acknowledge the aid of the guidance committee: Professors Katherine Hunt, John McCracken , William Reusch, Victoria McGuffin, and the late Professor Carl Brubacker from the Chemistry Department, and Professors Aaron Galonsky from NSCL and the Physics/Astronomy Department and Jerry Nolen now Director of the ATLAS facility at Argonne. All of those who have been in the McHarris group, in one capacity or another, deserve acknowledgment: Wen-Tsae Chou, Wade Olivier for the tremendous help with the program development for the FFT search technique and the shell model calculations, Aracelys Rios, Yves Dardenne, Bin Lian for help with the initial FFT program, Tony Hsieh, and Nancy Davis; for help in various phases of the data analysis: Jill E. Johnson, Jeff Wesley, Ron Brown, and Christopher P. Maloney, MSU chemistry students completing their undergraduate degrees.

I would also like to bid adieu to those that I have shared office space with: Hong Ming Xu, Wen-Guang Gong, Cornelius Williams, Wen-Chien Hsi, James Dinius, Afshin Azhari, Ray Min-Jui Huang, and Omar Bjarki. To Rilla, the other Dr. McHarris, I say thanks for help with the figures, for the many discussions, — for everything. To my family, without whose generous emotional and financial help this work would not

have been possible, I give my deepest gratitude. To Professor William C. McHarris, someone wise once said that good teachers show their student the way but great teachers allow the student to look through their eyes and listen with their ears, to discover it for themselves. For encouraging the discovery process, I truely thank you.

Okemos

March, 1994

revised

March, 1999

C.V.H.

Contents

List of Tables

List of Figures

Chapter 1

Introduction

1.1 Historical Perspective

Between 300 BC and 1700 AD there existed a form of philosophical thinking that captured the interest of people from many different cultures. The basic structure of three of their major principles are relevant today: They believed in the notion that one metal could be changed into another; they searched for a substance or method that could catalytically influence this transmutation process; and they had an understanding of a cosmic unity of all matter. Their objectives were not reached, per se, but the concepts of transmutation in nature and a grand unification principle were centuries ahead of its time, so much so that Alchemy is often acknowledged to be a forerunner of modern chemistry. [tre81] Science had to wait until the discovery of oxygen (Lavoisier, 1775), electrons (Crookes, 1879, and Thompson, 1897) and x-rays (Röntgen, 1895) before the secrets of transmutation in nature were discovered (Antoine-Henri Becquerel, 1896) [eis58]. Two years later in 1898, Pierre and Marie Skłodowska Curie announced that the phenomenon reported by Becquerel was an atomic decay of one element into another [fri81]. This was remarkable insight since the notion of an atomic nucleus did not coalesce until 1911 when E. Rutherford noticed that α-particle scattering on thin metal foils occurred at very large angles. He suggested that this could be produced only by an intense electric field within the

atom. Therefore the positive charge and most of the mass were concentrated within an atomic core. The charge was balanced with electrons spherically distributed around the center [fri81].

A method to influence catalytically the transmutation process: The first laboratory transmutation reaction was performed by Rutherford in 1919. Nitrogen was bombarded by alpha particles from a natural radioactive source to produce (in retrospect) ^{17}O and protons. Just prior to this, researchers at several laboratories had developed devices for the acceleration of hydrogen and helium ions to energies at which artificially induced transmutations might occur. This was reported in 1930 when J. Cockcroft and E. Walton observed the first nuclear transmutation using protons artificially accelerated with an electrostatic accelerator of their own design. However, it wasn't until 1934 when Irene and Frederick Joliot-Curie discovered that boron and aluminum targets would become radioactive after exposure to α rays from polonium, that the concept of artificially induced radioactivity was actually understood.[fri81]

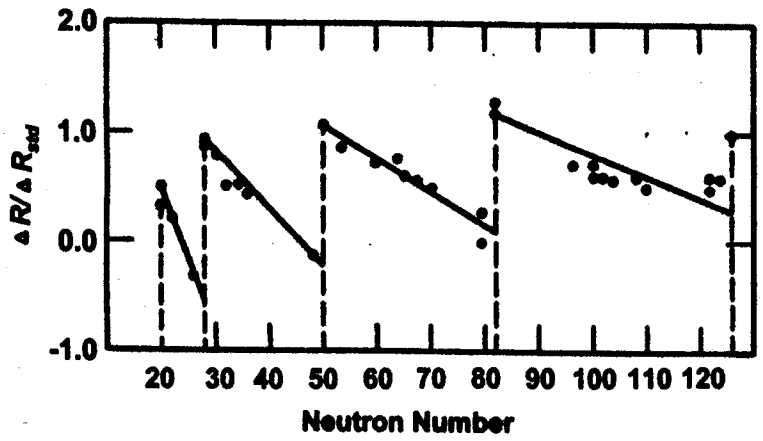

Figure 1.1: Early evidence for Nuclear Shell Structure: A plot of the change in nuclear charge radius, ΔR, for every pair of neutrons. The sudden changes at 20, 28, 50, 82 and 126 show transitions to the next shell and are now referred to as 'magic numbers'. [she76].

By 1913 Niels Bohr had advanced the theory of the structure of the atom to include electron orbitals surrounding the nucleus and introduced the concept of quantum

levels. Later, a quantum-mechanical description of the atom was developed in 1926 by E. Schrödinger and W. Heisenberg [fri81]. As early as the 1930's, speculations existed about an inner structure of the nucleus of the atom [eis58]. The discovery that the proton was a separate nuclear entity was made by J. Chadwick in 1932 [fri81]. According to Eisenbud and Wigner, the stability of certain groupings of protons and neutrons was noticed by W. Elsasser in 1934 [els34]. Figure 1.1 shows the evidence that inspired researchers to develop what was to be called the Shell Model of the nucleus – the change in nuclear charge radius, ΔR is plotted for every pair of neutrons. The sudden changes at 20, 28, 50, 82 and 126 show transitions to the next shell and are now referred to as 'magic numbers' [she76]. In 1949, Maria Goeppert-Mayer published the development of this mathematical model, providing "convincing evidence for the preferred nature of these numbers " [may49]. (Haxel, Jensen and Suess concurrently, yet independently, helped develop this model [hax50].) Spin and orbit coupling of the protons or neutrons caused the formation of energetically stable levels within the nucleus.

Since these early days, the model of the structure of the atomic nucleus has evolved in many directions. The present emphasis in nuclear structure studies is an attempt to explain what is referred to as superdeformed (*SD*) nuclear shapes. The *SD* bands have the properties of deformed prolate rotors (major to minor axes ratio less than 2:1) and have been observed only at high spin. The study of these bands may provide insight into the shape characteristics of the nucleus.

1.2 Objectives

In this work, we use the concept of transmutation to change ^{100}Mo into a highly excited ^{137}Pr intermediate nucleus using a beam of accelerated ^{37}Cl ions in order to study energy levels of the final reaction products. Our philosophical ancestors might

be intrigued by the process:

When fast-moving, high-energy particles move close enough to a target nucleus to overcome the coulomb repulsion, the force acting between the nuclei is an attractive one and the particle is captured. Within a time frame of less than 10^{-13} s. a γ ray, neutron or other type of particle can be emitted from the compound nucleus that has been formed. This type of transmutation reaction is called fusion-evaporation: two nuclei collide and fuse into a highly-energetic compound nucleus from which particles "boil off", leaving behind a residual nucleus. Because an accelerator produces particles that are travelling at a large fraction of the speed of light, there is a considerable amount of angular momentum taken up during the collision by the compound nucleus. This produces highly-energetic residual nuclei that can de-excite through a cascade of changes in rotation about the nuclear axis. These changes in rotation are accompanied by the emitting of a γ ray for each incremental change in spin. By detecting the energies of the photons, information can be obtained about the various spin states of each residual nucleus. This technique, referred to as in-beam γ-ray spectroscopy, is the one we used to investigate the various reactions.

We chose to examine the high spin rotational band structure of normally deformed (nonspherically shaped), odd-odd ^{132}Pr and to search for superdeformation in this nucleus, primarily because a moderate amount of structural information exists for the surrounding even-even and odd-mass nuclei and also because superdeformed rotational bands have been reported for other nuclides in this region: ^{132}Ce, ^{133,134,135,136,137}Nd, ^{130}La, and ^{131}Ce [god89, fir94], ^{133}Ce, and ^{134}Pr [hau94]. The N=73 isotones in this region exhibit superdeformation therefore ^{132}Pr would appear to be a good candidate for this study.

1.3 Synopsis

Most of the information has been written either to guide those who may want to follow this type of study or to jog my memory in the future. This work is divided into 12 chapters. Chapter 2 is a general description of electromagnetic properties of the nucleus, mainly from a classical perspective; Chapter 3 contains information about the various aspects of investigating fusion evaporation reactions. Both relativistic and classical kinematic calculations are included for the reaction under study. Chapters 4 and 5 include all of the necessary information from the experiment and the data analyses. Chapter 6 describes the development of mathematical spectral enhancement techniques as an aid to understanding the data. Chapter 7 contains information on our development of a γ-ray search routine based on a segmented Fast Fourier Transform method. Chapter 8 presents investigations into the possibility of spectral artefacts. Chapter 9 describes the mathematical development of the nuclear shell model and rotational and superdeformed bands. The rotational band results for ^{133}Pr and ^{132}Pr can be found in Chapter 10 along with Cranked Shell Model calculations and a discussion of the possible identification of the new bands found in ^{132}Pr. Chapter 11 contains a summary and recommendations for future developments are made in Chapter 12. The bulk of the spectra for ^{133}Pr and ^{132}Pr are contained in the various Appendices (D through F) along with tables of Q-Value calculations (A), various spin population matrices calculated for residual nuclei in the reaction under study (B), energy and efficiency calibration plots specific to each detector (C), and the necessary computer routines (G) that were developed in the course of this work.

"My efforts to cut out 50,000 words may sometimes result in my adding 75,000."

—Thomas Wolfe

Chapter 2

Electromagnetic Properties of the Nucleus

In the study of nuclear structure, the electromagnetic interaction of nuclei is used to probe the distribution and motion of nucleons in the nucleus.

2.1 The Nuclear Potential

The distribution of charge and currents within the nucleus produces inseparable electric and magnetic fields. The electric field $\mathbf{E}(\mathbf{r})$ is related to the gradient of the electrostatic potential :

$$\mathbf{E}(\mathbf{r}) = -\nabla \ \varphi(\mathbf{r}). \tag{2.1}$$

When the same reference is chosen for the electrostatic potential and for the potential energy, the electrostatic potential is related through the charge, q, to the central potential energy, $\mathbf{U}(\mathbf{r})$, of the nucleus : [rei80, kra88]

$$\mathbf{U}(\mathbf{r}) = -q \ \varphi(\mathbf{r}). \tag{2.2}$$

Two important properties of the nucleus, that are related to nuclear structure, the magnetic dipole moment and the electric quadrupole moment can be obtained by analyzing these fields. The nucleus might be approximated by the following example.

In fact, Coulomb's Law, on which the example is based, holds for the electrostatic repulsion between nuclei at distances greater than $\approx 10^{-14}$ meter. At smaller distances, the strong force dominates. [rei80]

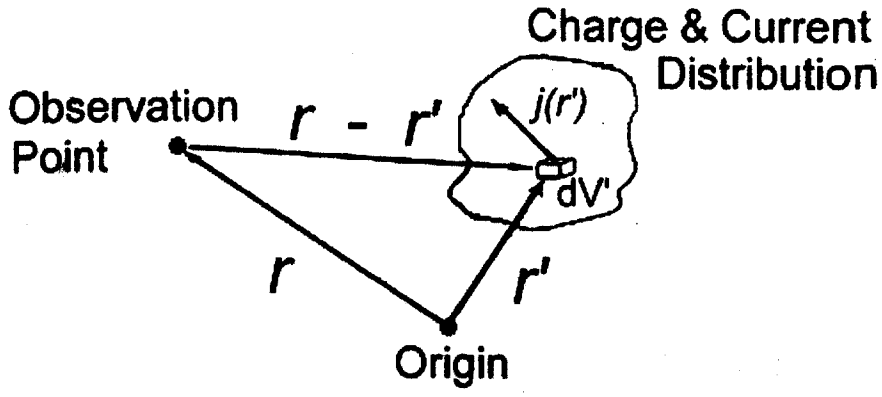

Figure 2.1: The nuclear potential described in terms of vectors. The total magnetic and electrostatic potentials are found from the integral over the entire current and charge distributions. [kra88].

Consider an arbitrary charge distribution of volume V', enclosed by a sphere of radius, a. See Figure 2.1. The charge is localized at the origin of coordinates with a charge density, $\rho(\mathbf{r}')$. The distance to the observation point, defined by vector $\mathbf{r}$ is large compared with a. The dv' represents a portion of the charge distribution whose location is defined by the vector $\mathbf{r}'$. The distance between this dv' and the observation point is $|\mathbf{r} - \mathbf{r}'|$. Then the potential at $\mathbf{r}$ is related to the charge density through a volume integral and can be written:

$$\varphi(\mathbf{r}) = \frac{1}{4\pi\epsilon_o} \int_V \frac{\rho(\mathbf{r}')}{|\mathbf{r} - \mathbf{r}'|} \, dv' \tag{2.3}$$

where ϵ_o is a constant of proportionality called the permittivity of free space. A binomial expansion of $|\mathbf{r} - \mathbf{r}'|^{-1}$ is made in terms of $\mathbf{r}'/r$. Terms higher than 2 are omitted. This yields:

$$\varphi(\mathbf{r}) = \frac{1}{4\pi\epsilon_o} \left(\frac{Q}{r} + \frac{\mathbf{p} \cdot \mathbf{r}}{r^3} + \sum_{i=1}^{3} \sum_{j=1}^{3} \frac{1}{2} \frac{x_i x_j}{r^5} Q_{ij} + \cdots \right) \tag{2.4}$$

where

$$Q \quad = (\text{monopole moment}) \quad = \int_{\mathrm{v}} \rho(\mathbf{r}')\ dv' \tag{2.5}$$

$$\mathbf{p} \quad = (\text{dipole moment}) \quad = \int_{\mathrm{v}} \mathbf{r}'\rho(\mathbf{r}')dv' \tag{2.6}$$

$$Q_{ij} \quad = (\text{quadrupole moment}) \quad = \int_{\mathrm{v}} (3x_i'x_j' - \delta_{ij}r'^2)\ \rho(\mathbf{r}')\ dv' \tag{2.7}$$

where δ_{ij} is the Dirac delta function and x_i, x_j are the Cartesian components of $\mathbf{r}$. The electric monopole moment is just the total charge. In quantum mechanical terms, the $(3x_i'x_j' - \delta_{ij}r'^2)$ term is known as the electric quadrupole operator [rei80].

From a magnetic point of view, the distribution of currents in Figure 1, is represented by the current density, $\mathbf{J}(\mathbf{r}')$ which specifies the magnitude and direction of the electric current per unit volume, dv'. The magnetic induction is obtained from the curl of the magnetic potential:

$$\mathbf{B} = \nabla \times \mathbf{A}. \tag{2.8}$$

The magnetic vector potential can be written:

$$\mathbf{A}(\mathbf{r}) = \frac{\mu_o}{4\pi} \int_{\mathrm{v}} \frac{\mathbf{J}(\mathbf{r}')}{|\mathbf{r} - \mathbf{r}'|}\ dv'. \tag{2.9}$$

where μ_o is a constant designed for mks system units compatibility and is specified by $\mu_o\epsilon_o = 1/c^2$; c, being the speed of light.

This can be expanded in a fashion similar to the electrostatic potential, resulting in the following form for the first non-vanishing term:

$$\mathbf{A}(\mathbf{r}) = \frac{\mu_o}{4\pi}\ \frac{\mu \times \mathbf{r}}{r^3} + \cdots \tag{2.10}$$

The quantity μ is defined as the magnetic dipole moment of the current distribution and can be written as:

$$\mu = \frac{1}{2} \int \mathbf{r}' \times \mathbf{J}(\mathbf{r}')\ dv'. \tag{2.11}$$

This can be rewritten in quantum mechanical terms of the charge density, $e|\psi(\mathbf{r}')|^2$ and the angular momentum,

$$\mu = \frac{e}{2m} \int \psi^*(\mathbf{r}') \ \ell \ \psi(\mathbf{r}') \ dv'. \tag{2.12}$$

This reduces to:

$$\mu_z = \mu = \frac{e\hbar}{2m} \ \ell. \tag{2.13}$$

If the wave function corresponds to a state of definite ℓ_z, only the z-component is non-vanishing. This μ_z is defined as the nuclear magnetic moment that corresponds to the maximum possible value of the z-component of the angular momentum. [kra88, rei80]. Each electromagnetic multipole moment has a parity. The parity of the electric moments is $(-1)^\ell$, where ℓ is the order of the moment. The parity of the magnetic moments is $(-1)^{\ell+1}$. It is important to note that all odd-parity static multipole moments vanish; i.e., the electric dipole, magnetic quadrupole, electric octupole, etc. To compute the expectation value of a moment, evaluate an integral of the form:

$$\langle moment \rangle = \int \psi^* \ \hat{\mathbf{O}} \ \psi \ dv \tag{2.14}$$

where $\hat{\mathbf{O}}$ is an electromagnetic operator. The parity of ψ does not affect the integral value. If $\hat{\mathbf{O}}$ has odd parity, the integrand is an odd function of the coordinates and the integral must vanish [kra88].

2.2 Nuclear Shapes and Vibrational Distortions

From the previous discussion, it should be clear that a spherical charge distribution gives only a monopole electric field (i.e.,the total charge); the higher order terms vanish. A circular current loop has only a magnetic dipole field. Therefore, if multipoles higher than the magnetic dipole are measured for a nucleus, the nucleus is not spherical [kra88]. This is the case in mid-shell regions, even-even and odd-mass nuclei exist

with stable and permanent quadrupole deformations. In these regions, the normally spherical shape is easily deformed by the collective motion of the extra particles outside closed shells coupled with the core. This results in collective excitation modes, referred to as phonon excitations, where a phonon is a vibrational quantum.

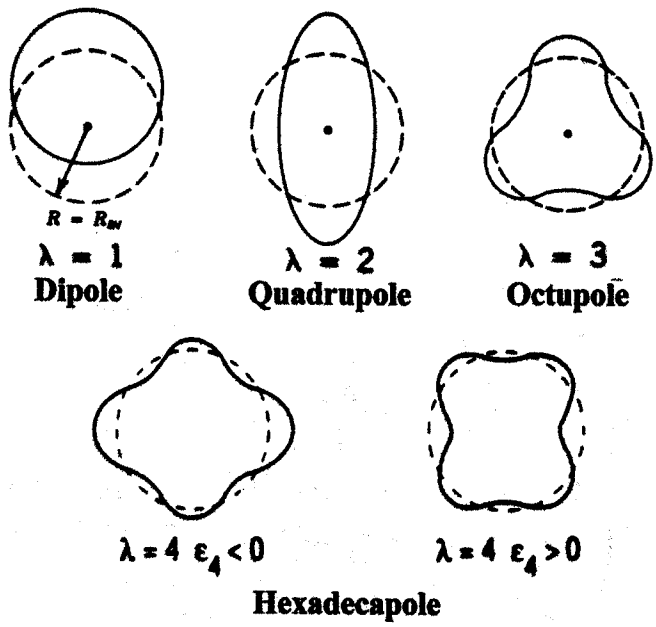

Figure 2.2: Nuclear distortions based on the spherical harmonic multipoles. Adapted from [kra88], [hyd64], and [cas90].

This deformed shape is significant because nuclei can be stabilized in non-spherical ground states and *the rotations of a deformed nuclear shape are the origins of rotational bands.*

In order to quantify these shapes, the nuclear radius, R, can be redefined in terms of spherical harmonics, $Y(\theta, \phi)$.

$$R = R_o \left[1 + \sum_{\lambda\mu} \alpha_{\lambda\mu} \; Y_{\lambda\mu}(\theta\phi) \right]. \tag{2.15}$$

where R_o is the radius of a spherical nucleus of the same volume. λ refers to the order of the spherical harmonics and μ is the projection of λ on a spaced fixed axis,

i.e., the angular momentum component. When this is expanded in powers of α, the coefficient of the spherical harmonics, then the shape oscillations are classified by their multipole order, λ and their parity, $\pi = (-1)^{\lambda}$. $\lambda = 2$ is referred to as a quadrupole deformation; $\lambda = 3$ is octupole, etc. The corresponding shapes are shown in Figure 2.2. Notice that the dipole vibration is merely a translational mode [hyd64, cas90].

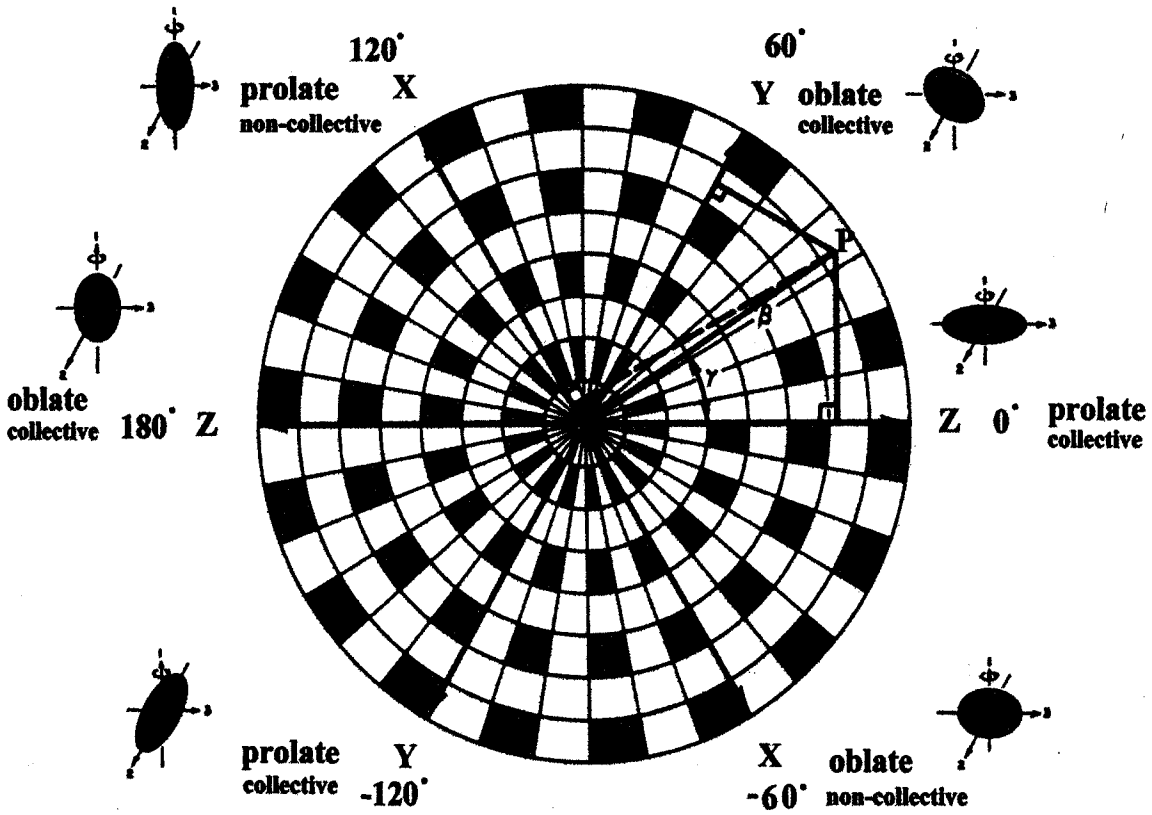

Figure 2.3: $\beta - \gamma$ Polar Plot. Adapted from [hyd64].

The quadrupole deformation is the most significant in nuclear spectroscopy because it has a large effect on the nuclear shape. These can be quantified using polar coordinates to define the ellipsoidal nuclear shape. For $\lambda = 2$, the expansion coefficients, α can be written in terms of β and γ. [cas90]:

$$\alpha_1 = \alpha_2 = 0 \qquad \alpha_0 = \beta \ \cos\gamma \qquad \alpha_2 = \alpha_{-2} = \beta \ \sin\gamma.$$

The β represents the extent of quadrupole deformation and γ, the degree of axial asymmetry. [1] The quadrupole deformation is best visually represented by a polar plot of β and γ - see Figure 2.3. The radius vector is β and γ is the polar angle. Any nuclear deformation (for example, point P) can be specified with these two parameters. A spherical shape would be represented by a point at the origin. There are three ellipsoid axes (x, y, z) superimposed on the polar plot at 60° to each other. If P is located on any of these three axes, the nucleus has rotational symmetry with respect to that axis. To put this in terms of the quadrupole moment, for a spherical nucleus the value of Q_{ij}, from equation 2.7 equals zero . If $Q_{ij} > 0$ the shape is called prolate deformed; if $Q_{ij} < 0$, the nuclear charge density along the z-axis is reduced causing a flattening of the spacial distribution. This is referred to as oblate. (Refer to Figure 2.4). The main difference between prolate and oblate shapes is that prolate is extended in one direction and compressed in two; oblate shapes are extended in two and compressed in one. [cas90]

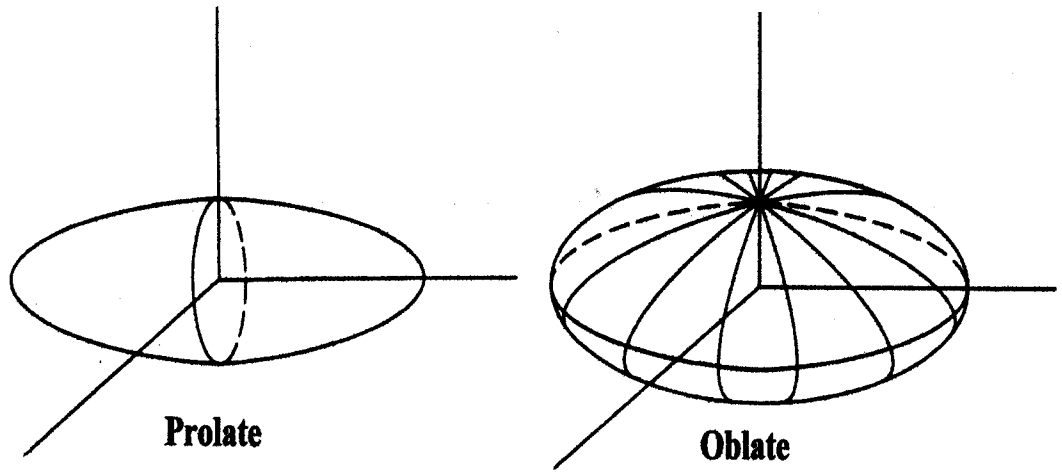

Figure 2.4: Prolate and Oblate static nuclear shapes generated from multipole order $\lambda = 2$.

In the $\beta - \gamma$ plot, the nucleus is prolate at $\gamma = 0°$ (for each x, y, z axis). If $\gamma = 60°$

[1] β is also related to the eccentricity of an ellipse: $\beta = 4/3\sqrt{\pi/5}\ \Delta R/(R_o A^{\frac{1}{3}})$ where Δ R is the difference between the semimajor and semiminor axes of the ellipse. [kra88].

or 180°, the nucleus is oblate. Notice that if $\gamma = 0°$, a prolate shape has $+\beta$ and an oblate shape has $-\beta$. Another shape classification exists called triaxial (non-axial), where there is a flattening of the nucleus in one of two directions perpendicular to the symmetry axis. This happens at $\gamma \neq (n\pi/3)$, i.e., 30°.

The β and γ parameters are also used to describe vibrational excitation states. The term β vibration refers to oscillations of the ground state in the β direction causing the formation of various spheroidal and ellipsoidal shapes. γ vibration refers to oscillations in the γ direction. This results in a cross sectional distortion of the nucleus (circle $\leftrightarrow$ ellipse) and has been referred to as a 'breathing' motion. See Figure 2.5.

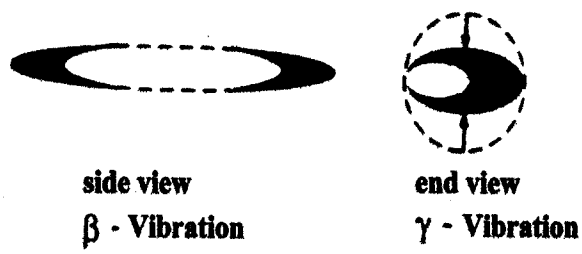

Figure 2.5: A pictorial description of β and γ vibrations for $\lambda = 2$. [cas90].

2.3 Radiation Fields of the Rotating Nucleus

Previously, we discussed how the nuclear charges and currents produce static magnetic and electric fields and how they can be analyzed in terms of expanded multipole moments. If the charge and current distributions vary with time – as they do in a rotating nucleus – a radiation field is produced. This field can also be analyzed in terms of multipoles. The total angular momentum is specified as the multipolarity of the radiation. [eis58] The electric field arises from the net charge; this is the zeroth (E0) or monopole moment and is related to $1/r^2$, where r is the nuclear radius. The first (E1), or dipole moment is related to $1/r^3$. The second (E2) or quadrupole

moment is associated with $1/r^4$. The magnetic multipole moments (M1,M2...) are similar except there is no known monopole. The parity of the radiation is defined by ℓ and the electromagnetic character (E or M). An E transition has parity, $\pi = (-1)^{\ell}$; an M transition has parity, $\pi = (-1)^{\ell+1}$. The radiation field has, for a given ℓ and π, $2\ell+1$ different states, characterized by $2\ell+1$ different values of the z component of the angular momentum: $\mu_z = -\ell, (-\ell+1), ..., (\ell-1), \ell$

2.3.1 Moment of Inertia

Besides the quadrupole moment, there is another important quantity that describes a deformed nucleus - the effective moment of inertia, $\Im$ about the axis of rotation. The kinetic energy of a rotating object is related to this $\Im$ and the frequency of rotation, ω.

$$E = \frac{1}{2}\Im\ \omega^2. \tag{2.16}$$

The orbital angular momentum, ℓ is a product of this rotational frequency and the effective moment of inertia:

$$\ell = \Im\ \omega \tag{2.17}$$

If we rearrange this in terms of ω and substitute the value into the previous equation, the energy can be written:

$$E = \frac{\ell^2}{2\Im} \tag{2.18}$$

Note that , if I represents the angular momentum quantum number, the quantum mechanical value for ℓ^2 is:

$$\ell^2 = I\ (I+1)\,\hbar^2 \tag{2.19}$$

By combining the last two equations we arrive at an expression that describes the energy of a rotating object in quantum mechanical terms: [kra88]

$$E = \frac{\hbar^2}{2\Im}\ I\ (I+1). \tag{2.20}$$

If the nucleus is described as a rigid body ellipsoid the moment of inertia can be written in terms of the mass A and nuclear radius, R_o:

$$\Im_{rigid} = \frac{2}{5} A R_o^2 \left(1 + 0.31\beta + 0.44\beta^2 \ldots\right) \tag{2.21}$$

where β refers to the shape deformation parameter described in Section 2.2.

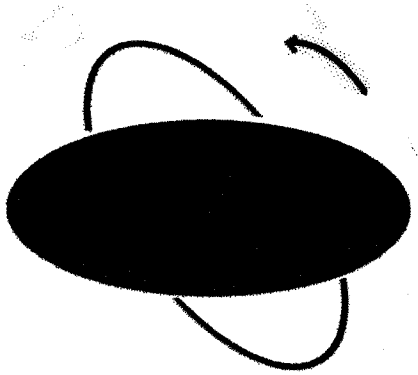

Figure 2.6: A pictorial description of the difference between the concepts of nuclear movement through rotation and through irrotational flow. The counterclockwise arrow shows rotation of a rigid rotor; the internal arrows depict an irrotational flow of a fluid.

The nucleus has often been described in terms of a liquid drop (hydrodynamic) model, wherein there is an irrotational flow of an incompressible fluid. Figure 2.6 is a pictorial description of the difference between the concepts of nuclear movement through rotation and through irrotational flow. The counterclockwise arrow shows rotation of a rigid rotor; the internal arrows depict an irrotational flow of a fluid. The nucleus arrives at an identical displacement in both cases, however, the the moment of inertia is differerent. $\Im$ then has the form:

$$\Im_{irrot} = \frac{2}{5} A R_o^2 \beta^2. \tag{2.22}$$

The actual experimental $\Im$ determined from the rotational band measurements is two and times larger than $\Im_{irrot}$ and closer than predicted to $\Im_{rigid}$ [hyd64]. These

variations in the description of the nuclear model and therefore $\Im$ have consequences for the rotational band sequence that will be described in Chapter 9 since $\Im$ is inversely proportional to the energy levels. (Equation 2.20)

2.3.2 Nuclear Gyromagnetic Factors

The quantity $e\hbar/2m$ in equation 2.13 is called the magneton. If the proton mass is used for m, the quantity is called the nuclear magneton, μ_N [kra88]. [2] Using equation 2.13, the magnitude of the nuclear magnetic moment, μ can be written:

$$\mu = g_\ell \ \ell \ \mu_N \tag{2.23}$$

where g_ℓ is the gyromagnetic factor associated with the orbital angular momentum, ℓ. For protons $g_\ell \doteq 1$; for neutrons $g_\ell = 0$. The intrinsic spin contribution, g_{si} of the nucleons can be written in the same form. To allow for the effects of both orbital and intrinsic spin contributions of a spherical nucleus, we can write [mor76]:

$$\mu = \sum_{i=1}^{A} [g_{\ell i} \ \ell_i \ + \ g_{si} \ \mathrm{s}_i] \ \mu_N/\hbar. \tag{2.24}$$

In an odd-odd nucleus, the orbital contribution can be written using the symbolism of Section 9.1.2 [sla84].

$$\mu = [Kg_K + g_R] \ \frac{J}{J+1} \tag{2.25}$$

where, g_K and g_R are the intrinsic and rotational gyromagnetic ratios, J refers to the spin state of the transition under study and

$$Kg_K = \Omega_1 g_{\Omega_1} \pm \Omega_2 g_{\Omega_2}. \tag{2.26}$$

The difference between g_K and g_R is approximately constant within a band and can be used to estimate the intrinsic structure of a particular band.

$$\frac{g_K - g_R^2}{Q_o} = \frac{0.871 \ E_\gamma^2}{(J+1)(J-1)} \times \frac{1}{\delta^2} \tag{2.27}$$

[2] $\mu_N = 3.1525 \times 10^{-8} eV/T$.
If the electron mass is used the quantity is called the Bohr magneton:
$\mu_B = 5.7884 \times 10^{-5} eV/T$.

where, Q_o is the intrinsic quadrupole moment, E_γ is in MeV. and δ^2 is the mixing ratio between transitions in different bands in a cascade. This ratio can be determined from angular distribution measurements. See [sla84].

2.3.3 Angular Distributions

The theoretical directional correlation function, $\omega(\vartheta)$ describing the angular distribution of γ rays emitted from a nuclear reaction, i.e., an oriented nuclear state can be stated by the following formula: [kra71, ste91]

$$\omega(\vartheta) = \sum_k Q_k B_k U_k A_k \; P_k(cos\vartheta) \tag{2.28}$$

where, Q_k is the solid angle correction factor; B_k specifies the orientation of the initial level; U_k corrects for the effect of unobserved intermediate radiations; A_k describes the properties of the γ rays observed; ϑ is the angle between detector axes; P_k are the ordinary Legendre polynomials. [3] This function can be rewritten as an expansion of a Legendre polynomial: [cam69]

$$\omega(\vartheta) = A_o [1 + A'_2 P_2(cos\vartheta) + A'_4 P_4(cos\vartheta) + \cdots] \tag{2.29}$$

Since the Q_k term, besides being a function of the size and shape of the detector and the source to detector distance is also a function of the γ ray energy, $A'_k = Q_k A_k$. The rest of the factors are incorporated into A_o. Using least squares regression analysis, fit to a Legendre polynomial (4th order), the coefficients A'_k/A_o that correspond to the multipolarity of the transition can be determined. One example of this type is shown in Figure 2.7 from reference [sla84].

The functions for transitions of known multipolarities can be plotted and used as 'templates' for transitions of unknown multipolarity.

Usually, the standard method of obtaining average intensity ratios to determine multipolarities is to gate on a known quadrupole transition then compare the peak

[3] i.e., $P_2(cos\vartheta) = (3\,cos^2\vartheta - 1)/2$ and $P_4(cos\vartheta) = (35\,cos^4\vartheta - 30\,cos^2\vartheta + 3)/8$.

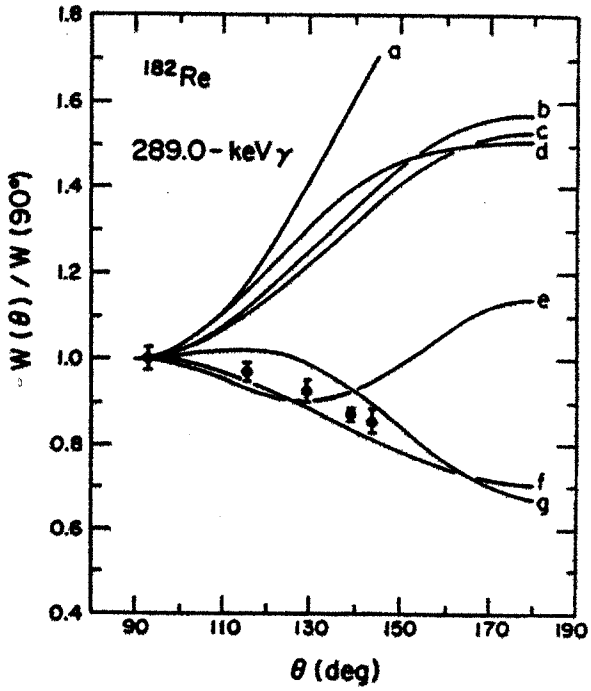

Figure 2.7: Angular distribution plots from various multipolarity transitions. From [sla84].

intensities at 90° with that at another angle. [fri81, kra71, pau87] This is referred to as an anisotropy parameter and can be determined with the following equation:

$$\mathcal{A} = \frac{\omega(180°) - \omega(90°)}{\omega(90°)} \tag{2.30}$$

where $\mathcal{A} = \sum A'_k/A_\circ$ If the unknown transition is a quadrupole (E2), the intensity ratio would be equal to or greater than 1.0. If the transition is a dipole (M1), the intensity ratio would be less than or equal to 0.7. If the transition has a mixed multipolarity, the intensity ratio would be between 0.7 and 1.0. This method is subject to a high degree of error. Peaks may contain more than one type of γ ray. If multiple gates are used to create a more selective spectrum, the intensities may be compromised by a low signal to noise ratio. Errors could be reduced if peak areas are generated for all detector angles, as shown in Figure 2.7.

2.3.4 Selection Rules

When considering transitions between different states, a set of empirical selection rules governing the parities have been observed. If the initial and the final transitions have the same parity, only even E multipoles and odd M multipoles are possible. If the transitions have opposite parity, the polarity of E is odd and the polarity of M is even. Note that there are no $\ell = 0$ transitions; the $0^+ \rightarrow 0^+$ transition deexcites by internal conversion. The I values must form a vector triangle: [kra88, eis58, may55]

$$|I_i - I_f| \leq \ell \leq I_i + I_f. \tag{2.31}$$

$$\Delta\pi \quad = no: \quad \text{even E, odd M} \tag{2.32}$$

$$\Delta\pi \quad = yes: \quad \text{even M, odd E} \tag{2.33}$$

In general:

- The lowest permitted multipole usually dominates.
- Transition rates of E and M multipoles decrease with increasing ℓ.
- An M ℓ-pole should give a lower rate than an E ℓ-pole.
- M ℓ-pole and E$(\ell + 1)$-pole have $\approx$ the same order of magnitude transition rates. They can occur in the same transition and often compete.
- If I_i and I_f differ by several units, the multipole radiation will be of high order and the transition, slow. By definition, this would be a nuclear isomer. [ste91, kra88]

2.4 Conversion Electron Production

Besides γ radiation and the production of electron-positron pairs, the excited nucleus can de-excitate through a competing process called internal conversion. This is an electromagnetic interaction that can be viewed as a "direct coupling of a bound atomic

electron and a nuclear multipole field which results in the emission of extranuclear electrons" [ada70]. In other words, the nucleus de-excites by transferring energy directly to an atomic electron. With this extra energy, the electron is ejected from the atom and a vacancy is created in one of the inner electronic shells. The atomic-orbital vacancy is often filled by an electron from the next level. This rearrangement results in the emission of x-rays and in an internal photoelectric process (Auger) with the emission of additional extranuclear electrons [kra88].

The conversion coefficient, α is the ratio of the electron emission rate, $\lambda_{electron}$ to the γ emission rate, λ_γ:

$$\alpha = \lambda_{electron} \,/\, \lambda_\gamma \tag{2.34}$$

The coefficient depends on four nuclear parameters: the nuclear charge (Z), the energy and the multipolarity and parity of the nuclear transition, and the atomic subshell from which the electron is ejected. Coefficients for the K, L and M shell have been separately determined and are listed in the *Nuclear Data Tables.* [ros78]. In general, the coefficients increase with decreasing energy, increasing mass of the residual nucleus, and increasing difference between the initial and final state of spin. [ada70].

2.5 γ Emission Rates

The matrix element of the multipole operators discussed in Section 2.1 determines the decay probability for each type of γ emission. The decay constant is defined as the probability per unit time. This is expressed as the average radiated power divided by the photon energy, $\hbar\,\omega$; [kra88]

$$\lambda(x\ell) = \frac{2(\ell+1)}{\epsilon_o \hbar \ell[(2\ell+1)!!]^2} \left(\frac{\omega}{c}\right)^{2\ell+1} [\mathcal{M}(x\ell)]^2. \tag{2.35}$$

$\mathcal{M}(x\ell)$ represents the matrix element of the individual multipole operators, $x\ell$. The double factorial means $(2\ell+1)\cdot(2\ell-1)\cdots 3\cdot 1$. When specific values are substituted for

the individual multipoles, the following estimates, often referred to as single particle Weisskopf estimates (or Moszkowski approximations for magnetic transitions), can be made:

$$\lambda(E1) = 1.0 \times 10^{14} A^{2/3} E^3 \quad (2.36)$$

$$\lambda(E2) = 7.3 \times 10^{7} A^{4/3} E^5 \quad (2.37)$$

$$\lambda(E3) = 34 A^2 E^7 \quad (2.38)$$

$$\lambda(E4) = 1.1 \times 10^{-5} A^{8/3} E^9 \quad (2.39)$$

$$\lambda(M1) = 5.6 \times 10^{13} E^3 \quad (2.40)$$

$$\lambda(M2) = 3.5 \times 10^{7} A^{2/3} E^5 \quad (2.41)$$

$$\lambda(M3) = 16 A^{4/3} E^7 \quad (2.42)$$

$$\lambda(M4) = 4.5 \times 10^{-6} A^2 E^9 \quad (2.43)$$

These estimates when combined with the selection rules, provide rough predictions about which multipole is emitted. For example, in a transition from $I^- = 15/2$ to $I^- = 11/2$ in the ^{133}Pr nucleus, with a transition energy, $E = 0.310$ MeV, the calculated emission probabilities are: $\lambda(M1) : \lambda(E2) : \lambda(M3) : \lambda(E4) = 1 : 8.7 \times 10^{-5} : 1.8 \times 10^{-12} : 8.1 \times 10^{-17}$ This large value for M1 suggests that the transition is mostly M1. However, it should be noted that in cases of deformed nuclei, the measured $\lambda(E2) \gg \lambda(M1)$ because this calculation does not account for collective effects where E2's contain an M1 contribution. The total decay rate is the sum of the decay rate of each transition that depopulates the state. If two transitions depopulate a state at a, and b energies, then the total decay rate can be written:

$$\lambda_t = \lambda_{t,a} + \lambda_{t,b} \quad (2.44)$$

The total decay rates are influenced by both γ and internal conversion rates, so that this can be written:

$$\lambda_t = \lambda_{\gamma,a}(1 + \alpha_a) + \lambda_{\gamma,b}(1 + \alpha_b) \quad (2.45)$$

If the relative intensities of the γ rays have been measured to be x and y, then the partial decay rates can be calculated: $\lambda_{\gamma,a} = x\ \lambda_t$ and $\lambda_{\gamma,b} = y\ \lambda_t$. This calculated value can then be compared with the partial decay rates of each transition determined from half-life ($t_{\frac{1}{2}}$) measurements (See Chapter 5), where

$$\lambda = \frac{ln\,2}{t_{\frac{1}{2}}} \tag{2.46}$$

Chapter 3

Nuclear Reaction – Theory

3.1 Kinematics of the Nuclear Reaction

The kinematics of a reaction describes the energetics — the energies, masses, momenta and angles involved in generating a nuclear reaction.

3.1.1 Q -Value Calculations

Consider a nuclear reaction of the form:

$$T\ (\ p_{in},\ p_{out}\ )\ P^*_{res}, \tag{3.1}$$

where, T is the target nucleus, p_{in} is the projectile, i.e., the input particle, p_{out} is the outgoing particle and P^*_{res} is the excited residual nucleus formed during the reaction. From a laboratory coordinate perspective, the reaction might proceed along the simplistic course shown in Figure 3.1A. The target, T is in the center with momentum vectors for the input particle, p_{in}, the outgoing particle, p_{out}, and the residual particle, P_{res} shown. The center-of-mass (cm) coordinate perspective for the identical reaction is shown in Figure 3.1B . A nuclear reaction produces polarized products; a directional anisotropy exists. The products are formed in a conical distribution about the beam direction axis; the angle θ describes the particle's direction from this axis.

Classical kinematic calculations were performed with the Oak Ridge software

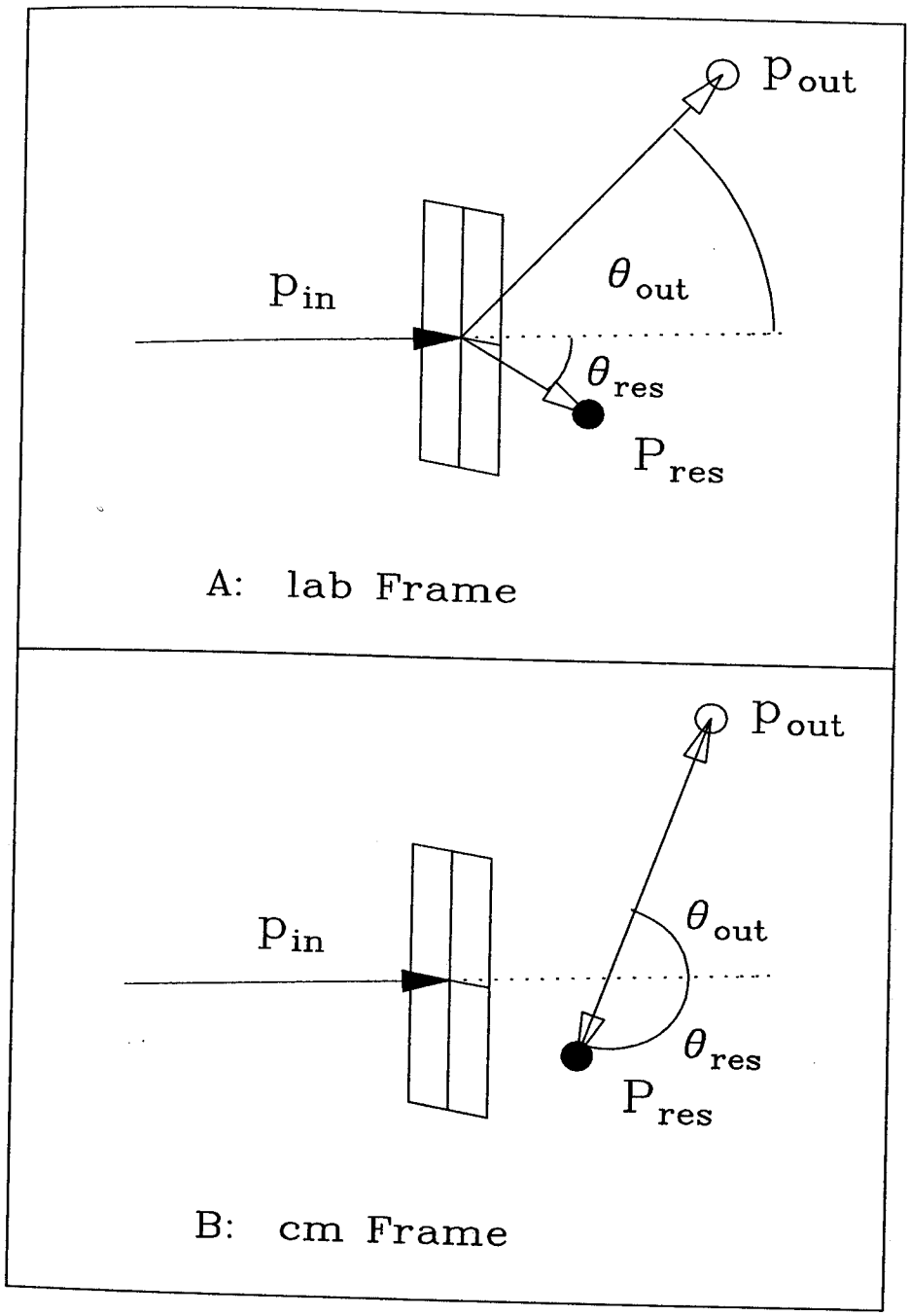

Figure 3.1: A) Simplistic view of a nuclear reaction from the laboratory frame perspective: The target is in the center with momentum vectors for the input particle, p_{in}, the outgoing particle, p_{out}, and the residual particle, P_{res} shown. θ is the angle, measured from the beam direction, for the residual (res) and outgoing (out) particles. B) The center-of-mass (cm) coordinate perspective for the identical reaction. Adapted from [ar83d].

Kineq for the various reactions from ^{37}Cl on ^{100}Mo. The linear relationship between the energy of p_{out} and P_{res} is shown in Figure 3.2. The lines represent the nuclei produced in this experiment. In decending order from the top are the nuclei: ^{130}La-α out, ^{134}Pr, ^{133}Ce, ^{129}La-α out, ^{133}Pr, ^{132}Ce, ^{128}La-α out, ^{132}Pr, ^{130}La-p out. Their corresponding reactions are listed in the tables in Appendix A.

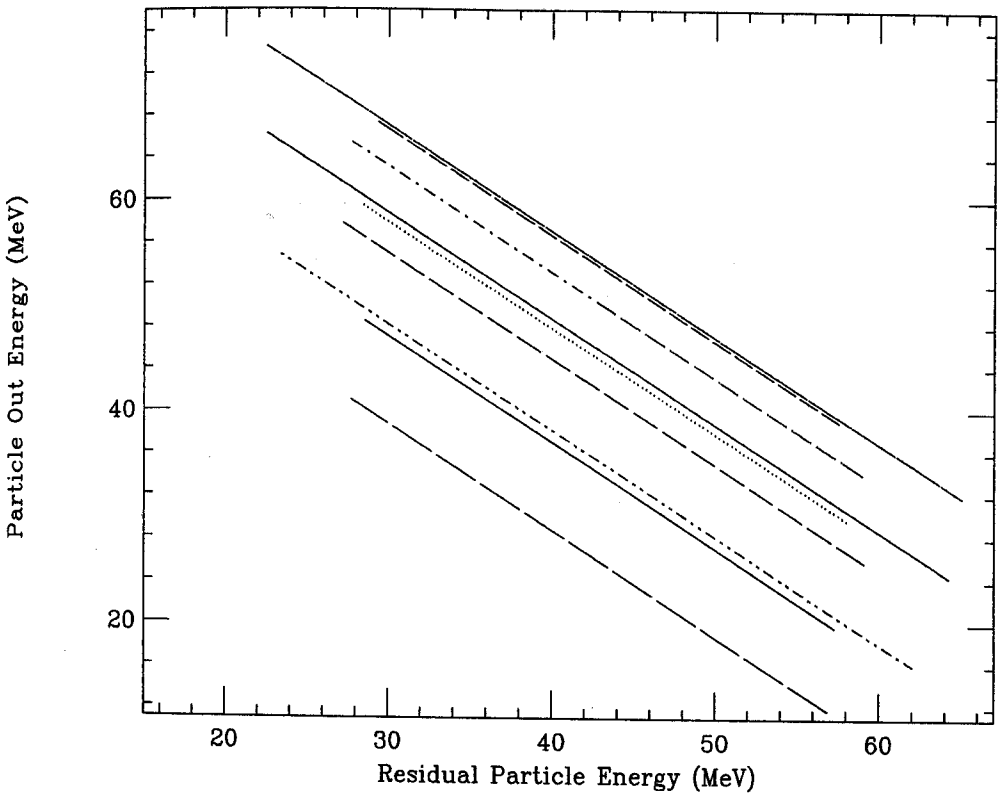

Figure 3.2: Classical Kinematic calulation using *Kineq*: A plot of the Residual Particle energy in MeV versus the particle out energy in MeV for the reaction: 160 MeV ^{37}Cl on ^{100}Mo. The lines represent the nuclei produced. In decending order, from the top are: ^{130}La-α, ^{134}Pr, ^{133}Ce, ^{129}La-α, ^{133}Pr, ^{132}Ce, ^{128}La-α, ^{132}Pr, ^{130}La-p.

The order of the nuclei does not strictly follow mass; the momentum must also be accounted for. So that total energy and linear momentum are conserved, the energetics of the reaction can be described in the following terms: [kra88, ar83d]

$$m_T c^2 + K_T + m_{p_{in}} c^2 + K_{p_{in}} = m_{p_{out}} c^2 + K_{p_{out}} + m_{P_{res}} c^2 + K_{P_{res}} \qquad (3.2)$$

where, m is the rest mass and K refers to the nonrelativistic kinetic energy. The heat or Q-value of the reaction is defined as the initial mass energy minus the final mass energy or, the final kinetic energy minus the initial kinetic energy.

$$Q = (m_T + m_{p_{in}} - m_{p_{out}} - m_{P_{res}}) c^2 \tag{3.3}$$

$$Q = K_{p_{out}} + K_{P_{res}} - K_T - K_{p_{in}} \tag{3.4}$$

A spontaneous reaction has a positive Q-value and is referred to as exothermic or exoergic; it is energetically possible even in the limit of zero beam energy. [eis58] A reaction which can occur only if the kinetic energy of the colliding particle exceeds the energy difference between products and reactants is called endothermic or endoergic and has a negative Q-value. This describes the reaction under study. Q-value calculations were performed for all of the possible products from the reaction ^{37}Cl on ^{100}Mo; the results are listed in the Tables in Appendix A. In addition, all Mo target isotopes were used, the relative abundances, of which, are listed in Table 4.1. 'Exact' nuclear masses, obtained from either Wapstra's Mass Table [wap85] or a set of mass formula coefficients [gar69], were used for the calculations. The method is listed in the Q-value tables as T or G, respectively.

It should be noted that these are ground state Q-values, i.e., Q_o. Excitation energies, E_{ex}, would be needed to determine the more precise Q_{ex}-value. [kra88] Since,

$$Q_{ex} = Q_o - E_{ex} . \tag{3.5}$$

3.1.2 Threshold Energy

The conservation of linear momentum, $\mathcal{P}$, along the beam direction and perpendicular to it provide the following equations: [kra88]

$$\mathcal{P}_{p_{in}} = \mathcal{P}_{p_{out}} \cos\theta_{out} + \mathcal{P}_{P_{res}} \cos\theta_{res} \tag{3.6}$$

$$0 = \mathcal{P}_{p_{out}} \sin\theta_{out} - \mathcal{P}_{P_{res}} \sin\theta_{res} \tag{3.7}$$

By combining the last two equations with equation 3.4 and eliminating θ_{res} and $K_{P_{res}}$ a relationship between θ_{out} and $K_{p_{out}}$ can be derived: [kra88, ar83d]

$$K_{p_{out}}^{1/2} \quad [m_{P_{res}} + m_{p_{out}}] \quad = \quad (m_{p_{in}} m_{p_{out}} K_{p_{in}})^{1/2} \cos\theta_{out} \tag{3.8}$$
$$\pm \left[m_{p_{in}} m_{p_{out}} K_{p_{in}} cos^2\theta_{out} + (m_{p_{out}} + m_{P_{res}})[m_{P_{res}} Q + (m_{P_{res}} - m_{p_{in}}) K_{p_{in}}] \right]^{1/2}$$

Using this information and a relativistic kinematic calculation from the Oak Ridge software, *Kineq*, a plot of the beam energy, $K_{p_{in}}$ versus $K_{p_{out}}$ for various θ_{out} values was generated. It is presented in Figure 3.3. For endothermic reactions, an interesting situation exists below 90°. There is no longer a one-to-one correspondence between the beam energy and the energy of the outgoing particle. Dual energies, hence dual velocities, for the outgoing particle are produced. The $\pm$ portion of equation 3.8 is responsible for this phenomenon. Another important observation is that the reaction does not continue to $K_{p_{in}} = 0$; there is a threshold energy, E_{th}, below which, the reaction will not occur. This is defined by the following: [ar83d, kra88]

$$E_{th} \quad = \quad (-Q) \; [\; m_{P_{res}} m_{p_{out}} \;] \; / \; [\; m_{P_{res}} + m_{p_{out}} - m_{p_{in}} \;] \tag{3.9}$$

$$E_{th} \quad = \quad (-Q)[1 + m_{p_{in}} \; / \; m_T] \tag{3.10}$$

For the reaction under study, threshold values were calculated, corresponding to the listed Q-values and are also presented in the Tables in Appendix A.

3.1.3 Energy Loss in Absorbers

When an ion beam impinges on the surface of the target, many different phenomena occur. The first is a sputtering action: at lower energies (keV) ions, neutral atoms and atomic clusters are ejected from the plasma formed at the point of contact on the surface. The plasma is a type of 'primordial soup' comprised of internally generated and sustained fields of electrons, atoms, ions and x-rays that etches away at the surface. Multiple chemical reactions occur, such as the formation of oligomers

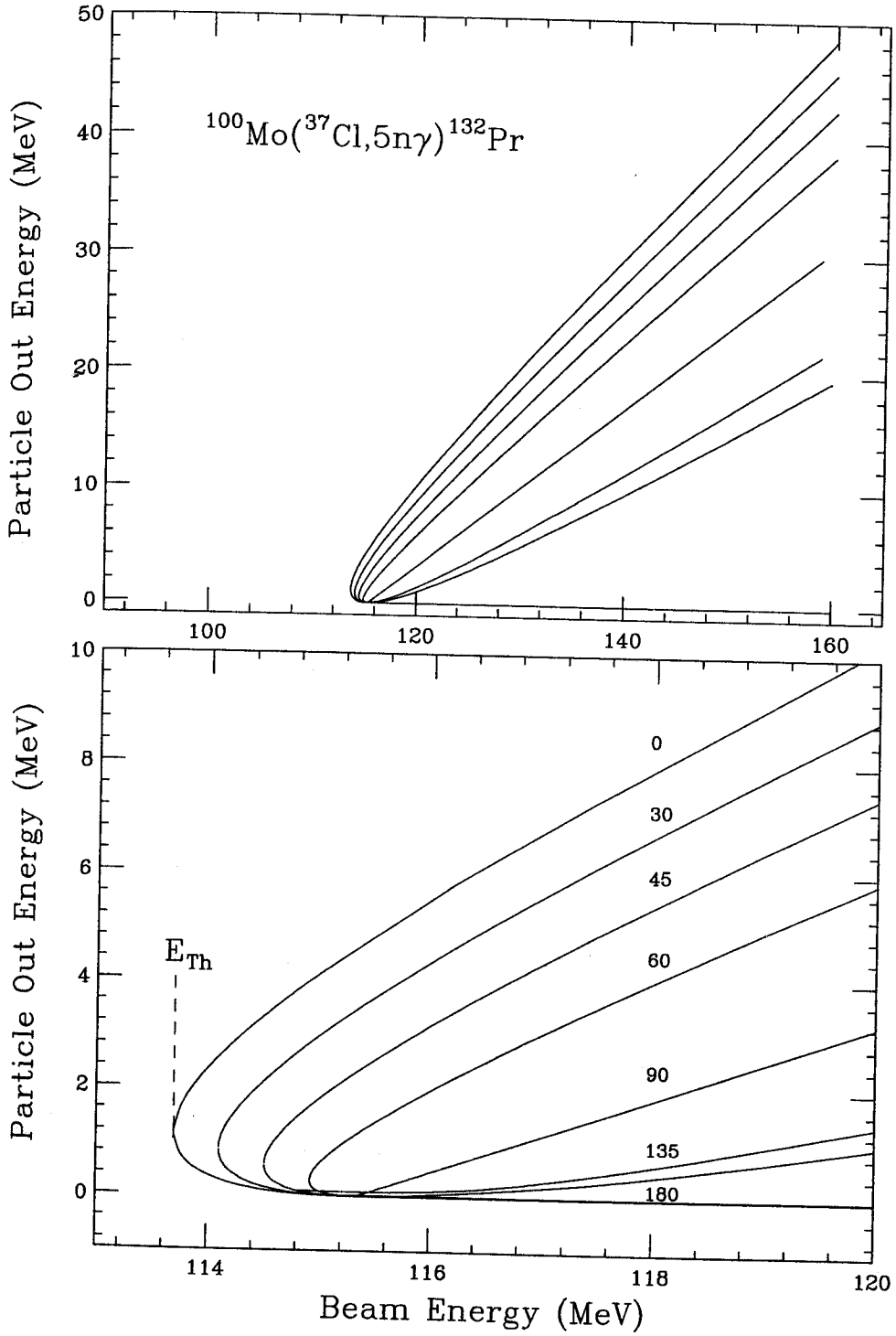

Figure 3.3: Threshold energy for ^{100}Mo(^{37}Cl, 5n γ)^{132}Pr relativistically calculated at multiple angles. Plots of the Beam energy versus the kinetic energy of the outgoing particle from the reaction are shown. The bottom frame is an expanded view of the energy threshold region containing dual energy values from angles 0° to 90°.

from surface and vacuum contaminants and the sputtered target components (T), for example, $[T_x(CH_2)_nH]^{\pm y}$ and $[T_x(H_2O)_n]^{\pm y}$. These reaction products are produced at angles transverse to the beam direction; they are normally reactions that are chemical, rather than, nuclear, in nature. A lattice phenomenon also occurs; much of the beam energy is converted into thermal movement of the bound atoms.

With energies in the MeV range, nuclear reactions occur and the energy lost to thermal motion becomes significant in determining which products are formed. There must be sufficient energy remaining in the beam, as it traverses the target, in order to induce specific endothermic reactions. This amount of energy is the E_{th} that has been discussed previously.

The Oak Ridge software *STOPX* [zie80] was used to determine energy loss values through the target. Table 3.1 shows the results of this calculation using a beam of ^{37}Cl at 160 MeV and two equally thin targets ($\approx$ 0.5 mg/cm^2) of a Mo composition listed in Table 4.1. Under normal operating conditions, the beam is never totally at maximum energy. There is a velocity distribution due to the flow characteristics of the ions in the beam which produces a ΔE in the energy. Also, the spot size of the beam and therefore, the beam intensity slightly change with the angle of the target and any mechanical vibrations that may be in the system. This ΔE is not accounted for in the energy loss calculations. Since the target was previously used, the sputtering process would have changed the surface, therefore, the exact thickness is not known. The Table lists calculations for a target of 0.48 to 0.55 mg/cm^2 and a 160 MeV beam. E^1_{abs} represents the amount of energy loss to the beam, i.e., the energy deposited in the target lattice. The reduced beam, E^1_{exit}, then enters the second foil and undergoes another $\approx$50 % attenuation ; the amount of energy deposited in the second foil is E^2_{abs} and the second exit beam is E^2_{exit}. Since the beam exit energy is significantly lower than the 113.7 MeV threshold energy needed to produce ^{132}Pr, another study was performed based on two, thin targets of equal thickness between 0.23 and 0.27

Table 3.1: Energy Loss Calculation: The beam throughput energy, E_{exit} and the amount of energy deposited in the Mo Target, E_{abs} with a ^{37}Cl Beam. The calculations were done with one beam energy, E0 and two equally thin targets, 0.48-0.55 mg/cm^2.

Target mg/cm^2	**E0** MeV	$\mathbf{E^1_{abs}}$ MeV	$\mathbf{E^2_{abs}}$ MeV	$\mathbf{E^1_{exit}}$ MeV	$\mathbf{E^2_{exit}}$ MeV
.48	160	78.07	40.7	81.93	41.07
.49	160	79.18	40.7	80.82	39.96
.50	160	80.66	40.7	79.34	38.85
.51	160	81.77	40.7	78.23	37.74
.53	160	83.99	40.7	76.01	35.52
.55	160	85.84	40.7	74.16	33.48

mg/cm^2. In addition, three beam energies were investigated, 145, 155, and 160 MeV. The results are listed in Table 3.2. As the beam energy increases more energy is lost to the target. As the target diminishes in thickness, the beam exit energy increases. Only a target of 0.25 mg/cm^2 or less would produce a beam exit energy $\geq E_{th}$ for ^{132}Pr.

Since the first foil is exposed to an unattenuated beam and the second foil receives a beam that is very much reduced in energy, the surfaces, after prolonged use, would be etched to different degrees. This prompted another study, one in which the foils have different thicknesses. Table 3.3 contains the results of a study in which the second foil has a thickness of 0.25 mg/cm^2 and the thickness of the first foil is varied between 0.15 and 0.24 mg/cm^2. Table 3.4 contains results of an identical calculation, except that the thickness of the second foil is held at 0.21 mg/cm^2. It is obvious from these studies that the target thickness plays a significant role in choosing what beam energy and, therefore, what reaction(s) will occur in the second foil. The initial beam energy is the key feature that selects the reaction(s) of interest in the first foil. Because the beam energy changes for each of the two targets, a dual set of reactions

Table 3.2: Energy Loss Calculation: The beam throughput energy, E_{exit} and the amount of energy deposited in the Mo Target, E_{abs} with a ^{37}Cl Beam. The calculations were done with three beam energies, E0 and two equally thin targets, 0.23-0.27 mg/cm^2.

Target mg/cm^2	**E0** MeV	$\mathbf{E}^1_{abs}$ MeV	$\mathbf{E}^2_{abs}$ MeV	$\mathbf{E}^1_{exit}$ MeV	$\mathbf{E}^2_{exit}$ MeV
.23	145	39.55	29.50	105.45	75.78
	155	42.14	31.61	112.86	81.33
	160	43.25	32.60	116.75	84.28
.24	145	41.03	30.16	103.97	73.56
	155	43.62	32.31	111.38	79.11
	160	44.73	33.34	115.27	81.69
.25	145	42.51	30.79	102.49	71.71
	155	45.10	32.97	109.90	76.89
	160	46.21	34.05	113.79	79.48
.26	145	43.99	31.35	101.01	69.50
	155	46.58	33.60	108.42	74.67
	160	48.06	34.71	111.94	77.26
.27	145	45.47	31.90	99.53	67.65
	155	48.43	34.19	106.57	72.45
	160	49.53	35.30	110.47	75.04

occurred with ^{132}Pr being preferrentially selected by the first target and ^{133}Pr, by the second target. These studies show that a low (.15 to .16 mg/cm^2) target thickness is most probable for the first target. The thickness of the target determines whether the residual particles are trapped within the lattice or whether they freely recoil into vacuum. This is referred to as the stopping power of the target; the value for this target was determined to be 5.7018 MeV/(mg/cm^2). The residual particles have been determined to have much higher energies, therefore, they pass through the target, as they are created, and into the vacuum.

3.1.4 Doppler Shift of γ - Rays

Again consider a nuclear reaction of the form: $T(p_{in}, p_{out})P^*_{res}$. If the target used is thin, the stopping power will not be great enough to contain the reaction products. Therefore, P^*_{res} will recoil freely into vacuum with its full initial velocity. Then another reaction will occur:

$$P^*_{res} \overrightarrow{\gamma} P_{res} , \tag{3.11}$$

the de-excitation of the excited nucleus via γ decay. The nucleus recoils with a momentum equal and opposite to that of the γ ray and there is a corresponding recoil kinetic energy, T_R given to the nucleus. Conservation of total energy and momentum can be written:

$$E_i = E_f + E_\gamma + T_R \tag{3.12}$$

where, E_i is the energy of P^*_{res} and E_f is the energy of P_{res}. [kra88] By substituting in the relativistic value for the kinetic energy and rearranging, the energy of the γ ray can be determined:

$$E_\gamma = \frac{1}{2}(E_i - E_f)(1 + \frac{E_f}{E_i}) \ \frac{[1-(v/c)^2]^{1/2}}{1-(v/c)cos\theta} \tag{3.13}$$

This is the relativistic Doppler-shift formula. [ale71]. It includes the velocity of P_{res}, v and the laboratory angle θ between the particle and the detector. If we substitute

Table 3.3: Energy Loss Calculation: The beam throughput energy, E_{exit} and the amount of energy deposited in the Mo Target, E_{abs} with a ^{37}Cl Beam. The calculations were done with three beam energies, E0 and two thin targets; the thickness of target 2 is 0.25 mg/cm^2 and that of target 1, varied.

Target mg/cm^2	**E0** MeV	$\mathbf{E}^1_{abs}$ MeV	$\mathbf{E}^2_{abs}$ MeV	$\mathbf{E}^1_{exit}$ MeV	$\mathbf{E}^2_{exit}$ MeV
.15	145	27.13	35.30	117.87	82.43
	155	28.65	37.71	126.35	88.72
	160	29.35	38.81	130.65	91.68
.16	145	28.76	34.82	116.24	81.33
	155	30.39	37.34	124.61	87.24
	160	31.16	38.44	128.84	90.20
.17	145	30.39	34.38	114.61	80.22
	155	32.12	36.71	122.88	86.13
	160	32.94	37.71	127.06	89.09
.18	145	32.01	33.90	112.99	79.11
	155	33.82	36.23	121.18	85.02
	160	34.67	37.34	125.33	87.98
.19	145	33.57	33.45	111.43	78.00
	155	35.52	35.75	119.48	83.91
	160	36.41	36.86	123.59	86.50
.20	145	35.15	32.97	109.85	76.89
	155	37.34	35.27	117.66	82.43
	160	38.07	36.37	121.93	85.39
.21	145	36.67	32.53	108.33	75.78
	155	38.81	34.82	116.19	81.33
	160	39.92	35.93	120.08	84.28
.22	145	38.07	32.09	106.93	74.67
	155	40.29	34.34	114.71	80.22
	160	41.40	35.45	118.60	82.80
.23	145	39.55	31.64	105.45	73.56
	155	42.14	33.90	112.86	79.11
	160	43.25	34.97	116.75	81.69
.24	145	41.03	31.24	103.97	72.45
	155	43.62	33.42	111.38	78.00
	160	44.73	34.49	115.27	80.59

Table 3.4: Energy Loss Calculation: The beam throughput energy, E_{exit} and the amount of energy deposited in the Mo Target, E_{abs} with a ^{37}Cl Beam. The calculations were done with three beam energies, E0 and two thin targets; the thickness of target 2 is 0.21 mg/cm^2 and that of target 1, varied.

Target mg/cm^2	**E0** MeV	$\mathbf{E}^1_{abs}$ MeV	$\mathbf{E}^2_{abs}$ MeV	$\mathbf{E}^1_{exit}$ MeV	$\mathbf{E}^2_{exit}$ MeV
.15	145	27.13	30.42	117.87	87.61
	155	28.65	32.46	126.35	93.89
	160	29.35	33.42	130.65	97.22
.16	145	28.76	30.01	116.24	86.13
	155	30.39	32.05	124.61	92.41
	160	31.16	33.01	128.84	95.74
.17	145	30.39	29.61	114.61	85.02
	155	32.12	31.64	122.88	91.31
	160	32.94	32.60	127.06	94.26
.18	145	32.01	29.24	112.99	83.91
	155	33.82	31.24	121.18	89.83
	160	34.67	32.20	125.33	93.15
.19	145	33.57	28.83	111.43	82.43
	155	35.52	30.83	119.48	88.72
	160	36.41	31.75	123.59	91.68
.20	145	35.15	28.46	109.85	81.33
	155	37.34	30.42	117.66	87.24
	160	38.07	31.35	121.93	90.20
.21	145	36.67	28.06	108.33	80.22
	155	38.81	30.02	116.19	86.13
	160	39.92	30.94	120.08	89.09
.22	145	38.07	27.69	106.93	79.11
	155	40.29	29.61	114.71	85.02
	160	41.40	30.53	118.60	87.98
.23	145	39.55	27.32	105.45	78.00
	155	42.14	29.20	112.86	83.91
	160	43.25	30.13	116.75	86.50
.24	145	41.03	26.95	103.97	76.89
	155	43.62	28.83	111.38	82.43
	160	44.73	29.76	115.27	85.39

$\Delta E_* = E_i - E_f$ and make the assumption that $P^*_{res}c^2 \equiv P_{res}c^2$, then the first two factors in the previous equation can be reduced.

$$\frac{1}{2}(E_i - E_f)(1 + \frac{E_f}{E_i}) = \Delta E - \frac{(\Delta E)^2}{2M^*_4c^2} = \ E^\circ_\gamma. \tag{3.14}$$

E°_γ is the energy of the γ- ray observed in the moving reference frame. By letting $\beta = v/c$ and substituting for E°_γ, we have derived a Doppler-shift formula that describes the energy of the Doppler shifted γ ray observed at the detector, $E_\gamma(\theta)$ in terms of only E°_γ, the velocity of the residual particle and the detector angle, θ.

$$E_\gamma(\theta) = E^\circ_\gamma \frac{(1-\beta^2)^{1/2}}{1 - \beta cos\theta} \tag{3.15}$$

For simplicity we can rewrite this as:

$$E_\gamma(\theta) = E^\circ_\gamma \times DS_{fac} \tag{3.16}$$

Experimentally, the $E_\gamma(\theta)$ can be described as the Doppler shifted peaks obtained using the isotropic *gs* calibration from Section 5.1. E°_γ is not a measured quantity but it can be simulated using the Doppler shifted calibration *gds*, wherein the energy peaks are rebinned in order to erase the effect of the Doppler shift. This process uses energies from various reaction products and consequently results in generating an average DS_{fac} for the reaction. This can be obtained by dividing the slope of the normalized isotropic calibration by the slope of the normalized Doppler shifted calibration, according to Equation 3.16. An average β was obtained from the experimentally averaged DS_{fac} by a process of successive iterations: $\beta = 0.0253$. [1] An example of this linear effect is shown in Figure 3.4, a plot of the cosine of the detector angle θ versus the inverse of the DS_{fac}. [2] The line represents the detector

[1] The value was obtained from three successive iterations and averaged over the β values obtained from detectors 2 through 5.

[2] There is a point, which belongs to detector 20, that shows a large excursion from linearity . This along with other evidence showing anomolies in peak intensity from this detector suggested that something had happened to it during the experiment. Therefore, information from detector 20 was not used in the gating procedures.

doppler shift correction normalized to the 88.5° detector (1) that was used for the data analysis in this experiment.

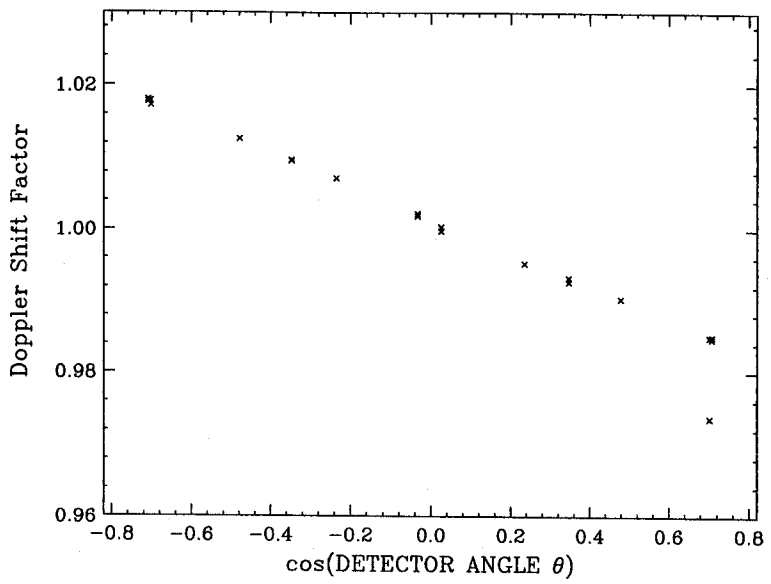

Figure 3.4: Plot of the cosine of the detector angle θ versus the inverse of the calculated Doppler Shift factor .

3.1.5 β-Velocity Correction Factor

According to Equation 3.14, the γ ray in the moving reference frame has been diminished in energy from the maximum amount available from the decay by the factor $(\Delta E)^2/2M_4^* c^2$. This is often referred to as the recoil correction term and is generally considered to be negligible, within the resolution capabilities of present detectors. [3] [kra88] There is another correction term that needs to be evaluated — the velocity of P_{res}, v. This is contained within β in the DS_{fac}. In the past, researchers have adjusted their data with a *gds* calibration to remove the Doppler shift without inves-

[3]However, with the emergence of a new generation of detectors that is being developed for Gammasphere, a re-evaluation is suggested once the resolution capabilities are determined.

tigation of whether this adjustment was valid for a multi-residual particle data set, or else, they have avoided the issue entirely by using a target that does not allow free recoil of the residual particles; hence, there would be no Doppler shift of the γ ray but the trade-off is a broadening of the peak, itself.[4] Free recoil allows for a better peak resolution and the added complexity of the Doppler shift was believed to be a simple, routine data adjustment. So, understandably, investigating the possibility that the expected, additional peaks observed in a high resolution γ ray spectrum might be artifacts does not appear to be a standard procedure.

However, because of the growing volume of data which display peaks in multiple, 'identical', superdeformed bands at very low intensities that differ by 1 or 2 keV., we feel that there are two questions in this regard that should be addressed: 1) Does the method of correcting for doppler shift cause variations in the expected energy? 2) Is a correction factor necessary to account for the variation in residual particle velocity?

In order to investigate these possibilities, classical kinematic calculations were performed using the Oak Ridge software *Kineq*. The calculations were performed for nine major nuclei that were predicted by the Q-value and *Cascade* calculations and/or appear in the experimental spectra. Some results are shown in Figure 3.5 – a plot of residual particle velocity (in cm/ns) versus the center of mass angle of the residual particle. [5] The lines represent the various nuclei produced in the experiment. At $\theta = 0°$ the order of the nuclei, from left to right are ^{134}Pr, ^{133}Pr, ^{132}Pr, ^{130}La-p, ^{133}Ce, ^{132}Ce, ^{128}La-α, ^{129}La-α, ^{130}La-α. The circled region represents the area where the

[4]Thermal motion in the target lattice is affected by the Doppler induced variations in velocity, resulting in a broadening of the absorption cross section. The peak exhibits a width proportional to $(E_{res}k_BT)^{1/2}$ where T is the Kelvin temperature, k_B is the Boltzmann constant and E_{res} is the recoil energy of the emitting nucleus. [ler91]

[5]For completeness, an analogous plot for the residual particle from the laboratory angle perspective is shown in Figure 3.6. This is a 3-D representation of Velocity versus Energy versus lab angle of the residual particle. A velocity of 0.7630 is located in the center of the figure, which is a series of nearly concentric saddle-shaped ellipses, representing each of the nuclei. At $\theta = 0°$ the order of the nuclei, starting at the center, from left to right are: ^{130}La-p, ^{132}Pr, ^{134}Pr, ^{133}Pr, ^{133}Ce + ^{132}Ce, ^{128}La-α, ^{129}La-α, ^{130}La-α. Because of the overlapping nature of the nuclei, the order differs in the other half of the plot, and the order, in either half, depends on the 3-D viewing angle.

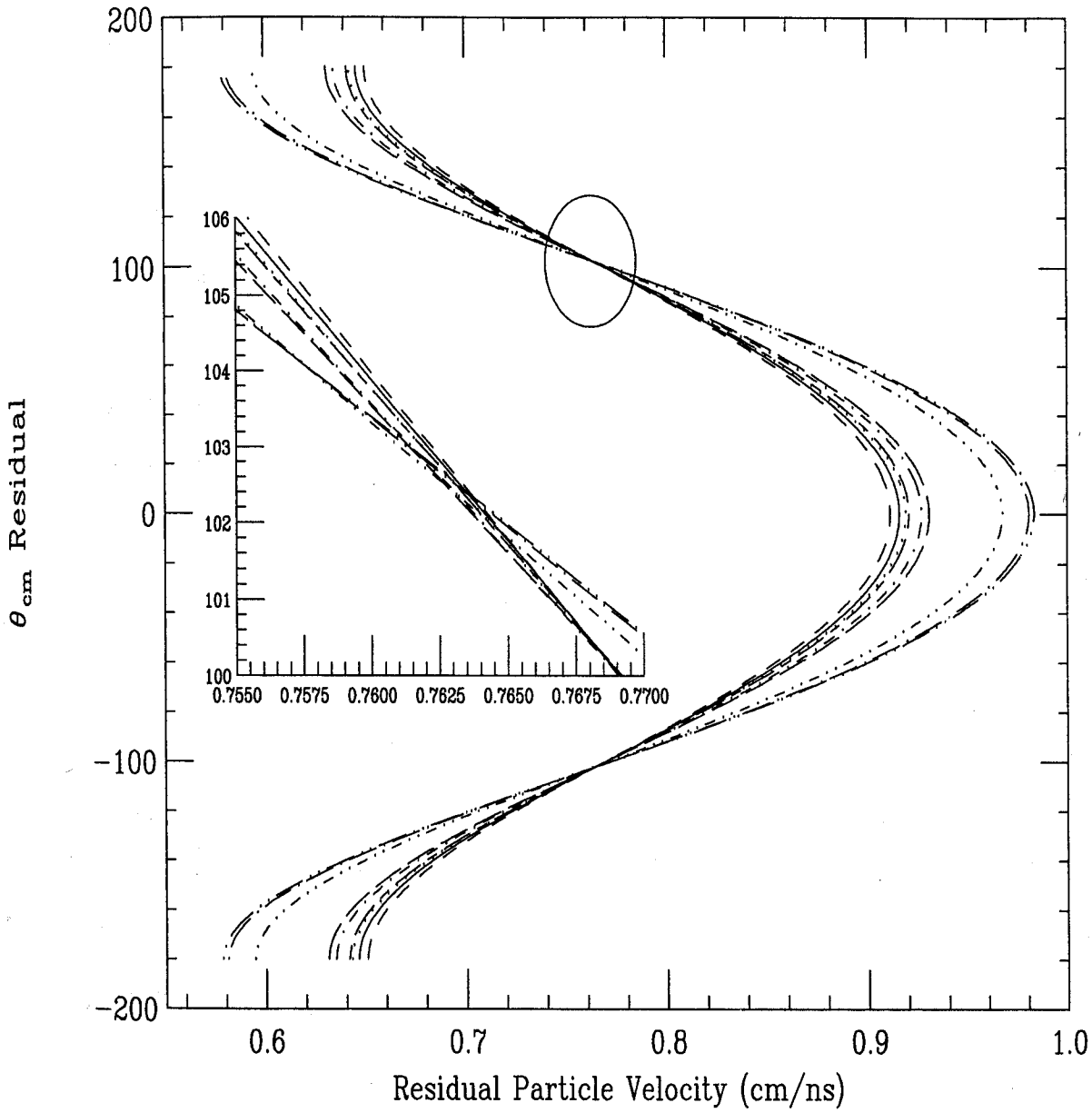

Figure 3.5: A classical Kinematic calculation using *Kineq* : A plot of the residual particle center-of-mass angle versus the residual particle velocity in cm/ns. An enlargement of the circled region is included. The lines represent the various nuclei produced in the experiment. At $\theta = 0°$ the order of the nuclei, from left to right are ^{134}Pr, ^{133}Pr, ^{132}Pr, ^{130}La-p, ^{133}Ce, ^{132}Ce, ^{128}La-α, ^{129}La-α, ^{130}La-α.

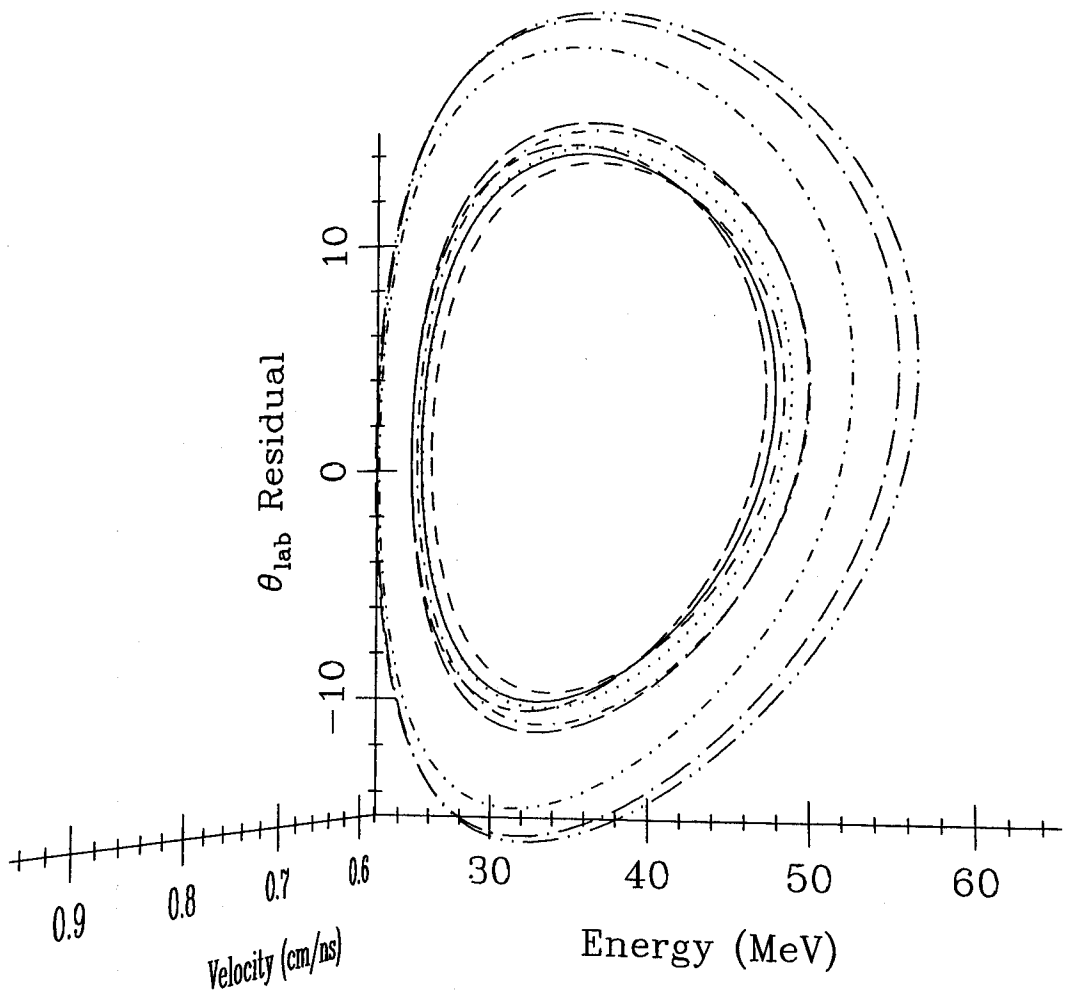

Figure 3.6: A classical Kinematic calculation using *Kineq* : A plot of the residual particle laboratory angle versus the residual particle velocity in cm/ns versus the residual particle energy in MeV. The saddle shaped ellipses represent the various nuclei produced in this experiment. At $\theta = 0°$ the order of the nuclei, starting at the center, from left to right are: ^{130}La-p, ^{132}Pr, ^{134}Pr, ^{133}Pr, ^{133}Ce + ^{132}Ce, ^{128}La-α, ^{129}La-α, ^{130}La-α. Note that the order depends on the viewing perspective.

velocities of all the nuclei converge. From the graph, this is at approximately, 102.5° and 0.7630 cm/ns. An enlargement of the circled region is included. At all other angles, the nuclei have velocities that vary, relative to each other. The maximum deviation occurs at angles of 0° and 180°. The value for β obtained from the mean of the velocities at 180° and 0° is: $\beta = 0.0260$. At 0°, ^{130}La-α has the highest velocity and ^{134}Pr has the lowest. At 180°, the roles are reversed showing ^{134}Pr with the highest velocity and ^{130}La-α with the lowest. This emphasizes the point that the last three nuclei, that appear to be separated from the rest, have the greatest velocity deviations over all angles. They were formed along with an α outgoing particle. Notice the positions of the two ^{130}La nuclei. At extreme angles, they are separated by a difference of 0.063 cm/ns which translates to two peaks, instead of one, for every transition of ^{130}La, separated by 2 kev at 1 MeV, 3 keV at 1.5 MeV., etc.

By plotting the residual particle velocity (cm/ns) versus the residual particle energy (MeV) (Figure 3.7) the nonrelativistic kinetic energy relationship can be observed. The original functions are nonlinear with overlap of three of the nuclei. Notice that there is a greater deviation in energy between the nuclei at high velocity than at low velocity. An expanded view of the circled area is included at the upper left side of the plot. One line exists for each mass number; 134 is at the top and 128, at the bottom. By multiplying the velocity by the square root of one half the mass and taking the square root of the energy, coincident, linear functions are produced, as shown in the lower right plot for all the nuclei. This may appear to be an obvious result; however, the exercise may be useful in determining whether the variations in velocity result in DS_{fac} values that can be adjusted to align all the nuclei.

Table 3.5 represents a single point comparison of the nuclei at one angle, 45°. The subscripts on the nuclei denote the outgoing particles, other than neutrons. The DS_{fac} values are calculated using equation 3.15 and the kinematic calculation results for the energy, E_{res}, and the velocity, v_{res} of the residual particle. By multiplying the

DS_{fac} by a peak energy, say 1000 keV, a useful comparison can be made for all nuclei. DS_{fac}A was calculated in the normal way. After multiplying by 1000 keV, the first six nuclei would have an average peak energy of 1020.69 keV; the nuclei with α outgoing particles would have an energy greater than this by 1 keV or more. This means that the transitions for these three nuclei would all be shifted by the difference between the average peak energy and their respective $DS_{fac} \times 1000$. The maximum deviation is 1.34 keV at a peak energy of 1000 keV. This may be significant enough, depending on the system resolution, to shift some peak centroids in a composite γ ray spectrum; however, when coincidence matrices are summed over detectors at multiple angles, as is customary for the large, 4π detector arrays, the effect may be even more critical. According to Figure 3.5, the DS_{fac} is a function of both angle and velocity; therefore the deviations between the nuclei would cause peak broadening and perhaps, multiple peak formation where only one is warranted. The effect becomes more pronounced as peak energies higher than 1000 keV are considered. If all nuclei could be shifted by a mutually agreeable DS_{fac} *and* an angle were chosen for normalization where all nuclei have similar velocities, then peak shifting and multiple peak abberations would be reduced. According to Figure 3.7, the velocity is a function of the inverse of the square root of energy and the square root of mass. By employing the following β correction factors, DS_{fac}B and C were calculated:

$$\beta' = \beta \times \sqrt{m_i \,/\, m_{ref}} \tag{3.17}$$

$$\beta'' = \beta \div \sqrt{E_i \,/\, E_{ref}} \tag{3.18}$$

With the mass correction factor, the DS_{fac}B shows that the peak energy at 1000 keV would converge to $\approx$ 1021.keV, except for the ^{130}La nuclei. By including ^{130}La, the maximum deviation would be 1.35 keV at 1000 keV. With the energy correction factor, DS_{fac}C shows an average peak energy at 1021.32 keV and a maximum deviation of 0.58 keV at 1000 keV. This represents a significant improvement.

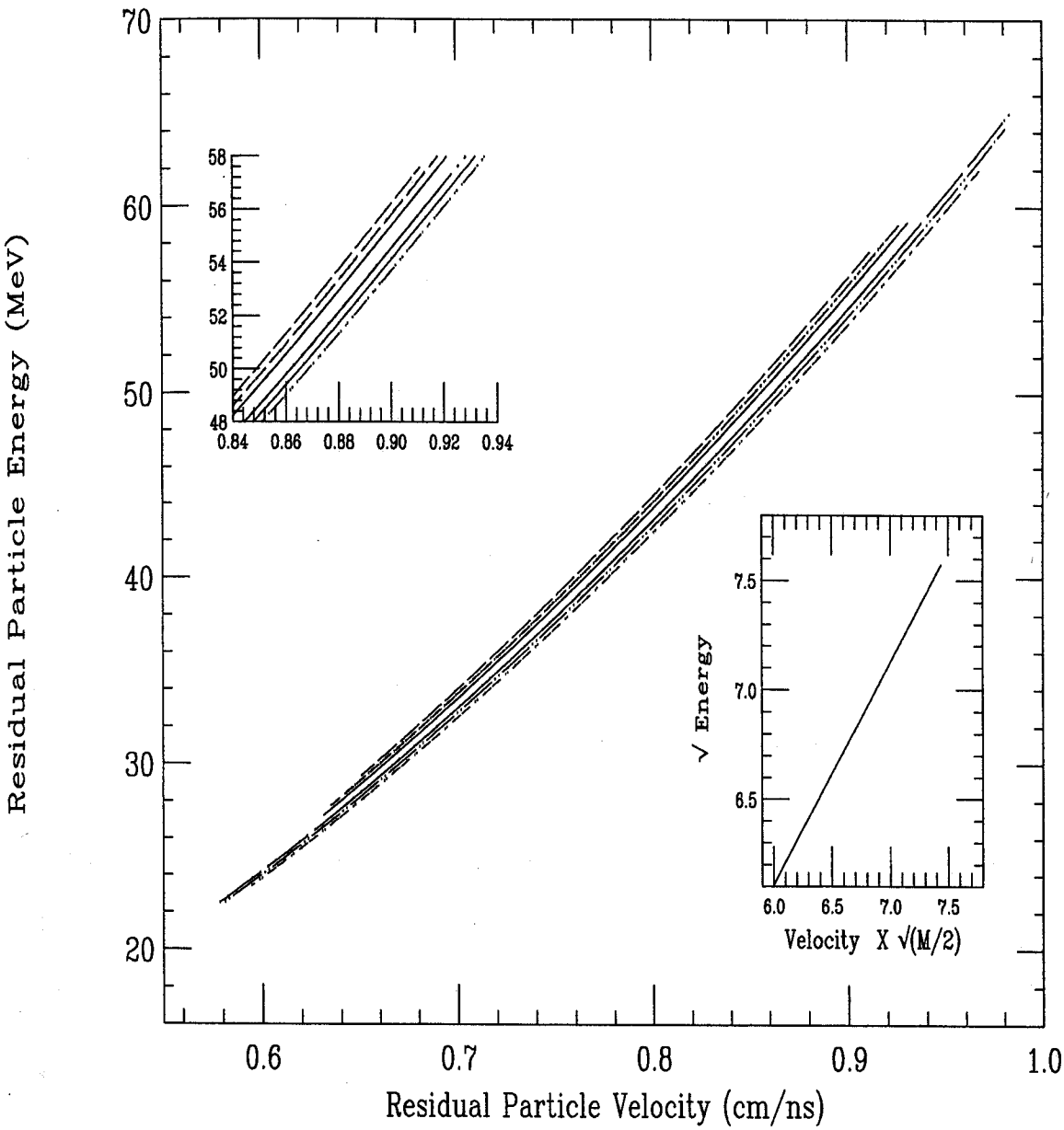

Figure 3.7: Classical Kinematic calculation using *Kineq*: A plot of Residual particle energy versus residual particle velocity. The upper left inset is an expanded view; the curves represent, from the top, A=134 to 132 and A=130 to 128. Three of the curves overlap. The lower right inset shows the effect of an axes change for the same data. The velocity multiplied by the square root of one half the mass of the residual particle is plotted versus the square root of the energy. All curves converge to one straight line.

Table 3.5: DS_{fac} calculations, based on results from classical kinematic calculations, for products from the reaction: ^{37}Cl on ^{100}Mo. $DS_{fac}A$ has no correction factor; $DS_{fac}B$ has a mass correction factor; and $DS_{fac}C$ has an energy correction factor.

Nucleus	θ_{cm} Res	$\mathbf{E}_{res}$	$\mathbf{v}_{res}$	$\mathbf{DS}_{fac}\mathbf{A}$	$\mathbf{DS}_{fac}\mathbf{B}$	$\mathbf{DS}_{fac}\mathbf{C}$
^{134}Pr	45.0517	53.4705	0.8779	1.02069	1.02117	1.02123
^{133}Pr	45.2079	53.7788	0.8837	1.02077	1.02117	1.02125
^{132}Pr	45.5087	53.0253	0.8808	1.02058	1.02090	1.02121
^{132}Ce	45.6907	54.3885	0.8921	1.02078	1.02110	1.02114
^{133}Ce	45.6417	54.4469	0.8892	1.02073	1.02113	1.02108
$^{130}La_p$	45.6548	52.6281	0.8842	1.02061	1.02077	1.02132
$^{130}La_\alpha$	45.2441	58.7915	0.9346	1.02195	1.02212	1.02148
$^{129}La_\alpha$	45.2948	58.0693	0.9324	1.02188	1.02196	1.02154
$^{128}La_\alpha$	45.2153	56.3240	0.9219	1.02166	1.02166	1.02166

The remaining questions that can be answered by the kinematic calculations are regarding the particles with dual velocities that are formed between 0° and 90° near the energy threshold of the reaction. 1) Are residual particles also formed with dual velocities? 2) Is the velocity difference between these otherwise identical particles enough to create two peaks instead of one for every transition from this nucleus?

Because equation 3.8 was derived by matrix elimination of E_{res} and its corresponding θ value, E_{res} does not show up as one of the results of the calculation. But this does not mean that E_{res} particles do not exist, rather, the values for their velocities are intractable with this particular calculation. Instead of reprogramming the software package, an attempt was made at estimating the residual particle velocities by drawing correlations from the classical results shown in Figure 3.7 and the relativistic results shown in Figure 3.3. Table 3.6 shows the results of these calculations to determine the dual residual particle velocities and DS_{fac} for ^{132}Pr at the energy threshold. Two angles were chosen, 0° and 45°, since the maximum difference in velocity occurs in this region. For the classical data, the sum of $E_{p_{out}}$ and $E_{P_{res}}$ is a constant for each

Table 3.6: Calculations to determine an estimate of the dual residual particle velocities and DS_{fac} for ^{132}Pr at the energy threshold. The values marked with * were obtained by subtracting the relativistic $E_{p_{out}}$ from the sum of ($E_{p_{out}}$ + $E_{P_{res}}$) of the classical calculation.

Calculation	Beam Energy MeV	E p_{out1} MeV	E P_{res1} MeV	v P_{res1} cm/ns	E total MeV
Classical 0°	114.2000	2.6826	28.5528	0.6463	31.2354
Classical 45°	114.5700	0.7748	30.8306	0.6716	31.6054
Calculation	Beam Energy MeV	E p_{out1} MeV	E p_{out2} MeV	E P^*_{res1} MeV	E P^*_{res2} MeV
Relativistic 0°	114.1990	2.7528	0.22392	28.4826	31.0114
Relativistic 45°	114.5700	0.92163	0.30258	30.6837	31.3028
Calculation	v P_{res1} cm/ns	v P_{res2} cm/ns	DS_{fac1}	DS_{fac2}	Δ keV at 1MeV
0°	0.64471	0.70195	1.02174	1.02370	1.96
45°	0.66839	0.68188	1.01576	1.01608	0.32

angle. The values for the two relativistic $E_{p_{out}}$ were then subtracted from this sum, generating two probable values for $E_{P_{res}}$. The classical data has a residual particle velocity to match $E_{P_{res}}$; therefore, proportional values for the newly generated $E_{P_{res1}}$ and $E_{P_{res2}}$ were then calculated. Using these velocities, the corresponding DS_{fac} were found and are listed in Table 3.6. If this is an accurate estimate of the velocities, the energy difference at 1000 keV would be 1.96 keV. at 0° and 0.32 keV. at 45°. Even though 1.96 keV is significant, most γ ray spectra are not collected at 0°. The deviations would decrease in value with angles higher than 45°. Again, *if* this is an accurate estimate of the velocities, by themselves, these deviations for dual residual particle velocities of ^{132}Pr would not be significant at normal resolutions. However, a synergistic effect with the velocity deviations shown in Figure 3.5 might be significant. Only ^{132}Pr was investigated in this regard. Also, there are no cross-sectional calculations available to determine relative intensities of the peaks with a velocity

variation.

3.2 Fusion Evaporation Reactions

Even if the proper kinetic energy is present in the projectile, the desired product does not have 100% probability of forming. The specific reaction probability depends on what is referred to as impact parameters between the projectile and target nuclei. If the projectile merely grazes the nuclear surface of the target, then an elastic or, perhaps, inelastic reaction occurs. With the proper spacial orientation, a nucleon (n, p, α) exchange reaction might occur. If the projectile just moves within the nuclear field of the target nucleus, a Coulomb excitation might happen. For a fusion reaction, the two nuclei must collide with a high percentage of the nuclear surfaces in contact.

3.2.1 *CASCADE* Calculations

Resonances

The fusion reaction isotherm proceeds through a resonance stage. The Eisenbud and Wigner version (circa 1958) of nuclear reaction theory appears to be very valid today. [eis58] They claim that "the general theory of nuclear reactions ... may be usefully organized about the concept of resonance." A reaction proceeds from reactants to products through a long-lived intermediate step referred to as a compound nucleus. The compound nucleus has a ground state in which the in-going particle is bound; it has low energy excited states which de-excite only by γ emission and other excited states with energy greater than the separation energy of the in-going particle. These last states have long lifetimes compared with the time the in-going particle takes to transverse the nucleus; they are referred to as 'quasi-stationary' states or resonance levels with energies that are not sharply defined. The energy uncertainty, Γ, is the energy width of the resonance level; it is related to the lifetime of the state by $\Gamma \times \tau =$

$\hbar$. Γ must be much smaller than the separation between adjacent levels in order for the resonant compound nucleus to exist.

Typical resonant behavior is shown in Figure 3.8. This is a result of the *CASCADE* calculation — a plot of the beam energy versus the reaction cross section, [6] σ, in millibarns, for the various products of the ^{37}Cl on ^{100}Mo reaction. The energy of the whole system (in the cm coordinate frame) at the maximum cross section is referred to as the resonance energy, E_λ of the reaction. The cross section for the formation of product x may be written:

$$\sigma_x = \pi \mathcal{M}_s^{-2} \frac{\Gamma_{\lambda s}\Gamma_{\lambda x}}{(E_\lambda - E)^2 + .25\Gamma_\lambda^2} \tag{3.19}$$

where $\Gamma_{\lambda s}$ is the probability of transition from the initial state of the incident particle to the state λ of the compound nucleus. $\mathcal{M}_s$ is the matrix element between these states. $\Gamma_{\lambda x}$ is the partial width of the λ level for the product, x. For this equation, only the $\ell = 0$ state is effective. [eis58]

Code

The computer code *CASCADE*, discussed by Pühlhofer, starts from an excited compound nucleus, calculates relative decay widths for neutron, protron, α particle and γ-ray emission and generates matrices containing the population of the daughter nuclei as a function of excitation energy and angular momentum. It calculates all possible decay sequences for all possible excitation energies. The decay of the compound nucleus is calculated from the Hauser-Feshbach formula. [puh77]

Figure 3.8 shows peaks of various Γ that correspond to unique reactions; the major products are marked on the plot. The peak maximum is the resonance energy for that particular nucleus. 160 MeV was experimentally determined to be the optimized

[6] The cross section of a process is defined as 'the probability that the process occurs if the incident beam consists of a single particle and the target contains one nucleus per unit area.' The unit, a Fermi or barn, is equal to an area of 10^{-24} cm^2. [eis58]

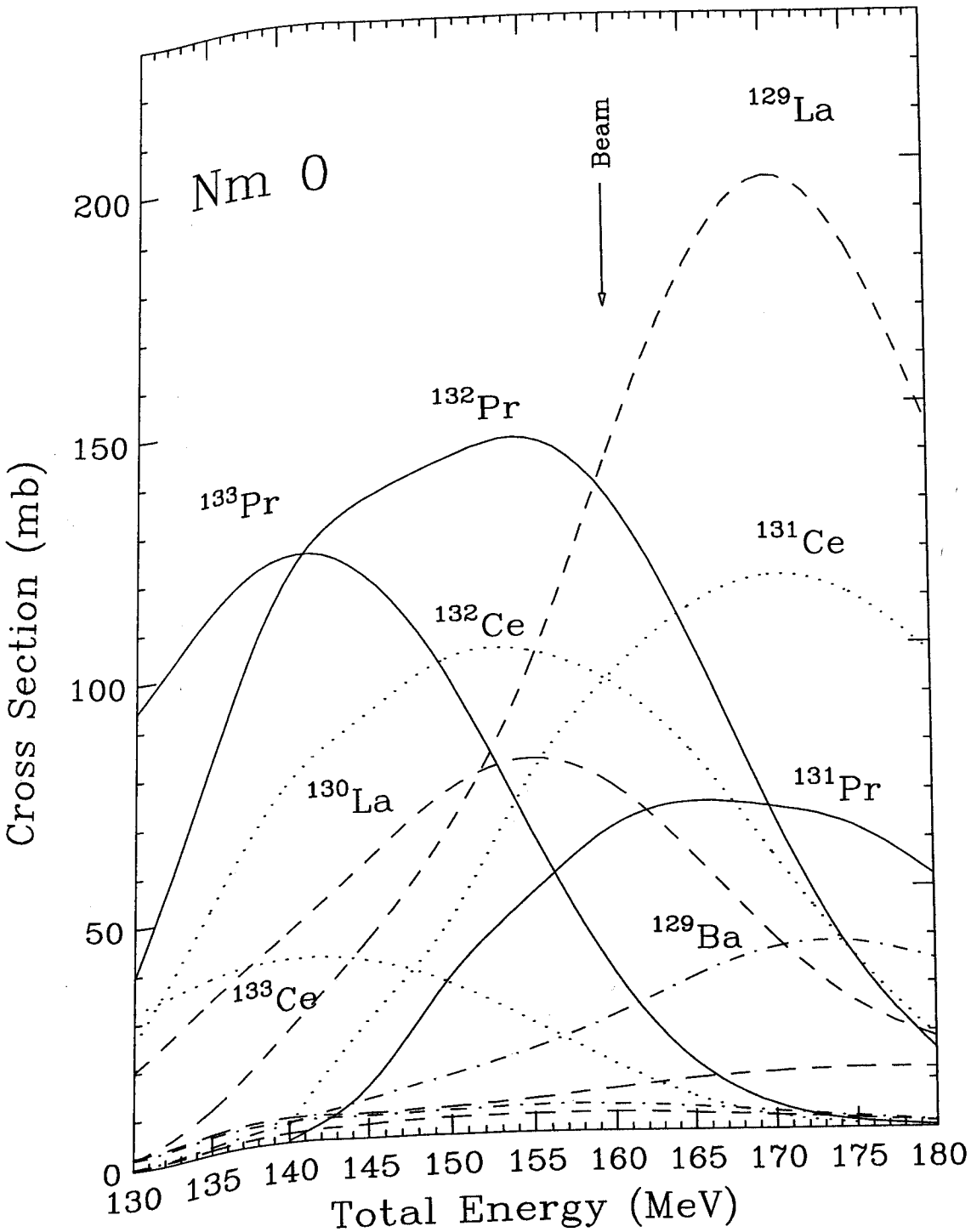

Figure 3.8: Cross section values calculated for various beam energies for Ba, La, Ce, and Pr isotopes created during the reaction: ^{37}Cl on ^{100}Mo, from *CASCADE* calculations using Nuclear Model 0. The experimental, 160 MeV. beam energy is marked.

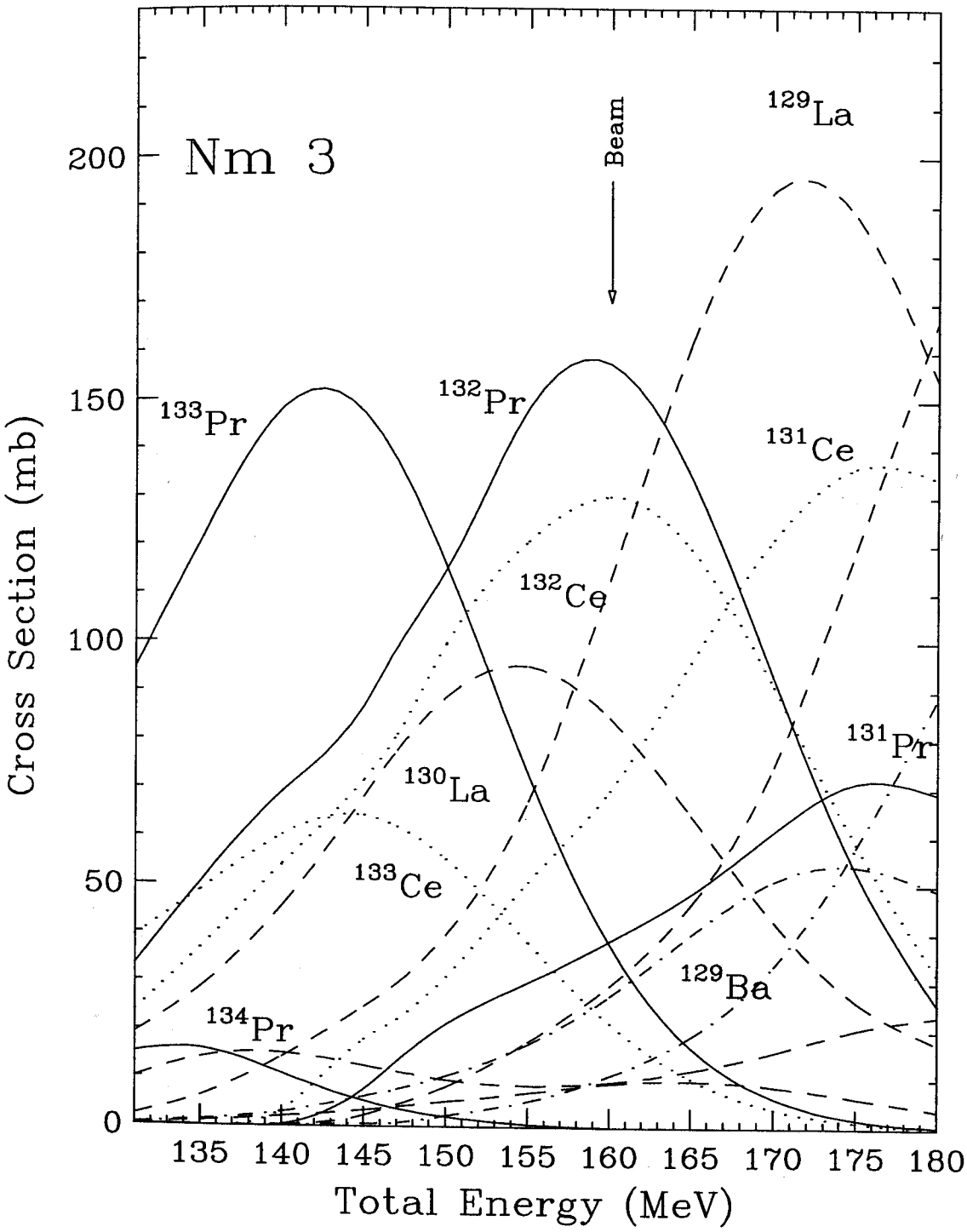

Figure 3.9: Cross section values calculated for various beam energies for Ba, La, Ce, and Pr isotopes created during the reaction: ^{37}Cl on ^{100}Mo, from *CASCADE* calculations using Nuclear Model 3. The experimental, 160 MeV. beam energy is marked.

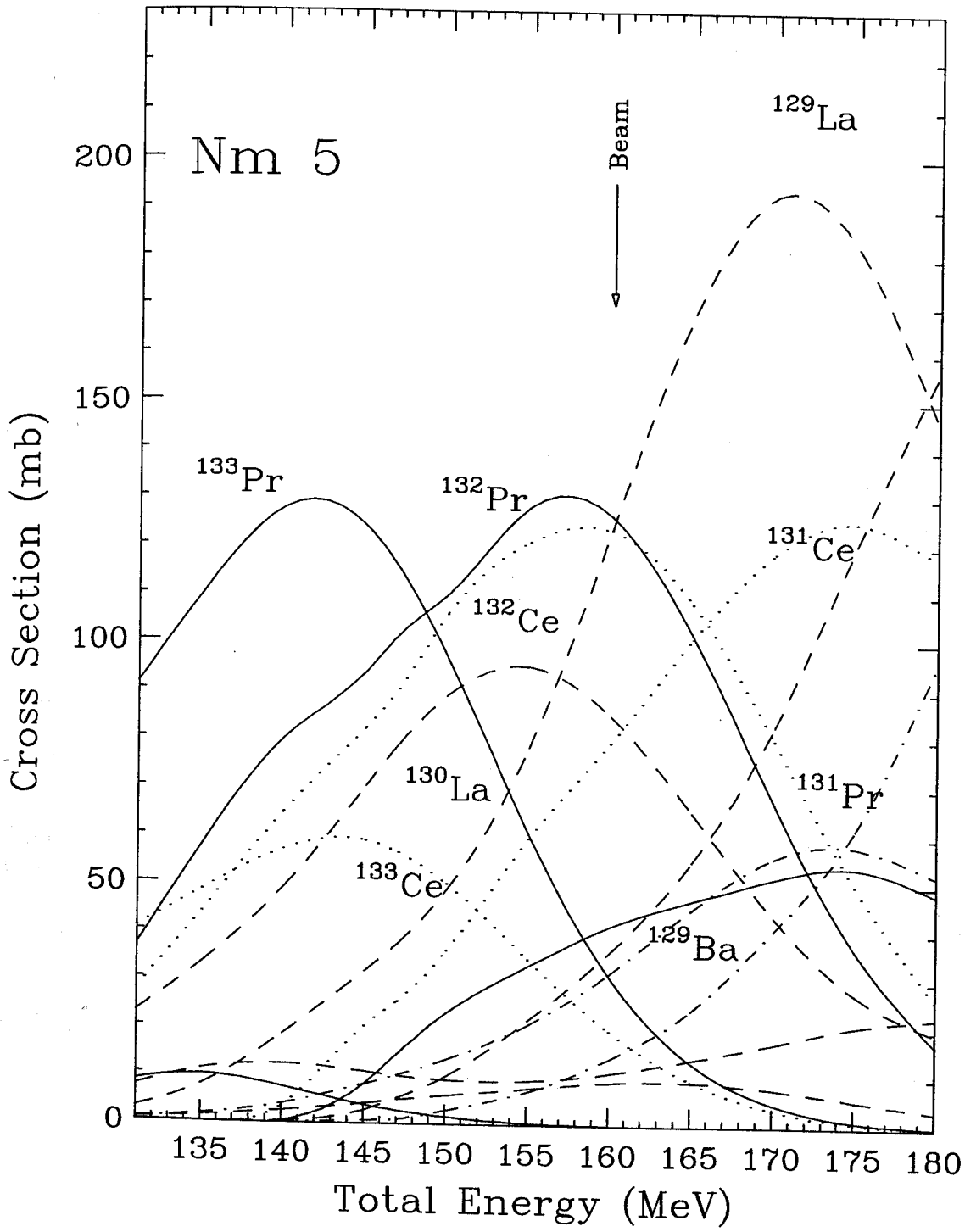

Figure 3.10: Cross section values calculated for various beam energies for Ba, La, Ce, and Pr isotopes created during the reaction: ^{37}Cl on ^{100}Mo, from *CASCADE* calculations using Nuclear Model 5. The experimental, 160 MeV. beam energy is marked.

beam energy for the production of ^{132}Pr (see Section 3.2.3). Since 160 MeV does not coincide with the peak maximum and a few of the other peak intensities, notably ^{133}Pr and ^{129}La, do not correspond with experimental results, a study was performed to investigate the use of the various existing mass models.

Nuclear Mass Models

Table 3.7 contains a list of the liquid-drop mass model formula names for the *CASCADE* calculations. Figure 3.8 was developed using nuclear model 0. There are four models available in the code; in addition, three of the four models are included with what is referred to as a Wigner term. All of the mass models are semiempirical, numerical attempts to adjust the mass defect to coincide with either masses measured with various instrumental techniques or logical explanations of nuclear behavior, such as shell effects. The Wigner term attempts to correct for a V-shaped deviation, not related to shell effects, in a plot of mass number versus mass defect. The nuclear model (Nm 0) described by Myers and Swiatecki calculates masses by extrapolating

Table 3.7: A list of the *CASCADE* calculation options for the nuclear mass model formulas.

Code	Nuclear Model Name	Reference
Nm 0	Myers- Swiatecki- Lysekil	[mye74]
Nm 1	Myers, droplet model	[mye76]
Nm 2	Myers, droplet model with Wigner term	
Nm 3	Groote- Hilf- Takahashi	[gro76]
Nm 4	Groote- Hilf- Takahashi with Wigner term	
Nm 5	Seeger	[see76]
Nm 6	Seeger with Wigner term	

smooth, average nuclear properties, such as neutron and proton density nonuniformities induced by electric forces and the dependence of the neutron skin thickness on

the position on the nuclear surface. It does not deal with shell effects. [mye74] The Myers Droplet Model (Nm 1) uses the following correction factors to calculate the mass excess or defect, Δ m.

$$\Delta m = M_N\, N + M_H\, Z + droplet\ term + shell\ correction\ term$$
$$+ even - odd\ term + Wigner\ term - 0.00001433\, Z^{2.39}\ MeV.$$

where, N is the number of neutrons; Z is the number of protons; M_N is the mass defect of the neutron, 8.07169 MeV.; M_H is the mass defect of the hydrogen atom, 7.28922 MeV. The last term corrects for the binding energy of atomic electrons. The Droplet Model term assumes that the nucleus has properties of a liquid droplet and accounts for shape permutations in ground state deformations and fission barriers. The even-odd term allows for the fact that separation between odd and odd-A mass surfaces is slightly smaller than the separation between the even and odd-A surfaces. A term is also included for shell structure. [mye76]

The Groote-Hilf-Takahashi model (Nm 3) uses a unique approach to correct for shell structure, that may be important for nuclei far from the line of stability. They have developed a nuclear level bunching technique that simulates 'magic' gaps in the energy levels and appropriate sub-shell behavior. [gro76] The Seeger nuclear model (Nm 5) is a combination of a smoothly varying droplet model plus a fluctuating shell correction term. The Nilsson energy levels are first determined, then normalized and the ground state energies are calculated. [see76]

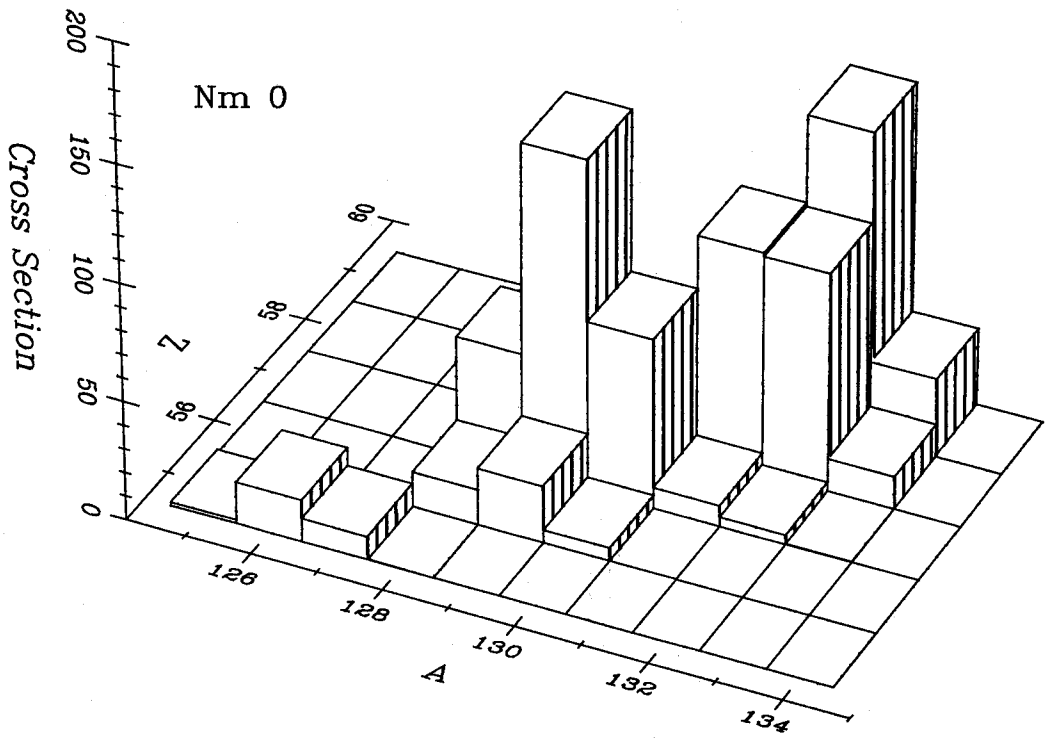

Figure 3.11: *Cascade* Nuclear Model Comparison for 160 MeV Cl on ^{100}Mo. A 3-D lego plot of atomic mass versus atomic number versus Cross Section for Nm 0 .

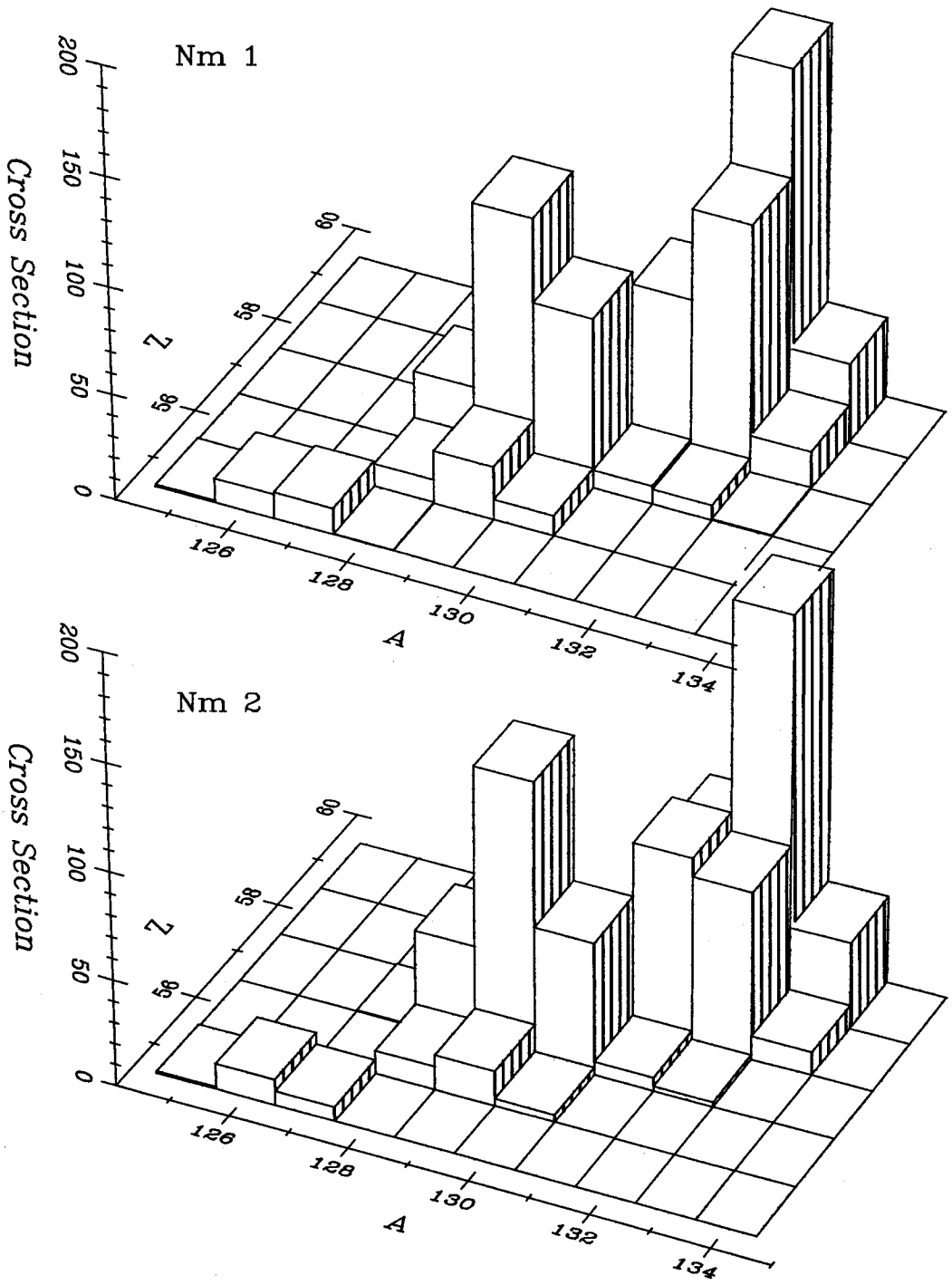

Figure 3.12: *Cascade* Nuclear Model Comparison for 160 MeV Cl on ^{100}Mo. A 3-D lego plot of atomic mass versus atomic number versus Cross Section for Nm 1 and Nm 2.

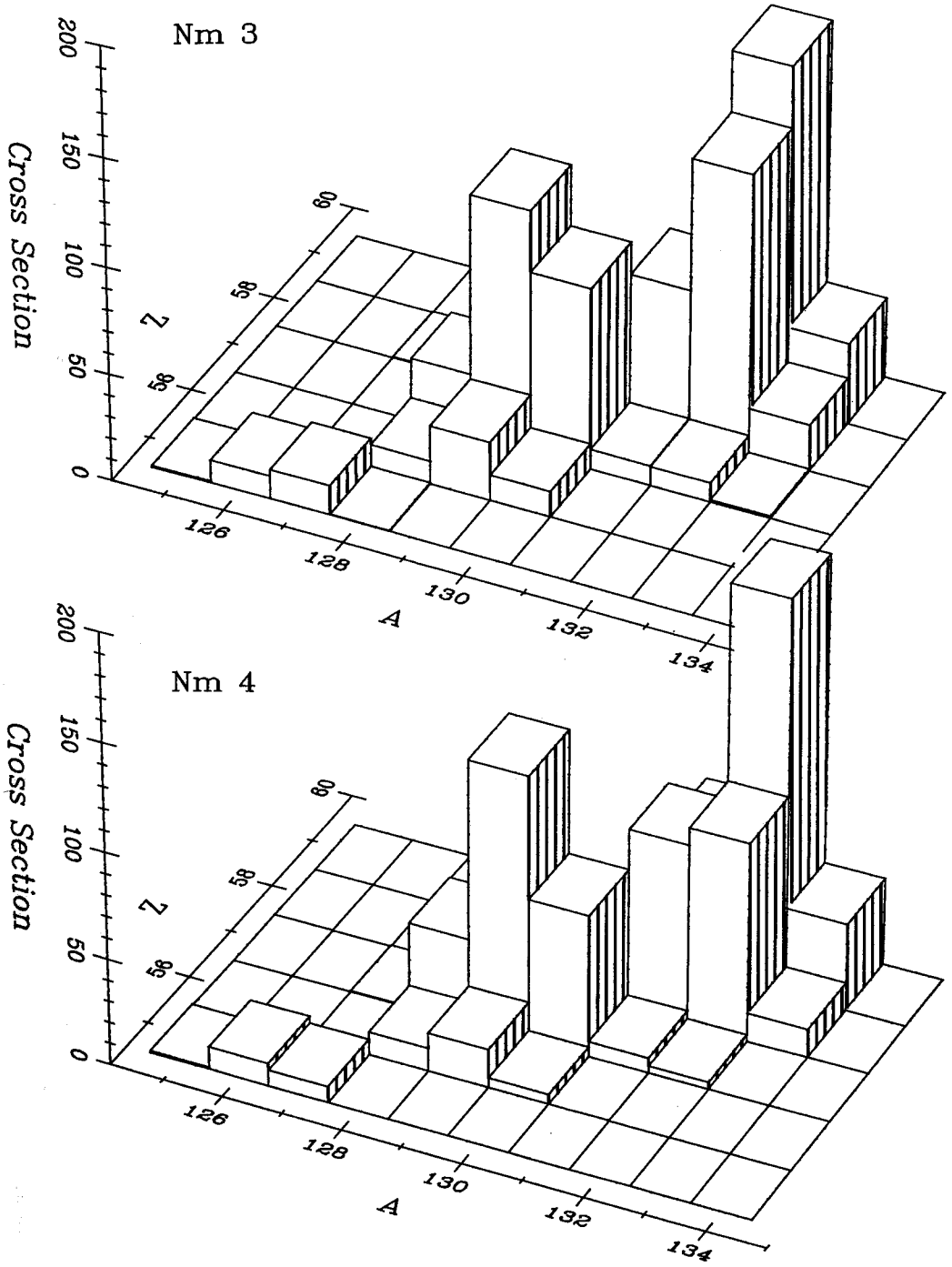

Figure 3.13: *Cascade* Nuclear Model Comparison for 160 MeV Cl on ^{100}Mo. A 3-D **lego** plot of atomic mass versus atomic number versus Cross Section for Nm 3 and **Nm 4**.

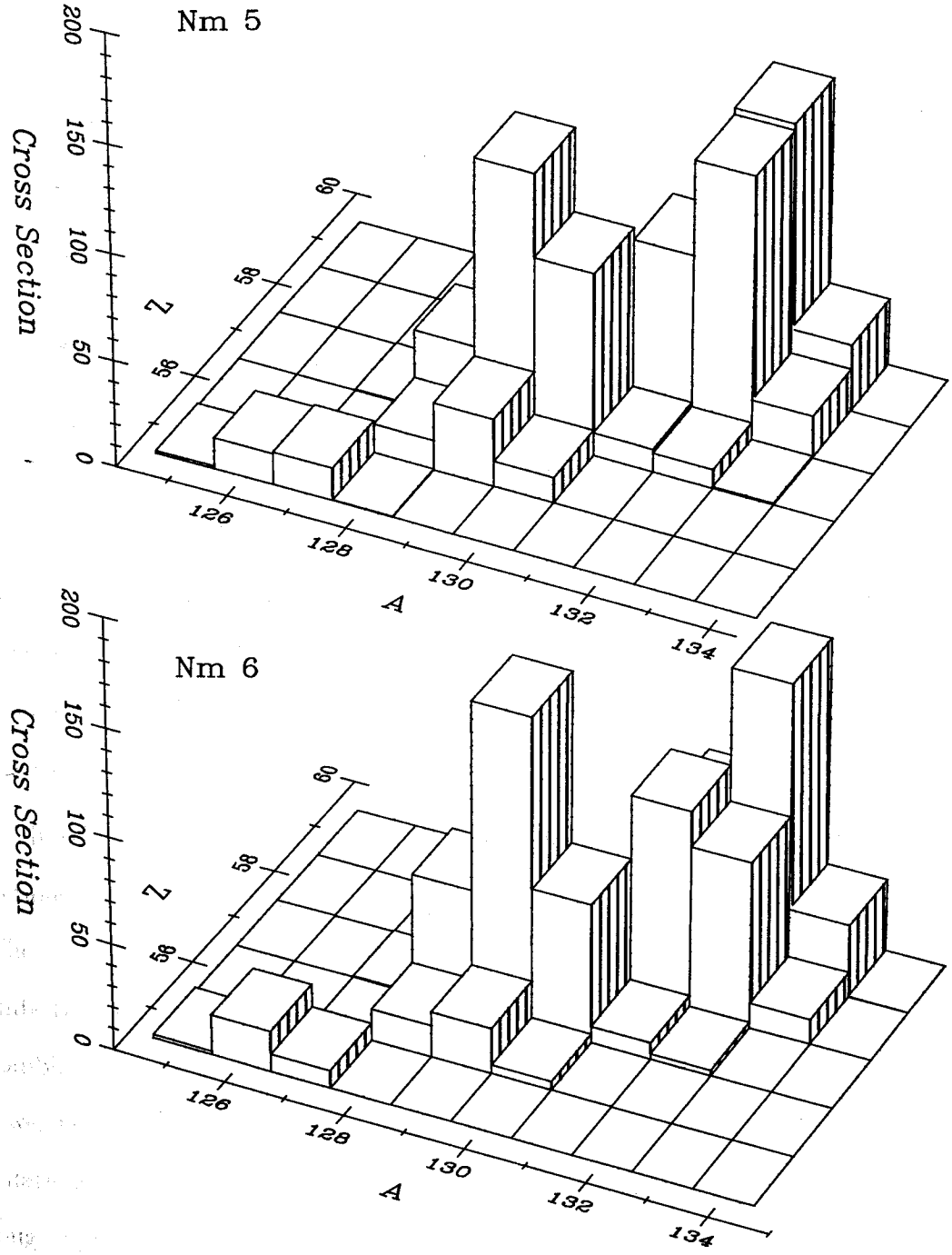

Figure 3.14: *Cascade* Nuclear Model Comparison for 160 MeV Cl on ^{100}Mo. A 3-D lego plot of atomic mass versus atomic number versus Cross Section for Nm 5 and Nm 6.

Figures 3.11, 3.12, 3.13, and 3.14 display the results of the *CASCADE* calculations for the ^{37}Cl on ^{100}Mo reaction, each using a different nuclear model. These are 3-D bar graphs: mass (A) versus proton number (Z) versus Cross Section in μbarn. Figure 3.15 contains 2-D bar graphs of the total cross section of the masses, A= 125-134, for each nuclear model code labeled 0-6. The nuclear models using the Wigner term are shaded. Based on these results, Figure 3.9 was developed for the Groote-Hilf-Takahashi nuclear model (Nm 3). The resonance energy, E_λ and Γ from this model better describes the experimental results for ^{132}Pr than do those for Nm 0 shown in Figure 3.8. The experimental intensity ratio of ^{129}La to ^{132}Pr is closer to this calculated cross sectional ratio. However, the experimental intensity at 160 MeV for ^{132}Ce relative to ^{132}Pr is much higher than the calculated cross section. Therefore, the Seeger nuclear model (Nm 5) was investigated. Figure 3.10 shows the results. ^{132}Ce relative to ^{132}Pr is closer to the experimental results than the other two models. However, the calculated ^{129}La intensity is too high and the ^{133}Pr and ^{133}Ce intensities are too low.

It is probable that the 'extra' intensities for the nuclei are produced by the reactions at the second foil in the target which was exposed to a lower energy beam. The *CASCADE* calculations do not account for two targets. The experimental results that we have observed at 160 MeV., may actually be better represented by a combination of the *CASCADE* cross section at 160 MeV. plus a cross section at a lower beam energy, closer to the resonance energy for ^{133}Pr. Since Monte Carlo calculations were not performed to more accurately estimate the target thickness, the rough approximation described before yields a second beam energy of $\ll$ 140 MeV. By summing the *CASCADE* results at 160 MeV plus 140 MeV and the results at 160 MeV plus 135 MeV, more reasonable correlations were obtained for the calculated cross sections versus the experimental intensities. Figures 3.16 and 3.17 present these summations using the Groote-Hilf-Takahashi model (Nm 3) and the Seeger model

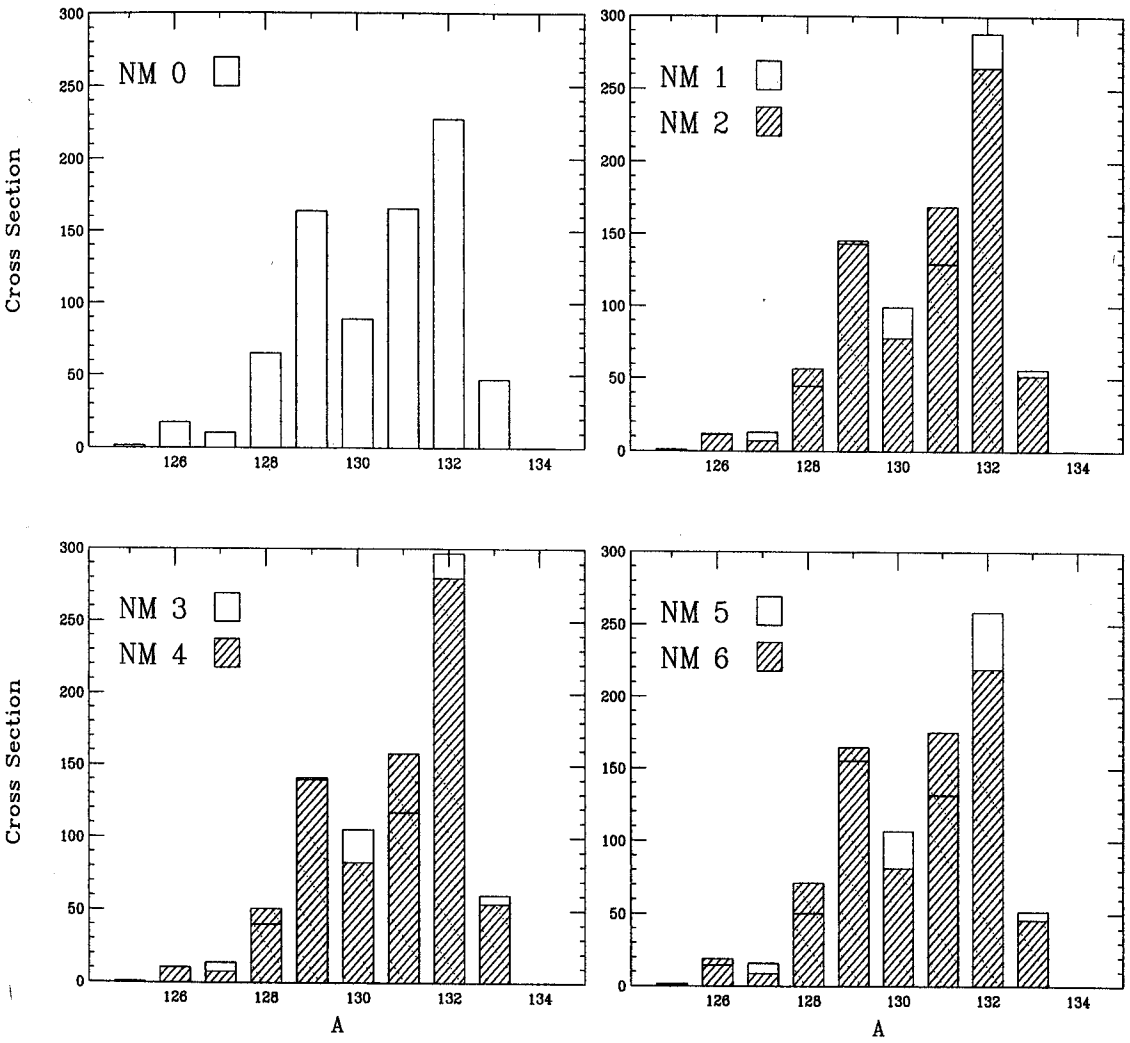

Figure 3.15: *Cascade* Nuclear Model Comparison for 160 MeV Cl on ^{100}Mo. A plot of the sum of the atomic mass (A) contributions for Z=55-59 versus Cross Section in μbarns for the Nuclear Mass Models (NM). The filled bargraph represents the corresponding model with Wigner term.

(Nm 5). There is very little differences in the summations with 140 MeV and those with 135 MeV, probably due to the nearly concentric Γ profiles. The summations done with Nm 3 and Nm 5 do not vary greatly. Although these summation plots describe the experimental results much more accurately than any of the single beam energy calculations, there are still some discrepancies. For example, the calculated ^{133}Ce and ^{134}Pr are too low and the ^{131}Ce too high. The higher experimental intensity for ^{132}Ce cannot be due to the second foil because its Γ profile is nearly identical with that for ^{132}Pr. In every case, ^{132}Pr is calculated as having the highest intensity but experimentally, ^{132}Ce and ^{133}Pr appear to predominate. (This appearance might be due to the multitude of low intensity transitions in which ^{132}Pr exists. A quantitative determination would involve using the relative abundances (branching ratios) of the transitions, most of which are unknown.)

The actual intensities observed in the experiment are the integrated sum of all of the cross sectional contributions of each individual nucleus from the beam energy down to the appropriate threshold energy, E_{th}. (See Appendix A.) These intensities are again changed by the sum of the integrated contributions from the second target. The discrepancies appear to be related to the choice of nuclear mass model used in the calculations.

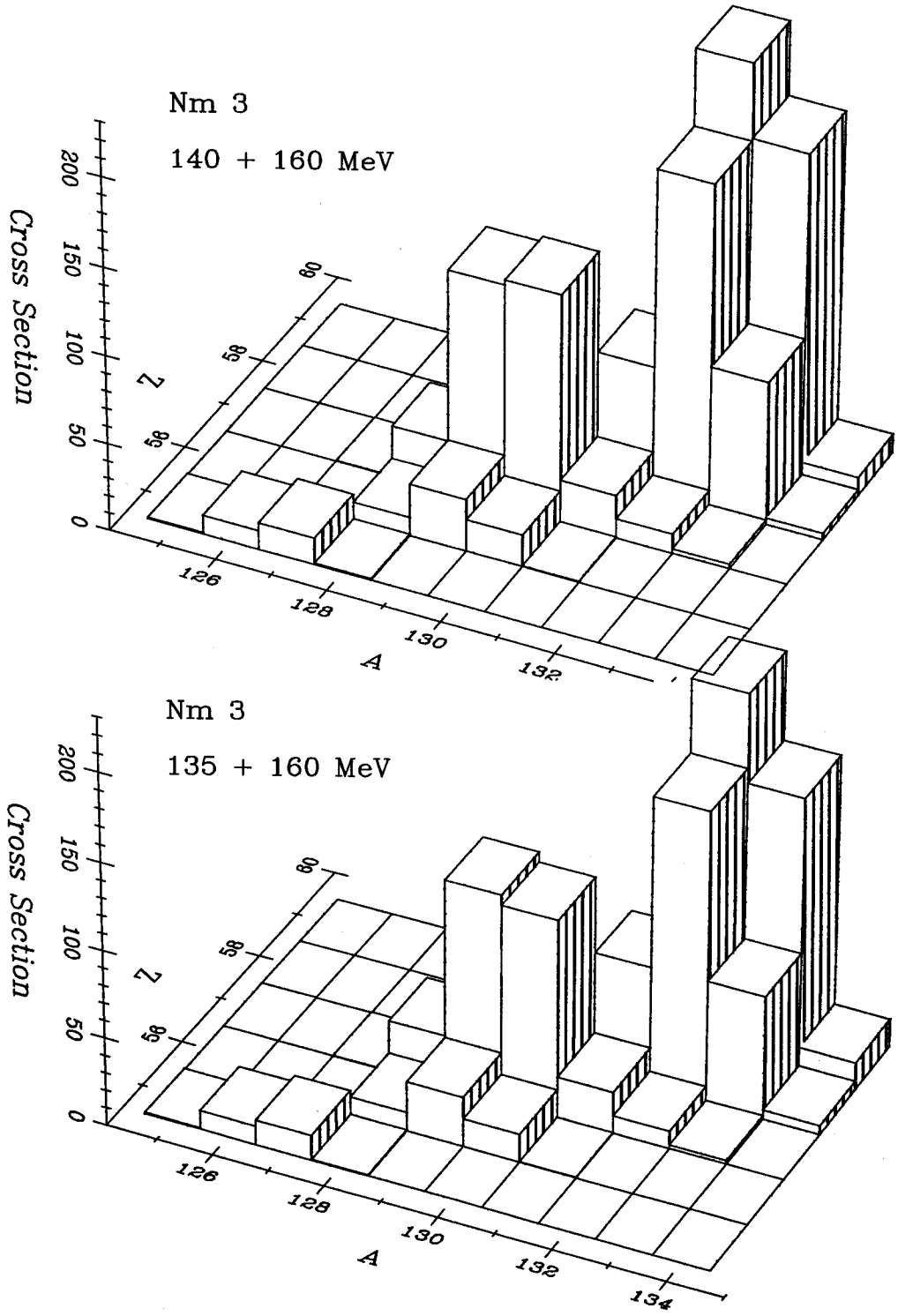

Figure 3.16: Sum of the *Cascade* cross sections for 160 MeV plus 140 MeV. Cl on ^{100}Mo and 160 MeV plus 135 MeV Cl on ^{100}Mo. A 3-D lego plot of atomic mass versus atomic number versus Cross Section for Nm 3.

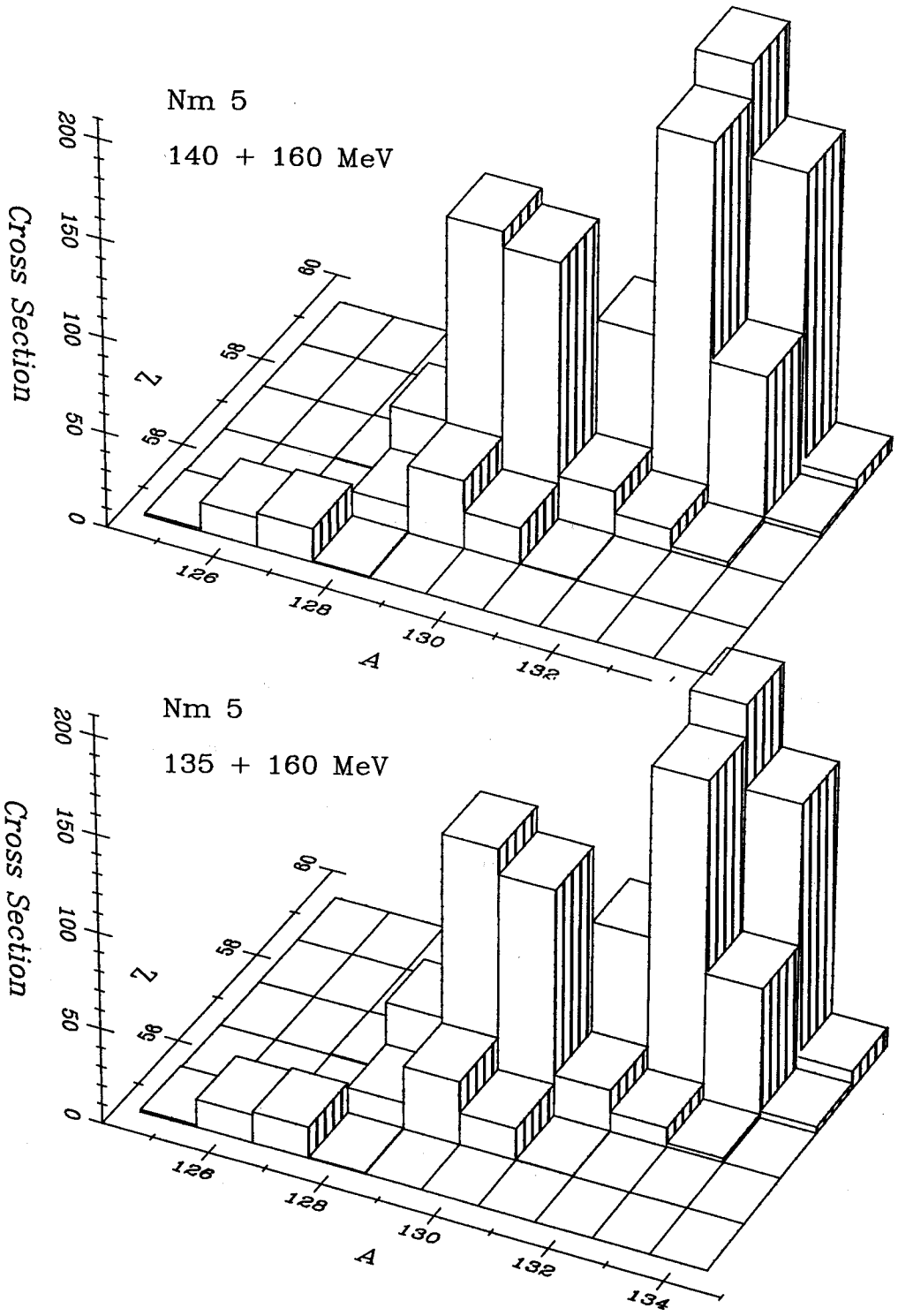

Figure 3.17: Sum of the *Cascade* cross sections for 160 MeV plus 140 MeV. Cl on ^{100}Mo and 160 MeV plus 135 MeV Cl on ^{100}Mo. A 3-D lego plot of atomic mass versus atomic number versus Cross Section for Nm 5.

3.2.2 Spin Population Matrices

The *CASCADE* calculations produce spin population matrices for every residual nucleus formed from the compound nucleus of the reaction. Cross sections and excitation energies [7] produced with a 160 MeV ^{37}Cl beam have been deduced for each unit of angular momentum (spin state) of the excited residual nucleus. [8] Figure 3.18 displays the results for the even spin states of ^{132}Pr. Part A is a 3-D representation of spin versus excitation energy versus cross section. There are two maxima observed; one at spin 14-15$\hbar$, the other at 42-43$\hbar$. This is more obvious on the accompaning contour plot in part B. The contour shows the log of the cross section as dotted curves. The edge of the plot from the upper right to the lower left approximates the yrast line, below which, no reactions occur. During this reaction, up to 54$\hbar$ of angular momentum were acquired by the residual nucleus, ^{132}Pr. The two maxima, both of which appear at approximately 18 MeV, might be interpreted as two separate decay modes. For comparison, a plot from Pühlhofer [puh77] for the reaction 76MeV ^{19}F on ^{27}Al is shown in Figure 3.23. The left side is a very simplified contour plot for one of the residual nuclei, showing particle threshold regions. The right side of the angular momentum versus excitation energy plot shows the most probable decay chains for the compound nucleus; the highest cross section is for the 2n,2α reaction. Another example is from [gui87]. Figure 3.24A shows three different fusion reaction contour plots for the production of ^{158}Er along with one for a transfer reaction. The curious thing is, ^{132}Pr is produced by only one decay mode, the 5n, yet two maxima exist. In the literature are results for ^{132}Pr from a lower spin study. [shi88] For comparison with the present experiment, identical *CASCADE* calculations were performed for their reaction ^{19}F on ^{117}Sn. Figure 3.19 shows the results in 3-D and contour plots.

[7] The excitation energy is the difference between the energy of the excited state and the energy of the ground state.

[8] This type of information may also be obtained by acquiring the outgoing particle (n, p, α) spectra along with γ rays during the reaction. [gui87] Only γ rays were acquired during this experiment.

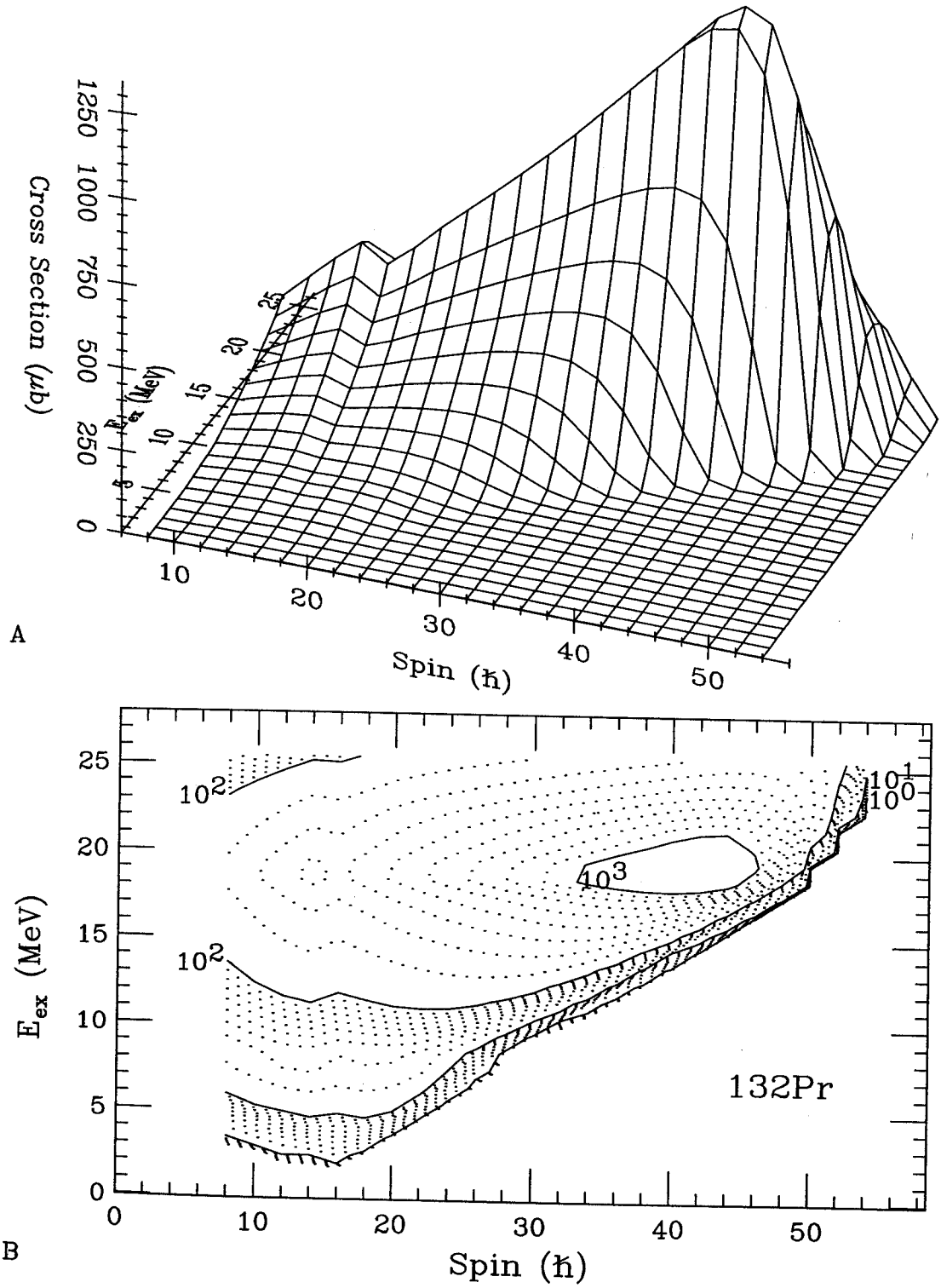

Figure 3.18: A) 3-D spin population matrix for ^{132}Pr, even spins, calculated from the ORNL experiment: 160 MeV. ^{37}Cl on ^{100}Mo, using nuclear model 3. B) The same data plotted in a contour format with the log of the cross section represented by the dotted curves.

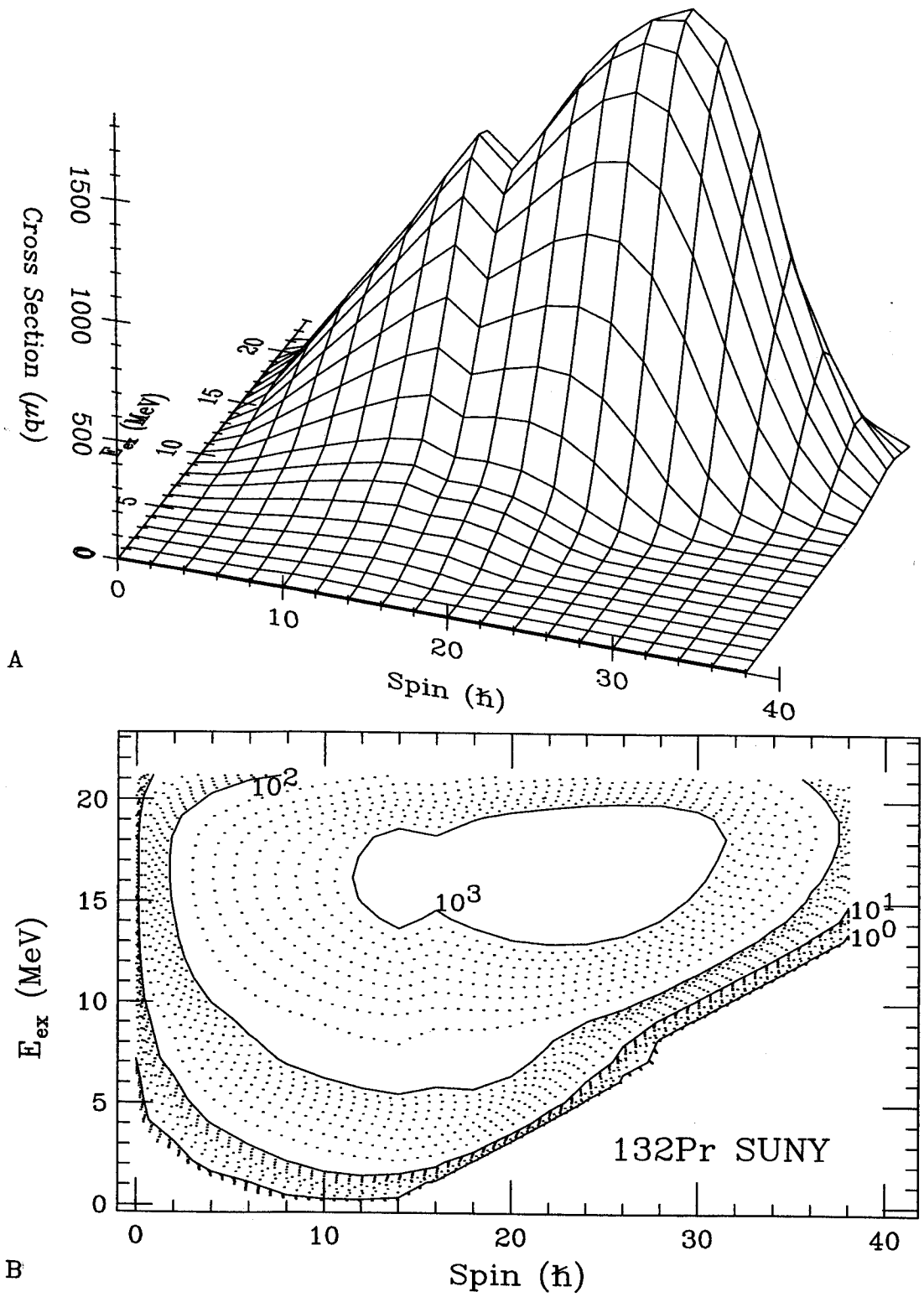

Figure 3.19: A) 3-D spin population matrix for ^{132}Pr, calculated from the Stonybrook experiment: 87 MeV. ^{19}F on ^{117}Sn from reference [hil86, shi88]. B) The same data plotted in a contour format with the log of the cross section represented by the dotted curves. Nuclear model 3 was used for the calculation.

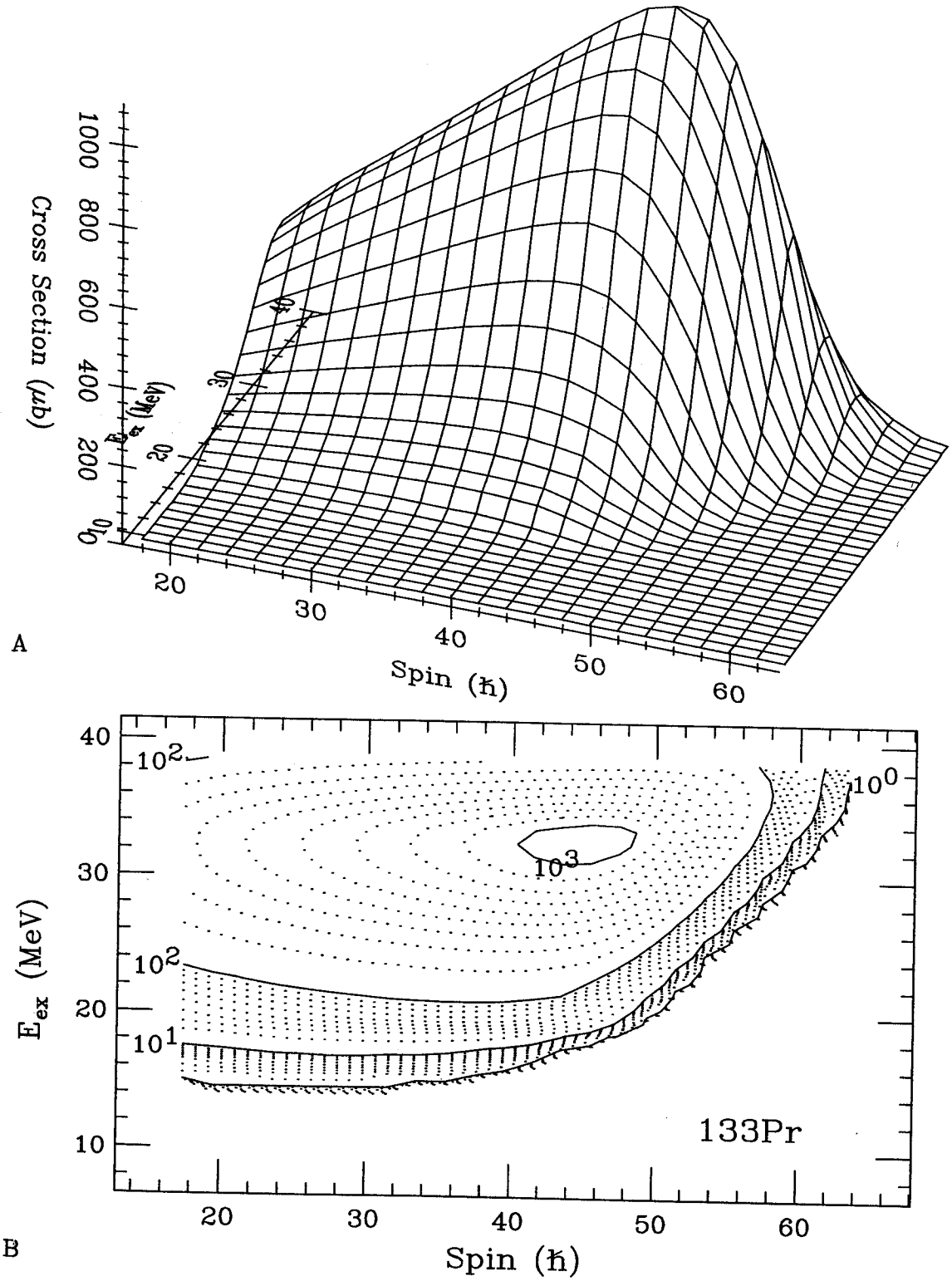

Figure 3.20: A) 3-D spin population matrix for ^{133}Pr, calculated from the ORNL experiment: 160 MeV. ^{37}Cl on ^{100}Mo, using nuclear model 3. B) The same data plotted in a contour format with the log of the cross section represented by the dotted curves.

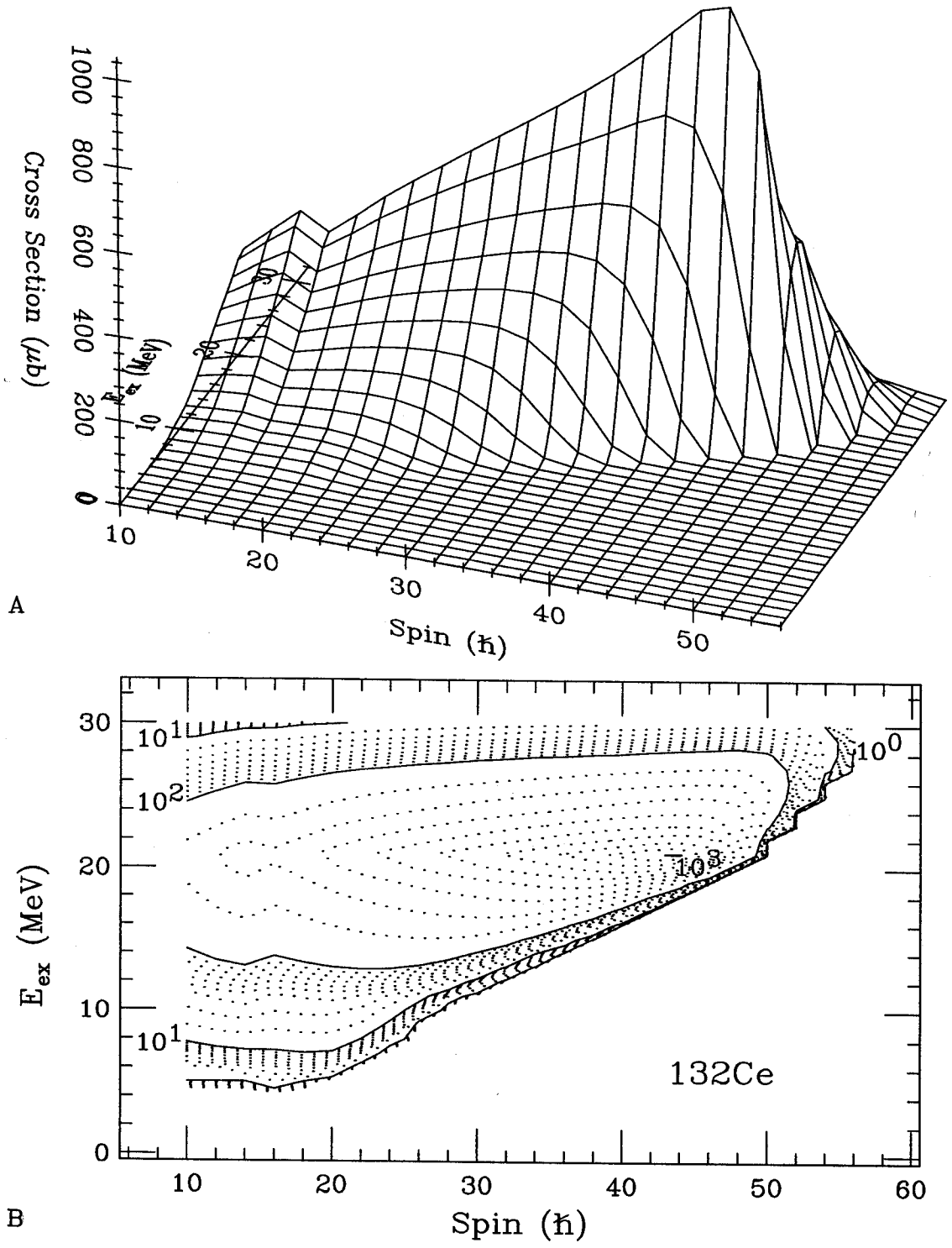

Figure 3.21: A) 3-D spin population matrix for ^{132}Ce, calculated from the ORNL experiment: 160 MeV. ^{37}Cl on ^{100}Mo, using nuclear model 3. B) The same data plotted in a contour format with the log of the cross section represented by the dotted curves.

A lower amount of angular momentum, $\approx 38\hbar$, was introduced into their reaction [9]. There are two maxima present; however, the cross sectional ratios are different and, although the first maximum is at the same spin position, 14-15$\hbar$, the second has nearly merged into the first at $\approx 26\hbar$. This suggests that this is a resonance related phenomenon [10]. Therefore, other residual nuclei from the present study were investigated. Figure 3.20 contains the results for ^{133}Pr. There is only one maximum and the profiles are very different. According to Figure 3.9, the Γ profile for $^{130}La_{\alpha}$ is similar to but slightly shifted from the profile for ^{132}Pr; the contour plot is shown in Figure 3.22. There is only one maximum; it coincides with the second maximum of ^{132}Pr but the probabilities are very different. However, Figure 3.9 shows the resonance profile for ^{132}Ce to be nearly identical with that for ^{132}Pr. Figure 3.21 shows the spin population matrix results for ^{132}Ce; the contour plot shows two maxima, the first at 15$\hbar$, the second at 43$\hbar$. The excitation energies at the maxima are slightly higher (21.03 MeV.) than those for ^{132}Pr (18.45 and 19.45 MeV.). However, the maxima for ^{132}Pr are wider so that an overlay of the two contour plots shows that an identical situation exists for these two nuclei: the same spin states are formed at identical excitation energies with nearly equivalent probability. This is understandable from the context that the compound nucleus is deexciting by the emission of 5 neutrons to form ^{132}Pr and by the emission of 3 neutrons and 1 proton to form ^{132}Ce. The only difference between the two processes is the exchange force between the neutron and proton.

[9] The Q-value for the ^{117}Sn(^{19}F, 4nγ)^{132}Pr reaction is -48.829 MeV.

[10] There is an interesting interpretation, from a heavy ion transfer reaction, for the observation of dual maxima. [gui87] Figure 3.24B is a contour plot for the reaction: ^{235}U(^{58}Ni,^{59}Ni)^{234}U. The lower spin maximum may be the 'entrance' channel for the ground state transitions and the higher one may define a band in the energy-angular momentum plane which is optimal for a 2 quasiparticle state. This is not exactly the same as what is observed for the present study since the two maxima for ^{132}Pr occur at the same excitation energy.

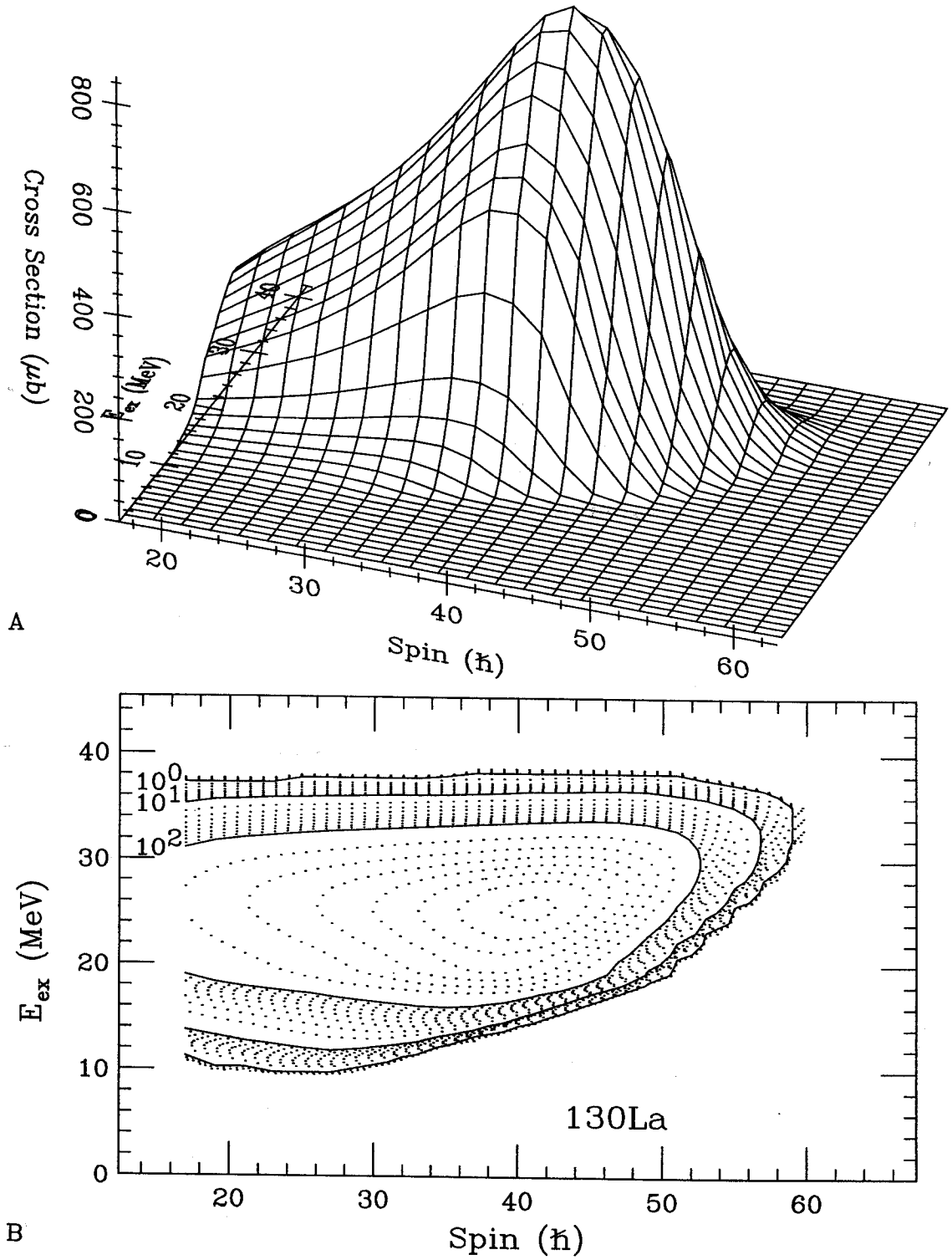

Figure 3.22: A) 3-D spin population matrix for ^{130}La, calculated from the ORNL experiment: 160 MeV. ^{37}Cl on ^{100}Mo, using nuclear model 3. B) The same data plotted in a contour format with the log of the cross section represented by the dotted curves.

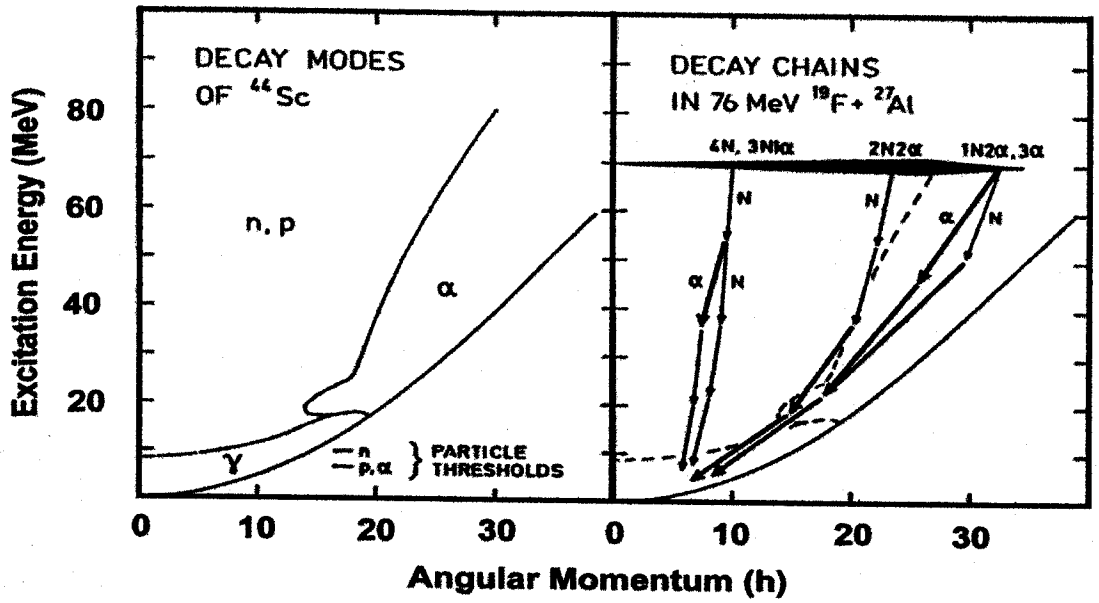

Figure 3.23: Angular momentum versus excitation energy plot for the reaction: 76 MeV ^{19}F on ^{27}Al. The left side is a very simplified contour plot showing particle threshold regions for ^{44}Sc, one of the residual nuclei. The right side of the plot shows the most probable decay chains for the compound nucleus. From [puh77].

3.2.3 Excitation Functions

After all is said and done in the theory and calculations, the fact remains that generating the nucleus of interest in a fusion-evaporation reaction is as much an art as it is a science. The final test is to determine the excitation functions. That is, experimentally determine peak ratios for a few nuclei of interest at various beam energies. Pre-experiment beam energies were tested on the Mo target at 145, 155 and 160 MeV. The results are shown in Figure 3.25. Experimental relative intensity ratios were obtained for a specific energy peak from ^{132}Pr, ^{132}Ce, ^{133}Ce, and ^{133}Pr. Only the ratios between the nuclei are relevant; the acquisition time at each beam energy is unknown, therefore, direct comparison of the different beam energy results cannot be made. Since, ^{132}Pr is the major nucleus of interest in this experiment, conditions were optimized to generate a high ratio of ^{132}Pr, this was at a beam energy of 160

MeV.

3.3 Summary

1) The γ -ray peak centroid deviations predicted by the kinematic calculations may cause energy shifts of 1 to 3 keV and may lead to multiple peak formation from detector coincidence arrays. These effects are valid for experiments that incorporate Doppler shifting of the γ -rays. The different velocities of the multiple residual particles must be accounted for. The dual velocities near the energy threshold for endothermic reactions may cause slight energy shifts in detectors with $\theta \leq 45°$. Every experiment is kinematically unique and must be investigated in order to determine exactly what the effects might be for that situation. In light of these results, it is understandable why some γ-ray energies from the same nucleus but different studies have shown up in the literature with energies differing by 1 to 2 keV and it may have consequences for some of the multiple, 'identical' bands reported.

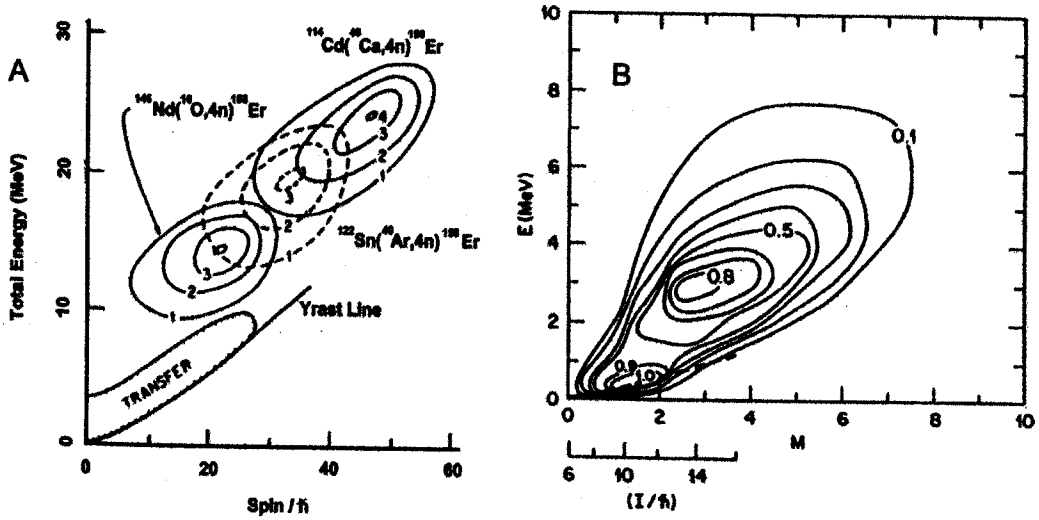

Figure 3.24: A) Three different fusion reaction contour plots for the production of ^{158}Er along with one for a transfer reaction near the yrast line. B) The observation of dual maxima on a contour plot for the reaction: ^{235}U(^{58}Ni,^{59}Ni)^{234}U. [gui87].

2) An energy calibration should not be based on a Doppler shift factor, DS_{fac} that was generated solely for one nucleus; if this is done the other nuclei may be shifted in energy and there is a risk of generating multiple peak artifacts, especially if the nucleus was formed along with an α particle. There are two ways to calibrate the energy of a γ ray spectrum. If the DS_{fac} method is used, an energy correction factor is recommended. If an energy calibration is obtained using the known energies of major peaks, as many nuclei as possible should be included and a normalizing detector should be chosen at an angle where the velocities of the residual particles are nearly equal.

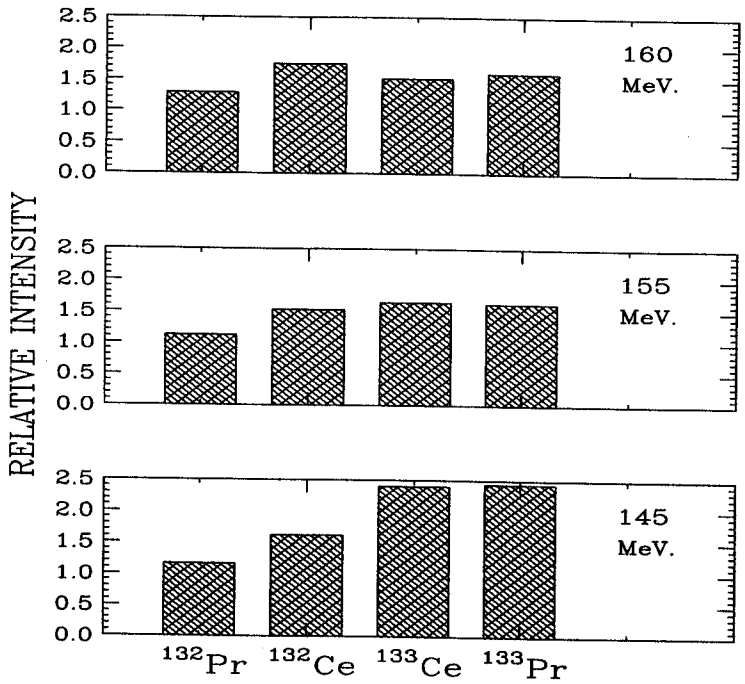

Figure 3.25: Excitation Function: Experimental relative intensity ratios obtained for specific energies from ^{132}Pr (283 keV), ^{132}Ce (325 keV), ^{133}Ce (170 keV), ^{133}Pr (310 keV) at three different Beam energies. a) 160MeV. b) 155 MeV. c) 145 MeV. All areas are normalized to the 130 keV peak for ^{132}Pr.

3) None of the nuclear mass models investigated totally describe the experimental findings. There appears to be a slight skewing in the calculations towards lower mass. Both target thickness studies and summed *CASCADE* calculations in-

dicate that dual beam reaction mechanisms predominate, producing ratios of nuclei that differ from the single beam predicted values.

Chapter 4

Experimental

The experiment was conducted at the Holifield Heavy Ion Research Facility (HHIRF) at Oak Ridge National Laboratory in Tennessee. [1] Information about the target, the beam accelerator facility, the γ-ray detector system and the electronics used for data acquisition is presented in this chapter.

4.1 Target

The target consisted of two, separated, thin layers of isotopically enriched ^{100}Mo, $\approx$ 0.5 mg/cm^2. It was constructed in such a way so that the reaction products would totally recoil into vacuum, resulting in doppler shifting of the γ rays, as discussed in Section 3.1.4. The Mo foils were supported by a Pb frame. The previously used target, borrowed from Lawrence Berkeley Laboratory was supplied with an isotopic and elemental spectrographic analysis. The analysis was performed at Oak Ridge National Laboratory. Table 4.1 lists the isotopes of Mo and their atomic percentage in the target. The limits quoted are an expression of the precision of this measurement only. The error is estimated at less than 1% from known sources of systematic errors. In addition, spectrographic analysis yielded a semi-quantitative estimate for Na (0.0015%) and Si (0.0020%). These are very likely normal surface contaminants

[1] As of October 1993, the official name is Holifield Radioactive Ion Beam Facility (HRIBF).

and not part of the bulk material.

Table 4.1: Isotopic Analysis of the ^{100}Mo target used in the present experiment.

Isotope	Atomic %	Precision
92	0.73	0.01
94	0.284	0.00
95	0.50	0.01
96	0.75	0.01
97	0.404	0.00
98	1.68	0.01
100	95.65	0.02

4.2 Beam

4.2.1 Electrostatic Accelerator Operation

In order to attain sufficient kinetic energy to initiate a nuclear reaction, a beam of particles must be accelerated to a large fraction of the speed of light. One of the most basic types of devices designed for this purpose is an electrostatic accelerator. An electrostatic accelerator operates on the principle that the simplest way to accelerate a charged particle is to move it through a static potential difference V between two electrodes. Then the particle with charge $+q$ is accelerated from the positive to the negative electrode, acquiring a kinetic energy of qV [kra88, bla69]. The Cockcroft Walton device was one of the earliest electrostatic machines. It incorporated an RC time constant voltage multiplication technique, composed of high voltage capacitors connected in series during the positive AC or charging cycle and in parallel, during the negative AC or discharging cycle. High voltages (10 MeV) with high currents (ma) were obtained but many sensitive experiments could not tolerate the high AC ripple that accompanied the voltage. The van de Graaff accelerator was developed to

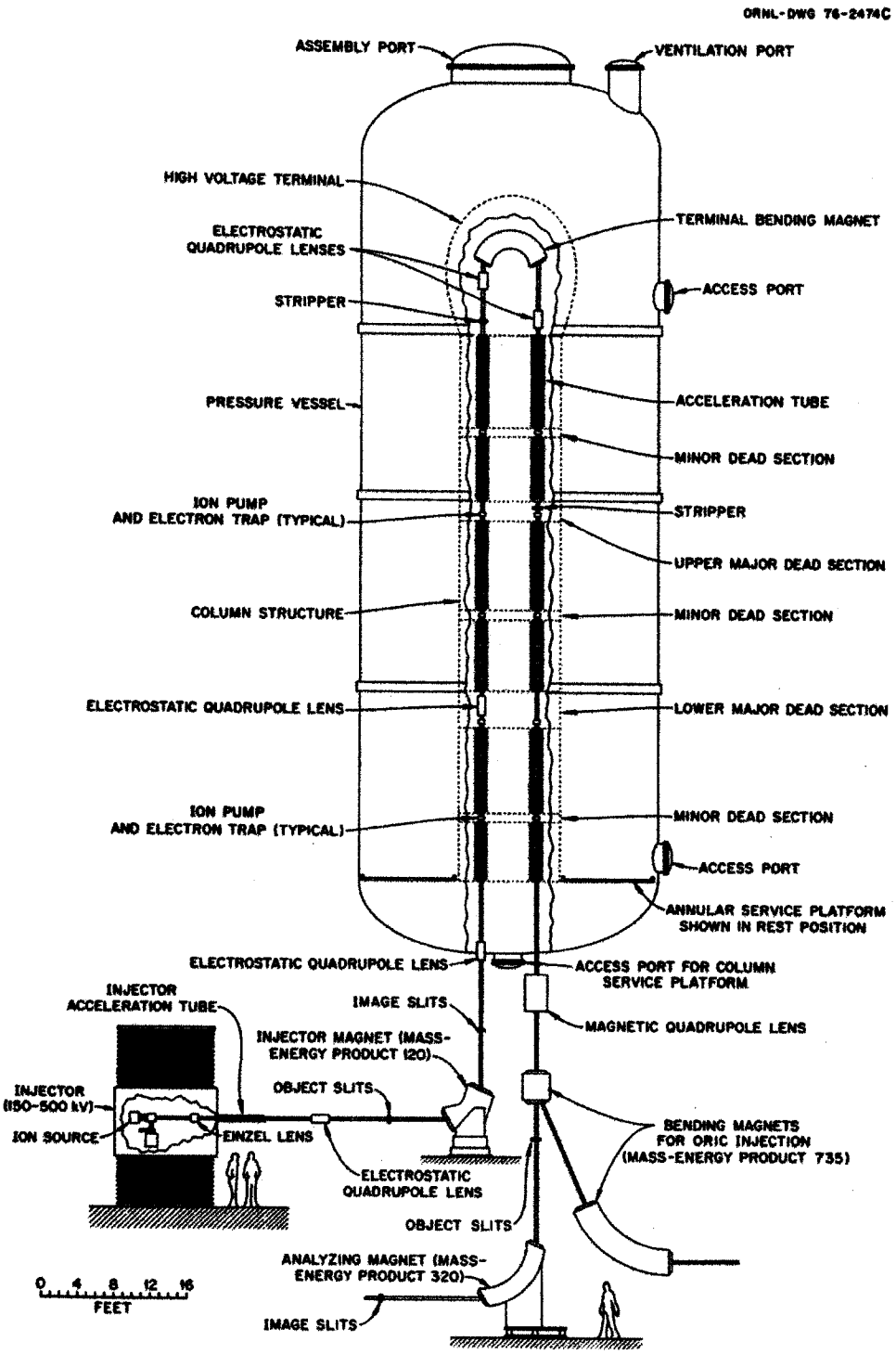

Figure 4.1: Schematic diagram of the Tandem Van de Graaff accelerator at Holifield Heavy Ion Research Facility, Oak Ridge National Laboratory. Drawing 76-2474C. From reference [hol87].

provide a smoother beam.

A van de Graaff type of accelerator works on the principle of electrostatics: Any charge on the inside of a hollow sphere is transferred to the external surface when contact is made between the surfaces. A moving belt maintains the charge between the high voltage terminal and ground and an insulating gas must be used to prevent discharging to ground. Stable ($\pm 0.1\%$) terminal voltages are produced with a current in the μa range. One of the mechanical drawbacks of this design is that the positive ion source is located within the high voltage terminal, making routine ion source maintenance and beam changes cumbersome. A double stage, tandem van de Graaff accelerator was then designed with the ion source outside the high voltage terminal. Negative ions must be produced in this ion source to be accelerated toward the positive terminal in the first stage. The negative ion beam then moves through a charge exchange chamber, gaining a positive charge, and is accelerated in the second stage toward the target at ground potential. Besides making the ion source more accessible, the tandem achieves much higher voltages than the single stage van de Graaff. A later enhancement of the design involved folding the tandem at the high voltage terminal, making a more compact, space efficient accelerator. The HHIRF tandem has this folded, vertical design.

4.2.2 HHIRF Facility

A view of the HHIRF folded, Tandem van de Graaff electrostatic accelerator [hol87] is presented in Figure 4.1. The high-tension terminal can be maintained up to 25 Mv relative to ground using a chain of metal (Pelletron) cylinders linked by insulating spacers. An insulating gas (2000 m^3 of pure SF_6 at 7 atm) surrounds the high-tension terminal and prevents it from discharging to ground. After exiting the ion source, the negative ions are injected into the accelerator vacuum system. Near the top of the column, the accelerated negative ions pass through a metal foil to remove electrons.

The positive ions created, are redirected, via electrostatic lenses and a magnet, down the column to achieve an increase in the kinetic energy. [kra88] The beam produced for this experiment started in the ion source as Cl^- and was accelerated to 160 MeV $^{37}Cl^{7+}$ at the target. The beam current, typically in tens of partical nanoamps (pna), is measured with a Faraday cup. A conventional beam current value can be calculated by multiplying the measured pna by the electric charge per particle.

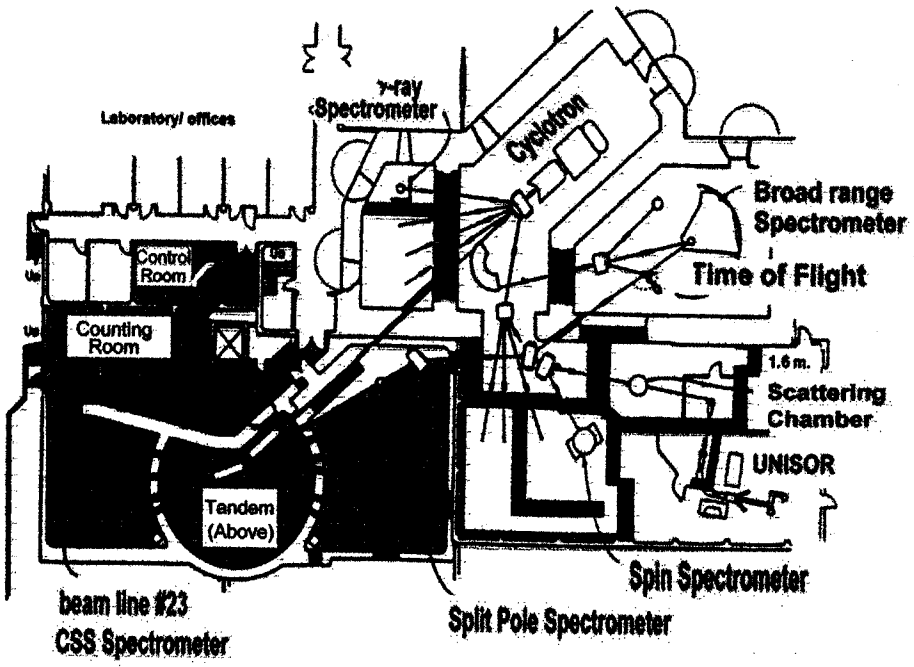

Figure 4.2: Partial floor plan of the HHIRF facility showing the relative placements of the tandem, beam line #23 and the compton suppression γ-ray spectrometer. Adapted from references [kra88, hol87].

Figure 4.2 displays a partial room layout of the HHIRF facility showing the relative placement of the vertical tandem with beam line 23 connecting to the compton suppression γ-ray spectrometer.

4.3 Detector System

There are two types of detectors used in this experiment; scintillation detectors [2] based on light emission, and semiconductors, in which a signal is created by means of electron/hole pair formation. In the Compton-suppression (CSS) spectrometer at HHIRF, both are combined into what is referred to as a 4π detector,i.e., a dodecahedral (i.e.,soccer ball) shaped device that contains multiple detectors covering a multitude of angles from the target for a 3-dimensional perspective. The general mechanical and theoretical operation of both types of detectors are discussed, then specific information about the CSS is presented.

4.3.1 Scintillation Counters

Bismuth-germanium oxide (BGO) and NaI (activated with 0.1- 0.2 % thallium) are scintillators; i.e., charged particles, x-rays, and γ rays impinging on the surface produce a flash of light within the material. NaI has a moderate density (3.7 g/cm^3); 35 eV of energy is needed to produce one electron/hole pair. Photons are produced through a complex cascade mechanism involving many of these pairs that are produced. BGO has a low light output relative to NaI(Tl) (10-15%) but is much more dense, making compact 4π detector arrays possible [nol85].

The hygroscopic NaI(Tl) crystal is sealed in a layer of aluminum coated with magnesium oxide for internal light reflection. The ionizing radiation produces e^-'s which emit visible light in the 330-500 nm region. The light induces the emission of photoelectrons from a photosensitive cathode (a cesium antimony alloy) in a photomultiplier tube and is converted into a signal pulse . The cathode is separated from the anode by a series of dynodes that provide multiplication stages for the photoelectron cascade. Electrons are accelerated toward successive dynodes, since each is

[2]The following types of crystals are used in Nuclear Physics experiments for their scintillation properties: NaI(Tl), CsI(Na,Tl, or undoped), BaF_2, BGO, $CdWO_4$, CsF, LiI(Eu), CaF_2(Eu).

maintained at progressively more positive voltage (800-1500 V total). Every photo-electron impinging on the first stage causes several secondary electrons to be ejected and accelerated to the next stage, forming a cascade of e^-'s to be collected at the anode with a gain between 10^5 and 10^7 [mal81]. The height of the signal resulting from the e^- pulse is proportional to the energy of the incident radiation.

4.3.2 Intrinsic Semiconductor Operation

An intrinsic semiconductor is a pure material that conducts by the excitation of valence electrons into equal numbers of holes (h^+'s) and electrons (e^-'s). Whether a material is a conductor, semiconductor or insulator is mainly dependent on the magnitude of the energy gap between the filled valence band and empty conduction band in the lattice structure. If this band gap is equal to zero, the material is a conductor; if it is much greater than zero, the material is an insulator; if it is slightly greater than zero ($\approx$ 1eV), it is a semiconductor [mal81].

An input of energy greater than the band gap is necessary for conduction. This energy may be provided by thermal excitation or photon radiation. When an e^- is promoted to the conduction band, a h^+ is simultaneously created in the valence band; under the influence of an electric field, the h^+'s and e^-'s can migrate through the lattice. [3]

In order to use the pure Ge crystal as a γ-ray detector, a reverse bias diode configuration is constructed. Electrical contacts must be made. Instead of using metals – the technology used in electronic diodes– a more efficient process has been developed: A thin layer (0.3 μm) of B^- is implanted into one side of the HPGe, and Li^+ is implanted in an inner core area (500 μm). See Figure 4.3. This constitutes a negative and positive contact for what is called n-type HPGe.

[3]The energy required to produce an e^-/h^+ pair for a Ge crystal, with a band gap of 0.67, is 2.96 eV at 77 K [fri81].

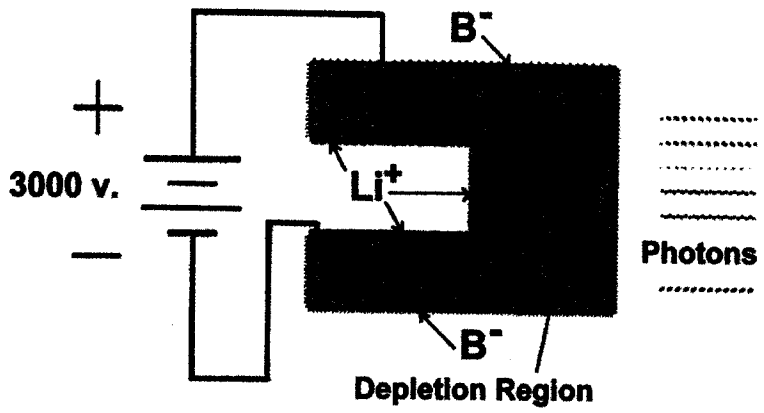

Figure 4.3: A pictorial view of a reverse biased HPGe crystal showing the Li^+ and B^- contacts and the depletion region of the p-n junction.

HPGe detectors can be manipulated at room temperature instead of liquid nitrogen temperature. (Taking a Ge(Li) detector to room temperature would cause random migration of the Li^+ ions and possibly ruin the depletion region [gou74] [4].) Because charge carriers are free to migrate in the crystal and their drift directions are opposite, they can cancel each other, resulting in the formation of a depletion region called a p – n junction, in which the concentration of charge carriers is lower than in the rest of the material. This reduces the conduction in this area to nearly zero. When a voltage is connected across the junction with a reverse bias, h^+'s and e^-'s move away from the junction. This creates a small thermally induced reverse current which increases with temperature. [5]

The detector signal is an induced current pulse that arises from the absorption of γ rays. The resulting electron-hole pairs created are swept out of the crystal by the electric field. The current pulse is integrated at the input of a charge sensitive pream-

[4]Using n-type HPGe, instead of p-type has the following advantages:
- A better signal is obtained since the radiation is not exposed to the inactive Li^+ drifted region which causes scattering and absorption loss of low energy photons.
- Fast neutrons generate negatively charged lattice defects which trap h^+s but not e^-. Since the h^+ collection process is of secondary importance in n-type HPGe, the signal is less sensitive to radiation damage[egg79].

[5]Liquid nitrogen cooling is used to reduce excessive thermal noise.

plifier [egg79]. If the photon- induced charged carrier production rate is considerably greater than the thermal production rate, the reverse bias current pulse is directly proportional to the photon flux. The drift velocity for e^-'s and h^+'s is approximately 10^7 cm/s for field gradients of 1000 V/cm [fri81]. The charge carrier transit times (pulse rise times) are in the subnanosecond range, making semiconductors suited for fast coincidence experiments.

4.3.3 Interaction of γ Rays in a Detector

Absorption of γ rays in the detector follows an exponential law:

$$I = I_o e^{-x\alpha}$$

where, I_o is the incident photon flux; I is the transmitted photon flux; x is the detector thickness and α is the absorption coefficient. There are three major processes that contribute to the photon absorption cross section: The photoelectric effect (pe), compton scattering (c), and pair production (pp). The values of the absorption coefficient α for each of these processes depend on the proton number Z and the photon energy E in the following manner:

$$\alpha_{pe} = \frac{Z^5}{E^{7/2}} \qquad \alpha_c = \frac{Z}{E^e} \qquad \alpha_{pp} = \frac{Z^2}{E^b}$$

where e and b are various positive values dependent on the photon energy. This can be seen in Figure 4.4, absorption coefficient versus γ ray energy.

Photoelectric Effect

In the photoelectric effect, low-energy photons are absorbed by a bound e^- in an atom in the detector lattice. An electron is ejected from the K or other shell of the atom with an energy equal to the photon energy minus the binding energy of the e^-. The photon energy is converted into the kinetic energy of the ejected atomic e^- and

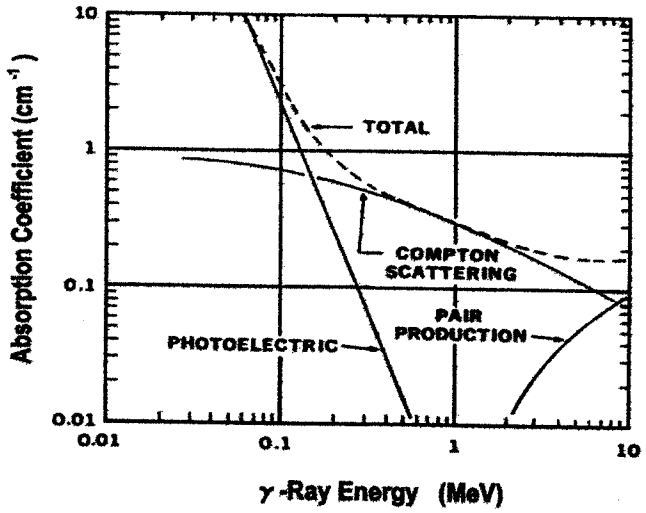

Figure 4.4: A plot of photon absorption coefficients versus energy for Germanium. From [gou74].

the x-rays or Auger electrons emitted during the atomic relaxation process [gou74]. If the x-rays escape from the detector, the photon energy recorded by the detector will be lower by their energy, resulting in an 'escape' peak at a lower energy than the photopeak [hor60].

Compton Scattering

Compton scattering is inelastic, incoherent scattering of photons by atomic e^-'s in the outer shells. The γ ray transfers part of its energy to the electron and is deflected from its original path. The energy of the recoiling e^- ranges from zero to a maximum value when θ equals zero and ϕ equals 180 degrees (ie., the photon is backscattered and the e^- is forward scattered.) This creates a broad energy distribution with a maximum value called the compton edge, located at a position lower in energy than the photopeak. In addition, the backscattered photon, now degraded in energy, can interact again with e^- in the detector material, producing yet another peak in the spectrum. The sum of the energies of the backscattered peak and the compton edge peak is equal to the energy of the γ ray photopeak. This is shown schematically in

Figure 4.5.

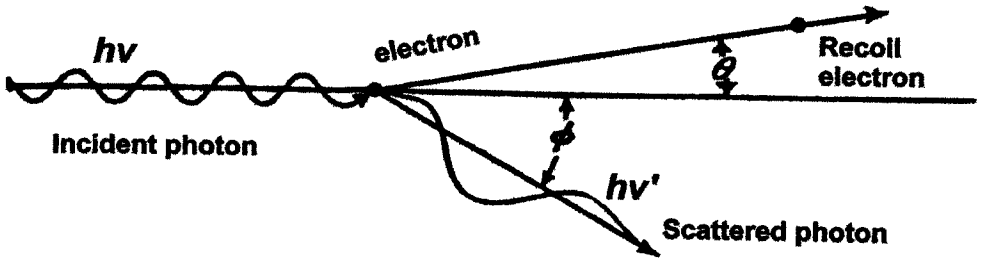

Figure 4.5: Compton Scattering.

Pair Production

Pair production becomes a significant method for photon interaction at energies greater than 2 $m_o c^2$ (1.022 MeV). At this energy, the photon can interact with an e^- in a negative energy state, promoting it into a positive energy state, and leaving behind a negative-energy hole called a positron (e^+). The e^- is swept out of the depletion region to be part of the photopeak (E). The positron forms a positronium ion with another e^- in the detector. If they have antiparallel spins, [6] they annihilate within 10^{-10}s., creating two photons, each with 511 keV energy (the rest mass of the e^-). If these photons leave without interacting with the detector, escape peaks can be formed at energies of E- 511 keV and E- 2(511 keV) [fri81].

In addition, peaks may be observed at energies higher than the photopeak. If two γ rays are related in a cascade fashion, a low intensity peak may appear that is the sum of both photopeak energies.

An illustration of these spectral characteristics is shown in the "Normal Spectrum" in Figure 4.6. Using γ rays obtained from a ^{60}Co source, this shows the photopeaks, compton edge, single- and double- escape peaks, positron-annihilation peak, and a backscattering peak.

[6] In order to conserve angular momentum three or more photons will be emitted if the spins are parallel. However, there is a very low probability for the occurance of this process[ary84].

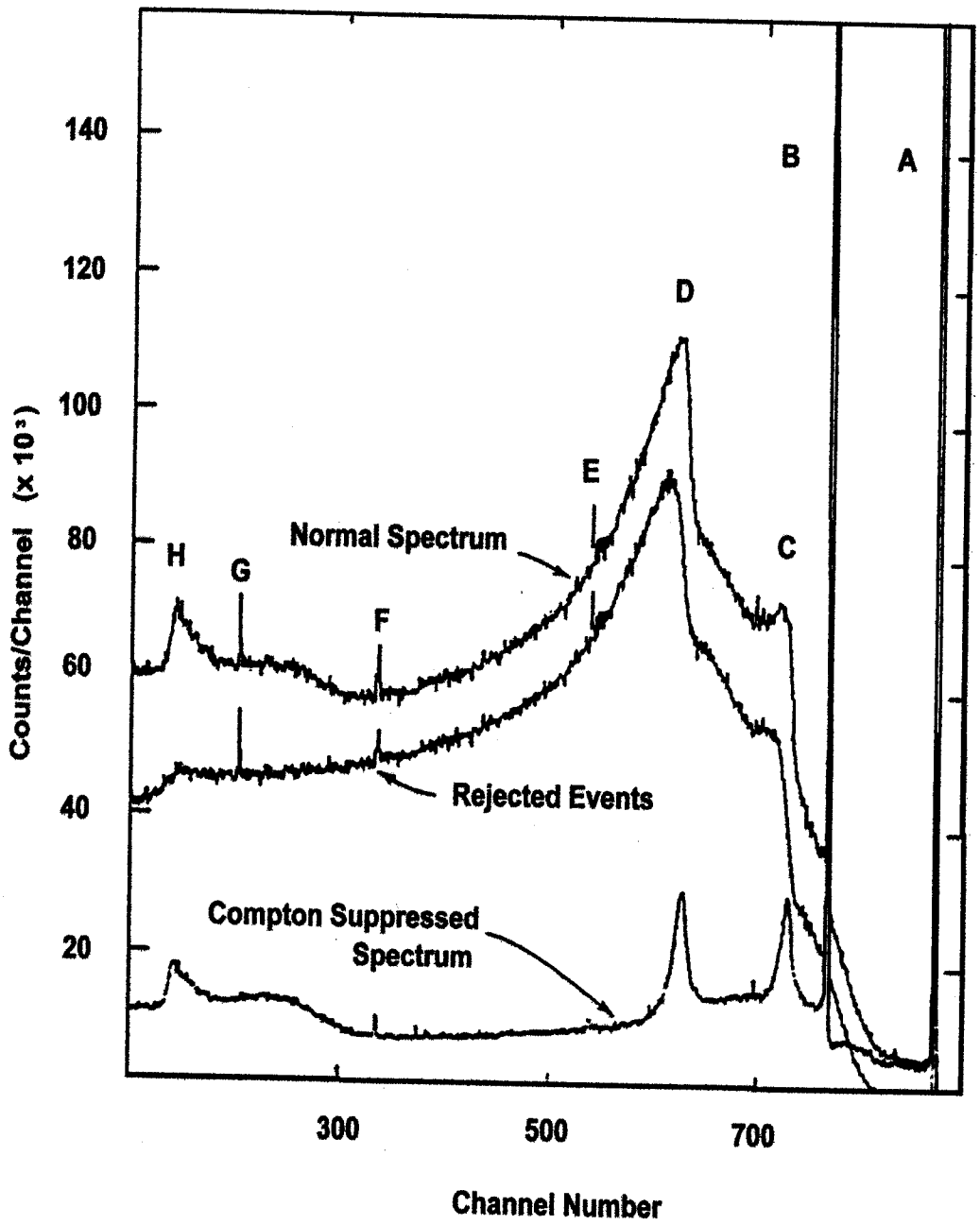

Figure 4.6: γ-ray spectra of ^{60}Co taken with the Compton- Suppression Spectrometer at HHIRF. The top spectrum is the normal compton plus photopeak spectrum; middle is the scattered events from the shield detectors; and bottom is the compton suppressed spectrum. *A*) 1333-keV photopeak; *B*) 1170-keV photopeak; *C*) 1333-keV compton edge; *D*) 1170-keV compton edge; *E*) 1333-keV single escape peak; *F*) 511-keV $\gamma\pm$ annihilation peak; *G*) 1333-keV double escape peak; *H*) compton backscattering. From [hol87].

Both the compton and escape peaks can be reduced relative to the photopeaks by placing the Ge detector inside a larger detector and electronically connecting them in anticoincidence so that only pulses from the internal detector that are not in coincidence with the outer or shield detector are recorded. This is referred to as an anti-compton or compton suppression spectrometer. The effect on the γ- ray spectrum of ^{60}Co can be seen in the compton- suppressed spectrum of Figure 4.6.

These photoprocesses described, occur in both scintillation and semiconductor detectors. Figure 4.7 compares a ^{137}Cs γ- ray spectrum taken with a NaI(Tl) scintillation detector and a Ge(Li) semiconductor detector. The peak full-width at half- maximum height measurement (FWHM) from the Ge(Li) detector is 1.85 keV compared with 56 keV from the NaI(Tl) detector. For this reason, high-efficiency scintillators are used in suppression shields which detect scattered radiation and low-efficiency, high-resolution Ge detectors are used to detect γ- ray photopeaks.

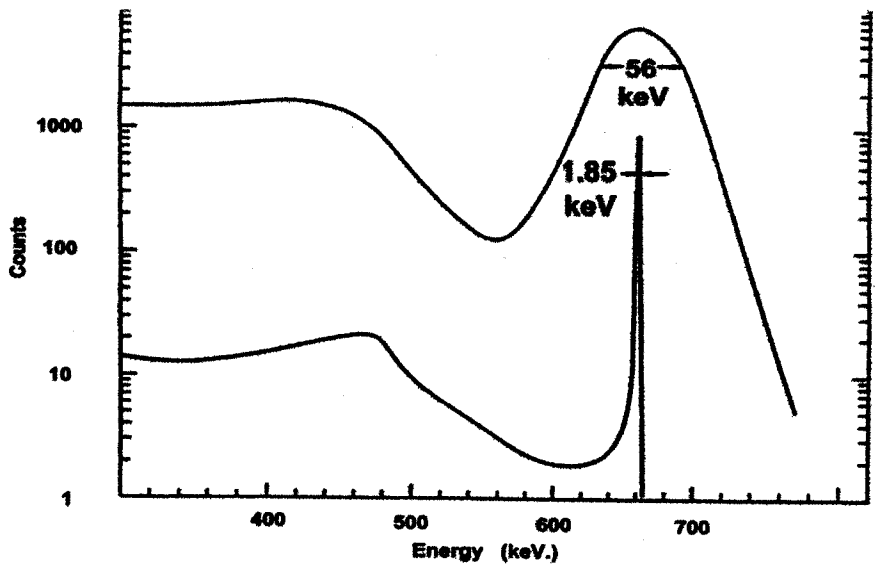

Figure 4.7: A comparison of γ ray spectra of ^{137}Cs taken with a NaI(Tl) scintillation detector (Top) and a Ge(Li) semiconductor detector (Bottom). From [fri81].

4.3.4 Compton-Suppression Spectrometer at HHIRF

The reaction was investigated using the Compact Ball compton-suppression γ- ray spectrometer at HHIRF, Oak Ridge National Laboratory. The beam from the Tandem is directed into beam line 23, passes through a series of quadrupole focusing electromagnets and a magnetic steerer assembly, and then into the target area. The target assembly is situated behind the vacuum beam line in the middle of the detector array. The detector array is mounted on a mechanical drive system that separates the Ball into halves, designated North (N) and South (S).

The spectrometer is a 4π arrangement of twenty one detector units. The structural geometry of the frame support for the detector and shields is shown in Figure 4.8. The N and S designations represent detector positions within the spectrometer frame. See Figure 4.8. The detector angles with respect to the beam direction (θ) and from the vertical axis perpendicular to the beam line (ϕ), are listed in Table 4.2. The shield codes represent the detector type and shape: B and N stand for BGO and NaI; P and H are pentagon and hexagon, respectively. There are detectors located at duplicate θ angles. These are grouped together in the table. For example, the first two detectors have a 44.89° θ angle.

A schematic view of a pentagonal BGO HPGe detector unit is shown in Figure 4.10. Each individual detector unit consists of four main elements: N-type intrinsic HPGe detector with LN_2 cooling, [7] BGO Catcher, BGO or NaI(Tl) shield, Pb collimators plus absorber foils. When all of the detectors are in place the CSS looks like the drawing in Figure 4.9. The two hemispherical sections of the frame are shown separated; the arrow indicates the direction of beam flow.

Ge detectors have the disadvantage that they compton scatter a lot of the γ radiation. The amount of photon absorption is only approximately 25% efficient

[7] For example, EG&G ORTEC HPGe detector GMX 30195-S CG-Duet, Bias 3000 volts negative, Serial No. 29-N10425B

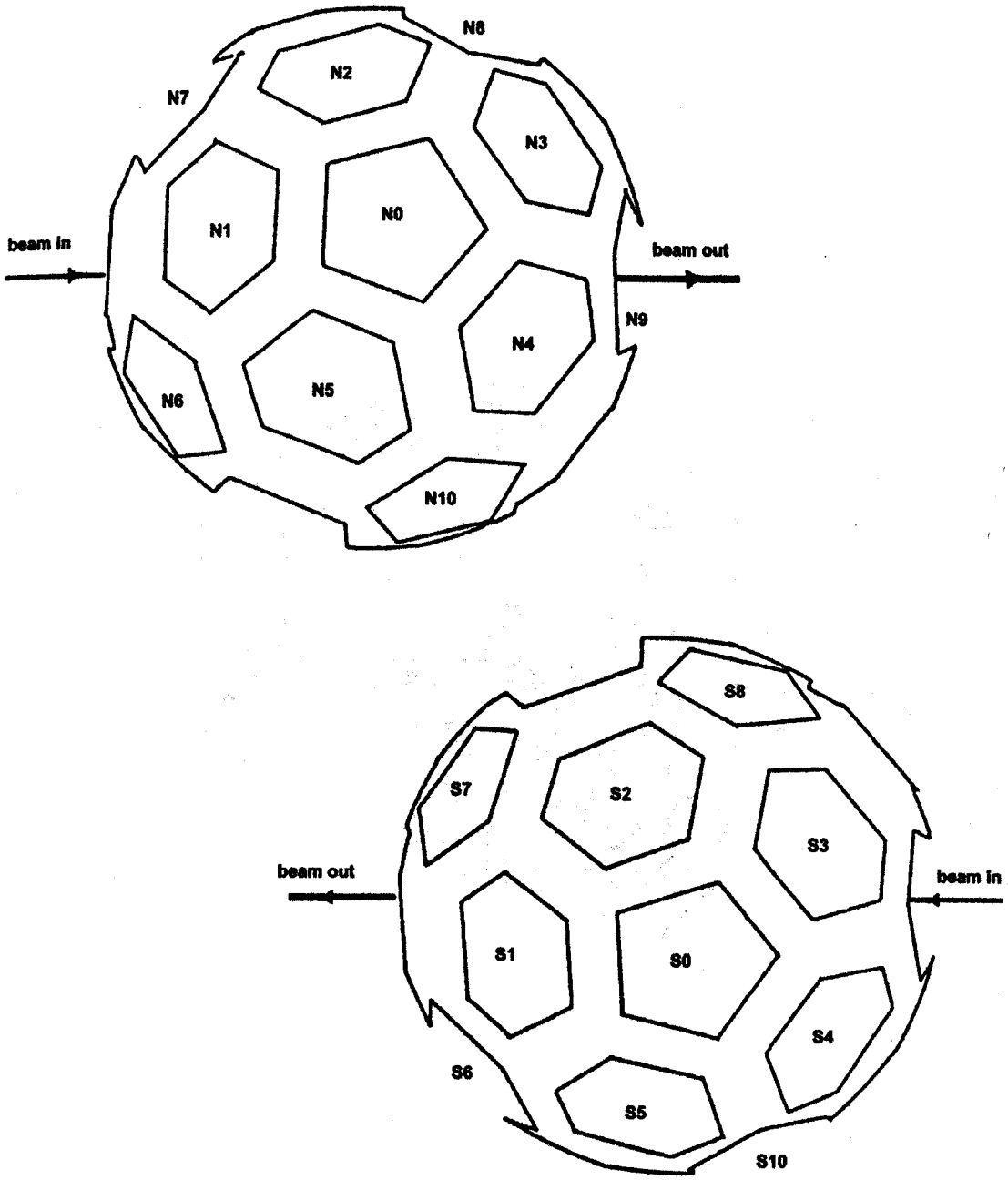

Figure 4.8: Geometry of the HHIRF Compact Ball Compton Suppression Spectrometer, showing the frame support for the detectors and shields. N and S designations represent detector numbers.

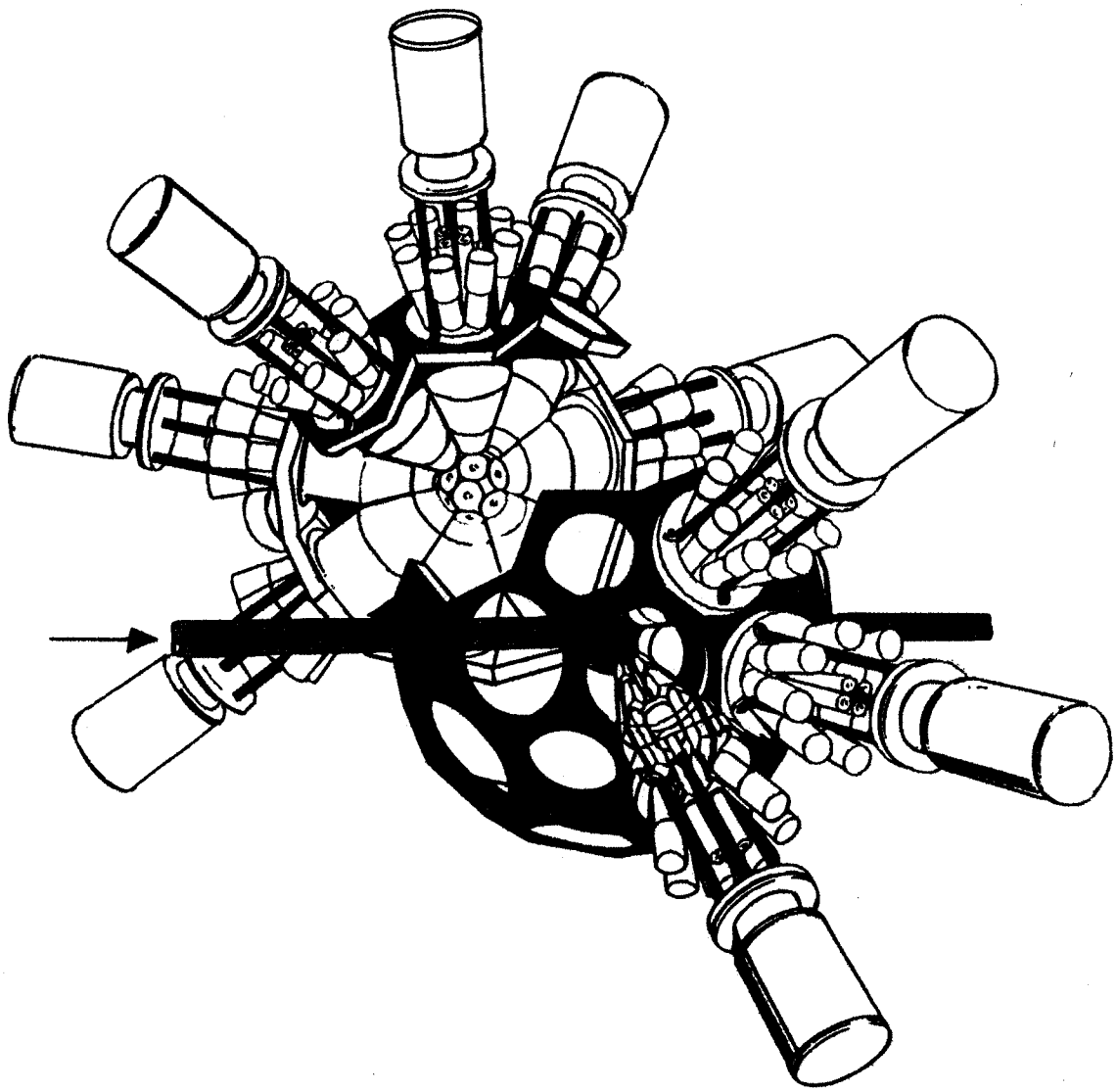

Figure 4.9: A drawing of the CSS Spectrometer with the hemispheres separated and all the detectors in place. The arrow indicates the beam direction.

compared with a NaI(Tl) detector. [8] In order to improve the signal to background ratio, Ge detectors are operated with a surrounding shield detector which collects the scattered radiation [nol85].

An annular BGO detector, located immediately behind each Ge crystal, is used to detect γ rays that are forward scattered from the Ge. This detector is constructed in two halves, each connected to a PM tube. Before being placed inside the shield, a disc shaped plastic collar was attached to the front of the Ge detector, separated by metal spacers. A cylindrical copper shield was attached to each unit between the detector crystals and the pre-amplifier electronics.

There are 12 BGO (6 hexagonal, 6 pentagonal) and 9 NaI (4 hexagonal, 5 pentagonal) shields used in the array, [9] each side viewed by a photomultiplier tube, for a total of 110 PMT shield signals (one pentagonal unit was not used). After the detector units were placed in the shields, Pb collimators with an internal conical shape and hexagonal or pentagonal external shape were attached [10] to the front of each shield. This was done in order to eliminate spurious peaks caused by compton scattering between detectors. This effect is described in reference [gie71]. Disk-shaped tin and copper absorbers were taped onto the Pb collimators in order to limit neutron damage and control the range of x-ray energies introduced to the detectors. γ-ray transmissions for various energies are listed individually in Table 4.3 for Sn and Cu absorbers and also listed as a % when the two absorbers are used simultaneously.

The BGO shields provide a background-suppression factor of 5 to 6; the NaI(Tl) shields provide a suppression factor that is half of this amount [hol87]. An illustration of the amount of suppression achieved with a BGO shield is shown in Figure 4.6. A standard ^{60}Co source was used to obtain the γ-ray spectra.

[8] Efficiencies are measured relative to a standard 76 mm $\times$ 76 mm NaI detector at 25 cm for ^{60}Co, 1333 keV peak.

[9] The 21st detector was not used in order to eliminate beam damage to the crystal surface. Its position is $N9$, directly in line with the beam.

[10] with VELCRO and masking tape

Table 4.2: The Positions of Ge Detectors and their Compton Suppression Shields in the CSS Spectrometer at HHIRF.

Angle θ	Angle ϕ	Detector	Shield Type	Position
44.89	35.97	4	BGO Pentagon	S7
	144.03	9	BGO Pentagon	S6
45.35	236.30	17	BGO Hexagon	N4
	303.70	20	BGO Hexagon	N3
61.45	90.00	7	BGO Hexagon	S1
69.67	189.72	18	BGO Pentagon	N10
	350.28	13	NaI Pentagon	N8
76.36	270.00	14	NaI Pentagon	N0
88.45	50.28	1	NaI Hexagon	S2
	129.72	10	NaI Hexagon	S5
0.00	90.00	not used	NaI Pentagon	N9
135.11	324.03	15	BGO Pentagon	N7
	215.97	12	BGO Pentagon	N6
134.65	123.70	6	BGO Hexagon	S4
	56.30	2	BGO Hexagon	S3
118.55	270.00	19	BGO Hexagon	N1
110.33	170.28	5	NaI Pentagon	S10
	9.72	3	BGO Pentagon	S8
103.64	90.00	8	NaI Pentagon	S0
91.55	309.72	16	NaI Hexagon	N2
	230.28	11	NaI Hexagon	N5

θ is measured with respect to the beam direction
ϕ is taken from the vertical axis perpendicular to the beam line.
N and S codes refer to the detector position in the CSS Spectrometer.
See Figure 4.8 for a pictorial view of the detectors' relative spacial positions.

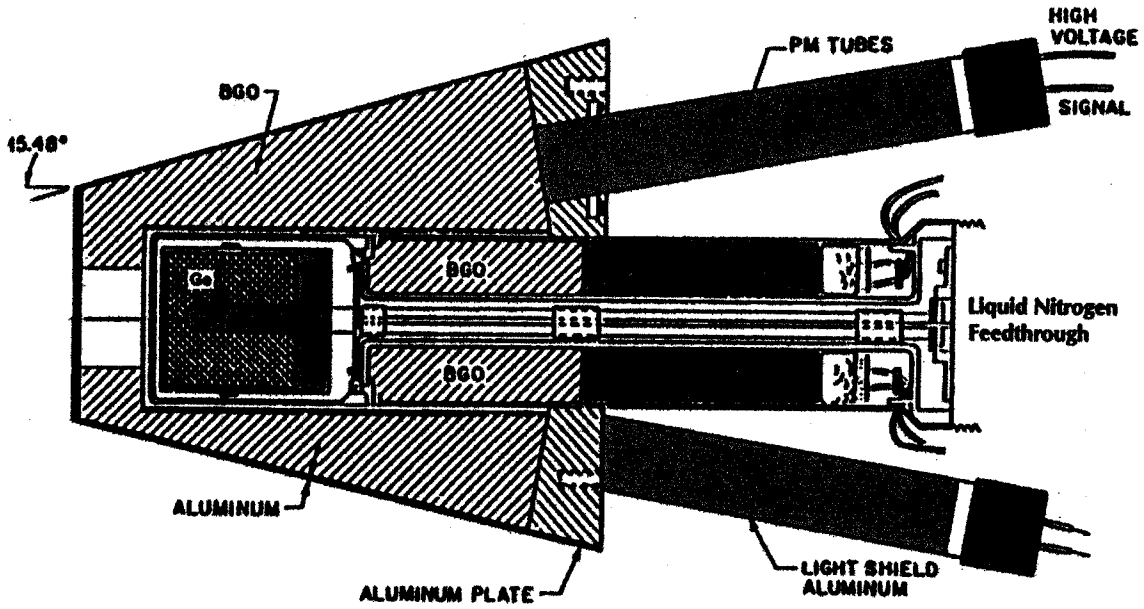

Figure 4.10: A cross sectional view of a single BGO Compton suppression unit used in the HHIRF Compact Ball CSS Spectrometer. From [hol87].

Table 4.3: Effective γ-Ray Transmission Through Tin and Copper Absorbers.

E_γ(keV)	Sn (.010in)	Cu (.005in)	% Total Transmission
75	.519	.90	46.7
100	.736	.95	69.9
150	.895	.975	87.3
200	.942	.982	92.5
250	.962	.986	94.9
300	.970	.987	95.7
400	.979	.989	96.8
500	.983	.991	97.4
600	.985	.991	97.6
800	.988	.993	98.1
1000	.992	.993	98.5

4.4 Electronics

4.4.1 Data Acquisition

The signals from the Ge preamp and the BGO catcher PMT are summed together. From each of the twenty detectors, two signals are generated; one for the energy, based on the pulse height and the other for the timing of the γ rays, based on pulse rate. The 110 signals from the NaI and BGO shields, are individually balanced for each shield (as described in the next section) and produce a timing signal. The standard NIM signals from the Ge and Shields are converted to ECL signals and used in most of the Camac modules[11]. The signal is converted to TTL for use in the Event Handler and back to NIM when the signal is sent to the 16 fold bit register to the computer.

The block diagram for the electronics used in the γ coincidence experiment is shown in Figure 4.11. The corresponding list of component acronyms and their unit

[11]Standard signal values are:
NIM : logic 1, -12mA to -36mA; logic 0, 0mA to -2mA
TTL : logic 1, 0 v. to +0.8v.; logic 0, +2v. to +5v
ECL : -0.8v to -1.7v

numbers are listed in Table 4.4 and continued in Table 4.5. In order to monitor the electronics, scalers are arranged in four places: after the logical manipulation of the Ge and Shield timing signals to create 'clean' and 'dirty' (units 26, 37), after the selection of triple coincidence events (u19) and for a signal from the Faraday cup on the primary beam line (u42). The Ge energy is amplified, sent to an ADC, then converted from NIM to TTL for use in the Event Handler (u1-6,21)). For accurate timing of the nanosecond range pulses from the Ge time signal, a Timing Filter Amplifier (TFA) , and a Constant Fraction Discriminator (CFD) (u9,10) were used to shape the signals. The CFD generates a trigger signal for the ADC, the Event Handler, the MALU, the TDC start and stop signals and the 16 fold bit register (u34). The TDC (also referred to as TAC) (u8) is used to convert the rate of the timing pulse to a digital value. The CFD was set to 50 ns. on width and the TFA was adjusted to E_γ (max) at approximately 4.8 MeV. The TAC range is 0-200 ns. with a calibration of 0.213 ns. per channel. The timing STOP signal was defined as 80 ns. plus two wires of 6 and 10 foot lengths with a calibration of 1.567 ns. per foot.

The timing of a γ-ray triples coincidence event is electronically defined with the CFD signal from the Ge (u10) and a timing signal from the shield detectors (u24). When a photon is absorbed in the Ge and then compton scattered into the shields, there is a time delay between these two events that were prompted by the same photon. In order to balance the timing, a time delay (130 ns) is placed on the Ge time signal (u29). This time delayed Ge signal and *Shield* signal are sent to a Programmable Logic Unit (PLU) (u30). Figure 4.12 shows the Truth Table for the PLU input signals and their corresponding output signals. If the Ge and *Shield* signals occur at the same time, a valid event has occurred. If the Ge signal, but not the *Shield* signal, occurs, then this is a compton scattering event that should not be included in the data set. Two boolean-logic AND signals have been designed for this purpose:

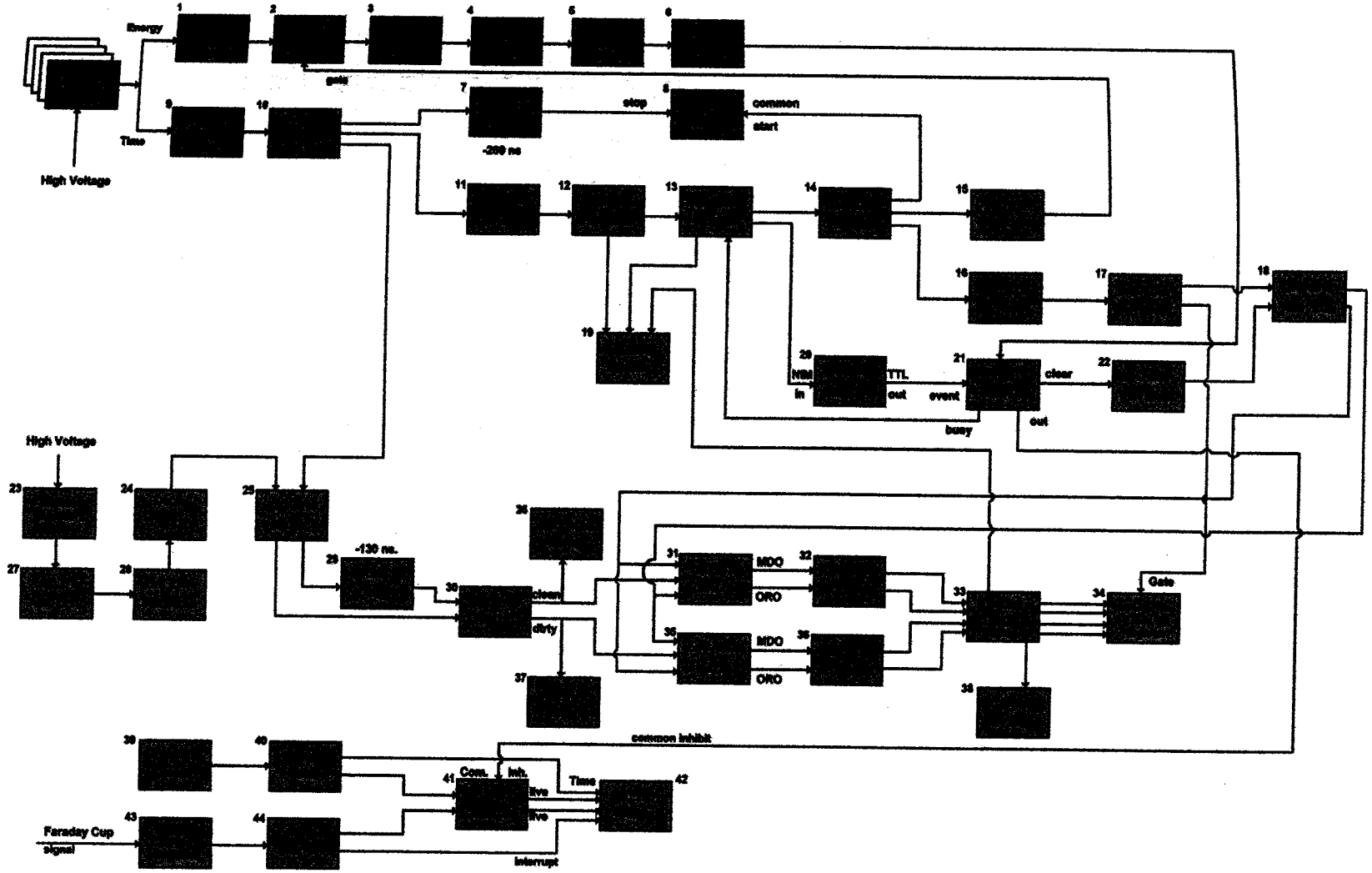

Figure 4.11: Block diagram of the electronics used in γ-coincidence experiments on the Compton Suppression Spectrometer.

Table 4.4: Electronic Unit Identification Chart

UNIT	MANUFACTURER	IDENTIFICATION
1	Ortec 671	Amplifiers (×20)
2	Nuclear Data 501	ADC (× 20)
3		ADC Interface
4	Camac	ADC Interface
5	LeCroy 688AL	Level Adapter (NIM/TTL)
6	LeCroy 429A	Fan In/Out Signal Multiplier
7	LeCroy 222	Delay Gate Generator (DGG)
8	LeCroy 2228A	Time to Digital Converter(TDC)
9	Ortec 474	Timing Filter Amplifier(TFA)(×20)
10	TC 454	Constant Fraction Discriminator(CFD)
11	LRS 380A	Multiplicity Logic Unit (MLU)
12	LeCroy 429A	Fan In/Out Signal Multiplier
13	LeCroy 365AL	4 fold Logic Unit (LU)
14	LeCroy 429A	Fan In/Out Signal Multiplier
15	Ortec 416A	Gate and Delay Generator (DGG)
16	LeCroy 222	DGG
17	LeCroy 429A	Fan In/Out Signal Multiplier
18	LeCroy 4616	NIM/ECL Signal Converter
19	LeCroy 2551	Scaler
20	LeCroy 688AL	NIM/TTL Signal Converter
21		Event Handler
22	LeCroy 429A	Fan In/Out Signal Multiplier

Table 4.5: Electronic Unit Identification Chart (continued)

UNIT	MANUFACTURER	IDENTIFICATION
23		Shield Detectors (×20)
24	LeCroy 705	Octal Discriminator
25	LeCroy 4616	NIM/ECL Signal Convertor
26	LeCroy 4434	Scaler
27	LeCroy 776	Amplifier (×20)
28	LeCroy 429A	Fan In/Out Signal Multiplier
29	LeCroy 4418	Delay
30	LeCroy 4506	PLU Programmable Logic Unit
31	LeCroy 4532	MALU Majority Logic Unit
32	LeCroy 4616	ECL/NIM Signal Convertor
33	TB 6000	Trigger Box
34	LeCroy 2141	16 Fold Bit Register
35	LeCroy 4532	MALU
36	LeCroy 4616	ECL/NIM Signal Convertor
37	LeCroy 4434	Scaler
38	TC 595	AR Meter (8 bit scale down for singles)
39		Pulser Timing Source (clock)
40		Gate Interface
41	LRS 622	Quad Col.
42	LeCroy 2551	Scaler
43		Digital Current Integrator
44		Gate Interface

$$\text{'Clean'} = \text{Ge} \bullet \mathit{Shield}$$

$$\text{'Dirty'} = \text{Ge} \bullet \overline{\mathit{Shield}}$$

Ge	*Shield*	$\overline{\mathit{Shield}}$	Clean	Dirty
0	0	1	0	0
0	1	0	0	0
1	0	1	0	1
1	1	0	1	0

Figure 4.12: PLU input and output logic signals: Truth Table Definitions

These signals can be pictorially described in Figure 4.6. The Clean spectrum is the compton suppressed spectrum. The Dirty spectrum represents the unsuppressed detector signal minus the compton suppressed signal, i.e., the rejected events. In order to better describe these signals, a pulse diagram is drawn in Figure 4.13: Signal pulses produced in the Ge (3) and Shield (4) detectors during a certain time window result in two Clean peaks and one Dirty peak.

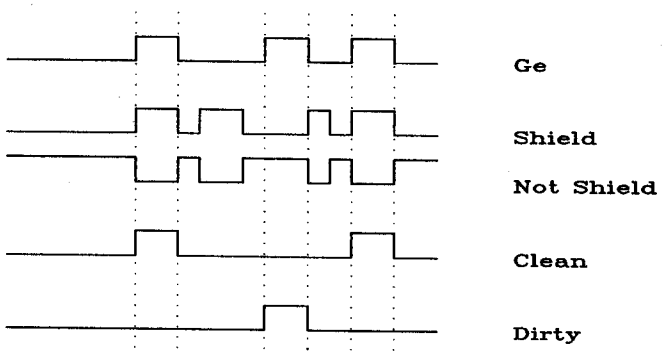

Figure 4.13: A pulse diagram illustrating the correspondence between the Ge detector and Shield signals.

The Clean and Dirty signals are then sent to the Majority Logic Unit (MALU) (u31,35) where a triple or single coincidence event is defined. There are two MALU output signals. The ORO output provides a logical OR of the 20 Clean signals and the 20 Dirty signals. These are single coincidence events. The MDO (majority discriminated output) has an adjustable threshold comparator in line. If less than three detectors fire for any event, the event is rejected. This is defined as a triple coincidence event. The output signal is 20 millivolts per detector. Four signals (Clean and Dirty singles and triples events) for every detector are sent to the Camac crate. Only the Clean signal (singles and triples) was recorded on tape for this experiment. Both Clean and Dirty signals were able to be viewed as a temporary histogram on the Chromatics graphics terminal during acqusition, or stored in what is referred to as an *spk* file.

During data acquisition, the Monitor Task software routine from the Event Handler is used to sort the energy and time signals into a buffer arrangement with detector codes. An example of this is shown in Figure 4.14. This is part of a block of the buffer structure, as written to tape. The buffer is read from right to left. The hexadecimal -1 value (FFFF) signals the end of an event. The next four bits contain a detector tag; each of the 20 detectors can be identified by an individual code that starts with 80XX. Following the detector tag, is a four bit value for the energy, then a value for the time signal, followed again by a detector tag, etc. Since triples coincidence data has been acquired, there will be three or more energy-time values between end of event markers. The Event Handler code (part of the Oak Ridge software) was used to acquire the data.

4.4.2 Experimental Preparation

Pre-experiment tests

Before placing the Ge detectors in the shields, the 110 PMT's from the shields were gain matched [ril88]. By positioning a 1μC ^{137}Cs source into each of the shields where the middle of the Ge crystal would be and monitoring the 662 keV peak on a Multichannel Analyzer, the peak amplitudes were adjusted using the PMT amplifier potentiometer while adjusting the shield supply voltage. Thresholds on the Octal Discriminator for each shield were adjusted using the 60 keV peak from a ^{241}Am source.

The Ge detectors were roughly gain matched using a 10μC ^{60}Co source positioned in the target area.

There were three standard tests done to check the operation of the Shields and Ge detectors: Rejection Ratio, False Veto, and Peak to Total. After the CSS was set up, including the collimators and absorbers, γ-ray spectra were acquired using the ^{60}Co source. A description of these tests is presented in Figure 4.15. A pictorial view of the Clean and Dirty spectra are used to illustrate the areas of the spectra needed to generate the test values. The results of these tests, for each detector, are listed in Table 4.6.

System Resolution Calculations

The resolving power of the entire system can be estimated using the following definitions and mathematical statements:

In order to find the gain in the peak to background ratio per γ-ray sort, i.e., R, the 'gain per fold', the following relationship is used. [12]

[12]This calculation was stated in a 9/18/93 Gammasphere newsletter, quarterly report.

```
Block number 25 (00000019), 8192 (2000) bytes

801BFFFF 03D703A8 80270390 036D8023 063407ED 800BFFFF 03D10000 80230596
801B03FF 0000000F FFFF04B9 00BD8027 03A60C54 802503DF 05DC801F 03E50EBD
802703EE 00000015 03ED0702 800F04A2 03560003 FFFF03F6 0DA08001D 061001B7
FFFF03CA 01F38027 03CF0746 801907FF 13D98015 03DD073F 8007FFFF 03CE047D
03EB082D 8011043A 0522000B FFFF03B6 06E38023 03F81097 800D03F3 0B748007
076B8005 FFFF03C5 0C6C8021 03FC079C 801903F7 0E188011 FFFF03F0 03688017
02478019 03D6021A 80150388 06288013 FFFF0684 00008027 03F401FB 801903B9
80150364 0C808005 FFFF03CD 038F8023 03EF053E 801903D5 00008001 FFFF0643
FFFF03CC 09338027 0691059E 801D03D9 0A40800F FFFF0688 00008027 03B205BA
037F0F9B 8007039A 09788005 FFFF03E5 0252801B 037B01F3 800503E2 0E558003
06840000 802703C6 06718025 03920E0B 802303BF 13038021 FFFF03E5 05D9801F
07AD800F 03F307CE 8007FFFF 03C70788 802703F0 0B868010 03F20A69 8001FFFF
06478021 047F0240 8017045E 00FA8013 03BD0FC2 8009FFFF 03C004B1 802103E1
801103EA 14568005 FFFF[redacted]0382
```

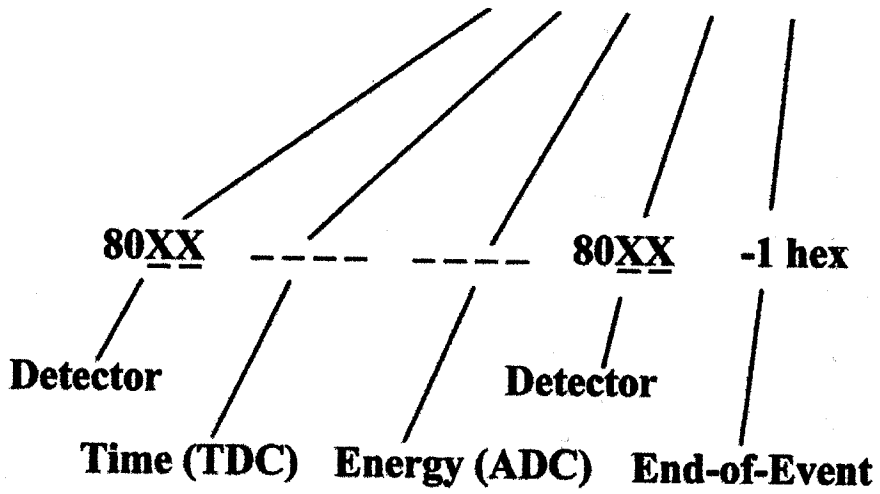

Figure 4.14: Structure of Triple Coincidence Buffer Events: The data is read from right to left. The detector identification tags are specified in the Event Handler code. By definition, a minimum of three detector-energy-time sequences must exist for every event; eg., the shaded area represents one event.

Rejection Ratio, R_r, represents the amount of compton suppression provided by the shields. The background from the clean (B_C) and dirty (B_D) spectra were integrated from channel 10 to just below the 1173 keV photopeak of ^{60}Co. R_r should be 5-6 for BGO and 3 for NaI.

$$R_r = \frac{B_C + B_D}{B_C}$$

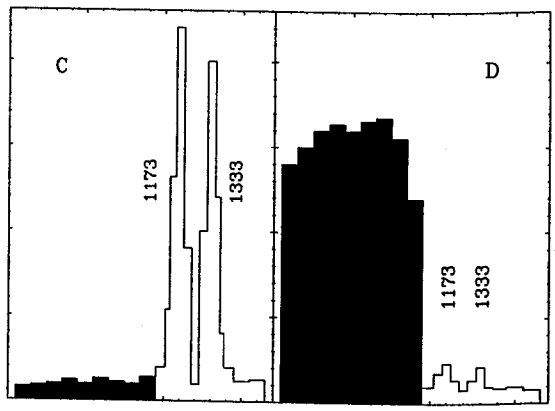

False Veto, the ratio P_D / P_C, represents the amount of real data rejected because of statistical noise. The 1333 keV peak was integrated for both clean and dirty spectra. The value should be $\approx$ 3% or less.

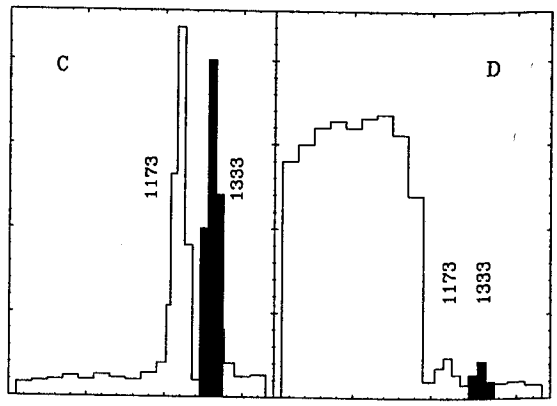

Peak to Total, P_C/T_C, for the integrated clean spectrum, should be 48 to 50% for BGO and $\approx$ 35% for NaI. T_C represents the total area from 100 keV to above the 1333 keV peak. P_C is the area of the 1173 plus 1333 keV peaks.

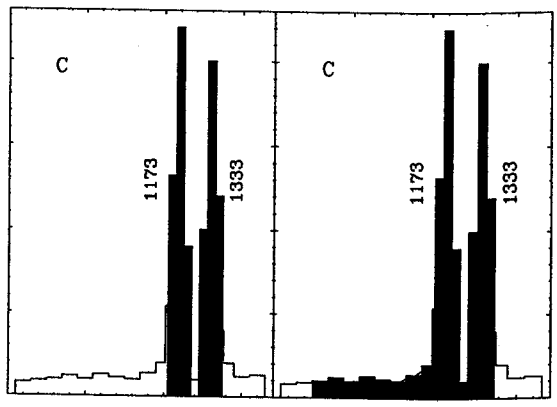

Figure 4.15: A description of the pre-experiment tests for Ge and shield detector operation. Top, Rejection Ratio; Middle, False Veto; Bottom, Peak to Total. C refers to the Clean spectrum of ^{60}Co; D, to the Dirty spectrum. The shaded areas represent the integrated regions that the test values were obtained from. (These are simulated spectra.)

Table 4.6: Standard Suppression Tests for the CSS

Detector	Shield	Rejection Ratio	Peak/Total(%)	False Veto(%)
1	NH	2.9	38	2.3
2	BH	5.3	49	2.6
3	BP	5.3	51	2.0
4	BP	4.1	42	1.3
5	NP	2.8	33	1.5
6	BH	5.3	49	2.6
7	BH	4.4	44	1.6
8	NP	2.8	33	1.4
9	BP	4.9	45	3.2
10	NH	3.1	34	2.2
11	NH	2.9	33	1.8
12	BP	4.8	44	2.3
13	NP	2.8	35	1.1
14	NP	2.7	31	1.5
15	BP	5.1	53	1.8
16	NH	3.1	35	1.6
17	BH	4.9	48	2.7
18	BP	4.9	48	2.3
19	BH	4.9	49	2.0
20	BH	5.0	50	2.5

Shield type and shape: N = NaI B = BGO H = Hexagonal P = Pentagonal

$$R = (SE\,/\,dE)\;(P\,/\,T) \tag{4.1}$$

where, SE is the average separation between γ-ray energies in the spectrum and dE is the effective energy resolution of the detector. Both are described in the Data Analysis Chapter. P/T is the effective peak to total ratio for the detector (described in the last section.)

The system resolving power, Rp, is related to the 'gain per fold' by a power

function:

$$Rp = R^f \tag{4.2}$$

where, f is the number of the γ ray sort, i.e., 'fold'.

'Fold' can be related to the total array efficiency:

$$N = \alpha \ N_\circ \ \varepsilon^f \tag{4.3}$$

where, N is the number of counts in the detected peak. α is the γ-ray branch of interest. $N_\circ$ is the total number of events. ε is the array efficiency for full energy γ rays.

By combining these three equations and making an estimate for N and $N_\circ$, a typical resolving power for the system can be obtained:

$$Rp = exp[(19.5 \ ln R \ ln \varepsilon / (ln R / ln \varepsilon \ - 1)] \tag{4.4}$$

where, $N = 100$ and $N_\circ = 10^5/sec \times 80 \ hours = 2.9 \times 10^{10}$. For a peak-to-background of one: $Rp \approx 1/\alpha$.

Chapter 5

Data Analysis

Approximately 250 million triple and higher coincidence events were recorded onto tape. [1] After the experiment, a one dimensional total energy composite histogram was generated for each detector from these triple coincidences. These represent a mixture of γ -rays from all of the reaction products. The 5n, 4n, p3n, and p4n reactions dominate, producing ^{132}Pr, ^{133}Pr, ^{133}Ce, ^{132}Ce. This is shown in Figure 5.1, a plot, from detector number 3, of channel number versus γ -ray intensity. The 130, 178, 240, 283 keV. peaks are a few of the transition energies from ^{132}Pr. This nucleus represents 25-30% of the total γ -rays. In order to study the rotational band structure of individual nuclei, their respective γ -rays must be separated. In this chapter we discuss the analytical means of distinguishing the γ -rays from each type of nucleus.

The first part contains observations and results from isotropic and doppler shifted energy calibrations and efficiency calibrations. The second part presents spectra (1-D histograms) from γ single events, post run radioactivities, simple-gate 2-D histograms with both prompt and delayed (time gated) spectra, multiple-gate 2-D histograms and Energy versus Time, 2-D histograms that produce time spectra for individual

[1] There were 29 γ triple event 9-track tapes (160 Mev. beam energy) and 10 other tapes for pre- and post-run calibrations, singles and radioactive decay data recorded. The length of time to generate one 2-D histogram was conservatively, between 29 and 60 hours, with the tape needing to be changed every 1 to 2 hours. When exabyte drives became available, the 29 tapes were copied to 2 single density 8 mm. tapes. 145 and 155 Mev data were not recorded in event format.

detectors.

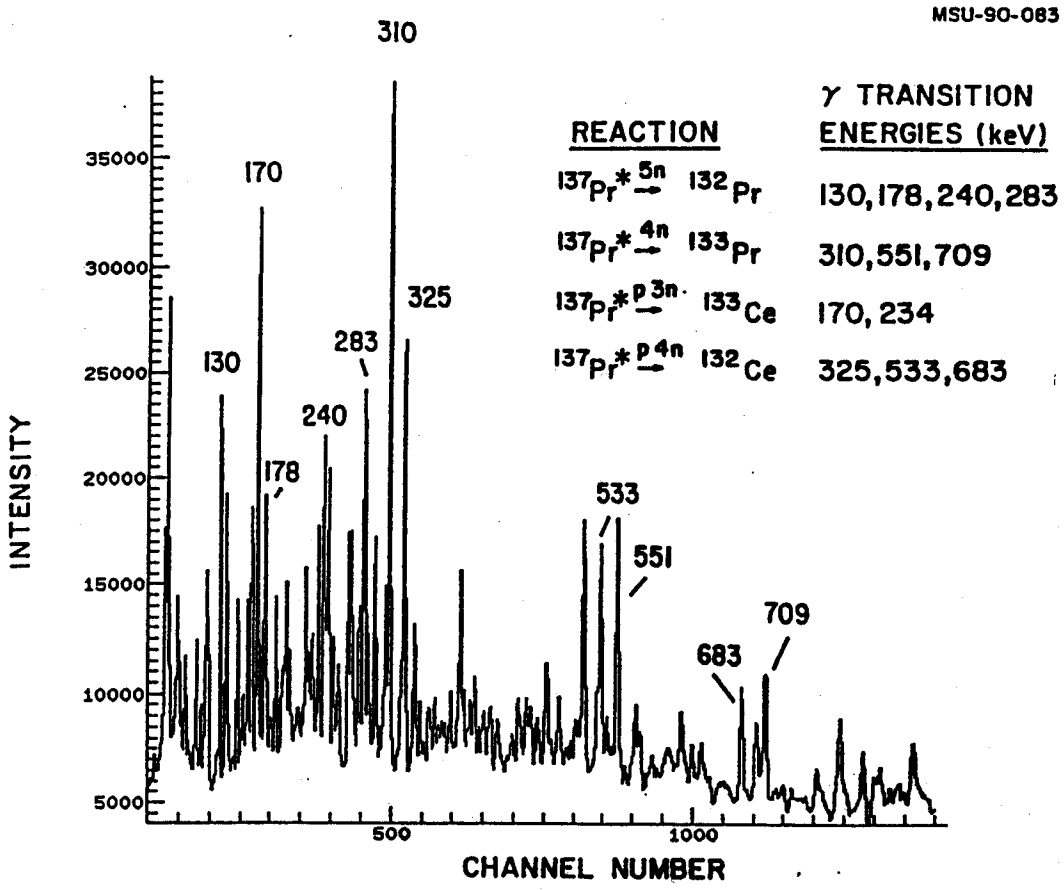

Figure 5.1: Composite Spectrum: Total plot of all photons from detector 3.

5.1 Calibration

5.1.1 Isotropic Energy Calibration

Before the experiment, γ ray spectra from the standard sources , ^{133}Ba, ^{60}Co, ^{152}Eu were acquired in order to generate isotropic calibrations for each detector. Even though the gain of each detector was adjusted before the experiment, a fine tuning

of the gain needed to be done after the data was collected. Table 5.1 contains the linear regression analysis results. Spectra for the standards acquired pre- and post-run are shown in Figure 5.3. The isotropic calibration plots for the 20 detectors are in Appendix C.1. The solid symbol represents the isotropic calibration points; the open symbol is the doppler corrected calibration.

In addition to determining the amount of gain adjustment per detector, the isotropic calibration (gs) was used to show the extent of doppler shifting that occurred during the reaction, to determine peak resolution, and to adjust the pre- and post-run standards and activities in event format. The parameters are located in Table 5.2 . Detector 1 was chosen to be the normalization detector, since it covers a θ angle of nearly 90°. Figure 5.2 shows the positive and negative shift in peak position relative to the 90° detector, as a function of detector θ angle. The theoretical implications of this function have been presented in Chapter 3.

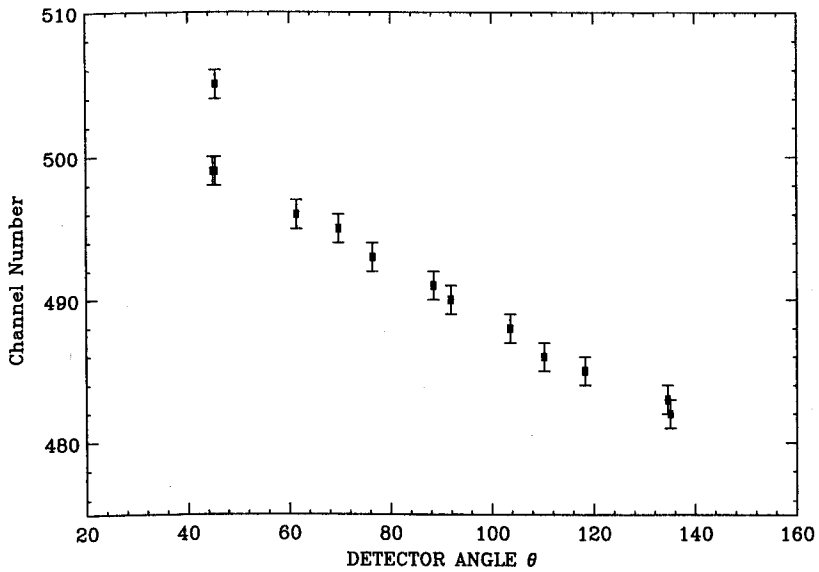

Figure 5.2: Angle effects observed for the gain shifted data: Each point represents the channel number centroid of the 310 keV. peak for every θ detector angle.

Table 5.1: Isotropic Standard Calibration: Linear Regression Results

Detector	**Slope**	**Intercept**	Σ**(Residuals)**^{2}
1	0.62144	5.2665	0.614
2	0.62645	29.2100	0.560
3	0.63518	-9.2867	0.608
4	0.62789	1.8033	2.085
5	0.63042	-7.9170	0.496
6	0.62934	-0.9735	1.278
7	0.62446	0.5879	0.656
8	0.62813	-0.8293	0.445
9	0.63084	-5.7282	0.965
10	0.63348	-8.9069	1.182
11	0.62582	1.9636	0.647
12	0.62969	1.2841	0.139
13	0.62224	3.6205	0.558
14	0.64504	-25.902	0.835
15	0.64204	-25.131	1.435
16	0.63172	-8.8883	0.270
17	0.62695	-1.5847	0.513
18	0.63117	-8.4134	1.042
19	0.63281	-11.570	0.415
20	0.62760	-2.6792	0.028

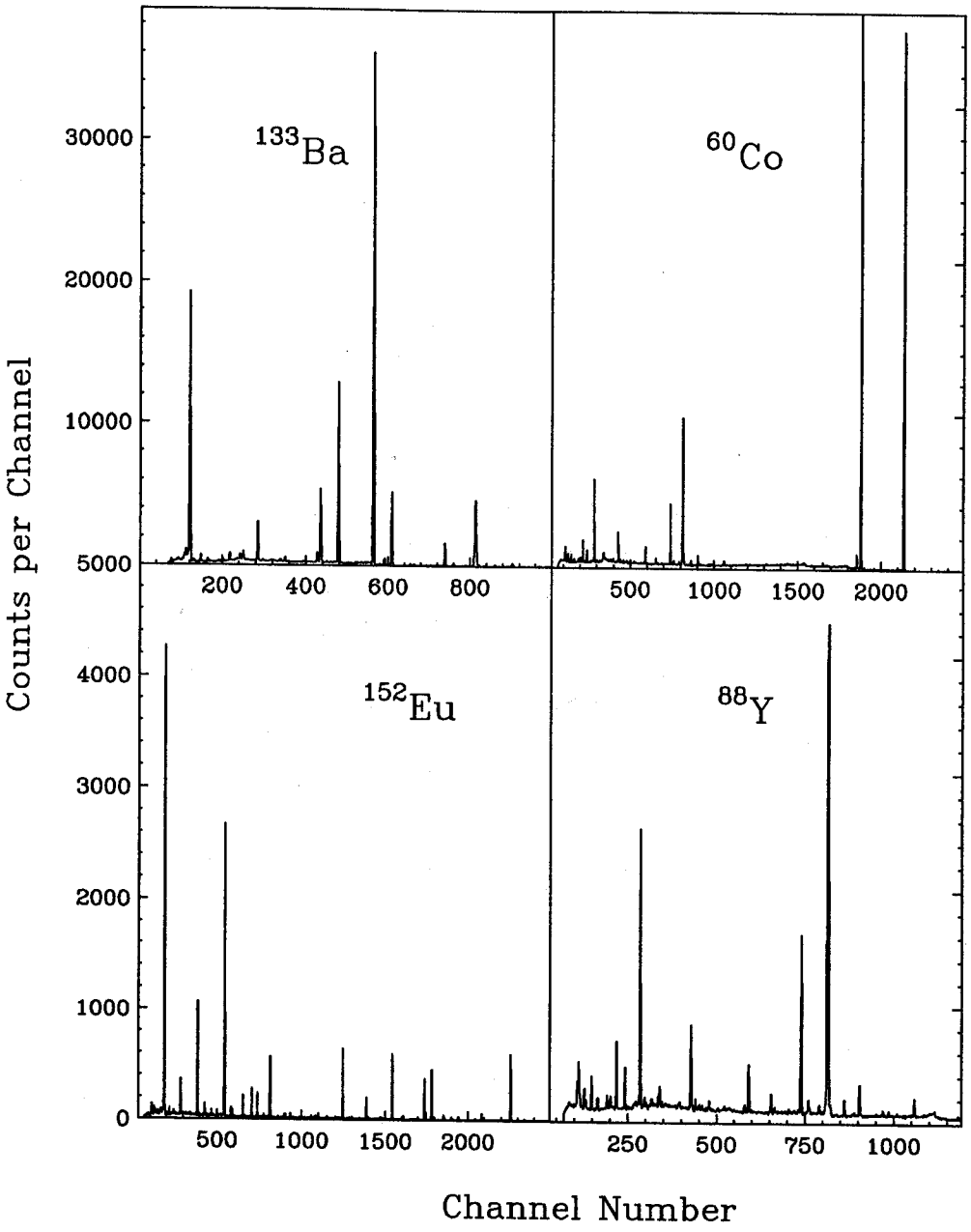

Figure 5.3: Spectra for the calibration standards: ^{133}Ba,^{152}Eu,^{60}Co, ^{88}Y.

Table 5.2: Isotropic (*gs*) and gain/doppler shift (*gds*) parameters used for raw data adjustment. A is the y-axis offset adjustment; B is the slope adjustment.

Detector	*gds*–**A**	*gds*–**B**	*gs*–**A**	*gs*–**B**
1	0.0000000	1.0000000	0.000000	1.0000000
2	77.5879974	1.0262530	77.058884	1.0080612
3	-48.3330002	1.0322570	-46.835327	1.0221077
4	-11.7760000	0.9951870	-11.144806	1.0103775
5	-43.4564018	1.0243540	-42.428009	1.0144489
6	-21.0079994	1.0303580	-20.080872	1.0127109
7	-15.9161997	0.9953650	-15.055725	1.0048586
8	-20.7381992	1.0181890	-19.616211	1.0107638
9	-36.1966019	1.0001611	-35.382904	1.0151253
10	-46.0421982	1.0199430	-45.614441	1.0193750
11	-10.9074001	1.0091590	-10.629318	1.0070465
12	-13.6529999	1.0314519	-12.814743	1.0132742
13	-6.1245999	0.9942050	-5.295502	1.0012852
14	-100.5065994	1.0332550	-100.310272	1.0379777
15	-98.6088028	1.0519750	-97.827942	1.0331490
16	-46.7771988	1.0189610	-45.553009	1.0165415
17	-23.2796001	0.9939310	-22.049286	1.0088652
18	-45.3428001	1.0090621	-44.026276	1.0156565
19	-55.8300018	1.0313550	-54.184784	1.0182953
20	-26.0816002	0.9835490	-25.571533	1.0099118

5.1.2 Gain and Doppler Shift Calibration

There are two ways to correct for doppler shift of the γ rays. One, is to determine the residual particle velocity then use formula 3.15 mentioned earlier in Chapter 3. The other, is to use energy peaks from various nuclei contained in the data run, i.e., the composite spectrum, Figure 5.1. Since we did not know, a priori, the average residual particle velocity, the second method was used. It should be emphasized that *all* the energy peaks are shifted by this process. [2]

Table 5.3: Energies and the source nuclei used for the Gain and Doppler Shift Calibration.

Nucleus	Energy (keV.)
^{132}Pr	130.3
^{133}Ce	170.0
^{132}Pr	178.5
^{133}Ce	234.8
^{132}Pr	240.5
^{132}Pr	266.7
^{132}Pr	283.7
^{133}Pr	310.3
^{132}Ce	325.4
^{132}Ce	533.69
^{133}Pr	709.0
^{133}Pr	812.6

[2] Although this may appear to be self-evident, it is often overlooked that peaks not generated by the reaction do not need this correction and therefore, become reverse-doppler shifted. This type of peak has many origins: radioactive decays, transitions at the bandheads (0^+ states), x-rays, $\beta^{\pm}$ anhilations, background transitions. Isotropic peaks of moderate intensity can usually be identified (in a 1-D histogram) by comparing the gain shifted, composite histograms from each detector —as is shown in Figure 5.4. The peaks that appear to be stationary are isotropic. The significance of some of these peaks is reduced considerably by the background subtraction technique. Other peaks are not reduced and become smeared, multiplet-appearing peaks in a 2-D spectrum that has had many detector comparisons added together. Modifications for these effects await development of a 2-D technique for noise reduction, background subtraction, and separation by residual particle velocity determination.

Table 5.4: Doppler Shifted Energy Calibration: Linear Regression Results

Detector	Slope	Intercept	Σ(Residuals)^2
1	0.62126	5.3028	10.183
2	0.63757	29.404	1.183
3	0.64130	-9.7107	0.870
4	0.61827	1.6447	2.081
5	0.63639	-8.1957	1.128
6	0.64012	-1.2229	1.477
7	0.61838	0.35897	1.635
8	0.63256	-1.1390	1.046
9	0.62136	-5.9407	1.879
10	0.63365	-8.9994	2.408
11	0.62695	1.9146	2.982
12	0.64080	1.0615	1.087
13	0.61766	3.4002	1.812
14	0.64192	-25.918	2.589
15	0.65355	-25.328	1.047
16	0.63304	-9.2274	0.923
17	0.61749	-1.9284	1.756
18	0.62689	-8.7823	1.506
19	0.64074	-12.040	1.544
20	0.61104	-2.7989	1.321

Channel number values for the peaks were obtained from a gaussian fit routine; the linear regression results are presented in Table 5.4 and the energies and their sources are listed in Table 5.3. The calibration range for detector 1 was extended by including the Pb x-ray energies at the low end and a few low intensity transitions at high energy. This gain and doppler shifted (*gds*) calibration was used to generate parameters for the raw data. In order to bring the doppler shifted peaks into alignment, the histograms from all 20 detectors were rebinned in order to have the same peak positions as detector 1.

A Fortran user-subroutine for the Oak Ridge software was written in order to

gain-shift and correct for doppler effect and adjust the TAC values of the raw data in event format. (See Appendix G.1 for a source code listing.) This was done by converting the event data to floating point, using parameters to adjust the data, then rebinning, using a random number technique and converting back to integer. The parameters for gain and doppler shift for the 20 detectors are written in Table 5.2. It should be noted that the offset values had to be doubled because the data were histogrammed with a resolution of 4096 channel numbers and the software data acquisition parameters specified 8192 channels. A random number technique was used in the rebinning process in order to stretch the count intensity into the recalculated channel number bins. If this were not done, positive and negative-going spikes would have been produced within the histogram. This process prevents these peaks from forming within the 1-D and 2-D histograms; however, it creates white noise within the 2-D Simple and Multiple gates. Some researchers refer to the white noise, itself, as spikes and have developed an elaborate sorting method to remove it with a statistical weighting given to each event. See reference [bea95]. The method development to remove the noise is described in Chapter 6.

In order to derive these parameters, two points in the initial spectrum, Λ_i were chosen –the lowest and highest energies in the range of interest. They were then converted to channel number , using the individual *gds* calibrations for each detector; then, shifted into the channel number position of two points in the final spectrum that are equal in energy. The following formulas describe this rebinning calculation to determine the y-axis offset, A and the slope adjustment, B parameters. Note that the final spectrum, Λ_f, refers to points in the 90° reference spectrum, i.e., detector 1.

$$\Lambda_f = A + [B \times \Lambda_i] \tag{5.1}$$

where,

$$B = [\Lambda_{f2} - \Lambda_{f1}] \Big/ [\Lambda_{i2} - \Lambda_{i1}]$$

Table 5.5: Time to Amplitude Converter (TAC) adjustment parameters.

Detector	**$TAC_{Centroid}$**	**TAC_o**	**Normalization Parameter**
1	506	317	1.000000
2	505	314	1.001980
3	506	305	1.000000
4	505	329	1.001980
5	504	306	1.003968
6	506	310	1.000000
7	504	298	1.003968
8	502	318	1.007968
9	504	321	1.003968
10	502	322	1.007968
11	507	313	0.998028
12	506	320	1.000000
13	506	303	1.000000
14	499	335	1.014028
15	507	341	0.998028
16	498	332	1.016064
17	485	323	1.043298
18	487	331	1.039014
19	483	322	1.047620
20	486	346	1.041152

$$A = \Lambda_{f1} - [B \times \Lambda_{i1}]$$

The rebinning calculations were contained within the user-subroutine linked to the Oak Ridge *SCAN* program, which had been modified to accommodate a large data array. [3] The subroutine was also linked to the *LEMO* program. The *SCAN* program produces a histogram on disk; the *LEMO* program does the same calculations but, instead of writing a histogram, it writes to another tape. It is most time efficient to use *LEMO*, converting the raw data tapes to the adjusted version, then *SCAN* to generate the 2-D histograms. Adjustments to align the Time to Amplitude Converter data were also done within this subroutine; these parameters are listed in Table 5.5, along with the TAC peak centroid values and the initial TAC channel number. [4]

Figure 5.4 was included in order to demonstrate this effect of gain correction and doppler shifting. In the raw data (A) the 310 keV. peak appears in erratic channel positions among the 20 detectors. Six of the detectors are represented in the figure by their θ angle. Note that the peak for the $\theta = 135.1°$ and $\theta = 44.9°$ data is located out of the view of the window. After the gain adjustment (B), the angle effect of doppler shifted γ rays can be seen. Peaks are regularly spaced as a function of θ angle. When the doppler shifting is counteracted (C) the peaks appear to move into alignment among the detectors. These prosesses were crucial to the analyses because the ensuing steps created arrays comparing γ rays from one detector with another. If the detectors were not in alignment, artifact peaks would have been formed.

[3] See [hol87] for CLX and CLY parameter adjustment. There is a 268 Mega-channel capacity for 2-D spectra; i.e., CLX $\times$ CLY $\times$ $\#bits$ $\times$ Word size(I^{*2}) = 268 Mega-channel.

[4] The timing was calibrated using 10 bits on the TDC or 1024 channel numbers. The channel numbers can be stretched or compressed with the *SCAN* program. 2048 TAC channels were used for the Energy versus Time arrays, but the timing range remains the same, i.e., 0 $\approx$ 200 ns.

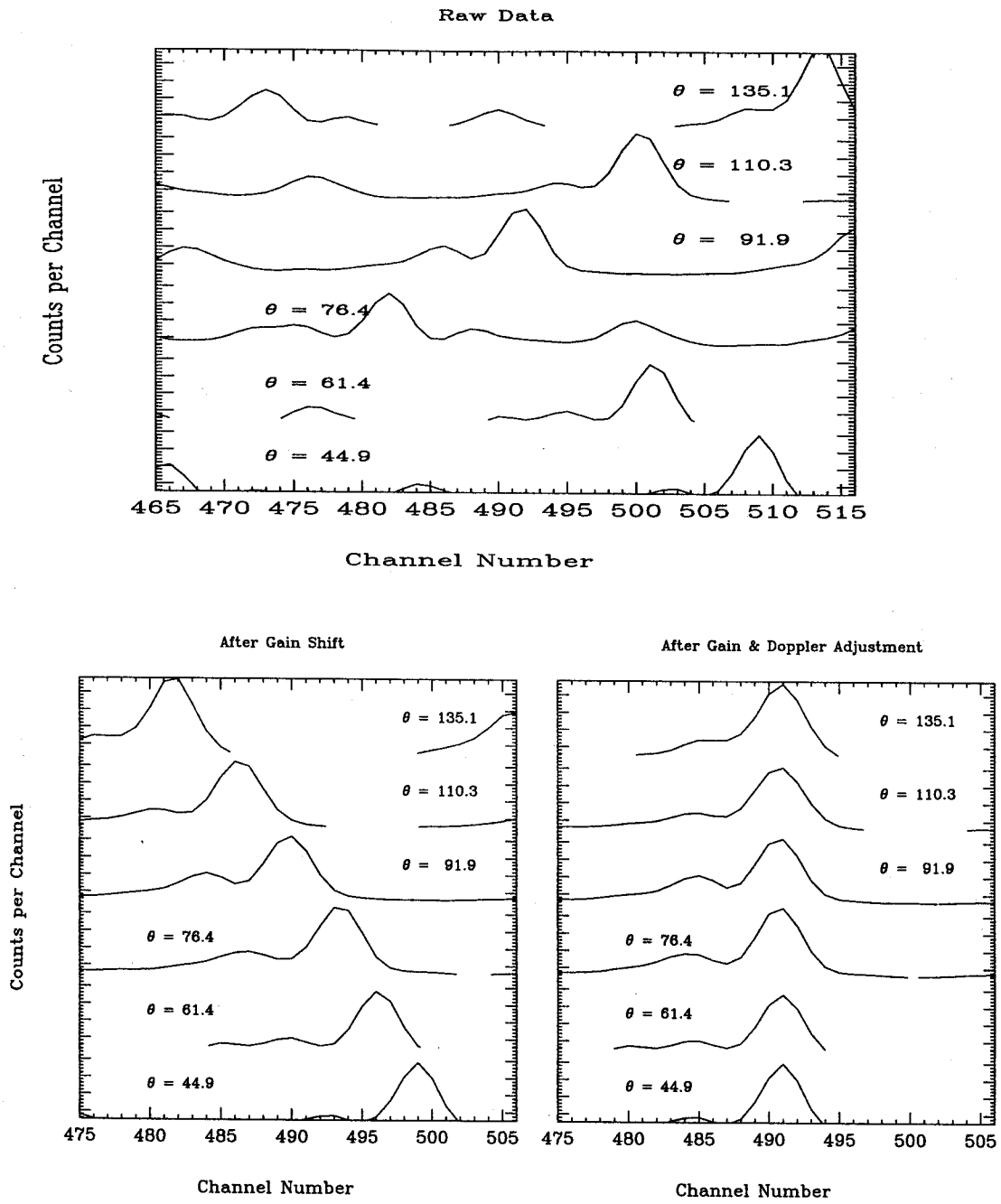

Figure 5.4: A graphical illustration of the effect on the raw data of gain shifting and doppler shifting. The 310 keV peak is plotted from various detectors, represented by their θ angle.

5.2 Detector Operation

5.2.1 Energy Resolution

Using the isotropic standard calibrations, the peak resolution, R_e (in keV.) for each detector was determined using the relationship:

$$R_e = R_{cn} \times (FS/4096)$$

$$\text{where,} \qquad FS = A + B(4096).$$

R_{cn} is the full width half maximum peak measurement determined experimentally and FS is the full scale energy (in keV.). A equals the linear regression intercept and B equals the linear regression slope from the isotropic detector calibrations, in Table 5.1. The number 4096 is derived from the number of ADC bits used for data acquisition, i.e., $2^{12} = 4096$, which determines the total number of usable channel numbers in the spectrum.

A peak resolution for various energies is listed in Table 5.6. For the ^{60}Co, 1333 keV peak, the resolution ranged from 2.11 keV (detector 12) to 2.60 keV (detector 17). The peak resolution also varies with energy. The mathematical relationships between the FWHM peak resolution, R (in channel number and keV.), the Energy, E_γ and channel number, cn were determined by linear regression analysis:[5]

$$R_e = 2.0236 - 0.47679 \times 10^{-2} \sqrt{cn} + 0.18240 \times 10^{-3} cn$$

$$R_e = 1.9968 - 0.19957 \times 10^{-4} E_\gamma + 0.12972 \times 10^{-6} E_\gamma^2$$

$$R_{cn} = 3.2547 - 0.76566 \times 10^{-2} \sqrt{cn} + 0.28651 \times 10^{-3} cn$$

Post run energy calibrations were done with ^{60}Co and ^{88}Y.

By comparing the FWHM peak resolution for pre and post-run ^{60}Co energy peaks, the condition of the detectors can be monitored. Neutron bombardment may induce

[5]In this case, the channel number, cn, refers to all spectra except the multiple gate histograms, which have exactly half the FWHM, the channel number and the resolution. These equations have been computed using data from detector 1.

Table 5.6: Isotropic Energy Resolution in keV Using the Full Width Half Maximum Height Measurements of Peaks in ^{133}Ba and ^{60}Co Standards.

Detector	FWHM 81 keV ^{133}Ba	FWHM 276 keV ^{133}Ba	FWHM 1173 keV ^{60}Co	FWHM 1333 keV ^{60}Co
1	1.99	2.01	2.14	2.21
2	1.95	1.88	2.33	2.42
3	1.80	1.79	2.11	2.21
4	1.80	2.02	2.21	2.22
5	2.12	2.09	2.37	2.41
6	2.03	1.95	2.40	2.54
7	1.98	1.94	2.12	2.19
8	1.90	1.93	2.21	2.31
9	1.78	1.95	2.24	2.38
10	1.72	1.95	2.38	2.55
11	1.95	1.96	2.13	2.31
12	1.97	2.01	2.11	2.11
13	1.80	1.74	2.32	2.44
14	2.12	2.02	2.23	2.49
15	1.98	1.89	2.11	2.22
16	2.00	2.18	2.29	2.36
17	2.18	2.22	2.53	2.60
18	2.12	2.13	2.33	2.40
19	1.95	2.00	2.11	2.15
20	1.75	1.97	2.09	2.13

crystal lattice defects, resulting in loss of resolution. Figure 5.5 shows the effect the neutrons had on detector resolution during this experiment. For 16 of the 20 detectors, a 2 to 9% loss of resolution was experienced. [6]

5.2.2 Efficiency Calibration

A photopeak efficiency calibration measures the response of the detector to photons over a wide range of energies. Theoretically, this response curve is determined by the photoelectric effect and compton scattering and, to a lesser degree, pair production

[6]See the footnote in the Efficiency section for a possible explanation for the anomolous value for detector 14 .

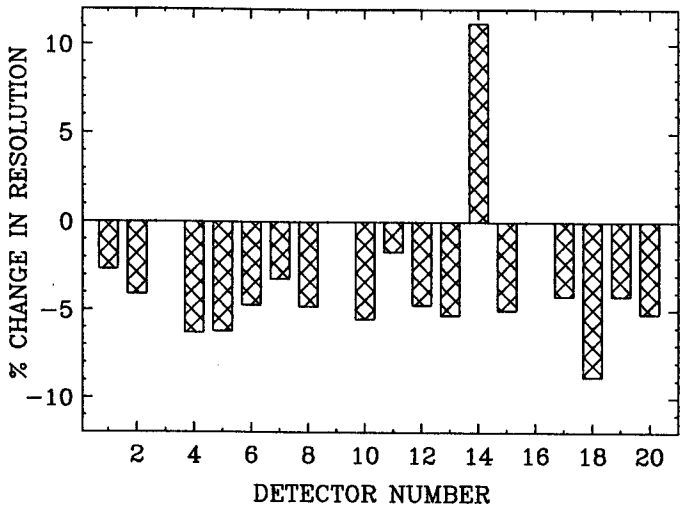

Figure 5.5: The effect of neutron damage during this experiment on detector resolution.

processes that contribute to the photon absorption cross section. It is affected by the size and geometry of the detector crystal and the angular distribution of the γ rays. The effect is an exponential one and the curve shape is governed by the 'Total' plot in Figure 4.4, a plot of photon absorption coefficients versus energy for Germanium.

There are at least three different methods that have been used to generate the efficiency calibration: A strictly theoretical method for absolute efficiency based on Monte Carlo calculations [cam69], various semi-empirical techniques [par69, don67, fre66], and an experimental determination followed by a Legendre polynomial least squares fitting routine. The formula for relative efficiency, ε, derived from the semiempirical approach is worth mentioning since it relates the active volume of the detector, V to photoelectric, τ and compton, σ absorption coefficients and γ ray energy, E. The symbol, k, is a constant relating absolute to relative efficiency.

$$\varepsilon = k\left[1 - \exp\left(-\tau V^{1/3}\right) + 0.012 V \sigma \exp\left(-0.8E\right)\right] \tag{5.2}$$

We have chosen to use the experimental method, with one exception. The Legendre fitting routine produces a fit that is not acceptable over the entire energy calibration

range. Therefore, a cubic spline fitting routine was used to generate an interpolated efficiency % at each channel number, based on the experimental peak areas. An extrapolation was also made to extend the energy range (40 to 2500 keV.). Then the Oak Ridge software was modified to automatically adjust the spectral peak intensities for photon transmission through absorbers and multiple detector efficiencies. A comparison of the absorber correction factor for tin and copper used in this experiment and a photon efficiency curve, averaged over all detectors are presented in Figure 5.6. The highest efficiency value produced by the spline fit was used to normalize the averaged efficiency curve to 100%. An absorber transmission adjusted efficiency curve is also included to describe the total effect on the energy peaks.

To generate experimental efficiency values, the following steps were followed: The experimental peak areas (I_x) must be divided by their respective relative abundance (RA_x) (or relative probability) obtained from reference [bro86]. [7] The energies and relative abundances are listed in Table 5.7. Within each set of energies from the four standards (^{88}Y, ^{60}Co, ^{152}Eu, ^{133}Ba) one energy peak was chosen to be the normalization standard, (I_n/RA_n). This is marked in the Table with an asterisk. The mathematical relationship is:

$$\varepsilon' = \frac{\varepsilon}{\varepsilon_o} = \frac{I_x}{RA_x} \Big/ \frac{I_n}{RA_n} \tag{5.3}$$

The resulting probability-adjusted and normalized peak areas, ε' needed to be corrected for the different acquisition times used for each standard run. This has been referred to as the "pair-point" adjustment method. [don67, par69]. It can be done graphically or by the following interpolation method: Choose two points, A and B, that are close in energy, from different source data sets. Using point A, interpolate an ε' value for point B, i.e., the energy peak not contained in that data set. Then derive a ratio of this interpolated value for B with the actual value for B, obtained

[7] Hamilton [ham75] refers to relative abundance as a branching ratio, defined as the number of γ photons per 100 disintegrations.

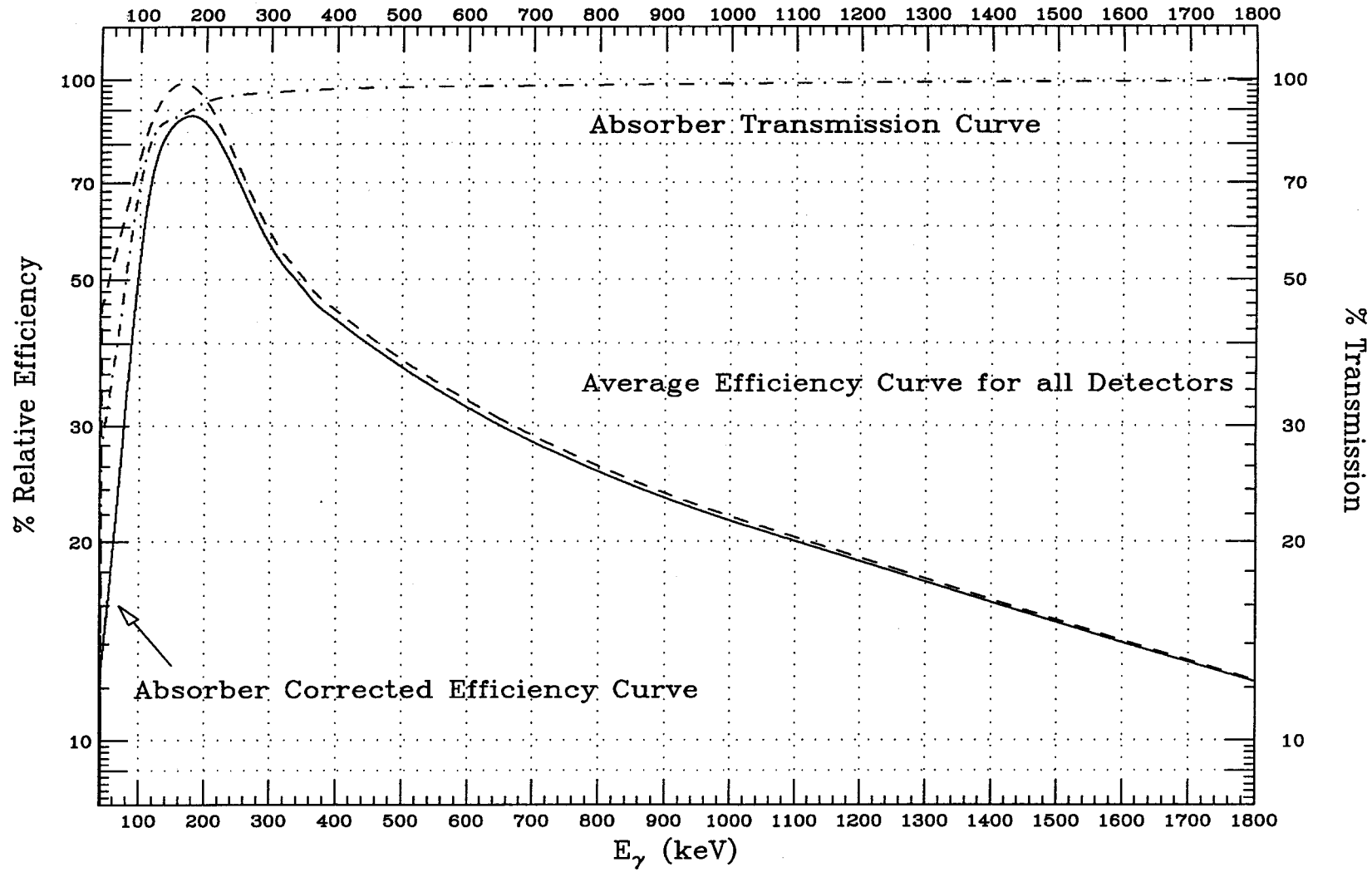

Figure 5.6: Absorber transmission, photon efficiency and absorber corrected efficiency curves, averaged over all detectors.

Table 5.7: Relative abundances (branching ratios) for the various peaks in the standard sources used for the Efficiency calibrations. Energies marked with * are the normalization energies for that source.

Source	Energy	RA
^{133}Ba	80.999	0.342
^{152}Eu	*121.783	0.284
^{133}Ba	*302.858	0.184
^{152}Eu	344.276	0.266
^{133}Ba	356.014	0.622
^{133}Ba	383.859	0.0892
^{152}Eu	443.976	0.0280
^{152}Eu	778.903	0.1298
^{88}Y	*898.021	0.927[1]
^{152}Eu	964.131	0.145
^{152}Eu	1112.116	0.136
^{60}Co	*1173.237	0.9920
^{60}Co	1332.501	0.9998
^{152}Eu	1408.011	0.208
^{88}Y	1836.074	0.9935

[1] Hamilton [ham75] reports this value as 0.914 ± 0.007.

from the second data set. Multiply all ε' values in the second data set by this ratio. They will then be aligned with the first data set. Then, by choosing the highest ε' value (302.858 keV.), all detectors were normalized to each other. [8] The resulting % relative efficiency plots are contained in Appendix C.2. An absorber transmission curve and an absorber adjusted efficiency curve are included in each plot.

[8] During the experimental setup, the positions of two detectors were switched without proper notation. Some of the standards were acquired before the switch, some after. Some of the peak areas for detectors 14 and 20 showed anomolous values. Therefore, for these two detectors, only one efficiency curve was generated and called detector 20. A curve for detector 14 was chosen by comparing the spectral baseline response with the other detectors. The curve for detector 11 that closely matched detector 14 was used.

5.3 Preliminary Spectra

5.3.1 Post Run Radioactive Decay

After the triple events were acquired, the beam was turned off and the γ rays from radioactive decays were recorded on tape. These activities can also be observed in the Energy versus Time arrays. Since they are isotropic contributions, they are observed throughout the array as background lines. These peaks can be used to confirm the production of certain reaction products. [9] Appendix D.3 contains the individual activities spectrum for each detector. Many of the peaks remain unidentified; a list of a few confirmation peaks can be found in Table 5.8. Most nucleids in this mass region decay by a type of β decay referred to as electron capture, ϵ. In this process an atomic electron is captured by the excited nucleus allowing a proton to be converted to a neutron [kra88].

According to our expectations, the γ rays appear to originate from two major reactions; the 5n,γ and 4n,γ. Their decay sequences are:

$$5n,\gamma \ : \qquad {}^{132}_{59}\mathrm{Pr} \xrightarrow{\epsilon} {}^{132}_{58}\mathrm{Ce} \xrightarrow{\epsilon} {}^{132}_{57}\mathrm{La} \xrightarrow{\epsilon} {}^{132}_{56}\mathrm{Ba}\ (\text{stable}) \tag{5.4}$$

$$4n,\gamma \ : \qquad {}^{133}_{59}\mathrm{Pr} \xrightarrow{\epsilon} {}^{133}_{58}\mathrm{Ce} \xrightarrow{\epsilon} {}^{133}_{57}\mathrm{La} \xrightarrow{\epsilon} {}^{133}_{56}\mathrm{Ba} \xrightarrow{\epsilon} {}^{133}_{55}\mathrm{Cs}\ (\text{stable}) \tag{5.5}$$

5.3.2 γ - Ray Energy versus Time Array

Triples

2-D Energy versus Time arrays (1500 $\times$ 2000 channels) were generated for the first ten detectors using triple coincidence data. TAC spectra were obtained for various energy peaks and TAC cuts were made, showing prompt and delayed energy spectra for each detector. Six different TAC gates were made on the array. These regions

[9] Note that the confirmation property of these peaks is at best, tentative. The peak may contain γ rays from more than one source. And a missing energy peak does not necessarily mean that the reaction product is not confirmed, but rather, a combination of low intensity and fast half life make the γ ray difficult to record.

Table 5.8: Energies of radioactive decays confirming the products of the ^{37}Cl on ^{100}Mo reaction.

Energy (keV.)	**Possible Decay Sequence**	**% RA**	$t_{1/2}$
76	$^{133}Ce \rightarrow {}^{133}La$	35	1.62 hr
97	$^{133}Ce \rightarrow {}^{133}La$	100	1.62 hr
477	$^{133}Ce \rightarrow {}^{133}La$	100	5.4 hr
357	$^{130}La \rightarrow {}^{130}Ba$	81	8.7 min
108	$^{131}La \rightarrow {}^{131}Ba$		
135	$^{132}La \rightarrow {}^{132}Ba$	44	24.3 min
465	$^{132}La \rightarrow {}^{132}Ba$		4.8 hr
540	$^{132}La \rightarrow {}^{132}Ba$		4.8 hr
663	$^{132}La \rightarrow {}^{132}Ba$		4.8 hr
1031	$^{132}La \rightarrow {}^{132}Ba$		4.8 hr
182	$^{132}Ce \rightarrow {}^{132}La$	82	3.5 hr
156	$^{132}Ce \rightarrow {}^{132}La$	11.5	3.5 hr
326	$^{132}Pr \rightarrow {}^{132}Ce$	100	1.6 min
496	$^{132}Pr \rightarrow {}^{132}Ce$	23	1.6 min
533	$^{132}Pr \rightarrow {}^{132}Ce$	19	1.6 min
358	$^{133}Ba \rightarrow {}^{133}Cs$	62.2	10.54 y
409	$^{134}Pr \rightarrow {}^{134}Ce$		17 min
372	$^{129}Cs \rightarrow {}^{129}Xe$	31	1.3 d
74	$^{133}Pr \rightarrow {}^{133}Ce$	74	6.5 min

are listed in Table 5.9 and correspond to the TAC channels (y-axis) in Figure 5.7. This is a truncated version of the 2-D arrays that are presented in Appendix D.1. The positioning of the small TAC profile along the y-axis and the composite energy spectrum along the x-axis is meant to emphasize how time and energy spectra are generated from this type of array. The energy spectrum is from the prompt TAC peak gate, i.e., a horizontal cut along the area where the TAC peak maximizes. The small time plot is a logarithmic display of a vertical energy cut at 114 keV.

Generating this type of 2-D array seems to be the proper method to use if an overall perspective is valued; i.e., the entire nuclear reaction is to be investigated. However, if only one or two nuclei are emphasized, more questions than answers are generated. In any case, we felt this was the best approach.

Table 5.9: Triples γ -t Spectral Gate Regions

Region	**Designation**	**TAC Channels**	**Time**(ns.)
1	Pre-prompt	80-800	8.52-85.2
2	Early Prompt	801-999	85.3-106.4
3	Prompt	1000-1020	106.5-108.6
4	Delayed Prompt	1021-1420	108.7-151.2
5	Late Delayed 1	1421-1720	151.3-183.2
6	Late Delayed 2	1721-1920	183.3-204.5

A few observations are noteworthy: The TAC region called pre-prompt contains background peaks, exclusively. A few peaks are pronounced enough to extend throughout the entire 2-D array and show up as a continuous vertical line. The Pb x-rays at $\approx$ 75 and 85 keV. are predominant in this region. This gate spectrum also resembles the activities spectrum. In the delayed prompt region the skewed profile of a metastable isomer appears at 597 keV and at two other channels in the last regions.

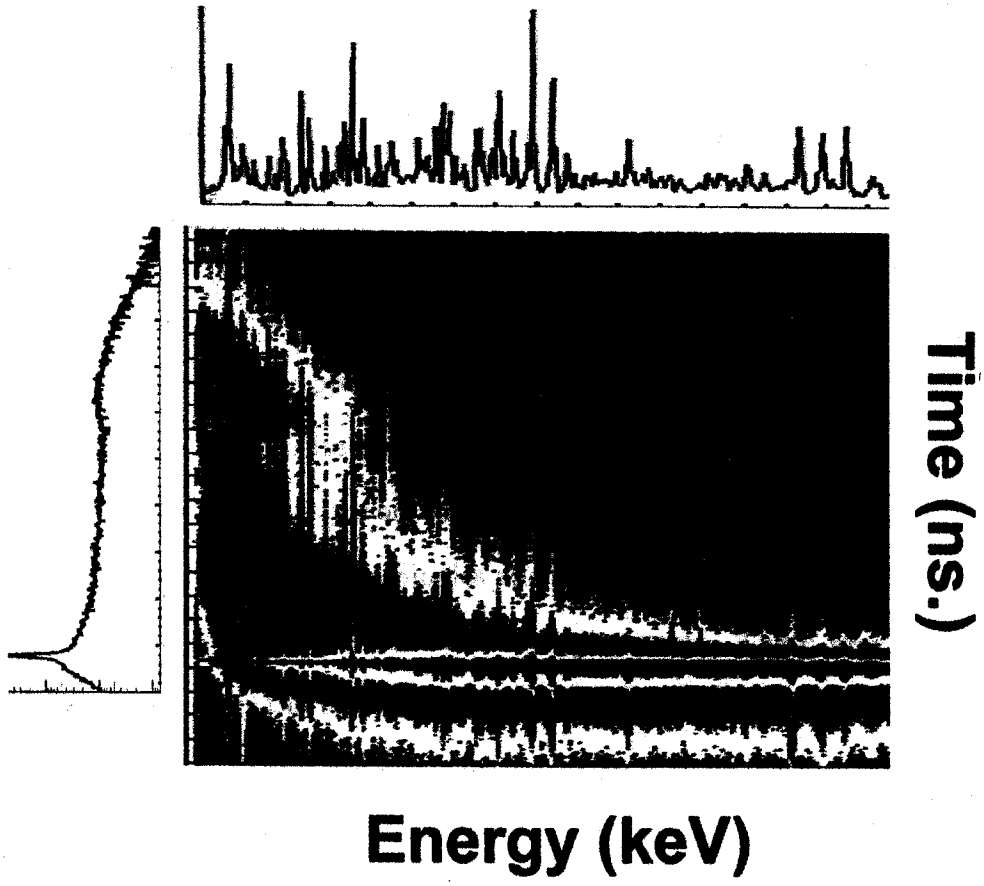

Figure 5.7: A portion of a two dimensional Energy versus time (TAC) array. A small TAC profile is positioned along the y-axis and a composite energy spectrum is positioned along the x-axis in order to emphasize the method of obtaining time and energy spectra from this array.

The most unexpected thing about the 2-D array is the elliptical shape that appears between 320 and 430 ns. on the Time axis and 50 to 150 keV. This is responsible for the wide, half-Lorentian shaped baseline in the last two TAC cuts, which, perhaps by coincidence resembles the shape of the peaks that had been referred to as metastable. The maximum intensity occurs at about 60 keV. There may be a connection between this profile and the x-rays produced by the reaction.

Singles

Single coincidence events were the initial reaction events to be recorded onto tape. Composite γ - Ray Spectra were generated from these events and are presented according to detector number in Appendix D.2. Very little rotational band information can be observed in these composite spectra; the background contributions are of such an intensity that they apparantly conceal the γ rays from the reaction. In fact, there is quite a similarity between the Singles and the Activities spectra. 2-D Energy versus Time arrays were also generated for the single events. There were two such histograms made; one, from the 60-1500 channel number region and the other, from the 1501-3000 channel number region. These are located in Appendix D.1. A comparison with the 2-D spectra from the triple events shows that the profiles are very similar. However, since the signal-to-background ratio is not intense, no further work was done on the Singles.

5.3.3 TAC Spectra

Composite TAC spectra were generated for each detector; these were merely used to generate the TAC parameters for aligning the raw data that are listed in Table 5.5. An example has been shown as part of Figure 5.7. Triple γ-t spectra were also made for a few energies from the Energy versus Time arrays. The half life of each transition may be determined from these profiles. Simple radioactive decay follows a first order

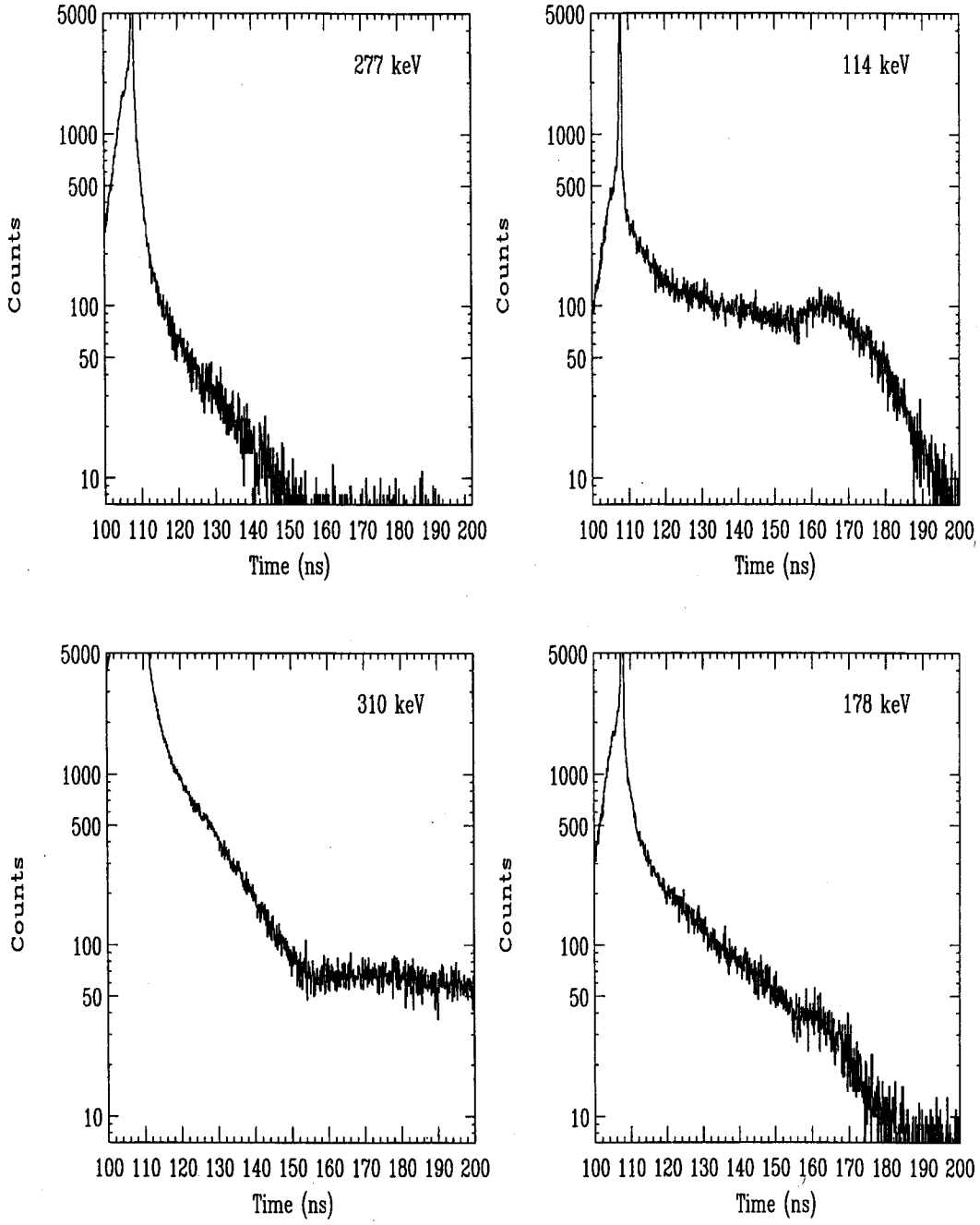

Figure 5.8: TAC profiles for select energies from the 2-D Energy versus Time array. Energies are marked on the plot.

decay pattern according to the well-known equation:

$$N(t) = N_{\circ}\ e^{-\lambda t} \tag{5.6}$$

where, λ is the decay constant,

$$\lambda = ln\ 2/\ t_{1/2}. \tag{5.7}$$

N is the number of radioactive nuclei present at time, t; $N_{\circ}$ is the initial number of nuclei, and $t_{1/2}$ is the half-life of the decay. This can be written in the form of an equation of a straight line:

$$log\ A = C - \ (m \times t) \tag{5.8}$$

where,

$$m = log\ 2/\ t_{1/2}. \tag{5.9}$$

A is the activity, C is the intercept of the line and m is the slope from which the half life can be obtained. By plotting the *log* of the TAC profile for an individual energy peak, the slope of the trailing edge of the prompt peak should yield a half-life value for the transition. An example of this is shown in Figure 5.8 for the 221 keV transition. The TAC profiles were obtained by summing the TAC counts across an energy peak. Many of the energy peaks contain a mixture of γ rays, therefore, their TAC peaks contain a mixture of activities. A plot of the *log* of their TAC prompt peaks does not yield a straight line on the tail of the peak. If the activities are from unrelated nuclei, if the half-lives are significantly different and if the intensity is sufficient, then the half-lives in the mixture may be determined. An example of this is shown in Figure 5.9 [ary84]. The longest half-life (60 hr) is determined from the last few points in the non-linear profile using linear regression analysis. The corresponding activity values for this nucleus is then subtracted from the total plot. This procedure is repeated until all of the activity has been accounted for. In this plot, a 60 hr, 10 hr and a 2 hr half-life nucleus have been separated from the mixture. An example

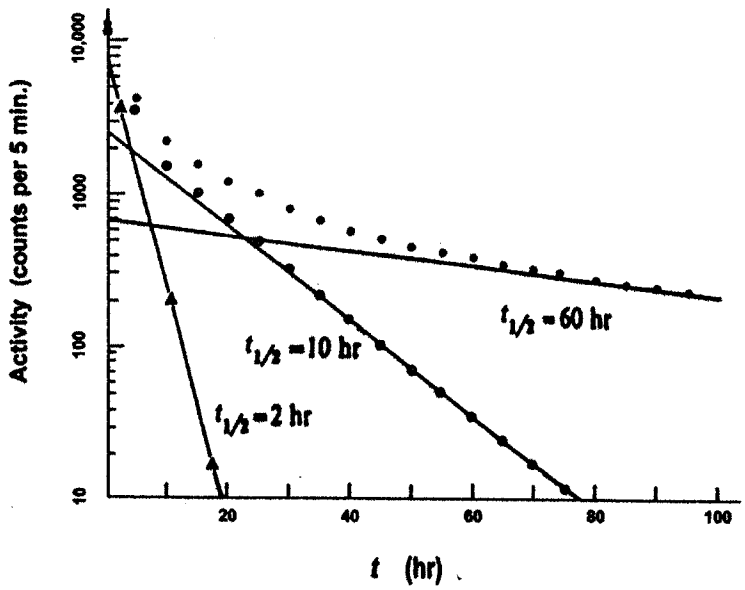

Figure 5.9: Halflife determination from a mixture of unrelated activities. [ar83b].

from this experiment is shown in Figure 5.8 for the 310 keV transition in ^{133}Pr. Many nuclei exhibit successive decays, i.e, a parent nucleus decays to a daughter nucleus then to a grand-daughter nucleus, and so on until a stable nucleus has been reached. An example of successive decay is shown in Figure 5.10 [ary84]. This is a plot of the relative number of atoms versus time for the decay of ^{105}Ru (N_1) to ^{105}Rh (N_2) to ^{105}Pd (N_3). This is a more complicated system and a deconvolution technique is necessary in order to separate the activities. Metastable isomers would exhibit this type of TAC profile, however, the situation is actually much more complicated since the (N_2) and (N_3) activities may or may not be found at the same energy. A TAC profile for any given energy peak may be the sum of unrelated activities and successive decays from that energy (metastable) or from a different energy peak. The contribution from different energies may be represented by the presence of a positive decay profile, i.e., the generation of another nucleus. If the successive decay is from a metastable isomer at the same energy, then the positive slope would not be observed since the y-axis represents the sum of the activities and this could not be more than

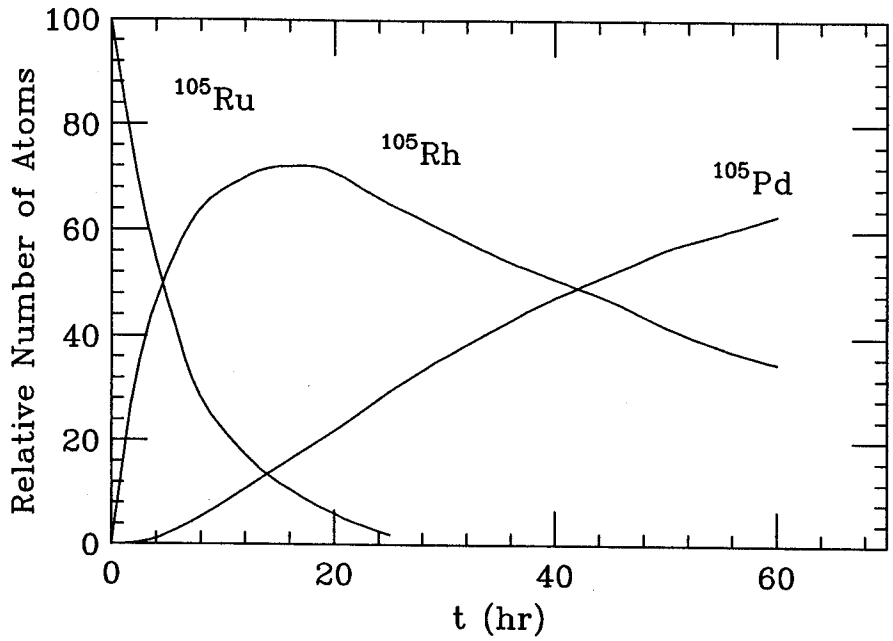

Figure 5.10: An example of successive decay: ^{105}Ru to ^{105}Rh to ^{105}Pd [ar83c].

100% for any parent nucleus. The half-life values for such complicated systems may have to be listed as a range instead of an actual half-life. If more selective TAC spectra could be obtained using the multiple energy gate technique, then the actual half-life values might be resolved. Multiple energy gate TAC spectra were not generated.

TAC profiles for transitions in the ^{132}Pr and ^{133}Pr nuclei are presented in Appendices E.4 and F.4 . Tables 5.10, 5.11 and 5.12 list their probable half-lives. By comparing the half-lives of transitions within a rotational band, it is generally observed that the higher spin transitions have a faster half-life and the lower spin components have a slower half-life.

Table 5.10: Half life determinations for ^{132}Pr from the composite triples γ- t array. The $t_{1/2}$ (ns.) should be considered upper limits and not absolute values. LR refers to the linear regression range used to determine $t_{1/2}$.

E keV	**band**	$t_{1/2}$ ns	**LR**	$\chi^2 \times 10^2$
114	1	32.69	120-135	0.958
178	1	12.69	120-135	0.941
229	1	10.54	120-135	2.276
277	1	10.33	120-135	2.706
311	1	8.29	120-135	4.730
352	1	8.28	120-135	8.320
408	1	6.38	115-130	7.664
130	2	22.0	130-150	
266	2	10.24	120-135	2.663
240	2	11.18	120-135	2.207
383	2	7.95	120-135	7.900
321	2	9.32	120-135	5.696
407	1	7.10	115-130	7.933
294	1	9.25	120-135	2.826
368	3	6.97	115-130	5.034
506	1	7.22	115-130	9.521
507	2	6.54	115-130	11.60
283	gs	10.04	120-135	4.342

Table 5.11: Half life determinations for ^{133}Pr from the composite triples γ- t array. The $t_{1/2}$ (ns.) should be considered upper limits and not absolute values. LR refers to the linear regression range used to determine $t_{1/2}$.

E keV	**band**	$t_{1/2}$ ns	**LR**	$\chi^2 \times 10^2$
388	1	7.61	120-135	1.879
530	1	8.72	115-130	1.820
698	1	9.75	115-125	1.111
939	1	3.62	112-120	9.953
414	1	7.81	120-135	2.563
567	1	7.50	120-135	3.869
606	1	6.11	120-135	3.219
452	2	7.11	115-130	1.462
488	2	6.63	115-130	1.070
632	2	5.60	115-130	2.263
909	2	3.45	112-120	2.704
667	2	9.01	117-132	5.278
623	2	8.02	120-135	7.764
477	2	7.59	120-135	2.281
400	2	7.64	120-135	1.760
720	2	4.46	112-120	2.563
682	2	6.29	115-125	1.755
310	3	8.74	120-135	2.933
551	3	6.19	115-130	2.034

Table 5.12: Half life determinations for ^{133}Pr (continued).

E keV	**band**	$t_{1/2}$ ns	**LR**	$\chi^2 \times 10^2$
149	4	18.22	120-135	2.891
245	4	10.51	120-135	3.426
327	4	8.98	120-135	0.828
395	4	7.66	120-135	1.589
448	4	7.42	120-135	1.939
170	4	15.49	140-155	0.312
763	4	6.90	115-125	4.224
768	4	6.51	115-125	6.176
164	5	20.8	130-145	0.380
251	5	9.89	135-150	1.381
337	5	8.55	130-145	1.982
409	5	8.68	125-140	2.281
472	5	8.06	120-135	3.157
196	6	12.73	120-135	0.383
244	6	11.04	120-135	0.358
351	6	8.72	120-135	0.818
404	6	8.14	120-135	1.674
454	6	7.49	120-135	2.479
501	6	7.41	120-135	2.537

5.3.4 Background Array

$E_{\gamma 1}$ versus $E_{\gamma 2}$ arrays were generated for the prompt and the three delayed TAC regions. See Figure 5.11. These consisted of a TAC gate of region one versus a TAC gate on the prompt or one of the delayed regions. Initially we expected to subtract these background arrays from the energy arrays from each region, in order to generate background subtracted spectra. However the background arrays produced more intense coincidences in the x-ray region than expected. Subtracting the arrays might have produced negative peaks, so, another background subtraction technique was devised. Gates at the valleys between peaks were summed together with gates from the highest energy region where no energy peaks were observed. This produced a general background spectrum that was normalized and subtracted from the energy peaks of interest. This procedure was followed for the multiple gate arrays, also.

5.4 Energy Spectra: Simple Gate

5.4.1 Prompt Region Spectra

In order to study rotational states the γ -rays must be sorted according to their respective nucleus. This involves constructing 2-D histograms: $E_{\gamma 1}$ versus $E_{\gamma 2}$ arrays. The 2-D array representing the sum of all triple coincidences determined from the detector comparisons is presented in Figure 5.12. A TAC gate was set during the array generation: everything that had previously been designated pre-prompt through prompt was included. By making a cut (gate) on either axis at an appropriate energy, A, all the energies in coincidence with A that occurred between the two detectors can be obtained within a 1-D histogram. The resulting spectra for ^{133}Pr and ^{132}Pr are displayed in Appendices F.1 and E.1. The size of the 2-D histograms restricts the amount of information analyzed. One 2900 $\times$ 2900 channel number array requires over 64,000 blocks on disk. The Oak Ridge Software is intensity limited, i.e., the scan

program does not spin the tape after a certain array intensity is reached. Therefore, out of a possible 400 2-D arrays, only about 60 were able to be run. (Two, 2-D arrays can be run at one time.) At this point, groups of the arrays were summed and gated. Then the gates from each of the groups were added. Spectral gates were obtained by summing gates across peaks and subtracting the background on each side of the peak. This procedure was followed for prompt and delayed and background spectra. The approximate resolution was 0.621 keV. per channel. After analyzing gates of approximately 30, 2-D histograms, it was determined that a second gate was necessary in order to obtain better signal to background ratio in the spectra.

Baseline Generation

The γ ray peaks in a typical spectrum are arranged on what appears to be a background envelope that is generated by the reaction. There is some speculation that this might be due to a residual effect from the Giant Dipole Resonances or, perhaps, merely an overlap of all the unresolved (and therefore, undocumented) x-rays and γ -rays and particle emission contributions (neutron activation, coulomb excitation, etc.) from the reaction. In any case, this envelope is not entirely removed when channel number gates are summed across a peak and the baseline gates are subtracted. A straight baseline is an advantage when adding spectra with varying total counts that contain low intensity peaks. Therefore a pseudo-baseline peak was generated from the background of a composite spectrum by manually clipping off each peak (using the workstation mouse and the *DAMS* software). This was normalized to each spectrum and subtracted in order to generate a straight baseline for the simple gates. This method was not a panacea –each spectrum had slightly differing envelopes and aberations sometimes occurred after baseline subtraction. —But, it was the impetus to create a new baseline method, which is described in Chapter 6.

5.4.2 Delayed Region Spectra

Three 2-D energy arrays were run for the three TAC regions beyond prompt. 1-D gates were generated from these arrays. ^{132}Pr appears to have some delayed transitions; ^{133}Pr does not. Many of the peaks present do not belong to either nucleus. Each delayed array was generated with the TAC gate range specified in Table 5.9 on each axis. This method can determine the energy coincidences between peaks that exist within those regions only. If time would have allowed, arrays with the prompt peak gate on one axis versus one of the delayed region gates could have been generated.

5.5 Energy Spectra: Multiple Gate

In order to increase the signal to background ratio and to selectively enhance peaks from one particular nucleus, a multiple gate technique was developed using triple coincidence data. For the first gate step, the program *LEMO* was used with a 2-D free form energy coincidence gate to write coincidences between detectors to tape. There is a software limitation of 4 gates per run. For the ^{133}Pr nucleus, 2-D gates were set for the 310, 551, 709 keV. peaks. The resulting 2-D array is presented in Figure 5.13. For ^{132}Pr, two 2-D gates from two different bands were chosen: 115, 178, 283, 130 keV. (See Figure 5.14). Coincidences from the four 90° detectors were compared with the rest of the detectors and the events were sorted onto a new tape. *SCAN* was then used with the new tape to generate a total energy versus total energy 2-D array. This had to be constructed in three to five steps because of the intensity limitation. Each step's 2-D histogram was gated. The procedure was similar to the simple gate process —with two exceptions. Peaks from the primary energies dominate the spectra and the process generated a diagonal line across the 2-D array that contains a sum of the Simple gates. A mask was designed to erase these contributions so that the coincidences of interest would be more apparant. The spectra had to be compressed

due to lack of computer storage space this resulted in an energy resolution of only 1.2 keV. per channel. This multiple gate deserves further comment. The first stage is not a gate where events containing 310, 551, 709 keV. peaks are merely filtered onto tape. This gate is truly a 2-D gate, i.e., all events that are in coincidence with what the 310, 551, 709 peaks are in coincidence with are filtered onto tape. In other words, anything in coincidence with the 310 simple gate **spectrum** is filtered in. This generates a data set that better describes the entire nucleus. Transitions that are related to, but not in direct linear coincidence with the primary gates are included.

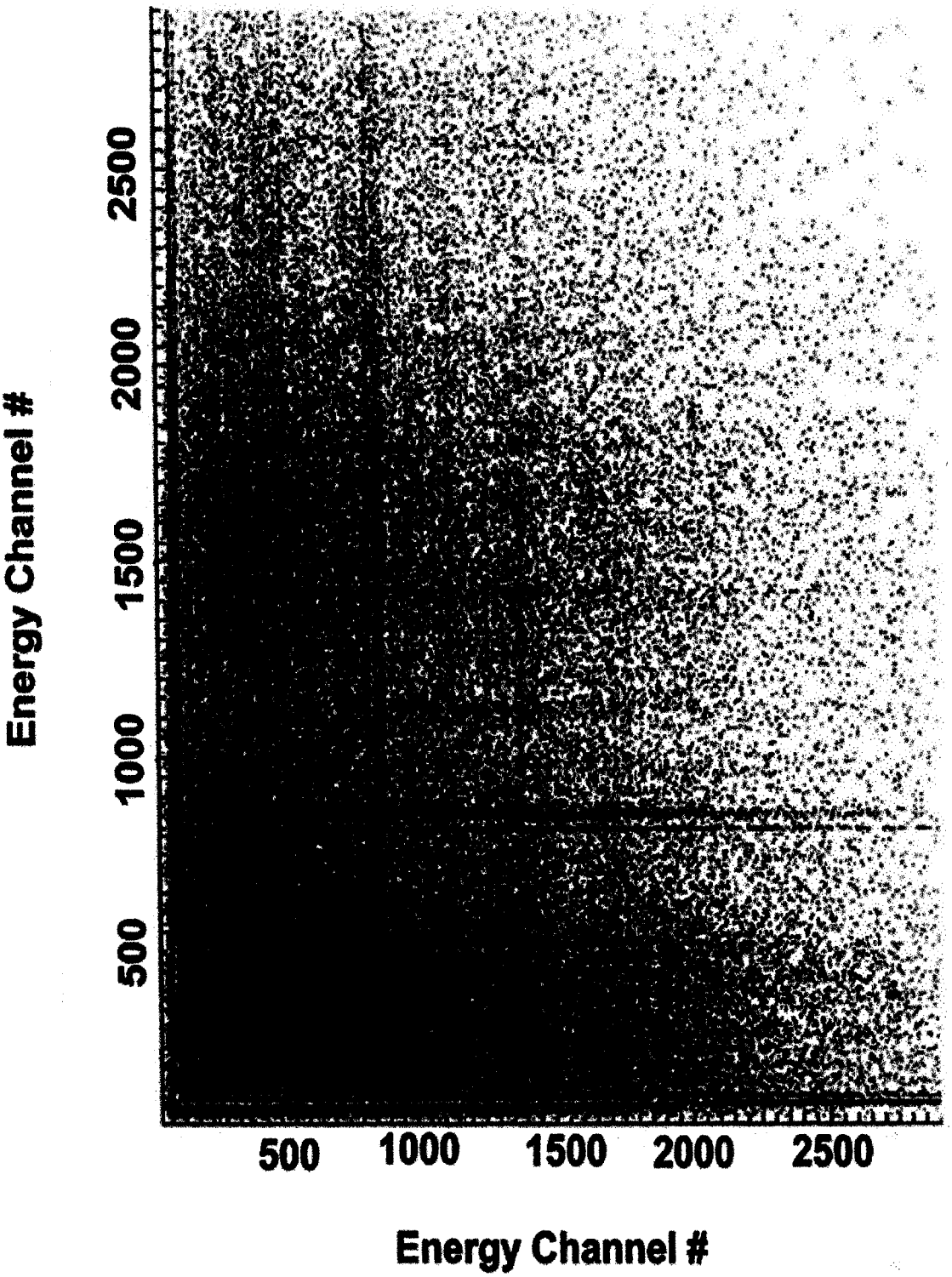

Figure 5.11: Background 2-D array: $E_{\gamma 1}$ versus $E_{\gamma 2}$ with a TAC gate on the pre-prompt region.

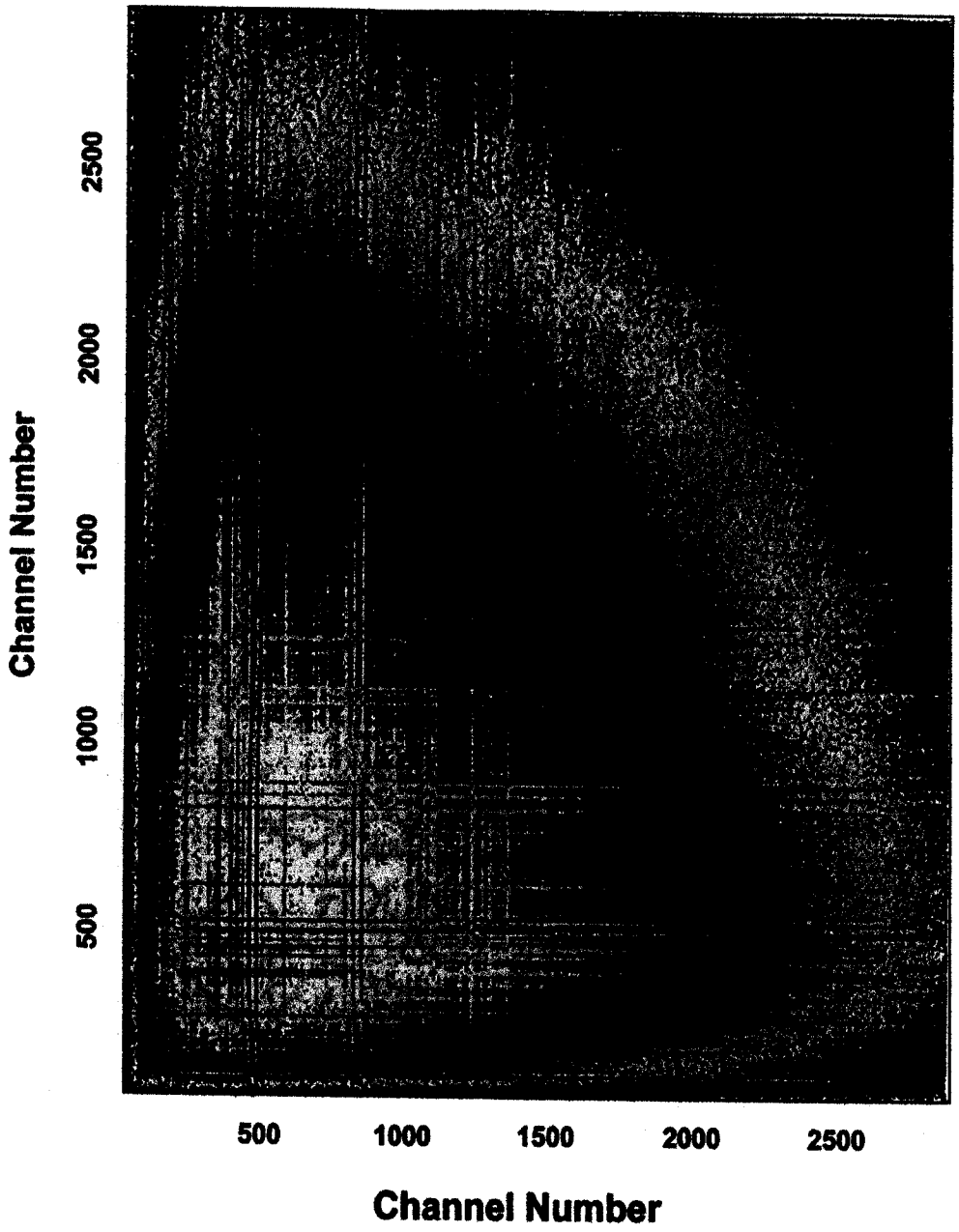

Figure 5.12: 2-D array of the sum of all triple coincidences from $E_{\gamma 1}$ versus $E_{\gamma 2}$ comparisons.

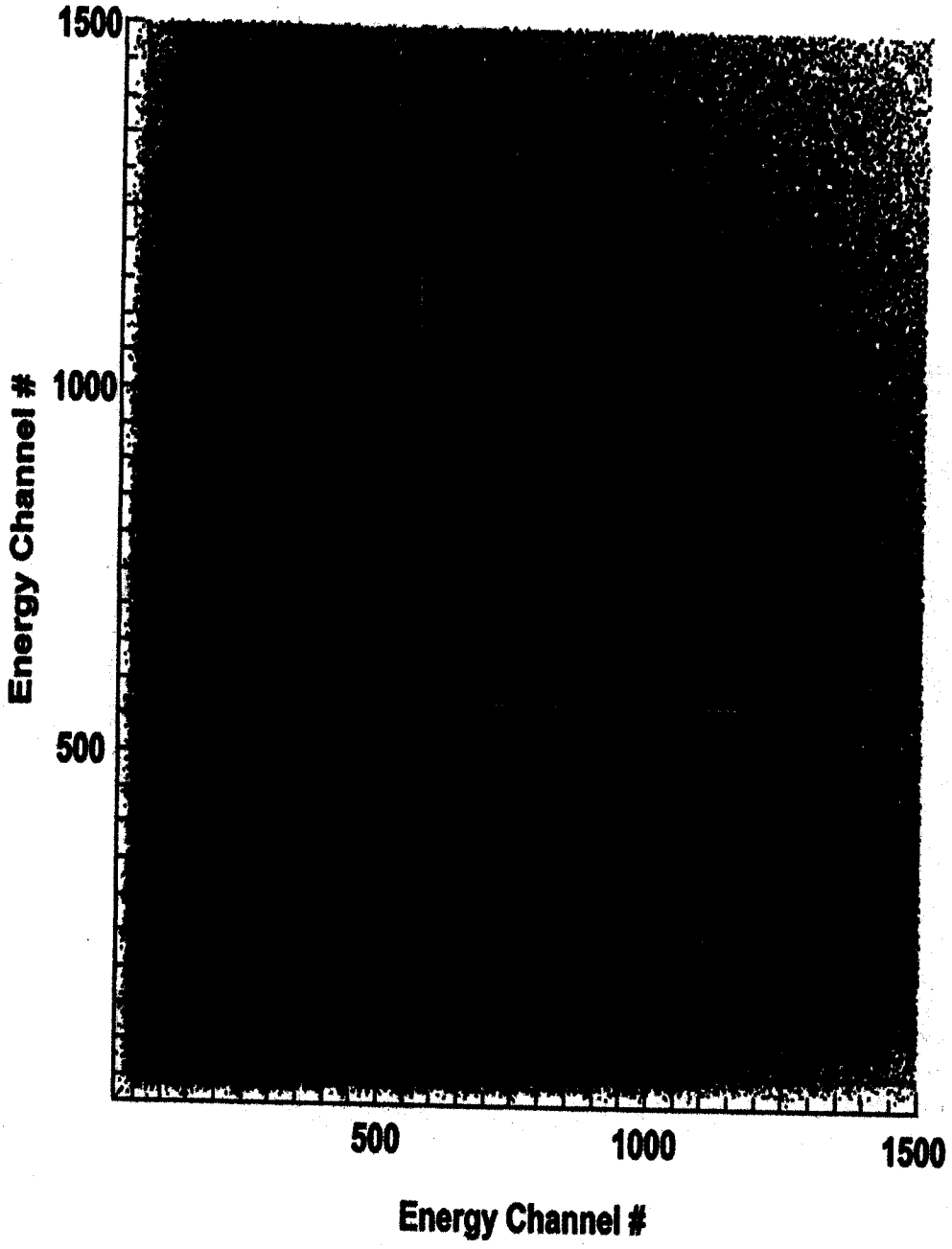

Figure 5.13: 2-D array from the multiple ^{133}Pr gate. The predominant perpendicular lines represent the primary gates at 310, 551, and 709 keV. The diagonal line contains the sum of the Simple gates from these primary energies.

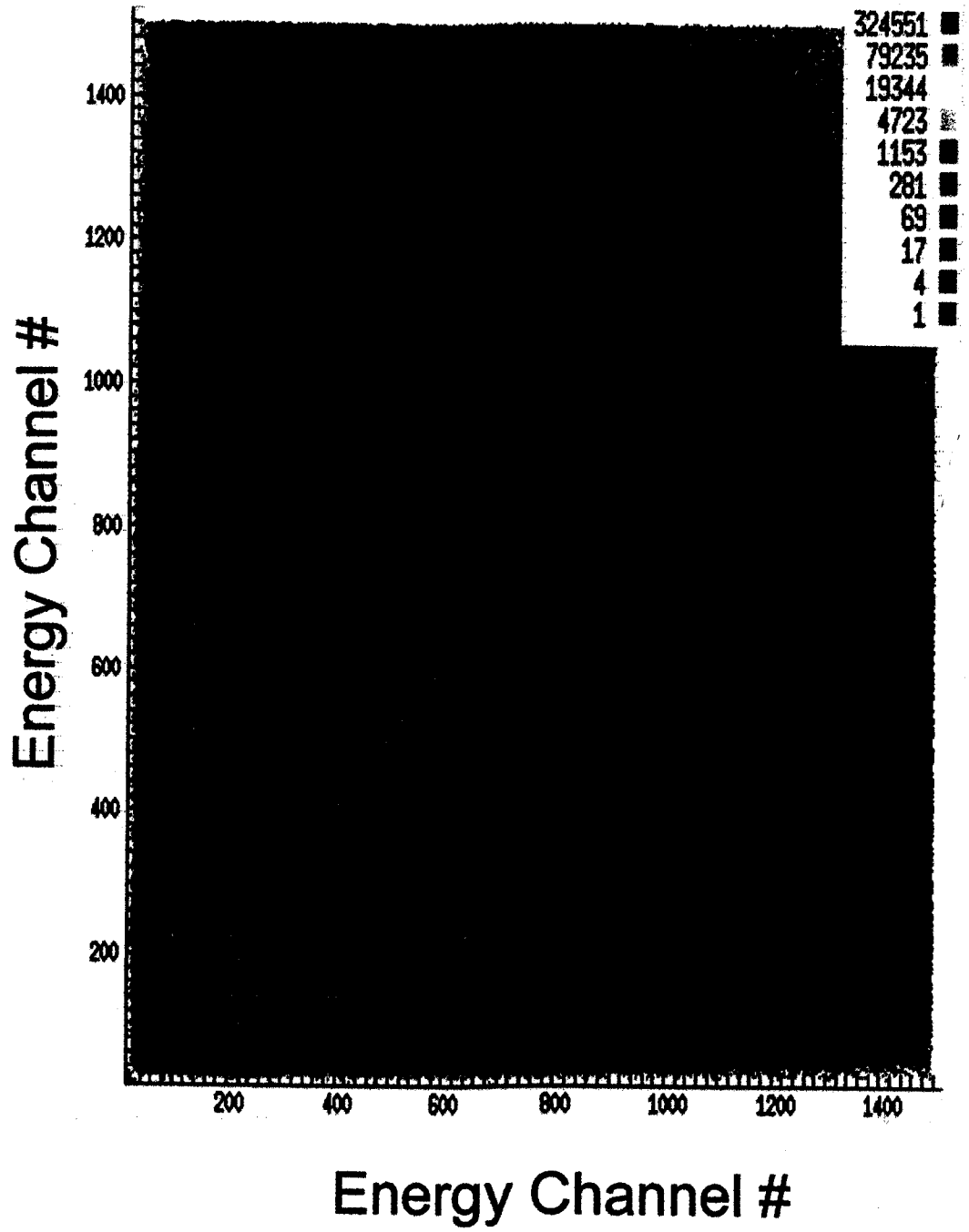

Figure 5.14: 2-D array from the multiple ^{132}Pr gate. The predominant perpendicular lines represent the primary gates at 115, 179, 283, 130 keV. The diagonal line contains the sum of the Simple gates from these primary energies.

Chapter 6

Spectral Enhancement Techniques

In this chapter we discuss the development of two spectral enhancement routines: a noise reduction technique using Fourier Transforms and a method to generate a baseline for individual spectra. Ordinarily, this might belong in the Data Analysis Chapter since the Fast Fourier Transformation (FFT) Technique has been routinely used for noise reduction in many types of spectral analyses. However, this is not the case in γ-ray spectroscopy. After the experimental data were analyzed, we felt the need for this additional work. Since FFT was not part of the standard γ-ray software, we had to develop it.

6.1 Introduction

About twenty years ago, spectroscopists used a form of Fourier transform (FT) for γ-ray spectroscopy, with some success. Some built the continuous FT algorithm into a smoothing technique, using a math filter that operated on the transformed coefficient vector [ino69, bli74, kek86, kek89]. Others constructed a deconvolution technique based on the Fourier transform [ver83, cab91, flo92]. These were designed specifically for each data set. Both methods improved spectral resolution; however, the computer software and hardware of the time may have prevented the routine use of a fast-fourier-transform (FFT). Inouye [ino69] in 1969, using the continuous FT,

speculated that a transform of a 4096-channel spectrum might require about 1/2 hour of computer time, and Blinowska and Wessner [bli74] in 1974 reported that a FFT of a 1024-channel spectrum required 50 seconds . Today, the forward and reverse FFT's are virtually instantaneous on a system such as Dec's VAXstation 4000.

With the advent of 4π spectrometers and the search for low intensity, superdeformed bands in nuclear structure studies, the need for FFT again arises. Even though the γ-ray signal-to-noise ratio from a single detector may be adequate, multistep coincidence measurements among various detectors produce large amounts of white noise within the resulting spectrum. High frequency noise is systematically introduced through the analysis processes, especially the process of rebinning doppler- and gain-shifted data via a random number sequence. When this is compounded with the necessity of investigating peaks below the 10% intensity level, the need for a potent noise reduction method becomes very apparant.

The application of a discrete FFT algorithm to γ ray spectra data analysis enhances low intensity components of a spectrum, removes high frequency noise and increases the signal-to-background ratio.

The data set obtained from the ^{37}Cl on ^{100}Mo reaction, provided a unique opportunity for this technique development. For example, most of the peaks of interest in the rotational band structure for the ^{132}Pr nucleus are below the 20% count level and peaks associated with superdeformed bands have considerably lower intensities. Three types of frequency components can be seen in each spectrum: low frequency, observed as a baseline abberation; high frequency noise; and medium frequency – the γ-ray peaks of interest. All three are naturally convoluted into a typical spectrum. The objective of this enhancement routine is to remove the low and high frequency components that are not part of the peaks of interest.

6.2 Fast Fourier Transform

To do this, the Oak Ridge User Software was modified to accommodate a discrete FFT program from the IMSL package [imsl], which uses a variation of the Cooley-Tukey algorithm [coo65]. The continuous Fourier transform [bri74] is defined as

$$\hat{f}(\omega) = \int_{-\infty}^{\infty} f(t) e^{-2\pi i \omega t} \, dt. \tag{6.1}$$

The discrete Fourier Transform [imsl] is an approximation of this integral for a non continuous function over the interval, T:

$$\hat{f}(\omega) \approx \int_{-T/2}^{+T/2} f(t) e^{-2\pi i \omega t} \, dt. \tag{6.2}$$

$$\hat{f}(\omega) = e^{\pi i \omega T} \int_{0}^{+T} f(t - T/2) e^{-2\pi i \omega t} \, dt. \tag{6.3}$$

The FFT is a discrete Fourier Transform that can be computed efficiently: [1]

$$\hat{x}_m = \sum_{n=1}^{N} x_n \omega_{nm}$$

where ω_{nm} is a function derived from $e^{-2\pi i(m-1)(n-1)/N}$. Using this, the vector $\vec{x}$ in n-space can be transformed into m-space.

All of these calculations are transparent to the software development because the IMSL MATH/LIBRARY provides a real, trignometric FFT that accepts a vector $\vec{s}$ of length N and returns a coefficient vector $\vec{c}$ with the following form, if N is even: [2]

$$\vec{c}_{2m-2} = +\sum_{n=1}^{N} \vec{s}_n \cos\left[\frac{(m-1)(n-1)2\pi}{N}\right] \qquad m = 2, \ldots, N/2+1$$

$$\vec{c}_{2m-1} = -\sum_{n=1}^{N} \vec{s}_n \sin\left[\frac{(m-1)(n-1)2\pi}{N}\right] \qquad m = 2, \ldots, N/2$$

$$\vec{c}_1 = +\sum_{n=1}^{N} \vec{s}_n.$$

[1] The transform of a vector of size N is most efficient when using a fixed number of points based on a product of small prime numbers. (ex., $1450 = 2 \times 5 \times 5 \times 29$.) If this condition is met, then the computation is proportional to $N \log N$; otherwise, the number of computational operations is equal to N^2.

[2] If N is odd, $\vec{c}_m$ is defined as above for m ranging from 2 to $(N+1)/2$.

The inverse FFT reverses the operation. If N is even, the form is: [3]

$$\vec{s}_m = \vec{c}_1 + (-1)^{(m-1)}\vec{c}_N \quad +2\sum_{n=2}^{N/2} \vec{c}_{2n-2} \cos\left[\frac{(m-1)(n-1)2\pi}{N}\right] \\ -2\sum_{n=2}^{N/2} \vec{c}_{2n-1} \sin\left[\frac{(m-1)(n-1)2\pi}{N}\right].$$

The spectra, $\vec{s}_m$, are transformed into another domain, $\vec{c}$, which may be thought of as a frequency domain. Then a limited range of frequencies —excluding the highest frequencies — are chosen to be transformed back into the original domain. Figure 6.1 shows the direct equivalence between frequency of the forward FFT and the channel number of the data. Because of this, the range for the reverse FFT can be set according to channel number. There is no mathematical manipulation of the forward transform, making the technique simple to use. To initialize the program, only the forward and reverse channel-number ranges need to be specified, along with input and output math operators. This constitutes the entire noise reduction technique.

An example of the extent of the noise reduction can be seen in Figure 6.2: A) is the original data, C), the same data after FFT and B) represents the difference between A and C, i.e., the noise that was removed.

6.3 Algorithm Development

There were three mathematical considerations that had to be built into the algorithm in order to produce an acceptable transformed spectrum. A flowchart is presented in Figure 6.3.

Zero Suppression:

Gated spectra often contain zero points in the baseline due to the position of the gate. This constitutes a non-continuous function, and the FFT produced has a ringing

[3] If N is odd, the equations are similar but are summed over $(N+1)/2$, and not $N/2$. See reference [imsl].

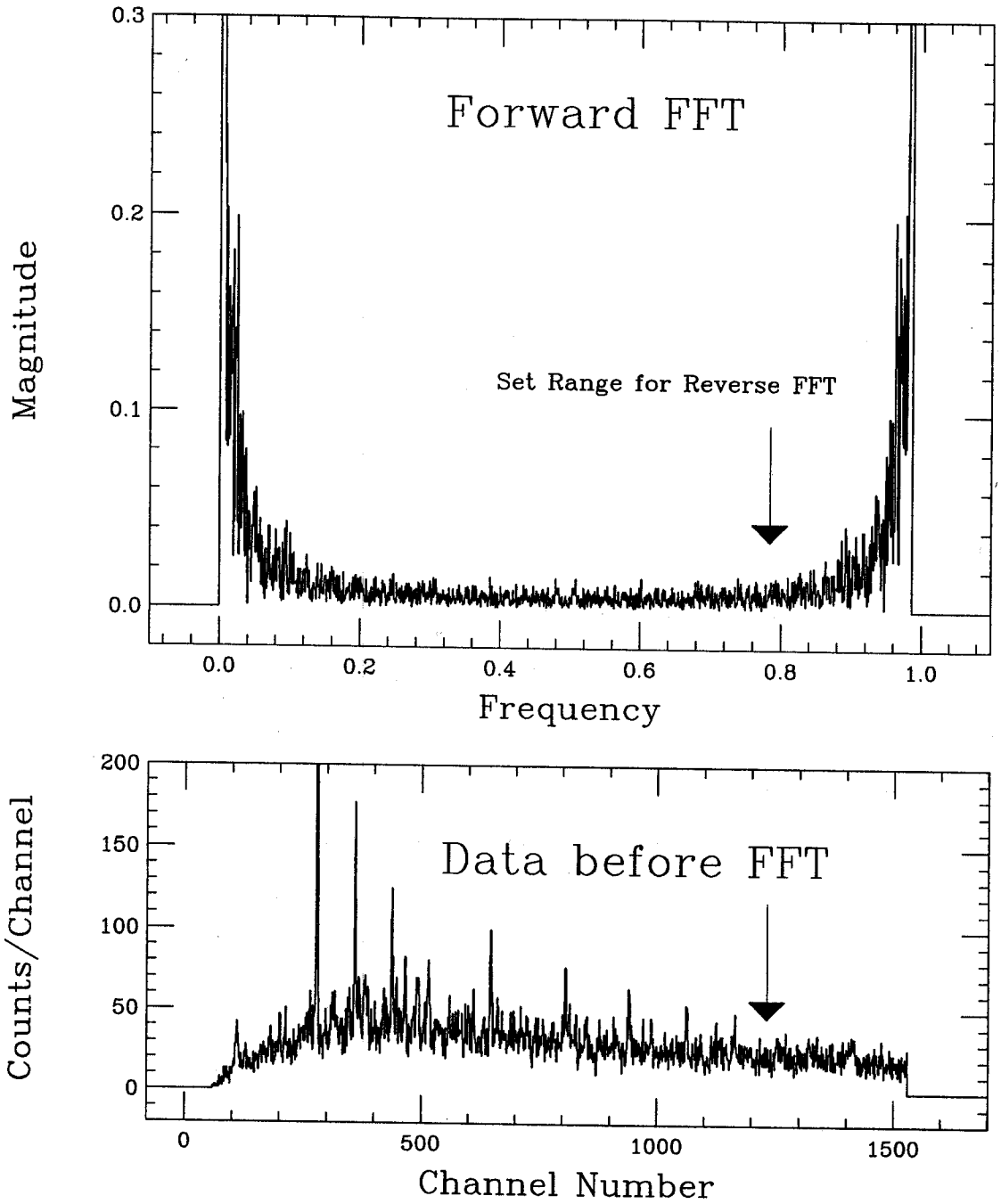

Figure 6.1: Equivalence between FFT frequency and spectral channel number: A plot of a forward FFT (linear) of a 240 keV gate. Since there is a direct relationship between points on the frequency axis and on the channel number axis, setting the range for the reverse FFT is based on channel number.

pattern superimposed on the spectrum. To resolve this, the zero points were removed, their channel number positions were retained, and the spectrum was compressed (shifted). After the reverse FFT, the spectrum was reconstructed with the zero points in place.

Baseline Offset:

An offset is added to the spectrum before FFT to avoid an arithmetic error in the math operator if a negative value is present. The offset is subtracted after the reverse FFT.

Mathematical operator:

If the data set intensities vary over many orders of magnitude, a linear FFT algorithm will be useful for only a portion of the data set. A series of math operators were included in order to extend the range. The software was written so that the user has a choice of math operators and each data set can be individually optimized. The common and natural log operators can work over a few orders of magnitude; the square root operator selectively enhances the small peaks (noise) for a very efficient removal of noise. By using a combination of operators, the best results, covering over eight orders of magnitude, are obtained. Taking the square root, then using the ln operator twice (LLS), yields the best results if a large, multiple spectra, data set is to be analyzed at one time. It is also possible to vary the input operator for the forward transform with respect to the output operator for the reverse transform. For example, a combination of $\ln/\log^{-1}$ provides extra enhancement for the low-intensity peaks. These techniques must be used selectively; there are advantages and disadvantages to both the LLS and $\ln/\log^{-1}$ methods. LLS can be used for multiple calls to the FFT routine on a data set with widely varying intensities. Using LLS twice on the same data set is preferable to using a high percentage of noise reduction

in a single attempt. LLS can be used on data that have been background subtracted or baselined with the SNIP routine (see below). The $\ln/\log^{-1}$ method is for single use only on individual spectra. It maximizes low intensity peaks and minimizes background. However, it must be performed before background subtraction since negative peaks are transformed into positive peaks, and it must be used before SNIP baseline subtraction if the relative peak ratios are to be retained. A comparison of the LLS and $\ln/\log^{-1}$ FFT methods on low, medium and high intensity single channel gates is displayed in Figures 6.4, 6.5, and 6.6. The original data are gates from the simple data array.

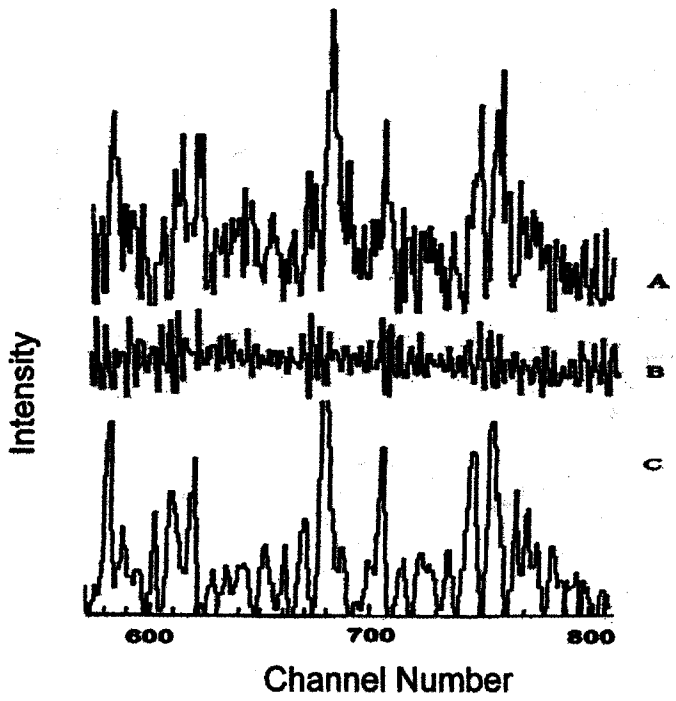

Figure 6.2: An example of the amount of noise rejection after FFT using an expanded view of the 240 keV gate: A) Original data, B) Subtracted Noise C) Data after FFT.

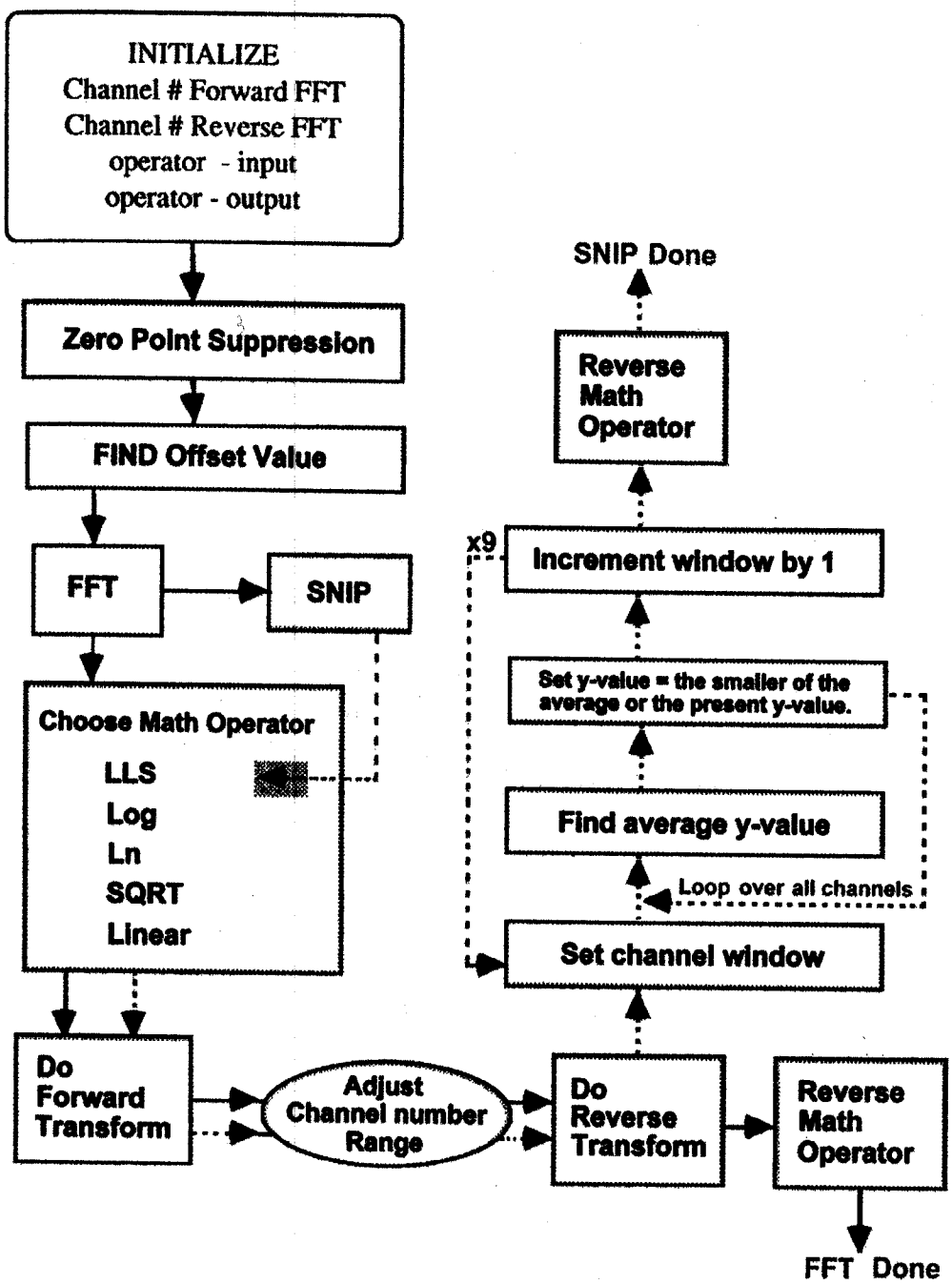

Figure 6.3: Flowchart of The FFT and SNIP spectral enhancement algorithms.

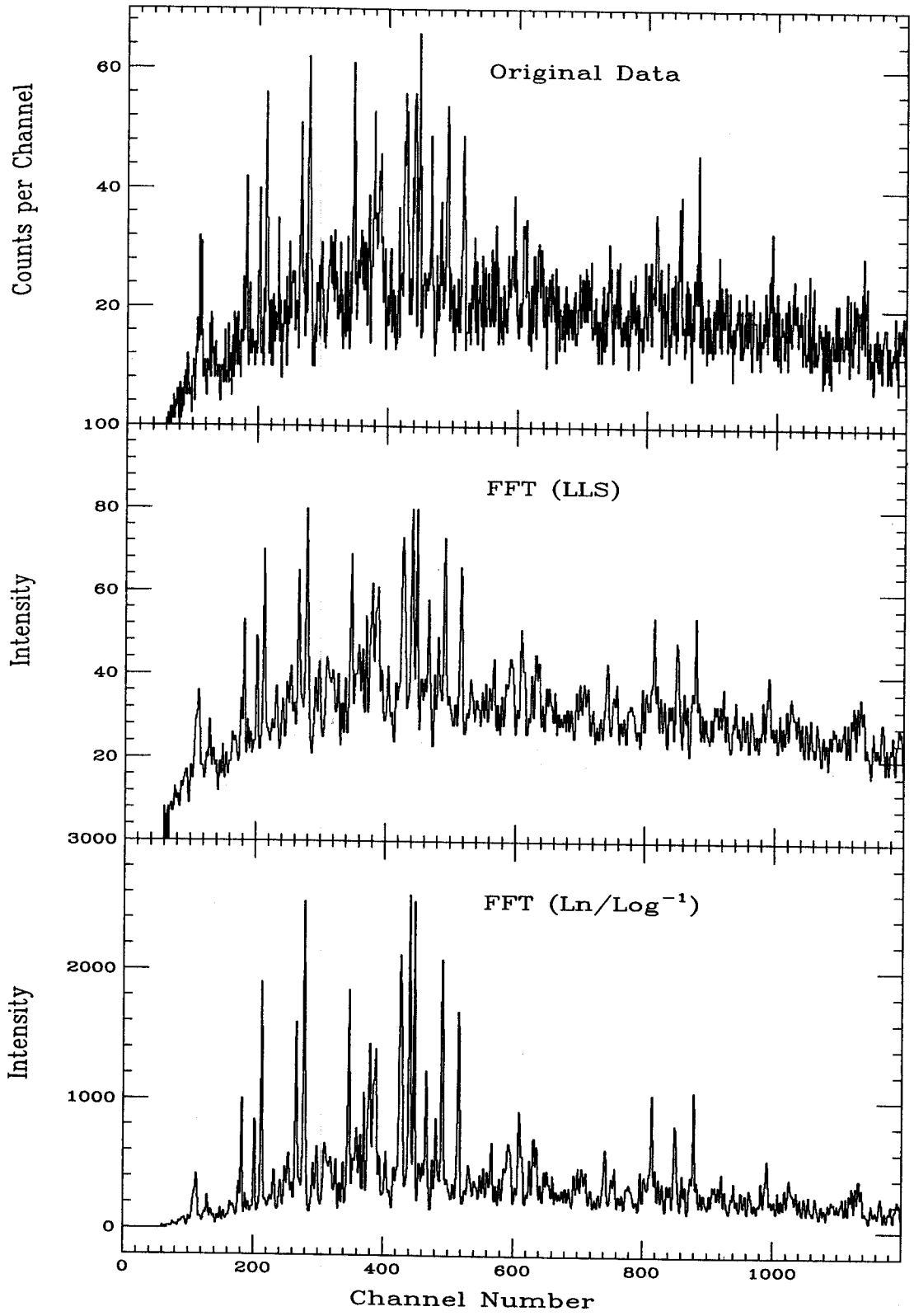

Figure 6.4: Comparison of the original (low intensity) channel number 174 gate with a first FFT (LLS) spectrum and a second FFT ($\ln/\log^{-1}$) spectrum.

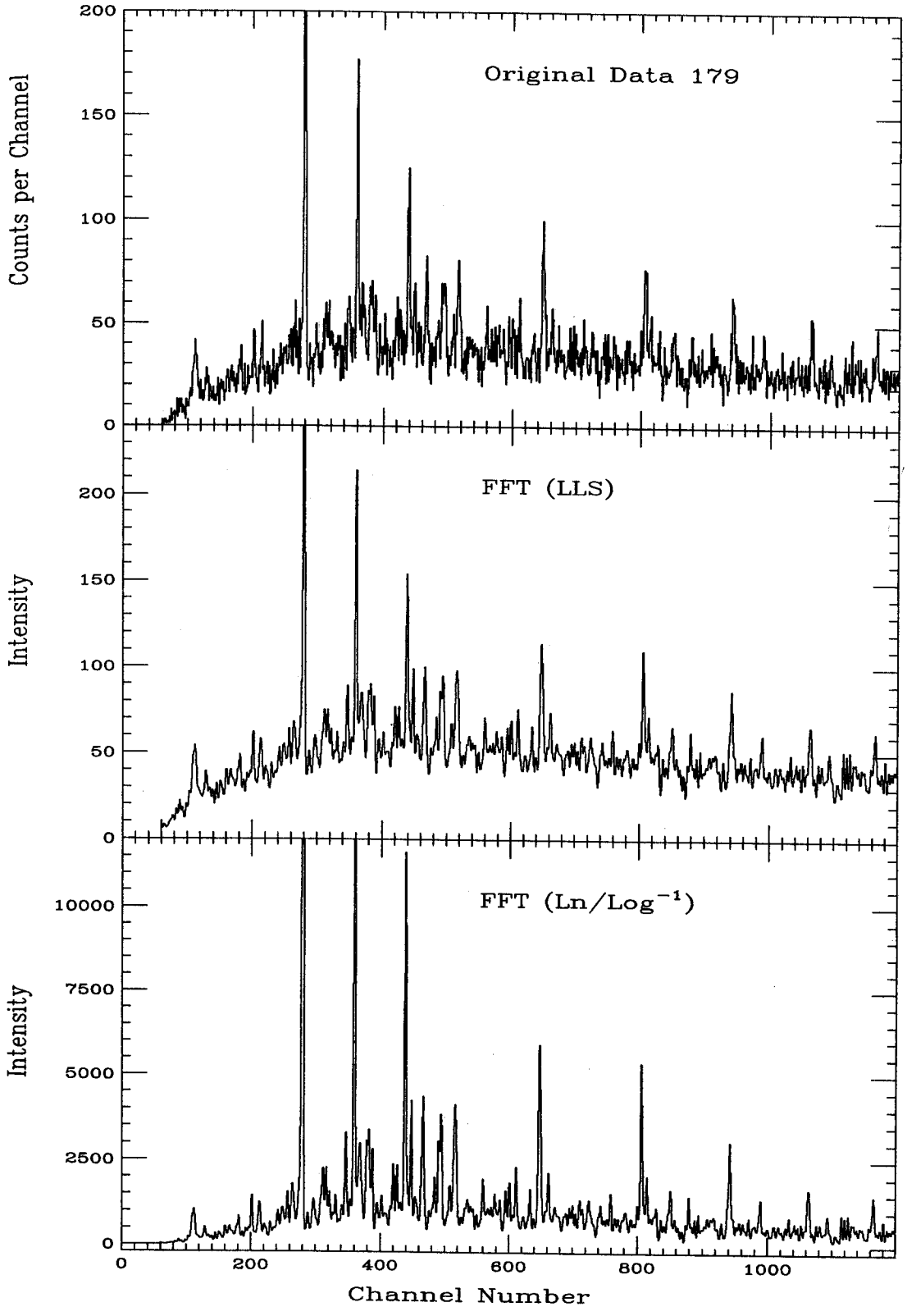

Figure 6.5: Comparison of the original (medium intensity) channel number 179 gate with a first FFT (LLS) spectrum and a second FFT (ln/log^{-1}) spectrum.

6.4 Baseline Generation -SNIP

In order to generate the low frequency component of a typical spectrum, another routine was added to the Oak Ridge software — a modification of the Statistics-Sensitive Nonlinear Iterative Peak clipping (SNIP) algorithm that was developed for proton induced x-ray emission spectroscopy [rya88]. This was preferable to the baseline spectrum generated by FFT because FFT induced unwanted oscillations in this frequency region.

Both SNIP and FFT routines require the same mathematical treatment for zero suppression of the channel-number axis (X) and baseline offset of the intensity axis (Y) of the spectra. The LLS combination of math operators is optional in the FFT algorithm but a requirement in SNIP, since it is used as a low statistics filter to compress the Y-axis range. The channel number intensity can be represented as: $z = \mathcal{F}(y)$ where

$$\mathcal{F}(y) = \ln\left[\ln\left(\sqrt{y - [offset] + 1} + 1\right) + 1\right] . \tag{6.4}$$

After the FFT routine, but before the application of the reverse operator, a multipass peak clipping loop replaces each value of $z(x)$. For each pass of the loop, a sampling interval ω is named. The average of the counts at each end of the sampling interval, $\bar{z}(x,\omega)$, is compared with the intensity at the center of the interval, $z(x)$, and the minimum value, $\bar{z}[x,\omega(x)]$, is written as the new channel count:

$$\left\{ \begin{array}{c} \bar{z}(x,\omega) = [z(x+\omega) + z(x-\omega)]/2 \\ \\ z(x) \end{array} \right\} \begin{array}{c} \text{MIN} \\ \Longrightarrow \\ (\text{MAX}) \end{array} \bar{z}\,[x,\omega(x)] . \tag{6.5}$$

After each pass, the sampling interval is incremented by 1 to reduce baseline oscillations; on the next to the last pass, the interval is reset to 1. The process is repeated

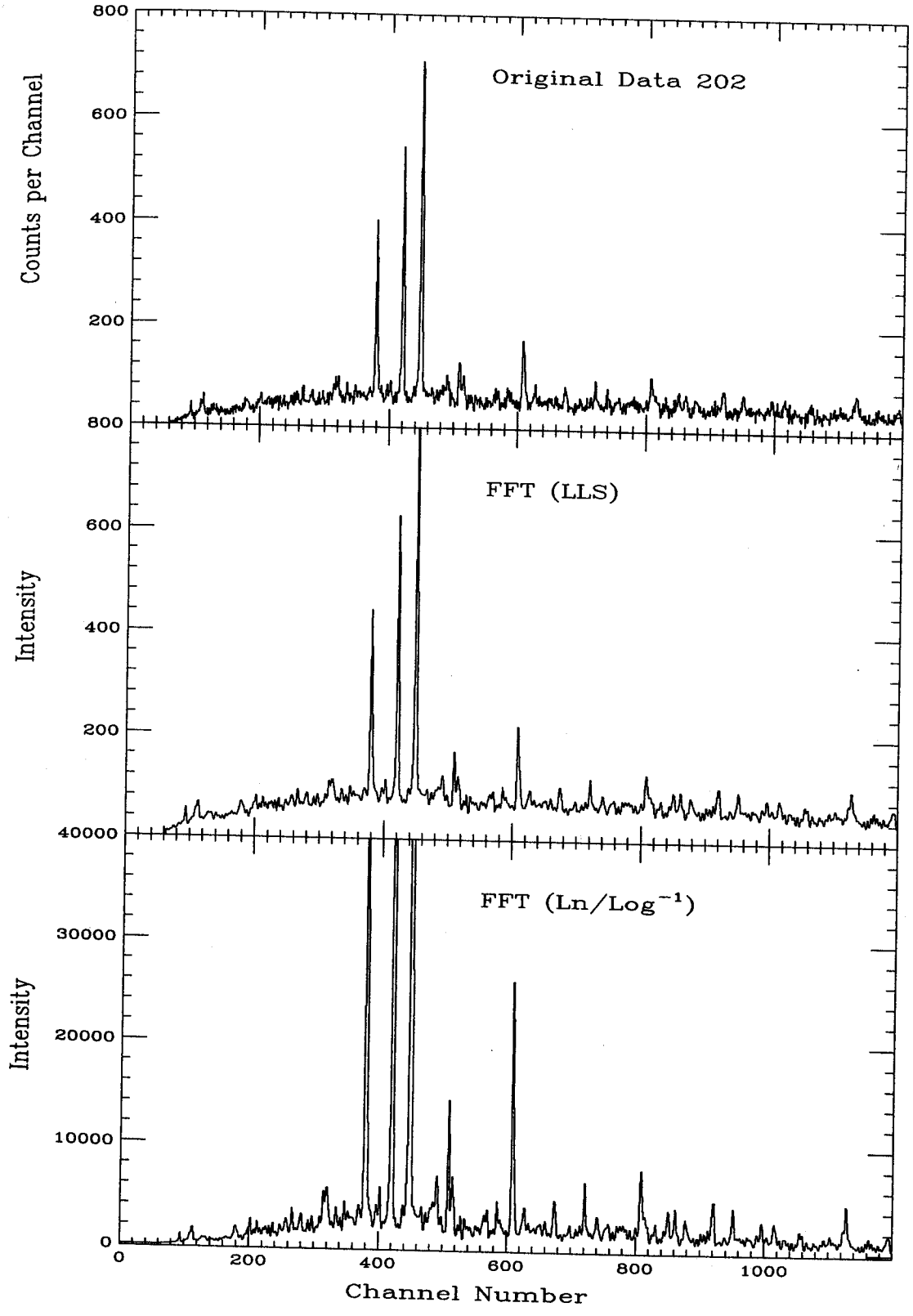

Figure 6.6: Comparison of the original (high intensity) channel number 202 gate with a first FFT (LLS) spectrum and a second FFT (ln/log^{-1}) spectrum.

for each channel.

A provision is made for low intensity spectra ($\leq$ 500 counts) to insure a realistic baseline that places negative peaks properly. For the first two passes through the loop, the maximum value of $z(x)$ and $\bar{z}(x,\omega)$ is averaged with the minimum value. The low-intensity spectra are subjected to twenty seven passes through the loop, whereas higher intensity spectra use nine loop passes. The reverse operator changes the results back to channel counts. Resulting baseline spectra generated by SNIP for low- and high-intensity conditions are shown in Figure 6.7, along with their corresponding energy spectra.

6.5 Comparison with a Smoothing Technique

A resolution study was performed to determine what effect FFT and a box-car averaging or smoothing technique had on the full-width at half-maximum height measurement (FWHM) of the peaks. Three single-channel gates with the intensity ratio 1: 2.3: 5.9 were chosen since they all contain a peak at 283 keV. The FWHM results for this peak in each data set are listed in Table 6.1. The original data are compared with the FFT (LLS) data, a three-point smooth, and a five-point smooth of the data. The resolution listed are given in keV ($\pm$0.05). There is no change in the resolution between the original data and the three-point smooth for medium- and high- intensity gates. However, there is a significant decrease in the resolution of the peak between the original and the three-point smoothed data from the low-intensity gate. The resolution of all three gates decreased using the five-point smooth, whereas the resolution of all three apparently increased after using FFT. A direct comparison of the effect of FFT and smoothing on a large part of the spectrum is shown in Figure 6.8: A) shows the original, low-intensity, single gate at channel 174. B) shows the first FFT (LLS) on the original data. FFT can be performed any number of times on the same data

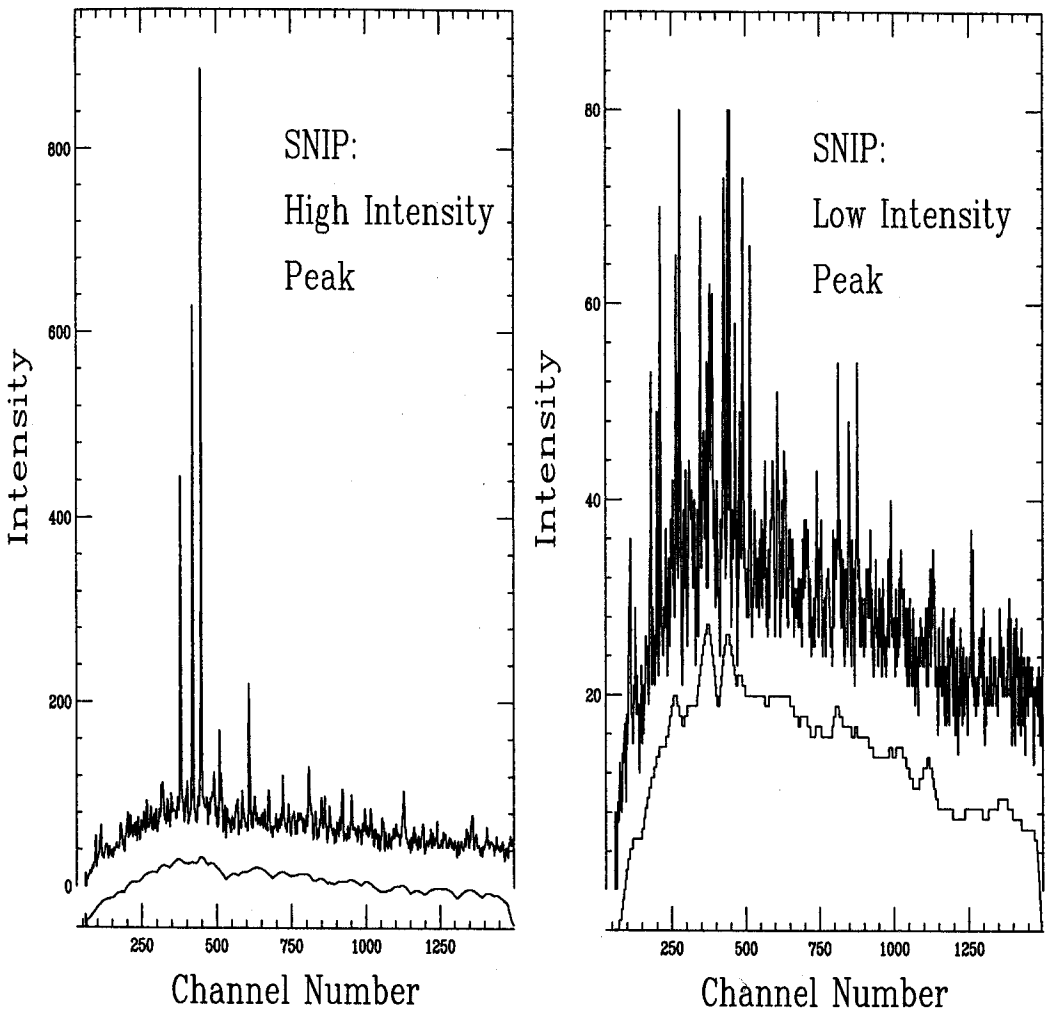

Figure 6.7: SNIP baseline generation for low and high intensity peaks.

in a successive manner. C) shows the second FFT ($\ln/\log^{-1}$) in succession. Compare these results with those from the averaging techniques: D) shows a three-point and E) a five-point smooth on the original data.

Table 6.1: FFT versus Smoothing: Resolution comparison for low- (174), medium- (179) and high-intensity (202) single-channel gates. The resolution (FWHM) of the 283 keV. peak from each gate is listed in keV.

FWHM	Low 174 gate	Medium 179 gate	High 202 gate
Original data	2.49	2.49	2.49
FFT (LLS)	1.87	1.87	1.87
3-point smooth	3.42	2.49	2.49
5-point smooth	4.36	3.11	3.74
Intensity ratio	1.0	2.3	5.9

6.6 Comments on the Source Code

The Fortran source code for the FFT and SNIP modifications of the Oak Ridge program *DAMS* is presented, without apologies for programming style, in Appendix G.2. The code can undoubtedly be improved upon since it was formulated by trial and error. There are a few quarks in the IMSL package that need to be mentioned: The space allocation for the FFT initialization limits the size of the vector length, N that can be transformed. Defining N must be done immediately prior to the call to the FFT subroutine, i.e., N cannot be a variable parameter set in an initialization step. In order to do FFT on spectra with more than 1500 channel numbers (i.e., the

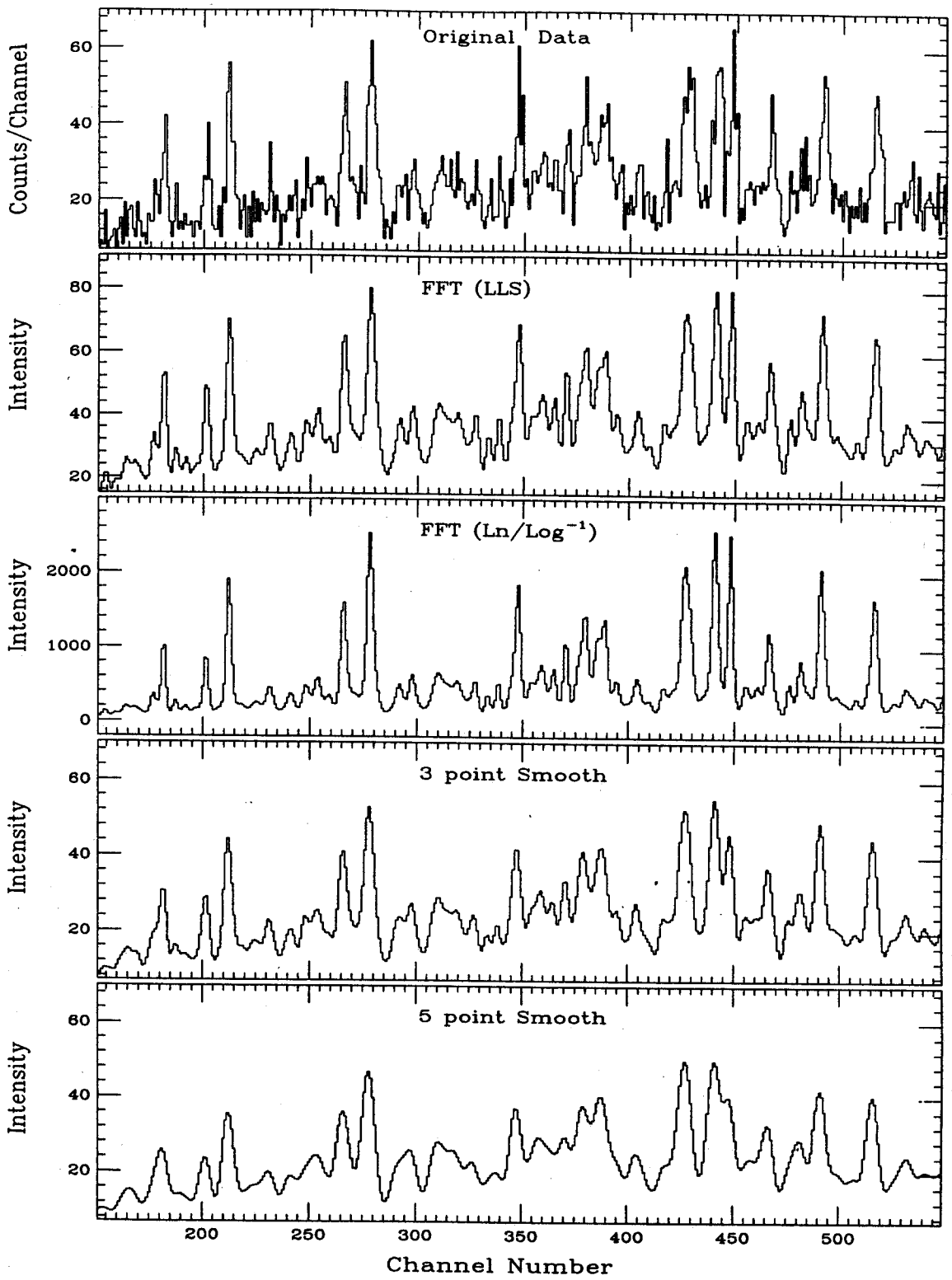

Figure 6.8: A) Original, single gate at channel 174. B) First FFT (LLS) on original data. C) Second FFT (ln/log^{-1}). D) Three point smooth on original data. E) Five point smooth on original data.

Simple gates), a *DAMS* command routine was written to perform the transformation in two steps. [4]

6.6.1 Summary

We have developed a FFT frequency exclusion technique for the removal of noise from spectra.

The Oak Ridge Holifield Nuclear Spectroscopy User Software has been modified to include FFT and SNIP spectral enhancement routines for both single and multiple spectra, using their command file (cmd) structure. This work shows that the application of a discrete FFT algorithm to multiply-gated γ-ray spectra enhances low-intensity components, removes high-frequency noise and increases the signal-to-background ratio. The method is extremely fast and uncomplicated; only a channel-number range and a math operator need to be specified. It is preferable to a three-point smoothing technique. Peaks beneath noise level can actually be seen once the noise frequencies have been removed. The technique is most beneficial for low- and medium-intensity gated spectra. As an added bonus, FFT appears to increase the resolution of the peaks.

The next step in the continuation of this work should be a two-dimensional FFT of the $E_{\gamma 1}$ versus $E_{\gamma 2}$ data array.

[4] Eventually, another version of the code was written in order to encompas 4095 channels within one FFT step.

Chapter 7

Segmented FFT Search Technique

A band-locator technique employing Fourier spectrum analysis has been developed for γ-ray spectra. This is a purely mathematical routine based on frequency-space descriptions of rotational bands. The objective is to distinguish a unique spectral pattern in the presence of a multitude of other frequencies. Conversion of the band into frequency space provides a pattern, segments of which can act as a template to be extracted from the frequency spectrum of the original data set. Summing the segments reconstructs the band. Computer experiments were designed to test the feasibility of locating superdeformed bands within γ-ray spectra. Search results are presented for rigid rotor bands and published superdeformed bands.

7.1 Introduction

For the past ten years or so, researchers have been searching for patterns of peaks in γ ray data that they believe represent superdeformed and hyperdeformed bands in nuclei. In this time, 161 superdeformed (SD) bands have been reported [sin96] in over 80 nuclei, many of which are multiple bands within the same nucleus or identical bands among neighboring nuclei that were established from the same experimental reaction. In order to facilitate the search process, computer algorithms were designed to locate SD bands within complex data arrays [has94, wil95]. The methodology is

based on logical tests of multiple detector coincidences [bea95] found in the data set and results in construction of a series of patterns that have SD potential. They work well on event data but they are very computer intensive and time consuming. Plus, the data must be in event format, which requires a large amount of computer storage.

The technique that we report here is unique in that it does not generate the SD band but, rather, it investigates the inherent frequencies of the total spectrum in order to find a match with a potential SD band. The premise is that if a specific SD pattern were present in the data, the ideal search routine would be able to find it within the total projection spectrum, without having to reanalyze the raw data events or construct new coincidence gates.

This premise is based on the *Principle of Superposition* which describes how any waveform can be unfolded into the summation of simpler parts based on linear combinations of harmonic multiples of the fundamental frequency. Fourier analysis was the earliest and most straightforward application of this principle and has been in use for more than 100 years in many different fields of chemistry, physics, and engineering. A more recent development — the Fast Fourier Transform (FFT) — is a series expansion of the earlier integral method [coo65]. We dub the mathematical technique that we have created and employed here a "segmented FFT routine" because just a small (5-20%) but very select fraction of the frequencies contained within the original spectrum is transformed back into energy space to reconstitute the data that are being sought. It has proven to be a powerful technique for analyzing complex spectra.

7.2 Algorithm description

All of the discrete peaks and bands within the data set can be represented by a single spectrum referred to as a total projection spectrum obtained from a very wide energy gate on a two dimensional $E_{\gamma 1}$ versus $E_{\gamma 2}$ data coincidence matrix. We will refer to

this single, composite energy spectrum as the data set that the FFT algorithm will operate on. (Any subset of this spectrum can also be used; e.g., a double or triple coincidence gate.)

The real, trignometric FFT function that is used here has been described in Chapter 6. This particular FFT algorithm [imsl] produces a frequency-domain output with a one-to-one correspondance, on the abscissa, between channel number and frequency. The ordinarily symmetric frequency plot is folded back onto itself to produce an output that represents both sine and cosine halves of the function. The positive and negative-going peaks reflect not only the frequency changes but also the variance in phase.

By converting the data set into frequency space, then transforming select segments, instead of the total frequency set, back into energy space, various parts can be separated. Figure 7.1 demonstrates the separation of the harmonics of a sawtooth wave. By retransforming select segments into energy space, the shape of the sawtooth wave starts to emerge since an increasing number of harmonics are added together. The first through the fifth harmonic can be easily observed by sequentially retransforming channels 7 through 42 from a 4095 channel spectrum consisting of four cycles of the sawtooth wave.

7.3 Method development

7.3.1 Spectral Analysis and Spectral Synthesis

In the same way that a sawtooth wave can be unfolded into spectral harmonics, a γ-ray spectrum can be analyzed into parts. By using sequential frequency segments of varying size, recognizable spectral parts, such as baseline, discrete peaks, noise, etc., can be extracted [ham94]. However, physically noninterpretable but artistically creative shapes also can be obtained if segments of random order or size are chosen.

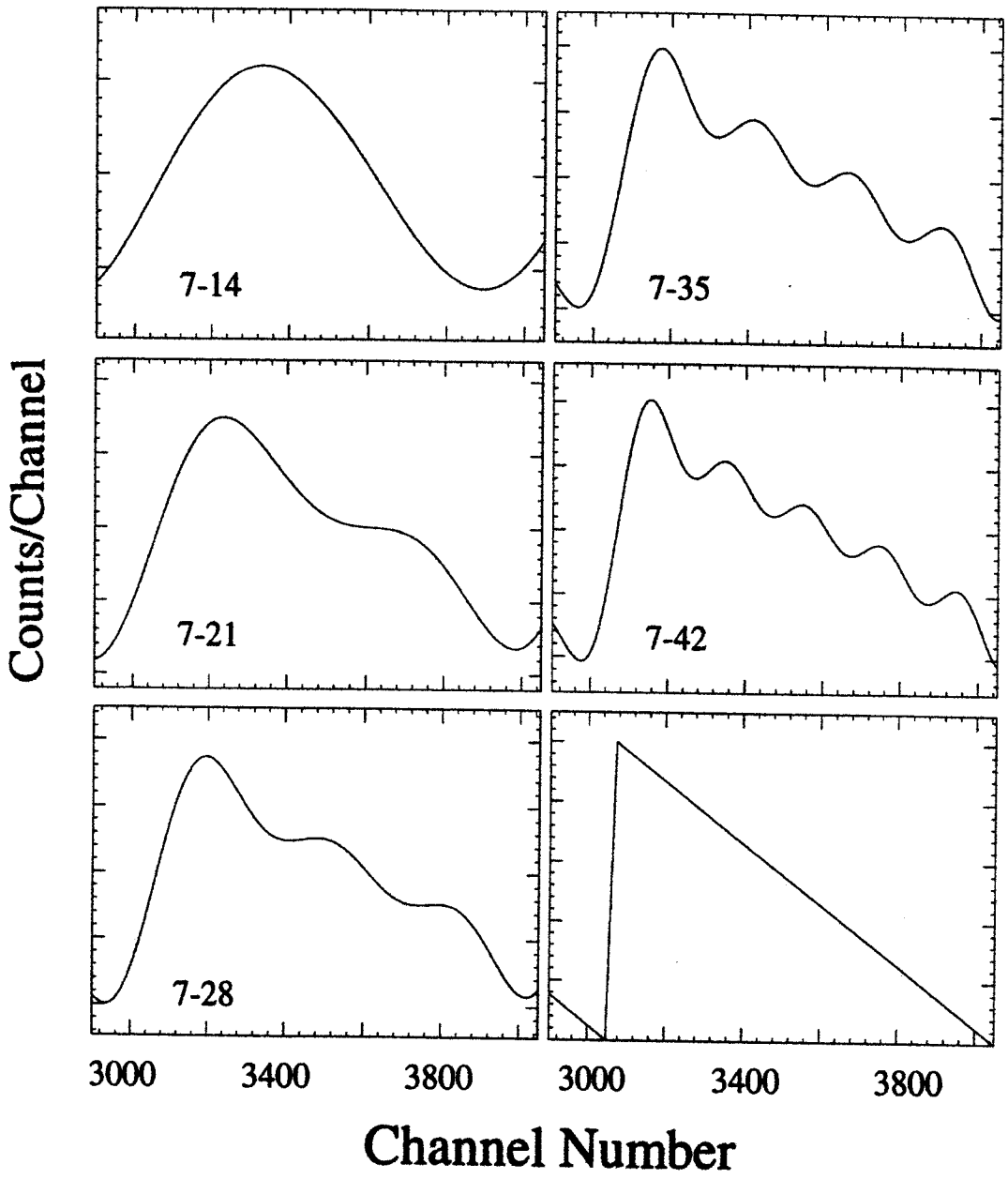

Figure 7.1: Separation of the first five harmonics of a sawtooth wave by retransforming an increasing number of frequency channels into energy space. The numbers on the frames represent the frequency channel number range that is retransformed into energy space.

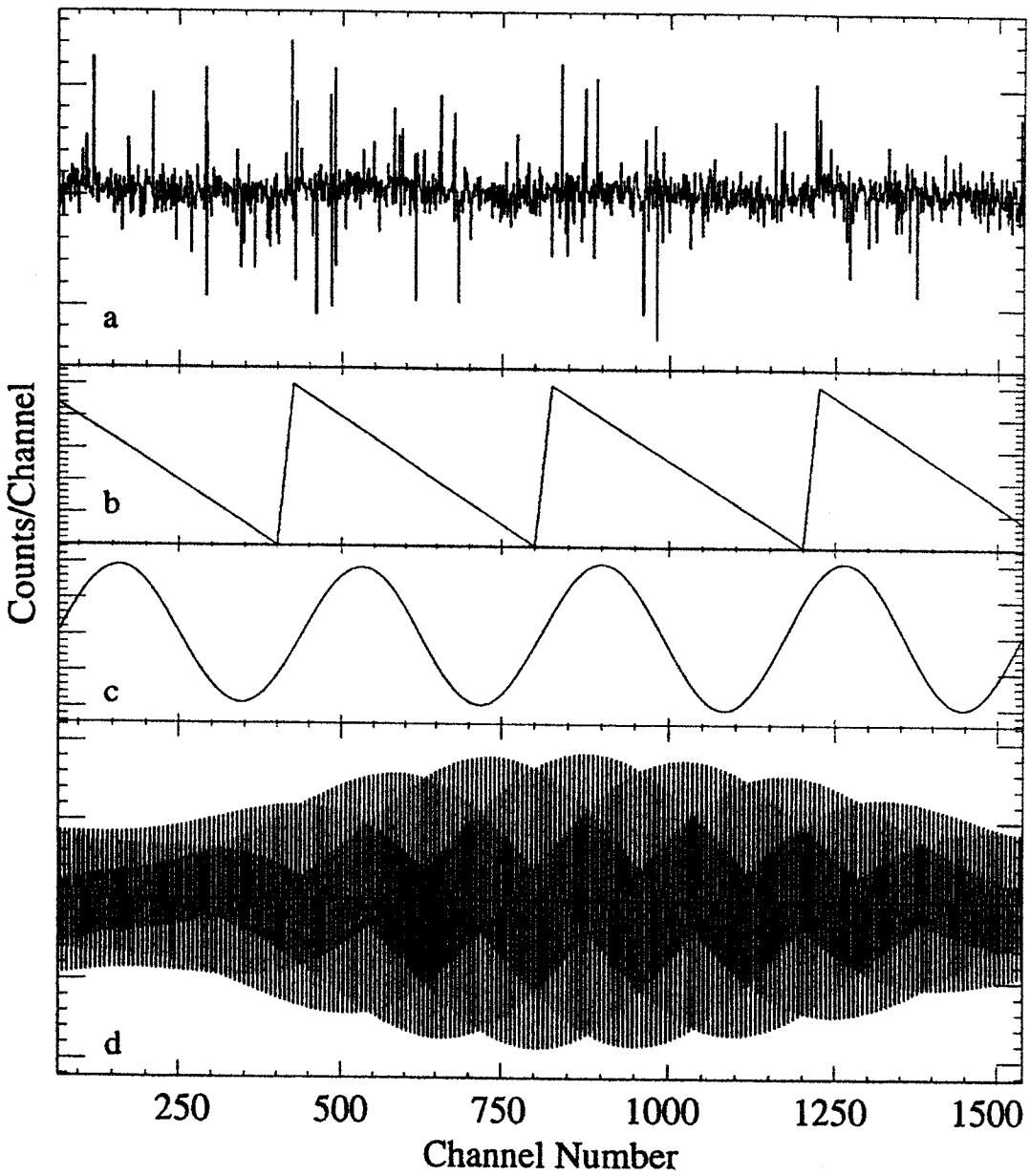

Figure 7.2: Analysis of a test spectrum: a) The original computer-generated test spectrum with a saw tooth wave (b) hidden within the baseline. By retransforming the frequency segment (channels 76-80), the first harmonic (c) of the sawtooth wave was revealed. d) The reverse transform of random frequency segments (e.g., channels 485-490) may result in physically non-interpretable yet artistically creative spectral shapes, which when summed together can regenerate the entire spectrum.

This method has the ability to extract various types of repetitive patterns from the spectrum, even if the pattern is unknown and its presence is not anticipated. For example, Figure 7.2a contains a computer test spectrum with a sawtooth wave hidden within the baseline. The intensity ratio of the sawtooth wave to noise is 2:25. By retransforming only frequency channels 76 to 80 (out of 1470) the first harmonic of the hidden sawtooth wave was revealed (Figure 7.2c). By transforming randomly-chosen frequency segments back into energy space, unrecognizable spectral parts can also be separated from the data set. (At first inspection this might appear to be irrelevant; however, it is this awareness that inspired the present segmented FFT technique development.) A multitude of irregular, artistically shaped energy space fragments can be produced that represent the retransformation of very small frequency segments (5/4095 channels or so). See Figure 7.2d. By summing these shapes, the total spectrum can be regenerated.

Figure 7.3 shows how an ordinary γ-ray spectrum can be synthesized in energy space using spectral parts generated by this method along with experimentally-determined parts. Spectral components range in frequency from low to high. The baseline, along with the frequency modulation that accompanies it, can be considered to be low-frequency components. Rotational bands and superdeformed bands span a much wider and higher frequency range. The highest frequency component in a spectrum appears to be systematic noise. By adding these spectral components, a realistic spectrum can be constructed (Figure 7.3f).

The converse must also be true, i.e., every spectrum can be analyzed into identifiable parts. In reality, this is a complicated process. Consider the reverse process on the summed spectrum of Figure 7.3. A reverse transform of frequency channels 1200-4095 can produce a good likeness of the highest frequency component (noise). The low frequencies can be approximated with a reverse transform of channels 1-10 to produce a likeness of Figure 7.3a and a transform of channels 1-51 to produce

Figure 7.3a plus Figure 7.3b. (These can also be exactly duplicated by using our modified SNIP routine described in Ref. [ham94]). For the medium-frequency region with discrete peaks from rotational and SD bands, a reverse transform of channels 60-1160 reproduces the peaks at the same centroid location with the same relative intensity; however, the transitions are all grouped together. In order to place these discrete peaks from within the same frequency range into their respective bands, a new method had to be developed. This is the essence of the segmented FFT technique.

7.3.2 Segmented FFT Technique

By employing this same methodology on incrementally smaller frequency segments, it became obvious that the discrete peaks contained within Figure 7.3f which are inter-related through a specific rotational band, can be separated from all other discrete peaks, since each rotational band exists as a unique mathematical function [ham96].

To demonstrate this, a simple example was chosen: It consists of a computer-generated, twelve-transition, rigid-rotor band with superdeformed characteristics (shown in Figure 7.4a). Analysis of this SD band using sequential frequency-increments of 20 channel numbers, yielded, not a variable number, but only two differing, yet very distinct spectral shapes as shown in Figure 7.5; i.e., the exterior contour of the spectra are nearly identical but the interior region contains a different pattern of peaks.

These repeating shapes can be explained by inspecting a frequency-space spectrum-transformation of this band, (Figure 7.4b). An enlargement reveals the positive and negative-going peak maxima (P) and the near-zero areas between the peaks that we refer to as valleys (V). By selecting frequency regions in Figure 7.4b that correspond in channel number to either peak maxima or valleys and then transforming these small frequency-region segments back into energy space, the two distinct types of spectral shapes appear. This is inherently due to the repetitive nature of the computer-generated SD band in energy space. Energy spectra in Figure 7.5a and

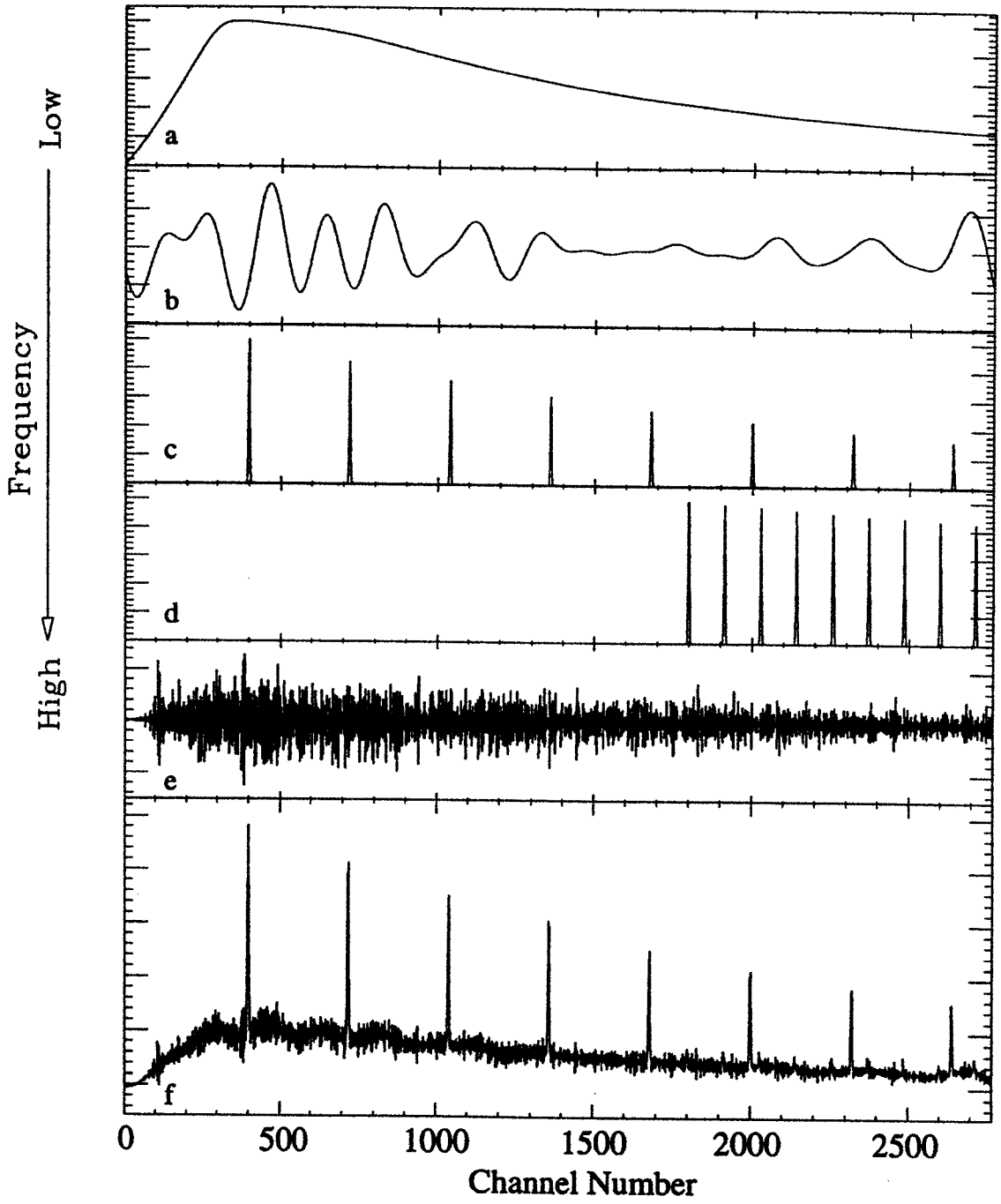

Figure 7.3: Spectral synthesis: By adding spectral components that range from low to high frequency, a realistic computer-generated spectrum can be constructed: a) baseline profile, b) baseline modulation, c) rotational band, d) superdeformed band, e) systematic noise, f) spectrum formed by summing varying amounts of spectra a) through e). All intensities are in counts per channel and are normalized to fit each window.

7.5c correspond to frequency-space, peak-centroid P segments. Energy spectra in Figure 7.5b and 7.5d correspond to V segments.

By summing all of the energy segments that belong to the frequencies at the peak maxima and adding to this the sum of the valley segments, the original SD band can be regenerated as shown in Figure 7.6. The task remained to prove that an application of a retransformation of identical peak regions to a complicated data set containing this SD band would indeed reveal this SD band.

Generating a Standard

Initially, a "standard" band is selected that will be used as a basis for the band search within the data set. This can be an experimentally-generated band from which the background has been removed, or it can be a computer-generated band calculated from a bandhead spin (I) and rotational constant (A) using the rigid rotor approximation formula: [1]

$$E_\gamma = E_{I+2} - E_I = A\,(4I + 6)\,. \tag{7.1}$$

The peak shape is then designed from a gaussian function, matching the statistical information from the actual data peaks for peak width (FWHM) variation, relative peak height, and calibration.

Conversion of this "standard" band into frequency space provides a pattern, segments of which can act as a template to be extracted from the frequency spectrum of the original data set. That is, the positive and negative peak maxima of the standard band in frequency space provide a centroid for the desired channel-number window for the segments. The template we refer to is a list of these peak centroid positions spanned by an arbitrary window. These frequency segments are then transformed

[1] Where $E_I = AI(I+1)$. For an SD band, $A = E_\gamma/[(4 \times I_{est}) + 6]$, where I_{est} is the estimated bandhead spin. E_γ is the lowest observed energy. For a normal deformed band, the experimental rotational constant is entered directly, not calculated.

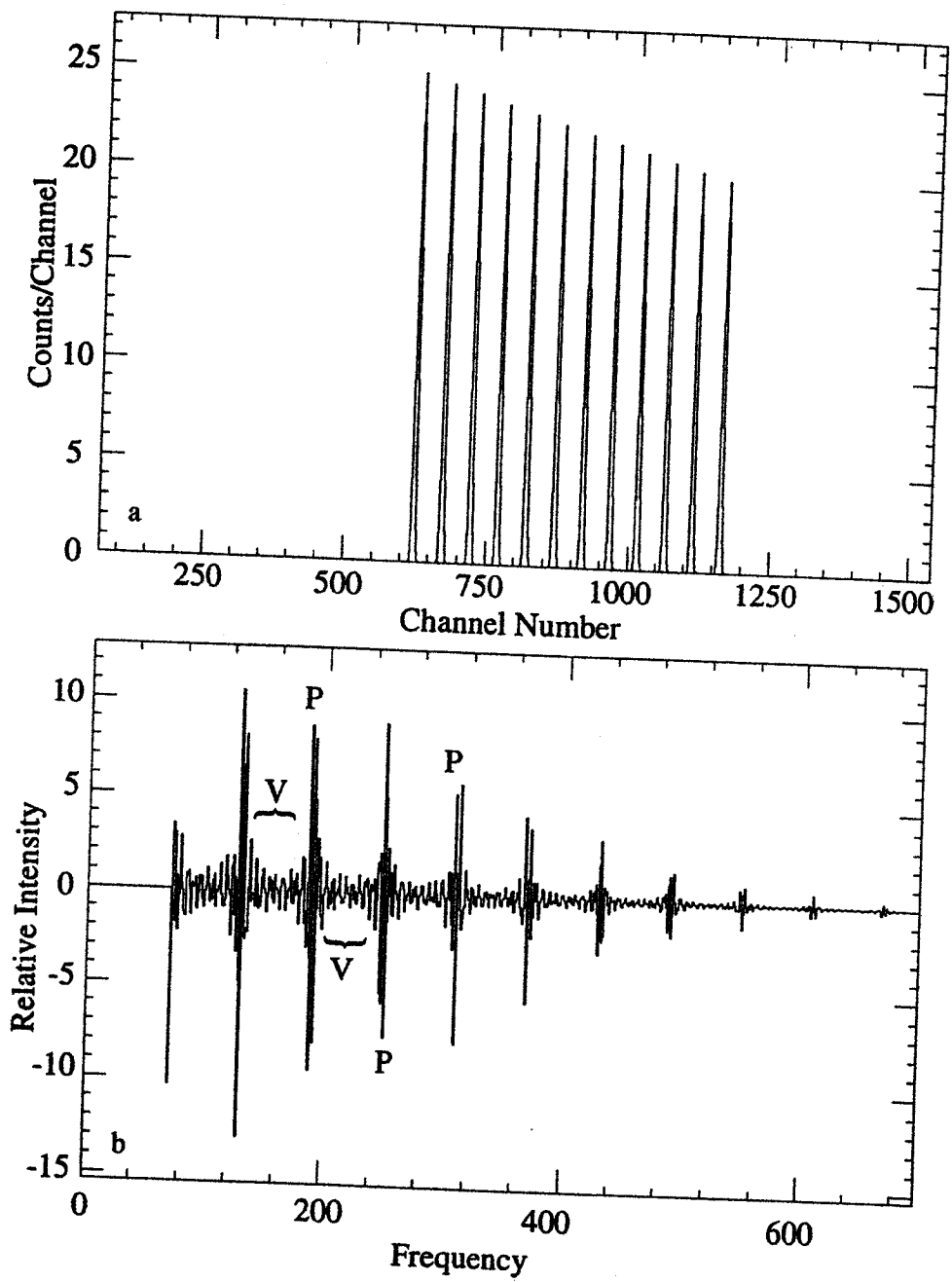

Figure 7.4: a) A computer-generated SD rigid-rotor, twelve-transition band in energy space can be transformed into frequency space. b) This expanded region of the frequency spectrum reveals the positive- and negative-going peak maxima (P) and the near-zero areas between the peaks that we refer to as valleys (V).

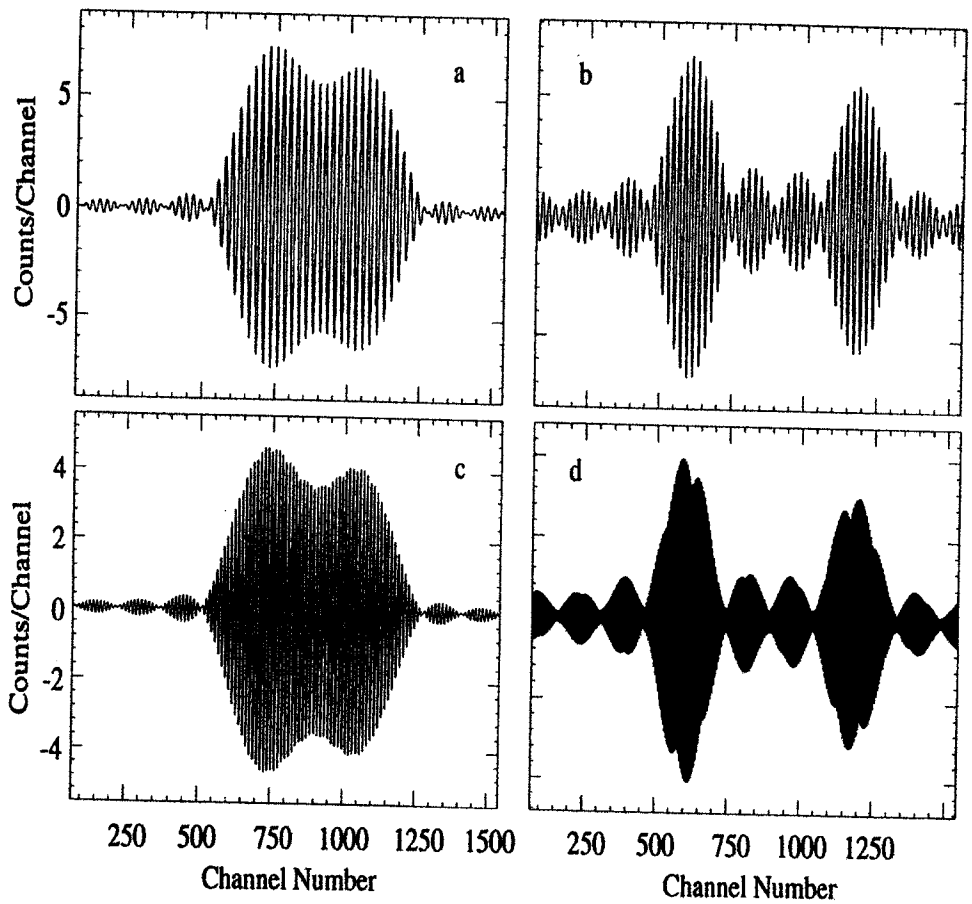

Figure 7.5: Uniquely shaped energy spectra: By selecting frequencies in Figure 7.4b that correspond to peaks or valleys and then retransforming these small frequency segments into energy space, only two distinct spectral shapes result: Energy spectra a) and c) correspond to frequency-space, peak-centroid P segments; b) and d) correspond to valley V segments. The channel numbers corresponding to the frequency segments that are retransformed into energy-space are written on each frame.

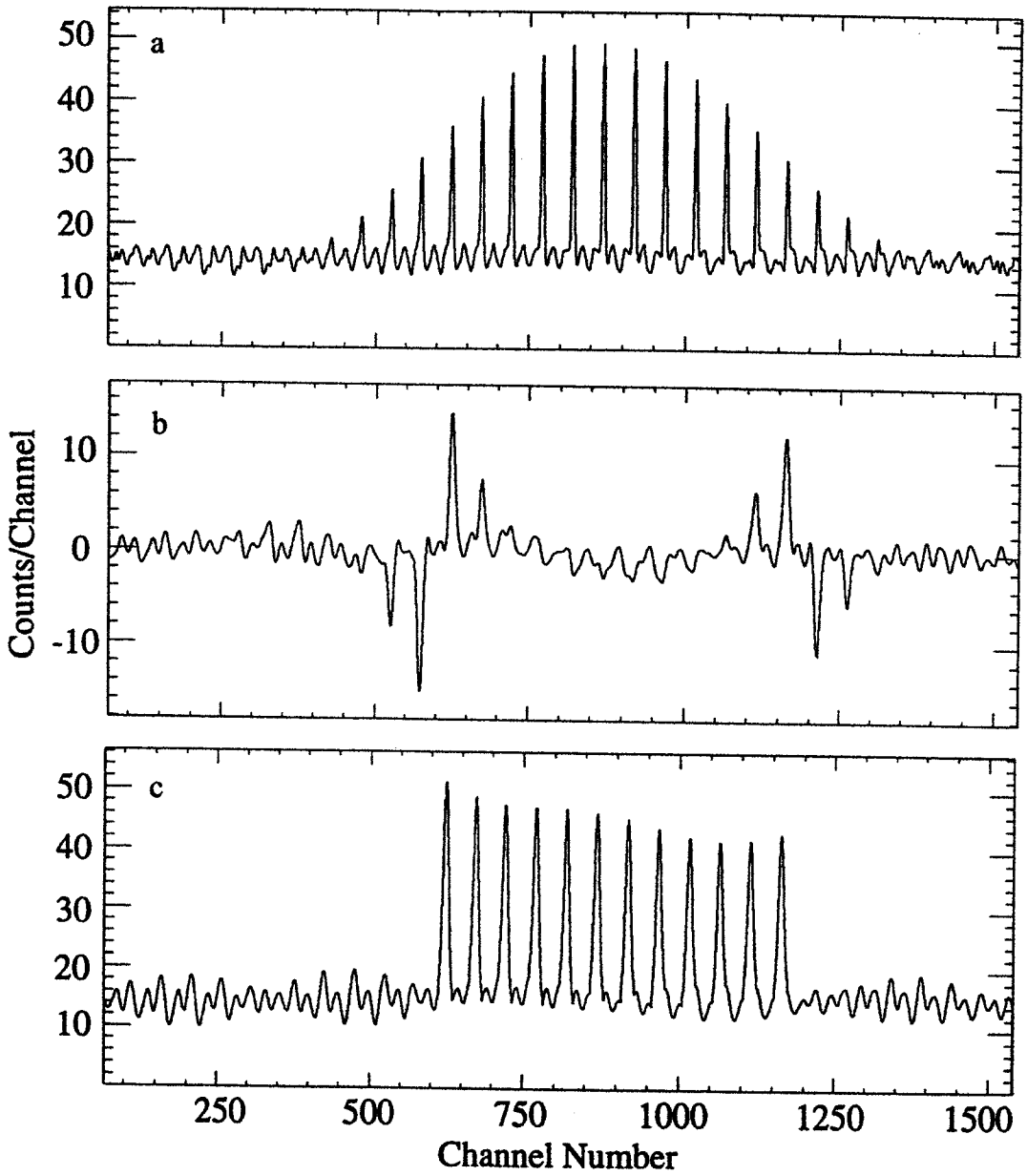

Figure 7.6: By adding a) the sum of the frequency P segments with b) the sum of the frequency V segments, c) the original SD band can be regenerated.

back into energy space and summed. The entire process is then repeated with the original data set. The summed, segmented-FFT spectra from the data set can be masked to eliminate spurious harmonic contributions by adding in the summed valley segments from the standard (as shown in Figure 7.6). The masked spectra from both the standard band and the data are then compared to determine the probability of the search result.

Search Parameters

In addition to comparing the data search result with the corresponding result from the standard SD spectrum, the following are necessary to locate a specified γ-ray band successfully:

- Match the standard peak width to that of the data set.
- Remove the baseline and crop the channel number range of the data file to match the range of the standard SD band.
- Use the largest possible range (usually 4K channels) for the forward transform algorithm. This allows use of wider segment windows.
- Use as few segment windows as necessary to locate a recognizable band. A low number of segment windows causes wide peaks to be produced by the search. A higher number of segment windows produces a spectrum with more accurate peak widths; however, this may introduce excessive stray harmonics.
- If necessary, mask out stray harmonics by adding in a normalized valley sum from the standard spectrum. If the mask intensity is adjusted to match the data, the results show a more normal-looking band with proper relative peak intensities.
- Do a control search on an unrelated spectrum using the same parameters.
- Perform a dose response experiment on a background spectrum in order to determine the relative amount of the band, below which it would be obscured.

Control Experiment

A "Control" search involves the application of the search template from the standard onto a completely unrelated data set (unrelated in channel binning, calibration, etc.). This result should show a spectrum very different from the data search results. If the results are not different, then either the data or the chosen search parameters may have introduced spurious, systematic peaks, altering the probability of fit. This would necessitate a change in the search parameters. An example of the results of a successful set of search parameters is shown in Figure 7.7a. There are no peaks of significant intensity in Figure 7.7b located at the peak centroids of interest, which are shown in the upper frame. The peaks that are present in the unrelated data set (lower frame) are of differing peak widths than the peaks being searched for.

Dose Response

A "Dose Response" experiment refers to a computer addition of successive amounts of the standard band into a background data set. By viewing the search results on each successive dose, it would become obvious whether or not spurious harmonics interfere with the peaks of interest from the standard band. By adjusting the number of segments in the search and the width of the channel number window of each segment, most interference can be controlled. The dose response also indicates a threshold limit for the relative count rate (ratio of standard to total counts), below which a specific band would be obscured.

7.4 Computer experiments

In order to determine what effects the various types of spectral components have on locating a specific band, studies were performed using a test data set consisting of either computer-generated spectra or real, experimental data. The peaks in the

computer-generated test set were formed with the same algorithm as was used to generate the standard band. In addition, a baseline, noise spikes, and various other types of bands were added together to form a realistic test set.

7.4.1 Rigid Rotor SD Band Studies

In order to determine whether the technique would be consistently applicable to spectra with slight variations in the peak parameters, the following tests were conducted.

Peak-Width Study

Five test spectra were generated to include 12 transitions in a SD band with FWHM peak widths set to 2, 3, 5, 7, or 10 channels. A forward transform was performed on each standard spectrum. The resulting frequency bursts look very different in character, with the wider peak widths producing a more compact frequency burst having four or five major peaks. On the other hand, the more narrow-width peaks produce results with an elongated frequency burst containing from 12 to 15 major peaks. See Figure 7.8. There is a linear relationship between the width of the energy peaks and the forward transform peak intensity. The narrower width energy peaks produce a lower intensity in the frequency spectrum; the wider energy peaks, a higher intensity thus accounting for the disproportionation in the relative intensities of the frequency peaks. This has some effect on the band search, when a channel number template is being established for the search. The wider peaks will be more intense in frequency space at the lower peak maxima, and the narrower peaks would have higher intensities at higher peak maxima. If a large number of windows were chosen in an attempt to account for the intensity differences, this might result in the addition of unnecessary interference from other components of the spectrum. In the various peak widths under scrutiny, all corresponding peaks appear to maximize at the same frequency-channel numbers, regardless of the relative intensity. Therefore, the same

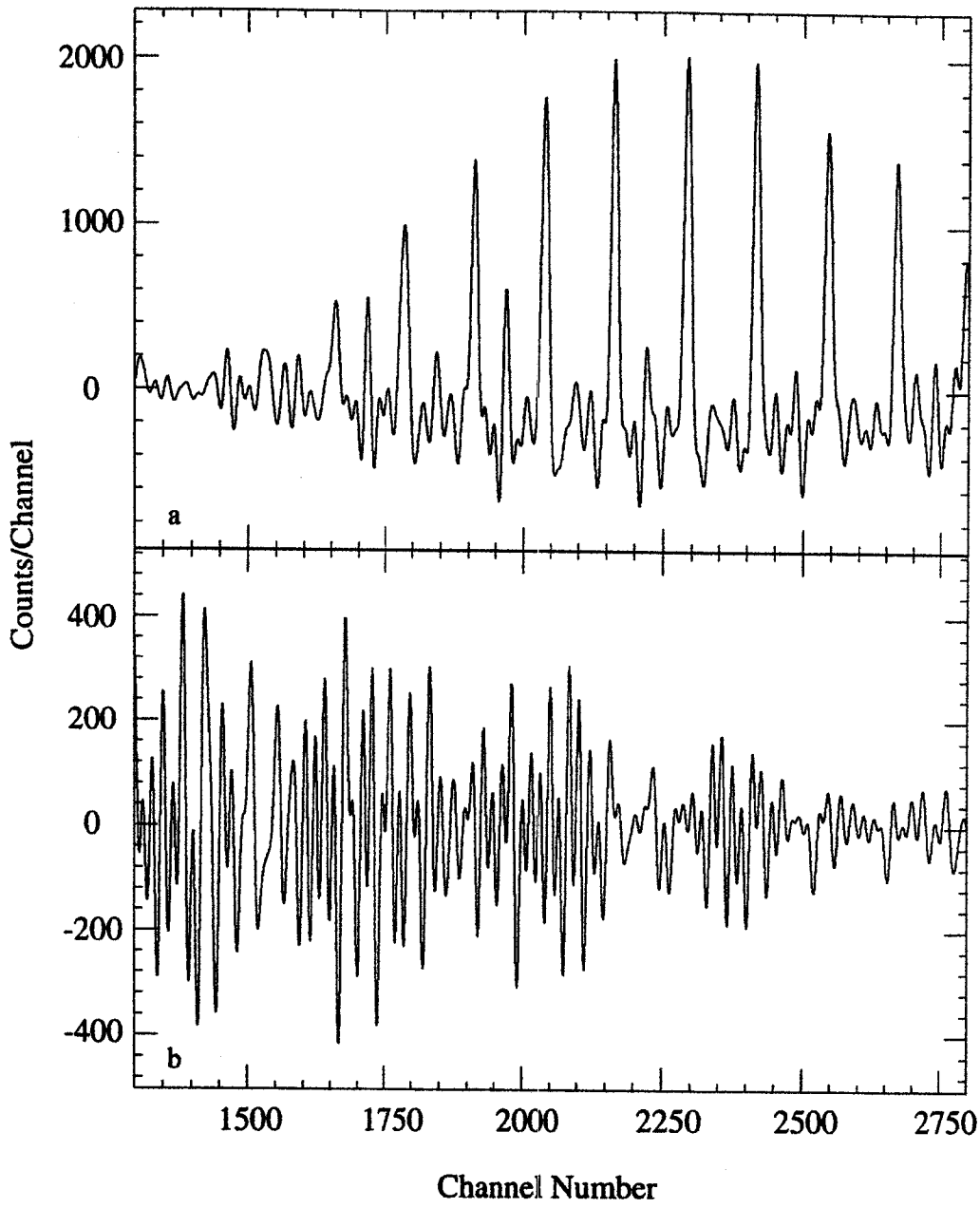

Figure 7.7: A comparison of search results for a) the ^{133}Ce SD standard band with b) search results from a "control", i.e., a search using the same template parameters on an unrelated data set. The lack of matching peaks indicates that the search template does not introduce spurious peaks into the ^{133}Ce SD analysis.

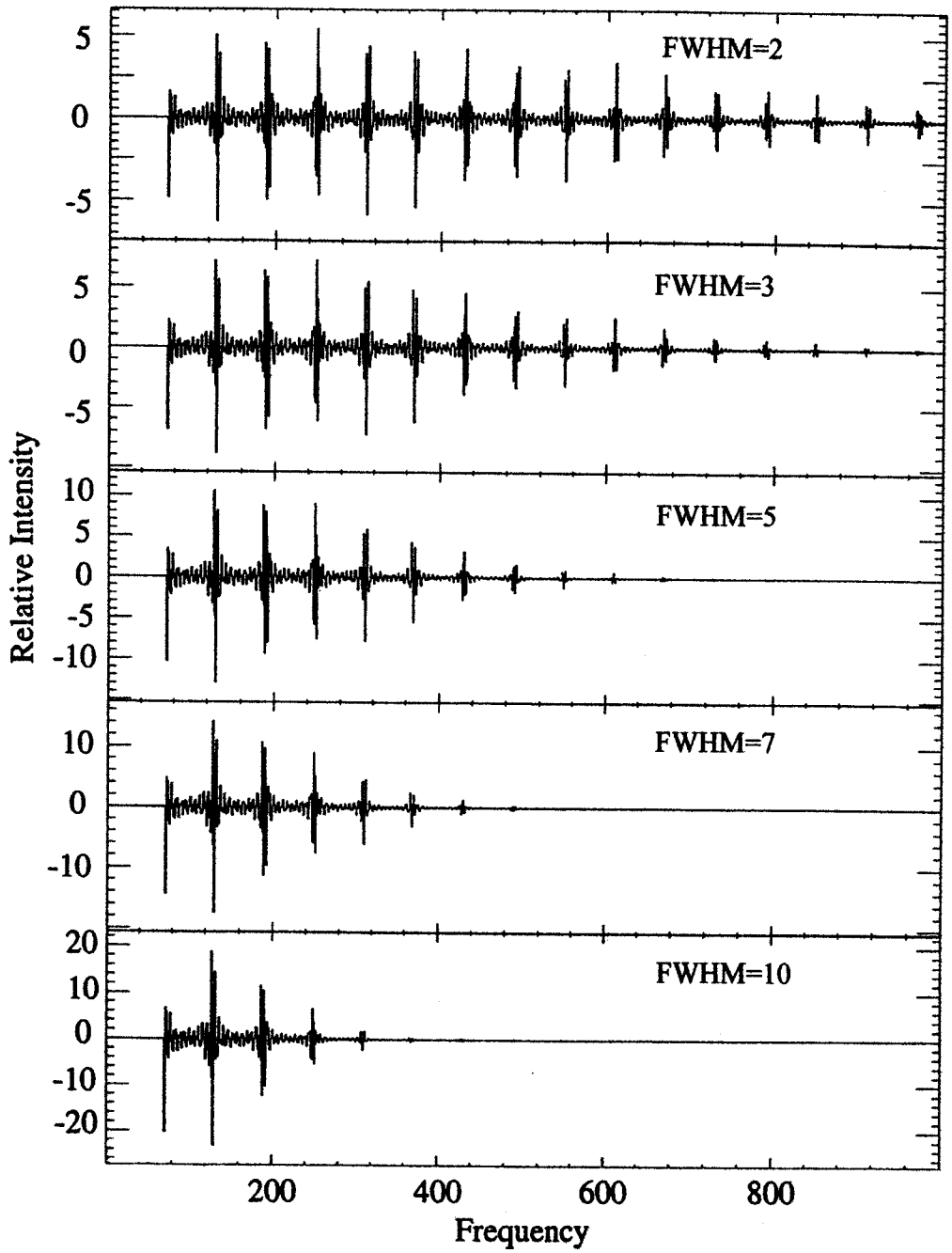

Figure 7.8: Peak-width study: These five frequency spectra are derived from the same rigid-rotor SD band as in Figure 7.4, with the exception that the energy peaks vary in width from 2 to 10 channels, full-width at half-maximum. Notice the variation in relative peak intensities in each.

template can be used for all peak widths.

Relative Peak Intensity Within the Band

We investigated whether the search technique would be equally effective if the relative intensity of the peaks in the band varied from that of the standard spectrum used for the search. Energy spectra with equal relative peak intensities and those with varying relative peak intensities produced identical frequency spectra. The search results produced energy spectra that reflected the variance in relative intensities.

Rotors with Bandhead Energy Offsets

Often the SD bands reported in the literature contain initial peaks (perhaps bandhead or linking transitions) that are offset from the rest of the band by varying amounts. We investigated the effect that this would have on the search results: The single initial peak that is out of cadence with the other peaks generates an entirely new set of overlapping harmonics in the frequency spectrum. This requires that an extra set of channel numbers be added to the search template. Therefore, along with the increase in segment windows is the probability of introducing extraneous peaks. However, a good likeness can be obtained with the search. For simplicity, the first peak can be omitted from the template without compromising the search results.

Random Staggering of Peak Centroid

The SD bands reported in the literature are not derived from rigid rotors, so a study was done to determine the effects of slightly randomized relative peak positions. A comparison was made between a twelve-transition rigid-rotor SD band and a SD band having the same number of peaks, except with slightly shifted centroids. For the rigid rotor SD band, the frequency spectrum consisted of about fourteen distinct peak regions with near-zero intensity valleys. However, the SD band with shifted

centroids shows about five distinct peaks with intense valley regions that rise to the level of the peak regions at higher channel numbers. The first five peaks in both have identical positions.

Figure 7.9 demonstrates these differences. Frame *a* presents the frequency spectrum of the SD band with the individual peak centroids staggered by 2 to 3 channels with respect to the rigid-rotor SD band used to generate the frequency spectrum in *b*. The first four energy peaks of the rigid-rotor SD band and the SD band with shifted peak centroids (dots) are shown in frame *c*. The corresponding search results for the first four peaks of the rigid-rotor SD band and the SD band with shifted peak centroids (dots) are in frame *d*. An identical search template, based on the first five frequency peaks, was used to generate both results. The search finds an identical match for the rigid-rotor SD peaks; however, for the other SD band (dots), the results show peak centroids that are occasionally slightly shifted with respect to the original. This is significant for two reasons: 1) When searching for an unknown band with a template derived from a standard band with equidistant peak centroids, bands that are more realistic than rigid rotors can be located. 2) If the search for a known band yields peaks that are slightly shifted with respect to the standard band, then the original peaks in the data set have centroids that are slightly different than those in the standard but their exact positions are not known.

7.4.2 Signal-to-Noise Intensity Study

A signal to noise intensity study was conducted to determine the lowest signal intensity that a band would need in order to be detected by the method in the presence of noise. Figure 7.10b shows a computer-generated test spectrum in energy space that contains the SD rigid-rotor band plus random-generated noise in a 1 to 3 intensity ratio. By retransforming eleven frequency segments in a six-channel window over the peak maximum (corresponding to approximately 5% of the total frequencies), a sig-

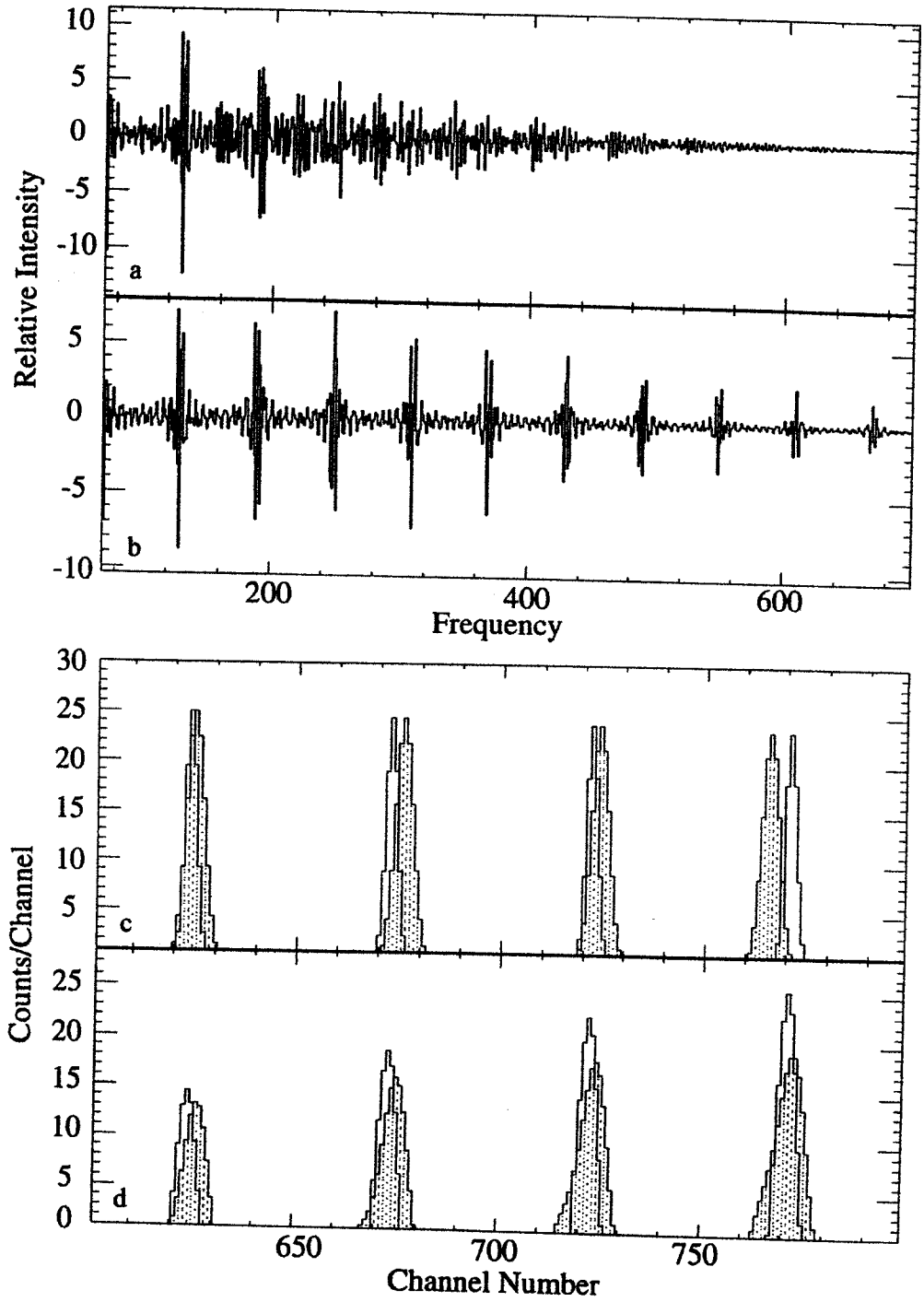

Figure 7.9: Study: Random staggering of peak centroid. a) Frequency spectrum of a SD band with the individual peak centroids staggered by 2 to 3 channels with respect to the rigid-rotor SD band used to generate the frequency spectrum in b). c) The first four energy peaks of the rigid-rotor SD band and the SD band with random staggering of peak centroids (dots). d) Search results for the rigid-rotor SD band and the SD band with random staggering of peak centroids (dots).

nificant regeneration of the SD band results (Figure 7.10c). The shape of the exterior contour of the peaks in the resulting band depends upon the number and size of the frequency segments chosen for retransformation. The higher the number, the more recognizable the band "shape." However, higher numbers also admit frequencies from other bands. Figure 7.11 shows the results of retransforming 7%, 15% and 19% of the total frequencies. A balance between recognizable "shape" and interfering band harmonics needs to be maintained. Clearly, a band with a signal-to-noise ratio of much less than 1 to 1 can be located with this method. Noise has no detrimental effect on locating SD bands in this part of the frequency spectrum, even if the bands have been obscured in energy space. (However, there is a slight probability that the sequence of noise peaks might generate a few overlapping peaks and add to the expected peak intensity in the search results. This is especially true when using a search template for a standard with equidistant peaks. See Figure 7.15 below.)

7.4.3 Multicomponent Study

A study was performed to determine the effect of the presence of other rotational bands on locating the SD band. A multicomponent, computer-generated test spectrum was constructed using *a*) the SD band, *b*) noise at twice the intensity of the SD band, and *c*) a normal rotational band with backbending. Some of the peaks within the backbending region overlapped with some SD peaks in energy space. The intensity of these interfering peaks was at least twice that of the SD peaks. Figure 7.12b shows the test spectrum in energy space. A retransformation of segmented frequencies into energy space reconstitutes the SD band even in the presence of interfering peaks (Figure 7.12c). Approximately 5% of the total frequencies were retransformed.

Note that if a smaller frequency window were used, less of the interfering peaks would be observed. In order to remove the harmonic contributions from the many components of the spectrum, a masking-out technique was used, resulting in Figure

7.12c. Comparison with a masked spectrum of the pure SD standard shows what part of the result belongs to the SD band.

The data set that is to be searched must have the lowest frequency region removed because these frequencies interfere with every other frequency, causing oscillations in the baseline of the search results. Compare the search results in Figure 7.12c with those in Figure 7.12d. The test spectrum for Figure 7.12c did not contain a baseline profile; the addition of a baseline to the multicomponent test spectrum skewed the results (Figure 7.12d). A simple way to remove these frequencies before the search is, first to use the modified SNIP routine from reference [ham94], then to subtract the baseline profile from the total spectrum.

7.5 Search for an unknown SD band

This method was investigated to determine whether a general search technique could be developed to locate an unknown band having equidistantly spaced peaks.

7.5.1 Relative Position of the Band in the Spectrum

Many SD bands that are intially observed at a certain point in the energy spectrum can have transitions extented to higher or lower positions, depending on the removal of overlapping, contaminant peaks in energy space. Therefore, a study was conducted with various spectra having identical peak spacing but different energy starting points. Computer-generated rigid-rotor spectra were designed with fifteen peaks, each separated by 90 channels. Band-head energy was set at 100, 300, various 500-800 starting points, 1000, 1500, 2000, 2800, and 3000 channels. The forward transforms of each were nearly identical in outward appearance. The relative frequency-peak intensities were slightly variable, but the main difference occurred in the valley regions. Figure 7.13 shows the differences and similarities for five of these frequency spectra. The

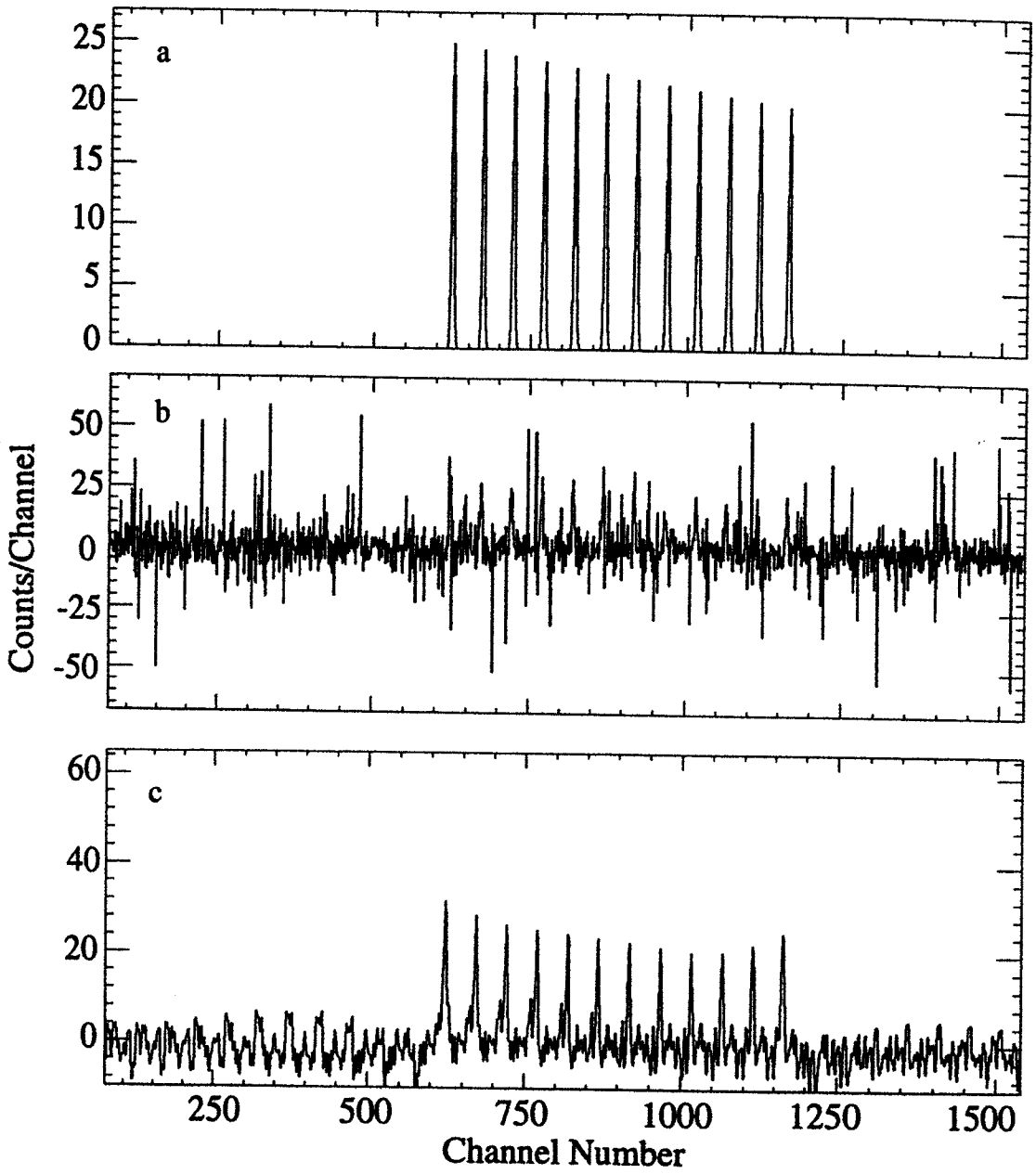

Figure 7.10: Signal/Noise intensity study. a) The original SD band. b) The energy spectrum contains the SD rigid-rotor band plus computer generated noise in a 1 to 3 intensity ratio. c) Retransforming 5% of the total frequencies results in a regeneration of the SD band.

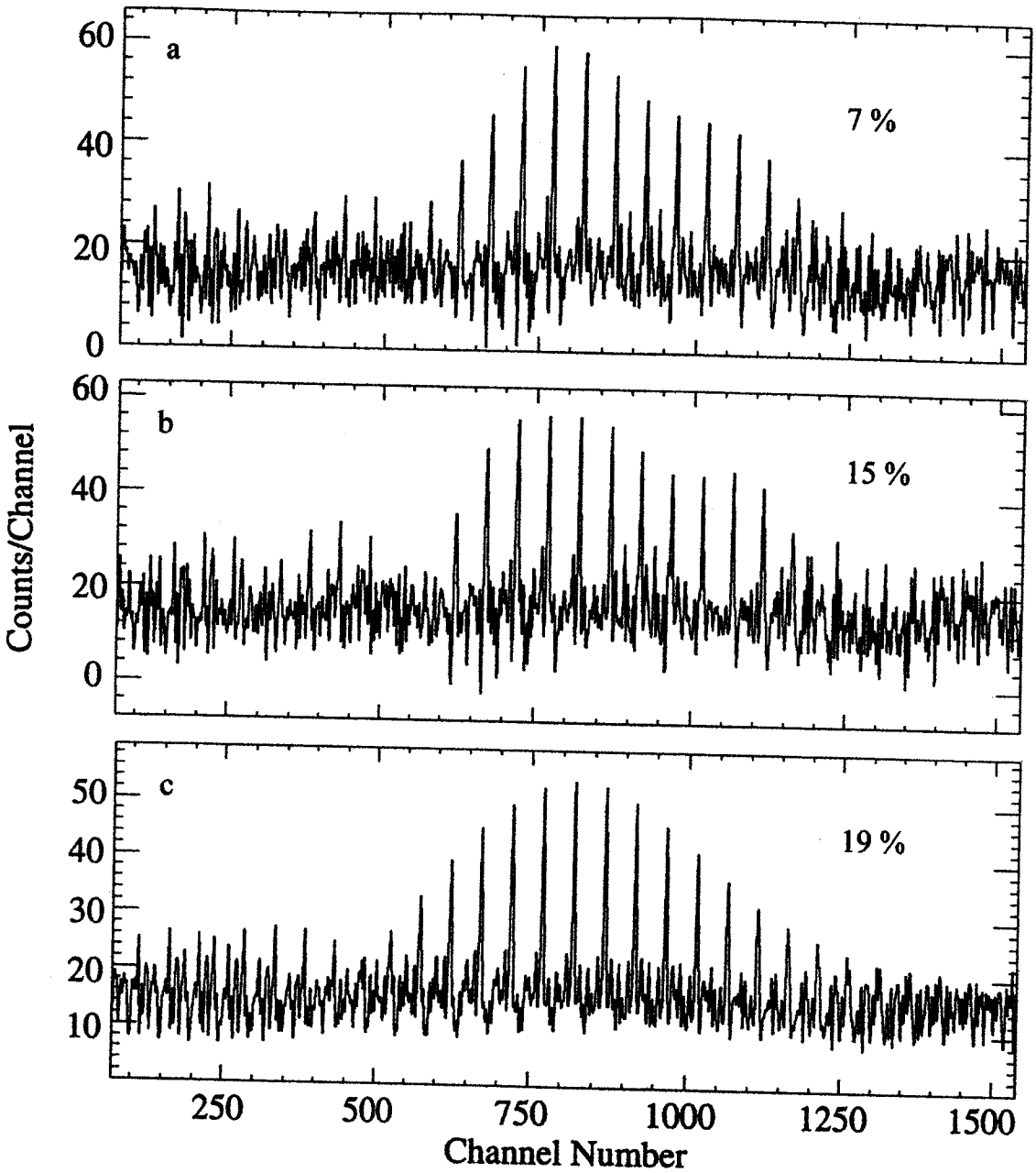

Figure 7.11: Comparison of frequency window widths: The energy space spectrum contains the SD rigid rotor band plus computer generated noise in a 1 to 3 intensity ratio. a) Retransforming 7% of the total frequencies results in a regeneration of the SD band. b) A retransformation of 15% of the total frequencies. c) A retransformation of 19% of the total frequencies. Only the peak sums are displayed; the valley mask has not been included.

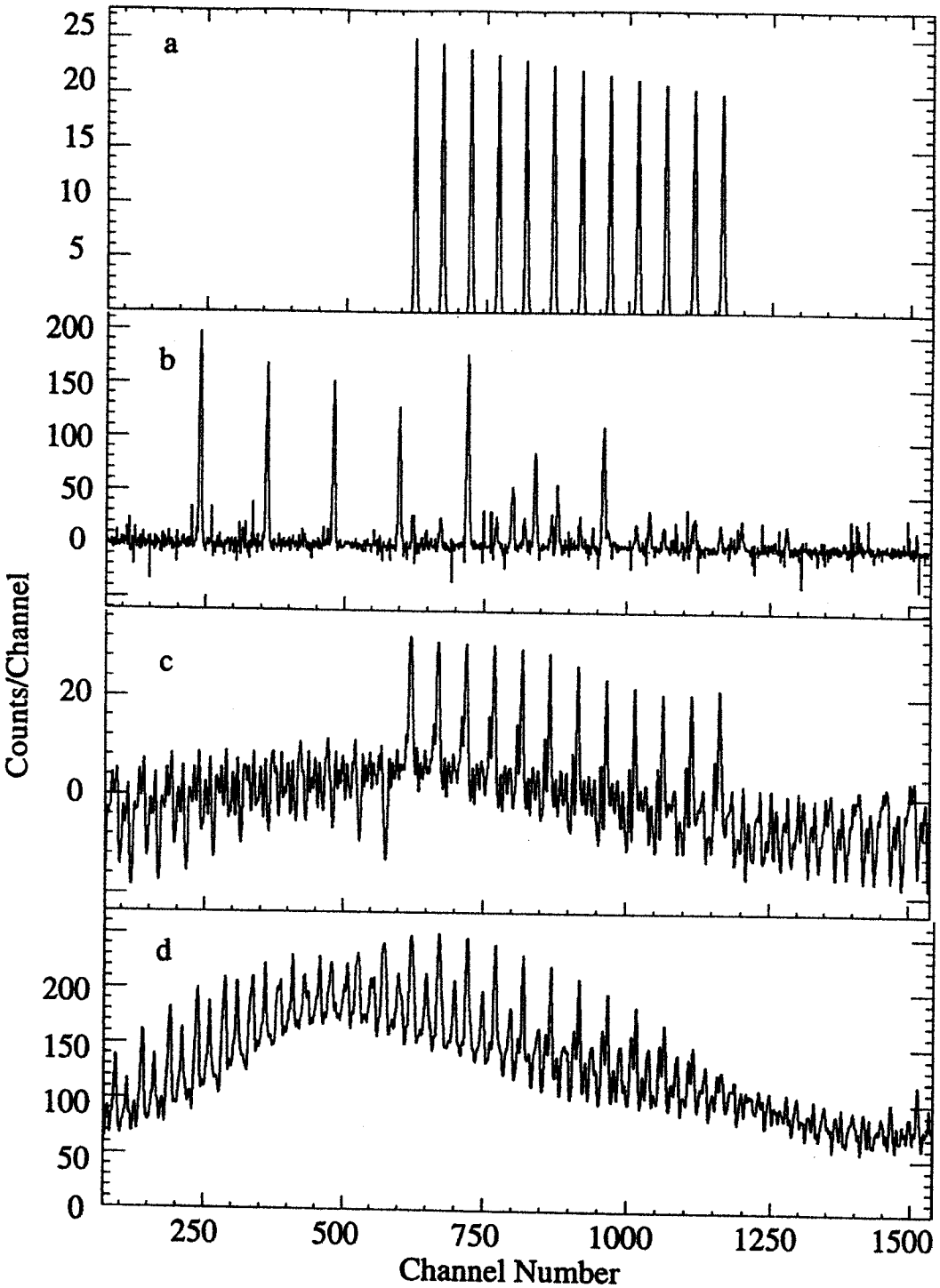

Figure 7.12: a) Computer generated SD rigid-rotor standard spectrum. b) Multicomponent test spectrum in energy space. c) The search result shows that a retransformation of frequency segments into energy space reconstitutes the SD band even in the presence of overlapping peaks in energy space. d) A search result on the spectrum in b) with the addition of a baseline profile (e.g., Figure 7.3a). This spectrum was not masked with the summed valley segments from the standard band.

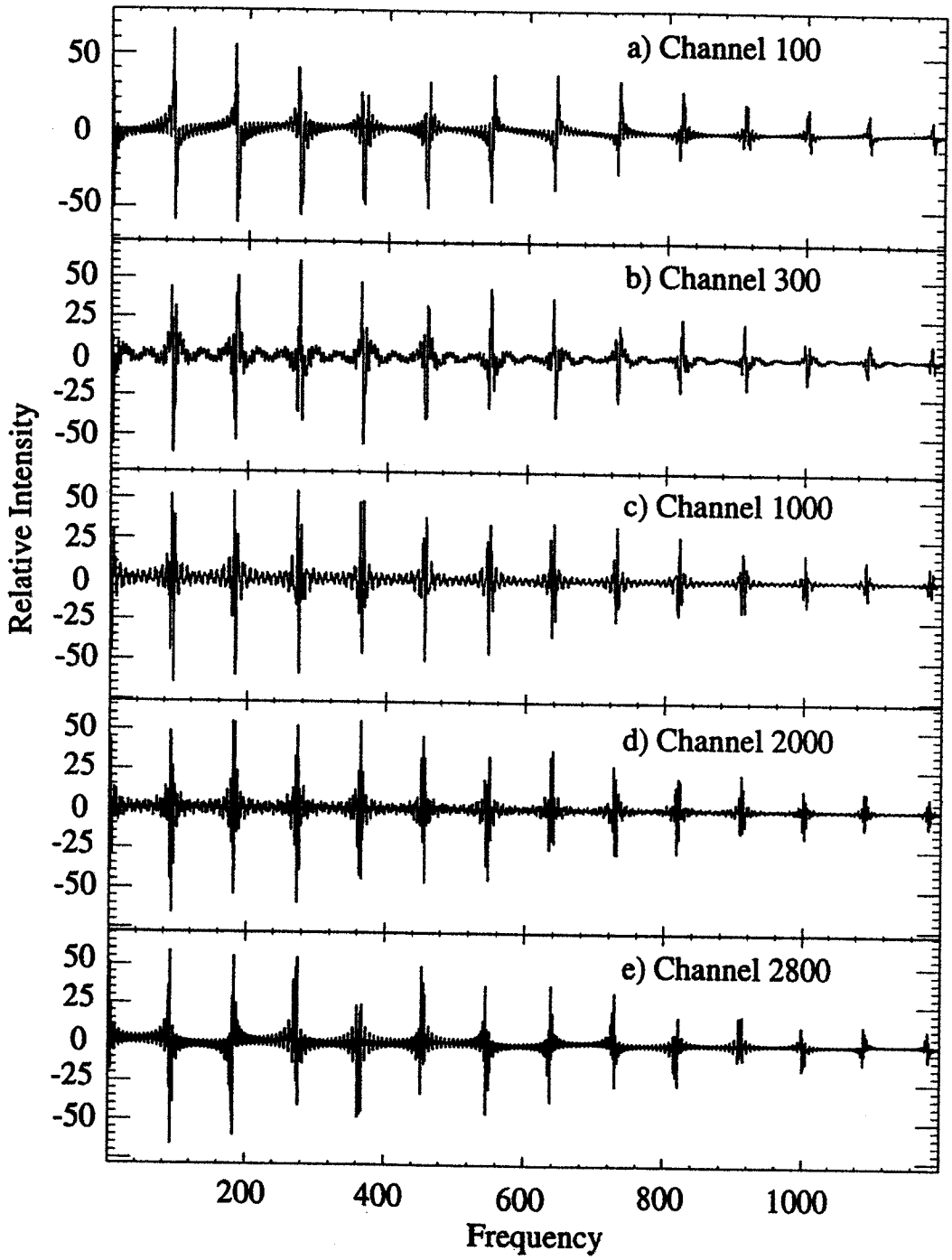

Figure 7.13: Study examining the effect that the relative position of the band in the energy spectrum might have on its corresponding frequency spectrum: Each energy spectrum contains fifteen transitions with a peak centroid spacing of 90 channels and identical relative peak intensities. The band-head energy varies with each spectrum. A portion of the corresponding frequency spectra are displayed. The band-head positions for each spectrum are: a) 100, b) 300, c) 1000, d) 2000, and e) 2800 channels.

channel numbers corresponding to band-head energies are written on each respective frame. The most important result is that the same search template can be used to locate each. The starting point of the band did not alter the search parameters.

7.5.2 Study of the Number of Band Transitions

At this point we examined the effect that the number of transitions in the band in energy space might have on its frequency spectrum. Each energy spectrum that we tested contained a band-head energy peak at channel 1000, with the peak centroid spacing set at a constant 90 channels. Every spectrum contained a different number of transitions in the band. The corresponding frequency spectra are displayed in Figure 7.14 for SD bands containing a) twelve, b) seven, c) five, and d) three transitions.

In general, the frequency-peak windows broadened with fewer peaks in the band. However, their centroids were identical, which means that this method could be used to scan through the entire spectrum, searching for peaks with a set spacing, using the same search template even if the number of band transitions in the data set differ from the number in the standard.

7.5.3 Multiple Band Template

We then conducted a study to determine whether one template could be effective in locating more than one SD band at various positions in the energy spectrum. A test spectrum was constructed of computer-generated noise plus three SD bands with peak centroid separations of 90 channels. The relative maximum peak heights of the three SD bands to the noise spectrum is 1:2:3:4. The first two bands are composed of fifteen transitions; the third has thirteen transitions. There is an irregular spacing (not a multiple of 90) between each band so that the cadence differs one from the other. Search results for a standard consisting of the three SD bands are shown in Figure 7.15, along with search results for the noise plus the three SD bands. No valley

mask had been added to the search results; therefore, the SD band shape is rounded. The search results are nearly identical for both with the original relative ratios of the maximum band intensity being preserved. The slight difference between the results can be attributed to a fortuitous presence of overlapping peaks in the noise spectrum. Search results on just the noise spectrum is shown in the last frame in Figure 7.15. A bracket identifies the region of overlap.

From this study, we conclude that a single search template can locate more than one band at various positions in the spectrum and with differing numbers of peaks, relative intensities, and cadence even if the band intensity is below noise level, as long as the peak centroids in each band are nearly (within 2 to 3 channels) equidistant. This is significant when searching for a completely unknown band.

7.6 Literature SD band search

The final test of the segmented FFT technique was a search for SD bands reported in the literature. Two studies were conducted.

7.6.1 ^{132}Ce SD-1 Band

Twelve components, with proper relative ratios, of the ^{132}Ce SD band 1 from Ref. [sin96, kir87] were entered into a computer file and gain matched to the calibration of a different, experimentally-determined data set. The intensity of the data set into which the SD band was placed was $\approx$ 15,000 counts at channel 1500, the start of the SD region (290,000 maximum intensity without baseline at a lower energy region). At the same channel number, the highest intensity of the SD band was 7,000.

The ^{132}Ce SD band in energy space was transformed into frequency space in order to design a search template. A six segment template was used with a window size of about 20 channels. The standard ^{132}Ce SD band along with the search results for the

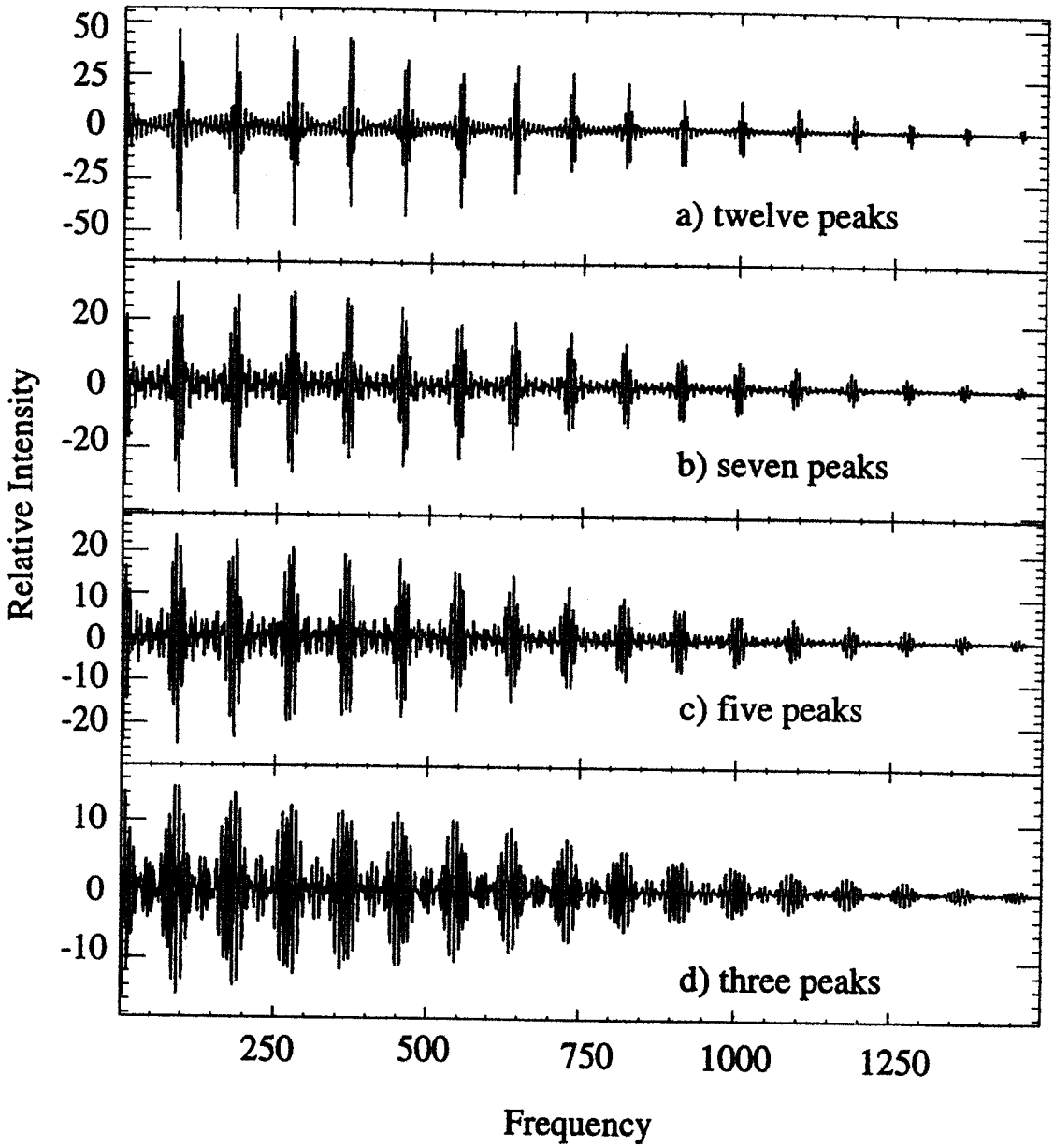

Figure 7.14: Study examining the effect that the number of transions in the band in energy space might have on its frequency spectrum. Each energy spectrum contains a band-head energy peak at channel 1000. The peak centroid spacing is constant at 90 channels. However, each energy spectrum contains a different number of transitions in the band. Their corresponding frequency spectra are displayed for SD bands containing a) twelve, b) seven, c) five, and d) three transitions.

standard can be found in Figure 7.16a and Figure 7.16b. The valley mask from the standard was not added. By comparing the standard search results with the results from the data tests, a good match is evident. A dose response study was performed by adding together various amounts of the data set and the standard spectrum. This is an extremely stringent test of the performance of the search technique. Three of the dose-response search results are shown in the remaining frames of Figure 7.16. The approximate ratios of the standard band intensity to the data-set background intensity are 1:2, 1:5, and 1:13, i.e., a signal-to-background ratio of 0.5, 0.2, and 0.077. The presence of the peaks are confirmed (albeit reduced in relative intensity) even at the lowest signal-to-background ratio.

High Frequency Region

When viewing the frequency spectrum for ^{132}Ce SD-1 in Figure7.17b, notice that there are two unusual regions that repeat the frequency burst. This type of structure does not appear in the rigid-rotor frequency spectra. They have been labeled $R1$, $R2$, and $R3$, and the high-frequency regions $R2$ and $R3$ have been enlarged ($\times 26$) for viewing purposes. These frequencies are approximately 1/80th the intensity of the initial frequency region. The frequency region coded $R1$ (channels 1200-1600) exactly reproduces the standard band when retransformed into energy space. When the frequency regions encoded $R2$ (channels 1900-2300) and $R3$ (channels 2300-2670) are retransformed into energy space, they nearly regenerate the original standard spectrum. Energy spectra having both positive and negative peaks are produced. (The exact SD peak centroids can be re-established by using a square function on the y-axis.) These structures appear to be frequency beat or resonance patterns that reproduce the entire spectrum.

These two high-frequency regions may have some significance in the SD search. If the band can be determined to be present using the segmented FFT search technique

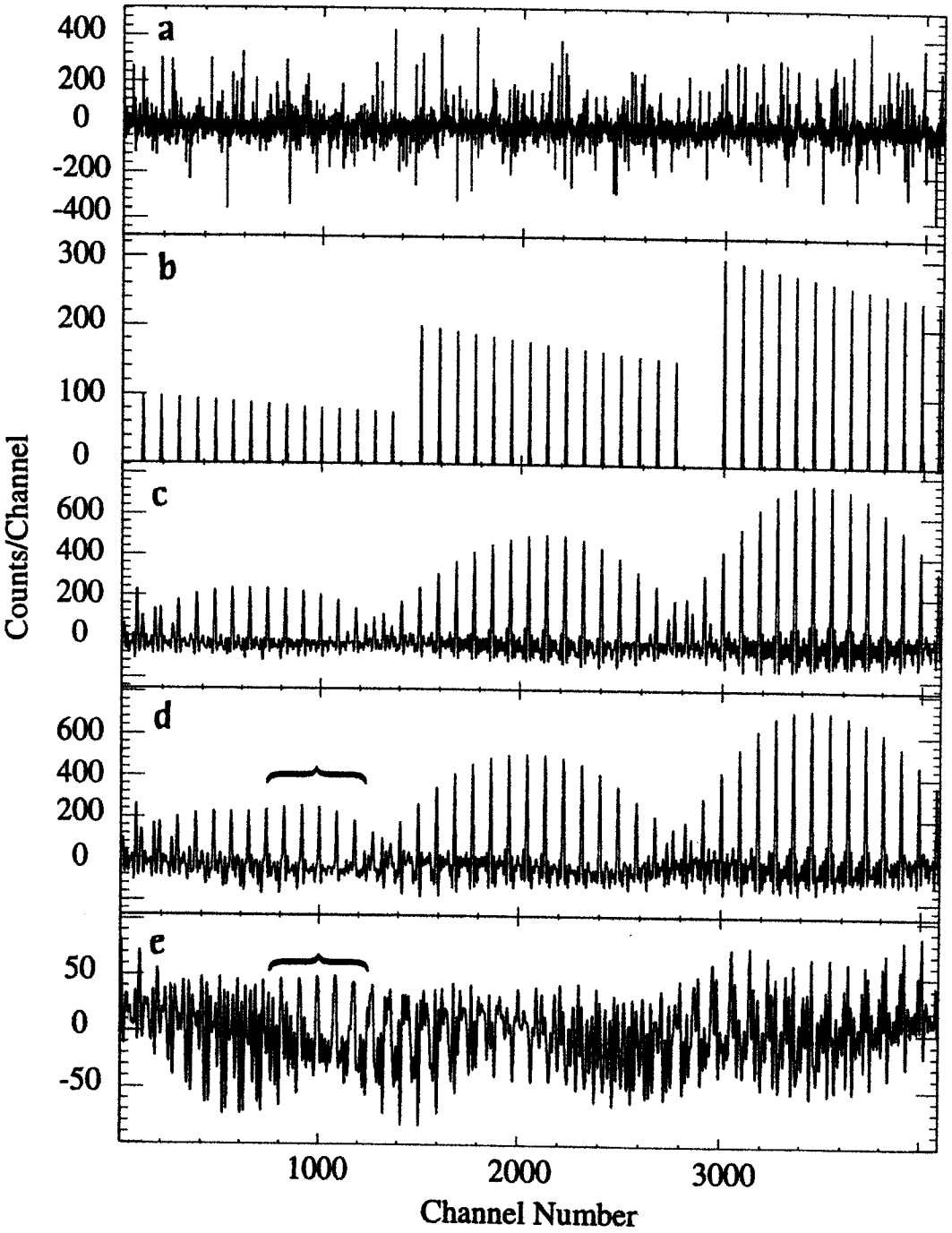

Figure 7.15: Study to determine the effectiveness of one template in locating the same SD band at various positions in the energy spectrum. a) Noise plus three SD bands with peak centroid separations of 90 channels. b) The three SD bands having relative maximum peak heights of 1:2:3. c) Search results for the three SD bands. d) Search results for the noise plus three SD bands. e) Search results for the noise without the SD bands.

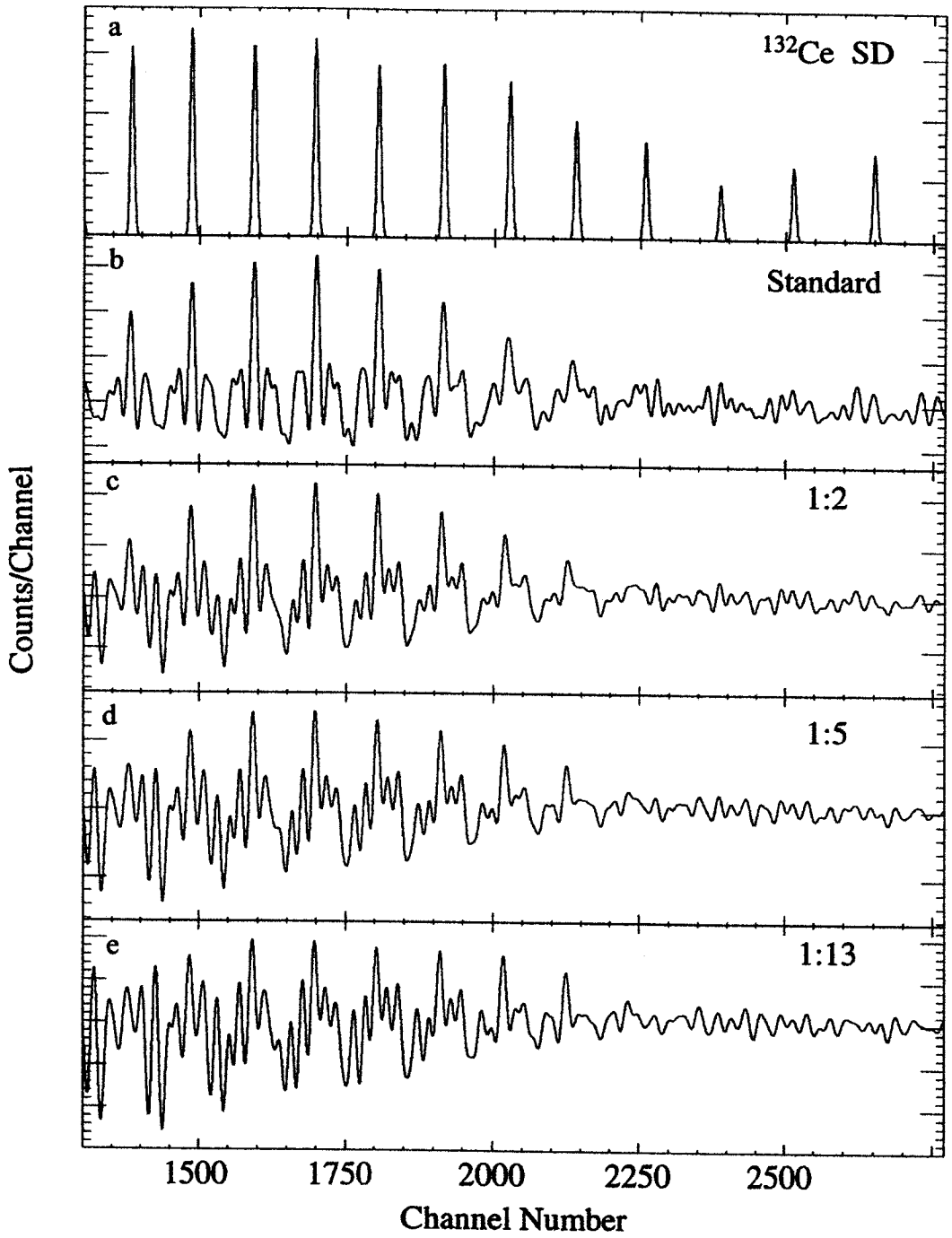

Figure 7.16: a) The standard ^{132}Ce SD band 1 generated from Ref. [sin96, kir87]. b) The search results from this standard band. The search results from a dose response study are shown in the remaining frames. The approximate ratios of the standard band intensity to the data-set background intensity are c) 1:2, d) 1:5, and e) 1:13. The presence of the peaks are confirmed even at the lowest signal-to-background ratio.

on region $R1$, then perhaps the same type of search on either of the other regions would provide the appropriate confirmation of its presence. If a search on the $R1$ region were obliterated by extraneous peaks, then perhaps a search on the two higher-frequency regions, where the regular discrete peaks are diminished in intensity, would provide some information.

7.6.2 ^{133}Ce SD-3 Band

We performed a segmented FFT search on the actual data set from the published ^{133}Ce SD band 3, acquired on a large multi-detector array [hau95]. The methodology that they used to generate the SD band is a standard one, commonly used in the field. The typical procedure in an SD band search is to obtain triple coincidence events from a high spin γ-ray experiment folded into a (2×2) $E_{\gamma 1}$ versus $E_{\gamma 2}$ data array or a (3×3) $E_{\gamma 1}$ versus $E_{\gamma 2}$ versus $E_{\gamma 3}$ data cube. (A 4×4 gamma hypercube could be constructed if higher-fold event data had been acquired.) Then a search technique is used to predict the location of peaks with a selected regular spacing. And finally, gates or slices of the data array are generated at the predicted peak locations and summed. From this histogram a background is subtracted, resulting in a difference spectrum having positive and negative peaks that reflect the predominance of nuclei within the data and reveal the enhanced peaks — the SD band.

We were provided with spectra representing 1) the sum of doubly-gated SD peaks (i.e., a gate on a cube, where one of the three γ-rays is from a discrete transition and another γ-ray is from a SD transition) and 2) a background spectrum formed from the equivalent of a total energy gate on the (2×2) array.

A standard for the FFT search routine was constructed from the ^{133}Ce SD band spectrum formed from the difference between the sum of the double gated SD data and the background data. The search template consisted of 11 segments. The FFT technique was tested on the standard, the sum of the double gated SD peaks, and the

background spectrum. By subtracting the search results for the background from the search results for the data (spectrum c from spectrum b in Figure 7.18), the difference spectrum formed (spectrum d in Figure 7.18) appears to be nearly identical with the standard (spectrum a). The Segmented FFT technique works. It is sensitive enough to find SD bands within the sum of SD gated spectra and also within background spectra. The SD3 band in ^{133}Ce appears to be enhanced by a factor of two between the background and the sum of the gates on the SD peaks.

7.7 Practical Application

Since peak positions are not known, a priori, to setting gates for the SD band in the data, how could a potential SD band be located with this technique? Based on the appearance of published SD bands, the peaks have nearly equidistant spacing. With this information, we can search the data set for peaks with a template designed for a band with a specific distance between peaks. Within the SD band the displacements between peaks actually vary slightly. The FFT search technique can accomodate this feature when locating an unknown band. If two peaks are separated by C channels, then their 1st harmonics are too. If a third peak is located $C \pm 10$ channels away from the second peak, the method will locate the peak based on a different harmonic. Another way of viewing the results is that each peak centroid can be located within a window.

The width, number and order of the segment windows determine an approximate channel number range, r within which peak centroids can be located, i.e., by selecting a template with a 100 channel number peak separation, peaks within $100 \pm r$ channel numbers will show up in the search results. The range can be adjusted wide to perform a search in survey mode, then, when a band is located, the range can be narrowed to find the exact location and spacing of the peaks.

7.7.1 Steps to locating a potential SD band

After obtaining a data set from a high spin γ-ray experiment in the form of an array:

1a) Create a 1-D histogram of the data set from a total energy gate on each axis. A spectrum created by summing gates over all the discrete peaks in the rotational bands of the nucleus of interest would also be a good choice since this would reduce some of the background and make the analysis more specific for a particular nucleus. b) Remove the baseline from the data set and choose a channel number range for the search.

2) Determine a list of potential peak spacings within a band based on comparison with other SD bands in the mass region, e.g., 60 through 170 channel number spacings.

3) Create computer-generated standard SD bands with these peak spacings.

4) Create a sequence of templates that represent these standard bands. Adjust the segment parameters so that a wide window is chosen and select the first six or seven segments. This will insure that more than one peak spacings will show up in the search for each template. (Survey mode) This will also create wide or low resolution peaks in the results.

5) Run a series of search templates that differ by 10 channel numbers on the 1-D histogram, i.e., 60, 70, 80 etc.

6) If the results show peaks maximizing for a specific template, then narrow the segment window, increase the number of segments in the search template and decrease the search template spacings to find the exact location of peaks. For example, if the survey mode search resulted in peaks that maximize at 120 channel number spacings, then rerun the search with templates representing 118, 119, 121, etc. channel spacings.

7) Repeat the entire process for the remaining channel number ranges in the data set.

As an example, let us presume that the specific peak locations of SD3 in ^{133}Ce are unknown and then procede to find them with a survey scan for an unknown band. First, we had constructed templates representing peak spacings ranging from 60 to 170 channel numbers. Then the search routine was performed on the standard SD3 band in the channel range 1850 to 2500. These results are shown in Figure 7.19. The peak intensity for the series of templates maximizes at 120 and 130 channel numbers, meaning that a band has been located with those approximate peak centroid spacings. Band and peak harmonics will cause the appearance of extra peaks at the beginning and end of the channel range used in the search. (See Figure 6.) To make the results more clear, we present an expanded view for the channel number range 1850 to 2500 in Figure 7.20. Since the 130 channel number template results showed the highest intensity peaks, this template was used in a search on the background data set for ^{133}Ce. These results are presented in Figure 7.21. There are more peaks present than the five expected from SD3 in ^{133}Ce. Therefore, the same template was run on standards made for SD1 and SD2 in ^{133}Ce. An overlap of the individual search results for the three SD standards are shown in frame *b*: SD1 (solid), SD2 (dot dash), and SD3 (dash). By summing these results, frame *c* was created. Now, a comparison between the search results for the background data set *a* and the three standards *c* looks comparable. However, there is yet another set of peaks present in the data set results. This becomes obvious when frame *c* is subtracted from frame *a*. There appears to be another band with peak-centroid maxima at channels 1857, 1988, 2118, 2222, and 2353. This might be another SD band comparable in intensity to SD3.

In general, the survey search on the background data set from ^{133}Ce located peak maxima accurately. The results are listed in Table 7.1. The channel number maxima of the standard peaks calculated from published energy values, A, can differ by 1 or 2 channel numbers compared with the search results of the same standards, B. The last peak in SD3 shows a greater deviation than this, perhaps indicating that the 750

channel number range for the search should be lowered. Summing the results for the three standards D can result in a slight shift in the apparent peak maxima.

The most notable comparison is between the search result for the data set, C, and the summed result for the three standard SD bands, D. For SD1 there is a 1 to 2 channel number deviation; for SD2, a 10 channel number deviation; and for SD3, a 1 to 4 channel number deviation. If a more precise number than this were necessary to obtain gated spectra, then search templates representing smaller peak spacings should be used.

Table 7.1: A comparison of the peak centroids between (A) the three SD bands in ^{133}Ce , (B) the FFT 130 search result on each standard, (C) the FFT 130 search result on the data set and (D) the results from (B) summed over each SD band. Data are listed for the channel number range 1850 to 2500.

A	B	C	D
SD1			
1873	1875	1872	1873
2005	2005	2001	2003
2135	2135	2130	2133
2263	2265	2261*	2263
2396	2395	2381	2392
SD2			
1973	1972	1964	1972
2103	2103	2094	2104
2235	2234	2224	2235
2367	2365	2355	2365
SD3			
1907	1905	1900	1901
1967	1968**	***	***
2037	2035	2030	2031
2162	2164	2160	2161
2295	2294	2289	2292
2414	2424	2418	2422

* This is a shoulder on a larger peak.
** Significantly reduced in intensity.
*** This peak was not found.

7.8 Conclusions

We have developed an extremely sensitive search technique for superdeformed bands. Our initial objective was to construct a fast method that would locate the same peaks within a simple total projection of all the energies within the data set. The Segmented FFT technique works through a mathematical investigation of the peaks that are present in the total spectrum. Peaks will be located depending on the presence of their spectral harmonics. The important features of this technique are: 1) the extreme sensitivity allows SD bands to be located within a total energy projection spectrum, as well as a spectrum generated without background subtraction from the sum of energy gates on the band and 2) the method is extremely fast. Once the parameters and conditions have been optimized, the analysis is complete within minutes instead of weeks that other methods require. 3) The technique can be used to confirm the presence of a known SD band or to locate a potential SD band prior to setting gates on a data array. When using a template for a known band, the Segmented FFT routine can be a diagnostic tool that cannot be matched by any of the other search techniques.

The Segmented FFT search routine can be used to: 1) search for the presence of 'identical' bands from another nucleus or a band that was located in a different experiment; 2) search for multiple SD bands within the same data set; and 3) more importantly, to investigate the 'source' of a particular SD band by quickly searching through a total energy gate from each detector. It may be able to answer questions such as: Does the SD band occur preferentially at specific angles. Do certain SD transitions originate with a known rotational band transition.

7.8.1 Software development

This search routine has been designed to be part of a modified *DAM*, *D*isplay *A*nd *M*anipulation module from the Oak Ridge National Laboratory γ-ray software package. It is also a separate Fortran routine that can be run on any VAX/VMS system. Both are linked with the trignometric, Fast Fourier Transform algorithm, which is part of the package from *IMSL*, Inc. [imsl].

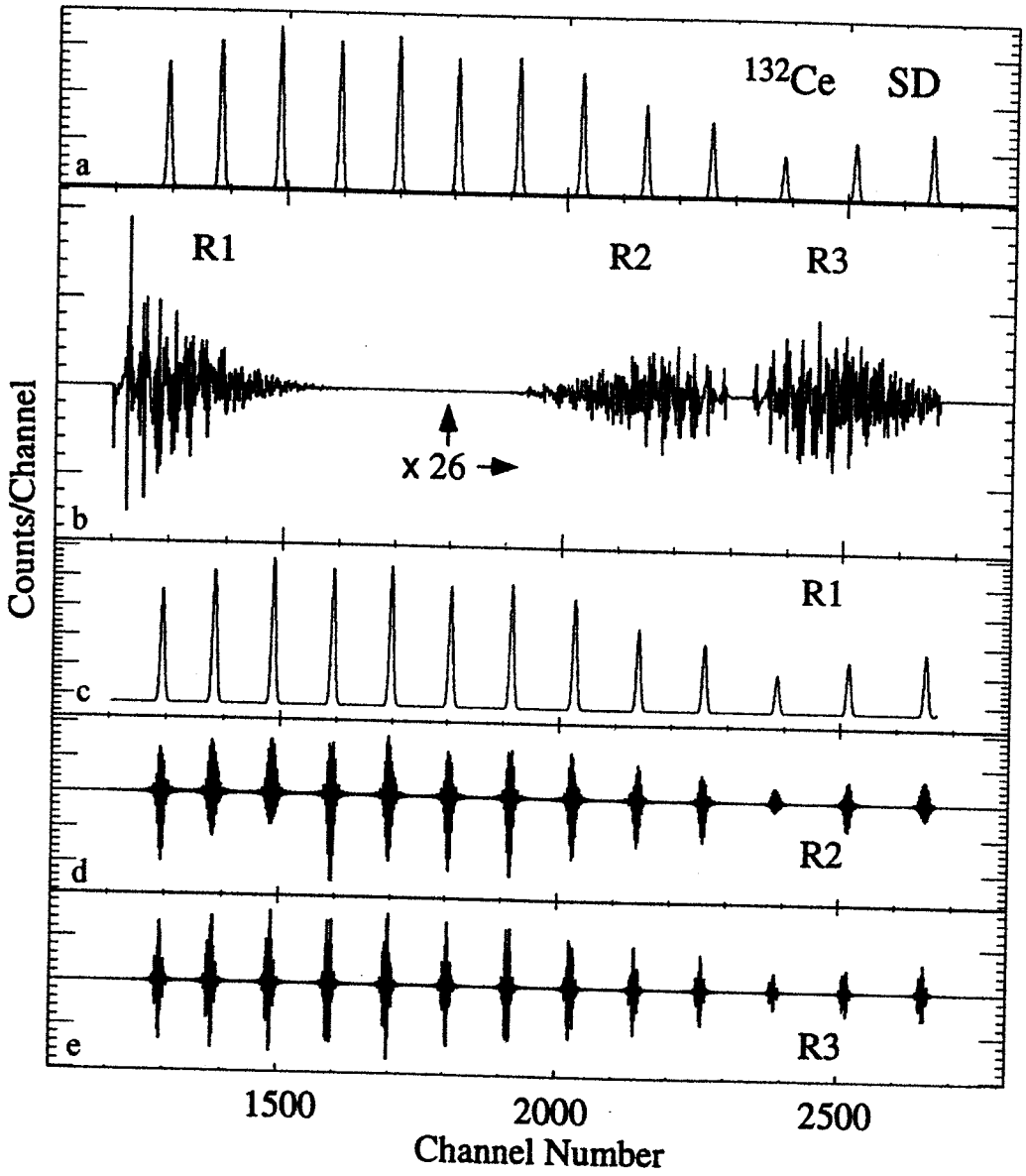

Figure 7.17: a) The ^{132}Ce SD band 1 from Ref. [sin96, kir87] in energy space. b) The corresponding forward transform or frequency space spectrum of this standard band. Notice that there are three regions that repeat the frequency burst, encoded $R1$, $R2$, and $R3$. The second two have been enlarged ($\times 26$) for viewing purposes. When each of the frequency regions is retransformed into energy space, it nearly regenerates the original spectrum, and the SD peak centroids are re-established. The retransformation for each region is shown in energy space in c) $R1$, d) $R2$, and e) $R3$.

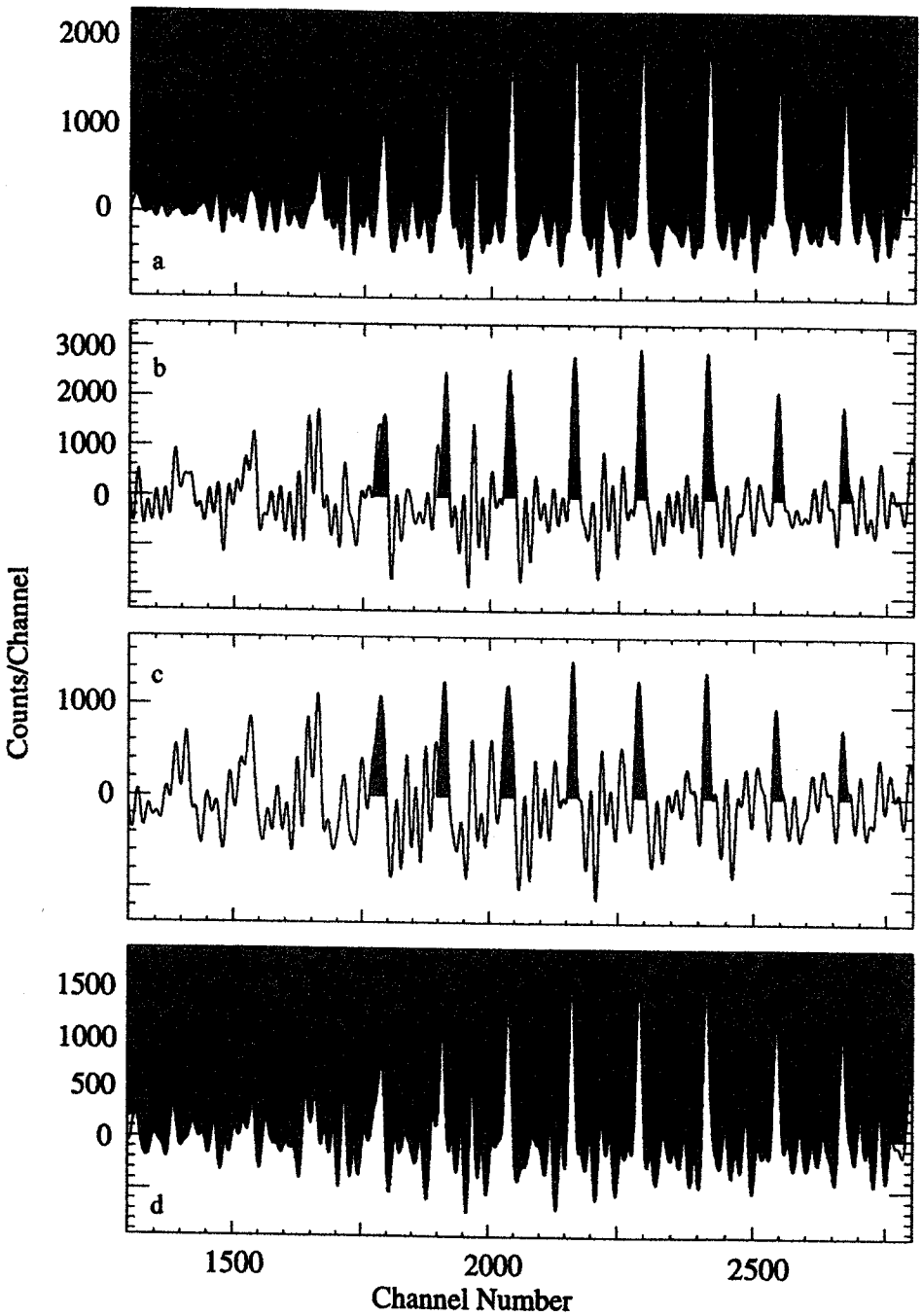

Figure 7.18: Search results for ^{133}Ce SD band 3 in: a) The standard ^{133}Ce SD band 3 spectrum formed from the difference between the sum of the double gated SD data and the background data. b) Sum of the double gated SD peaks. c) Background spectrum. d) The difference spectrum formed by subtracting the search results, spectrum c) from spectrum b).

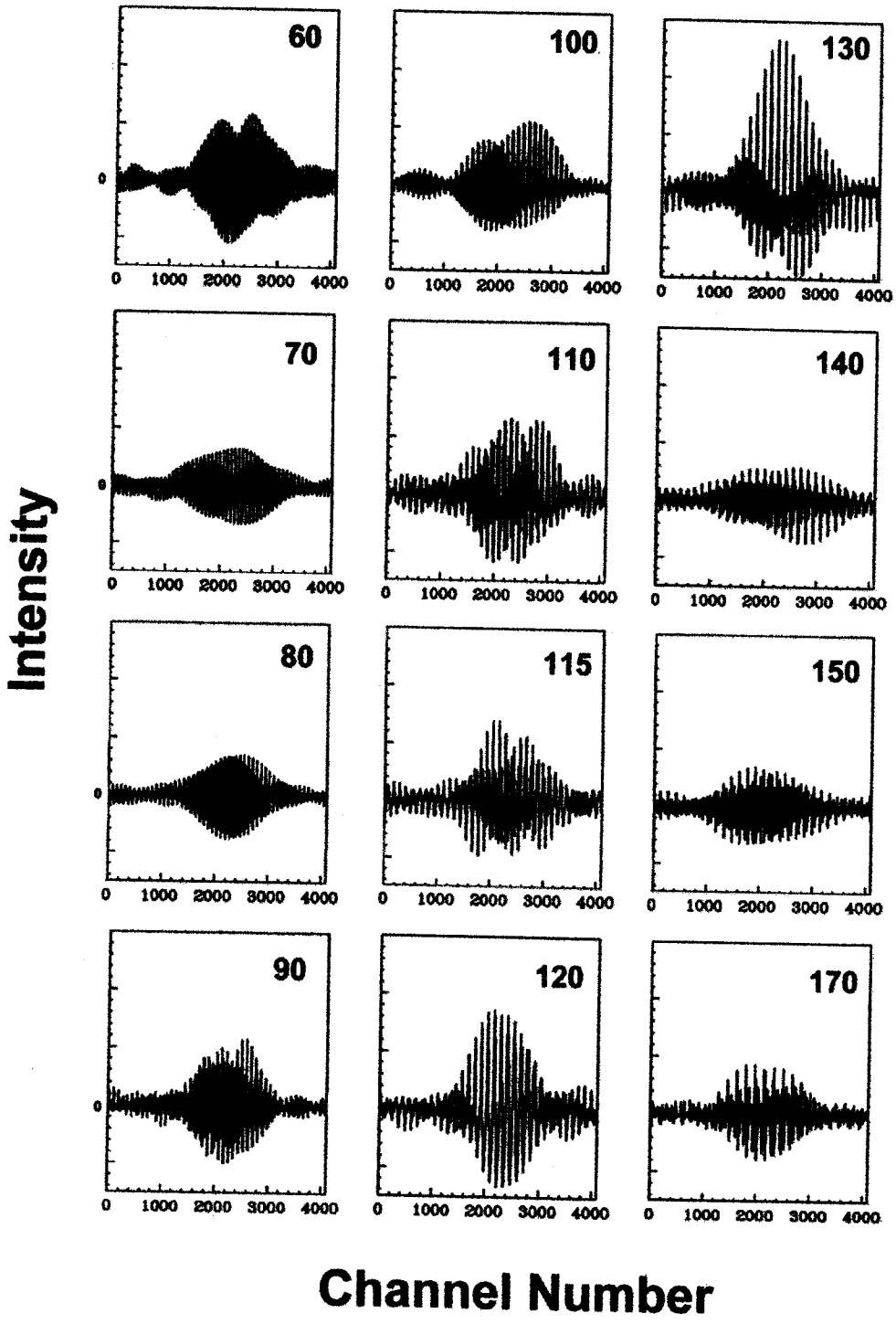

Figure 7.19: FFT search in survey mode: Comparison of the results for ^{133}Ce SD3 standard using various search templates. The numbers on each frame represent the equidistant peak spacings reflected in the templates.

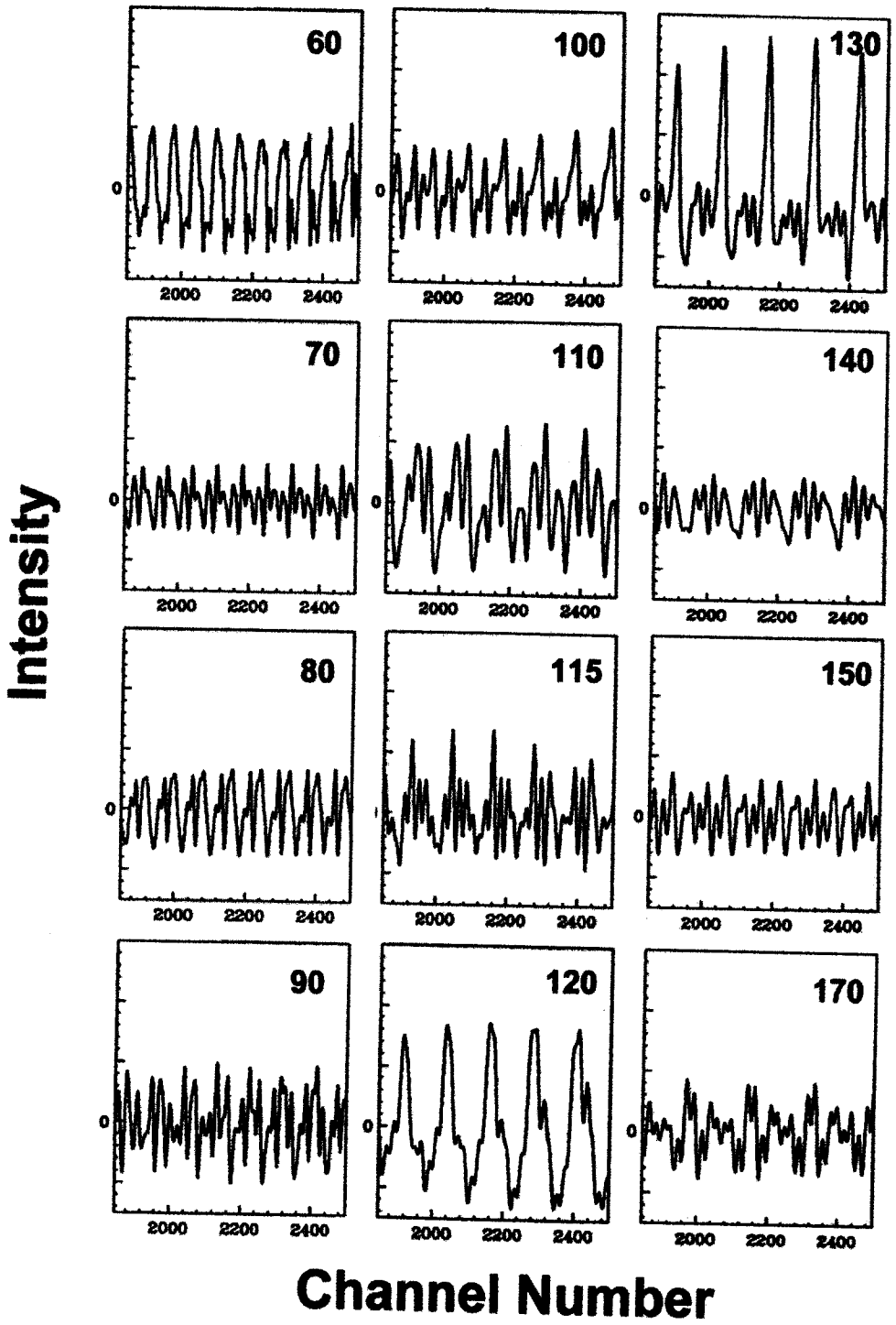

Figure 7.20: FFT search in survey mode: Comparison of the results for the ^{133}Ce SD3 standard spectrum displaying the 1850 to 2500 channel number range. The numbers on each frame represent the equidistant peak spacings reflected in the templates. The intensity maximizes in frames 120 and 130, indicating the presence of peaks with those approximate spacings.

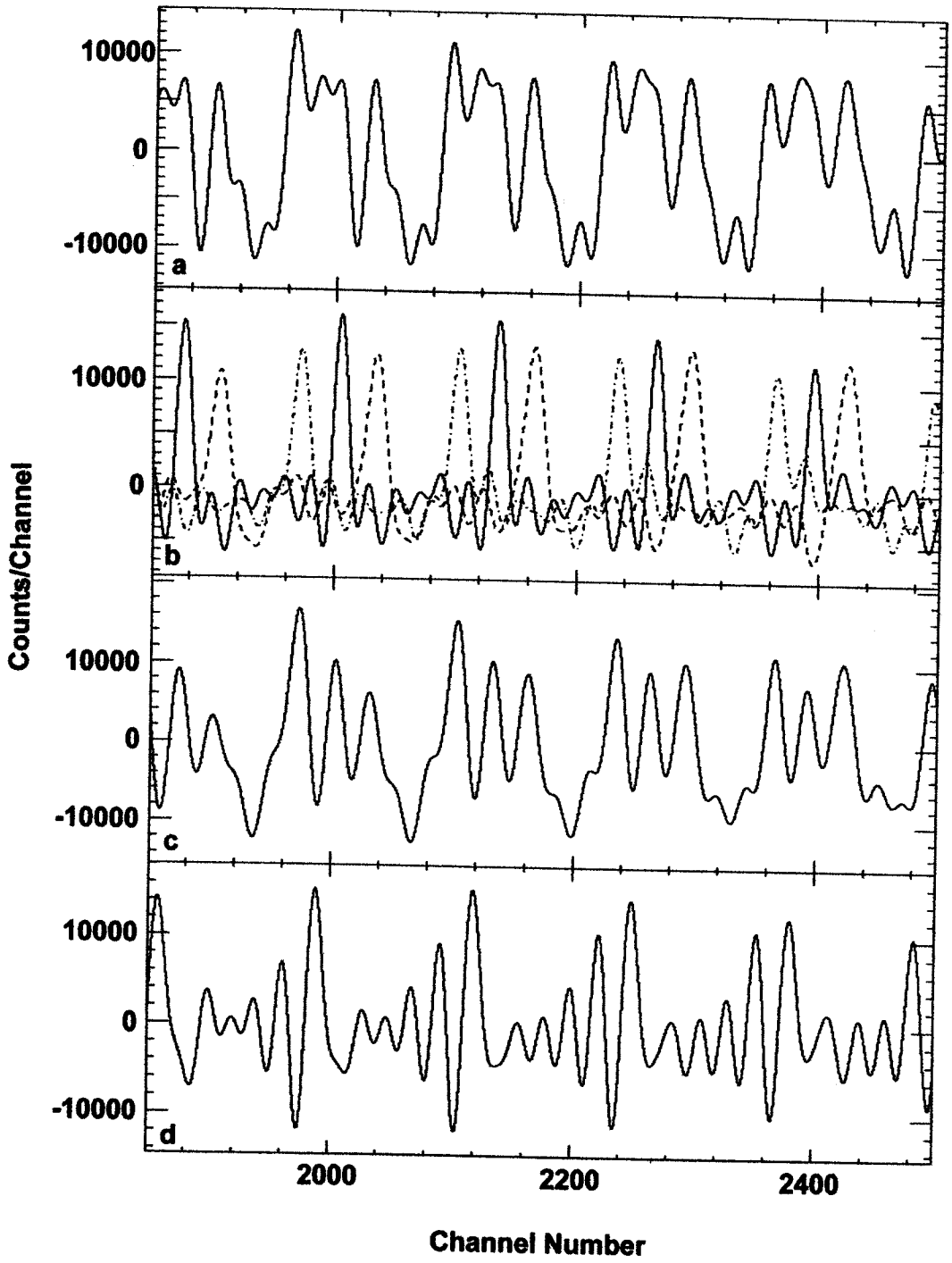

Figure 7.21: 130 channel number template search: Comparison between a) the results for the background spectrum, b) individual results for ^{133}Ce SD1 (solid), SD2 (dot dash), and SD3 (dash), c) a sum of the results for ^{133}Ce SD1 plus SD2 plus SD3, d) the difference between a) and c) showing potential SD peaks.

Chapter 8

Spectral Artefacts

The surprising results of the application of the Segmented Fast Fourier Transform (FFT) technique on published Superdeformed (SD) data show an unusual phase shift that we believe will have significant impact on the search for SD bands. The results point to a situation where minor changes in the x-axis can actually generate regularly spaced artefact peaks that to some extent resemble the popular description of SD bands. Calibration techniques were investigated in order to find potential sources of these artefacts.

8.1 Introduction

The typical procedure in an SD band search is to generate an array of triple coincidence events, then, use a search or a gating technique to generate a sum of the gated spectra that contains an enhanced count rate of peaks with a selected regular spacing. From this histogram a background is subtracted, resulting in a difference spectrum having positive and negative peaks that reflect the predominance of nuclei within the data and reveal the enhanced peaks – the "SD band".

The Segmented FFT technique works without enhancing the count rate of regularly spaced peaks. It is sensitive enough to find SD bands within the sum of SD gated spectra and also within background spectra.

8.2 Segmented FFT Search

We performed the segmented FFT method on published ^{133}Ce SD band data acquired on a large multi-detector array [hau95]. The methodology that they used to generate the SD band is a standard one, commonly used in the field. The FFT technique was tested on: a standard ^{133}Ce SD band-3 spectrum formed from the difference between the sum of the double gated SD data and the background data; the sum of the double gated SD peaks; and, a background spectrum formed from the sum of single gated spectra. By subtracting the search results for the background from the search results for the data, (spectrum C from spectrum B in Figure 7.18), the difference spectrum formed (spectrum D in Figure 7.18) appears to be nearly identical with the standard. However, we were surprised to find that the peak centroids in the search results from the double gated SD spectra and the background do not exactly match the corresponding centroids in either the standard SD spectrum or the difference spectrum. There is a slight and varying phase shift in the peaks, indicating that a compression or expansion of the x-axis has occurred between the gated SD spectrum and the background spectrum. See Figure 8.1.

8.3 Rebinning Experiment

We devised a method to investigate the source of this phase shift. Since calibration fluctuations would be an obvious choice, an unrelated data set acquired on the CSS spectrometer at HRIBF [ham90] was rebinned from the raw data in four different ways to simulate minor calibration changes. Regression analysis was performed on data points acquired from 20 detectors using ^{133}Ba, ^{152}Eu, ^{60}Co, and ^{88}Y isotropic calibration standards. Table 8.1 outlines the study parameters. One test set was a simple linear regression. Another set included four parameters and produced coefficients of x^0, x^1, x^2, and x^3 or x^4. The choice of whether to include the x^3 or x^4 coefficient was

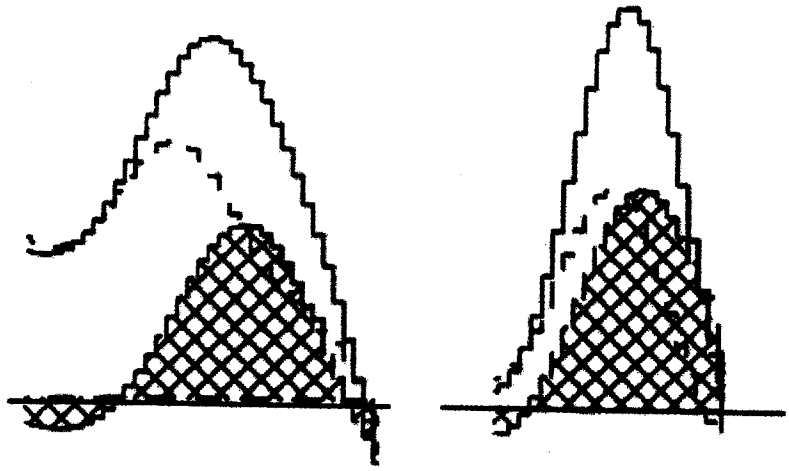

Figure 8.1: Two examples of peaks from the segmented FFT search show a phase shift in the data (solid), background (dash), and difference (crosshatch) peak centroids, suggesting that a compression or expansion of the x-axis had occurred between the double gated SD data and the single gated data used as background.

based on the best fit. Since many software programs used to analyze high resolution γ ray data only include provisions for two or three coefficients of calibration, two other test sets were included in the study: one included only the first three coefficients from the four parameter test set; the other included only the first two coefficients from the same test set. Table 8.2 lists the actual calibration coefficients for the detectors. This corresponds to the Tests 1 through 3. The two-parameter calibration coefficients for Test 4 can be found in Table 5.1.

By comparing spectra from the same detector that differ only by these minor calibration changes, we would be able to observe whether or not spurious, artefact-peaks can be formed during routine data analyses. If these calibration changes were too small to affect the peak energy, then subtracting two test sets would produce an empty set. However, if the calibration changes shifted the peaks out of phase between the test sets, then a subtraction would produce many positive and negative peaks, the centroids of which would reflect the areas of the peaks not cancelled by

the subtraction. This resulted in 12 test comparisons for each of the 20 detectors.

Table 8.1: Calibration rebinning experiment:

	x^0	x^1	x^2	x^3 or x^4	Regression Analysis
Test 1	*	*	*	*	4 parameter fit / 4 used
Test 2	*	*	*	-	4 parameter fit / 3 used
Test 3	*	*	-	-	4 parameter fit / 2 used
Test 4	*	*			2 parameter fit / 2 used

Figure 8.1 shows examples of the results. Many artefact peaks formed during the test comparisons. In fact, none of the 20 detectors produced empty sets. Some, such as the Test 1 minus Test 4 for detector 1 (Test 1 1m4), would just add to the noise level of the spectrum and blur the clarity of the small peak centroids; however, many have a peak intensity that would be significant, had they been formed in a routine data analysis, such as the background subtraction process. An expansion of the Test 2m3 comparison for detector 1 shows many small peaks of equivalent intensity that are separated by nearly equal distances. Two "Phantom" SD bands can be observed that are comparable in intensity and spacing to those reported in the A=130 region. The Test 2m3 comparison simulates what would happen if low resolution software were used with data that should be calibrated to three coefficients. The production of artefact peaks depends not only on whether certain coefficients are dropped during the analysis but also on the individual detector calibrations. Groups of SD-like peaks show up at various locations in the energy spectrum, depending on minor differences in the coefficients.

8.4 Recalibration Experiment

Would corresponding subtle changes in calibration between the data and background spectra produce changes in the published SD band in ^{133}Ce? An experiment using a

Table 8.2: Standard Isotropic Energy Calibrations for each Detector using a four-parameter fit.

Detector	x^0	x^1	x^2	x^3	x^4	$\Sigma(res)^2$
1	5.1643	0.62212	-0.67622E-6	0.13407E-9	-	0.049
2	29.146	0.62695	-0.42585E-6	-	0.25132E-13	0.026
3	9.3838	0.63575	-0.45489E-6	-	0.26920E-13	0.055
4	1.6367	0.62892	-0.77678E-6	-	0.37634E-13	0.052
5	-8.005	0.63094	-0.41963E-6	-	0.27235E-13	0.078
6	-1.1119	0.63022	-0.82449E-6	0.14483E-9	-	0.135
7	0.48908	0.62508	-0.40920E-6	-	0.2996E-13	0.043
8	-0.92759	0.62878	-0.68229E-6	0.15424E-9	-	0.028
9	-5.8594	0.63162	-0.63414E-6	-	0.41314E-13	0.042
10	-9.0429	0.63427	-0.59441E-6	-	0.28351E-13	0.032
11	1.88110	0.62632	-0.37310E-6	-	0.1687E-13	0.063
12	1.25060	0.62990	-0.17996E-6	-	0.12522E-13	0.051
13	3.5159	0.62294	-0.71719E-6	0.15494E-9	-	0.037
14	-26.060	0.64594	-0.91350E-6	0.19591E-9	-	0.345
15	-25.368	0.64340	-0.13866E-5	0.30993E-9	-	0.035
16	-8.9695	0.63223	-0.53683E-6	0.12291E-9	-	0.032
17	-1.6782	0.62752	-0.45118E-6	-	0.28409E-13	0.057
18	-8.5890	0.63229	-0.12009E-5	0.28481E-9	-	0.103
19	-11.650	0.63327	-0.36743E-6	-	0.23288E-13	0.046
20	–NA –					

histogram rebinning technique was designed to simulate this. The background spectrum was subtracted from the double gated data spectrum after both were adjusted with the original three parameter calibration, i.e., $E = C_0x^0 + C_1x^1 + C_2x^2$. This is the standard difference spectrum to which everything else is compared. Four of the SD peaks are shown in Figure 8.3a. The data spectrum was then subjected to various calibration adjustments. The background spectrum with the original calibration was subtracted from each adjusted data spectrum. The first two recalibrations (Figure 8.3b and 8.3c) involved decreasing the x^2 coefficient by $2X10^{-7}$ and increasing the coefficient by the same amount. For the next test, the x^2 coefficient was set equal to zero (Figure 8.3d). In the fourth test, the coefficient was changed from approximately $-0.7X10^{-6}$ to $-2.7X10^{-6}$. In the last test, an arbitrary value of $0.2X10^{-9}$ was added to the calibration as an x^3 coefficient. The equivalent converse experiment was also performed, i.e., adjusted background spectra were subtracted from a data spectrum with the original calibration. Both experiment sets gave equivalent results. The most obvious change in the SD band is the appearance of many additional peaks. A slight variation in the quadratic coefficient causes peak centroid shifting and changes in the relative peak intensities. Truncation of the highest coefficient produces an increase in the overall signal; however, the original four peaks no longer are readily apparant.

8.5 Discussion

We have shown how easily artefacts can be produced and the extent to which they can affect the spectrum. Locating the cause of the artefacts during data analysis is important. Some potential sources of artefact peak generation may be the following:

- Software: Low resolution truncation of higher calibration coefficients. The method chosen to re-apportion the Y-axis intensity level in rebinning techniques. The use of single, rather than double precision values.
- The use of a background spectrum with a different multiplicity than the gated spec-

trum.

- The effects of low resolution gain shifting or doppler shifting.
- Calibration of all nuclei in the experiment based on the γ-ray transitions from one nucleus.
- Linear normalization of all detectors in an array instead of including their non-linear coefficients.
- The use of SD search techniques that generate a spectrum with changes in the x-axis.

8.6 Conclusions

1) The segmented FFT search results suggest that a compression or expansion of the x-axis had occurred somewhere in the analysis of the double gated data spectrum and/or the single gated background spectrum from which the SD band was generated.

2) The rebinning experiment shows that artefact peaks with spacings and intensities that approximate SD bands may be formed by any compression or expansion of the x-axis.

3) The recalibration experiment demonstrates that subtle changes to the quadratic and cubic coefficients in a calibration may produce drastic changes in the SD difference spectrum: peak shifts, the appearance of a multitude of additional peaks and the disappearance of "SD peaks".

Artefact SD peaks can be generated during data analysis. There may be a need to re-evaluate many published SD spectra from this new perspective.

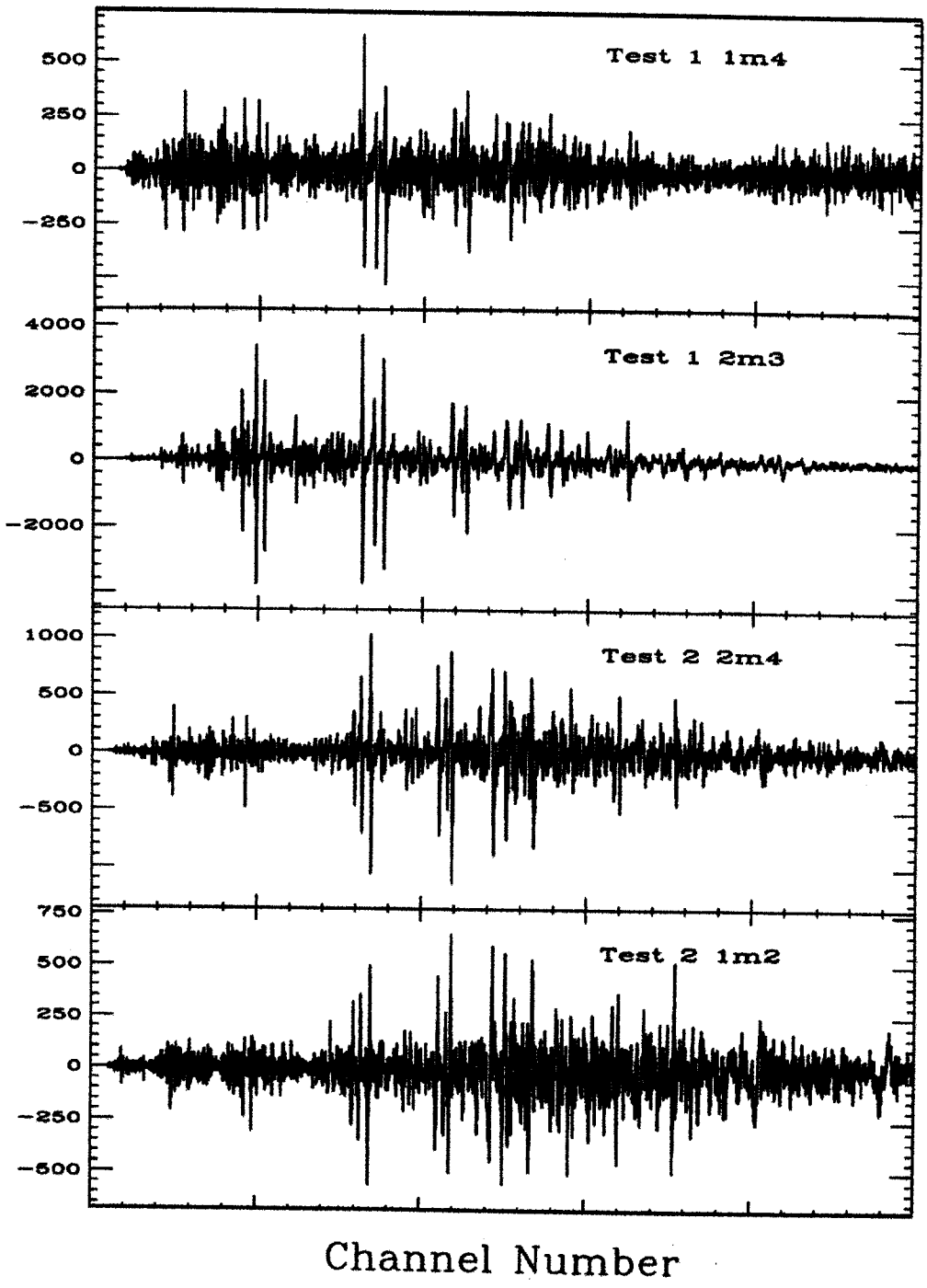

Figure 8.2: Examples of artefact peaks formed during the test comparisons from the calibration rebinning experiment: from the top, Test 1 1m4, Test 1 2m3, Test 2 2m4, Test 2 1m2.

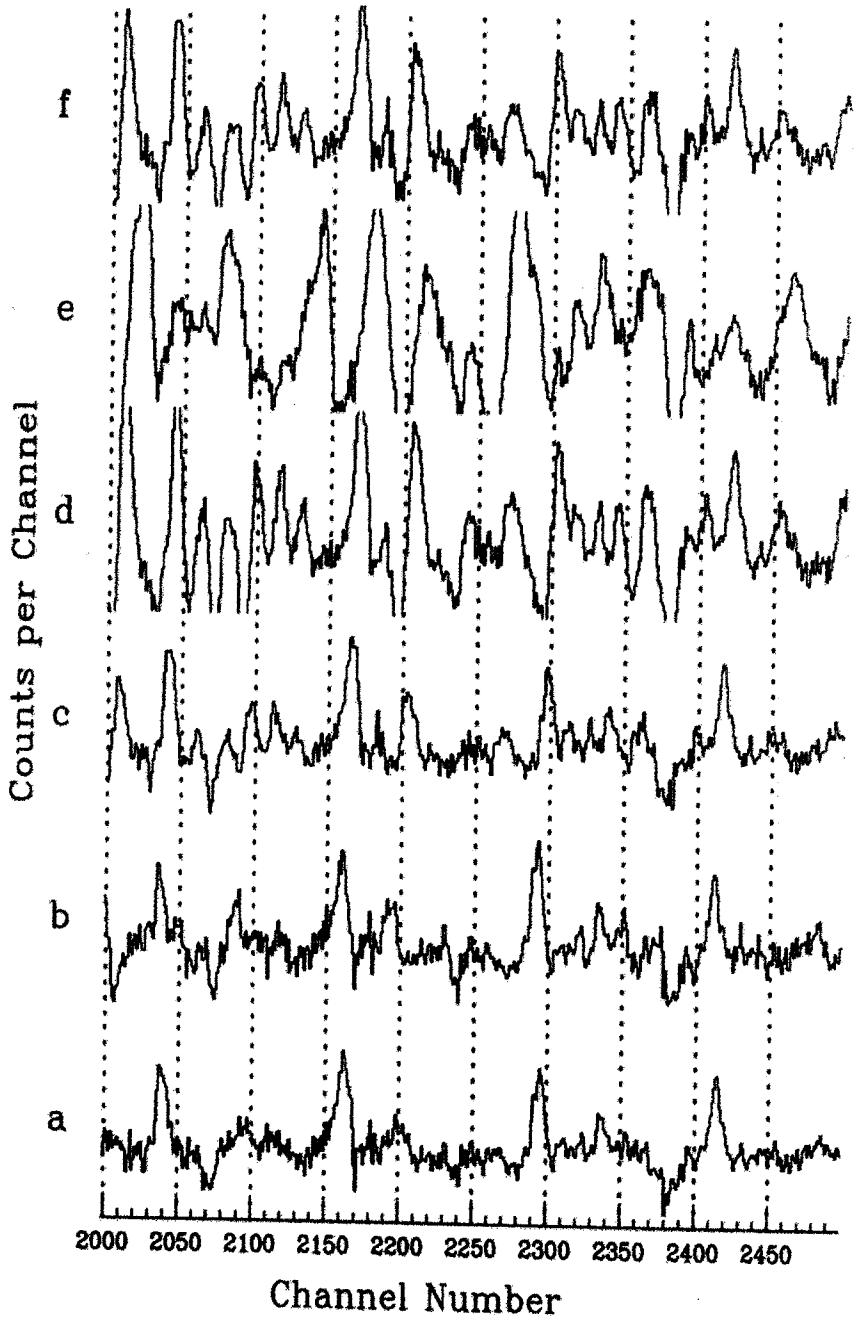

Figure 8.3: Results of the recalibration experiment employing subtle changes in calibration between the data and background spectra show changes in the published SD band in ^{133}Ce. a) Represents four of the SD peaks with the original calibration. b-e) Represent changes to the quadratic term. f) Includes a cubic term to the calibration. See text.

Chapter 9

Nuclear Energy Level -Theory

In this Chapter we incorporate the basic concepts of the nuclear potential introduced in Chapter 2 and develop it into a nuclear structure model so that a true understanding of the nature of this experiment can be realized.

9.1 Nuclear Models

A nuclear model is merely a mathematical attempt to describe what is going on in nature. To be useful, it must account for measured nuclear properties and predict new ones. [kra88] The most successful nuclear model is the Shell model in which like nucleons of opposite spin pair together and orbit within the self sustaining fields generated by the nucleus. This development will be expounded on in the following pages. Another model is a Hydrodynamic one in whch nuclear matter is described in terms of the physics of a 'liquid drop'. This has been mentioned previously in the mass model calculations in Chapter 3. There are other nuclear models that will only be mentioned here. One is an α cluster model of nuclear structure where it is postulated that internuclear material exists in basic units of two protons and two neutrons, ie., a stable α particle. Nuclear shells are then constructed based on this idea. Another nuclear structure model is referred to as the molecular model. When the combined angular momentum of the target plus projectile in a nuclear reaction

is too high to form a compound nucleus, a 'molecular' structure may form that has vibrational and rotational properties like a diatomic molecule. [kra88]

In the atomic case, solution of the three-dimensional Schrödinger equation determines which energy levels can be designated for each electron. The nuclear situation is much more complicated because the potential is due to a self-sustaining field generated by the nucleons themselves. This means that every isotope has a unique set of nucleons that creates a correspondingly unique field. To solve each would be an impossible chore, therefore, generalizations are made that determine trends for specific types of nuclei. We will discuss spherical nuclei and deformed (nonspherical) nuclei. These are categorized by the proximity of their nucleons to filled shells.

9.1.1 Evolution of the Spherical Shell Model

In the Shell model, two like-particles couple with opposite spins according to the Pauli principle. Therefore, the nucleus can be described in terms of two distinct sets of orbitals, one for protons and another for neutrons. Spherical nuclei contain all nucleons in closed shells (filled orbitals). As more nucleons are added, the nuclear field takes on a distinctly deformed shape. Highly deformed nuclei are found midway between closed shells.

The success of the shell model is due to its ability to explain the experimentally observed stability of specific numbers of nucleons – 2, 8, 20, 28, 50, 82, 126 that occur within spherical nuclei. See Figure 1.1. According to Mayer [may68], an approximation had to be made to simplify the perception of the movement of the nucleons, in order to generate a nuclear potential. If an arbitrary nucleon is considered, the assumption can be made, to good approximation, that the effect of all other nucleons on the chosen one can be averaged to a static potential. Initially, researchers investigated harmonic oscillator and infinite square well potentials. The resulting orbital levels are shown in Figure 9.1 [kra88, hyd64]. Only the first three stable energy levels could

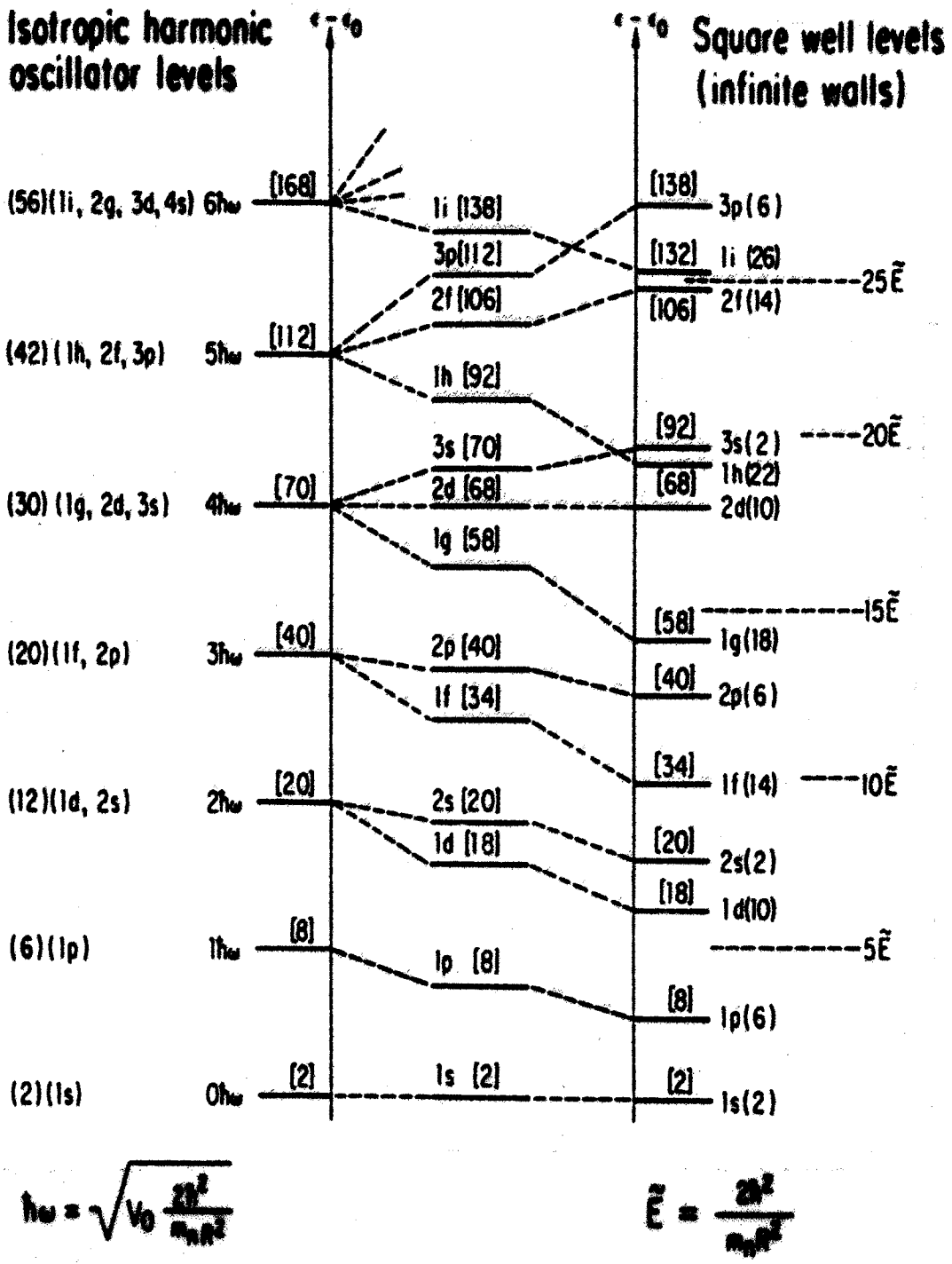

Figure 9.1: Energy levels obtained by solving the Schrödinger equation using an infinite well potential (right) and a harmonic oscillator potential (left). The center levels are produced with a potential intermediate between these two. The numbers in parentheses indicate the nucleon occupancies [kra88, hyd64, may55].

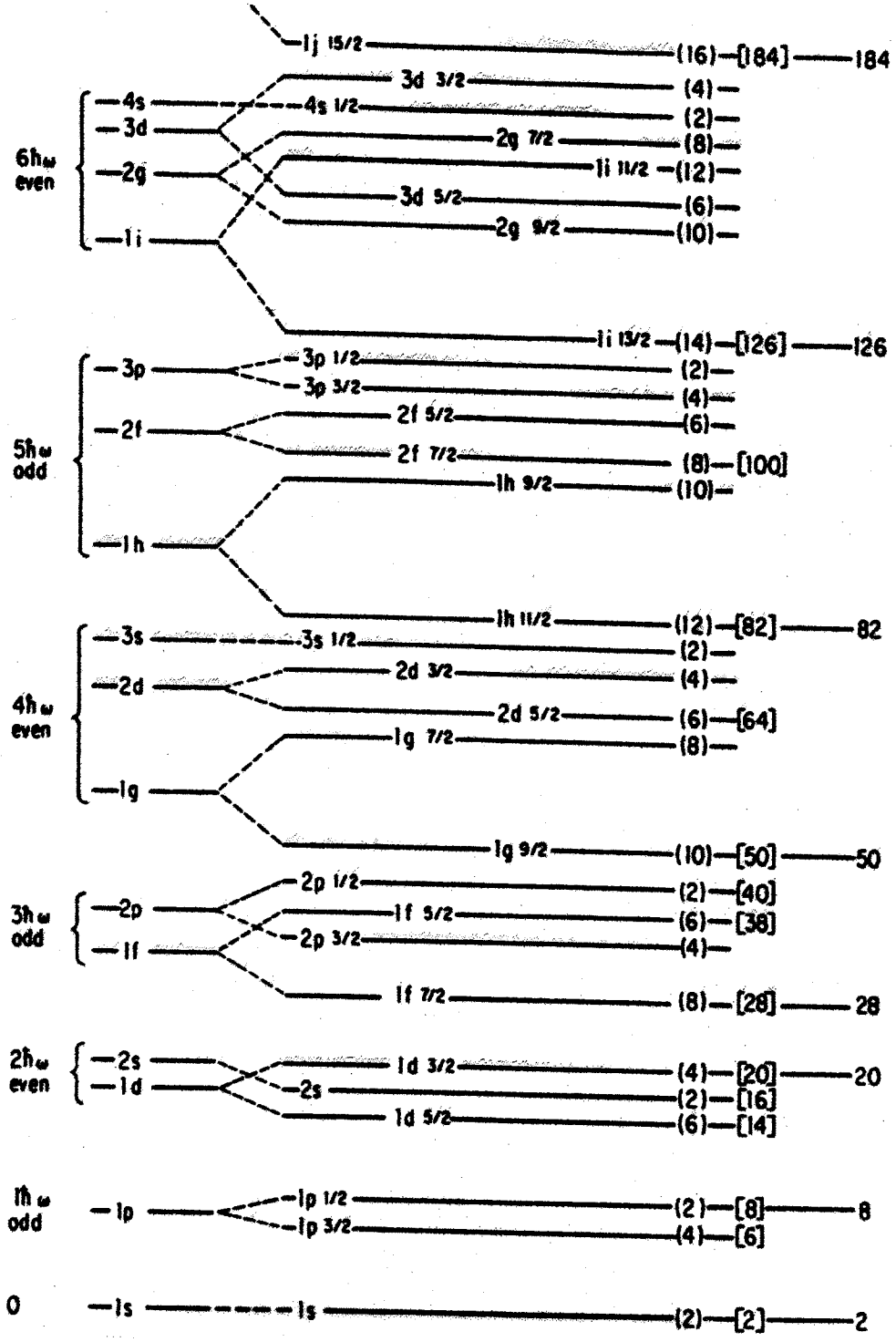

Figure 9.2: The effect of spin-orbit coupling produces the 'magic' shell-gap numbers. Shown are energy levels calculated with a potential intermediate between a square well and an harmonic oscillator and on the right, the shell model results calculated with the intermediate potential plus a spin orbit parameter [kra88, hyd64, may55].

be accounted for. A linear interpolation between these levels lifted the degeneracy of the orbitals, but produced the same null results in accounting for the magic numbers. When a term was added to this intermediate potential to acccount for the coupling between the particle's spin and orbital angular momentum, the proper experimental subshell levels were produced (Figure 9.2). Each of the states are labeled with the total angular momentum, $j = \ell + s$. For each nucleon, $s = \pm\frac{1}{2}$. Therefore, j can have the values $|\ell \pm \frac{1}{2}|$. The spin-orbit interaction can be written: $V_{so}(r)\,(\ell \cdot s)$ with $V_{so}(r)$ being the intermediate potential. [1] The energy separation between states with $\ell > 0$ can be computed using the the expectation value of $< \ell \cdot s >$.

$$< \ell \cdot s >_{j=\ell+\frac{1}{2}} \; - \; < \ell \cdot s >_{j=\ell-\frac{1}{2}} \quad = \quad \frac{1}{2}(2\ell+1)\,\hbar^2 \tag{9.1}$$

Consider the example 1d ($\ell = 2$) orbital with a degeneracy [2] of $2(2\ell+1) = 10$. The possible j values are $|\ell \pm \frac{1}{2}|$ resulting in $d_{\frac{5}{2}}$ and $d_{\frac{3}{2}}$ levels, referred to as a spin orbit doublet. The nucleons are regrouped between the levels based on a degeneracy value of $(2j+1)$. [3] This results in 6 particles in the $d_{\frac{5}{2}}$ level and 4 in the $d_{\frac{3}{2}}$ level.

This variation of the shell model is known as the extreme independent particle model because the unpaired valence particle determines most of the properties of the nucleus. It can account for the ground state spins and parities in most odd-A nuclei with $A < 150$. For example, if the valence particle of a specific nucleus is in a $d_{5/2}$ state, the spin of the ground state of that isotope is $\frac{5}{2}$ and the parity is even (since $\pi = (-1)^{\ell}$). [kra88]

Nordheim coupling rules

For an even-even nucleus, all particles are coupled and the ground state is 0^+. For an odd-mass nucleus, the ground state can be estimated as discussed above. However,

[1] $V_{so}(r) = -V_o/(1 + exp[(r-R)a])$. where a is the 'skin thickness' (0.524 fm), $R = 1.25\,A^{\frac{1}{3}}$ and the well depth V_o is about 50 MeV.

[2] Degeneracy refers to occupancy level.

[3] With spin orbit coupling, m_s and m_ℓ are no longer valid quantum numbers therefore they cannot be used to label states or determine degeneracies.[kra88]

for an odd-odd nucleus, empirical rules are used to estimate the ground state spin and parity. These are called the Nordheim coupling rules [4] [fri81, har69]. The ground state is built upon the effective mathematical coupling of the spin and angular momentum of both odd particles and may have a value ranging from $|j_1 - j_2|$ to $|j_1 + j_2|$, where j is the total angular momenta.

- I. If $(\ell_1 + \ell_2 + j_1 + j_2)$ is even, then $I = |j_1 - j_2|$.
- II. If $(\ell_1 + \ell_2 + j_1 + j_2)$ is odd, then $I \approx |j_1 + j_2|$.
- III. If the ground state is a combination of particles and holes, then the result is less certain with $I = j_1 + j_2 - 1$.

The parity is determined by the orbital angular momentum, ℓ . If ℓ_1 and ℓ_2 are both either even or odd, then the parity is even. If one is even and the other is odd, then the nucleus had odd parity.

9.1.2 Collective Model

The Collective nuclear model accounts for various collective motions in the nuclear core and also describes the rotation of deformed nuclei.

Deformation

The importance of nuclear deformation was realized around 1950, when Rainwater [rai50] measured the nuclear quadrupole moments of odd-mass nuclei and found them to be much larger than expected for a single odd nucleon moving in a spherical field. Deformation seems to increase by adding more nucleons. Figure 9.3 shows a schematic view of the chart of the nuclides with the known regions of deformation circled. These regions are located between areas where the magic shell gap numbers overlap.

In the last section we described a spherical nucleus with nucleons in the $d_{\frac{3}{2}}$ level. All four $(2j + 1)$ particles are equivalent because the projections of their angular

[4] The Nordheim coupling rules are useful in the mass range $20 < A < 120$.

momenta on the symmetry axis are at the same energy. In the situation where a

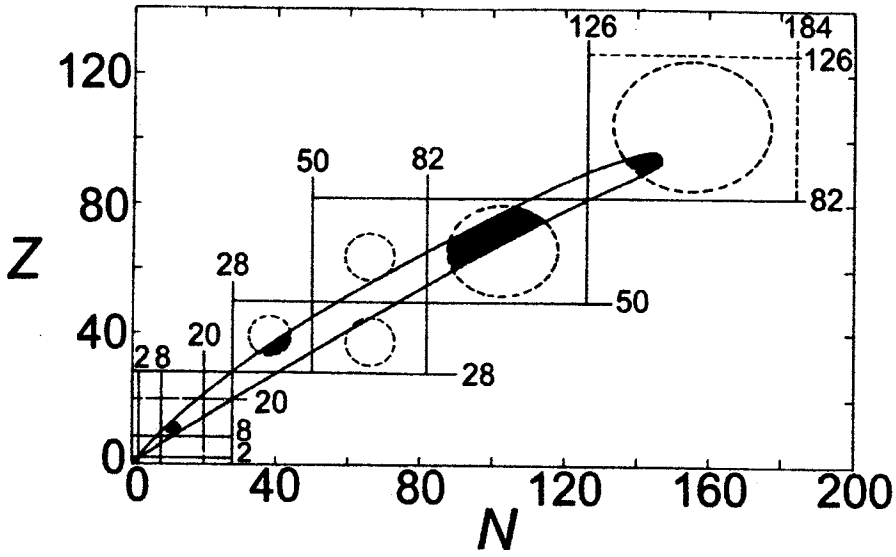

Figure 9.3: A schematic N versus Z chart of the nuclides showing regions of nuclei with stable, static deformation. The overlap with the magic numbers shows that these regions occur midshell [hyd64].

deformed potential exists, this degeneracy is lifted by the spacial orientation of the orbit. The energy depends on the component of j along the symmetry axis of the core. This is shown schematically in Figure 9.4. As the nuclear potential is changed into a deformed shape, the eight-fold spherically degenerate $f_{\frac{7}{2}}$ state splits into four (2j+1)/2 levels labeled with a new quantum number Ω that extends numerically from j in integral decrements to $\frac{1}{2}$. Figure 9.4 contains a description for both limiting deformations outside of a spherical shape, i.e., oblate and prolate. For a prolate deformation, the state with the orbital nearest to the plane perpendicular to the axis of elongation is the least stable. Therefore the highest Ω has the highest energy. The reverse is true for the oblate deformation. The stability increases with increasing Ω. See Figure 9.5.

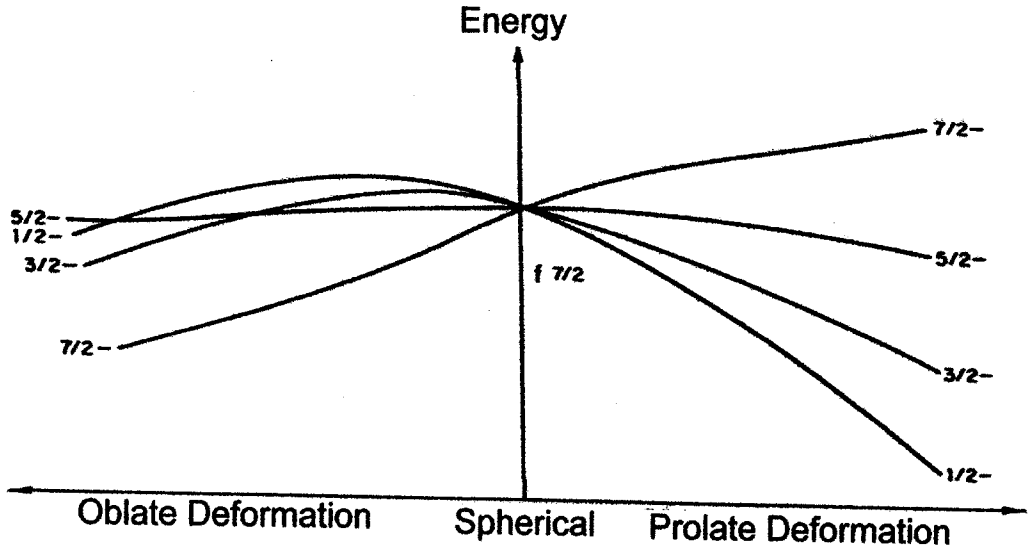

Figure 9.4: Single particle orbits with $j = \frac{7}{2}$ and their possible projections along the symmetry axis for prolate and oblate deformations. Only the positive projections are shown [kra88].

Nilsson Levels

A state in a spherical nucleus is completely characterized by the energy, the angular momentum (j), the nuclear magnetic moment (μ_z) which is the z component of the angular momentum, and the parity. However, in a nonspherical nucleus the wave functions become mixed and the quantum numbers that describe a spherical nucleus are no longer valid. Figure 9.6 shows the important quantum numbers for an odd mass (A) and an odd-odd nucleus (B) [mch65, hyd64, cho89]. In an odd mass nucleus, **j** is the angular momentum of the odd particle, Ω is the projection of **j** on the symmetry axis Z', **R** is the collective rotational angular momentum, **I** is the total angular momentum of the system, i.e., the nuclear spin, M is the projection of **I** on a space-fixed axis Z, K is the projection of **I** on the symmetry axis Z', Λ is the projection of the particle's orbital angular momentum on the symmetry axis and Σ is the projection of the particle's spin angular momentum on the symmetry axis. It should be noted that in this case, $\Omega = K$.

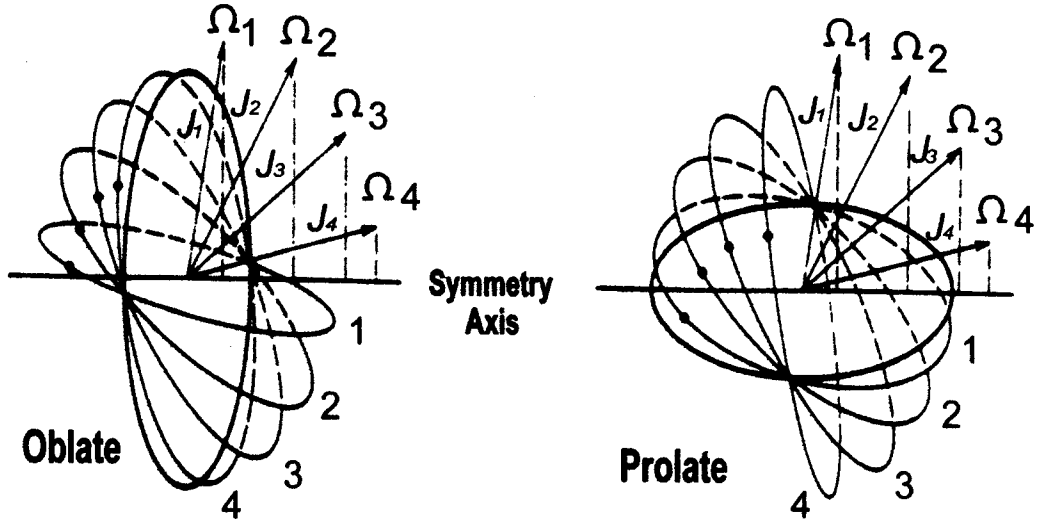

Figure 9.5: Variation of the stability of the Ω states with deformation [kra88].

In an odd-odd system, the spin and orbital angular momentum of the last unpaired neutron and protron contribute to the collective angular momentum and give rise to a doublet band; then $K = |\Omega_p \pm \Omega_n|$. Each nonspherical nuclear orbital is referred to as a Nilsson state and can be described with the labels:

$$\Omega^{\pi} \; [\, N \, n_z \, \Lambda \, \Sigma \,] \tag{9.2}$$

where, π is the parity, n_z is the number of nodes perpendicular to the symmetry axis and N is the total number of oscillation quanta[5] and is generally used as a counting number. It should be noted that $\Omega = \Lambda + \Sigma$ for an odd-odd system, therefore, Σ is often omitted from the brackets since it is the difference of the other two and can only be equal to $\pm\frac{1}{2}$ [mch65].

Nilsson Diagrams

When viewing a Nilsson diagram, the deformation parameter (either ϵ or β) is plotted along the x-axis and energy as a function of rotational frequency, along the y-axis.

[5]The term, oscillation quanta, refers to the energy levels generated by the harmonic oscillator. See Figure 9.1.

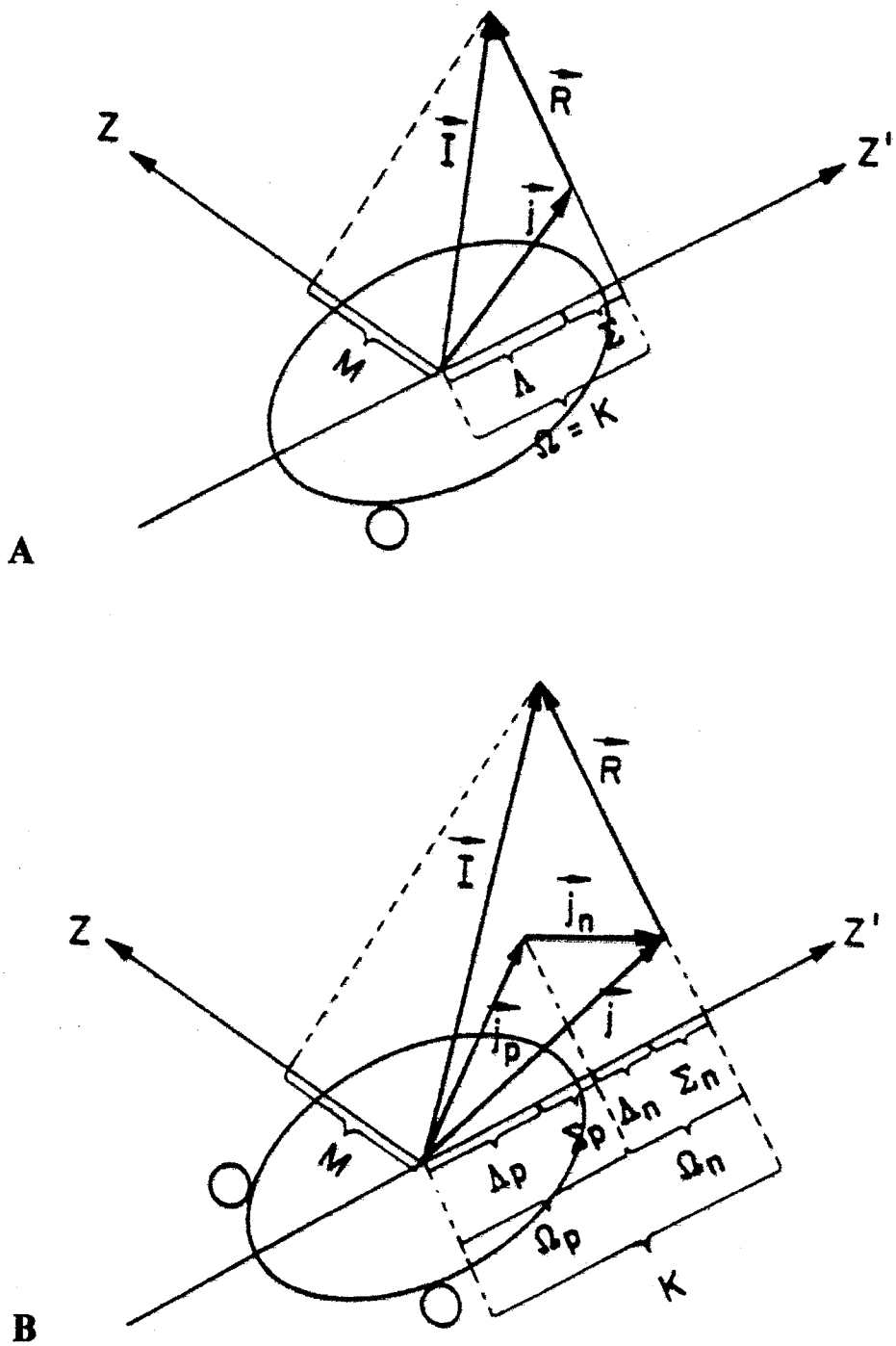

Figure 9.6: A) Schematic of the angular momentum coupling for an odd mass nucleus. B) Schematic of the angular momentum coupling for an odd-odd nucleus. See the text for an explanation of the symbols [mch65].

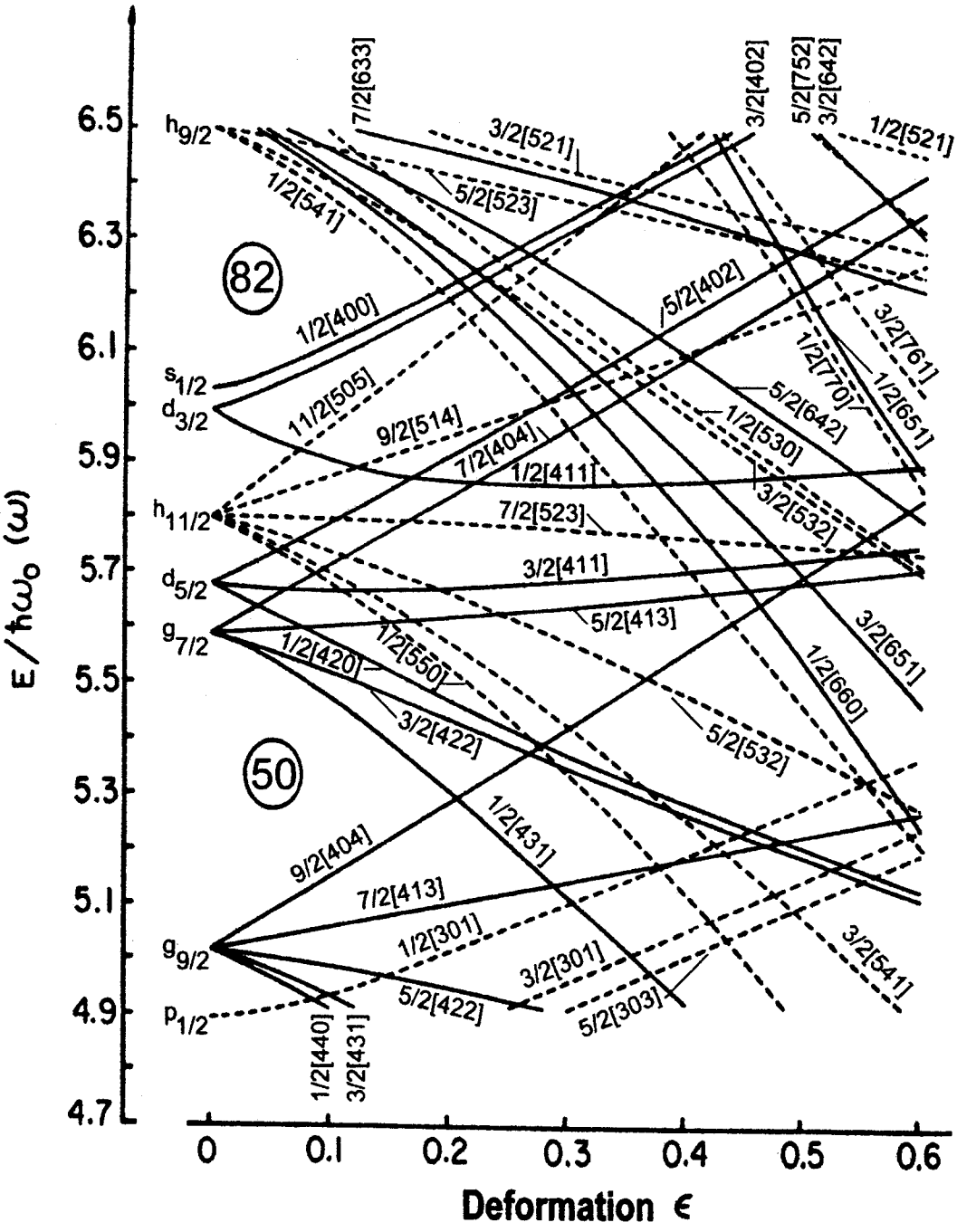

Figure 9.7: Nilsson energy level diagram for the 50 through 82 shell-gap regions [kra88].

(See Figure 9.7.) The shell model energy levels (from Figure 9.2) are listed along the left side of the figure. This represents the structure for a spherical nucleus with zero deformation. As deformation increases, the degeneracies are lifted and each state splits into $\frac{1}{2}(2j+1)$ levels with an occupancy of two particles in each. The circled numbers in the figure represent the shell gap magic numbers. The Nilsson labels are noted on each state. Even parity states are designated with solid lines; odd parity, with dashed lines.

Between energy gaps there are grouped together a number of states of a certain parity, called normal parity states, and a single state of opposite parity called a unique (or abnormal) parity state. There are states, referred to as intruder states, that are formed at high deformation (angular momentum) when a high j orbital state suddenly turns downward in a plot of energy versus deformation and mingles with much lower j states.

The point where one level intercepts another is called a bandcrossing. It is at the bandcrossing where the alignment of a nucleon pair [hil86] with the core are considered to take place.

Hamiltonian

The total Hamiltonian can be written in the form: [mch65, cho89]

$$\mathcal{H} = \mathcal{H}_{int} + \frac{\hbar^2}{2\Im(R^2)} = \mathcal{H}_{int} + \mathcal{H}_{rot} + \mathcal{H}_{cor} + \mathcal{H}_{pn} + \mathcal{H}_{irot} \qquad (9.3)$$

where R is the rotational angular momentum of a nuclear system consisting of particles coupled to a rotor having a symmetry axis in a static potential field. Each term can be expressed independently:

$$\mathcal{H}_{irot} = \frac{\hbar^2}{2\Im}[(J_p^2 - \Omega_p^2) + [(J_n^2 - \Omega_n^2)] \qquad (9.4)$$

$\mathcal{H}_{irot}$ is an intrinsic contribution from the rotational degree of freedom.

$$\mathcal{H}_{pn} = \frac{\hbar^2}{2\Im}(J_{p+}\,J_{n-} + (J_{p-}\,J_{n+}) \tag{9.5}$$

This represents the coupling of particle degrees of freedom through rotational motion which can connect proton and neutron states that have Ω's differing by 2 units. This can shift odd and even members of a band with respect to each other, i.e., the $K = 0$ bands.

$$\mathcal{H}_{rot} = \frac{\hbar^2}{2\Im}(I^2 - K^2) \tag{9.6}$$

where $K = \Omega = |\Omega_p \pm \Omega_n|$ for odd-A and odd-odd nuclei.

$$\mathcal{H}_{intr} = \mathcal{H}_{sp}(p) + \mathcal{H}_{sp}(n) + \mathcal{V}_{pn} \tag{9.7}$$

where $\mathcal{V}_{pn}$, the residual proton neutron interaction, is the reason for the splitting of the $K = |\Omega_p \pm \Omega_n|$ doublet in an odd-odd system.

$$\mathcal{H}_{cor} = -\frac{\hbar^2}{2\Im}(I_+\,J_- + I_-\,J_+) \tag{9.8}$$

As the nucleus rotates, Corolis force tries to decouple particles from the core and align them along the rotational axis. This force can become strong enough at some rotational frequency to overcome the pairing interaction between nucleons. High j – low Ω orbitals (see Figure 9.5) are most susceptible to this force [hil86].

$$\mathcal{H}_{cor} = -\frac{\hbar^2}{2\Im}[(I_+\,J_{p-} + I_-\,J_{p+}) + (I_+\,J_{n-} + I_-\,J_{n+})$$

where $I_\pm$ and $J_\mp$ are normal shift operators.

The matrix elements of $\mathcal{H}_{cor}$ are single particle operators and have the form: [mch86] [cho89] [ste71]

$$\mathcal{M}_{cor} = \frac{-\hbar^2}{2\Im}\,[j(j+1) - (\Omega \pm 1)]^{\frac{1}{2}}\,[I(I+1) - K(K \pm 1)]^{\frac{1}{2}} \tag{9.9}$$

If the Coriolis force is small, it can be treated as a perturbation on the energy levels [cho89]. If the Coriolis force is large, it can cause splitting of rotational bands, often referred to as doubly decoupled bands.

9.2 Rotational Bands

Nuclear cascade

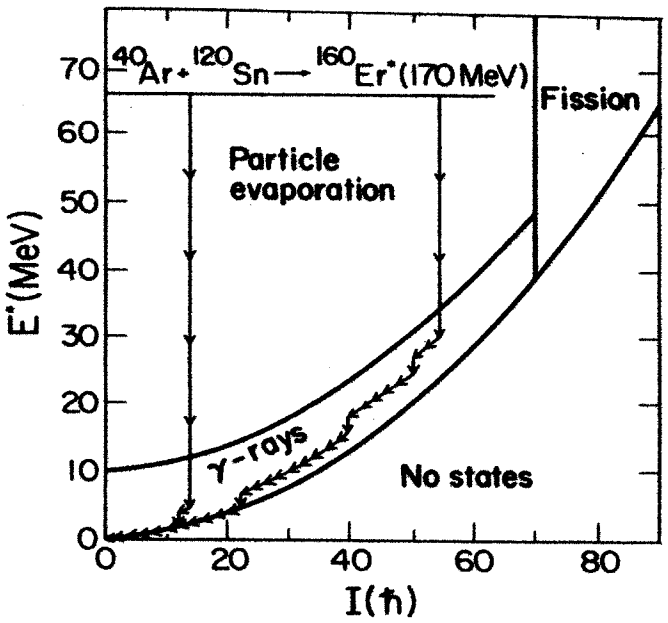

Figure 9.8: A general plot of excitation energy versus angular momentum for a nuclear reaction. The nucleus de-excites via either an yrast mechanism or a statistical cascade. Below the yrast line there are no energy levels .

In a nuclear reaction, the compound nucleus may decay by various modes: particle evaporation, γ-ray de-excitation, or fission. This is shown schematically in Figure 9.8. At a point in spin where the excitation energy approximates the neutron binding energy, the nucleus fissions [dia84]. At lower spins, particle evaporation occurs. This has been described in Chapter 3. The residual nucleus with the highest spin must be created from the compound nucleus via a low particle evaporation number. Since particle evaporation does not remove significant amounts of angular momentum, the

nucleus then de-excites by γ-ray emission. The parabolic line drawn from zero to high spin is the yrast line, below which no states exist. The γ-ray transitions can be one of two types [dia84]: 1) statistical transitions move the nucleus toward the yrast line and originate in a region of high level density and high spin referred to as the 'continuum'. 2) yrast-like transitions carry away much of the angular momentum resulting in orderly cascades that parallel the yrast line to the ground state. Nuclei tend to de-excite by two major γ-ray methods: single particle alignments and collective motions of the entire nuclear system [dia84]. The difference is shown schematically in Figure 9.9. For nuclei near closed shells, excitation of shell model states occurs. The angular momentum is removed by the alignment, along the rotational axis, of the spin from the individual particles outside of the closed shell. This is shown on the right side of the Figure for ^{212}Rn. The transitions do not exhibit a regular pattern and many multipolarities exist. Collective motion of the nucleus includes both vibrational and rotational modes. Spherical nuclei exhibit only vibrational modes but the converse does not necessarily hold true. Deformed nuclei may also have vibrational modes of de-excitation. However, they can produce very complicated effects on top of rotational modes. A pure vibrational mode can be caused by either quadrupole (γ or β vibrations See Figure 2.5 in Chapter 2.2.) or octupole vibrations [hyd64] and are referred to as phonon bands. The left hand side of Figure 9.9 depicts a collective rotation of a prolate spheroid and a corresponding example of a rotational cascade in ^{238}U. This is a smoothly decreasing cascade of E2 transitions [6] that approximates the equation for a rigid rotor.

Rotational Mode

The energies of a rigidly rotating object in quantum mechanical terms has been described in Equation 2.20 from §2.3.1. Since the residual nucleus in a reaction

[6] Deformed nuclei may also generate cascades of M1 transitions.

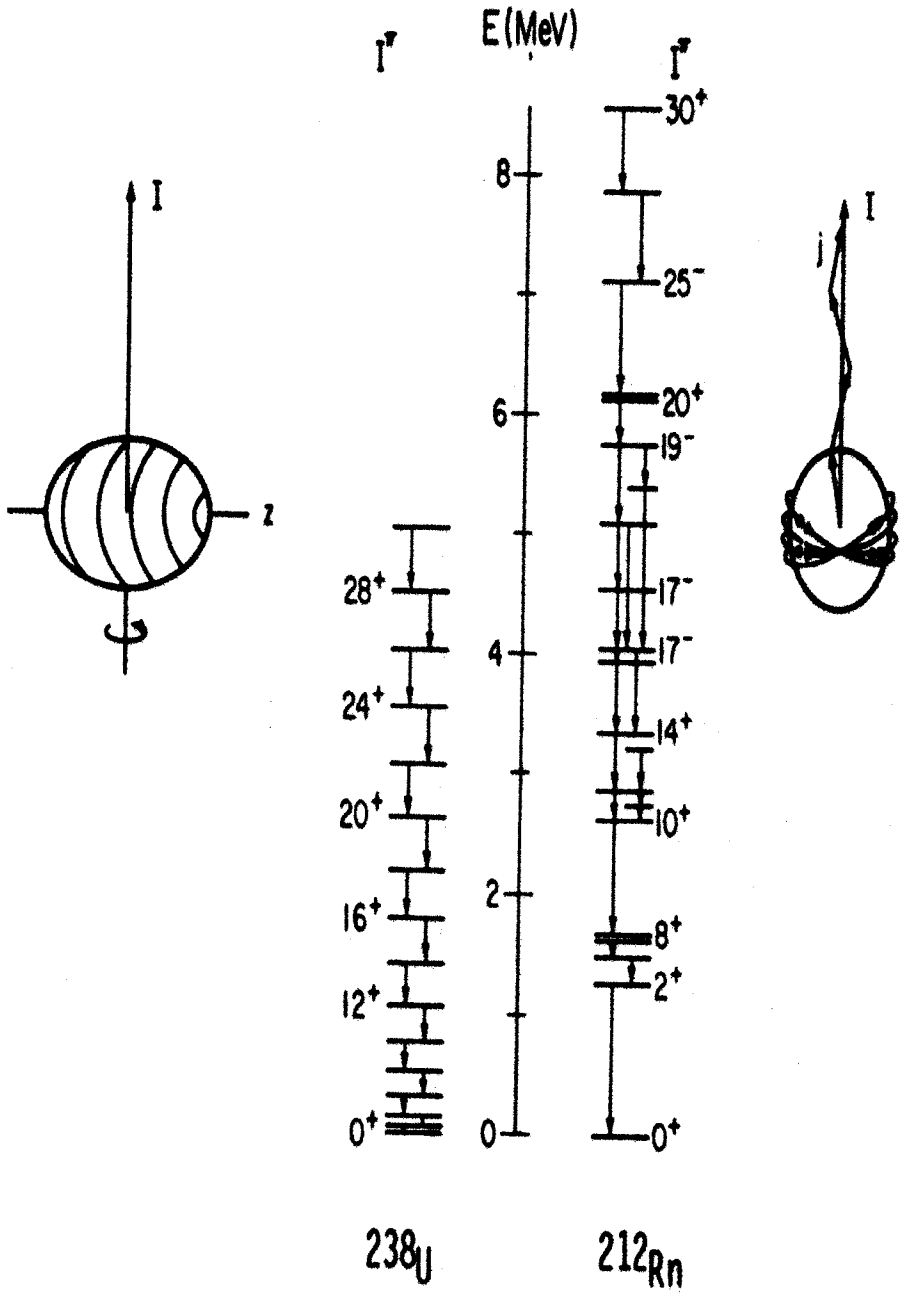

Figure 9.9: The left hand side of Figure 9.9 depicts a collective rotation of a prolate spheroid and a corresponding example of a rotational cascade in ^{238}U. The right side shows a cascade of single particle states in ^{212}Rn along with a simplistic view of how the angular momentum from the single particles may couple with the core. [dia84].

deexcites in steps of equal units of angular momentum, I, this corresponds to a generally decreasing rotational energy for each nuclear excited state. This forms a sequence of energy transitions known as a rotational band. Since the rotational angular momentum is always perpendicular to the symmetry axis[7] all transitions in a rotational band have the same quantum number, K [hyd64].

Equation 2.20 holds for a rigid rotor. This formula holds true for nuclei only when there is complete separation of rotational from vibrational and intrinsic motions [hyd64]. For even-even nuclei, a correction is needed for the rotational-vibrational interaction and is reflected in the B term[8] in the corrected formula:

$$E_I = E_\circ + \frac{\hbar^2}{2\Im}\, I\,(I+1) + B\, I^2\,(I+1)^2. \tag{9.10}$$

For odd-odd and odd-A nuclei, the B term reflects both the rotational-vibrational interaction plus a rotational-particle coupling interaction due to the Coriolis force. In the special case of $K = \frac{1}{2}$, a decoupling term, a must be added [9] [hyd64].

$$E_I = E_\circ + \frac{\hbar^2}{2\Im}\left[I\,(I+1) + a(-1)^{I+1/2}\,(I+\frac{1}{2})\delta_{K,\frac{1}{2}}\right] \tag{9.11}$$

The new terms are due to the effect of the Coriolis force acting in the rotating system. The decoupling constant a is the Coriolis matrix element which can be derived from two consecutive transitions of the same signature [cho89].

Signature Splitting

A band from an odd-A or an odd-odd nucleus can split into two parts called signatures, due to the two quantum numbers associated with angular momentum. The Coriolis matrix term could shift members of one signature up in energy and the members of the other down in energy [cho89]. This can be observed in the transition

[7] This follows the right hand rule.

[8] The B term is usually evaluated empirically from the spacings of the first few transitions in the rotational band [hyd64].

[9] δ represents the Kronecker symbol.

energies as a staggered ordering of the energies with increase in spin. The signature splitting of a rotational band depends on the asymmetry shape factor, γ; the specific valence orbitals and the strength of the pairing force. A reduction of the pairing force will decrease the rotational frequency needed to decouple and align a nucleon pair [hil86]. Therefore, some bands have a slight signature splitting while others are totally decoupled with one signature observed with a high intensity (referred to as favored) while the other might not be observed at all.

Bandcrossing

Diamond in reference [dia84] describes the mechanism of rotational band formation in the following way: If the nucleus were rigid the moment of inertia would be constant. However, values of $\Im$ for a deformed nucleus at low spin have been measured to be a factor of 2 to 3 smaller than the value for a rigid rotor. This is due to the pairing interaction [10]. With an increase in angular momentum, the increasing Coriolis interaction reduces the pairing correlations. Therefore, the $\Im$ value increases with increasing spin. Since the Coriolis force is also proportional to the j of the particle, it acts more strongly on the high-j nucleons in a shell. Experimentally, this can be observed on a plot of spin versus rotational frequency. "The gradually increasing slope is interrupted occasionally by a sharp increase where it is energetically more favorable to align a pair of high-j nucleons completely while keeping the pairing correlations among lower-j nucleons." [dia84].

Backbending

A nucleus with high excitation energy may not always follow the initial decay path within one rotational band. It can, instead, flip over into another decay route (i.e.,

[10]Mathematically, the pairing force is the last parameter in the binding energy equation that describes the nuclear mass. It refers to the gain in stability (an energy lowering effect) that occurs when two like-nucleons couple with opposite spin.

another band) [eis87]. A decrease in energy with increasing spin occurs at a band crossing. Backbending is the term used for this phenomenon. It describes the crossing of the paired ground-state band with a band [11] built on a state formed by the breaking and alignment of a pair of high-j nucleons [jai92]. There are a few related plots that can reveal the cross over point: 1) the moment of inertia versus the squared rotational frequency and 2) the aligned angular momentum versus the rotational frequency. 3) the spin versus the rotational frequency [12] The first plot is used for bands that have crossings that are not obvious by inspection of the transition energies. A few of these plots for the yrast band in ^{158}Er [dia84] are shown in Figure 9.10. The second plot shows two bandcrossings; one starting at 8^+, the other at 24^+. The difference between the extrapolated dashed lines represents the gain in the aligned spin that occured at each bandcrossing. This aligned spin is plotted in the lower part of the figure for each crossing.

Coupled States

Transitions in the deformed nucleus can be due to 1) the uncoupling of proton or neutron pairs and their alignment along the axis of rotation; 2) the coupling of quasi-particle orbitals; 3) the promotion of one particle to another orbital; 4) the breaking of proton or neutron pairs and their recoupling within the same orbital with different angular momentum [hil86, kra88]. Breaking a pair of nucleons would require between 1 and 2 MeV of energy [13]. Therefore, the states would appear at or higher than this

[11] Often referred to as the S band.

[12] Rotational frequency, ω usually refers to one half of the transition energy in MeV. This is derived from the expression [wil86]:

$$\omega(I) = \frac{dE(I)}{dI} = \frac{E(I+1) - E(I-1)}{(I+1) - (I-1)} = \frac{E_\gamma}{2} \tag{9.12}$$

[13] This is referred to as the pairing gap, 2Δ, where $\Delta = 0.8 - 1.2 MeV.$ is the pairing force. The energy depends on the level density of states within the particular nucleus.

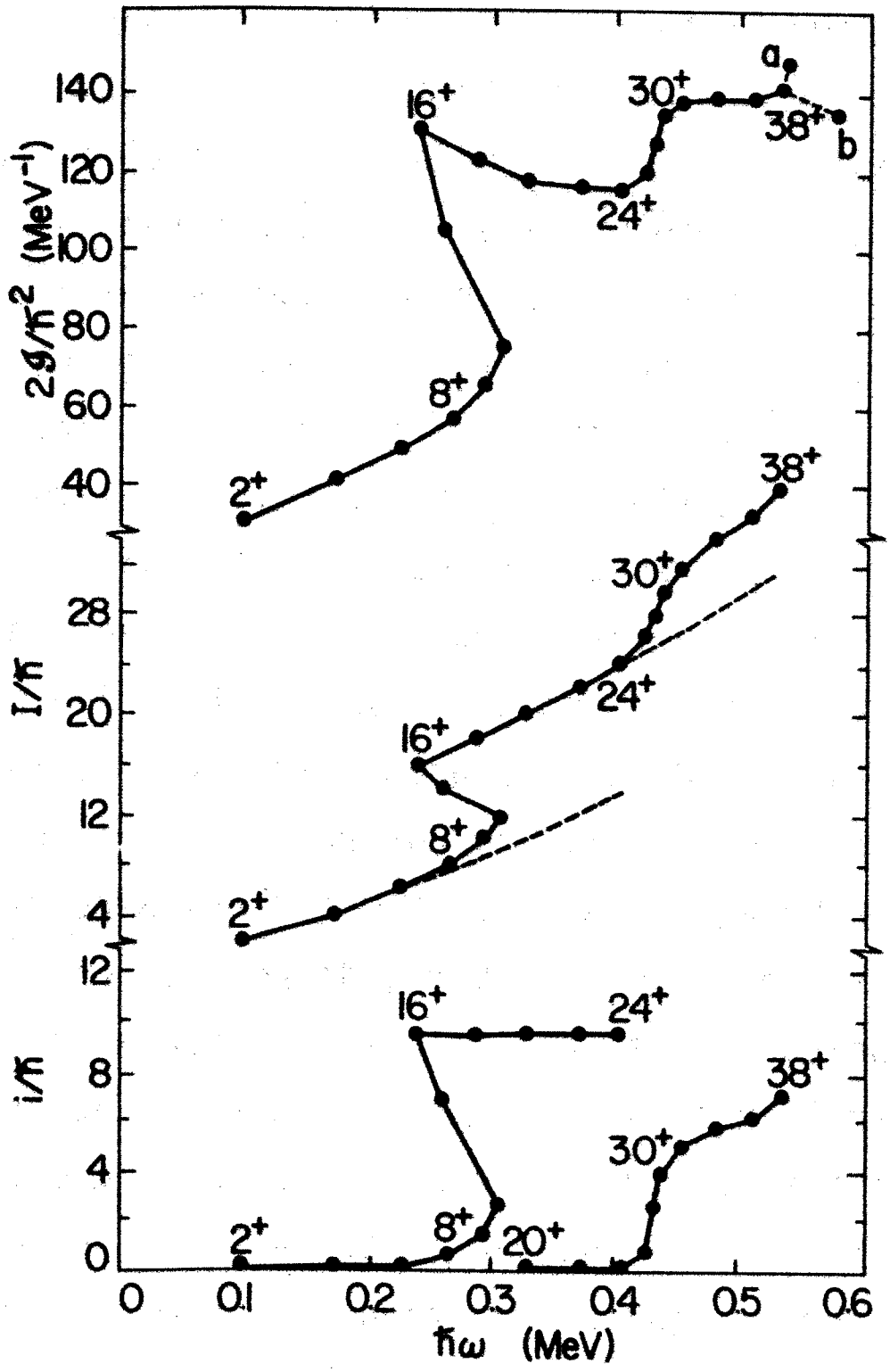

Figure 9.10: Examples of backbending plots for the yrast band in ^{158}Er using the moment of inertia, the total spin and the aligned spin versus the rotational frequency. From [dia84].

energy in an energy level diagram [kra88, hey94]. The coupling between the resulting two odd particles then determines the spin and parity of the levels. In quantum mechanics, coupling angular momenta of j_1 and j_2 results in values from the sum (j_1+j_2) to (j_1-j_2) in integer steps.

In order to interpret complex spectra within an energy level scheme, the states must be described as combinations instead of pure shell model states [kra88]. For example:

$$\psi(2^+) = a\psi(\nu h_{\frac{11}{2}} \otimes h_{\frac{11}{2}}) + b\psi(\nu d_{\frac{3}{2}} \otimes d_{\frac{3}{2}}) + c\psi(\nu d_{\frac{3}{2}} \otimes s_{\frac{1}{2}}) + \cdots$$

Where, a, b, c represent the expansion coefficients of the wave function, the symbol $\otimes$ means angular momentum coupling, and ν refers to neutron orbital (π would refer to a proton orbital). For a coupling of quasiparticles in an odd-odd system, orbital designations such as $(\nu h_{\frac{11}{2}} \otimes \pi h_{\frac{11}{2}})$ may be observed.

Quasiparticle States

For nuclei near or at closed shells, the fermi level is a diffuse ground state, above which there are no particles [hey94]. When many particles are present outside closed shells, the scattering of pairs leads to a stable probability distribution for the occupancy of single-particle orbitals. The pairing correlations lead to a major modification in the nuclear ground state distribution. (See Figure 9.11a, b.) Particles in this type of distribution may be considered to be part particle and part hole because around the fermi level particles oscillate between the patterned (particle) and nonpatterned (hole) areas. Because of this, they are referred to as quasiparticles.

Blocking

The presence of an odd particle at the fermi level leads to the blocking of certain orbital excitations because the pairing interaction has effectively been removed. (See

Figure 9.11c.)

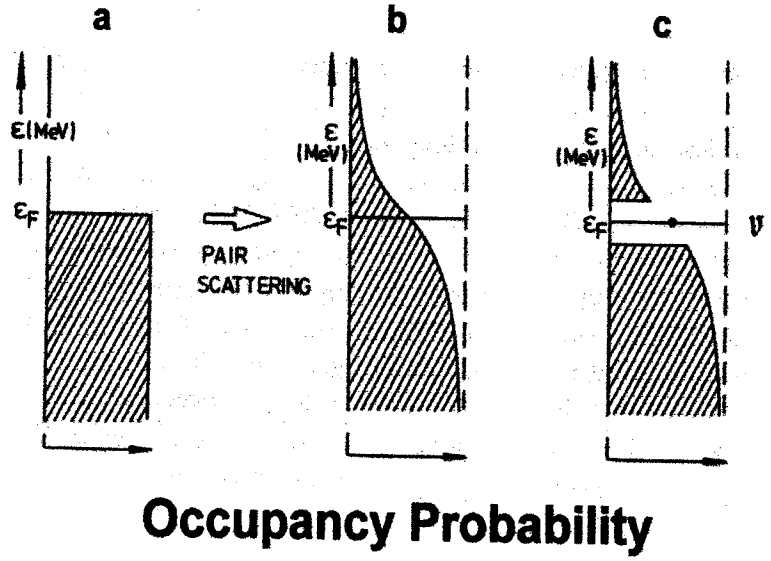

Figure 9.11: a) Schematic depiction of nucleons in a closed shell occupying all levels up to the fermi level. b) A depiction of a smeared pair distribution around the fermi level. c) Blocking of the pairing force with the addition of an odd particle at the fermi level. Adapted from [hey94].

9.3 Energy Level Diagrams

Understanding the theory of rotational bands and analyzing the data lead to the construction of an energy level diagram for a particular nucleus:

• Obtain the ground state and parity of the nucleus. Use the Nordheim coupling rules if the nucleus is odd-odd.

• To determine the potential orbital configuration for each band, look at the Nilsson diagram and using the proper deformation value, find the last proton or neutron that matches the ground state spin and parity. ex.,[hil88] For ^{133}Pr, Z=59, and $\epsilon \approx 0.2$. Therefore, the choices of Nilsson orbitals are : $\frac{3}{2}^+[411]$, $\frac{5}{2}^+[413]$, or $\frac{3}{2}^-[541]$ (intruder). The second is the obvious choice for a nucleus with a $\frac{5}{2}^+$ ground state based on a $g_{\frac{7}{2}}$ proton.[14]

[14]The assignments for the yrast and/or ground state bands are often chosen based on systematics or comparisons with the neighboring nuclei. This habit can lead to oversights and misassignments

• Order the experimentally determined γ rays by their coincidence relationships and their intensities.

• Using angular distribution data and experimentally determined conversion coefficients from conversion electrons acquired in coincidence with the γ rays, obtain the spin and parity of the levels.

• Estimate the lifetimes of the states from the γ-γ-t measurements. [15]

9.3.1 Cranked Shell Model

Routhian

The Hamiltonian describes a nucleus in a static potential near the ground state. In order to analyze a nucleus in a deformed rotating field, the Routhian $\mathcal{H}'$ must be used instead of the Hamiltonian $\mathcal{H}$ of the system [ben79].

$$\mathcal{H}'_{qp} = \mathcal{H}'_{sp} - \Delta(P^+ + P) - \lambda\hat{N} \tag{9.13}$$

where the single particle Routhian incorporates a deformed Woods-Saxon potential and is defined:

$$\mathcal{H}'_{sp} = \mathcal{H}_{sp}(\epsilon) - \omega J_x \tag{9.14}$$

The Routhian[16] can be described as the Hamiltonian in a frame of reference rotating with an angular frequency, ω about the x-axis. J_x is the single particle angular momentum, ϵ represents a set of deformation parameters. P^+ is the creation operator for the pair field, the strength of which is determined by the pairing gap parameter, δ. The chemical potential, λ determines the expectation value of the particle number, $\hat{N}$.

---

of spin and parity [liu96].

[15] These can be determined more accurately using a Doppler Shifted Attenuation Measurement (DSAM) experiment.

[16] A modified Hartree-Fock-Boguljubov (HFB) theoretical analysis is used.

The eigenfunctions of the Routhian are configurations of independent quasiparticles. The lowest eigenstate corresponds to an yrast state and the sequence of these states obtained by enlarging ω constitutes the yrast line. From this Routhian, we can calculate 1) excitation energies of quasiparticle configurations with respect to a reference configuration (usually the even-even core nucleus); 2) aligned angular momentum; and 3) total Routhian surfaces (TRS), also known as potential energy surfaces.

Aligned Spin

The rotational alignment, I_x is an important parameter used to characterize a rotational band. It is the projection of the total angular momentum, I, along the rotational axis. [ben79, cho89]

$$I_x(I_m) = \left[(I_m + \frac{1}{2})^2 - K^2\right]^{1/2} \tag{9.15}$$

I_m is the average value of the two spins (i.e., $I + 2 \rightarrow I$) in the transition.

Another method to determine I_x involves the Harris formula [har65]:

$$i_x = I_x(\omega) - (J_0 + J_1\omega^2)\omega \tag{9.16}$$

The nuclear collective motion is characterized by the inertial parameters, J_0 and J_1, which are derived from linear regression analysis of the data points. The alignment or aligned spin, i_x is the projection of the angular momentum j along the rotational axis. A sharp increase in i_x accompanies backbending; this can be seen in the last plot in Figure 9.10. This method is often used to obtain the bandcrossing frequency.

PE Surfaces

In Figure 9.12 a schematic representation is drawn for potential versus β, the quadrupole deformation, for various regions of valence particles [kra88]. This is a simplistic, cross-sectional view of the $\beta - \gamma$ polar plot shown in Figure 2.3. Closed shell nuclei would

show potential energy in a symmetrical, parabolic function about the origin. This is region I. As deformation increases, the parabola becomes wider until the function becomes negative and takes on a distorted appearance at high β values. Prolate deformed nuclei show a second minimum potential energy well in this region III.

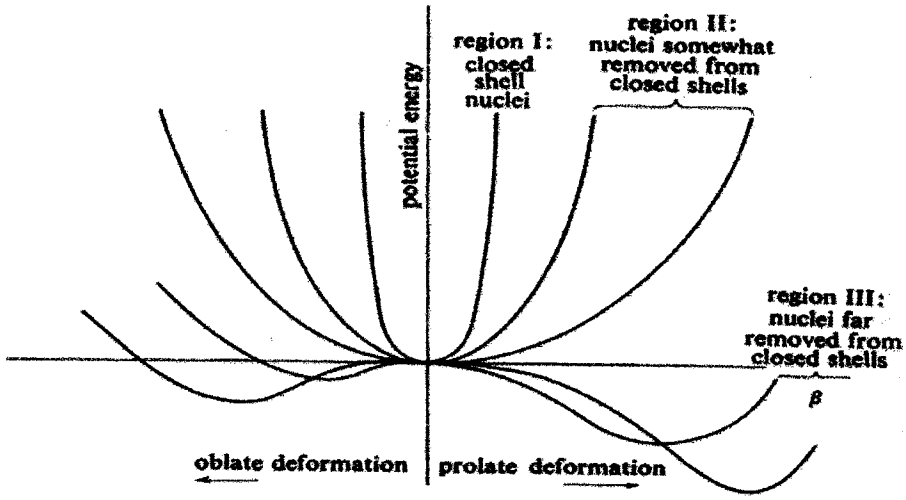

Figure 9.12: A schematic Potential Energy versus β deformation plot showing an approximate view of a 1-D PE surface for various regions of valence particles. Deformed nuclei are expected to be in region III [kra88].

The TRS plots provided by the Cranked Shell model calculations are potentially useful in predicting a second minimum in the potential energy surface that has been associated with superdeformation. As an example, in the Kr isotopes in Figure 9.13, the nuclei change from a spherical to a deformed structure. Two of these isotopes are shown. The transition of the deformed isomer as the ground state configuration can gradually be followed through the isotopes [eis87]. For a given γ angle, one can observe how the potential changes with β, which has the same linear scale along any given γ line. The translation between potential energy contour plots and 1-D PE curves is the following: Cross-sectional cuts through the PE surface at two different γ angles are plotted as a function of β. The collective prolate configurations are found along the $\gamma = 0$o line and collective oblate structures are found along the $\gamma = 60$o

line. The ^{76}Kr isotope shows spherical and prolate deformed configurations while ^{78}Kr has a slightly less prolate deformed structure plus a triaxial configuration.

9.4 Superdeformed Bands

The concept of superdeformation came about when Polikanov and co-workers [pol62] discovered that the half-lives of some spontaneously-fissioning actinide isomers were orders of magnitude lower than expected. Later it was explained that these isomers have a second minimum in the potential energy surface. They are prolate shape nuclei with a major to minor axis ratio of nearly 2 to 1 (β=.5).

Researchers felt that if SD were present in nuclei below the fission limit it might originate with high spins in a region where the energy level density is considered to be too high to be able to resolve discrete peaks. So they tried to measure nuclear properties averaged over many states in this continuum region. A method based on the moments of inertia was devised to find SD bands [and79] that could be attributed to this second PE minimum well region. There are two definitions for the moment of inertia that are of interest here, the kinematic and the dynamical. Kinematic describes the alignment of orbital angular momentum of individual particles and dynamical refers to collective rotation [shi90].

The kinematic moment of inertia can be described as the first derivative of the energy with respect to spin. [shi90, dia84]

$$\frac{\Im^{(1)}}{\hbar^2} = I\left(\frac{dE}{dI}\right)^{-1} = \frac{I}{\hbar\omega} \tag{9.17}$$

The dynamic moment of inertia is the second derivative of the energy with respect to spin.

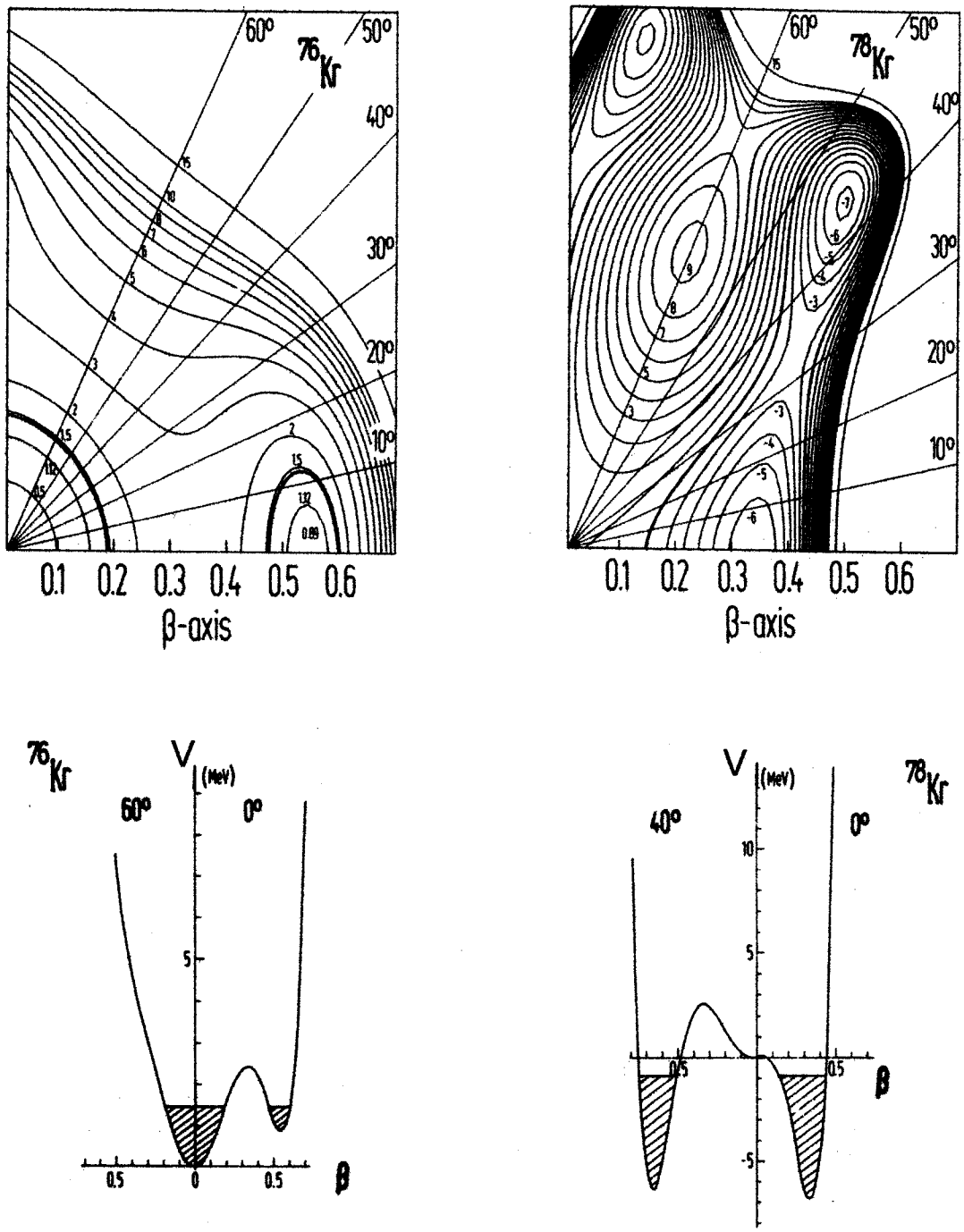

Figure 9.13: An example from ^{76}Kr and ^{78}Kr of the way potential energy contour plots translate to 1-D PE curves. β cuts at two different γ angles are plotted along the horizontal showing their corresponding minima in the potential energy. [eis87].

It can be obtained from the first derivative.

$$\frac{\Im^{(2)}}{\hbar^2} = \left(\frac{d^2E}{dI^2}\right)^{-1} = \frac{dI}{\hbar d\omega} \tag{9.18}$$

Researchers noticed in a $E_{\gamma 1}$ versus $E_{\gamma 2}$ correlation matrix that interesting patterns appeared along the diagonal where no γ-ray counts should exist[17]. The pattern appears to be a series of ridges parallel with the positive diagonal and they felt that this might be due to a superdeformed band. This is displayed in Figure 9.14a, a correlation matrix for ^{152}Dy. The vertical and horizontal stripes are due to the discrete peaks below spin 40. Ridges can be seen along the positive diagonal. In order to separate the ridges from the discrete peaks, another matrix is created from the first: $\Delta E_\gamma = |E_{\gamma 1} - E_{\gamma 2}|$ is plotted versus $E_\gamma = (E_{\gamma 1} + E_{\gamma 2})/2$. When cuts are made along and parallel with the negative diagonal of this matrix, the width between the ridges can be measured. Figure 9.14b is an example of this for the ^{135}Nd nucleus. The arrows indicate the position of the ridges [bec87]. The width of the valley along the diagonal between ridges can be determined by the difference in γ-ray energies and is related to the dynamical moment of inertia [cho89, nya84]:

$$Width = 2\Delta E = 8(d^2E_\gamma/dI^2) = 8(d\omega/dI) = 8\hbar^2/\Im^{(2)}_{band} \tag{9.19}$$

From this, the dynamic moment of inertia $\Im^{(2)}_{band}$ for a SD band in ^{135}Nd was estimated to be $59\hbar^2 MeV^{-1}$. Other nuclei, such as ^{152}Dy showed $\Im^{(2)}_{band}$ with values greater than $80\hbar^2 MeV^{-1}$ [nya84]. This corresponds to a quadrupole deformation of $\beta \approx .5$ which matches a deformation of a prolate shaped rotor with a 2:1 axis ratio. This is what the researchers had hoped to find to confirm their theory that the ridges in the correlation matrix were due to superdeformation. The lower value found for ^{135}Nd showed a less extremely deformed nucleus with an axis ratio of 3:2 (β= .35-.4). Hence, this was declared to be a new region of superdeformation around A=130.

[17]The positive diagonal in the correlation matrix is the place where $E_{\gamma 1}$=$E_{\gamma 2}$ and in theory no two γ rays should exist with the same energy.

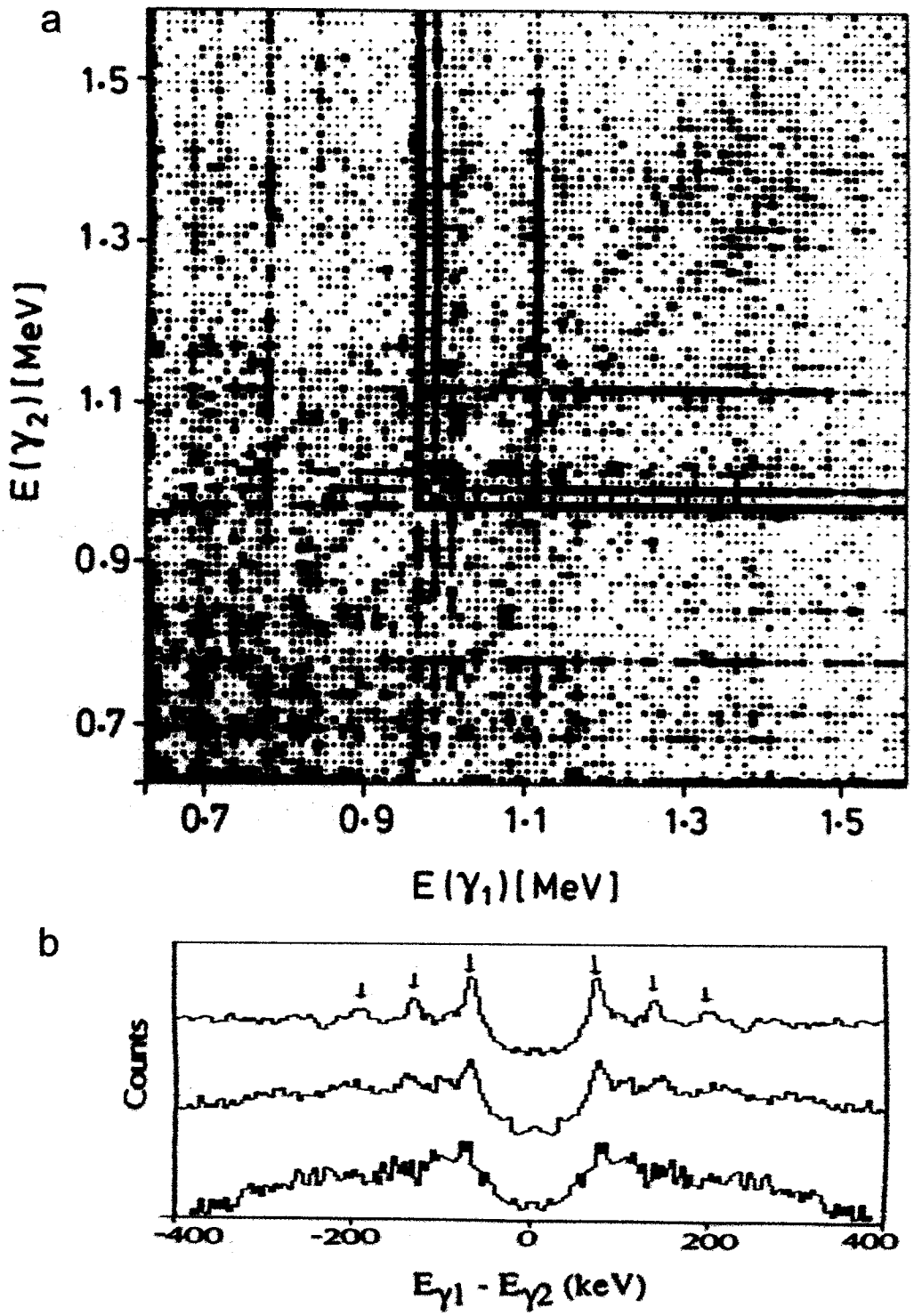

Figure 9.14: a) Correlation spectrum for ^{152}Dy. The ridges parallel and close to the $E_{\gamma 1}$=$E_{\gamma 2}$ diagonal for energies between 0.80 and 1.35 MeV. are taken to represent an SD band [nya84]. b) Three cuts perpendicular to the $E_{\gamma 1}$=$E_{\gamma 2}$ diagonal in a correlation spectrum for ^{135}Nd. The arrows indicate where the ridges are located [bec87].

And, it was in this region that the first discrete SD peaks were observed for ^{132}Ce [nol85]. From the positions of the ridges, gates were made on the original correlation matrix and summed together. This produced a set of peaks that resembled a ridgid rotational band with the exceptions that the intensities of the transitions were nearly the same, the spacings between peaks were very regular and they did not follow the normal, gating-coincidence relationships (i.e., a gate on one member of the band did not produce peaks at the positions of the other members). In 1989, the first set of multiple SD bands were declared for ^{153}Dy [joh89]. This is shown in the three bands in Figure 9.15. The correlation method did not always indicate where the SD peaks were located because the high intensity of the discrete peaks often obliterated the signal from the ridge patterns[18] . Therefore, methods were devised to search the correlation matrix for peaks that existed in regular patterns. The correlation matrix moved into another dimension with the event data being sorted into an $E_{\gamma 1}$ versus $E_{\gamma 2}$ versus $E_{\gamma 3}$ array to make the analysis more nucleus specific. This is described in Chapter 7.

Since this early research, superdeformed rotational bands (SD) have been declared to have the properties of deformed prolate rotors (β= .35 –.5) and appear to originate at high spin from quasiparticle alignments in highly deformed intruder orbitals such as the $i_{13/2}$ neutron orbital. Many bands have been published [sin96] since the inception of this research. A large number of them are referred to as 'identical' bands because the same band appears in neighboring nuclei, many of which originated with the same nuclear reaction.

Many N=73 isotones in the A=130 mass region have been reported to exhibit deformation, so the ^{132}Pr nucleus is a good candidate for this study.

[18]SD bands have been observed to be between 0.1 and 1% of the total intensity.

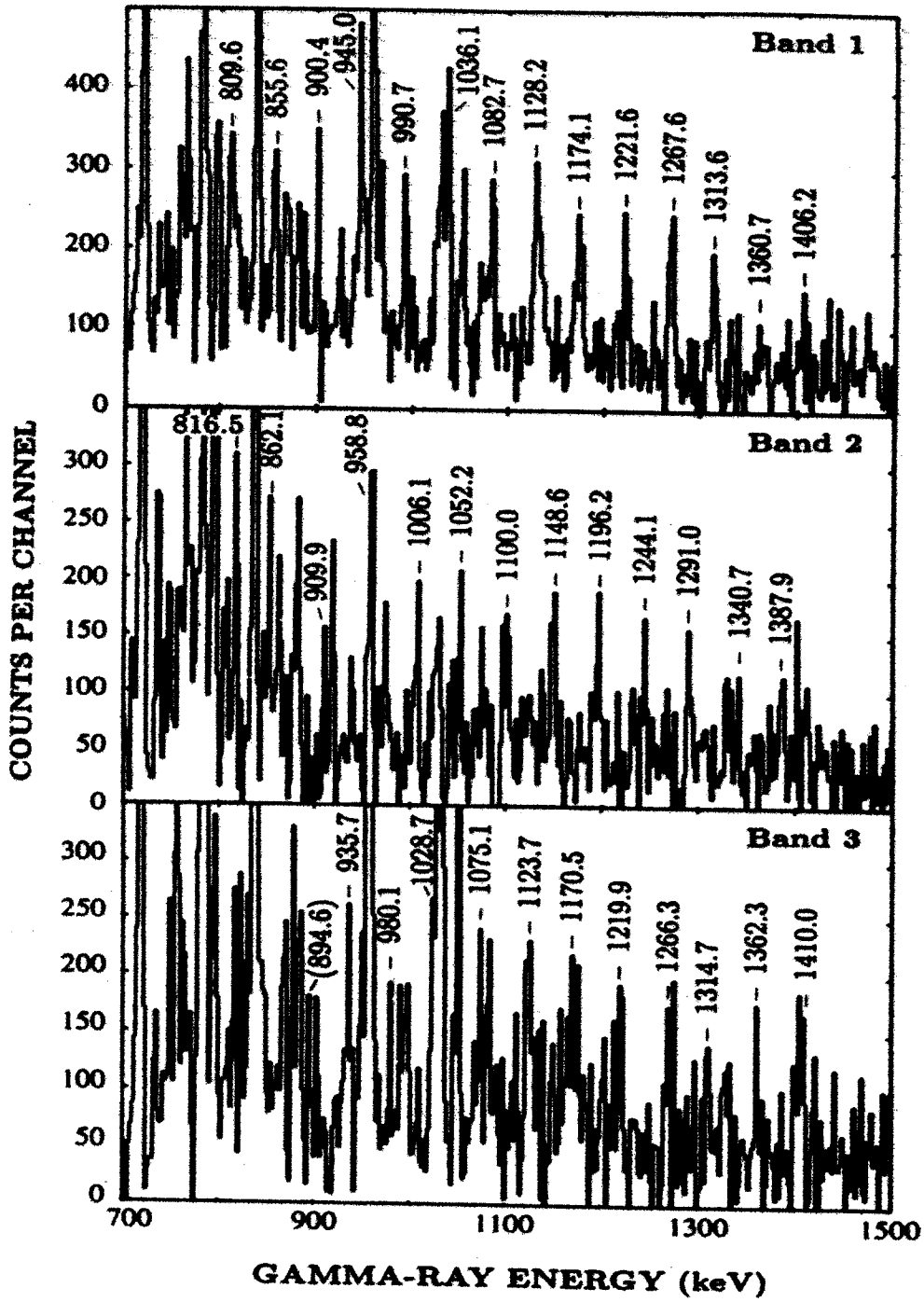

Figure 9.15: Summed, gated spectra for three SD bands in ^{153}Dy [joh89].

Chapter 10

Results

In this chapter, we describe the rotational band results for ^{132}Pr and ^{133}Pr and we propose specific structures for semi-identical bands in the ^{132}Pr nuclide based on either cranked shell model (CSM) calculations using a Woods-Saxon potential[naz85] or on systematics of occupied orbitals observed in neighboring nuclides.

10.1 Introduction

Superdeformation has been observed in several regions of the chart of nuclides. (for a recent compilation, see [sin96]). These areas tend to encompass nuclides that exist with significant static ground-state deformations. See Figure 9.3. One of the regions of recent study is the nuclides around A=130. Several groups have characterized a number of nuclides in this region, observing both highly deformed regular bands and SD bands (see, for example [hau94, pau87]).

Identical Bands (IB) are defined to be those which differ from a selected reference band structure by less than a few percent in terms of either absolute energies of their transitions or the dynamic moments of inertia for corresponding transitions. In either case, the rotational structure may be dependent on core effects with minimal contributions of the unpaired particles to observable features. The unpaired particle interactions that must exist can be postulated to balance or compensate any core

driving effects or be of negligible magnitudes.

SD bands are logical candidates for identical behavior. The uncoupled particles that form the structure are necessarily, by virtue of the high deformation, not strongly interacting with the core structure. It should be usual, then, to see more than one band structure which is identical to either a common core structure or another rotational band within these superdeformed nuclides.

Odd-odd nuclides have the advantage of being close to both superdeformation and identical behavior in that they start out with two particles that are not paired to core interactions. The particles in highly deformed nuclides cannot, without creating a driving effect toward a spherical nucleus, occupy a strongly-coupled orbital. Their existence in highly deformed and necessarily minimally interacting systems provides an origin from which to create these highly deformed (SD) and (IB) bands.

Searches for highly deformed rotational structures in the mass A$\sim$130 region have been extensive [god89, fir94]. Recently, Hauschild, *et al.* reported SD bands in ^{134}Pr[hau94] and triaxial bands in ^{133}Ce [hau95]. These examples demonstrate the range of rotational structures that occur in this mid-proton and mid-neutron shell region. While the cores of these nuclei are intrinsically γ–soft [1] [wys88], the occupation of one or more high–j quasi–particle orbital usually drives the nucleus to a stable deformed structure. However, the deformation driving effects of protons occupying the lower end of the Z=50 to Z=82 shell are often in competition with the effects of the neutron contributions at the higher end of the N=50 to N=82 shell. ^{132}Pr, with 9 protons from the Z=50 shell closure and 9 neutron holes from the N=82 shell closure, is an excellent example of this situation and thus a good candidate for investigating these competing effects.

Shi, *et al.* studied the rotational structure of ^{132}Pr and reported the observation

[1] γ–soft is a term used to describe a nucleus with a relatively flat potential-energy surface with respect to the triaxiality parameter, γ [pau90].

of three bands[shi88], two prolate and one β–soft with triaxial character stabilized at $\gamma \simeq -10$. Our investigation has extended the previously observed bands to higher spins (§10.2) and also characterized four new bands (§10.3).

We have attempted to assign plausible particle configurations to these bands by means of Cranked Shell Model and Total Routhian Surface calculations. While these models do not provide information about the structures which is specific enough for positive identification, they do, in some instances, eliminate possible structures.

10.2 ^{132}Pr Rotational Bands

Using the reaction ^{100}Mo(^{37}Cl (160MeV), 5n γ)^{132}Pr, rotational band transition energies have been deduced from singly- and multiply-gated spectra. The simple gates were selected from a 2×2 $E_{\gamma 1}$ vs. $E_{\gamma 2}$ data array. In order to generate the multiple gates, events in coincidence with the γ-ray spectra from four major transitions (116, 130, 178, 283 keV) were scanned into a 2-D array; then selected energy gates were summed to represent the band (§5). Each band represents a sum of transitions in ^{132}Pr that have been noise filtered using the FFT technique (§6), background subtracted and baselined.

The coincidence spectra for the odd-odd ^{132}Pr nucleus, in general, confirm the three bands observed in a previous (lower spin) study [shi88] using the reaction, ^{117}Sn(^{19}F (87MeV), 4n γ)^{132}Pr . We have observed a few differences. We have seen additional energy transitions that extend the rotational band, decay scheme to higher spin states. The 193 keV. linking transition between bands 1 and 2 that was listed in the previous reaction was not found in our data. Our higher spin reaction produced a band 3 that is much higher in intensity than reported, plus we have extended it by five transitions. The relative ratios in the $\Delta I = 2$ sidebands in bands 1 and 2 to the $\Delta I = 1$ transitions are much lower in our data compared with Shi's. We have

found a low energy transition (62 keV.) not seen before, that is in coincidence with the 283 keV. transition. Its placement within the level scheme is not known exactly. Adjustment for conversion coefficients indicates that it is of significant intensity. It is also in coincidence with a 58 keV peak.

10.2.1 Energy Level Diagrams

In ^{132}Pr the proton Fermi level is at the lower midshell – 9 protons above the closed shell at 50. The neutrons are in the upper part of the shell – 23 above the closed shell. This may also be viewed as 9 hole-particles away from the next closed shell at 82.

In an odd-odd nucleus, two quasiparticle states are formed by coupling the odd proton and odd neutron to a deformed even-even core. According to the Gallagher Moszkowski coupling rule [gal58] there would be two combinations formed: $K = |\Omega_p - \Omega_n|$. However, depending on deformation, the K values may or may not be a valid quantum number. Valence quasiparticles play a role in determining deformation properties. The shape driving effects of the valence proton and neutron are opposite; the protons drive the nucleus toward $\gamma = 0$ –a prolate shape and the neutrons drive the nucleus toward a $\gamma \approx -60°$, oblate shape [shi88]. For reference the energy level diagram is shown in Figure 10.1.

10.2.2 Band Based on $\pi h_{11/2} \otimes \nu g_{7/2}$

According to Shi and co-workers [shi88] the spin and parity of band 1 is 7^- and the ground state can be determined from systematics from ^{131}Ce. The odd proton is in the $h_{\frac{11}{2}}\ \frac{3}{2}^-[541]$ Nilsson orbital and the odd neutron is in the $g_{\frac{7}{2}}\ \frac{7}{2}^+[404]$ orbital. This yrast band is generally thought to be the $K = 2$ band and can be described with the $\pi h_{11/2} \otimes \nu g_{7/2}$ configuration.

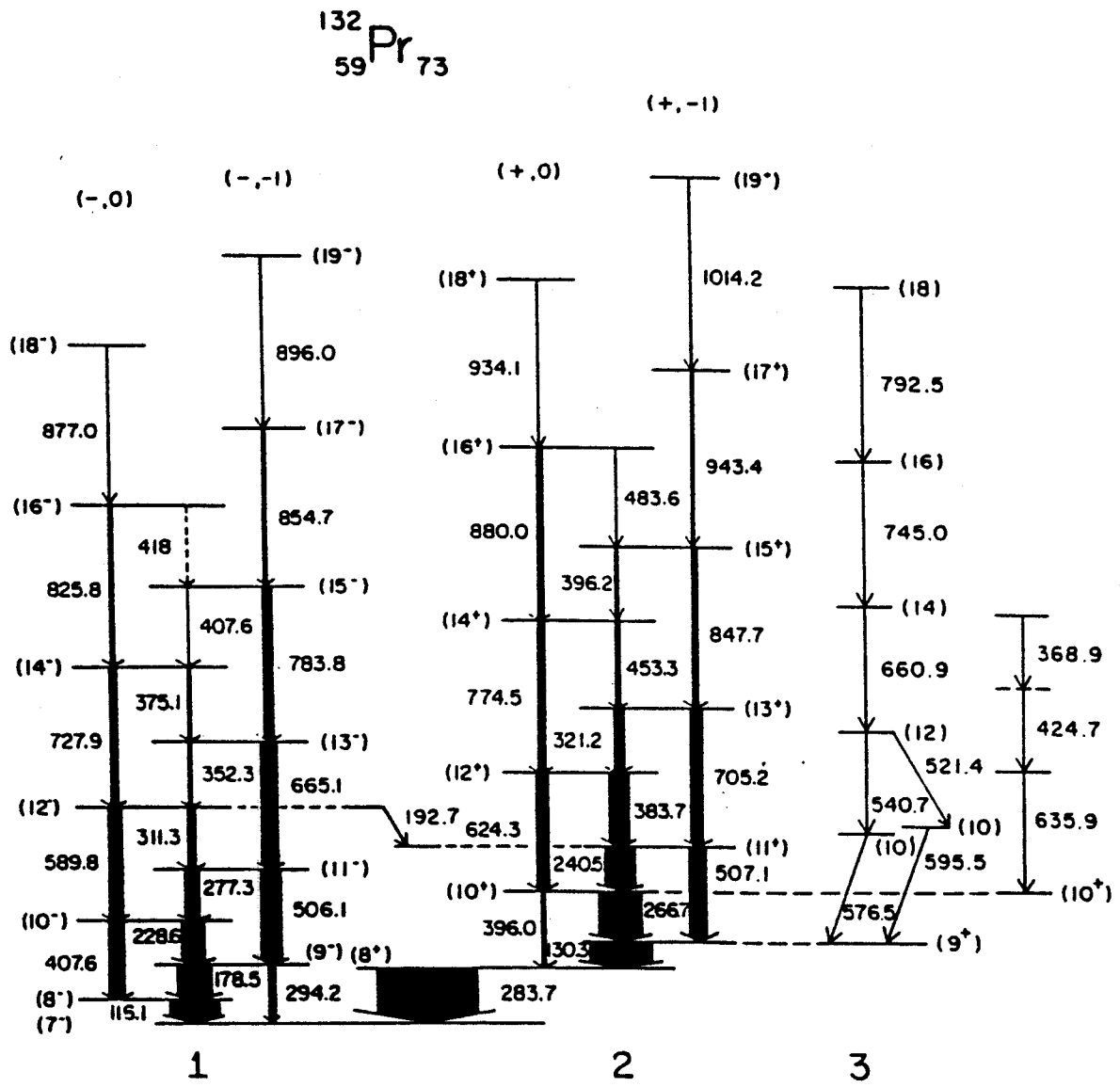

Figure 10.1: Nuclear energy level diagram for the γ ray cascade in ^{132}Pr. From [shi88].

10.2.3 Band Based on $\pi h_{11/2} \otimes \nu h_{11/2}$

The bandhead spin and parity of band 2 , the most intense of the 3 bands, is thought to be $I^{\pi} = 8^{+}$ [shi88]. The description of this band is based on the systematics of ^{130}La. It is believed that there is a perpendicular coupling of the spins of the low Ω $h_{\frac{11}{2}}$ proton and high Ω $h_{\frac{11}{2}}$ neutron. The odd proton is in the $h_{\frac{11}{2}}$ $\frac{3}{2}^{-}[541]$ orbital and the odd neutron is in either the $h_{\frac{11}{2}}$ $\frac{7}{2}^{-}[523]$ orbital or the $\frac{9}{2}^{-}[514]$ orbital. Since the odd neutron is in a high Ω orbital, a small $\Delta I = 1$ signature splitting is produced. This is evident in the M1 cascade.

10.2.4 Structure based on $\pi h_{11/2} \otimes \nu i_{13/2}$

This band 3 can be described as originating with a neutron in an intruder orbital, $i_{\frac{13}{2}}$ $\frac{1}{2}^{+}[660]$ from two major shells up that couples with the $h_{11/2}$ proton. Since both neutron and proton are in low Ω orbitals, a maximally signature-split band is created. This is referred to as a doubly decoupled band. Usually only one of the signatures predominates.

We have seen five additional energy transitions, extending the decay scheme. Figure 10.4 shows the spectrum from a 2-D Multiple gate.

In coincidence with this band 3, we see many transitions from band 1 and band 2. The band appears to feed into the $(14^{-} \rightarrow 12^{-})$ transition from band 1 and the $(17^{+} \rightarrow 15^{+})$ transition from band 2.

The width and the bimodal appearance of the peak centered at 1009 keV suggest that there are actually two transitions present, separated by about 2 keV. This indicates that backbending is occurring at this point. The sequence may be 913, 1011, 1008, 1114 keV. However, because of the presence of many low intensity peaks, there is the possibility that the backbend extends lower in energy, beyond the 1008 keV transition.

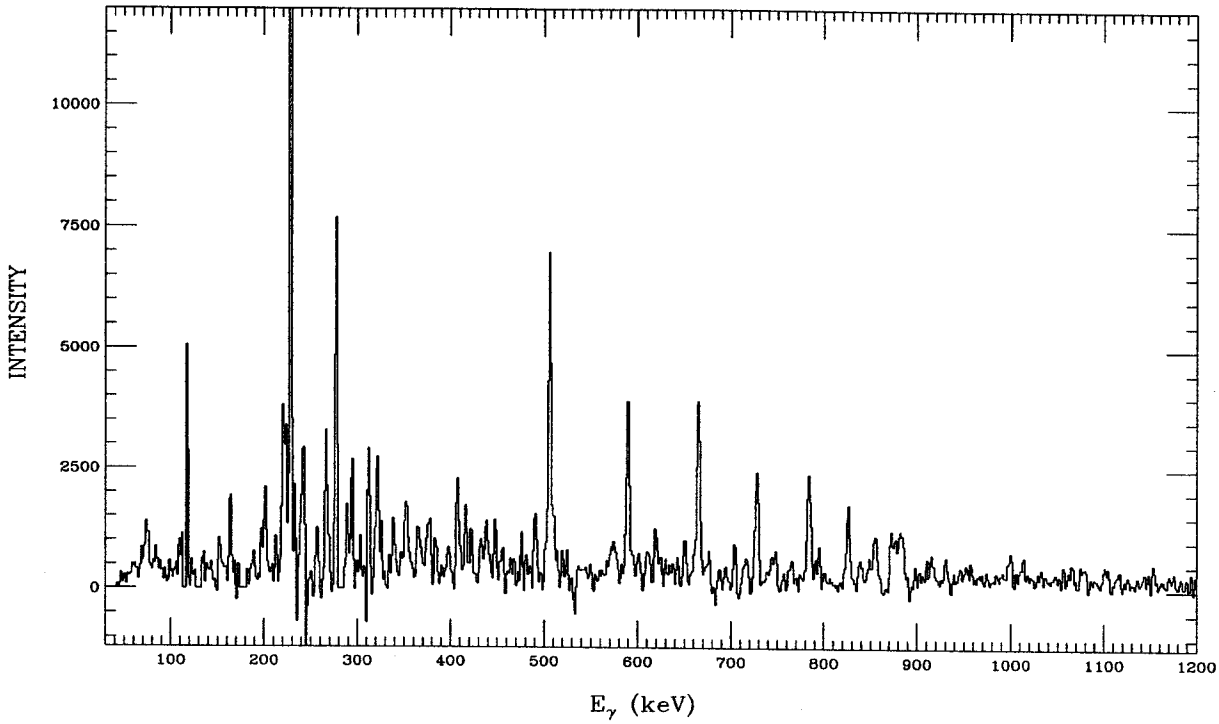

Figure 10.2: ^{132}Pr spectrum representing the yrast rotational band 1, from a 2-D multiple gate technique.

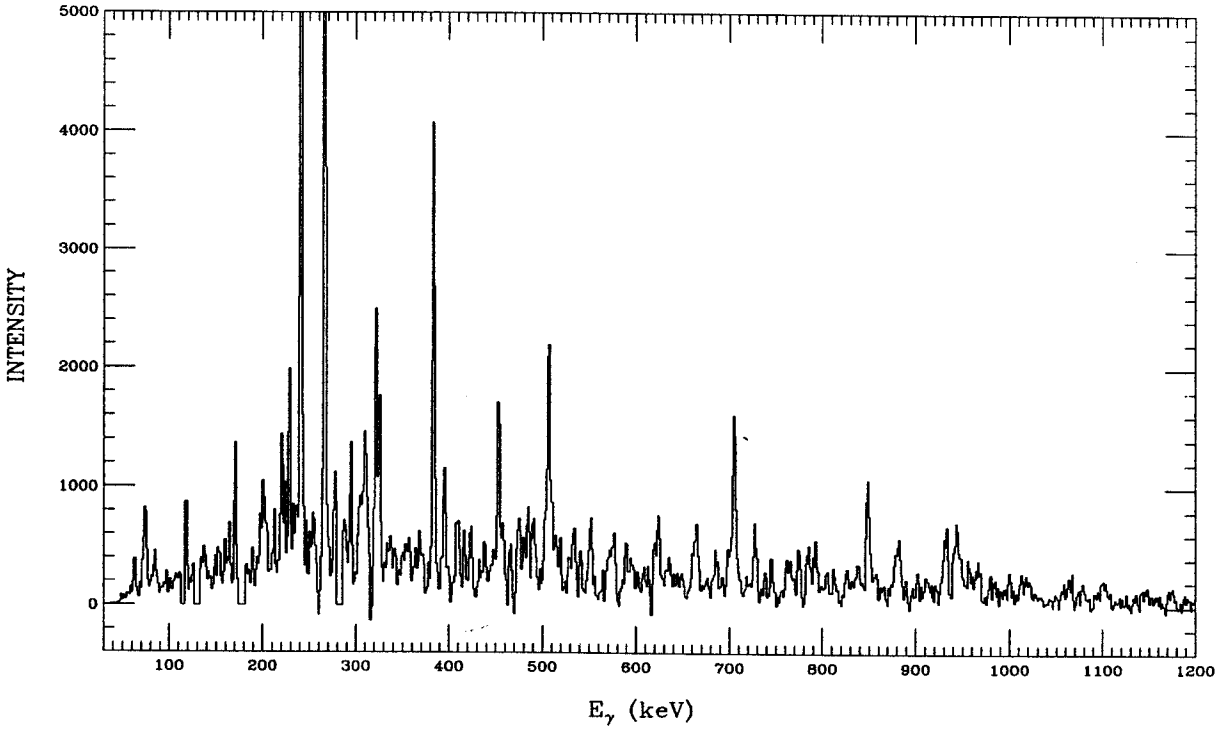

Figure 10.3: ^{132}Pr spectrum representing rotational band 2, from a 2-D multiple gate technique.

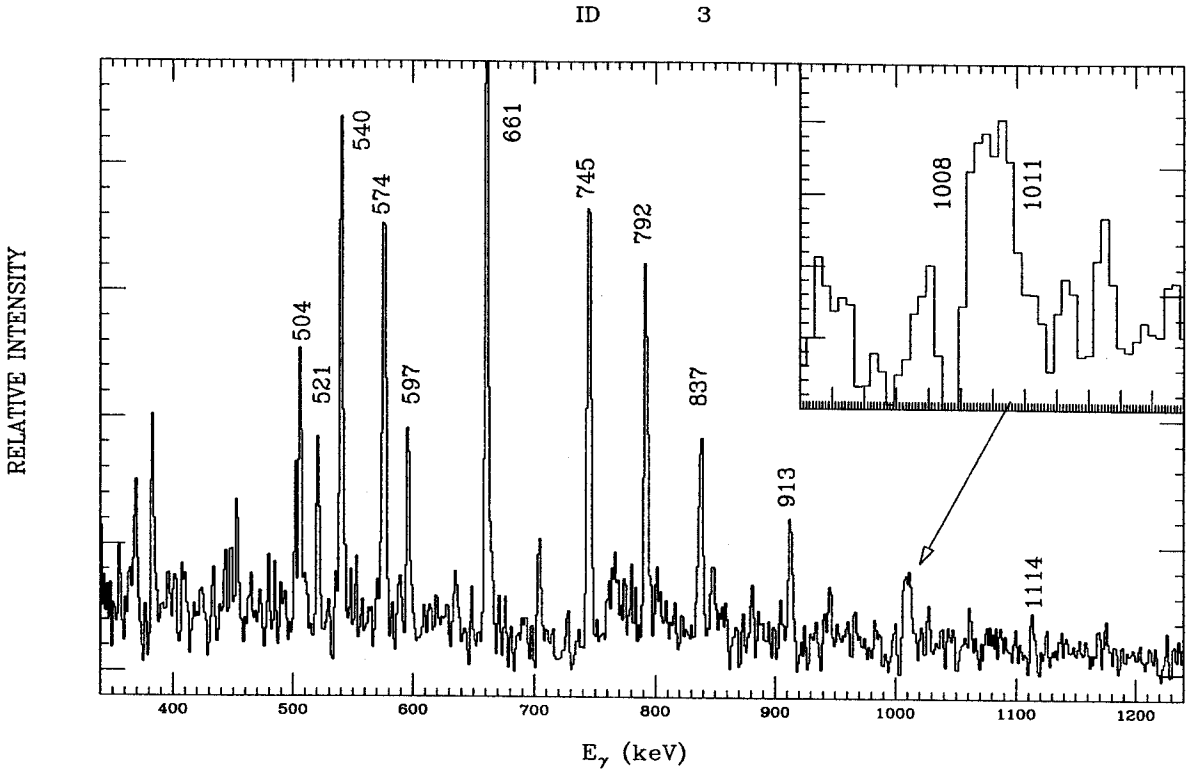

Figure 10.4: ^{132}Pr spectrum representing rotational band 3, from a 2-D multiple gate technique. The upper right hand corner contains an expanded view of the 1008 and 1011 keV peaks.

The initial part of the band appears to be a sequence of staggered transitions. If this is the case, then the band cannot be a doubly-decoupled band since this type of stair-step pattern in the transitions would indicate the presence of a signature splitting within the same band. This precludes a total decoupling wherein each signature forms a separate sequence.

10.2.5 Multiple peak region

In the energy region between 325 and 800 kev. many low intensity peaks ($\leq$ 10%) can be seen when gated spectra are summed together (Figure 10.5). There is the possibility that these are actually multiple, low intensity bands with closely related moments of inertia. SD bands of this nature have recently been discovered in the A-150 and A-190 regions [ste90, aza91] and have been attributed to quasiparticle pseudo-spin alignments. The potential for multiple SD peaks is evident and will be

discussed in the next section.

10.3 Four Highly Deformed Rotational Bands in ^{132}Pr.

Most of the transitions in ^{132}Pr under high spin conditions are below the 20% relative intensity level and there is a very evident fine structure below the 7% intensity level in the energy region between 325 and 800 keV.

Multiple peaks exist, separated by about 5 keV. This is displayed in Figure 10.5: Sum of the simple gates at 62, 130, 240, 115, 266, 283, 178 keV from the singly-gated $E_{\gamma 1}$ vs. $E_{\gamma 2}$ array for the ^{132}Pr nucleus. The inner figure is an expanded view of the region containing low-intensity multiple peaks. The 378 keV gate is marked. Since the possibility exists that these are actually multiple, low intensity bands with closely related moments of inertia from which SD transitions may arise, a double gating method was developed to better select the ^{132}Pr transitions. Triples events in coincidence with four major transitions in the ground band structure of ^{132}Pr (116, 130, 178, 283 keV) were scanned into a 2-D array; then selected energy gates were summed to represent each band. The gated spectra from this array were then processed with the FFT technique to yield the final spectrum. By gating on the 378 keV peak from the multiple peak region, many low-intensity peaks can be seen in coincidence. They might be described as four very low intensity bands. The peaks are regularly spaced with nearly identical intensities. This coincides with the description of a SD band for the neighboring odd-odd ^{130}La nucleus. Table 10.1 lists the bands from both nuclei. Tables 10.2 and 10.3 lists other SD bands reported in this mass region. Figure 10.6 shows the 378-keV gated spectrum from the 2D array containing all valid events in the experiment. The SD transitions are marked with symbols, other γ rays in ^{132}Pr are labeled with their transition energies.

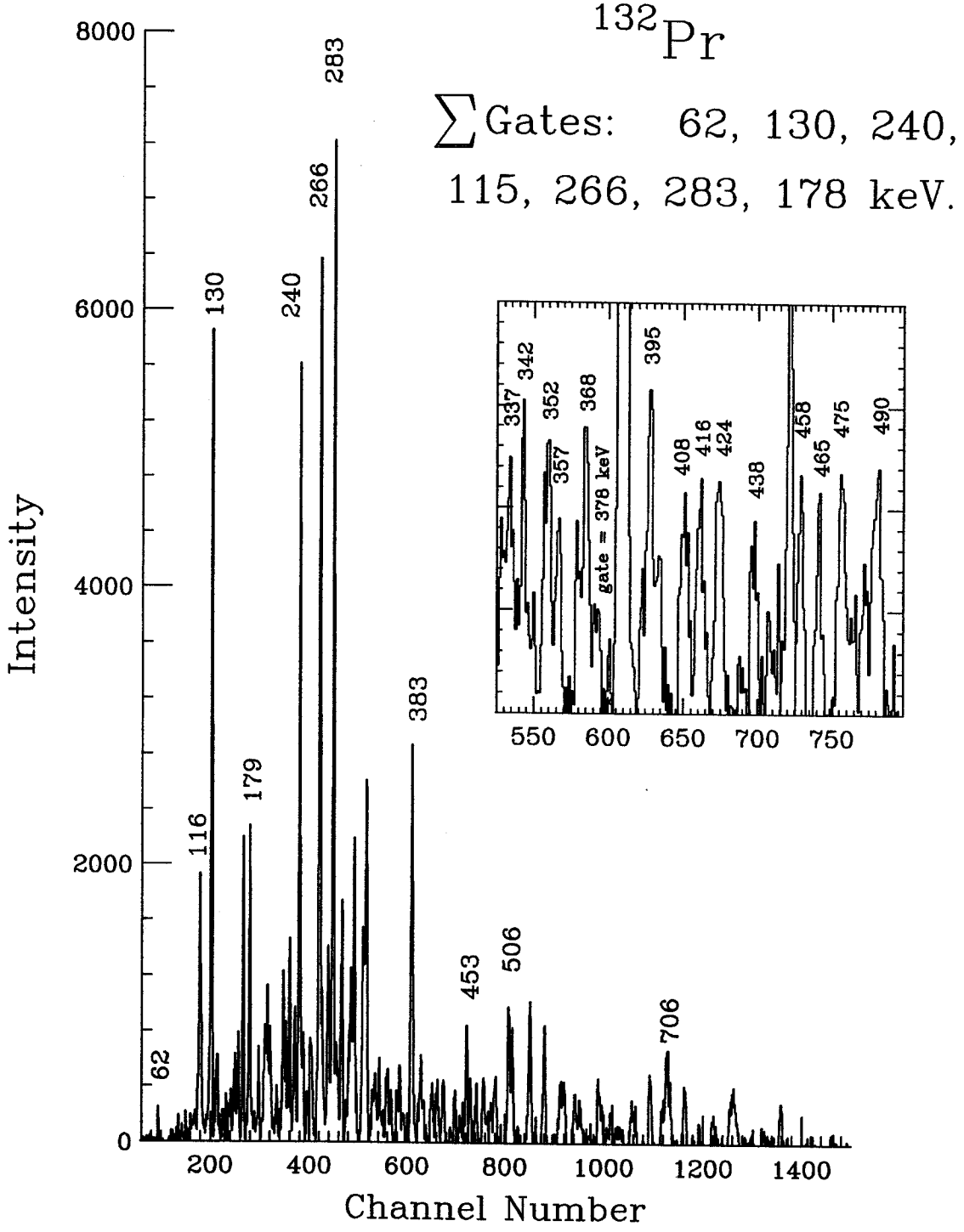

Figure 10.5: Sum of the simple gates at 62, 130, 240, 115, 266, 283, 178 keV for the ^{132}Pr nucleus. The inset is an expanded view of the region containing low-intensity multiple peaks from which the SD bands emerge. The 378 keV gate is marked.

Table 10.1: Comparison of SD bands in ^{130}La from [pau90] and ^{132}Pr from present study.

^{132}Pr E_γ	Δ	E_γ	Δ	E_γ	Δ	$E\gamma$	Δ	^{130}La E_γ	Δ
Band 1		Band 2		Band 3		Band 4		1412	
									93
								1319	
									90
								1229	
									81
1186								1148	
	87								75
1099		1083		1075		1025		1073	
	80		73		78		72		75
1019		1010		997		953		998	
	74		83		85		73		77
945		927		912		880		921	
	71		78		91		66		71
874		849		821		814		852	
	88		87		83		84		90
786		762		738		730		762	
	80		77		73		80		
706		685		665		650			
	88		87		76		79		
618		598		589		571			
	83		80		77		82		
535		518		512		489			
	91		100		77		82		
444		418		435		407			

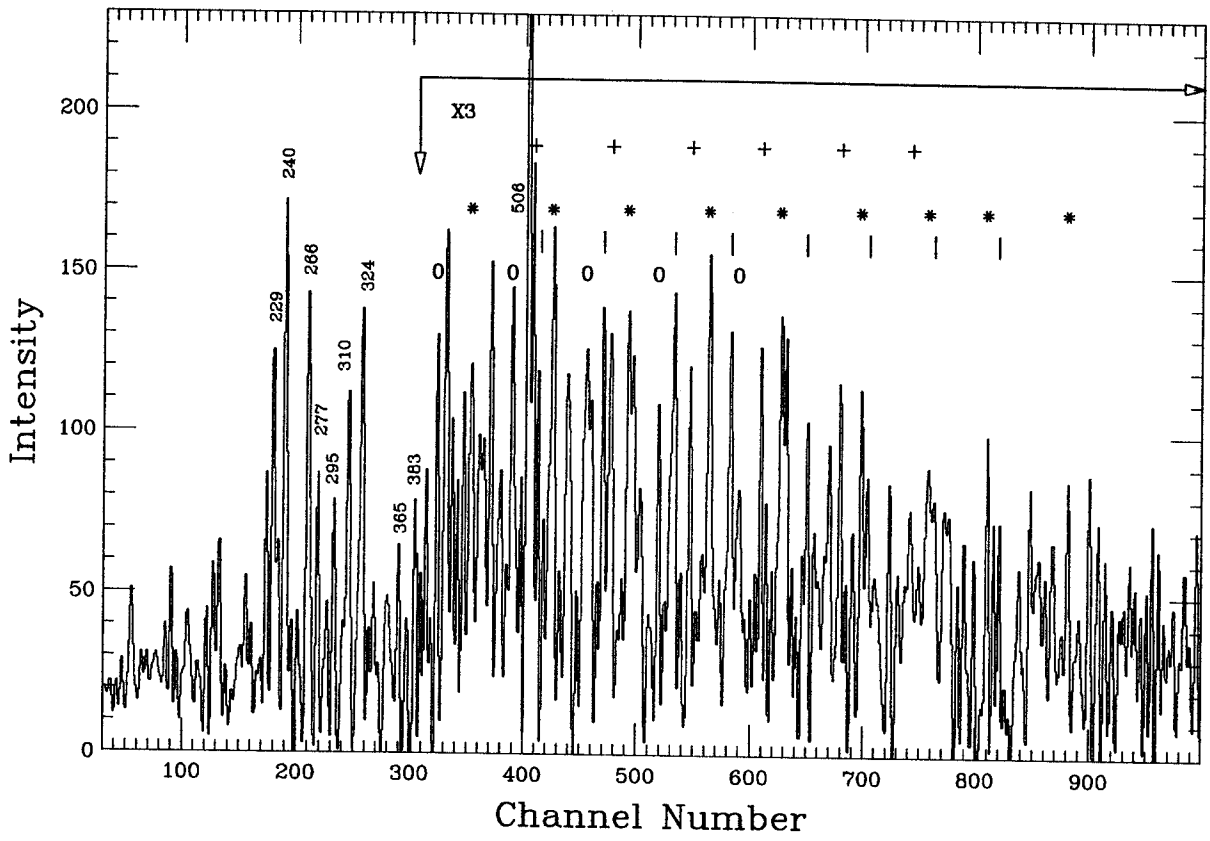

Figure 10.6: Spectrum gated on 378-keV transition. The four new bands are marked with plotting symbols, other transitions in ^{132}Pr are labeled with transition energies.

10.3.1 Discussion

The four rotational bands observed in the present study were extremely weakly populated (not more than 0.1% of the total ^{132}Pr production). The energy difference between transitions (Δ) is very close. This spacing describes a nuclear shape of $\beta \approx$ 0.4 for a nucleus in the $A \simeq 130$ mass region. Because of the weak population of these states, gates on the individual peaks did not result in a reconstruction of the transitions.

Multiple IB's have been observed in the $A \approx 190$ region, where these cases have demonstrated identical character to a specific core rotational band for the immediate region with the IB clustered throughout neighboring nuclides [aza91]. The bands observed in ^{132}Pr do not appear to originate in the same manner.

The observation of four semi-identical bands in one nuclide is a stringent test of current thought of identical behavior. While truly identical bands provide an even more exacting arena, these bands illustrate the extent to which minimal interactions of odd (unpaired) particles can produce rotational structures. This behavior is not necessarily limited to superdeformed nuclides. It can also provide insight into behaviors observed in other identical structures.

Alignment

To compare the individual characteristics of the four SD bands in the ^{132}Pr, we have calculated limits on the aligned angular momentum. We also calculated the dynamic moments of inertia, and total incrementally aligned angular momentum for each band. It is readily seen that the underlying core structure is very similar in each of the four bands. Their aligned momentum, plotted in Figure 10.7, is nearly indistinguishable given the range of possibilities in choosing the bandhead spins. Figure 10.8 shows the total alignment variation of band 1 with different choices for the bandhead spin.

Table 10.2: Superdeformed Band Comparison for N=73 Isotones: $^{133}_{60}$Nd, $^{131}_{58}$Ce, $^{130}_{57}$La from [fir94].

^{133}Nd E_γ	Δ	^{131}Ce E_γ	Δ	^{130}La E_γ	Δ
		1732			
			93		
1631		1639			
	88		87		
1543		1552			
	85		83		
1458		1469			
	81		87		
1377		1382		1412	
	77		79		93
1300		1303		1319	
	74		77		90
1226		1226		1229	
	68		73		81
1158		1153		1148	
	66		71		75
1092		1082		1073	
	63		69		75
1029		1013		998	
	62		69		77
967		944		921	
	63		69		70
904		875		852	
	68		70		90
836		805		762	
	74		72		
762		733			
	79		71		
683		662			
	79		70		
604		592			
	90				
514					
	73				
441					
	96				
345					

Table 10.3: Superdeformed Band Comparison for N=74 Isotones: $^{133}_{59}$Pr and $^{132}_{58}$Ce from [fir94].

^{133}Pr E_γ	Δ	^{132}Ce(1) E_γ	Δ	^{132}Ce(2) E_γ	Δ	^{132}Ce(3) E_γ	Δ
						2201	
							87
						2114	
							84
						2030	
							100
						1930	
							94
						1836	
							94
						1742	
							90
						1652	
							85
						1567	
							79
				1548		1488	
					90		79
(1489)		1533		1458		1409	
	77		85		66		74
(1412		1448		1392		1335	
	91		88		72		71
(1321)		1360		1320		1264	
	56		76		72		69
1265		1284		1248		1195	
	73		77		69		68
1192		1207		1179		1127	
	71		73		70		67
1121		1134		1109		1060	
	72		68		67		65
1049		1066		1042		995	
	73		67		67		66
976		999		975		929	
	68		73		68		64
908		926		907		865	
	68		62		60		56
840		864		847		809	

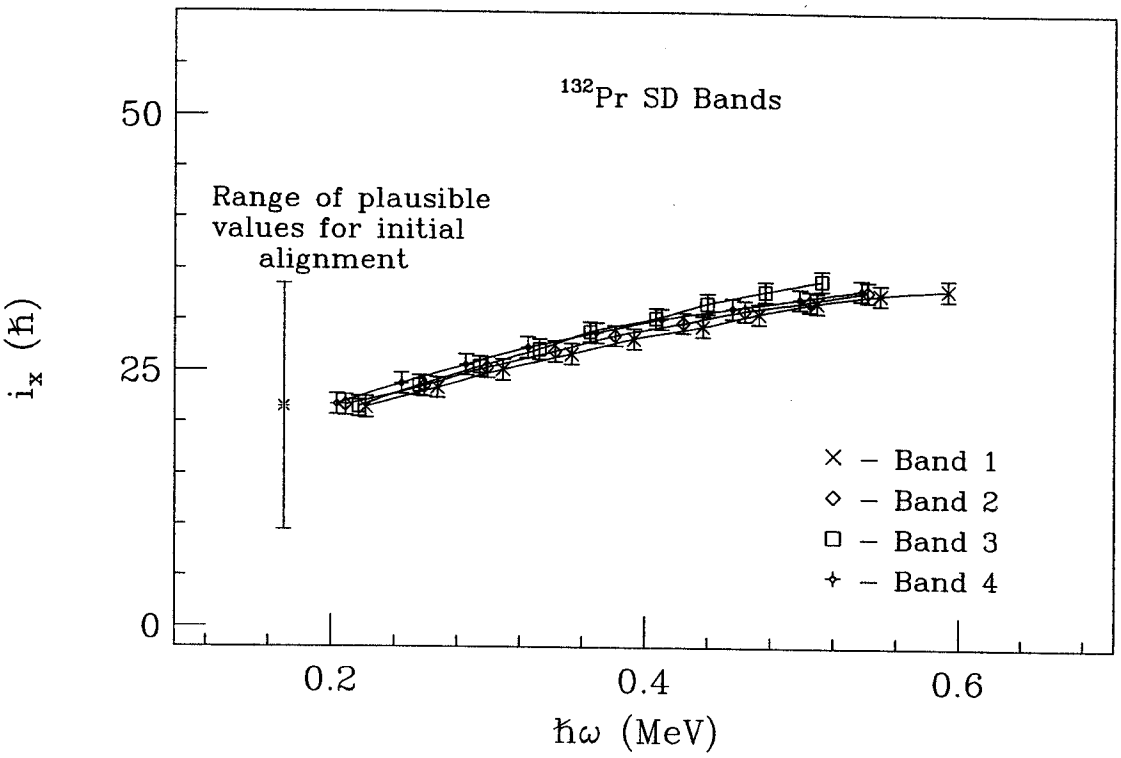

Figure 10.7: Aligned angular momentum of the SD bands in ^{132}Pr. The large range of plausible values for initial alignment results from the uncertainty in the assignment of the bandhead spins and true K quantum number for the band.

Incremental Alignments

Incremental alignments allow excellent comparisons of bands which arise from the same intrinsic structures. One difficulty which is often encountered in calculating incremental alignments is choosing the proper core reference band. We chose the SD band in ^{132}Ce since it has one less proton and one less proton hole than ^{132}Pr. Stephens *et al.* proposed that the incremental alignment of SD truly "identical" bands is quantized to values of ± 1, ± 0.5, or 0 units of angular momentum [ste90a]. Figure 10.9 illustrates that these bands do not follow this behavior. Each band does, however, cluster about different, but fairly constant values of alignment. This is still a strong indication of a correlation between these semi-IB and some other SD core

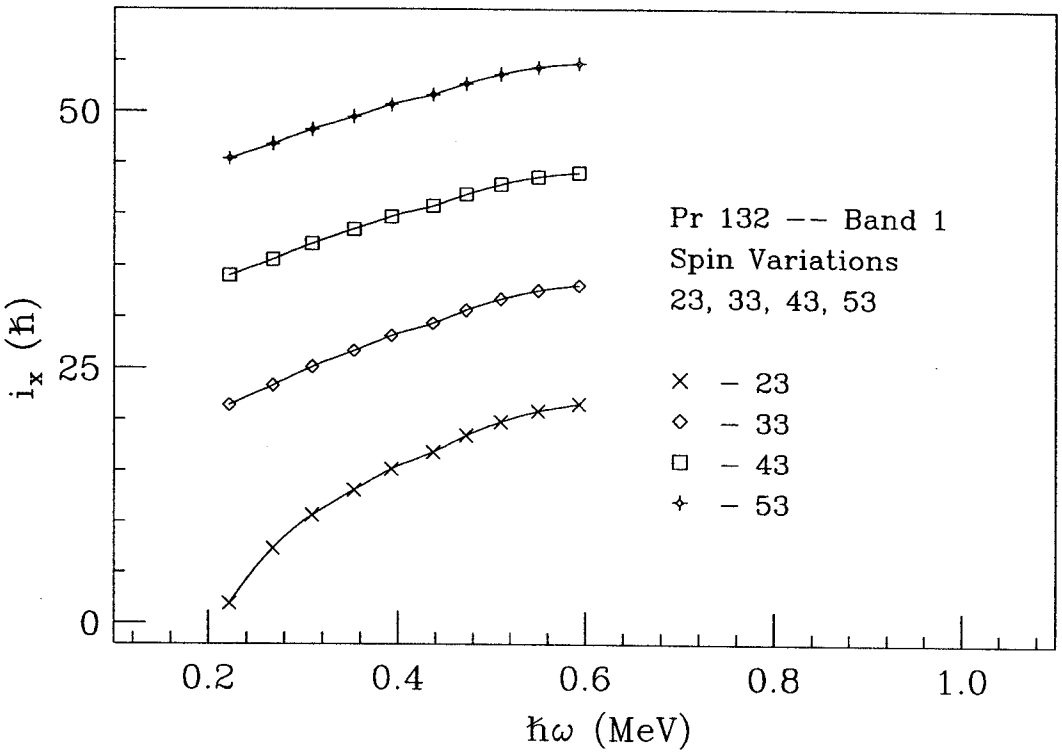

Figure 10.8: ^{132}Pr total alignment plot.

band, perhaps ^{130}La.

Moments of inertia

Similarly, analysis of the kinematic and dynamic moments of inertia can provide a little insight into fundamental structures. Figure 10.10 shows the dynamic moments of inertia of the four bands. The range of values, from about 42 to 60$\hbar^2$ MeV^{-1}, is typical of superdeformed bands in this region[fir94]. This can be seen in a few examples of SD bands reported for neighboring nuclei. See Figure 10.11 from reference [sin96]. The nuclei and SD band identification numbers are marked. A few of the SD band plots, ^{132}Ce SD-1,$^{131}CeSD-1$,^{133}Ce SD-2, $^{133}CeSD-1$, and ^{135}Nd, start around 60$\hbar^2$ MeV^{-1} at low rotational frequency and continue to decrease smoothly toward higher rotational frequencies. Others have considerable oscillations in the dynamic moment of inertia with increasing rotational frequency. The dynamic moments of inertia of the 4 bands in ^{132}Pr parallel this behavior. There appears to be a staggering effect

in SD-1 and SD-2.

The oscillations of the angular momentum in the yrast SD band of ^{149}Gd have been linked to a possible perturbation around the rotation axis, resulting in a $\Delta I = 2$ staggering [fli93]. We generated second derivative plots to see whether a corresponding trend existed in the 4 bands. Figure 10.12 points out the staggering effect in the bands.

TRS calculations

Total Routhian Surface (TRS) calculations have provided reasonable descriptions of general shapes and driving forces observed in nuclei in the mass ~130 region. A series of TRS[wys88] calculations of plausible structures for ground state configurations of ^{132}Pr was performed. The calculations showed, for nearly all possible configurations, the ^{132}Pr nucleus exists as a well-behaved prolate rotor (though somewhat soft to triaxial deformations) with the β_2 deformation parameter ranging from 0.2 to 0.35 and β_4 and γ parameters centered near zero values for these structures. Representative surfaces, calculated at a rotational frequency of $\omega = 0.30\ \hbar^2/\text{MeV}$, are shown for two proton and neutron configurations in Figure 10.3.1. Total Routhian Surfaces of ^{132}Pr are presented with: (a) The odd neutron occupying lowest available negative parity-positive signature orbital (-,+) and the odd proton occupying the lowest negative parity - negative signature orbital, and (b) Neutron (+,-) and proton (-,+) configuration. Note that both configurations yield structures which are prolate deformed with a $\beta_2 \approx 0.24$.

When the rotational frequencies were varied from $\omega = 0.101,\ 0.304,\ 0.507$, to $0.710\ \hbar^2/\text{MeV}$ a second minimum appeared in the potential energy surface. Figure 10.14 shows this formation between $\beta_2 \approx 0.3 - 0.4$. This initially occurs above spin $I = 17$, with the most intense minimum occurring around $I = 44$. Perhaps this is the structure from which the four IB bands arise.

These results of TRS calculations, in addition to providing a survey of general trends of shape and shape stability of the nuclide, were used to extract specific deformation information to calculate Routhians of proton and neutron structures for ^{132}Pr.

CSM calculations

Using the results from the TRS calculations as a guide, we also performed CSM calculations. Deformation parameters of β_2=0.24, β_4=-0.004, and γ=0.00 are consistent with minima typically observed in the surveying TRS calculations. Given these parameters, we observe the ground state configuration consists of a $g_{7/2}$ proton coupled to an $h_{11/2}$ neutron. Figures 10.15 and 10.16 shows the single particle Routhians as a function of rotational frequency. The proton levels are nearly unchanged over the range of interest, $\hbar\omega$=0.2-0.6, while the neutrons exhibit significant changes in energies of orbitals of interest. These energy changes in the neutron orbitals drive the nucleus toward a stable prolate shape while the proton orbitals have little effect. More importantly, the high level density for both particles, especially neutrons, allows for many possibilities in construction of multiple quasi-particle structures.

Single Particle Routhians

Figure 10.17 shows single particle Routhians as a function of rotational frequency for protons and neutrons at β_2=0.30, β_4=-0.004, and γ=0.00.

Given these deformation parameters, we observe the ground state configuration consists of a $g_{7/2}$ 7/2 [404] neutron coupled to an $h_{11/2}$ 3/2 [541] proton . The more important aspect of the calculations is the usefulness in identification of highly deformation-driving orbitals which are within a few MeV above the Fermi surface. These are the prime candidates for components of bandhead structures of SD bands.

No such orbitals exist for proton excitations to encourage a more deformed struc-

ture until rotational frequencies on the order of 0.8 MeV are achieved. At this point the highly mixed $g_{9/2}$ 1/2[651] crosses the $d_{5/2}$ 3/2[411] and becomes low enough in energy to be populated. It is doubtful that this band crossing comes into play in the rotational structure of SD bands. Most of the available proton orbitals are fairly constant in excitation energy, both in terms of rotational frequency and quadrupole deformations. They would serve only to hold spectator nucleons and provide several similar states which can be occupied to construct semi-identical bandhead configurations. These include the positive parity $g_{7/2}$ 5/2[413] and $d_{5/2}$ 3/2[411] as well as the negative parity $h_{11/2}$ 5/2[532].

The neutrons in this region however, do have several highly mixed, but very good candidates for high deformation effects. An intruder $i_{13/2}$ 3/2[651] and the $i_{11/2}$ 1/2[640] orbital diving in from the next shell both show significant decreases in single-particle energies with increased rotational frequency.

The most promising structures appear to be similar to the decoupled and doubly-decoupled bands which tend to be built on opposite parity orbitals from the next oscillator shell. An example of this behavior is found in the ^{134}Pm nucleus.[wad91] It is most likely the SD structures in ^{132}Pr have similar types of highly aligned $h_{9/2}$ or at least aligned negative parity 5^{th} shell neutron contributions coupled to static proton structures from the 4^{th} shell.

10.4 ^{133}Pr Rotational Bands

During this experiment, rotational bands were also obtained for the reaction: ^{100}Mo(^{37}Cl (160MeV),4nγ)^{133}Pr.

The odd-mass ^{133}Pr nucleus had previously been studied under lower spin conditions [hil86, hil88, fos90] using the ^{118}Sn(^{19}F (92MeV),4nγ)^{133}Pr reaction[hil86]. We present information from a higher spin perspective, using a simple and a multiple

gate technique. The simple gates were selected from a 2×2 $E_{\gamma 1}$ vs. $E_{\gamma 2}$ data array. To construct the multiple gate, triples events in coincidence with spectra from three major transitions (310, 551, 709 keV) were scanned into a 2-D array. Then selected energy gates from this array were summed to represent the band.

10.4.1 Energy Level Diagrams

Odd-mass $^{133}_{59}Pr_{74}$ with one additional neutron exhibits a more complicated rotational energy-level decay scheme than ^{132}Pr. For comparison the energy level diagram is presented in Figure 10.18. The nucleus has one odd proton, 4 proton pairs and 12 neutron pairs outside of shell gap 50. The ground state is thought to be a prolate deformed, positive parity I=$\frac{5}{2}$ state [ben85, eks72]. There are six bands that describe the de-excitation of this nucleus.

10.4.2 Band Based on $\pi h_{11/2} \otimes \nu h_{11/2}$

The yrast band is built on a decoupling of two $h_{11/2}$ protons. The proton alignment can be seen around 0.43 MeV. when backbending occurs within the band. A 130 keV transition to the ground state does not appear in the spectra. This is thought to be an isomeric state that de-excites by either a delayed γ or by conversion electrons.

10.4.3 Bands Based on $\pi h_{11/2} \otimes \nu g_{5/2}$

There are three $\Delta I = 2$ rotational bands based on the $\pi\ g_{\frac{7}{2}}\ \frac{5}{2}^{+}[413]$ orbital configuration.

10.4.4 Band Based on $\pi h_{11/2} \otimes (\nu h_{11/2})^n$

We present information to extend the band, designated collective oblate, [hil88] by a few energy transitions. This band has been designated the $\pi h_{11/2} \otimes (\nu h_{11/2})^n$ orbital configuration.

Figure 10.19 is a spectrum representing rotational band 6 for ^{133}Pr. It was produced by the 2-D multiple gate technique. This band has been published before [fos90]. The reported sequence is 196, 244, 296, 351, 403, 454, 501, 546, 587, 626, 662, 686 keV. The low intensity segment, after 587 keV, is in dispute with our results. While we do see peaks at 626 and 662 keV using our simple gate technique, these peaks disappear when using our, more selective, 2-D multiple gate technique. The sequence is more likely concluded with: 587, 684, 788 keV.

(Also show the simple gate segment.)

10.5 Summary

We have extended the rotational band structure of ^{132}Pr and ^{133}Pr. In addition, four possibly-superdeformed (SD$^{?}$) or identical rotational bands were observed in this study of high-spin states in odd-odd ^{132}Pr. These bands exhibit remarkably similar transition energies and dynamic moments of inertia. Although the differences in energies and moments are too great to classify them as truly "identical," we have termed them "semi-identical." While somewhat surprising because of so many occurring in one nucleus, their systematics is consistent with more general classes of identical bands in nuclides arising both from the coupling of similar configurations *and* the decoupling of specific particles. The spacings of successive transitions is comparable to those observed in superdeformed bands in the region. Cranked Shell Model (CSM) and Total Routhian Surface (TRS) calculations using a Woods-Saxon potential suggest a small set of plausible structures.

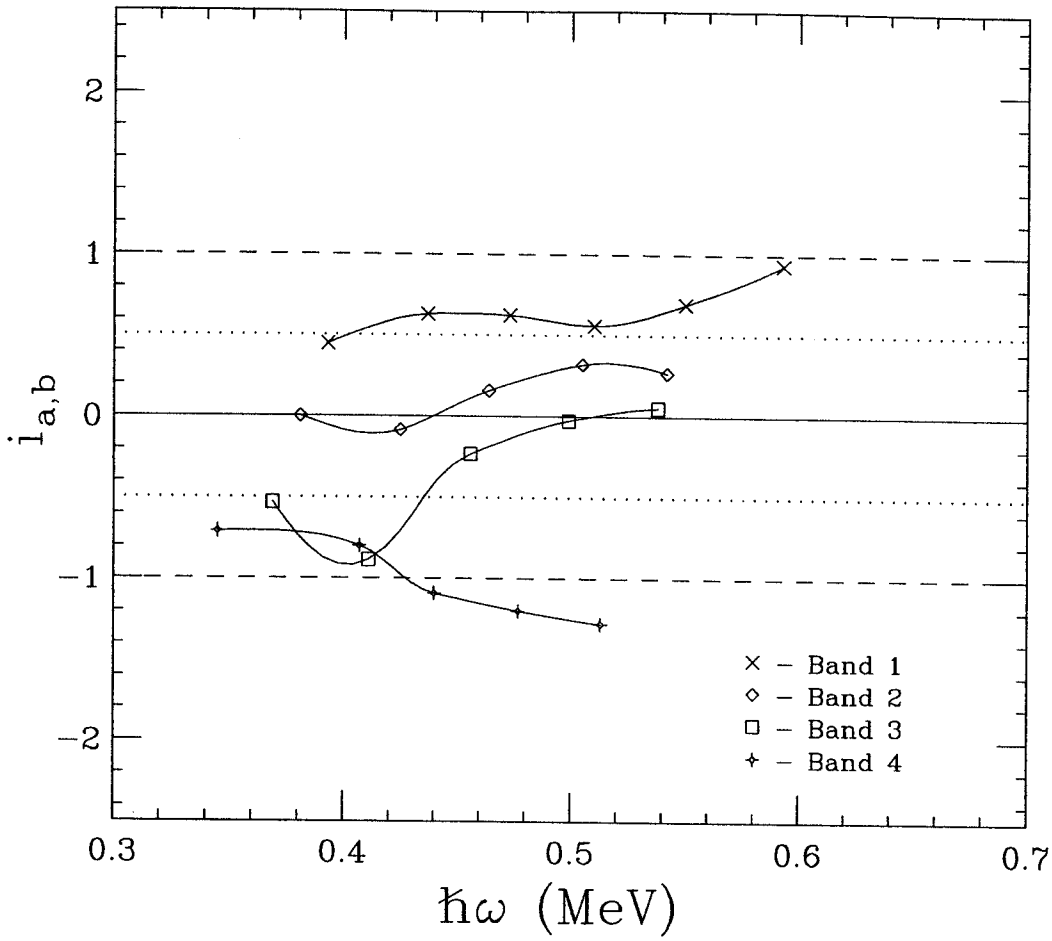

Figure 10.9: Aligned incremental angular momentum of SD bands in ^{132}Pr. Identical bands generally cluster about values of ± 0.5 or ± 1.

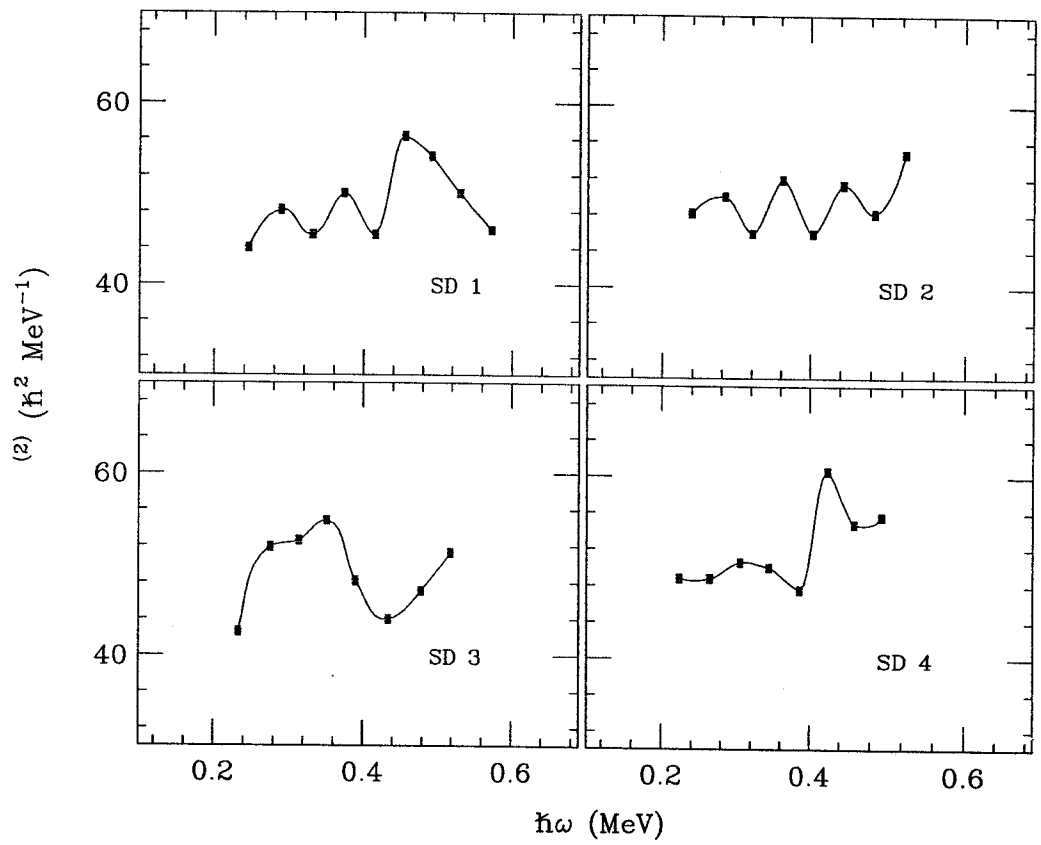

Figure 10.10: Dynamic moments of inertia for the 4 highly-deformed (SD) bands in ^{132}Pr.

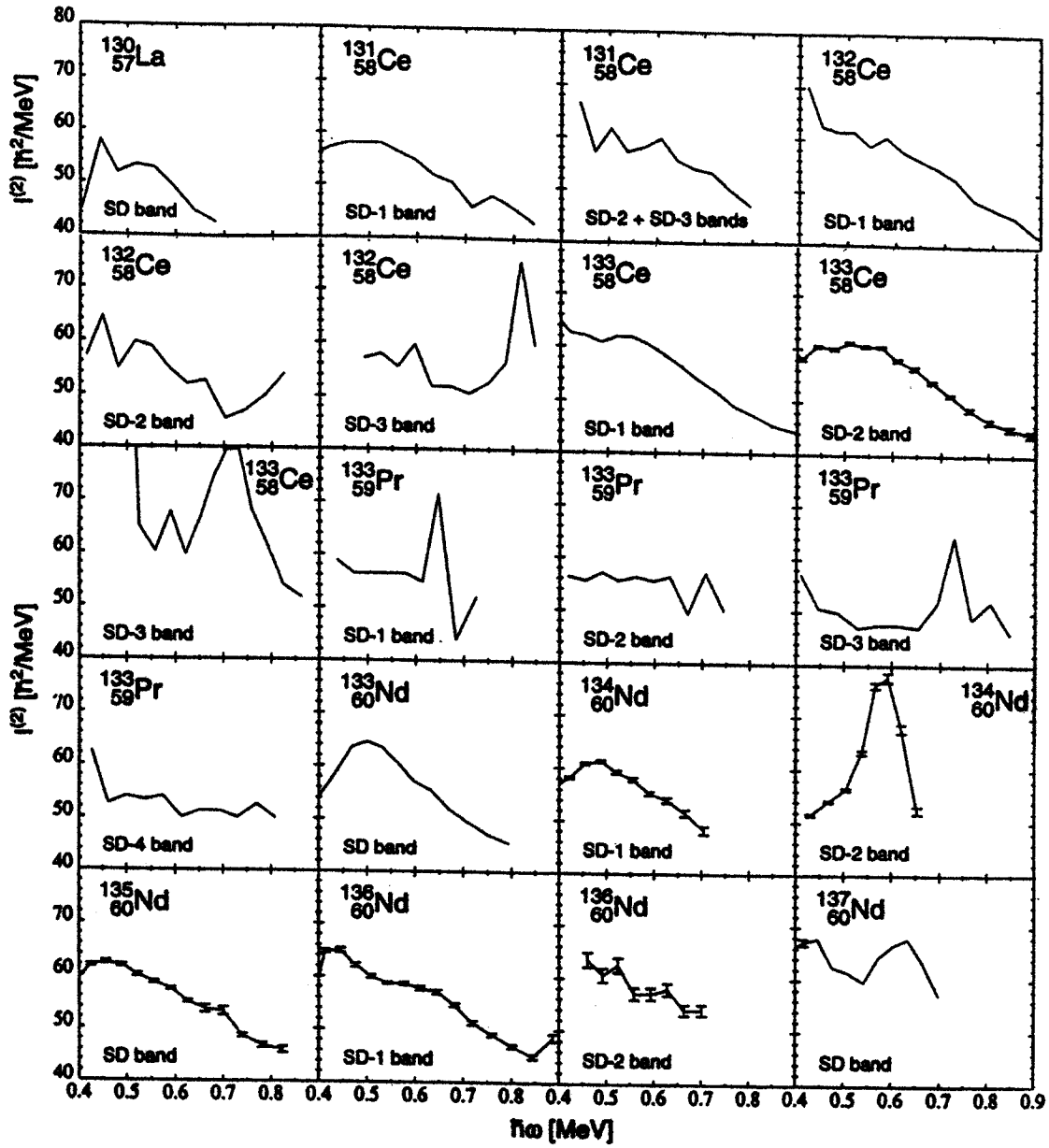

Figure 10.11: Dynamic moment of inertia plots for SD bands in $A = 130 - 137$ mass region.

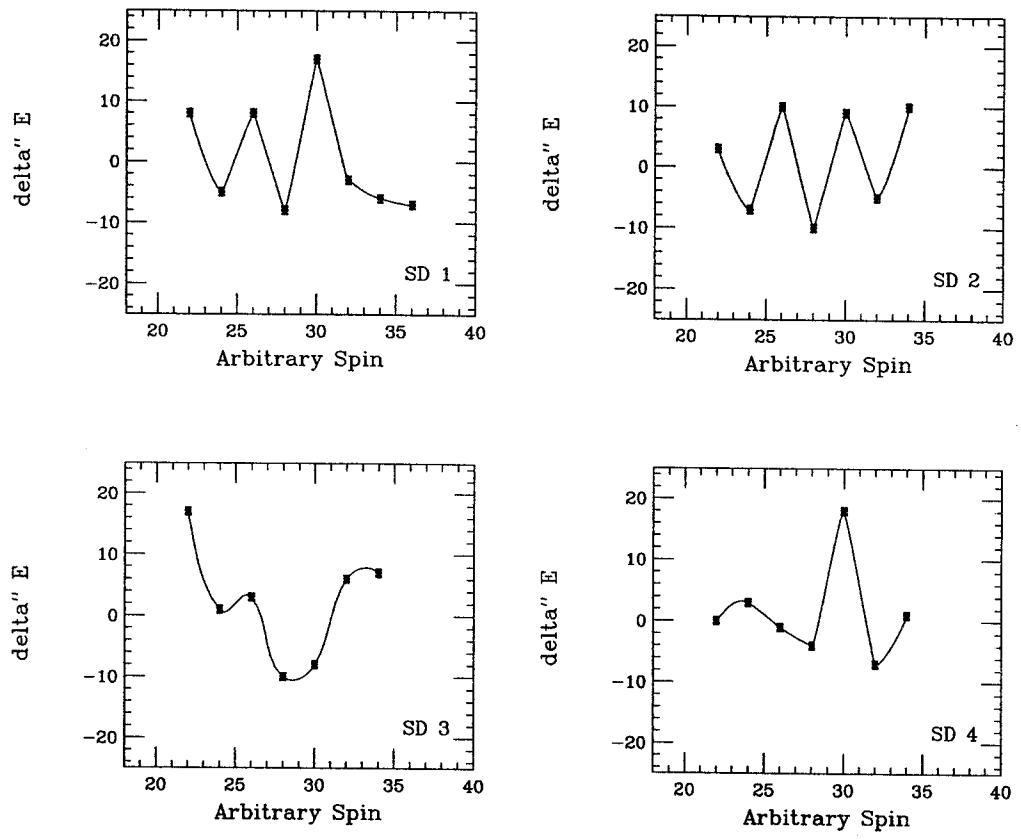

Figure 10.12: Second derivative energy plots for the four highly-deformed (SD) bands in ^{132}Pr.

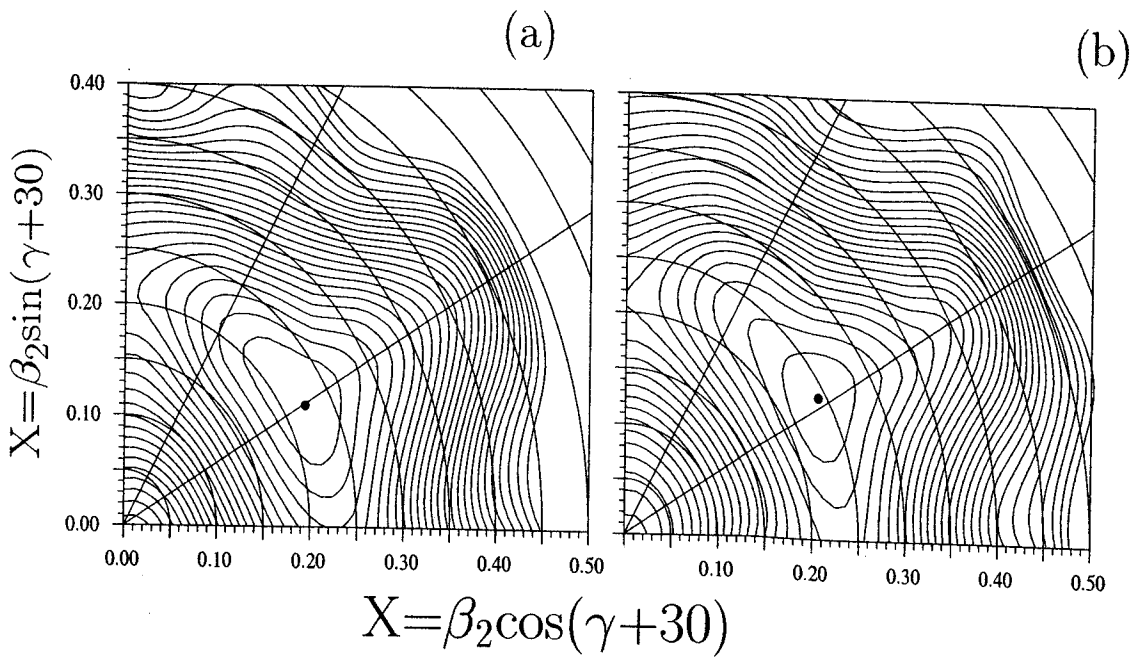

Figure 10.13: Total Routhian Surfaces of ^{132}Pr with: (a) The odd neutron occupying lowest available negative parity-positive signature orbital (-,+) and the odd proton occupying the lowest negative parity - negative signature orbital, and (b) Neutron (+,-) and proton (-,+) configuration. Note that both configurations yield structures which are prolate deformed with a $\beta_2 \approx 0.24$.

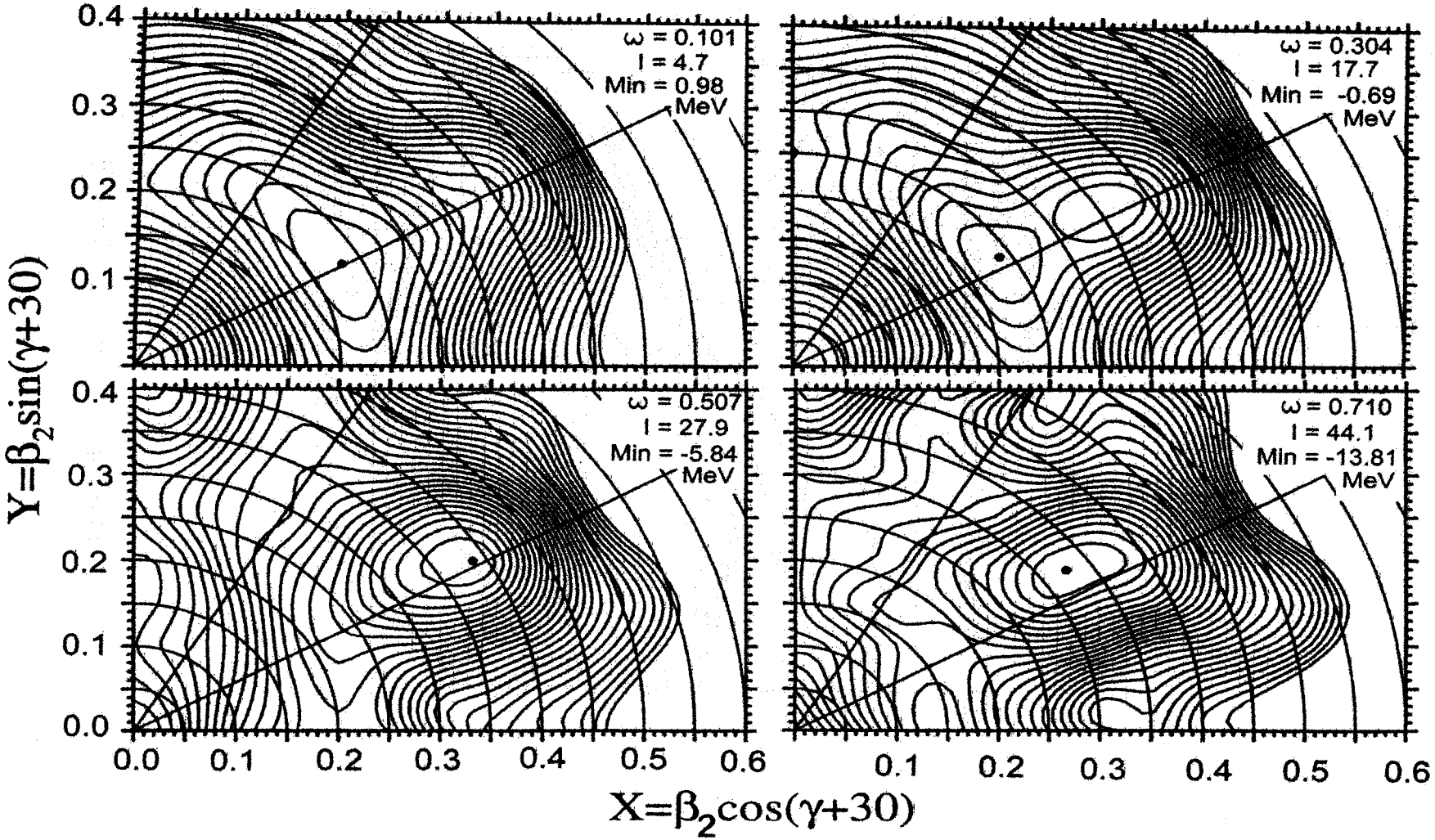

Figure 10.14: Total Routhian Surfaces of ^{132}Pr calculated with the neutron (+,-) and proton (-,+) configuration, as in Figure 10.13 , and a variation in the rotational frequency. Note that in addition to the prolate deformed minimum at $\beta_2 \approx 0.24$, a second minimum appears between $\beta_2 \approx 0.3$- 0.4 as the spin increases beyond $I = 17$.

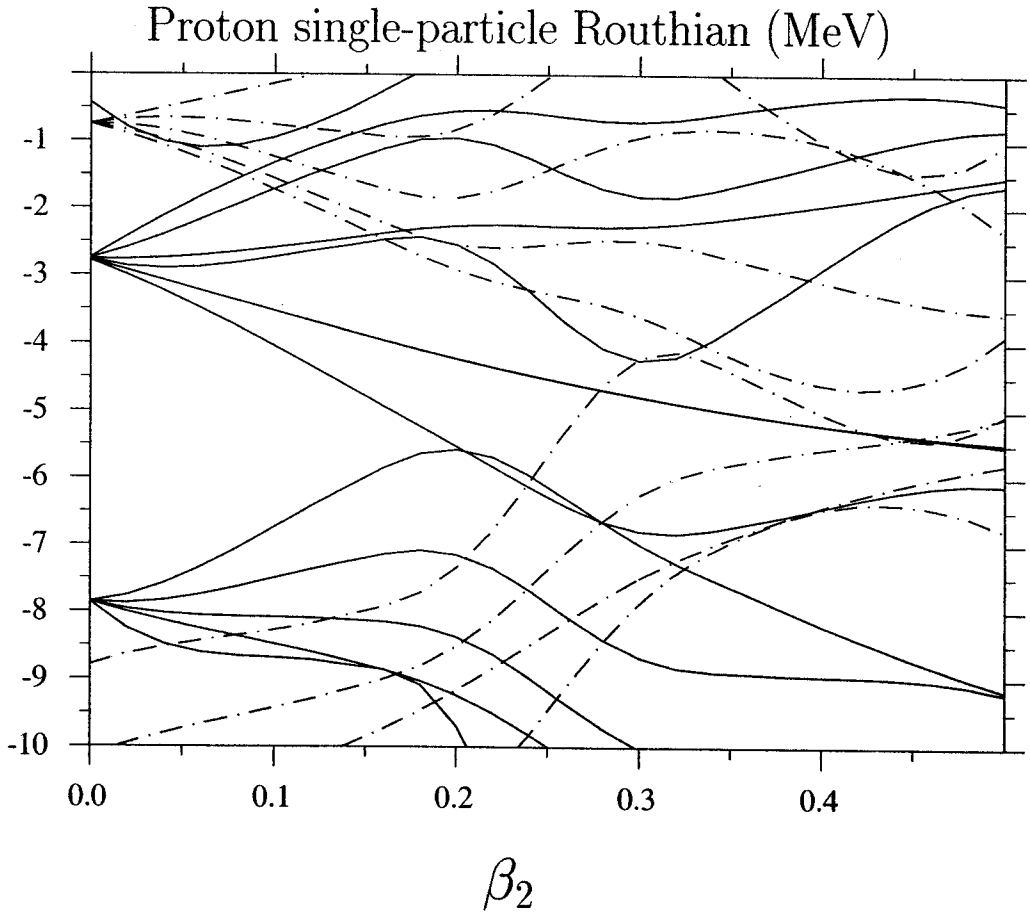

Figure 10.15: ^{132}Pr total routhian plot for protons.

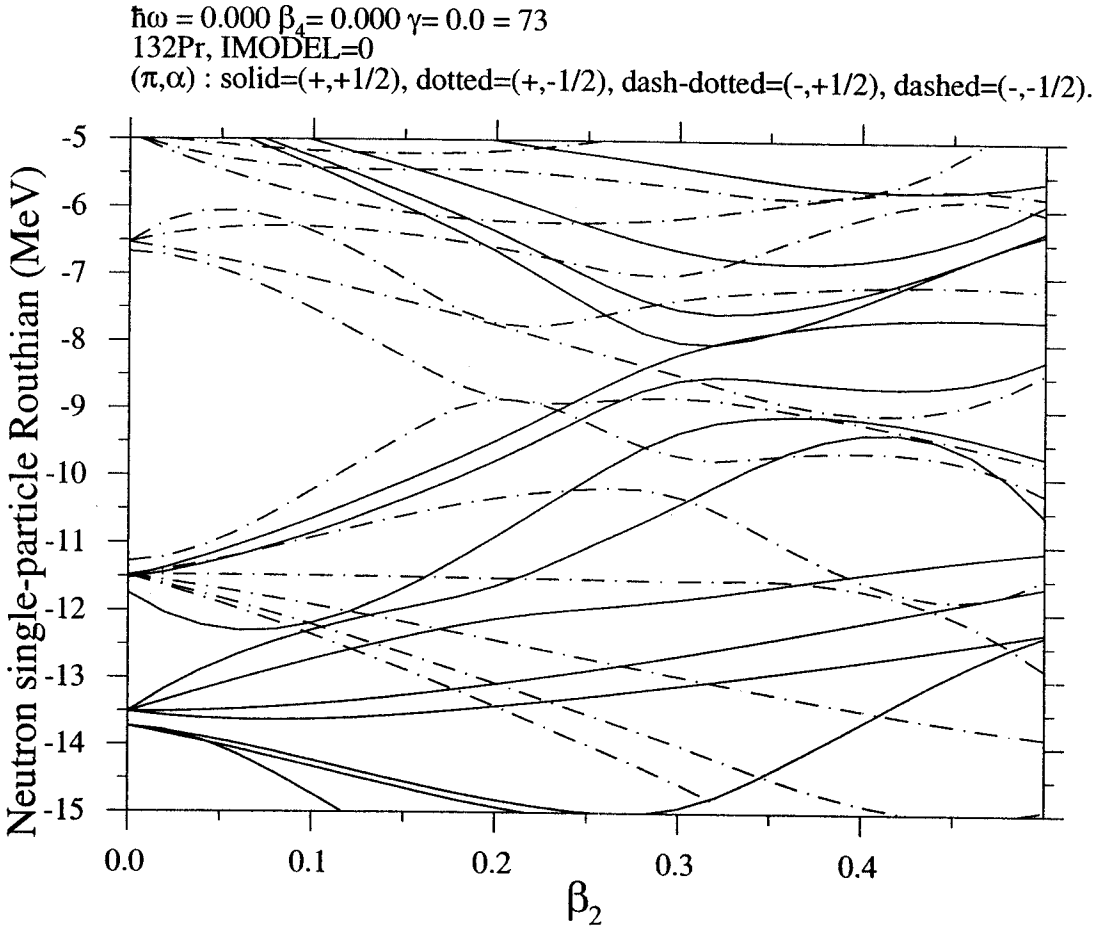

Figure 10.16: ^{132}Pr total routhian plot for neutrons.

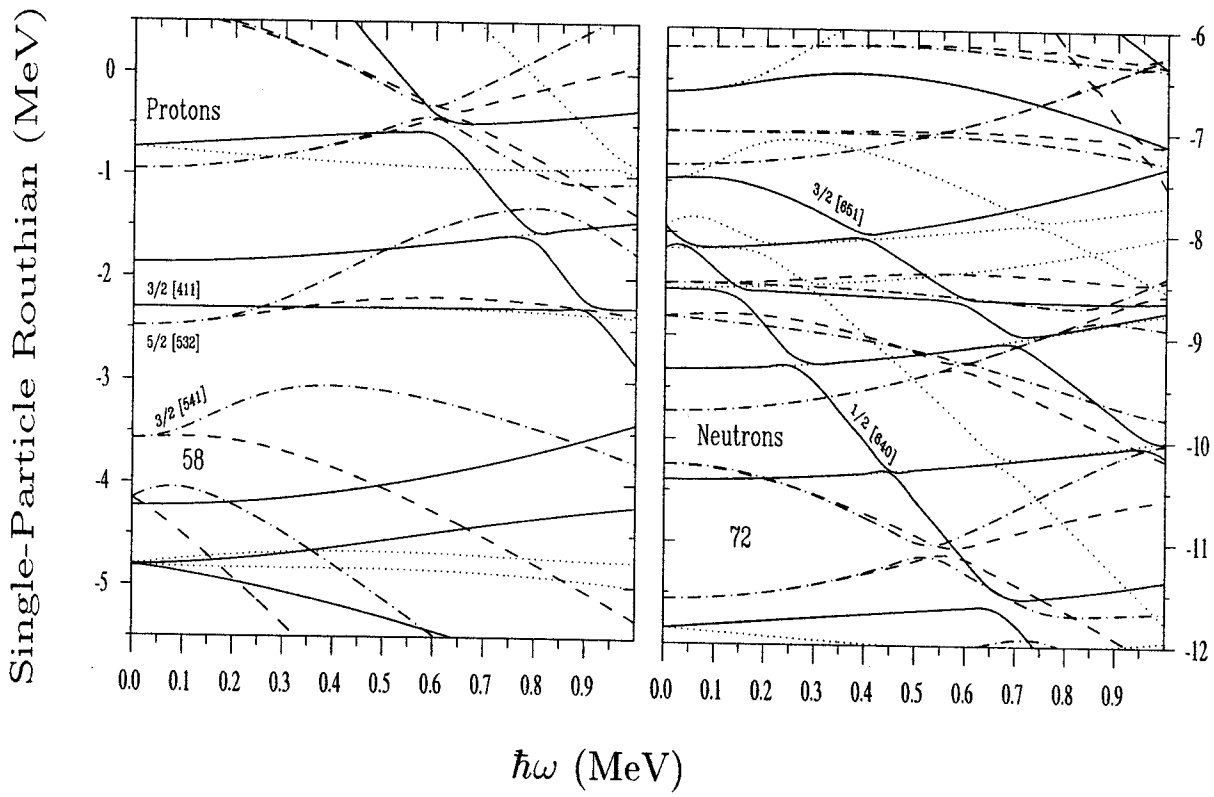

Figure 10.17: Single particle Routhians calculated at β_2=0.30 β_4=-0.004 and γ=0.0 Routhians for particles of particular interest are labeled. All Routhians follow the convention of (parity,signature) (π,α) are denoted: solid=(+,+), dot=(+,-), dot-dash=(-,+), and dash=(-,-). (a) Protons with blocking of the lowest (-,+) level and (b) Neutrons with blocking of the lowest (+,-) level.

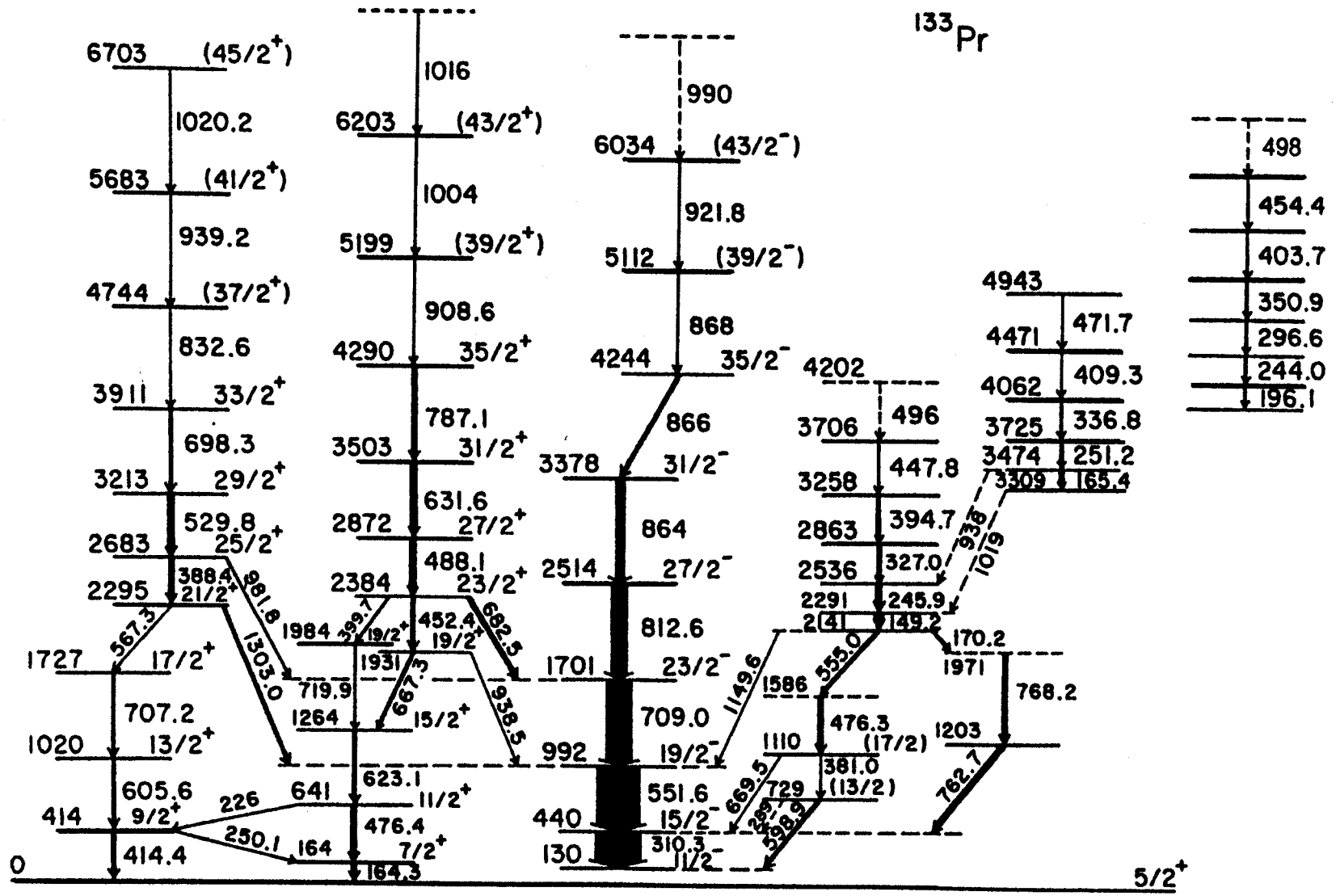

Figure 10.18: Nuclear energy level diagram for the γ ray cascade in ^{133}Pr. From [hil86,hil88].

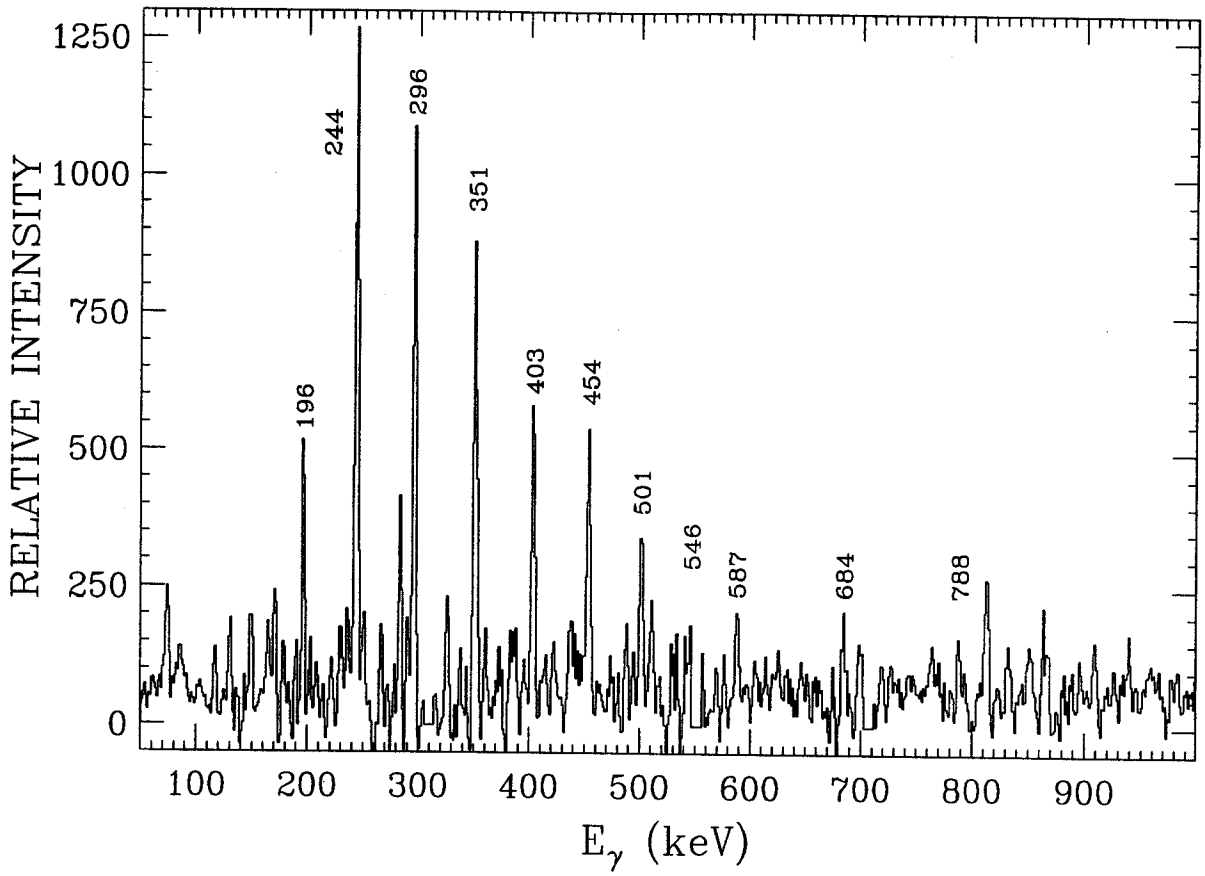

Figure 10.19: ^{133}Pr spectrum representing rotational band 6, from a 2-D multiple gate technique. (The 546 keV peak has been partially erased by the 551 keV primary gate.)

Chapter 11

Summary

We have investigated the reaction $^{100}Mo(^{37}Cl(160MeV), xn\gamma)^{137}Pr^*$ with an in-beam γ-ray spectroscopic technique. Using triple coincidence data, we have explored the rotational band structure of ^{132}Pr and ^{133}Pr and have extended some bands to higher spin states.

The primary motivation for this research was a search for superdeformation in this $A \approx 130$ nuclear mass region. Using a multiply-gated data array specific for ^{132}Pr, we have found a set of low intensity peaks that might be described as four regularly spaced, weakly populated rotational bands which have very similar rotational characteristics. The spacings of successive transitions are comparable to those observed in superdeformed bands in the region. Cranked Shell Model (CSM) and Total Routhian Surface (TRS) calculations using a Woods-Saxon potential suggest a small set of plausible structures based on the proton $g_{\frac{7}{2}}$ and neutron $h_{\frac{11}{2}}$ orbitals.

During the course of the data analysis, we noticed that the accepted method of rebinning the data events with a random number technique to correct for gain and doppler shifting, actually produced noise within the spectra. This was compounded by the fact that each detector had a different calibration and we were making comparisons between 20 detectors. Due to the low signal-to-background intensities of many of the individual coincidence spectra, we had to develop a Fast Fourier Transform frequency

exclusion technique for the removal of this noise. Other researchers approached this situation from a different perspective. They referred to this noise as spikes and felt that it was proportional to the multifold nature of the analysis and was generated by the method of analyzing higher-fold events. They developed a method that effectively removed most of the spikes but the γ-ray energies were occasionally slightly shifted, depending on where the spikes had been located [bea95].

During the course of this work, we have developed an extremely fast and sensitive Segmented FFT search routine based on the investigation of spectral spherical harmonics. It is a very efficient diagnostic tool for studying and locating SD bands. We decided to continue our investigation in an unconventional way because of 1) the extremely low intensity ($< 0.1\%$) in the four bands; 2) all four bands were found within one single coincidence gate instead of a statistical cascade from many gates; 3) the fact that the 378 keV transition seen in coincidence with them has not been placed in the rotational band scheme; and 4) the sum of individual gates on the peaks within the four bands do not reconstruct the bands. This suggested that perhaps these bands had another source, other than superdeformation.

Therefore, we studied the reaction kinematics for the possibility of artefact formation from doppler shifted γ rays, due to differences in residual particle velocities and found that there might be a 2 to 10 keV deviation produced in the mid to high energy region, depending on how the data was doppler shifted, gain matched and calibrated. During the course of the segmented FFT search technique development, we found that there was a slight irregularity between the data and background peak positions in a published SD band, pointing to the possibility that a change had occurred in the x-axis energy values during the analysis. So we conducted a rebinning experiment to investigate how much of a change would cause this effect. We found that extremely small deviations based on a cubic or quartic term in the calibration could be responsible. We then investigated whether this small change could affect the SD peaks. In

fact, we found that the SD peaks could disappear with these small changes between the calibration of the data set and the background. The question remains: Since this is so, could the reverse also be true– that SD peaks appear because of these small deviations in calibration. This would suggest that many of the published SD bands were spectral artefacts.

In the 12 years or so since Twin and co-workers published the first discrete SD band in ^{132}Ce over 160 of such bands have been discovered in more than 80 nuclei. Many of the reported bands are termed 'identical' and they occur within nuclei from the same experiment [sin96]. Most of the SD bands published in the past 5 to 6 years have been generated from one of two large Ge detector systems. It appears that they use the now standard method of spike removal which slightly shifts the energy peaks. This shifting could be eliminated with an internal calibration based on known transitions within the spectrum. However, all gates would need to be individually recalibrated. What appears to be happening is that the gates with slightly different energy shifts are summed together then a background from a different multiplicity array (one without energy shifts or at least shifts caused by a different multifold analysis) is subtracted. It is conceivable that this method has produced artefacts that have been interpreted to be SD bands. In addition, some of the SD bands look very much like a normal rotational band from a neighboring nucleus. Researchers may argue that this is the basis for 'identical' bands. However, we speculate, based on the background arrays that we have generated from this experiment, that 'identical' bands may be just a product of coincidences between the photons of interest and those within the background.

We rebinned our own ^{132}Pr data set with different event locating parameters. Then we tested a total energy gate to see whether the four bands could be located. A survey search showed that the bands existed in the original region of the spectrum. We then searched for SD bands from neighboring nuclei produced by our reaction.

These bands, reported in the literature, do not appear in our data set even though the nuclear reaction for the SD in ^{133}Pr is identical to our experiment with the exceptions of a 5 MeV lower beam energy and a larger detector array [1]. What does appear for the ^{132}Ce SD bands is an identical structure shifted lower in energy by a few hundred keV. The main difference is in the method of analysis of very low intensity peaks.

The major rotational bands from this study appear to be equivalent with those presented in the literature.

Perhaps the major contribution from this work is the inception of a new perspective on the analysis of SD bands and the creation of a new set of tools with which to accomplish this.

[1] Some evidence for SD-1 in ^{133}Pr does appear in the Simple-gated data set. However, the evidence disappears in the more selective Multiply-gated array. This is counter-intuitive to what is expected to confirm the existance of the band.

Chapter 12

Recommendations

We feel that a true understanding of SD can only be achieved by developing a more sophisticated perspective for the entire nuclear reaction under study. In order to do this the following steps are recommended:

12.1 Reaction Kinematics

1) Kinematic computer modeling of reaction under study. One program should be written to incorporate all kinematic factors and a 3-D array with Doppler shift (DS_{fac}) corrections for residual particles and γ rays.

2) Improve the *CASCADE* program to include the reaction kinematics: energy loss in the Target; threshold energy; velocity of the residual, etc. The *CASCADE* code should incorporate Monte Carlo calculations to account for target composition and thickness. A mass model formula should be chosen that best represents the mass range of the residual particles. Modifications in the cross sections should be made for the use of dual targets.

3) Residual particle velocity selection for γ rays. Perhaps a reversal of the method used to determine correction factors to the β residual particle velocity could be used to differentiate the γ rays from various nuclei, i.e., if a particular peak exhibits certain

changes in resolution and centroid position then it may backcalculate to a certain β value determination and therefore to a residual particle identification. This will work only if peak resolution is high enough and a high number of ADC bits are used to record the data. This may require the following:

12.2 Data Analysis

Because of time, space, and computer constraints, only a few peaks (3 from ^{133}Pr and 4 from ^{132}Pr) were actually filtered into the 2-D arrays. With today's faster computers and almost unlimited storage capacity, it would be useful to modify the Oak Ridge software to allow creation of the arrays from the event data that has been stored on the internal disk. This would considerably speed-up the process of the array construction. The following proposed developments would greatly enhance the existing data analysis methodology.

1) A 2-D FFT development along with a modified second derivative, centroid location technique and a deconvolution method development would be useful. Perhaps a pattern recognition algorithm would be necessary that incorporates a 2-D (actually multiple or n-tuple) sorting of the (E vs T) array from each detector.

2) Nuclei sorting method based on the collective E2 region: During the course of this work we developed a technique for baseline subtraction based on FFT, a log-log-square root method to describe the intensity and a previously published baseline method referred to as SNIP [rya88]. While producing a modified-SNIP spectrum for every channel in the $E_{\gamma 1}$ versus $E_{\gamma 2}$ data array, we observed that the baselines from γ-rays in the same nucleus were nearly identical. It was easy to distinguish between the baselines belonging to ^{133}Pr and ^{132}Pr. Furthermore, the baselines belonging to specific nuclei in individual bands showed a similarity that might be used to help identify the placement of a specific transition within an energy level diagram. This

may be due to the fact that much of the baseline profile is due to a summation of collective E2 transitions [dia84] that would, of course be nucleus specific. Since the SNIP spectra are automatically generated by our modified Oak Ridge software, it would be possible to generate a nucleus sorting method that could either search for a profile belonging to a specific nucleus and/or separate the array into sub-arrays based on the outcome of the separations. Pattern recognition software might be useful here.

3) A real 3-D determination of the position of γ rays (polar plots). A type of E2, M1, determination, but much more specific.

4) 2-D background subtraction in the (E vs. T) array: During the course of this work we generated 2-D background arrays pertaining to various time gates. True coincidences exist between certain background peaks and the actual transitions in the data. These should be subtracted prior to data analysis. This would require Factor Analysis.

5) Multi-fold selection gates on the event data prior to generating the arrays would be very useful. Presently, we acquired data in the form of triples and higher-fold. To generate arrays based on fold selection would potentially eliminate the occurance of 'spikes' in the data.

6) TAC profiles and half-life determination: Is the 62 keV area an example of successive decay or are the peaks due to x-rays? In fact, if they are due to x-rays, are they from conversion electrons?

12.3 Noise Reduction

Electrical and mechanical noise (and the subsequent beat pulses produced from them) interfere with the clarity of the data signal. High resolution spectra are most susceptible. Microphonic effects can translate mechanical noise into electrical. Lengths of cable add voltages to the system since an appreciable capacitance exist in the wire.

This is governed by $Q = CV$ (charge = capacitance times voltage). Vibrations in the cables produce a capacitance that varies in time (dC/dt). The derivative [srs96] shows how this affects the signal, i:

$$C\frac{dV}{dt} + V\frac{dC}{dt} = \frac{dQ}{dt} = i \tag{12.1}$$

The following are suggestions for the construction of a detector system that would eliminate or at least minimize noise.

1) The platform that holds the mechanical track to separate the detector frame into halves, supports the entire detector system. This platform should rest upon a pneumatic pad that can be raised or lowered as needed. (This can be regulated by the high pressure from compressed air.) High resolution spectra should be acquired only with the detector floating, i.e., isolated from building vibrations. Mechanical pumps should not be located on the pneumatic platform.

2) Each detector should be weighted or appropriately secured to the system frame at the base of the detector can in order to balance the effect of their angular positions. (The force vectors to the normal should be eliminated since this may cause eratic undulations of the can, depending on angle and position of the noise source.)

3) Electrically isolate the entire detector system.

4) The automatic liquid nitrogen feeds should fill only during non acquisition times. The LN2 inlet tubes should be secured to the detector can or its support arm, plus the system frame in order to eliminate vibrations.

5) The detector parts internal to the system frame (i.e., filters, lead collimators, etc.), should be secured together within an internal frame. This should be made of a non-conducting composite material– ceramic perhaps.

6) The inlet from the beam line to the detector system should be isolated for vibration reduction (using a corrugated line). There should be an additional steering

mechanism here.

7) The target support could be located within the internal frame.

8) Use differential pumping. There should be separate pumps on the beam line and the target frame. UHV on the detector system would eliminate noise from the scattering of the primary or secondary (residuals) beam with air and/or oil molecules.

9) The preamp cables should be electrically shielded (low-noise, twisted pairs) and secured to to the frame to eliminate vibrations and the antenna effect of R_f pickup.

10) Because of the proximity of the liquid nitrogen inlet tubes to the electric cables, thermocouple effects may be induced into the signal. There is a type of emf created by temperature differences between two different metals at an electrical junction. This may produce a slowly varying low frequency effect as the liquid nitrogen evaporates plus a fast rising pulse when the liquid nitrogen starts to refill the system. Reference [srs96] suggests using a compensation junction, i.e., a second junction in reverse polarity which generates an emf to cancel the thermal potential of the first. Also, relocating the inlet tube and surrounding it with insulation would be helpful.

The Search for Superdeformation in Odd-Odd Praseodymium-132

Volume II

By

Christine Veronica Socha Hampton

A DISSERTATION

Submitted to
Michigan State University
in partial fulfillment of the requirements
for the Degree of

DOCTOR OF PHILOSOPHY

Department of Chemistry

1999

Appendices

Appendix A

Q_o-Value and E_{th} Calculations

Q_o-value calculations were performed using the OAK RIDGE software *KINEQ*, for possible products from the reaction ^{37}Cl on ^{100}Mo. The specific reaction formulae, along with the Q_o-value results are listed in the following Tables. The Tables, although extensive, are not all-inclusive because there is a seven particle-out specification limit within the program *KINEQ*. In addition, all significant Mo target isotopes were used, the relative abundances, of which, are listed in Table 4.1. 'Exact' nuclear masses, obtained from either Wapstra's Mass Table [wap85] or a set of mass formula coefficients [gar69], were used for the calculations. The method is listed in the Q_o-value tables as T or G, respectively. The column marked $\mathbf{m\ p}_{out}$ lists the total mass of the outgoing particles; $\mathbf{m\ P}_{residual}$ refers to the mass of the residual nucleus. Since the reaction under study is endothermic, energy threshold values, E_{th}, have also been included in the Tables for each reaction product. It should be emphasized that these are ground state Q_o-value calculations.

Table A.1: Calculated Q_o-Values and threshold energies, E_{th} for the Production of Pr Isotopes with a ^{37}Cl Beam on a Mo Target.

Reaction	**m p_{out}**	**m $P_{residual}$**	**Q_o-Value**	**Method**	**E_{th}**
$^{100}Mo(^{37}Cl,n)^{136}Pr$	1.008665	135.912633	-44.639119	T	61.15
$^{100}Mo(^{37}Cl,2n)^{135}Pr$	2.017330	134.913138	-53.180488	T	72.85
$^{100}Mo(^{37}Cl,3n)^{134}Pr$	3.025995	133.915435	-63.391857	T	86.84
$^{100}Mo(^{37}Cl,4n)^{133}Pr$	4.034660	132.916187	-72.163226	T	98.86
$^{100}Mo(^{37}Cl,5n)^{132}Pr$	5.043326	131.919118	-82.964595	T	113.66
$^{100}Mo(^{37}Cl,6n)^{131}Pr$	6.051991	130.920205	-92.048269	G	126.10
$^{100}Mo(^{37}Cl,7n)^{130}Pr$	7.060656	129.923524	-103.211310	G	141.39
$^{98}Mo(^{37}Cl,n)^{134}Pr$	1.008665	133.915435	-49.176319	T	67.74
$^{98}Mo(^{37}Cl,2n)^{133}Pr$	2.017330	132.916187	-57.947688	T	79.82
$^{98}Mo(^{37}Cl,3n)^{132}Pr$	3.025995	131.919118	-68.749057	T	94.70
$^{98}Mo(^{37}Cl,4n)^{131}Pr$	4.034660	130.920205	-77.832731	G	107.21
$^{98}Mo(^{37}Cl,5n)^{130}Pr$	5.043326	129.923524	-88.995772	G	122.59
$^{98}Mo(^{37}Cl,6n)^{129}Pr$	6.051991	128.924860	-98.311648	G	135.42
$^{98}Mo(^{37}Cl,7n)^{128}Pr$	7.060656	127.928799	-110.052814	G	151.60
$^{96}Mo(^{37}Cl,n)^{132}Pr$	1.008665	131.919118	-53.285219	T	73.82
$^{96}Mo(^{37}Cl,2n)^{131}Pr$	2.017330	130.920205	-62.368893	G	86.40
$^{96}Mo(^{37}Cl,3n)^{130}Pr$	3.025995	129.923524	-73.531934	G	101.87
$^{96}Mo(^{37}Cl,4n)^{129}Pr$	4.034660	128.924860	-82.847810	G	114.77
$^{96}Mo(^{37}Cl,5n)^{128}Pr$	5.043326	127.928799	-94.588976	G	131.04
$^{96}Mo(^{37}Cl,6n)^{127}Pr$	6.051991	126.930697	-104.428291	G	144.67
$^{96}Mo(^{37}Cl,7n)^{126}Pr$	7.060656	125.935201	-116.694851	G	161.67
$^{92}Mo(^{37}Cl,n)^{128}Pr$	1.008665	127.928799	-60.319400	G	84.57
$^{92}Mo(^{37}Cl,2n)^{127}Pr$	2.017330	126.930697	-70.158715	G	98.37
$^{92}Mo(^{37}Cl,3n)^{126}Pr$	3.025995	125.935201	-82.425275	G	115.57
$^{92}Mo(^{37}Cl,4n)^{125}Pr$	4.034660	124.937748	-92.868652	G	130.21
$^{92}Mo(^{37}Cl,5n)^{124}Pr$	5.043326	123.942829	-105.673298	G	148.17
$^{92}Mo(^{37}Cl,6n)^{123}Pr$	6.051991	122.945936	-116.638101	G	163.54

Table A.2: Calculated Q_o-Values and threshold energies, E_{th} for the Production of Ce Isotopes with a ^{37}Cl Beam on a Mo Target.

Reaction	**m p_{out}**	**m $P_{residual}$**	**Q_o-Value**	**Method**	E_{th}
^{100}Mo(^{37}Cl,p)^{136}Ce	1.007825	135.907137	-38.736780	T	53.06
^{100}Mo(^{37}Cl,p,n)^{135}Ce	2.016490	134.909115	-48.651149	T	66.65
^{100}Mo(^{37}Cl,p,2n)^{134}Ce	3.025155	133.908887	-56.509518	T	77.41
^{100}Mo(^{37}Cl,p,3n)^{133}Ce	4.033821	132.911356	-66.880887	T	91.62
^{100}Mo(^{37}Cl,p,4n)^{132}Ce	5.042486	131.911495	-75.082256	T	102.86
^{100}Mo(^{37}Cl,p,5n)^{131}Ce	6.051151	130.914265	-85.733625	T	117.45
^{100}Mo(^{37}Cl,p,6n)^{130}Ce	7.059816	129.914759	-94.264994	T	129.14
^{98}Mo(^{37}Cl,p)^{134}Ce	1.007825	133.908887	-42.293980	T	58.26
^{98}Mo(^{37}Cl,p,n)^{133}Ce	2.016490	132.911356	-52.665349	T	72.54
^{98}Mo(^{37}Cl,p,2n)^{132}Ce	3.025155	131.911495	-60.866718	T	83.84
^{98}Mo(^{37}Cl,p,3n)^{131}Ce	4.033821	130.914265	-71.518087	T	98.51
^{98}Mo(^{37}Cl,p,4n)^{130}Ce	5.042486	129.914759	-80.049456	T	110.27
^{98}Mo(^{37}Cl,p,5n)^{129}Ce	6.051151	128.918160	-91.288278	G	125.75
^{98}Mo(^{37}Cl,p,6n)^{128}Ce	7.059816	127.918968	-100.112460	G	137.91
^{96}Mo(^{37}Cl,p)^{132}Ce	1.007825	131.911495	-45.402880	T	62.90
^{96}Mo(^{37}Cl,p,n)^{131}Ce	2.016490	130.914265	-56.054249	T	77.65
^{96}Mo(^{37}Cl,p,2n)^{130}Ce	3.025155	129.914759	-64.585618	T	89.47
^{96}Mo(^{37}Cl,p,3n)^{129}Ce	4.033821	128.918160	-75.824440	G	105.04
^{96}Mo(^{37}Cl,p,4n)^{128}Ce	5.042486	127.918968	-84.648622	G	117.27
^{96}Mo(^{37}Cl,p,5n)^{127}Ce	6.051151	126.922828	-96.316061	G	133.43
^{96}Mo(^{37}Cl,p,6n)^{126}Ce	7.059816	125.924231	-105.693946	G	146.42
^{92}Mo(^{37}Cl,p)^{128}Ce	1.007825	127.918968	-50.379046	G	70.64
^{92}Mo(^{37}Cl,p,n)^{127}Ce	2.016490	126.922828	-62.046485	G	86.99
^{92}Mo(^{37}Cl,p,2n)^{126}Ce	3.025155	125.924231	-71.424370	G	100.14
^{92}Mo(^{37}Cl,p,3n)^{125}Ce	4.033821	124.928681	-83.640395	G	117.27
^{92}Mo(^{37}Cl,p,4n)^{124}Ce	5.042486	123.930635	-93.532256	G	131.14
^{92}Mo(^{37}Cl,p,5n)^{123}Ce	6.051151	122.935579	-106.209215	G	148.92
^{92}Mo(^{37}Cl,p,6n)^{122}Ce	7.059816	121.938097	-116.626166	G	163.53

Table A.3: Calculated Q_o-Values and threshold energies, E_{th} for the Production of La Isotopes with a ^{37}Cl Beam on a Mo Target.

Reaction	**m p_{out}**	**m $P_{residual}$**	**Q_o-Value**	**Method**	E_{th}
$^{100}Mo(^{37}Cl,2p)^{135}La$	2.015650	134.906951	-45.852810	T	62.81
$^{100}Mo(^{37}Cl,2p,n)^{134}La$	3.024316	133.908457	-55.327179	T	75.79
$^{100}Mo(^{37}Cl,2p,2n)^{133}La$	4.032981	132.908135	-63.098548	T	86.44
$^{100}Mo(^{37}Cl,2p,3n)^{132}La$	5.041646	131.910100	-72.999917	T	100.00
$^{100}Mo(^{37}Cl,2p,4n)^{131}La$	6.050311	130.910078	-81.051286	T	111.04
$^{100}Mo(^{37}Cl,2p,5n)^{130}La$	7.058976	129.912397	-91.282655	T	125.05
$^{98}Mo(^{37}Cl,2p)^{133}La$	2.015650	132.908135	-48.883010	T	67.33
$^{98}Mo(^{37}Cl,2p,n)^{132}La$	3.024316	131.910100	-58.784379	T	80.97
$^{98}Mo(^{37}Cl,2p,2n)^{131}La$	4.032981	130.910078	-66.835748	T	92.06
$^{98}Mo(^{37}Cl,2p,3n)^{130}La$	5.041646	129.912397	-77.067117	T	106.16
$^{98}Mo(^{37}Cl,2p,4n)^{129}La$	6.050311	128.912633	-85.358486	T	117.58
$^{98}Mo(^{37}Cl,2p,5n)^{128}La$	7.058976	127.915317	-95.929855	T	132.14
$^{96}Mo(^{37}Cl,2p)^{131}La$	2.015650	130.910078	-51.371910	T	71.17
$^{96}Mo(^{37}Cl,2p,n)^{130}La$	3.024316	129.912397	-61.603279	T	85.34
$^{96}Mo(^{37}Cl,2p,2n)^{129}La$	4.032981	128.912633	-69.894648	T	96.83
$^{96}Mo(^{37}Cl,2p,3n)^{128}La$	5.041646	127.915317	-80.466017	T	111.47
$^{96}Mo(^{37}Cl,2p,4n)^{127}La$	6.050311	126.916284	-89.437386	T	123.90
$^{96}Mo(^{37}Cl,2p,5n)^{126}La$	7.058976	125.919589	-100.588060	G	139.35
$^{92}Mo(^{37}Cl,2p)^{127}La$	2.015650	126.916284	-55.167810	T	77.35
$^{92}Mo(^{37}Cl,2p,n)^{126}La$	3.024316	125.919589	-66.318484	G	92.98
$^{92}Mo(^{37}Cl,2p,2n)^{125}La$	4.032981	124.920938	-75.645587	G	106.06
$^{92}Mo(^{37}Cl,2p,3n)^{124}La$	5.041646	123.924795	-87.310339	G	122.42
$^{92}Mo(^{37}Cl,2p,4n)^{123}La$	6.050311	122.926612	-97.074278	G	136.11
$^{92}Mo(^{37}Cl,2p,5n)^{122}La$	7.058976	121.930969	-109.203385	G	153.12

Table A.4: Calculated Q_o-Values and threshold energies, E_{th} for the Production of La Isotopes with a ^{37}Cl Beam on a Mo Target: α Particle out.

Reaction	**m p_{out}**	**m $P_{residual}$**	**Q_o-Value**	**Method**	E_{th}
$^{100}Mo(^{37}Cl,\alpha)^{133}La$	4.002603	132.908135	-34.802670	T	47.67
$^{100}Mo(^{37}Cl,\alpha,n)^{132}La$	5.011268	131.910100	-44.704039	T	61.24
$^{100}Mo(^{37}Cl,\alpha,2n)^{131}La$	6.019934	130.910078	-52.755408	T	72.27
$^{100}Mo(^{37}Cl,\alpha,3n)^{130}La$	7.028599	129.912397	-62.986777	T	86.29
$^{100}Mo(^{37}Cl,\alpha,4n)^{129}La$	8.037264	128.912633	-71.278146	T	97.65
$^{100}Mo(^{37}Cl,\alpha,5n)^{128}La$	9.045929	127.915317	-81.849515	T	112.13
$^{100}Mo(^{37}Cl,\alpha,6n)^{127}La$	10.054594	126.916284	-90.820884	T	124.42
$^{98}Mo(^{37}Cl,\alpha)^{131}La$	4.002603	130.910078	-38.539870	T	53.09
$^{98}Mo(^{37}Cl,\alpha,n)^{130}La$	5.011268	129.912397	-48.771239	T	67.18
$^{98}Mo(^{37}Cl,\alpha,2n)^{129}La$	6.019934	128.912633	-57.062608	T	78.60
$^{98}Mo(^{37}Cl,\alpha,3n)^{128}La$	7.028599	127.915317	-67.633977	T	93.16
$^{98}Mo(^{37}Cl,\alpha,4n)^{127}La$	8.037264	126.916284	-76.605346	T	105.52
$^{98}Mo(^{37}Cl,\alpha,5n)^{126}La$	9.045929	125.919589	-87.756020	G	120.88
$^{98}Mo(^{37}Cl,\alpha,6n)^{125}La$	10.054594	124.920938	-97.083123	G	133.73
$^{96}Mo(^{37}Cl,\alpha)^{129}La$	4.002603	128.912633	-41.598770	T	57.63
$^{96}Mo(^{37}Cl,\alpha,n)^{128}La$	5.011268	127.915317	-52.170139	T	72.27
$^{96}Mo(^{37}Cl,\alpha,2n)^{127}La$	6.019934	126.916284	-61.141508	T	84.70
$^{96}Mo(^{37}Cl,\alpha,3n)^{126}La$	7.028599	125.919589	-72.292182	G	100.15
$^{96}Mo(^{37}Cl,\alpha,4n)^{125}La$	8.037264	124.920938	-81.619285	G	113.07
$^{96}Mo(^{37}Cl,\alpha,5n)^{124}La$	9.045929	123.924795	-93.284037	G	129.23
$^{96}Mo(^{37}Cl,\alpha,6n)^{123}La$	10.054594	122.926612	-103.047976	G	142.76
$^{92}Mo(^{37}Cl,\alpha)^{125}La$	4.002603	124.920938	-47.349709	G	66.39
$^{92}Mo(^{37}Cl,\alpha,n)^{124}La$	5.011268	123.924795	-59.014461	G	82.74
$^{92}Mo(^{37}Cl,\alpha,2n)^{123}La$	6.019934	122.926612	-68.778400	G	96.43
$^{92}Mo(^{37}Cl,\alpha,3n)^{122}La$	7.028599	121.930969	-80.907507	G	113.44
$^{92}Mo(^{37}Cl,\alpha,4n)^{121}La$	8.037264	120.933429	-91.270748	G	127.97
$^{92}Mo(^{37}Cl,\alpha,5n)^{120}La$	9.045929	119.938301	-103.880566	G	145.65
$^{92}Mo(^{37}Cl,\alpha,6n)^{119}La$	10.054594	118.941103	-114.561677	G	160.63

Table A.5: Calculated Q_o-Values and threshold energies, E_{th} for the Production of Ba Isotopes with a ^{37}Cl Beam on a Mo Target.

Reaction	**m p_{out}**	**m $P_{residual}$**	**Q_o-Value**	**Method**	E_{th}
$^{100}Mo(^{37}Cl,3p)^{134}Ba$	3.023476	133.904483	-50.842840	T	69.65
$^{100}Mo(^{37}Cl,3p,n)^{133}Ba$	4.032141	132.905986	-60.314209	T	82.63
$^{100}Mo(^{37}Cl,3p,2n)^{132}Ba$	5.040806	131.905040	-67.504578	T	92.48
$^{100}Mo(^{37}Cl,3p,3n)^{131}Ba$	6.049471	130.906900	-77.307947	T	105.91
$^{100}Mo(^{37}Cl,3p,4n)^{130}Ba$	7.058136	129.906279	-84.801316	T	116.17
$^{98}Mo(^{37}Cl,3p)^{132}Ba$	3.023476	131.905040	-53.289040	T	73.40
$^{98}Mo(^{37}Cl,3p,n)^{131}Ba$	4.032141	130.906900	-63.092409	T	86.91
$^{98}Mo(^{37}Cl,3p,2n)^{130}Ba$	5.040806	129.906279	-70.585778	T	97.23
$^{98}Mo(^{37}Cl,3p,3n)^{129}Ba$	6.049471	128.908640	-80.856147	T	111.38
$^{98}Mo(^{37}Cl,3p,4n)^{128}Ba$	7.058136	127.908234	-88.549516	T	121.98
$^{96}Mo(^{37}Cl,3p)^{130}Ba$	3.023476	129.906279	-55.121940	T	76.36
$^{96}Mo(^{37}Cl,3p,n)^{129}Ba$	4.032141	128.908640	-65.392309	T	90.59
$^{96}Mo(^{37}Cl,3p,2n)^{128}Ba$	5.040806	127.908234	-73.085678	T	101.25
$^{96}Mo(^{37}Cl,3p,3n)^{127}Ba$	6.049471	126.911130	-83.855047	T	116.17
$^{96}Mo(^{37}Cl,3p,4n)^{126}Ba$	7.058136	125.911259	-92.046416	T	127.52
$^{92}Mo(^{37}Cl,3p)^{126}Ba$	3.023476	125.911259	-57.776840	T	81.01
$^{92}Mo(^{37}Cl,3p,n)^{125}Ba$	4.032141	124.914641	-68.998209	T	96.74
$^{92}Mo(^{37}Cl,3p,2n)^{124}Ba$	5.040806	123.915382	-77.759578	T	109.03
$^{92}Mo(^{37}Cl,3p,3n)^{123}Ba$	6.049471	122.919204	-89.390947	T	125.34
$^{92}Mo(^{37}Cl,3p,4n)^{122}Ba$	7.058136	121.920170	-98.362316	T	137.92

Table A.6: Calculated Q_o-Values and threshold energies, E_{th} for the Production of Cs Isotopes with a ^{37}Cl Beam on a Mo Target.

Reaction	**m p_{out}**	**$P_{residual}$**	**Q_o-Value**	**Method**	E_{th}
$^{100}Mo(^{37}Cl,4p)^{133}Cs$	4.031301	132.905427	-59.010870	T	80.84
$^{100}Mo(^{37}Cl,4p,n)^{132}Cs$	5.039966	131.906428	-68.015239	T	93.18
$^{100}Mo(^{37}Cl,4p,2n)^{131}Cs$	6.048631	130.905442	-75.167608	T	102.97
$^{100}Mo(^{37}Cl,4p,3n)^{130}Cs$	7.057296	129.906751	-84.458977	T	115.70
$^{98}Mo(^{37}Cl,4p)^{131}Cs$	4.031301	130.905442	-60.952070	T	83.96
$^{98}Mo(^{37}Cl,4p,n)^{130}Cs$	5.039966	129.906751	-70.243439	T	96.76
$^{98}Mo(^{37}Cl,4p,2n)^{129}Cs$	6.048631	128.906025	-77.637808	T	106.94
$^{98}Mo(^{37}Cl,4p,3n)^{128}Cs$	7.057296	127.907753	-87.319177	T	120.28
$^{96}Mo(^{37}Cl,4p)^{129}Cs$	4.031301	128.906025	-62.173970	T	86.13
$^{96}Mo(^{37}Cl,4p,n)^{128}Cs$	5.039966	127.907753	-71.855339	T	99.54
$^{96}Mo(^{37}Cl,4p,2n)^{127}Cs$	6.048631	126.907426	-79.621708	T	110.30
$^{96}Mo(^{37}Cl,4p,3n)^{126}Cs$	7.057296	125.909462	-89.590077	T	124.11
$^{92}Mo(^{37}Cl,4p)^{125}Cs$	4.031301	124.909722	-63.633870	T	89.22
$^{92}Mo(^{37}Cl,4p,n)^{124}Cs$	5.039966	123.912268	-74.077239	T	103.86
$^{92}Mo(^{37}Cl,4p,2n)^{123}Cs$	6.048631	122.912988	-82.818608	T	116.12
$^{92}Mo(^{37}Cl,4p,3n)^{122}Cs$	7.057296	121.916090	-93.779977	T	131.49

Table A.7: Calculated Q_o-Values and threshold energies E_{th} for the Production of Cs Isotopes with a ^{37}Cl Beam on a Mo Target: α Particle out.

Reaction	**m p_{out}**	**m $P_{residual}$**	**Q_o-Value**	**Method**	E_{th}
^{100}Mo(^{37}Cl,2α)^{129}Cs	8.005207	128.906025	-35.261590	T	48.30
^{100}Mo(^{37}Cl,2α,n)^{128}Cs	9.013872	127.907753	-44.942959	T	61.57
^{100}Mo(^{37}Cl,2α,2n)^{127}Cs	10.022537	126.907426	-52.709328	T	72.21
^{100}Mo(^{37}Cl,2α,3n)^{126}Cs	11.031202	125.909462	-62.677697	T	85.86
^{100}Mo(^{37}Cl,2α,4n)^{125}Cs	12.039867	124.909722	-70.991066	T	97.25
^{100}Mo(^{37}Cl,2α,5n)^{124}Cs	13.048532	123.912268	-81.434435	T	111.56
^{98}Mo(^{37}Cl,2α)^{127}Cs	8.005207	126.907426	-38.493790	T	53.02
^{98}Mo(^{37}Cl,2α,n)^{126}Cs	9.013872	125.909462	-48.462159	T	66.75
^{98}Mo(^{37}Cl,2α,2n)^{125}Cs	10.022537	124.909722	-56.775528	T	78.21
^{98}Mo(^{37}Cl,2α,3n)^{124}Cs	11.031202	123.912268	-67.218897	T	92.59
^{98}Mo(^{37}Cl,2α,4n)^{123}Cs	12.039867	122.912988	-75.960266	T	104.63
^{98}Mo(^{37}Cl,2α,5n)^{122}Cs	13.048532	121.916090	-86.921635	T	119.73
^{96}Mo(^{37}Cl,2α)^{125}Cs	8.005207	124.909722	-41.311690	T	57.23
^{96}Mo(^{37}Cl,2α,n)^{124}Cs	9.013872	123.912268	-51.755059	T	71.70
^{96}Mo(^{37}Cl,2α,2n)^{123}Cs	10.022537	122.912988	-60.496428	T	83.81
^{96}Mo(^{37}Cl,2α,3n)^{122}Cs	11.031202	121.916090	-71.457797	T	98.99
^{96}Mo(^{37}Cl,2α,4n)^{121}Cs	12.039867	120.917239	-80.599166	T	111.66
^{96}Mo(^{37}Cl,2α,5n)^{120}Cs	13.048532	119.920803	-91.990535	T	127.44
^{92}Mo(^{37}Cl,2α)^{121}Cs	8.005207	120.917239	-46.329590	T	64.96
^{92}Mo(^{37}Cl,2α,n)^{120}Cs	9.013872	119.920803	-57.720959	T	80.93
^{92}Mo(^{37}Cl,2α,2n)^{119}Cs	10.022537	118.922489	-67.362328	T	94.45
^{92}Mo(^{37}Cl,2α,3n)^{118}Cs	11.031202	117.926740	-79.393697	T	111.32
^{92}Mo(^{37}Cl,2α,4n)^{117}Cs	12.039867	116.928898	-89.475066	T	125.45
^{92}Mo(^{37}Cl,2α,5n)^{116}Cs	13.048532	115.933117	-101.476435	T	142.28

Table A.8: Calculated Q_o-Values and threshold energies E_{th} for the Production of I Isotopes with a ^{37}Cl Beam on a Mo Target.

Reaction	**m p_{out}**	**m $P_{residual}$**	**Q_o-Value**	**Method**	E_{th}
$^{100}Mo(^{37}Cl,6p)^{131}I$	6.046951	130.906112	-74.226930	T	101.69
$^{100}Mo(^{37}Cl,6p,n)^{130}I$	7.055617	129.906711	-82.856299	T	113.51
$^{98}Mo(^{37}Cl,6p)^{129}I$	6.046951	128.904983	-75.103130	T	103.45
$^{98}Mo(^{37}Cl,6p,n)^{128}I$	7.055617	127.905808	-83.942499	T	115.63
$^{96}Mo(^{37}Cl,6p)^{127}I$	6.046951	126.904470	-75.304030	T	104.32
$^{96}Mo(^{37}Cl,6p,n)^{126}I$	7.055617	125.905621	-84.447399	T	116.99
$^{92}Mo(^{37}Cl,6p)^{123}I$	6.046951	122.905592	-74.364930	T	104.27
$^{92}Mo(^{37}Cl,6p,n)^{122}I$	7.055617	121.907593	-84.300299	T	118.20
$^{100}Mo(^{37}Cl,\alpha,2p)^{127}I$	10.020857	126.904470	-48.391650	T	66.29
$^{100}Mo(^{37}Cl,\alpha,2p,n)^{126}I$	11.029522	125.905621	-57.535019	T	78.82
$^{100}Mo(^{37}Cl,\alpha,2p,2n)^{125}I$	12.038187	124.904617	-64.671588	T	88.60
$^{100}Mo(^{37}Cl,\alpha,2p,3n)^{124}I$	13.046852	123.906205	-74.221757	T	101.68
$^{98}Mo(^{37}Cl,\alpha,2p)^{125}I$	10.020857	124.904617	-50.456050	T	69.50
$^{98}Mo(^{37}Cl,\alpha,2p,n)^{124}I$	11.029522	123.906205	-60.006219	T	82.66
$^{98}Mo(^{37}Cl,\alpha,2p,2n)^{123}I$	12.038187	122.905592	-67.506588	T	92.99
$^{98}Mo(^{37}Cl,\alpha,2p,3n)^{122}I$	13.046852	121.907593	-77.441957	T	106.68
$^{96}Mo(^{37}Cl,\alpha,2p)^{123}I$	10.020857	122.905592	-52.042750	T	72.10
$^{96}Mo(^{37}Cl,\alpha,2p,n)^{122}I$	11.029522	121.907593	-61.978119	T	85.86
$^{96}Mo(^{37}Cl,\alpha,2p,2n)^{121}I$	12.038187	120.907391	-69.861488	T	96.78
$^{96}Mo(^{37}Cl,\alpha,2p,3n)^{120}I$	13.046852	119.909842	-80.215857	T	111.13
$^{92}Mo(^{37}Cl,\alpha,2p)^{119}I$	10.020857	118.910025	-54.187650	T	75.98
$^{92}Mo(^{37}Cl,\alpha,2p,n)^{118}I$	11.029522	117.912773	-64.819019	T	90.88
$^{92}Mo(^{37}Cl,\alpha,2p,2n)^{117}I$	12.038187	116.913460	-73.530388	T	103.10
$^{92}Mo(^{37}Cl,\alpha,2p,3n)^{116}I$	13.046852	115.916777	-84.691757	T	118.75

Table A.9: Calculated Q_o-Values and threshold energies, E_{th} for the Production of Xe Isotopes with a ^{37}Cl Beam on a Mo Target.

Reaction	**m p_{out}**	**$P_{residual}$**	**Q_o-Value**	**Method**	E_{th}
$^{100}Mo(^{37}Cl,5p)^{132}Xe$	5.039126	131.904142	-65.102900	T	89.19
$^{100}Mo(^{37}Cl,5p,n)^{131}Xe$	6.047791	130.905069	-74.038269	T	101.43
$^{100}Mo(^{37}Cl,5p,2n)^{130}Xe$	7.056456	129.903507	-80.654538	T	110.49
$^{98}Mo(^{37}Cl,5p)^{130}Xe$	5.039126	129.903507	-66.439000	T	91.52
$^{98}Mo(^{37}Cl,5p,n)^{129}Xe$	6.047791	128.904778	-75.694069	T	104.27
$^{98}Mo(^{37}Cl,5p,2n)^{128}Xe$	7.056456	127.903529	-82.602038	T	113.78
$^{96}Mo(^{37}Cl,5p)^{128}Xe$	5.039126	127.903529	-67.138200	T	93.01
$^{96}Mo(^{37}Cl,5p,n)^{127}Xe$	6.047791	126.905180	-76.747369	T	106.32
$^{96}Mo(^{37}Cl,5p,2n)^{126}Xe$	7.056456	125.904279	-83.979738	T	116.34
$^{92}Mo(^{37}Cl,5p)^{124}Xe$	5.039126	123.905892	-67.355300	T	94.44
$^{92}Mo(^{37}Cl,5p,n)^{123}Xe$	6.047791	122.908467	-77.825269	T	109.12
$^{92}Mo(^{37}Cl,5p,2n)^{122}Xe$	7.056456	121.908167	-85.617638	T	120.05
$^{100}Mo(^{37}Cl,\alpha,p,n)^{127}Xe$	10.021697	126.905180	-49.834989	T	68.27
$^{100}Mo(^{37}Cl,\alpha,p,2n)^{126}Xe$	11.030362	125.904279	-57.067358	T	78.18
$^{100}Mo(^{37}Cl,\alpha,p,3n)^{125}Xe$	12.039027	124.906394	-67.109227	T	91.93
$^{100}Mo(^{37}Cl,\alpha,p,4n)^{124}Xe$	13.047692	123.905892	-74.712496	T	102.35
$^{98}Mo(^{37}Cl,\alpha,p)^{126}Xe$	9.013032	125.904279	-42.851820	T	59.03
$^{98}Mo(^{37}Cl,\alpha,p,n)^{125}Xe$	10.021697	124.906394	-52.893689	T	72.86
$^{98}Mo(^{37}Cl,\alpha,p,2n)^{124}Xe$	11.030362	123.905892	-60.496958	T	83.33
$^{98}Mo(^{37}Cl,\alpha,p,3n)^{123}Xe$	12.039027	122.908467	-70.966927	T	97.76
$^{98}Mo(^{37}Cl,\alpha,p,4n)^{122}Xe$	13.047692	121.908167	-78.759296	T	108.49
$^{96}Mo(^{37}Cl,\alpha,p)^{124}Xe$	9.013032	123.905892	-45.033120	T	62.38
$^{96}Mo(^{37}Cl,\alpha,p,n)^{123}Xe$	10.021697	122.908467	-55.503089	T	76.89
$^{96}Mo(^{37}Cl,\alpha,p,2n)^{122}Xe$	11.030362	121.908167	-63.295458	T	87.69
$^{96}Mo(^{37}Cl,\alpha,p,3n)^{121}Xe$	12.039027	120.911442	-74.416827	T	103.09
$^{96}Mo(^{37}Cl,\alpha,p,4n)^{120}Xe$	13.047692	119.911936	-82.948196	T	114.91
$^{92}Mo(^{37}Cl,\alpha,p)^{120}Xe$	9.013032	119.911936	-48.678620	T	68.25
$^{92}Mo(^{37}Cl,\alpha,p,n)^{119}Xe$	10.021697	118.915382	-59.959989	T	84.07
$^{92}Mo(^{37}Cl,\alpha,p,2n)^{118}Xe$	11.030362	117.916208	-68.801358	T	96.47
$^{92}Mo(^{37}Cl,\alpha,p,3n)^{117}Xe$	12.039027	116.920245	-80.632727	T	113.06
$^{92}Mo(^{37}Cl,\alpha,p,4n)^{116}Xe$	13.047692	115.921608	-89.974096	T	126.15

Appendix B

Spin Population Matrices

The *CASCADE* calculations produce spin population matrices for residual nuclei formed from the compound nucleus of the reaction. Cross sections and excitation energies produced with a ^{37}Cl beam on a ^{100}Mo target have been deduced for each unit ($\hbar\omega$) of angular momentum (spin state) of the excited residual nucleus. Note that the excitation energy (E_{ex}) is calculated as the difference between the energy of the excited state (Q_{ex}) and the energy of the ground state (Q_o). This type of information may also be obtained by acquiring the outgoing particle (n, p, α) spectra along with γ rays during the reaction. [gui87]

This Appendix contains the Spin Population matrices for ^{132}Pr, ^{133}Pr, and ^{132}Ce using the Seeger nuclear Mass Model (Nm 5) at various beam energies. Chapter 3 contains results using the Groote-Hilf-Takahaski nuclear model (Nm 3) at 160 MeV.

Part A of each plot is a 3-D representation of spin ($\hbar\omega$) versus excitation energy (E_{ex}) versus cross section (μbarns). At times, there are various maxima observed which (it is speculated) might be interpreted as separate decay modes. This is more obvious on the accompaning contour plot in part B. The contour shows the log of the cross section as dotted curves. The edge of the plot from the upper right to the lower left approximates the yrast line, below which, no reactions occur.

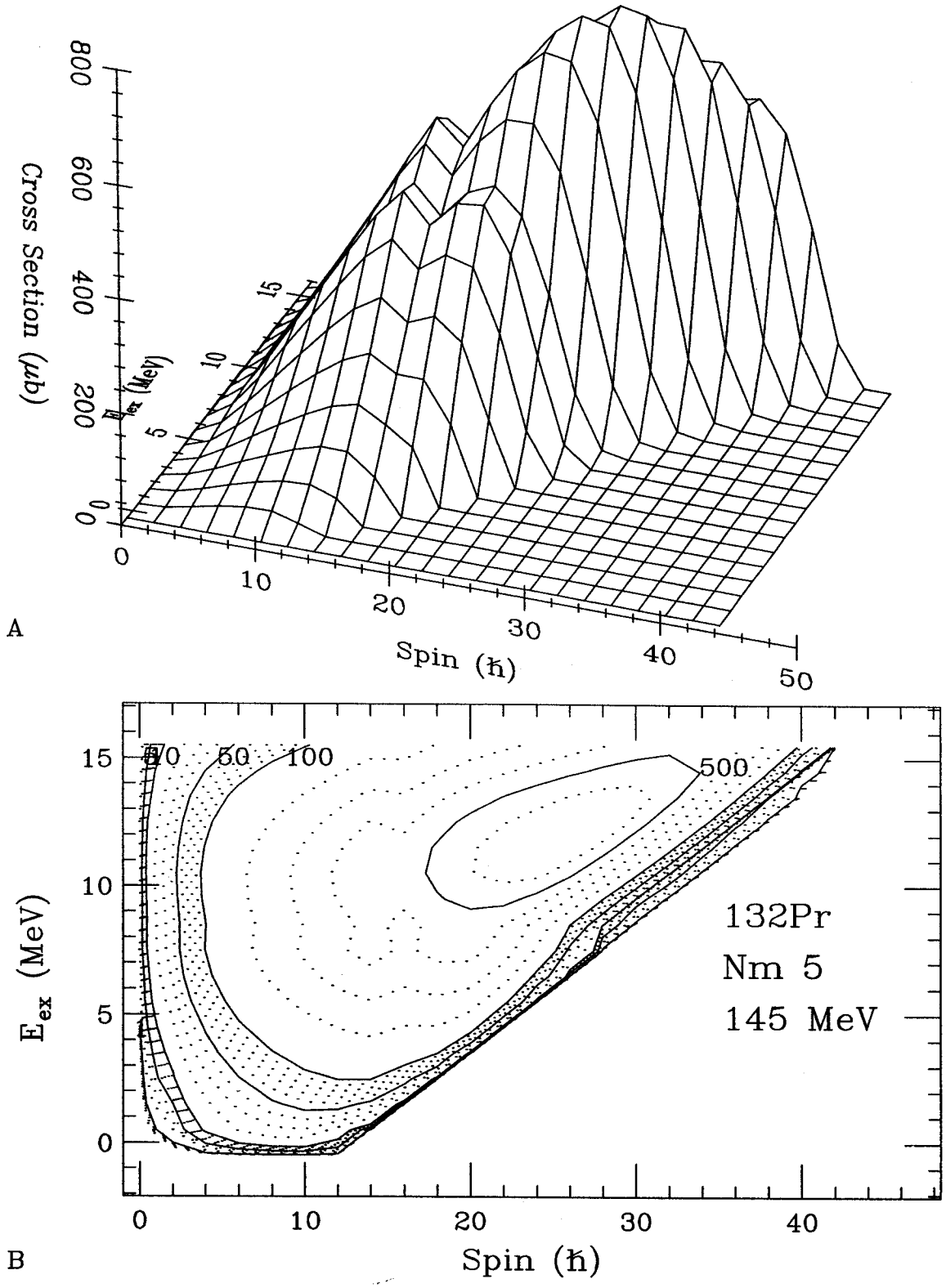

Figure B.1: A) 3-D spin population matrix for ^{132}Pr, calculated for the reaction: 145 MeV. ^{37}Cl on ^{100}Mo using the Seeger nuclear mass model (Nm 5). B) The same data plotted in a contour format with the log of the cross section represented by the dotted curves.

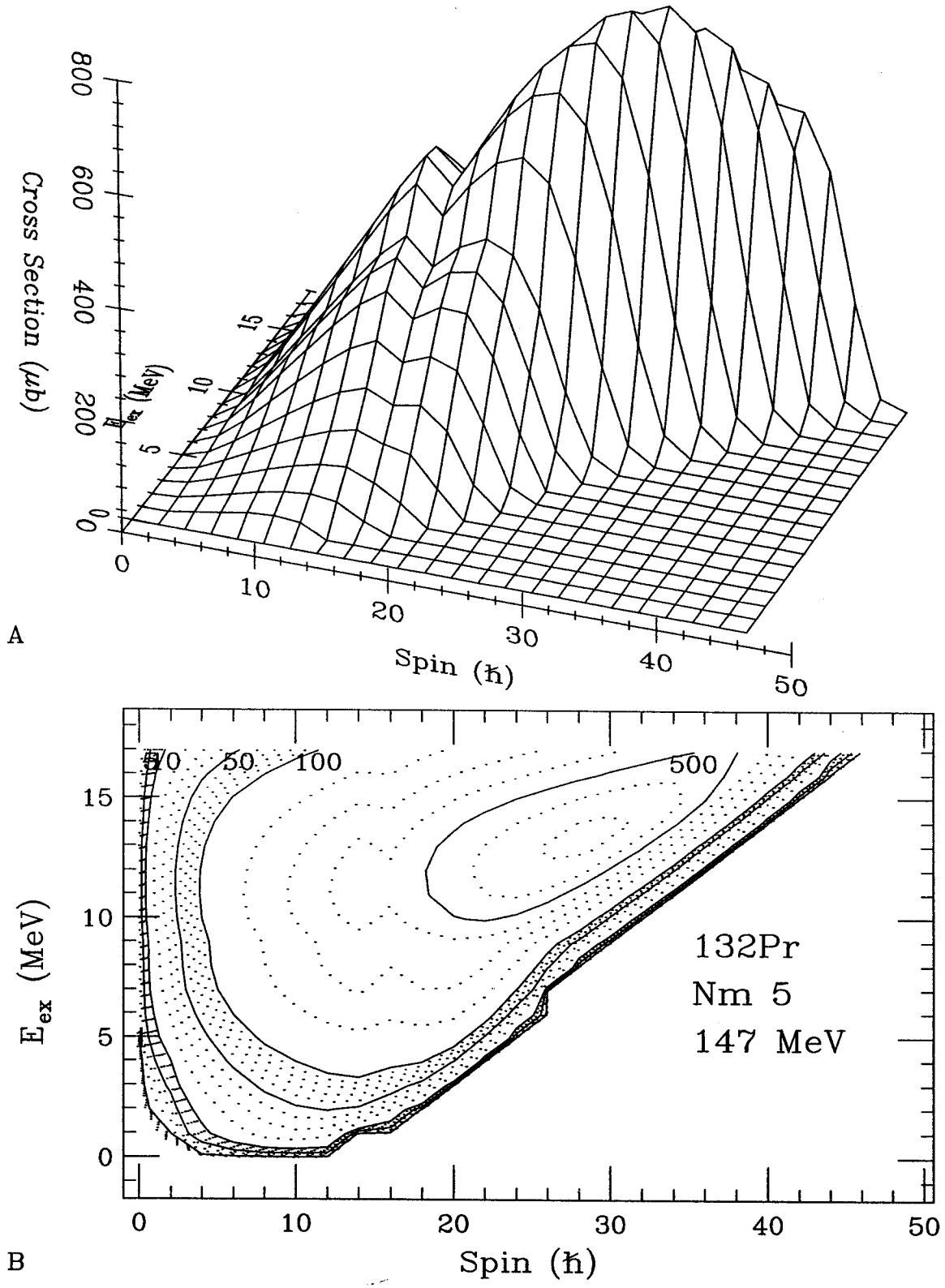

Figure B.2: A) 3-D spin population matrix for ^{132}Pr, calculated for the reaction: 147 MeV. ^{37}Cl on ^{100}Mo using the Seeger nuclear mass model (Nm 5). B) The same data plotted in a contour format with the log of the cross section represented by the dotted curves.

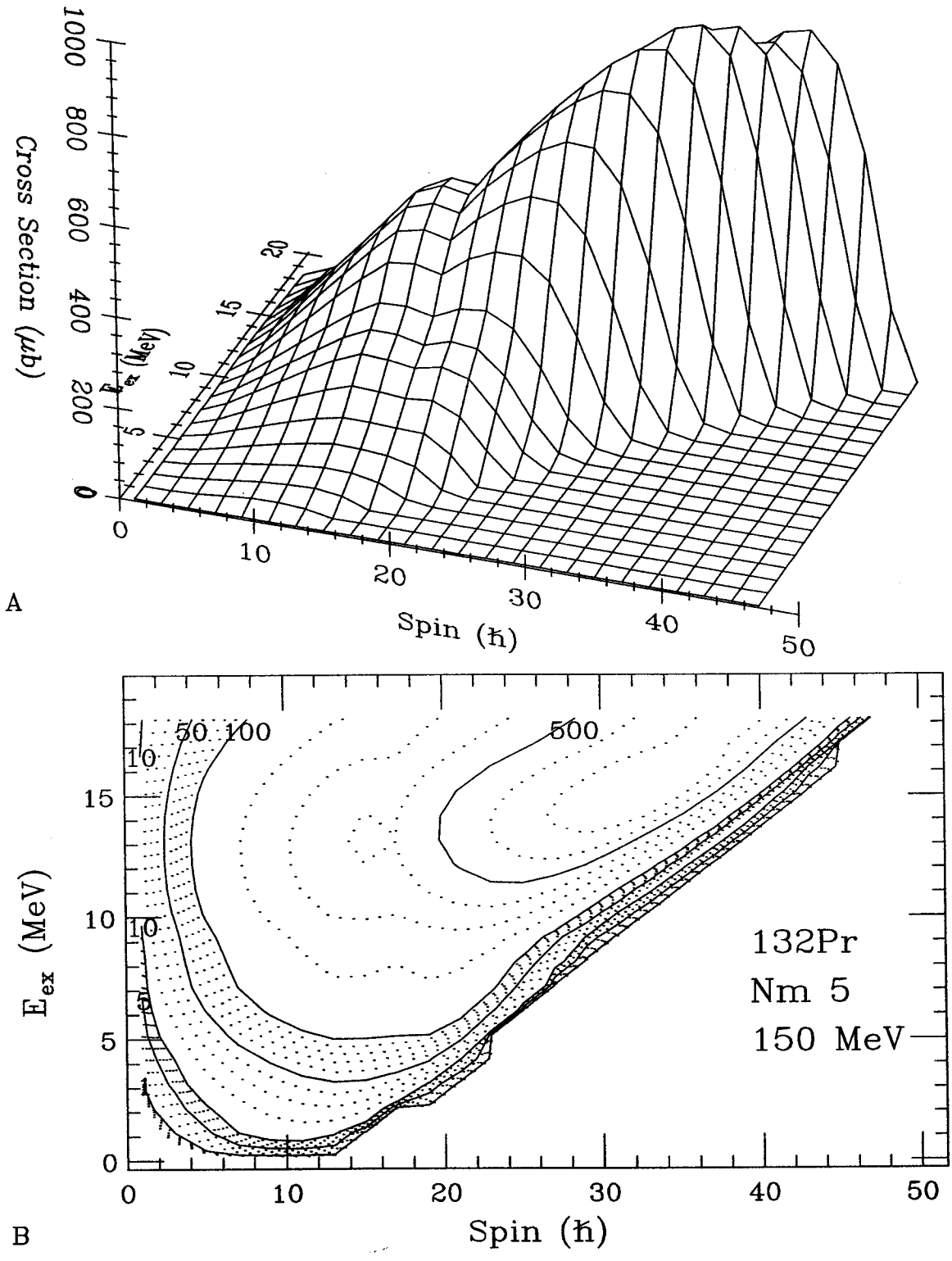

Figure B.3: A) 3-D spin population matrix for ^{132}Pr, calculated for the reaction: 150 MeV. ^{37}Cl on ^{100}Mo using the Seeger nuclear mass model (Nm 5). B) The same data plotted in a contour format with the log of the cross section represented by the dotted curves.

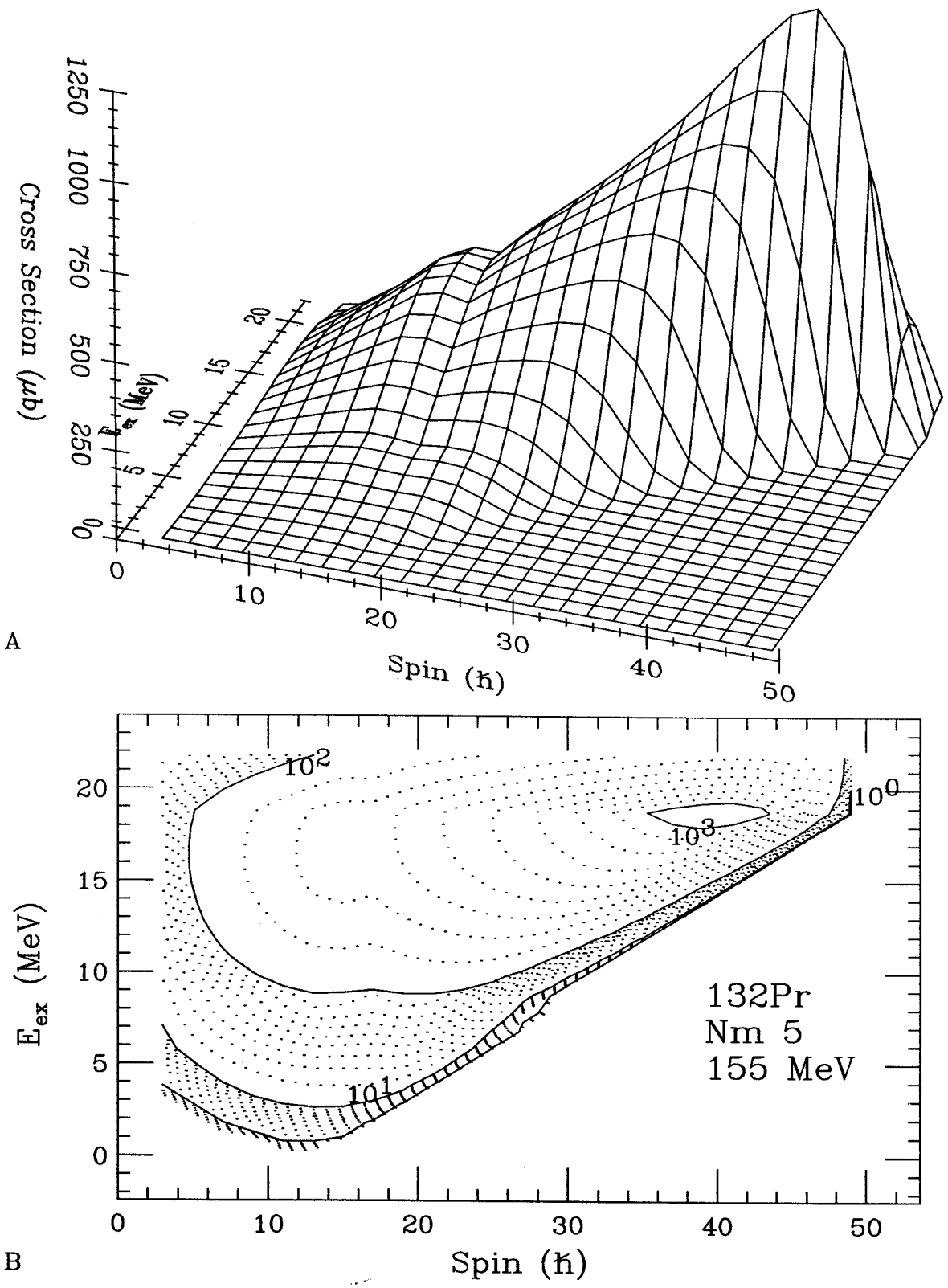

Figure B.4: A) 3-D spin population matrix for ^{132}Pr, calculated for the reaction: 155 MeV. ^{37}Cl on ^{100}Mo using the Seeger nuclear mass model (Nm 5). B) The same data plotted in a contour format with the log of the cross section represented by the dotted curves.

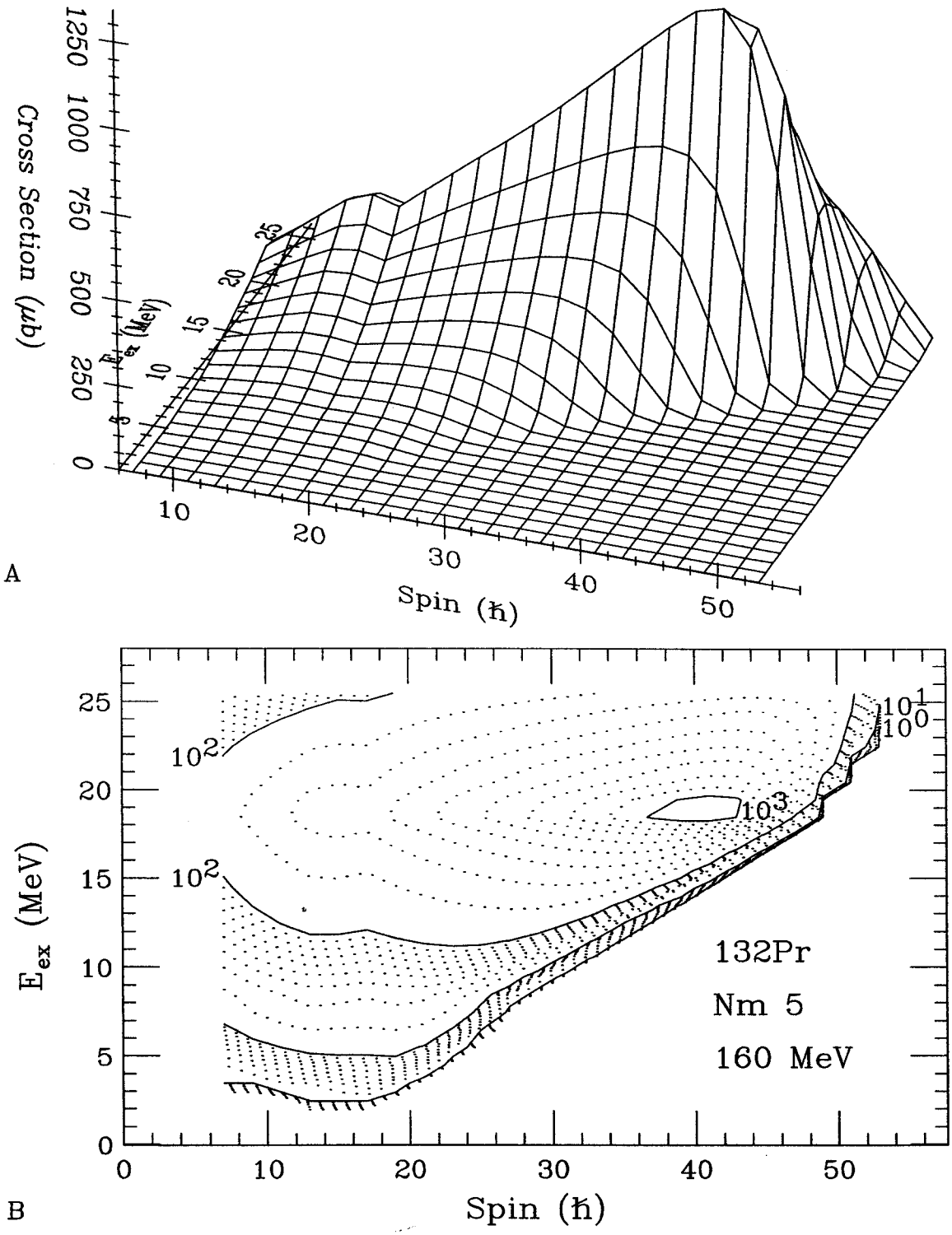

Figure B.5: A) 3-D spin population matrix for ^{132}Pr, calculated for the reaction: 160 MeV. ^{37}Cl on ^{100}Mo using the Seeger nuclear mass model (Nm 5). B) The same data plotted in a contour format with the log of the cross section represented by the dotted curves.

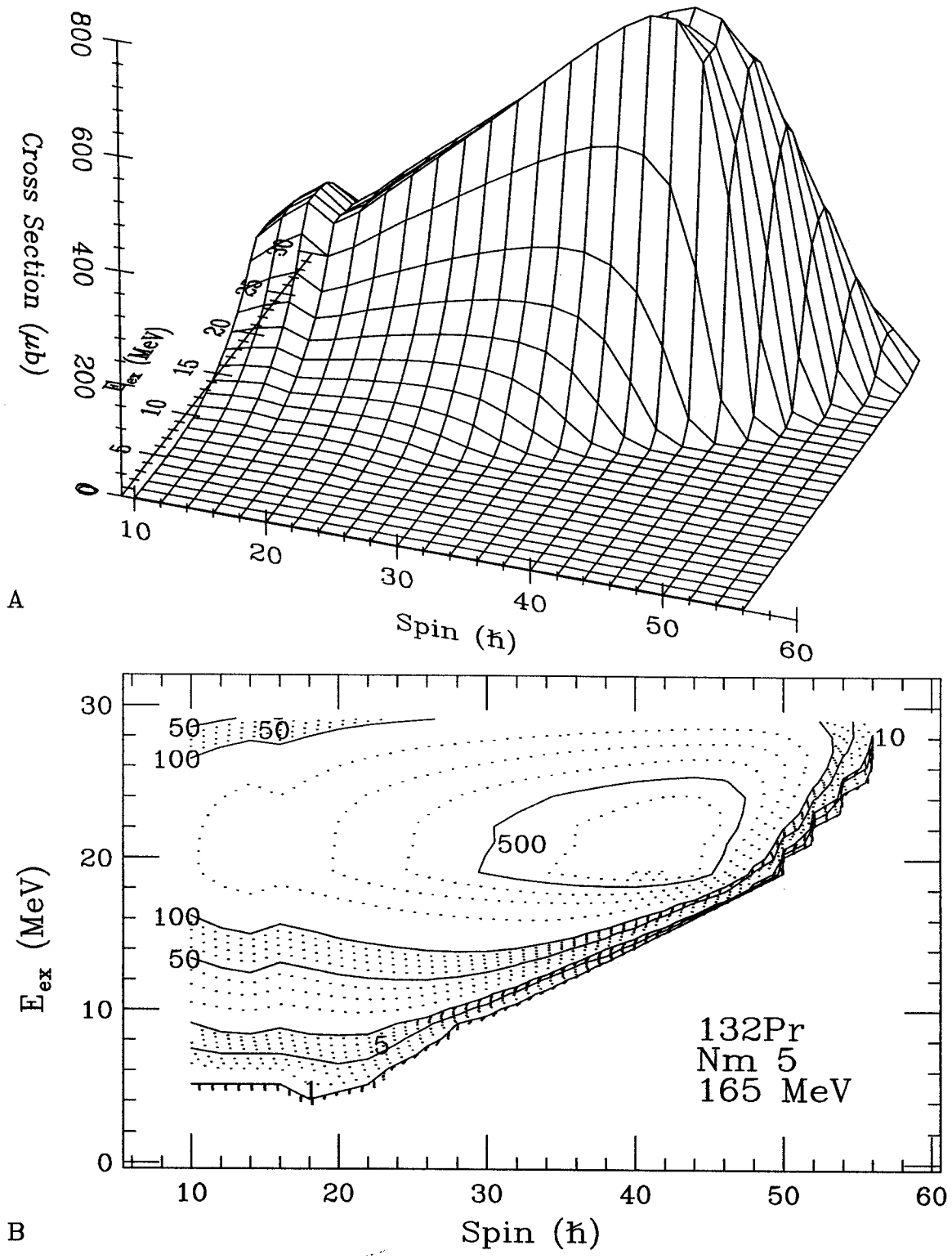

Figure B.6: A) 3-D spin population matrix for ^{132}Pr, calculated for the reaction: 165 MeV. ^{37}Cl on ^{100}Mo using the Seeger nuclear mass model (Nm 5). B) The same data plotted in a contour format with the log of the cross section represented by the dotted curves.

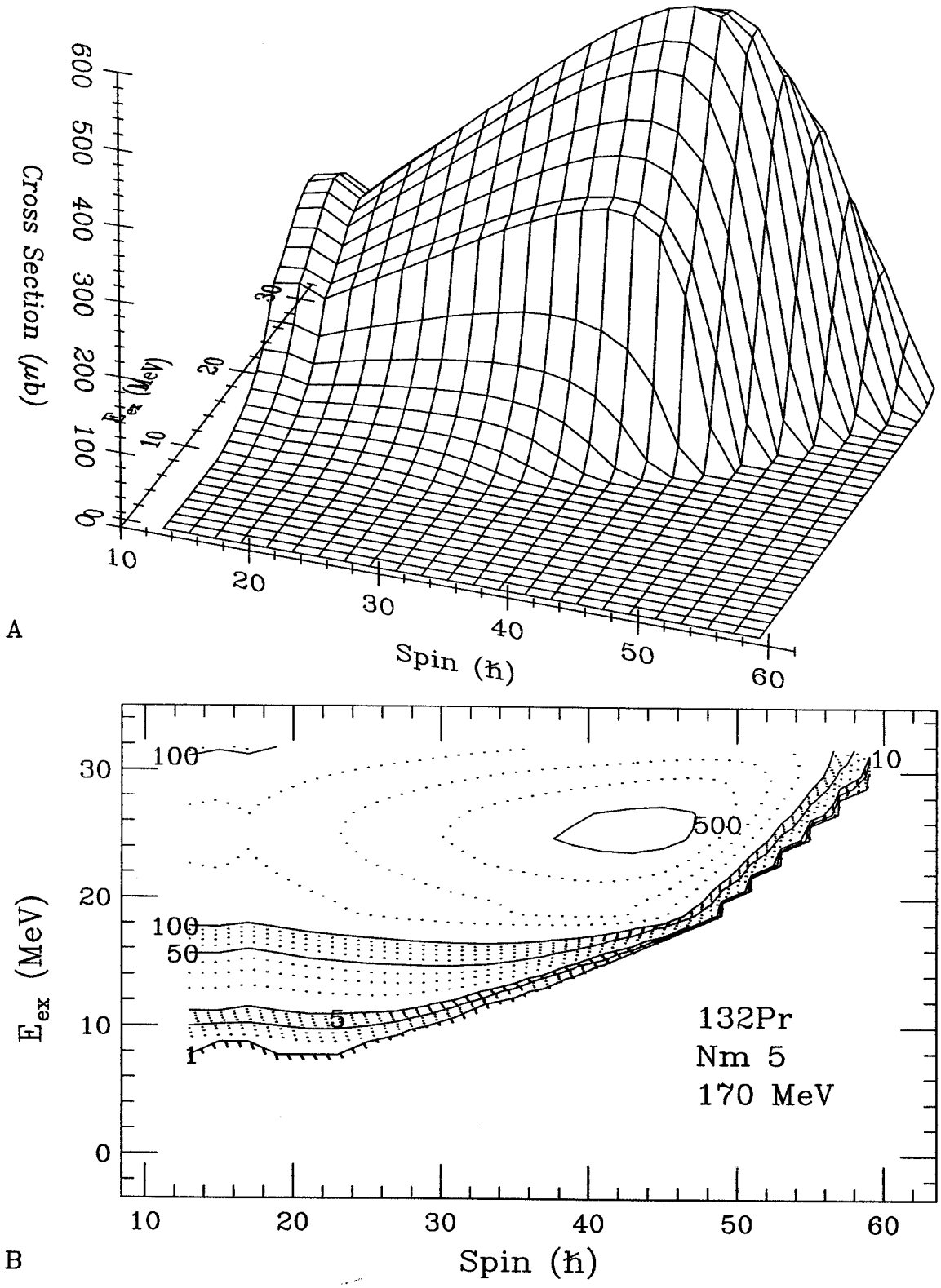

Figure B.7: A) 3-D spin population matrix for ^{132}Pr, calculated for the reaction: 170 MeV. ^{37}Cl on ^{100}Mo using the Seeger nuclear mass model (Nm 5). B) The same data plotted in a contour format with the log of the cross section represented by the dotted curves.

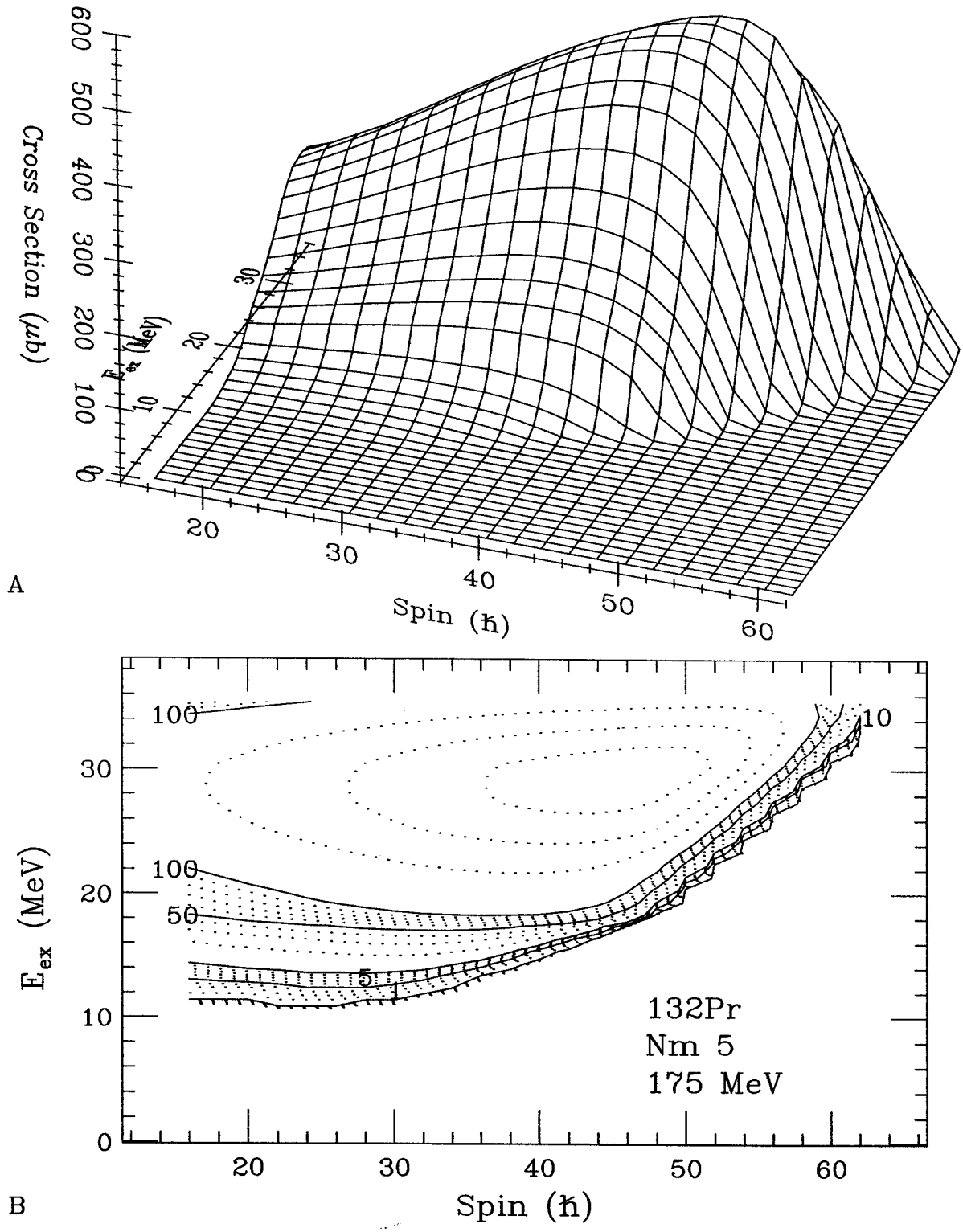

Figure B.8: A) 3-D spin population matrix for ^{132}Pr, calculated for the reaction: 175 MeV. ^{37}Cl on ^{100}Mo using the Seeger nuclear mass model (Nm 5). B) The same data plotted in a contour format with the log of the cross section represented by the dotted curves.

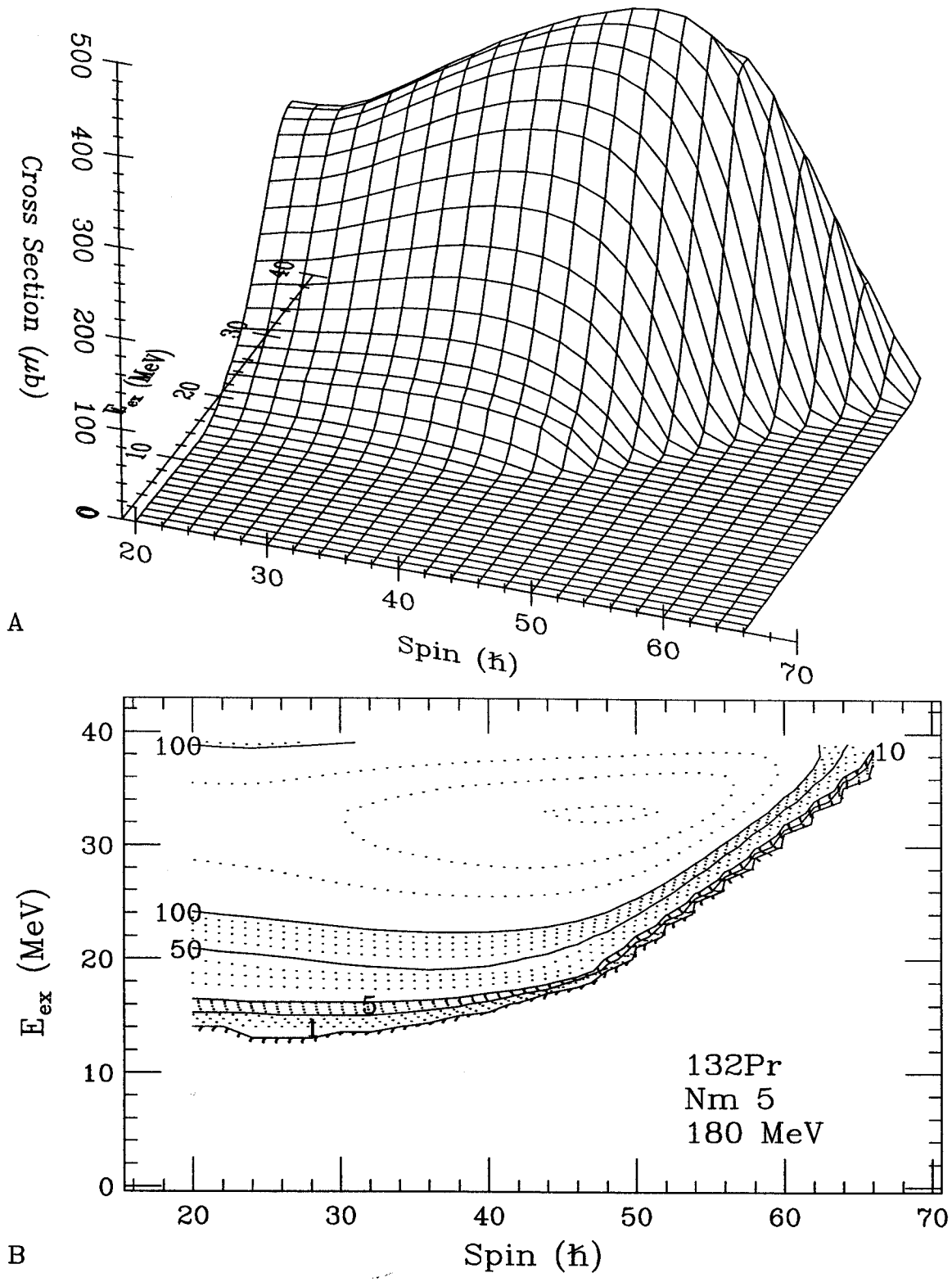

Figure B.9: A) 3-D spin population matrix for ^{132}Pr, calculated for the reaction: 180 MeV. ^{37}Cl on ^{100}Mo using the Seeger nuclear mass model (Nm 5). B) The same data plotted in a contour format with the log of the cross section represented by the dotted curves.

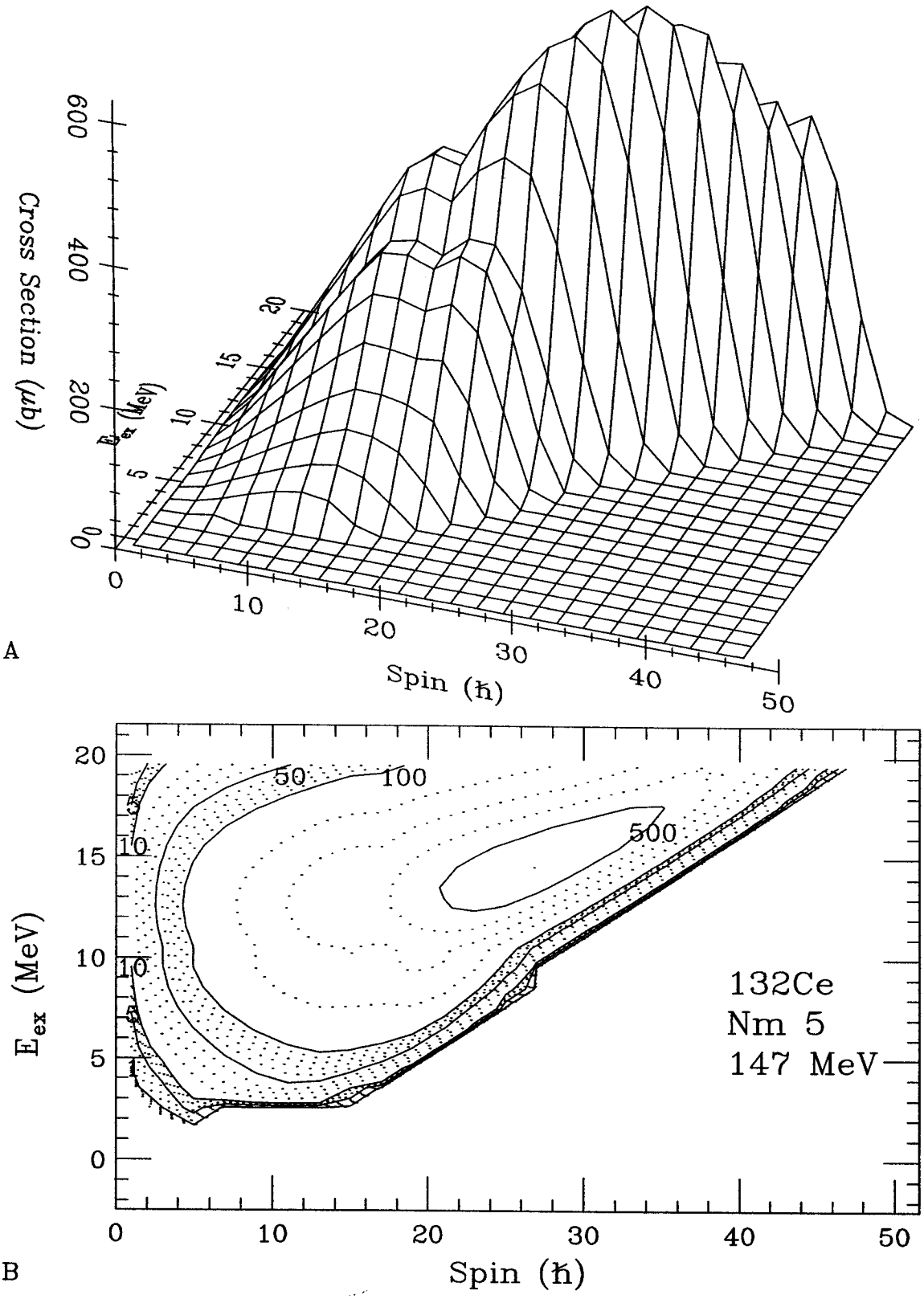

Figure B.10: A) 3-D spin population matrix for ^{132}Ce, calculated for the reaction: 147 MeV. ^{37}Cl on ^{100}Mo using the Seeger nuclear mass model (Nm 5). B) The same data plotted in a contour format with the log of the cross section represented by the dotted curves.

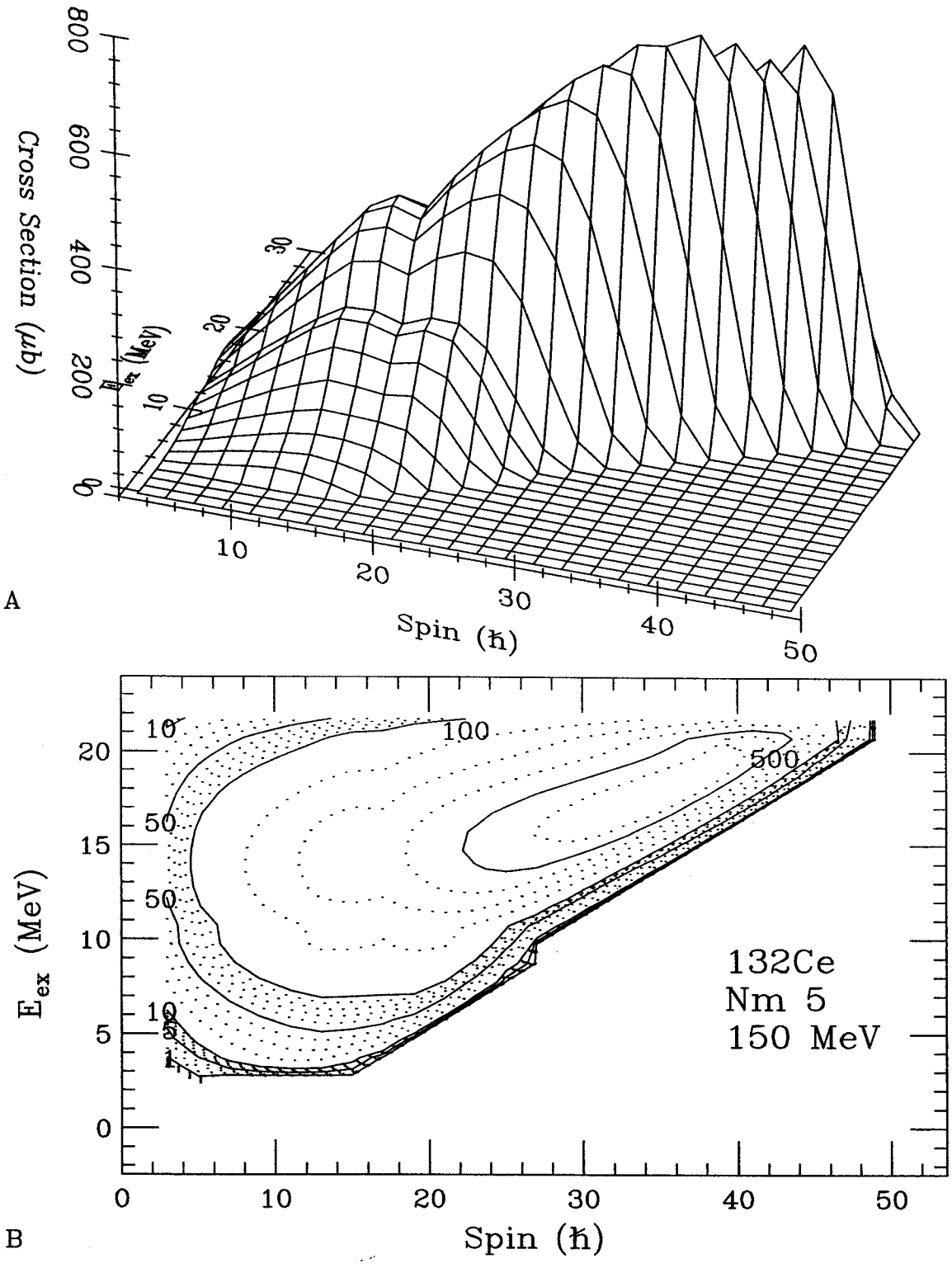

Figure B.11: A) 3-D spin population matrix for ^{132}Ce, calculated for the reaction: 150 MeV. ^{37}Cl on ^{100}Mo using the Seeger nuclear mass model (Nm 5). B) The same data plotted in a contour format with the log of the cross section represented by the dotted curves.

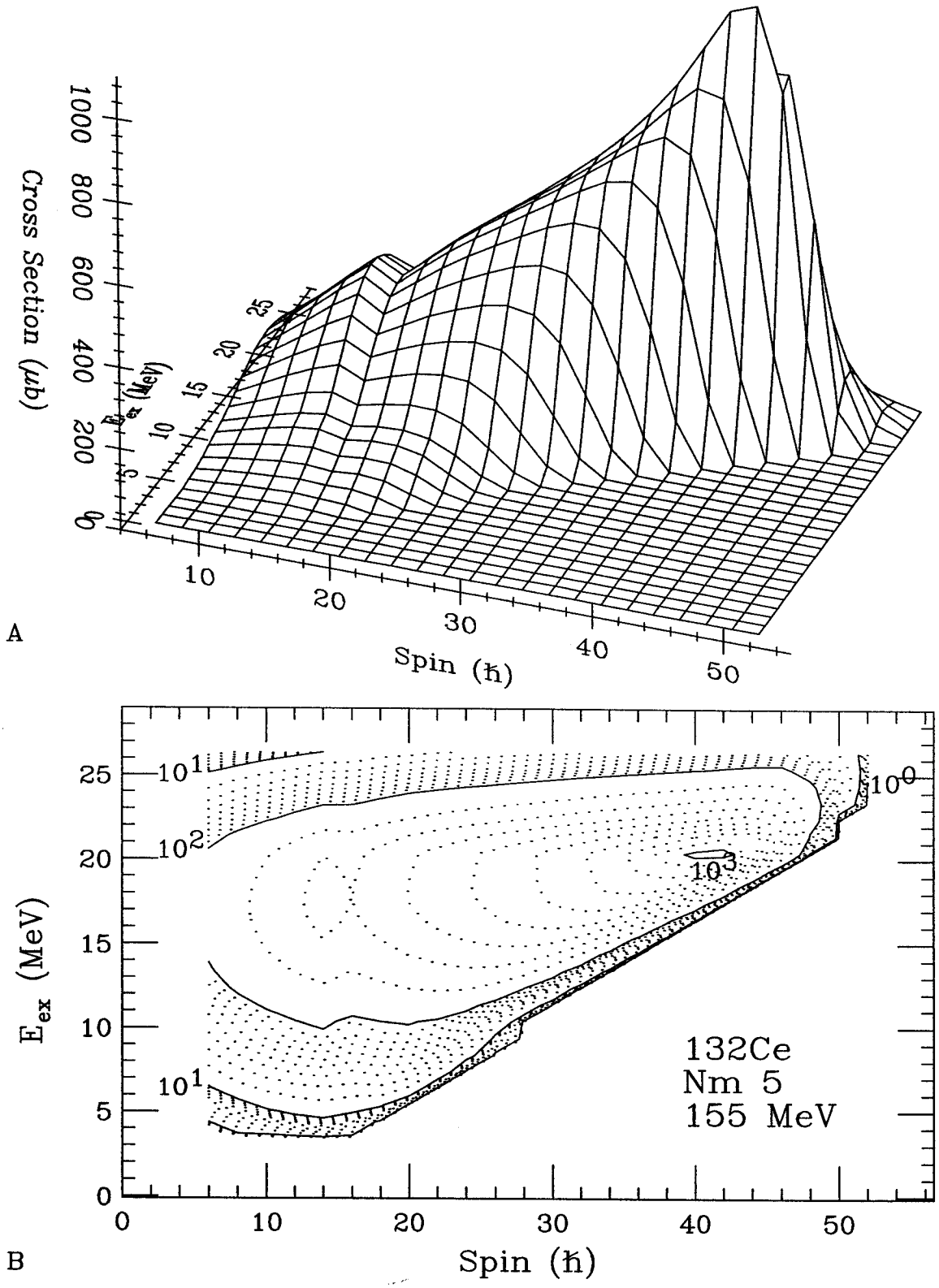

Figure B.12: A) 3-D spin population matrix for ^{132}Ce, calculated for the reaction: 155 MeV. ^{37}Cl on ^{100}Mo using the Seeger nuclear mass model (Nm 5). B) The same data plotted in a contour format with the log of the cross section represented by the dotted curves.

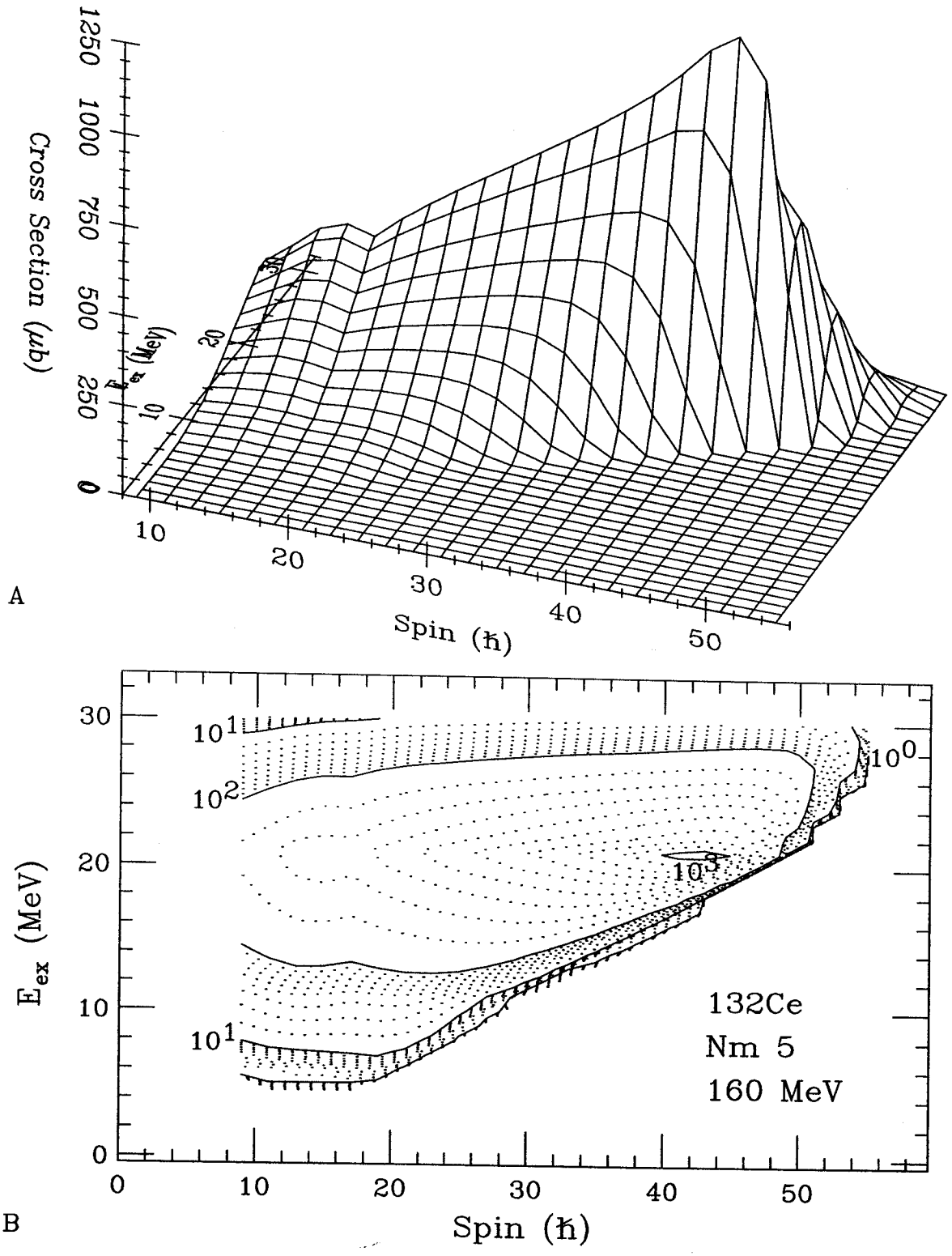

Figure B.13: A) 3-D spin population matrix for ^{132}Ce, calculated for the reaction: 160 MeV. ^{37}Cl on ^{100}Mo using the Seeger nuclear mass model (Nm 5). B) The same data plotted in a contour format with the log of the cross section represented by the dotted curves.

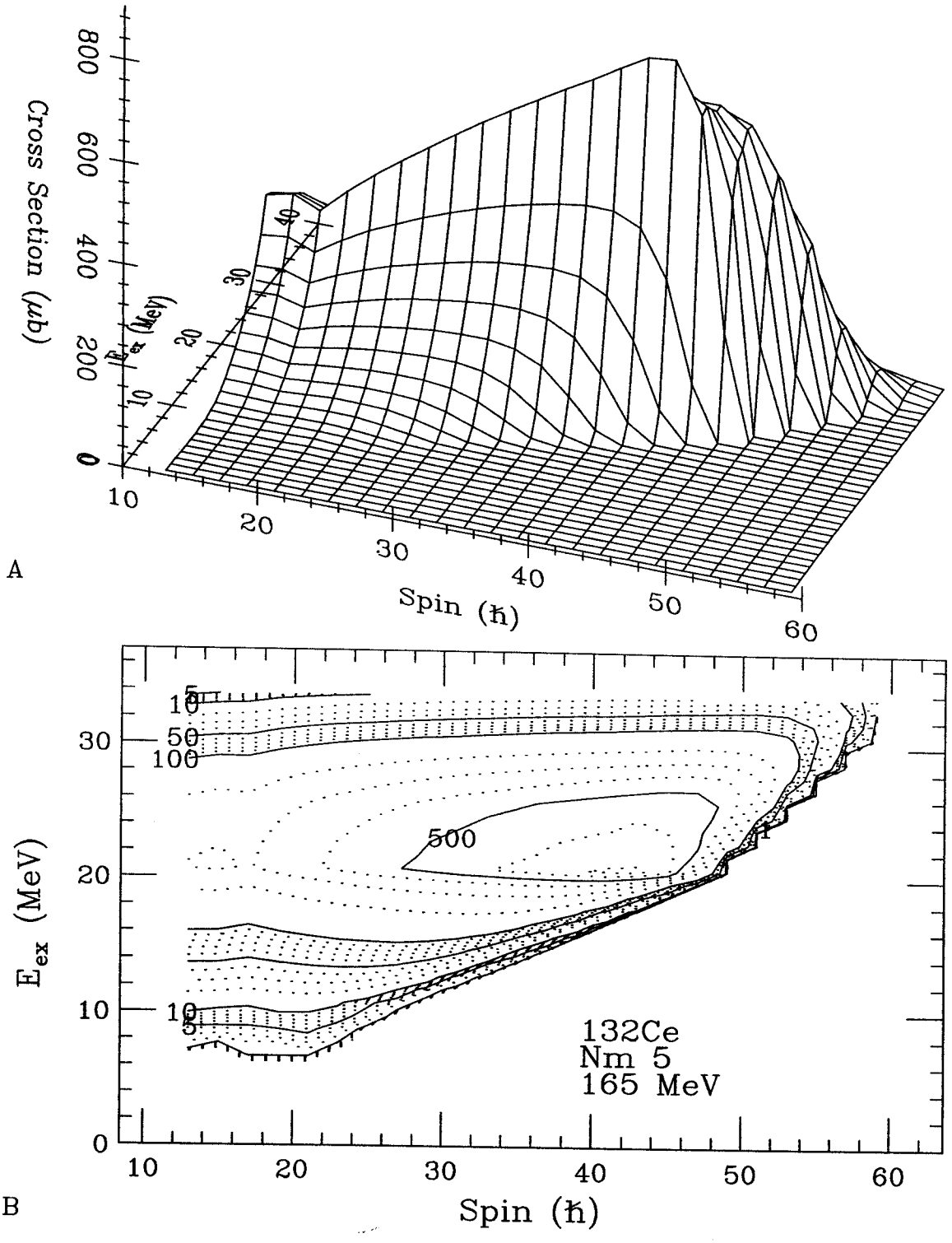

Figure B.14: A) 3-D spin population matrix for ^{132}Ce, calculated for the reaction: 165 MeV. ^{37}Cl on ^{100}Mo using the Seeger nuclear mass model (Nm 5). B) The same data plotted in a contour format with the log of the cross section represented by the dotted curves.

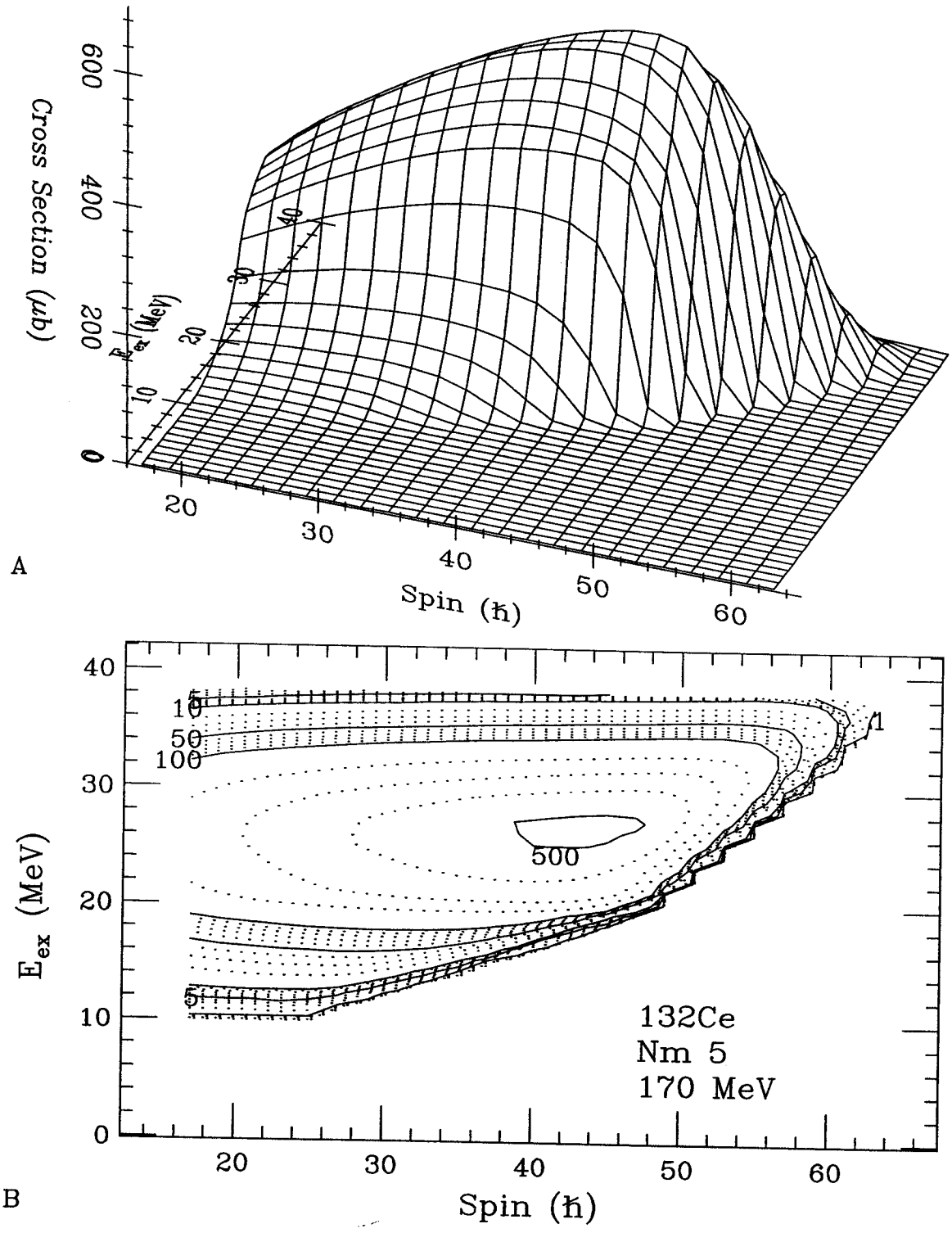

Figure B.15: A) 3-D spin population matrix for ^{132}Ce, calculated for the reaction: 170 MeV. ^{37}Cl on ^{100}Mo using the Seeger nuclear mass model (Nm 5). B) The same data plotted in a contour format with the log of the cross section represented by the dotted curves.

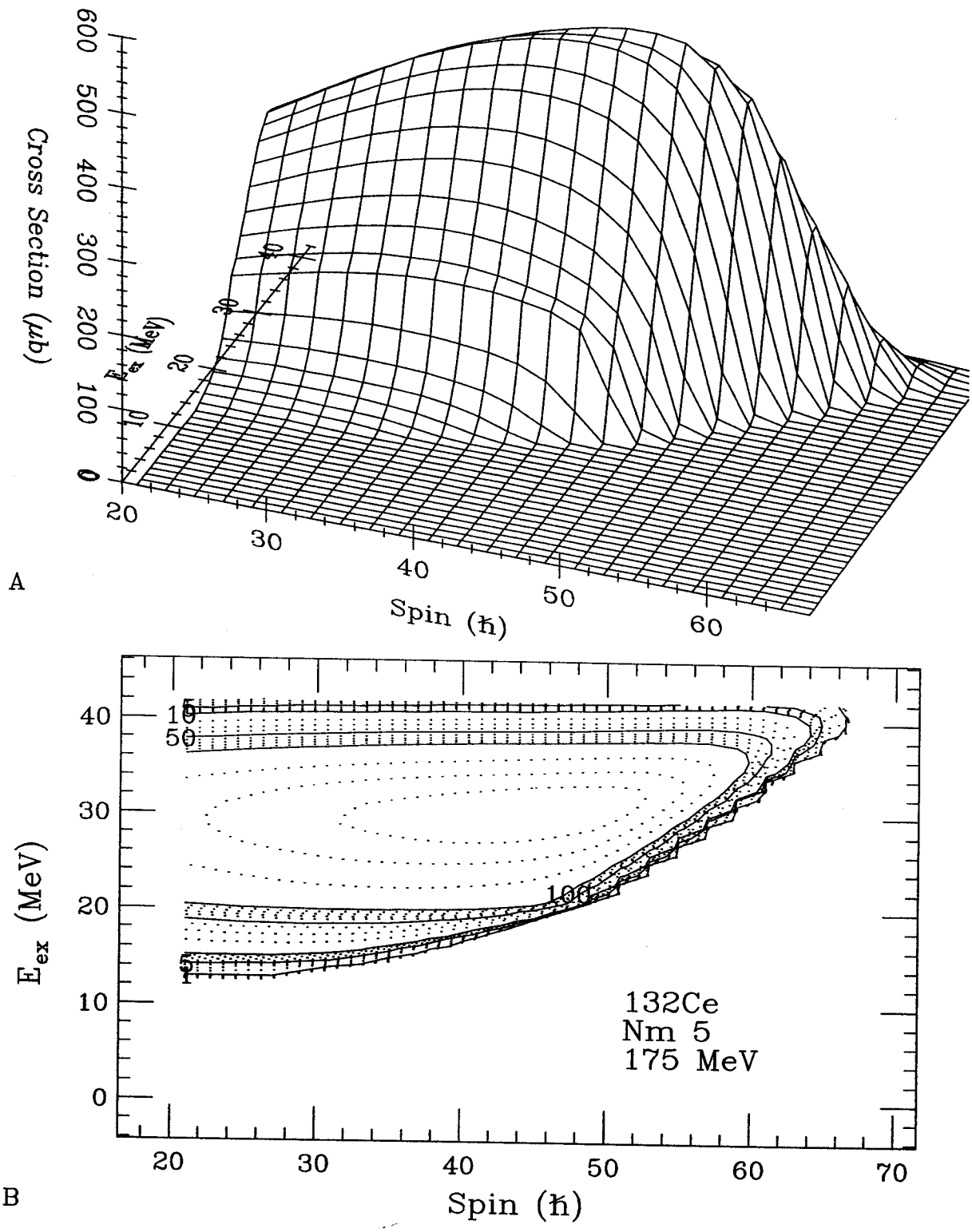

Figure B.16: A) 3-D spin population matrix for ^{132}Ce, calculated for the reaction: 175 MeV. ^{37}Cl on ^{100}Mo using the Seeger nuclear mass model (Nm 5). B) The same data plotted in a contour format with the log of the cross section represented by the dotted curves.

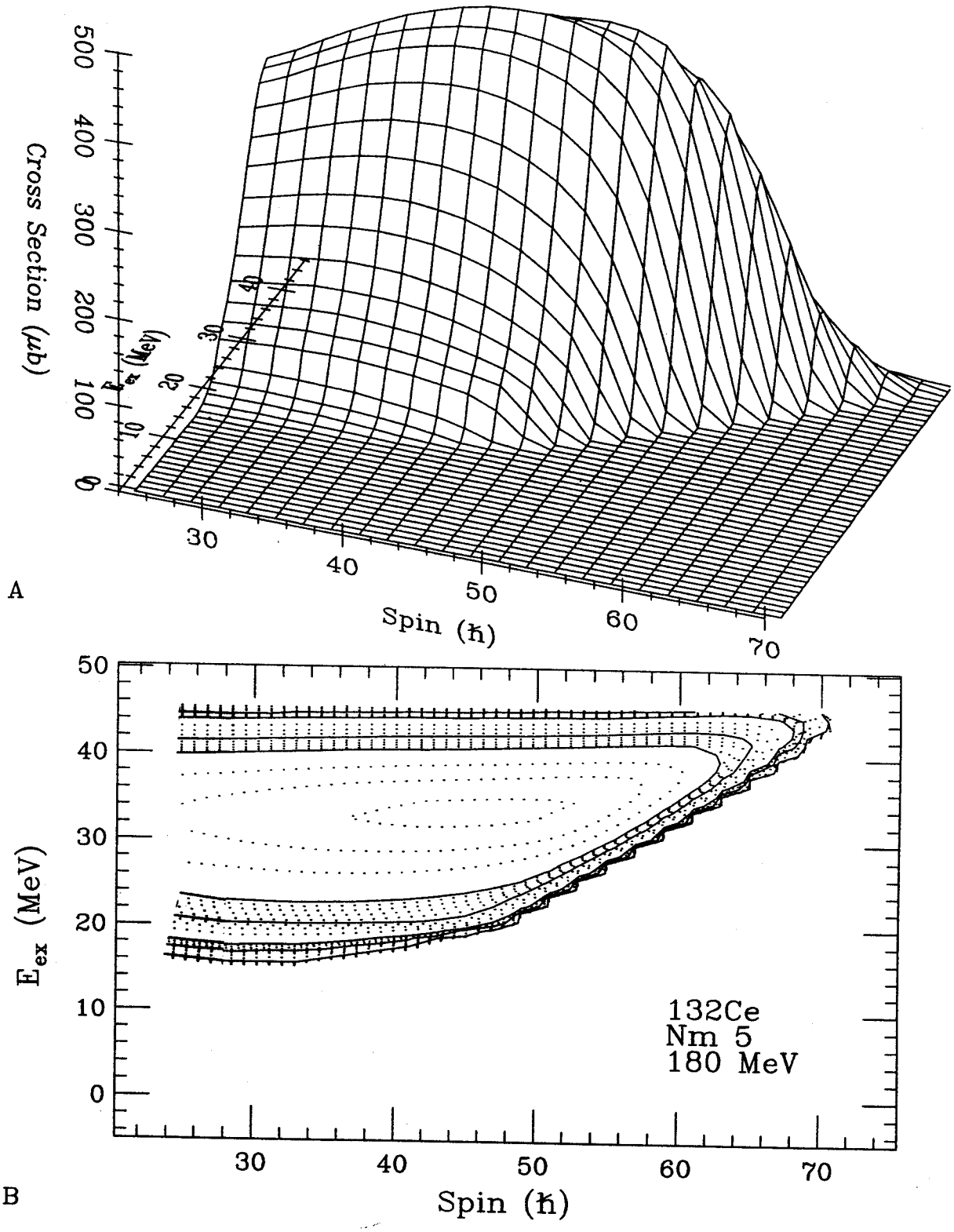

Figure B.17: A) 3-D spin population matrix for ^{132}Ce, calculated for the reaction: 180 MeV. ^{37}Cl on ^{100}Mo using the Seeger nuclear mass model (Nm 5). B) The same data plotted in a contour format with the log of the cross section represented by the dotted curves.

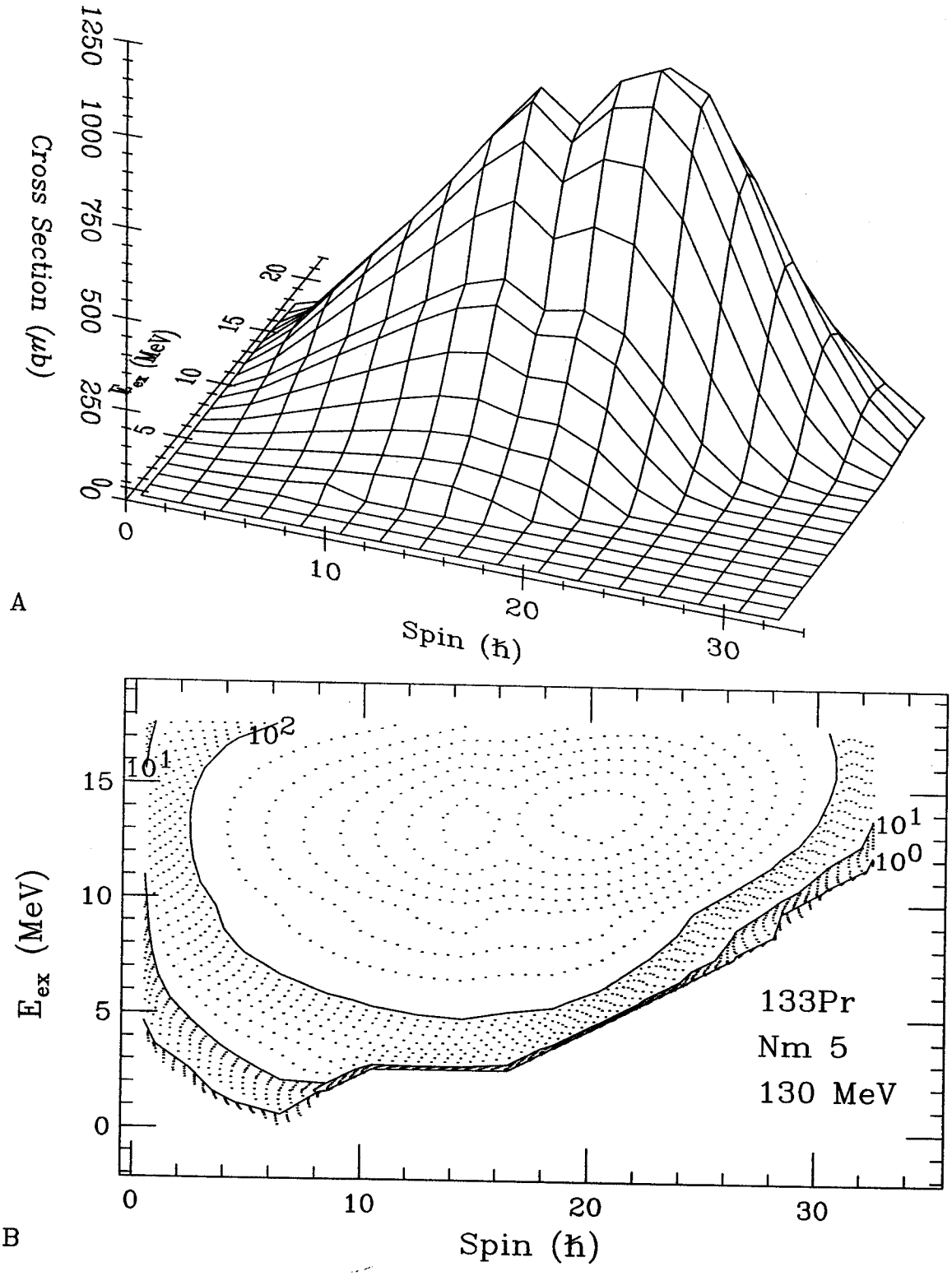

Figure B.18: A) 3-D spin population matrix for ^{133}Pr, calculated for the reaction: 130 MeV. ^{37}Cl on ^{100}Mo using the Seeger nuclear mass model (Nm 5). B) The same data plotted in a contour format with the log of the cross section represented by the dotted curves.

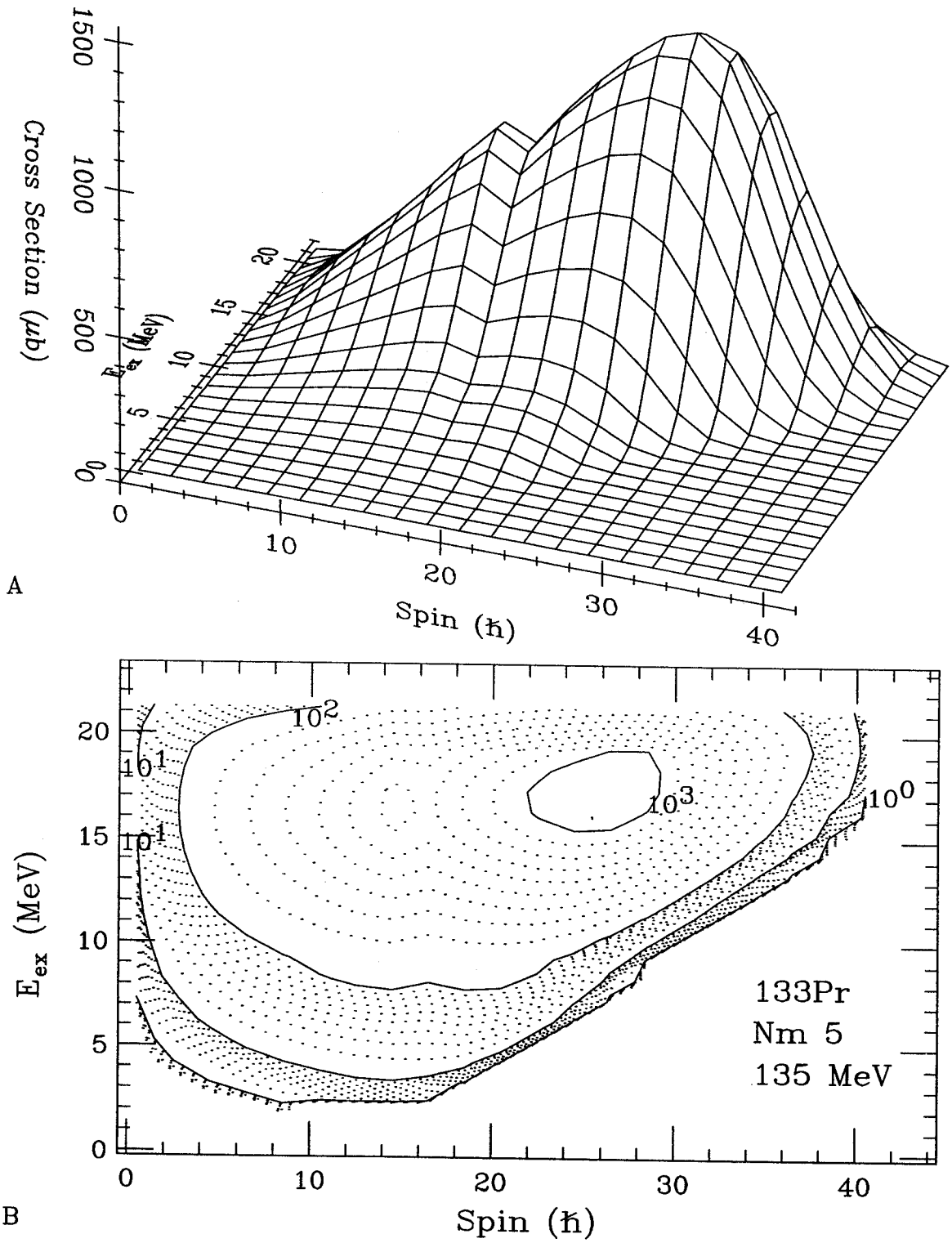

Figure B.19: A) 3-D spin population matrix for ^{133}Pr, calculated for the reaction: 135 MeV. ^{37}Cl on ^{100}Mo using the Seeger nuclear mass model (Nm 5). B) The same data plotted in a contour format with the log of the cross section represented by the dotted curves.

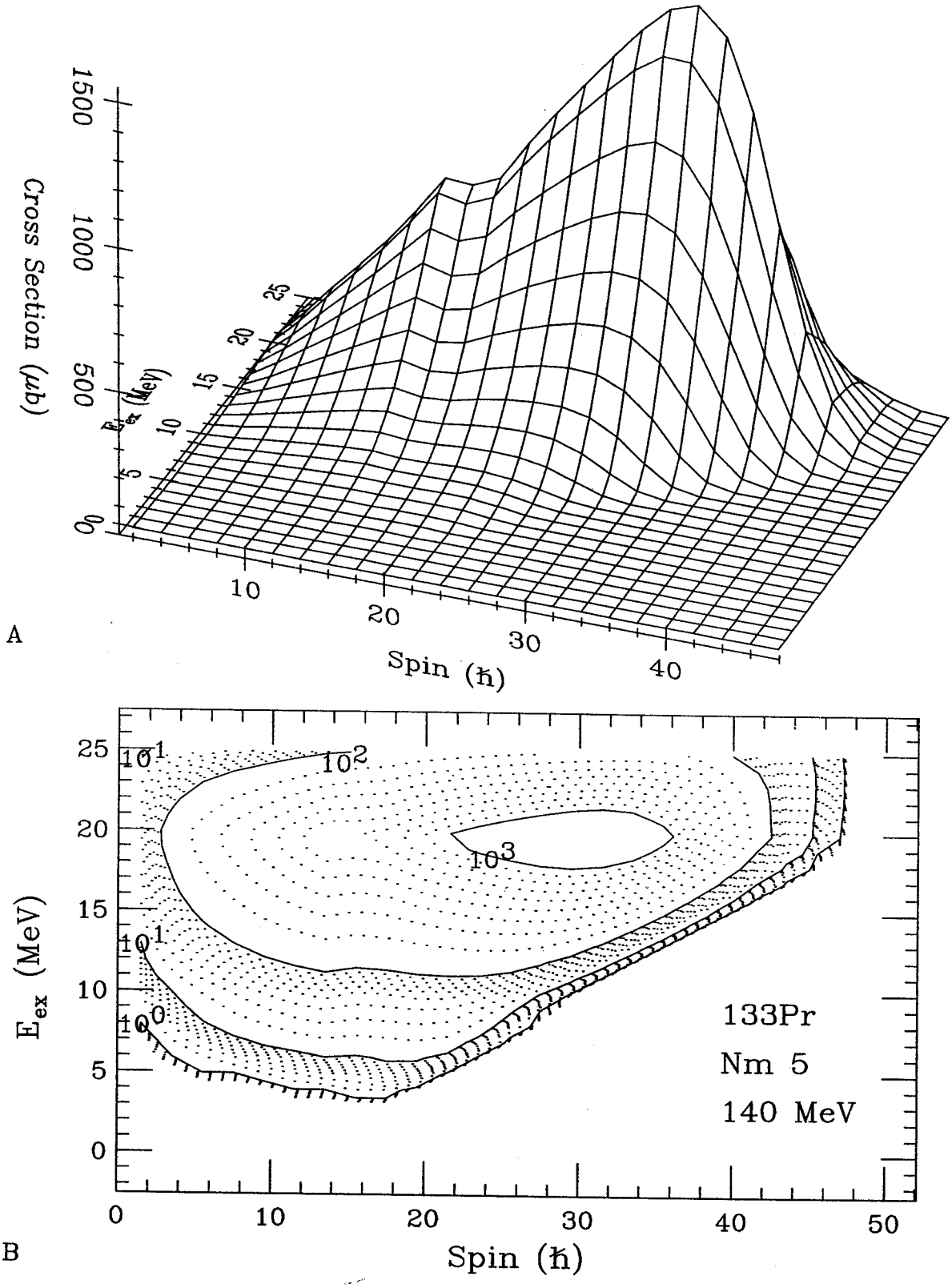

Figure B.20: A) 3-D spin population matrix for ^{133}Pr, calculated for the reaction: 140 MeV. ^{37}Cl on ^{100}Mo using the Seeger nuclear mass model (Nm 5). B) The same data plotted in a contour format with the log of the cross section represented by the dotted curves.

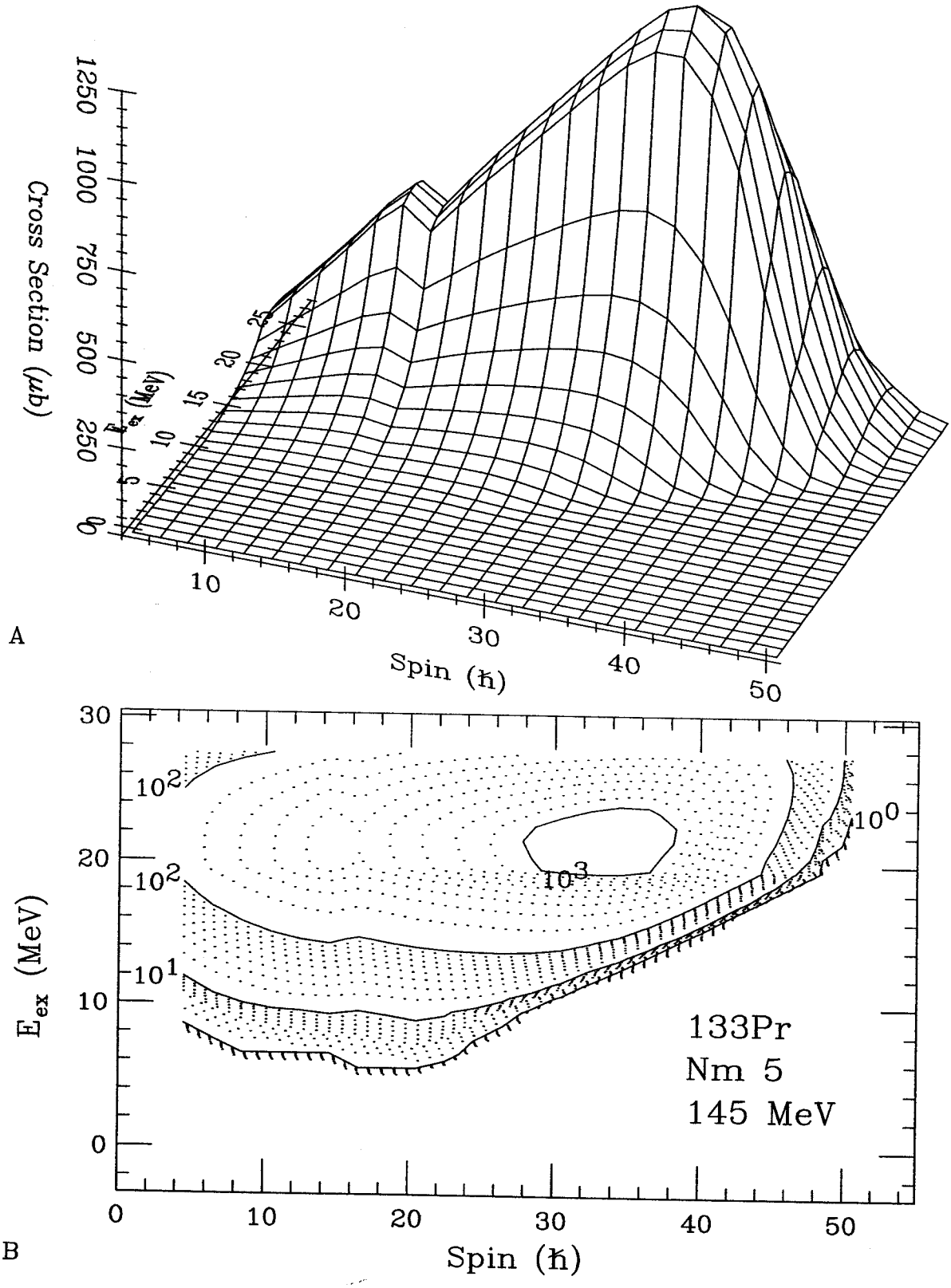

Figure B.21: A) 3-D spin population matrix for ^{133}Pr, calculated for the reaction: 145 MeV. ^{37}Cl on ^{100}Mo using the Seeger nuclear mass model (Nm 5). B) The same data plotted in a contour format with the log of the cross section represented by the dotted curves.

Appendix C

Detector Calibration Plots.

C.1 Energy: Isotropic & Doppler Shifted

The following Appendix contains isotropic (*gs*) calibration plots for the 20 detectors. Superimposed, are the calibration plots for the gain and doppler shifted calibration (*gds*). The solid symbol represents the isotropic calibration points; the open symbol is the doppler corrected calibration. The standard sources, ^{133}Ba, ^{60}Co, ^{152}Eu were used to generate isotropic calibrations for each detector. Table 5.1 contains the linear regression analysis results. Spectra for the standards acquired pre- and post-run are shown in Figure 5.3. Energy peaks from various nuclei in the reaction were used for the gain and doppler-shift calibration. Channel number values for the peaks were obtained from a gaussian fit routine; the linear regression results are presented in Table 5.4 and the energies and their sources are listed in Table 5.3. The calibration range for detector 1 (the normalization detector) was extended by including the Pb x-ray energies at the low end and a few, low-intensity, reaction transitions at high energy.

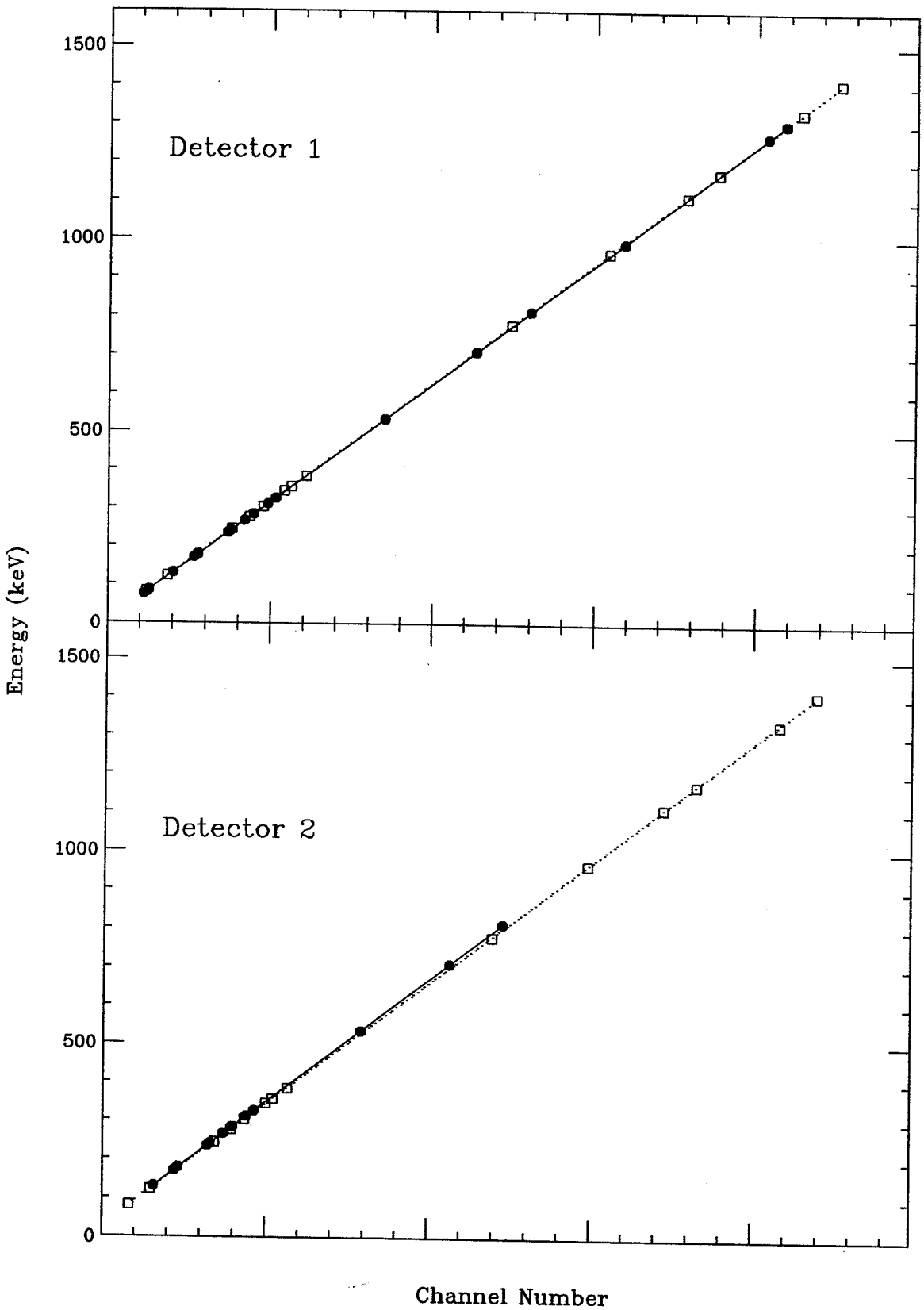

Figure C.1: Energy calibration plots for detector numbers 1, and 2. The open symbol represents the isotropic calibration points; the solid symbol is the doppler corrected calibration.

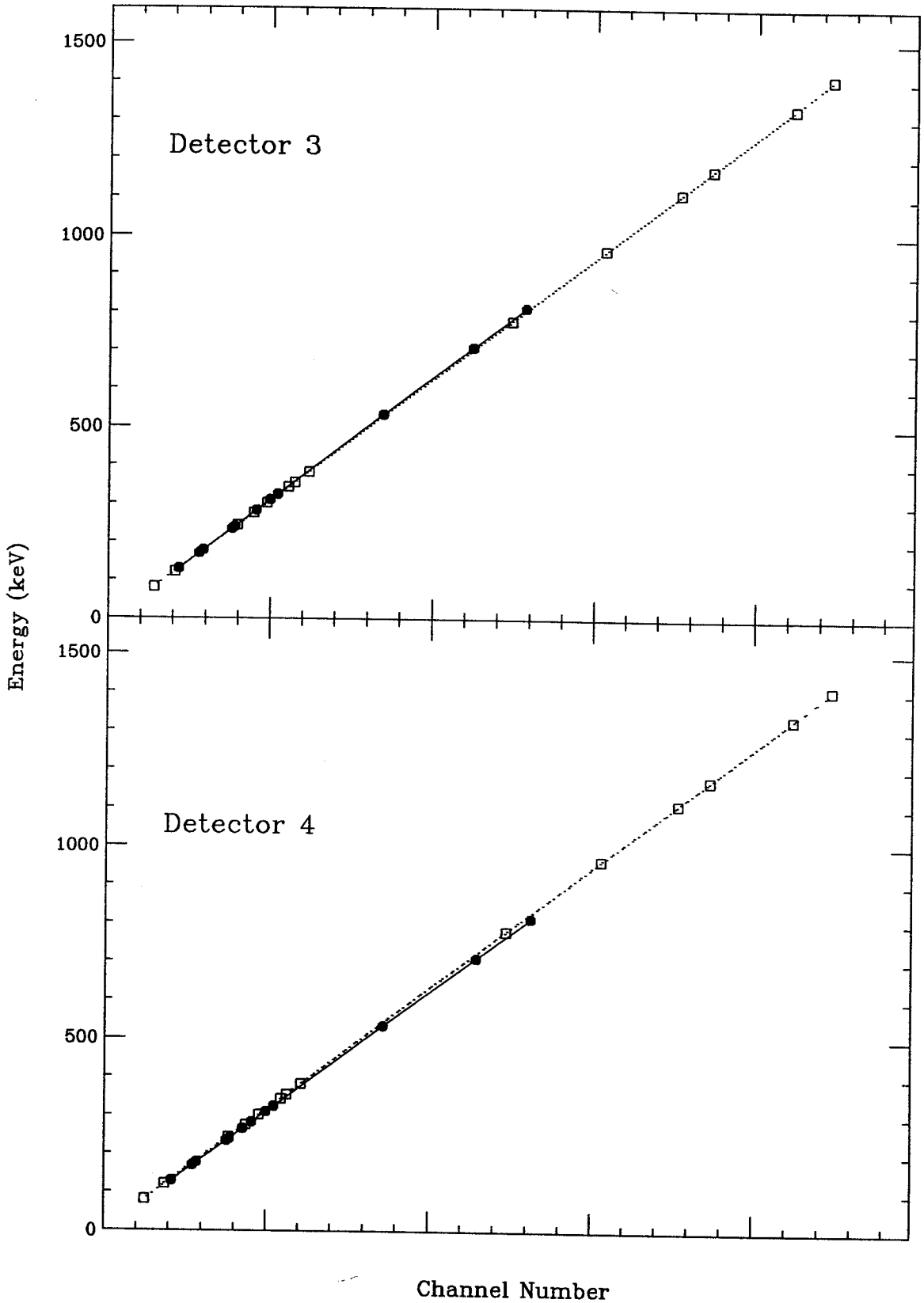

Figure C.2: Energy calibration plots for detector numbers 3, and 4. The open symbol represents the isotropic calibration points; the solid symbol is the doppler corrected calibration.

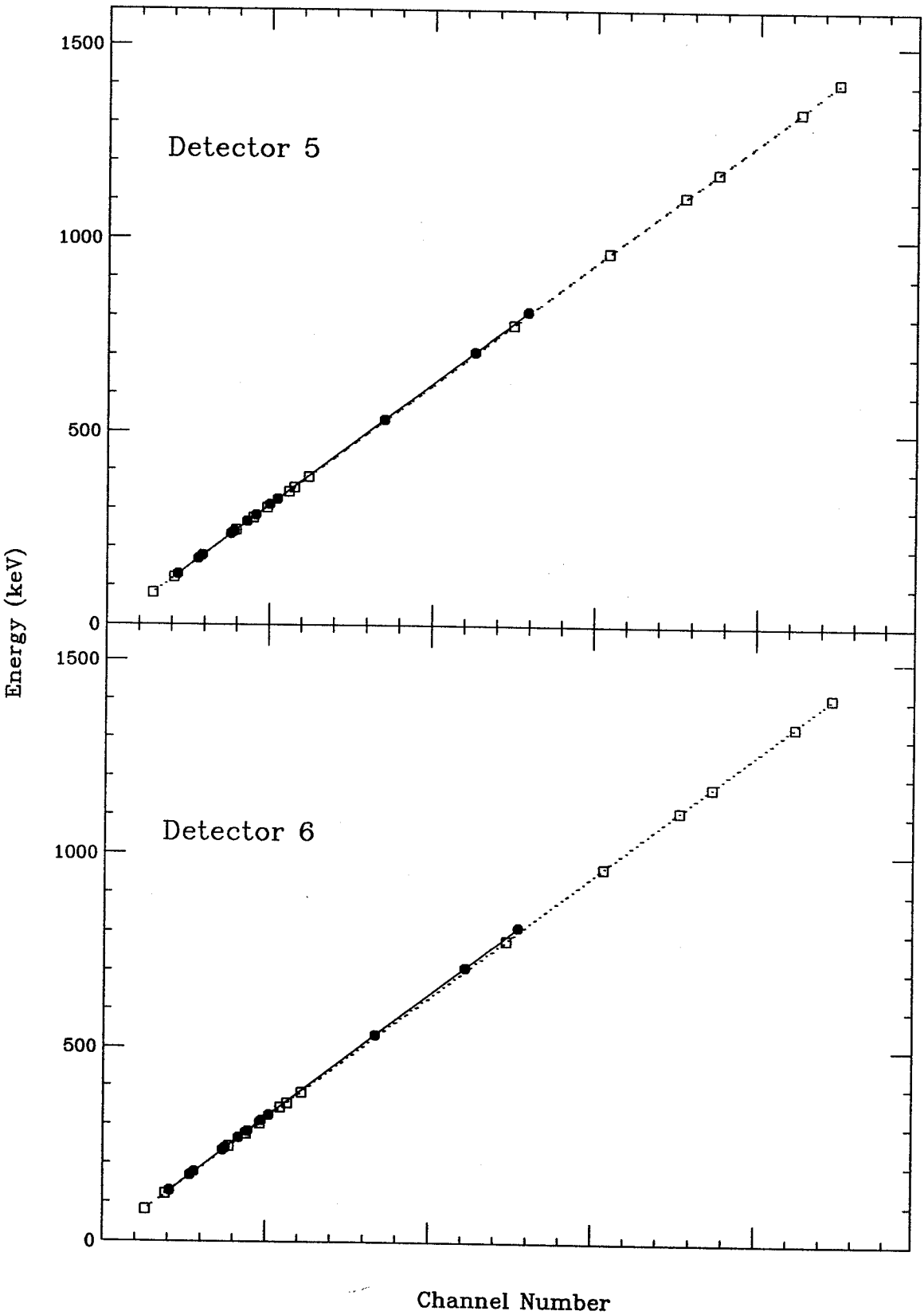

Figure C.3: Energy calibration plots for detector numbers 5, and 6. The open symbol represents the isotropic calibration points; the solid symbol is the doppler corrected calibration.

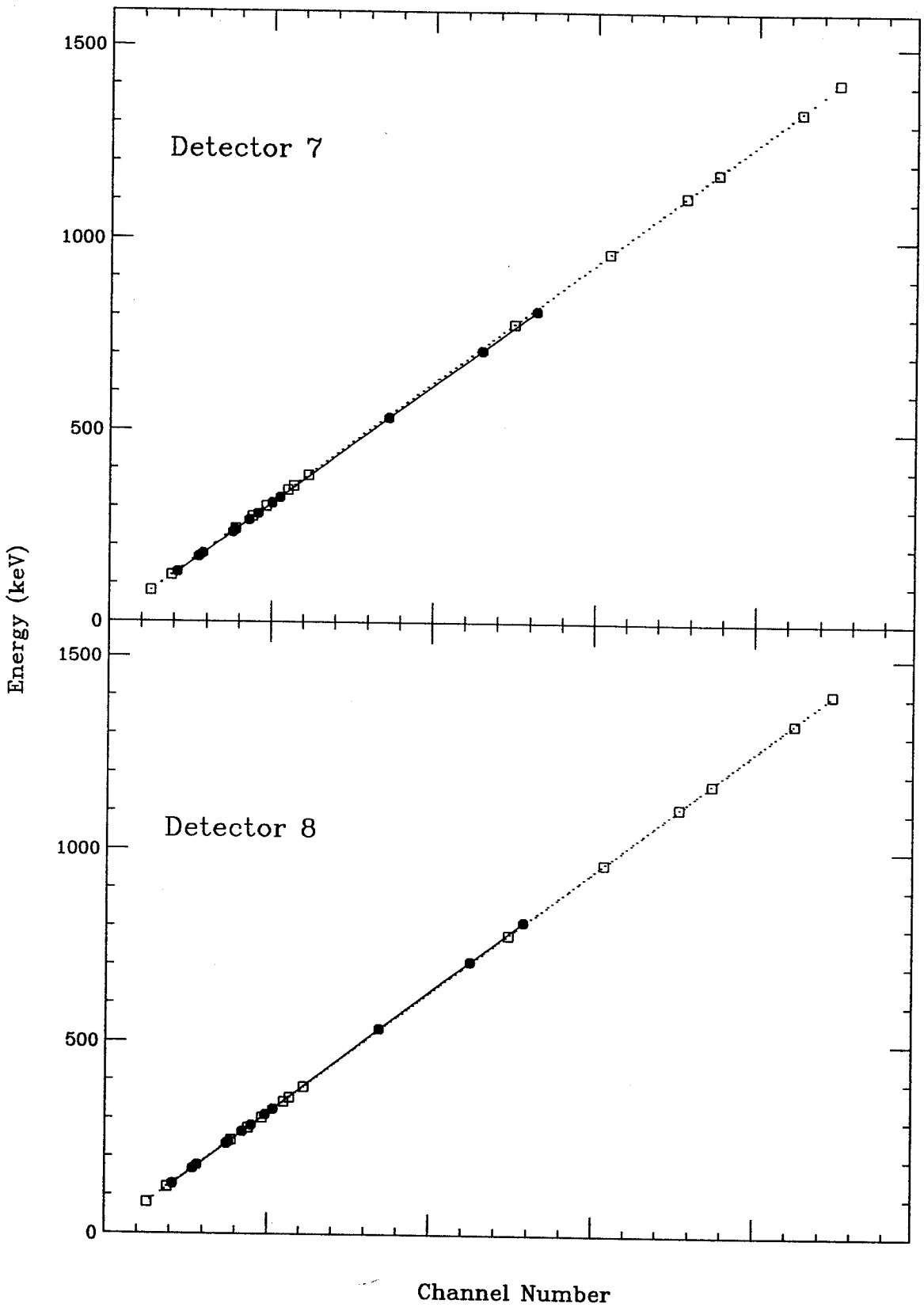

Figure C.4: Energy calibration plots for detector numbers 7, and 8. The open symbol represents the isotropic calibration points; the solid symbol is the doppler corrected calibration.

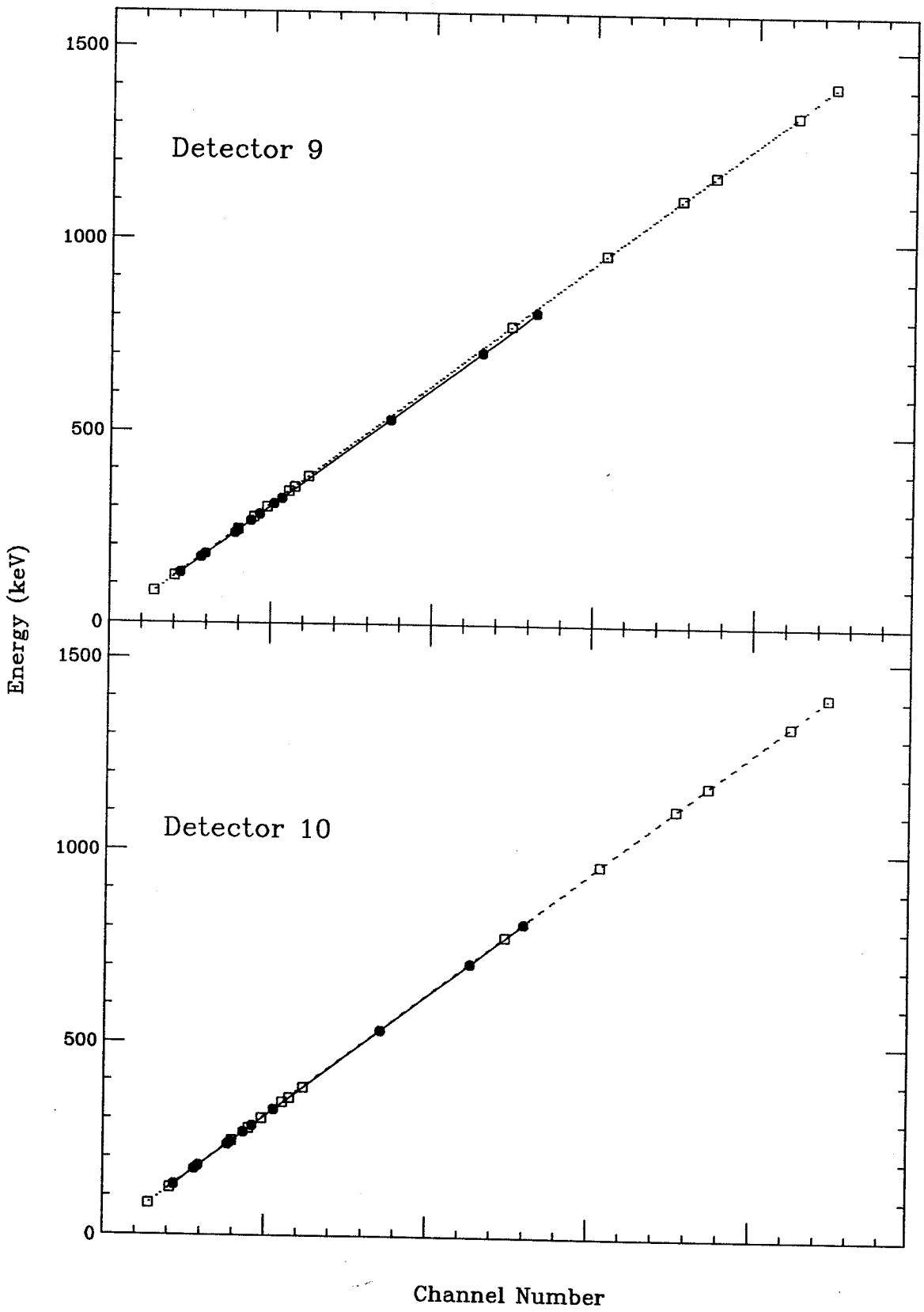

Figure C.5: Energy calibration plots for detector numbers 9, and 10. The open symbol represents the isotropic calibration points; the solid symbol is the doppler corrected calibration.

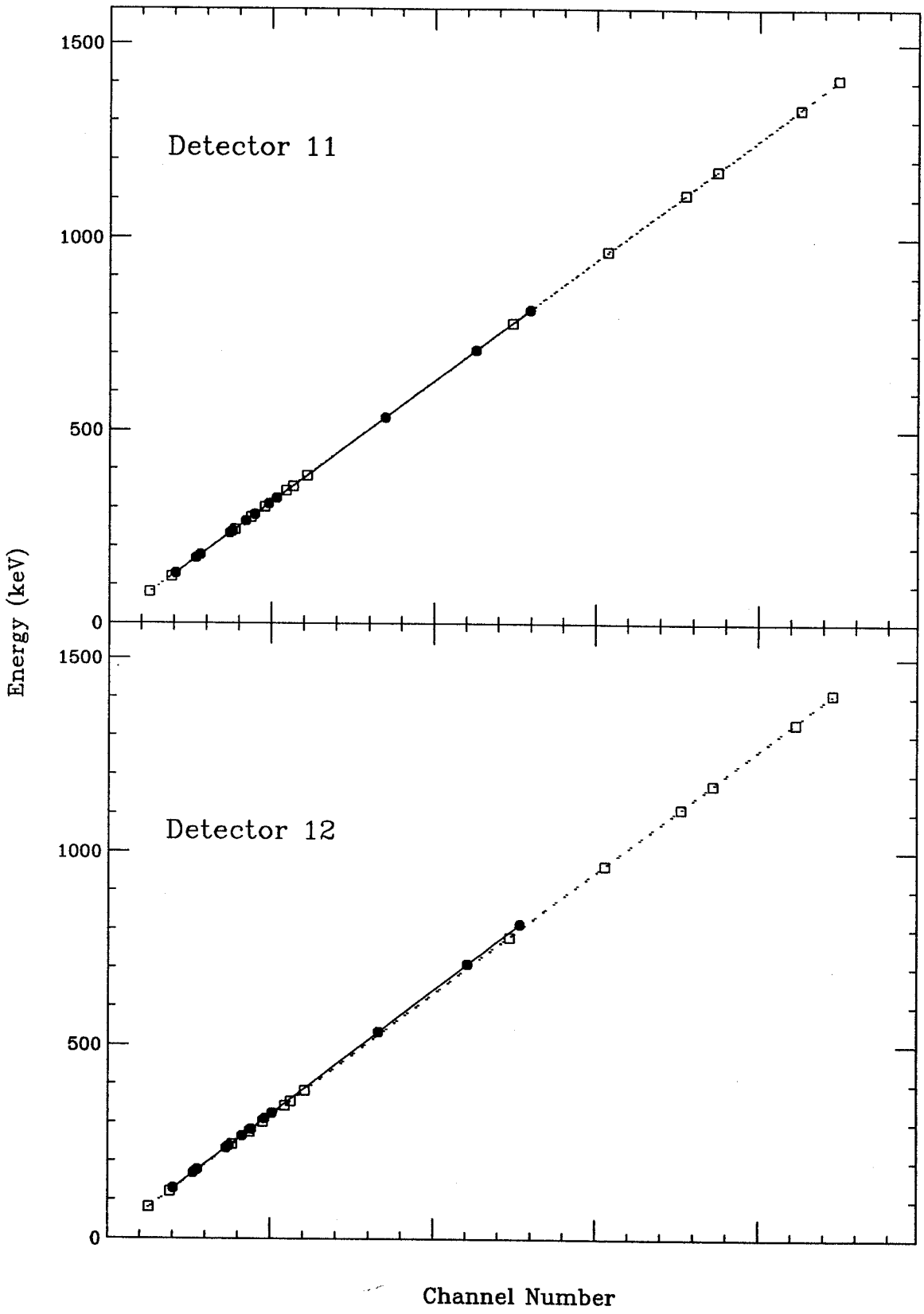

Figure C.6: Energy calibration plots for detector numbers 11, and 12. The open symbol represents the isotropic calibration points; the solid symbol is the doppler corrected calibration.

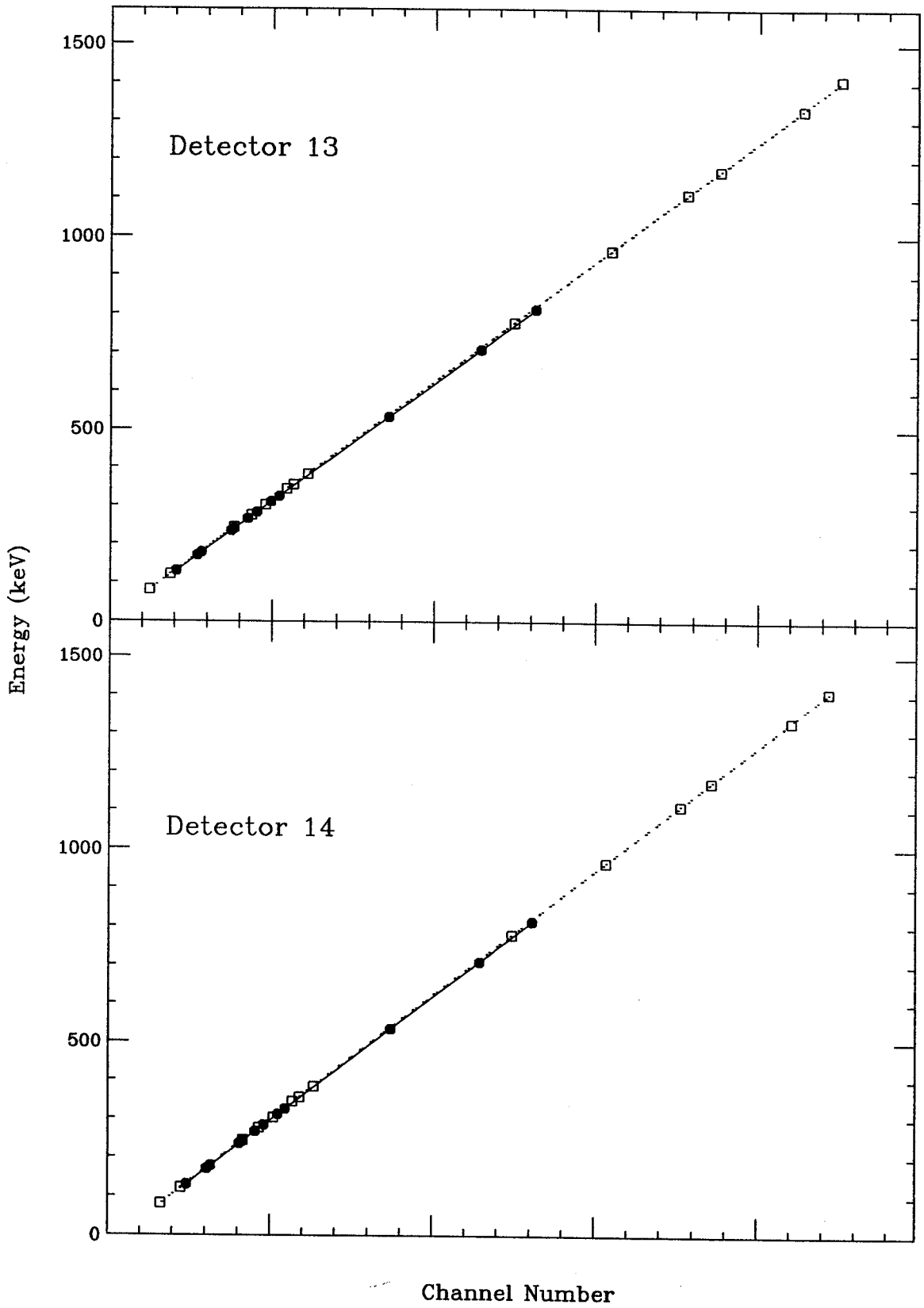

Figure C.7: Energy calibration plots for detector numbers 13, and 14. The open symbol represents the isotropic calibration points; the solid symbol is the doppler corrected calibration.

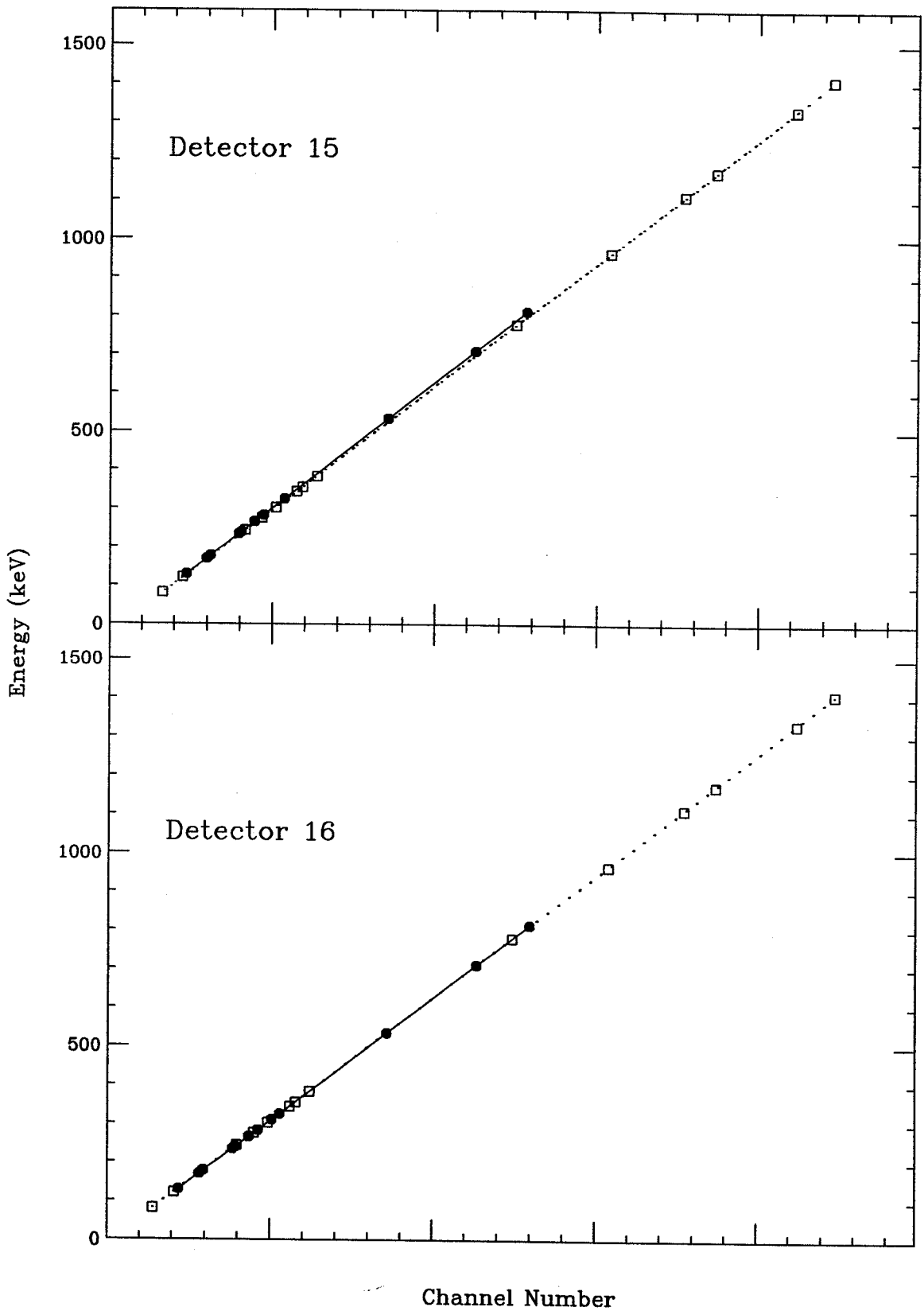

Figure C.8: Energy calibration plots for detector numbers 15, and 16. The open symbol represents the isotropic calibration points; the solid symbol is the doppler corrected calibration.

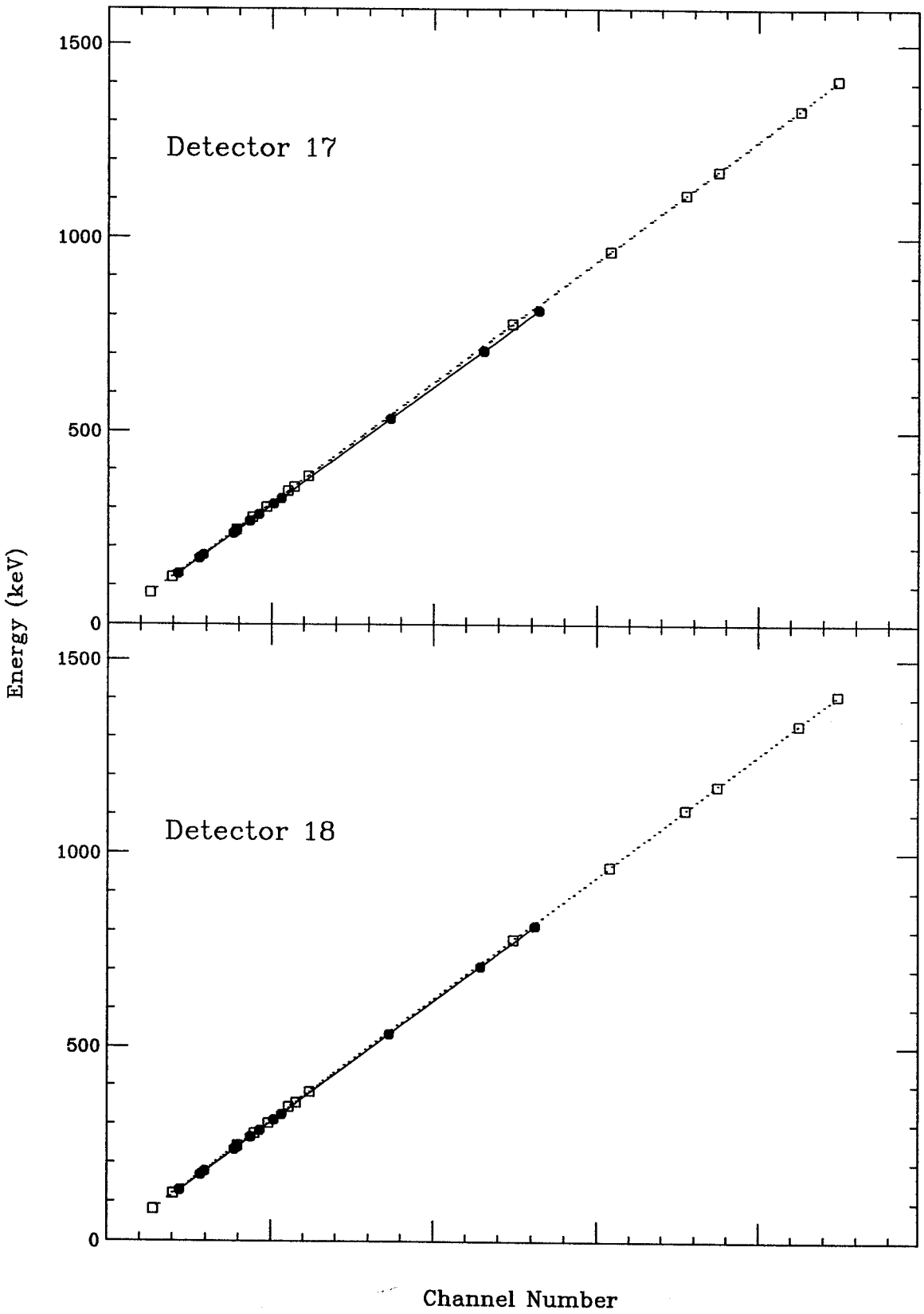

Figure C.9: Energy calibration plots for detector numbers 17, and 18. The open symbol represents the isotropic calibration points; the solid symbol is the doppler corrected calibration.

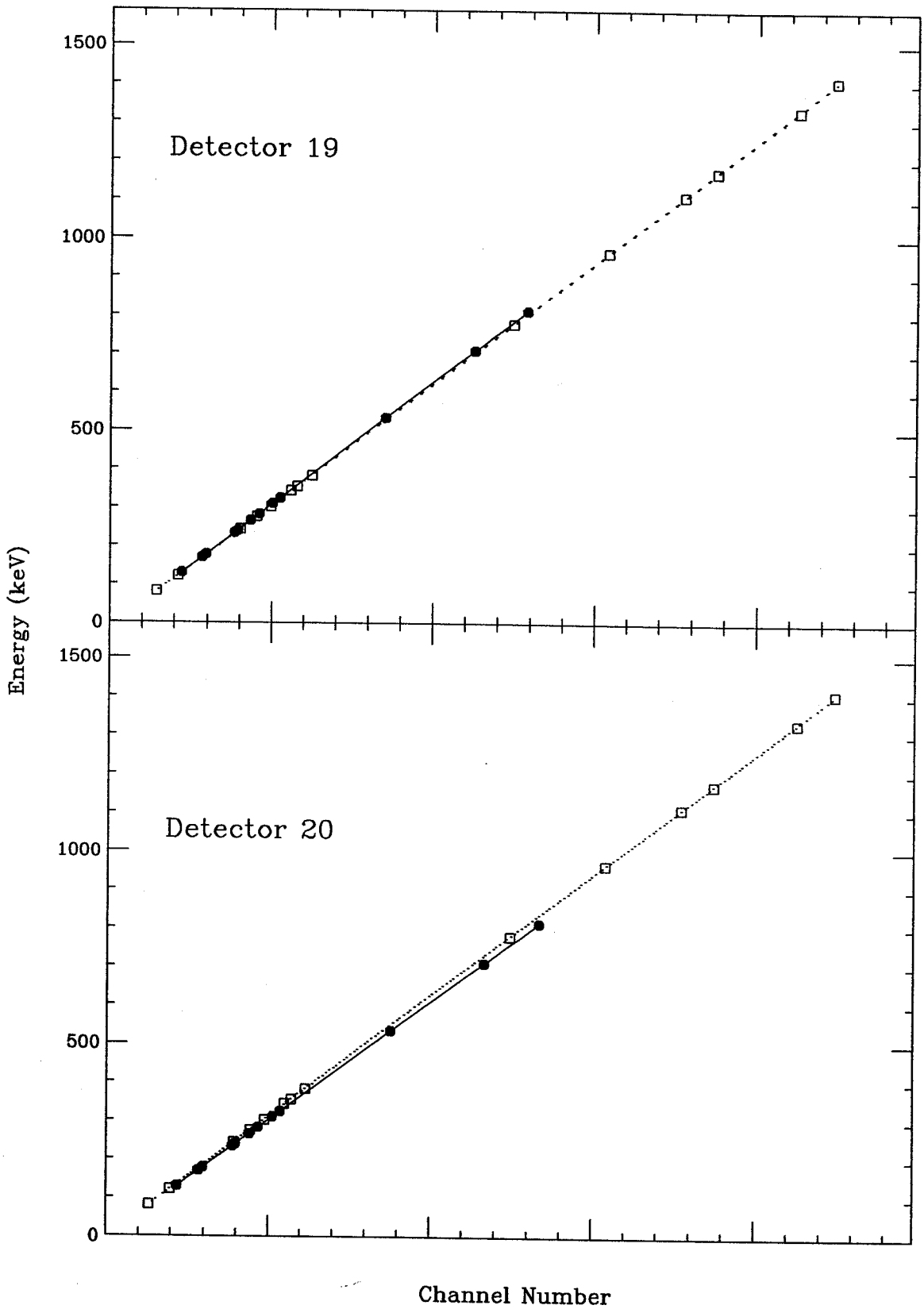

Figure C.10: Energy calibration plots for detector numbers 19, and 20. The open symbol represents the isotropic calibration points; the solid symbol is the doppler corrected calibration.

C.2 Photon Efficiency

A photopeak efficiency calibration measures the response of the detector to photons over a wide range of energies. The effect is an exponential one and the curve shape is governed by the 'Total' plot in Figure 4.4, a plot of photon absorption coefficients versus energy for germanium. A cubic spline fitting routine was used to generate an interpolated efficiency percentage at each channel number, based on the experimental peak areas. A photon efficiency curve, averaged over all detectors, is presented in Figure 5.6. The highest efficiency value produced by the spline fit was used to normalize the averaged efficiency curve to 100% for this figure. In addition, an effective efficiency curve, adjusted for the transmission of photons through the absorber foils, is also included in this figure to describe the total system effect on the energy peaks. This Appendix contains equivalent curves for the individual detectors; they have not been normalized to 100% in order to preserve the relative response among the detectors. The dashed line is the efficiency curve; the dot-dash line is the absorber transmission curve; the solid line is the absorber-corrected efficiency curve.

The Oak Ridge software was modified to automatically adjust the spectral peak intensities for photon transmission through absorbers and for multiple detector efficiencies. The method can be found in the command *EFF* in the program *DAMFT1*, a modified *DAMS* program. An extrapolation of the data was also made to extend the energy range beyond 1800 keV shown in the plots, i.e., 40 to 2500 keV. This can be obtained from the computer files.

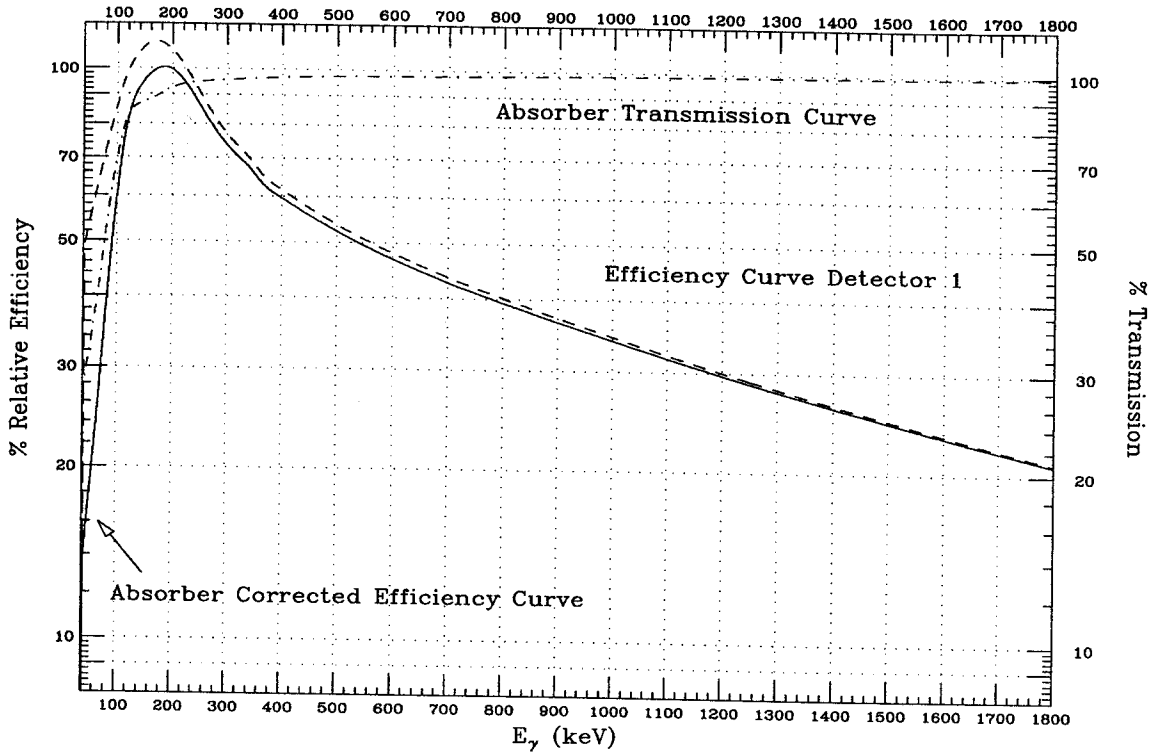

Figure C.11: Efficiency calibration, Absorber Transmission and Absorber-adjusted Efficiency curves for Detector 1.

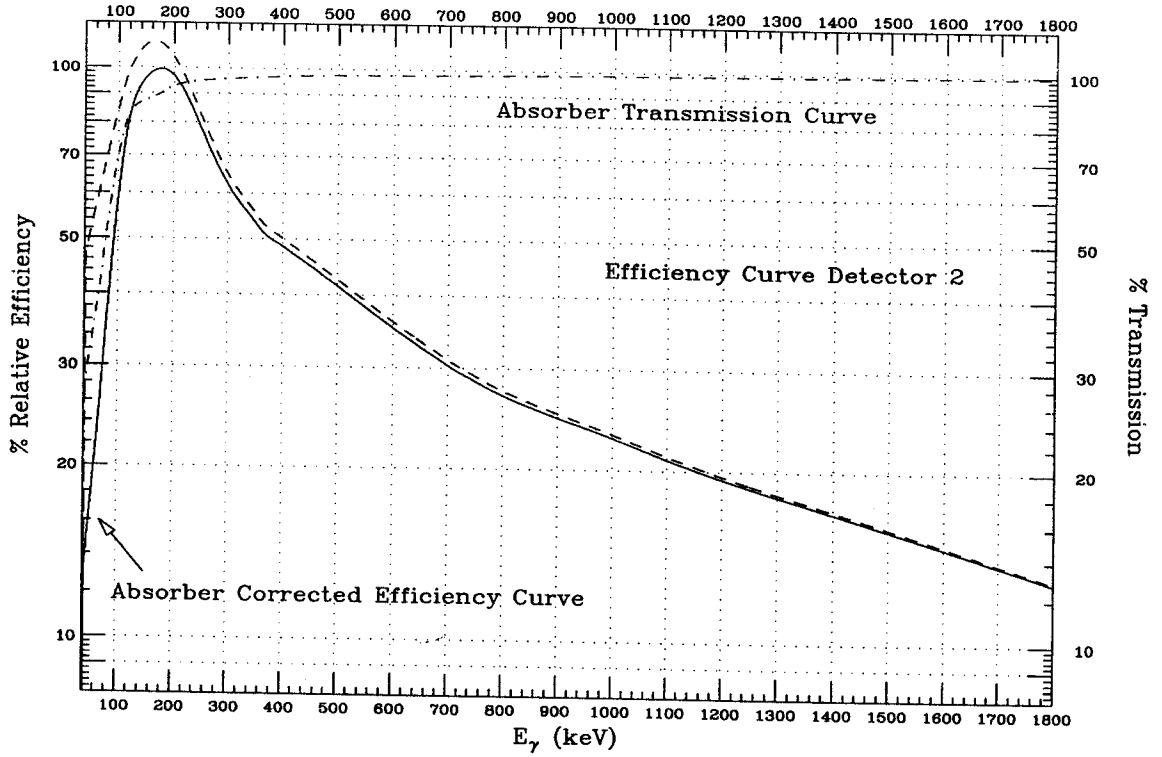

Figure C.12: Efficiency calibration, Absorber Transmission and Absorber-adjusted Efficiency curves for Detector 2.

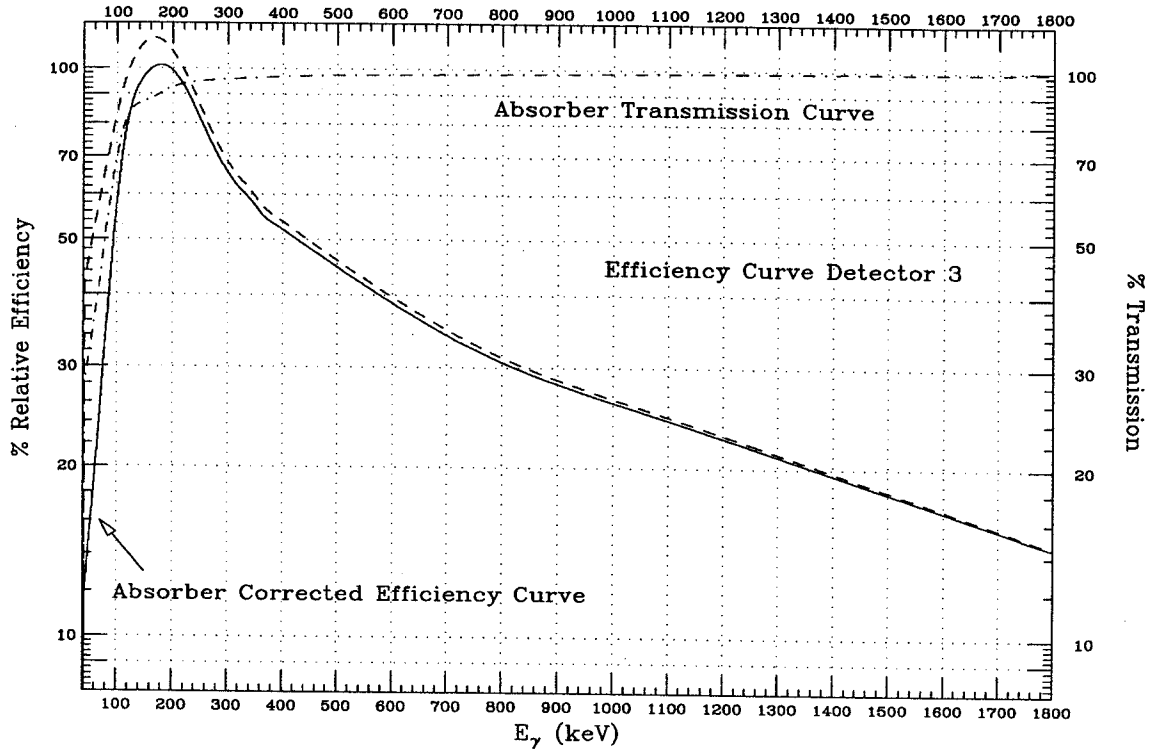

Figure C.13: Efficiency calibration, Absorber Transmission and Absorber-adjusted Efficiency curves for Detector 3.

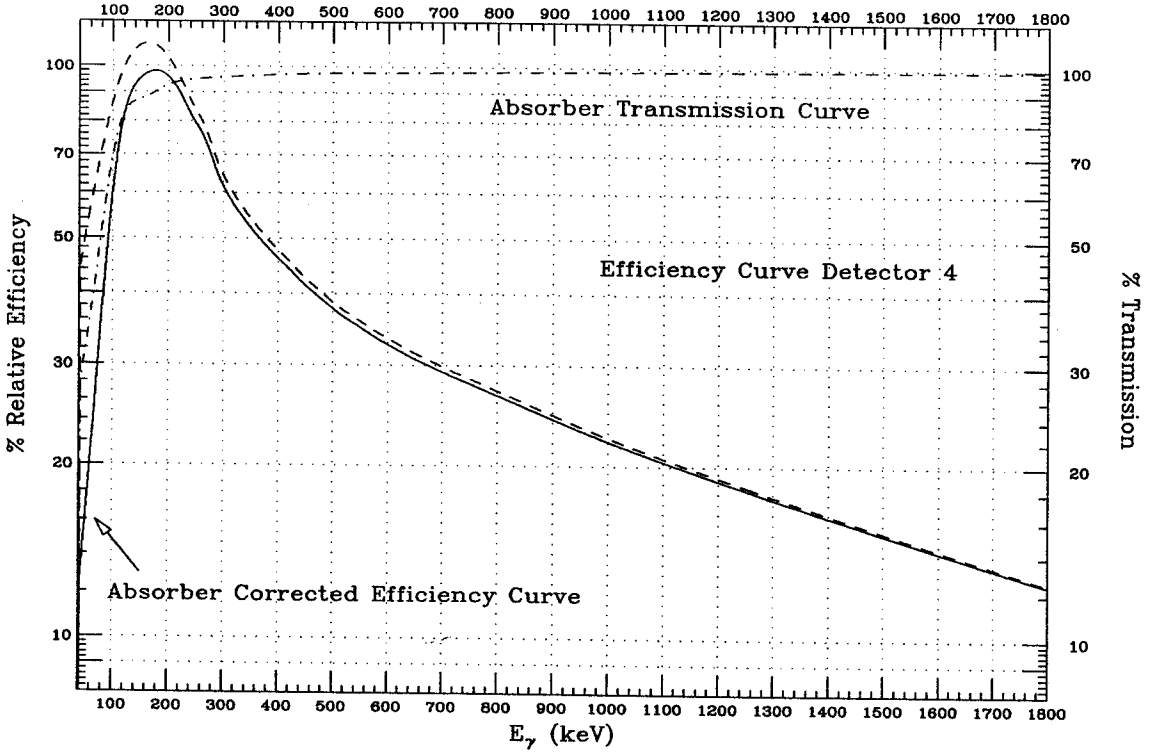

Figure C.14: Efficiency calibration, Absorber Transmission and Absorber-adjusted Efficiency curves for Detector 4.

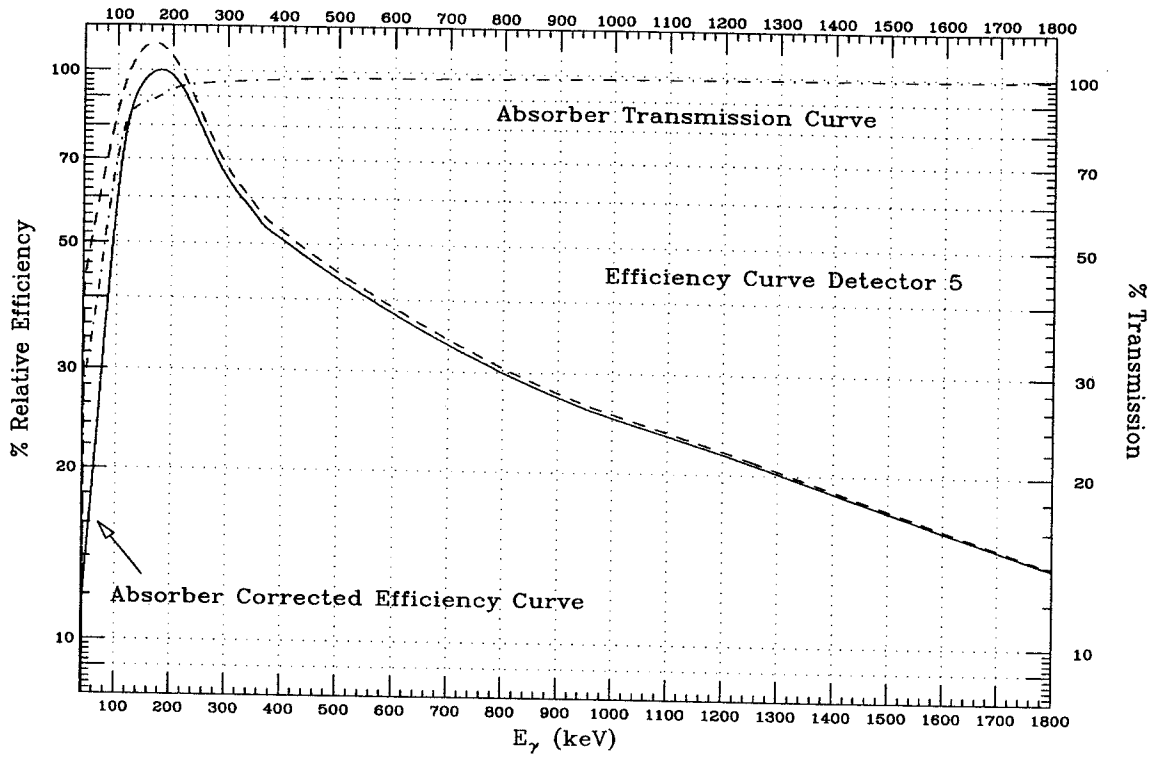

Figure C.15: Efficiency calibration, Absorber Transmission and Absorber-adjusted Efficiency curves for Detector 5.

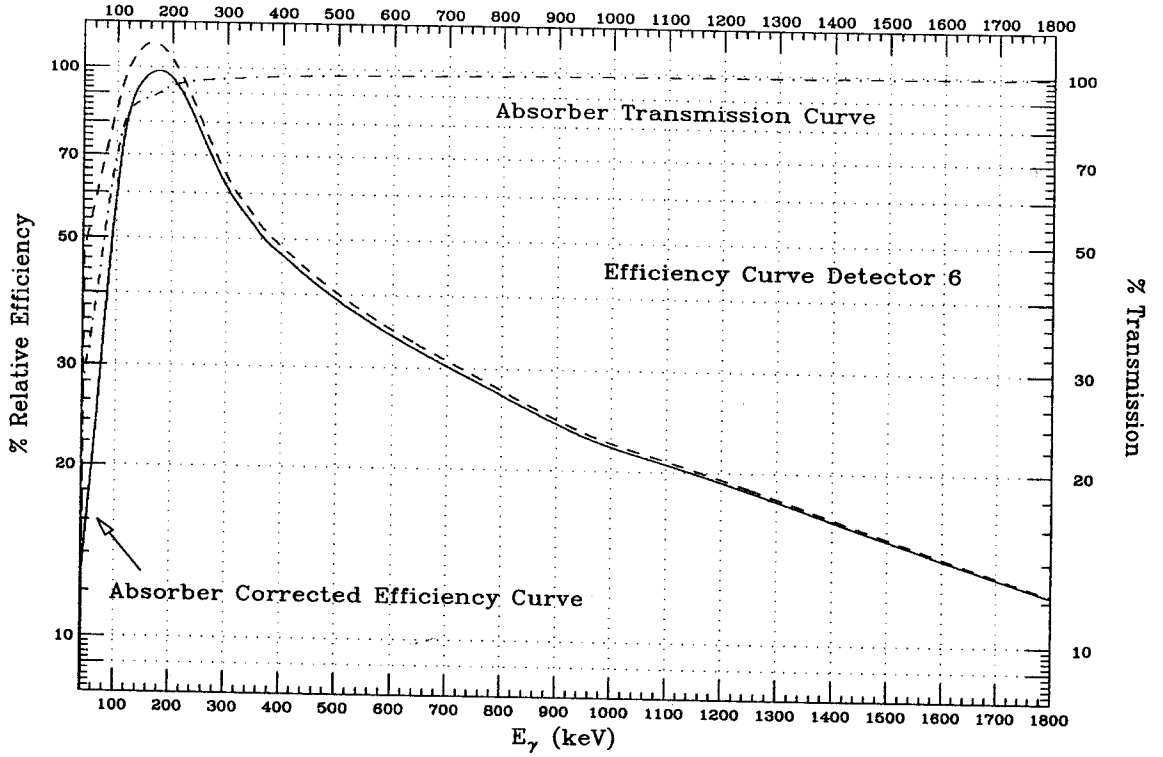

Figure C.16: Efficiency calibration, Absorber Transmission and Absorber-adjusted Efficiency curves for Detector 6.

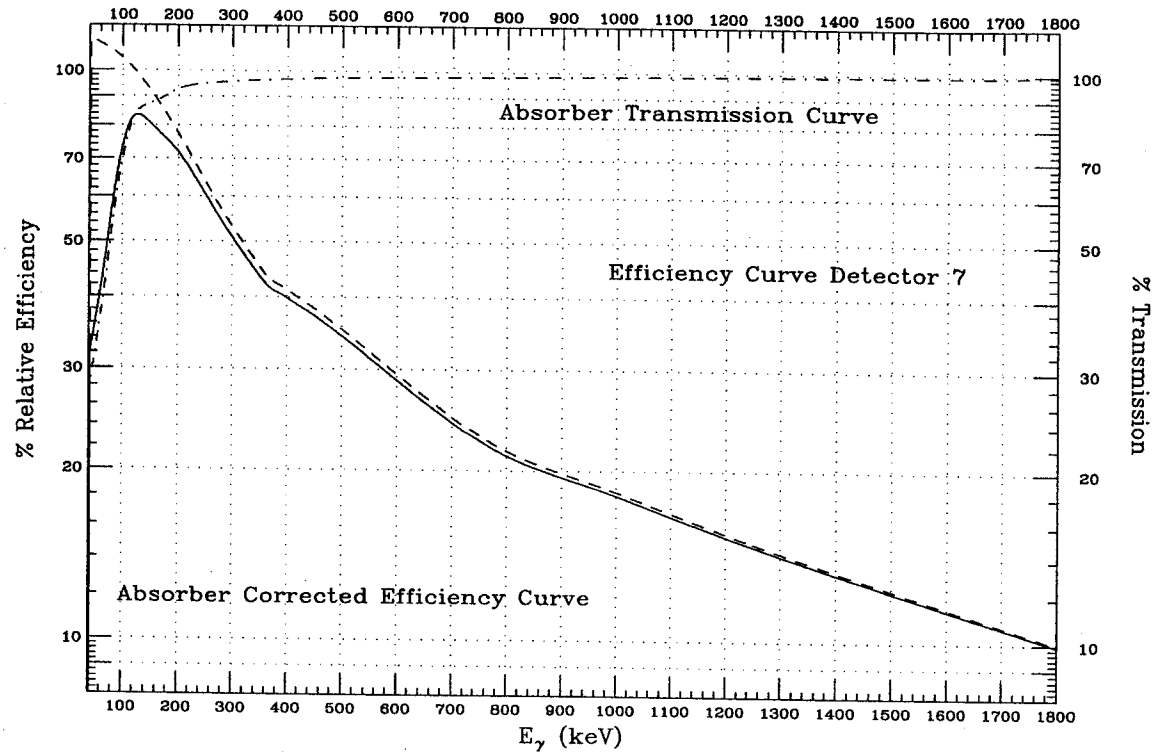

Figure C.17: Efficiency calibration, Absorber Transmission and Absorber-adjusted Efficiency curves for Detector 7.

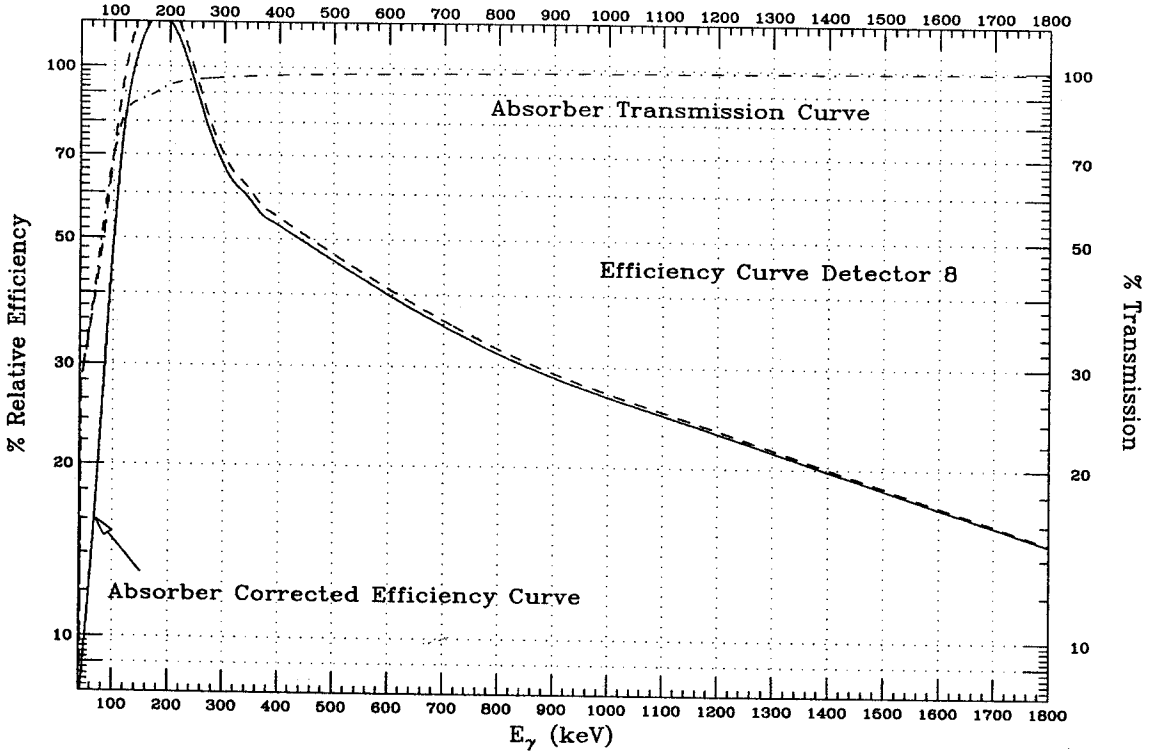

Figure C.18: Efficiency calibration, Absorber Transmission and Absorber-adjusted Efficiency curves for Detector 8.

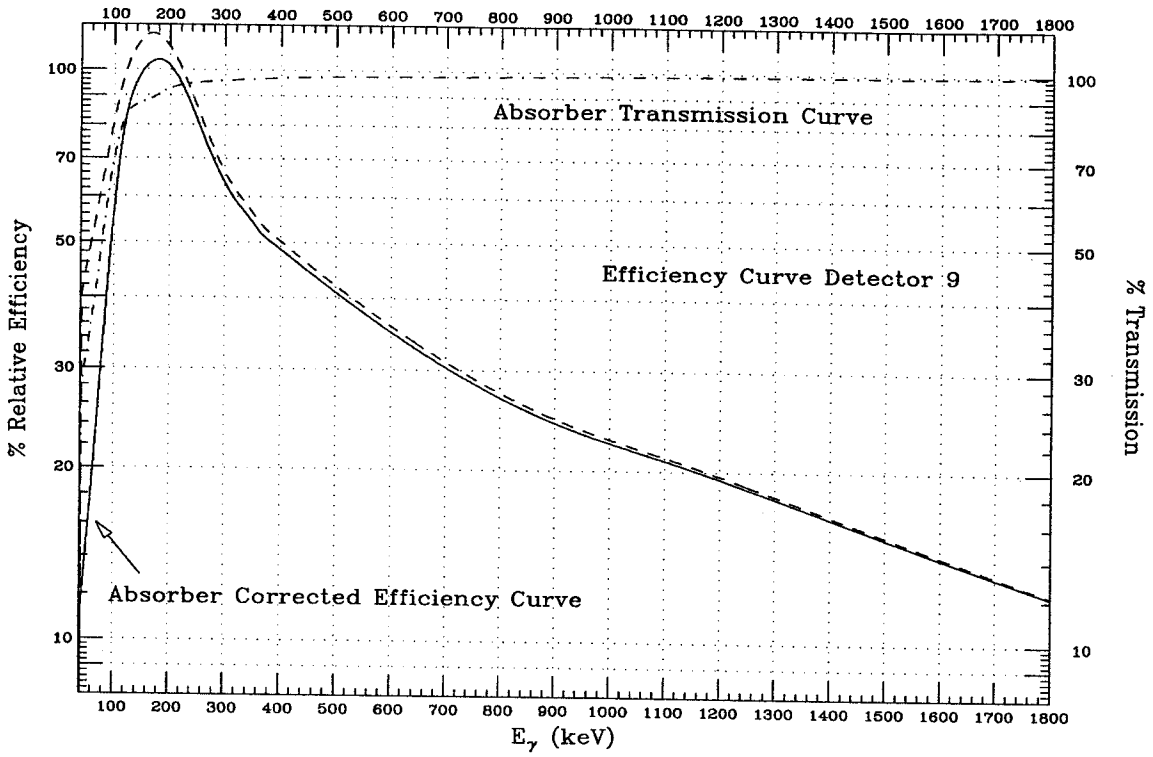

Figure C.19: Efficiency calibration, Absorber Transmission and Absorber-adjusted Efficiency curves for Detector 9.

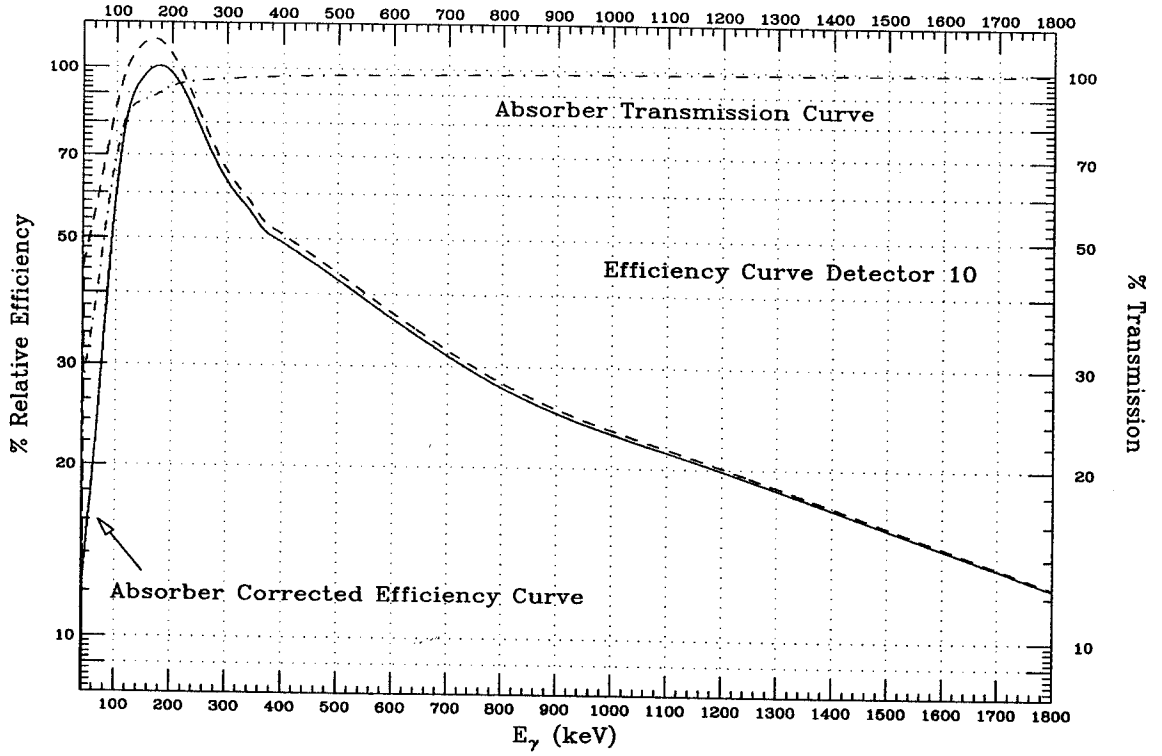

Figure C.20: Efficiency calibration, Absorber Transmission and Absorber-adjusted Efficiency curves for Detector 10.

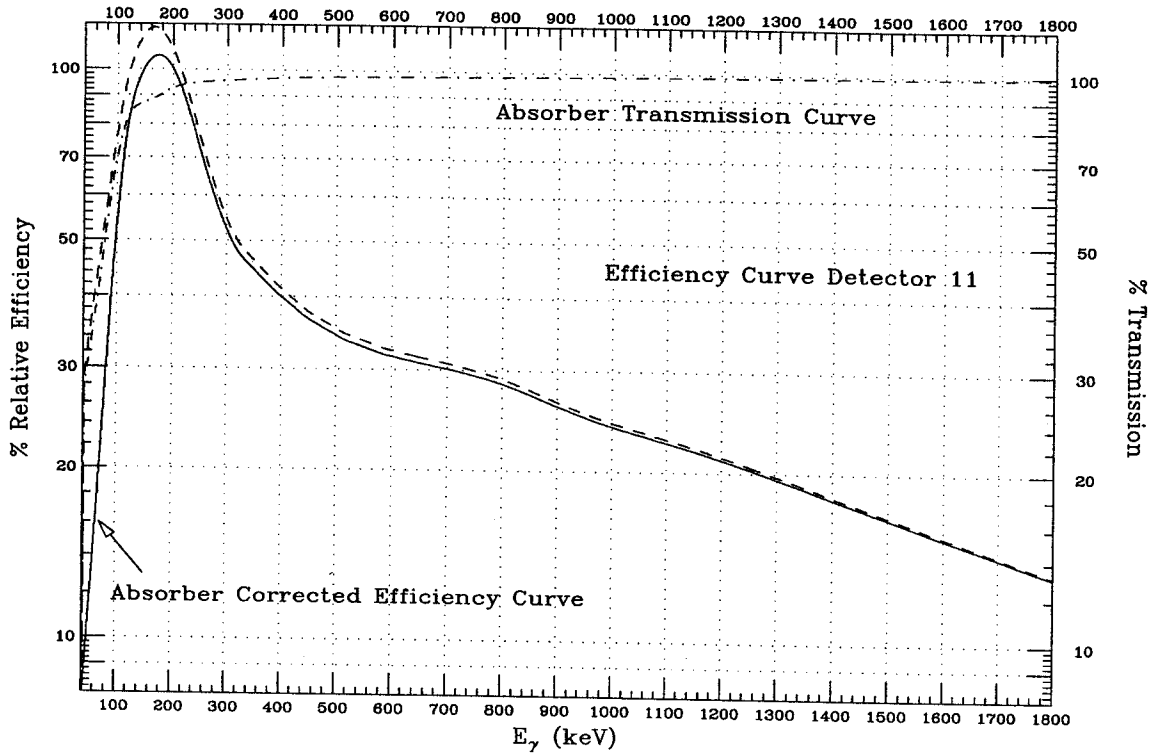

Figure C.21: Efficiency calibration, Absorber Transmission and Absorber-adjusted Efficiency curves for Detector 11.

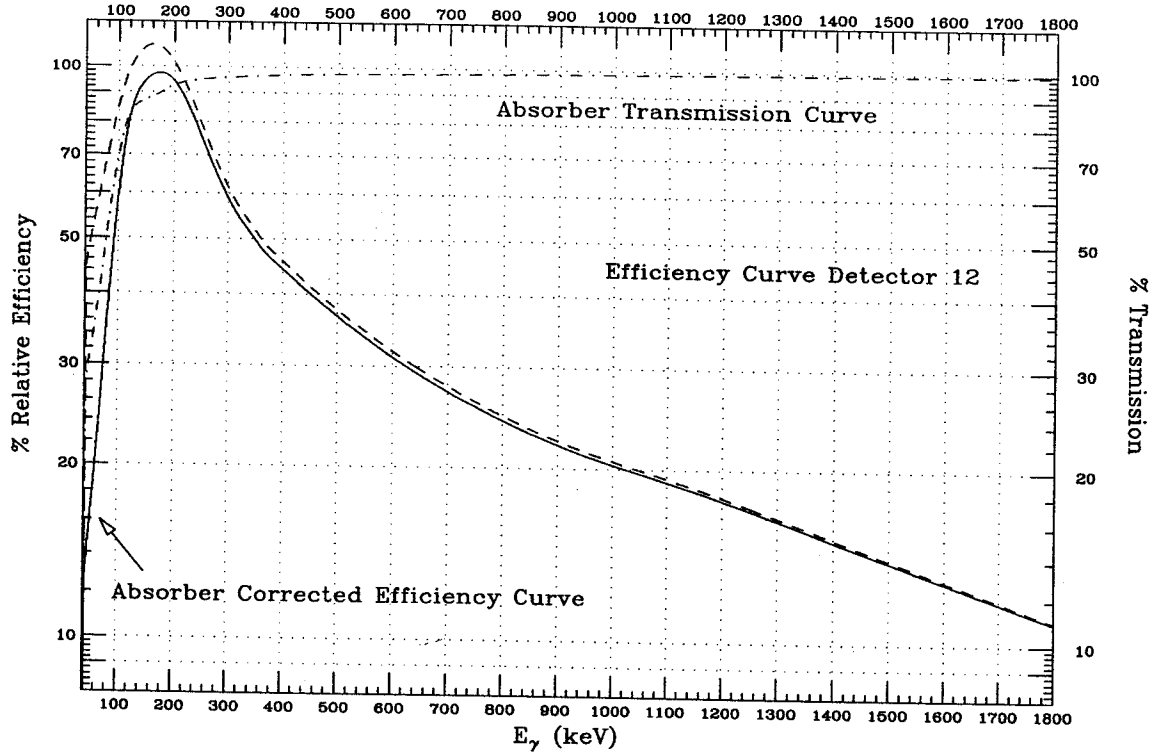

Figure C.22: Efficiency calibration, Absorber Transmission and Absorber-adjusted Efficiency curves for Detector 12.

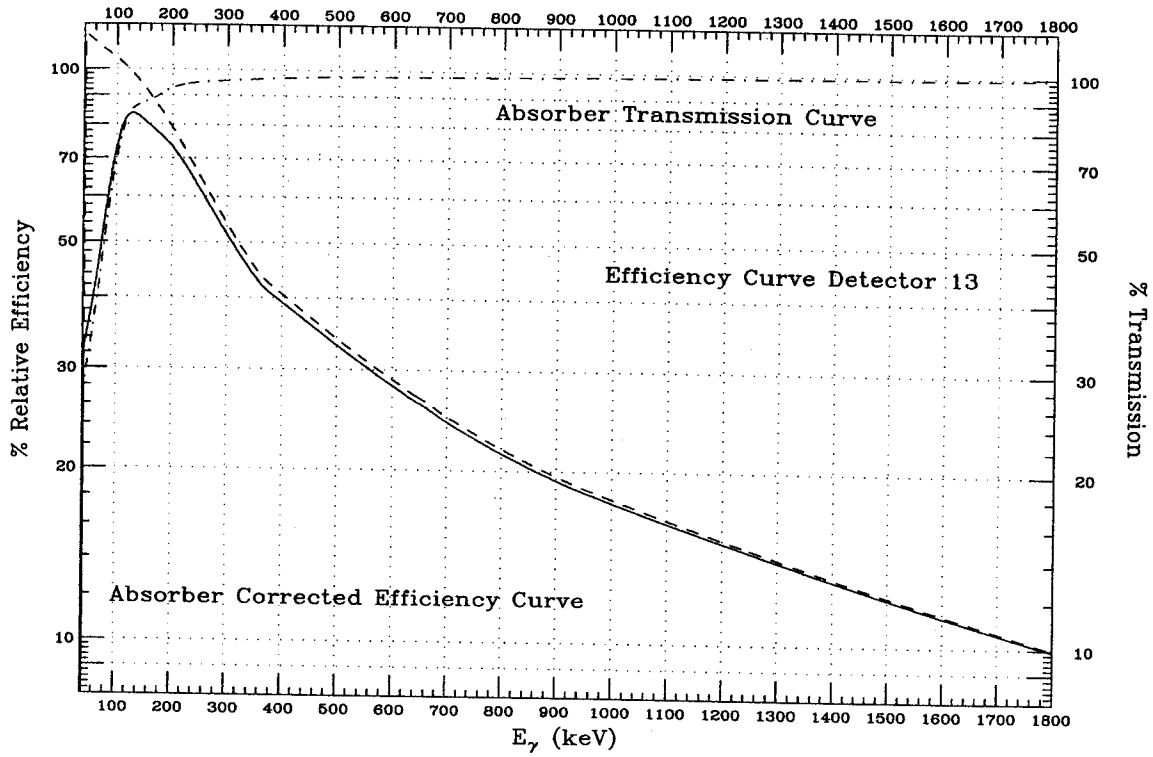

Figure C.23: Efficiency calibration, Absorber Transmission and Absorber-adjusted Efficiency curves for Detector 13.

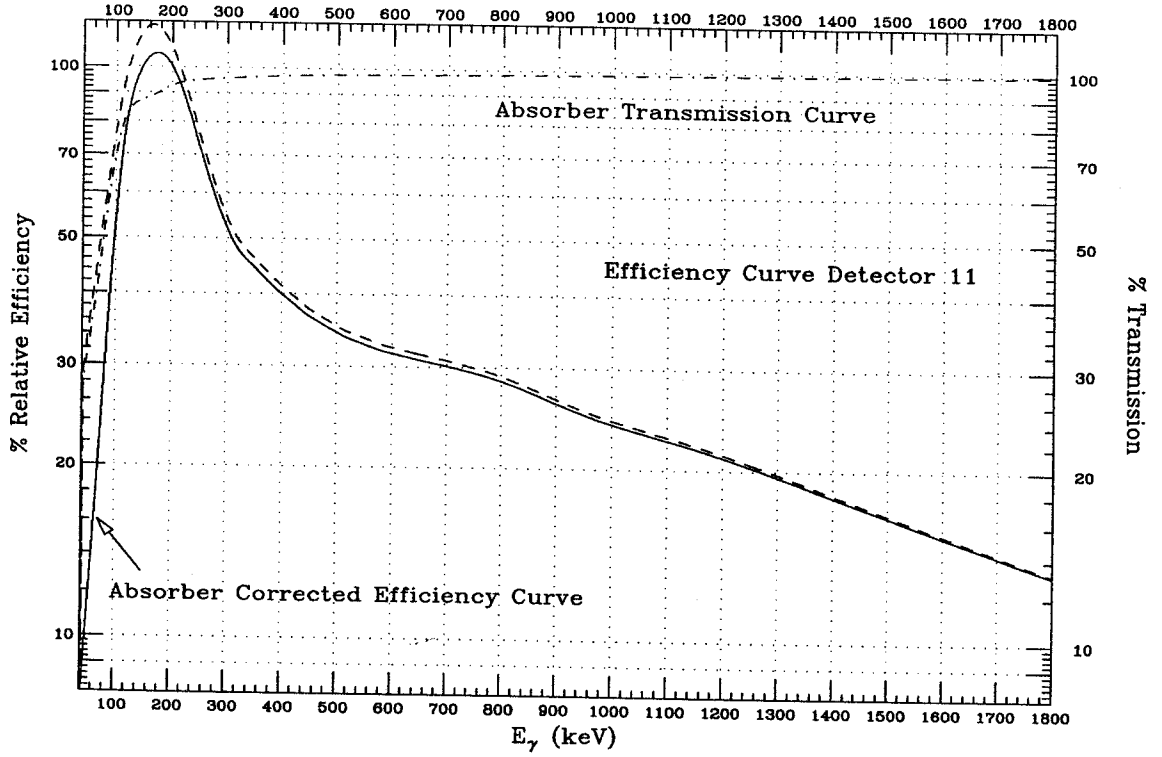

Figure C.24: Efficiency calibration, Absorber Transmission and Absorber-adjusted Efficiency curves for Detector 14.

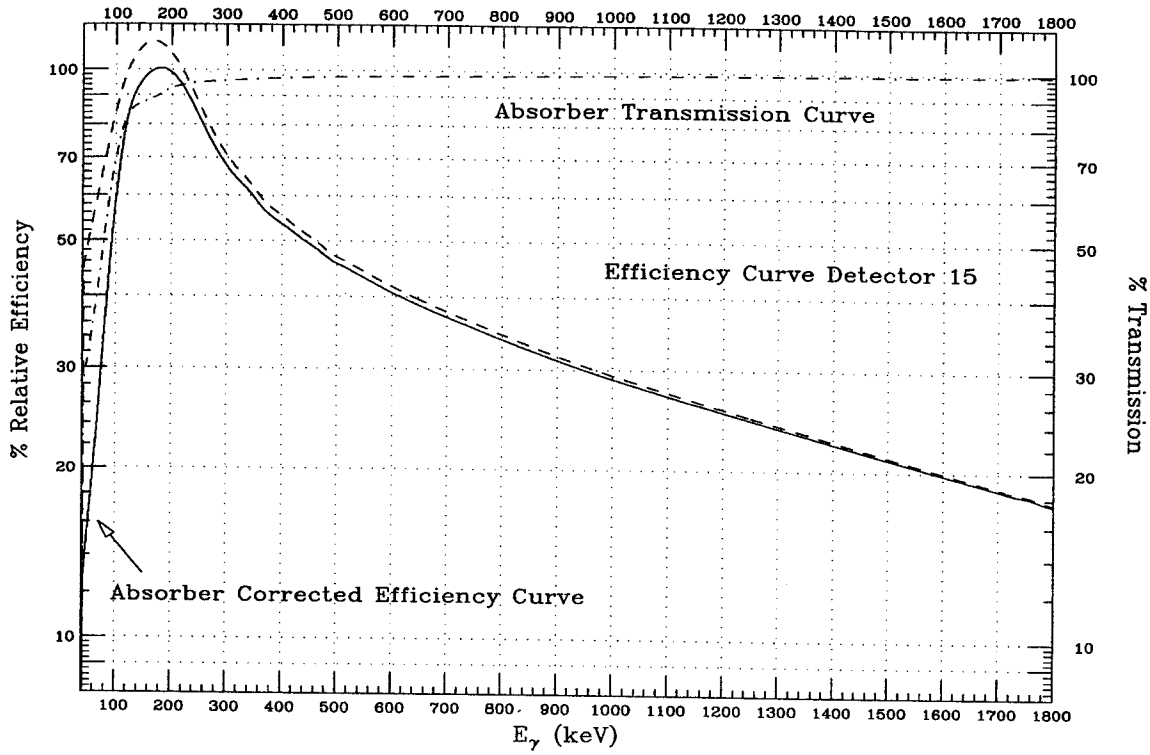

Figure C.25: Efficiency calibration, Absorber Transmission and Absorber-adjusted Efficiency curves for Detector 15.

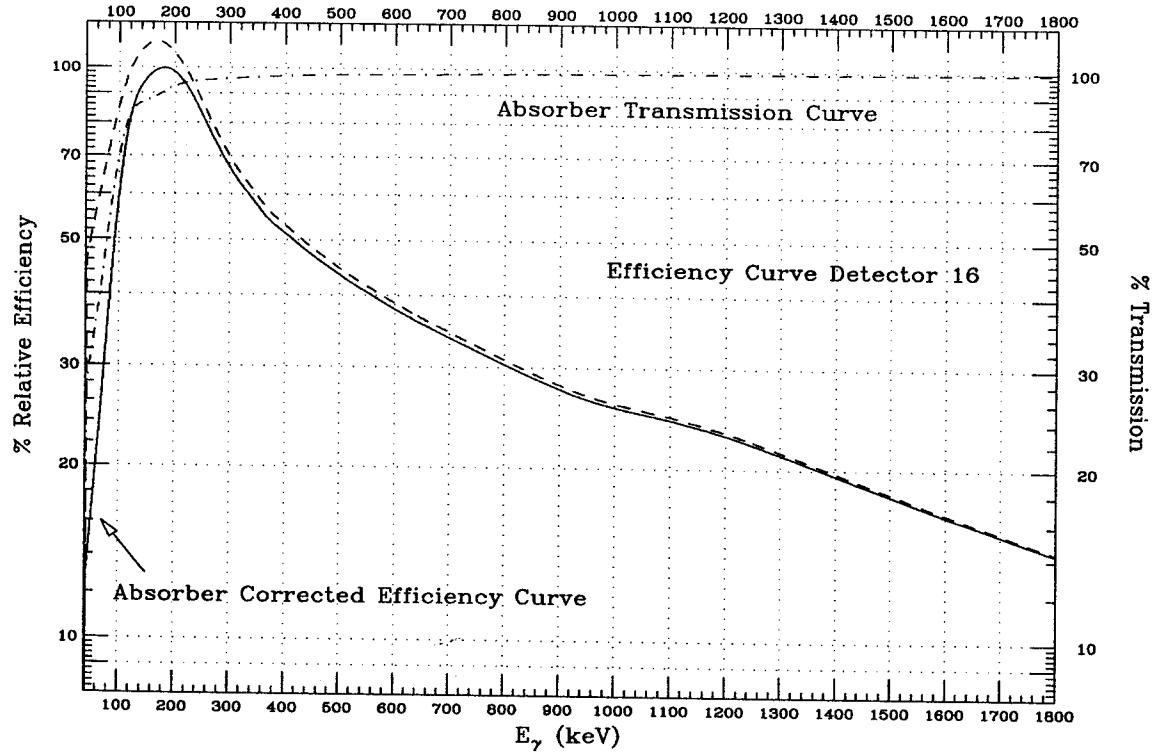

Figure C.26: Efficiency calibration, Absorber Transmission and Absorber-adjusted Efficiency curves for Detector 16.

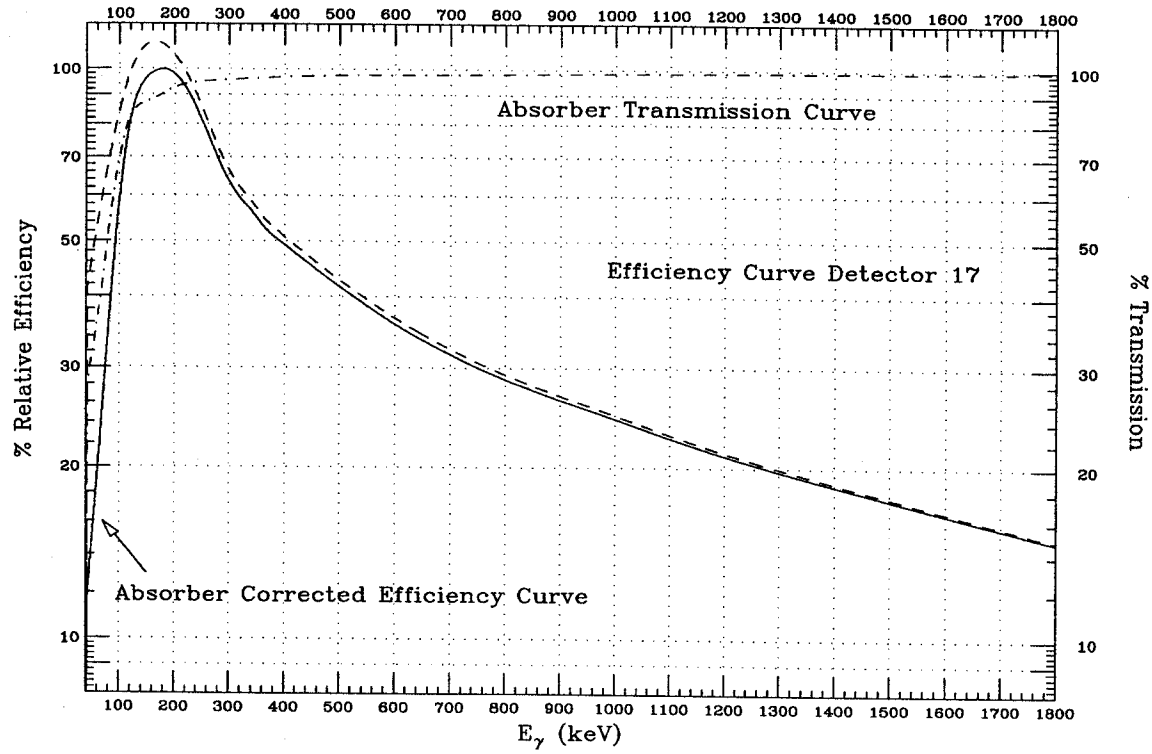

Figure C.27: Efficiency calibration, Absorber Transmission and Absorber-adjusted Efficiency curves for Detector 17.

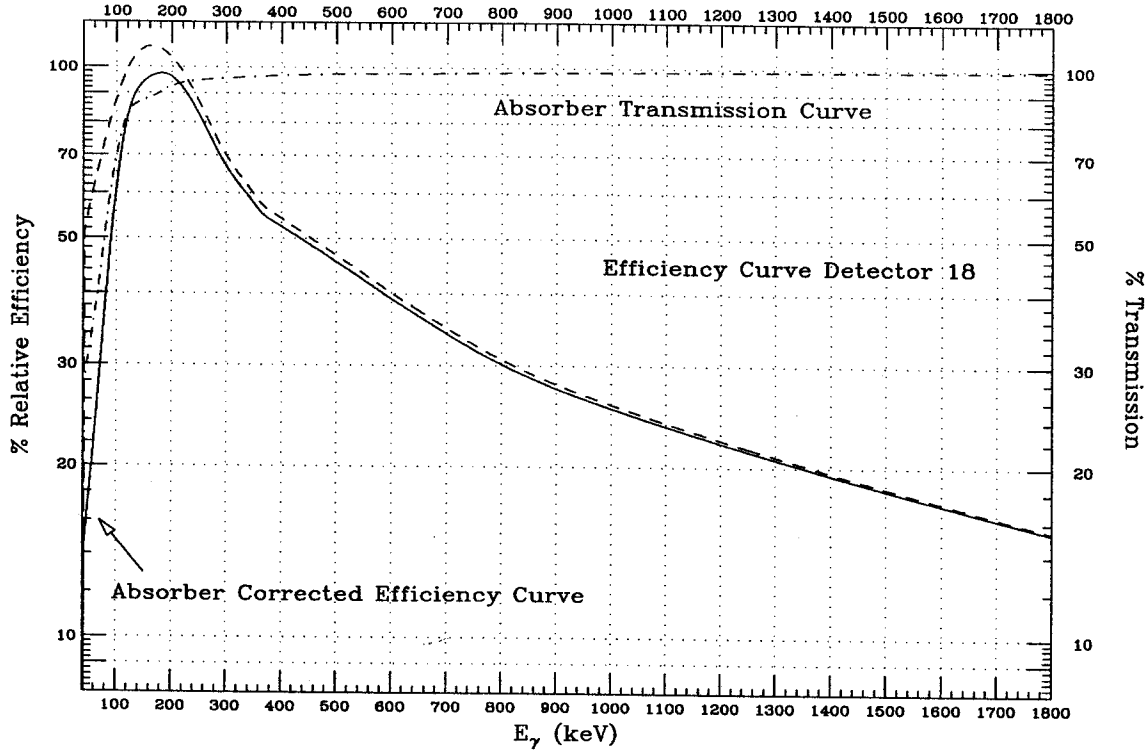

Figure C.28: Efficiency calibration, Absorber Transmission and Absorber-adjusted Efficiency curves for Detector 18.

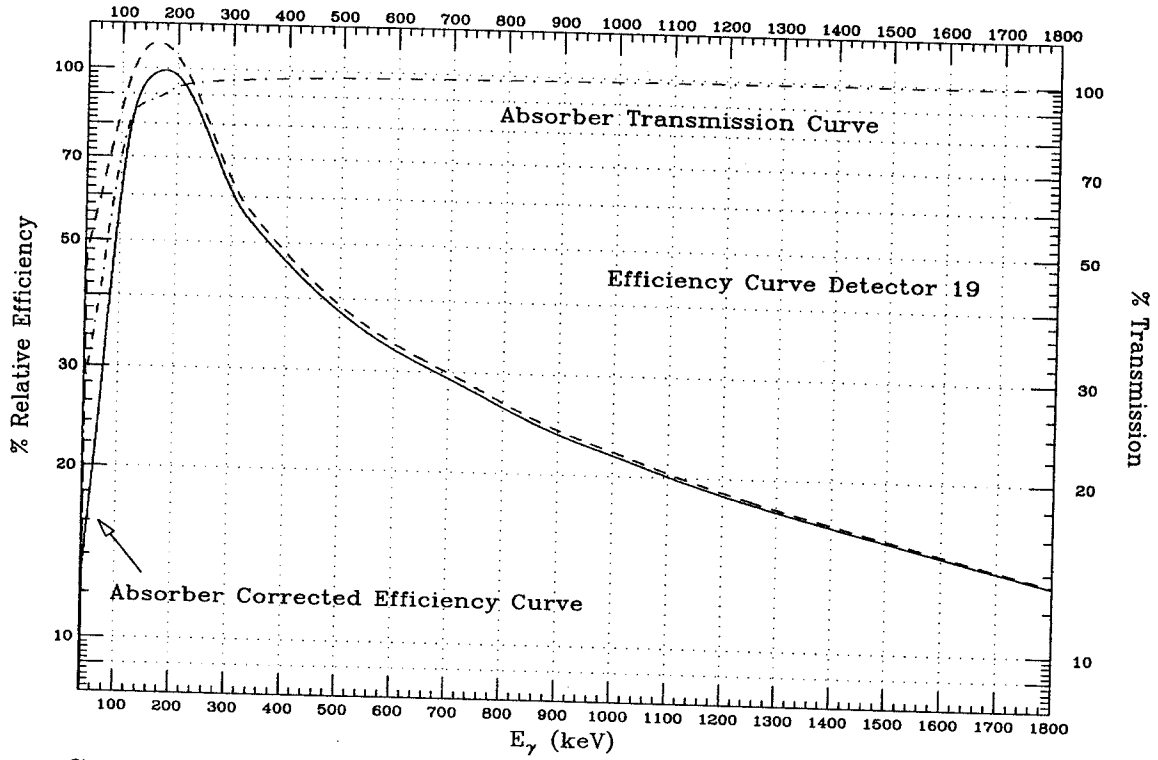

Figure C.29: Efficiency calibration, Absorber Transmission and Absorber-adjusted Efficiency curves for Detector 19.

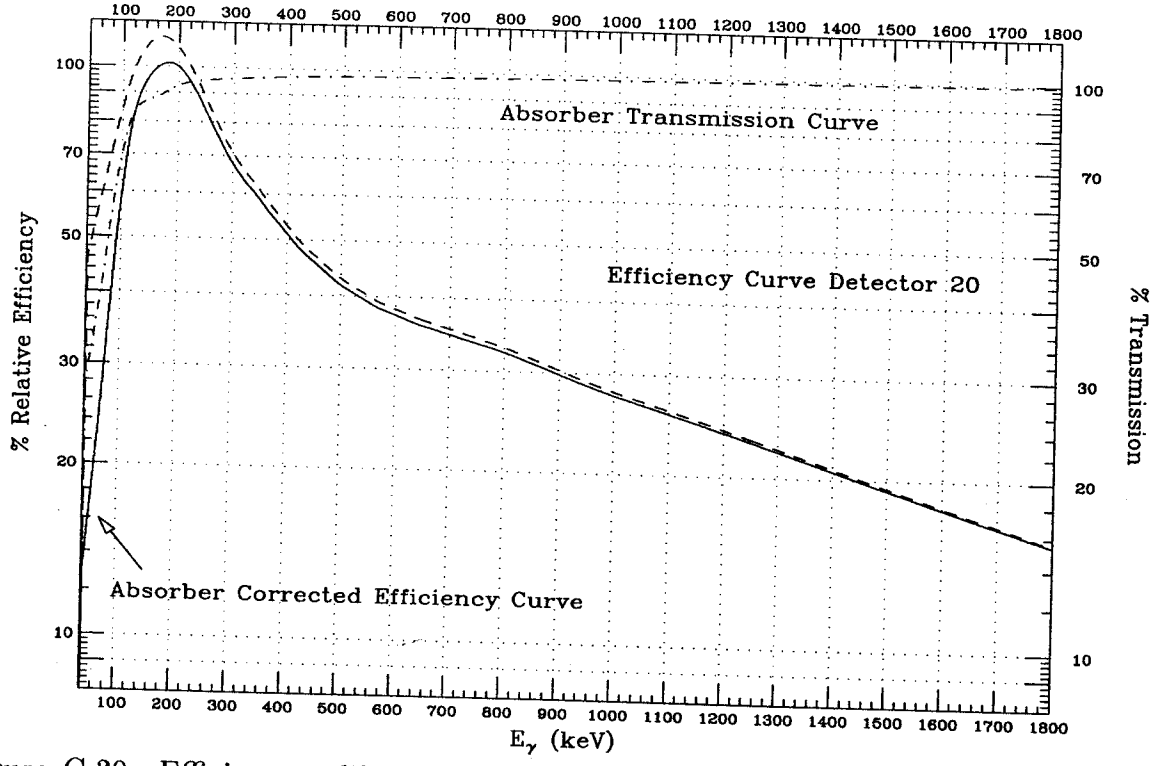

Figure C.30: Efficiency calibration, Absorber Transmission and Absorber-adjusted Efficiency curves for Detector 20.

Appendix D

Preliminary Spectra

D.1 Energy versus Time arrays

2-D Energy versus Time arrays (1500×2000 channels), using triple coincidence data, were generated for the first ten detectors. Six different 1-D TAC cuts were made on these arrays to show prompt and delayed energy spectra for each detector. The TAC timing regions per cut are listed in Table 5.9. There were two 2-D Energy versus Time arrays generated for the single coincidence events; one, from the 60-1500 channel number region and the other, from the 1501-3000 channel number region. These are also included in this Appendix, without any corresponding 1-D TAC cuts.

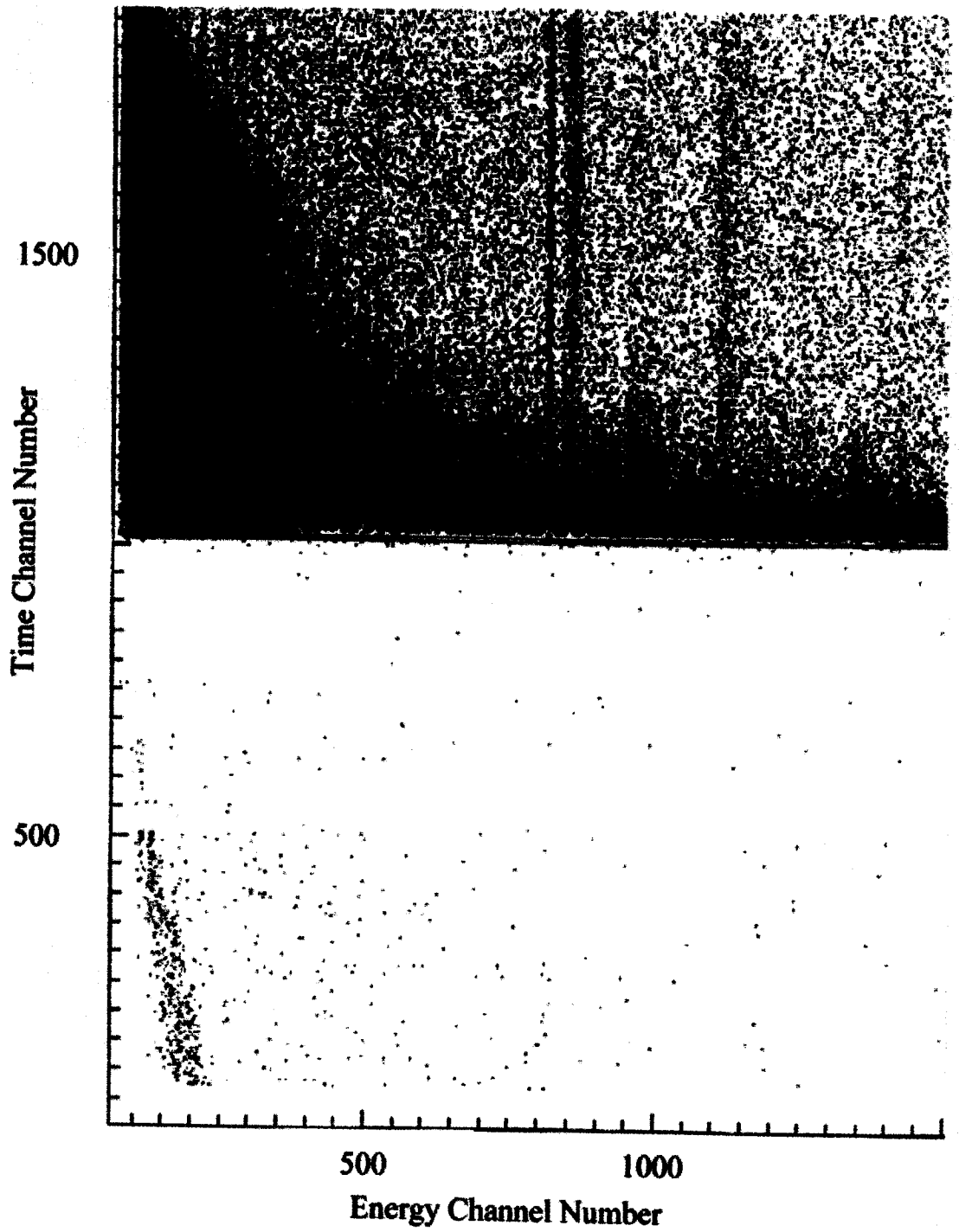

Figure D.1: Time versus E_γ plot for single events from channels 60-1500.

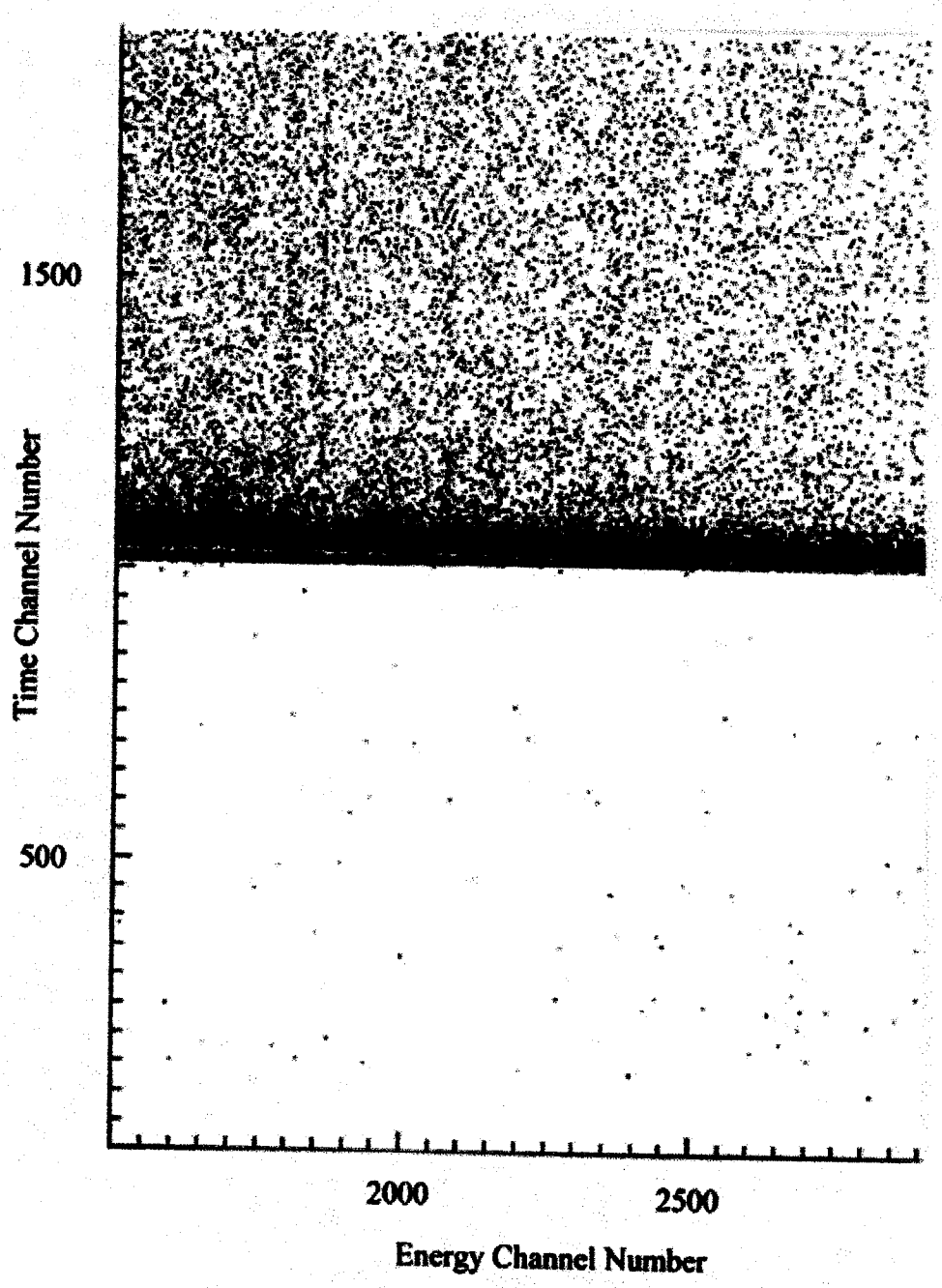

Figure D.2: Time versus E_γ plot for single events from channels 1500-3000.

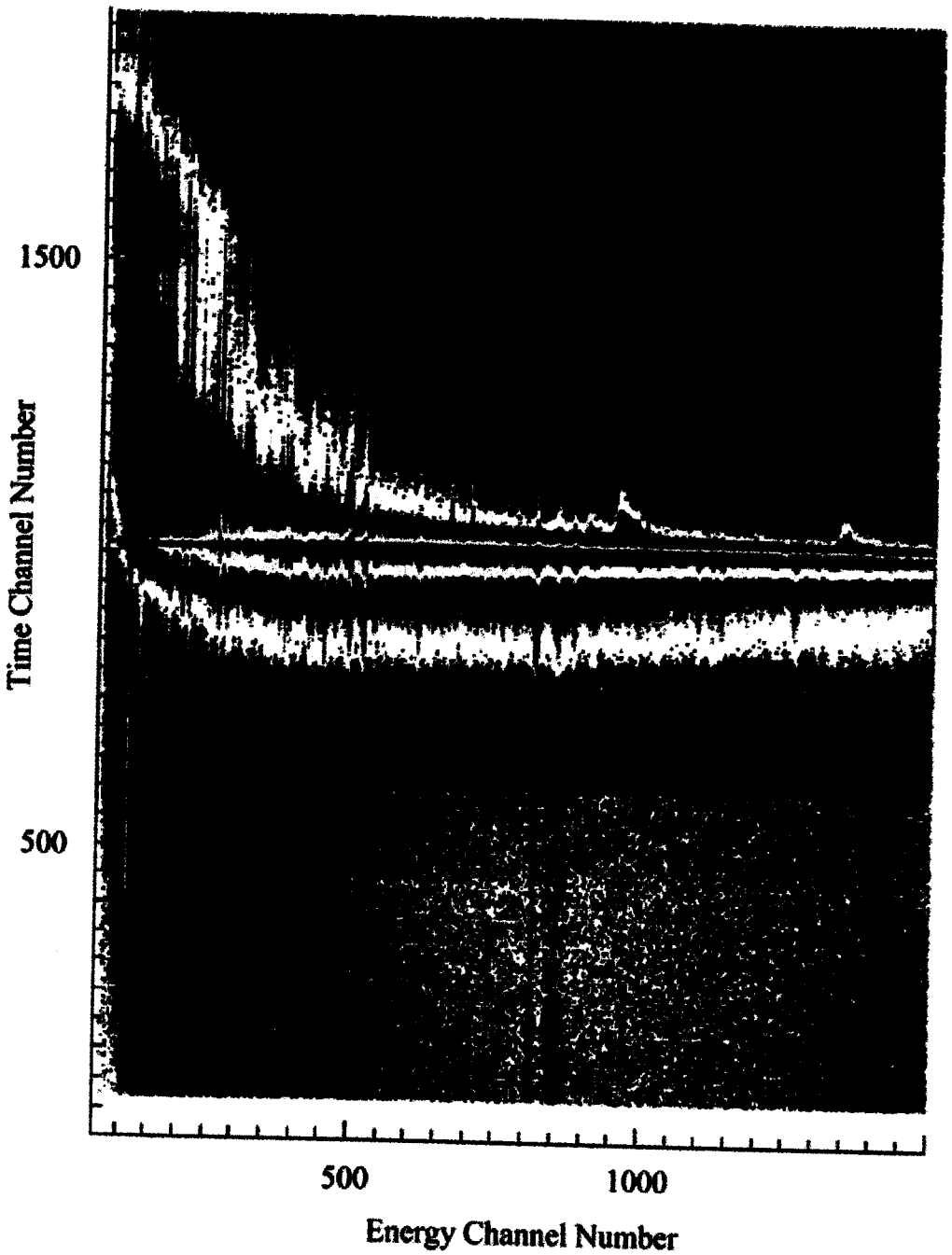

Figure D.3: Time versus E_γ plot for triple events from detector 1.

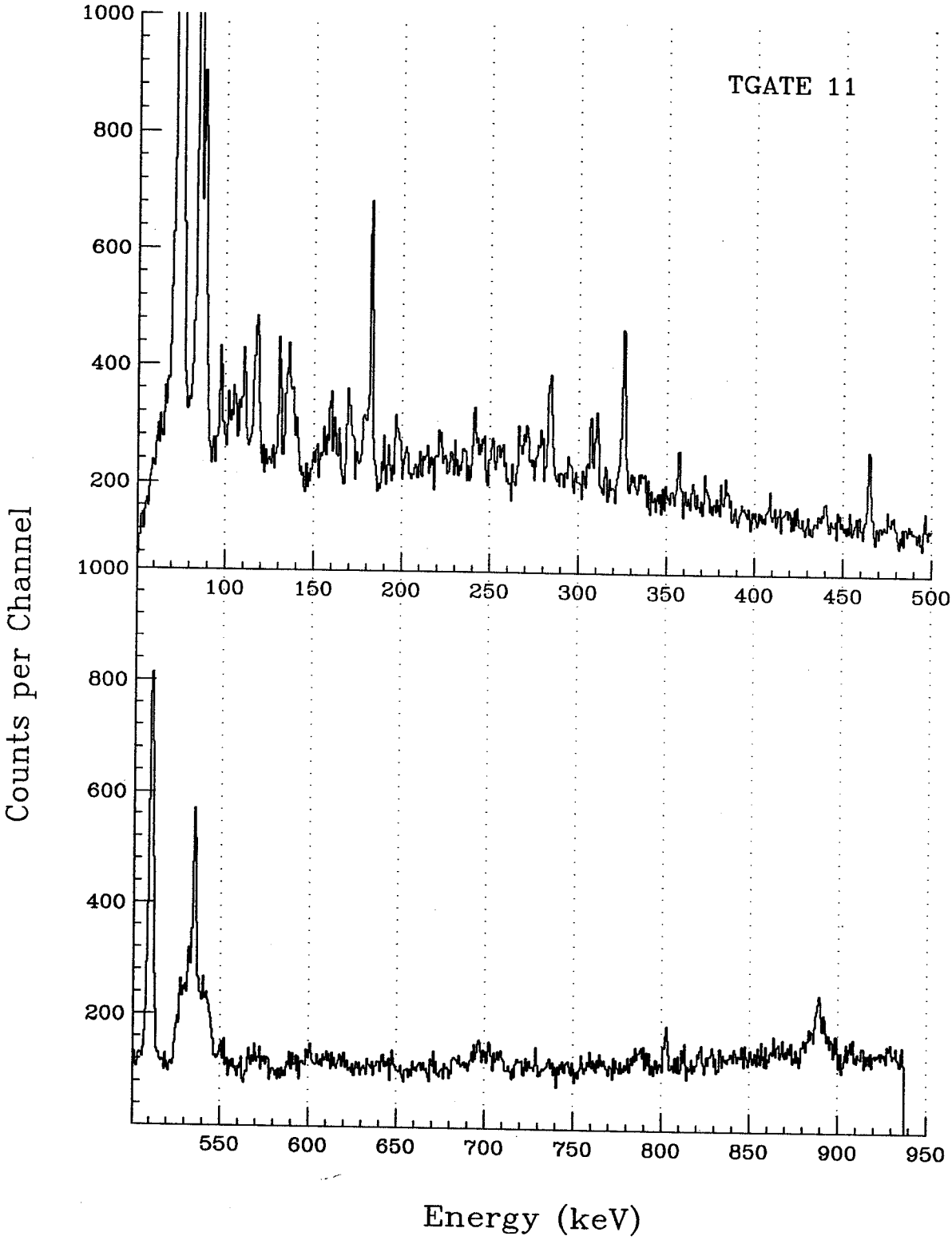

Figure D.4: Composite energy spectrum from TAC gate region 1, detector 1.

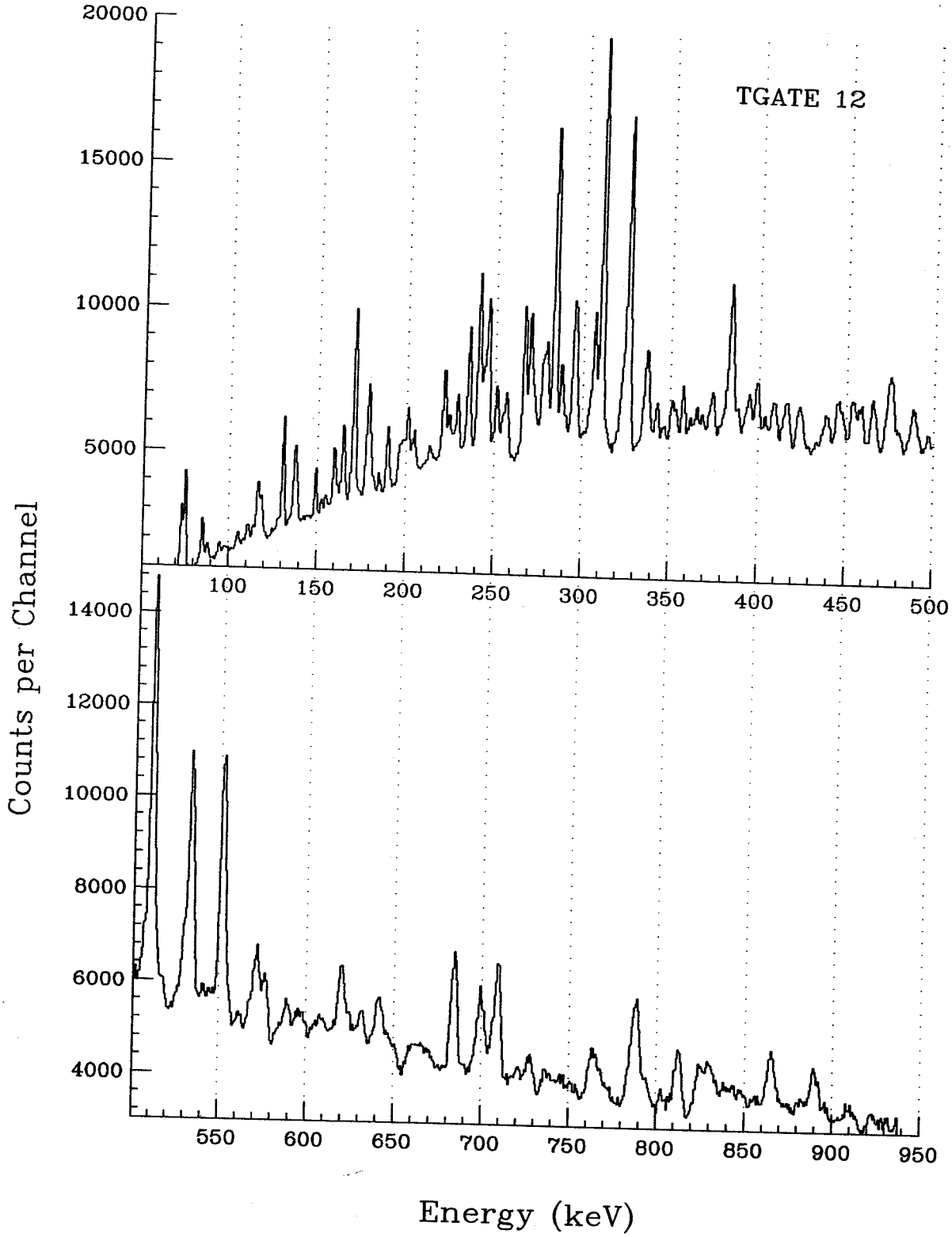

Figure D.5: Composite energy spectrum from TAC gate region 2, detector 1.

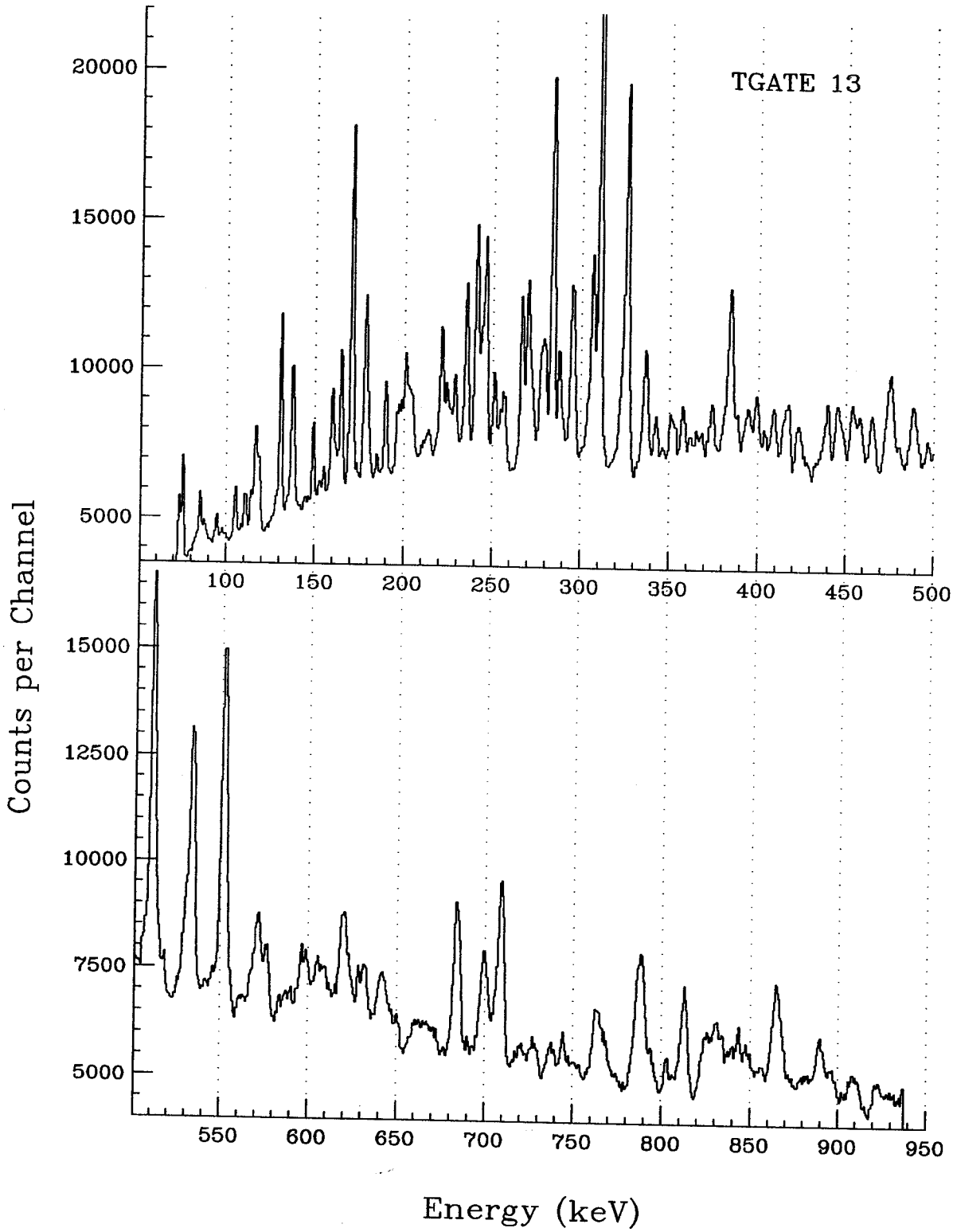

Figure D.6: Composite energy spectrum from TAC gate region 3, detector 1.

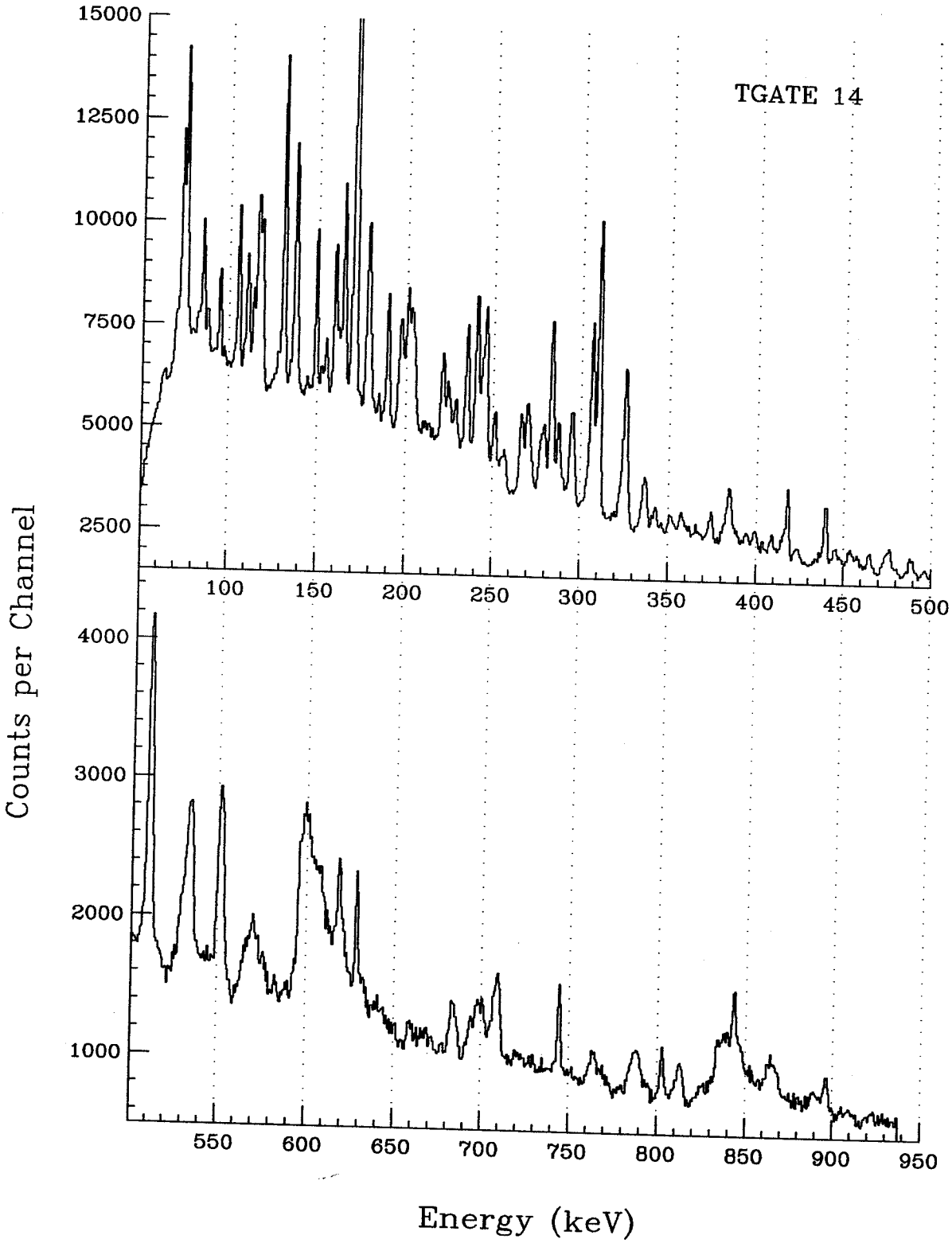

Figure D.7: Composite energy spectrum from TAC gate region 4, detector 1.

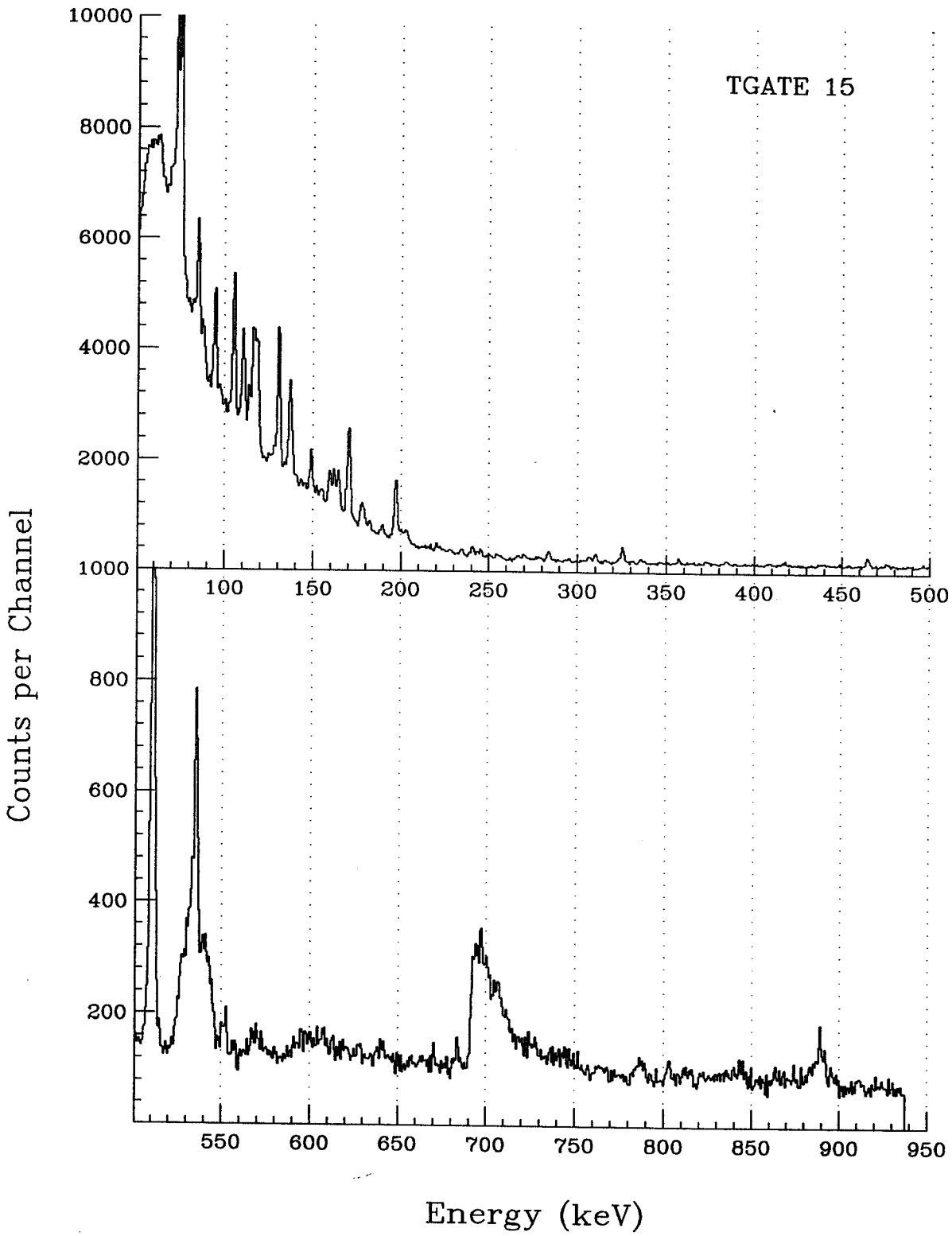

Figure D.8: Composite energy spectrum from TAC gate region 5, detector 1.

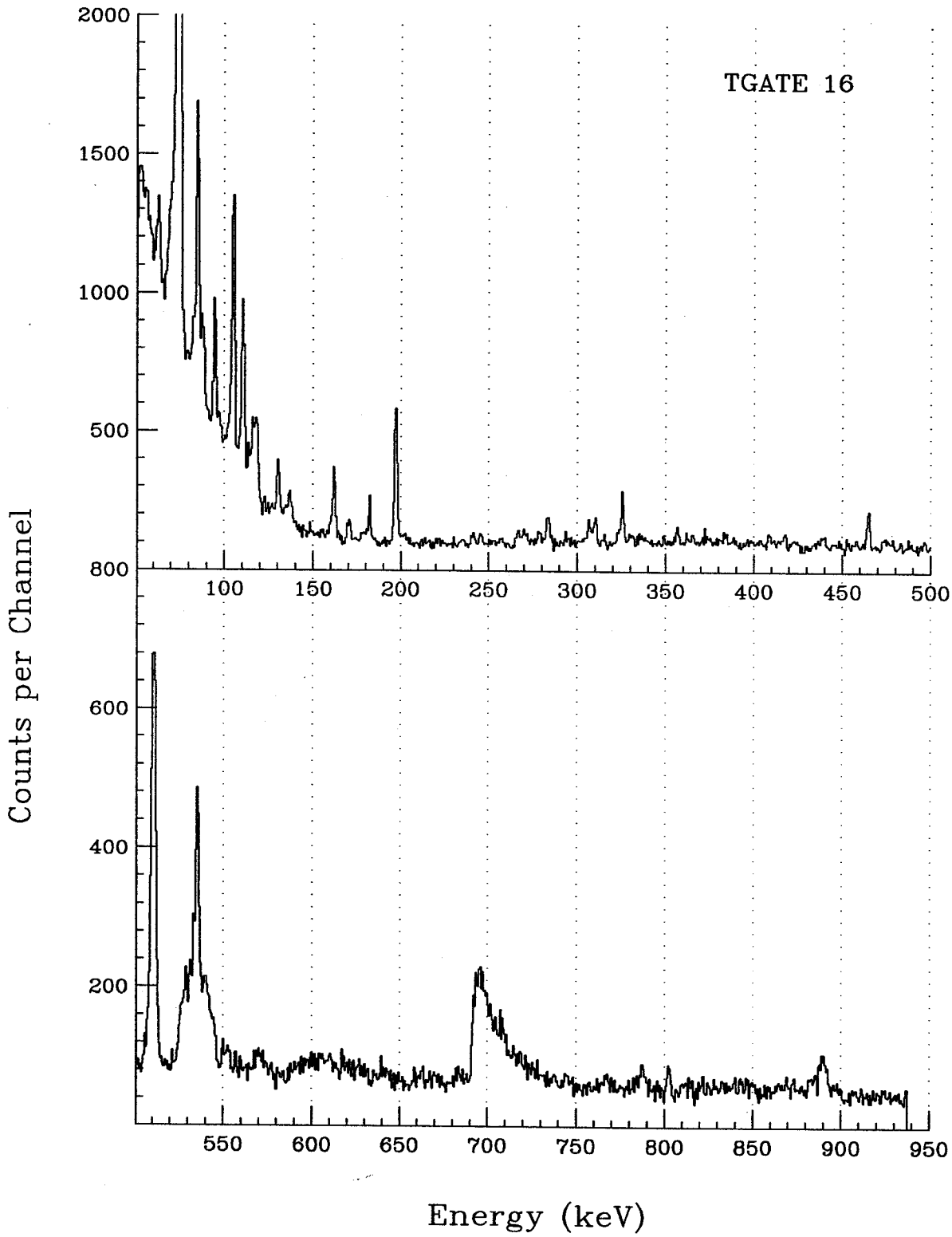

Figure D.9: Composite energy spectrum from TAC gate region 6, detector 1.

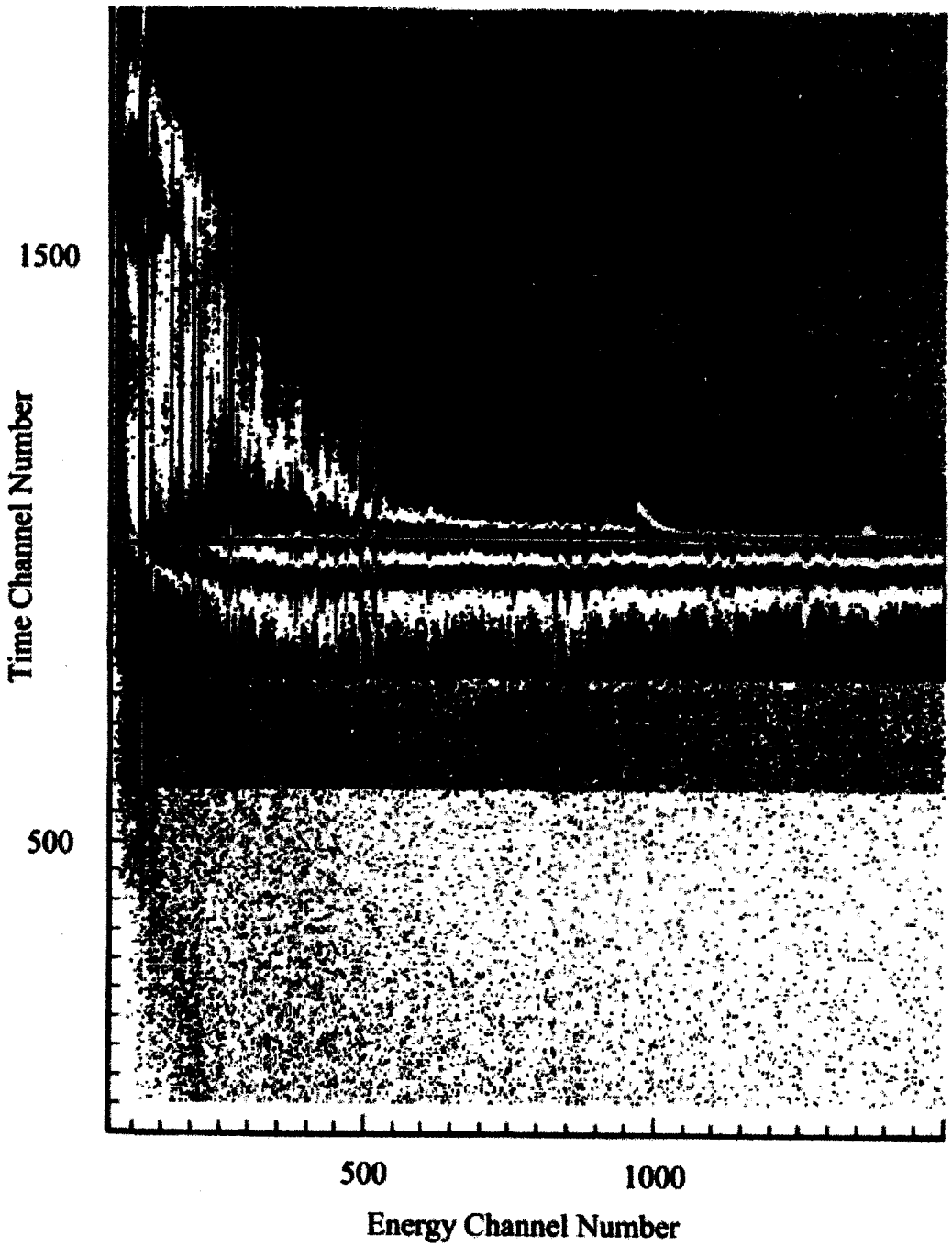

Figure D.10: Time versus E_γ plot for triple events from detector 2.

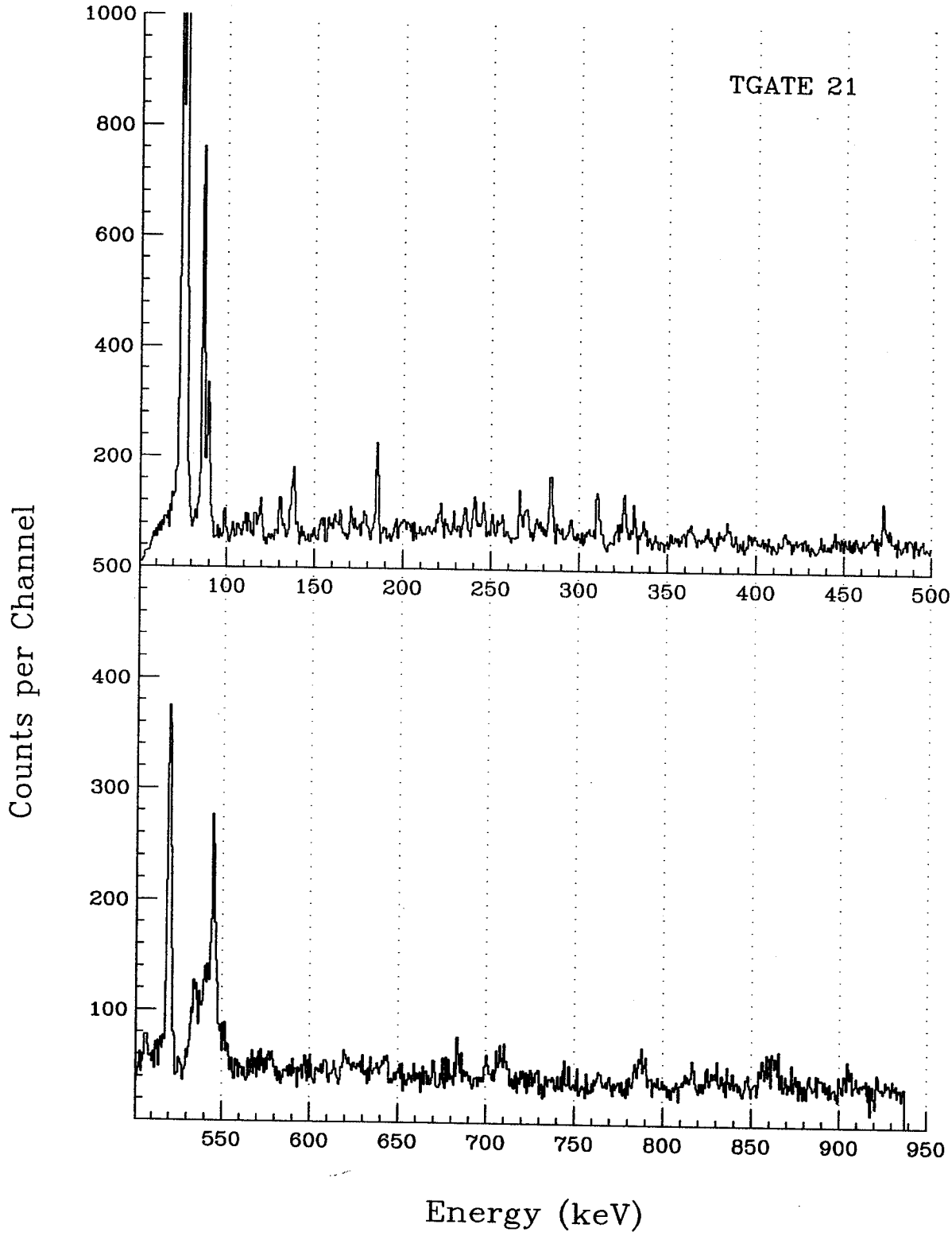

Figure D.11: Composite energy spectrum from TAC gate region 1, detector 2.

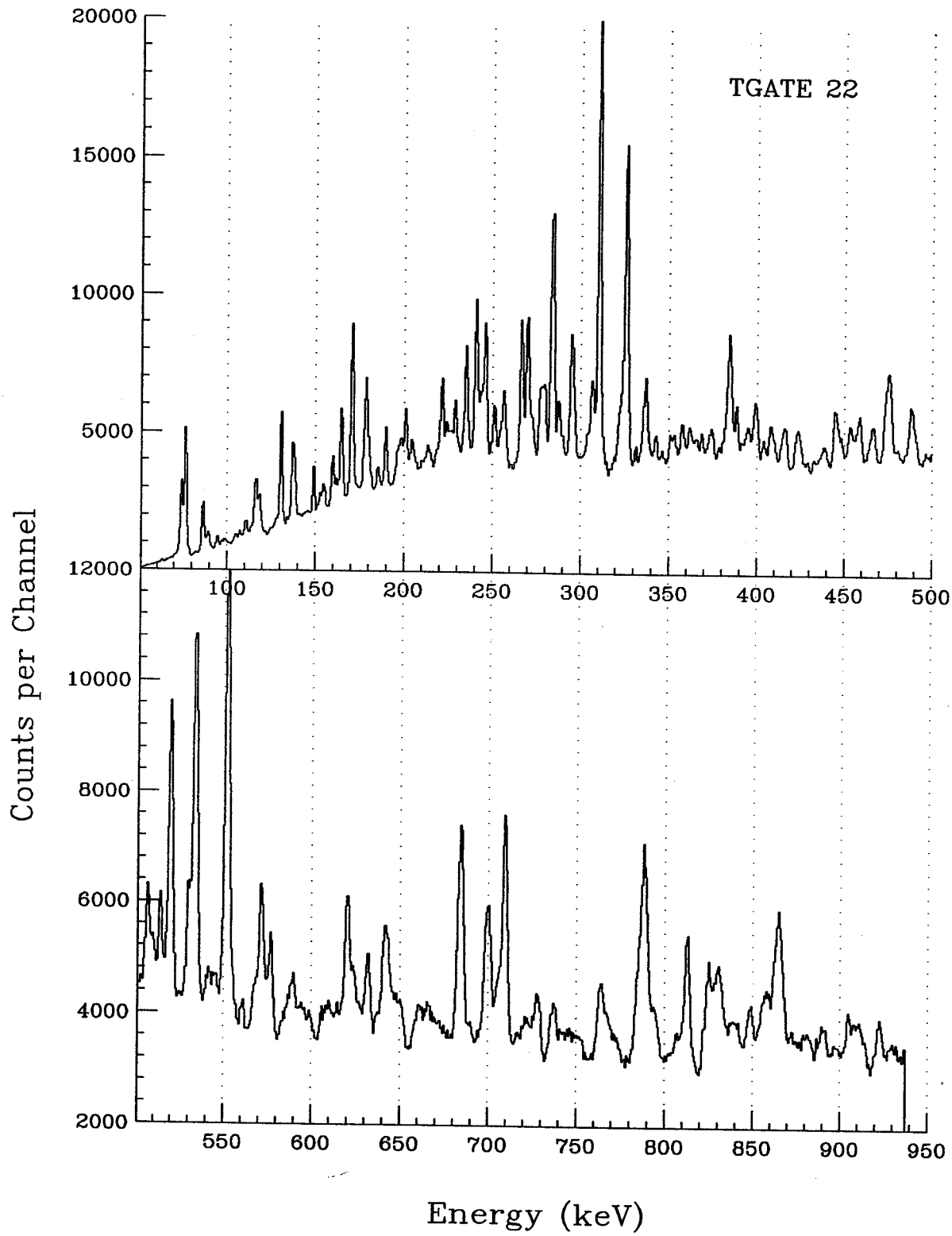

Figure D.12: Composite energy spectrum from TAC gate region 2, detector 2.

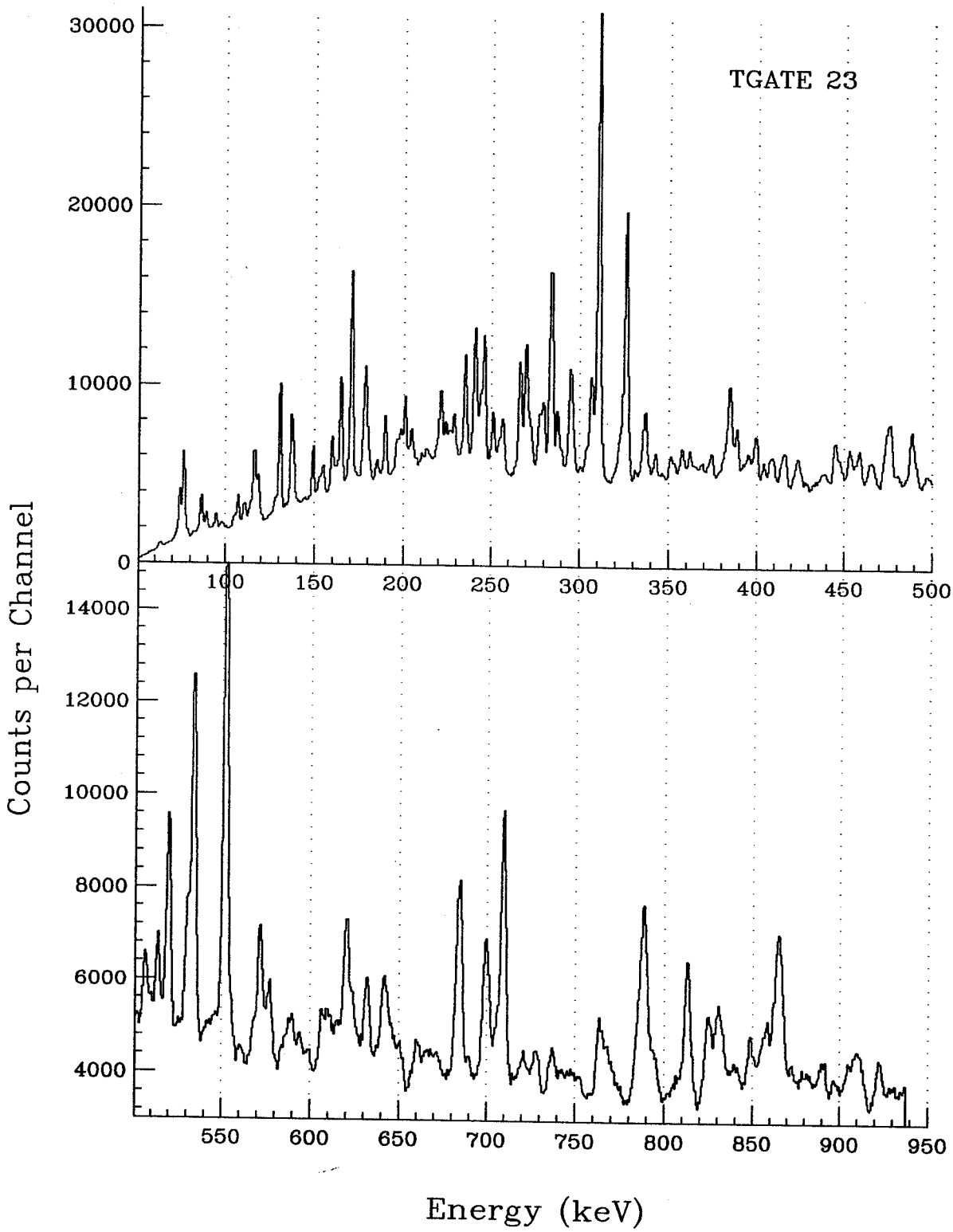

Figure D.13: Composite energy spectrum from TAC gate region 3, detector 2.

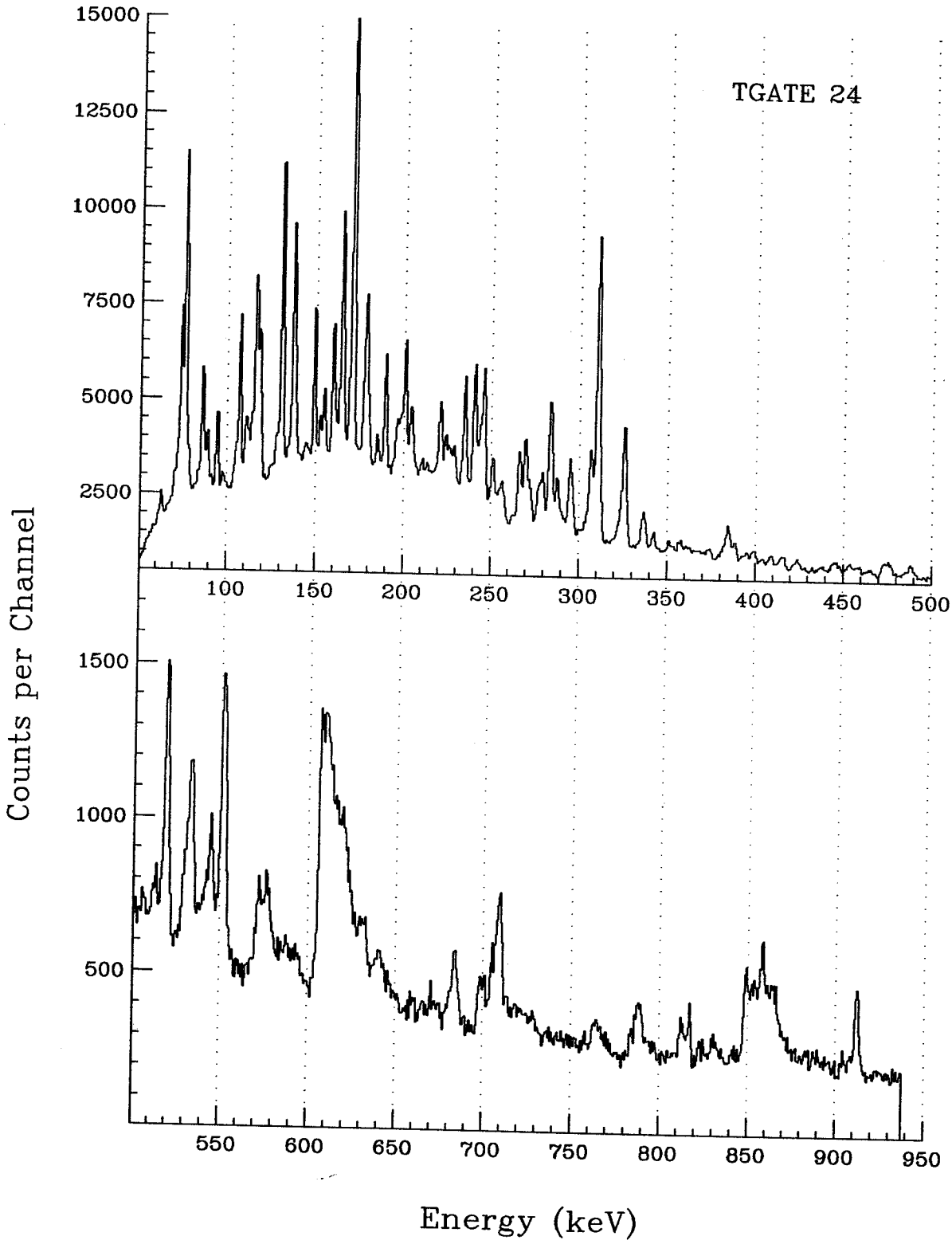

Figure D.14: Composite energy spectrum from TAC gate region 4, detector 2.

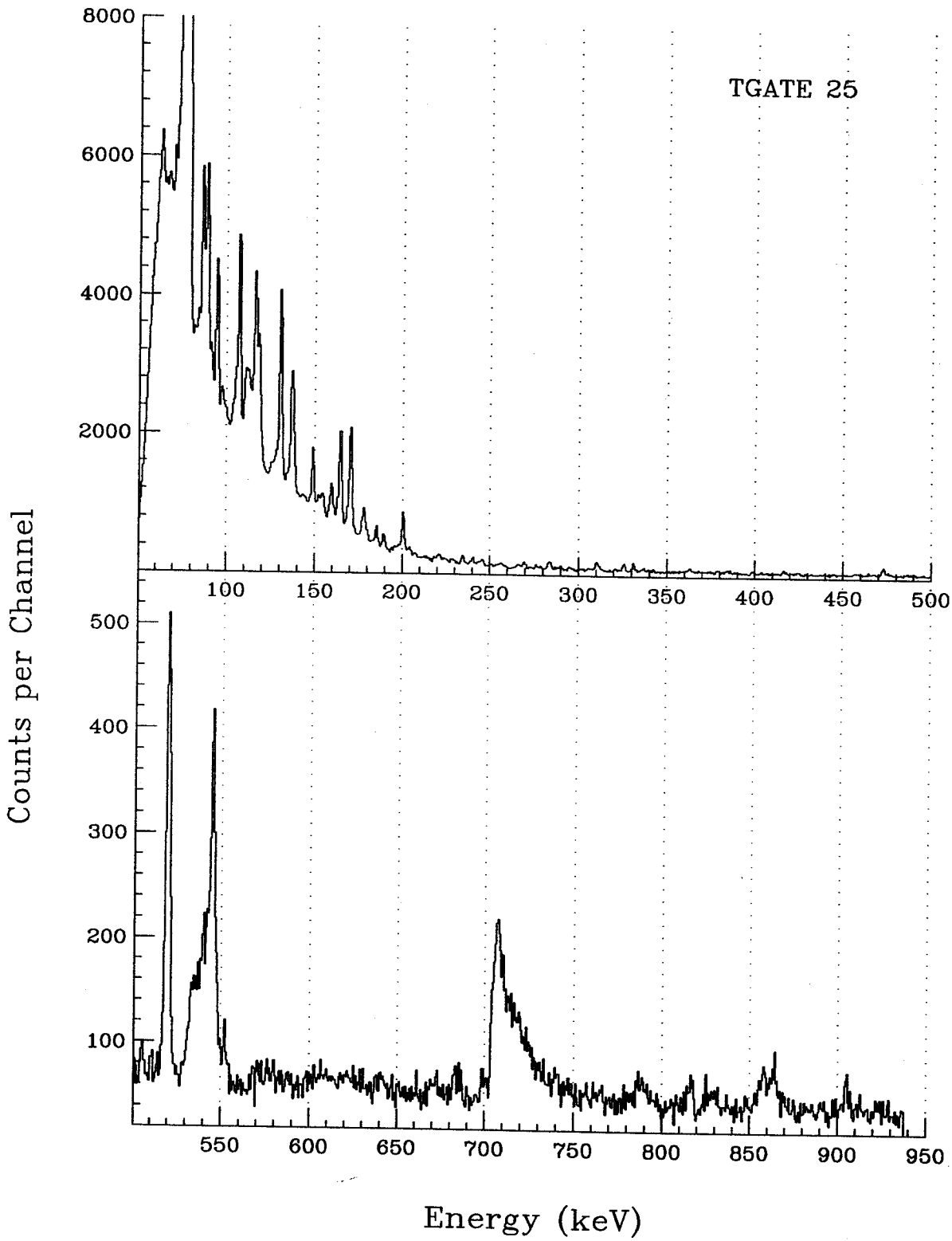

Figure D.15: Composite energy spectrum from TAC gate region 5, detector 2.

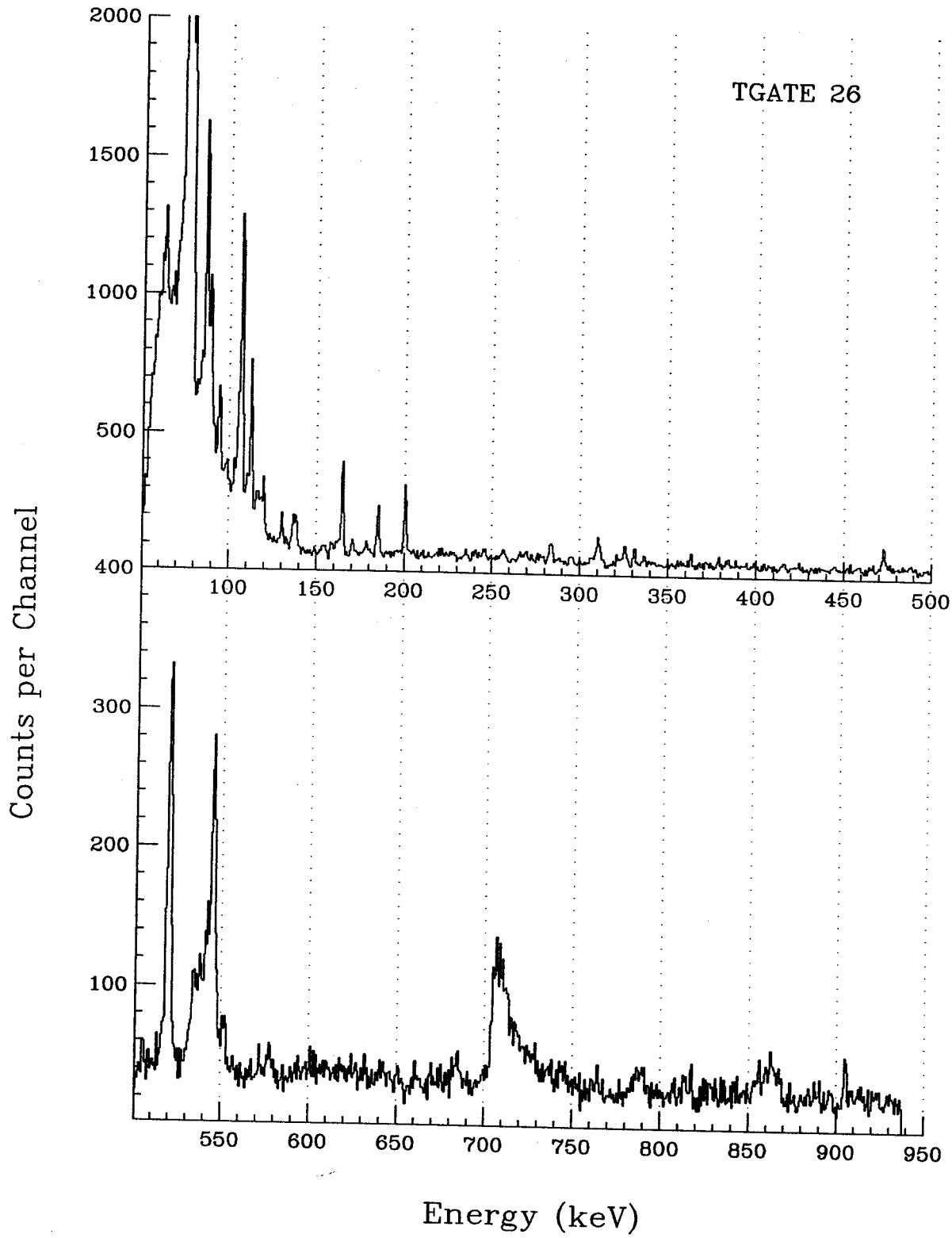

Figure D.16: Composite energy spectrum from TAC gate region 6, detector 2.

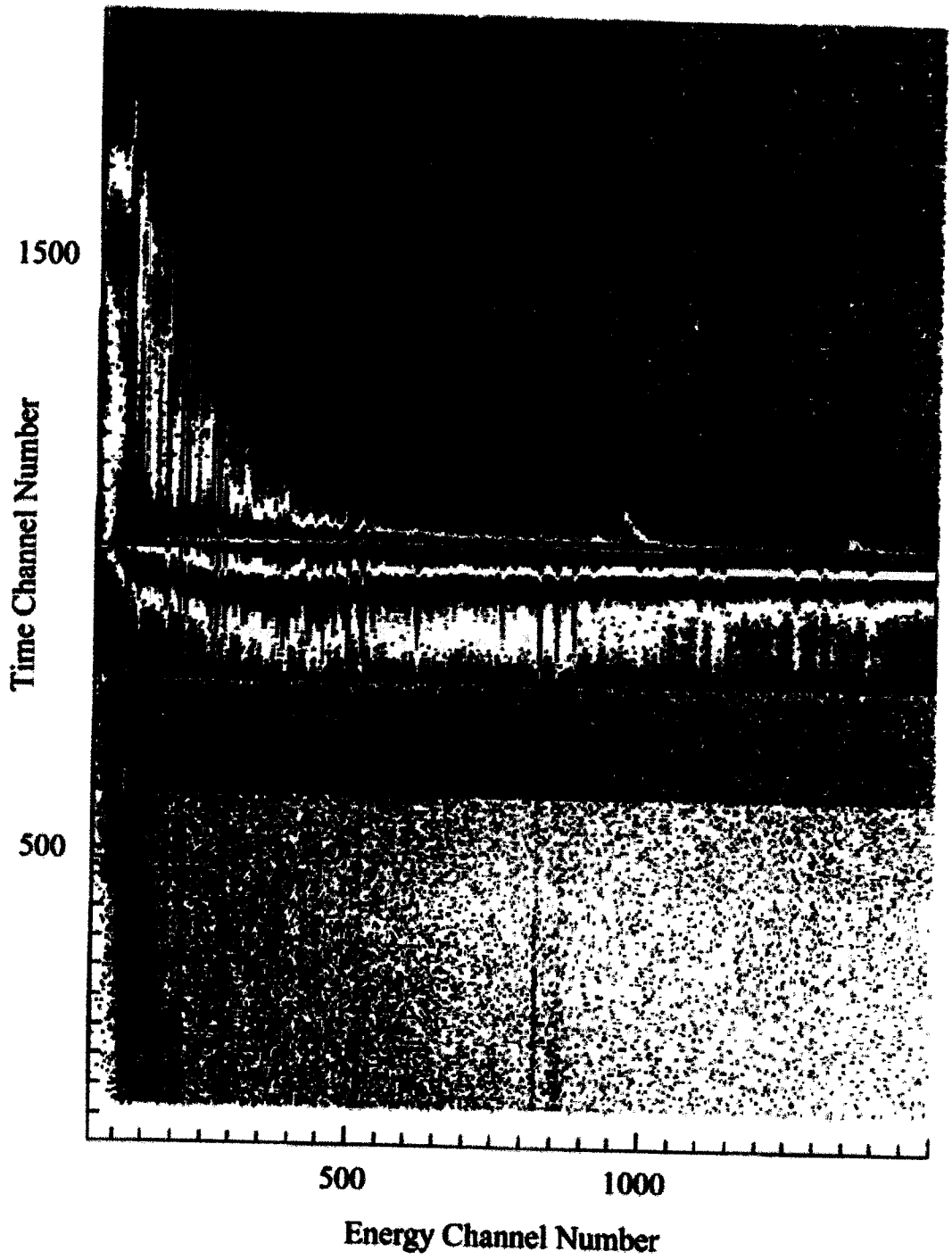

Figure D.17: Time versus E_γ plot for triple events from detector 3.

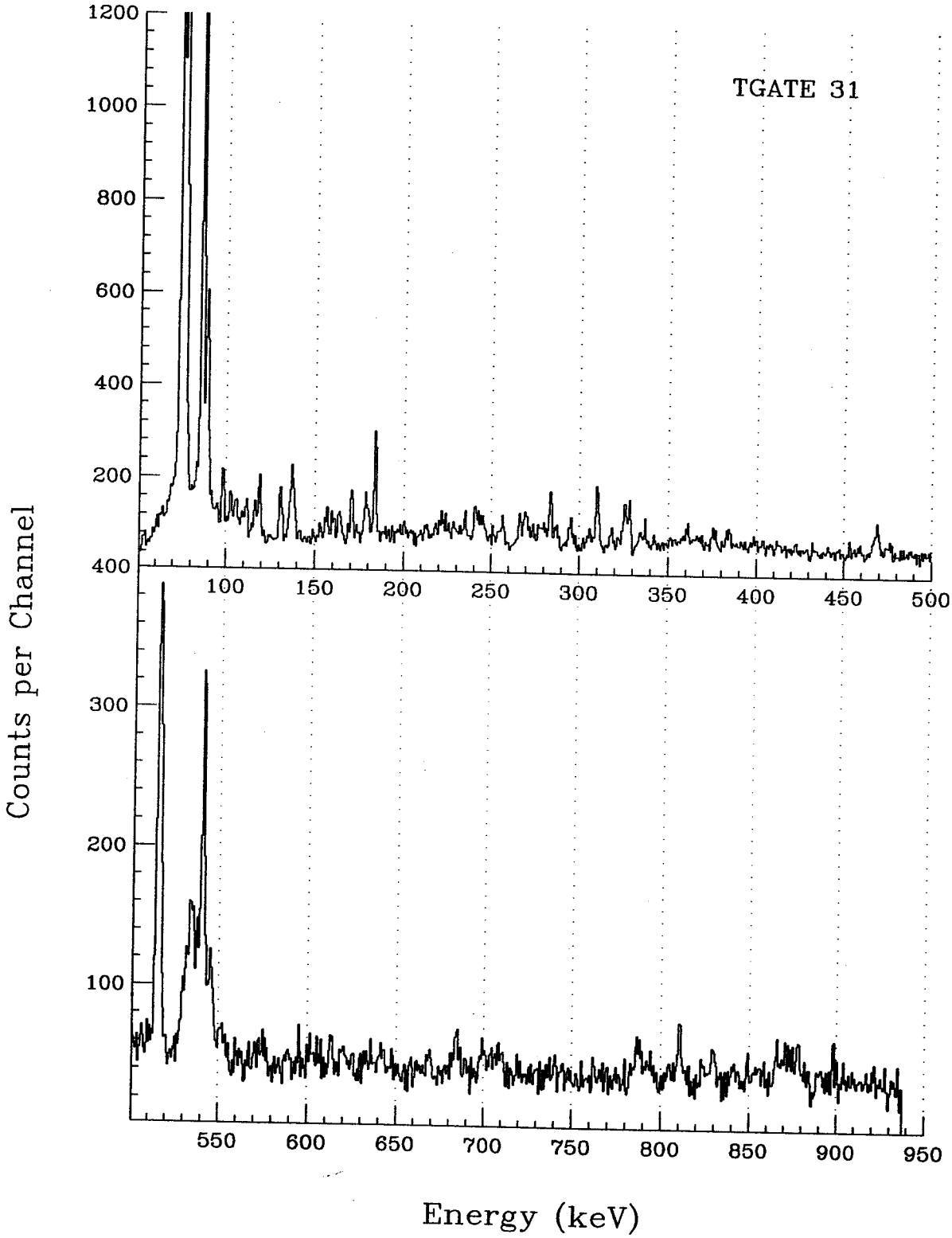

Figure D.18: Composite energy spectrum from TAC gate region 1, detector 3.

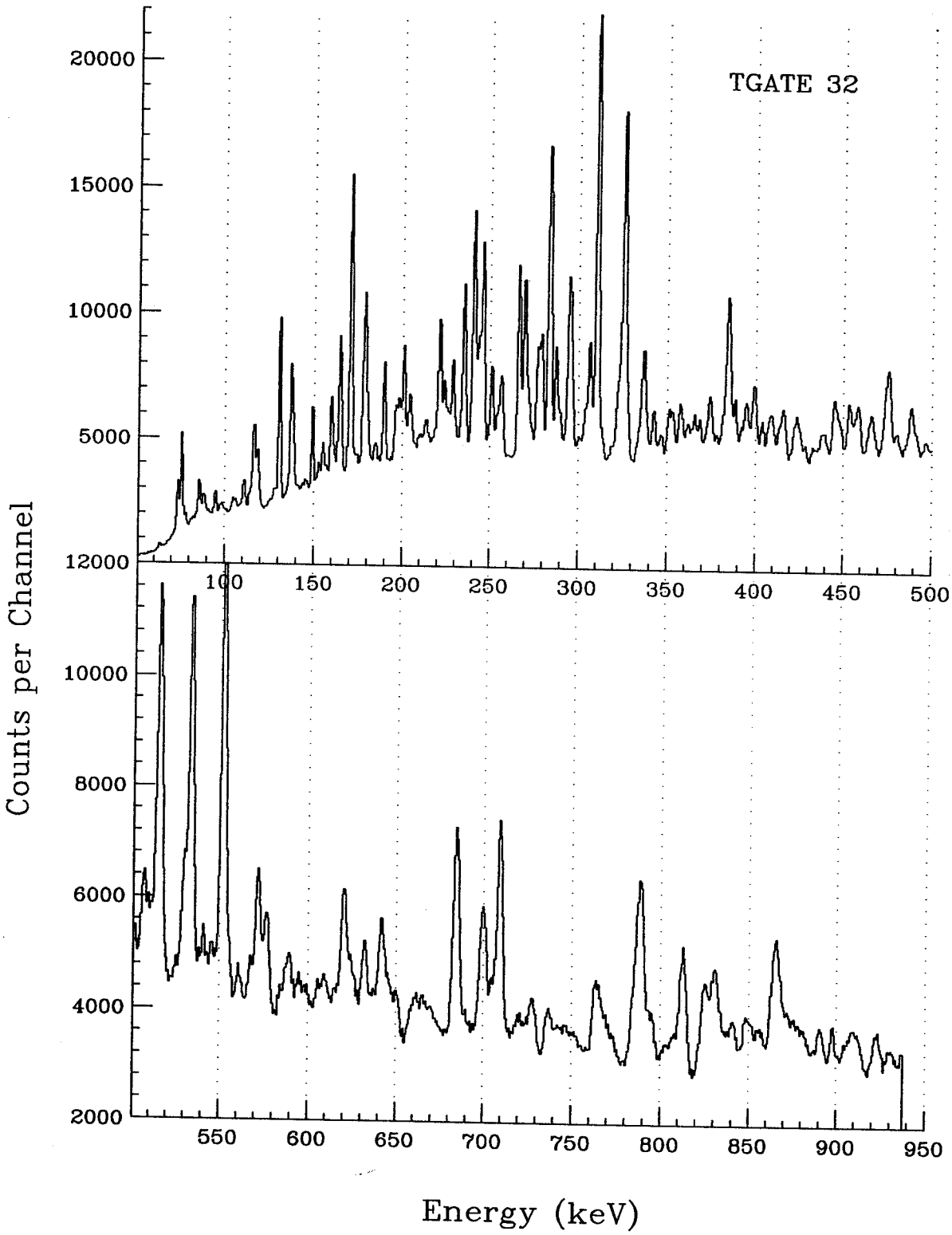

Figure D.19: Composite energy spectrum from TAC gate region 2, detector 3.

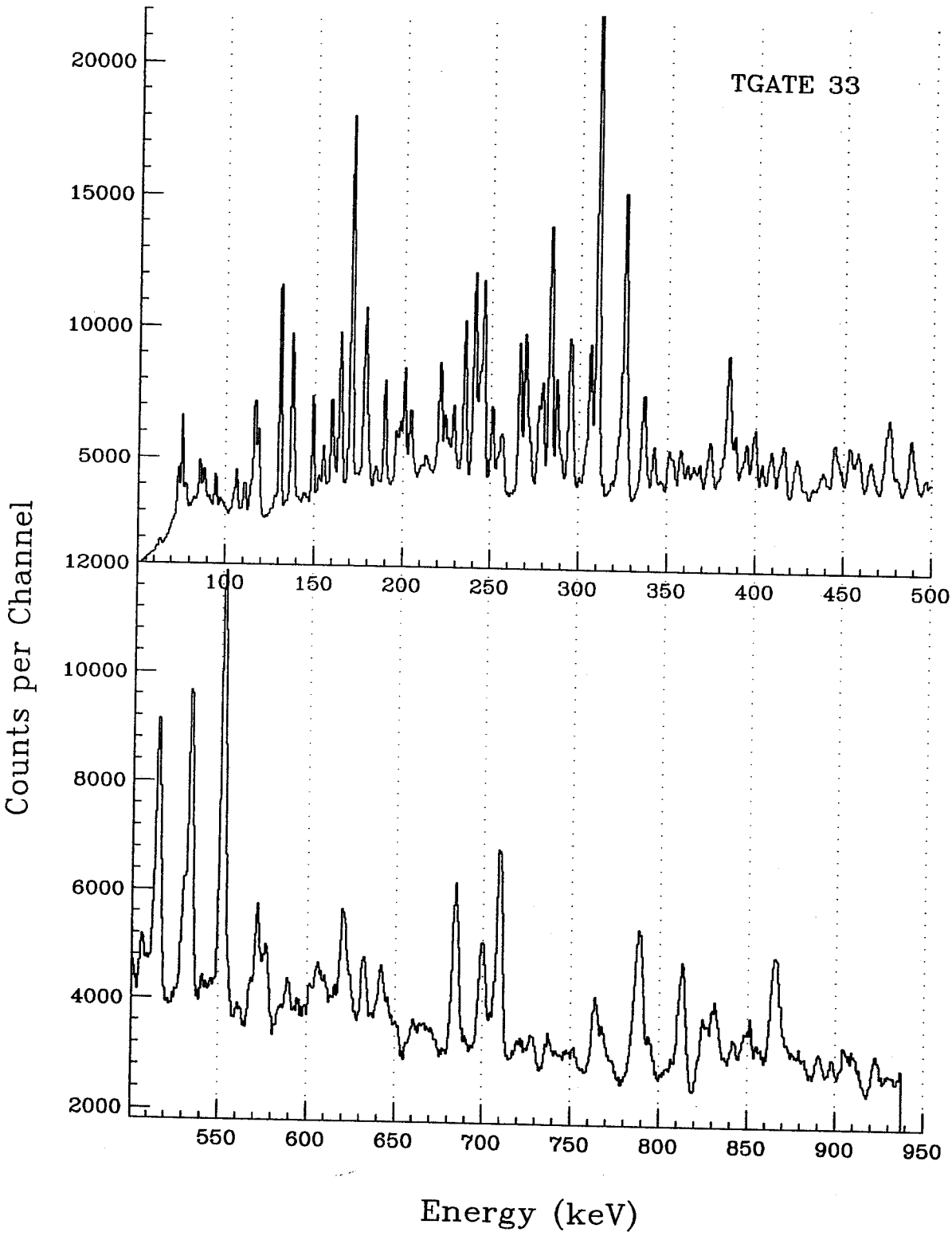

Figure D.20: Composite energy spectrum from TAC gate region 3, detector 3.

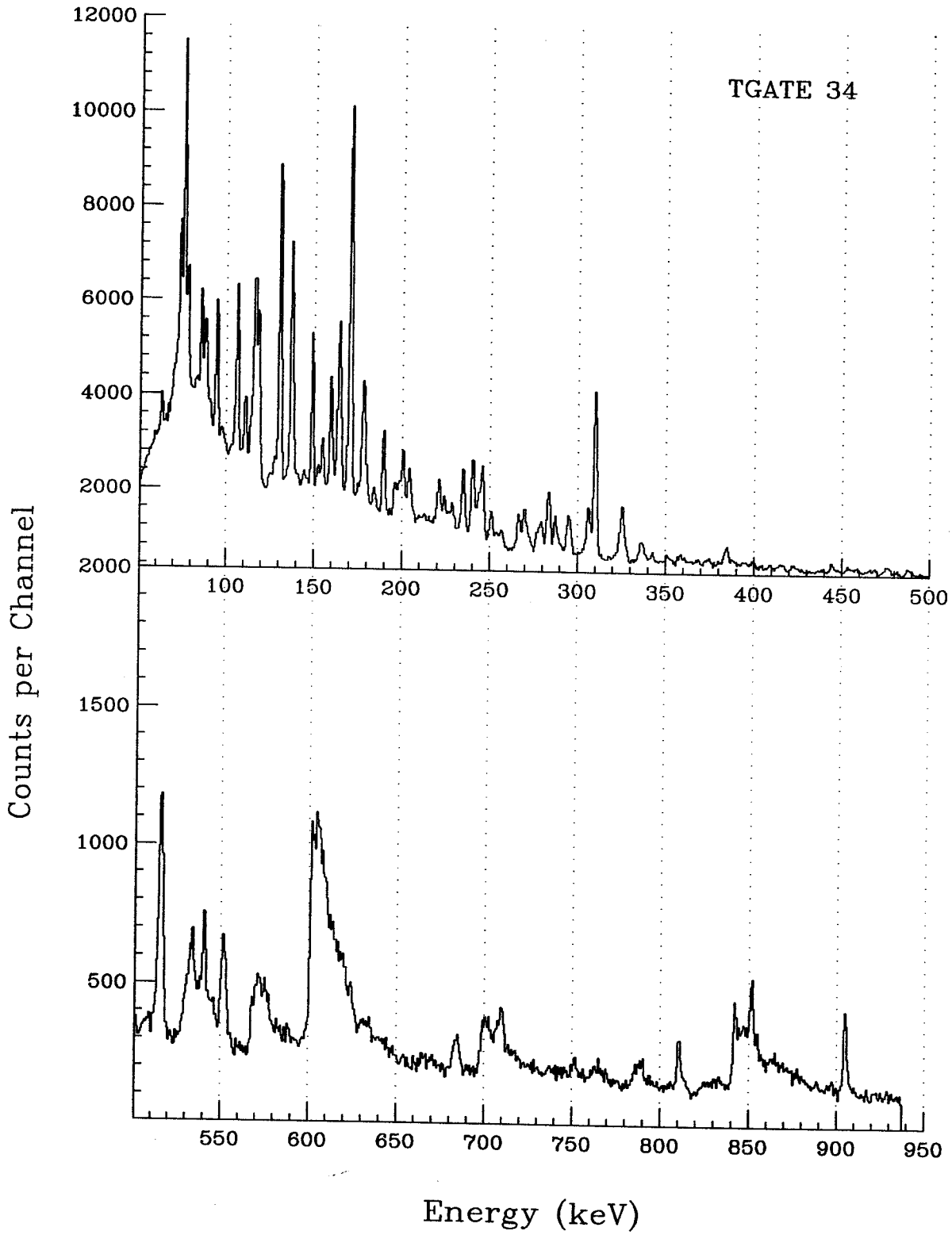

Figure D.21: Composite energy spectrum from TAC gate region 4, detector 3.

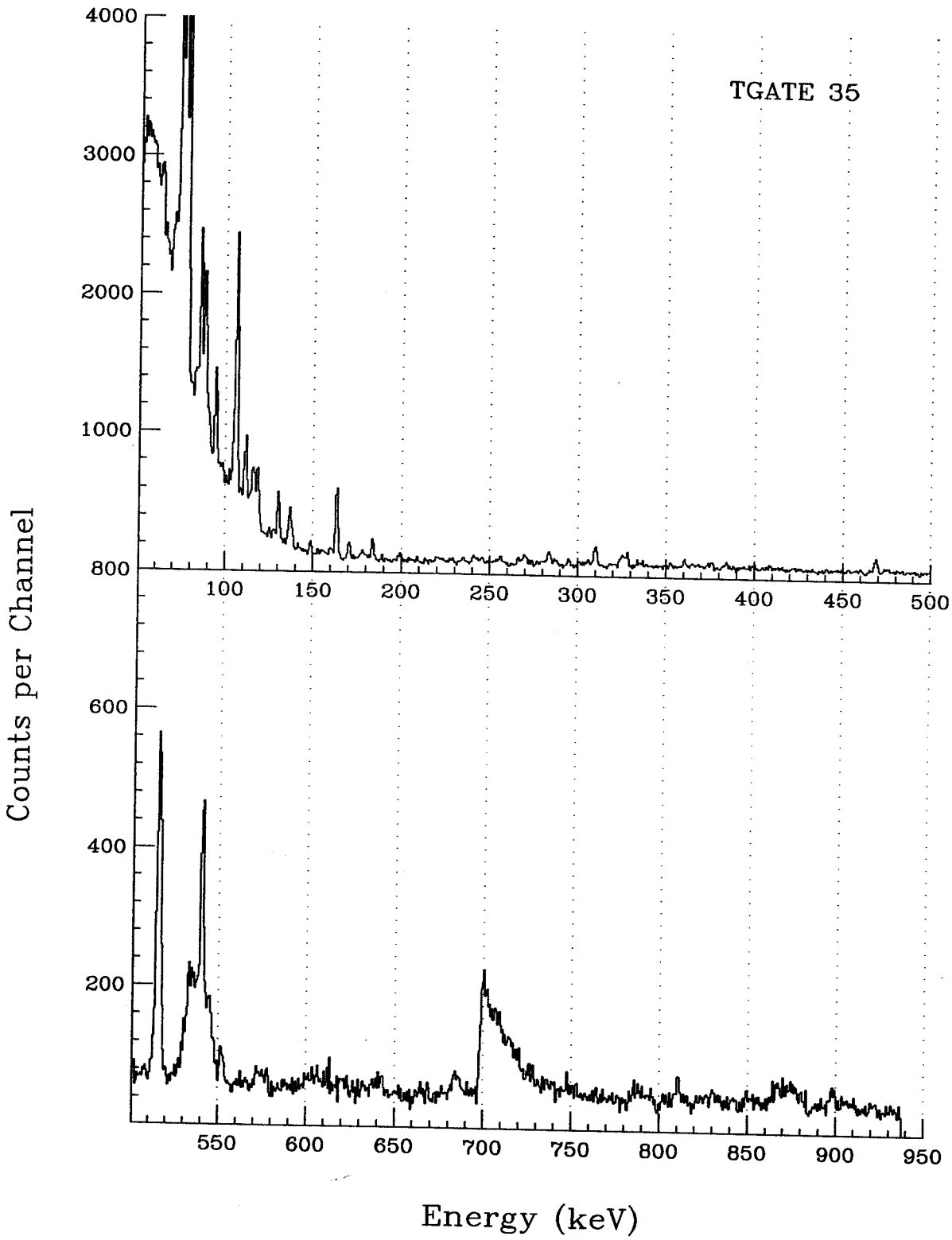

Figure D.22: Composite energy spectrum from TAC gate region 5, detector 3.

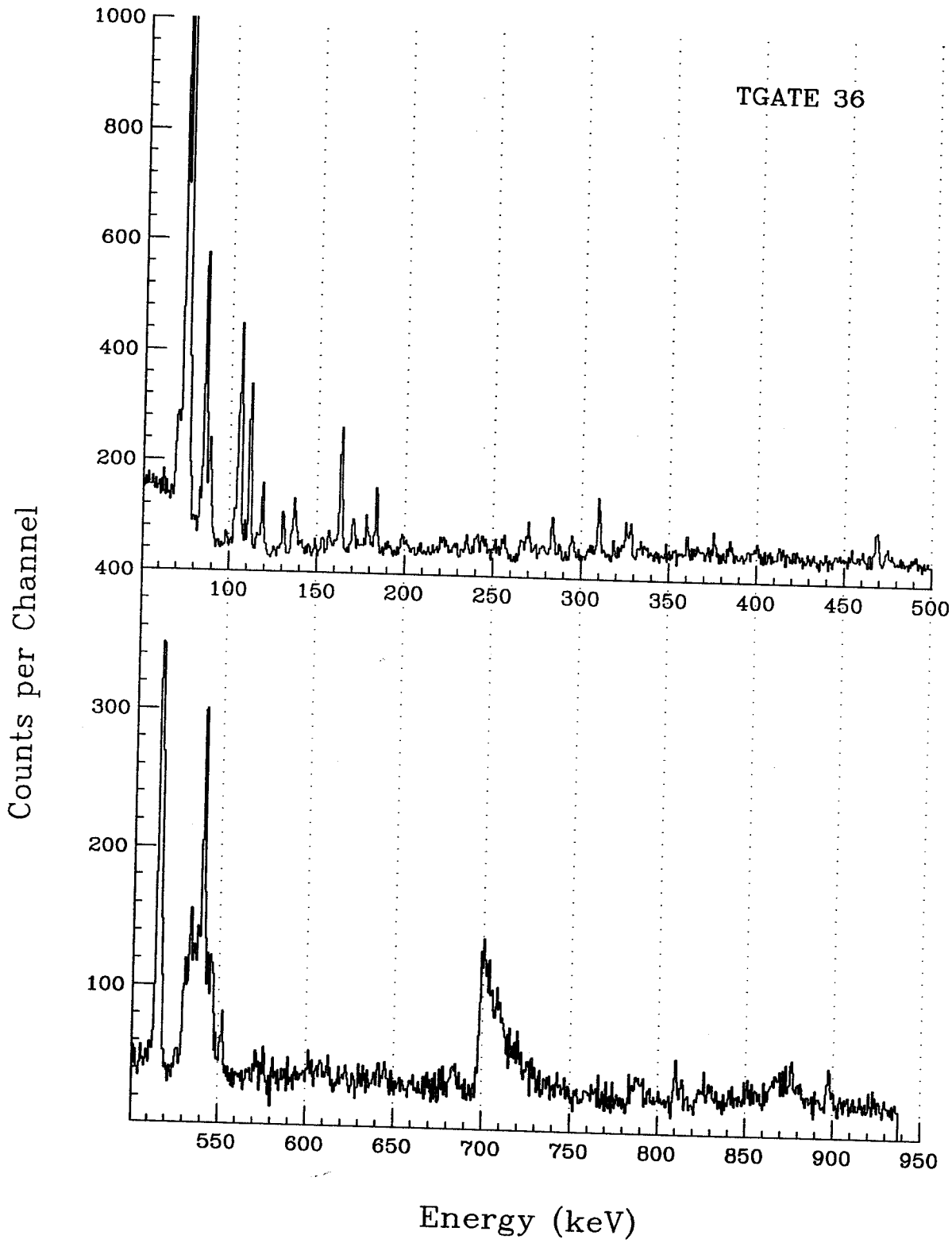

Figure D.23: Composite energy spectrum from TAC gate region 6, detector 3.

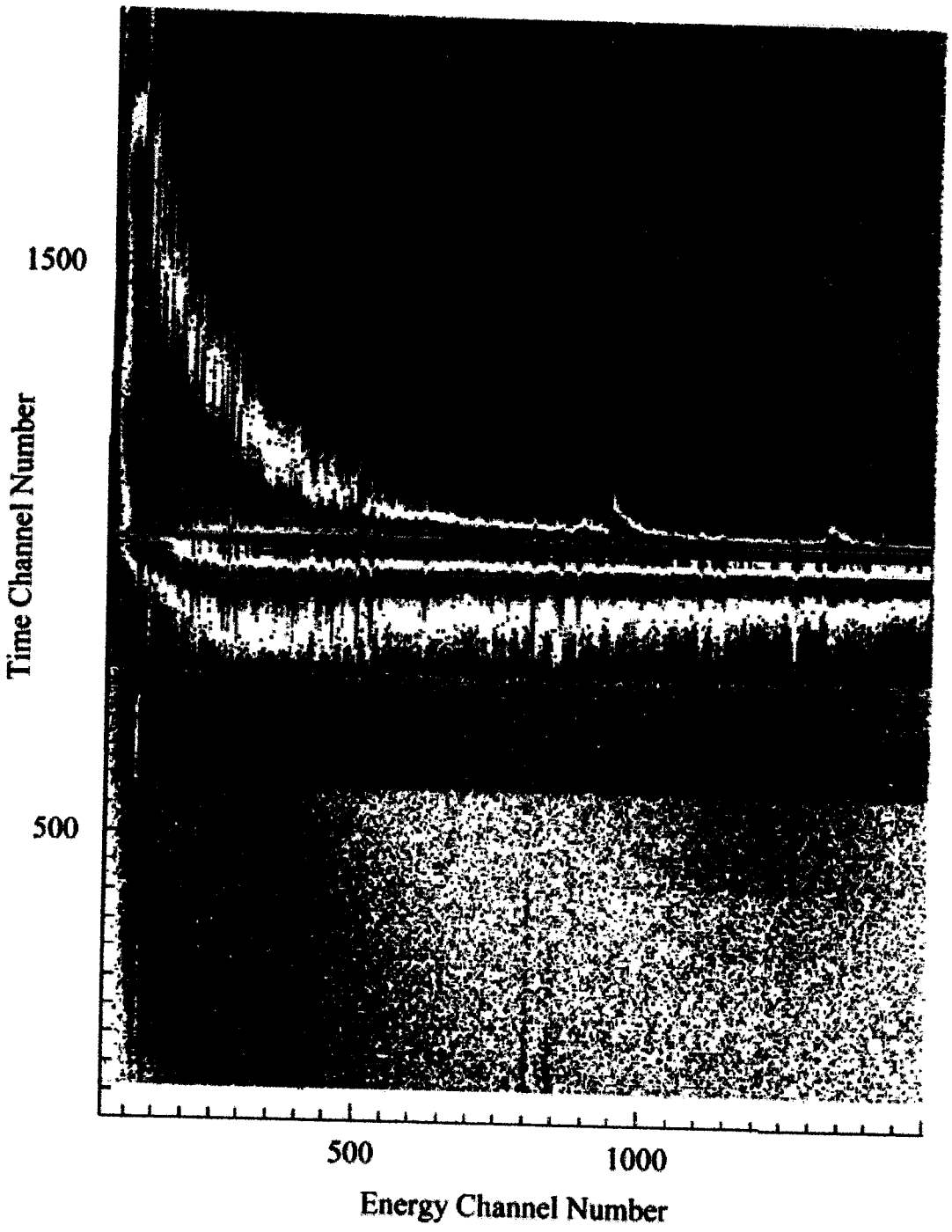

Figure D.24: Time versus E_γ plot for triple events from detector 4.

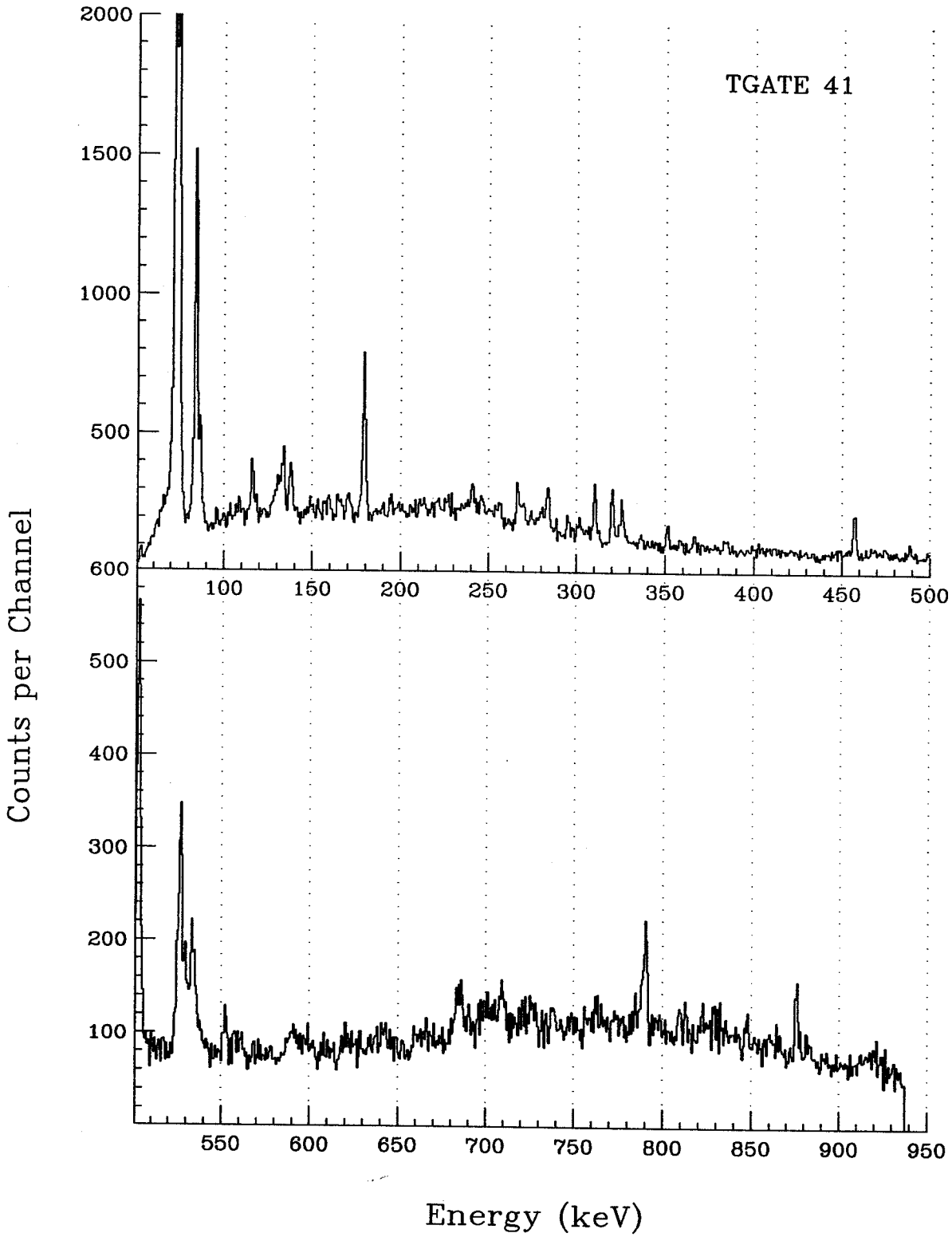

Figure D.25: Composite energy spectrum from TAC gate region 1, detector 4.

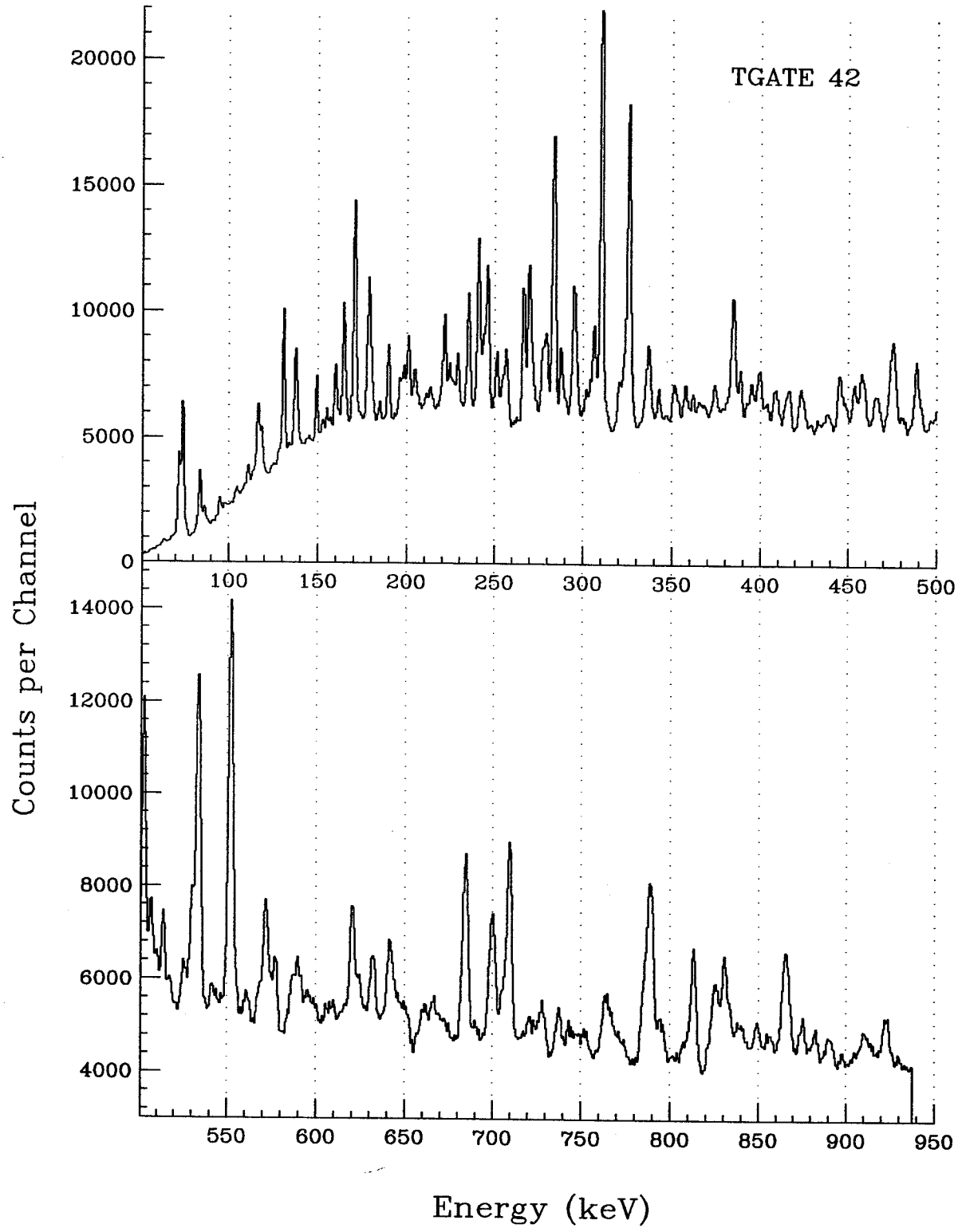

Figure D.26: Composite energy spectrum from TAC gate region 2, detector 4.

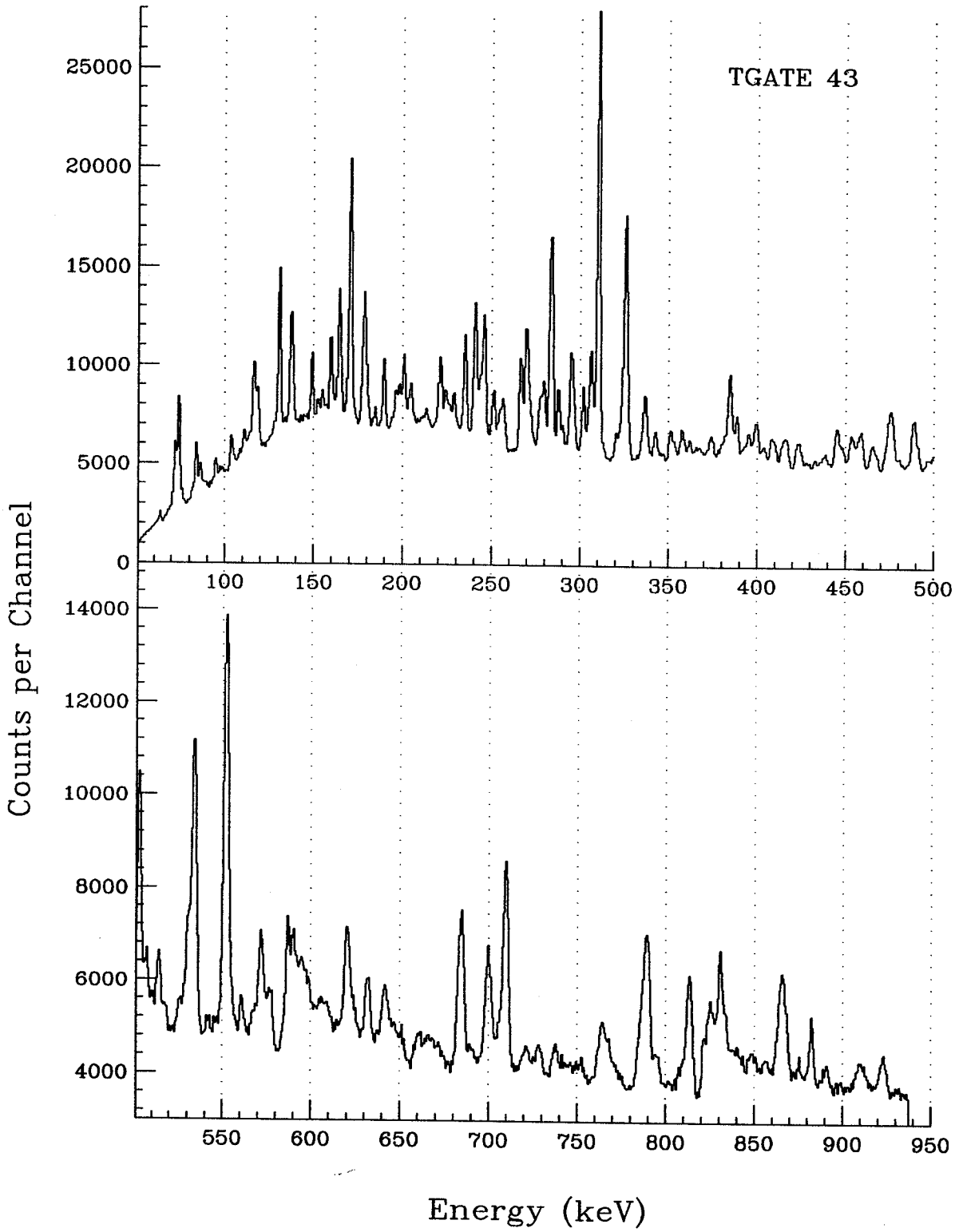

Figure D.27: Composite energy spectrum from TAC gate region 3, detector 4.

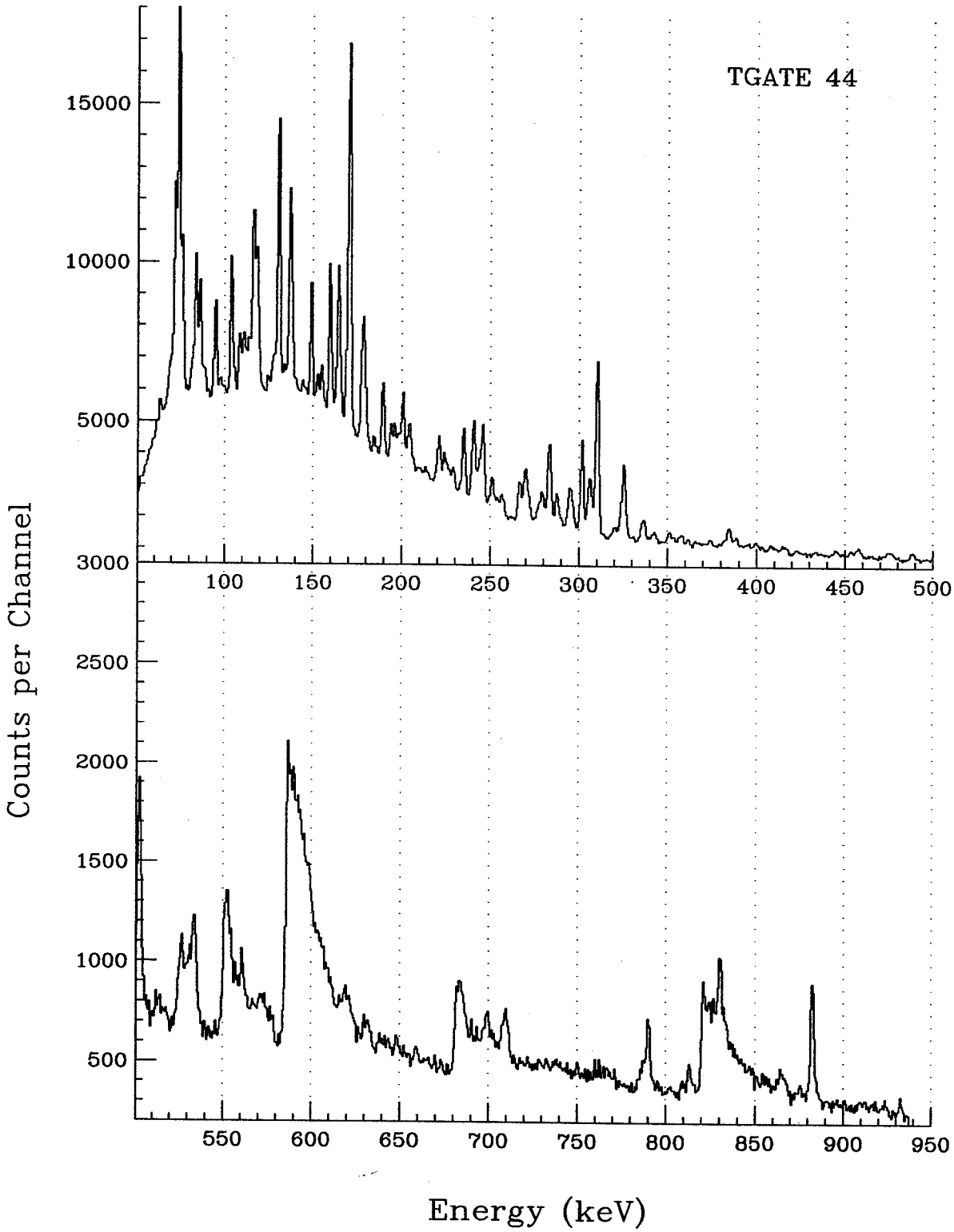

Figure D.28: Composite energy spectrum from TAC gate region 4, detector 4.

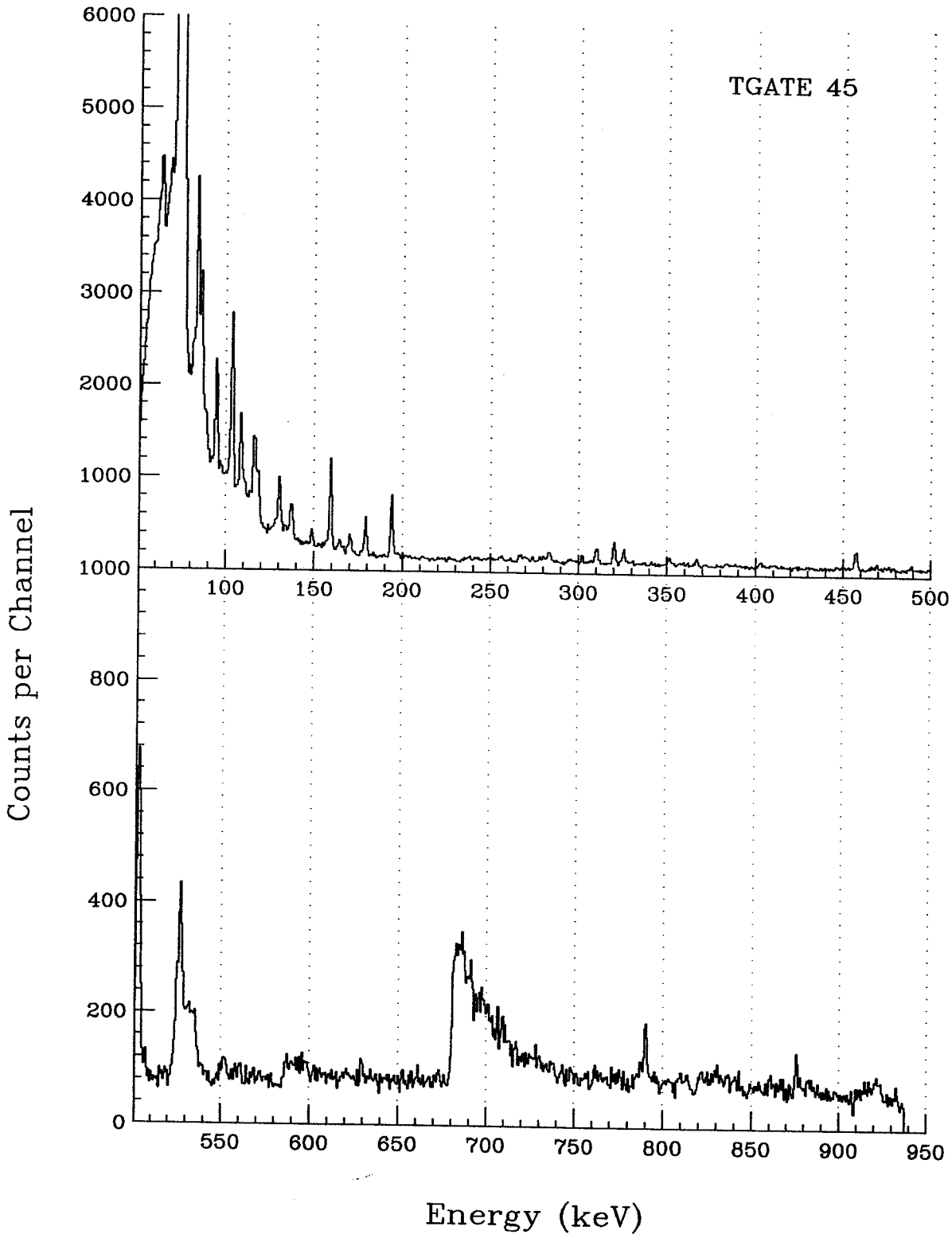

Figure D.29: Composite energy spectrum from TAC gate region 5, detector 4.

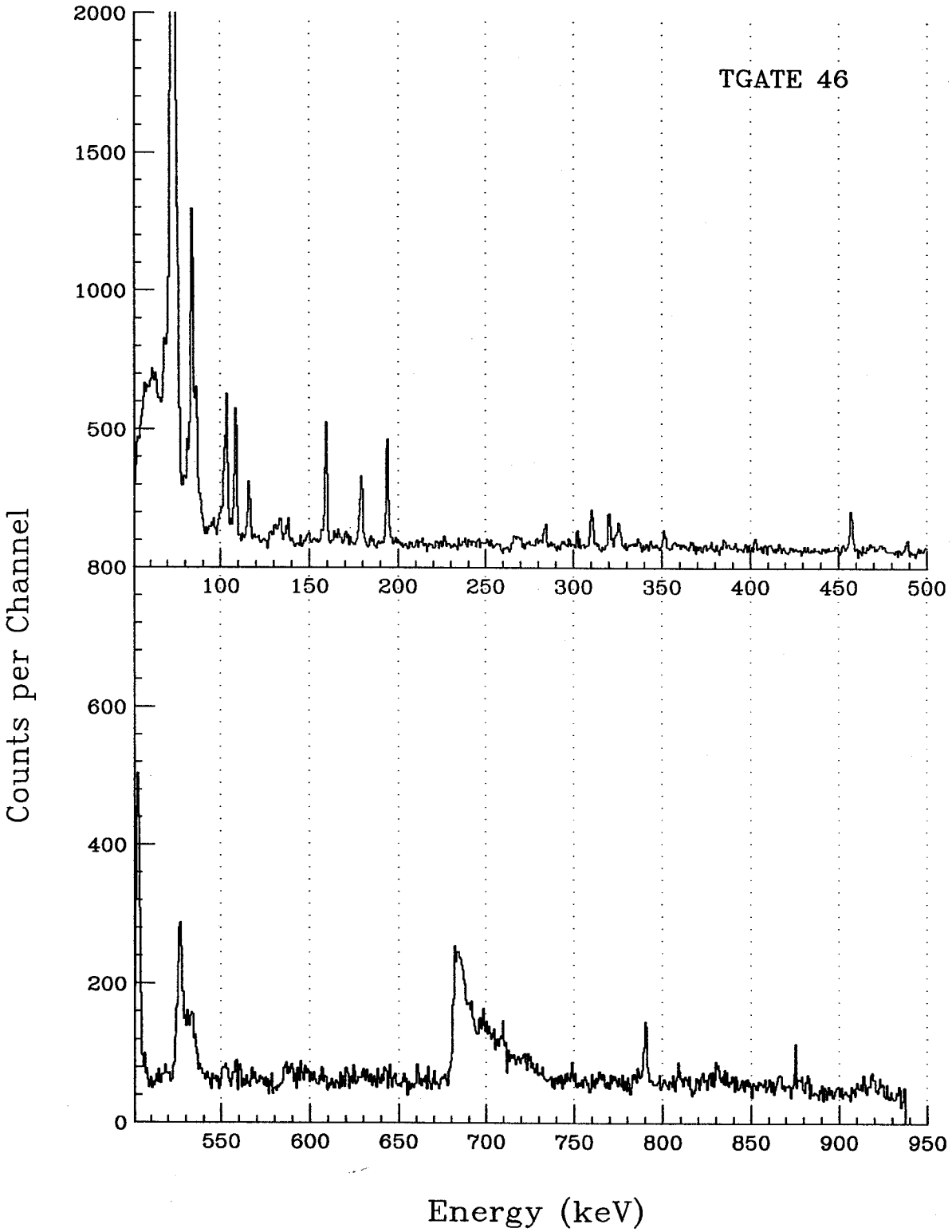

Figure D.30: Composite energy spectrum from TAC gate region 6, detector 4.

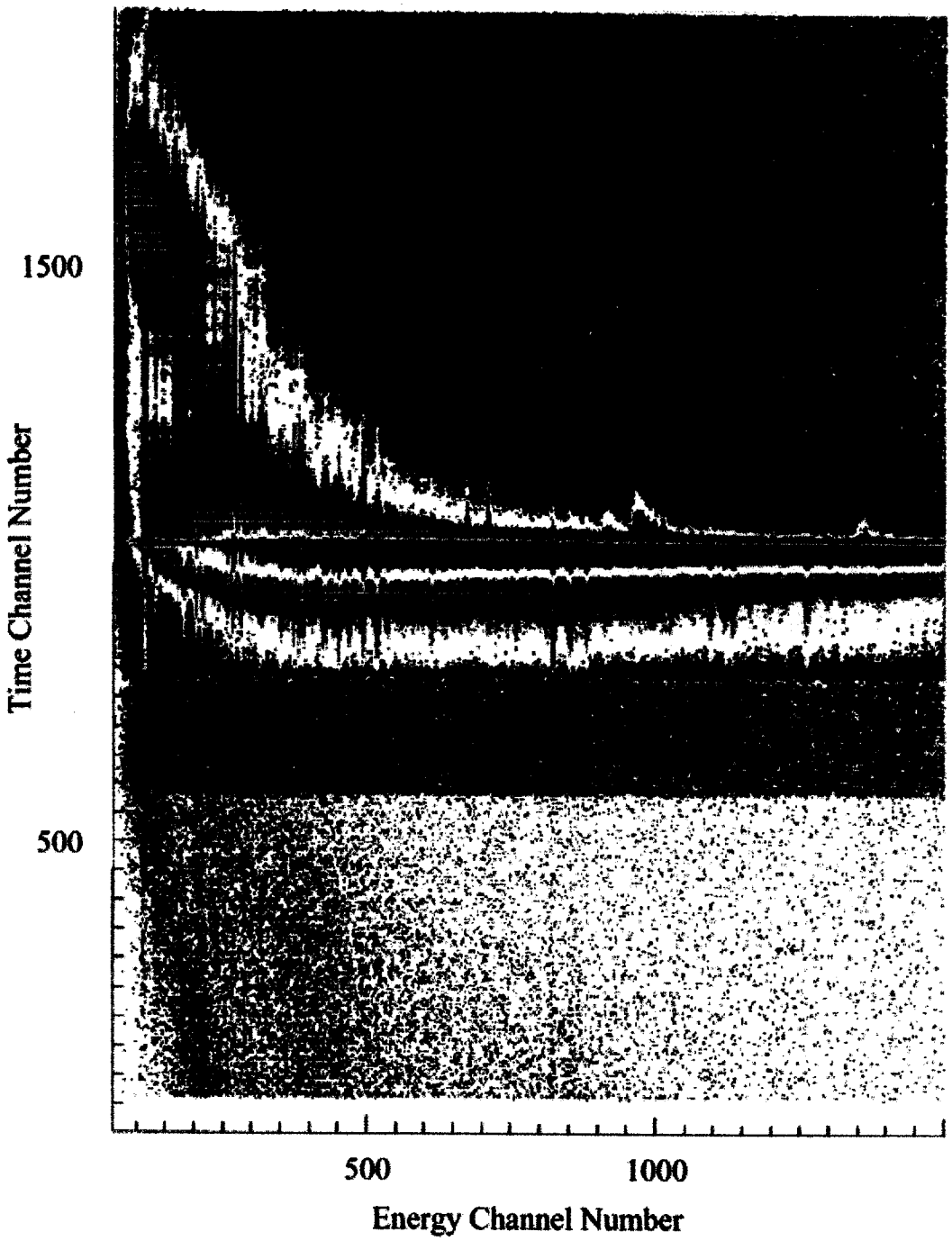

Figure D.31: Time versus E_γ plot for triple events from detector 5.

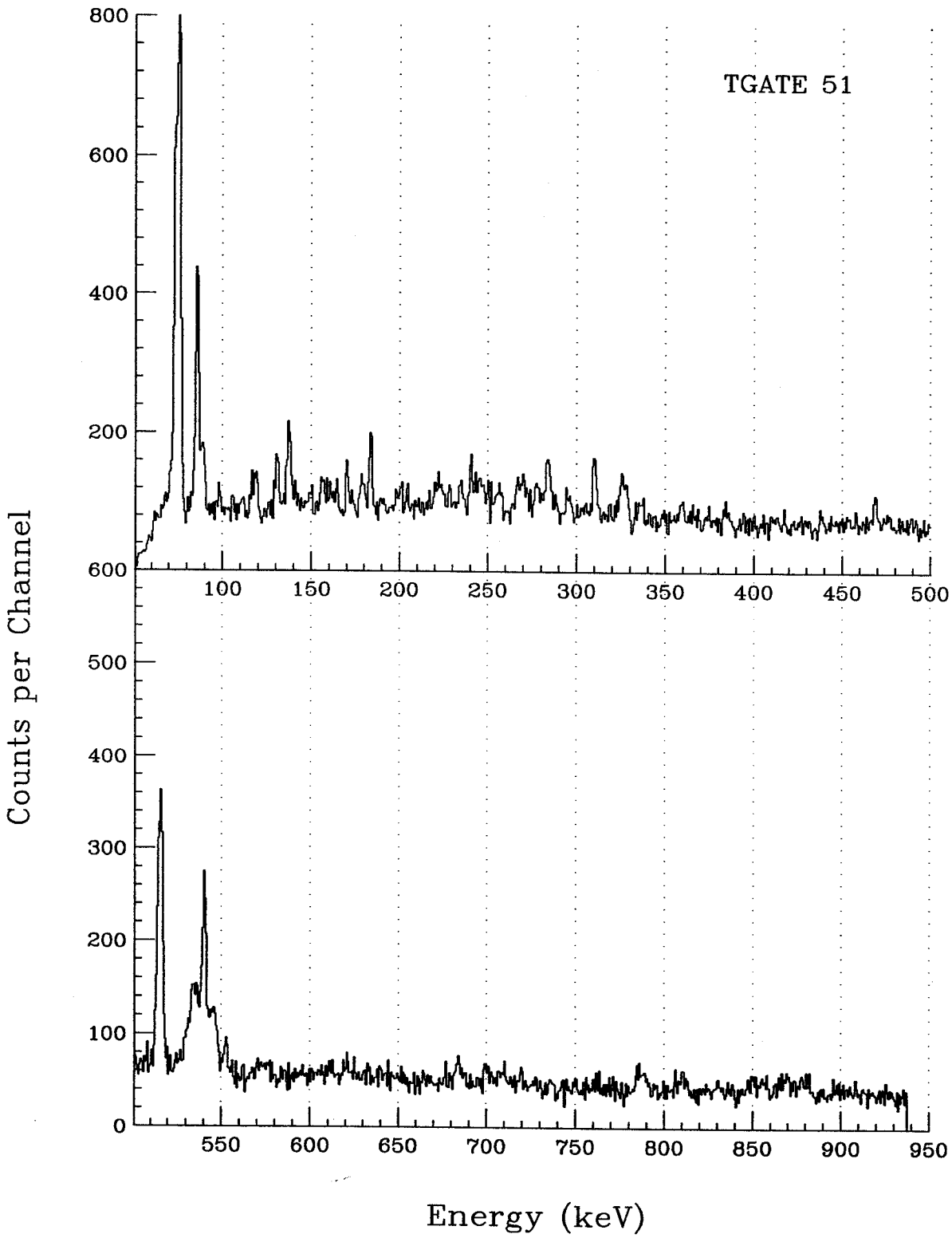

Figure D.32: Composite energy spectrum from TAC gate region 1, detector 5.

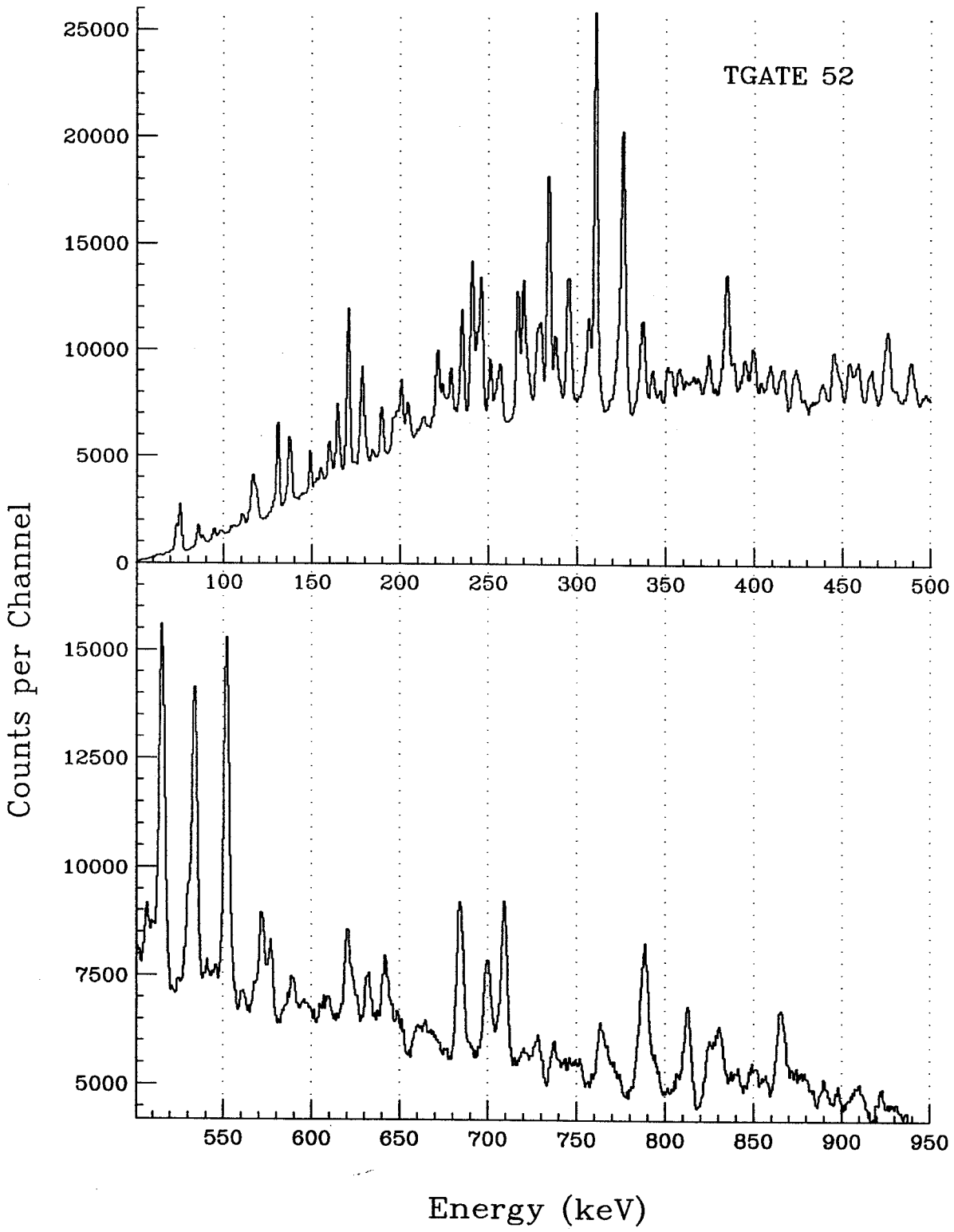

Figure D.33: Composite energy spectrum from TAC gate region 2, detector 5.

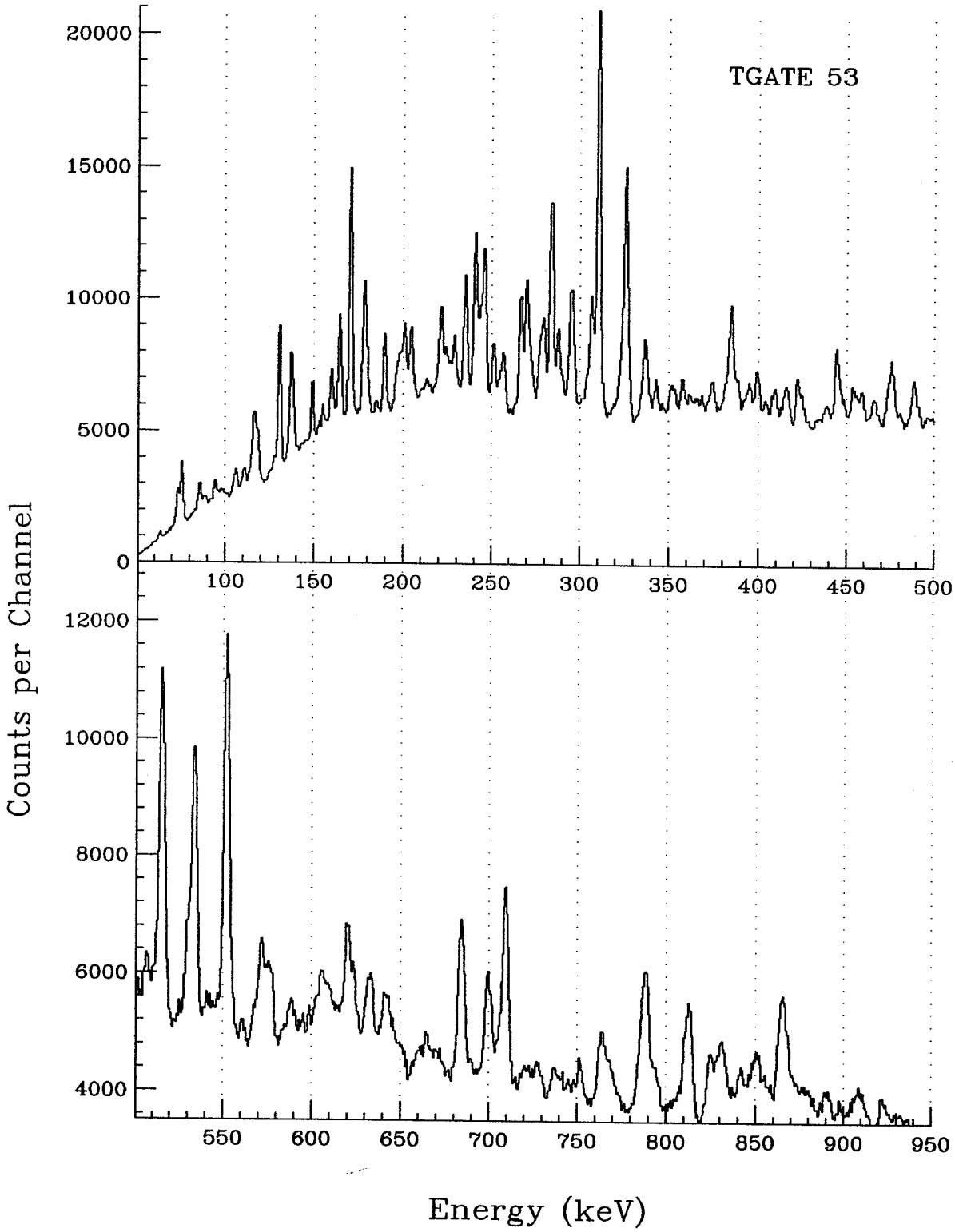

Figure D.34: Composite energy spectrum from TAC gate region 3, detector 5.

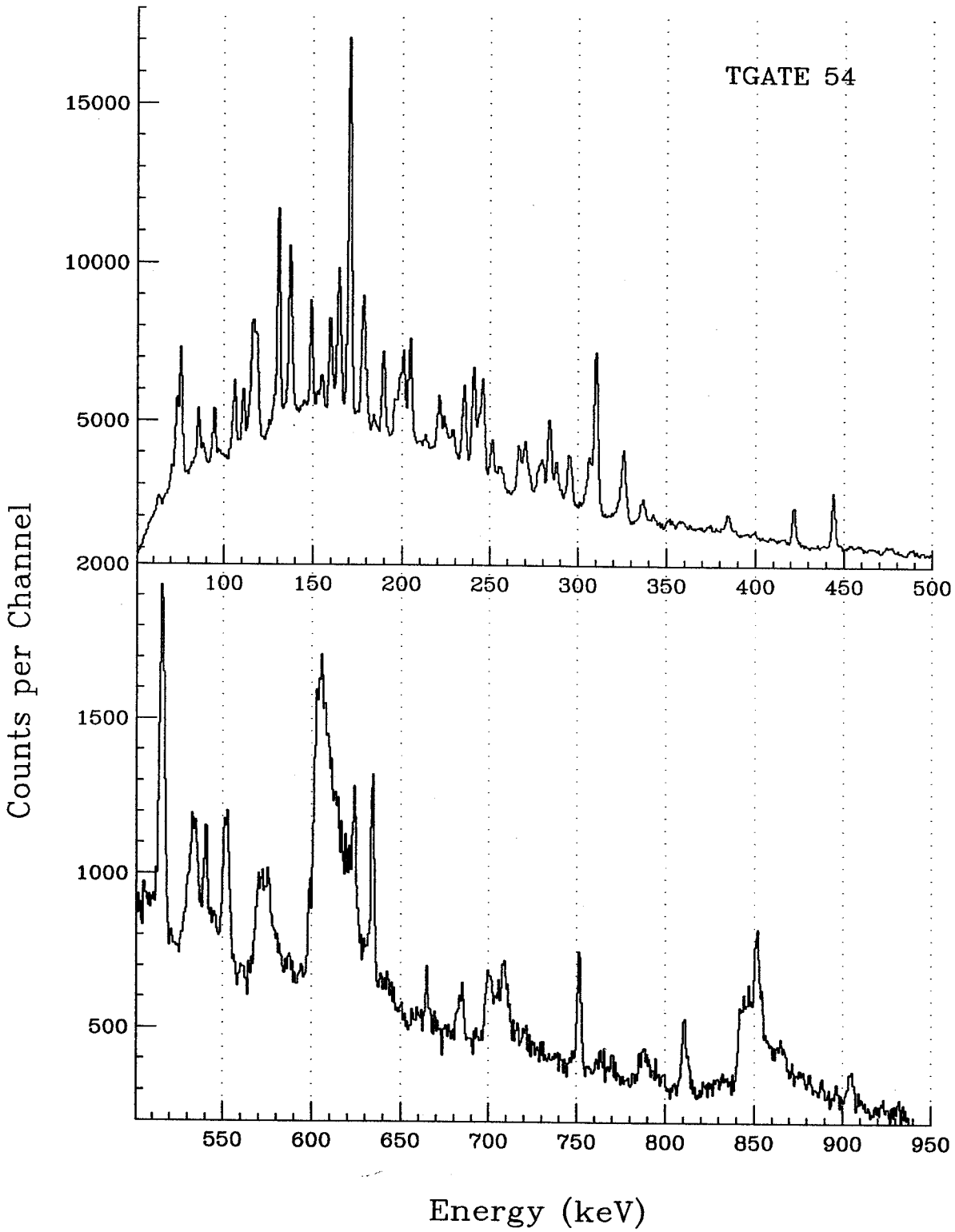

Figure D.35: Composite energy spectrum from TAC gate region 4, detector 5.

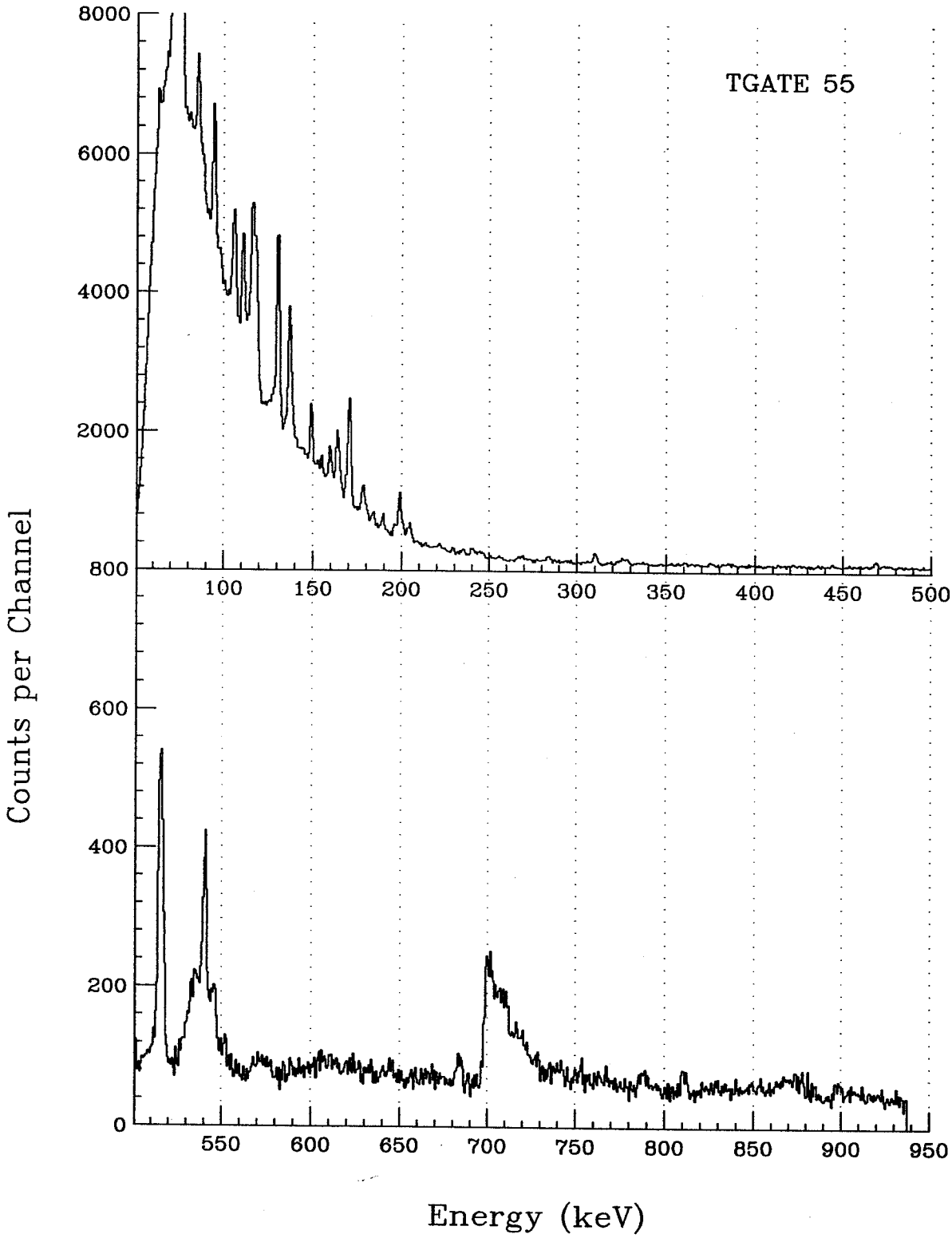

Figure D.36: Composite energy spectrum from TAC gate region 5, detector 5.

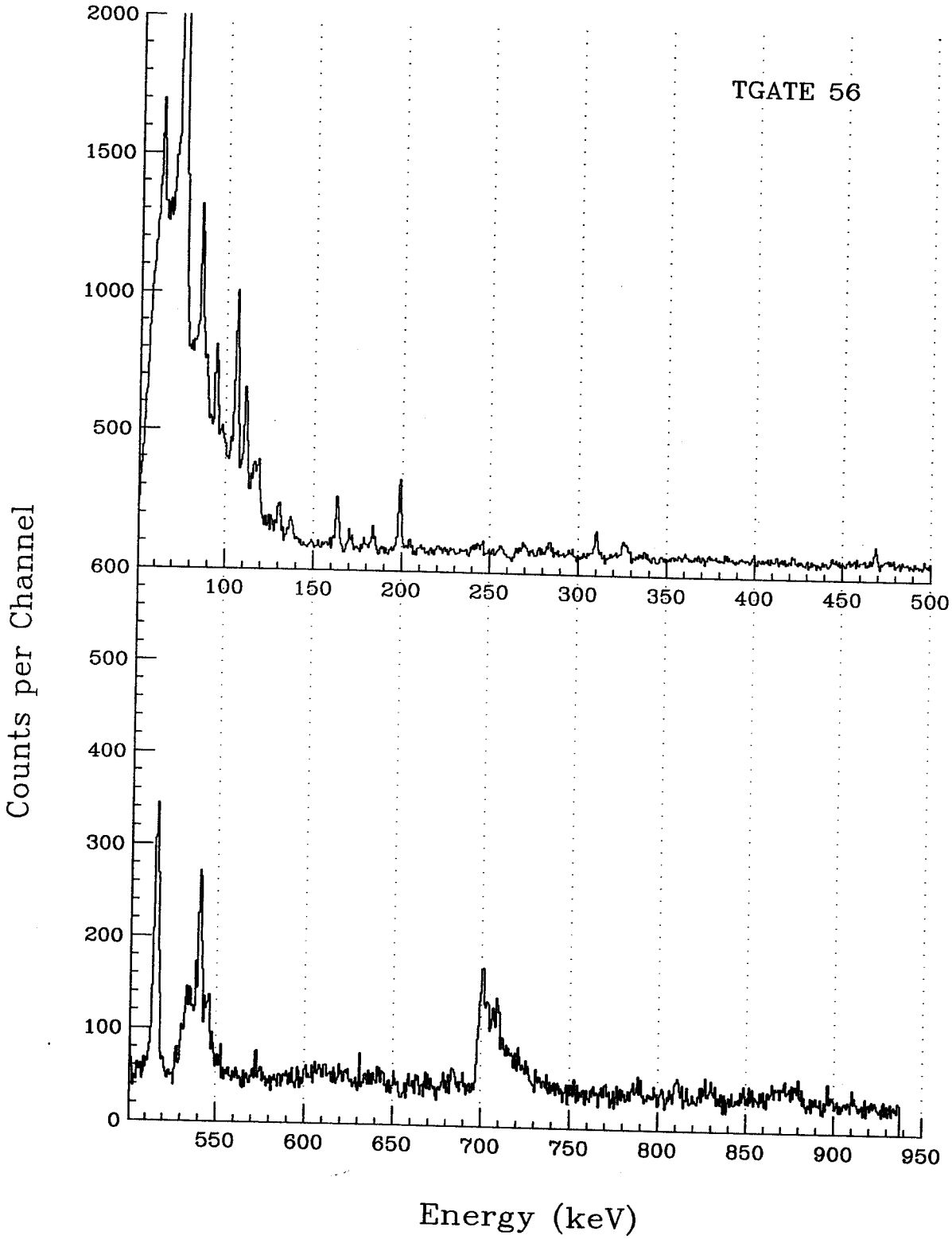

Figure D.37: Composite energy spectrum from TAC gate region 6, detector 5.

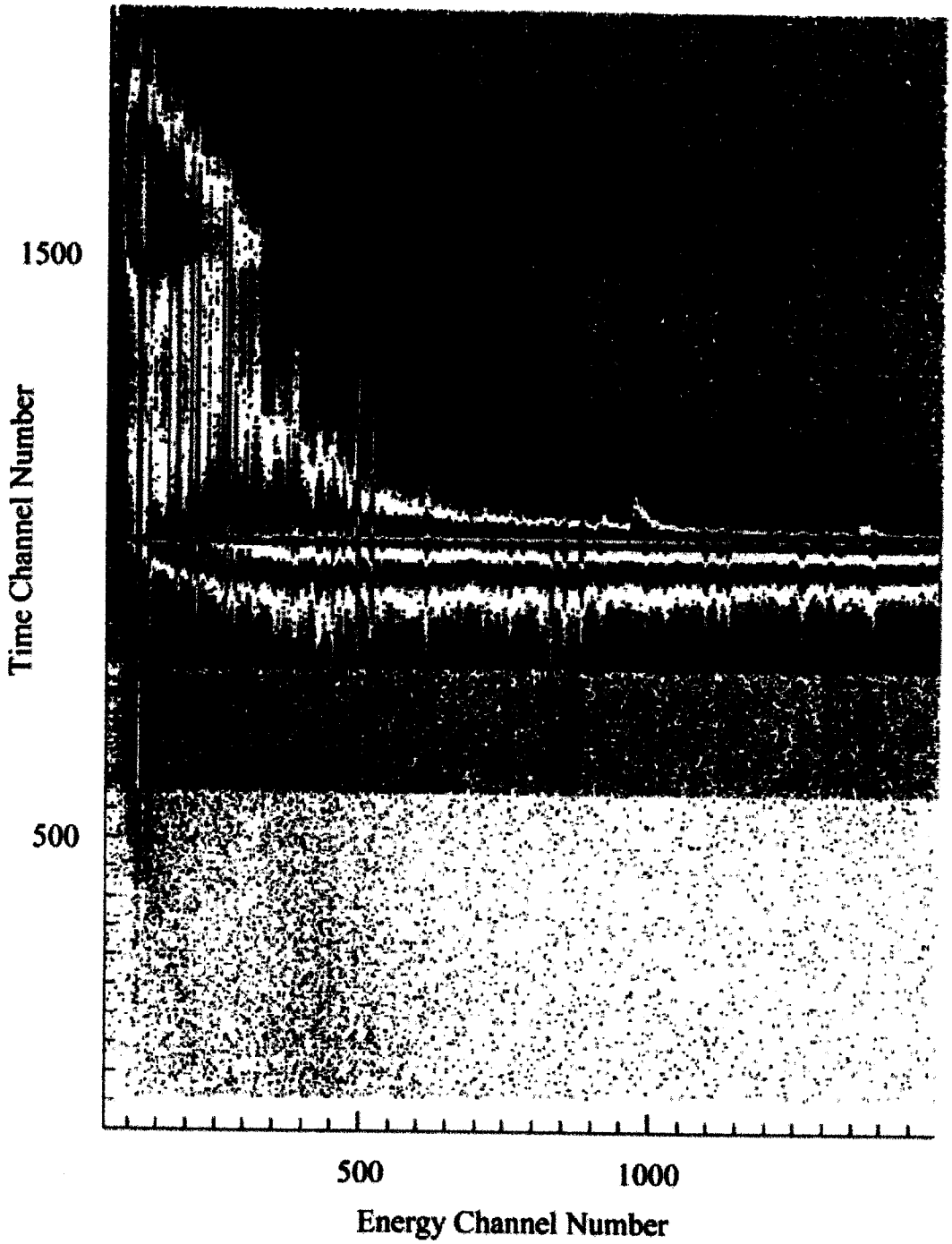

Figure D.38: Time versus E_γ plot for triple events from detector 6.

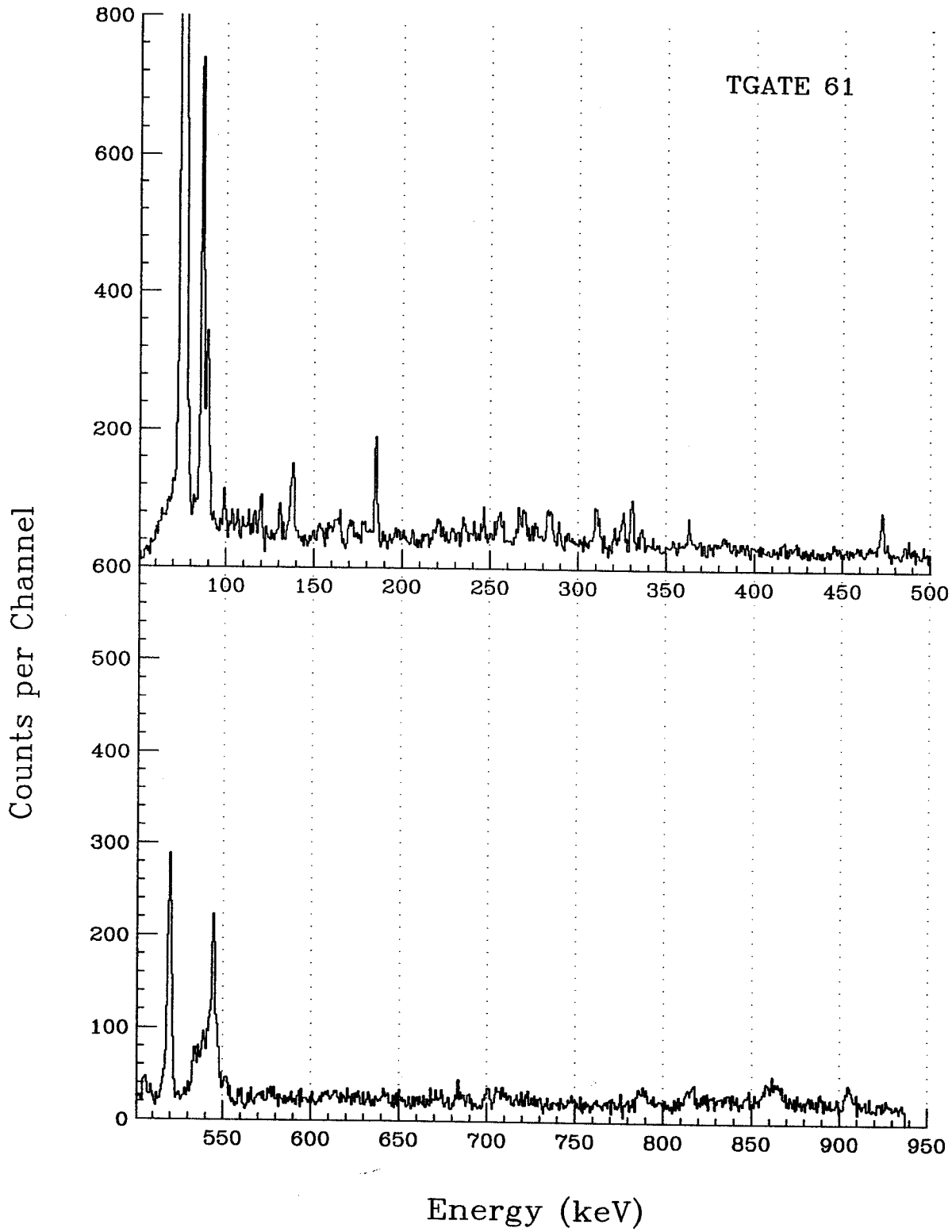

Figure D.39: Composite energy spectrum from TAC gate region 1, detector 6.

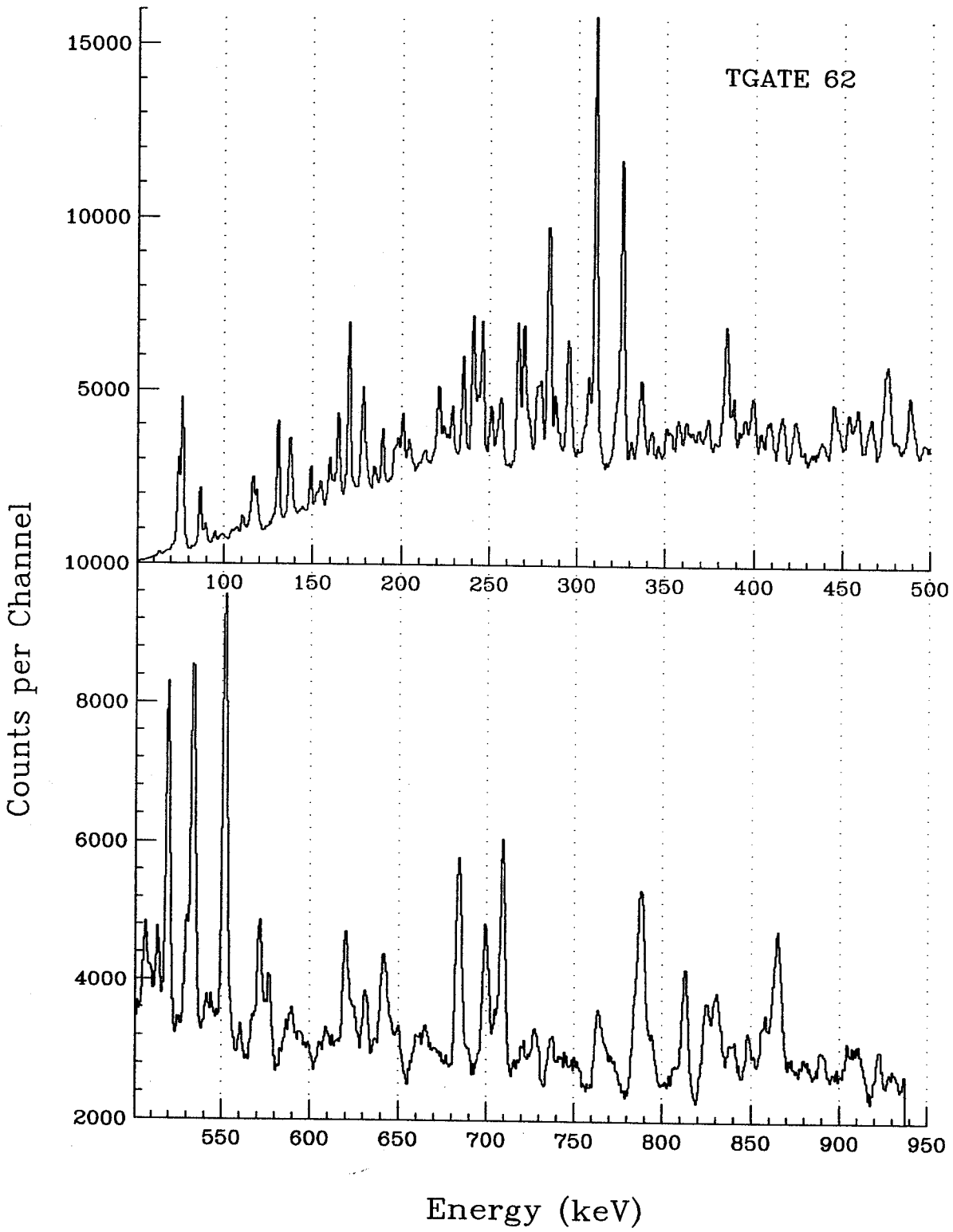

Figure D.40: Composite energy spectrum from TAC gate region 2, detector 6.

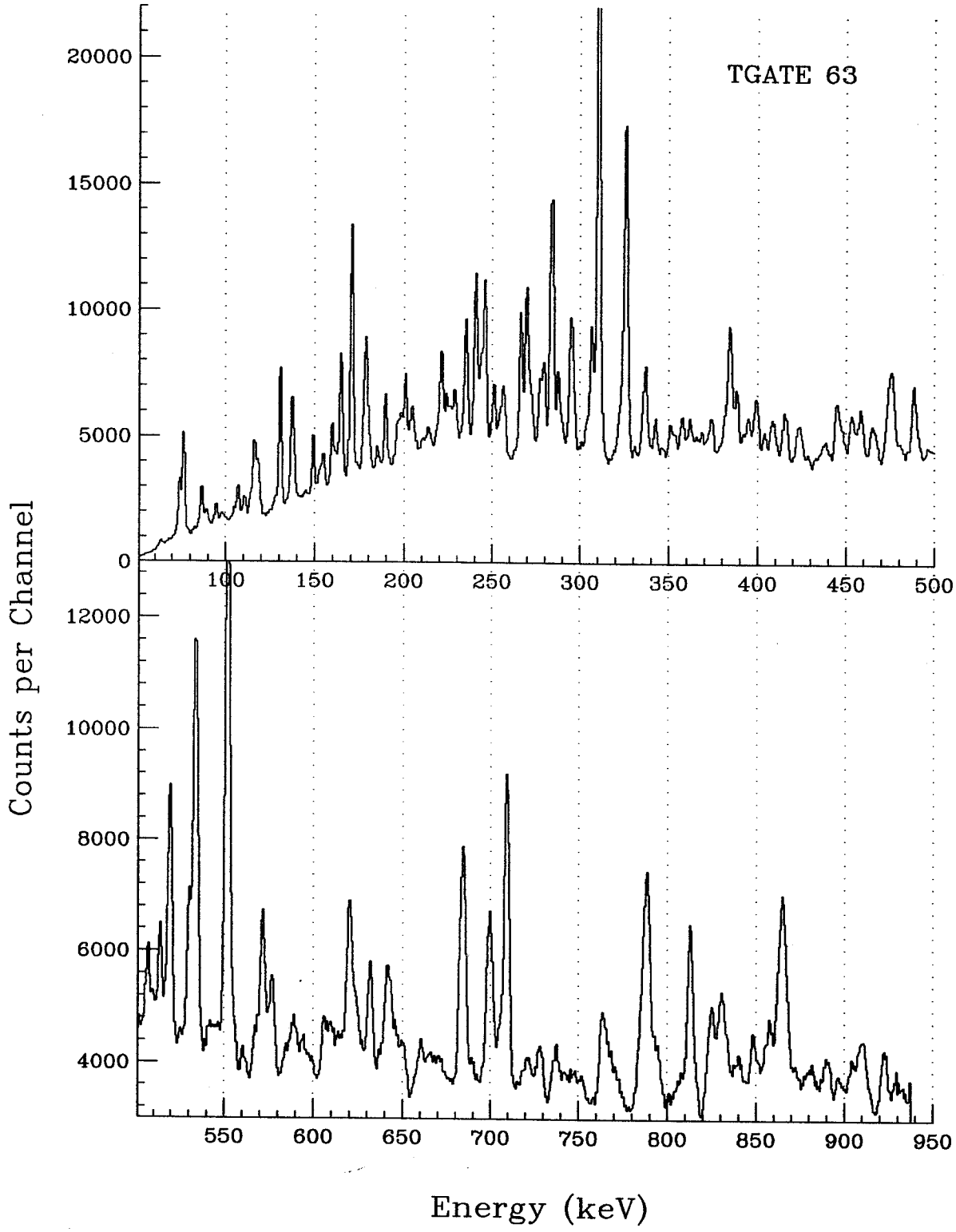

Figure D.41: Composite energy spectrum from TAC gate region 3, detector 6.

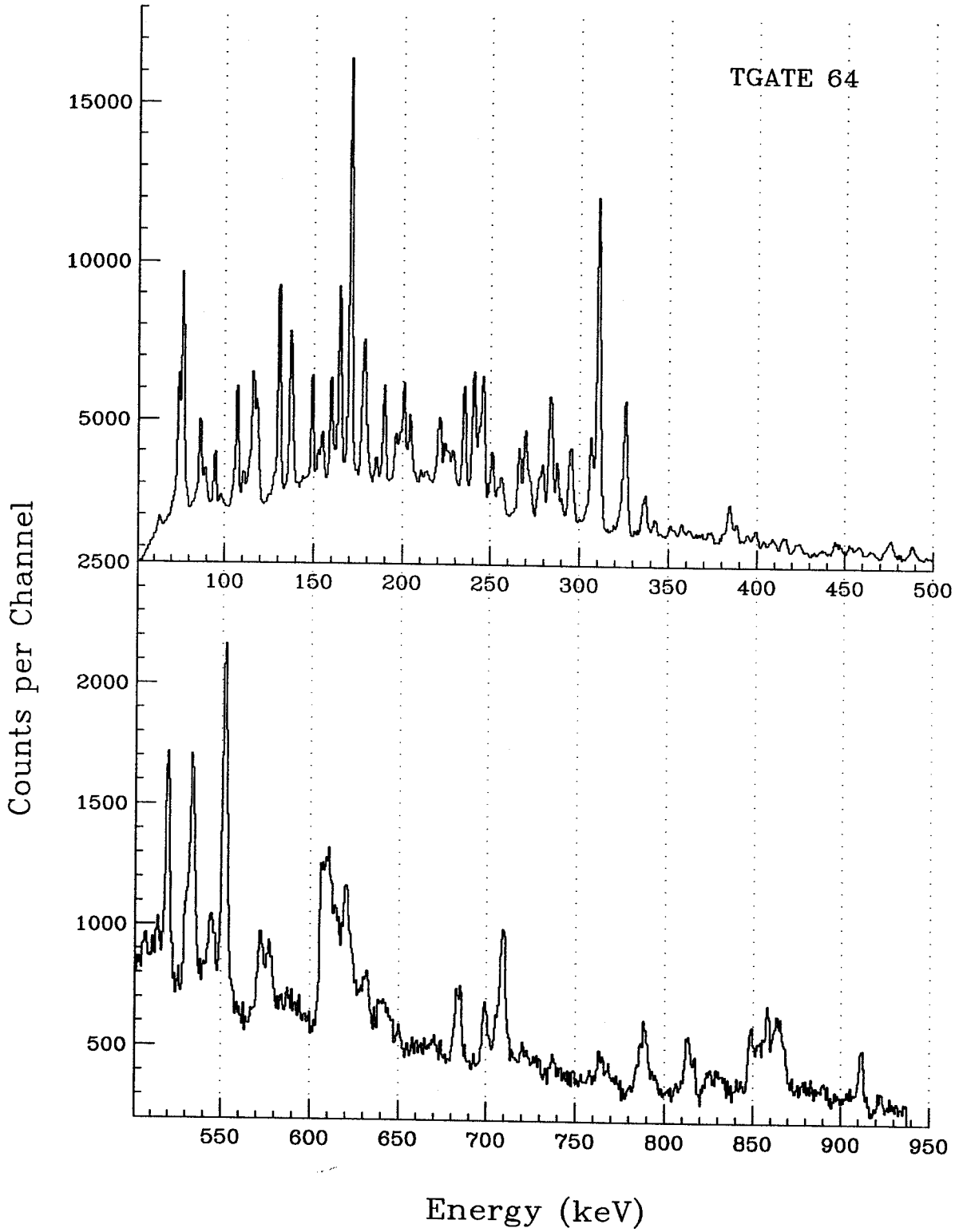

Figure D.42: Composite energy spectrum from TAC gate region 4, detector 6.

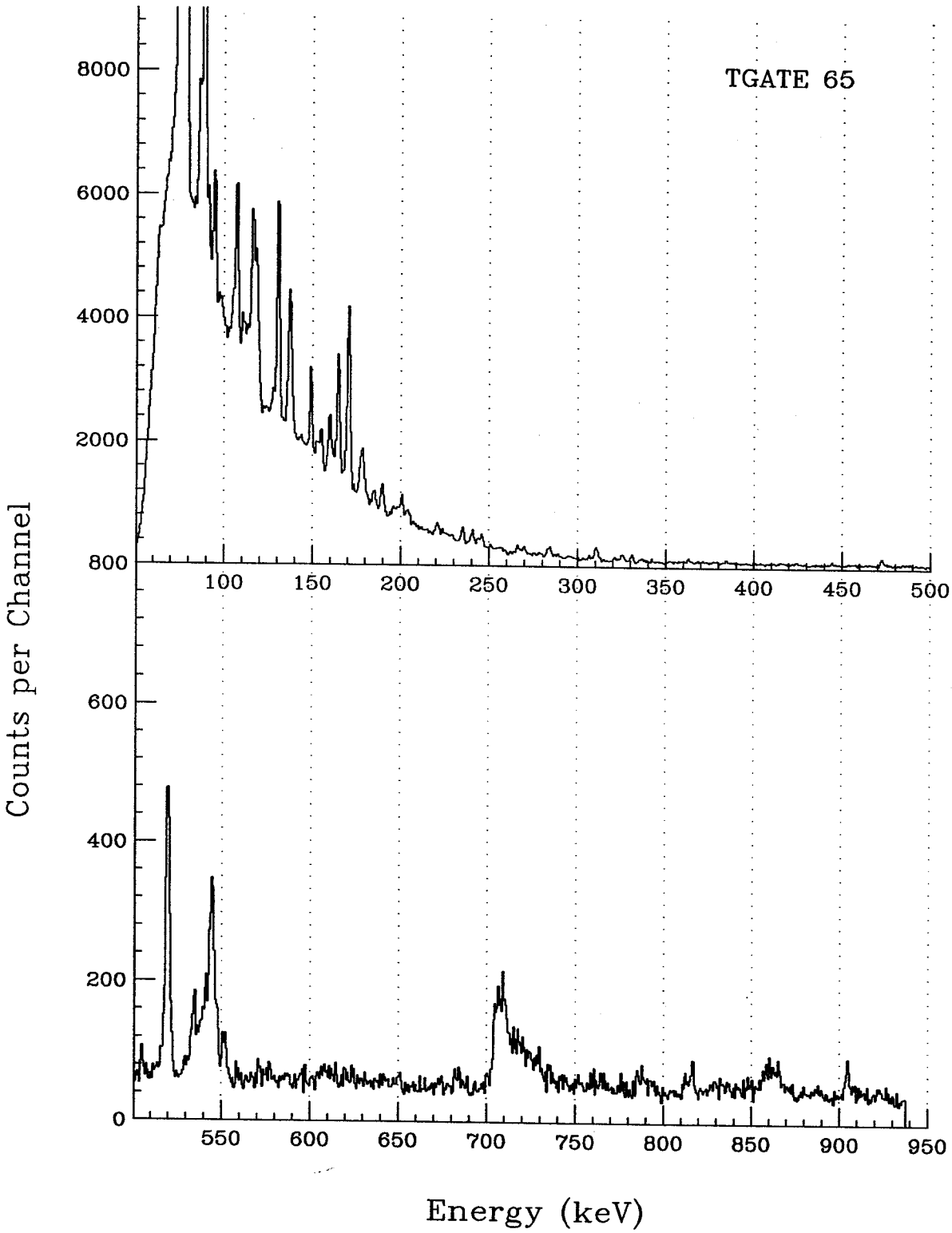

Figure D.43: Composite energy spectrum from TAC gate region 5, detector 6.

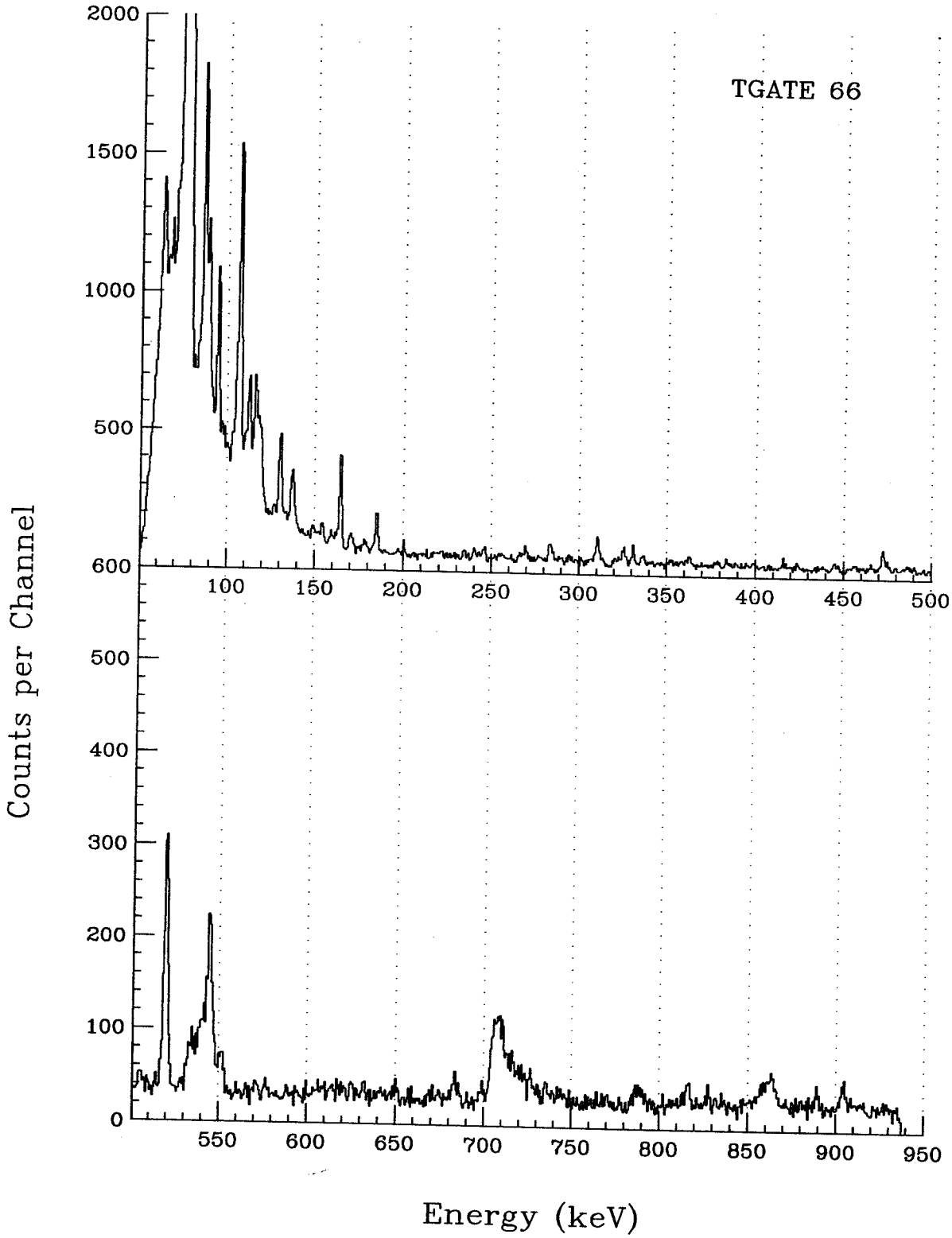

Figure D.44: Composite energy spectrum from TAC gate region 6, detector 6.

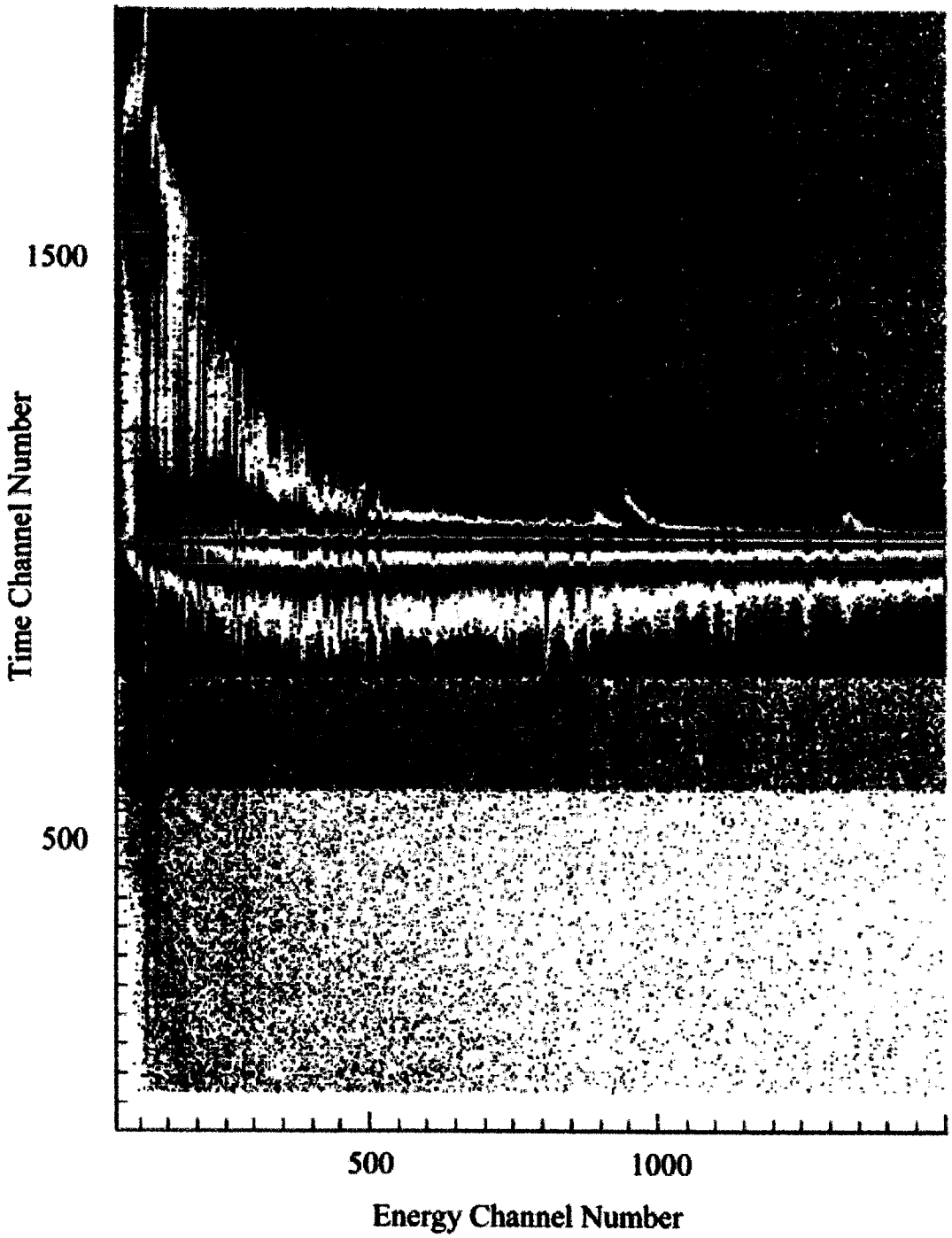

Figure D.45: Time versus E_γ plot for triple events from detector 7.

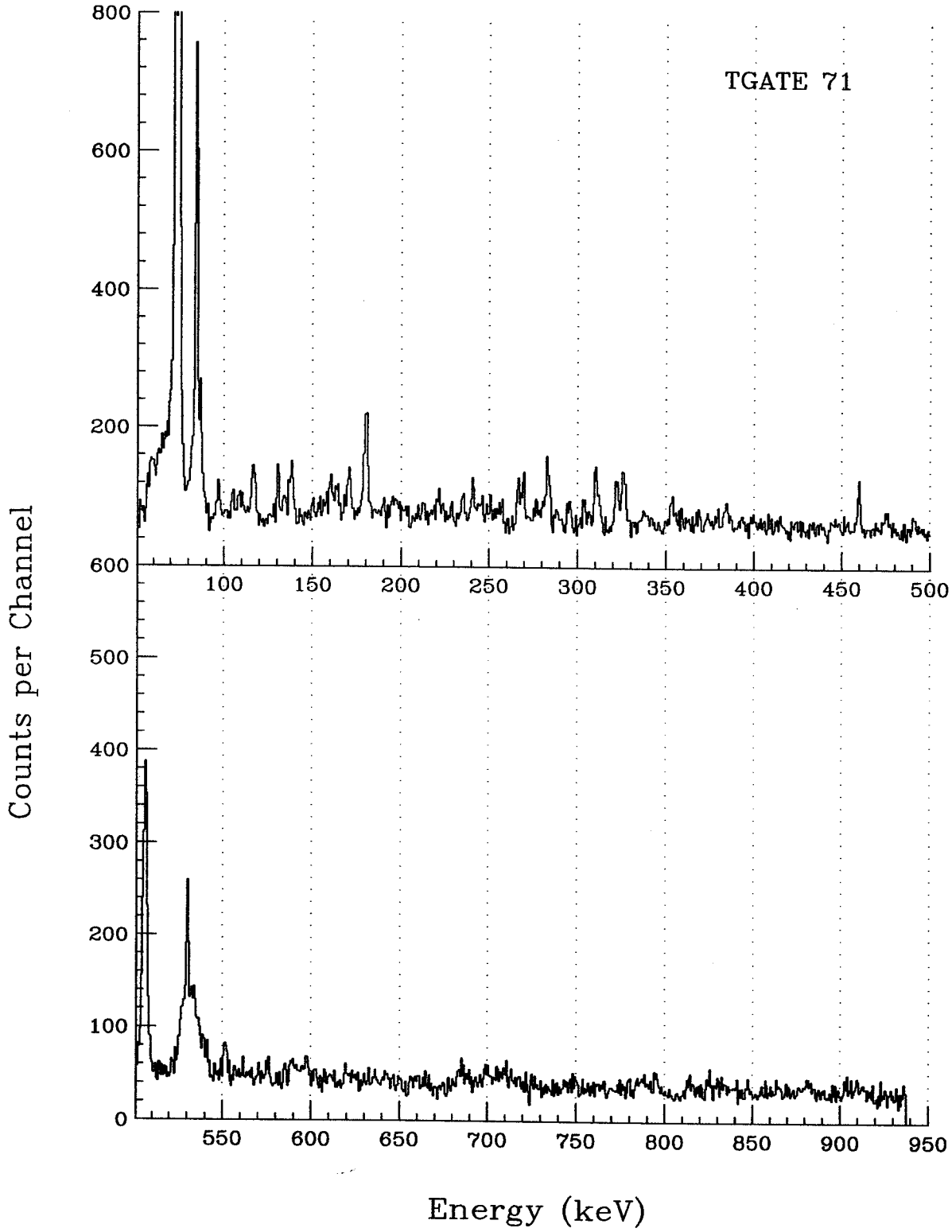

Figure D.46: Composite energy spectrum from TAC gate region 1, detector 7.

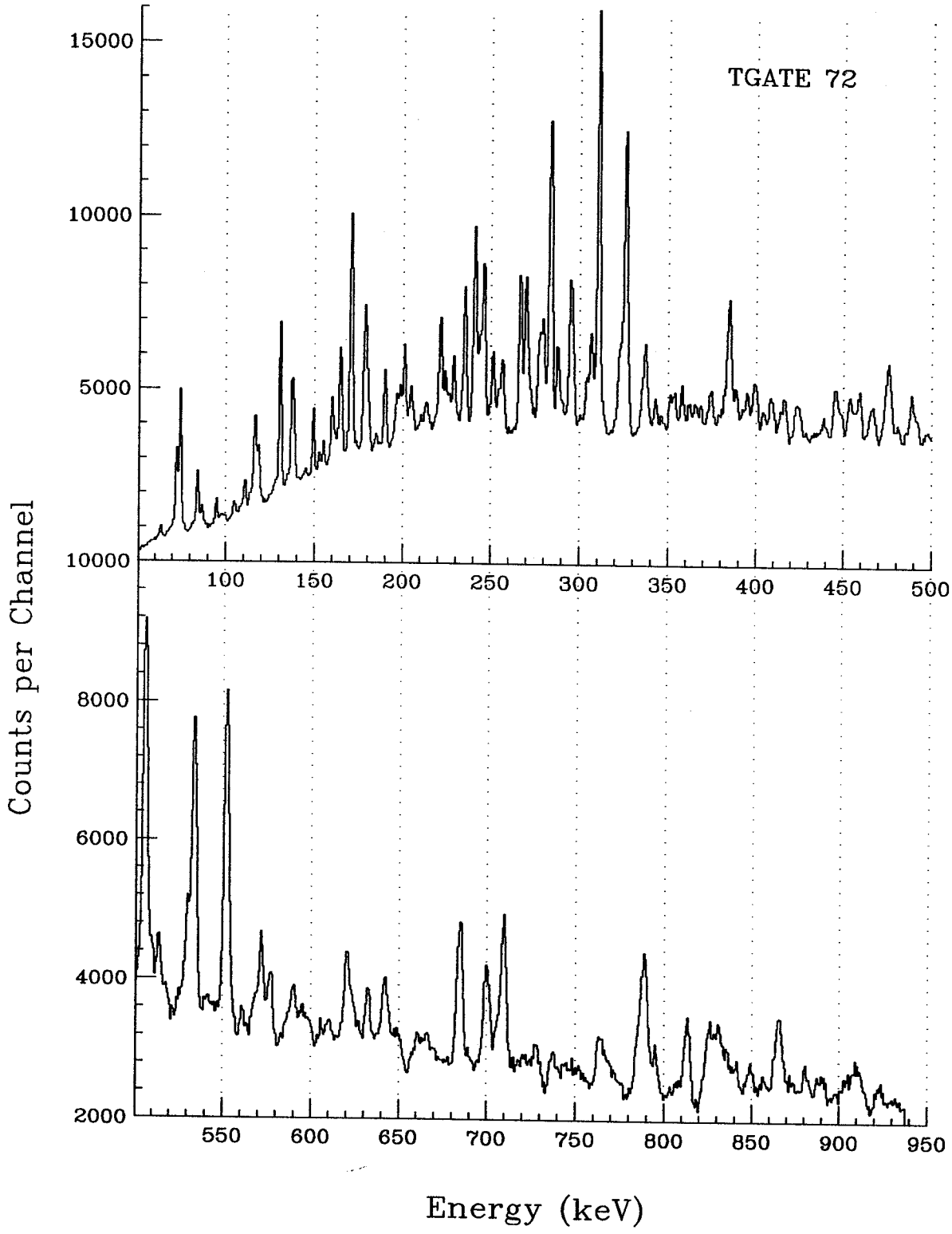

Figure D.47: Composite energy spectrum from TAC gate region 2, detector 7.

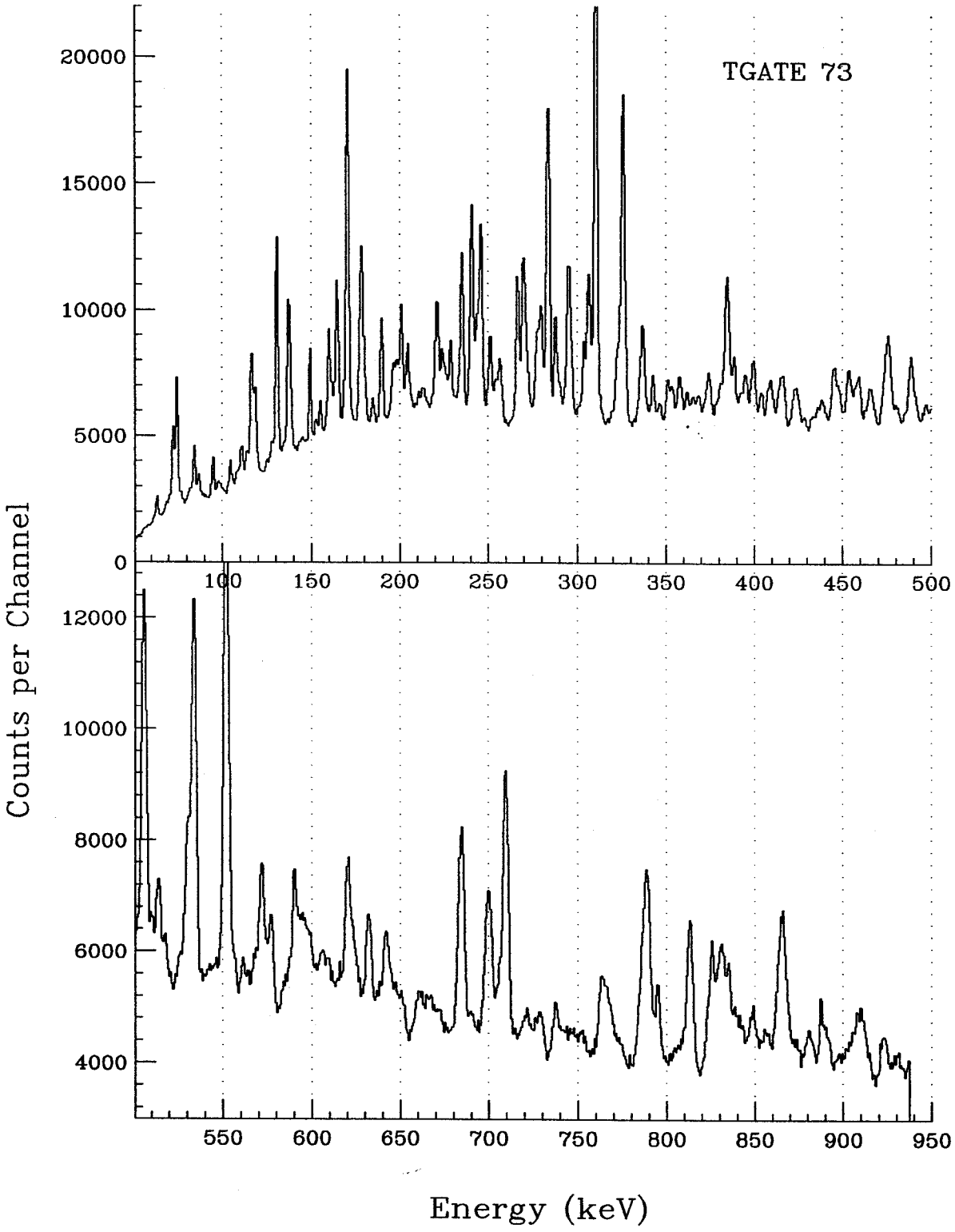

Figure D.48: Composite energy spectrum from TAC gate region 3, detector 7.

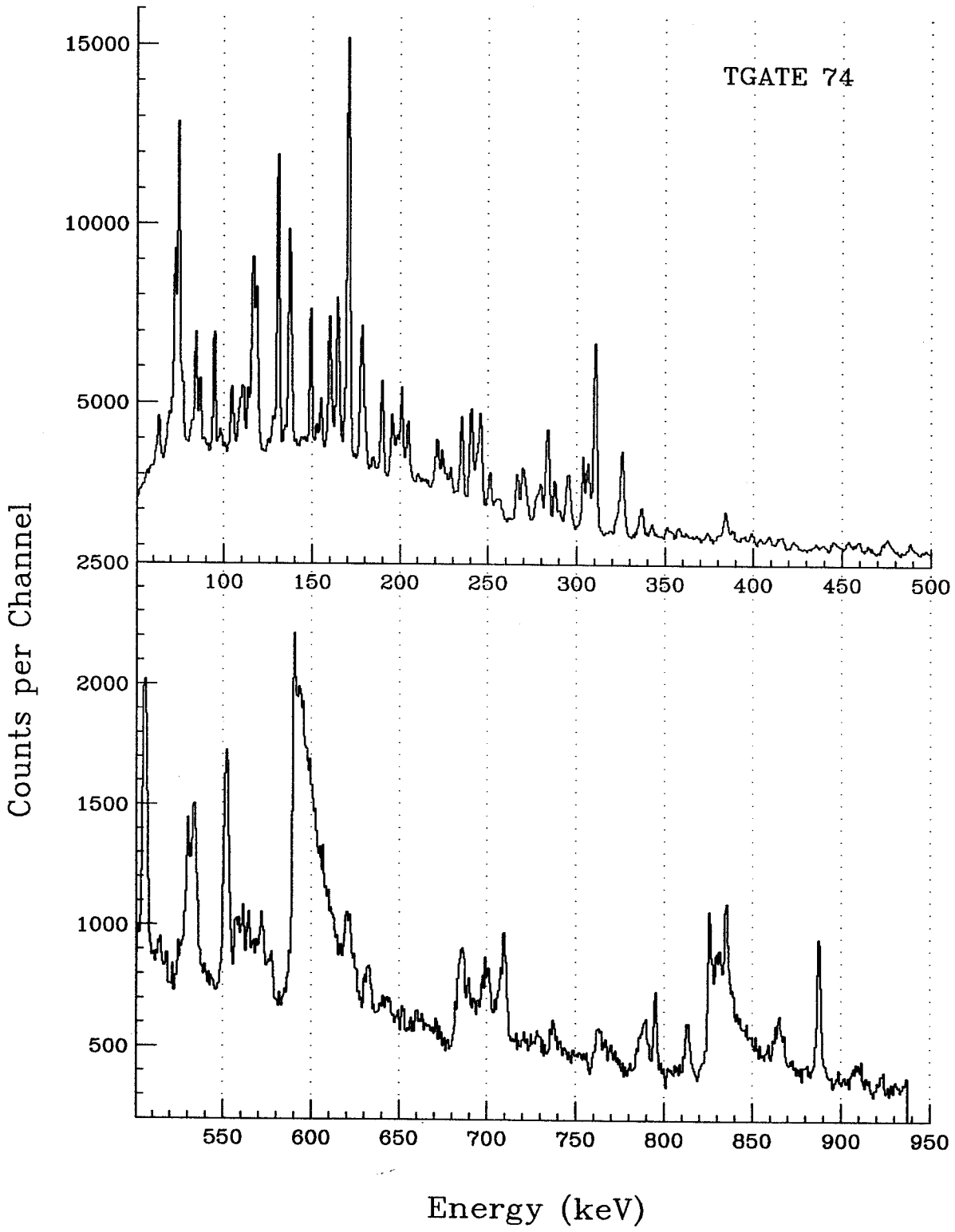

Figure D.49: Composite energy spectrum from TAC gate region 4, detector 7.

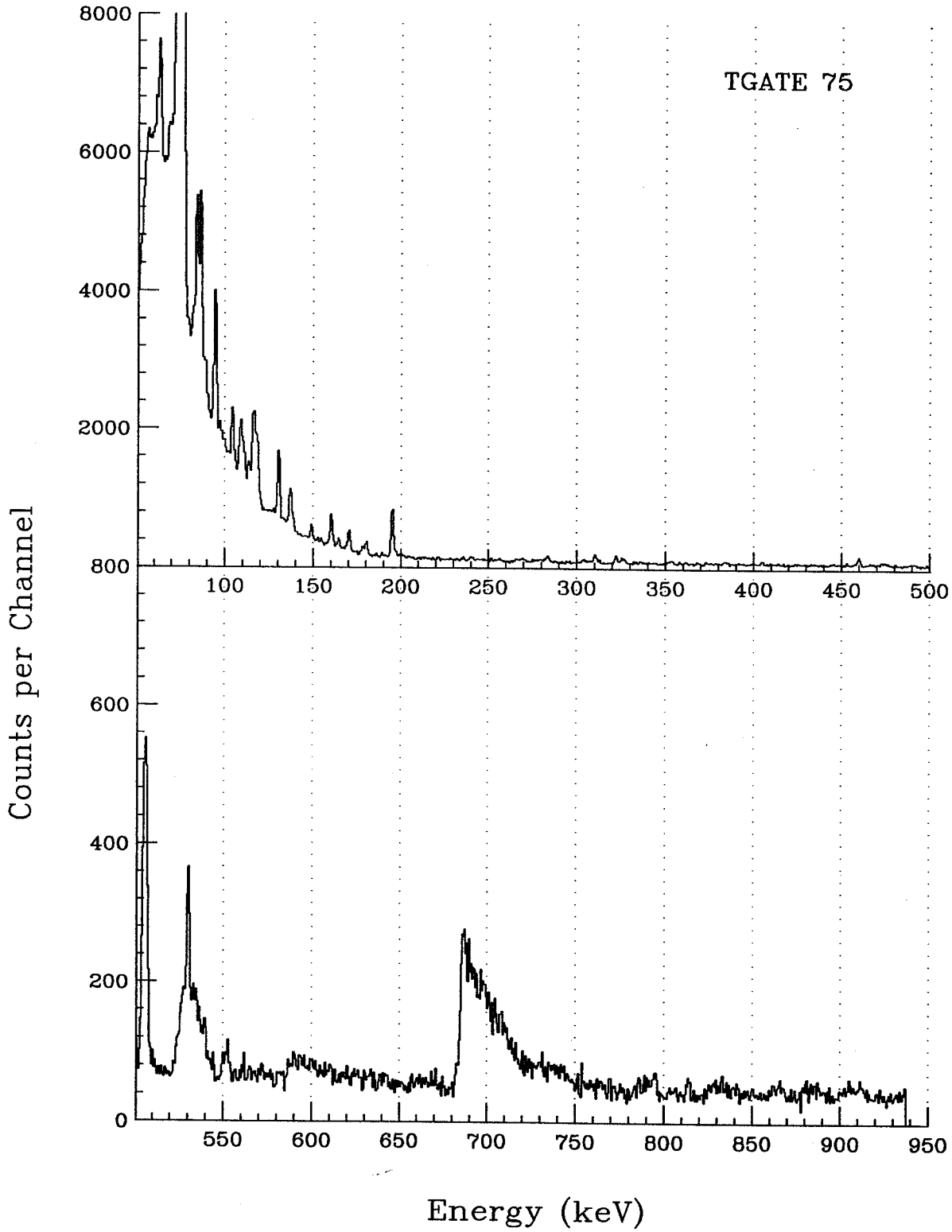

Figure D.50: Composite energy spectrum from TAC gate region 5, detector 7.

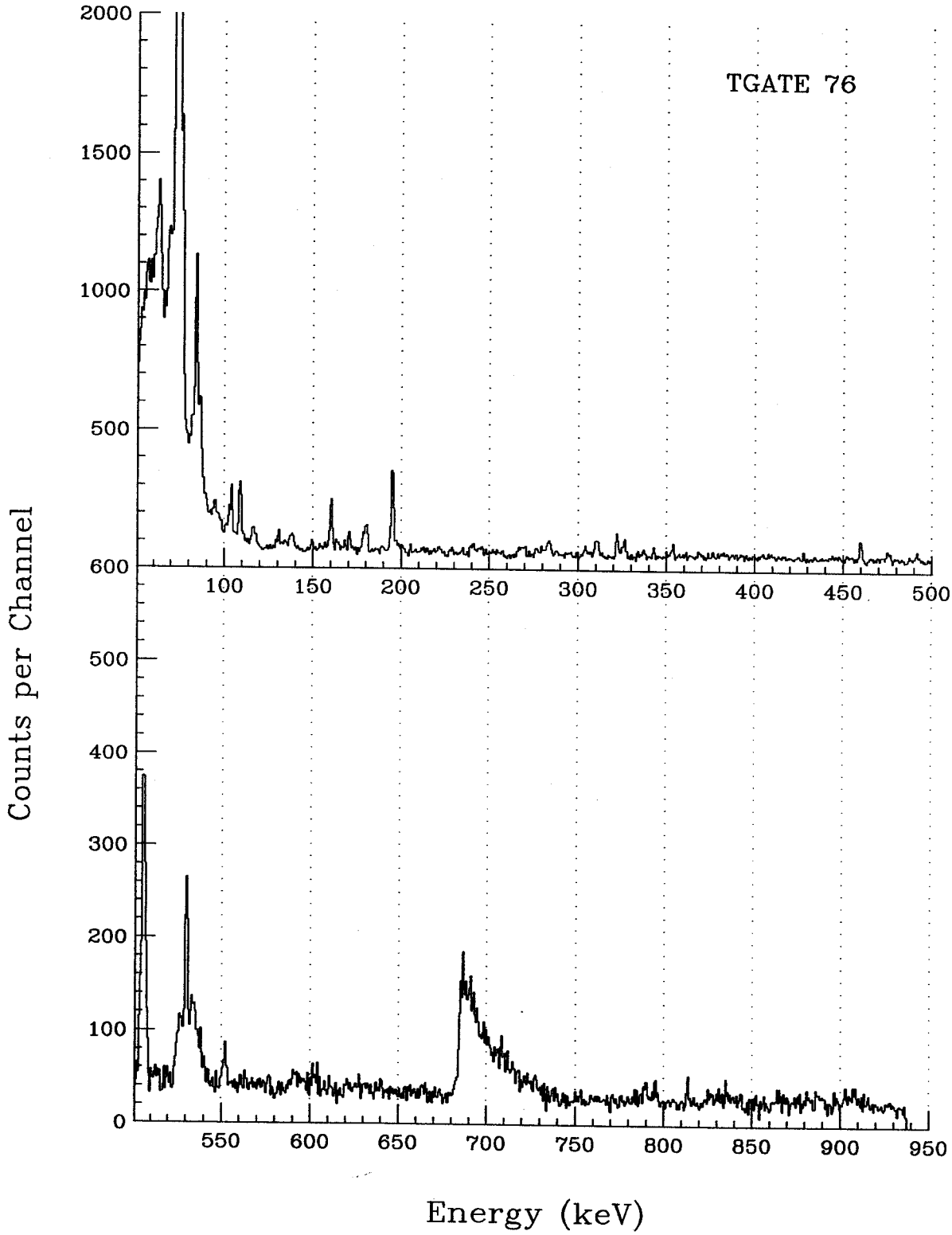

Figure D.51: Composite energy spectrum from TAC gate region 6, detector 7.

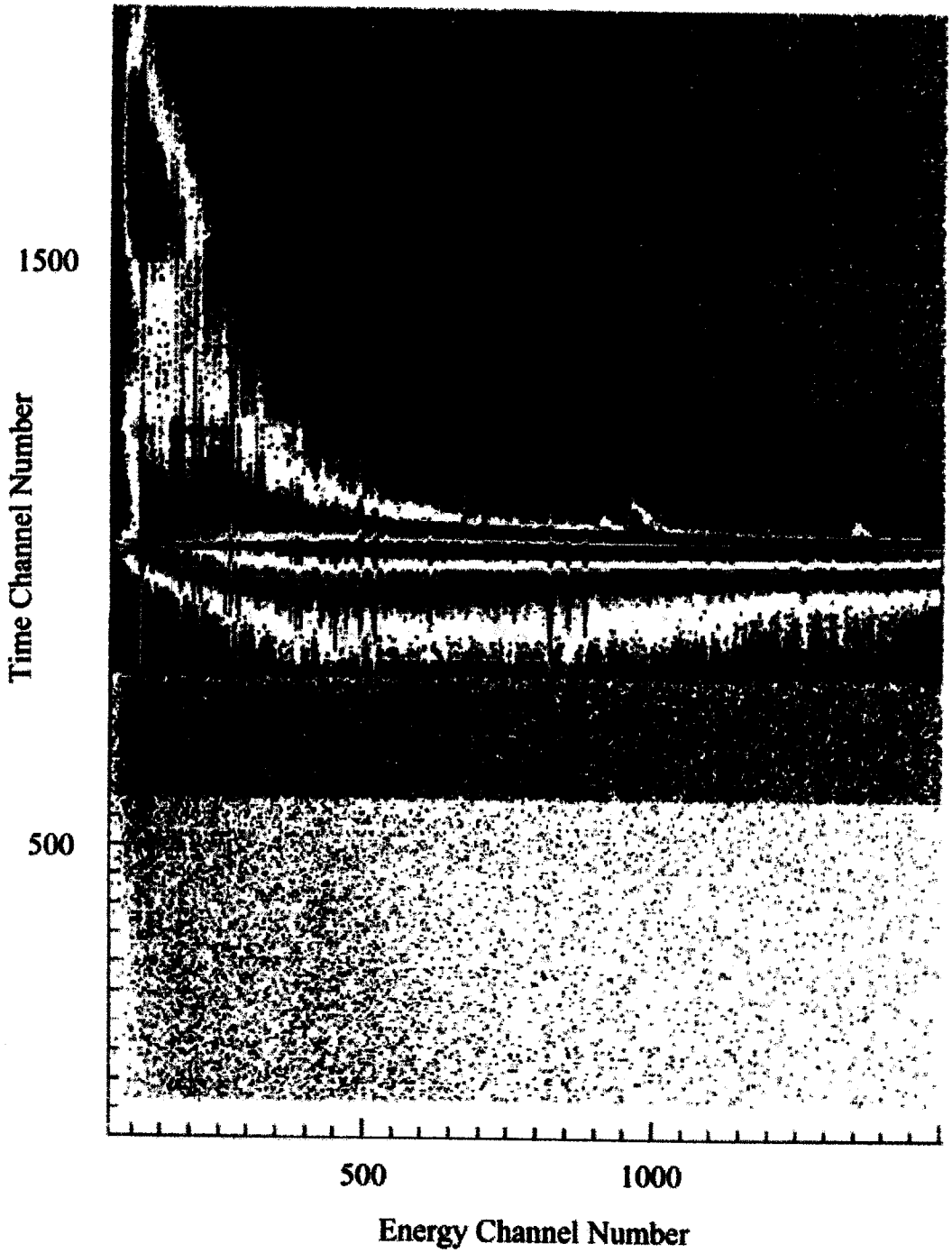

Figure D.52: Time versus E_γ plot for triple events from detector 8.

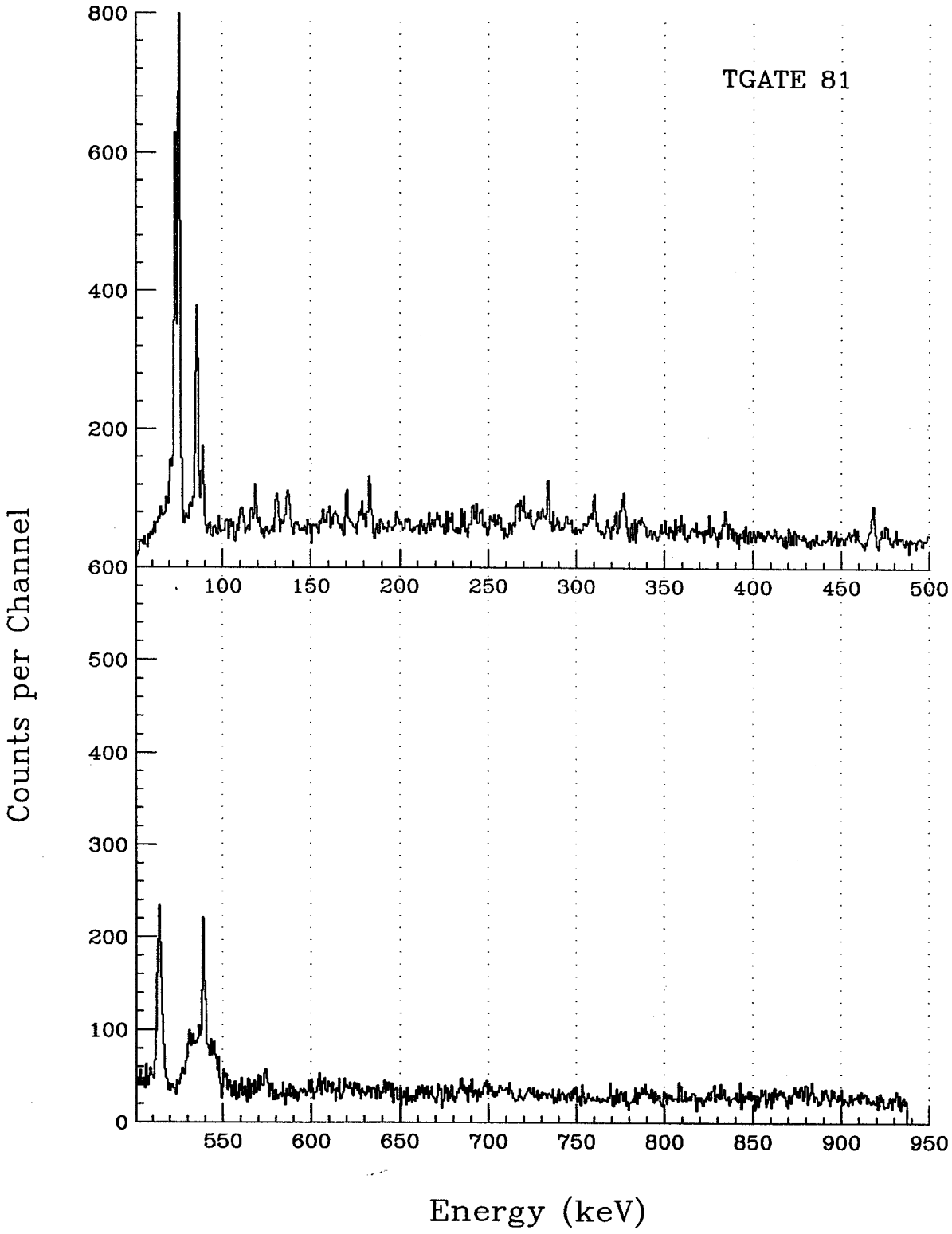

Figure D.53: Composite energy spectrum from TAC gate region 1, detector 8.

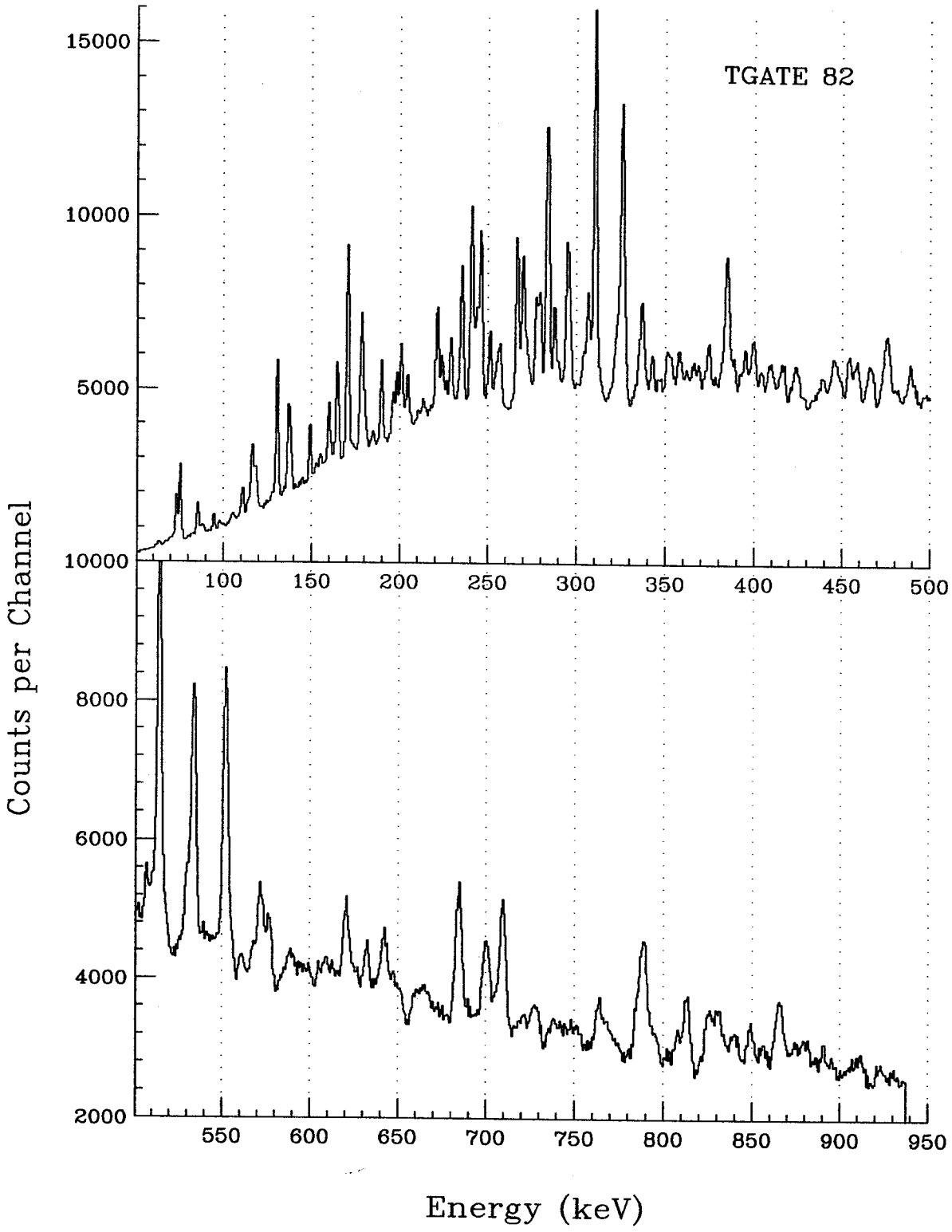

Figure D.54: Composite energy spectrum from TAC gate region 2, detector 8.

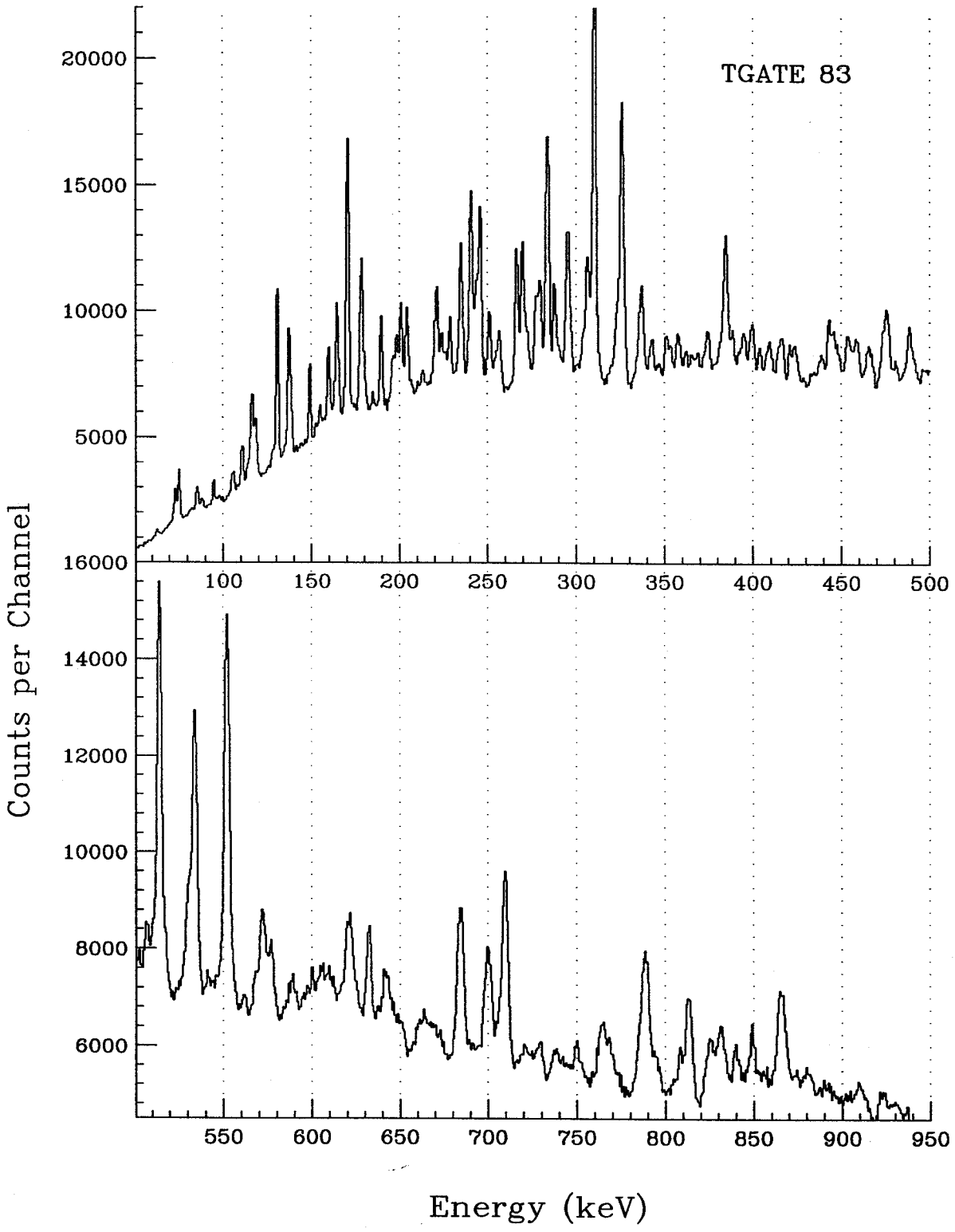

Figure D.55: Composite energy spectrum from TAC gate region 3, detector 8.

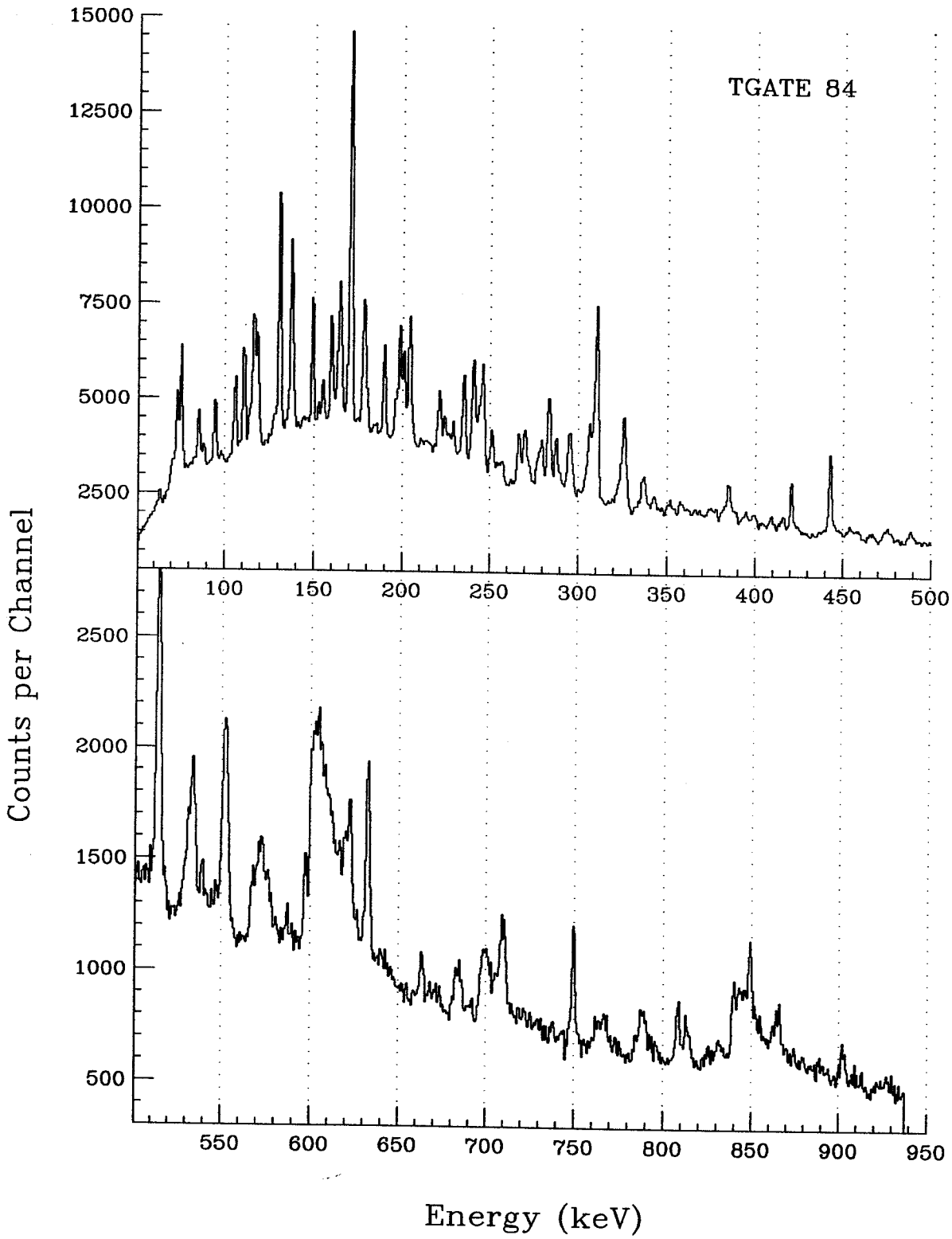

Figure D.56: Composite energy spectrum from TAC gate region 4, detector 8.

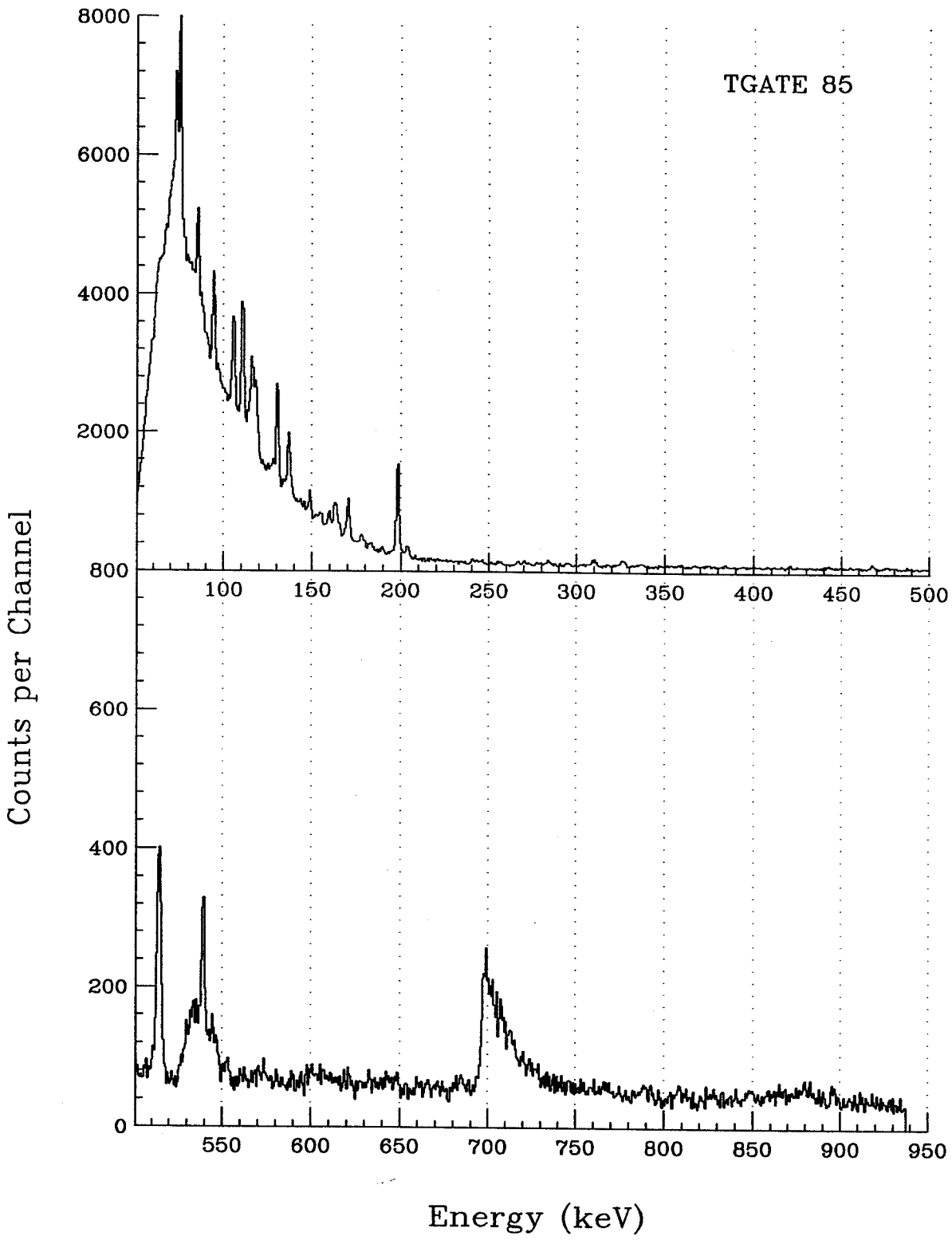

Figure D.57: Composite energy spectrum from TAC gate region 5, detector 8.

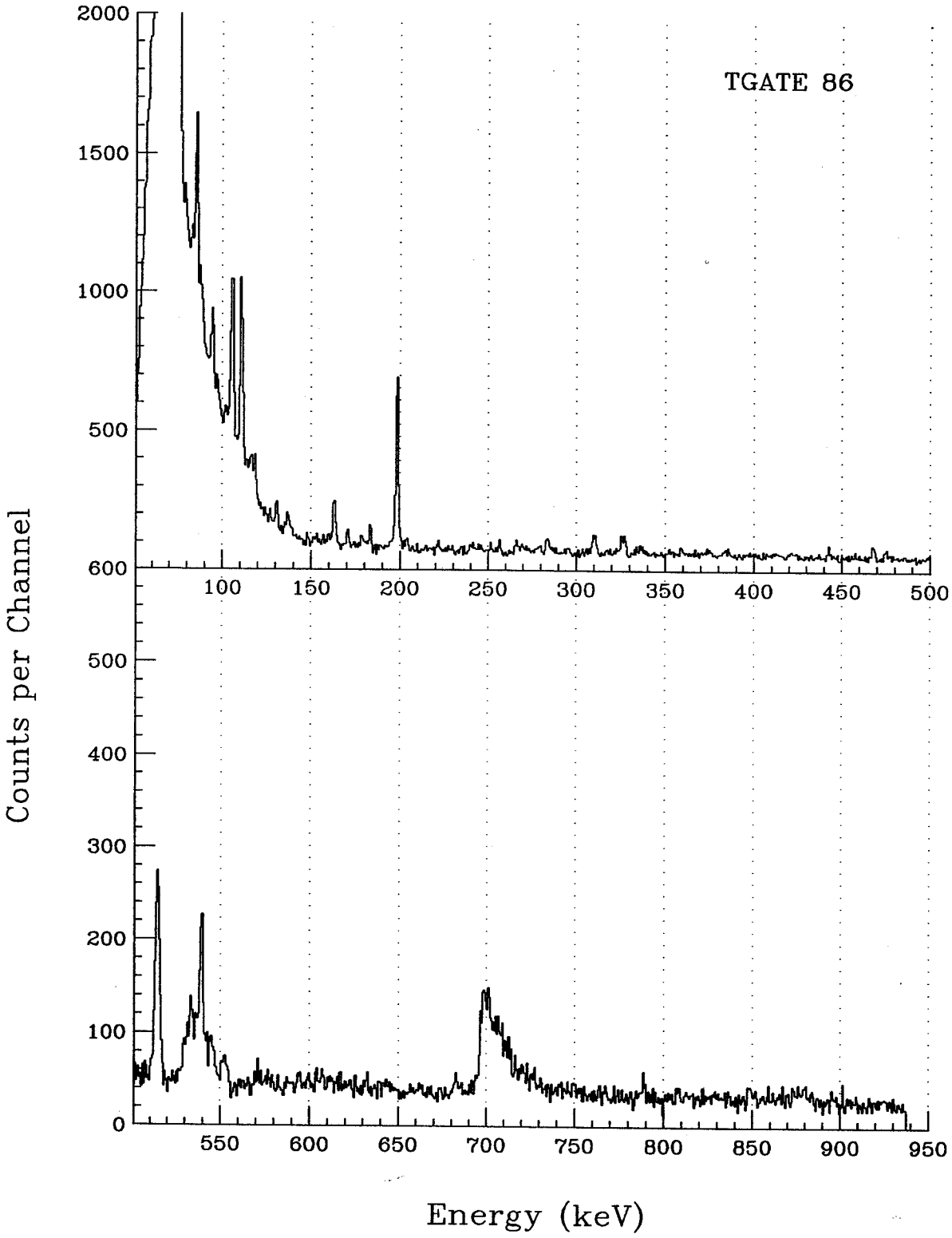

Figure D.58: Composite energy spectrum from TAC gate region 6, detector 8.

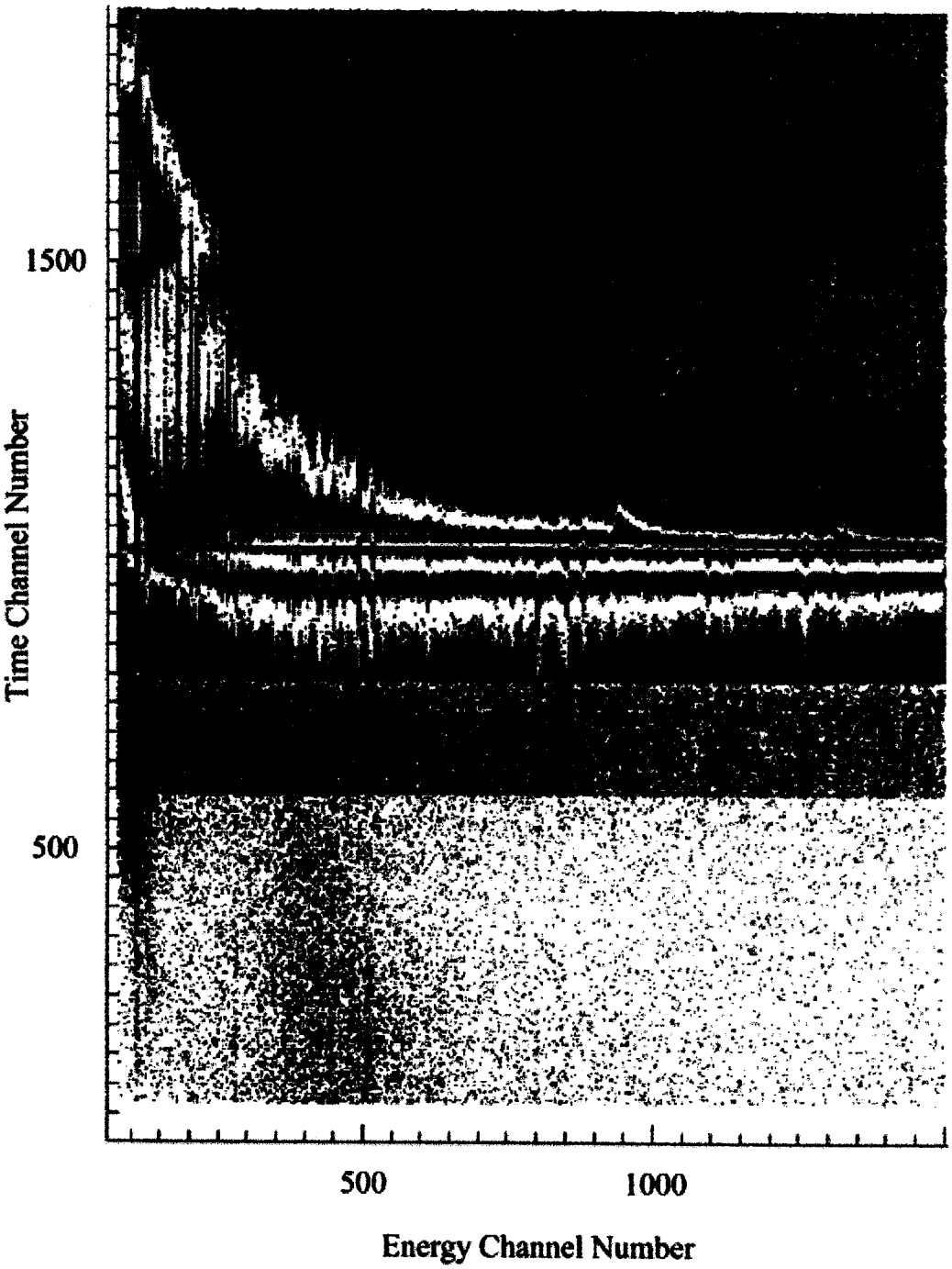

Figure D.59: Time versus E_γ plot for triple events from detector 9.

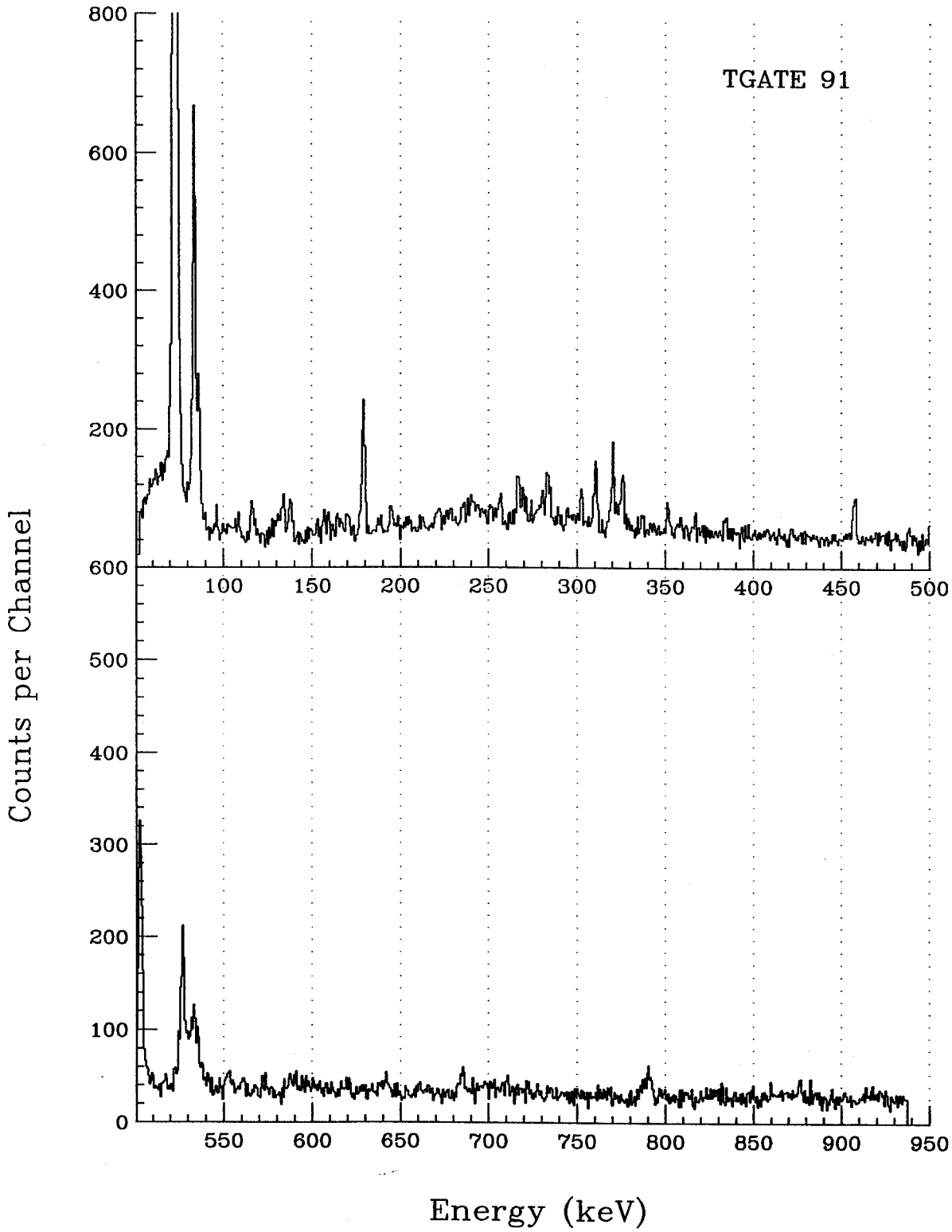

Figure D.60: Composite energy spectrum from TAC gate region 1, detector 9.

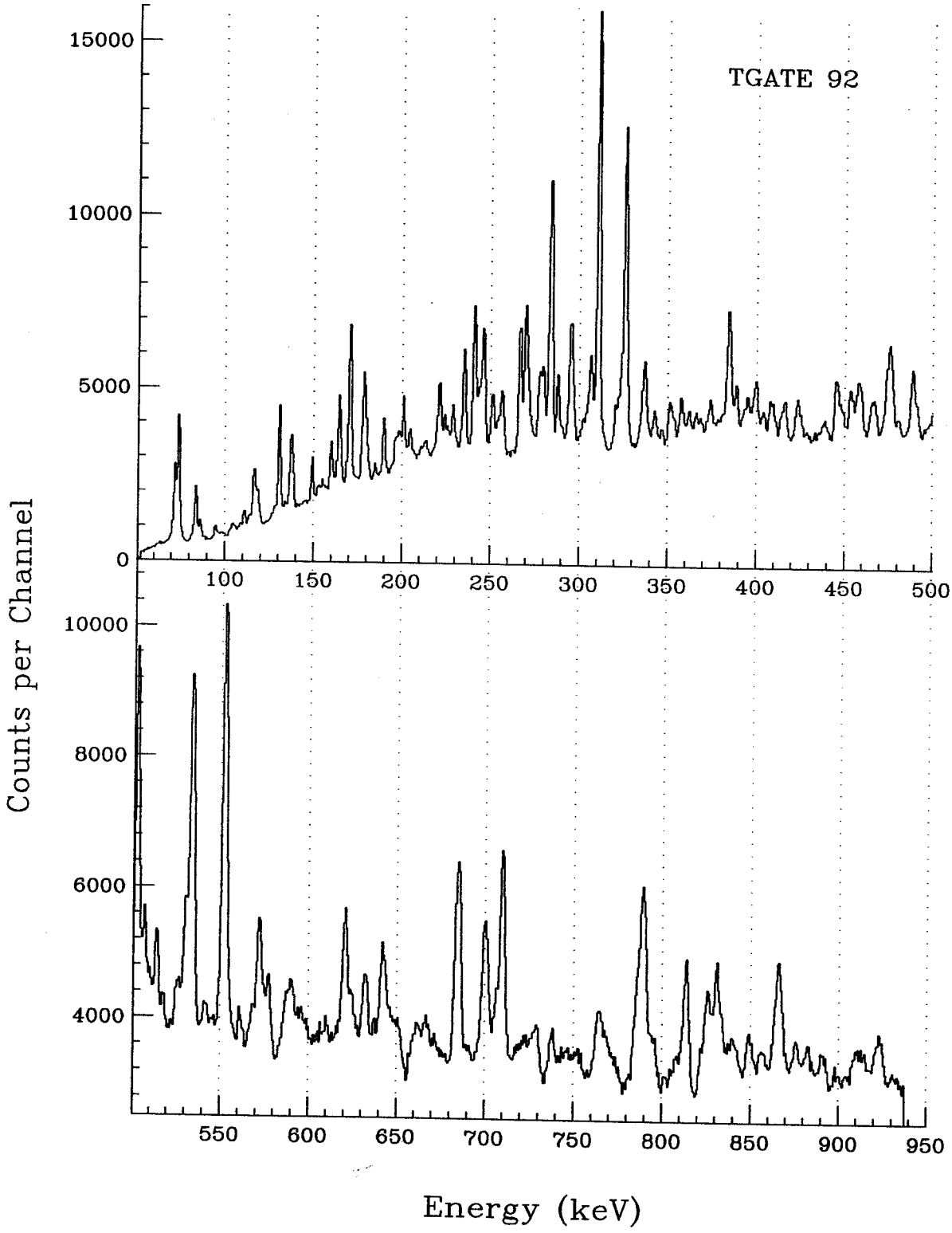

Figure D.61: Composite energy spectrum from TAC gate region 2, detector 9.

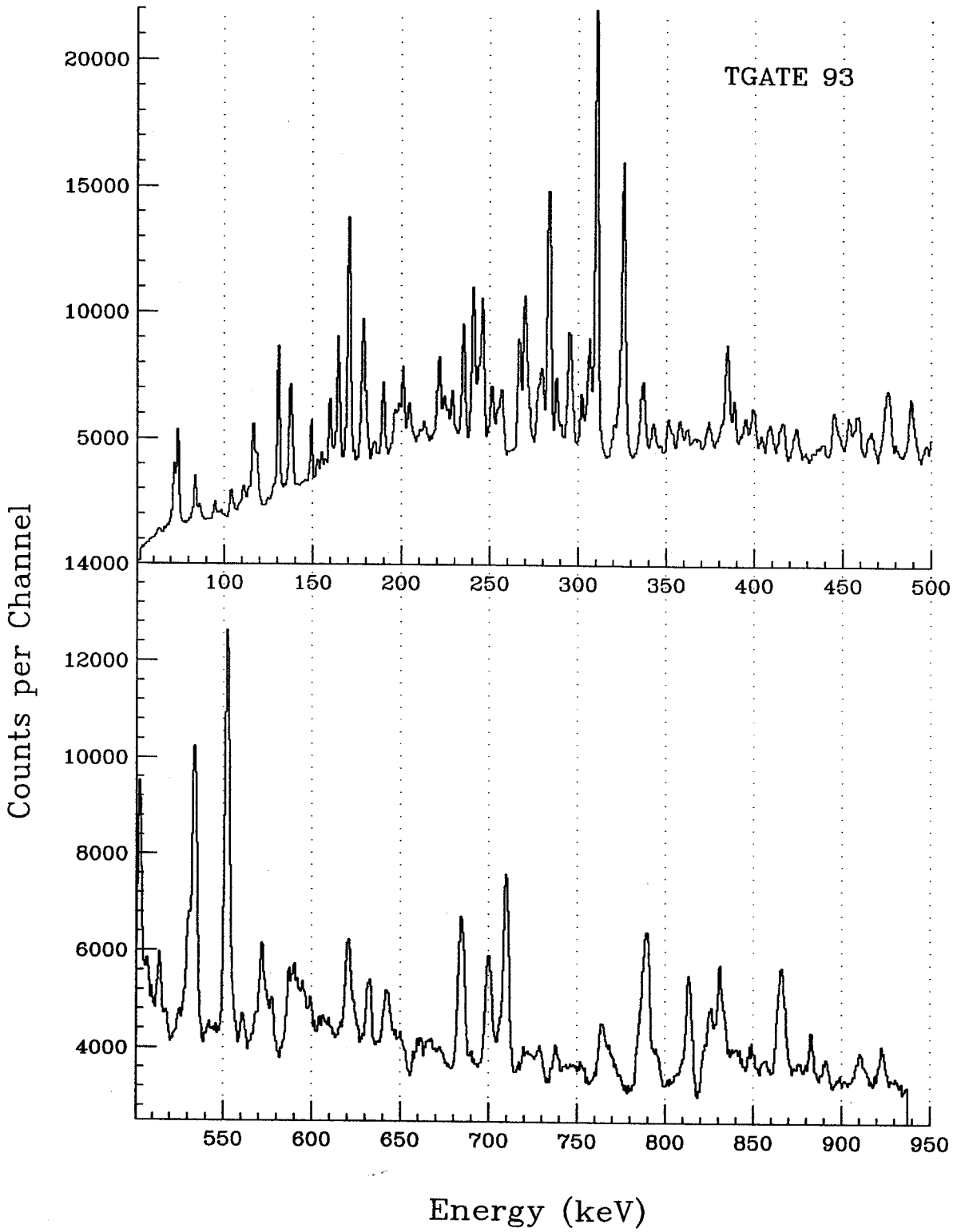

Figure D.62: Composite energy spectrum from TAC gate region 3, detector 9.

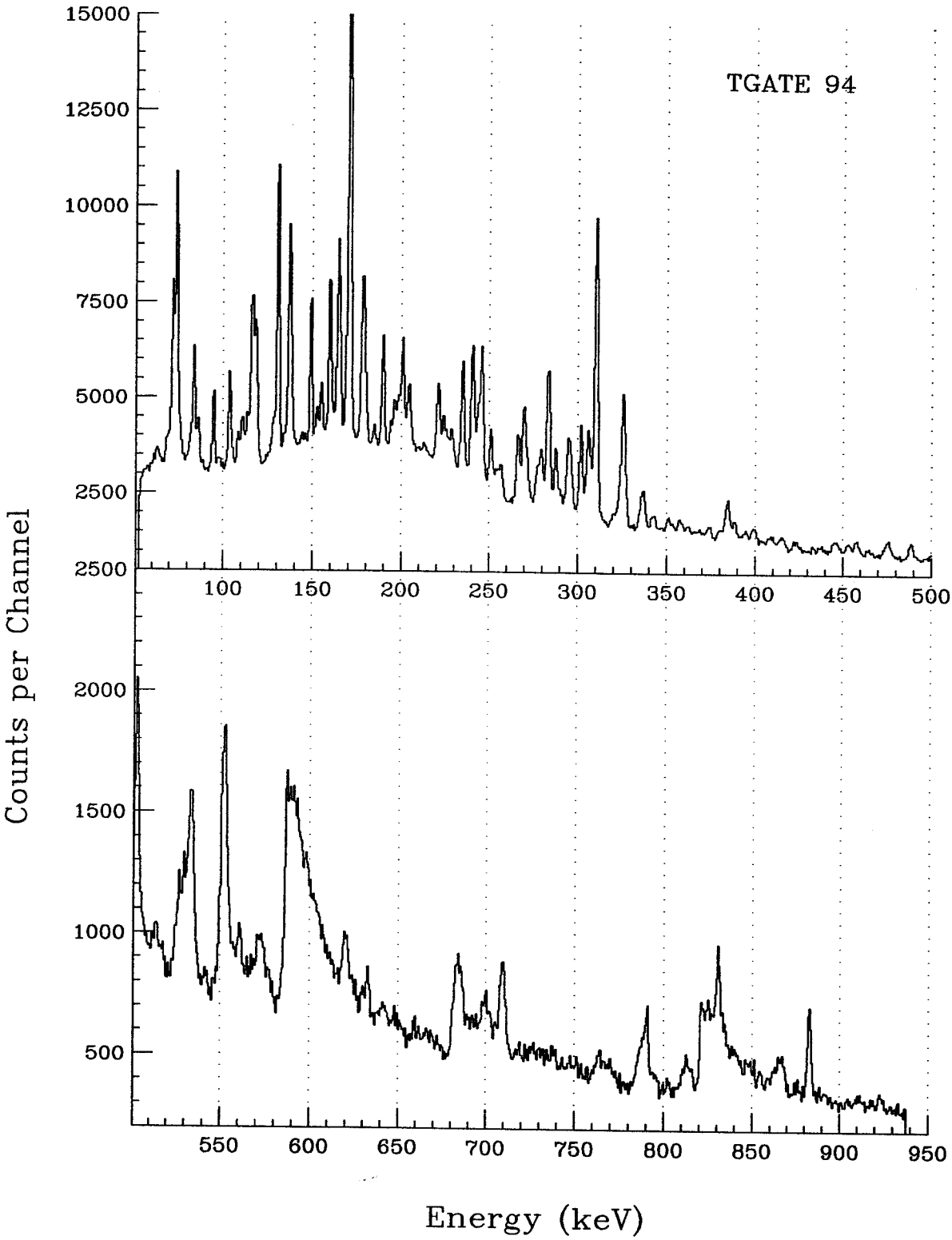

Figure D.63: Composite energy spectrum from TAC gate region 4, detector 9.

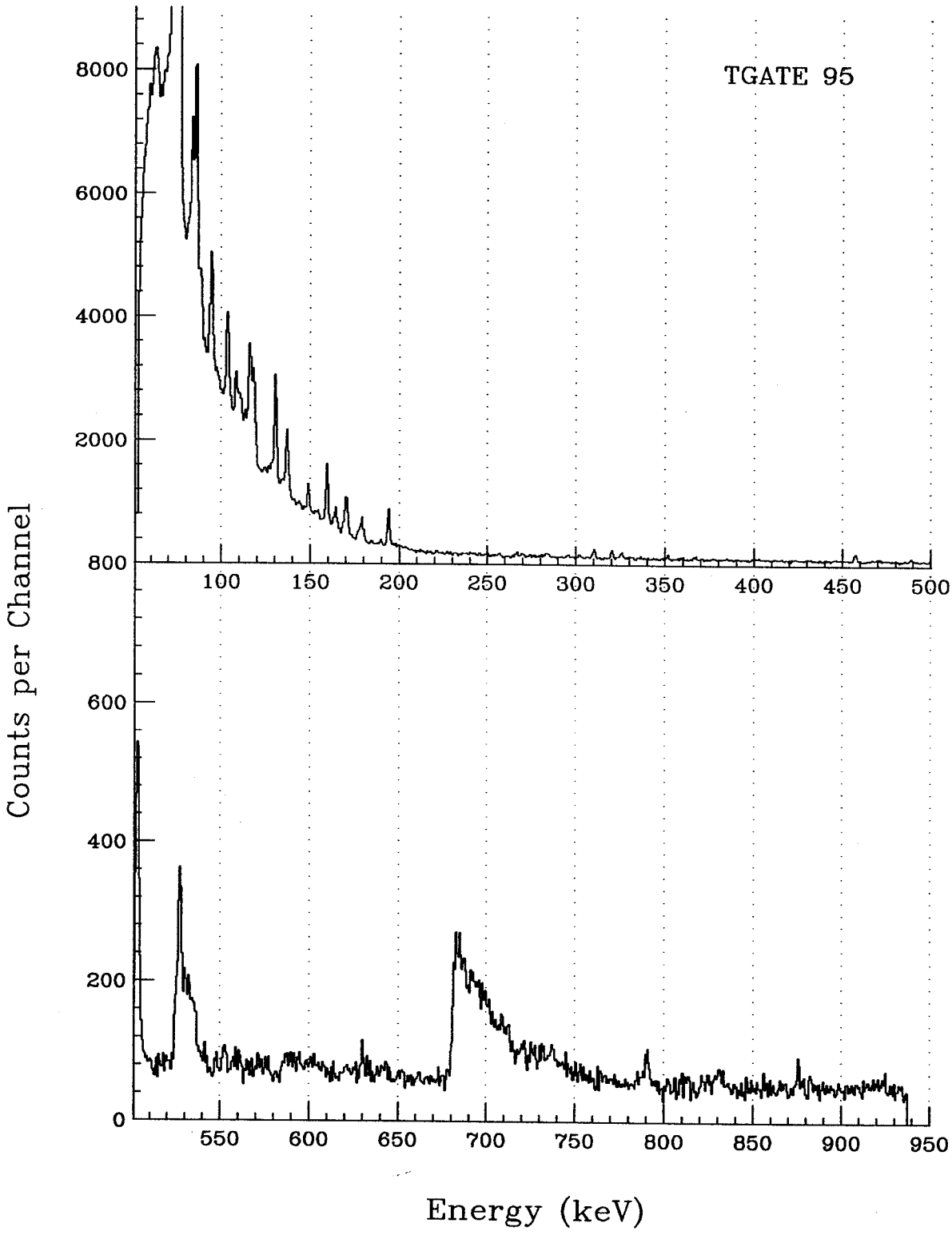

Figure D.64: Composite energy spectrum from TAC gate region 5, detector 9.

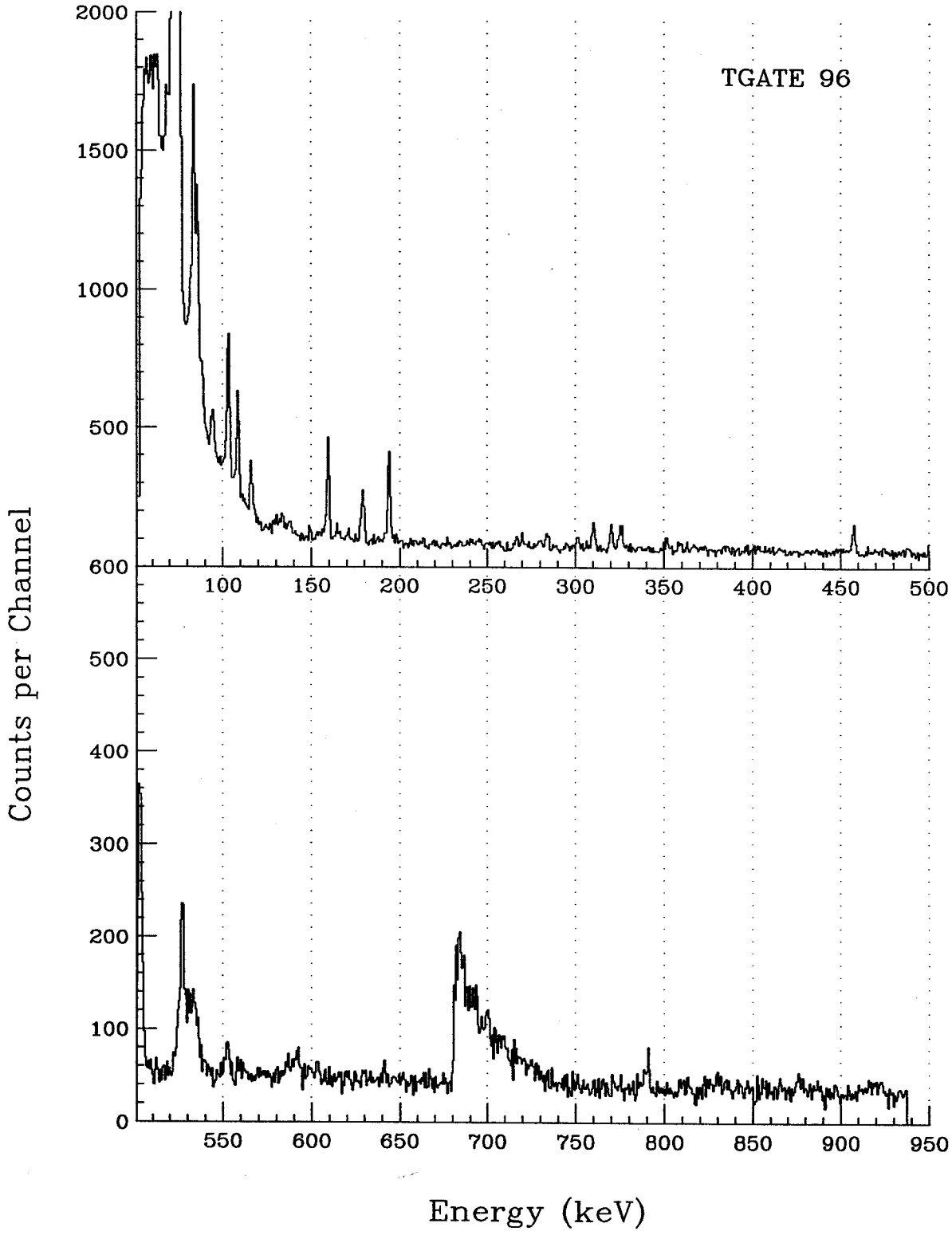

Figure D.65: Composite energy spectrum from TAC gate region 6, detector 9.

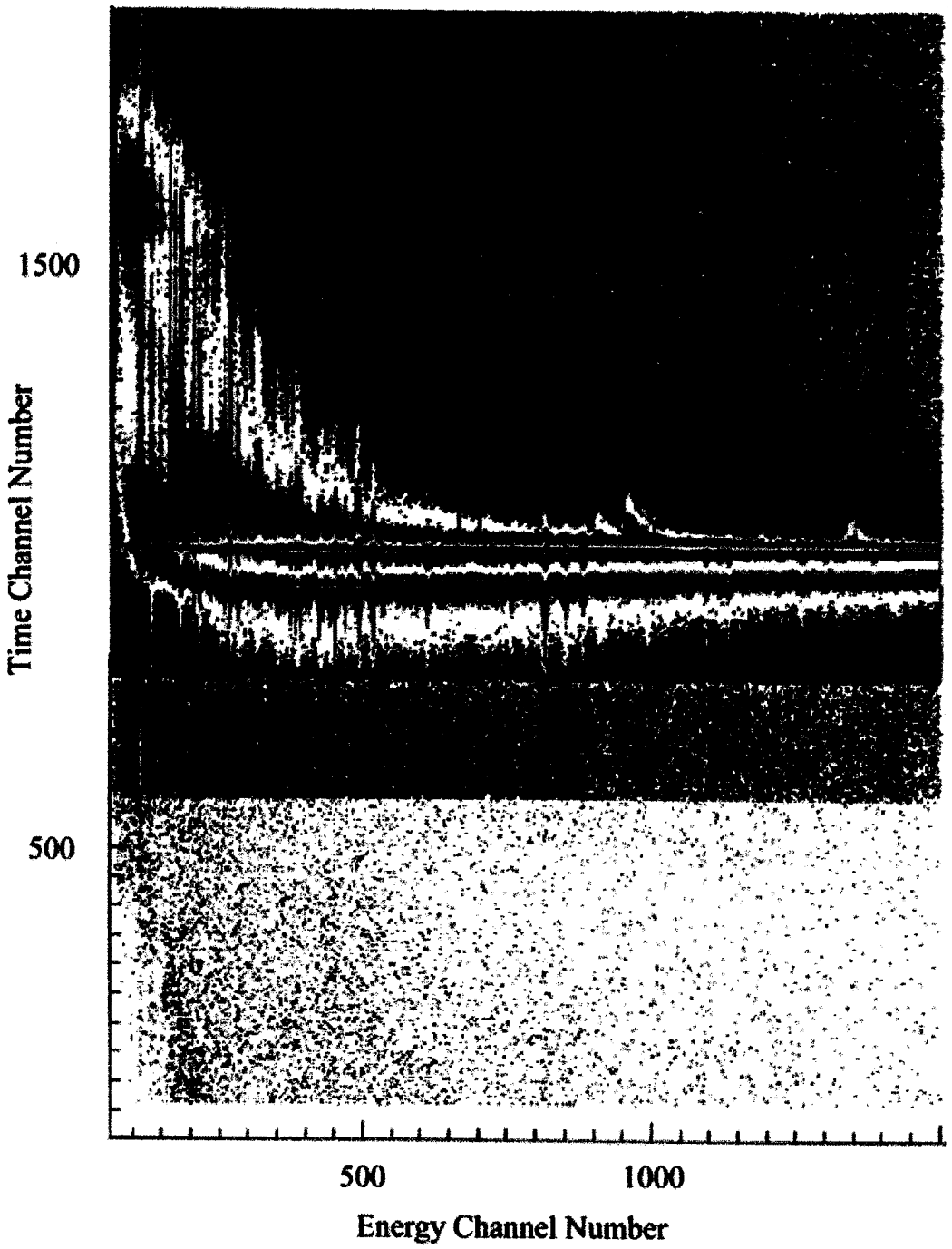

Figure D.66: Time versus E_γ plot for triple events from detector 10.

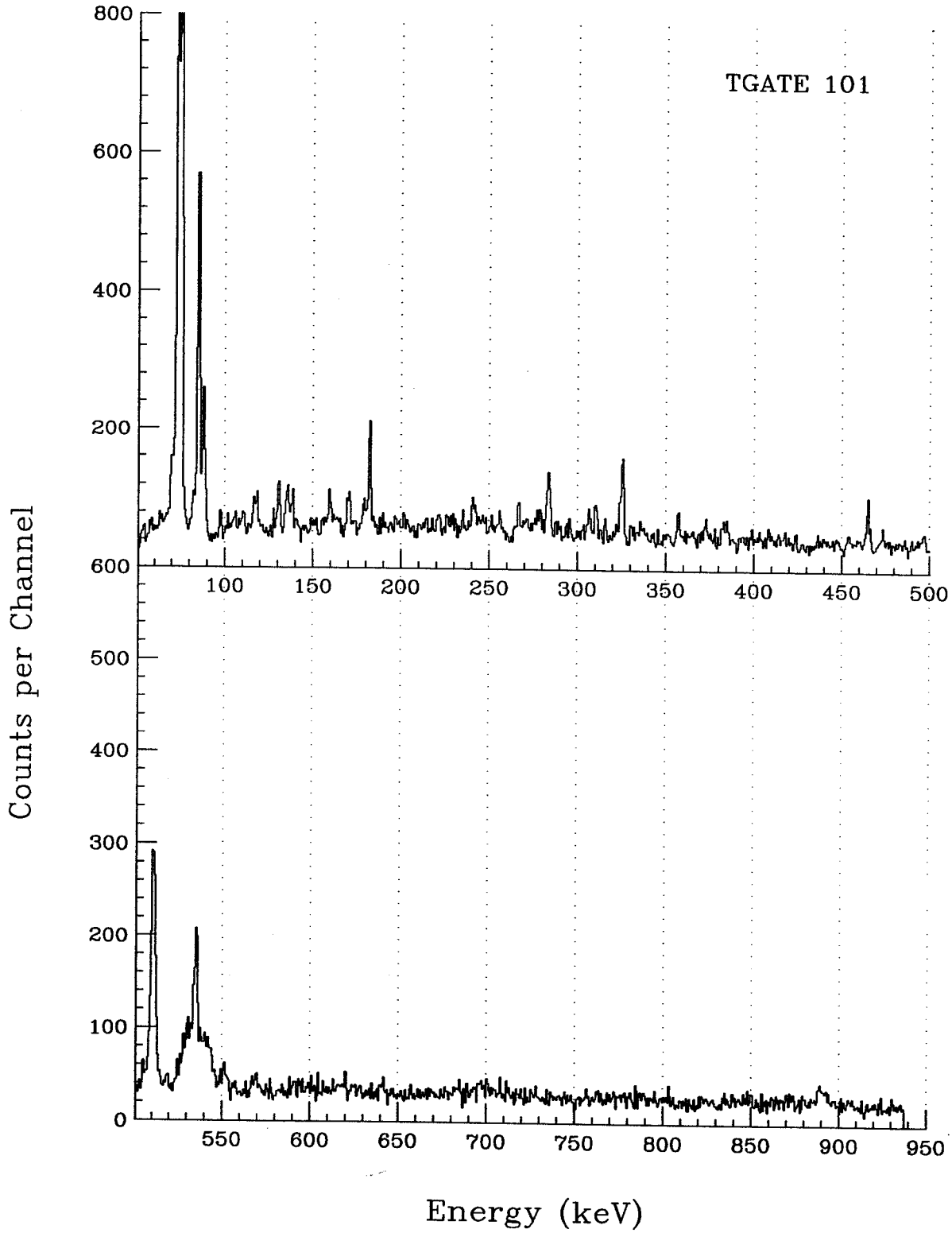

Figure D.67: Composite energy spectrum from TAC gate region 1, detector 10.

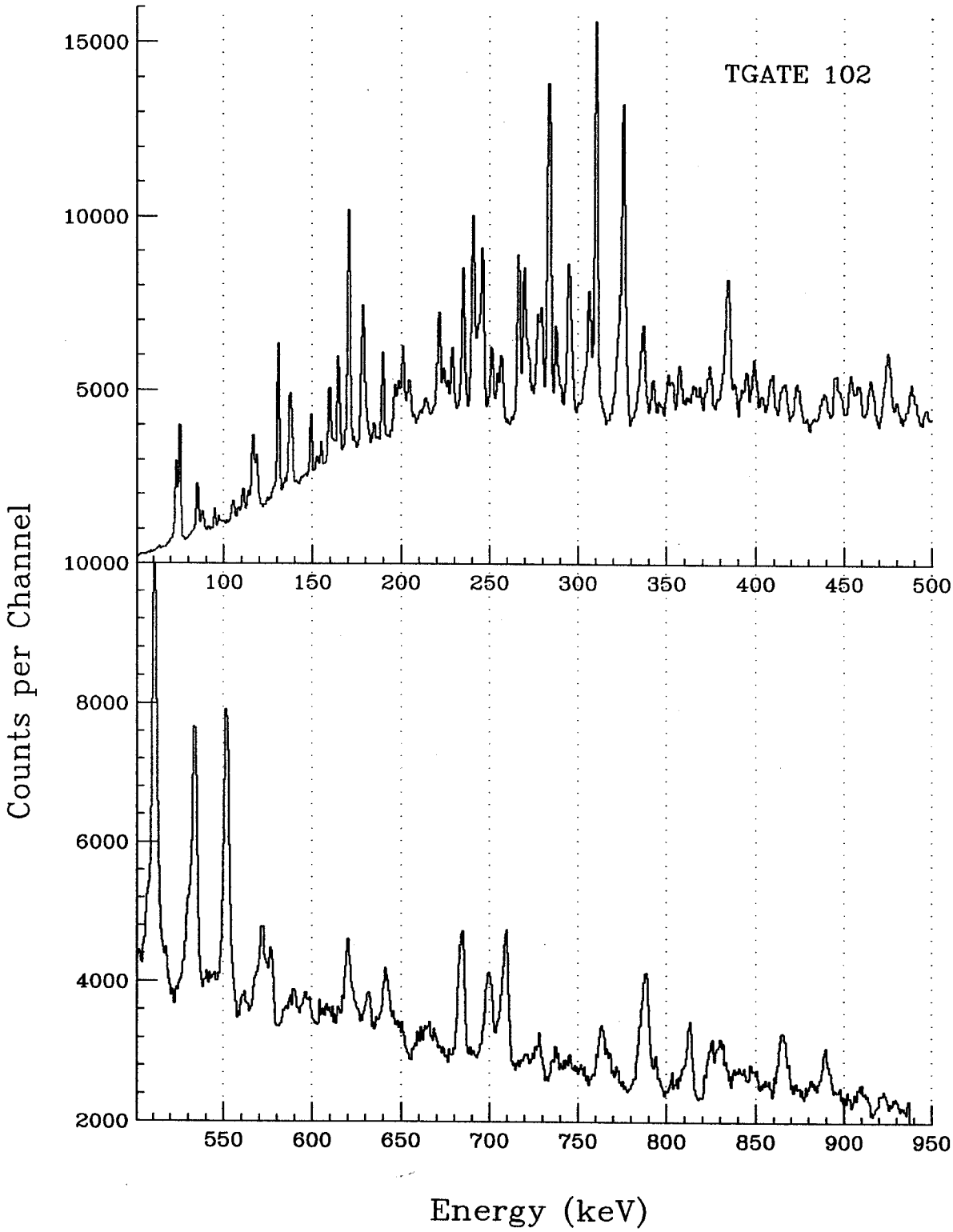

Figure D.68: Composite energy spectrum from TAC gate region 2, detector 10.

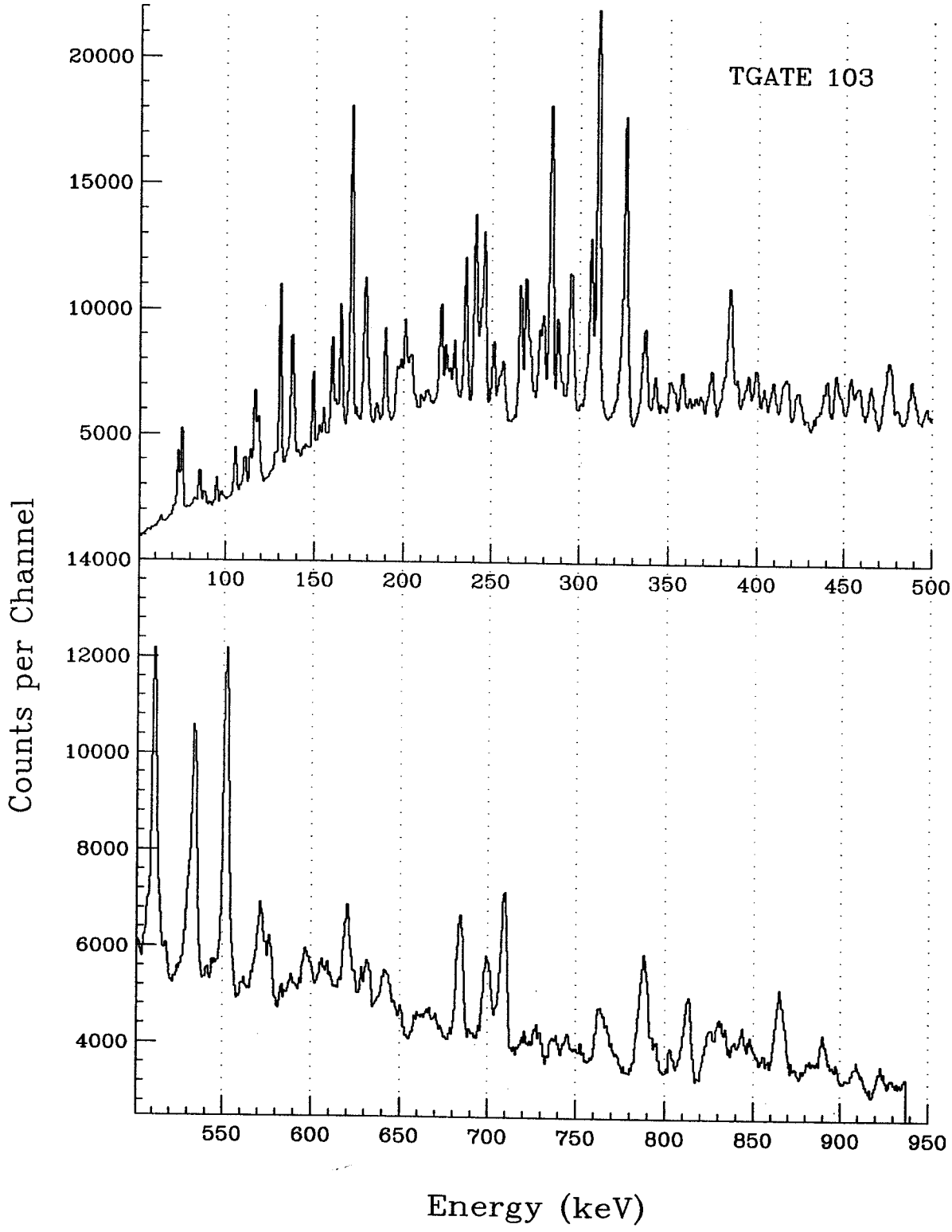

Figure D.69: Composite energy spectrum from TAC gate region 3, detector 10.

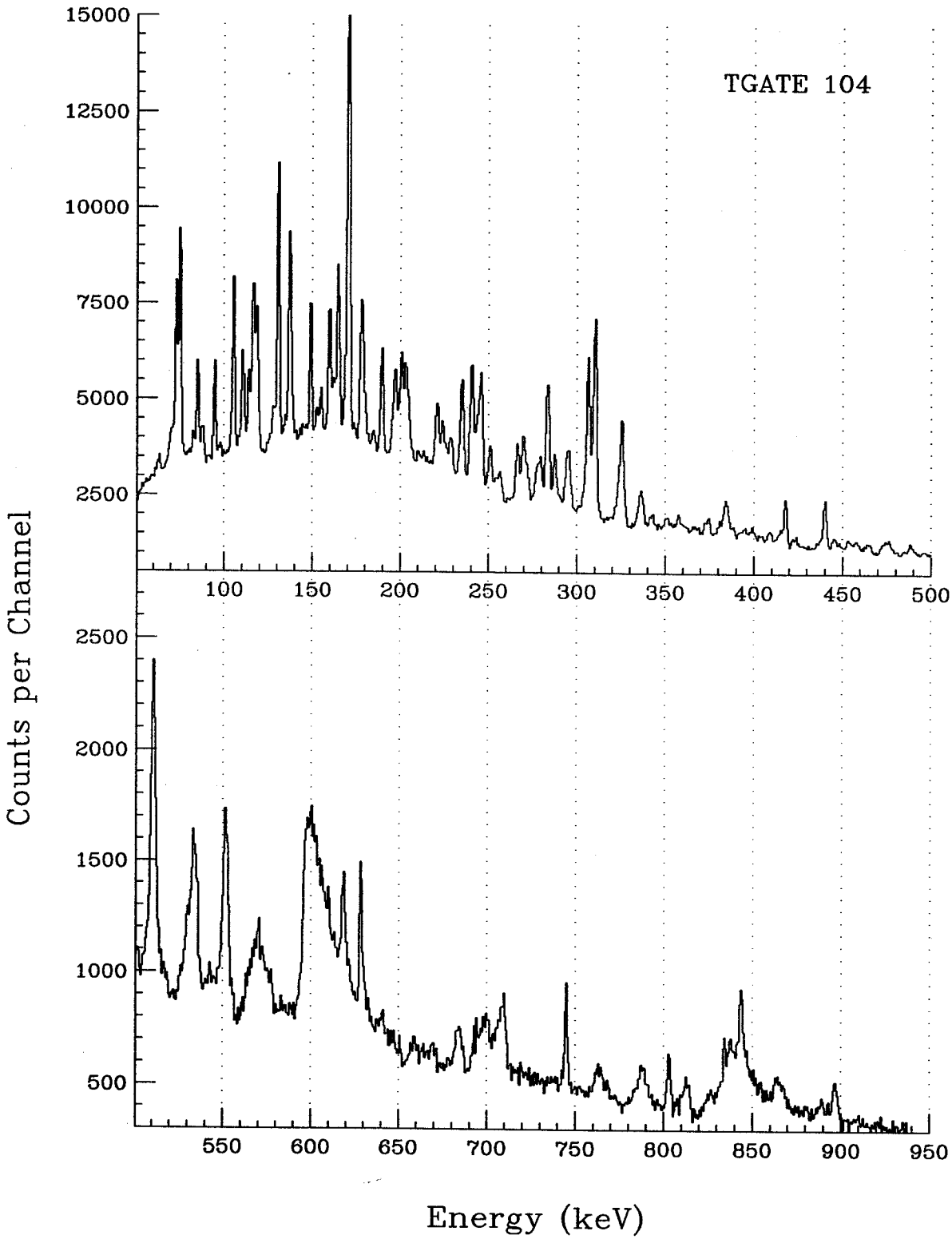

Figure D.70: Composite energy spectrum from TAC gate region 4, detector 10.

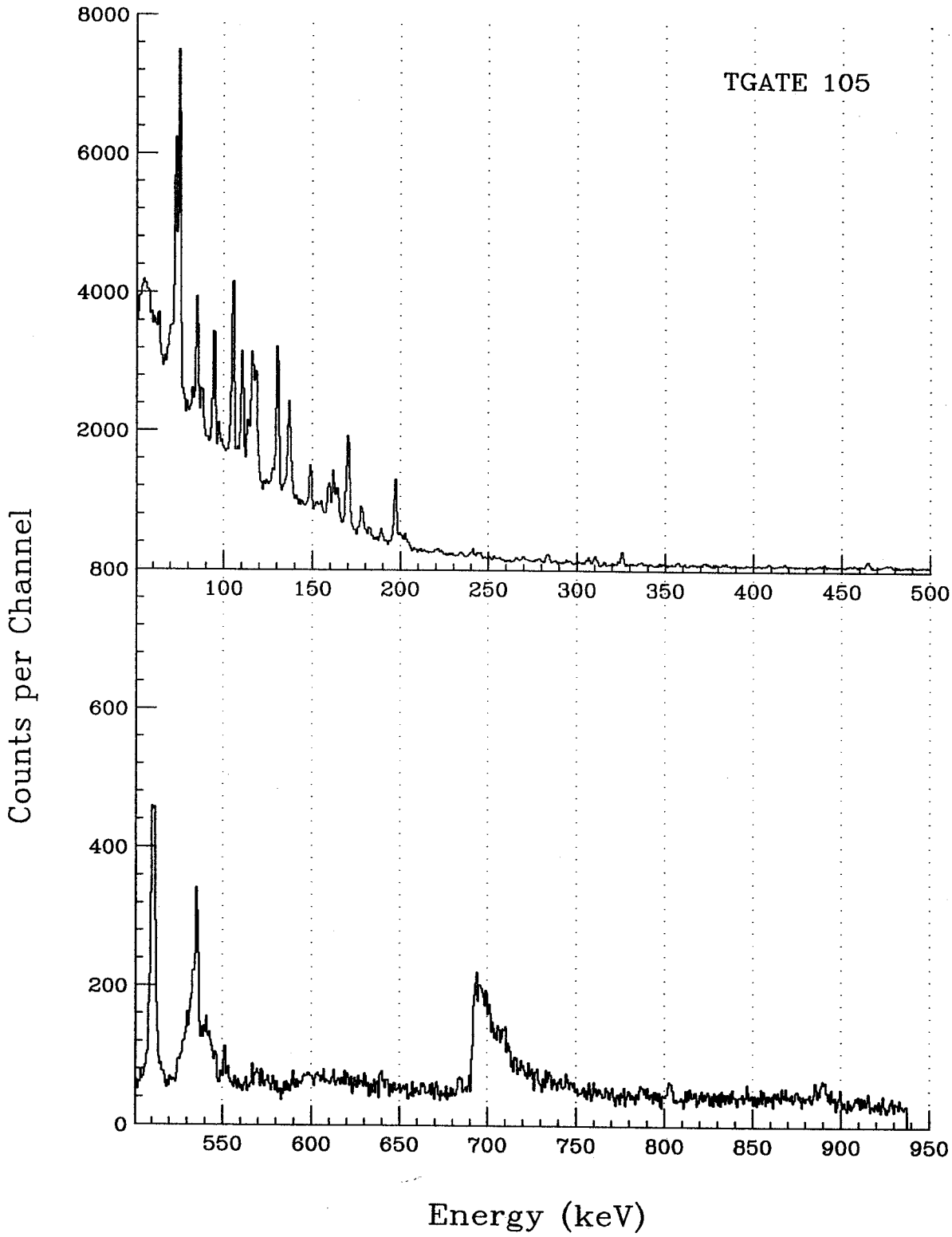

Figure D.71: Composite energy spectrum from TAC gate region 5, detector 10.

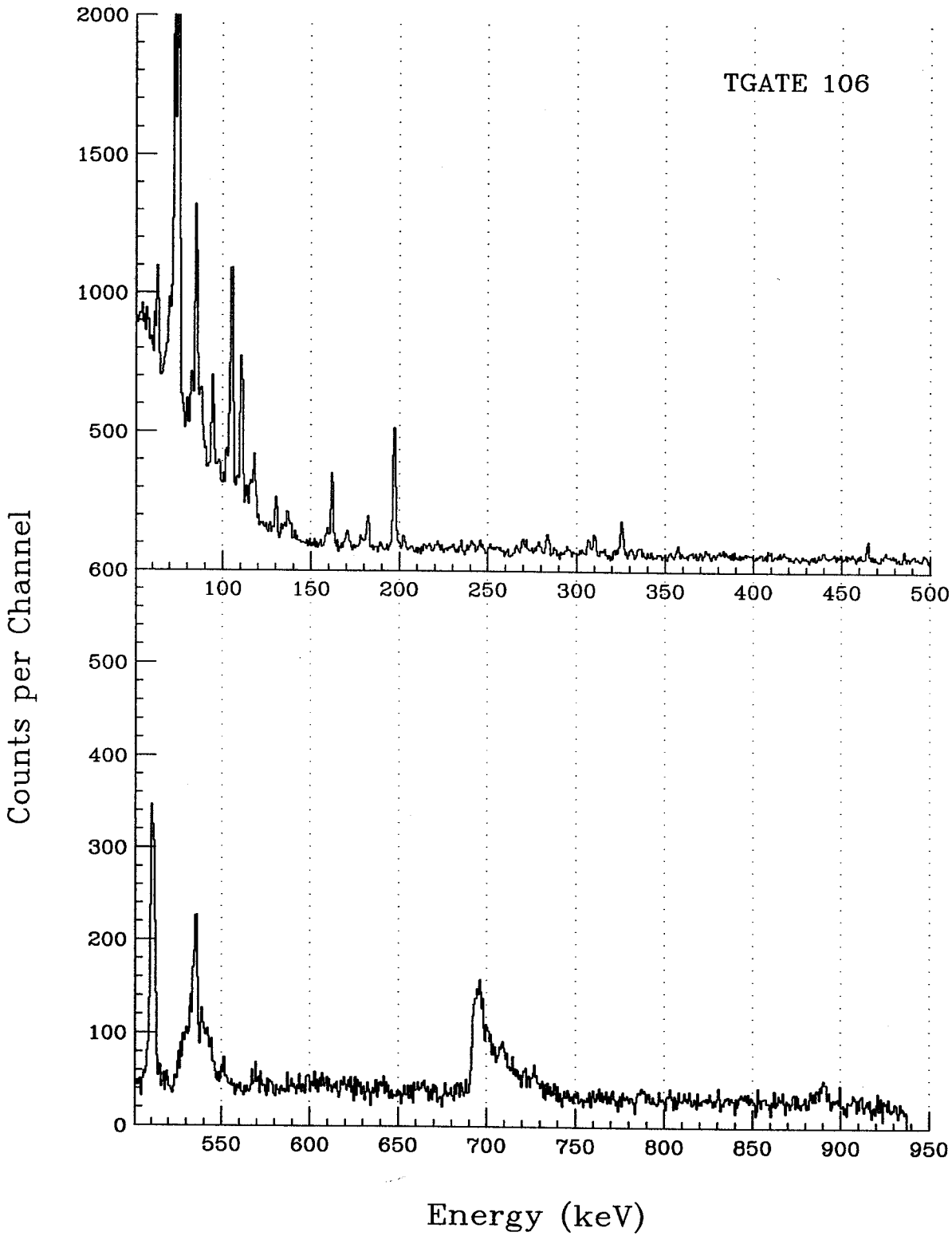

Figure D.72: Composite energy spectrum from TAC gate region 6, detector 10.

D.2 Singles

Single coincidence events were the initial reaction events to be recorded onto tape. Every clean event that was registered in the detectors was saved. There was no multiple-coincidence requirement between the detectors, hence the name 'singles'. Composite γ - ray spectra were generated from these events according to detector number and are presented in this Appendix.

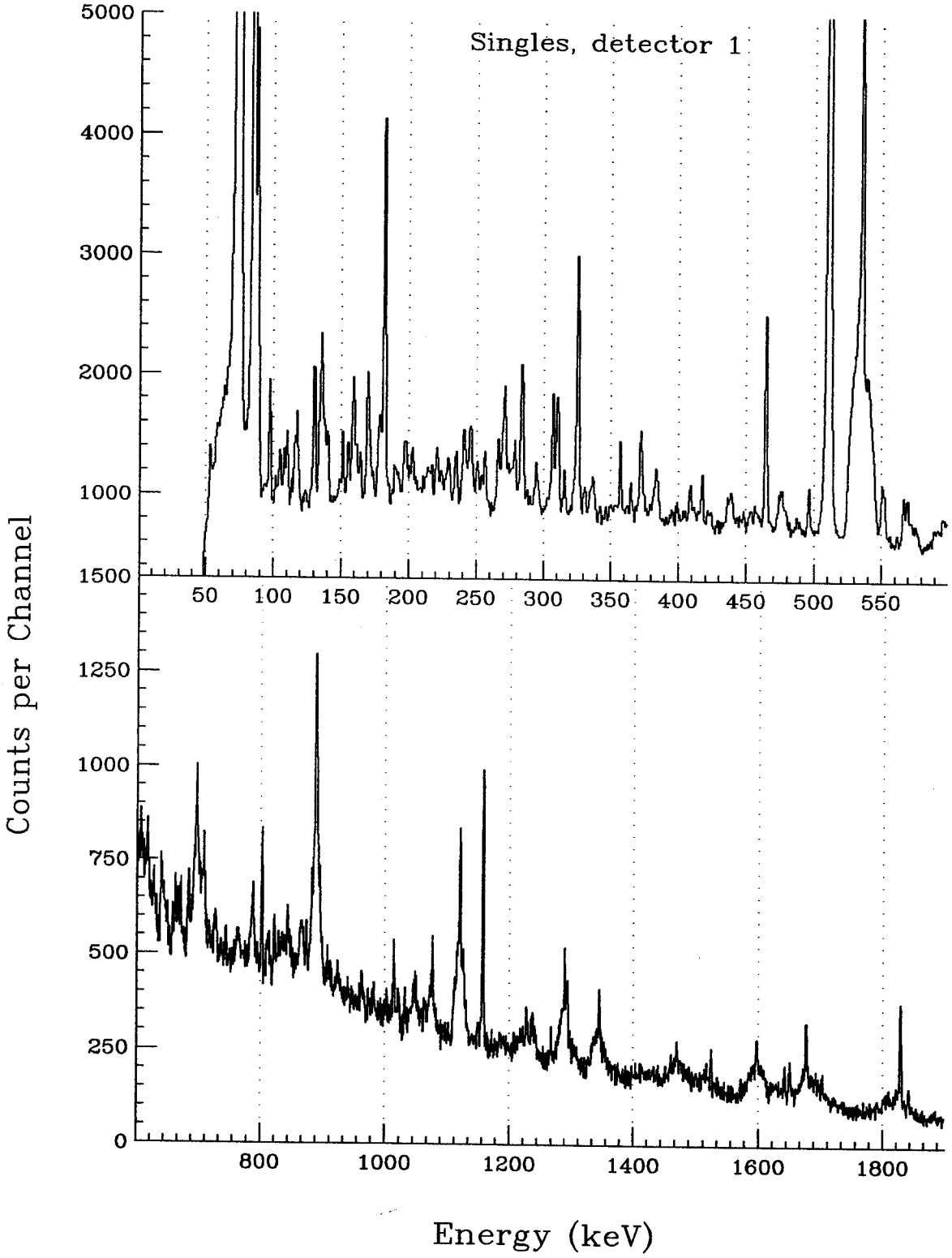

Figure D.73: Composite Singles spectrum of all nuclei in the reaction ^{37}Cl on ^{100}Mo, detector 1.

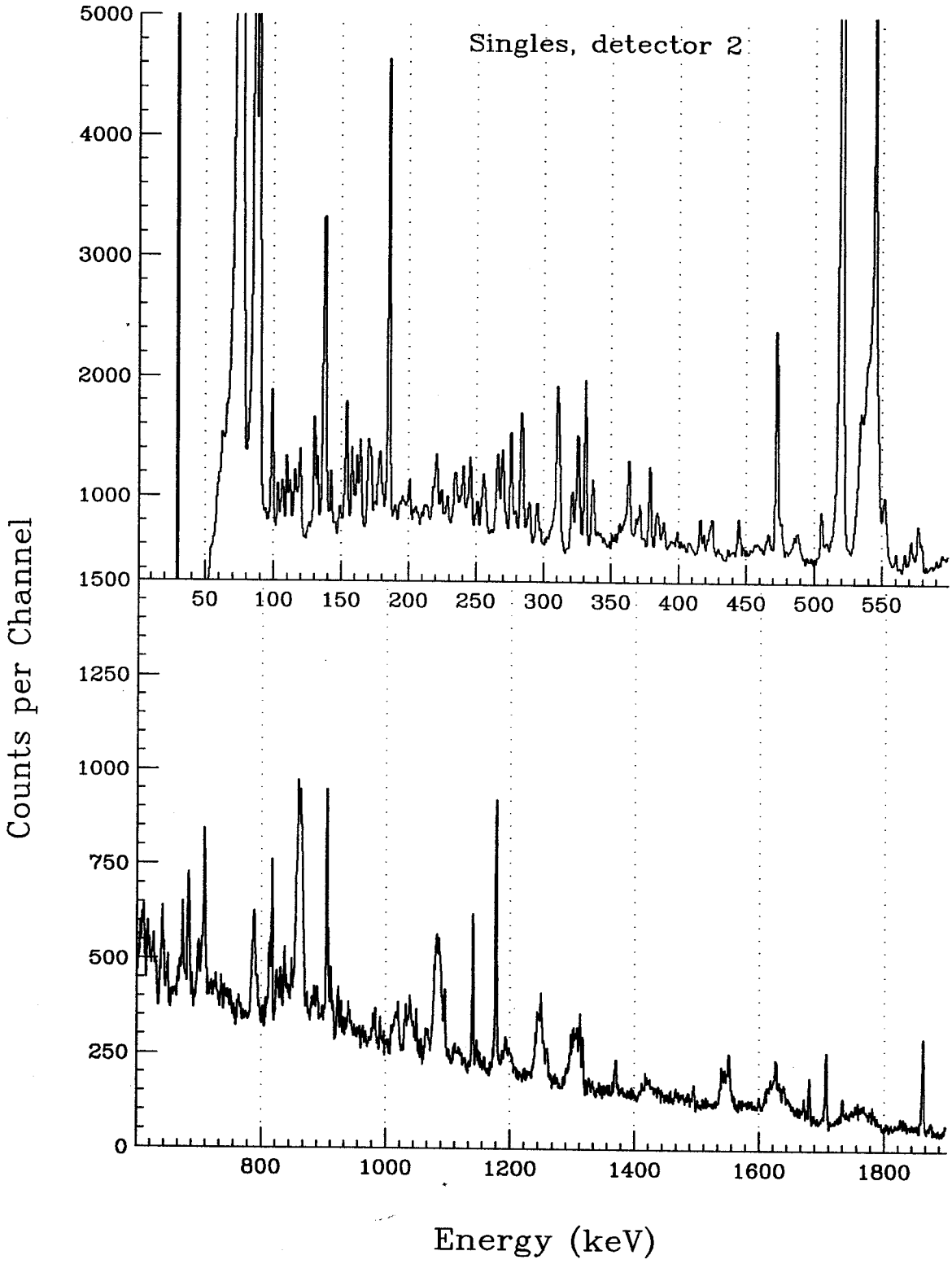

Figure D.74: Composite Singles spectrum of all nuclei in the reaction ^{37}Cl on ^{100}Mo, detector 2.

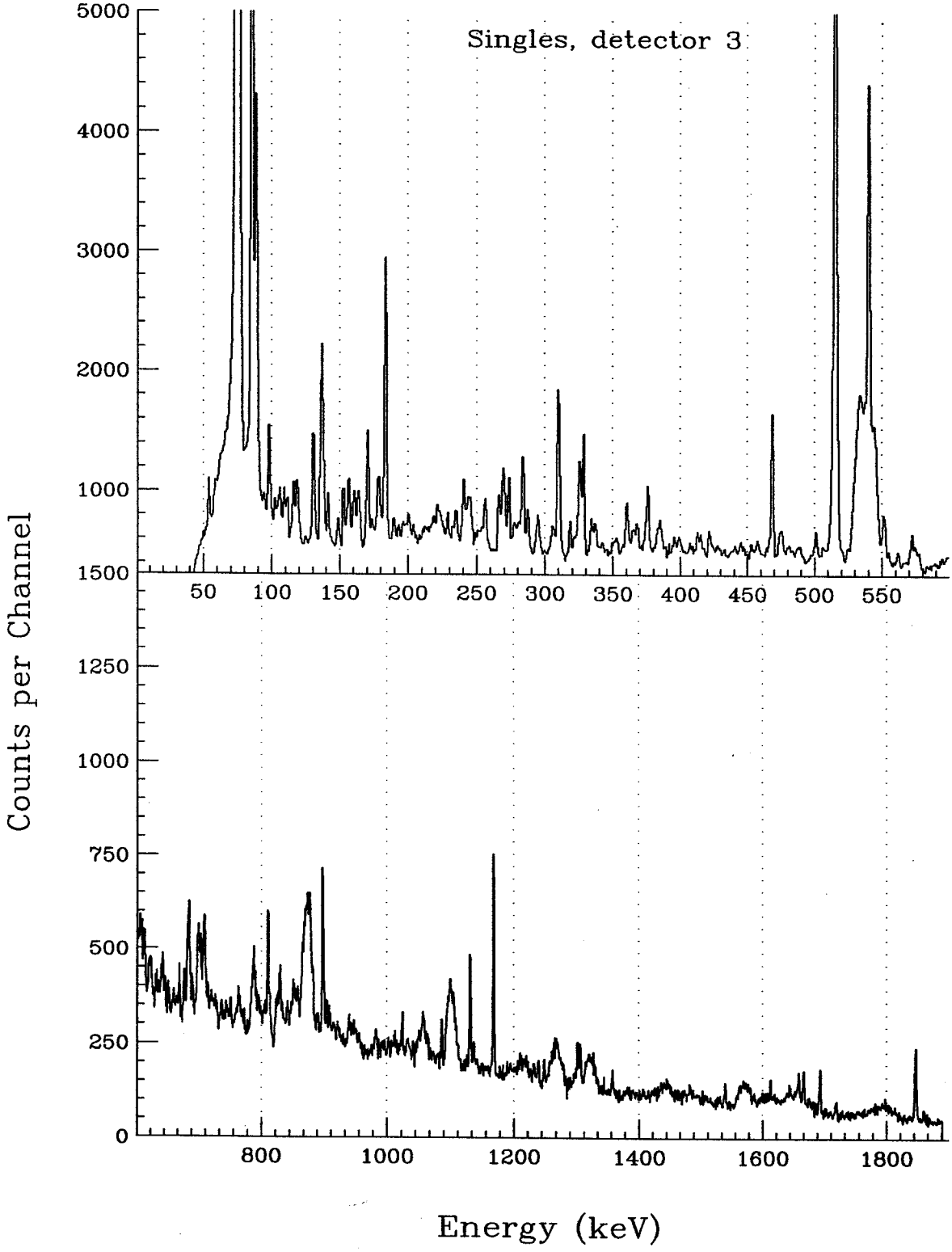

Figure D.75: Composite Singles spectrum of all nuclei in the reaction ^{37}Cl on ^{100}Mo, detector 3.

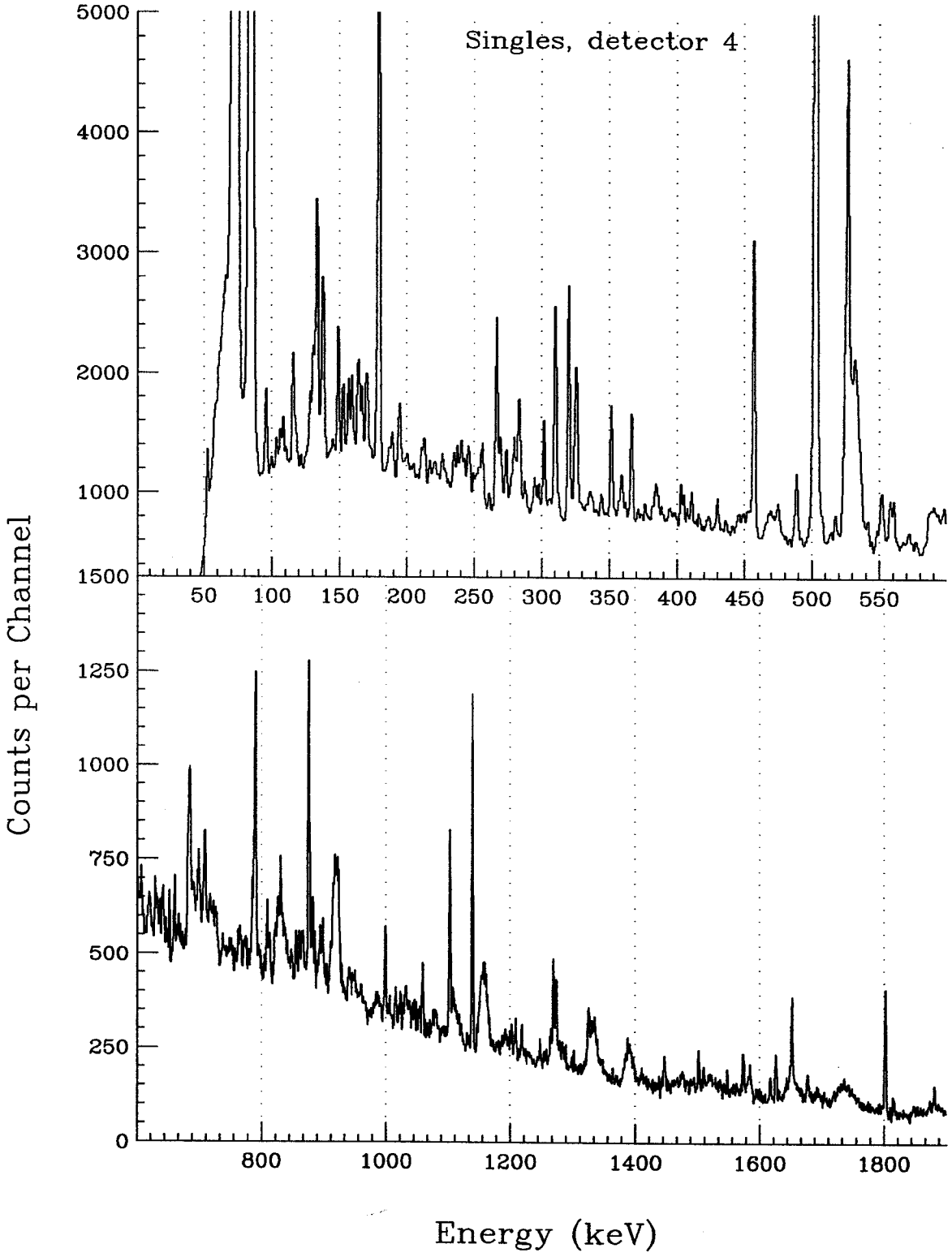

Figure D.76: Composite Singles spectrum of all nuclei in the reaction ^{37}Cl on ^{100}Mo, detector 4.

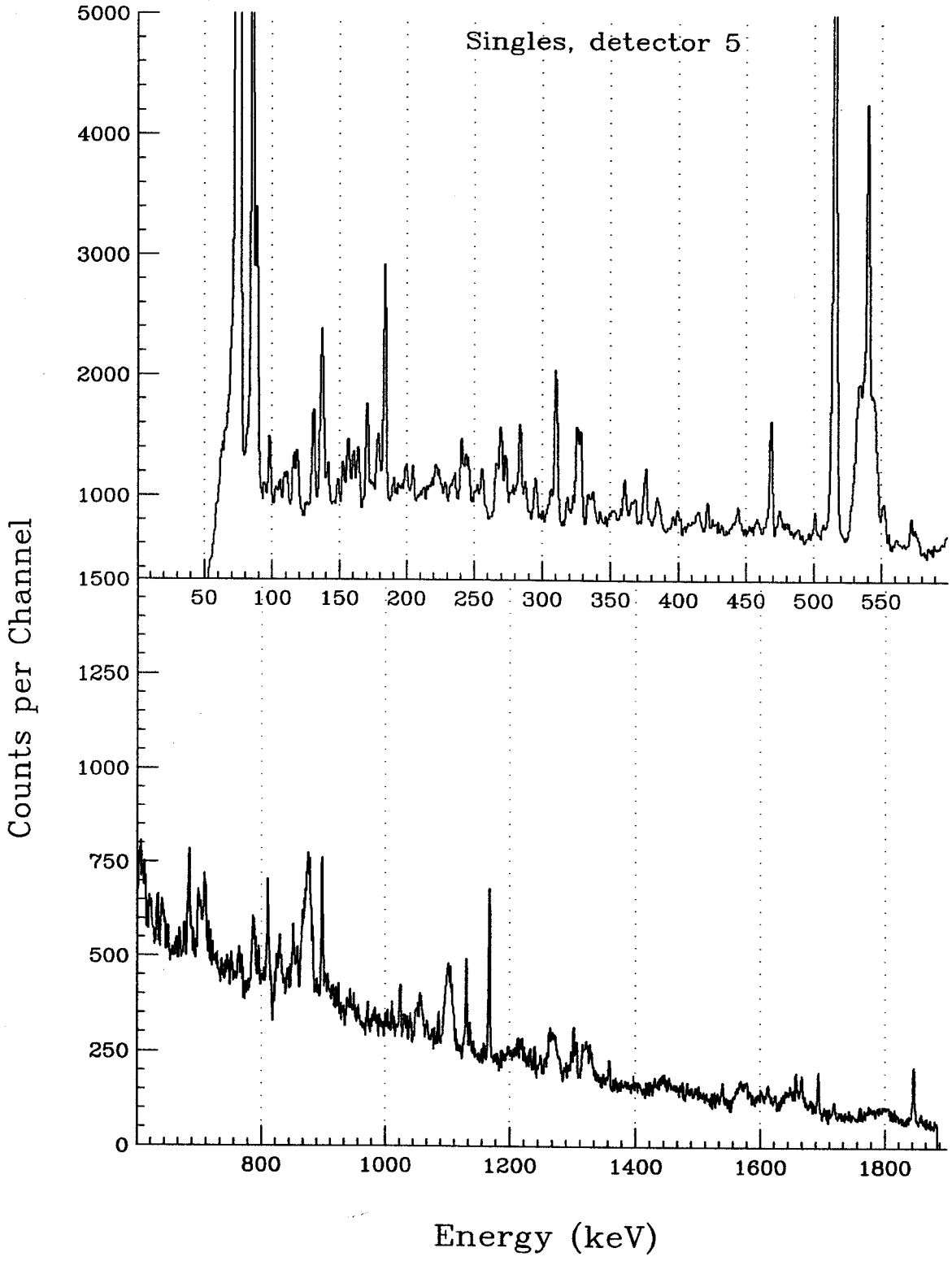

Figure D.77: Composite Singles spectrum of all nuclei in the reaction ^{37}Cl on ^{100}Mo, detector 5.

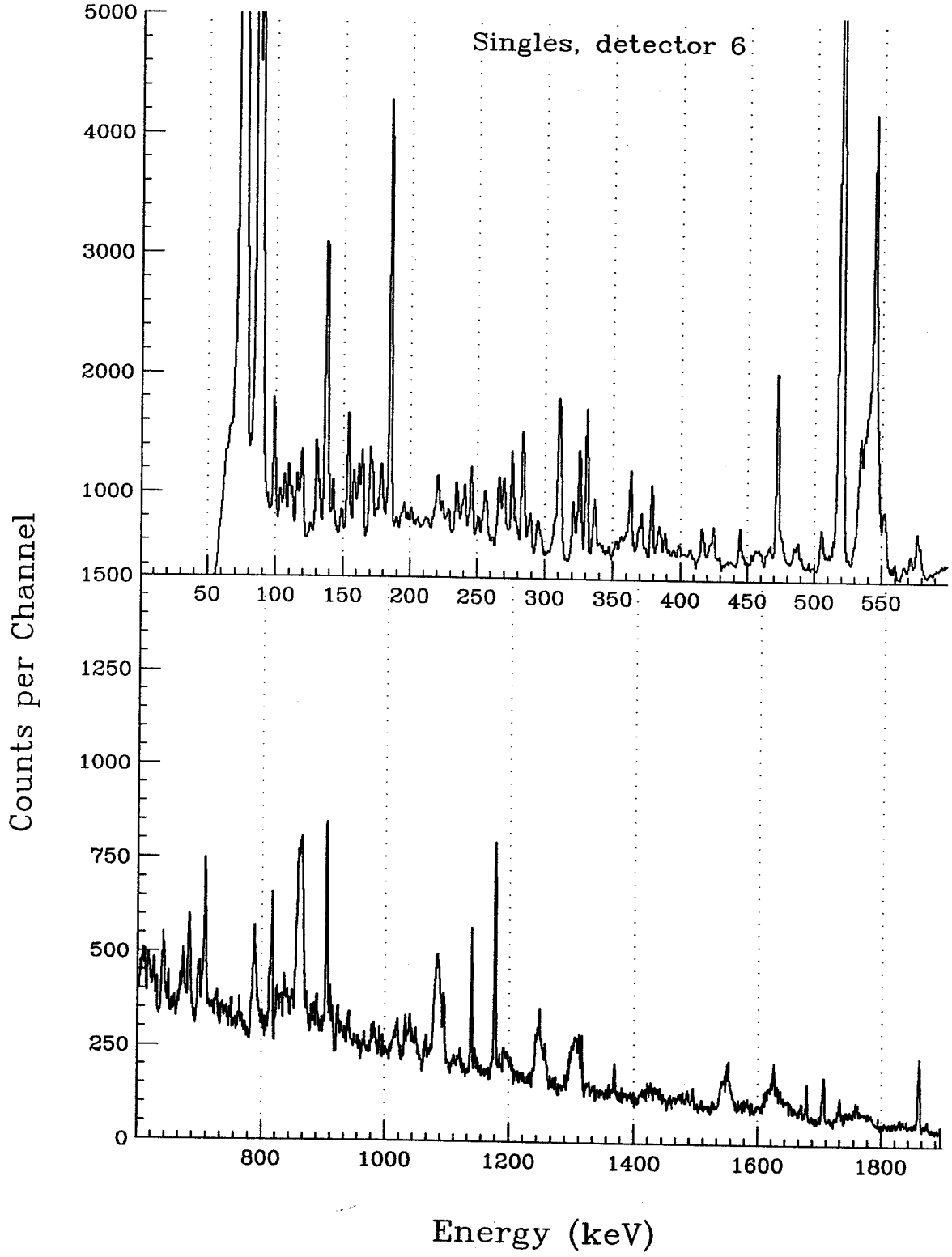

Figure D.78: Composite Singles spectrum of all nuclei in the reaction ^{37}Cl on ^{100}Mo, detector 6.

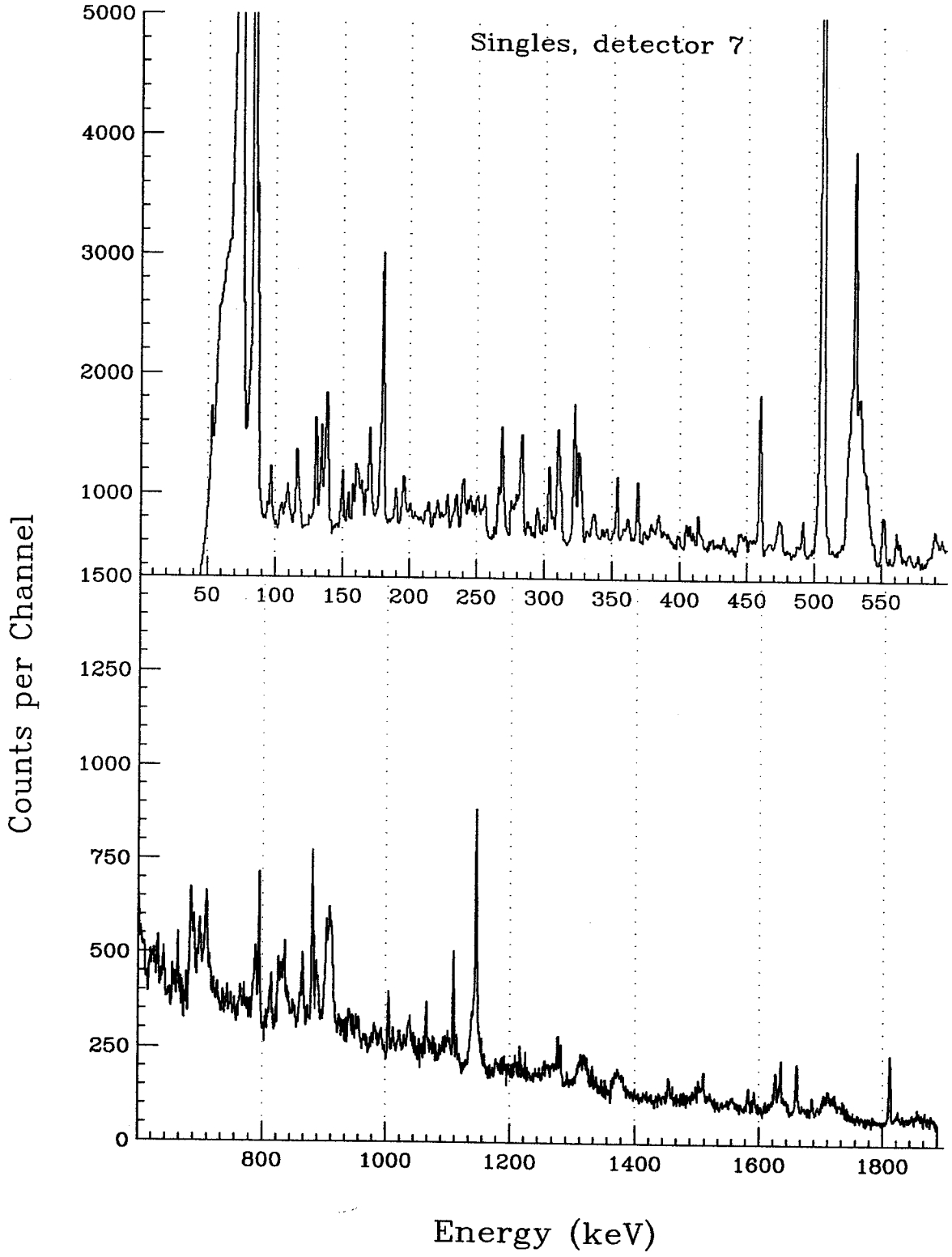

Figure D.79: Composite Singles spectrum of all nuclei in the reaction ^{37}Cl on ^{100}Mo, detector 7.

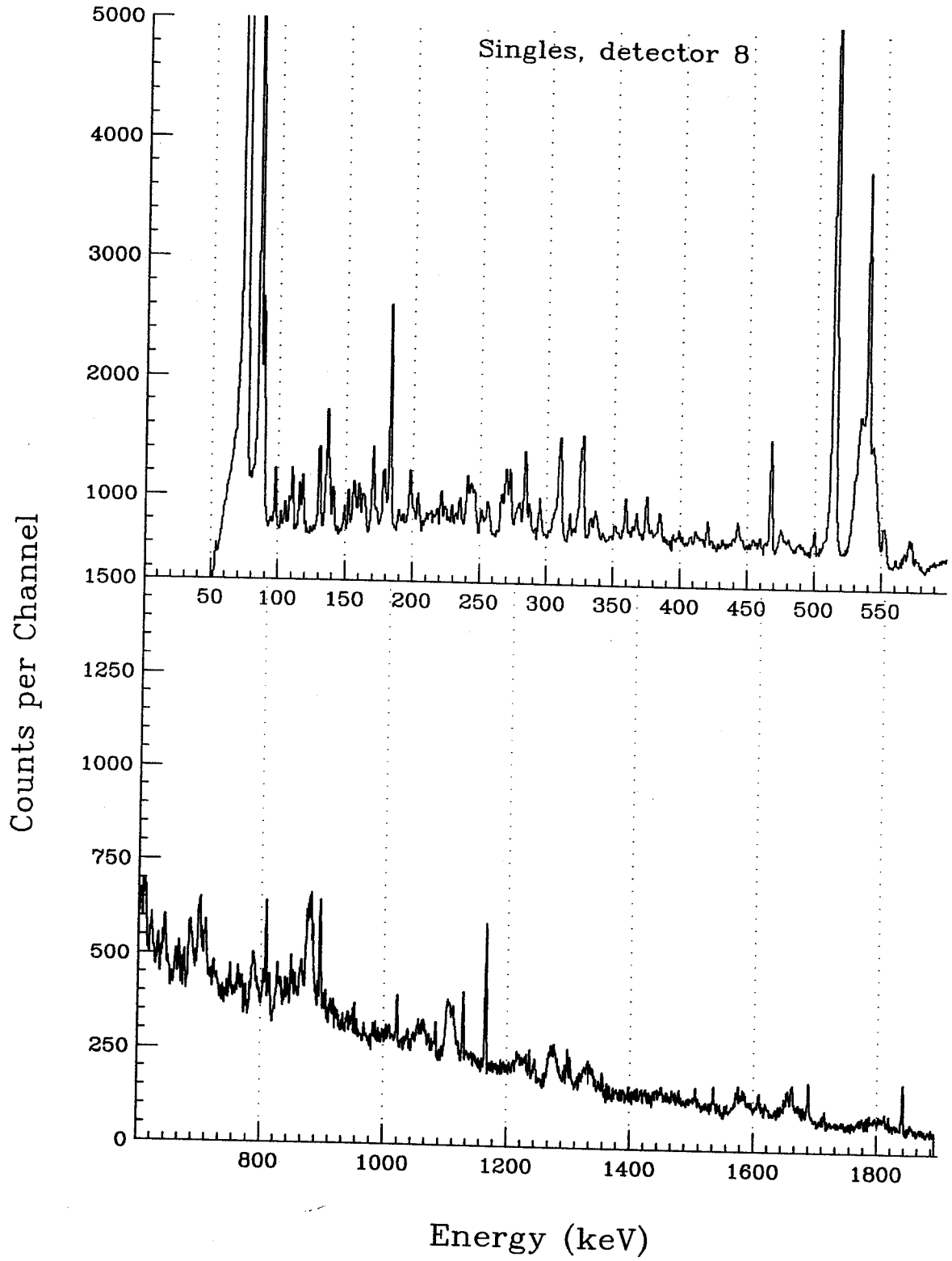

Figure D.80: Composite Singles spectrum of all nuclei in the reaction ^{37}Cl on ^{100}Mo, detector 8.

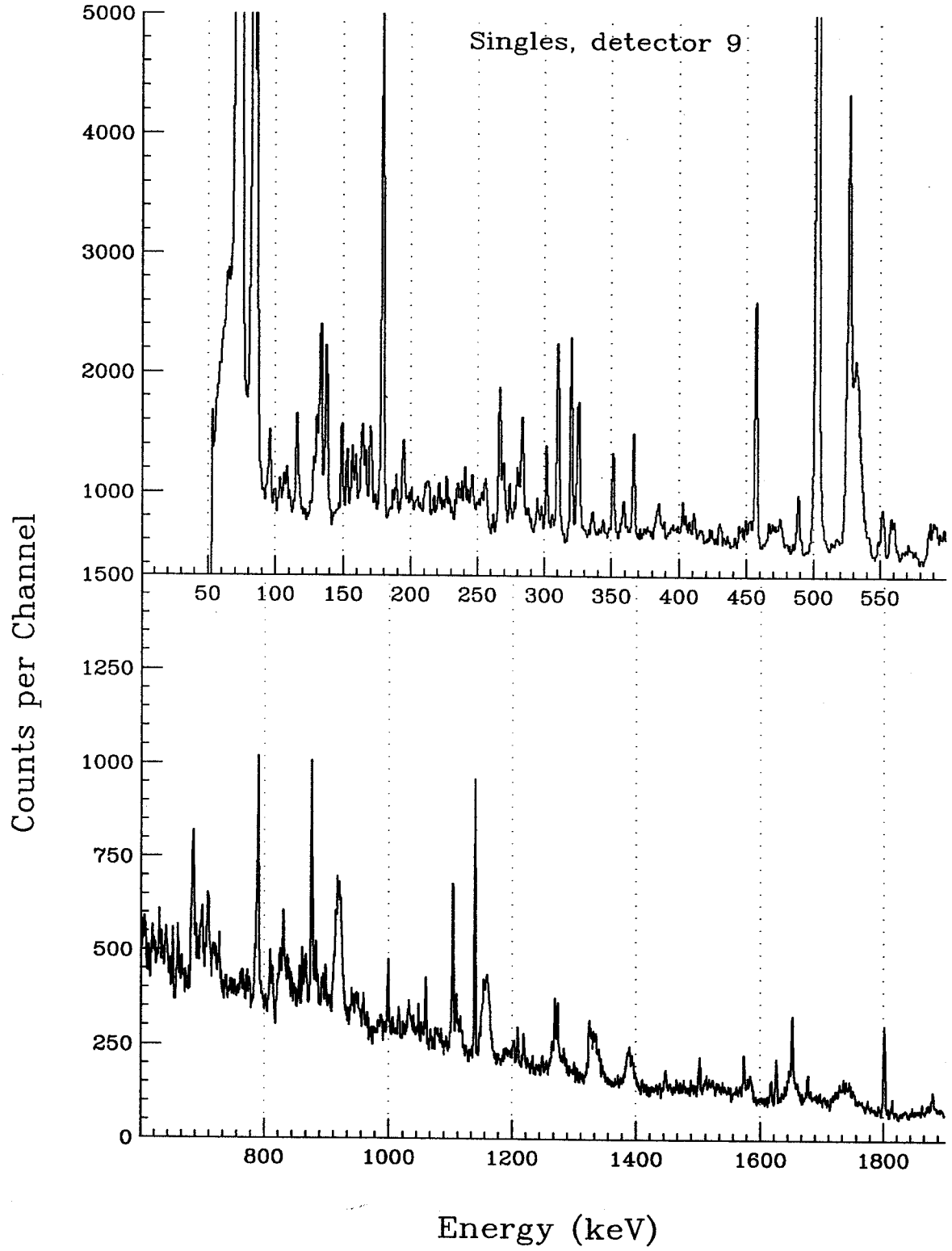

Figure D.81: Composite Singles spectrum of all nuclei in the reaction ^{37}Cl on ^{100}Mo, detector 9.

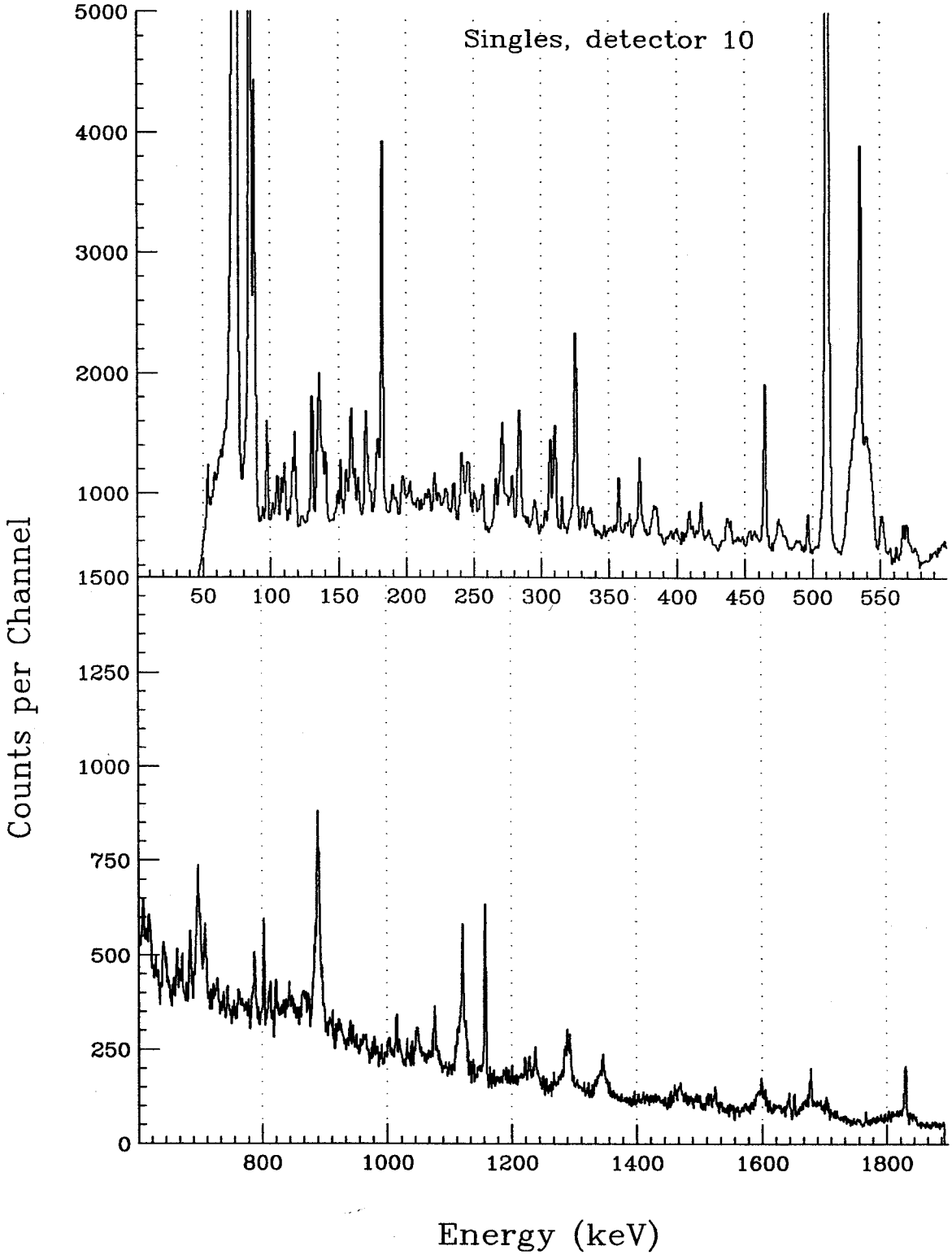

Figure D.82: Composite Singles spectrum of all nuclei in the reaction ^{37}Cl on ^{100}Mo, detector 10.

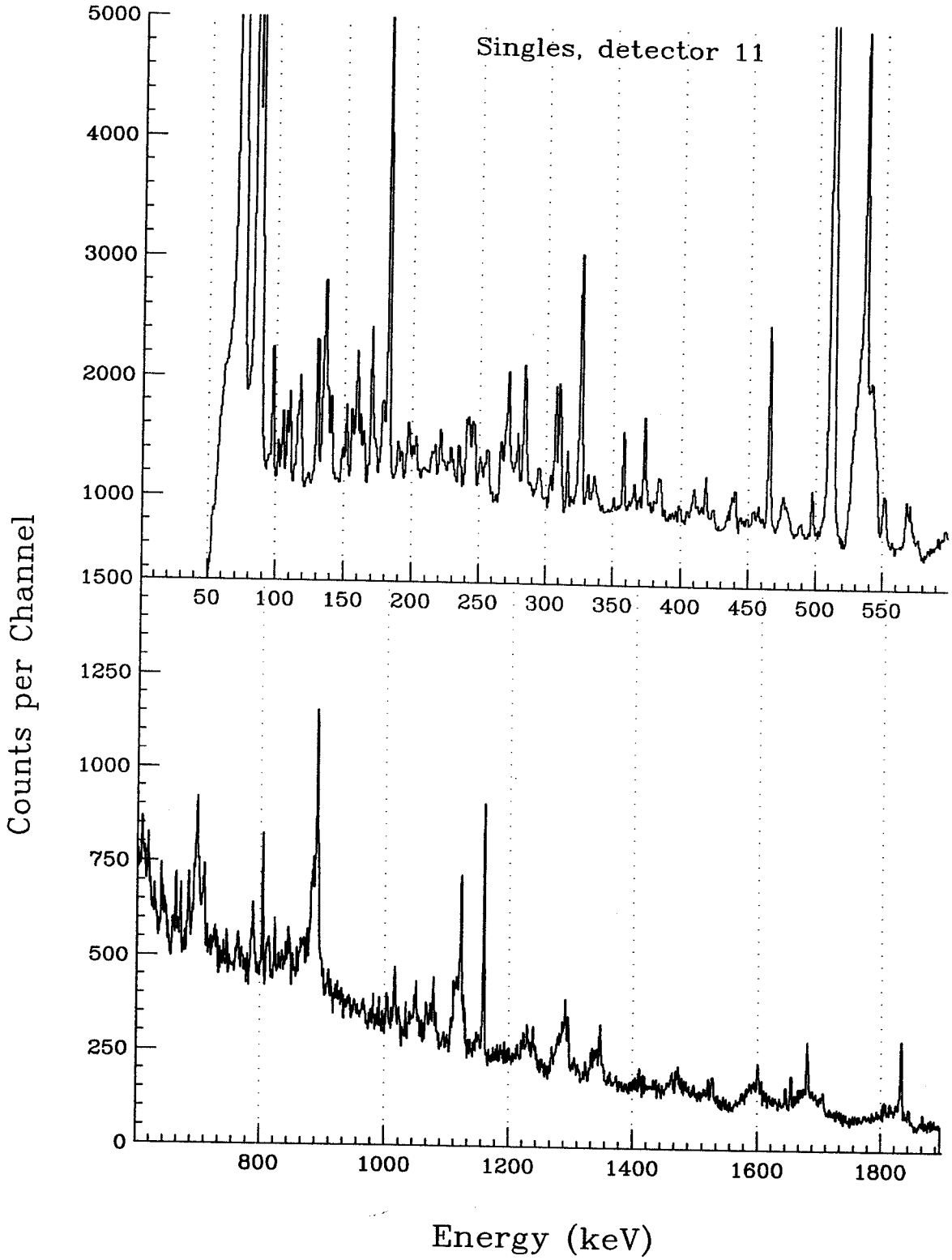

Figure D.83: Composite Singles spectrum of all nuclei in the reaction ^{37}Cl on ^{100}Mo, detector 11.

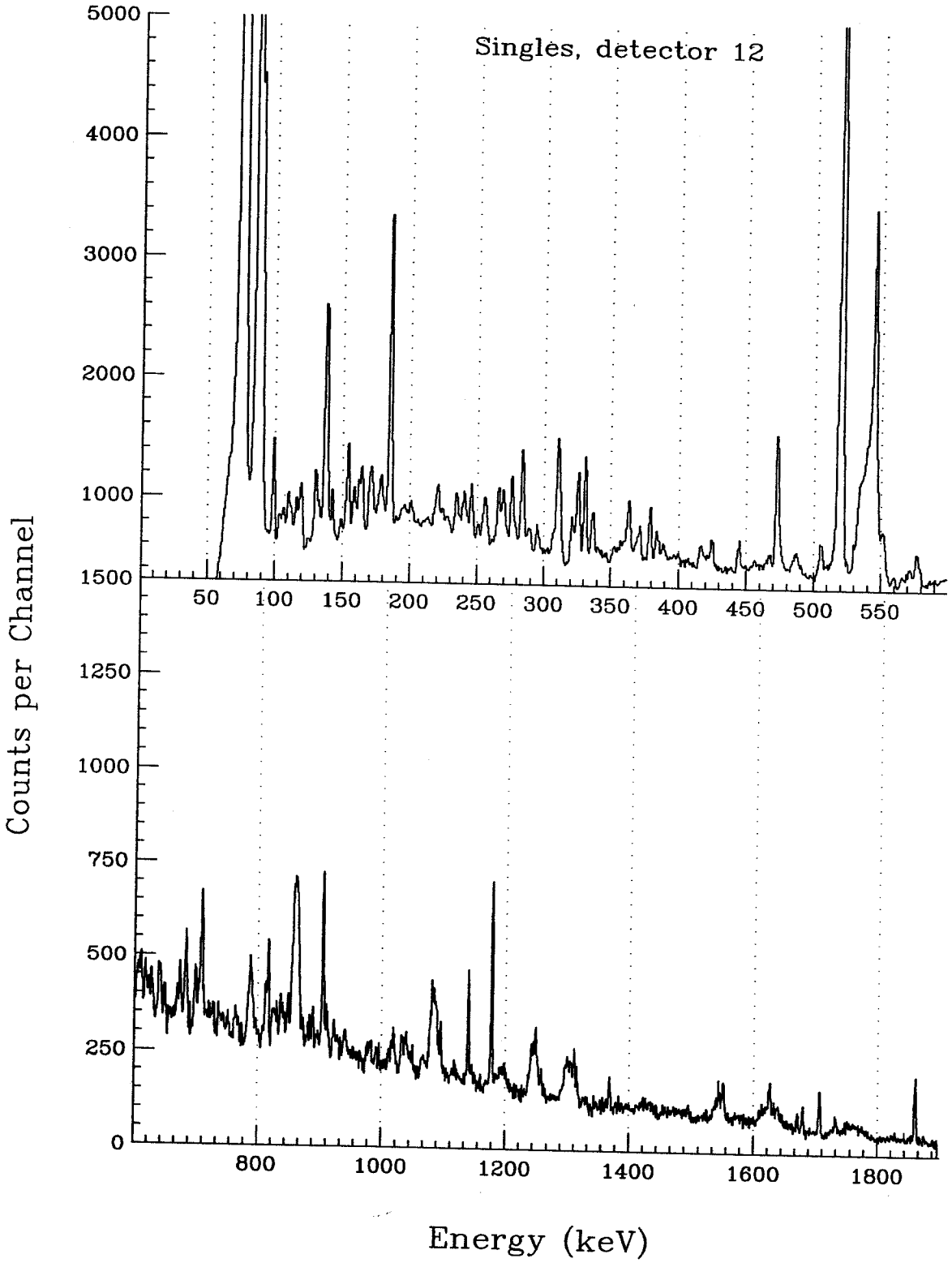

Figure D.84: Composite Singles spectrum of all nuclei in the reaction ^{37}Cl on ^{100}Mo, detector 12.

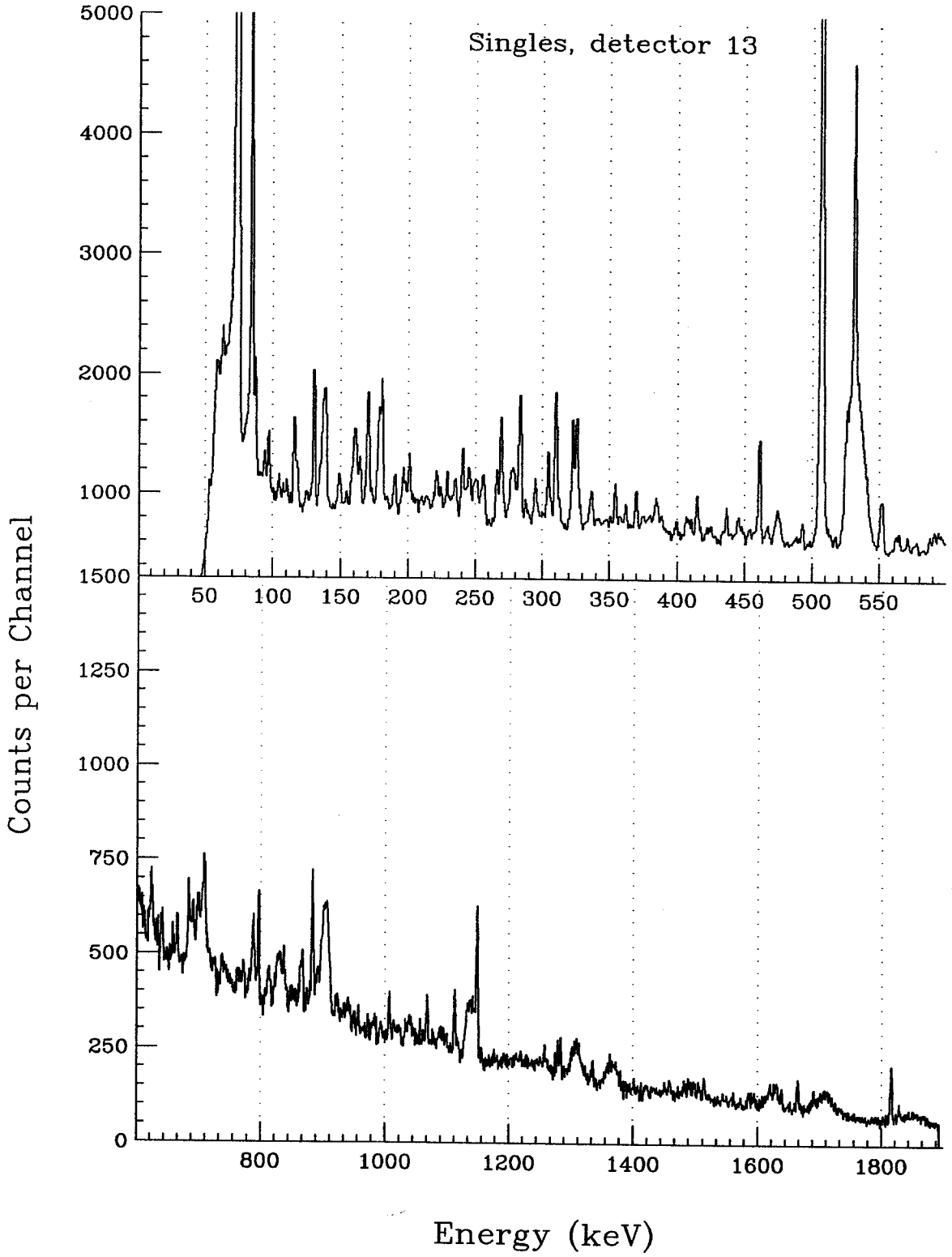

Figure D.85: Composite Singles spectrum of all nuclei in the reaction ^{37}Cl on ^{100}Mo, detector 13.

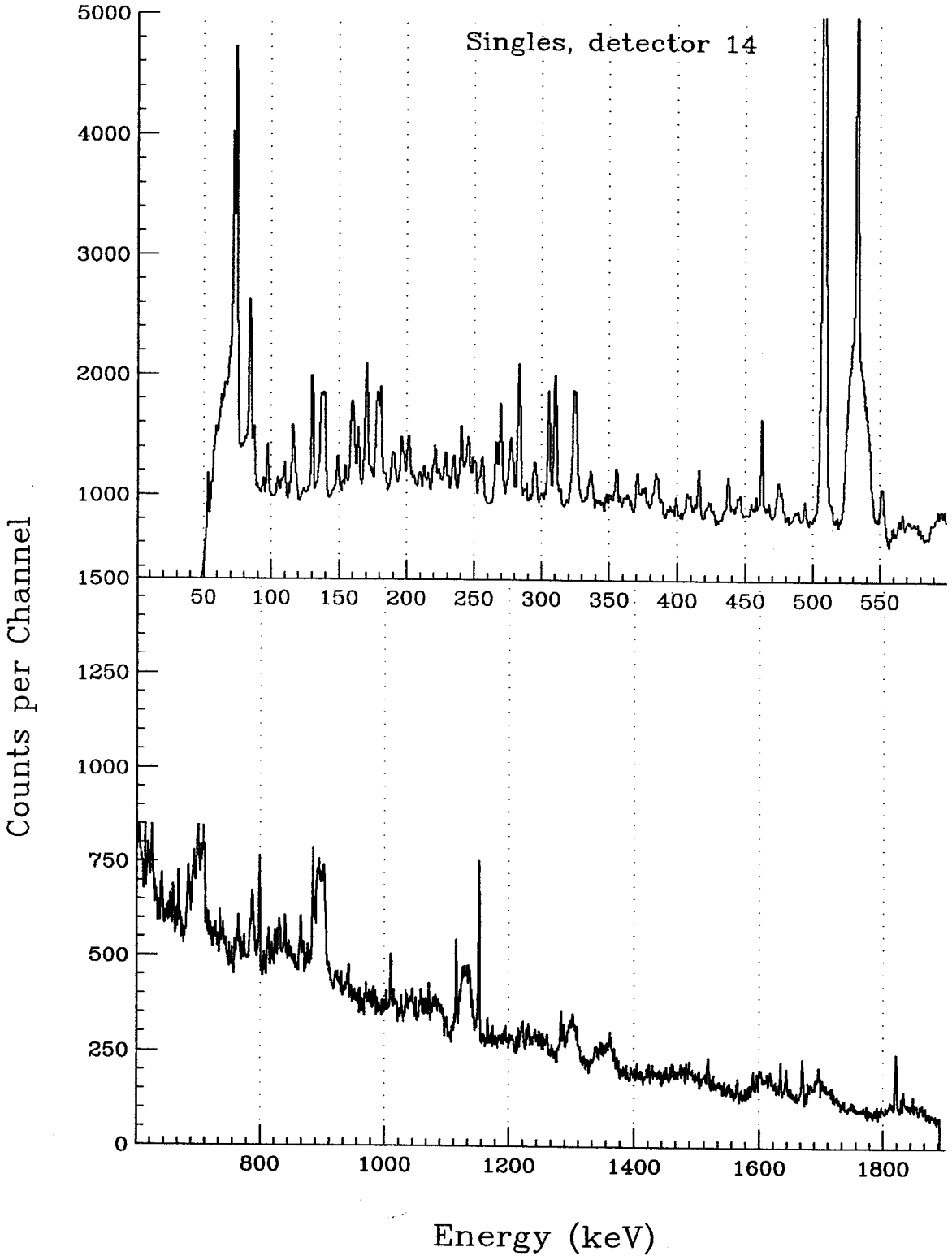

Figure D.86: Composite Singles spectrum of all nuclei in the reaction ^{37}Cl on ^{100}Mo, detector 14.

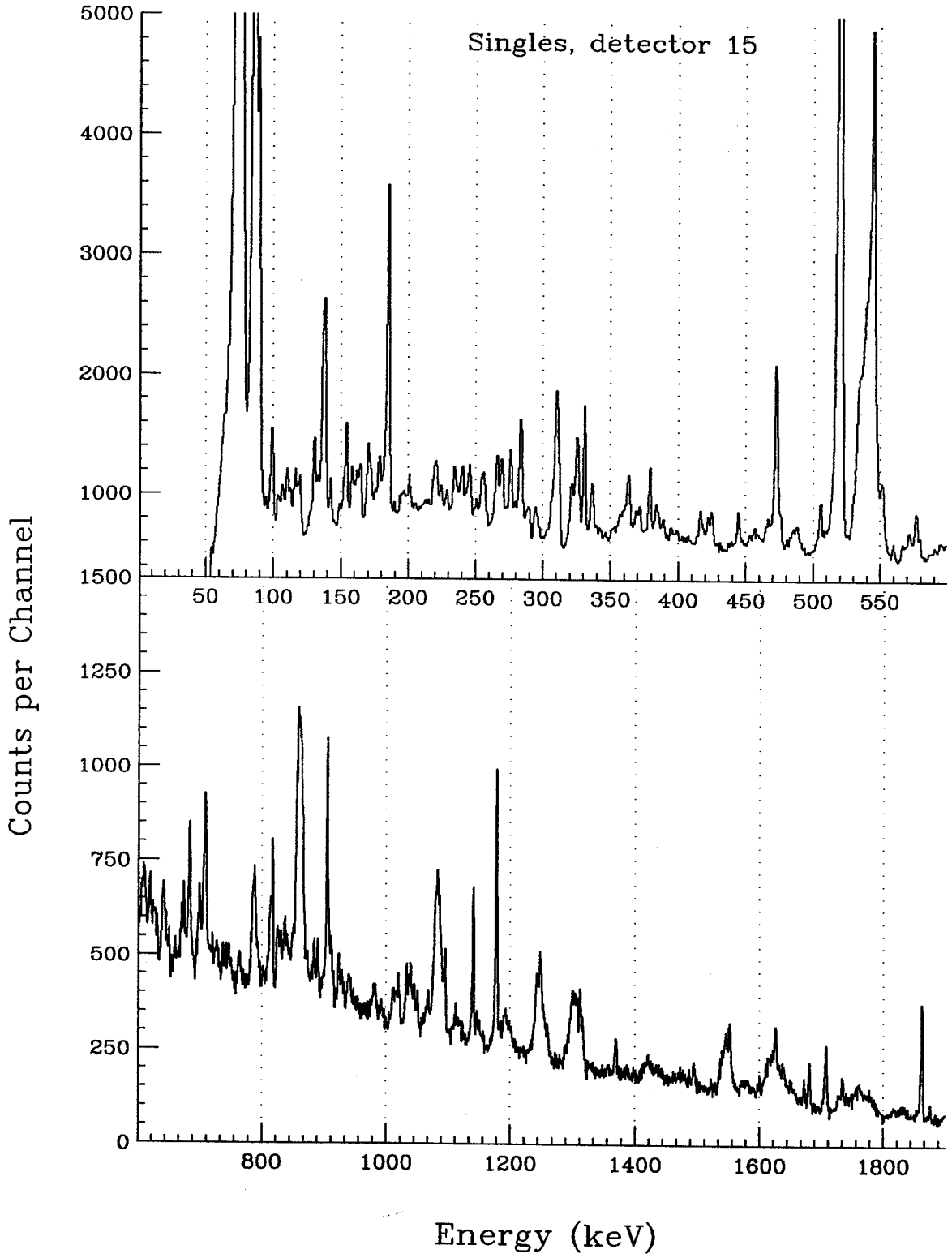

Figure D.87: Composite Singles spectrum of all nuclei in the reaction ^{37}Cl on ^{100}Mo, detector 15.

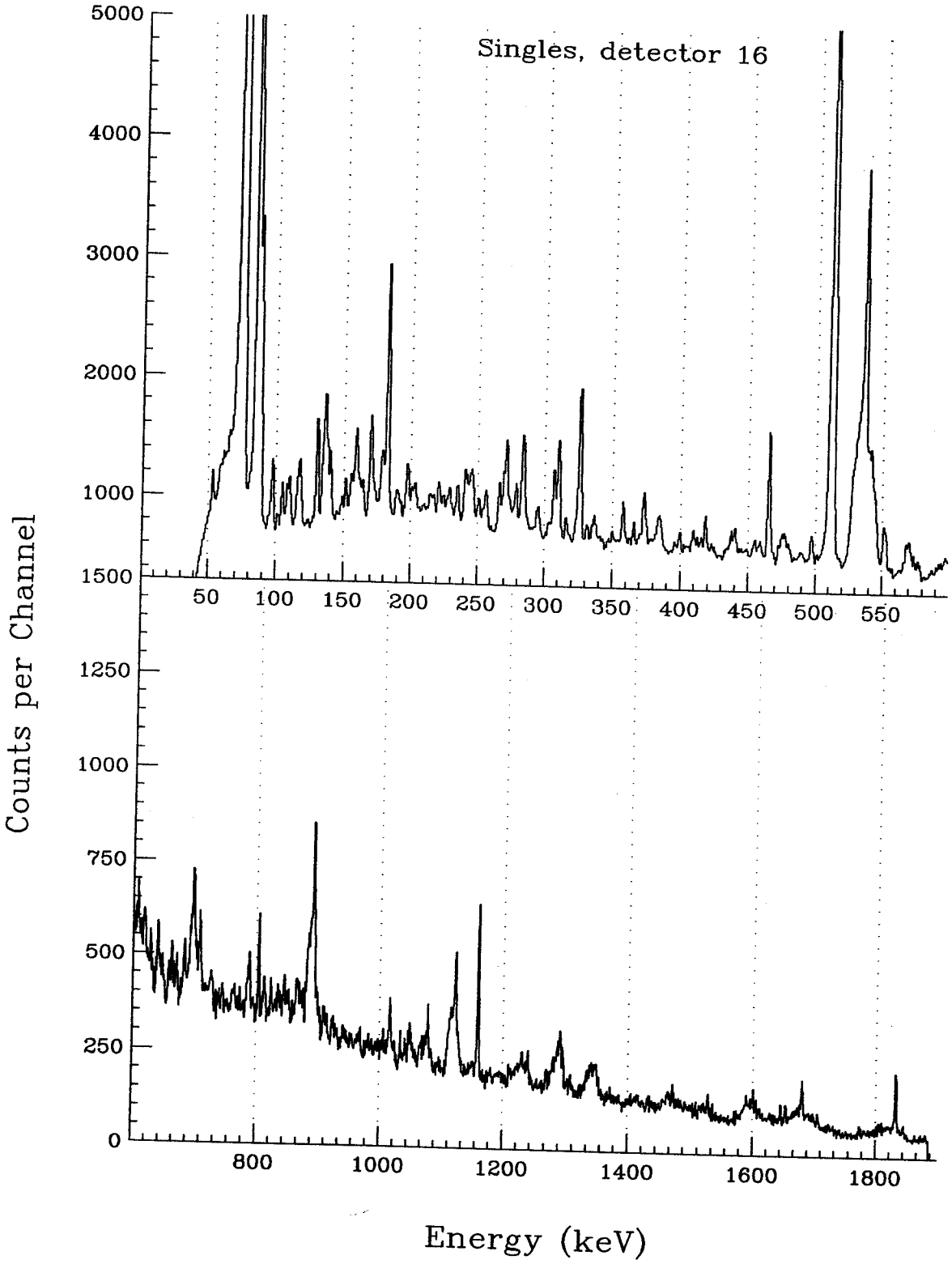

Figure D.88: Composite Singles spectrum of all nuclei in the reaction ^{37}Cl on ^{100}Mo, detector 16.

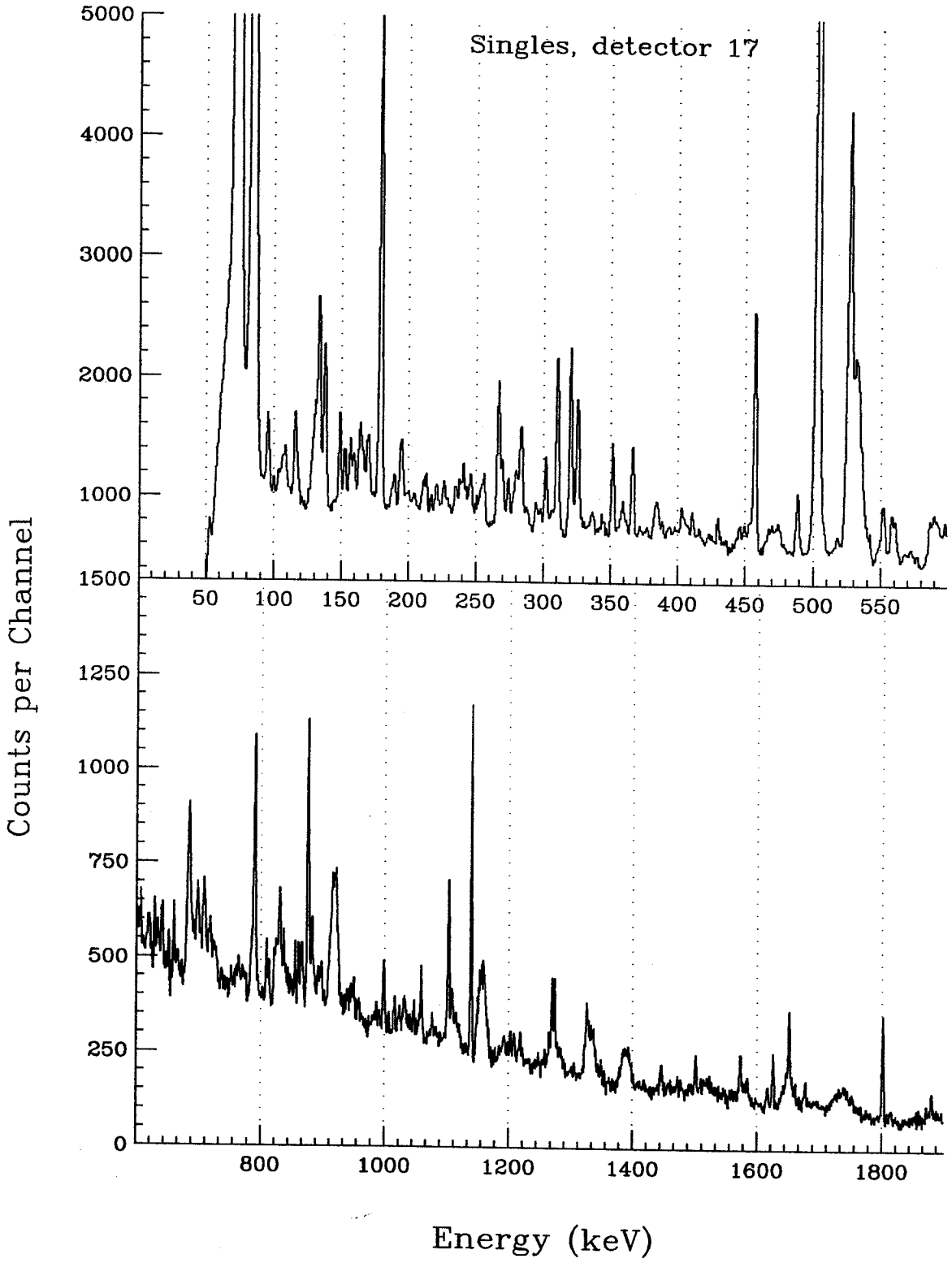

Figure D.89: Composite Singles spectrum of all nuclei in the reaction ^{37}Cl on ^{100}Mo, detector 17.

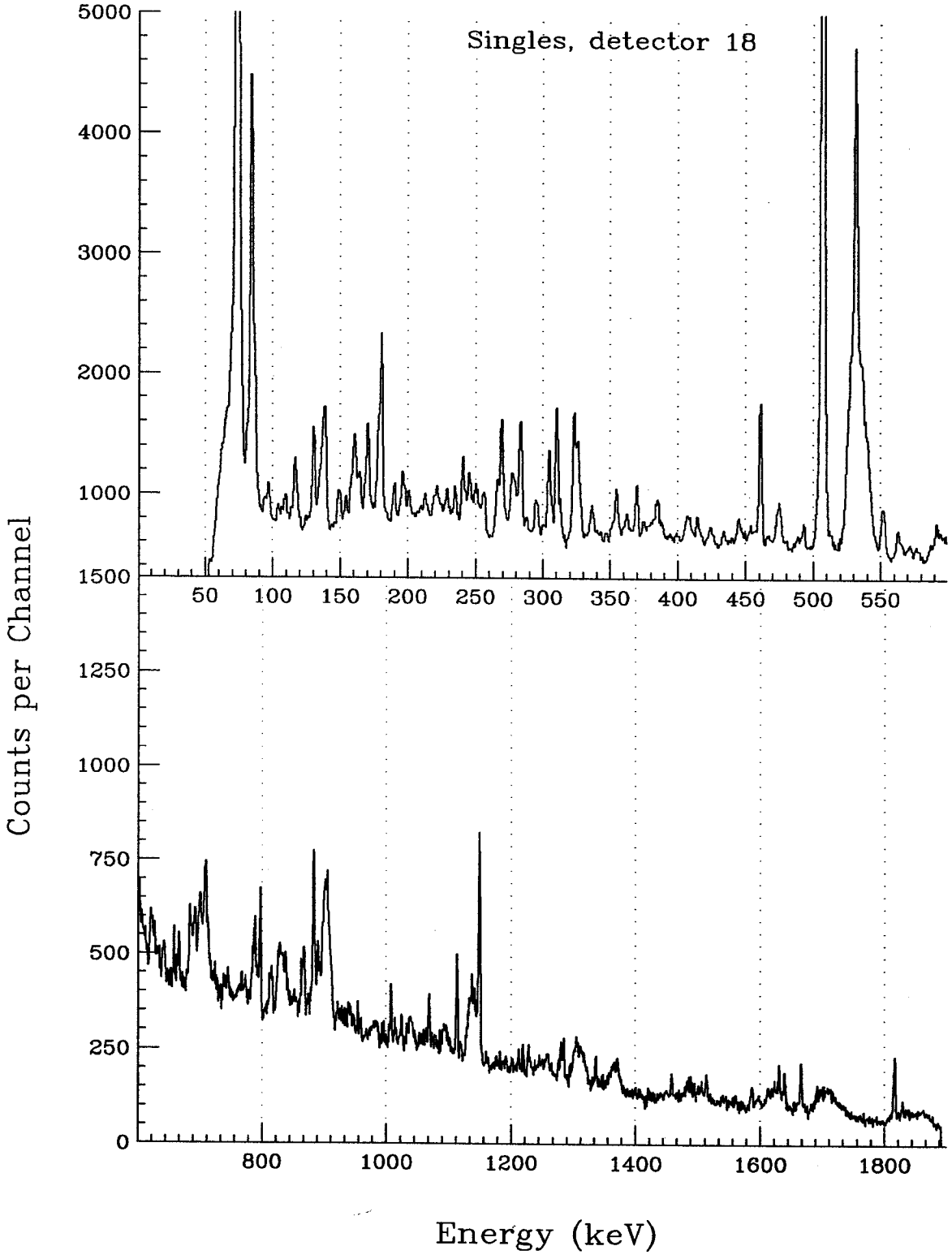

Figure D.90: Composite Singles spectrum of all nuclei in the reaction ^{37}Cl on ^{100}Mo, detector 18.

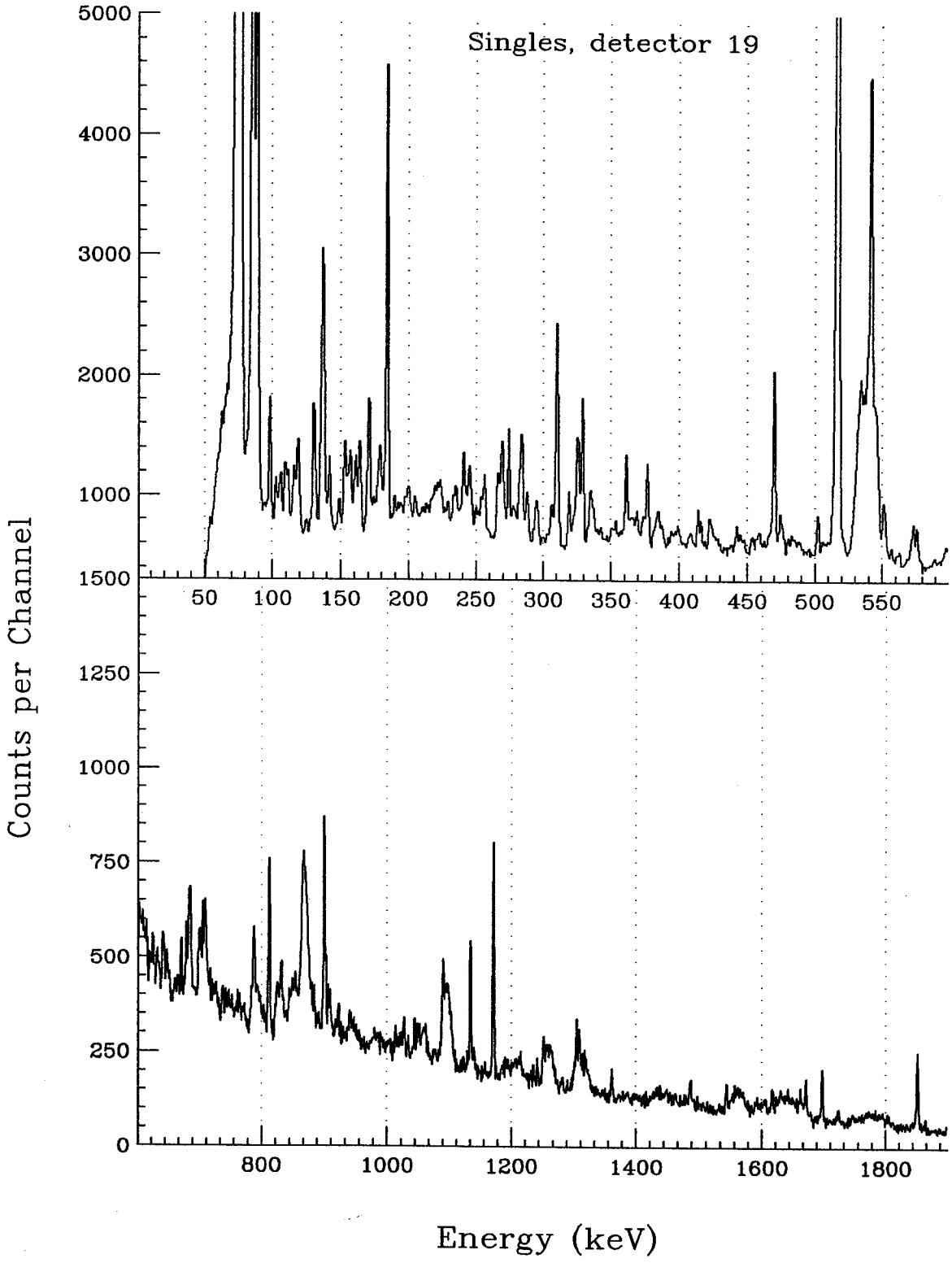

Figure D.91: Composite Singles spectrum of all nuclei in the reaction ^{37}Cl on ^{100}Mo, detector 19.

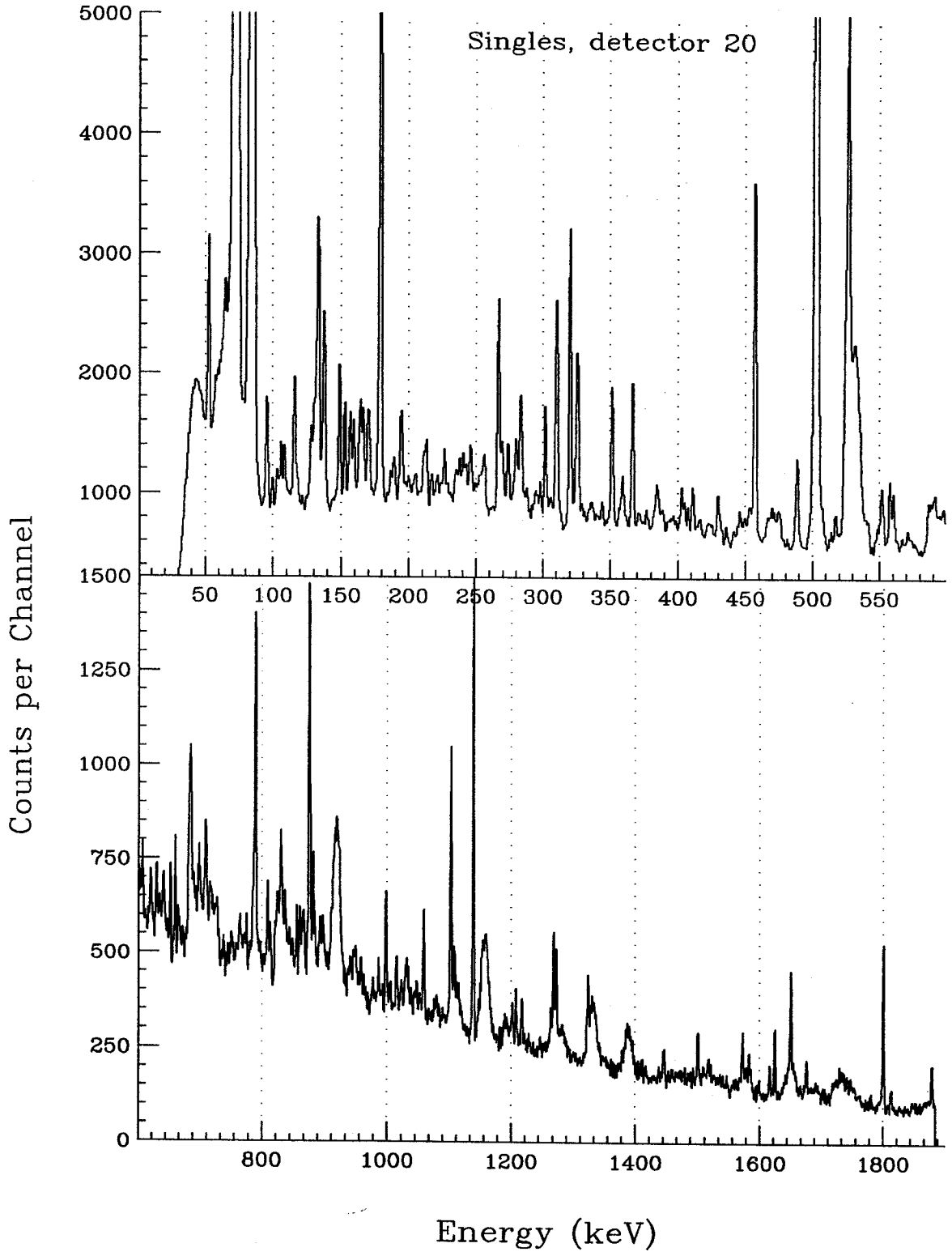

Figure D.92: Composite Singles spectrum of all nuclei in the reaction ^{37}Cl on ^{100}Mo, detector 20.

D.3 Post-Run Activities

γ rays from radioactive decays (mostly β decay) were recorded post experiment. These peaks can be used to tentatively confirm the production of certain reaction products. Peaks may contain γ rays from more than one source; a missing energy peak does not necessarily mean that the reaction product is not confirmed, but rather, a combination of low intensity and long half life may make the γ ray difficult to record. The post-run γ rays appear to originate from the two major reactions: the 5n,γ and 4n,γ. However, many of the peaks remain unidentified; a list of a few confirmation peaks can be found in Table 5.8. This Appendix contains the individual activities spectrum for each detector. The spectra have been attenuated for display purposes. In many cases, the two largest peaks, the 182 keV. and 511 keV., have been truncated in order to view the rest of the peaks.

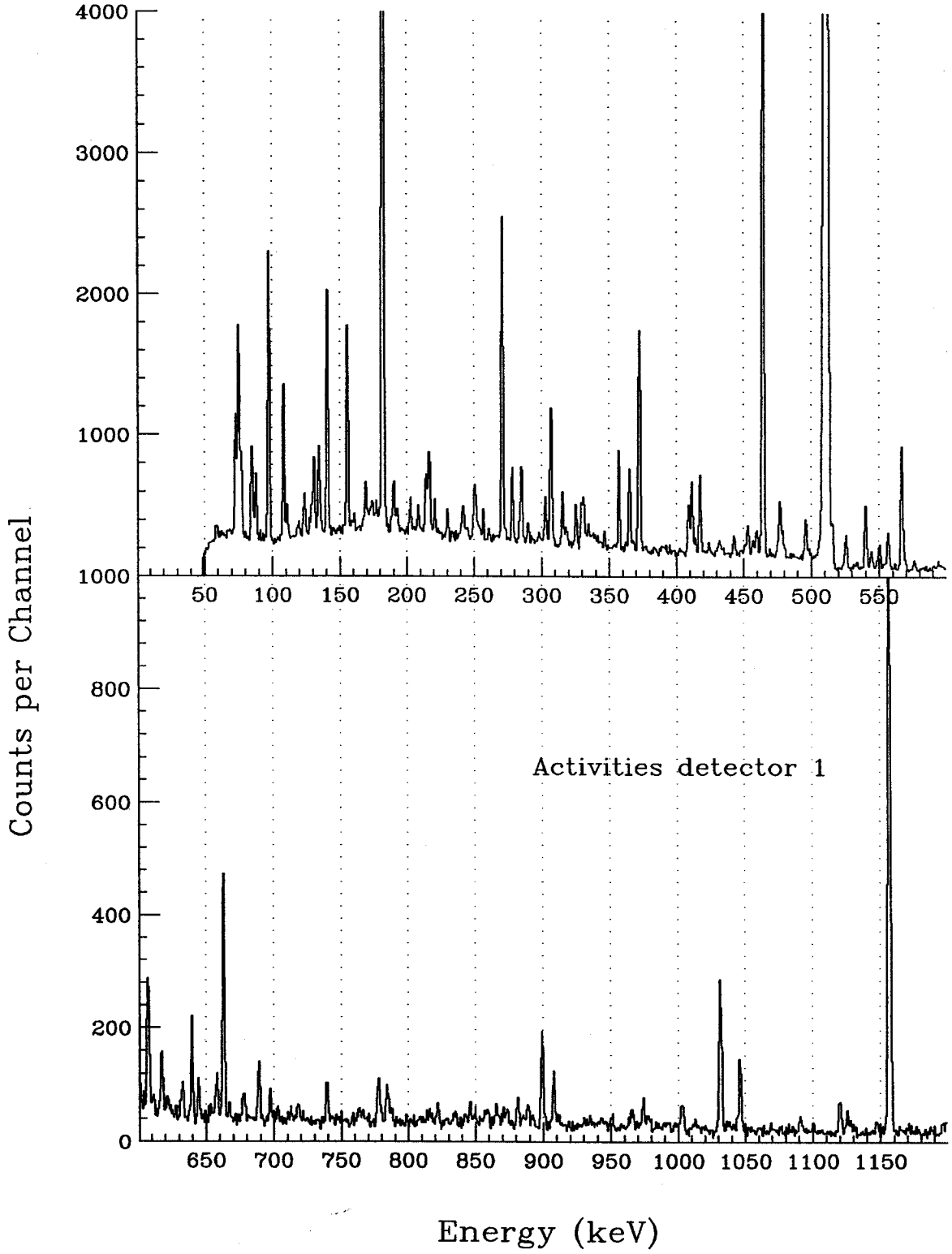

Figure D.93: Post-Run Activities spectrum of all nuclei in the reaction ^{37}Cl on ^{100}Mo, detector 1.

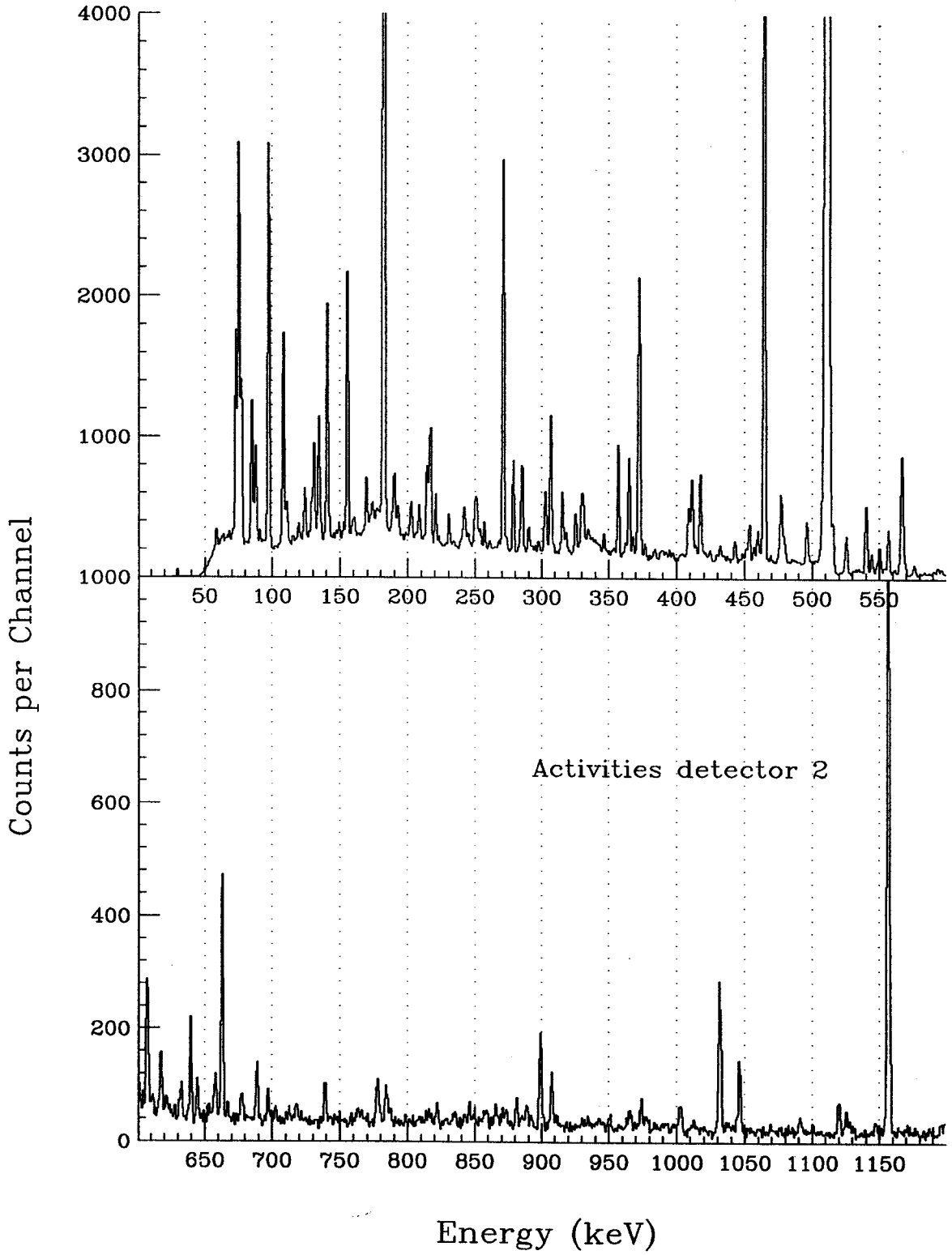

Figure D.94: Post-Run Activities spectrum of all nuclei in the reaction ^{37}Cl on ^{100}Mo, detector 2.

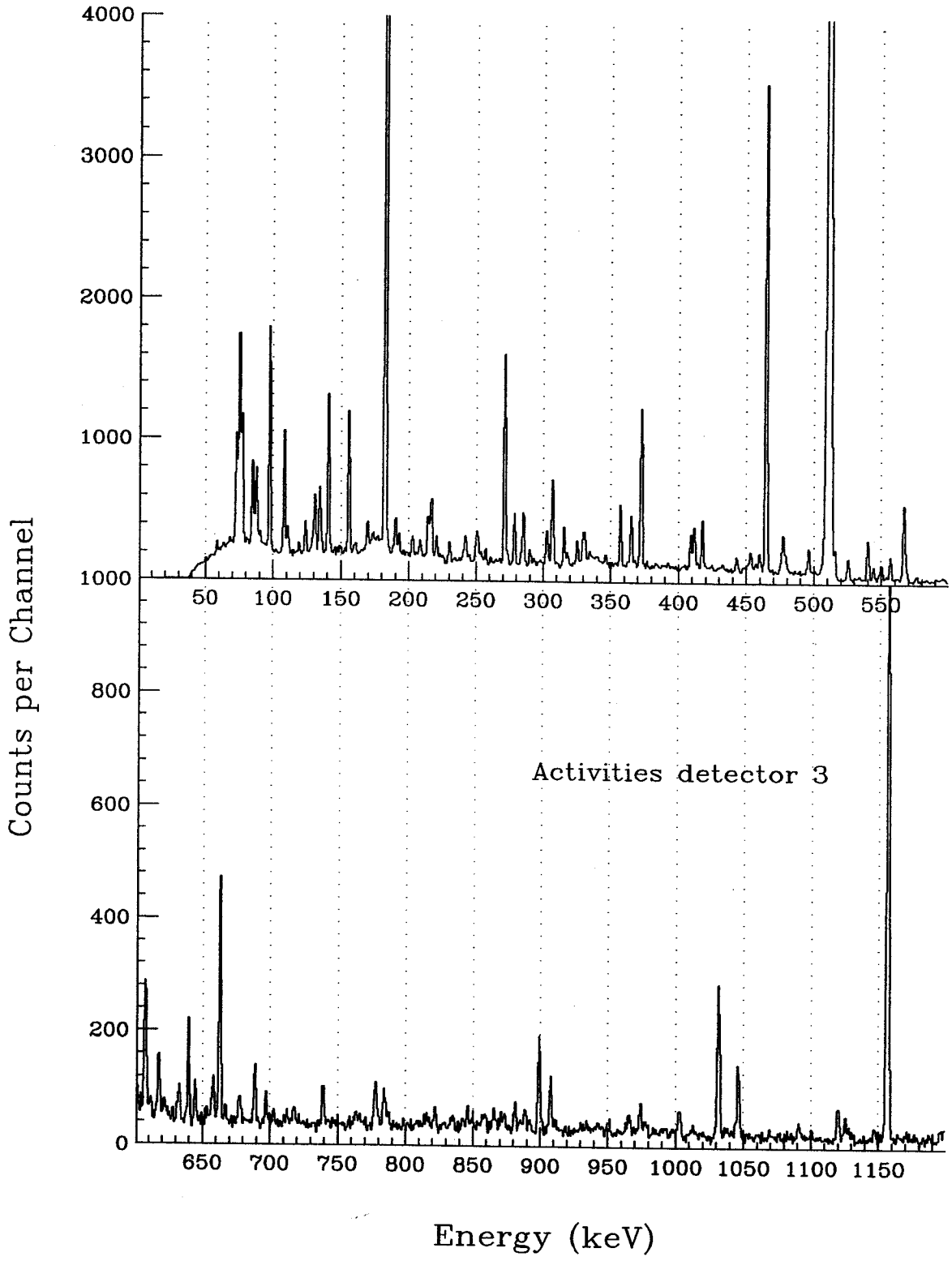

Figure D.95: Post-Run Activities spectrum of all nuclei in the reaction ^{37}Cl on ^{100}Mo, detector 3.

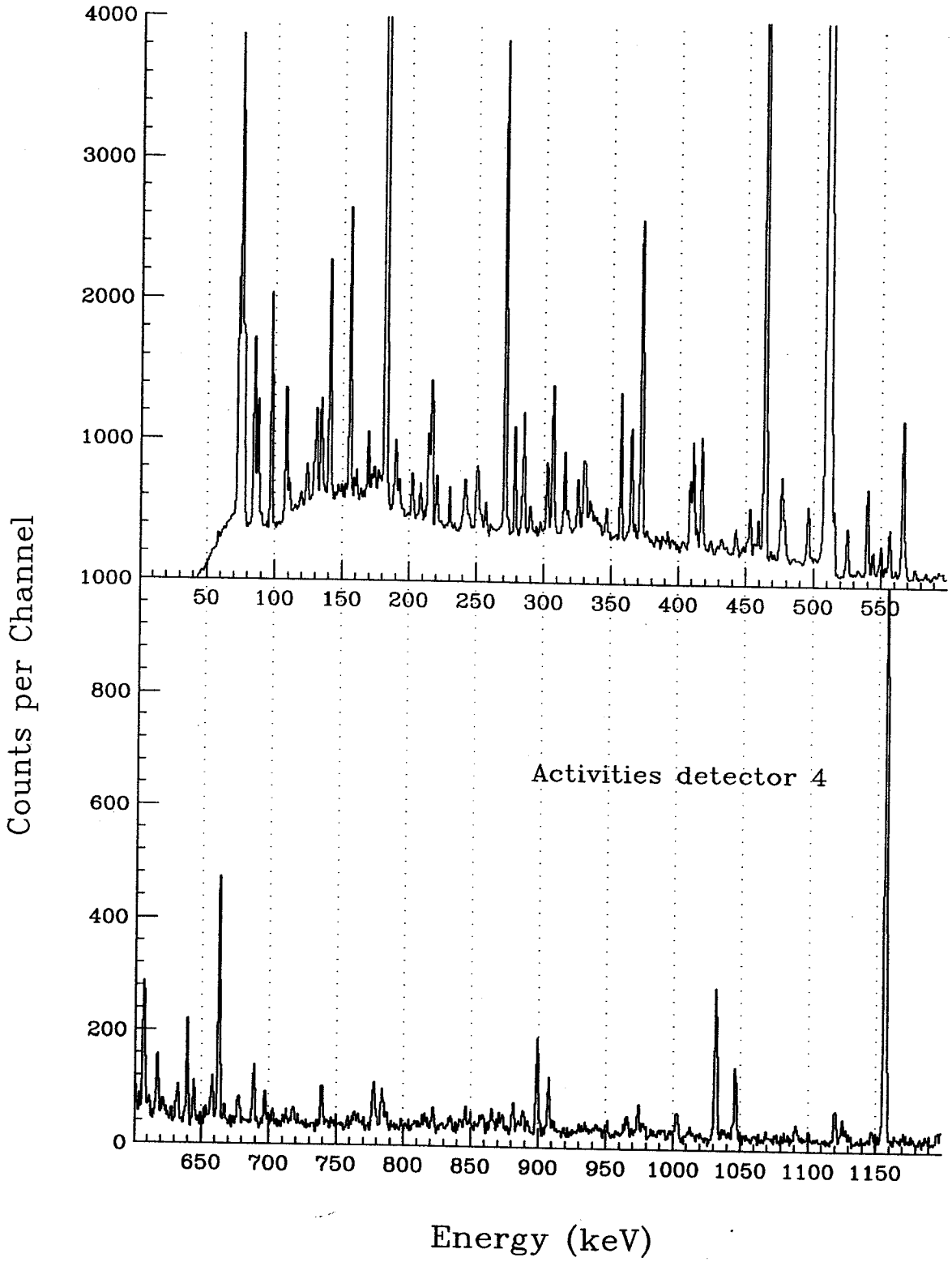

Figure D.96: Post-Run Activities spectrum of all nuclei in the reaction ^{37}Cl on ^{100}Mo, detector 4.

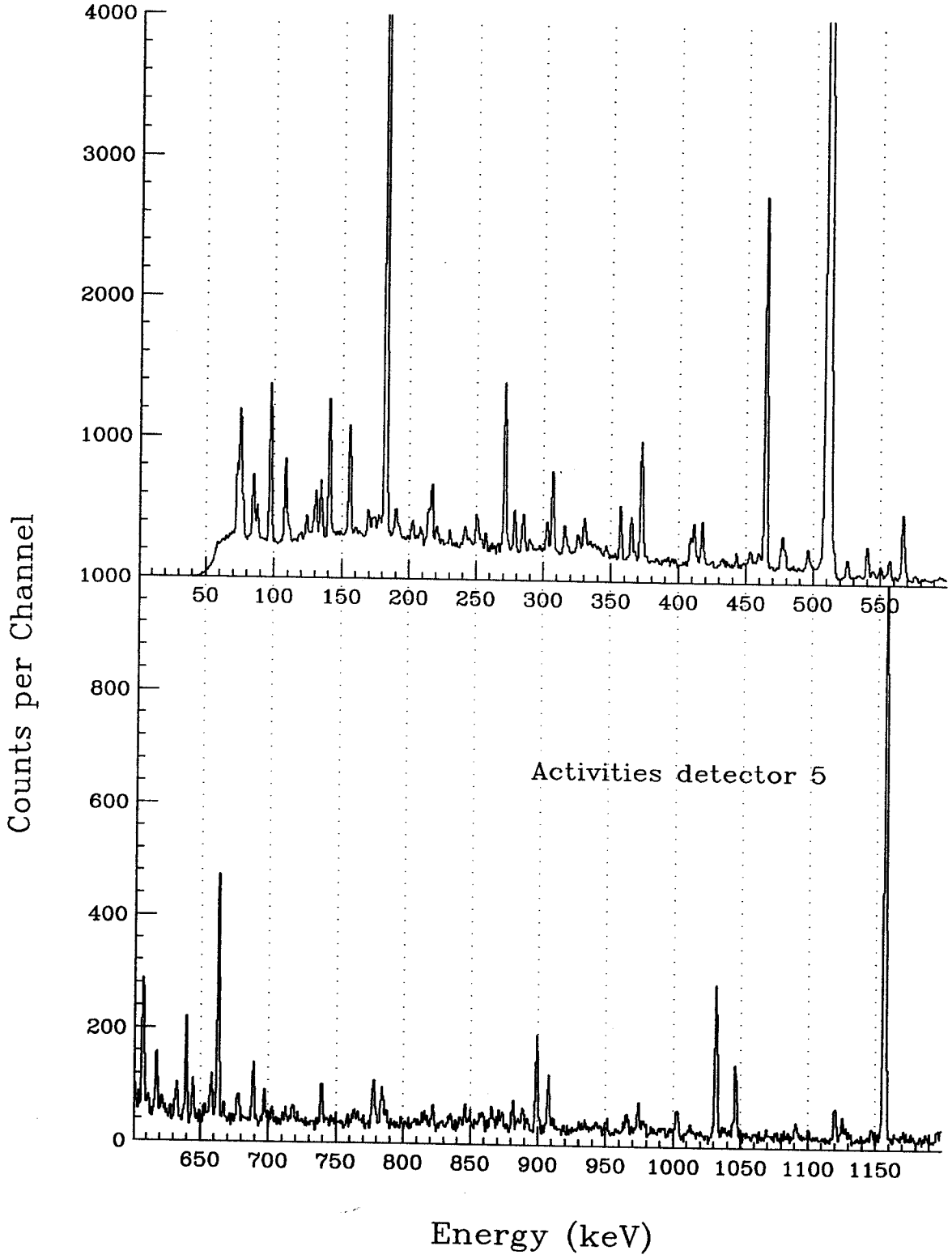

Figure D.97: Post-Run Activities spectrum of all nuclei in the reaction ^{37}Cl on ^{100}Mo, detector 5.

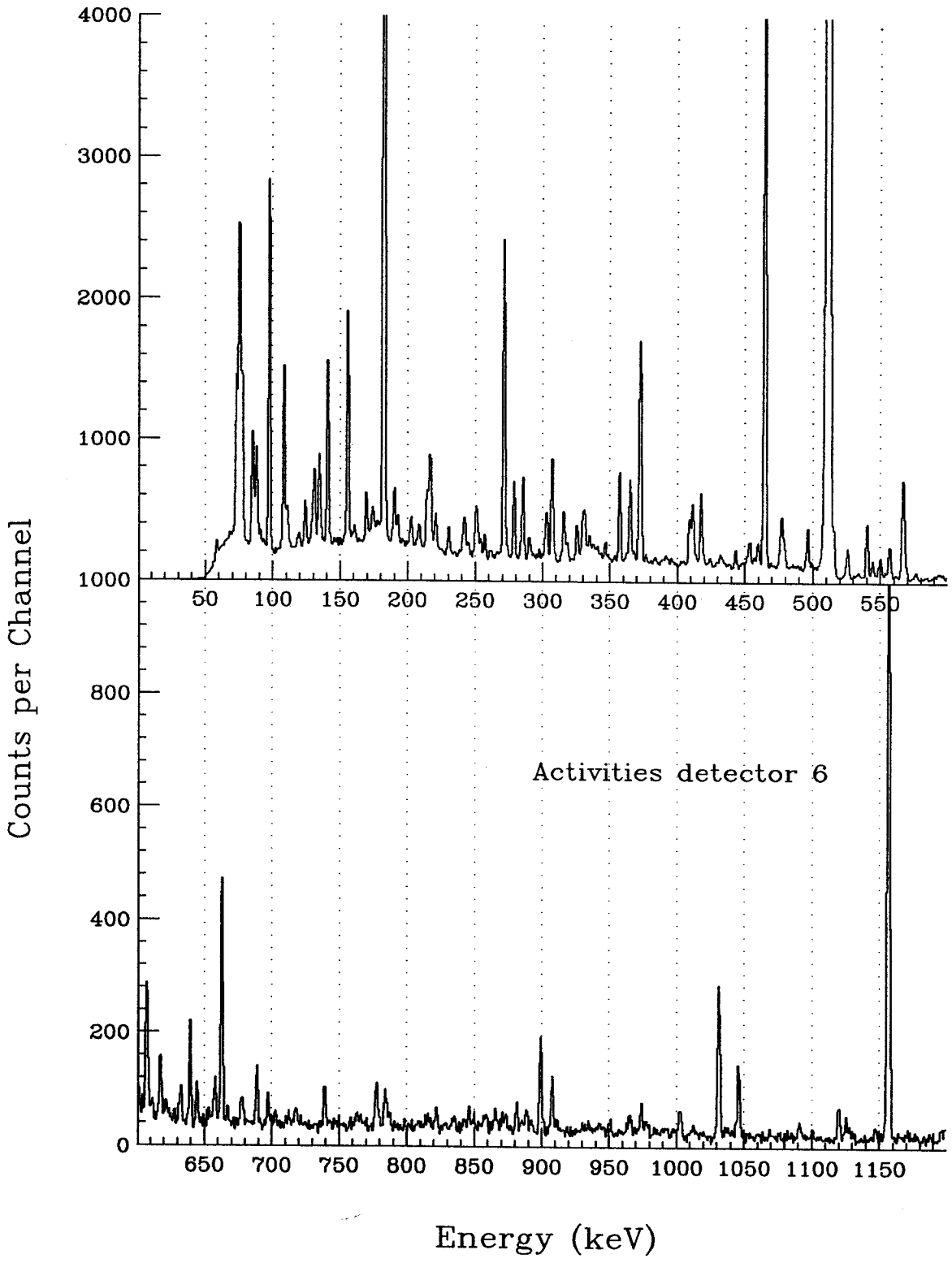

Figure D.98: Post-Run Activities spectrum of all nuclei in the reaction ^{37}Cl on ^{100}Mo, detector 6.

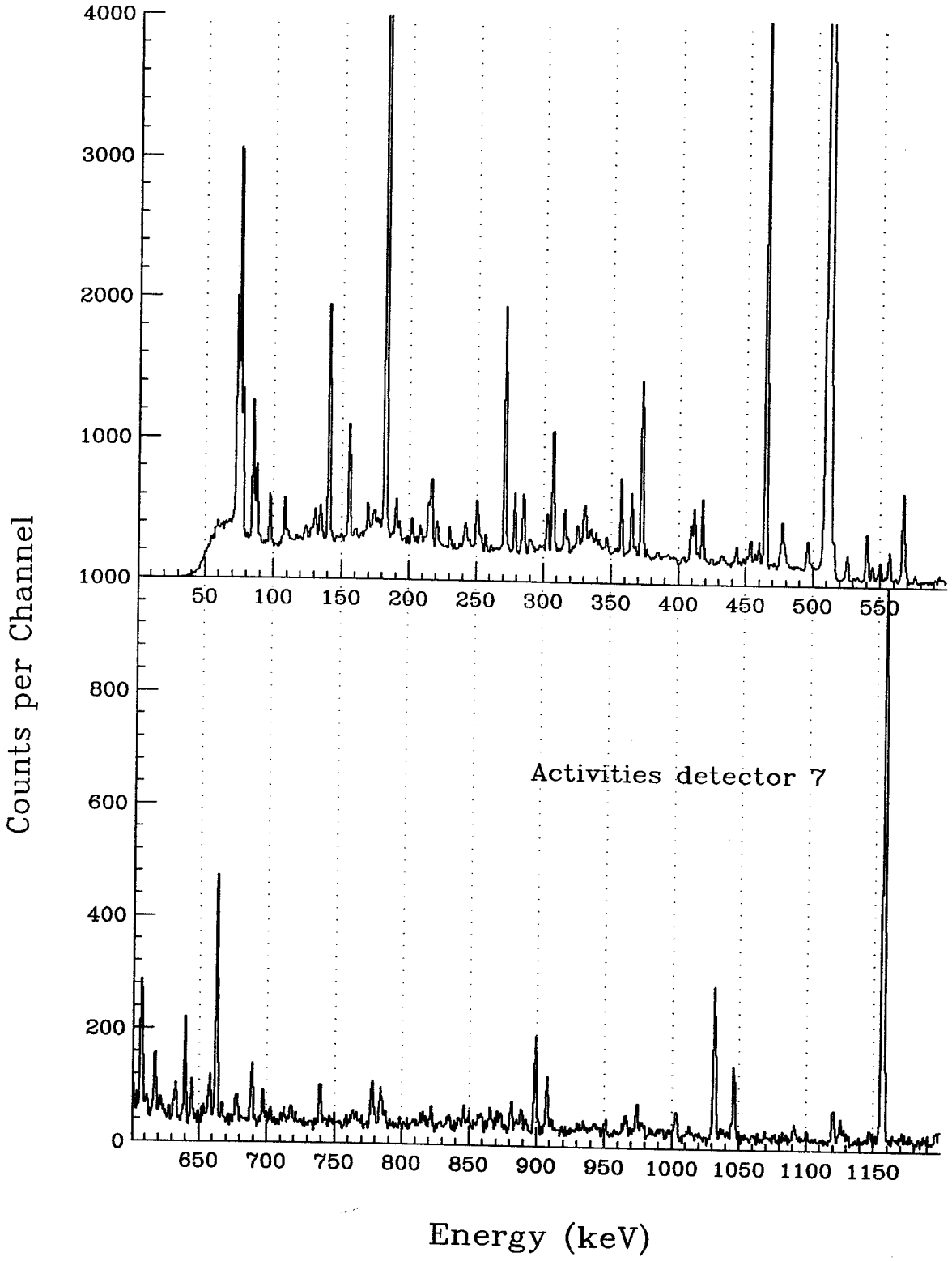

Figure D.99: Post-Run Activities spectrum of all nuclei in the reaction ^{37}Cl on ^{100}Mo, detector 7.

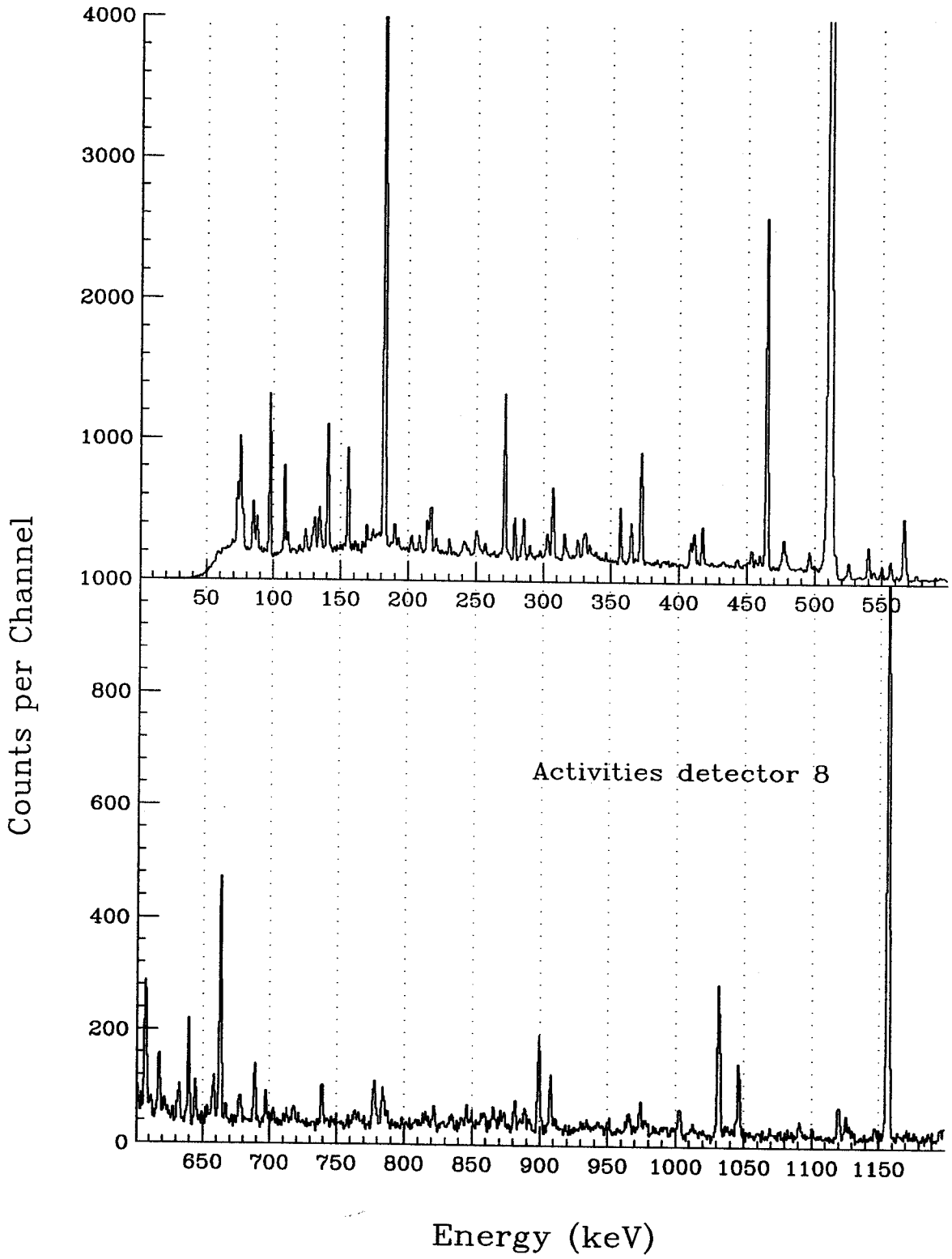

Figure D.100: Post-Run Activities spectrum of all nuclei in the reaction ^{37}Cl on ^{100}Mo, detector 8.

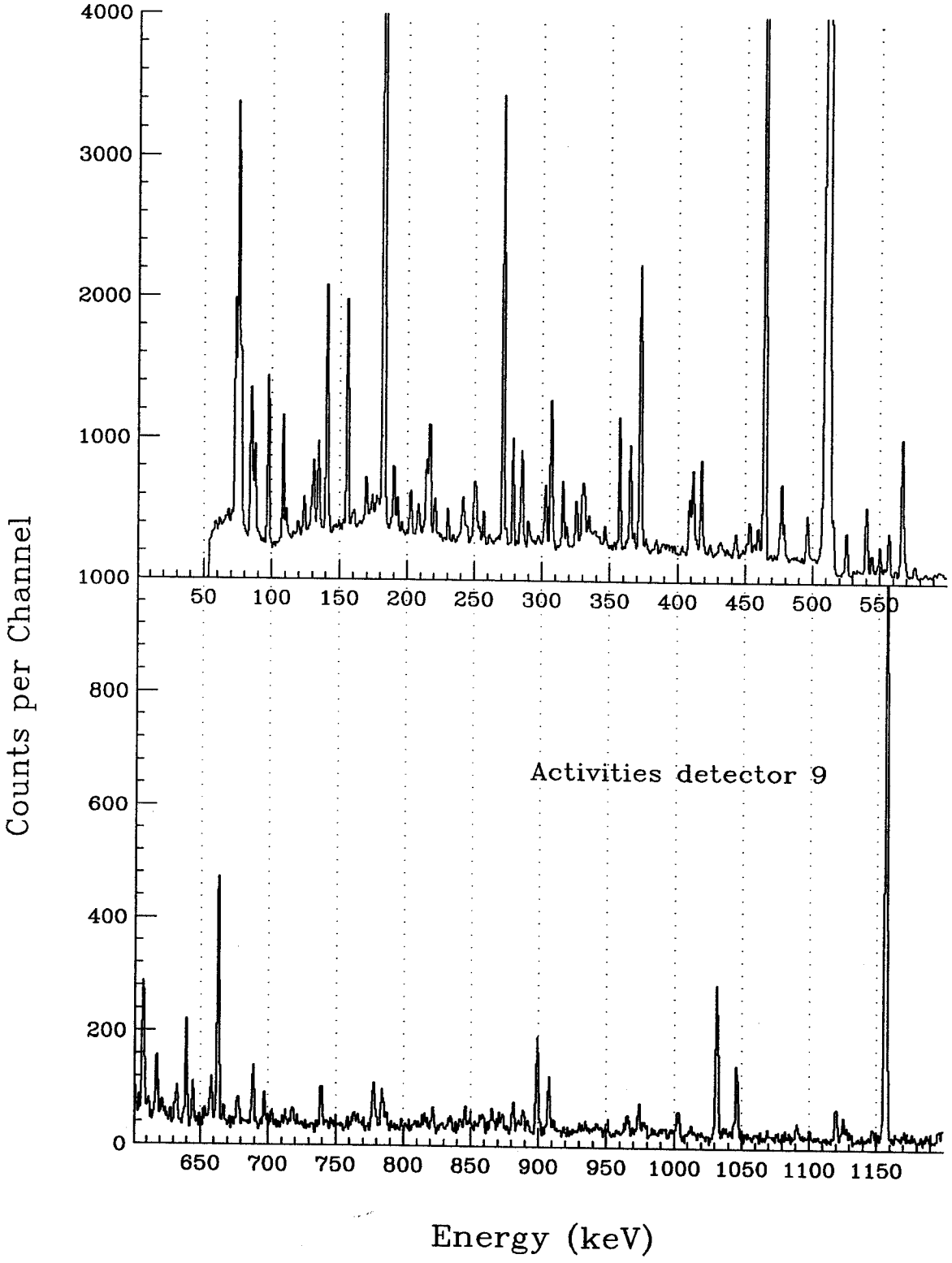

Figure D.101: Post-Run Activities spectrum of all nuclei in the reaction ^{37}Cl on ^{100}Mo, detector 9.

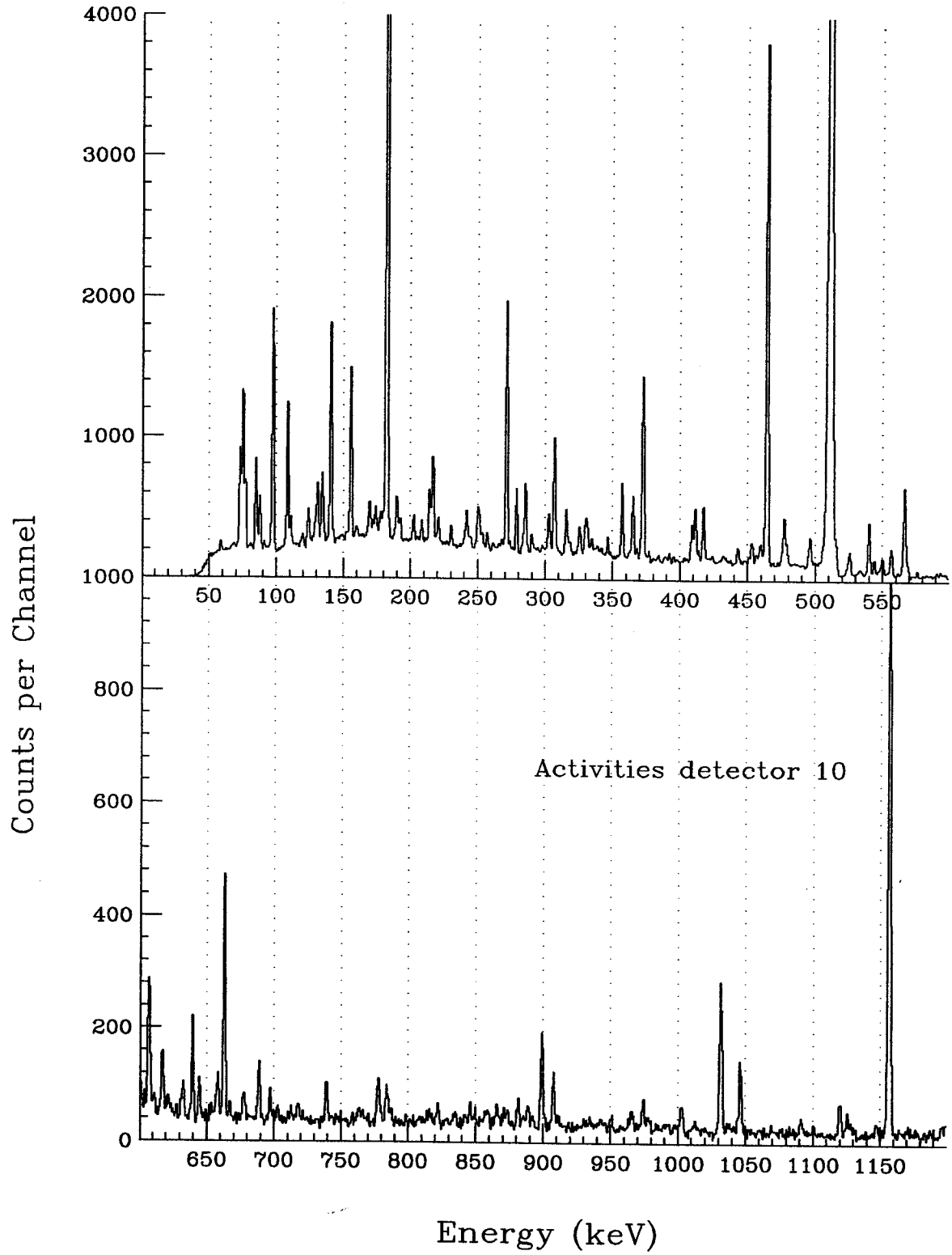

Figure D.102: Post-Run Activities spectrum of all nuclei in the reaction ^{37}Cl on ^{100}Mo, detector 10.

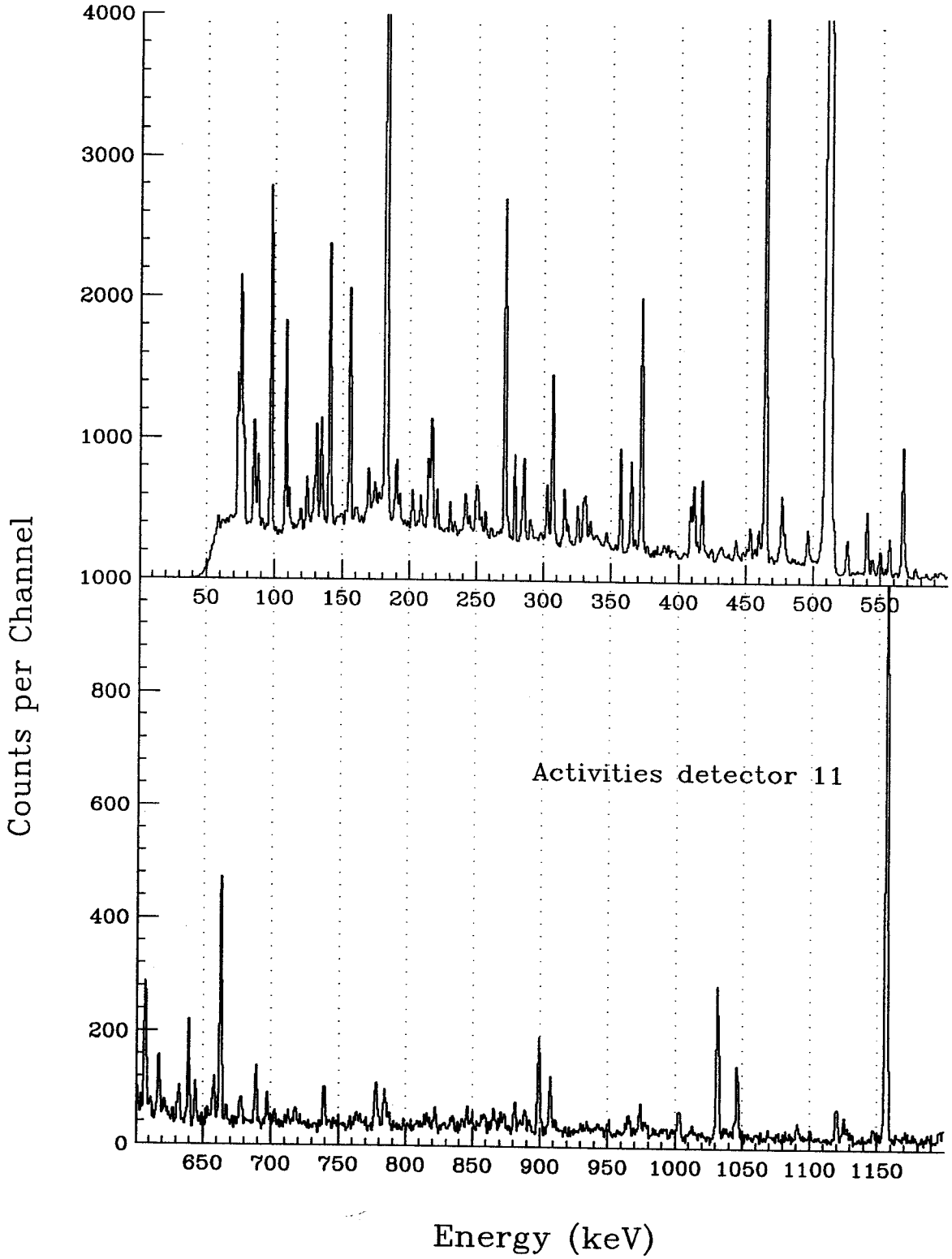

Figure D.103: Post-Run Activities spectrum of all nuclei in the reaction ^{37}Cl on ^{100}Mo, detector 11.

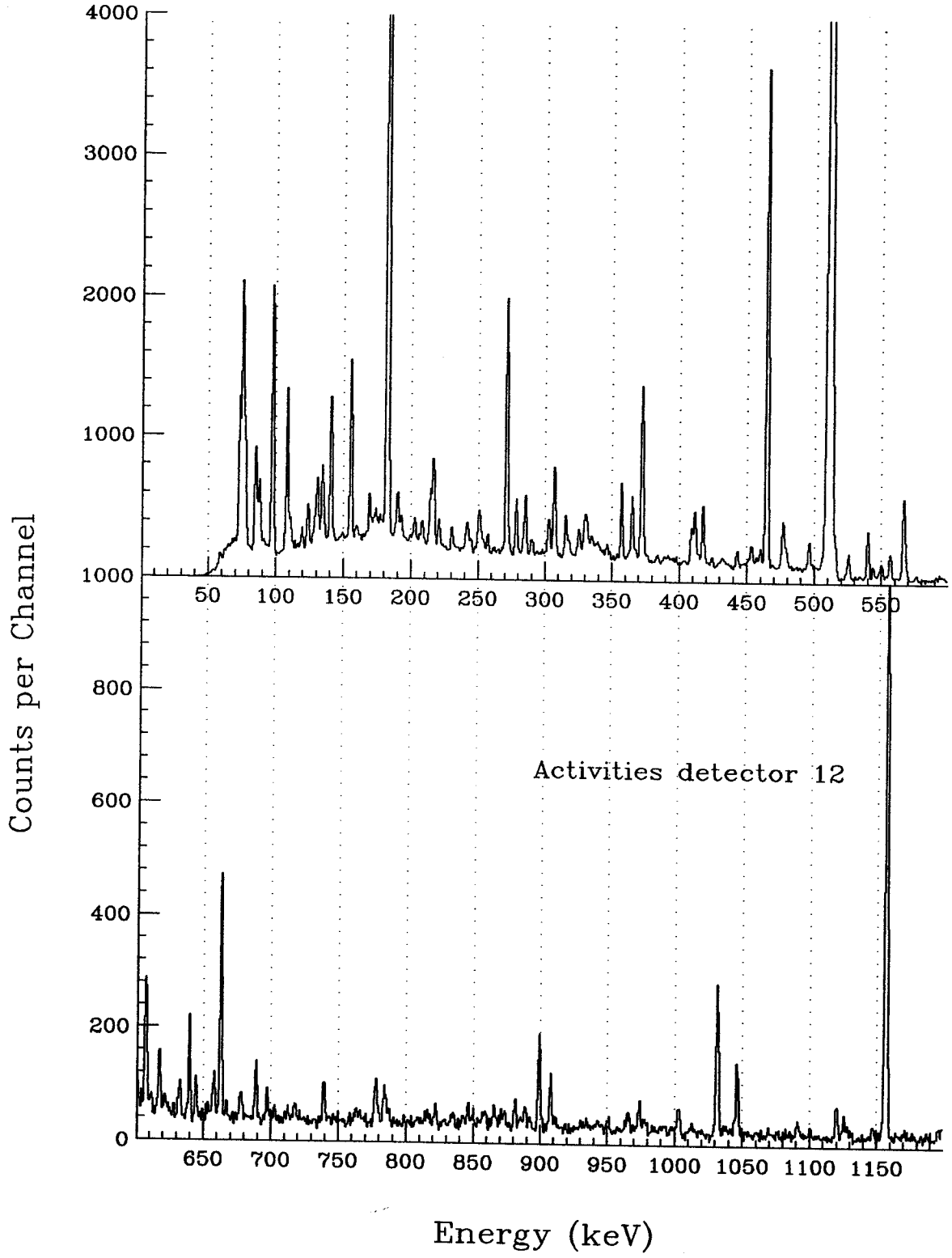

Figure D.104: Post-Run Activities spectrum of all nuclei in the reaction ^{37}Cl on ^{100}Mo, detector 12.

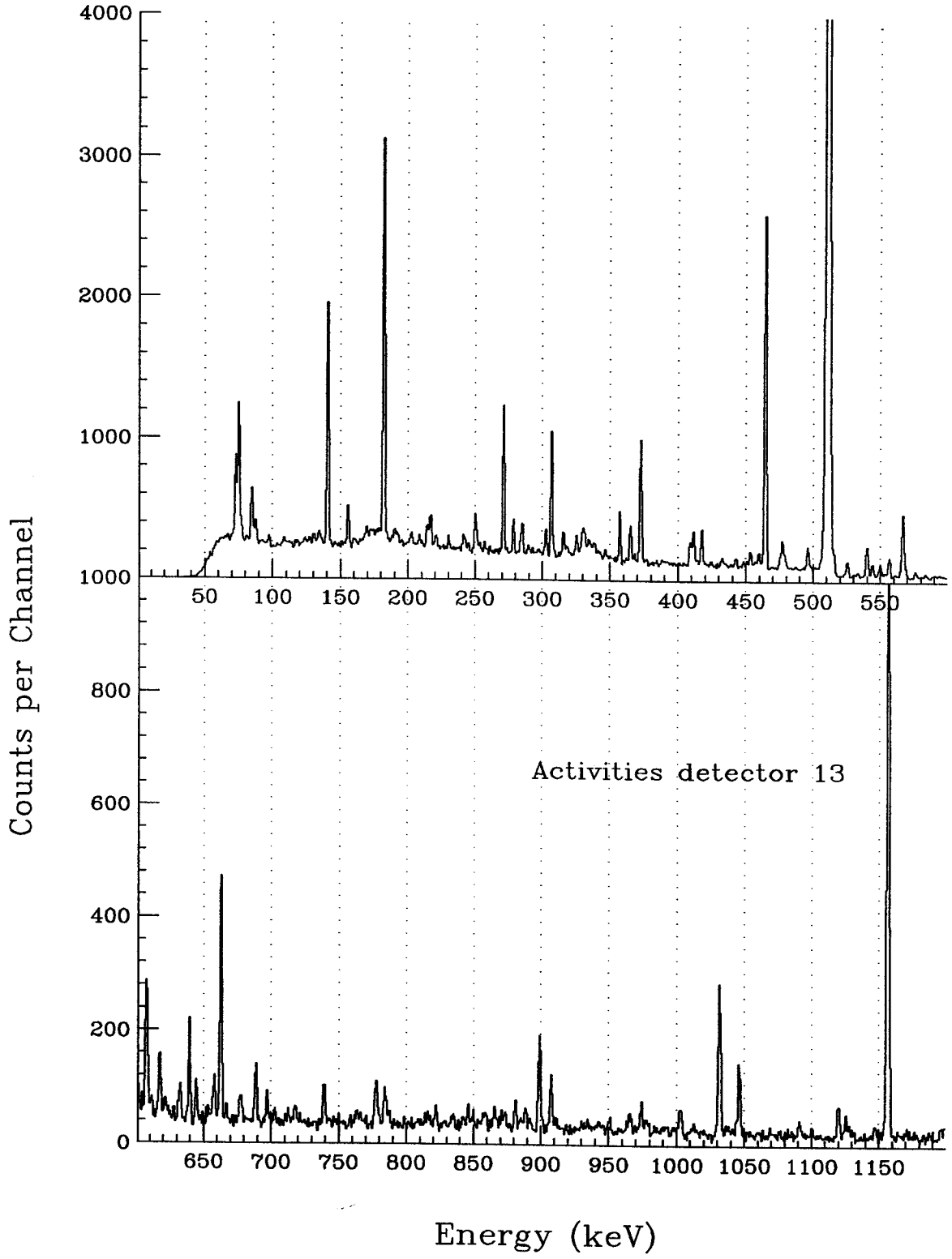

Figure D.105: Post-Run Activities spectrum of all nuclei in the reaction ^{37}Cl on ^{100}Mo, detector 13.

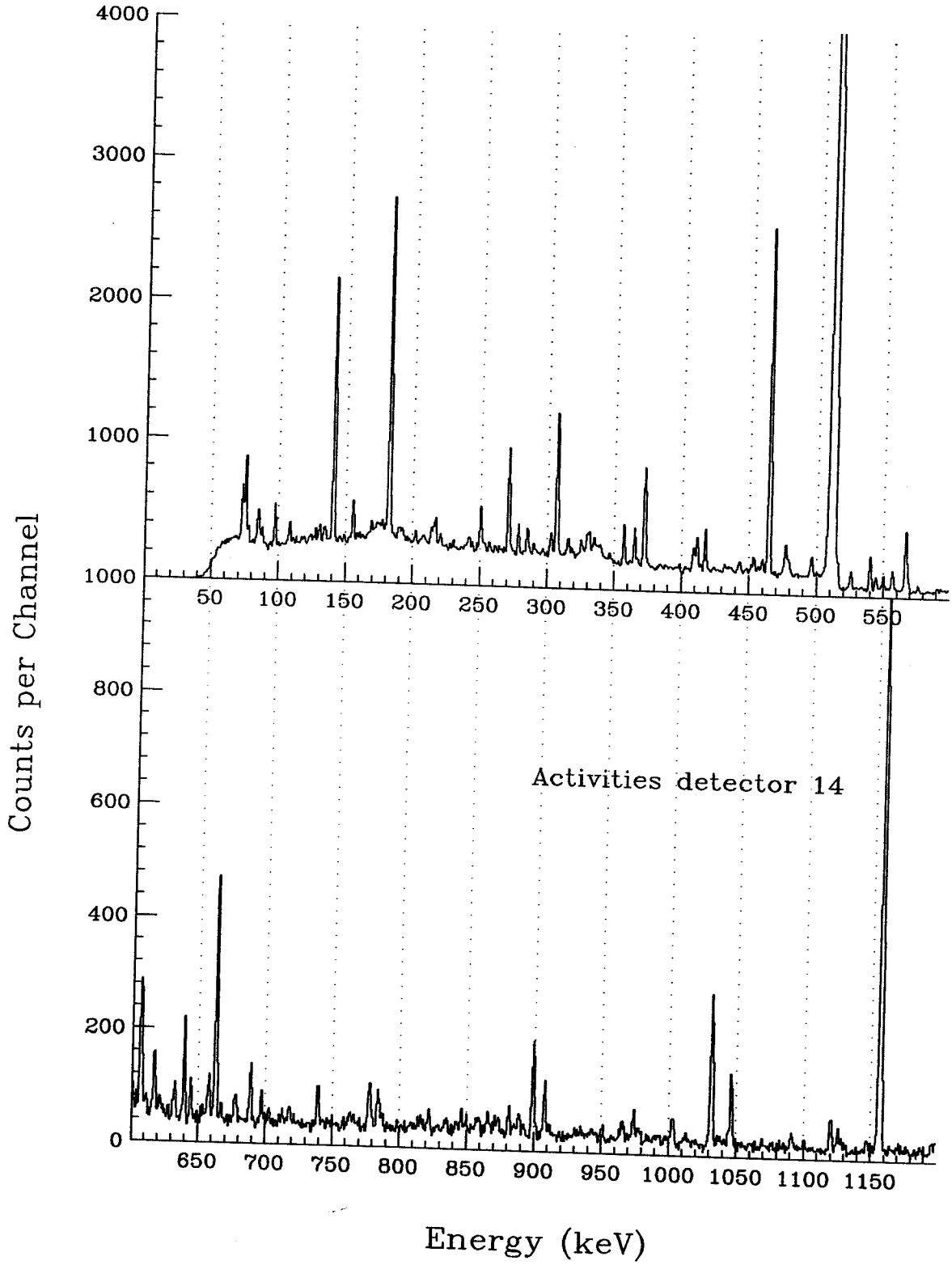

Figure D.106: Post-Run Activities spectrum of all nuclei in the reaction ^{37}Cl on ^{100}Mo, detector 14.

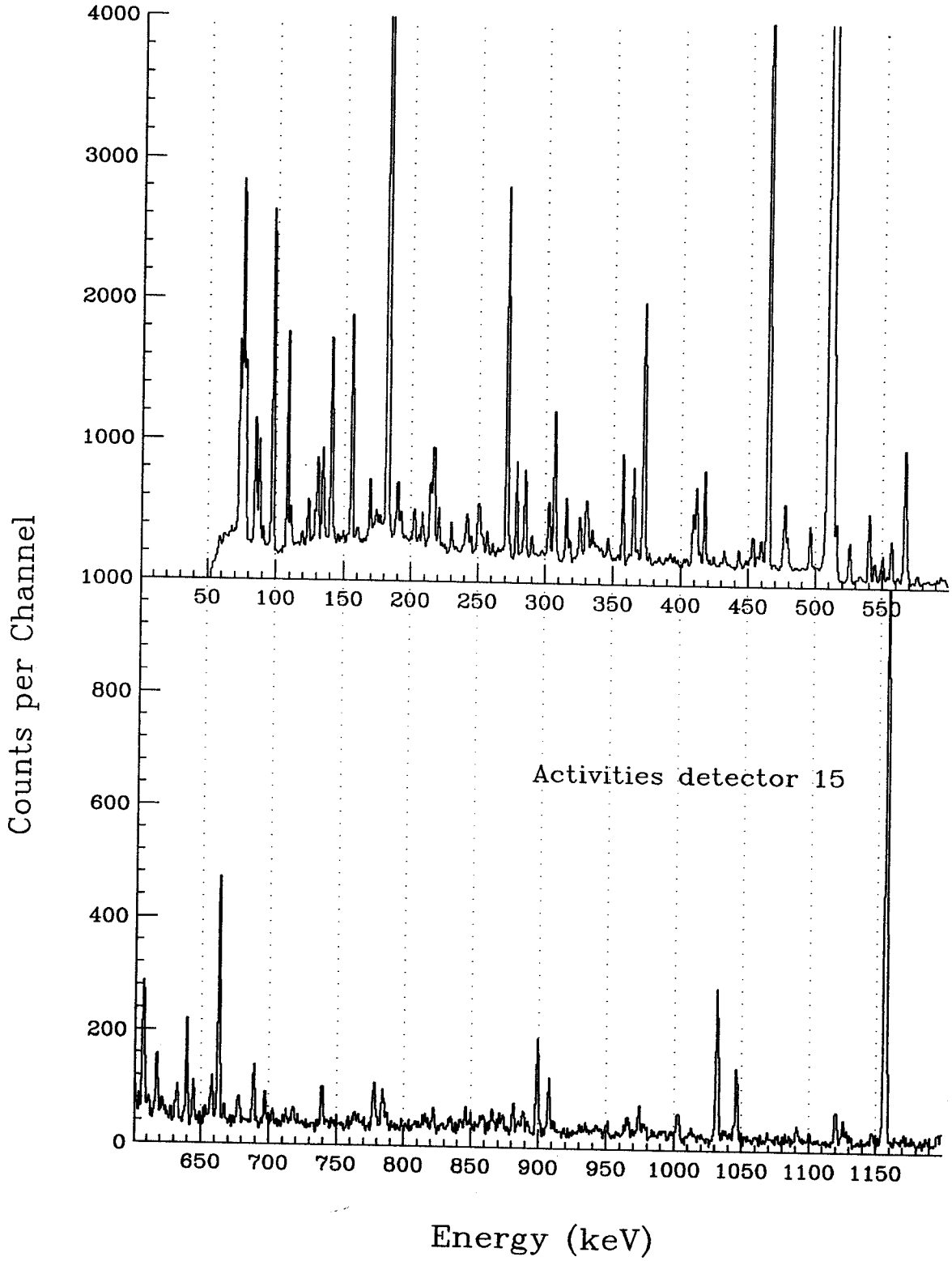

Figure D.107: Post-Run Activities spectrum of all nuclei in the reaction ^{37}Cl on ^{100}Mo, detector 15.

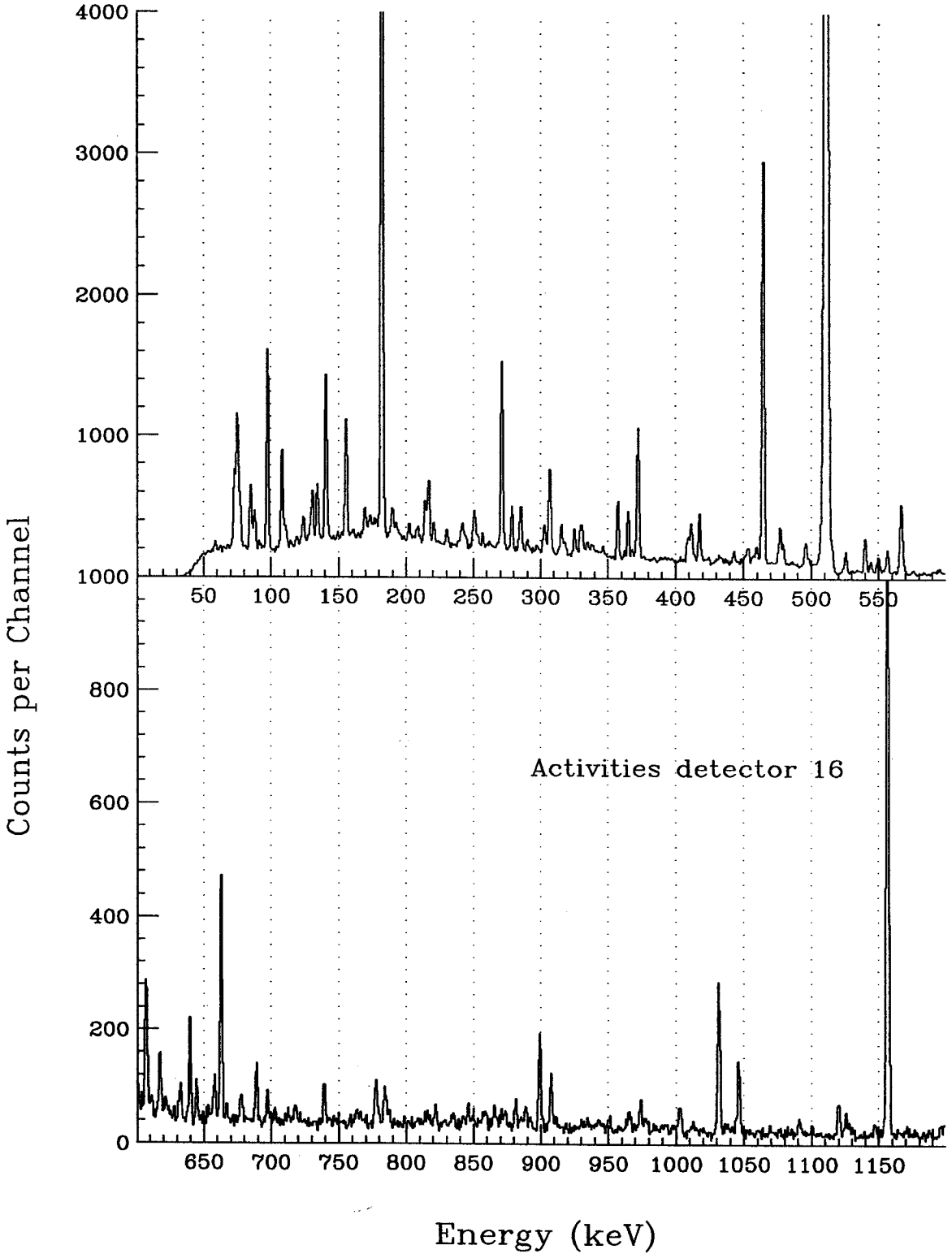

Figure D.108: Post-Run Activities spectrum of all nuclei in the reaction ^{37}Cl on ^{100}Mo, detector 16.

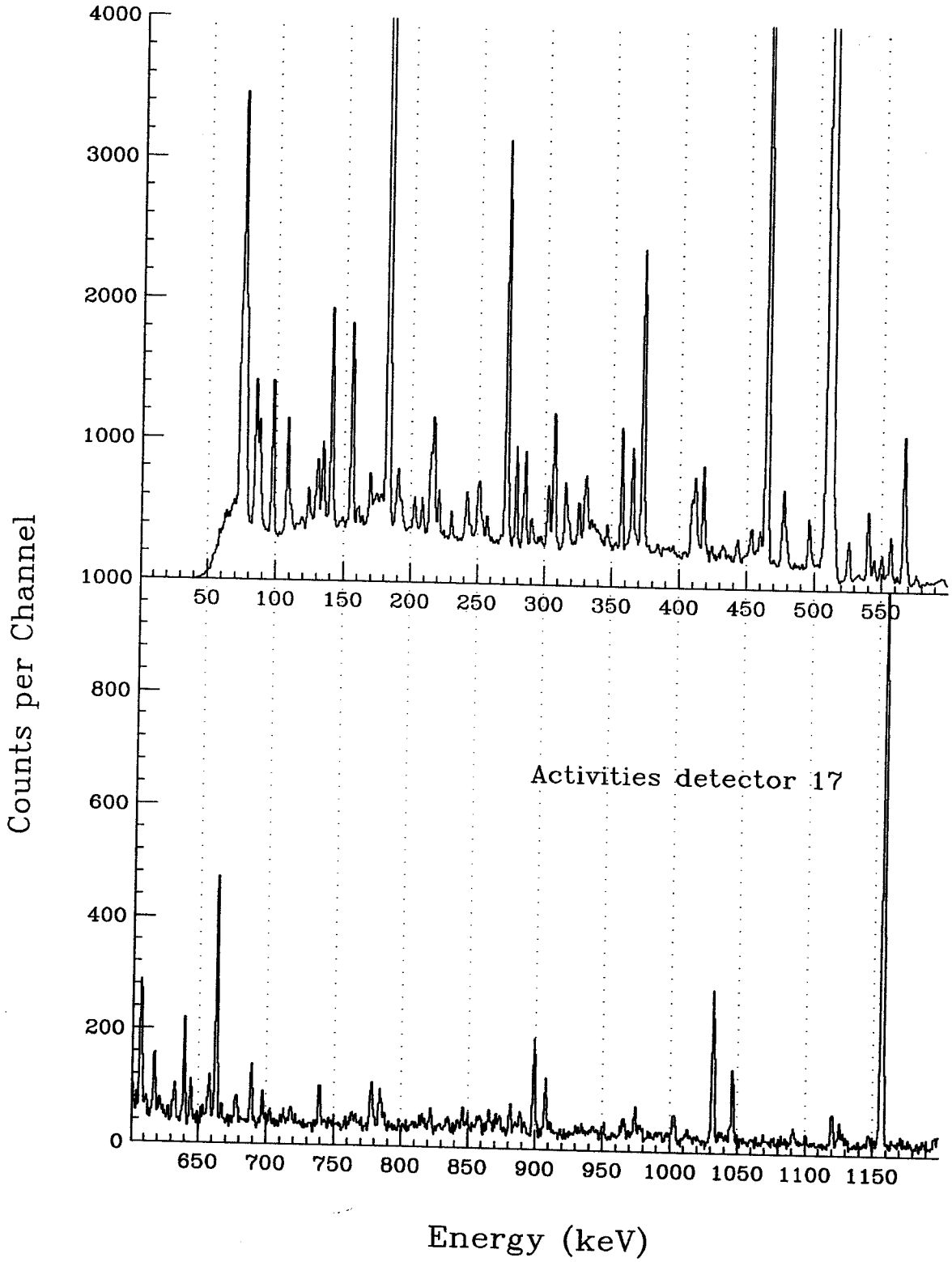

Figure D.109: Post-Run Activities spectrum of all nuclei in the reaction ^{37}Cl on ^{100}Mo, detector 17.

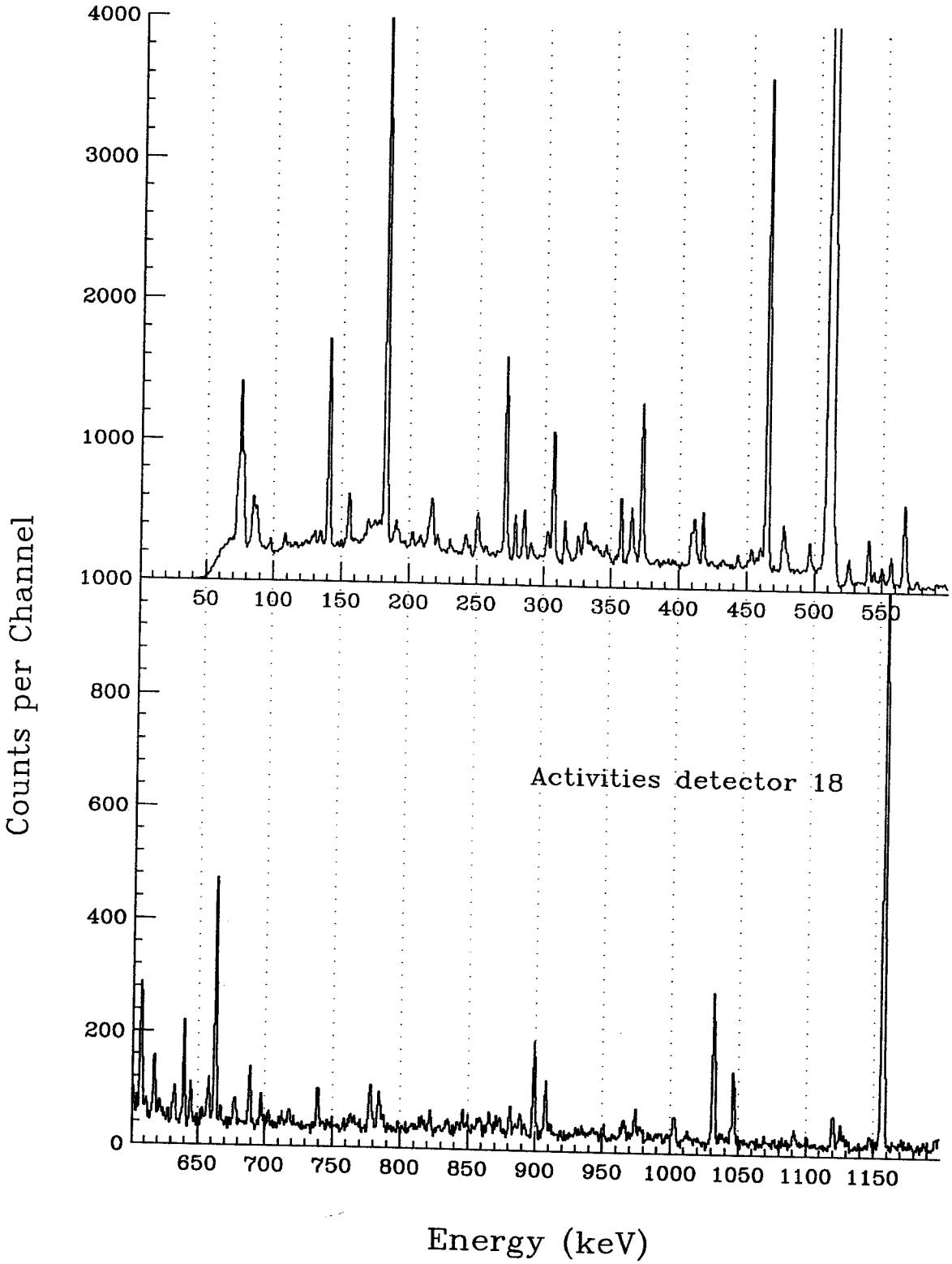

Figure D.110: Post-Run Activities spectrum of all nuclei in the reaction ^{37}Cl on ^{100}Mo, detector 18.

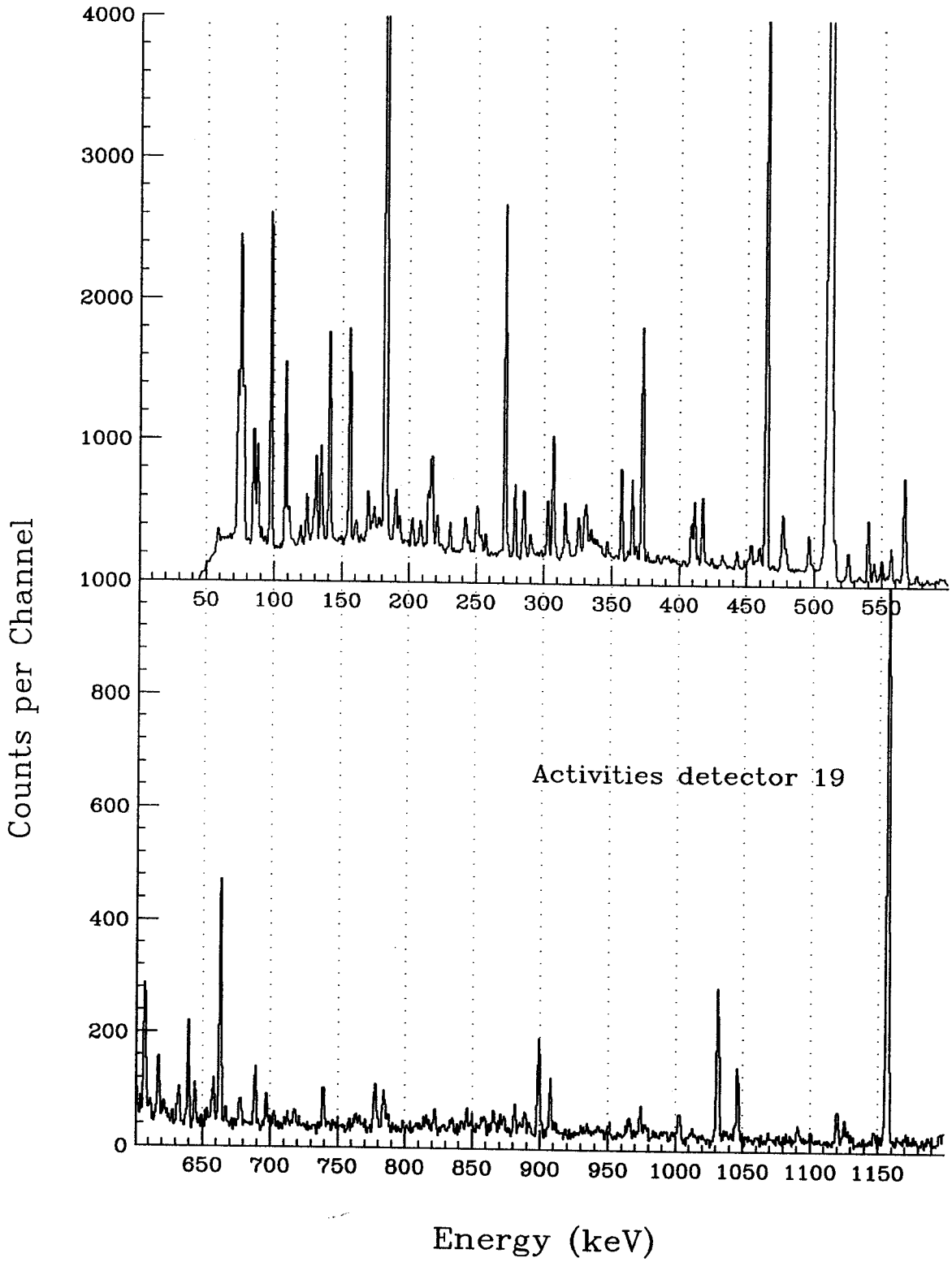

Figure D.111: Post-Run Activities spectrum of all nuclei in the reaction ^{37}Cl on ^{100}Mo, detector 19.

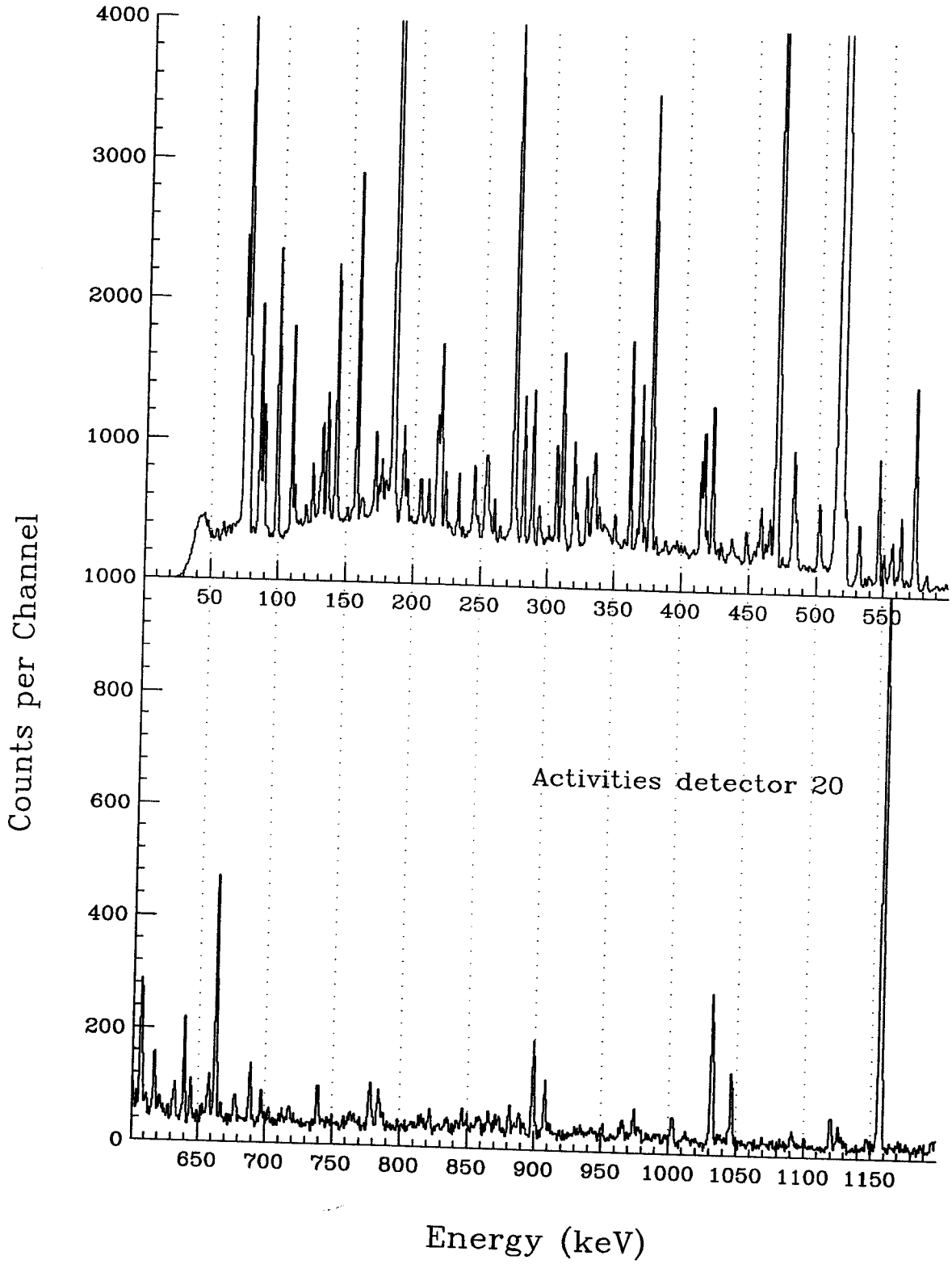

Figure D.112: Post-Run Activities spectrum of all nuclei in the reaction ^{37}Cl on ^{100}Mo, detector 20.

Appendix E

^{132}Pr Spectra.

The Simple- and Multiple-gated histograms ('gates') for ^{132}Pr displayed in this Appendix have complementary information. The energy peaks from the primary gates at 115, 178, 283, and 130 keV. for ^{132}Pr will not be seen in the Multiple gates; however, their contribution is a major one in the Simple gates. The Simple gates have twice the ADC resolution as the Multiple gates but they are not necessarily nuclei specific. Therefore, 1) more 'contaminant' peaks are present in the Simple gates; 2) the Simple gate's higher energy regions have a much lower signal to background ratio than the Multiple gates have. Many higher-energy peaks will not be seen in the Simple gates. The Multiple gates were designed to be nuclei specific but in some cases contaminant peaks from neighboring nuclei cannot be separated.

Without FFT, much of the individual Simple-gate information cannot be used (see Chapter 6). In many of the following spectra, the LLSI/O mode was chosen for display since the resulting spectral intensities closely match the original counts in the data set. The FLGI/O FFT mode was also used (mostly for the multiple gates) since it emphasizes the smaller peaks. Note that the y-axis values do not reflect the actual count number. During the FFT process an offset and a mathematical operator change this value. Therefore, the y-axis should be viewed in a qualitative manner.

E.1 Simple Gates ^{132}Pr

$E_{\gamma x}$ versus $E_{\gamma y}$ arrays were constructed, representing the sum of all triple coincidence events determined from detector comparisons. This is presented in Figure 5.12. A TAC gate was set during the array generation: everything that had previously been designated pre-prompt through prompt was included. By making a cut (gate) on either axis at an appropriate energy, A, all the energies in coincidence with A that occurred between the two detectors were obtained within the 1-D histogram. A few of the resulting spectra for ^{132}Pr are displayed in this Appendix. In the appendices to follow, each spectrum has been enhanced using the FFT and SNIP routines described in Chapter 6. For comparison purposes, the ^{132}Pr Simple-gated spectra contained in this Appendix have not been enhanced.

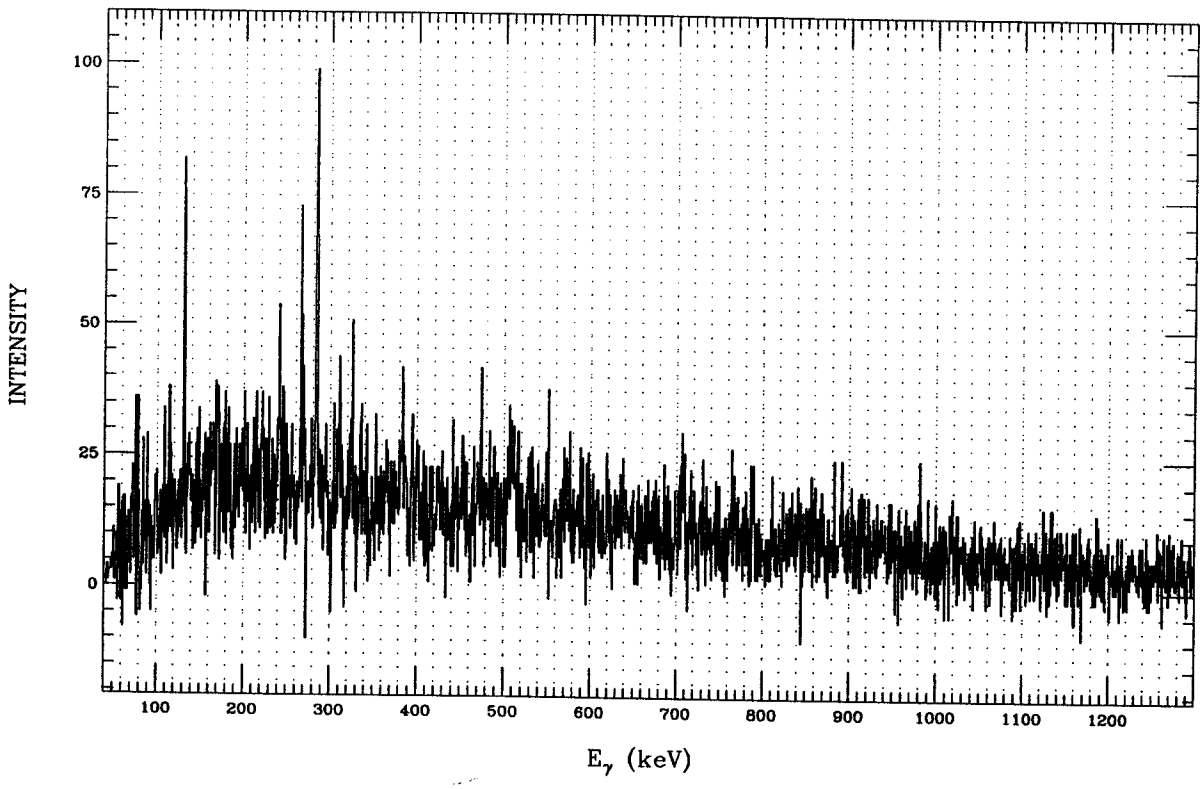

Figure E.1: ID 62. Simple gate from ^{132}Pr, gs band.

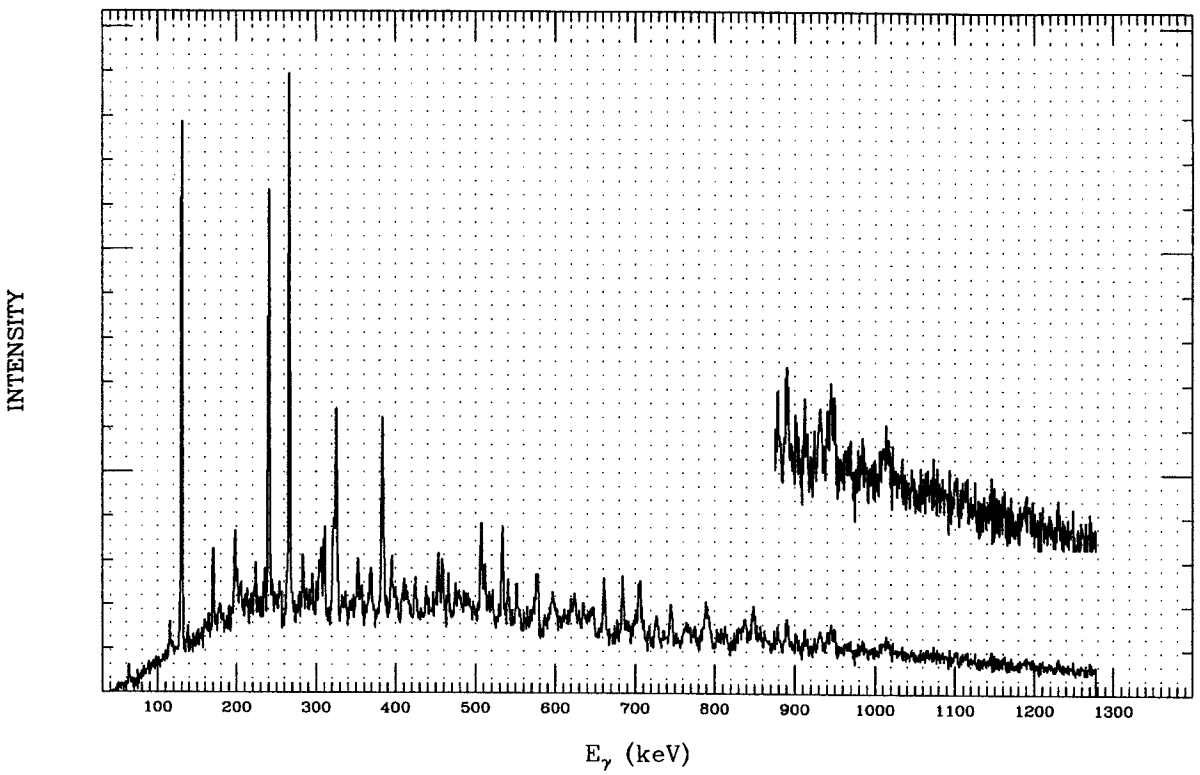

Figure E.2: ID 283. Simple gate from ^{132}Pr, gs band.

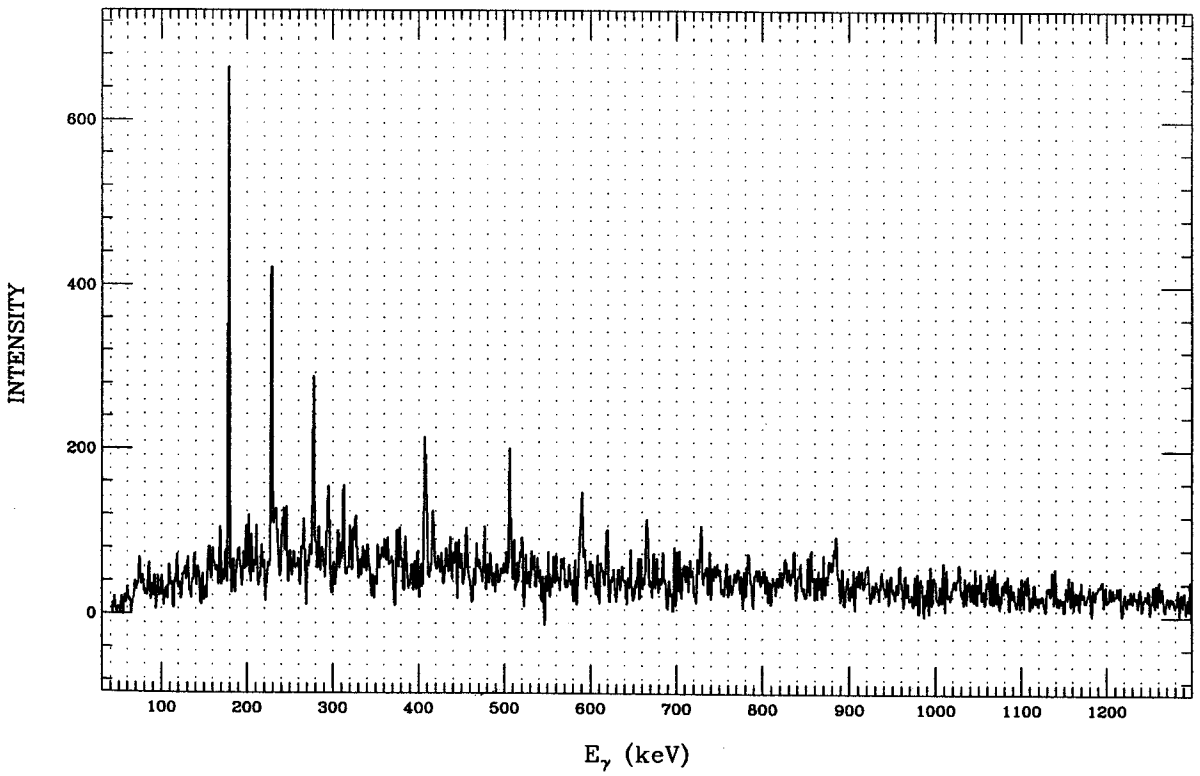

Figure E.3: ID 115. Simple gate from ^{132}Pr, band 12.

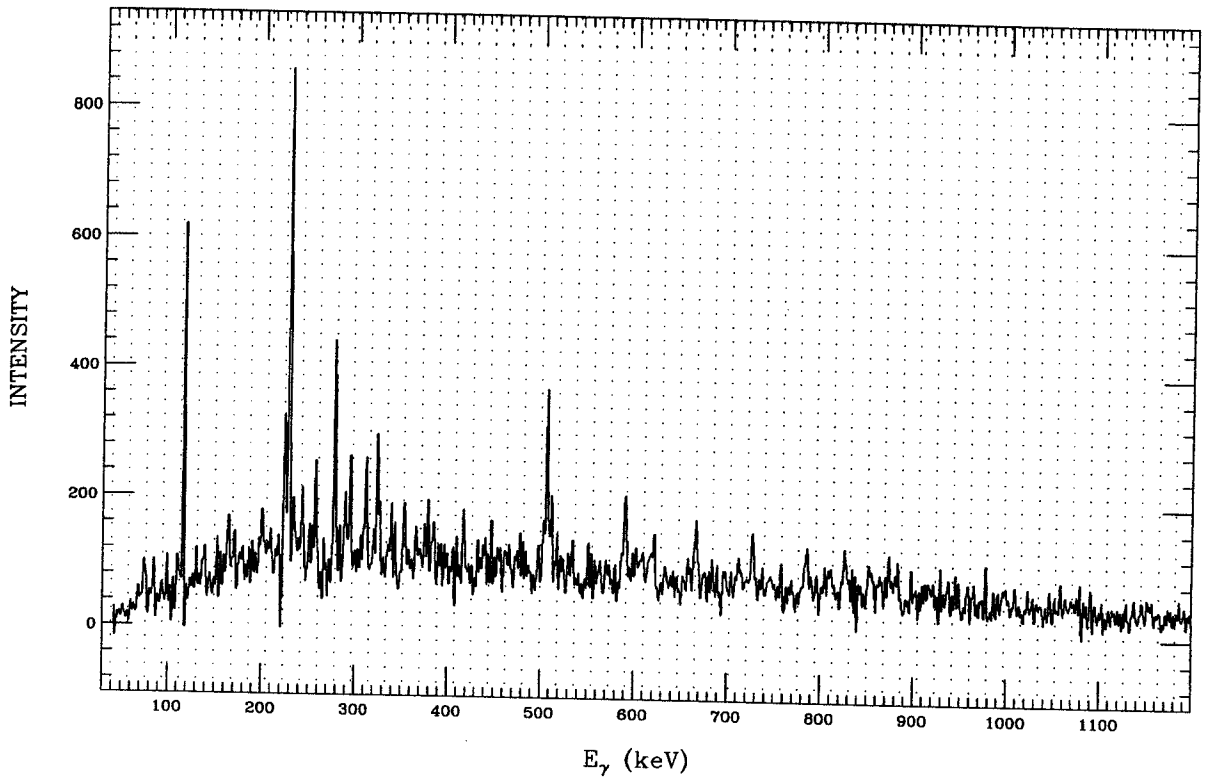

Figure E.4: ID 179. Simple gate from ^{132}Pr, band 12.

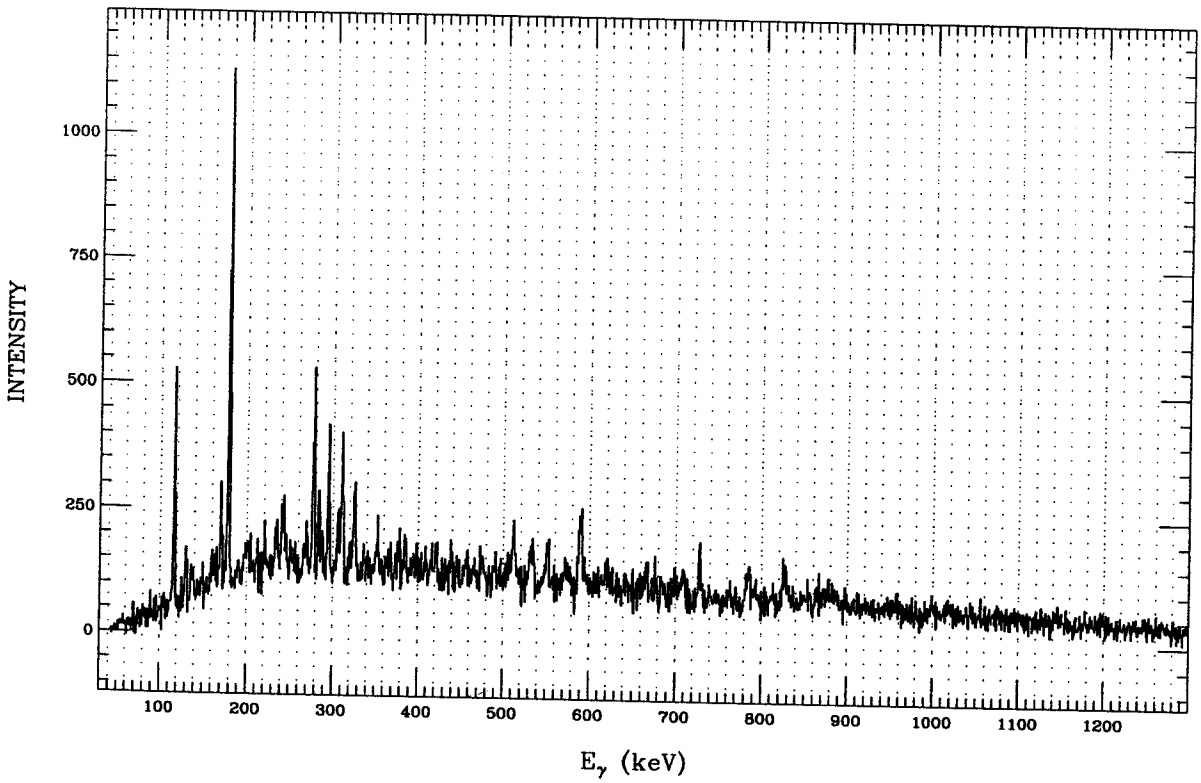

Figure E.5: ID 229. Simple gate from ^{132}Pr, band 12.

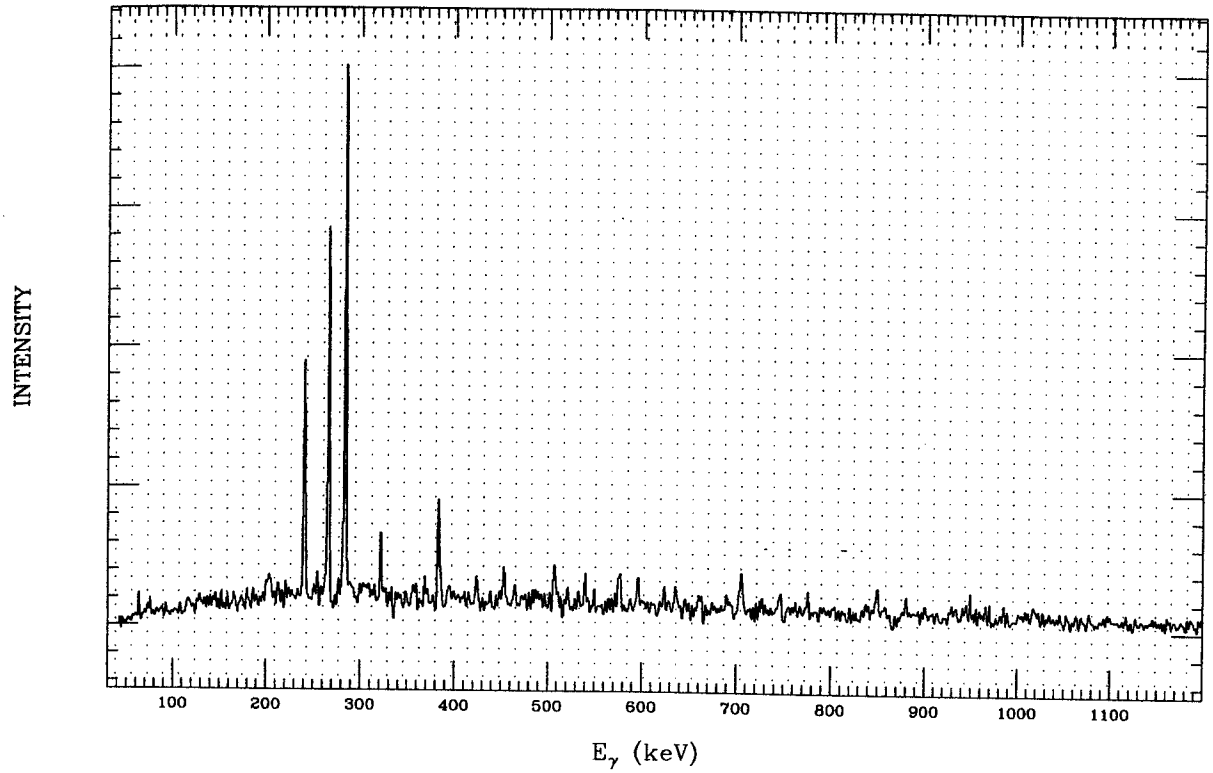

Figure E.6: ID 130. Simple gate from ^{132}Pr, band 22.

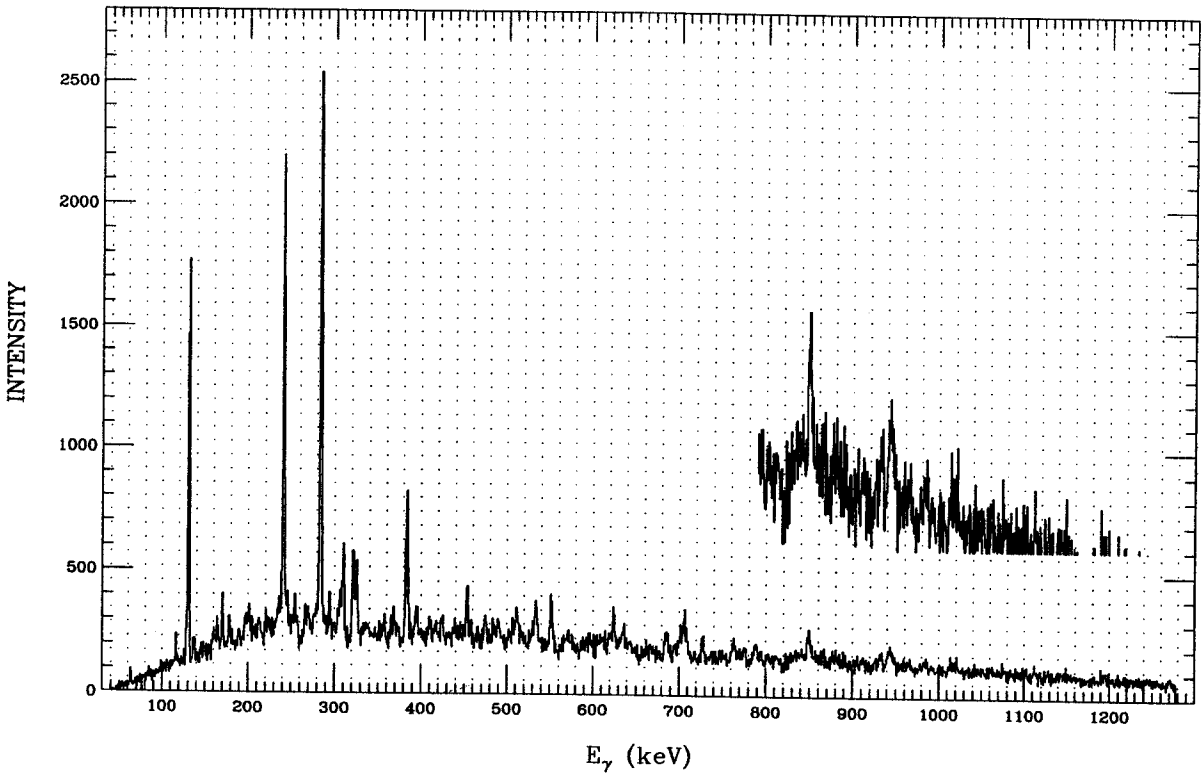

Figure E.7: ID 266. Simple gate from ^{132}Pr, band 22.

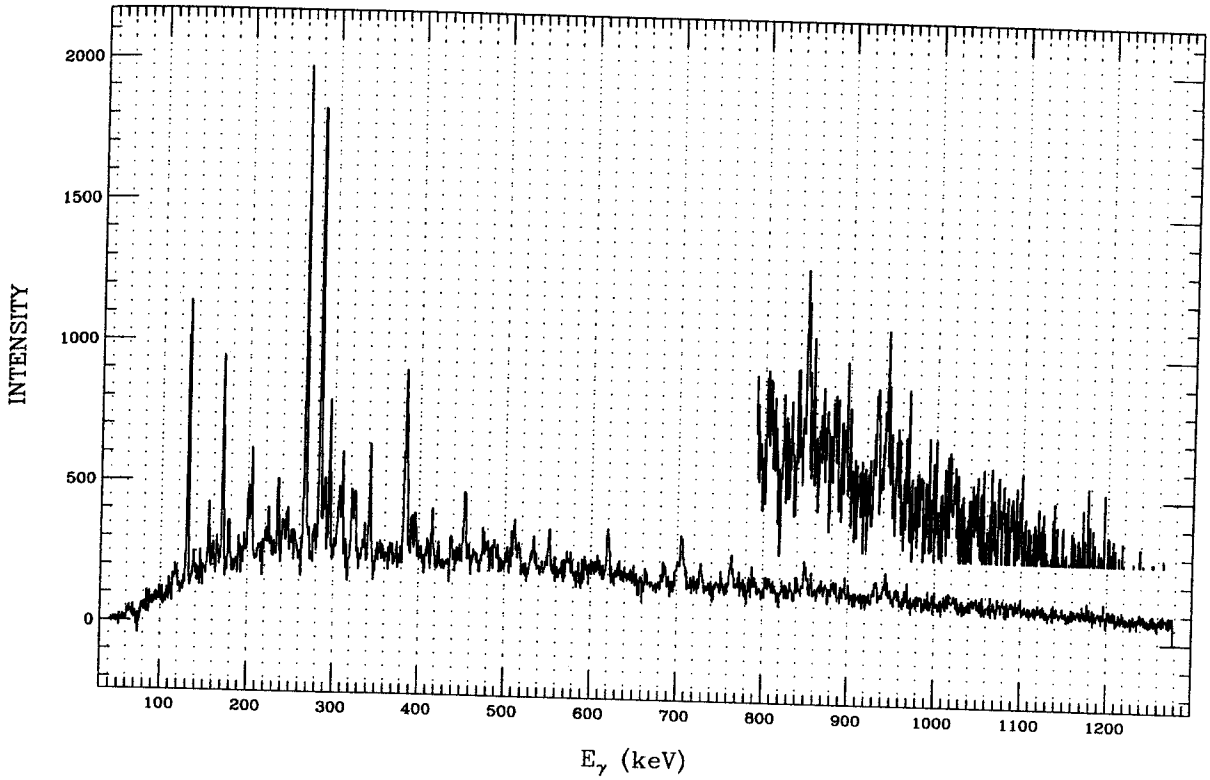

Figure E.8: ID 240. Simple gate from ^{132}Pr, band 22.

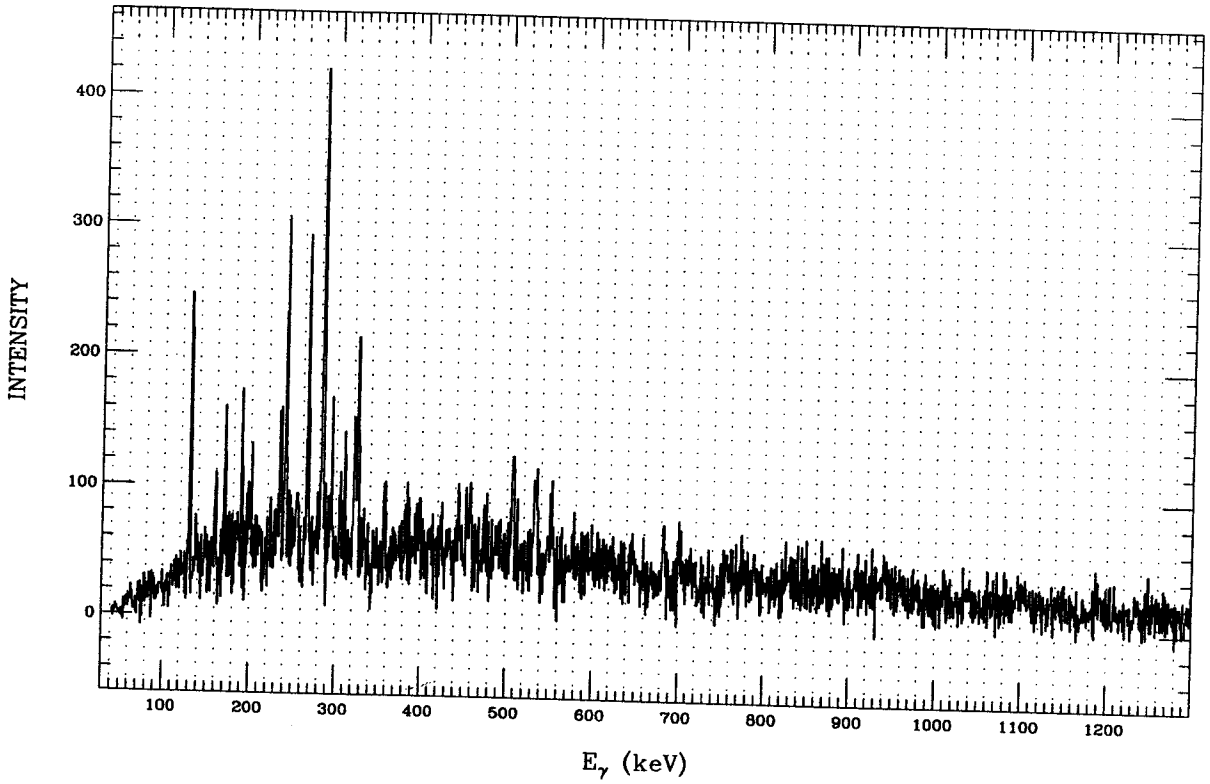

Figure E.9: ID 384. Simple gate from ^{132}Pr, band 22.

E.2 Multiple Gates ^{132}Pr

A multiple gate technique was developed using triple coincidence data for ^{132}Pr. For the first gate step, the program *LEMO* was used with a 2-D free form energy coincidence gate (.ban file) to write coincidences between detectors to tape. Coincidences from the four 90° detectors were compared with the rest of the detectors and the events were sorted onto a new tape. For ^{132}Pr, four 2-D primary gates from different bands were chosen: 115 and 178, 283, 130 keV. For the second gate step, *SCAN* was used with the new tape to generate a total energy versus total energy 2-D array. See Figure 5.14. This 2-D histogram was then gated, generating the spectra contained in this Appendix. Each spectrum has been enhanced using the FFT and SNIP routines described in Chapter 6.

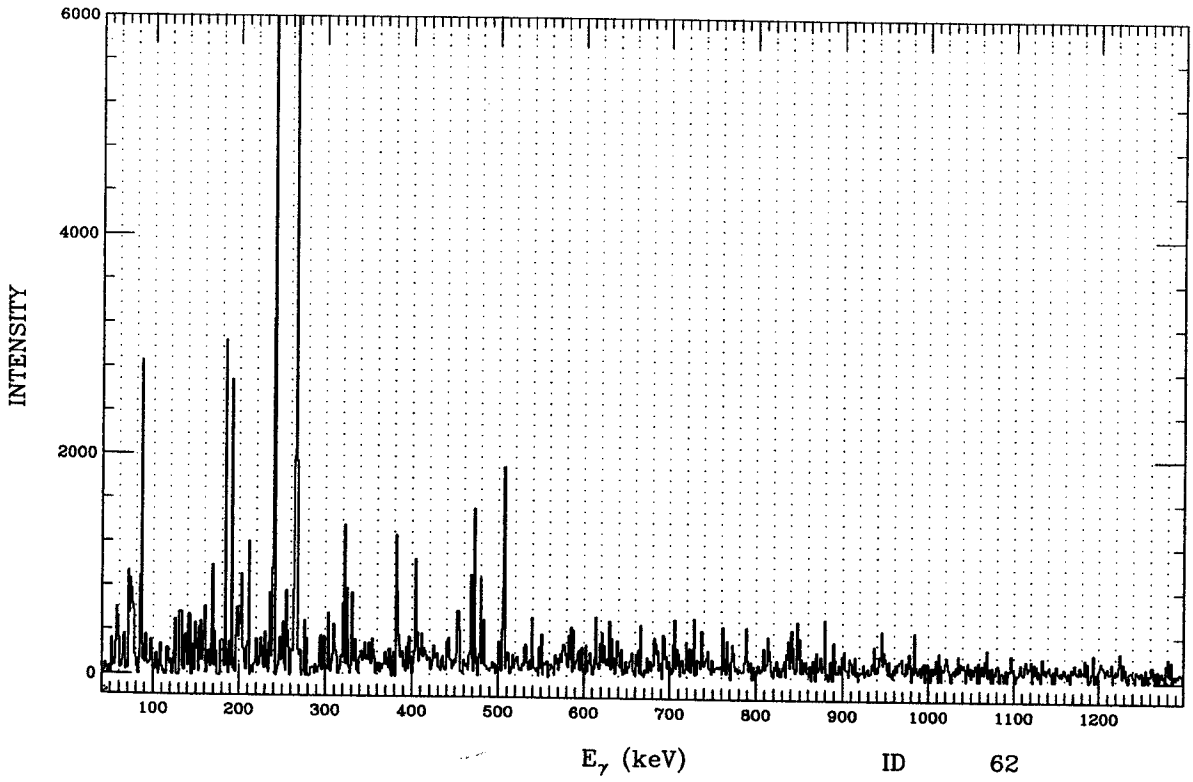

Figure E.10: ID 62. Multiple gate from ^{132}Pr, gs band.

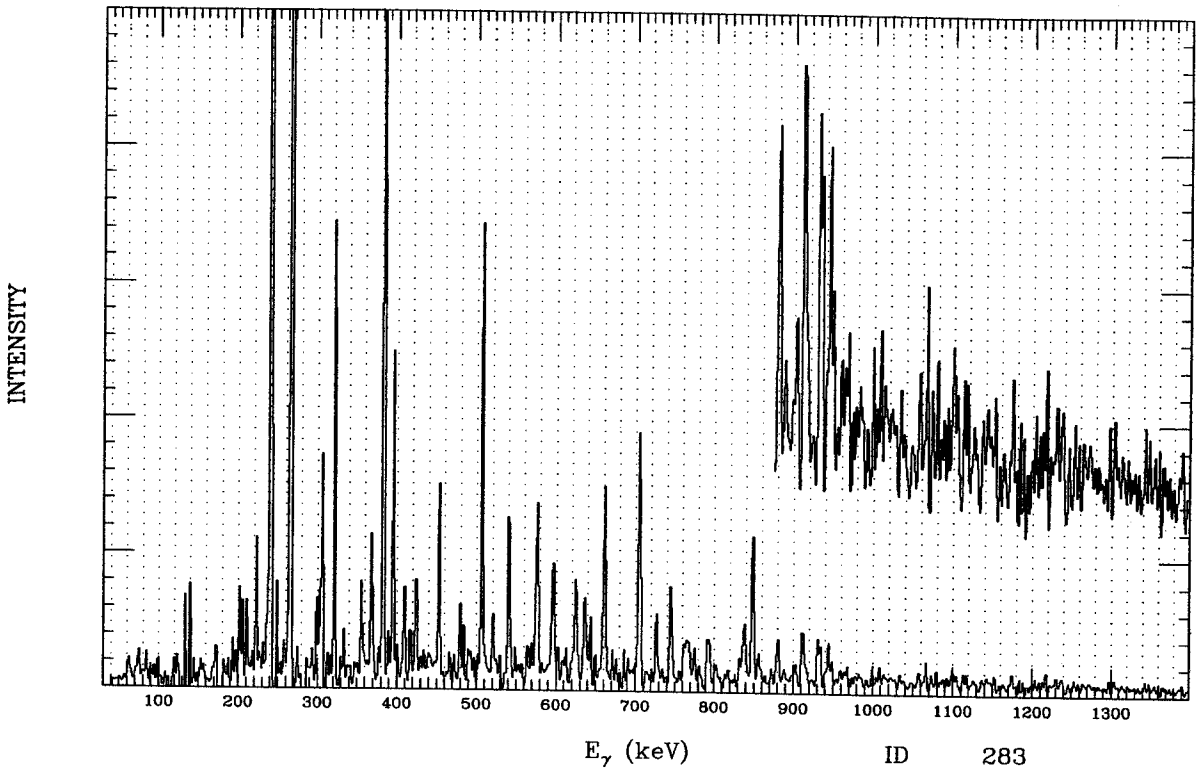

Figure E.11: ID 283. Multiple gate from ^{132}Pr, gs band.

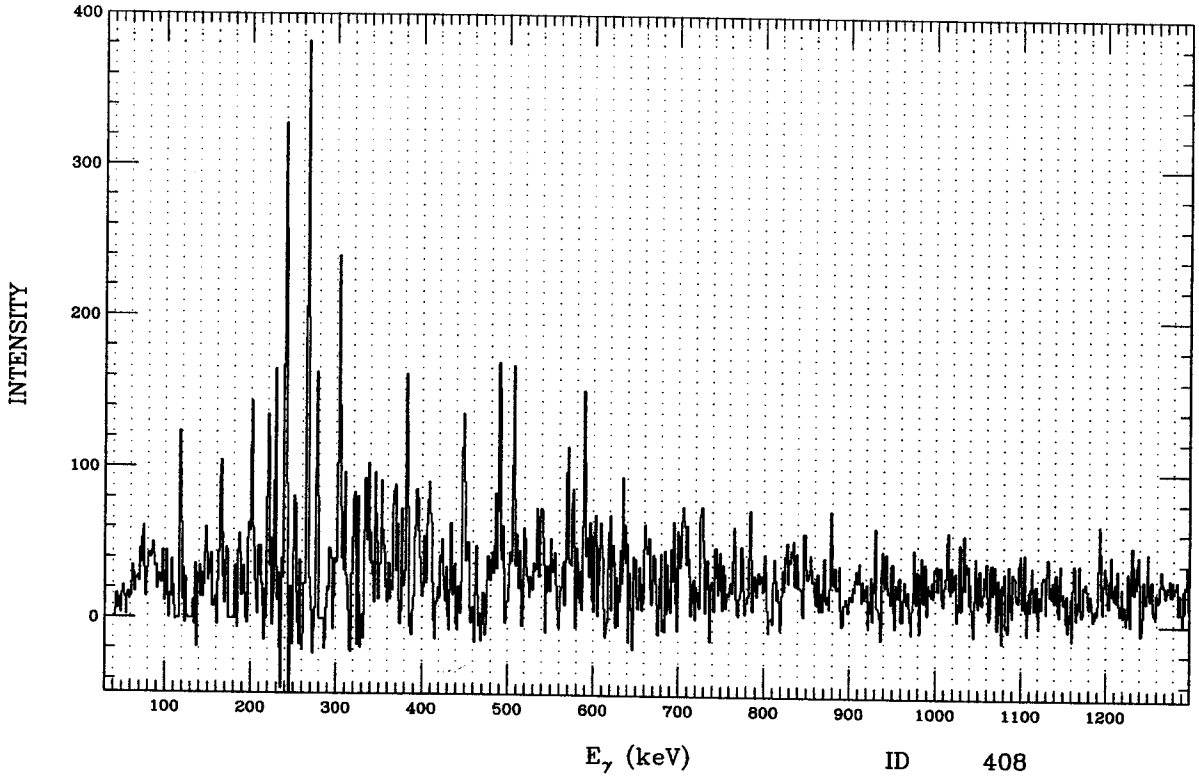

Figure E.12: ID 407. Multiple gate from ^{132}Pr, band 11.

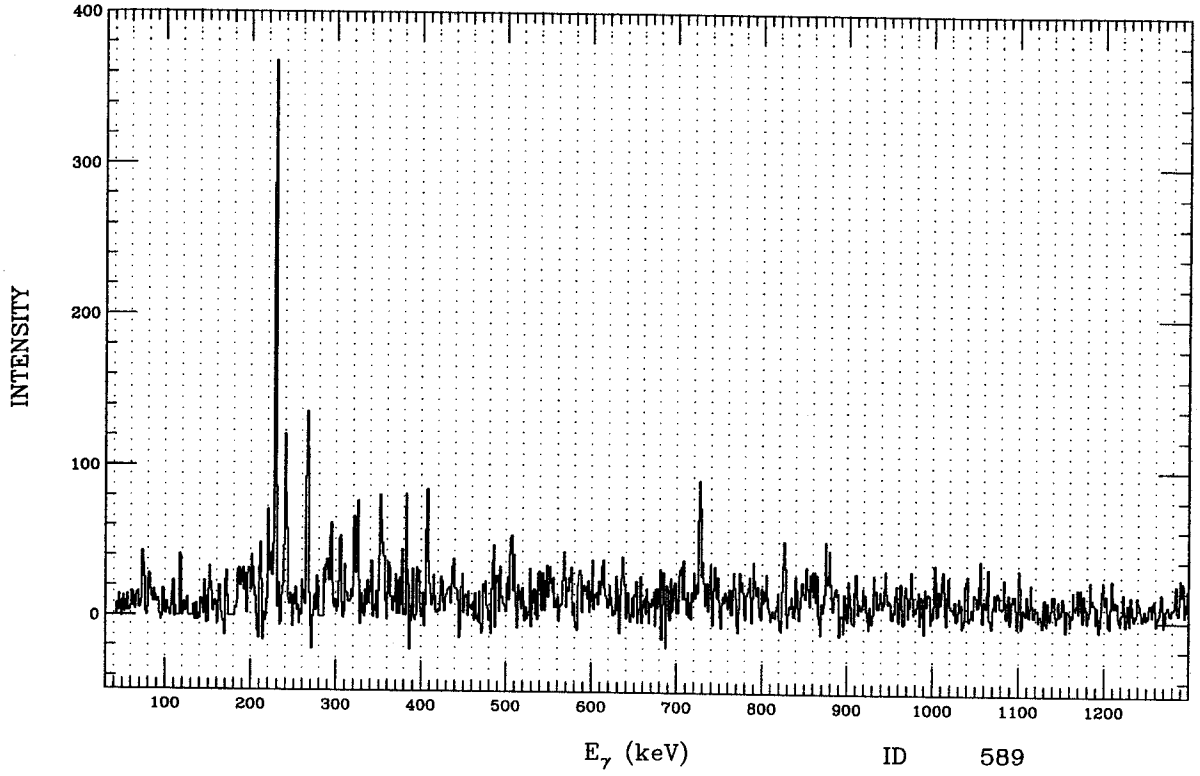

Figure E.13: ID 590. Multiple gate from ^{132}Pr, band 11.

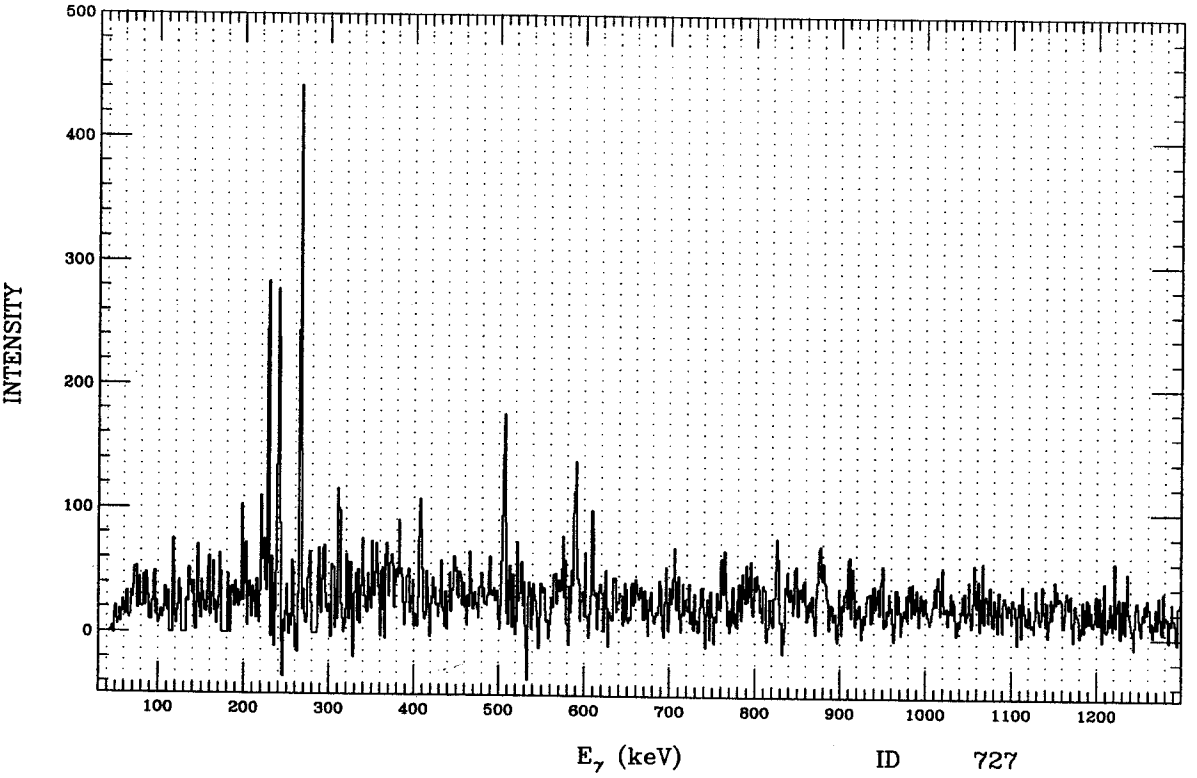

Figure E.14: ID 728. Multiple gate from ^{132}Pr, band 11.

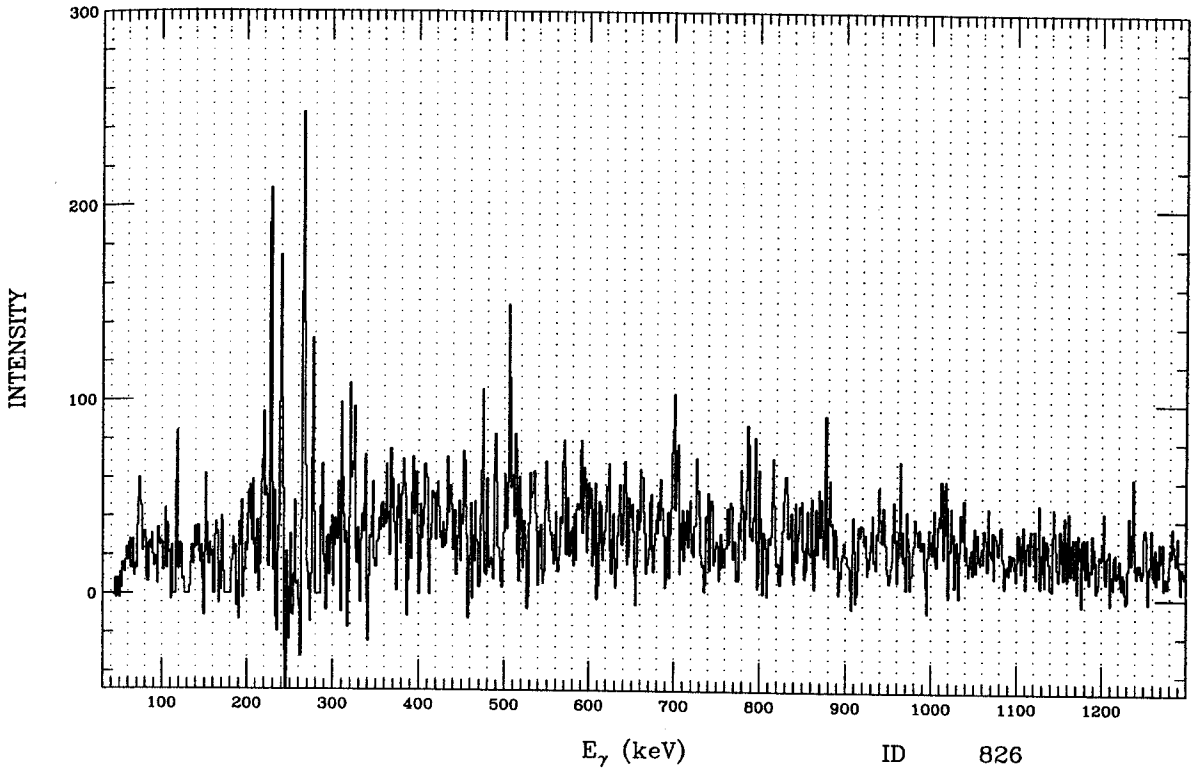

Figure E.15: ID 826. Multiple gate from ^{132}Pr, band 11.

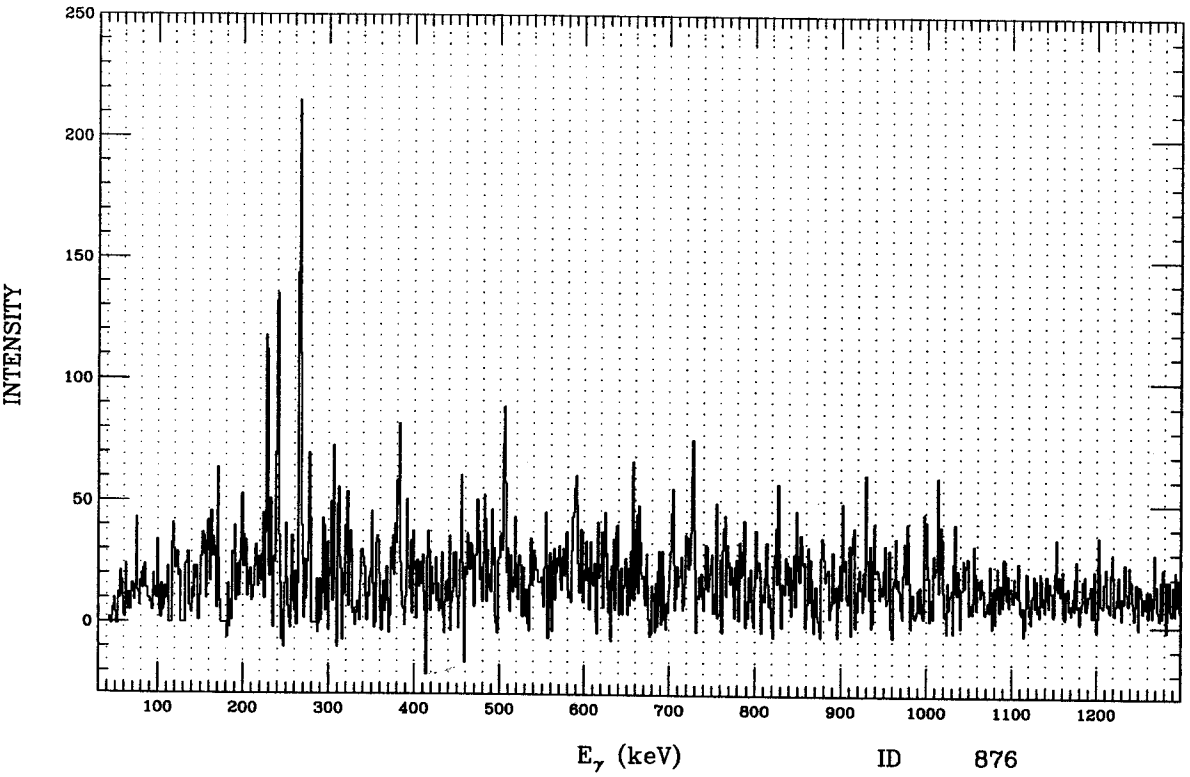

Figure E.16: ID 877. Multiple gate from ^{132}Pr, band 11.

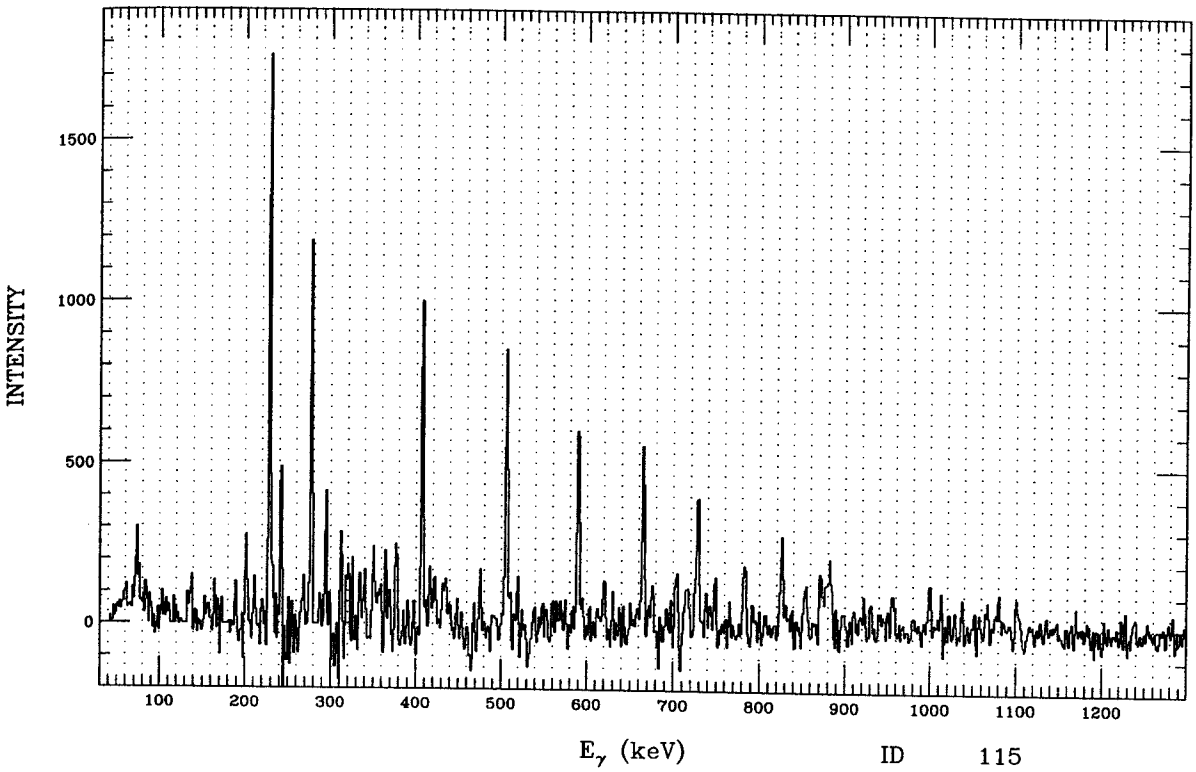

Figure E.17: ID 115. Multiple gate from ^{132}Pr, band 12.

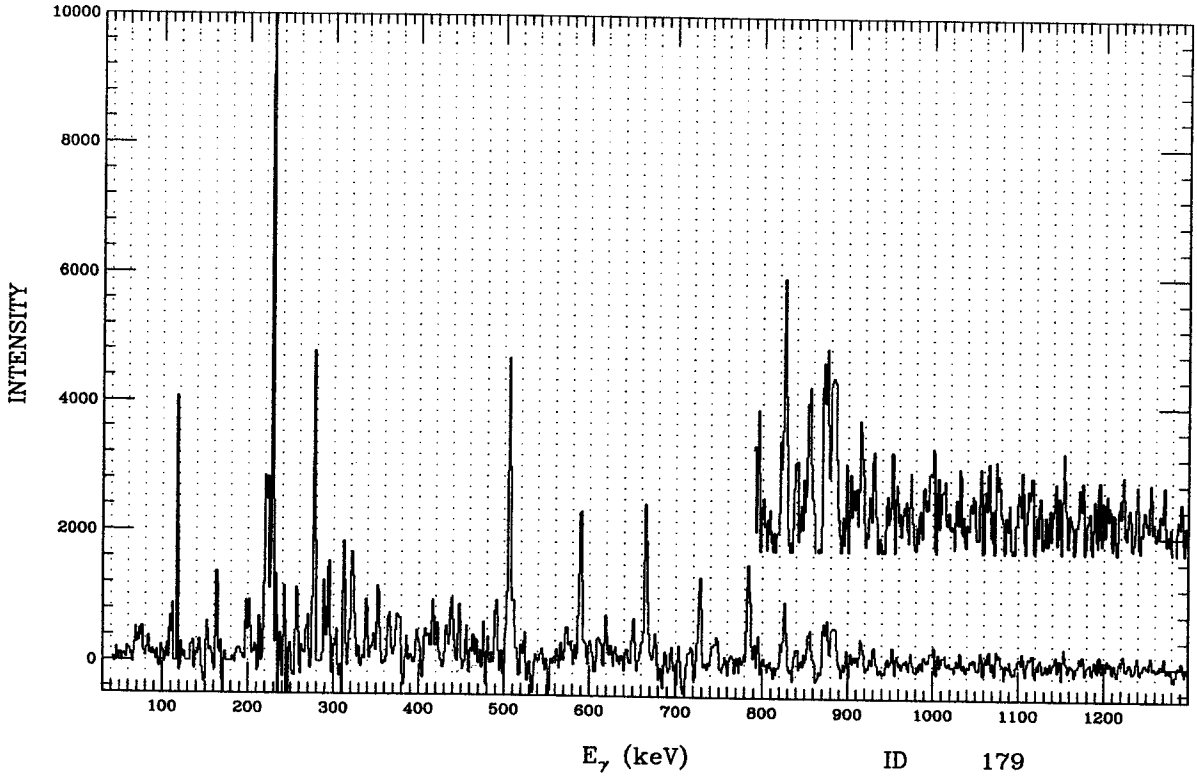

Figure E.18: ID 179. Multiple gate from ^{132}Pr, band 12.

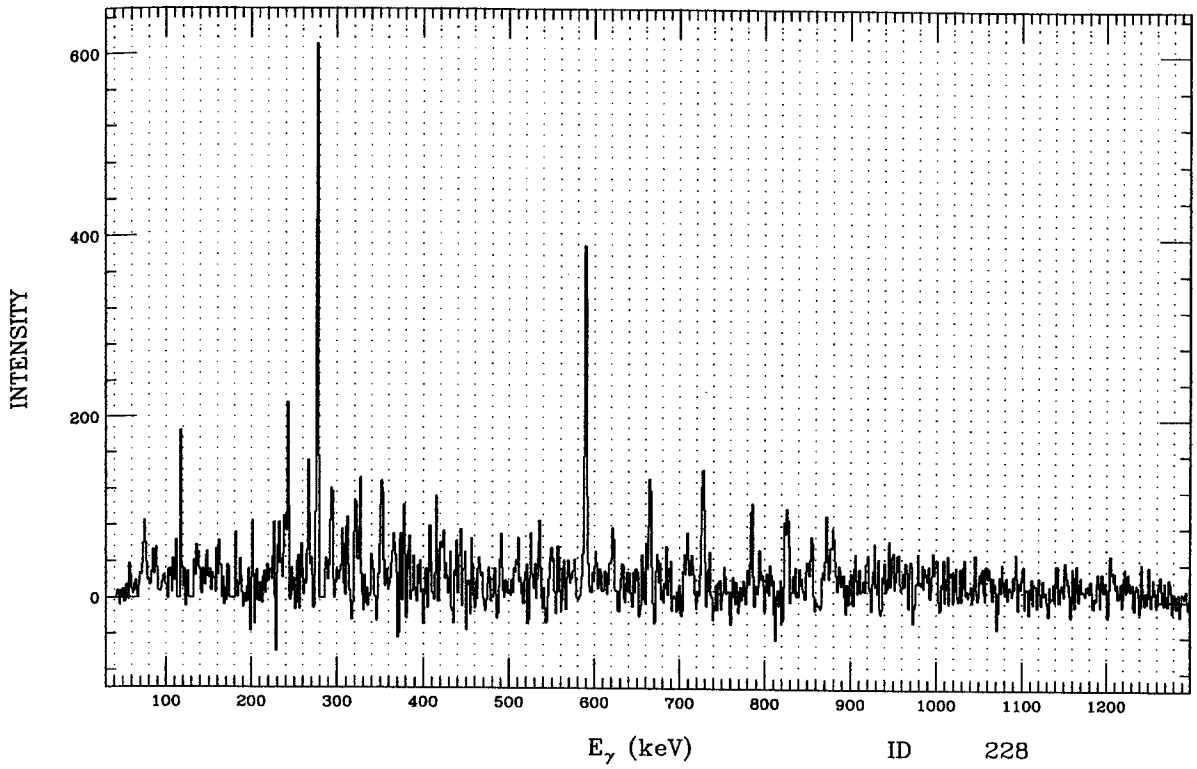

Figure E.19: ID 229. Multiple gate from ^{132}Pr, band 12.

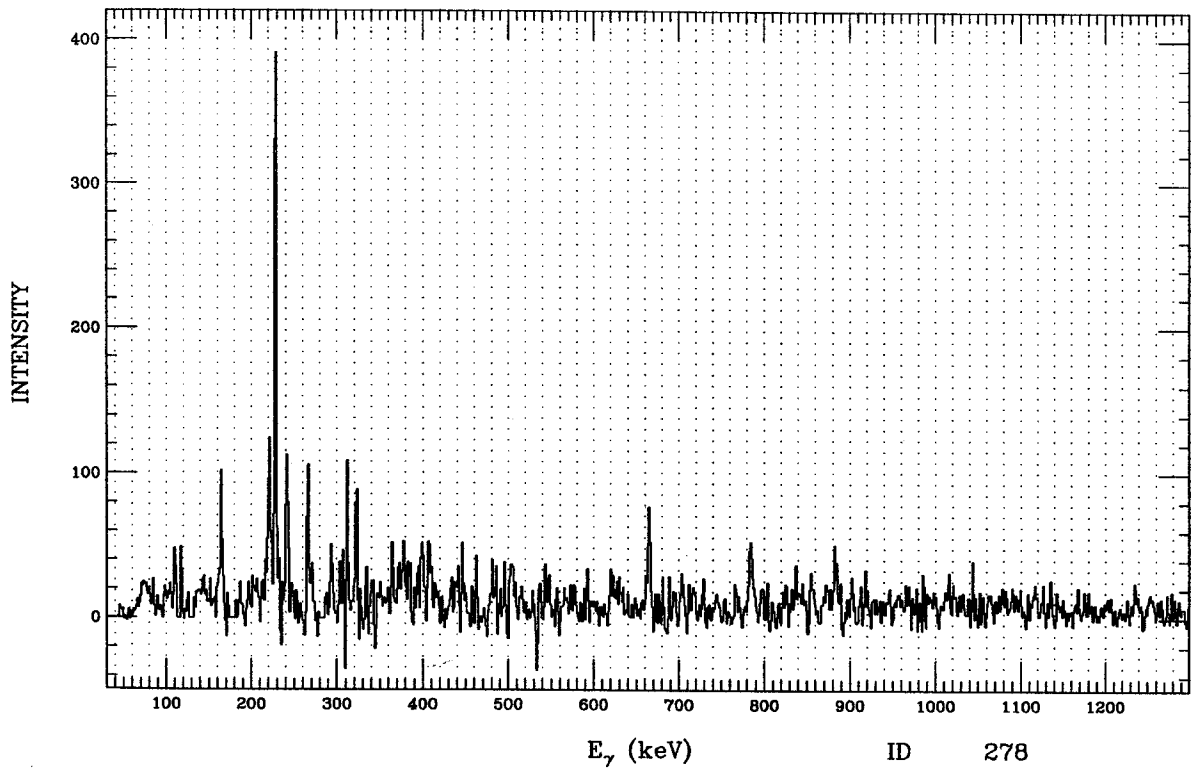

Figure E.20: ID 277. Multiple gate from ^{132}Pr, band 12.

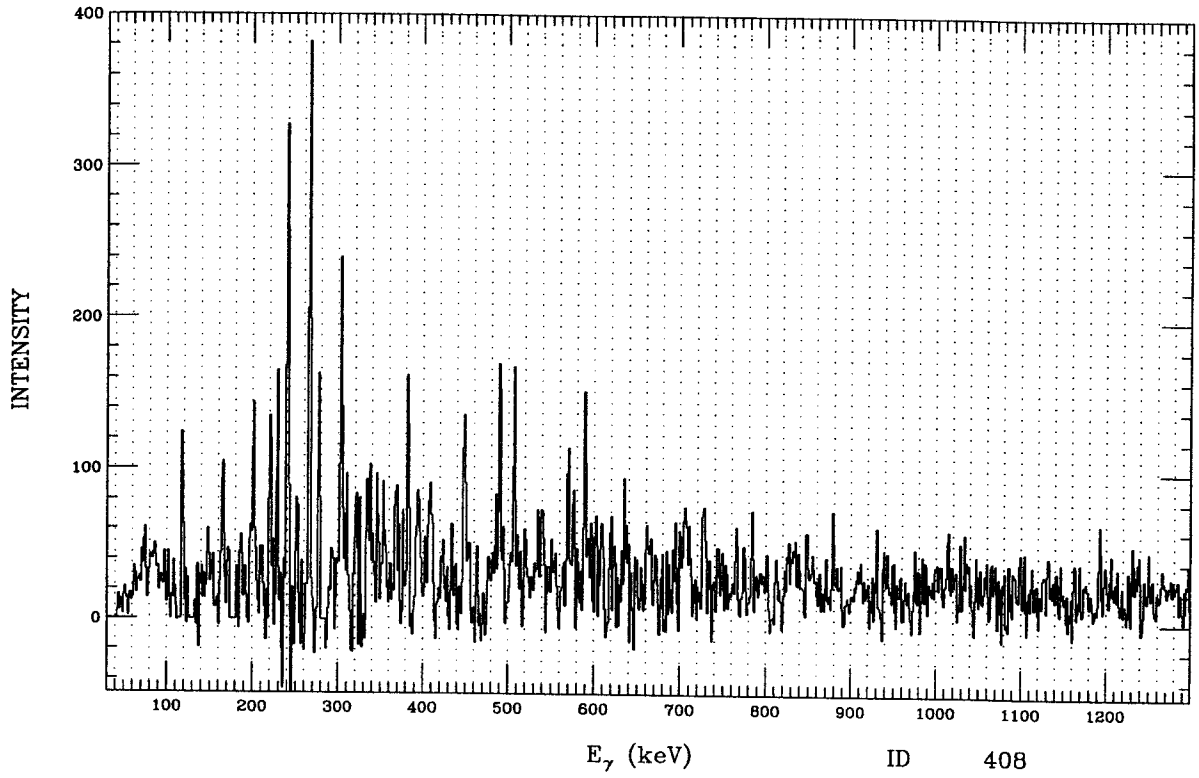

Figure E.21: ID 407. Multiple gate from ^{132}Pr, band 12.

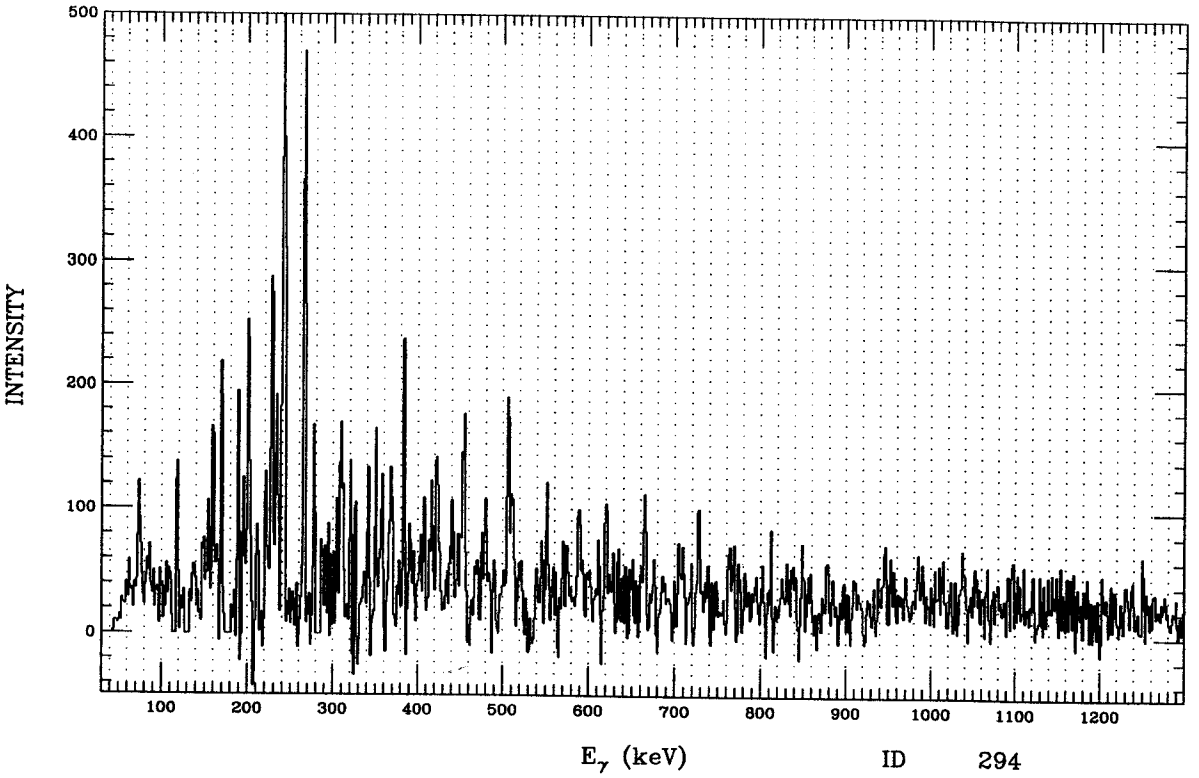

Figure E.22: ID 294. Multiple gate from ^{132}Pr, band 13.

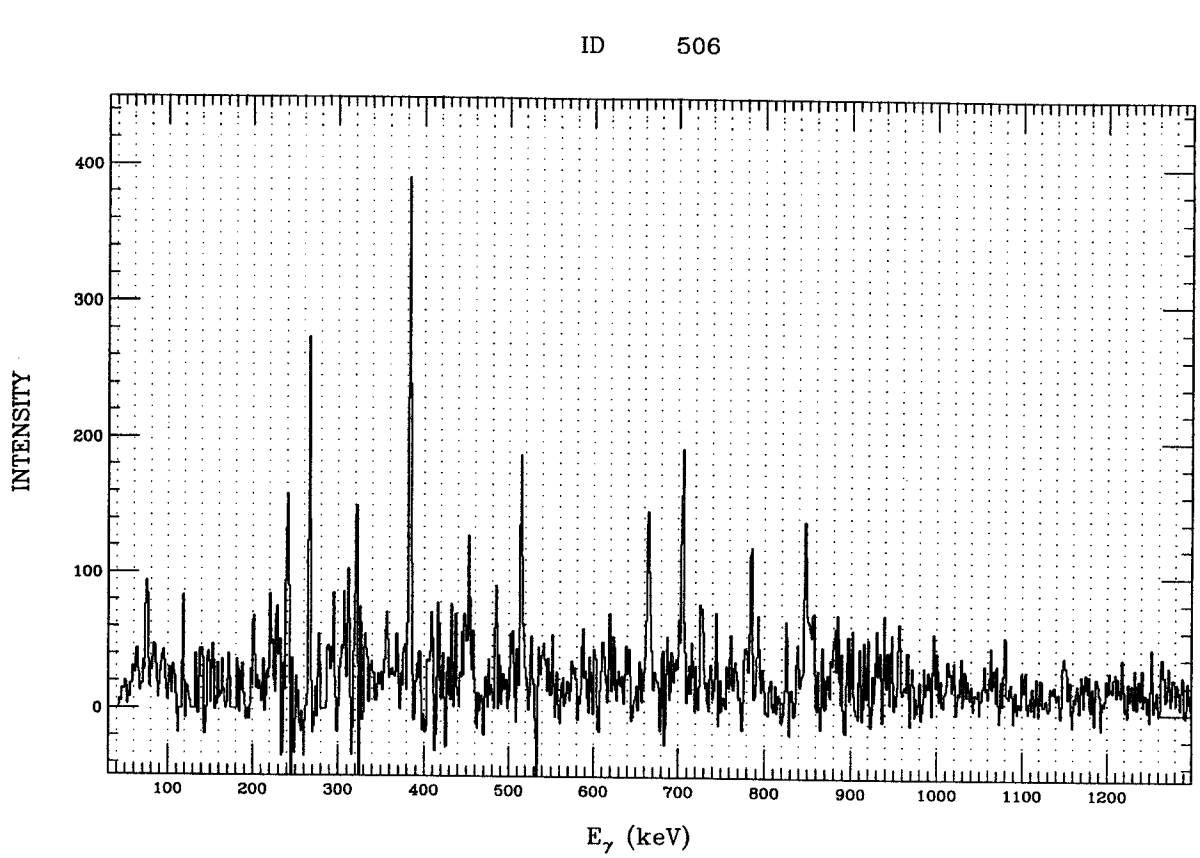

Figure E.23: ID 506. Multiple gate from ^{132}Pr, band 13.

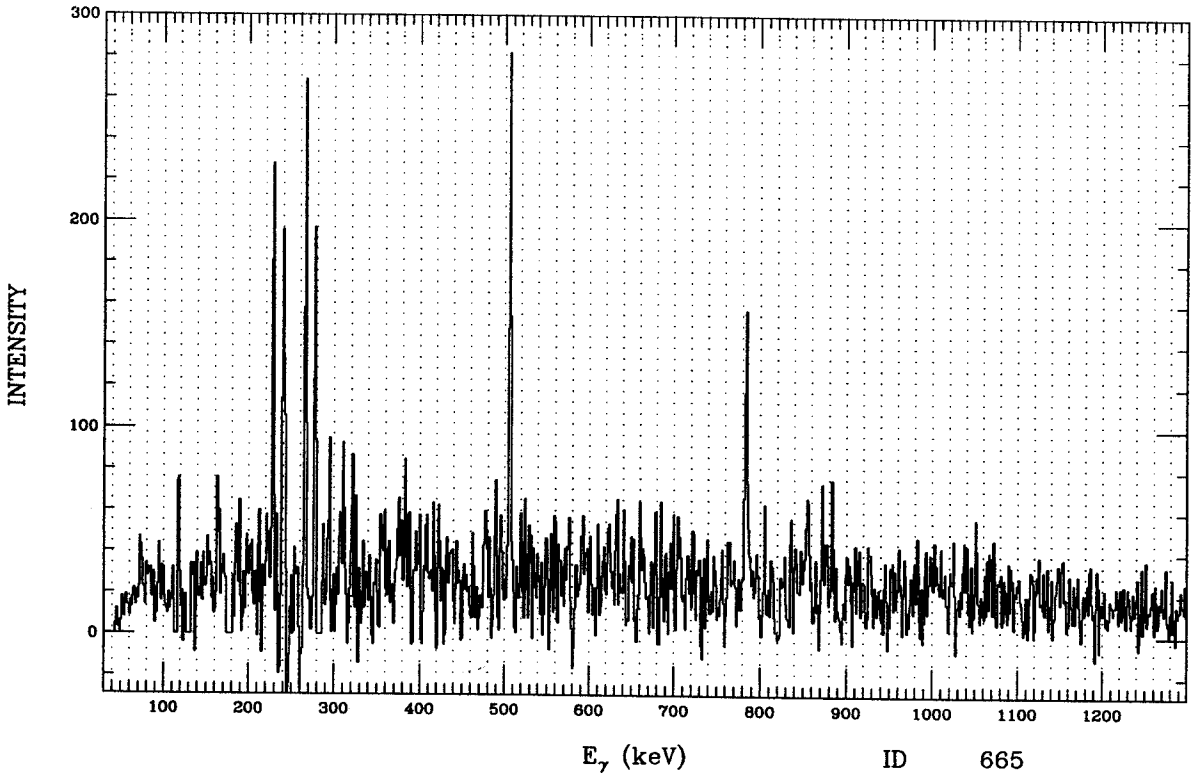

Figure E.24: ID 665. Multiple gate from ^{132}Pr, band 13.

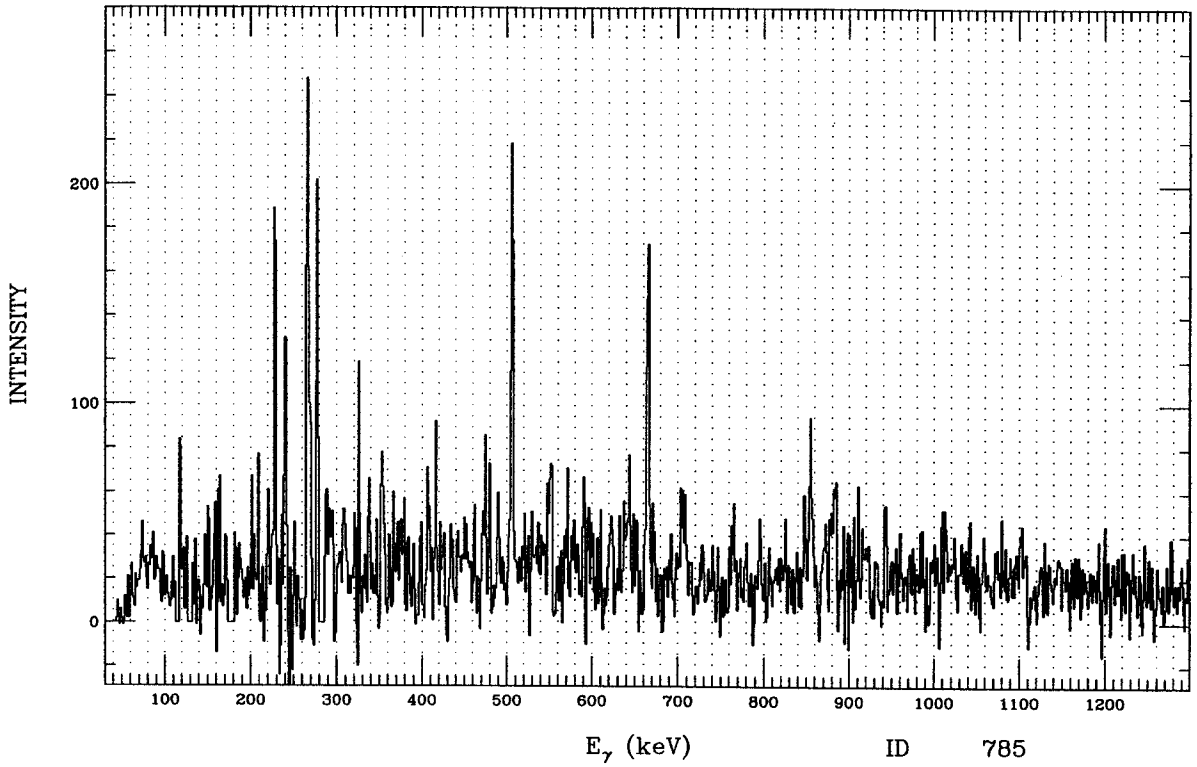

Figure E.25: ID 784. Multiple gate from ^{132}Pr, band 13.

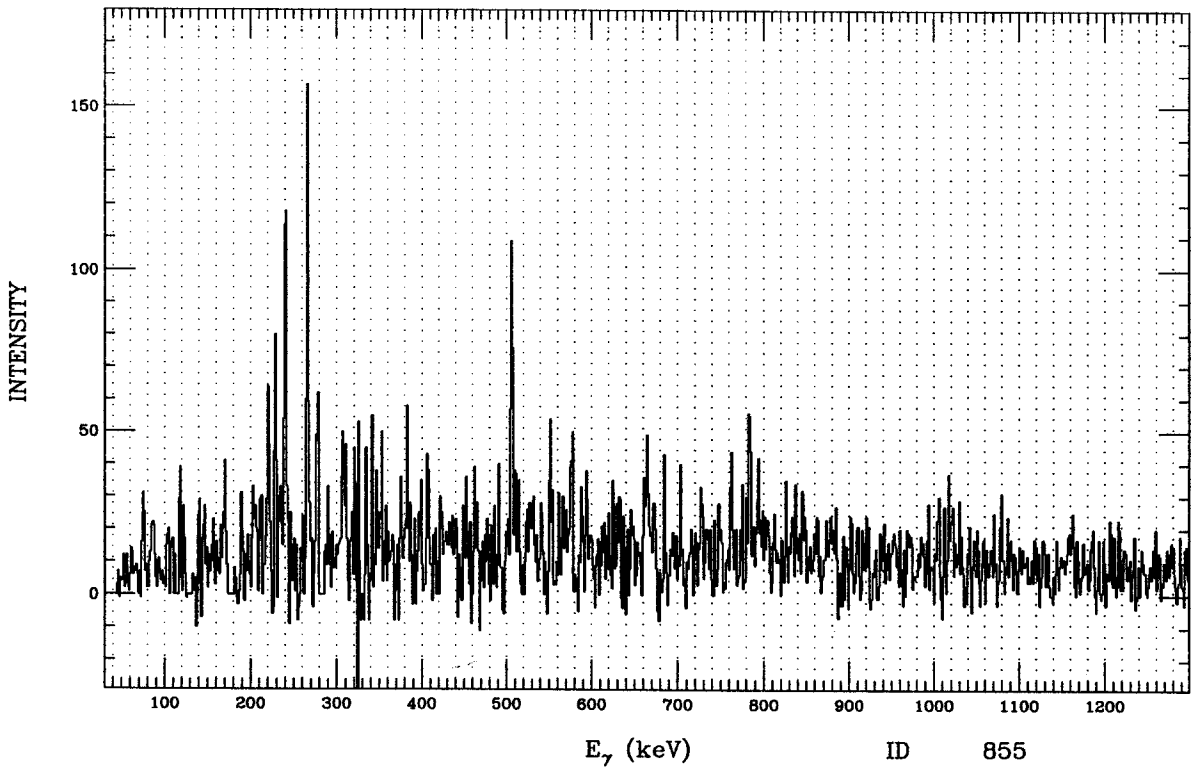

Figure E.26: ID 855. Multiple gate from ^{132}Pr, band 13.

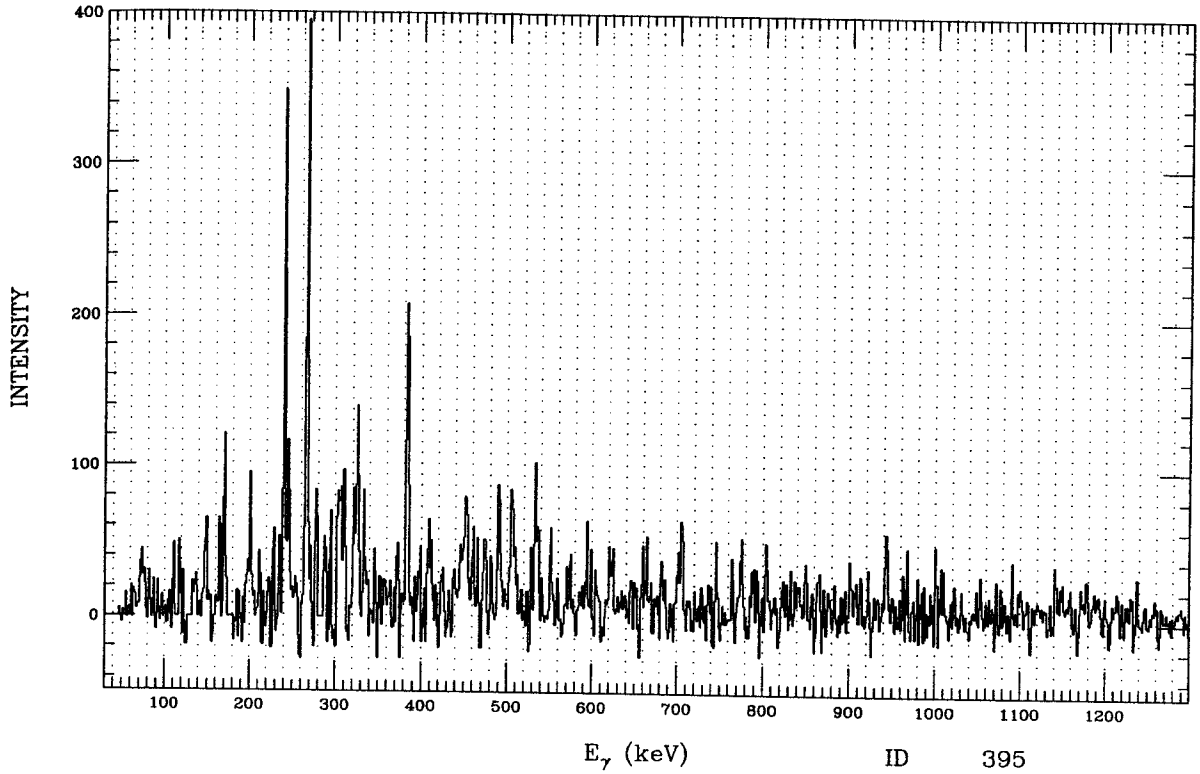

Figure E.27: ID 396. Multiple gate from ^{132}Pr, band 21.

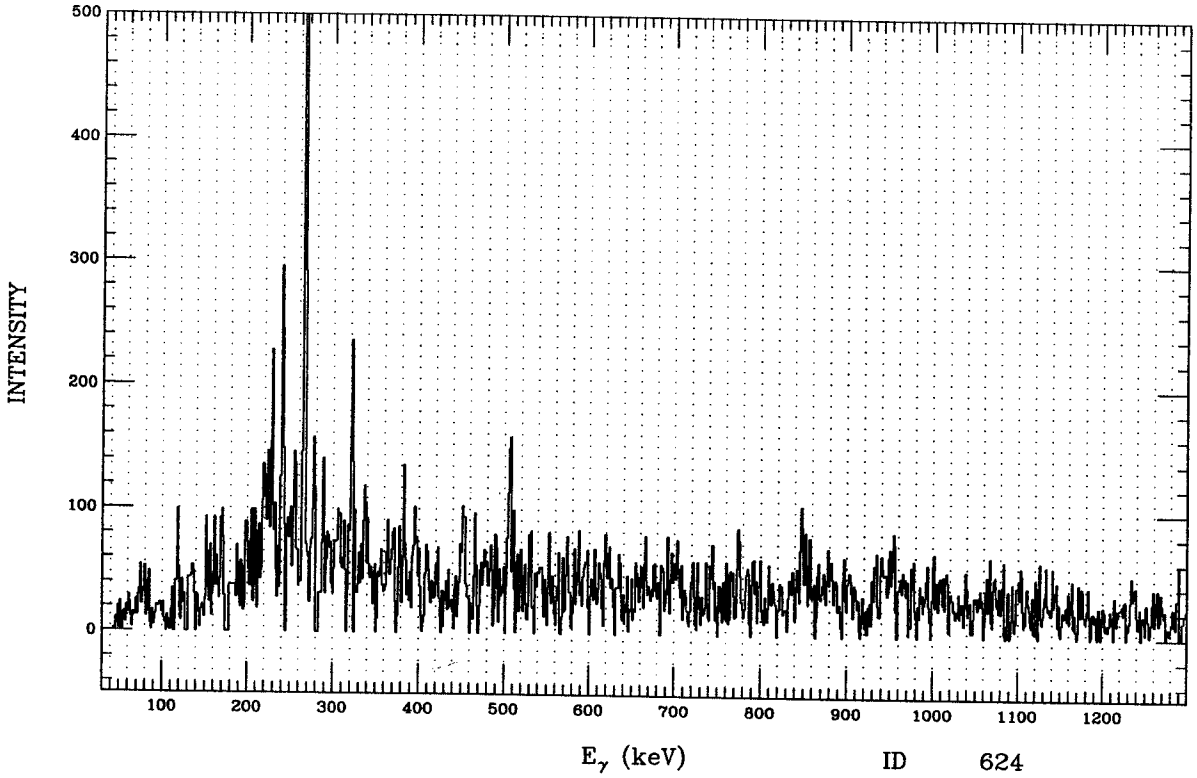

Figure E.28: ID 624. Multiple gate from ^{132}Pr, band 21.

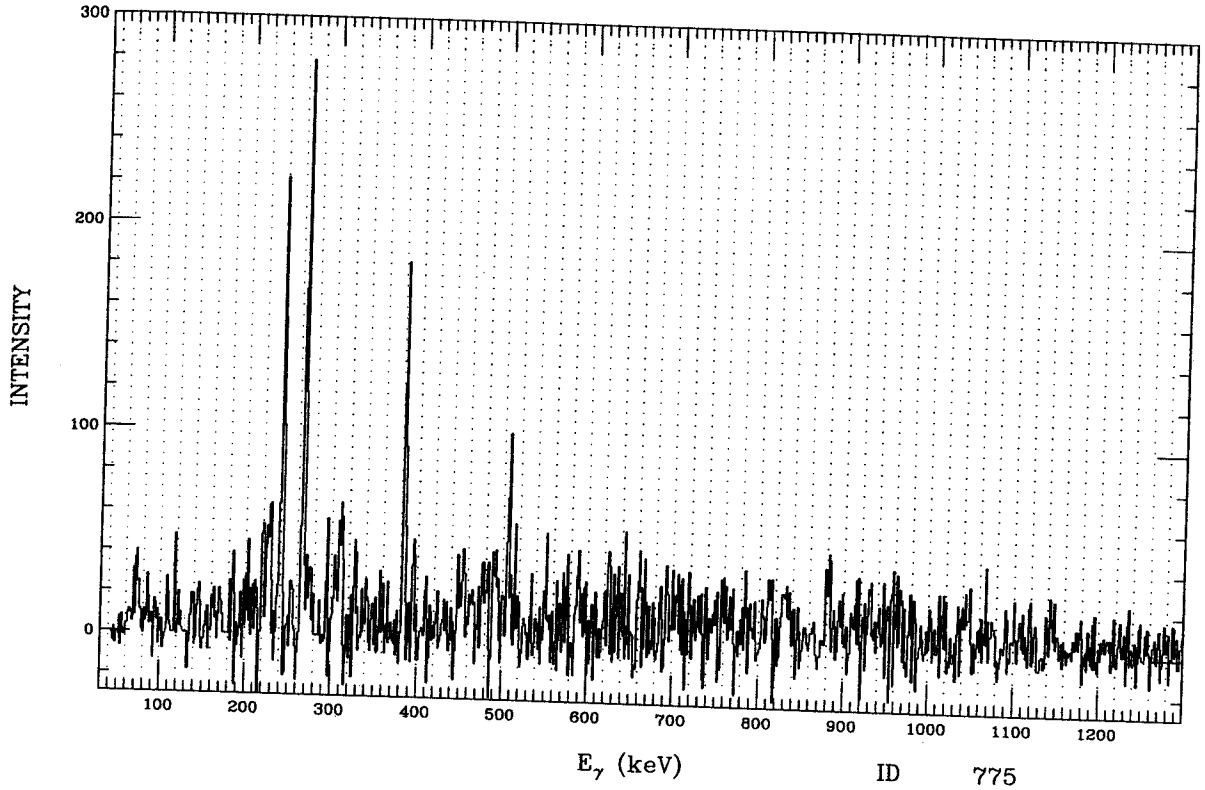

Figure E.29: ID 775. Multiple gate from ^{132}Pr, band 21.

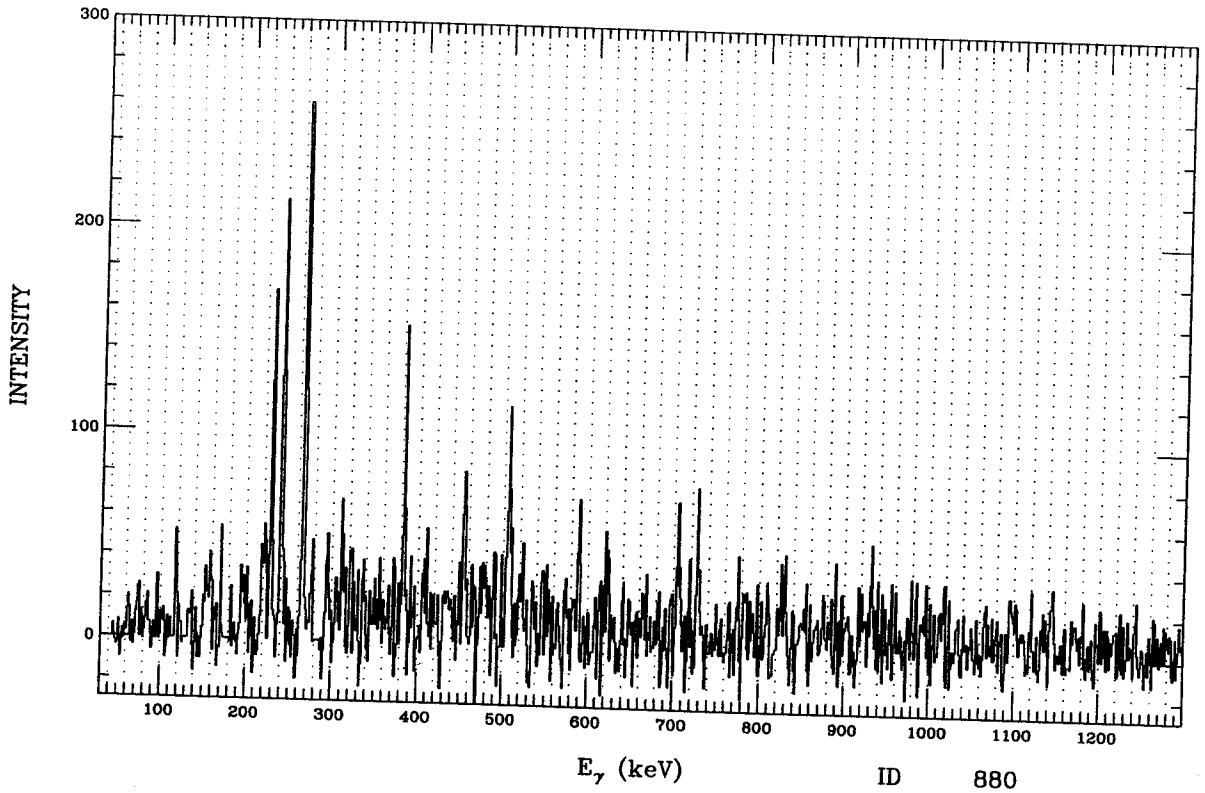

Figure E.30: ID 880. Multiple gate from ^{132}Pr, band 21.

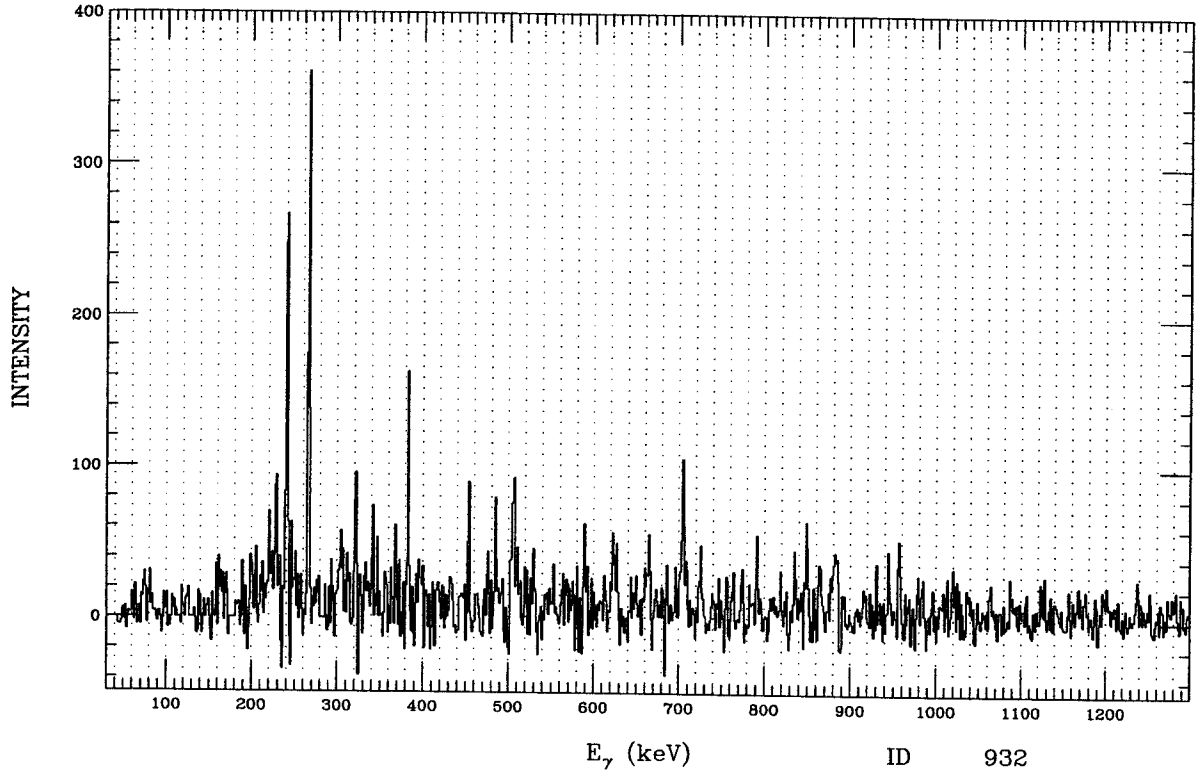

Figure E.31: ID 934. Multiple gate from ^{132}Pr, band 21.

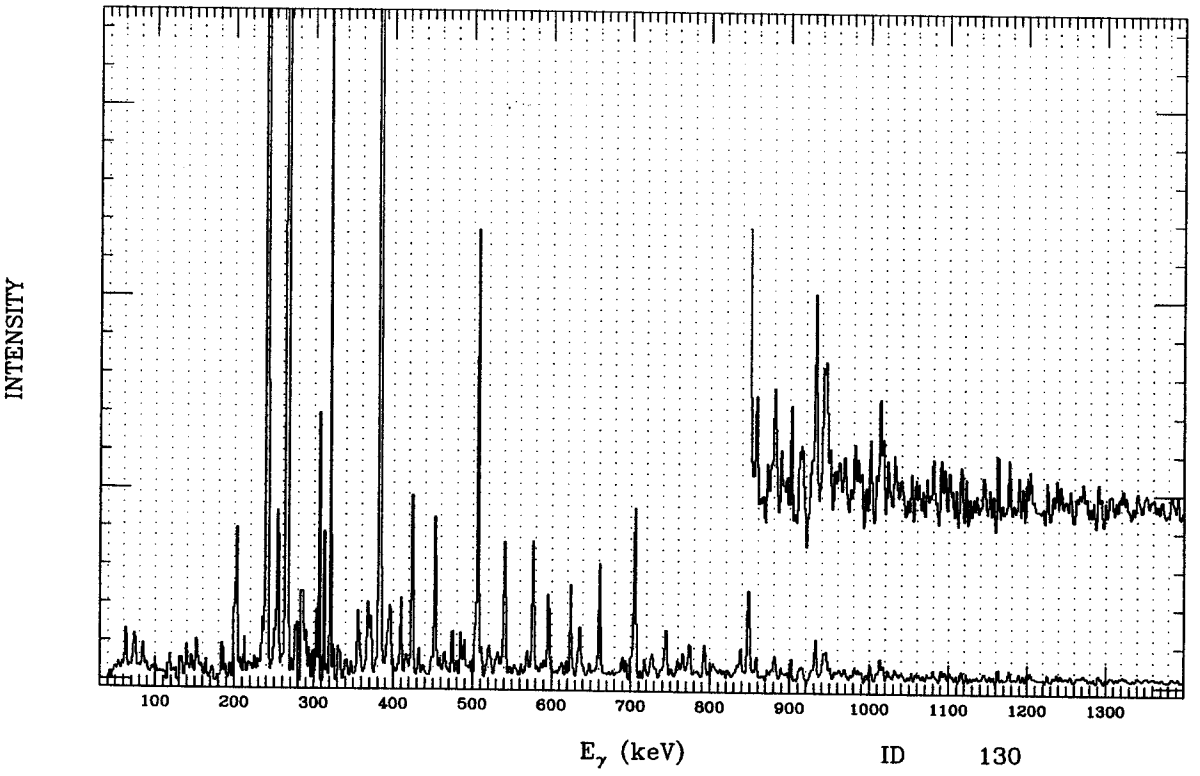

Figure E.32: ID 130. Multiple gate from ^{132}Pr, band 22.

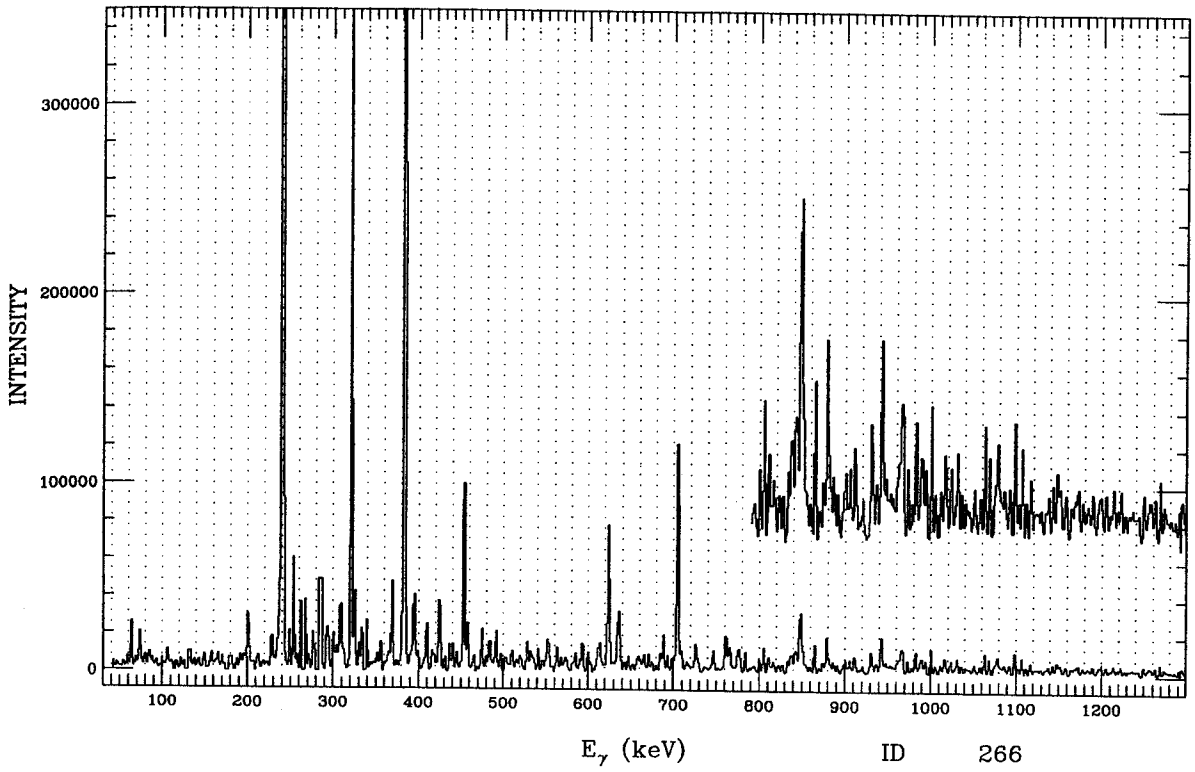

Figure E.33: ID 266. Multiple gate from ^{132}Pr, band 22.

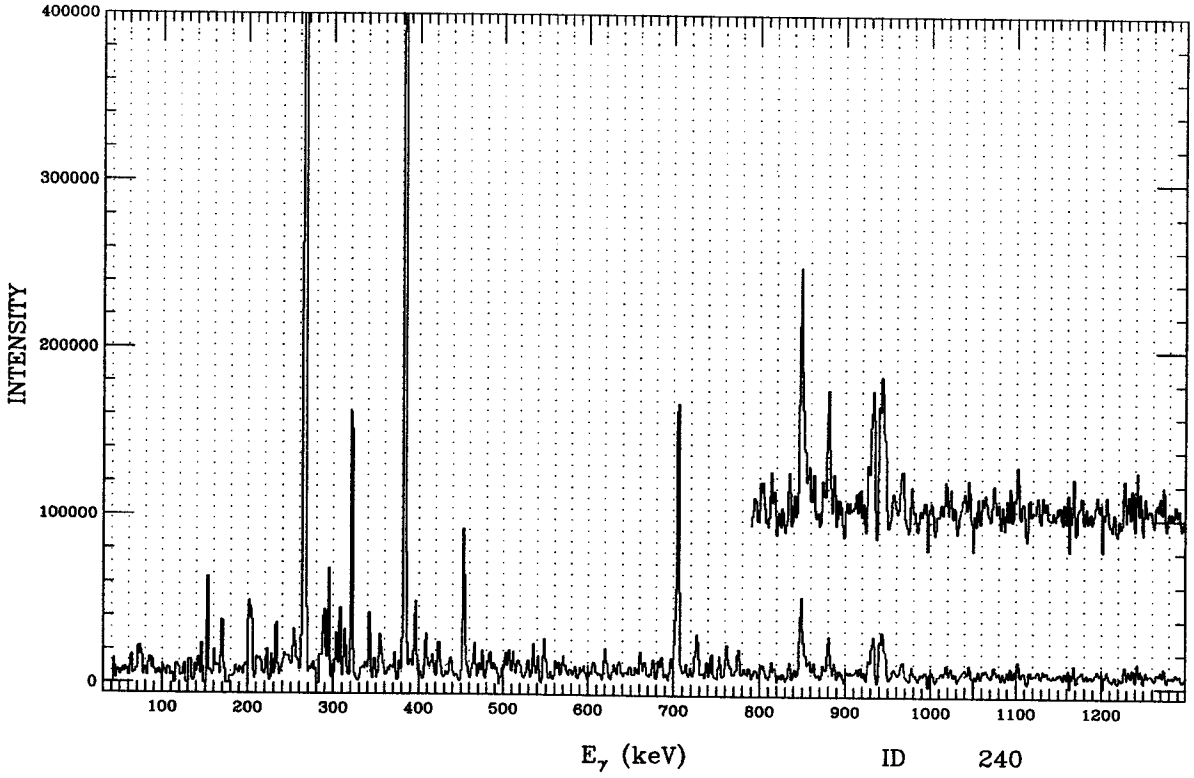

Figure E.34: ID 240. Multiple gate from ^{132}Pr, band 22.

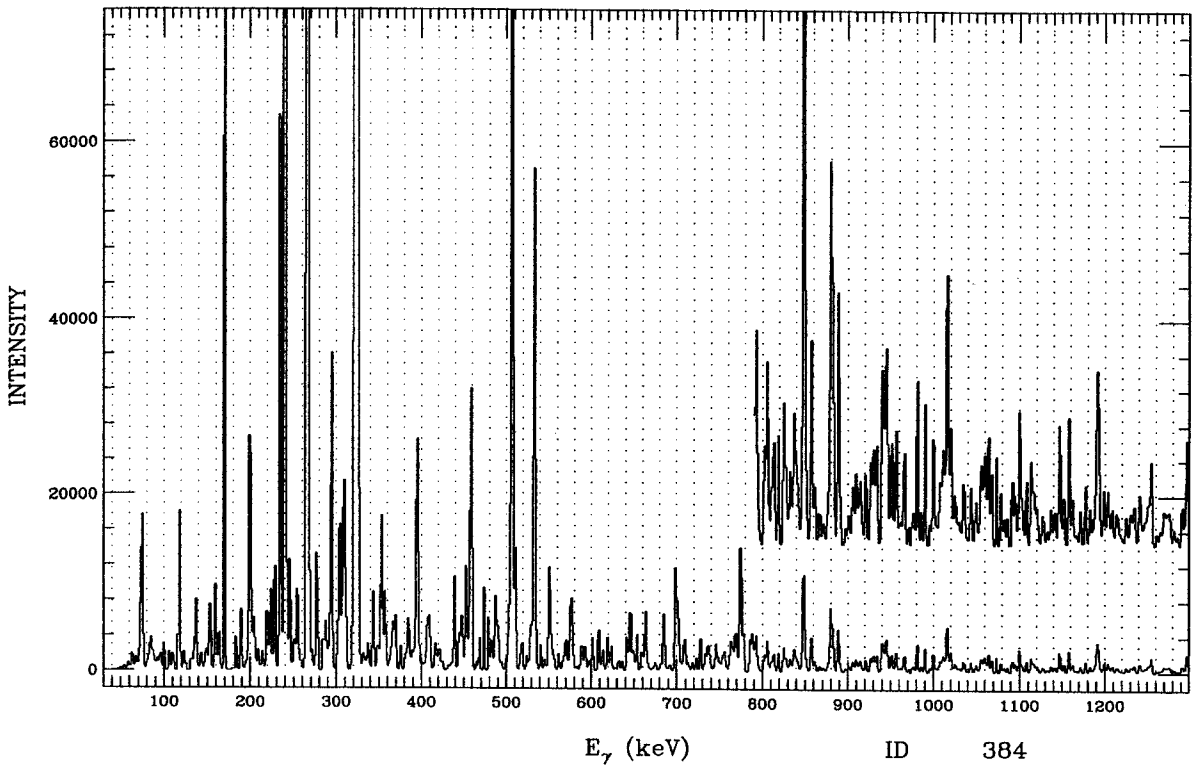

Figure E.35: ID 384. Multiple gate from ^{132}Pr, band 22.

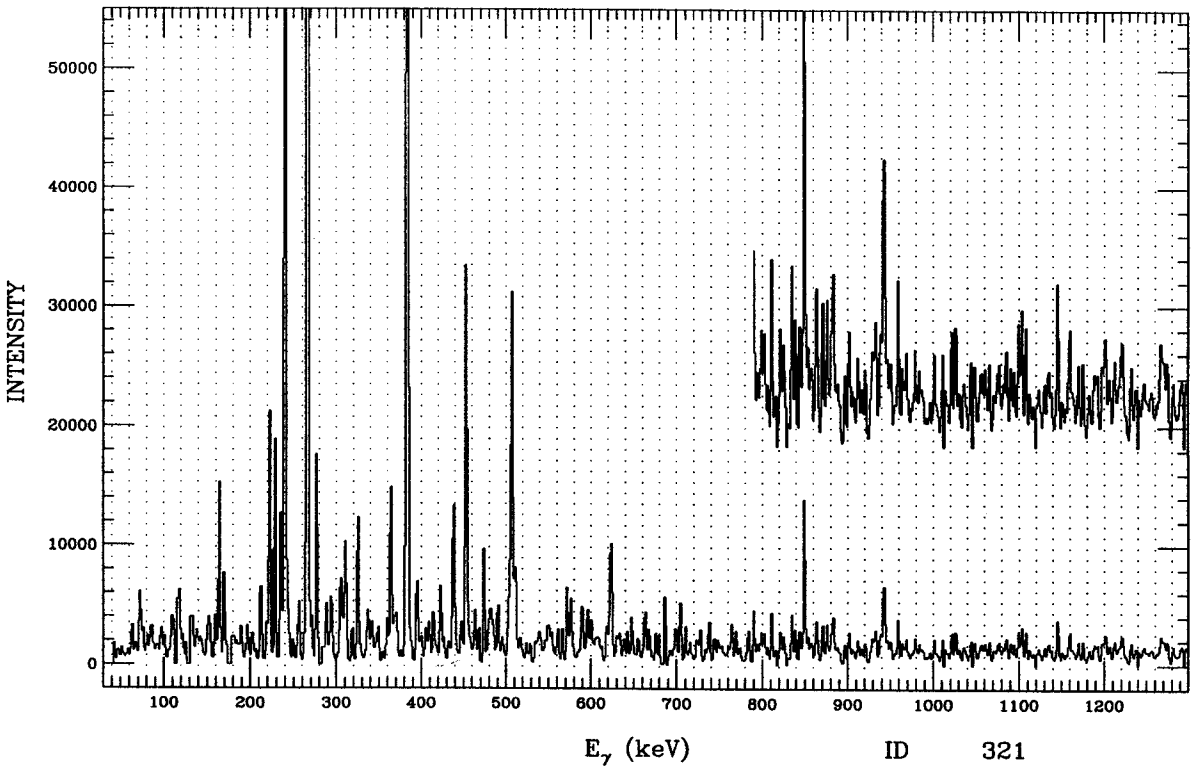

Figure E.36: ID 321. Multiple gate from ^{132}Pr, band 22.

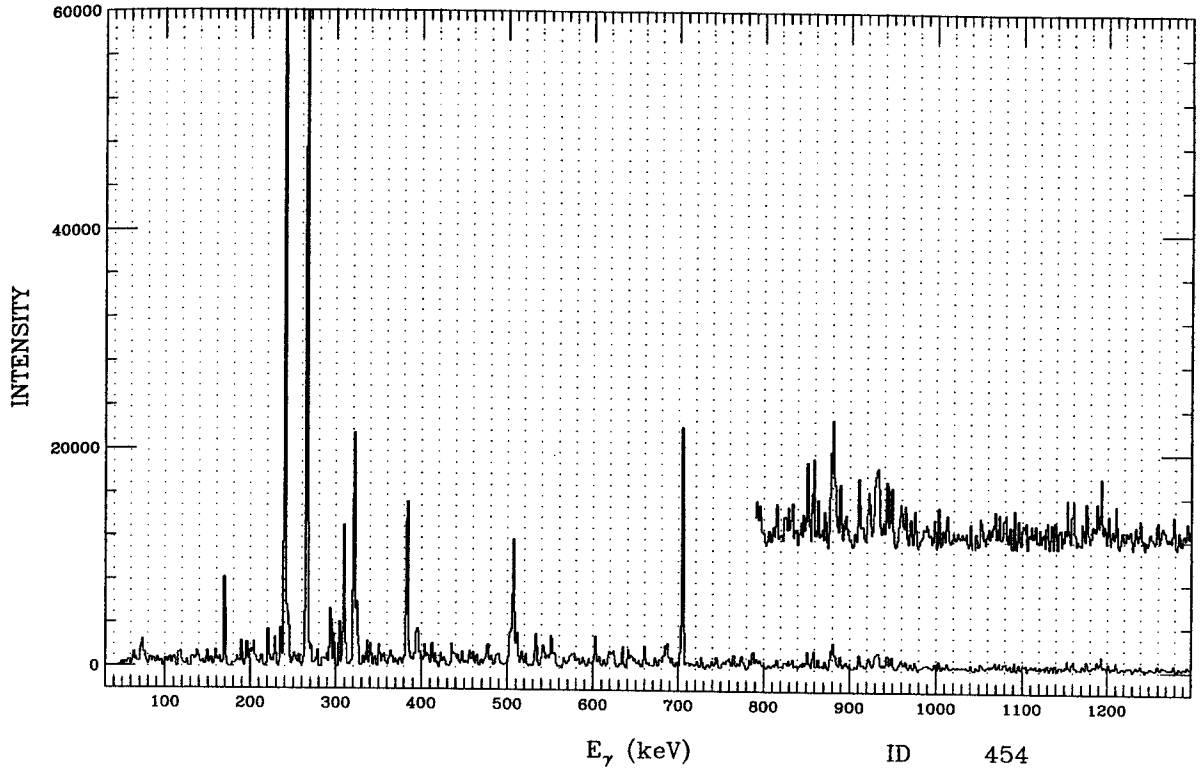

Figure E.37: ID 453. Multiple gate from ^{132}Pr, band 22.

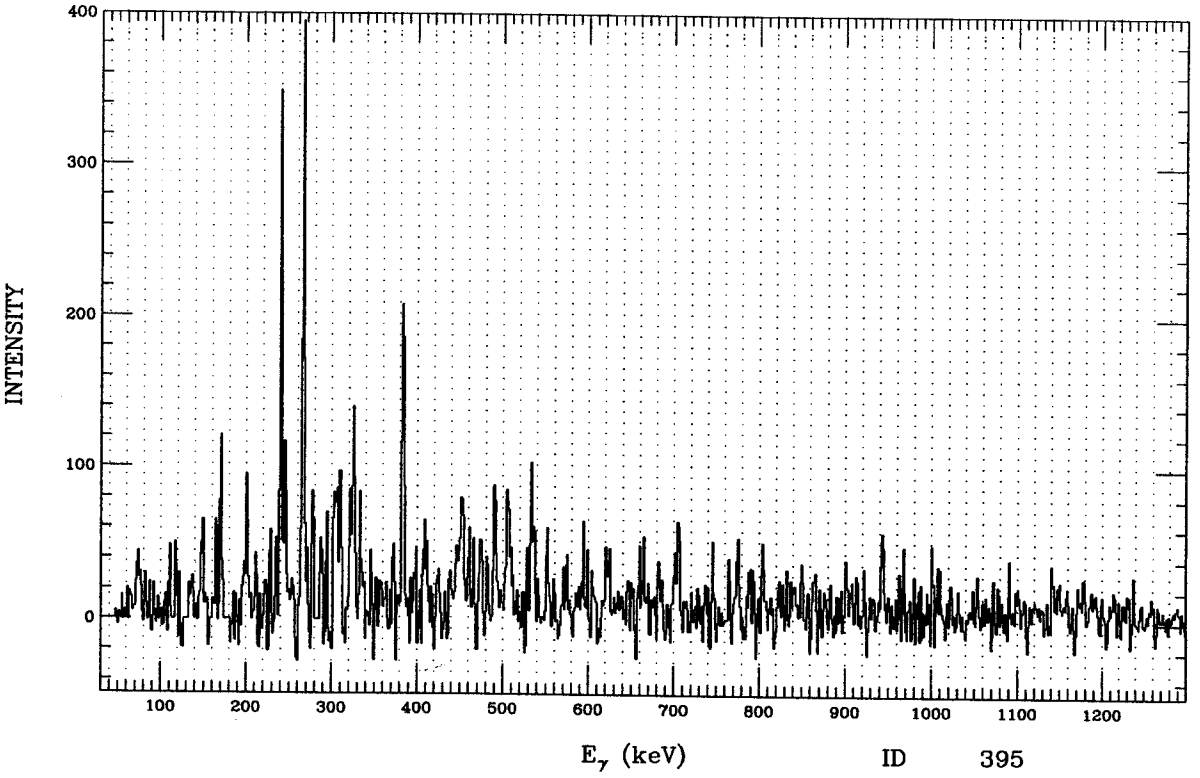

Figure E.38: ID 396. Multiple gate from ^{132}Pr, band 22.

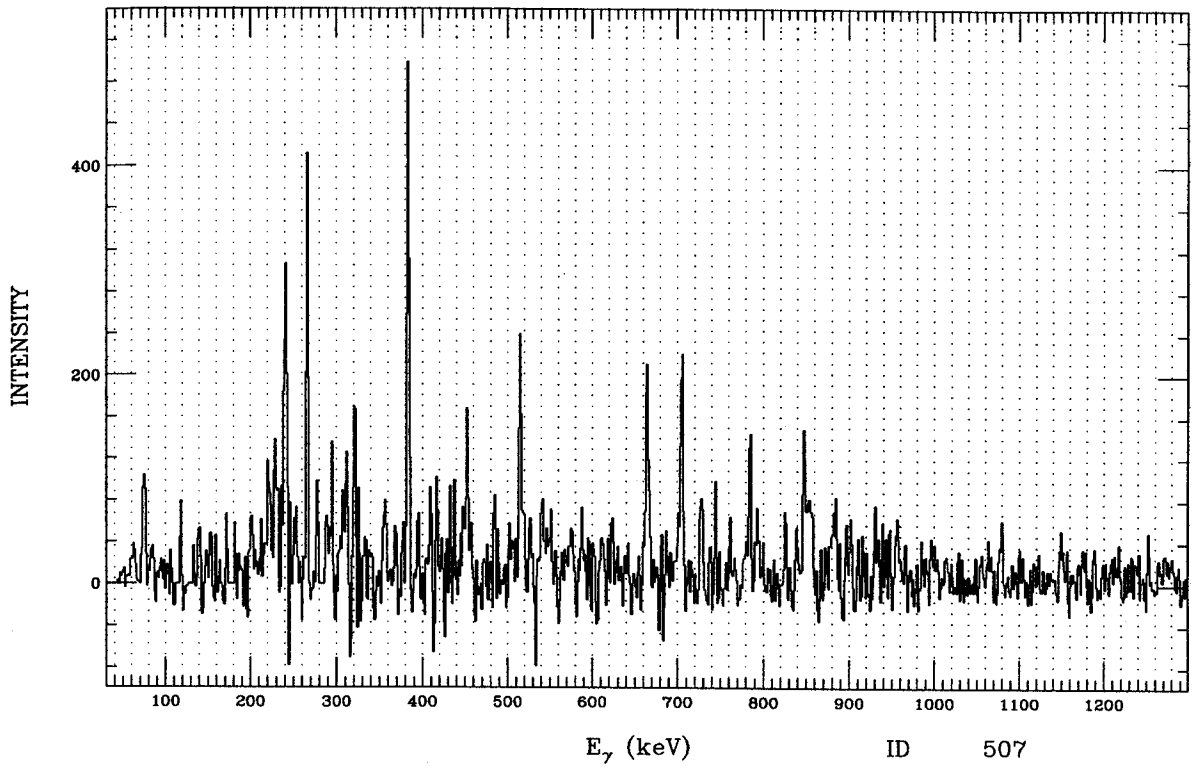

Figure E.39: ID 507. Multiple gate from ^{132}Pr, band 23.

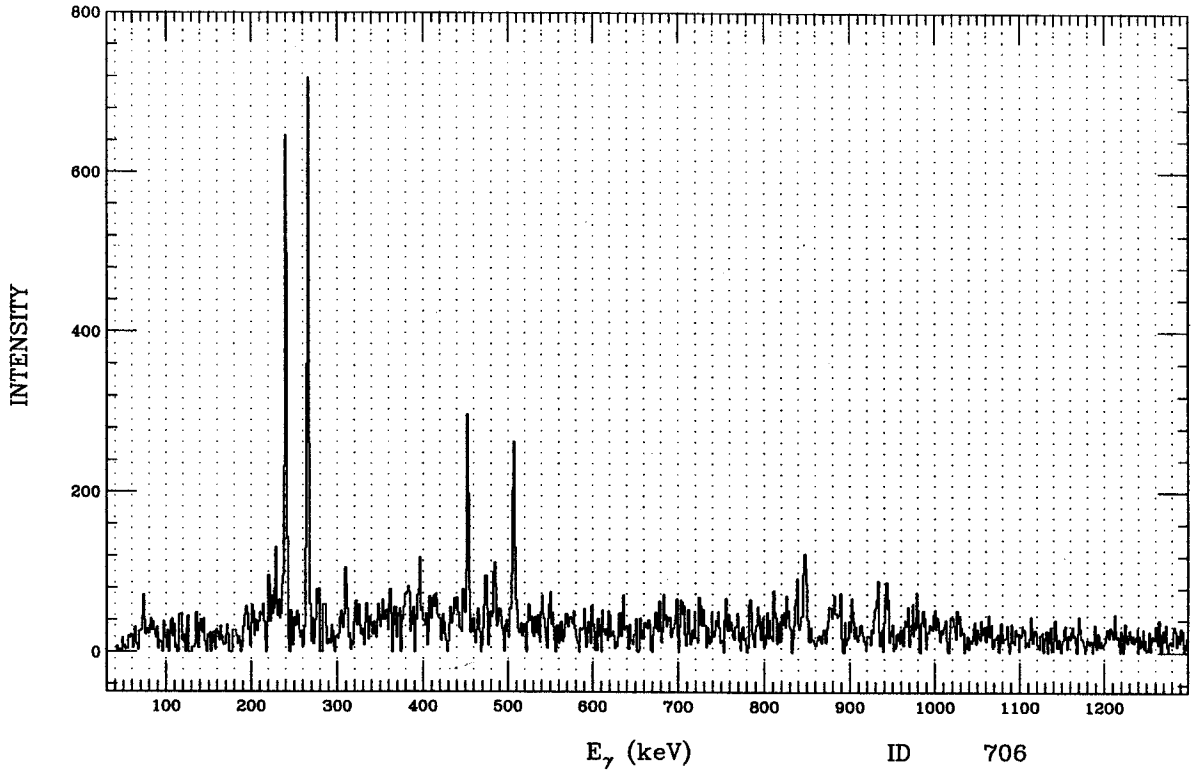

Figure E.40: ID 705. Multiple gate from ^{132}Pr, band 23.

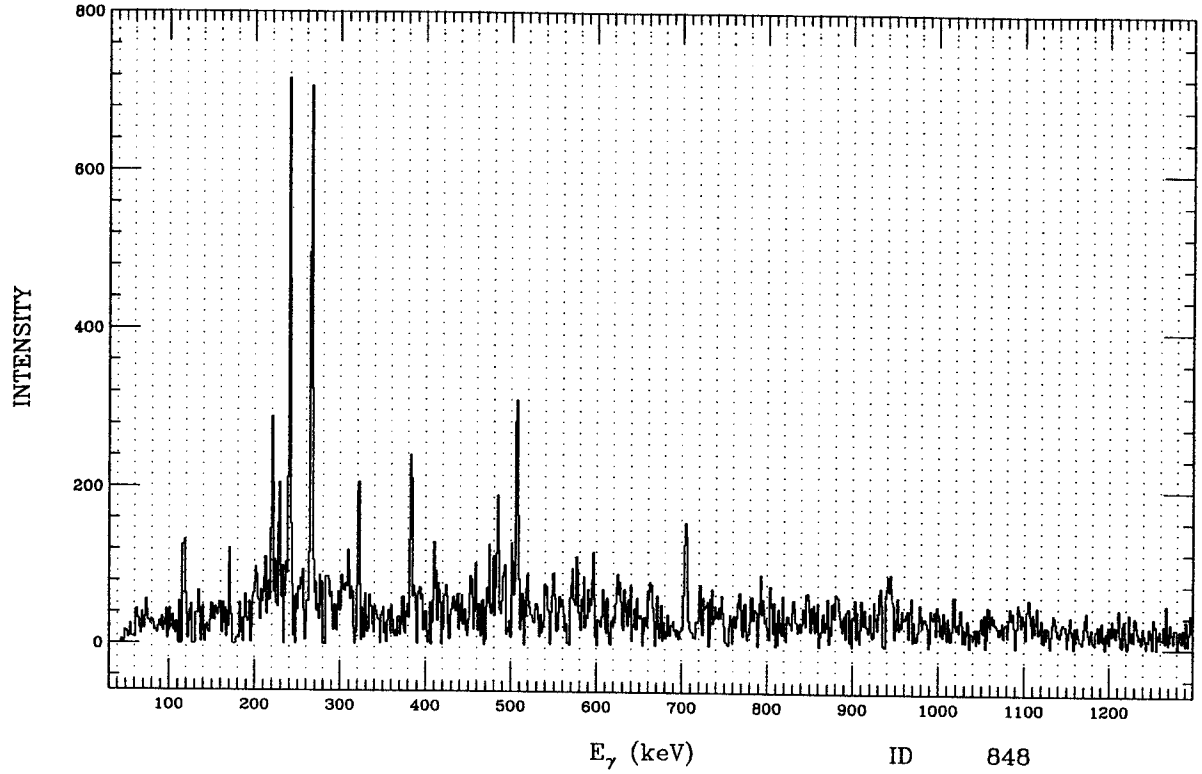

Figure E.41: ID 848. Multiple gate from ^{132}Pr, band 23.

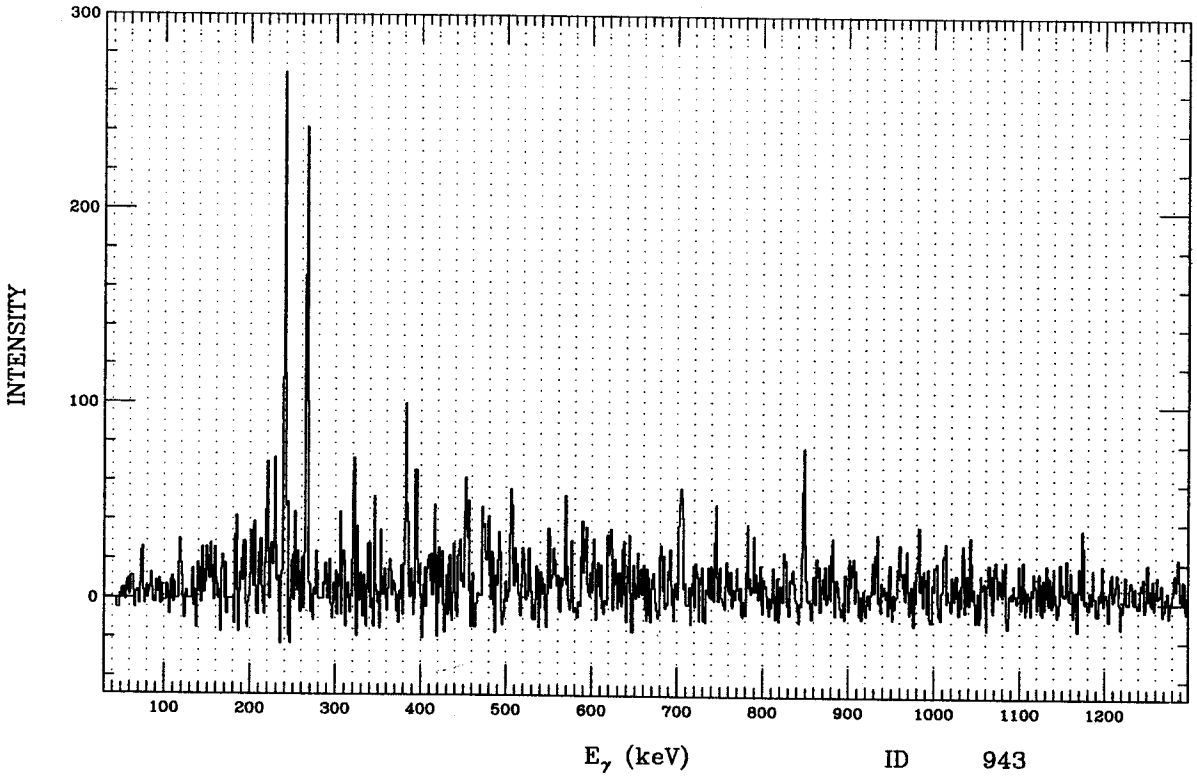

Figure E.42: ID 943. Multiple gate from ^{132}Pr, band 23.

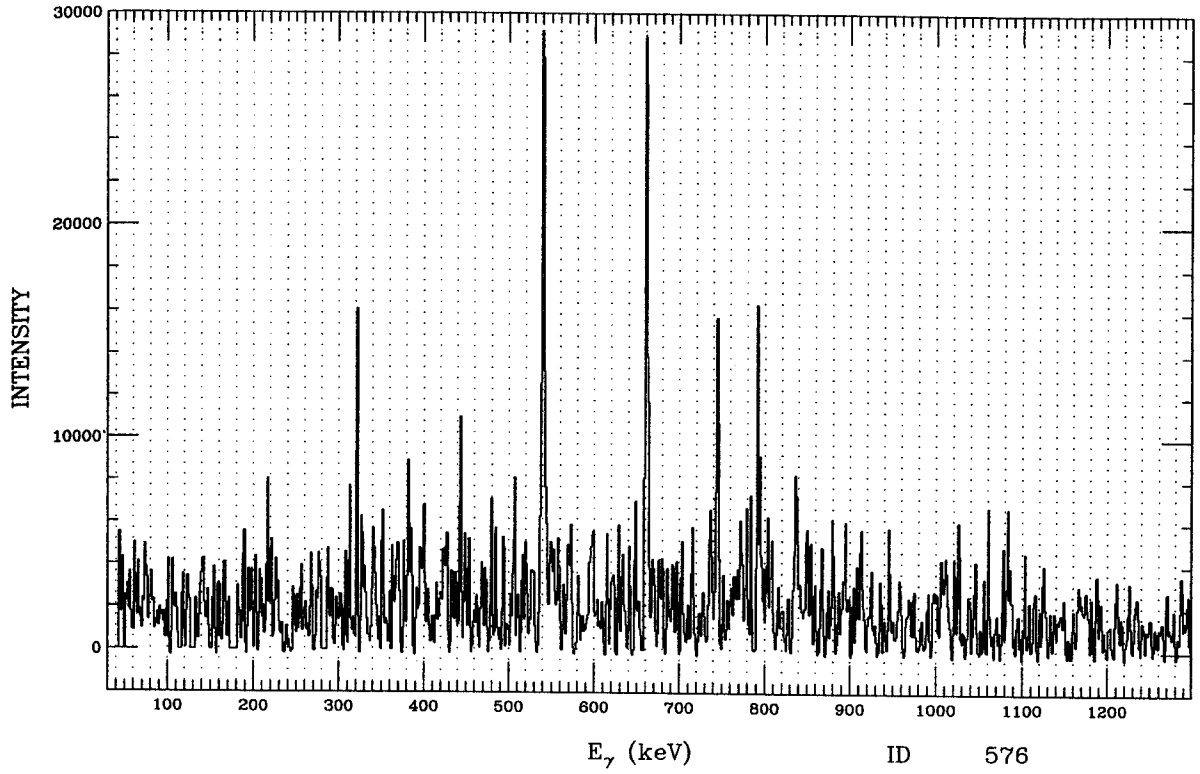

Figure E.43: ID 576. Multiple gate from ^{132}Pr, band 3a.

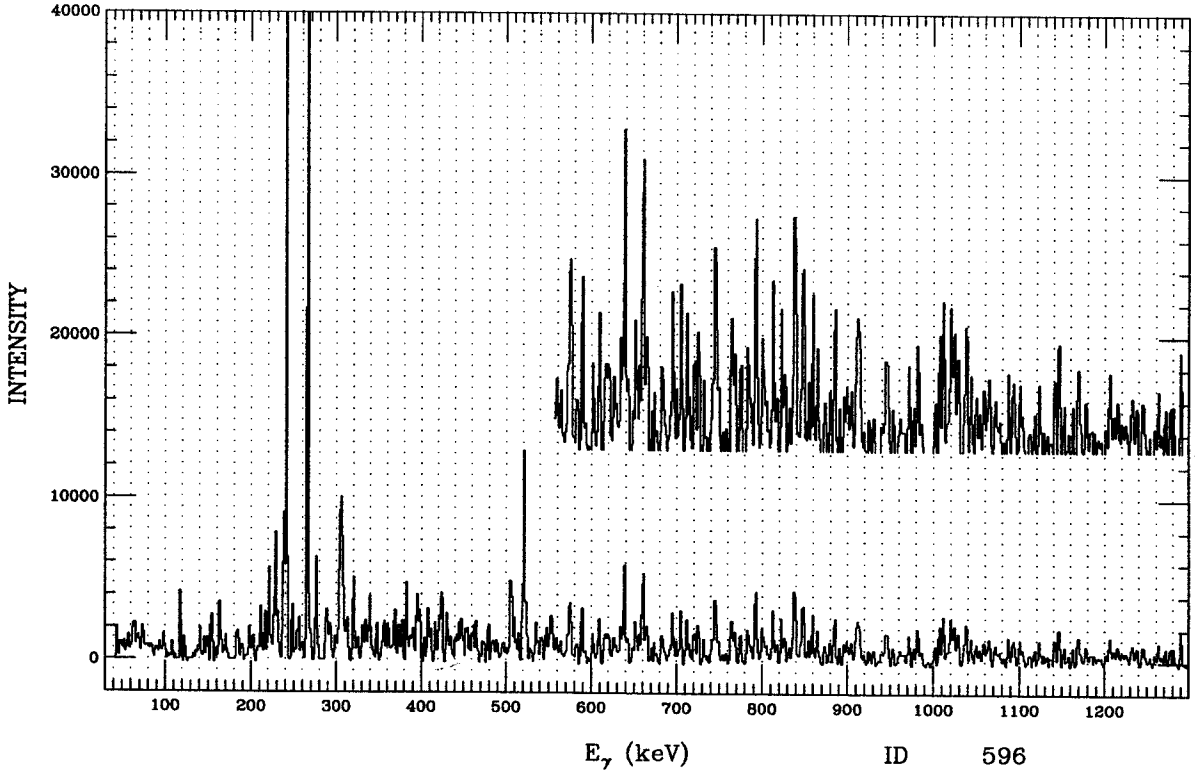

Figure E.44: ID 595. Multiple gate from ^{132}Pr, band 3a.

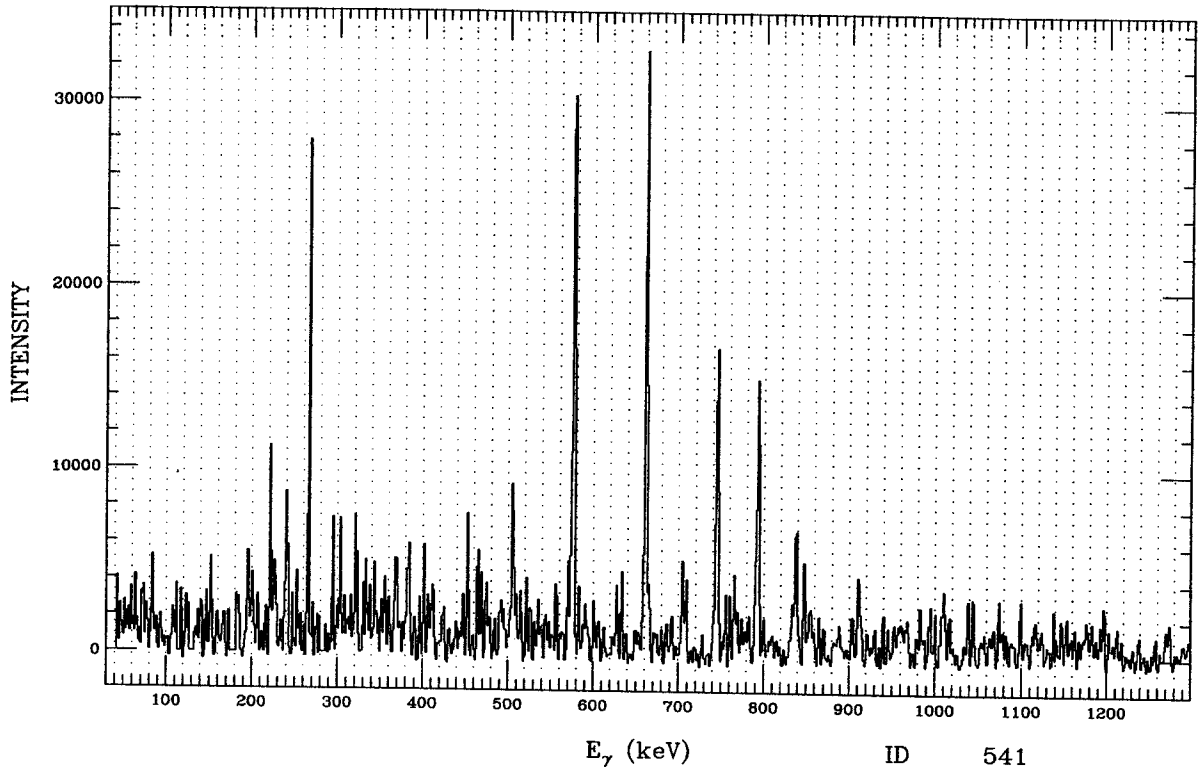

Figure E.45: ID 541. Multiple gate from ^{132}Pr, band 3a.

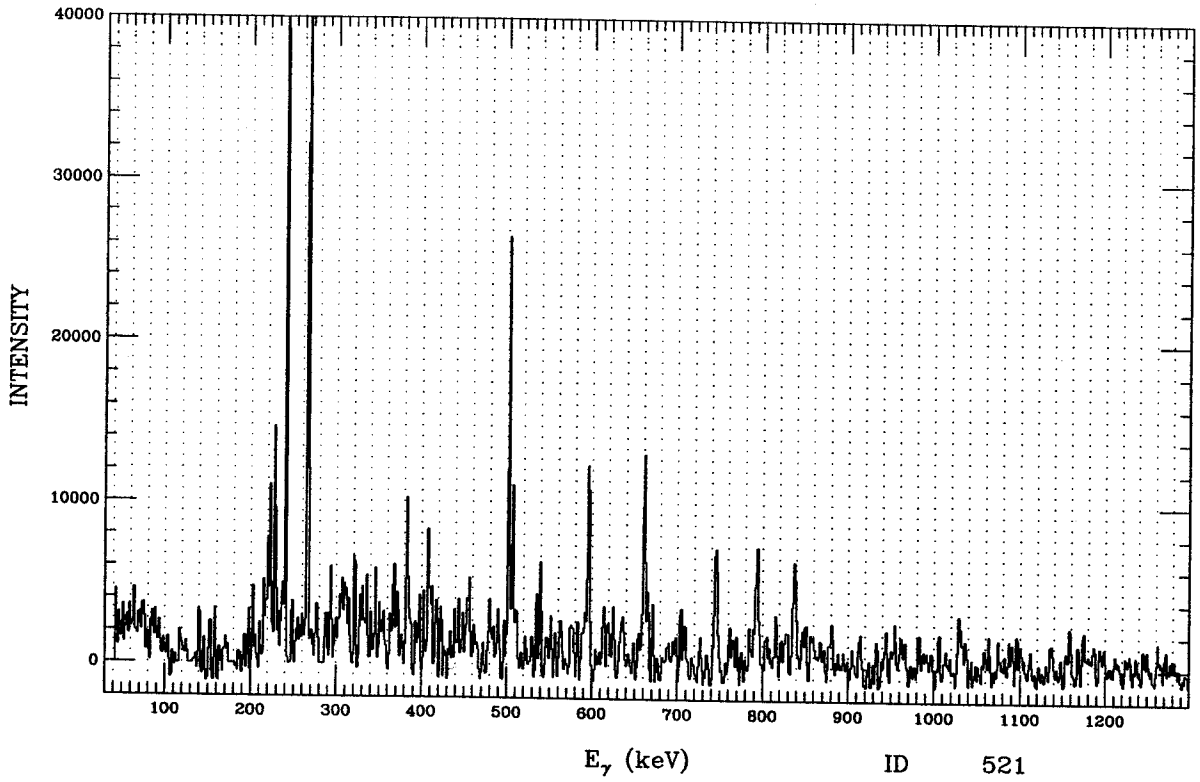

Figure E.46: ID 521. Multiple gate from ^{132}Pr, band 3a.

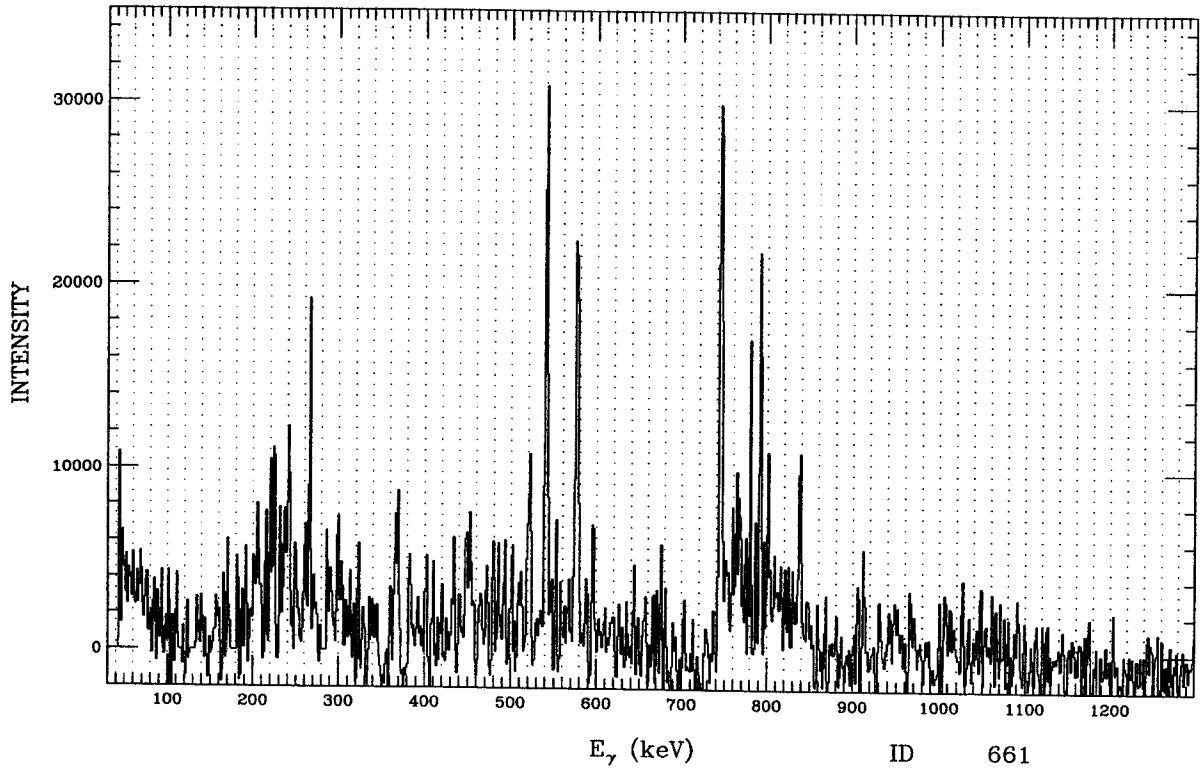

Figure E.47: ID 661. Multiple gate from ^{132}Pr, band 3a.

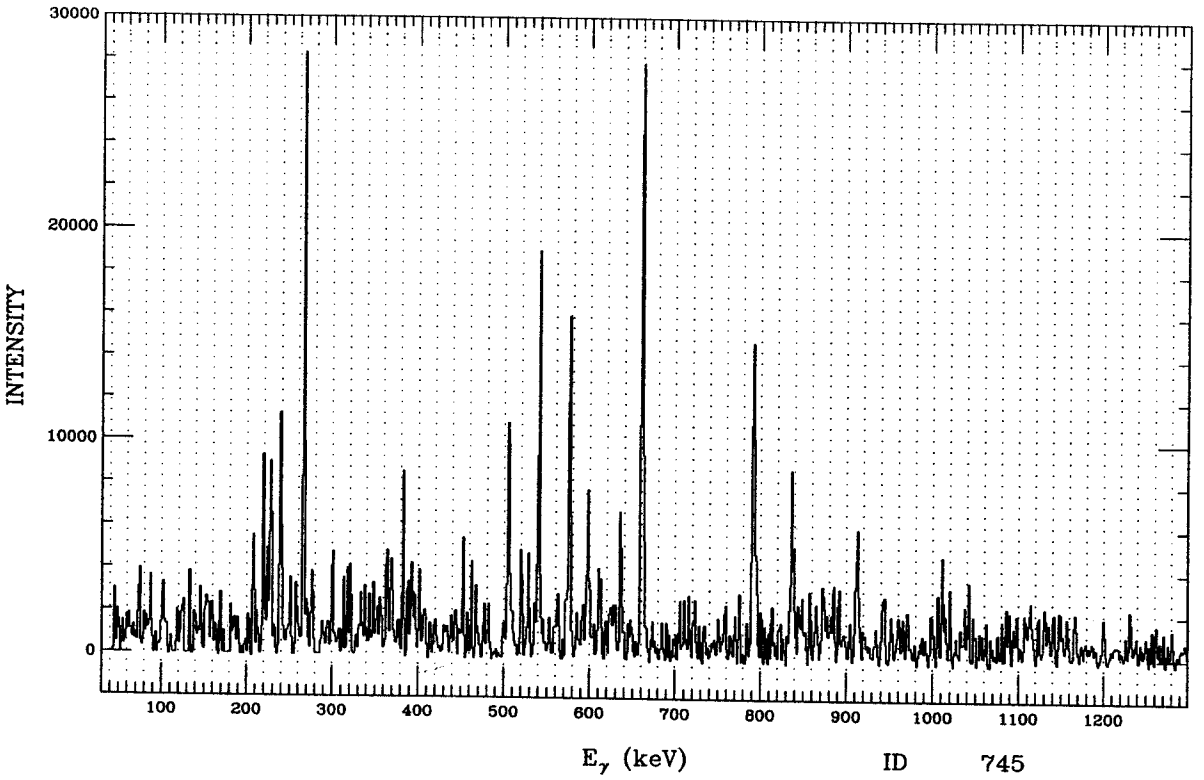

Figure E.48: ID 745. Multiple gate from ^{132}Pr, band 3a.

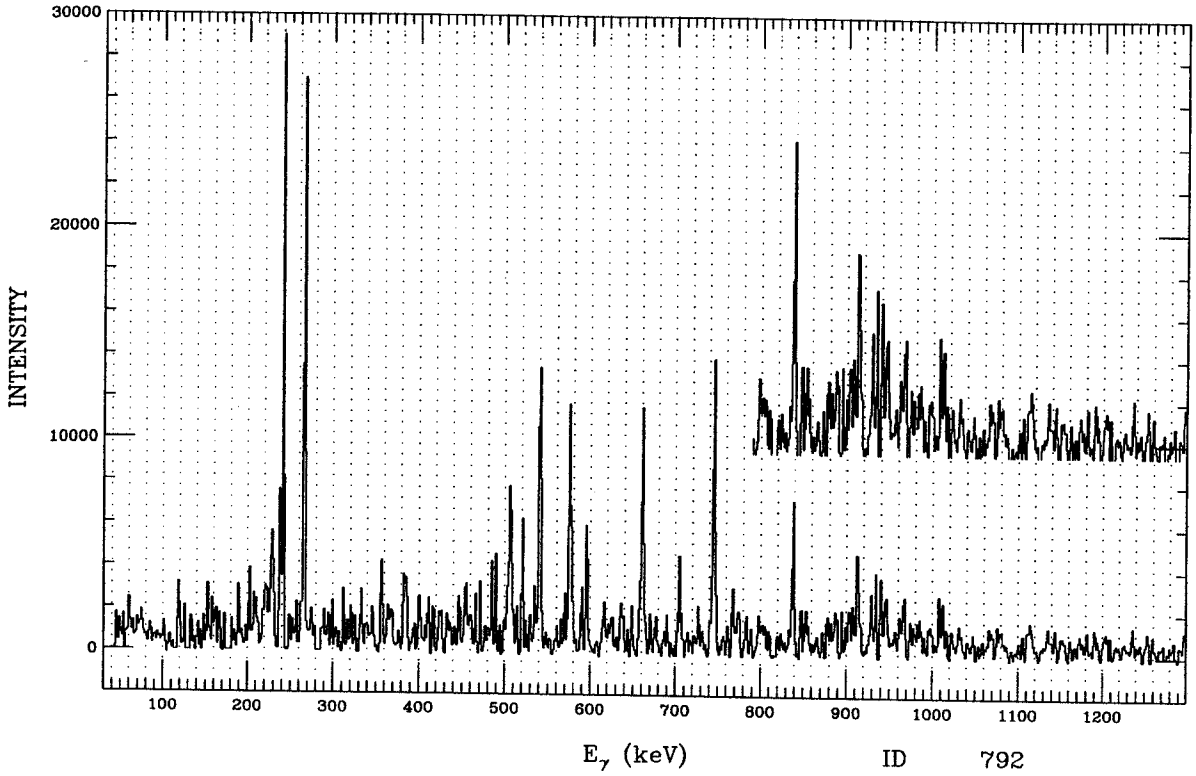

Figure E.49: ID 792. Multiple gate from ^{132}Pr, band 3a.

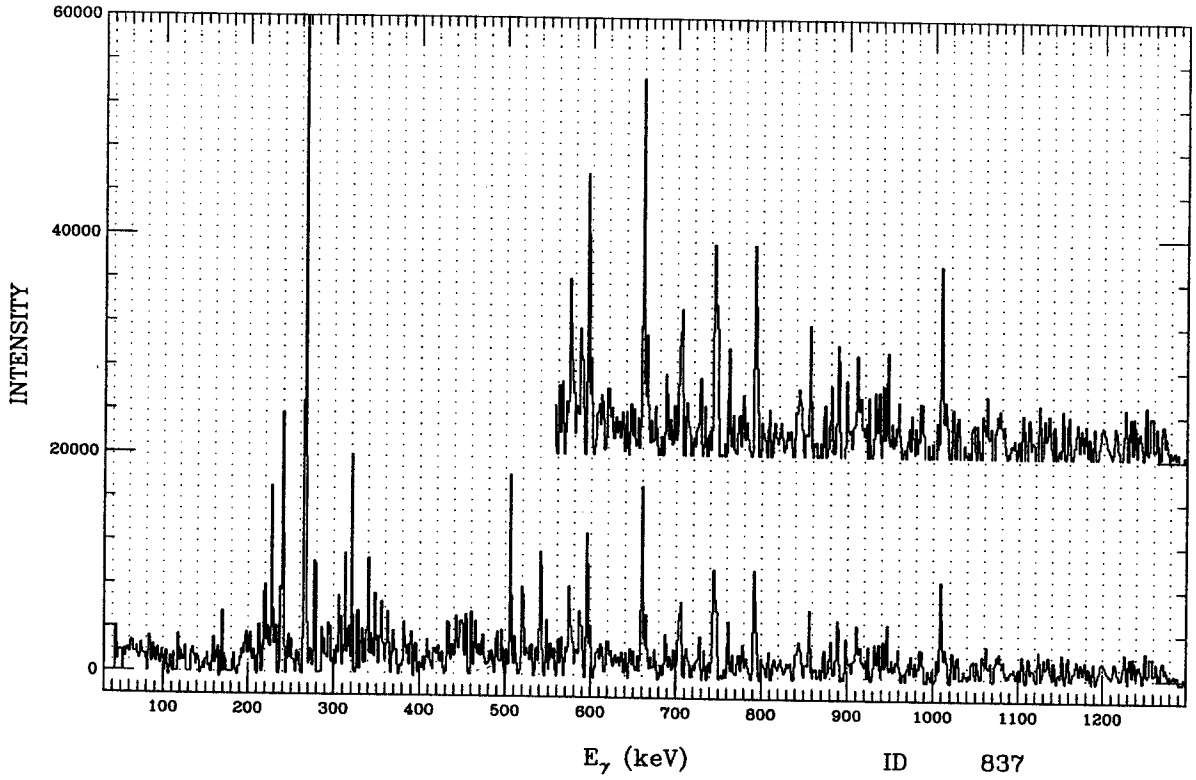

Figure E.50: ID 837. Multiple gate from ^{132}Pr, band 3a.

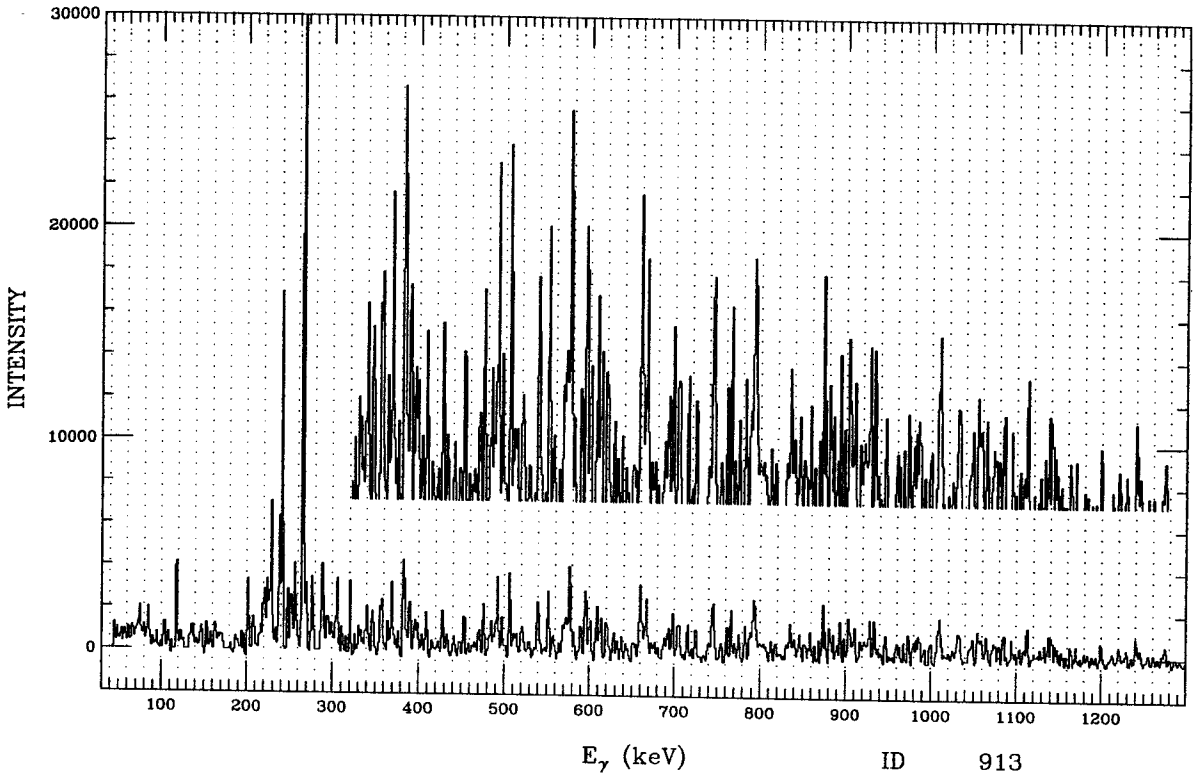

Figure E.51: ID 912. Multiple gate from ^{132}Pr, band 3a.

E.3 Rotational Bands ^{132}Pr

Spectra for the rotational bands in ^{132}Pr are listed in this Appendix. They were constructed by summing gates that fit the coincidence requirements. (See E.2 and E.1.) Each channel number gate, defining an energy peak, was subjected to the FFT noise reduction routine and summed over the peak. Local background was subtracted where indicated and a general background spectrum was also subtracted. The band numbers reflect individual rotational bands described in Figure 10.1.

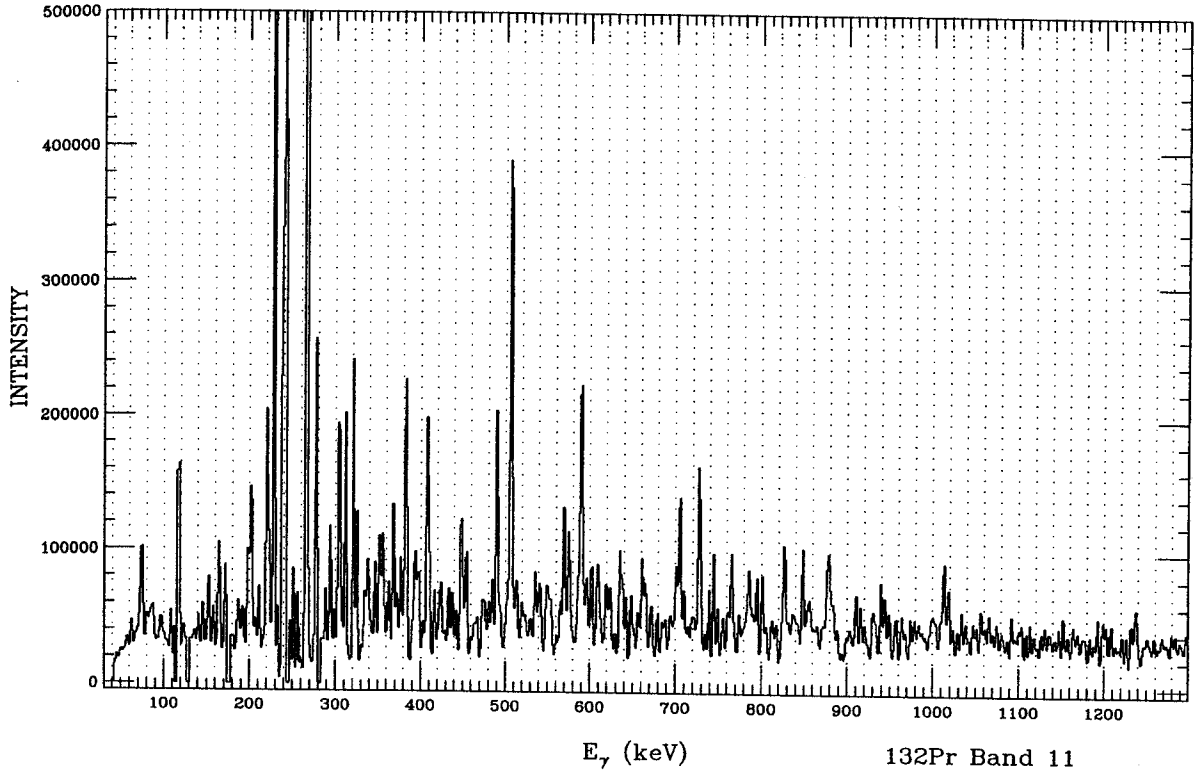

Figure E.52: Sum of gates at 407, 590, 728, 826, 877 keV for band 11 in ^{132}Pr, Multiple gate.

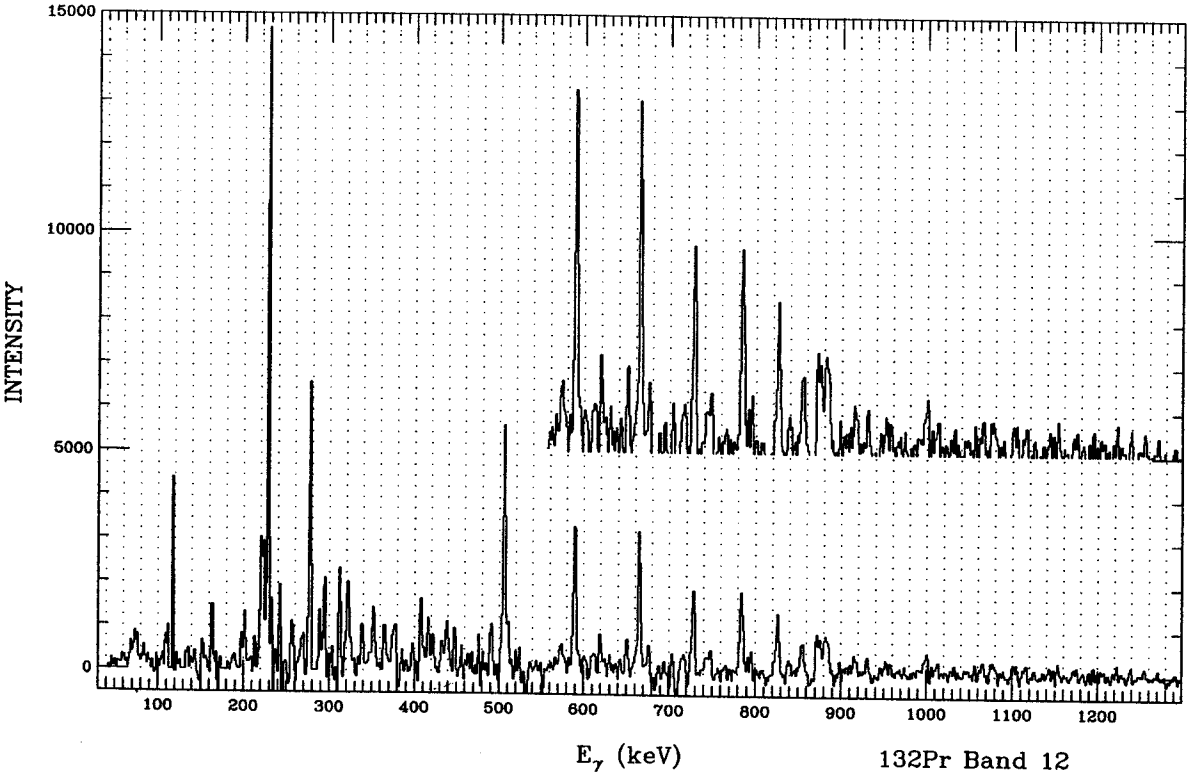

Figure E.53: Sum of gates at 115, 179, 229, 277 keV for band 12 in ^{132}Pr, Multiple gate.

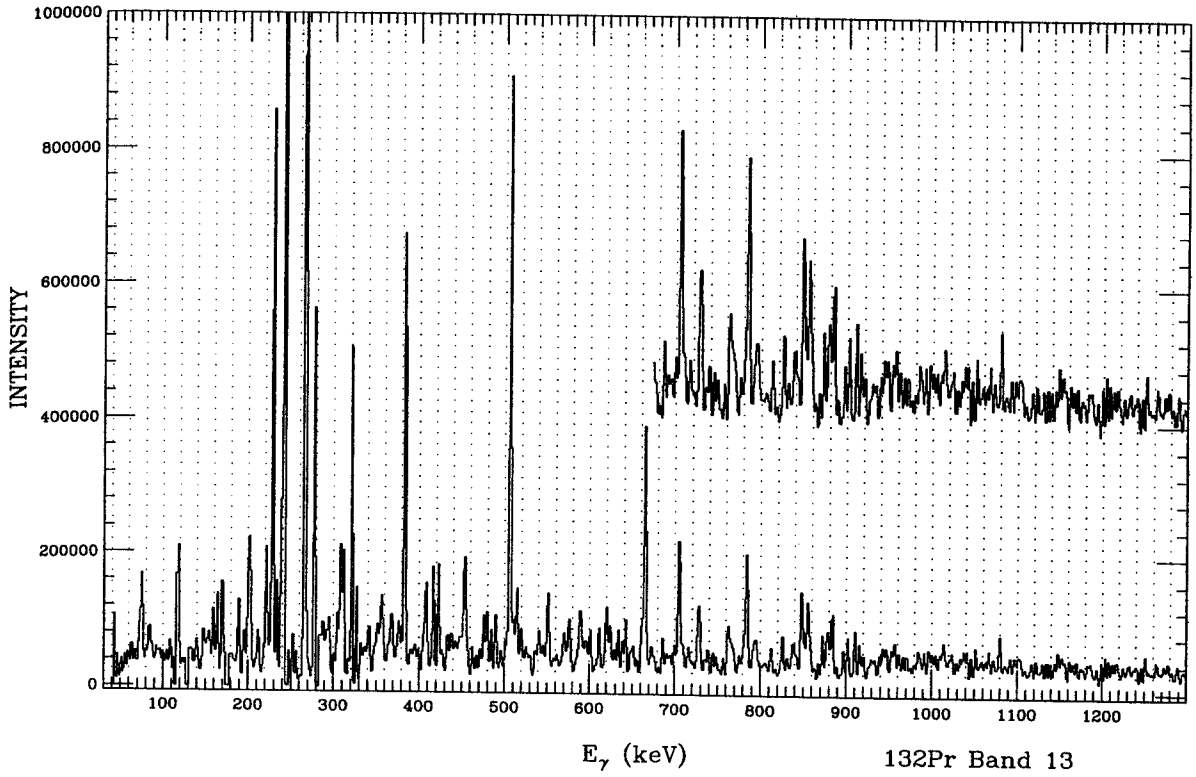

Figure E.54: Sum of gates at 294, 506, 665, 784, 855 keV for band 13 in ^{132}Pr, Multiple gate.

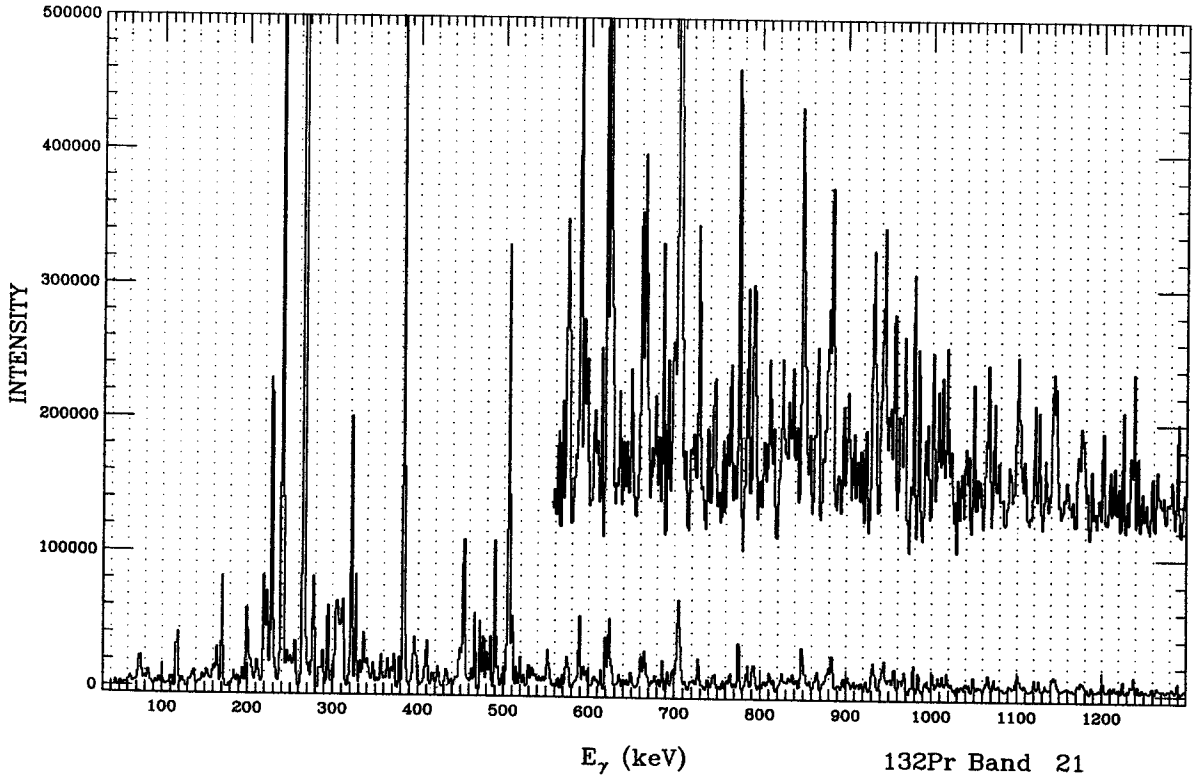

Figure E.55: Sum of gates at 396, 624, 775, 880, 934 keV for band 21 in ^{132}Pr, Multiple gate.

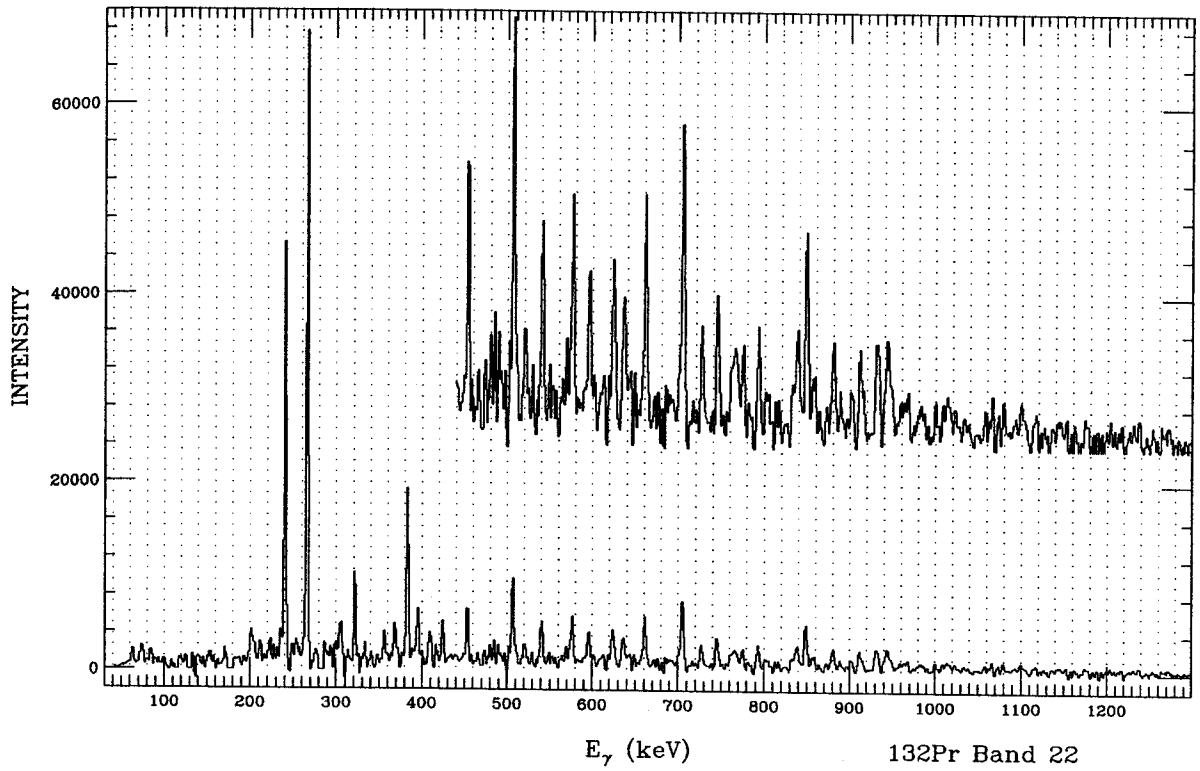

Figure E.56: Sum of gates at 130, 267, 240, 384, 321, 453, 396, 483 keV for band 22 in ^{132}Pr, Multiple gate.

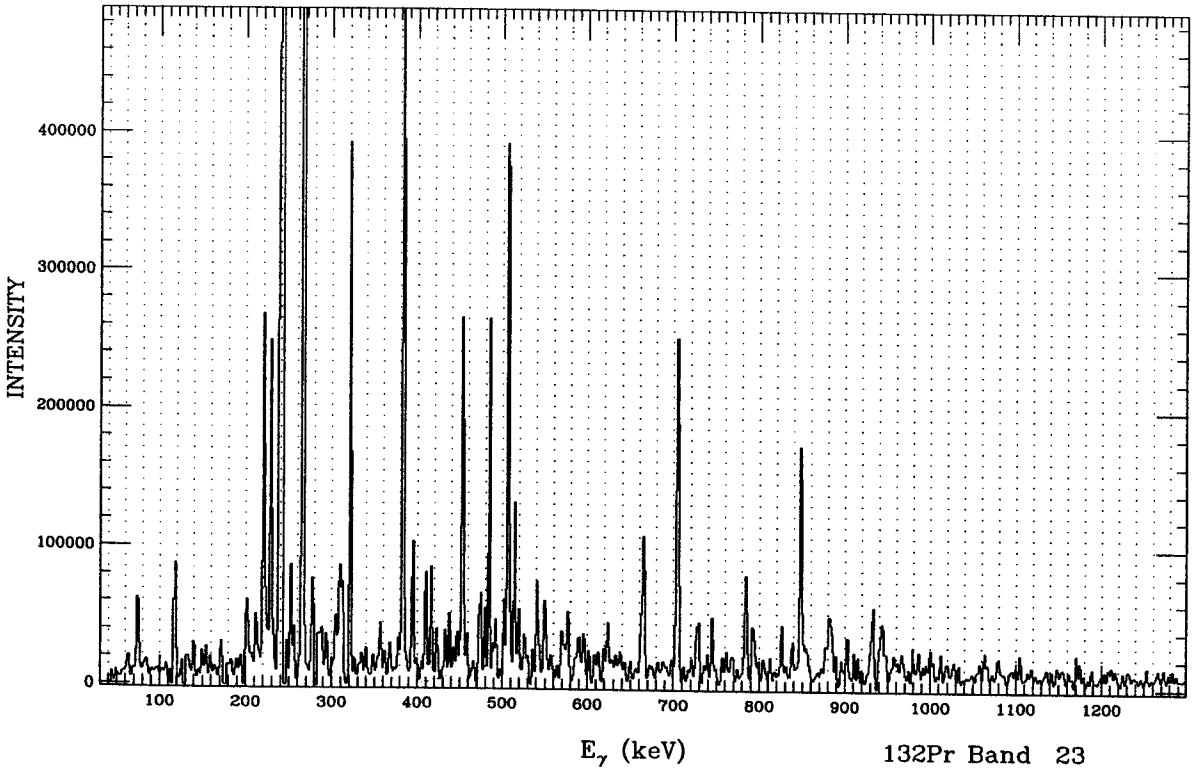

Figure E.57: Sum of gates at 396, 624, 775, 880, 934, 1019, 1130, 507, 705, 848, 943 keV. for band 23 in ^{132}Pr, Multiple gate.

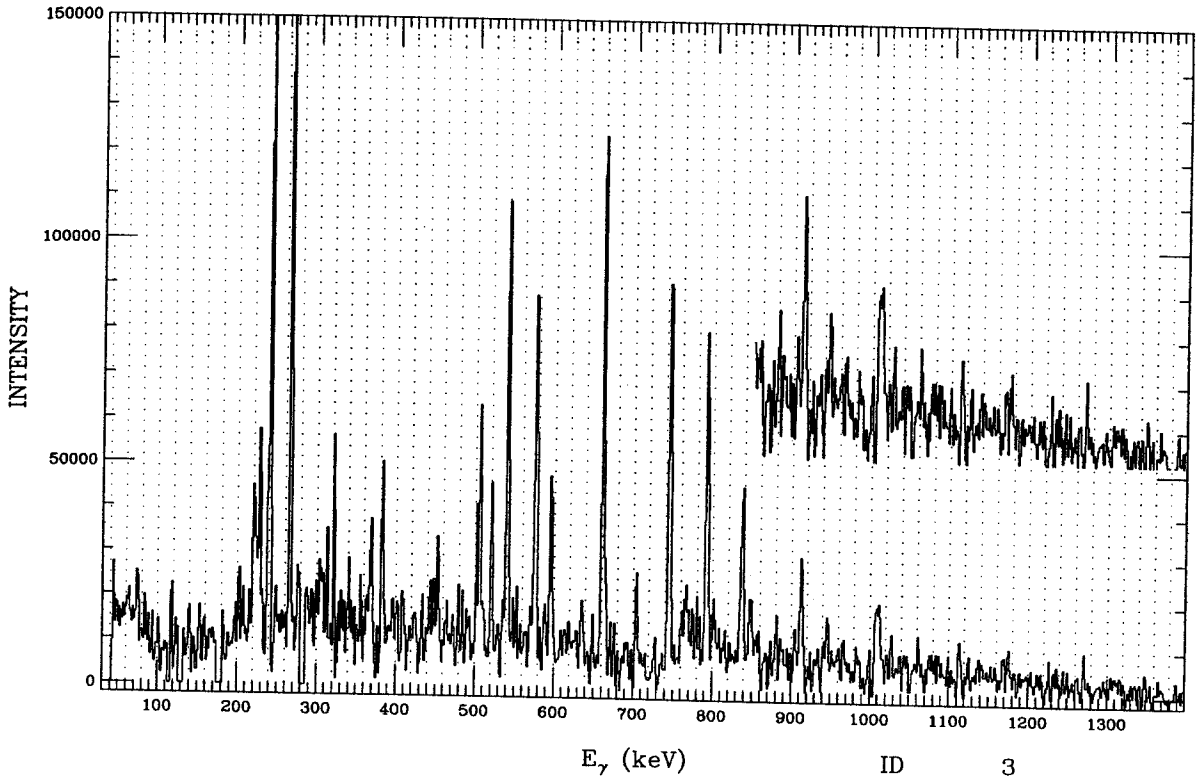

Figure E.58: Sum of gates at 576, 595, 541, 521, 661, 745, 792, 837, 912 keV. for band 3 in ^{132}Pr, Multiple gate.

E.4 TAC Spectra ^{132}Pr

γ-γ-t (TAC) spectra were made for a few energies from triples in the Energy versus Time arrays. By plotting the *log* of the TAC profile for an individual energy peak, the slope of the trailing edge of the prompt peak should yield a half-life value for the transition. The TAC profiles were obtained by summing the TAC counts across an energy peak. Many of the energy peaks contain a mixture of γ rays, therefore, their TAC peaks contain a mixture of activities. TAC profiles for transitions in ^{132}Pr are presented in this Appendix. Table 5.10 lists their probable half lives.

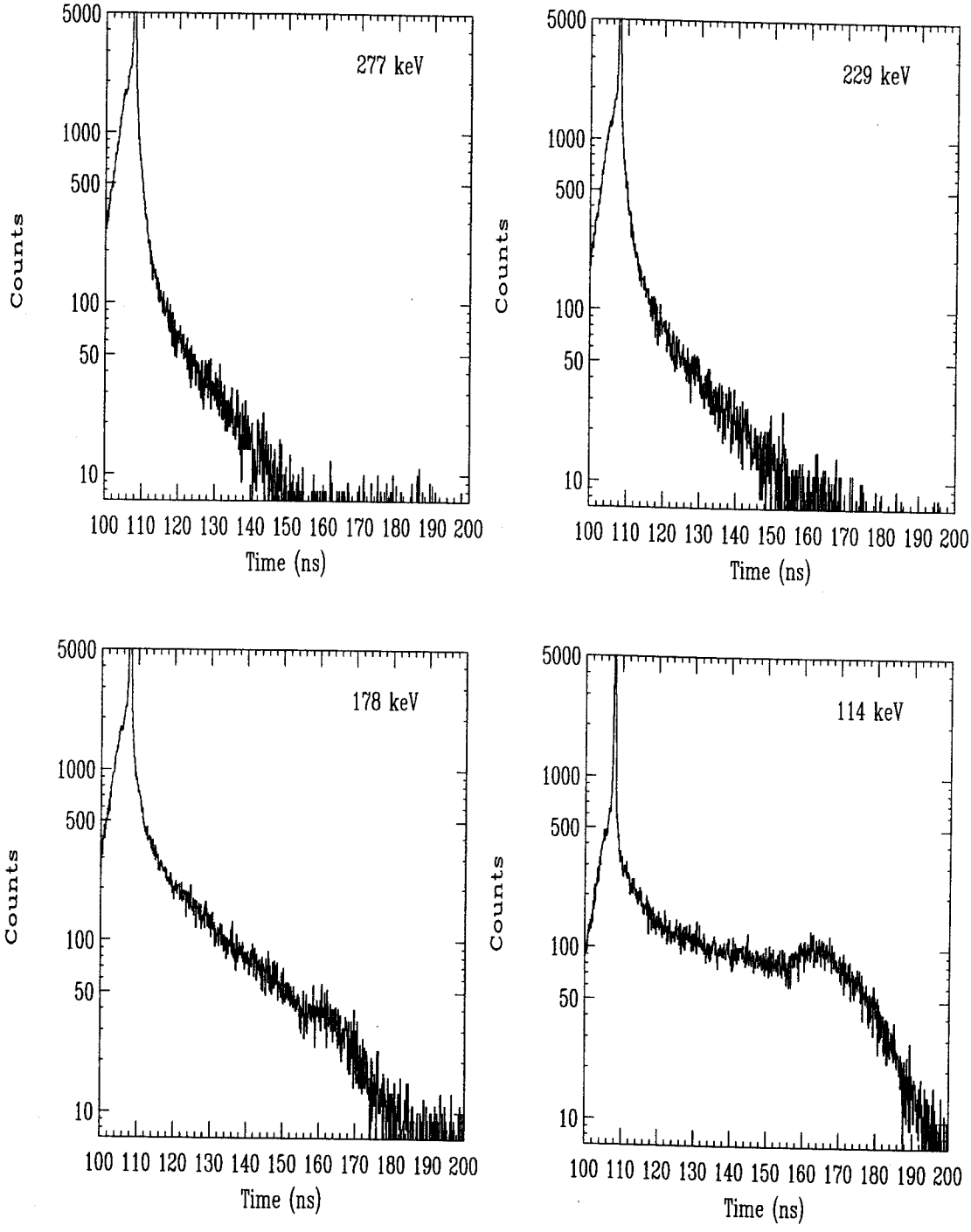

Figure E.59: Energy gated TAC spectra for 114, 178, 229, 277 keV.

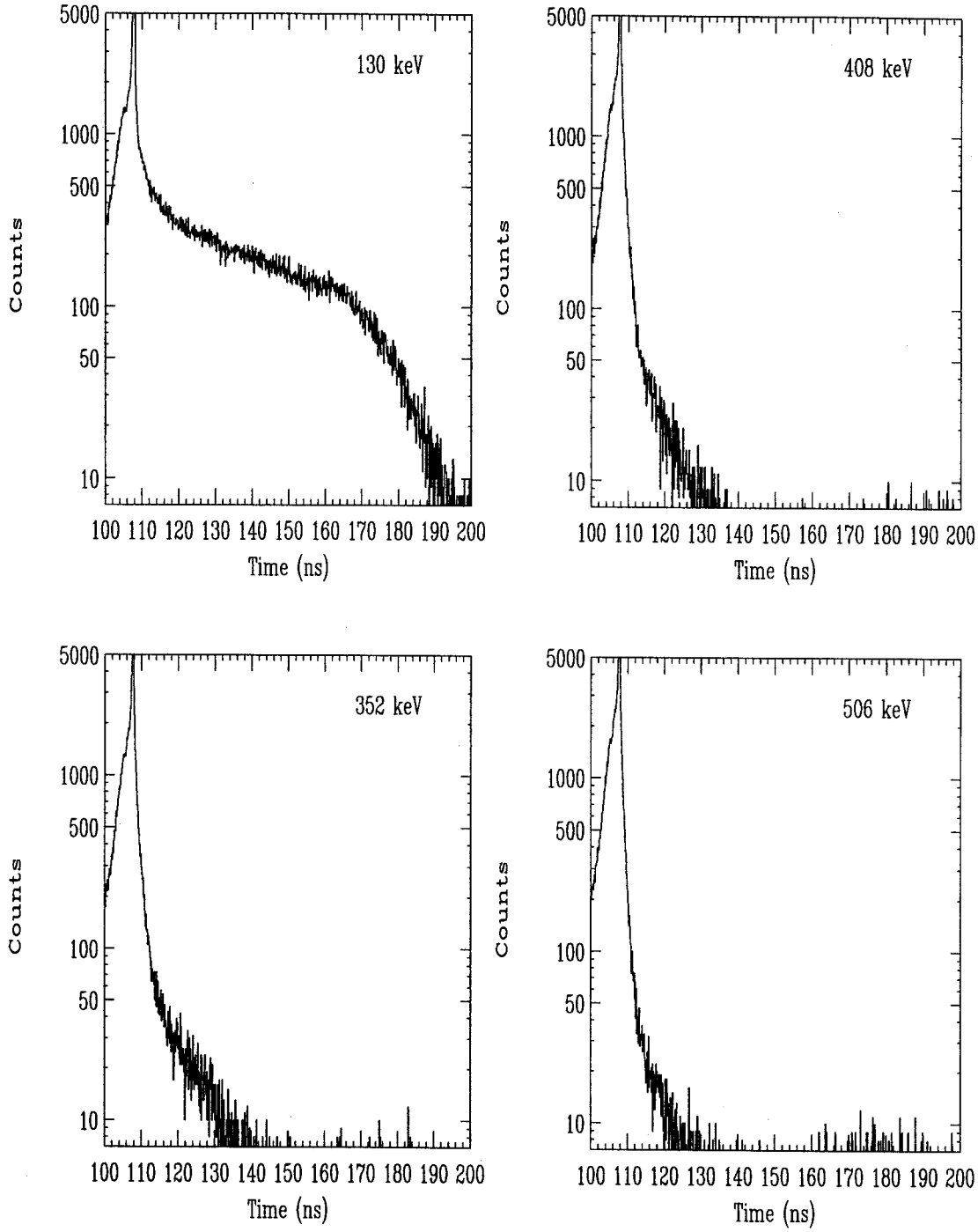

Figure E.60: Energy gated TAC spectra for 506, 352, 408, 130 keV.

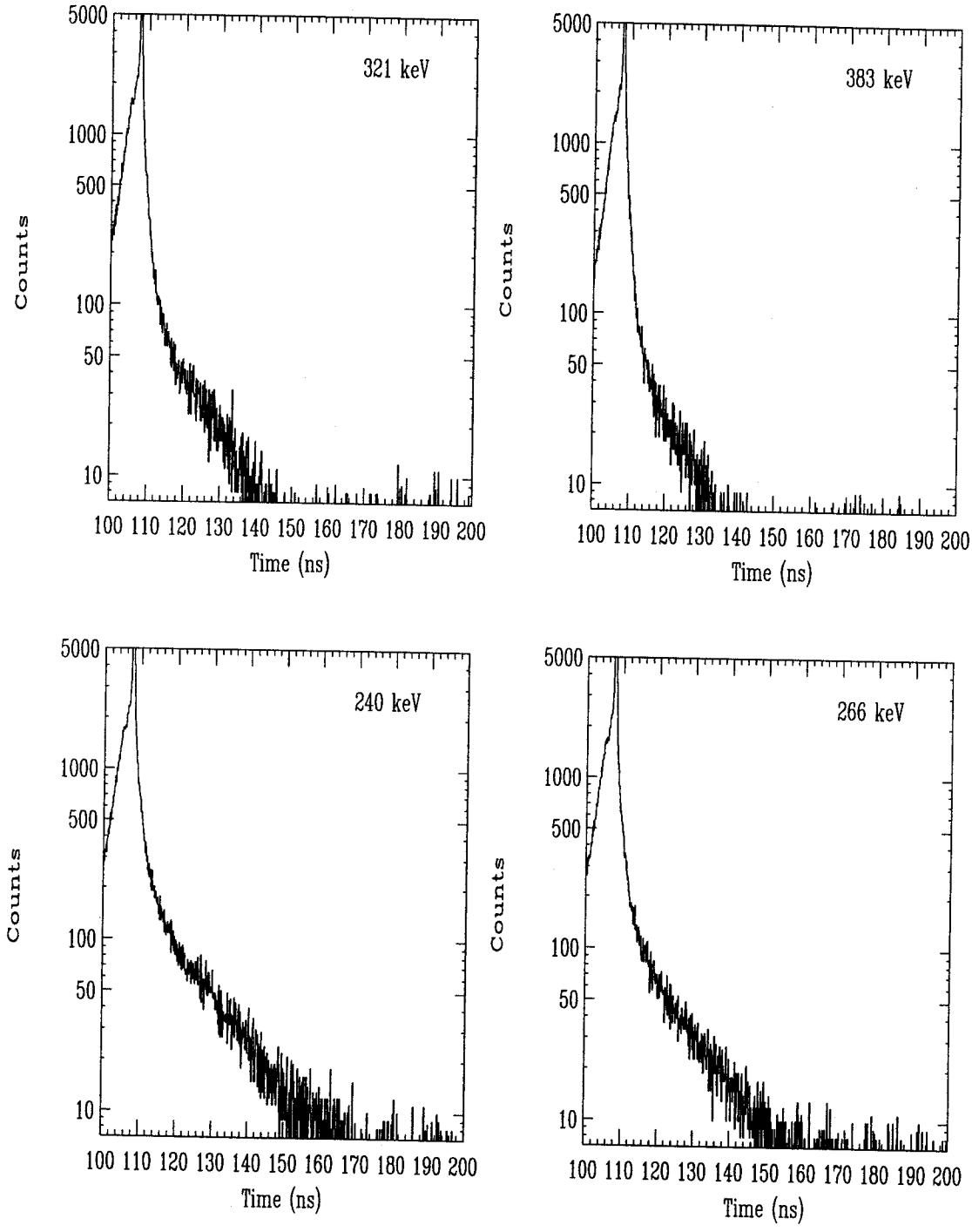

Figure E.61: Energy gated TAC spectra for 266, 240, 383, 321 keV.

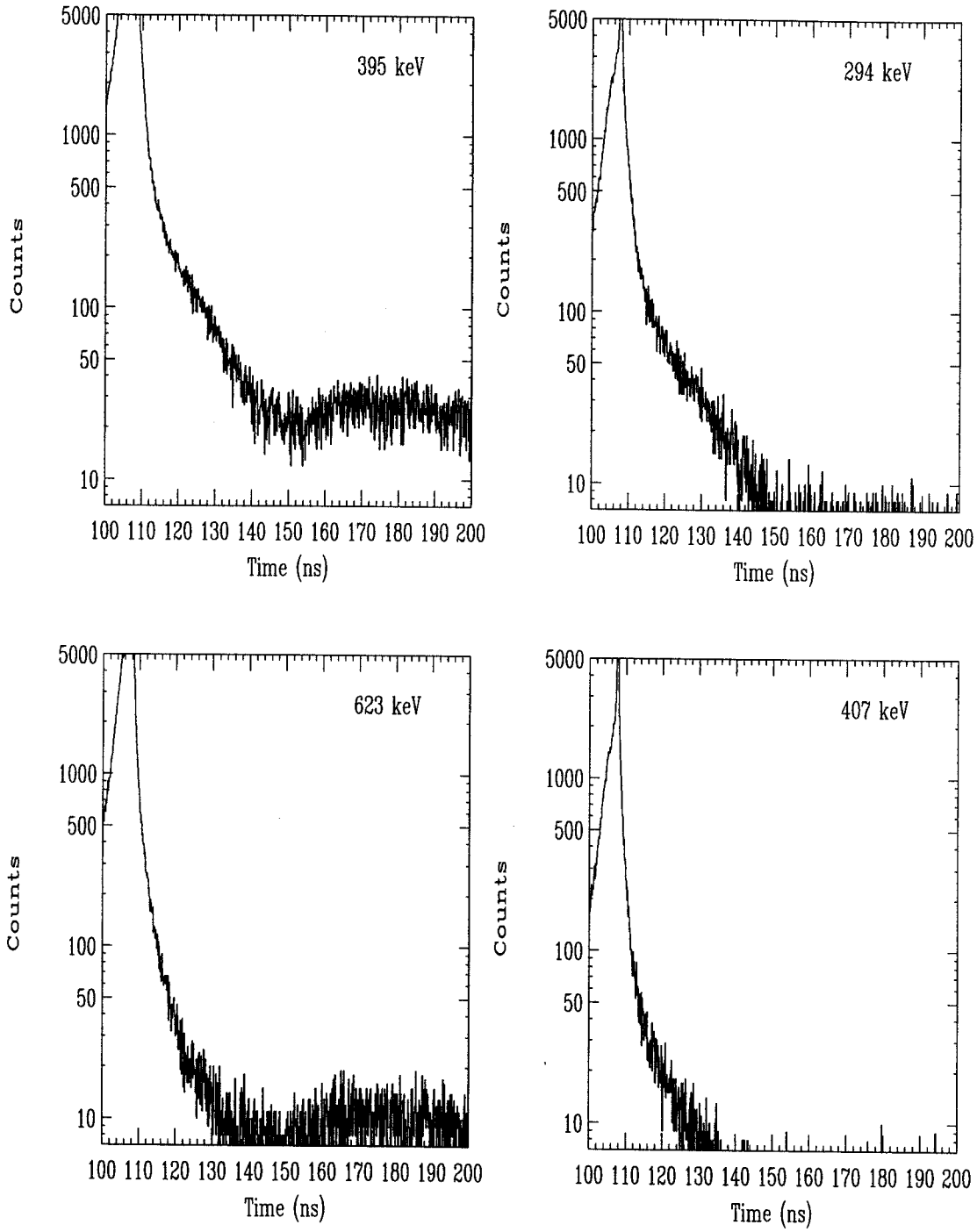

Figure E.62: Energy gated TAC spectra for 407, 623, 294, 395 keV.

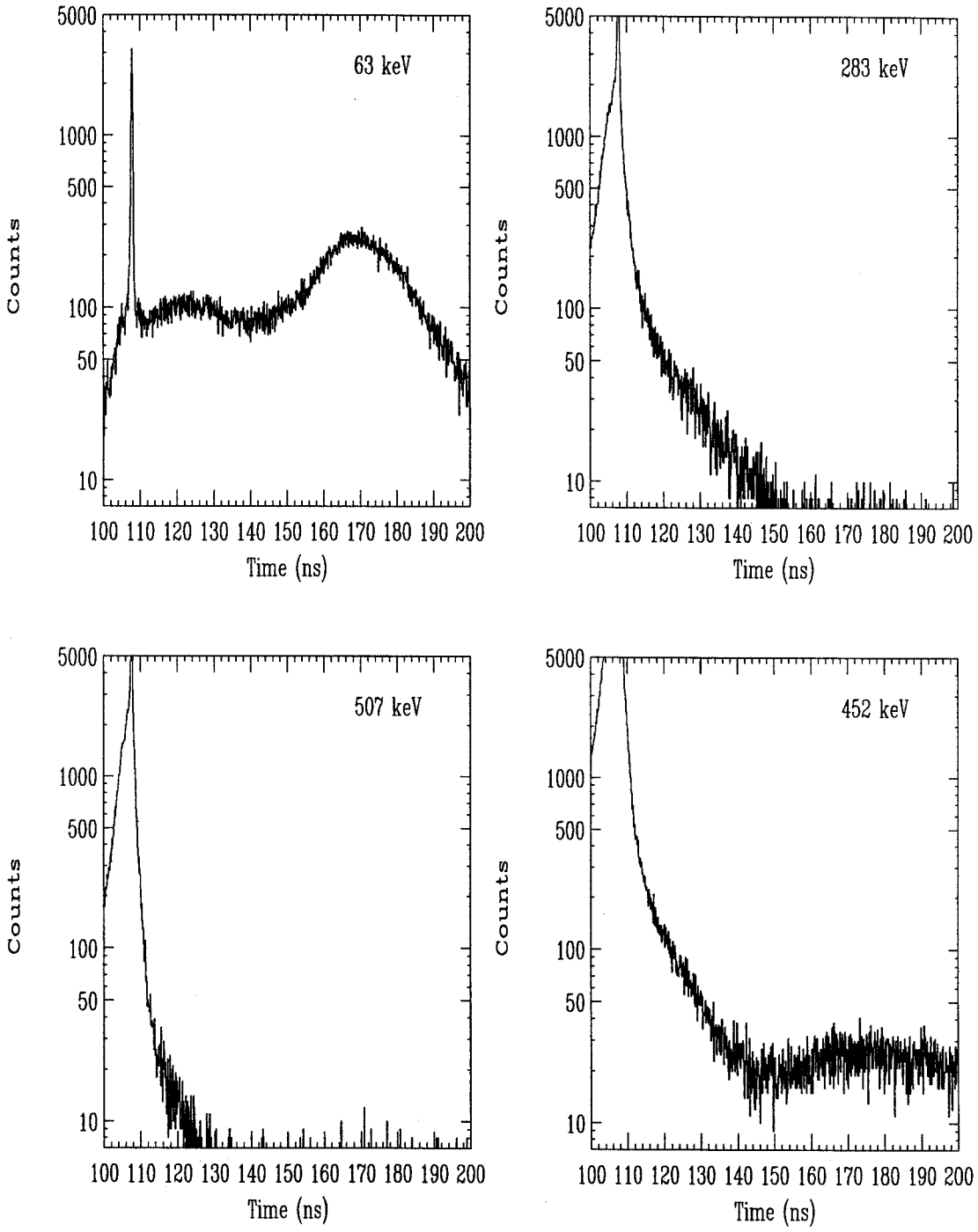

Figure E.63: Energy gated TAC spectra for 452, 507, 283, 63 keV.

Appendix F

^{133}Pr Spectra.

The Simple- and Multiple-gated spectra (gates) for ^{133}Pr displayed in this Appendix have complementary information. The energy peaks of the primary gates at 310, 551 and 709 keV for ^{133}Pr will not be seen in the Multiple gates; however, their contribution is a major one in the Simple gates. The Simple gates have twice the ADC resolution as the Multiple gates but they are not necessarily nuclei specific. Therefore, 1) more 'contaminant' peaks are present in the Simple gates; 2) the Simple gate's higher energy regions have a much lower signal to background ratio than the Multiple gates have. Many higher-energy peaks will not be seen in the Simple gates. The Multiple gates were designed to be nuclei specific but in some cases contaminant peaks from neighboring nuclei cannot be separated.

Without FFT, much of the Simple gate information cannot be used (see 6). In the following spectra, the FLGI/O FFT mode was chosen for display since it emphasizes the smaller peaks. Note that the y-axis values do not reflect the actual count number. During the FFT process an offset and a mathematical operator change this value. Therefore, the y-axis should be viewed in a qualitative manner.

F.1 Simple Gates ^{133}Pr

$E_{\gamma 1}$ versus $E_{\gamma 2}$ arrays for ^{133}Pr were constructed, representing the sum of all triple coincidences determined from detector comparisons. This is presented in Figure 5.12. A TAC gate was set during the array generation: everything that had previously been designated pre-prompt through prompt was included. By making a cut (gate) on either axis at an appropriate energy, A, all the energies in coincidence with A that occurred between the two detectors were obtained within the 1-D histogram. The resulting spectra for ^{133}Pr are displayed in this Appendix. Each spectrum has been enhanced using the FFT and SNIP routines described in Chapter 6.

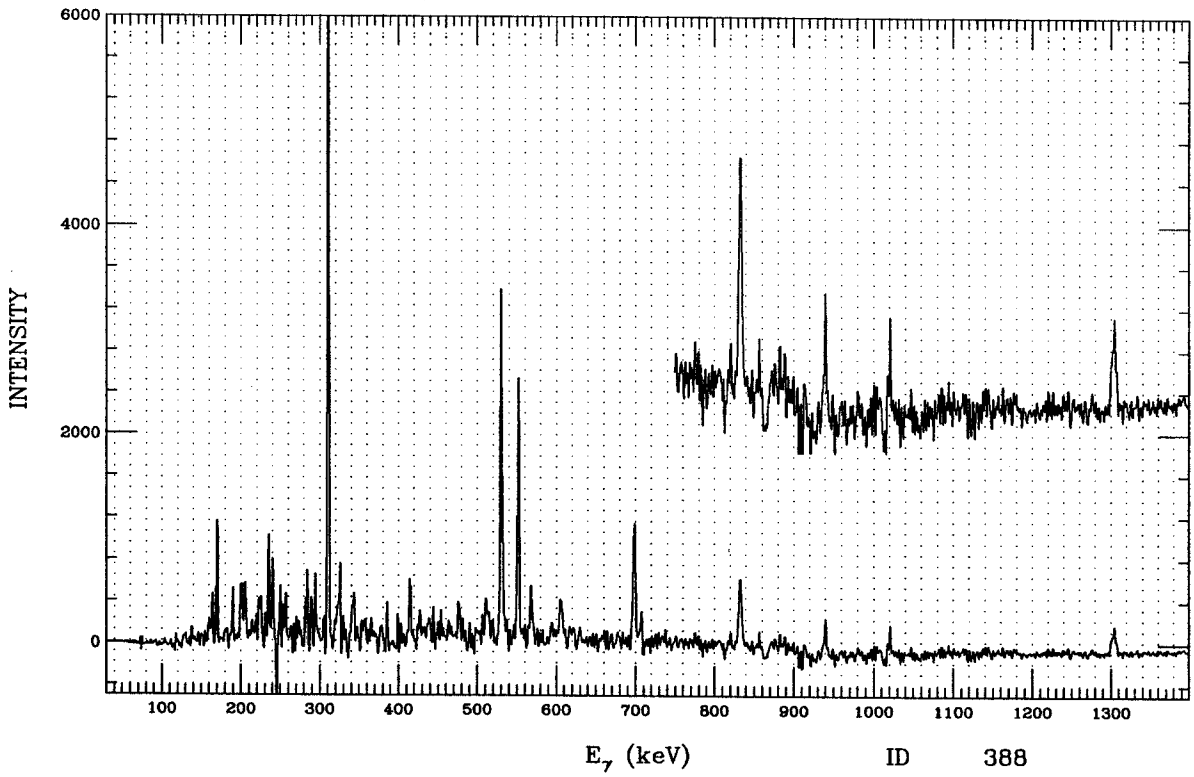

Figure F.1: ID 388. Simple gate from ^{133}Pr, band 1.

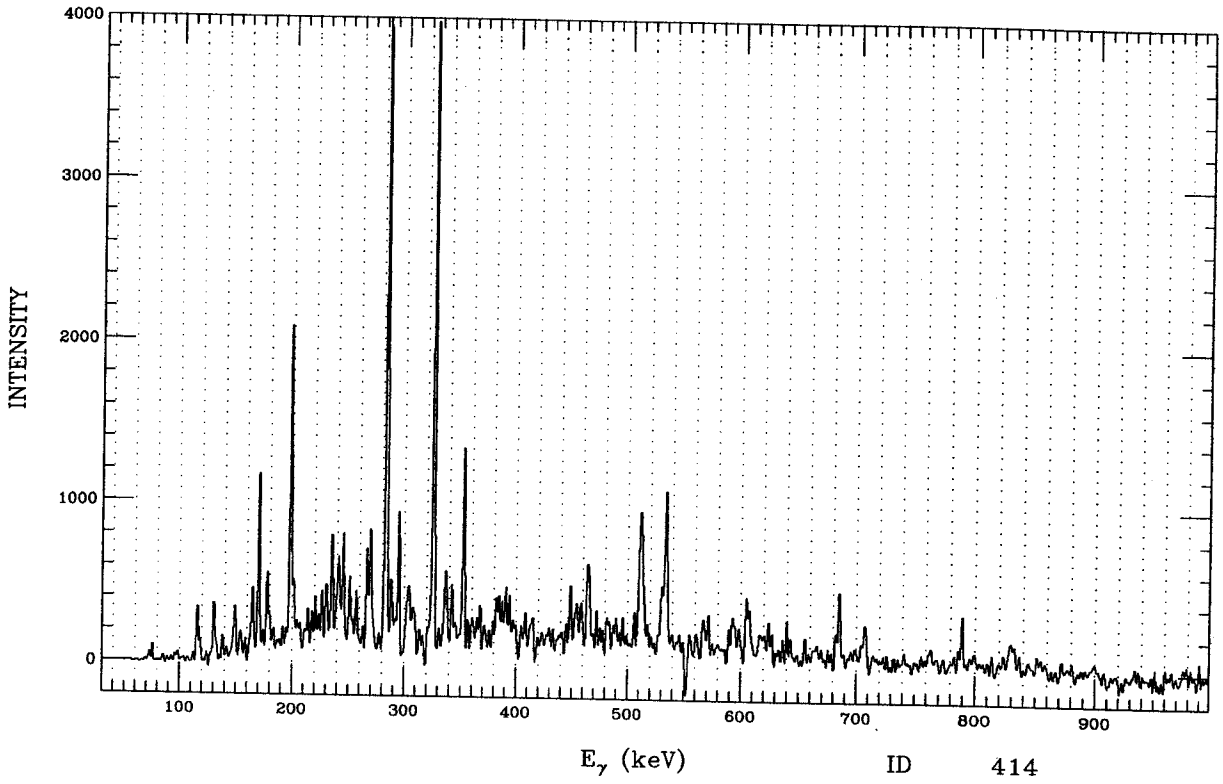

Figure F.2: ID 414. Simple gate from ^{133}Pr, band 1.

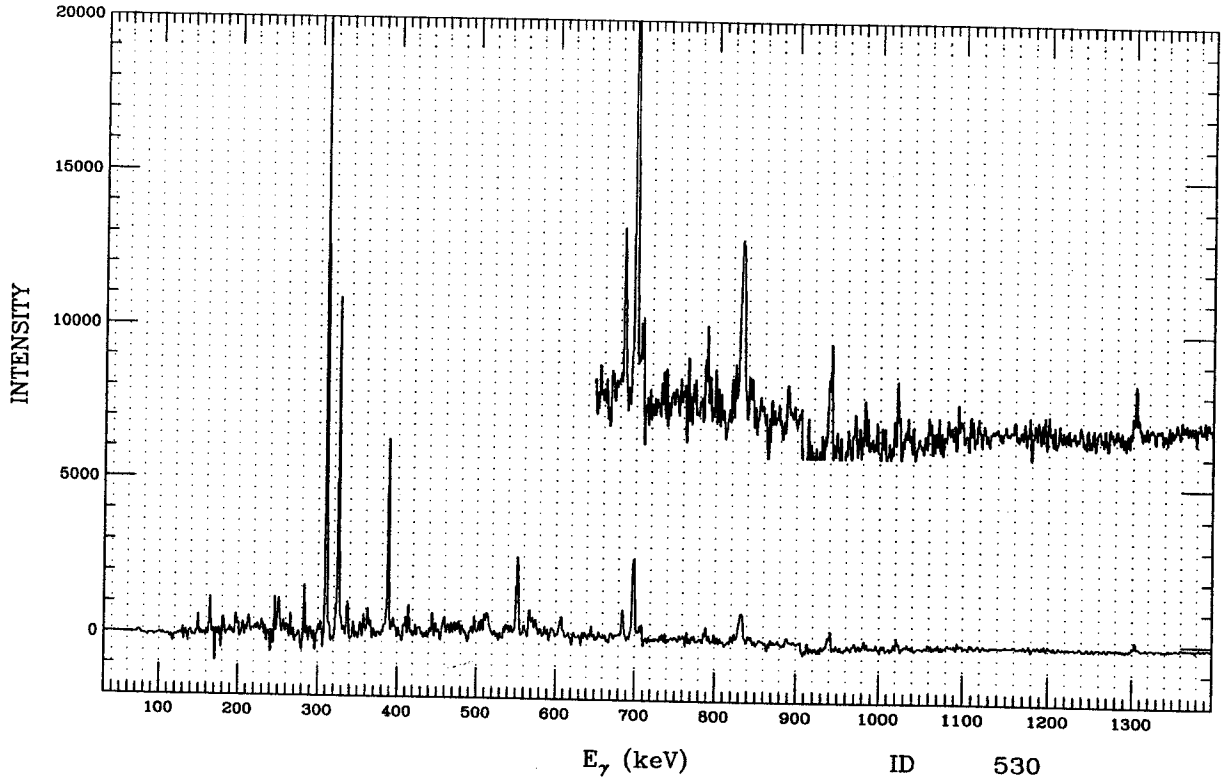

Figure F.3: ID 530. Simple gate from ^{133}Pr, band 1.

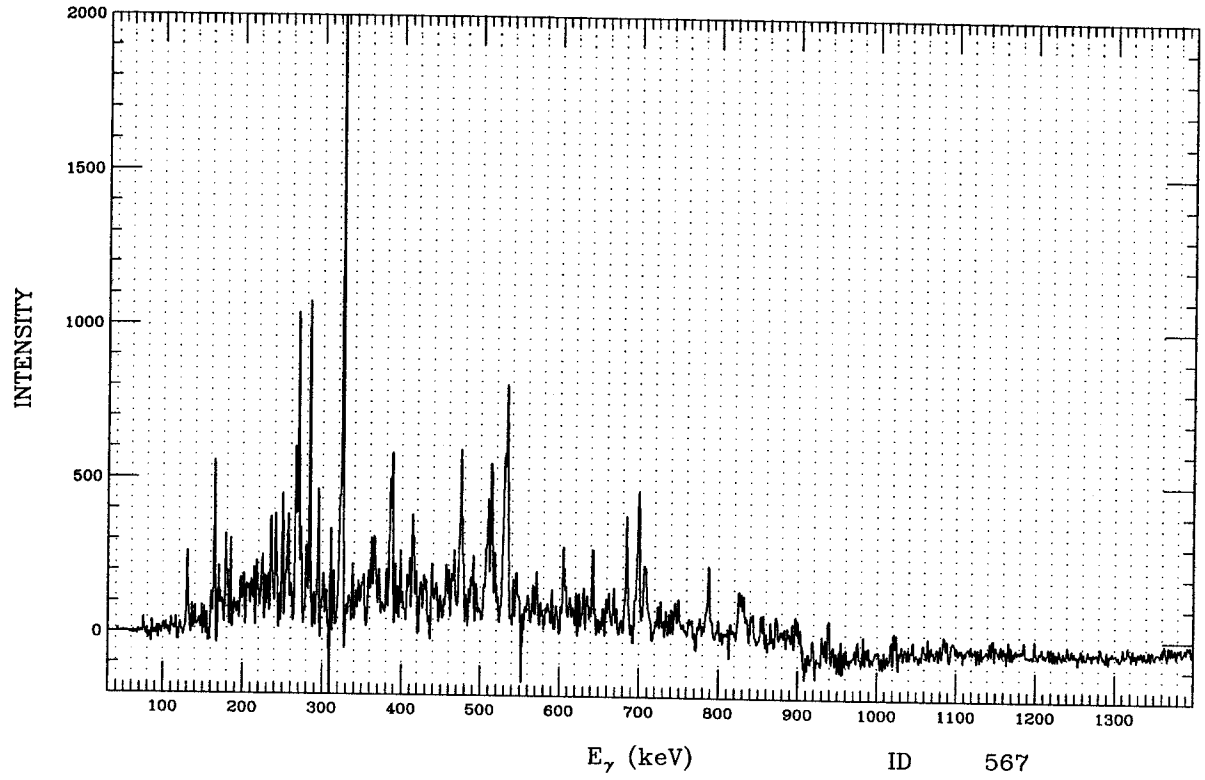

Figure F.4: ID 567. Simple gate from ^{133}Pr, band 1.

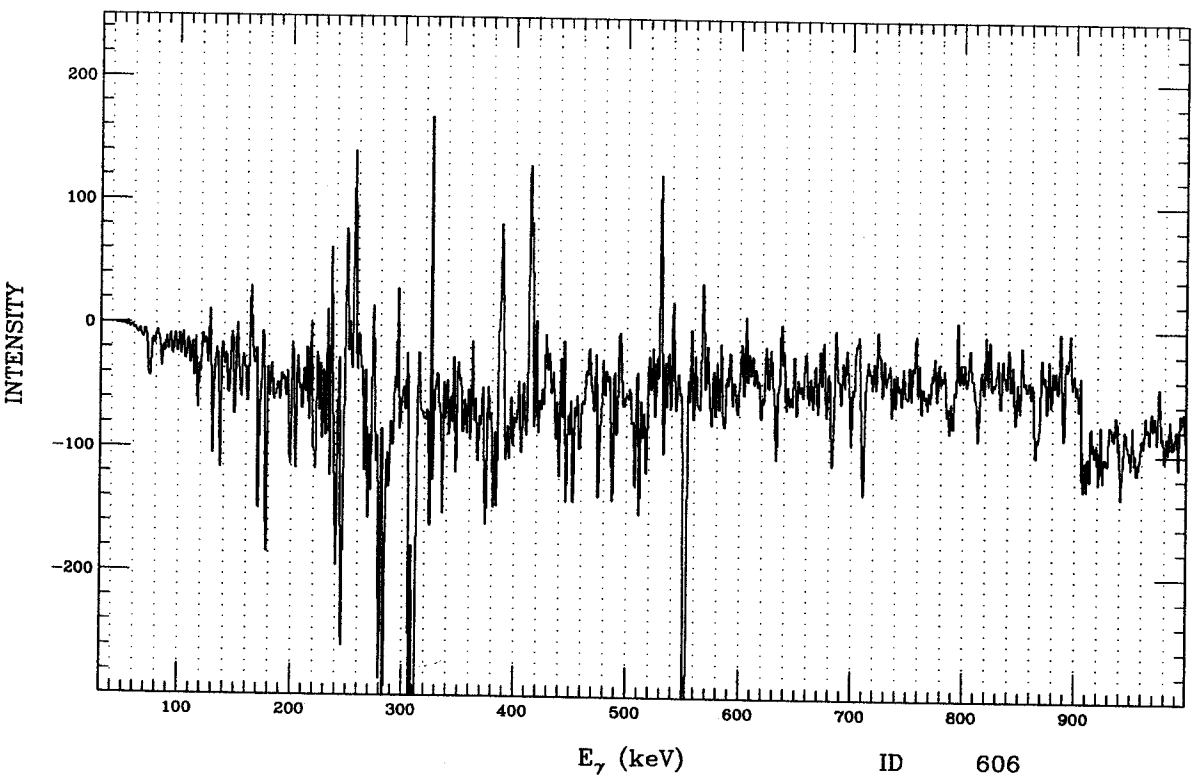

Figure F.5: ID 606. Simple gate from ^{133}Pr, band 1.

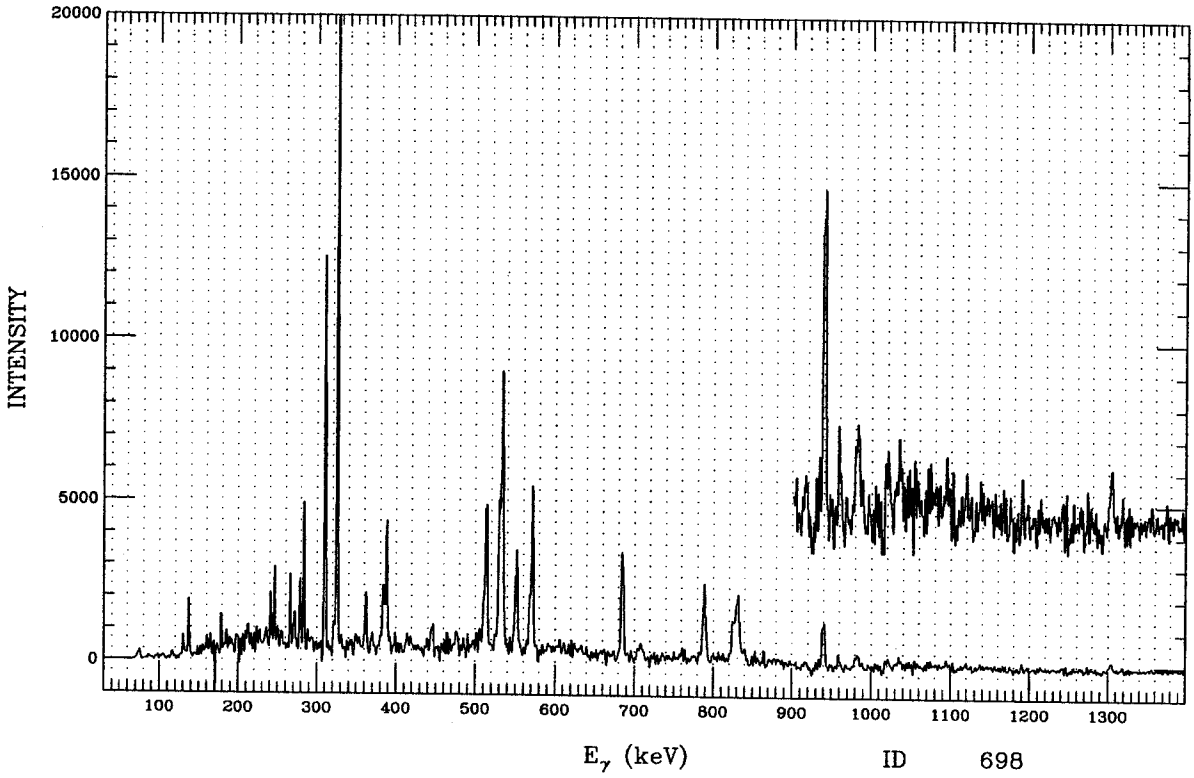

Figure F.6: ID 698. Simple gate from ^{133}Pr, band 1.

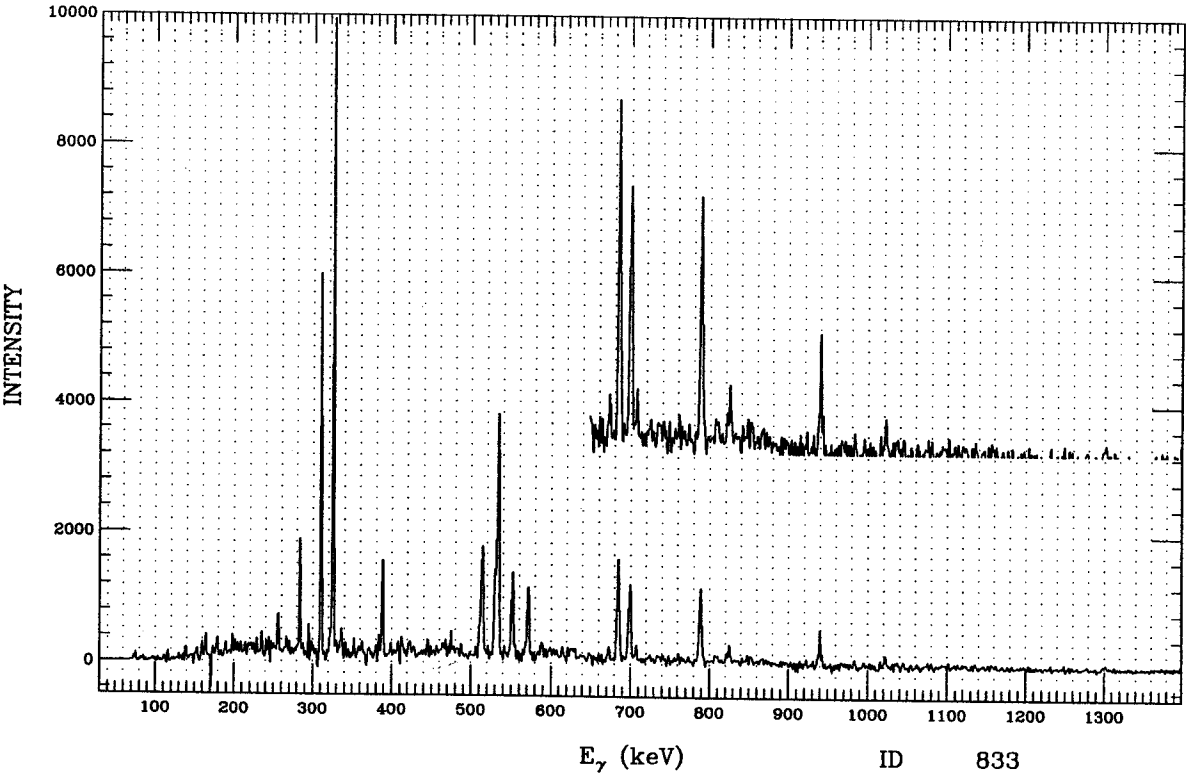

Figure F.7: ID 833. Simple gate from ^{133}Pr, band 1.

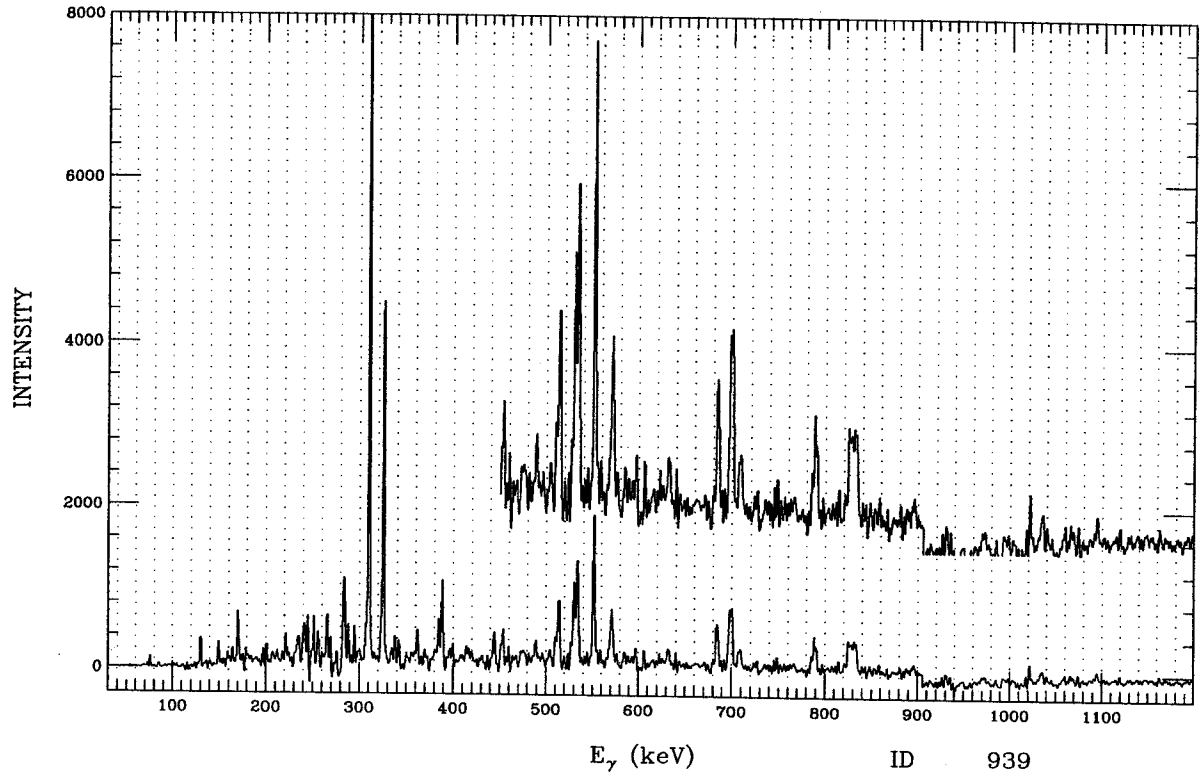

Figure F.8: ID 939. Simple gate from ^{133}Pr, band 1.

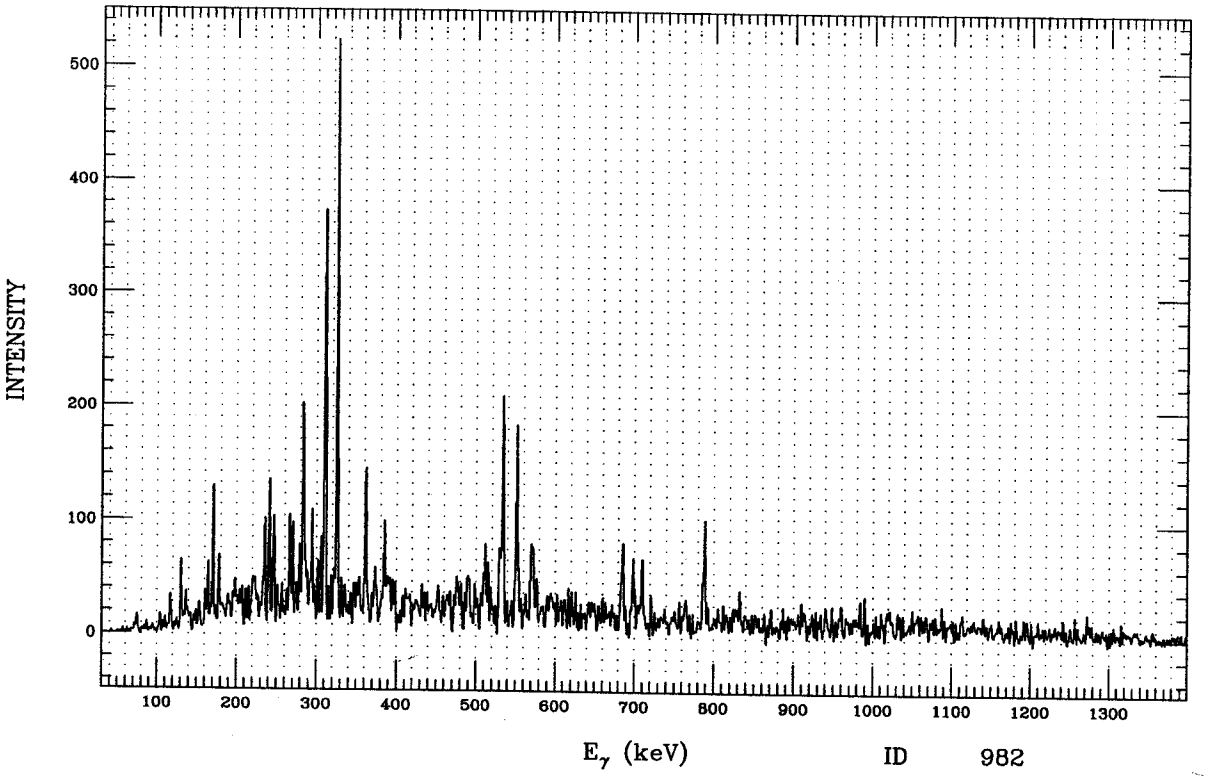

Figure F.9: ID 982. Simple gate from ^{133}Pr, a link between bands 1 and 3.

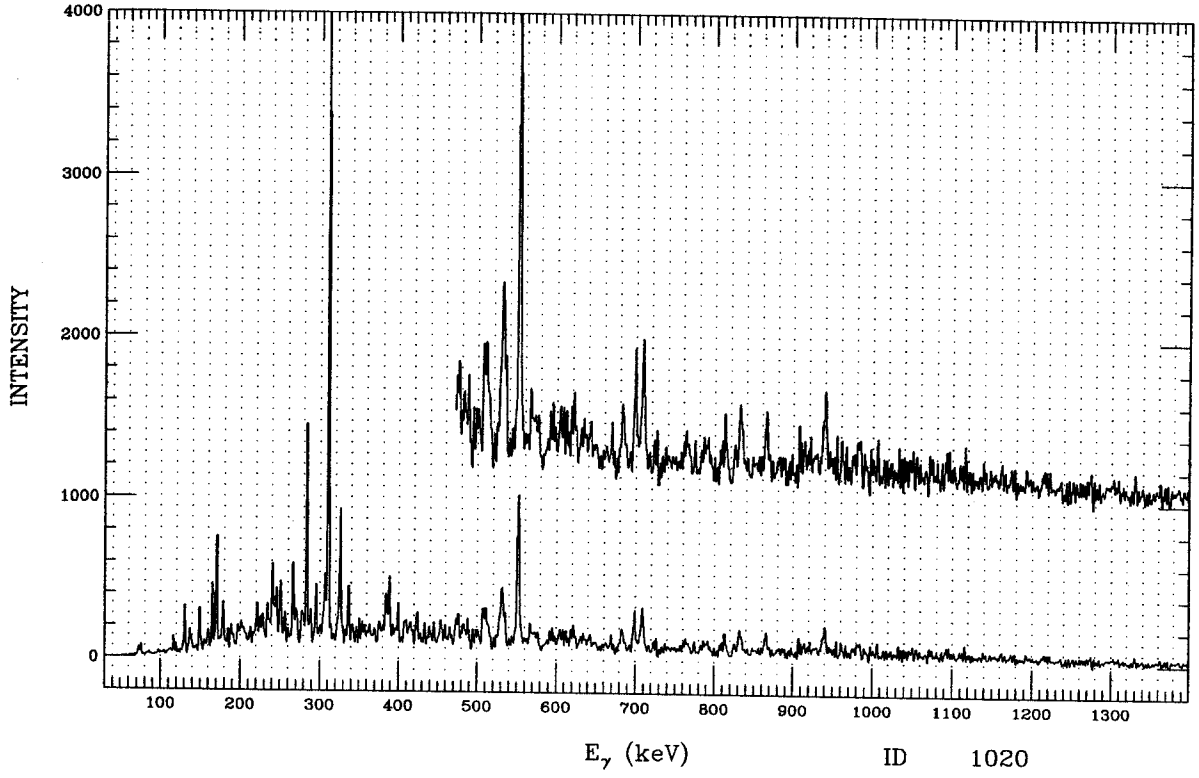

Figure F.10: ID 1020. Simple gate from ^{133}Pr, band 1.

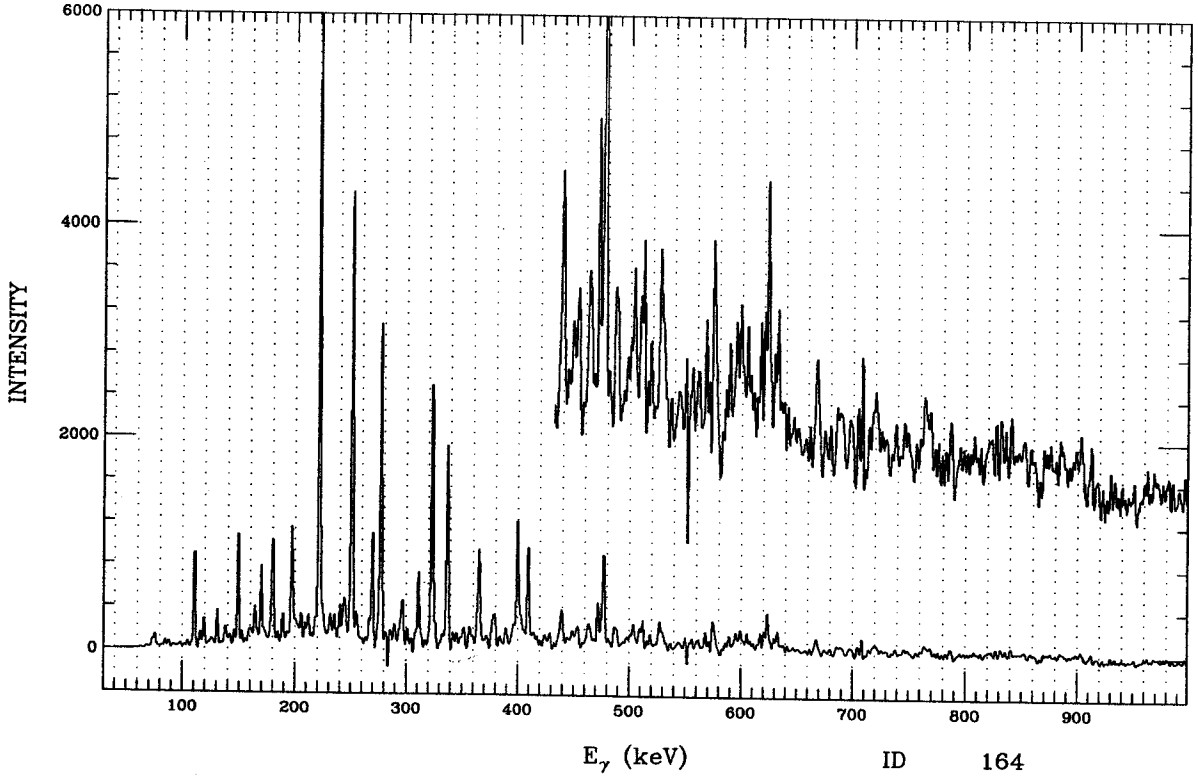

Figure F.11: ID 164. Simple gate from ^{133}Pr, band 2 (or 5).

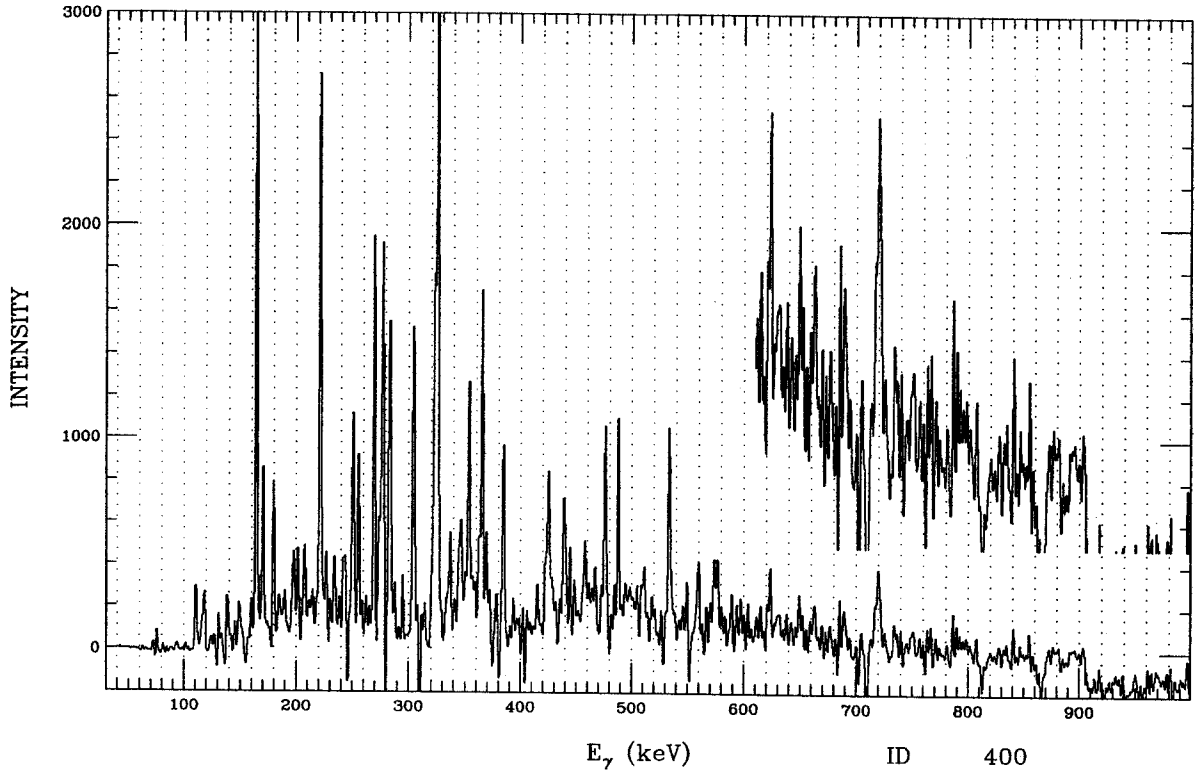

Figure F.12: ID 400. Simple gate from ^{133}Pr, band 2.

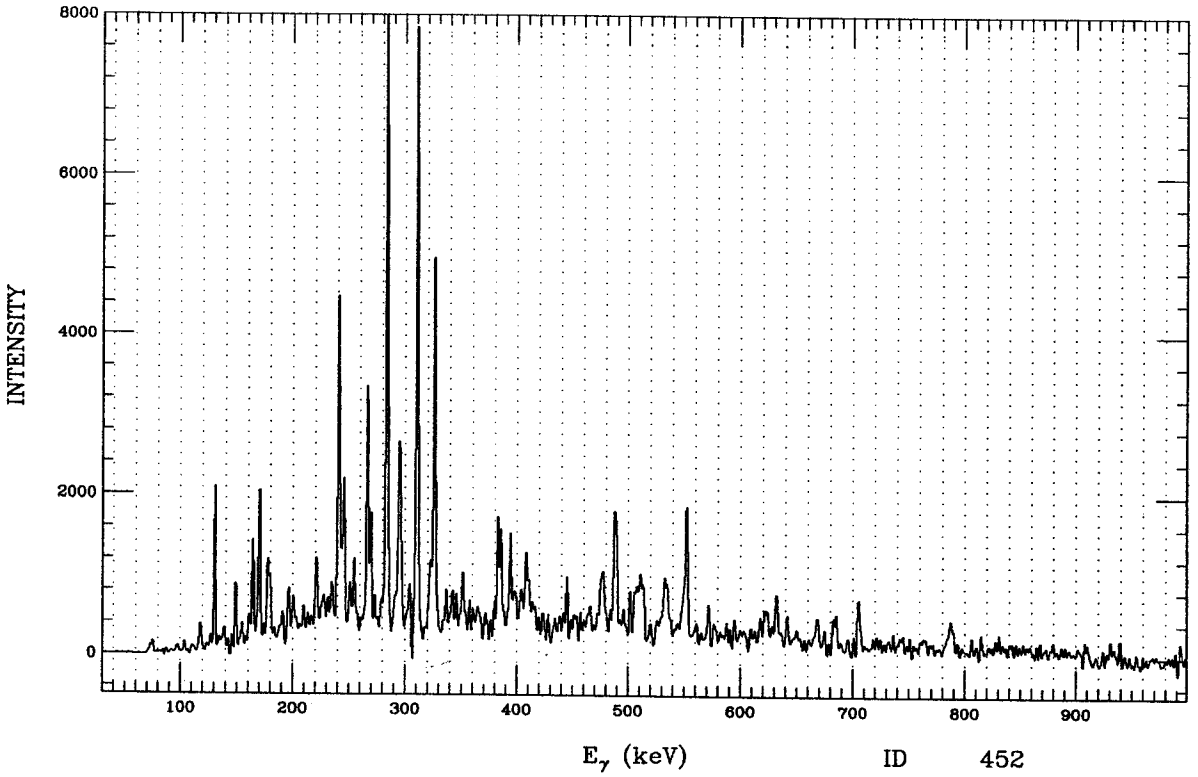

Figure F.13: ID 452. Simple gate from ^{133}Pr, band 2.

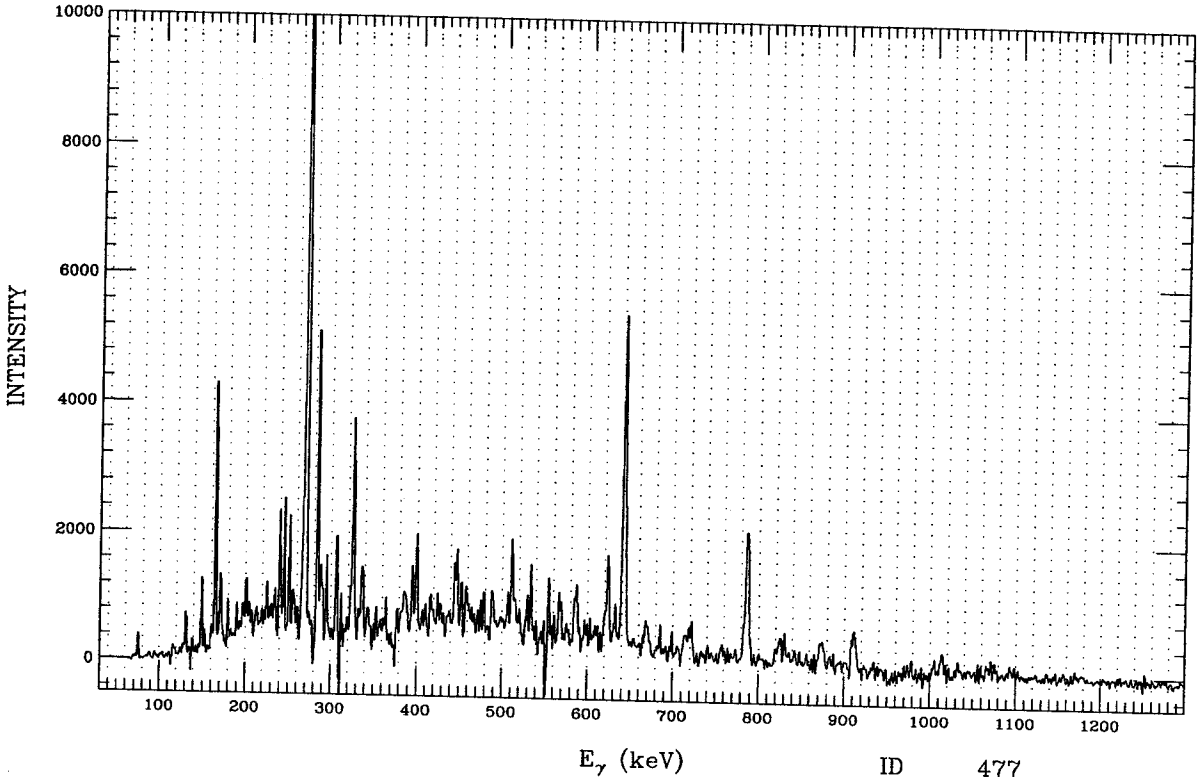

Figure F.14: ID 477. Simple gate from ^{133}Pr, band 2.

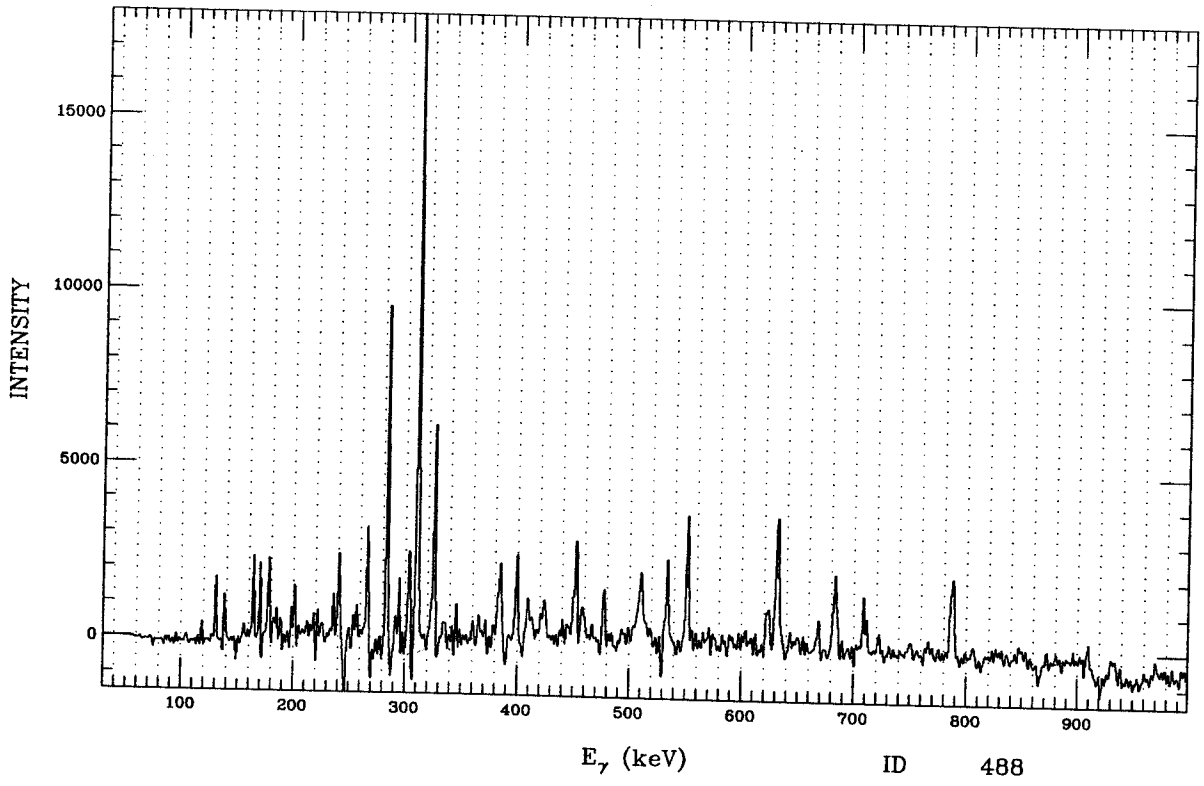

Figure F.15: ID 488. Simple gate from ^{133}Pr, band 2.

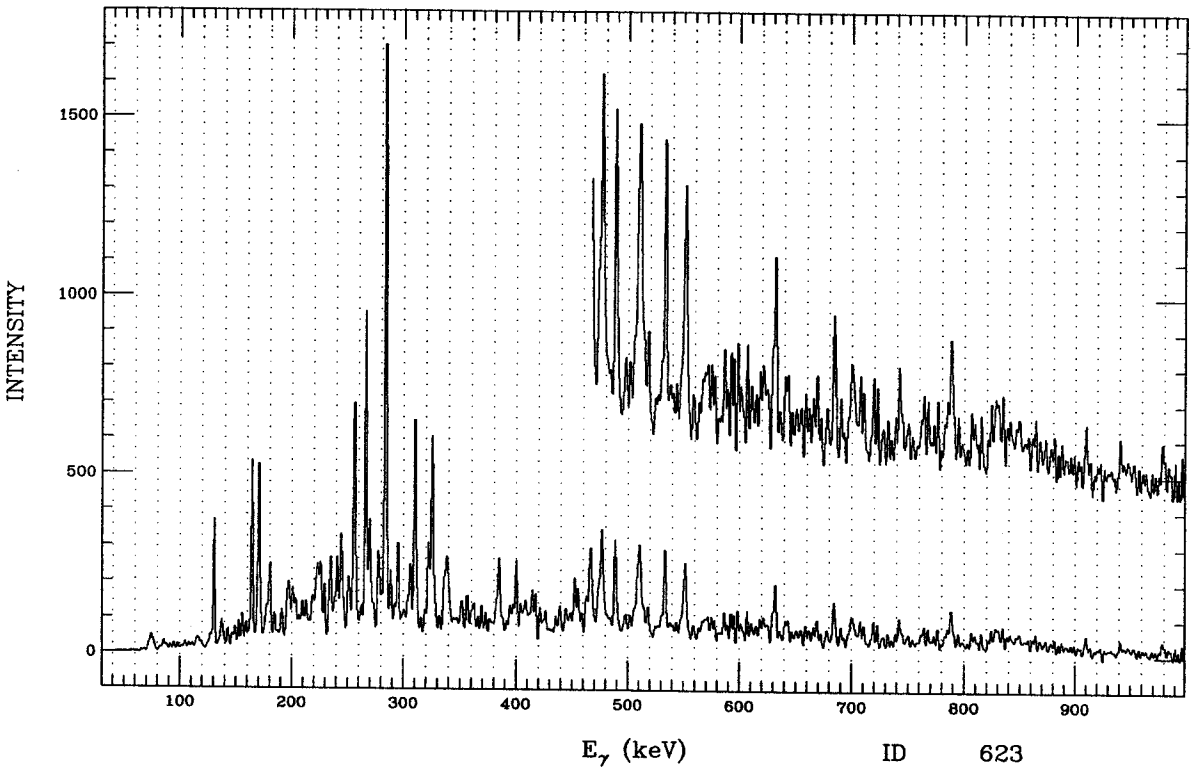

Figure F.16: ID 623. Simple gate from ^{133}Pr, band 2.

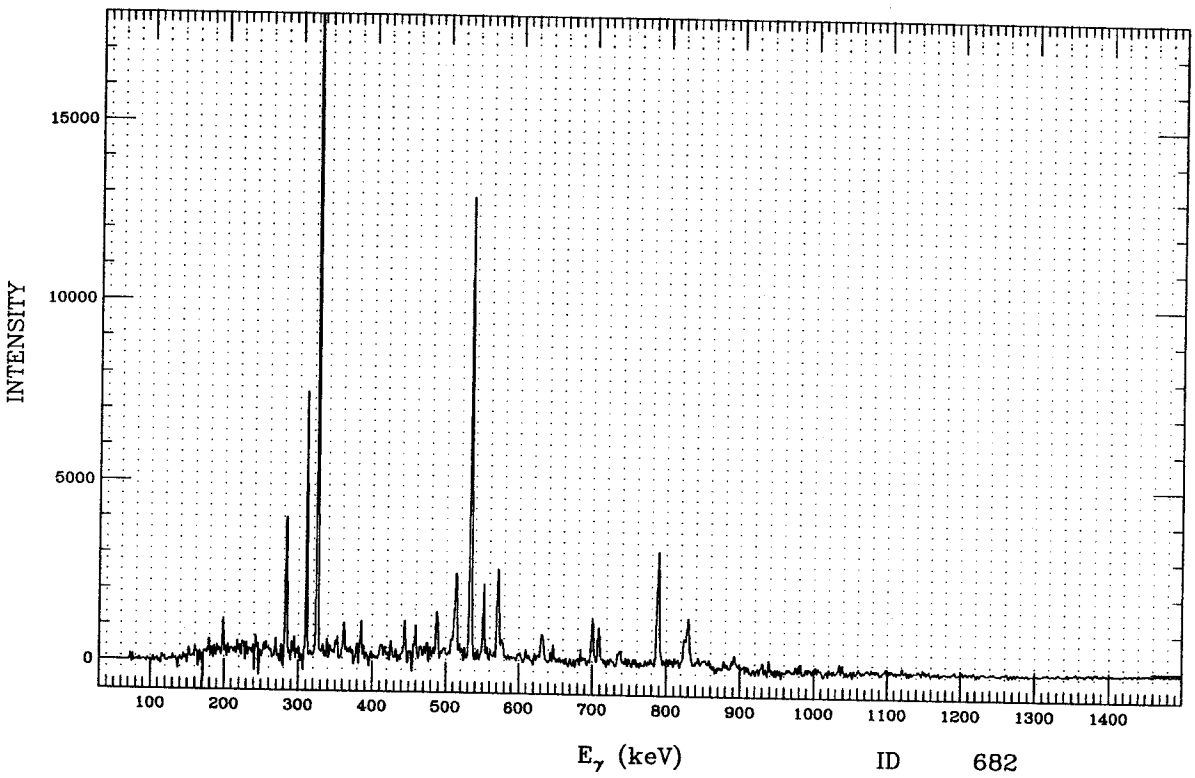

Figure F.17: ID 682. Simple gate from ^{133}Pr, a link between bands 2 and 3.

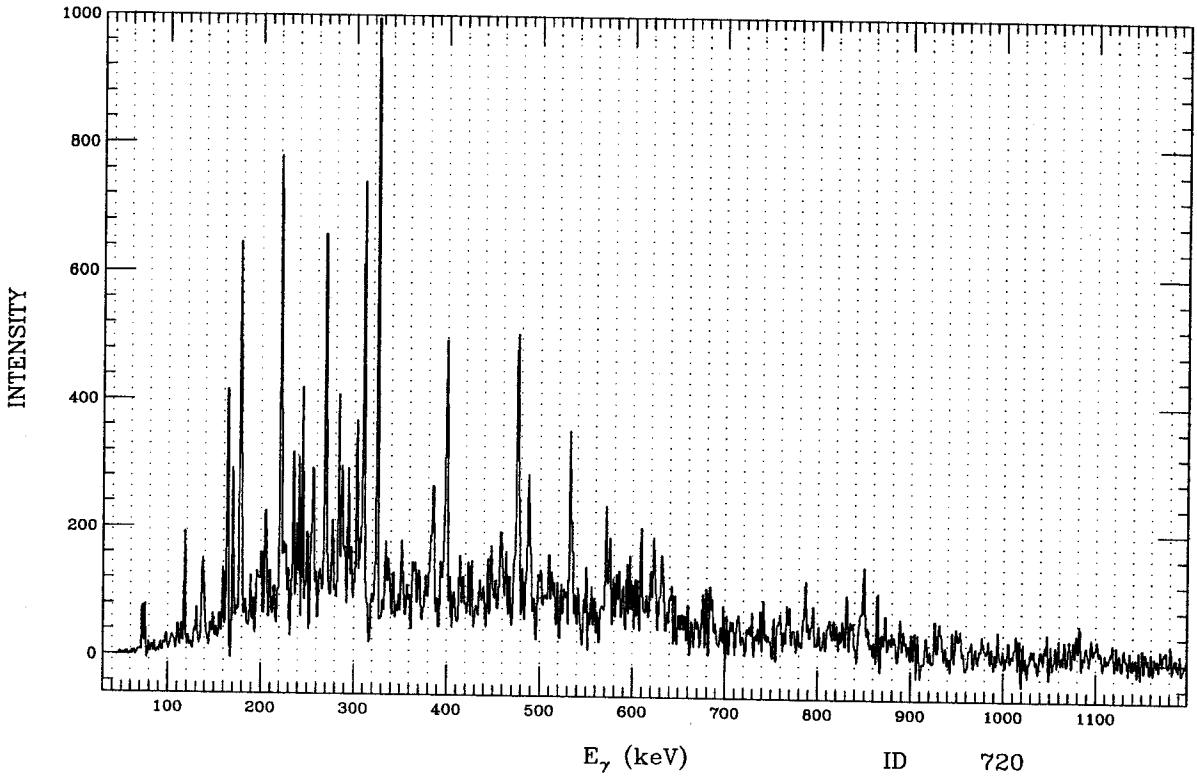

Figure F.18: ID 720. Simple gate from ^{133}Pr, band 2.

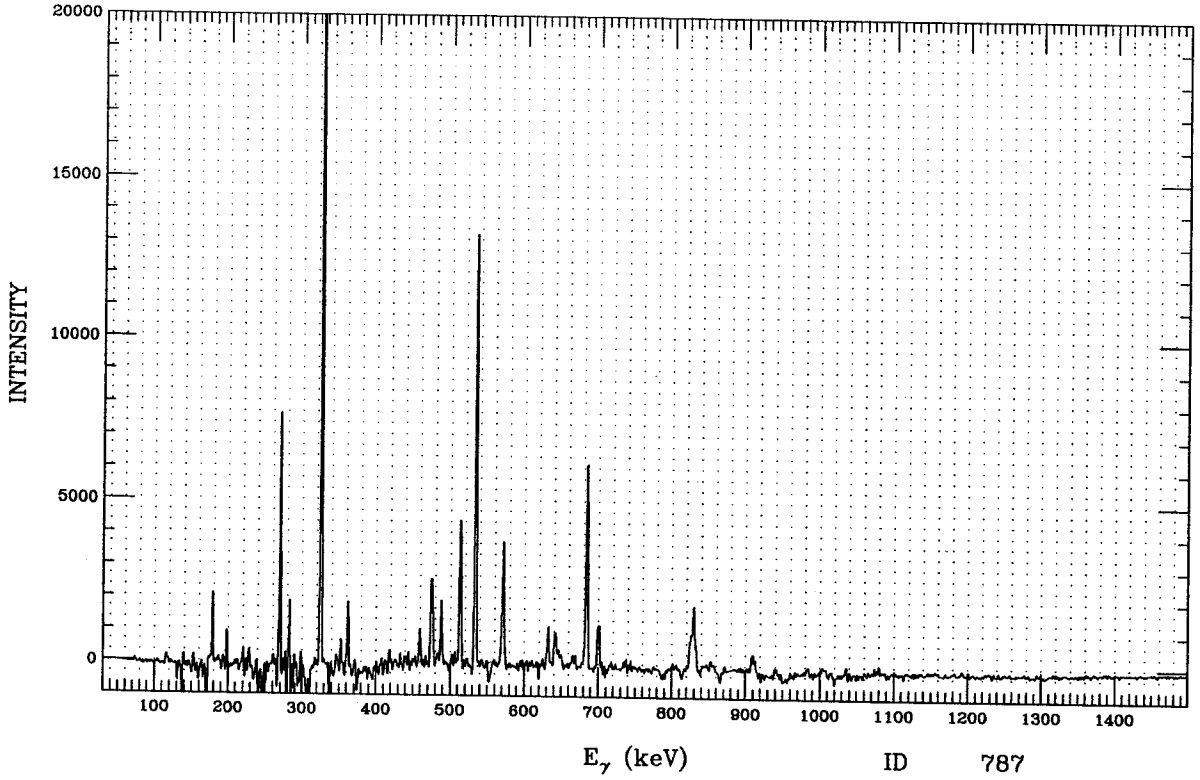

Figure F.19: ID 787. Simple gate from ^{133}Pr, band 2.

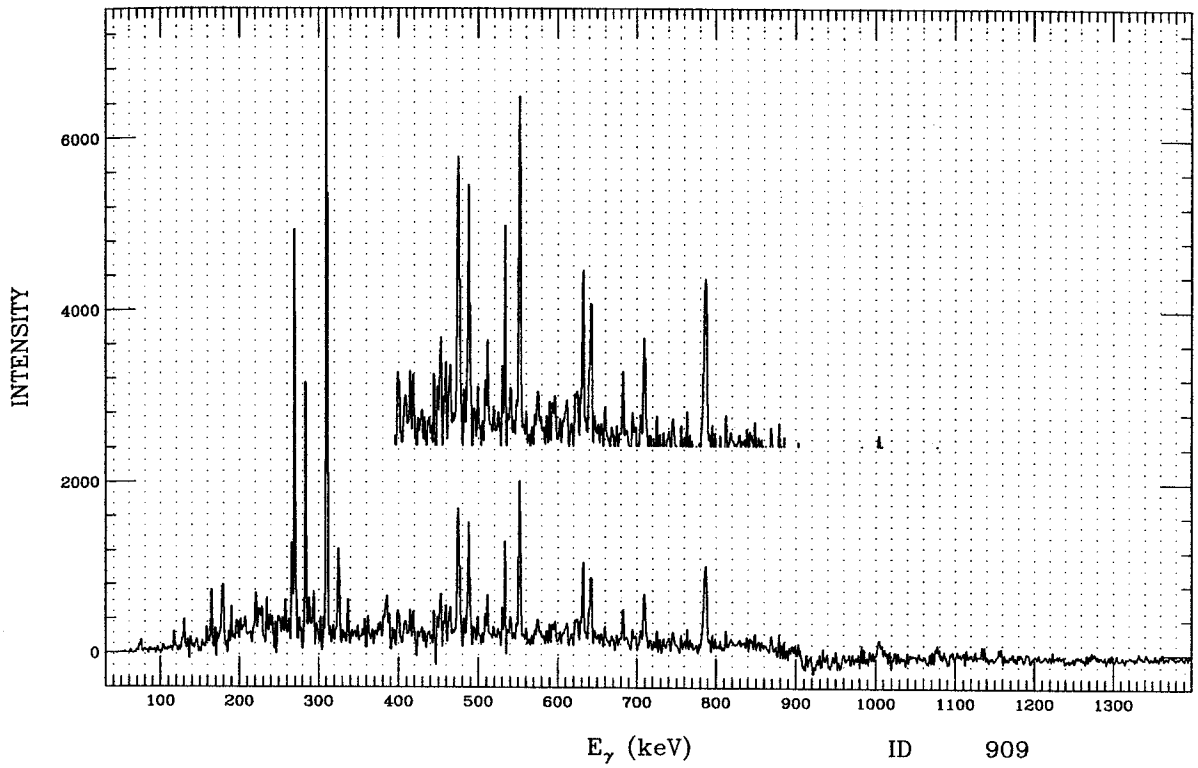

Figure F.20: ID 909. Simple gate from ^{133}Pr, band 2.

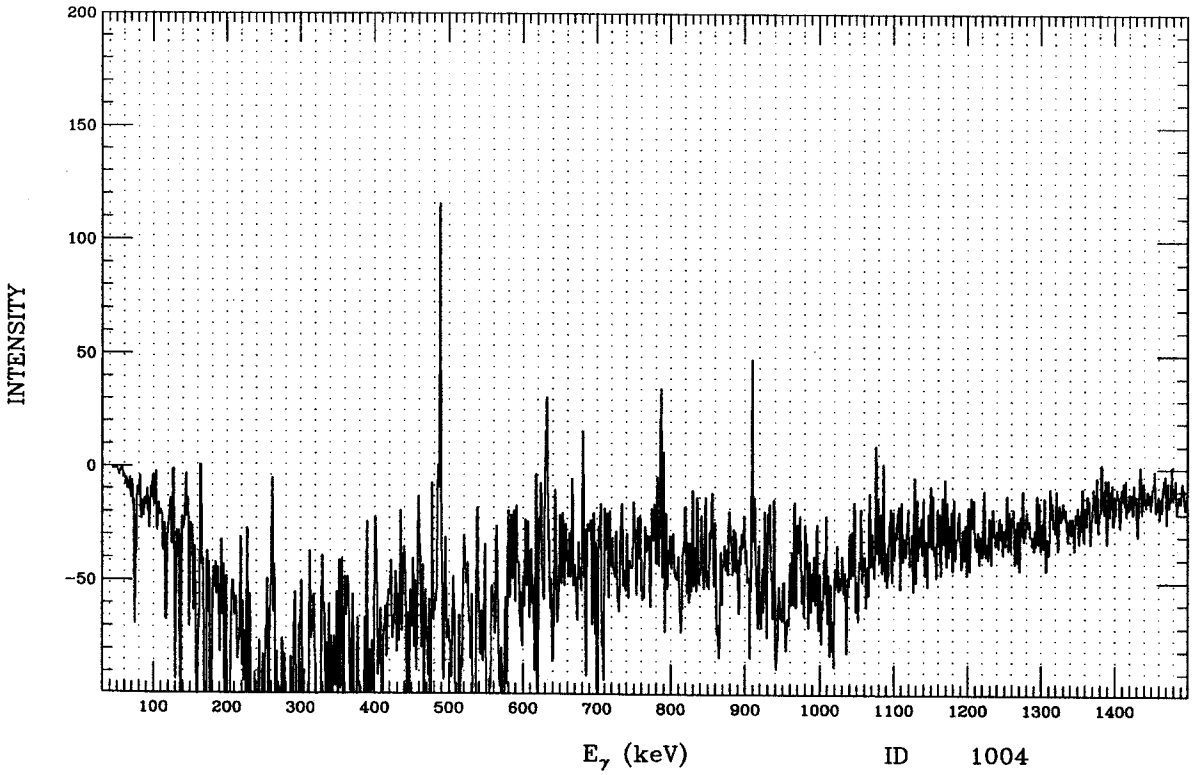

Figure F.21: ID 1004. Simple gate from ^{133}Pr, band 2.

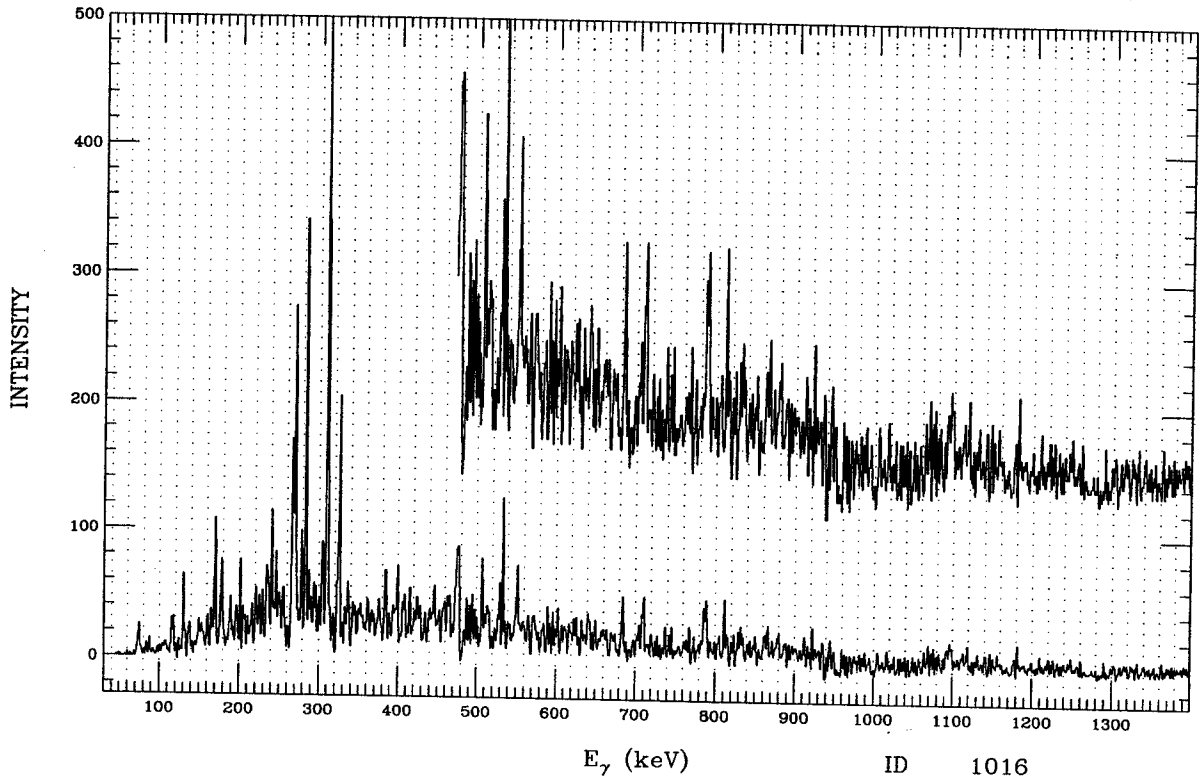

Figure F.22: ID 1016. Simple gate from ^{133}Pr, band 2.

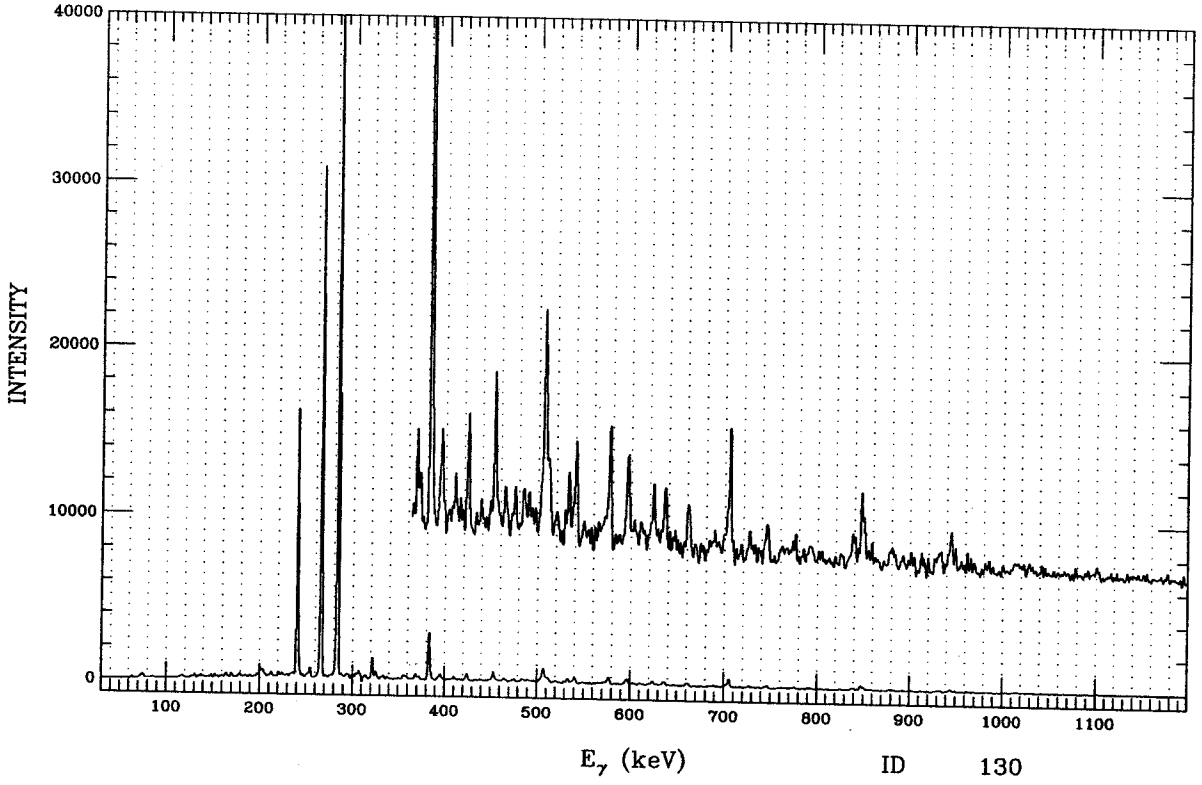

Figure F.23: ID 130. Simple gate from ^{133}Pr array, for the ^{132}Pr nucleus.

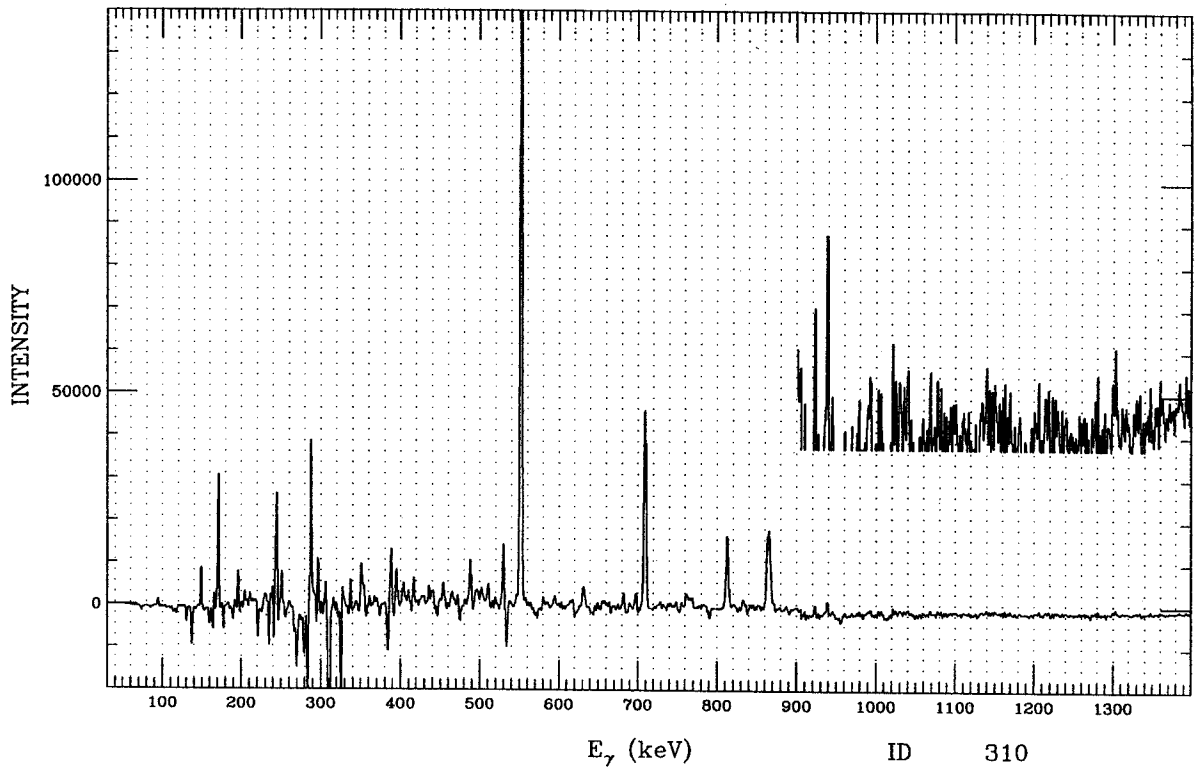

Figure F.24: ID 310. Simple gate from ^{133}Pr, band 3.

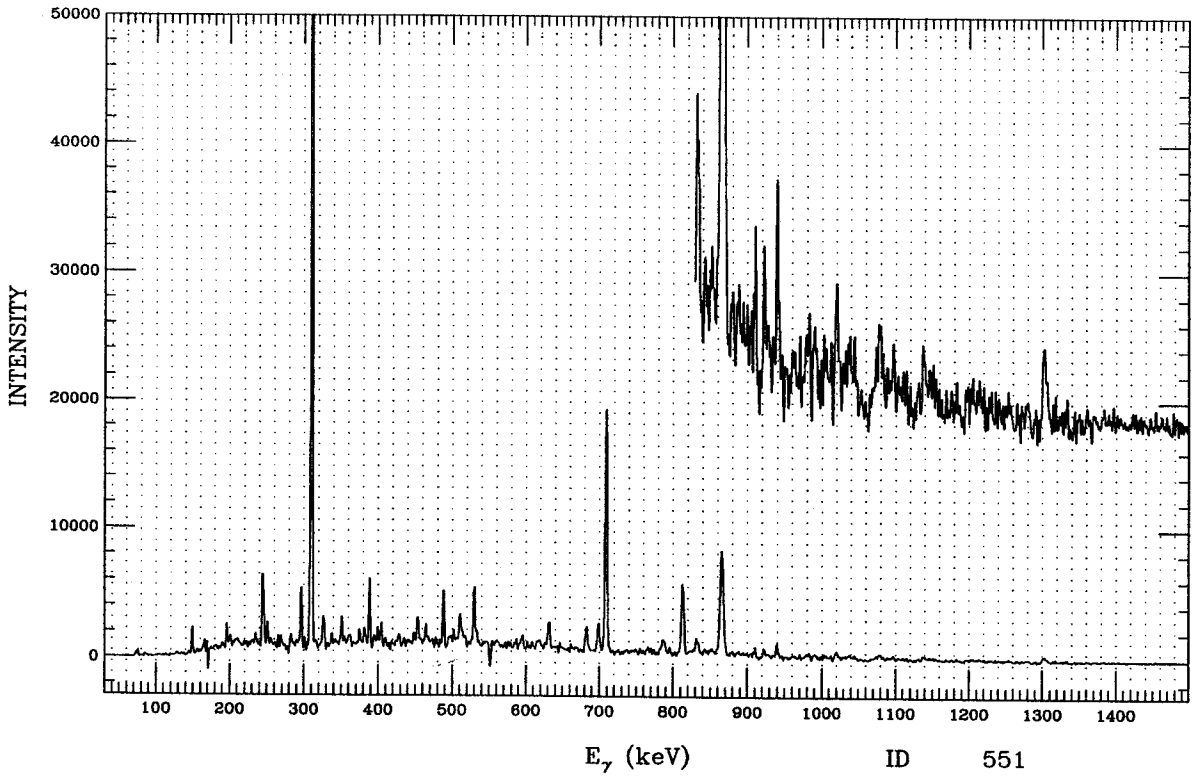

Figure F.25: ID 551. Simple gate from ^{133}Pr, band 3.

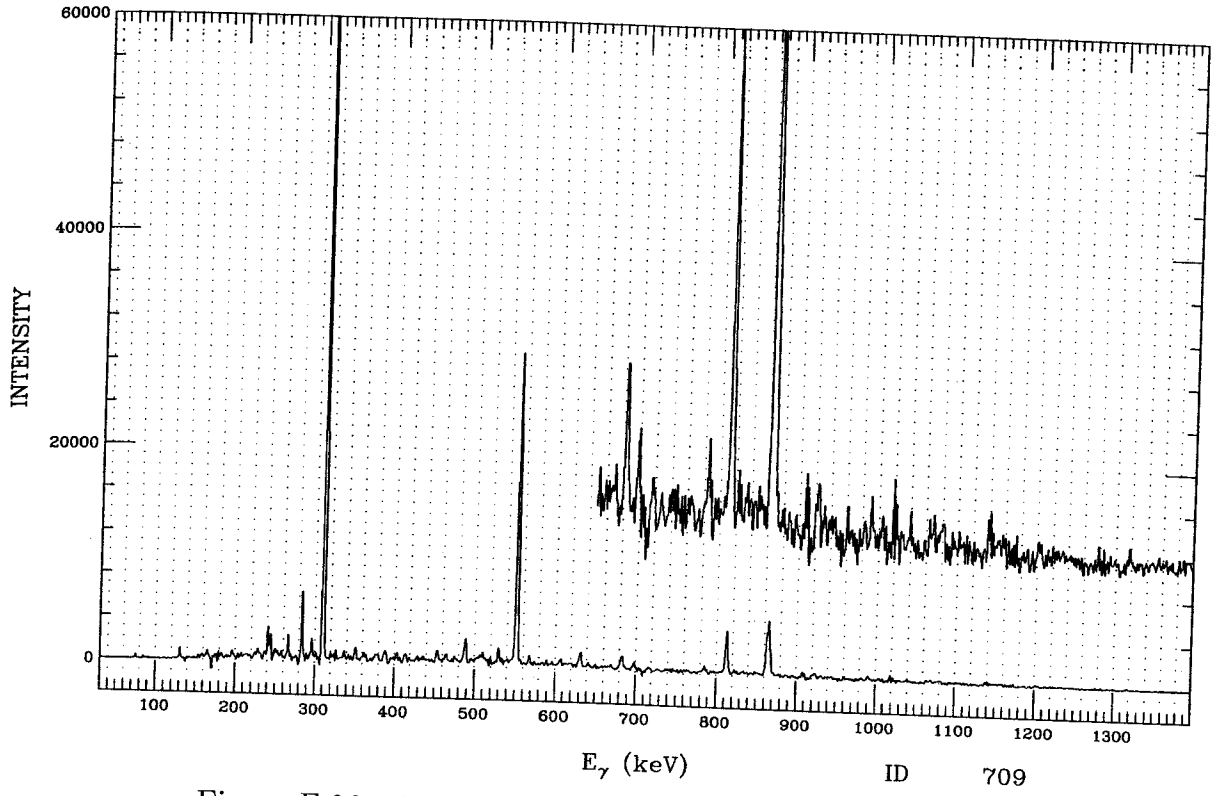

Figure F.26: ID 709. Simple gate from ^{133}Pr, band 3.

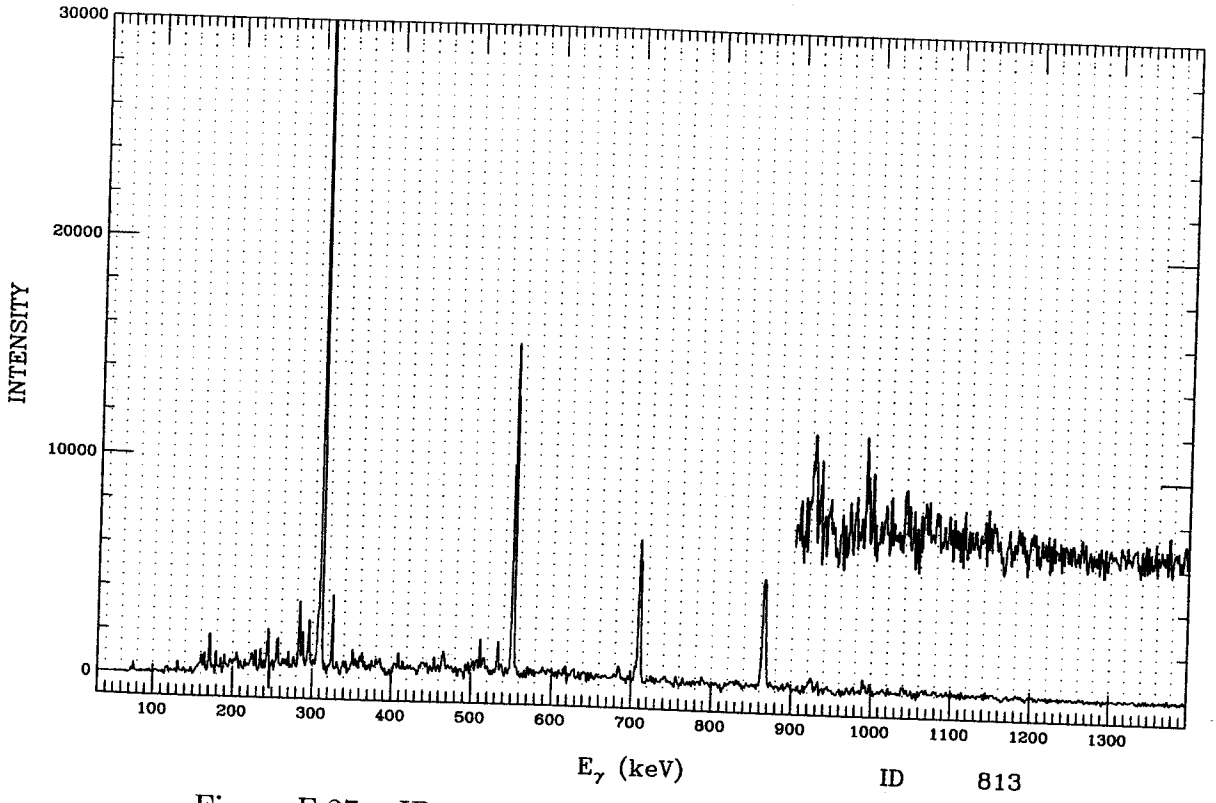

Figure F.27: ID 812. Simple gate from ^{133}Pr, band 3.

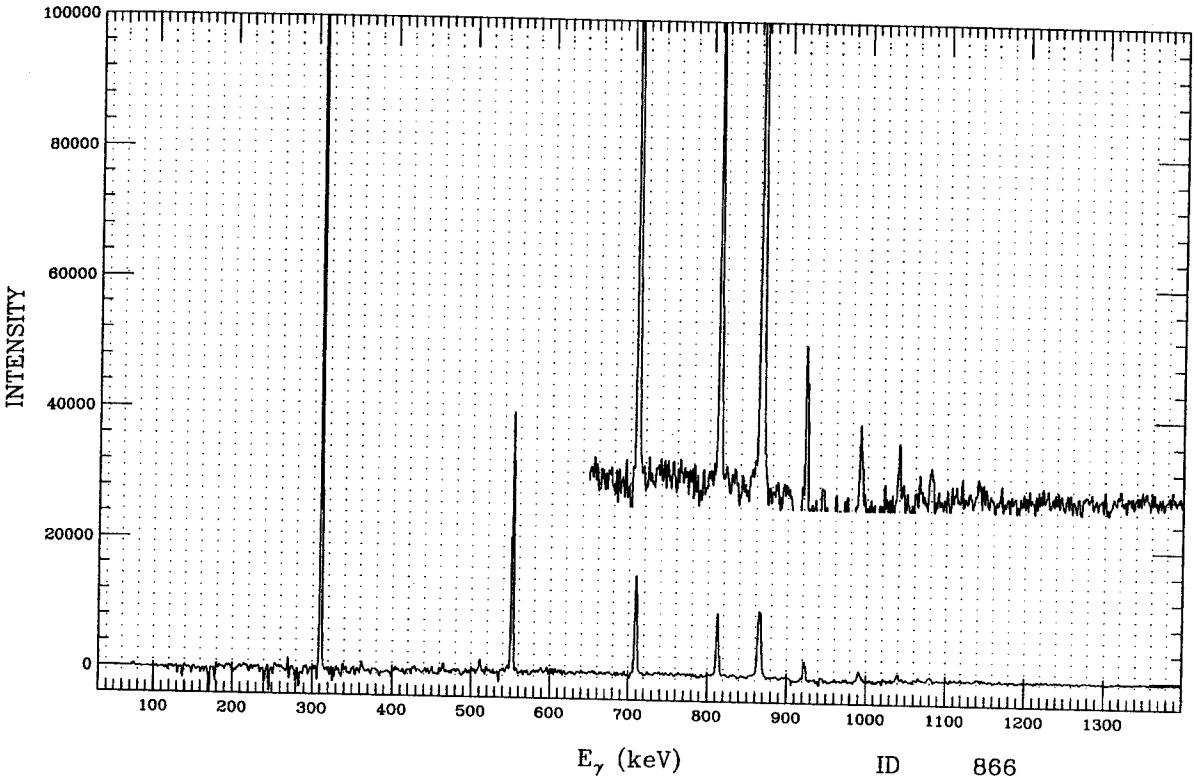

Figure F.28: ID 864-868 triplet. Simple gate from ^{133}Pr, band 3.

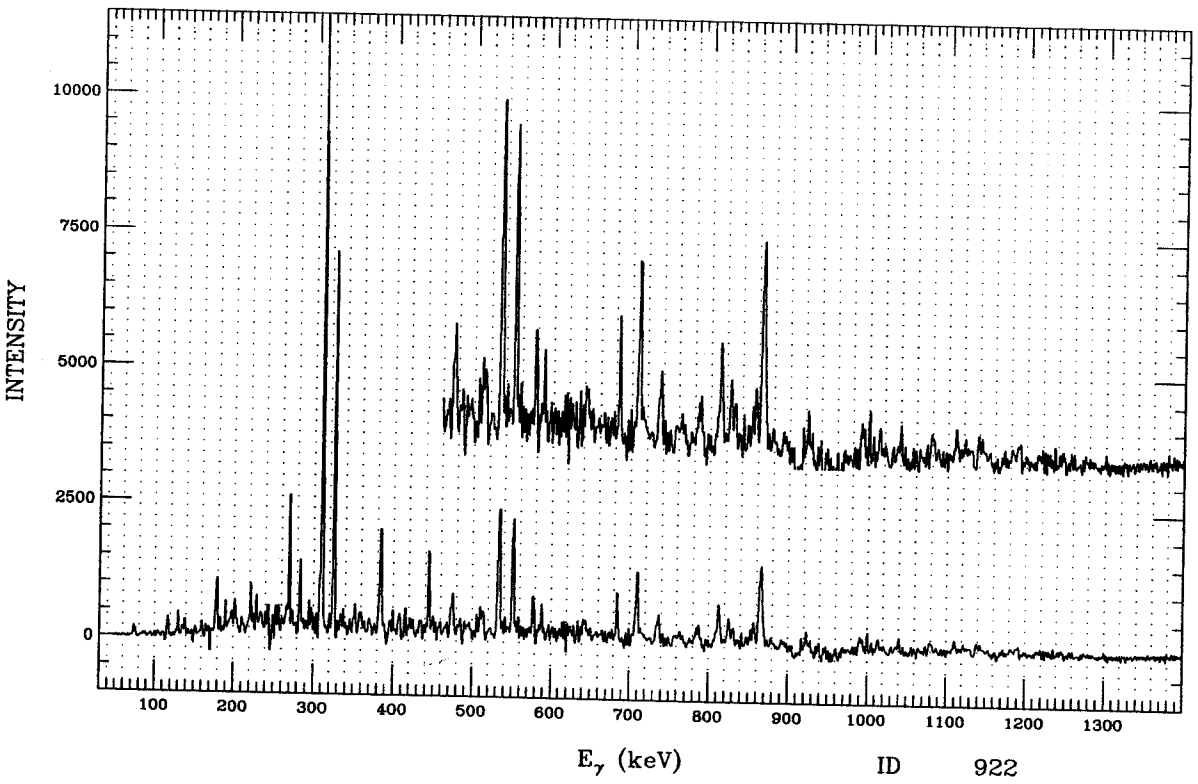

Figure F.29: ID 922. Simple gate from ^{133}Pr, band 3.

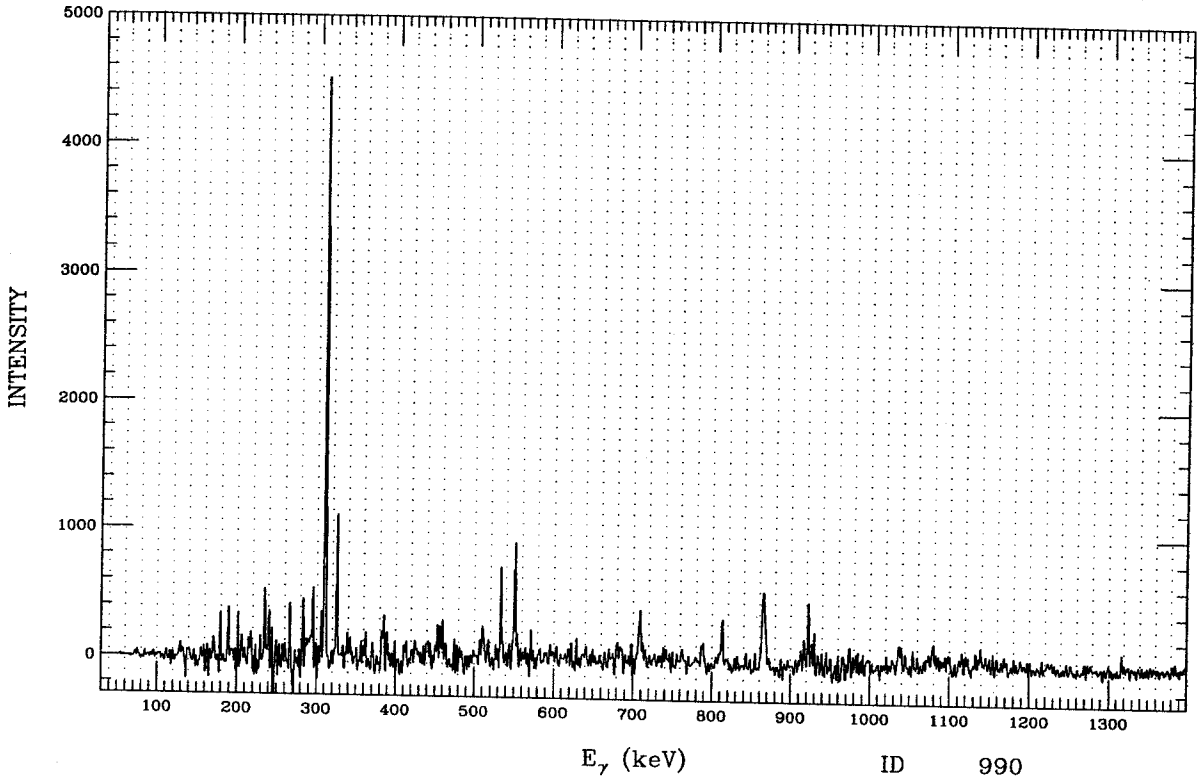

Figure F.30: ID 990. Simple gate from ^{133}Pr, band 3.

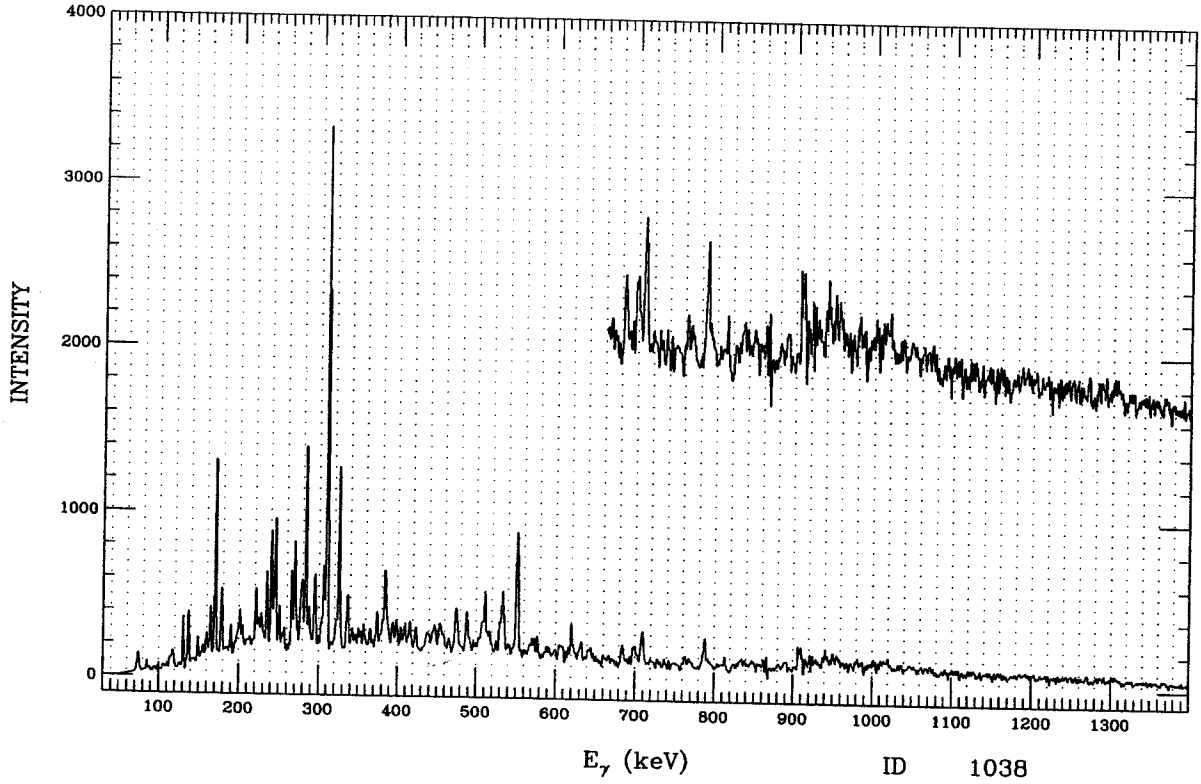

Figure F.31: ID 1037. Simple gate from ^{133}Pr, band 3.

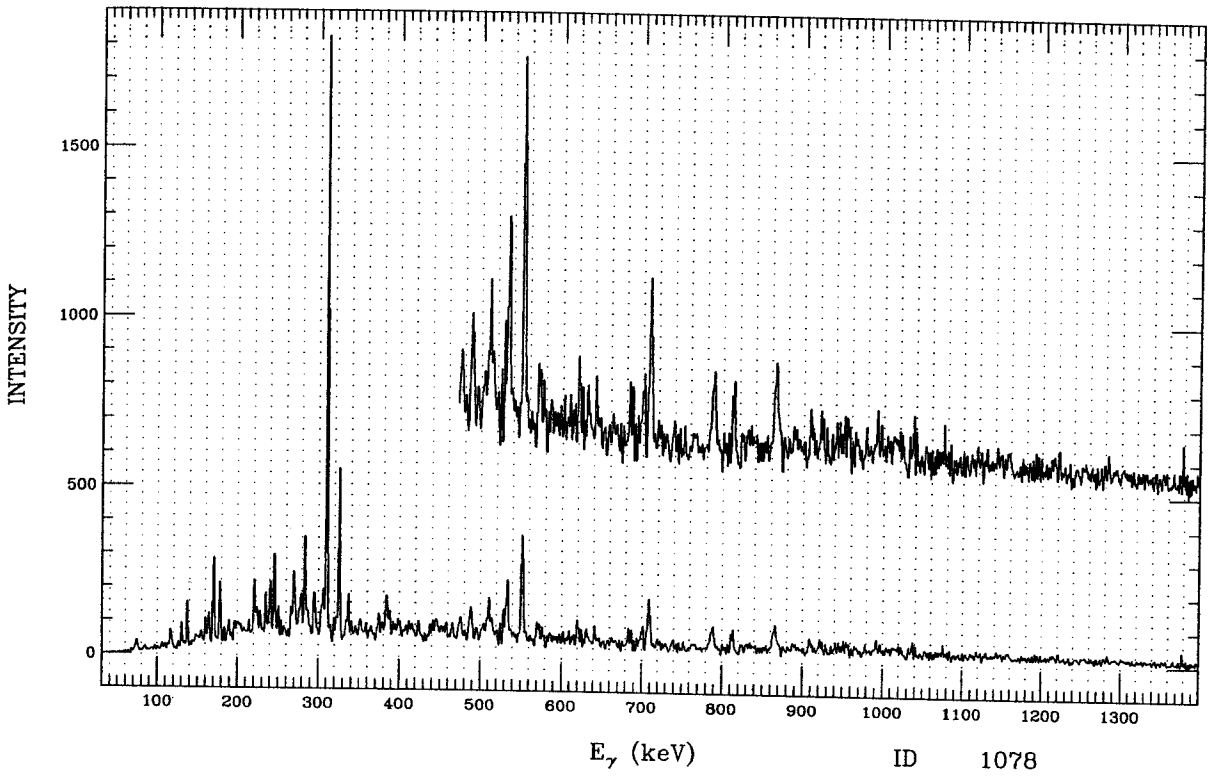

Figure F.32: ID 1078. Simple gate from ^{133}Pr, band 3.

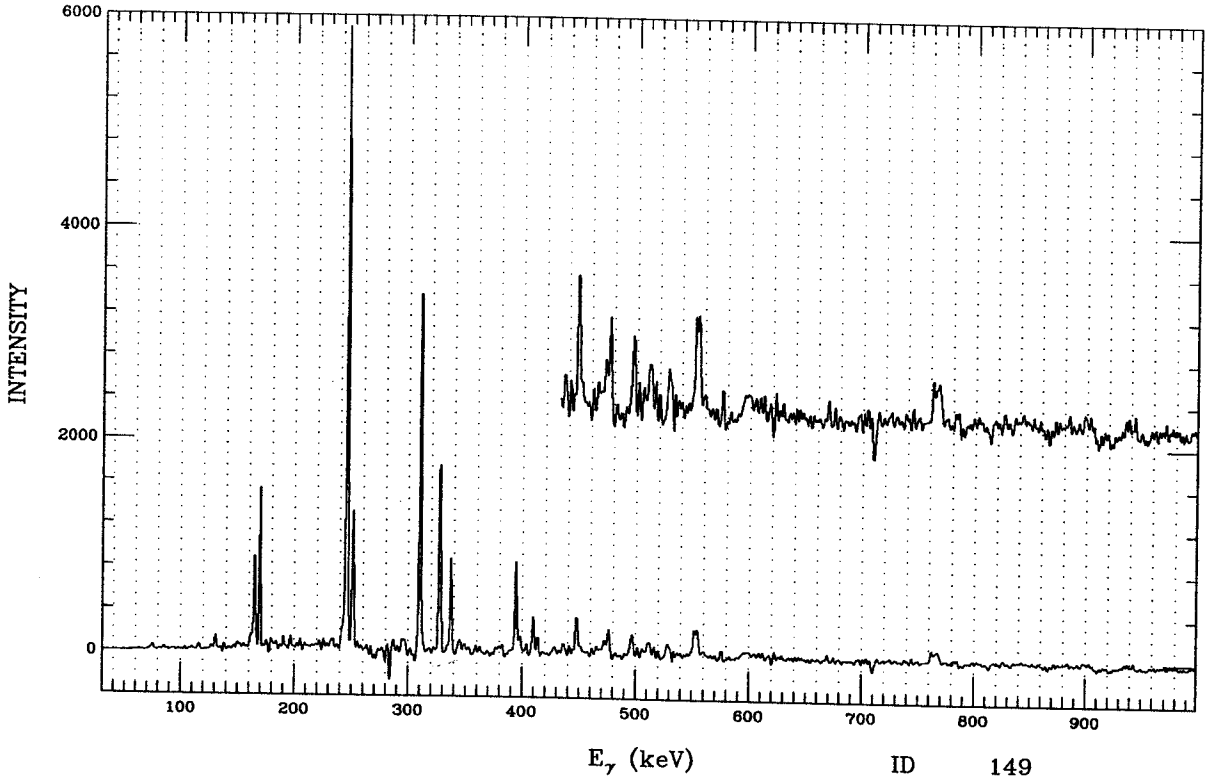

Figure F.33: ID 149. Simple gate from ^{133}Pr, band 4.

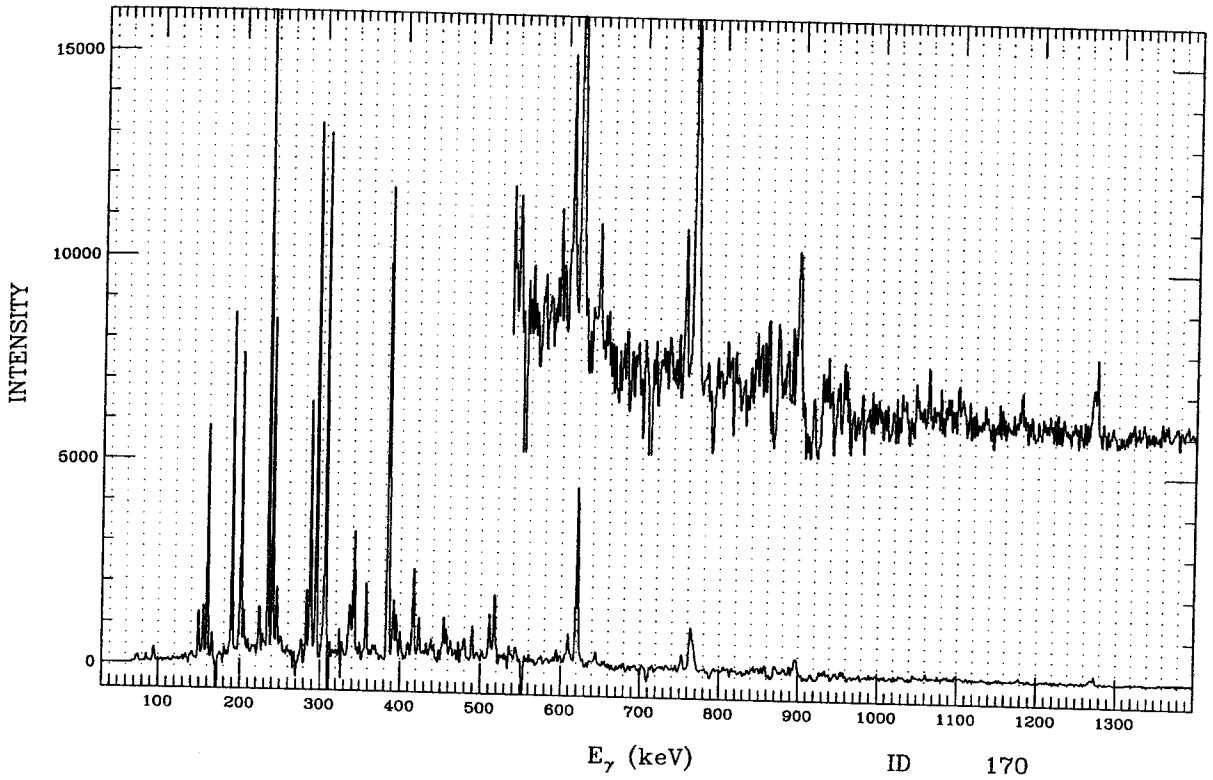

Figure F.34: ID 170. Simple gate from ^{133}Pr, band 4.

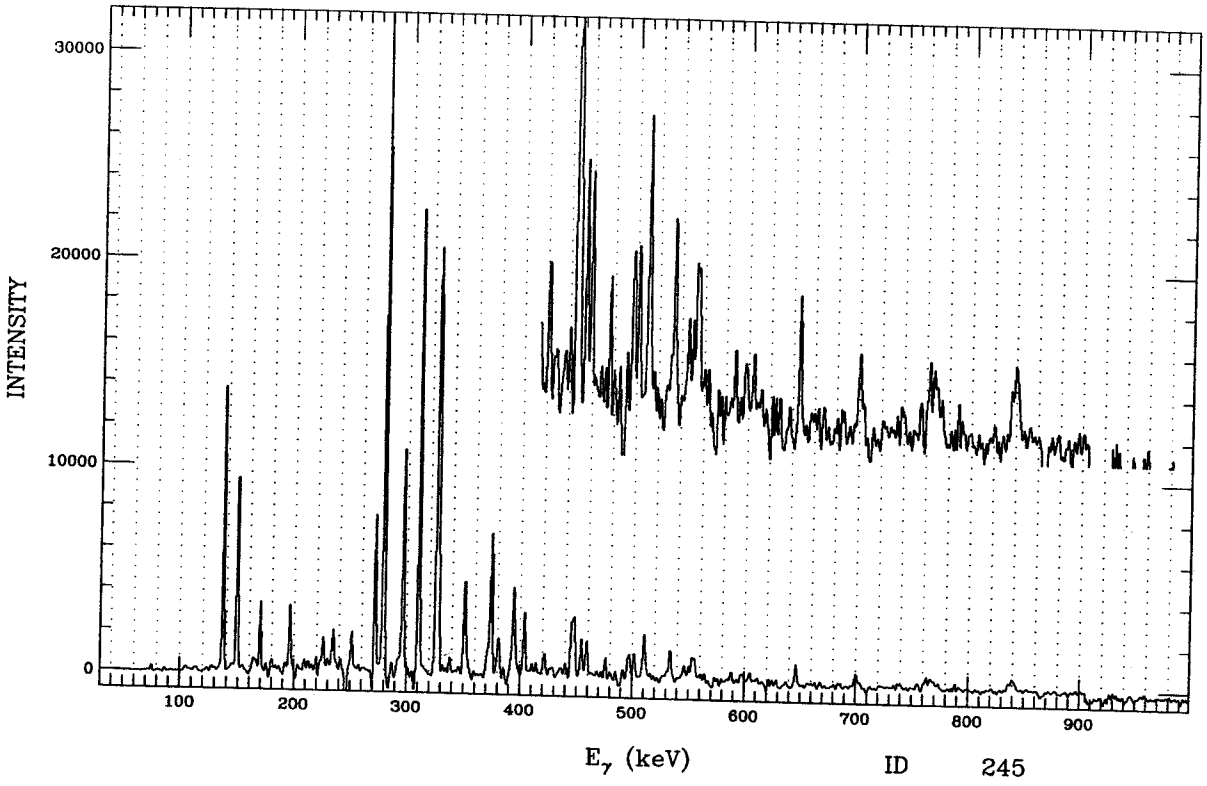

Figure F.35: ID 245. Simple gate from ^{133}Pr, band 4.

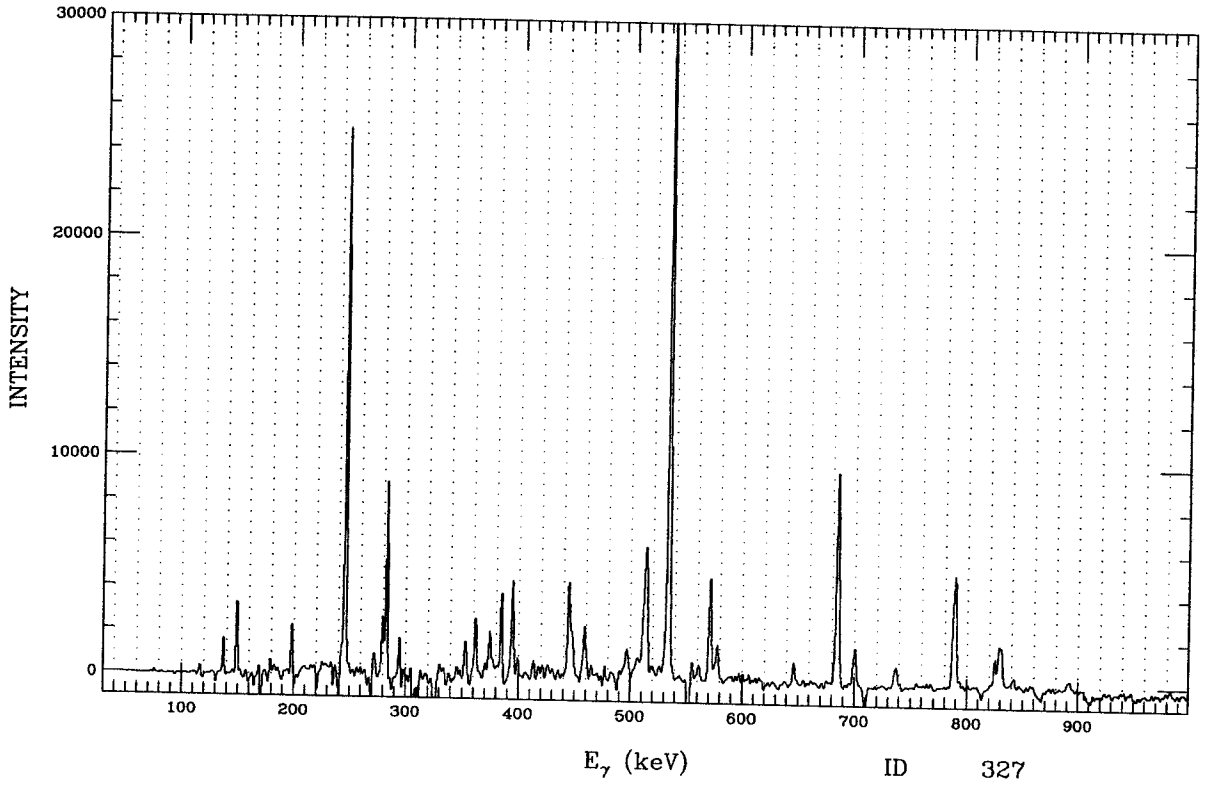

Figure F.36: ID 327. Simple gate from ^{133}Pr, band 4.

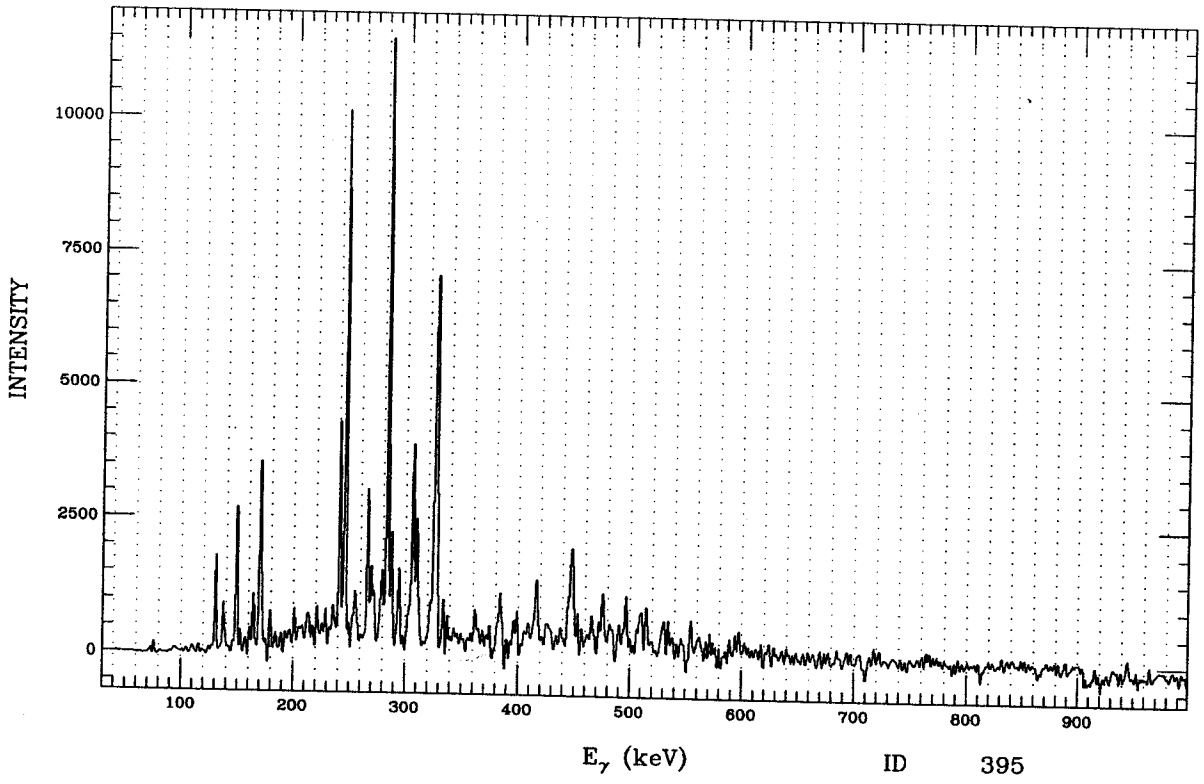

Figure F.37: ID 395. Simple gate from ^{133}Pr, band 4.

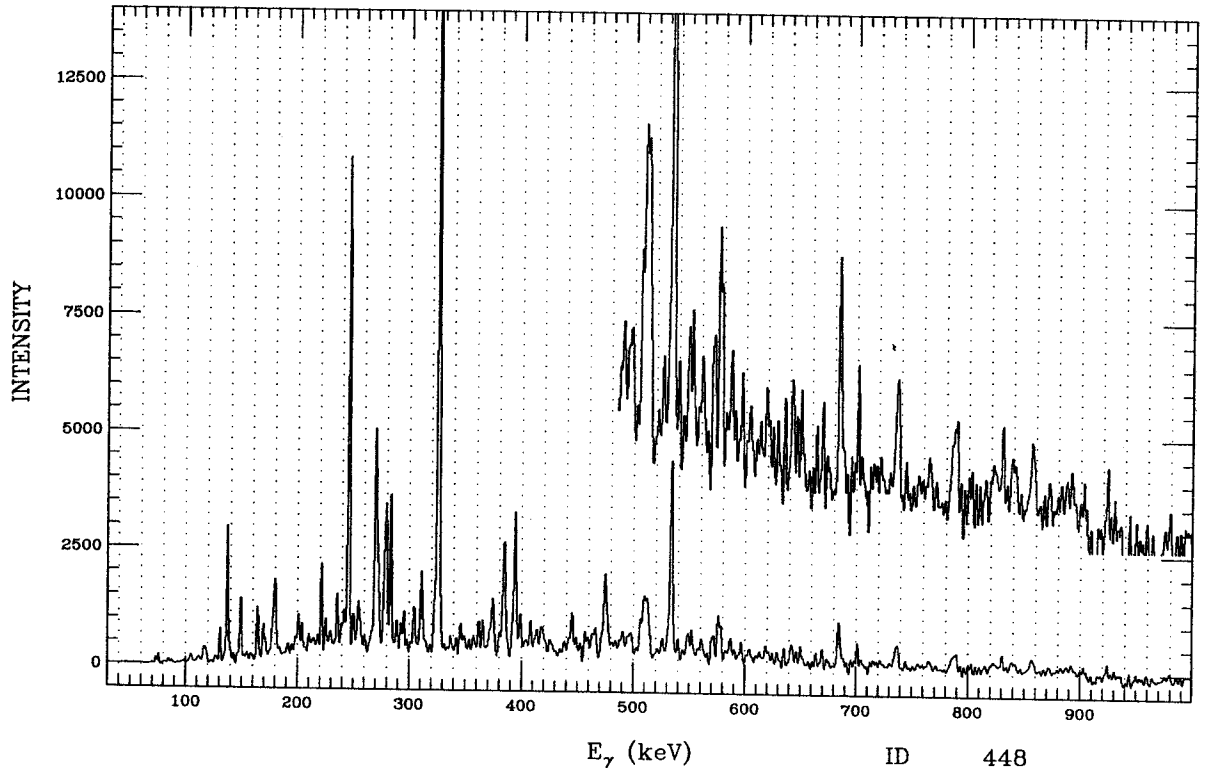

Figure F.38: ID 448. Simple gate from ^{133}Pr, band 4.

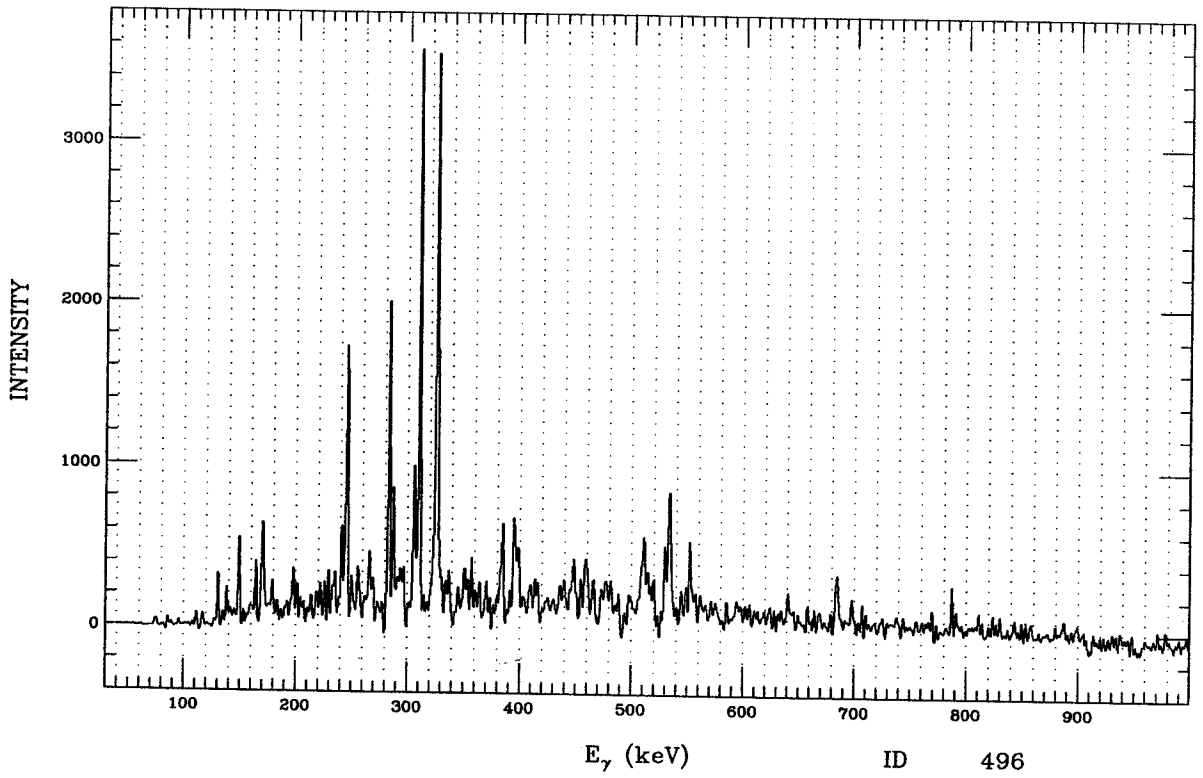

Figure F.39: ID 496. Simple gate from ^{133}Pr, band 4.

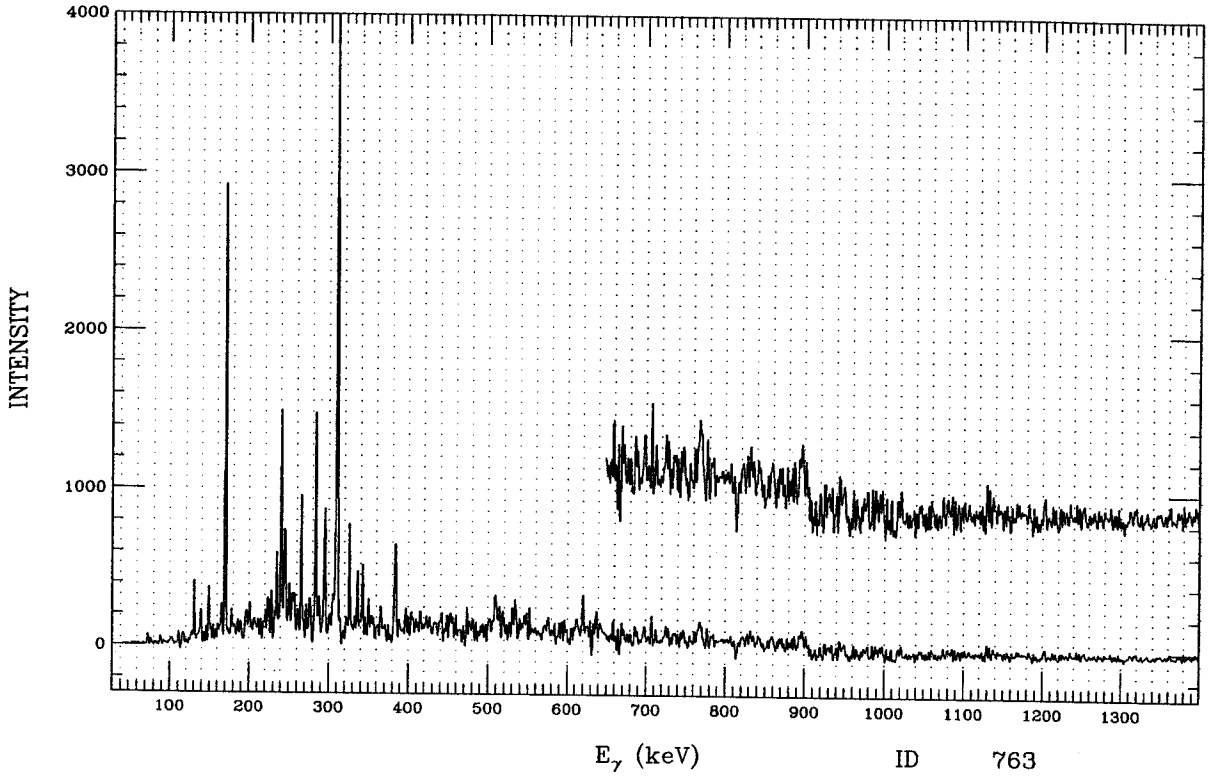

Figure F.40: ID 763. Simple gate from ^{133}Pr, band 4.

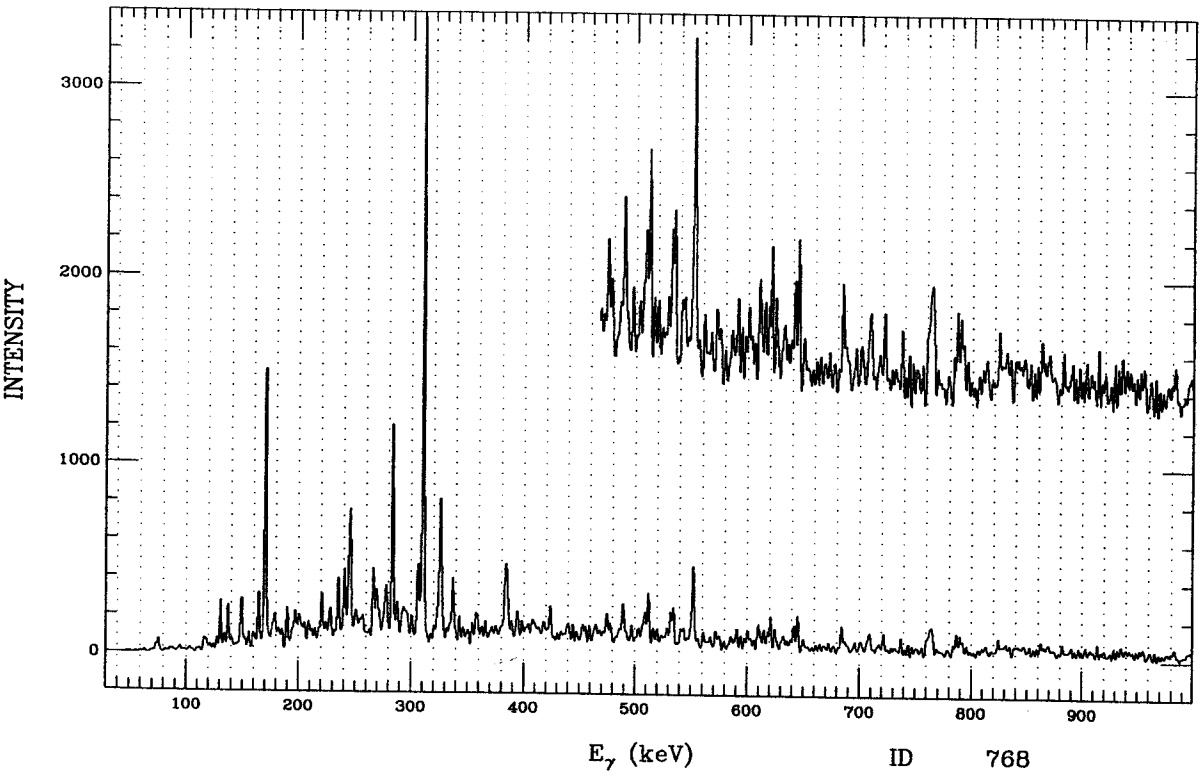

Figure F.41: ID 768. Simple gate from ^{133}Pr, band 4.

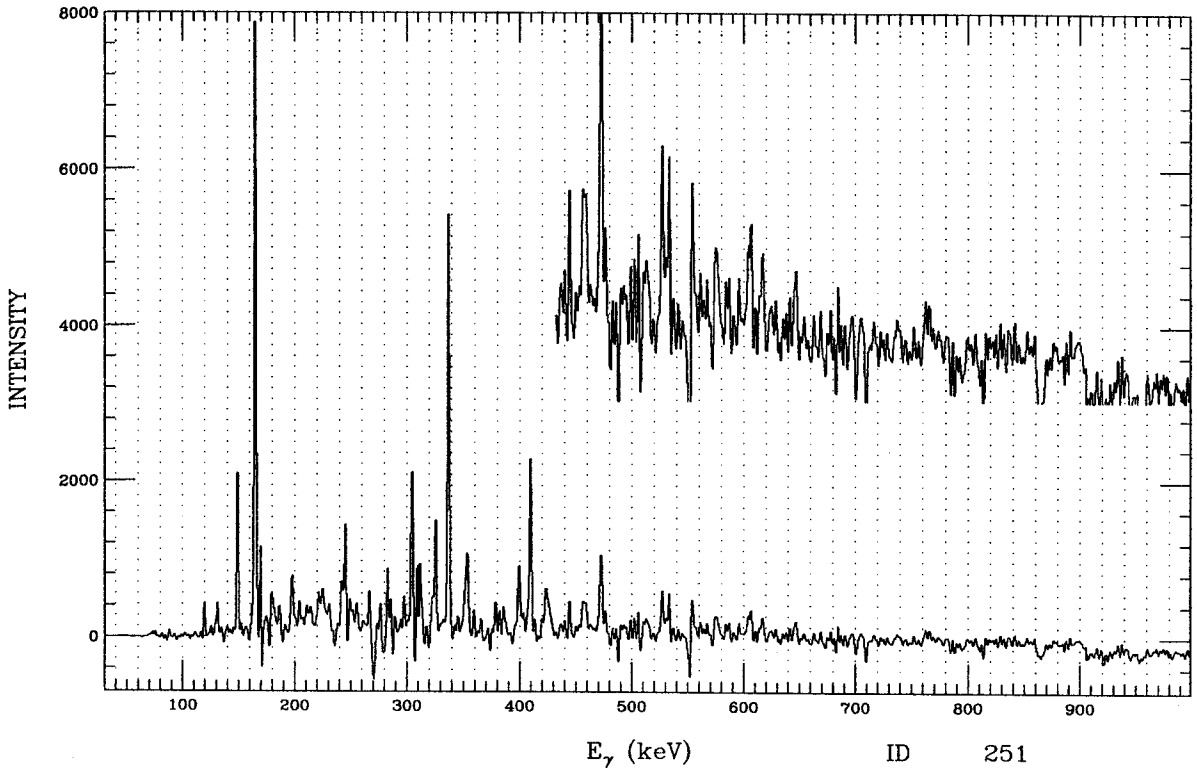

Figure F.42: ID 251. Simple gate from ^{133}Pr, band 5.

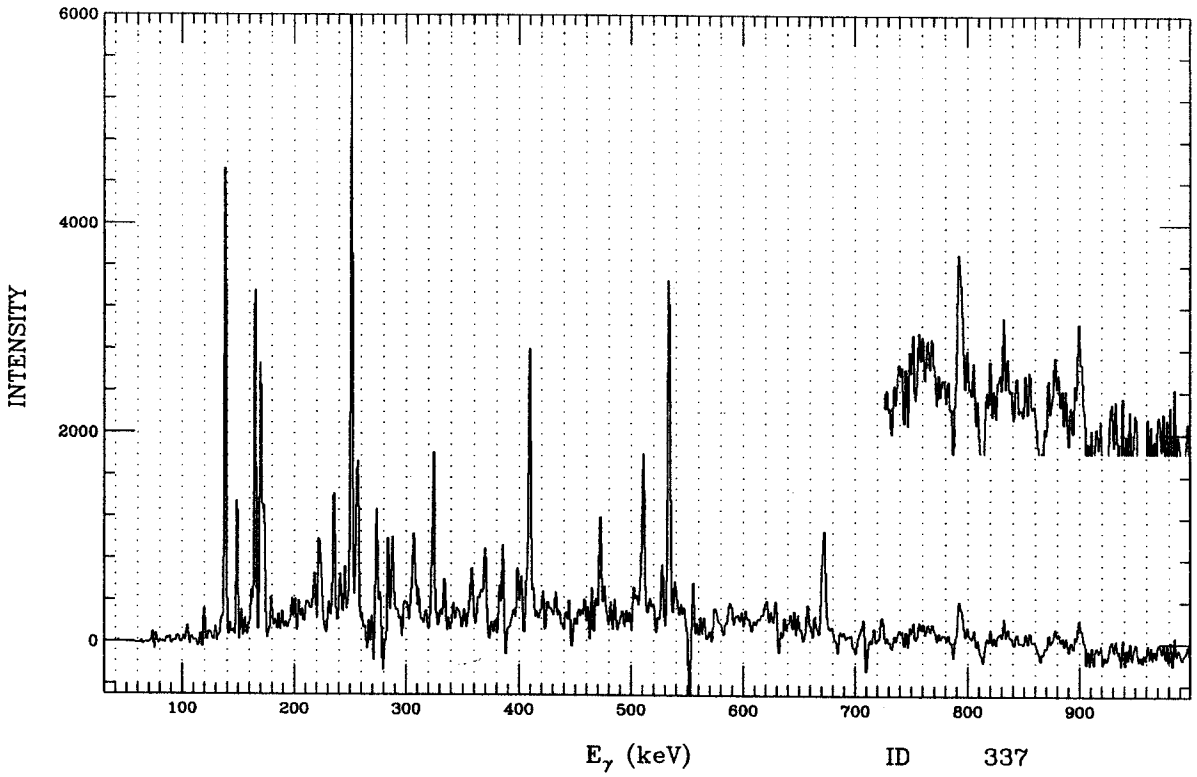

Figure F.43: ID 337. Simple gate from ^{133}Pr, band 5.

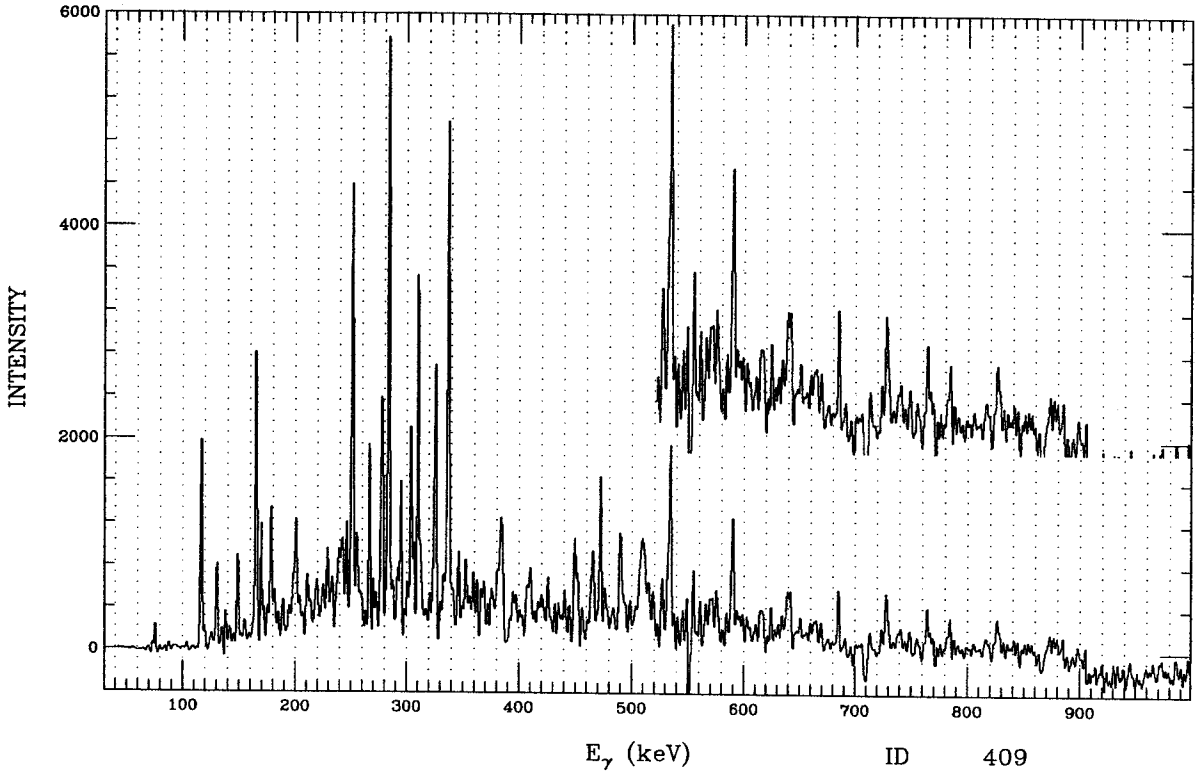

Figure F.44: ID 409. Simple gate from ^{133}Pr, band 5.

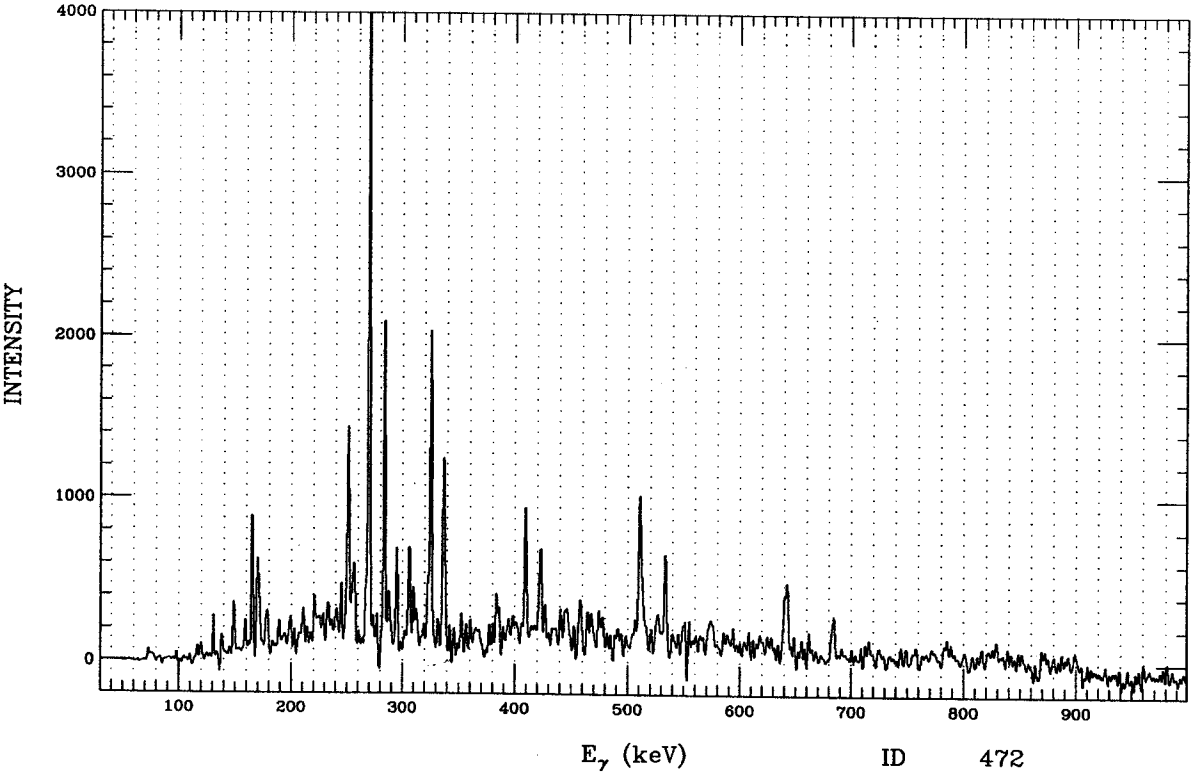

Figure F.45: ID 472. Simple gate from ^{133}Pr, band 5.

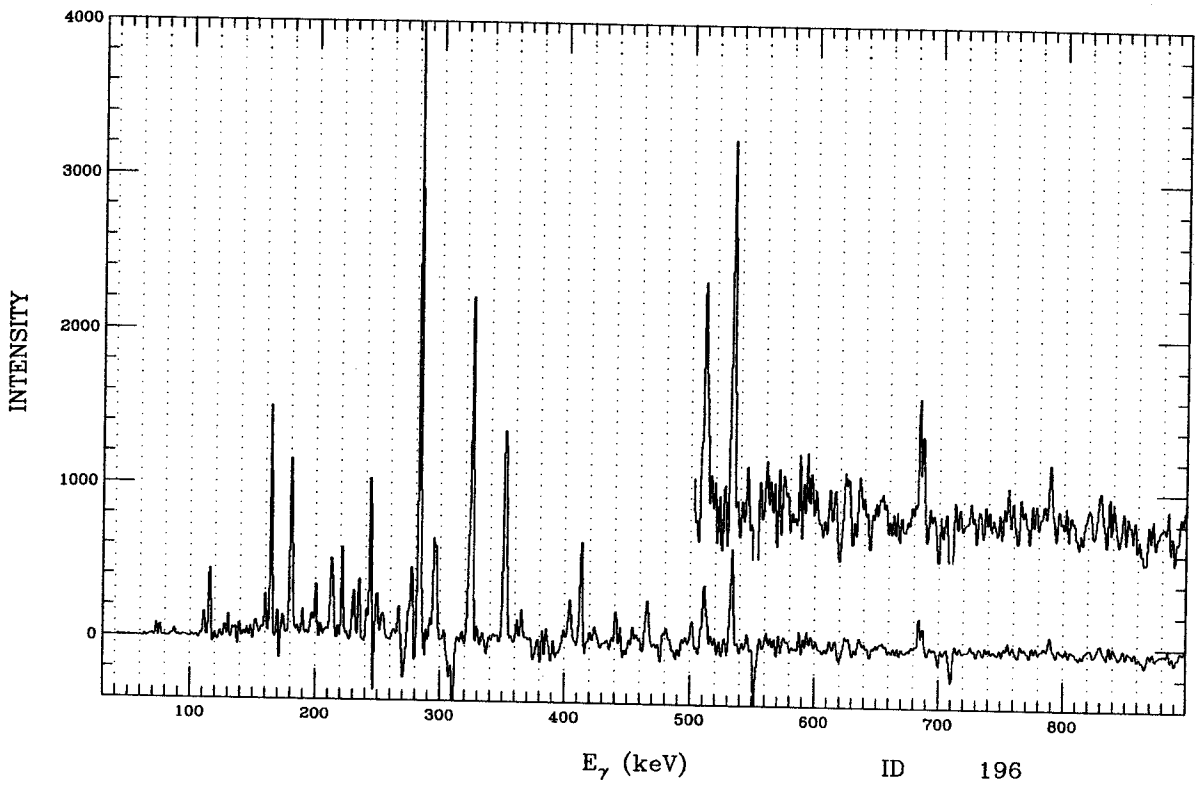

Figure F.46: ID 196. Simple gate from ^{133}Pr, band 6.

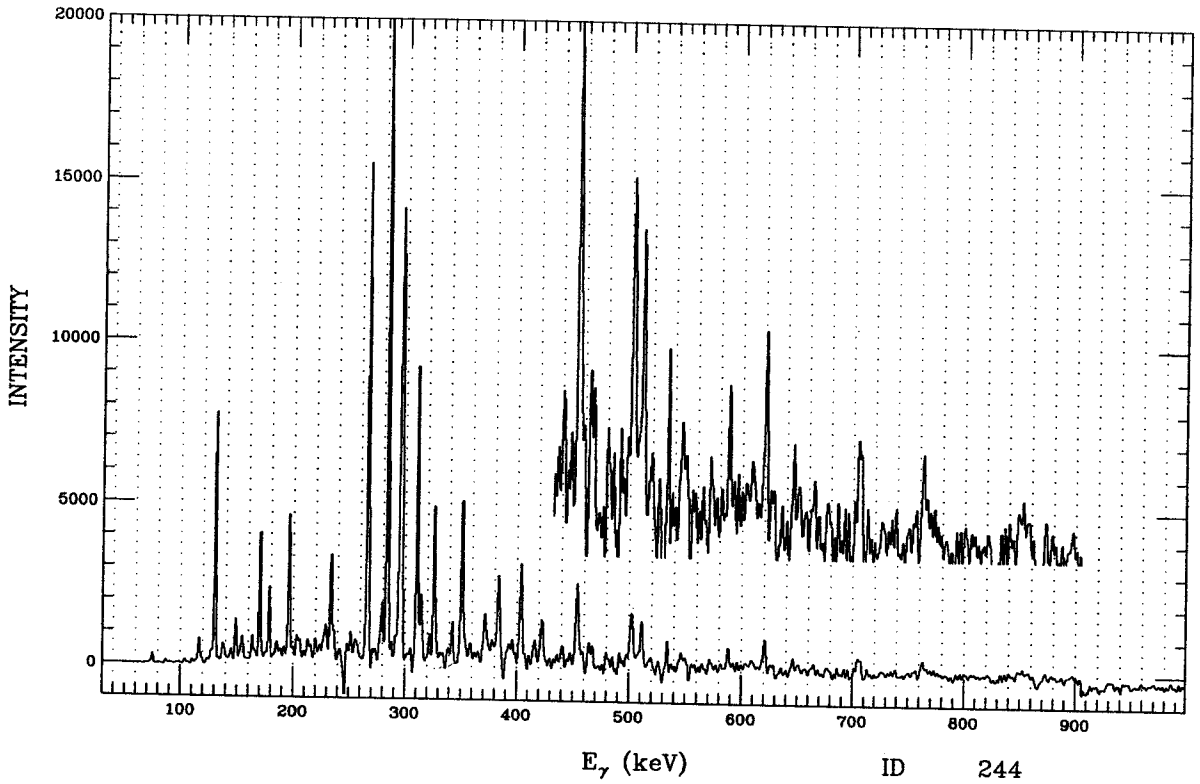

Figure F.47: ID 244. Simple gate from ^{133}Pr, band 6.

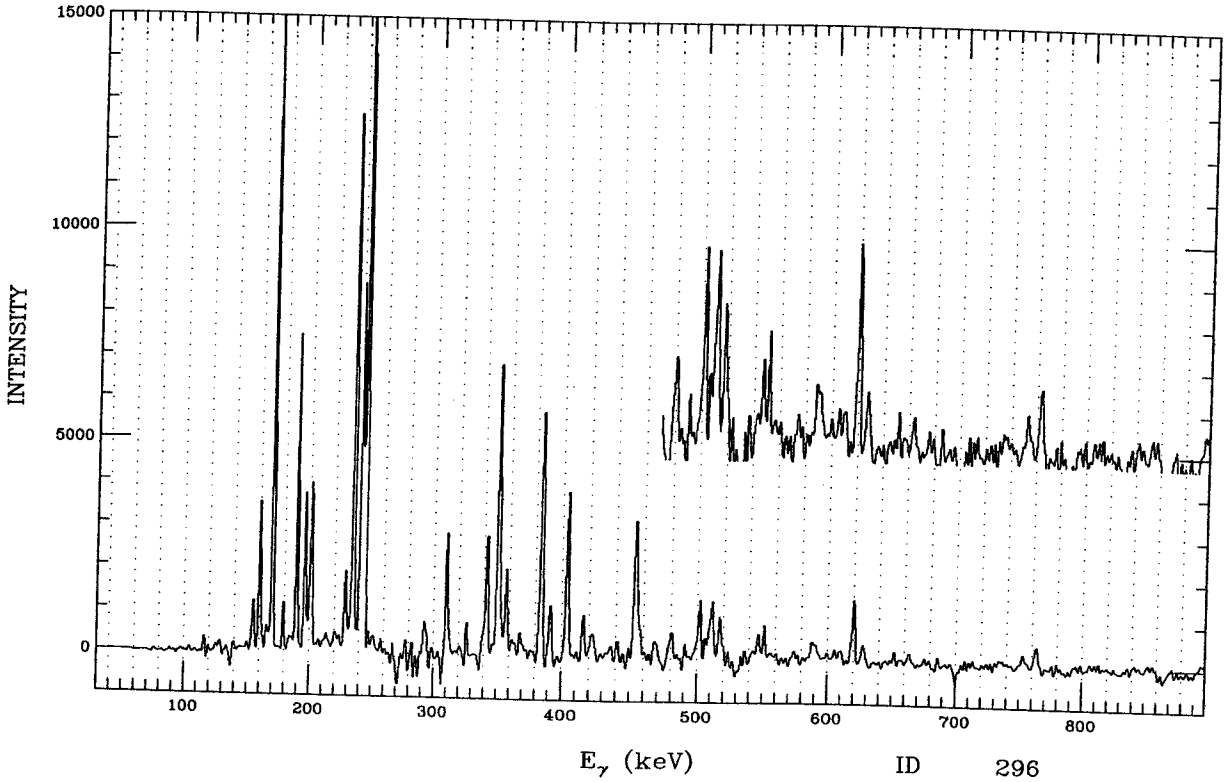

Figure F.48: ID 296. Simple gate from ^{133}Pr, band 6.

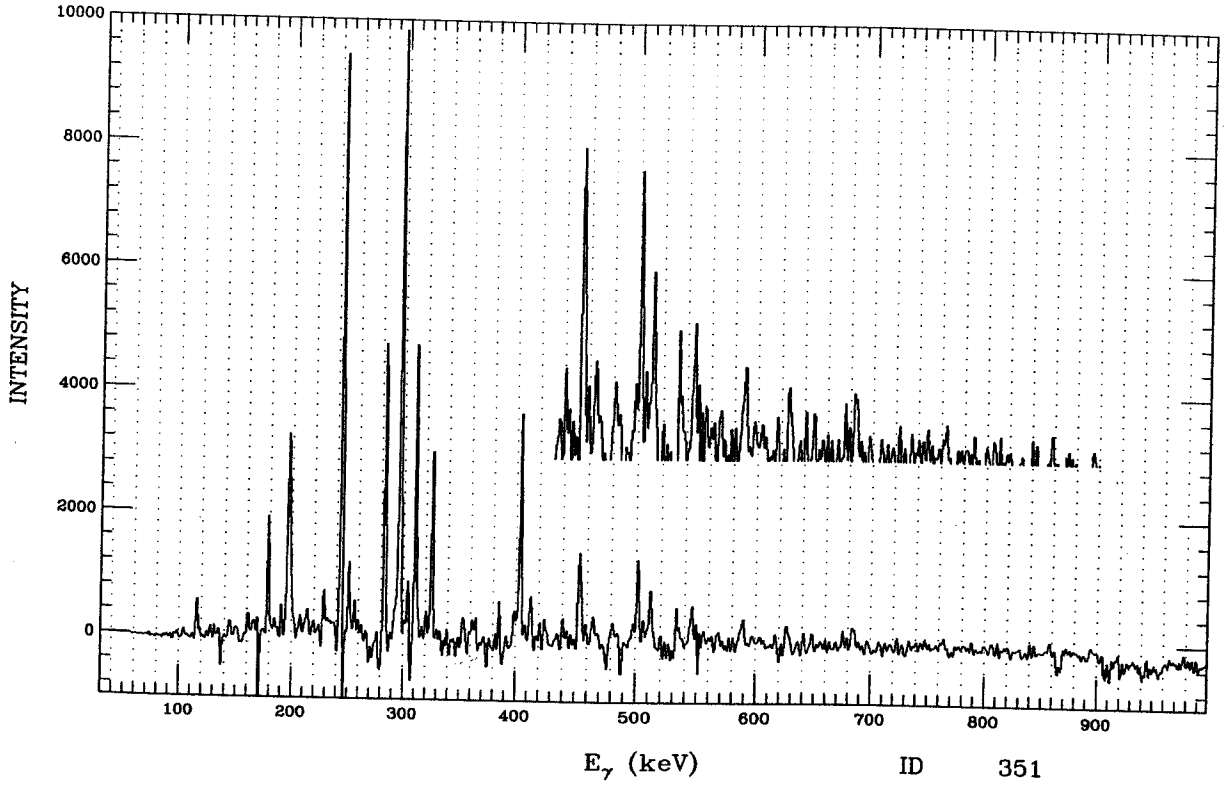

Figure F.49: ID 351. Simple gate from ^{133}Pr, band 6.

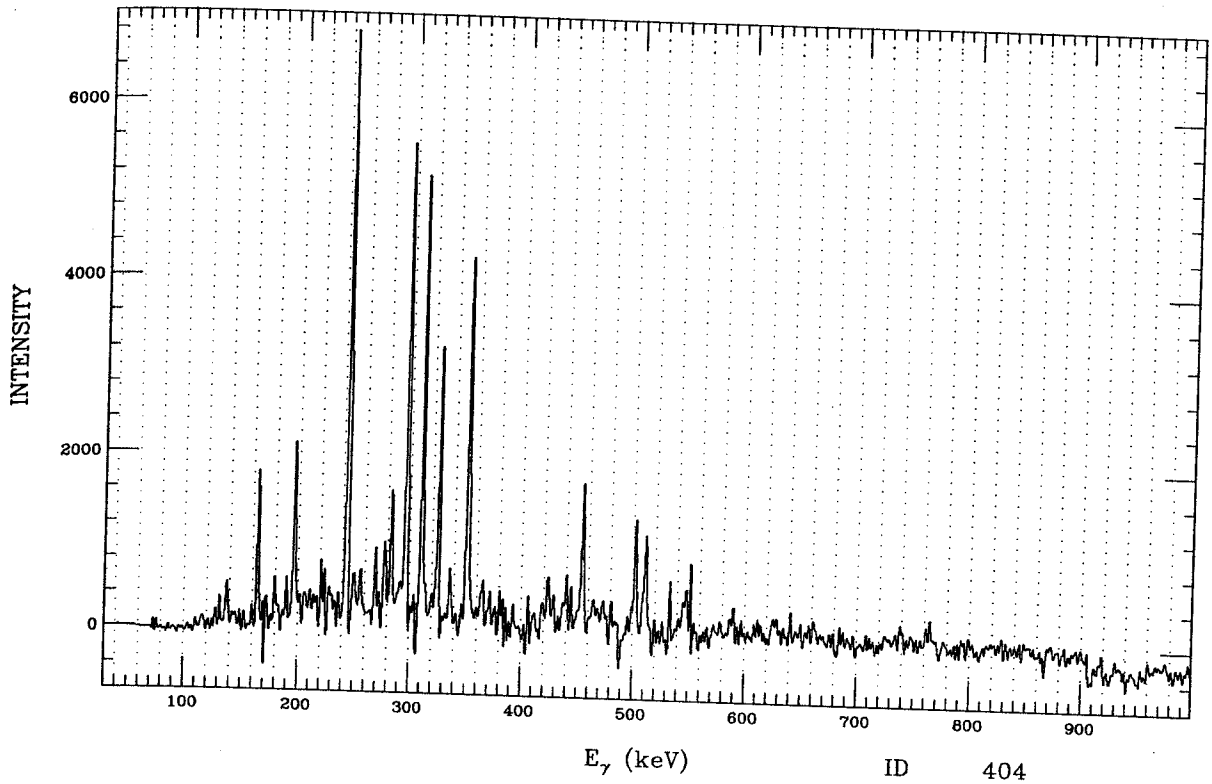

Figure F.50: ID 404. Simple gate from ^{133}Pr, band 6.

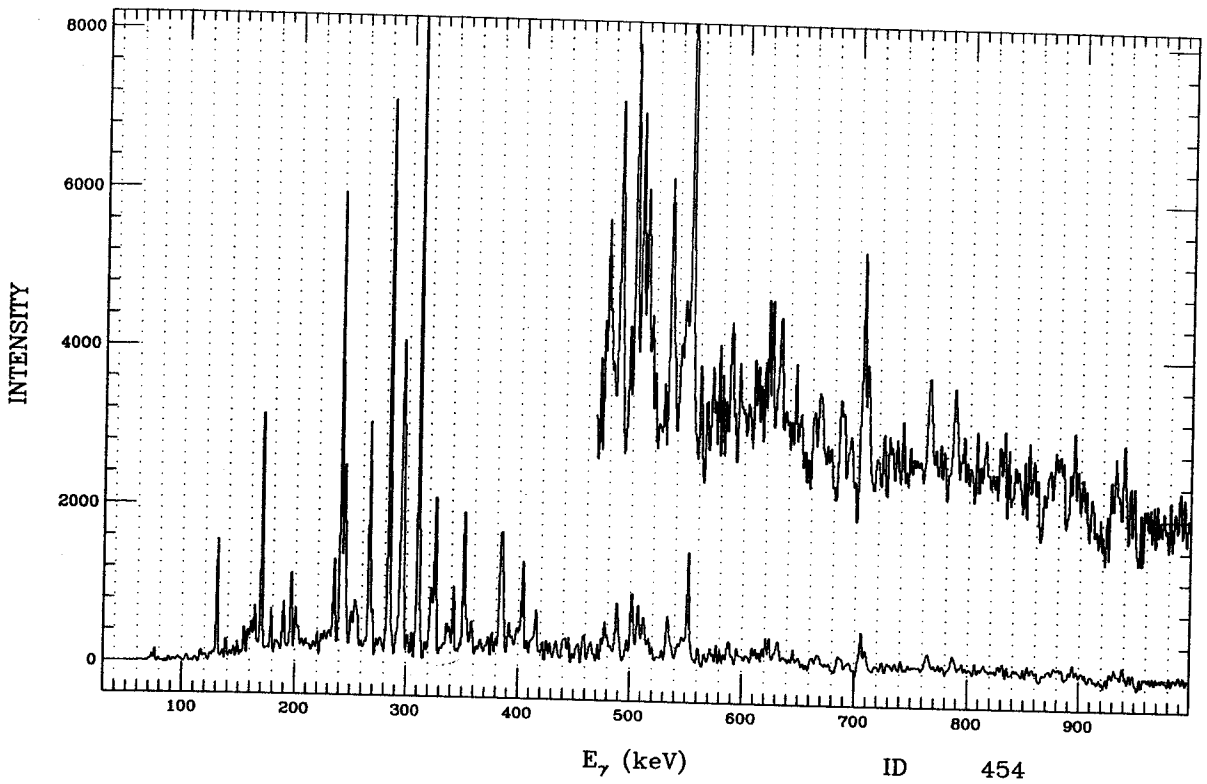

Figure F.51: ID 454. Simple gate from ^{133}Pr, band 6.

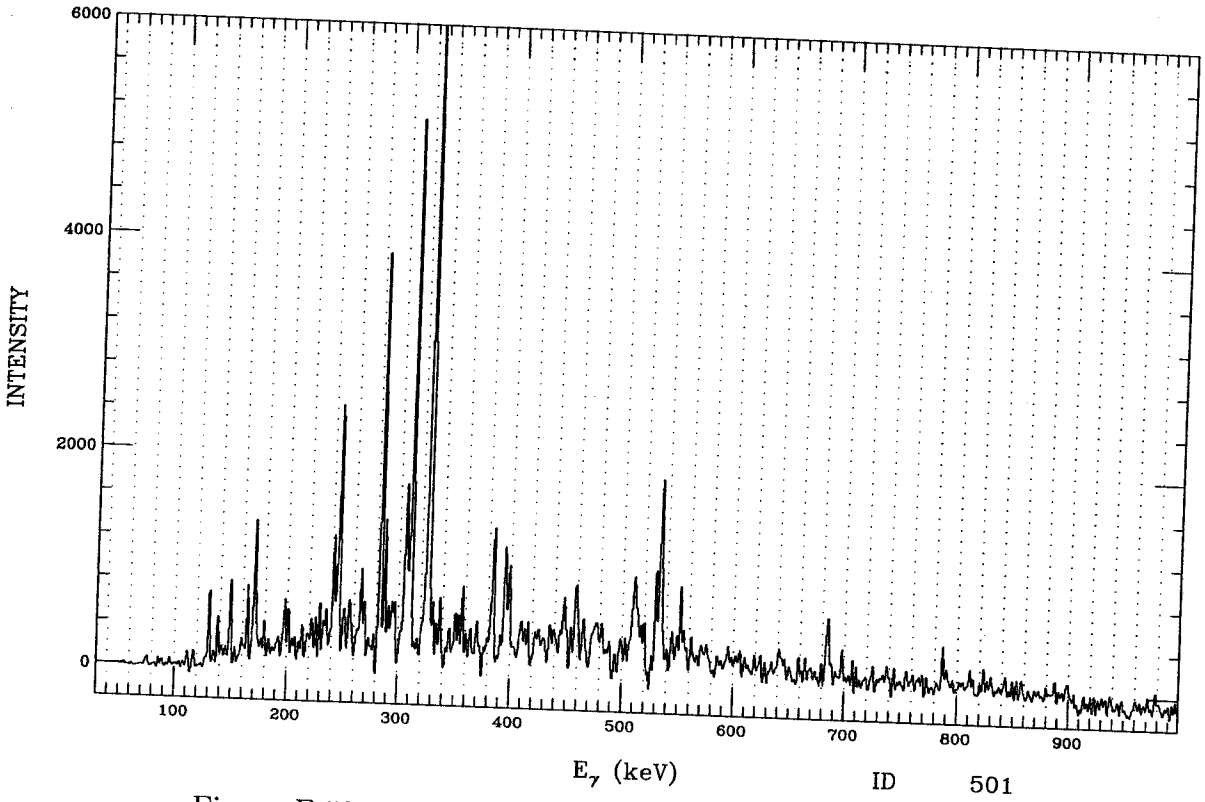

Figure F.52: ID 501. Simple gate from ^{133}Pr, band 6.

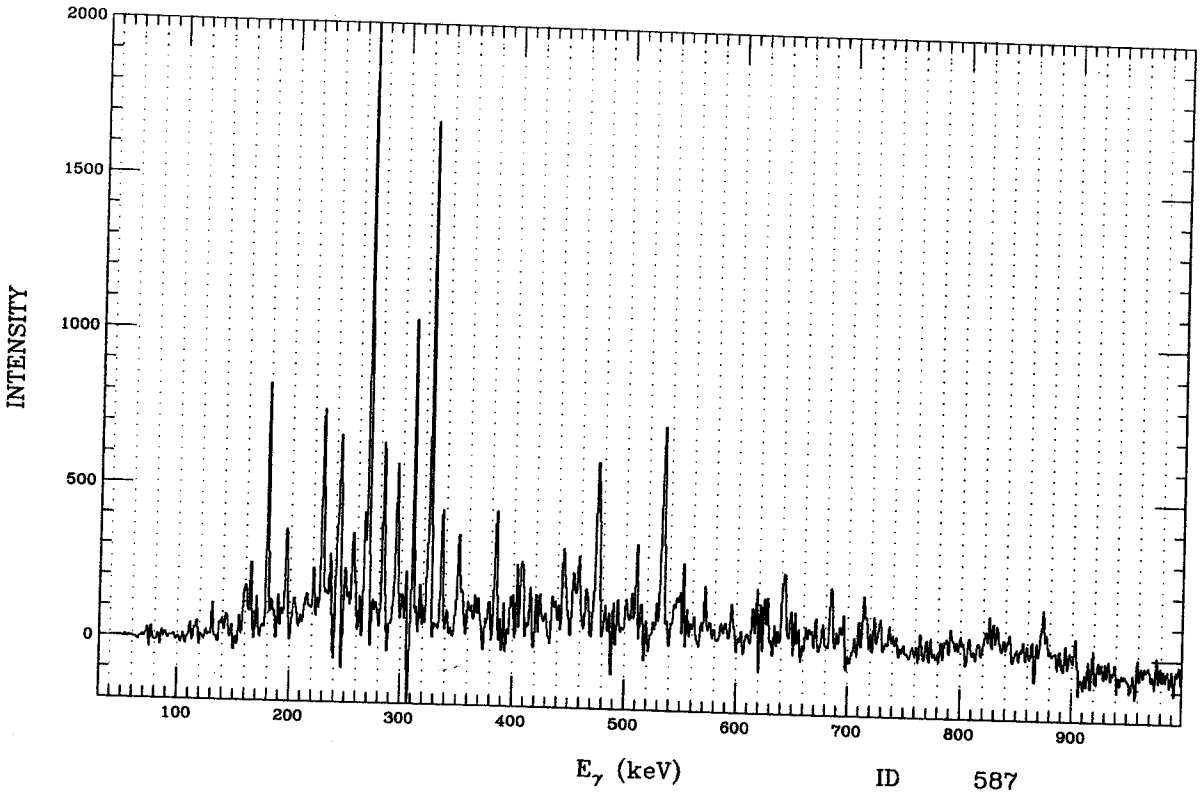

Figure F.53: ID 587. Simple gate from ^{133}Pr, band 6.

F.2 Multiple Gates ^{133}Pr

A multiple gate technique was developed for ^{133}Pr using triple coincidence data. For the first gate step, the program *LEMO* was used with a 2-D free form energy coincidence gate (.ban file) to write coincidences between detectors to tape. Coincidences from the four 90° detectors were compared with the rest of the detectors and the events were sorted onto a new tape. For the ^{133}Pr nucleus, 2-D primary gates were set for the 310, 551, 709 keV. peaks. For the second gate step, *SCAN* was used with the new tape to generate a total energy versus total energy 2-D array, presented in Figure 5.13. The 2-D histogram was then gated, generating the spectra contained in this Appendix. Each spectrum has been enhanced using the FFT and SNIP routines described in Chapter 6.

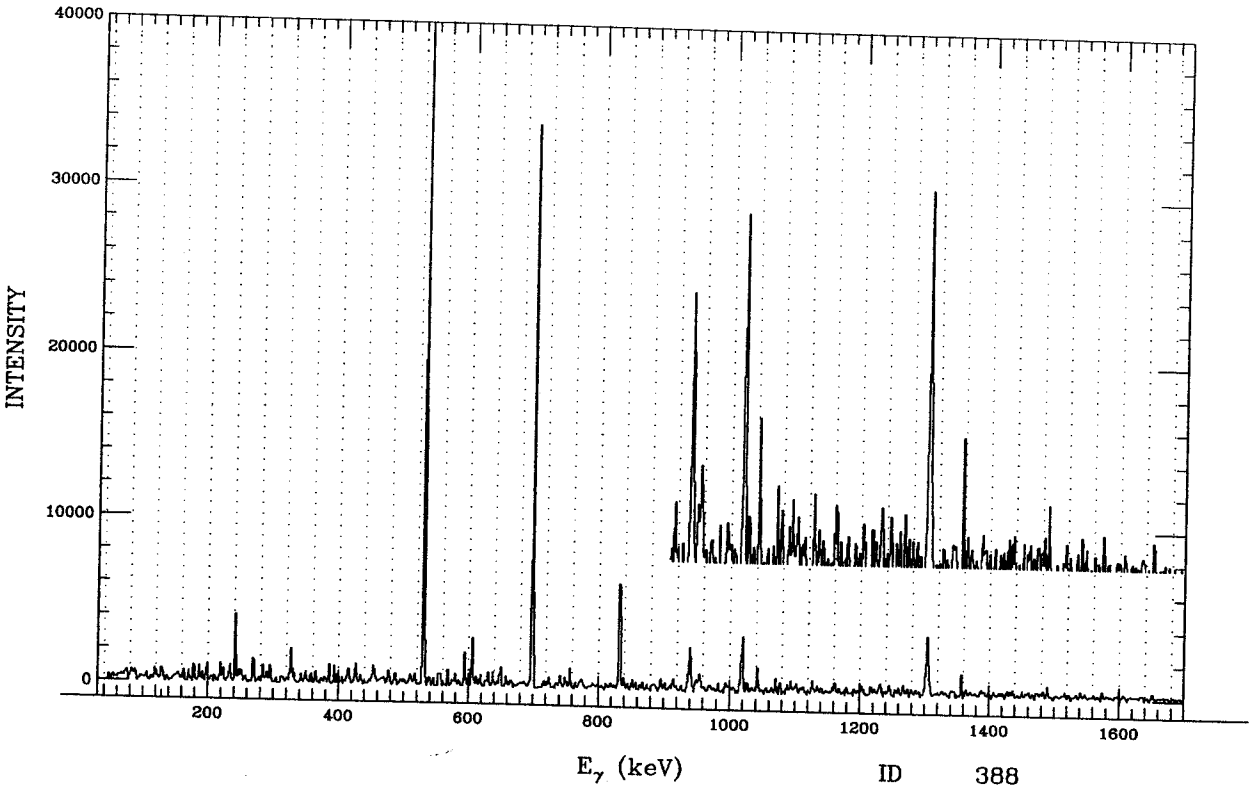

Figure F.54: ID 388. Multiple gate from ^{133}Pr, band 1.

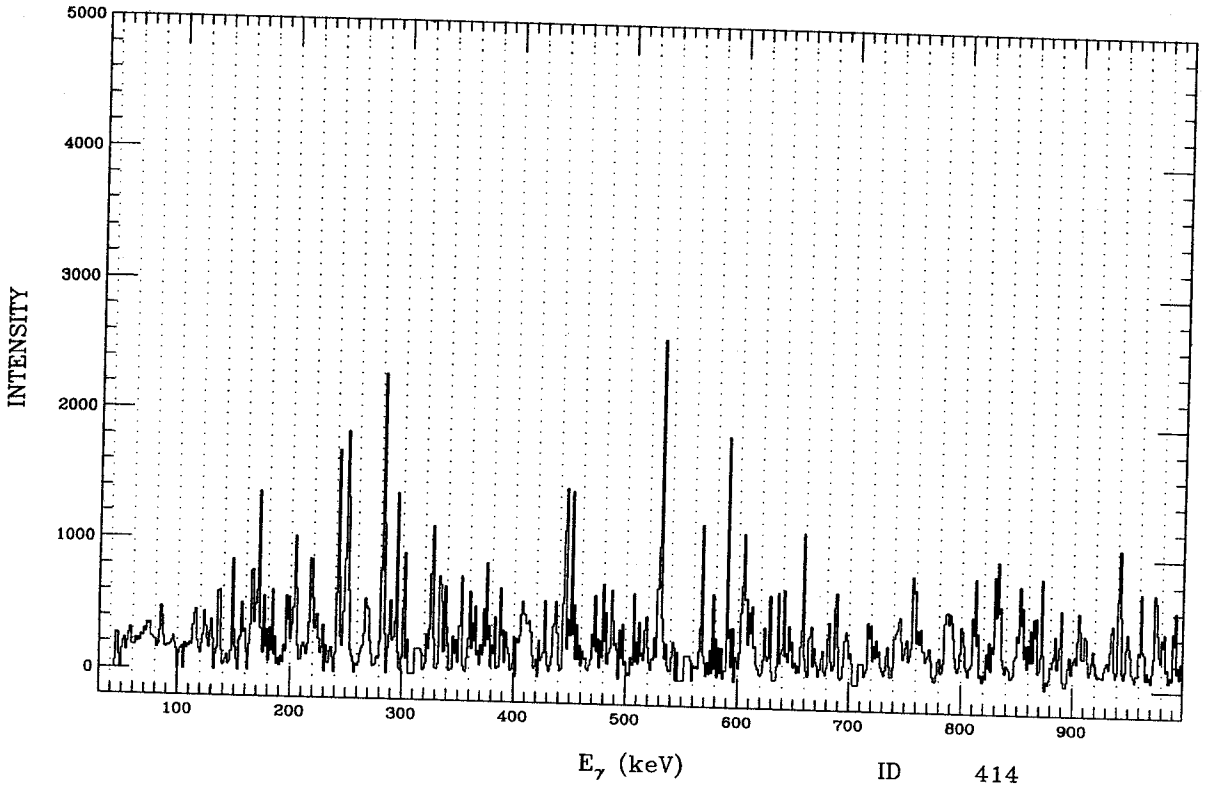

Figure F.55: ID 414. Multiple gate from ^{133}Pr, band 1.

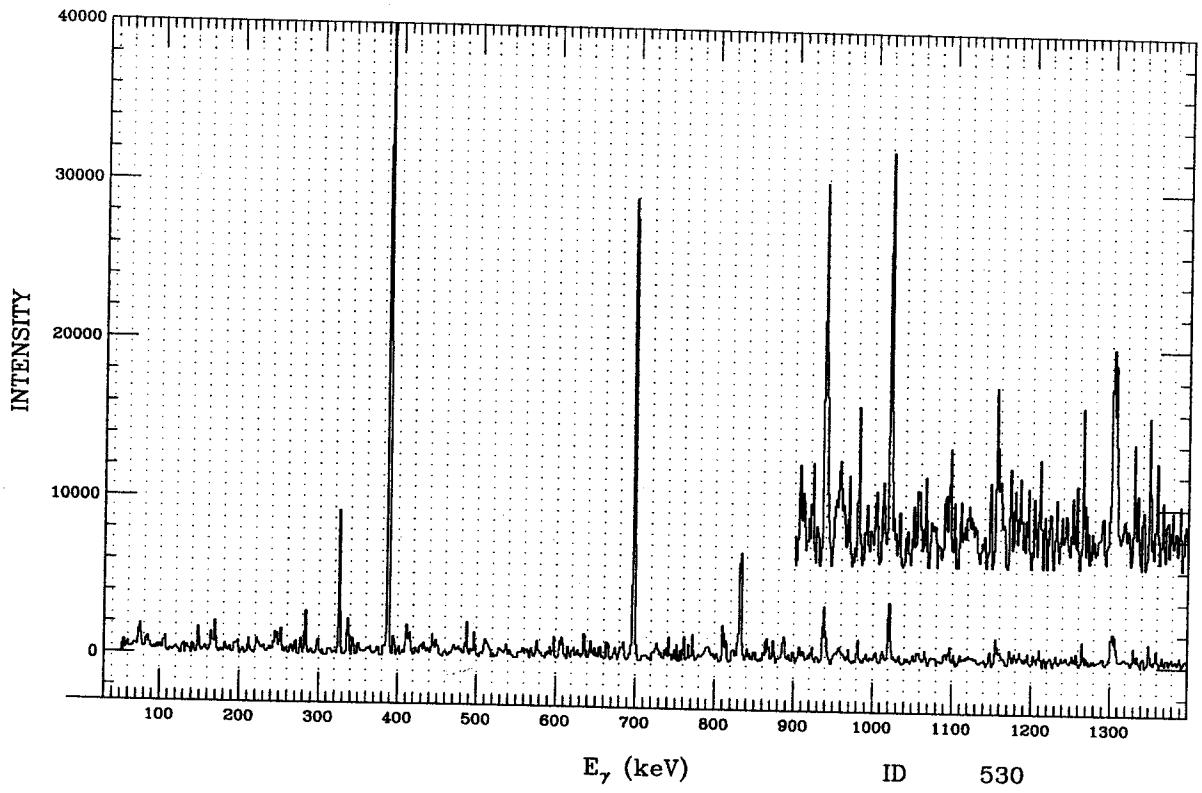

Figure F.56: ID 530. Multiple gate from ^{133}Pr, band 1.

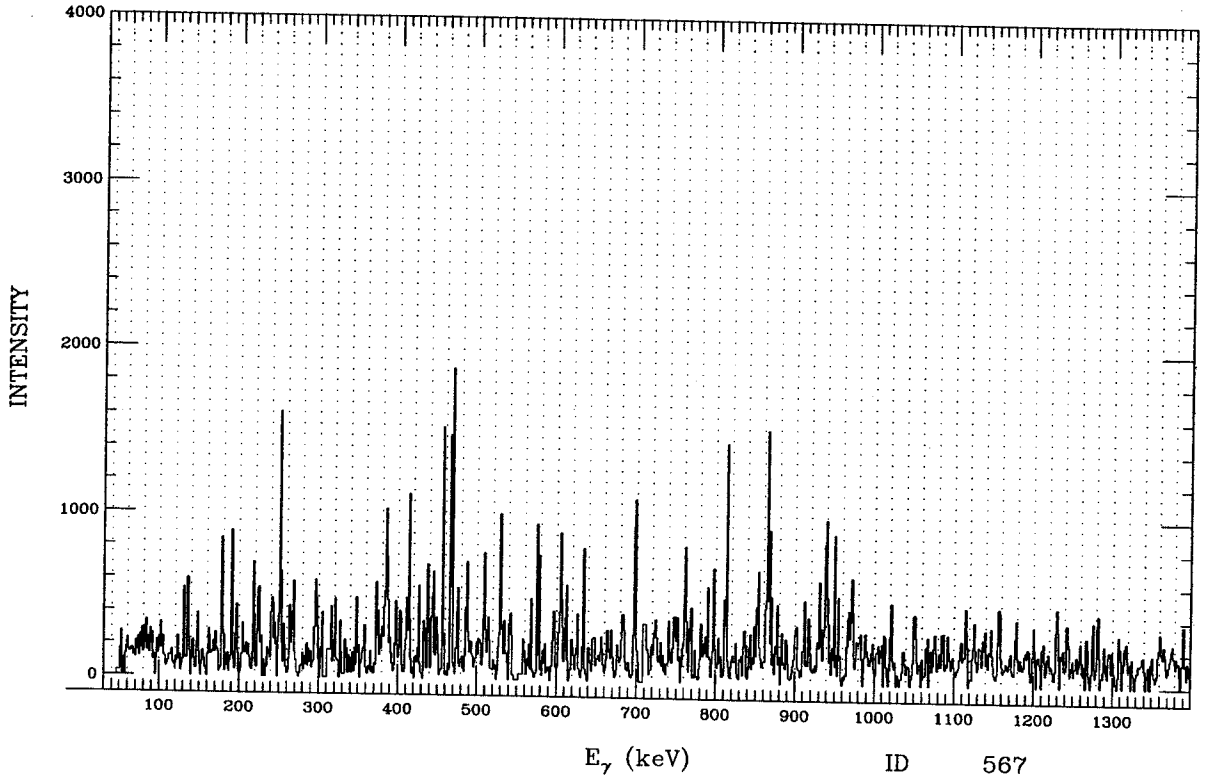

Figure F.57: ID 567. Multiple gate from ^{133}Pr, band 1.

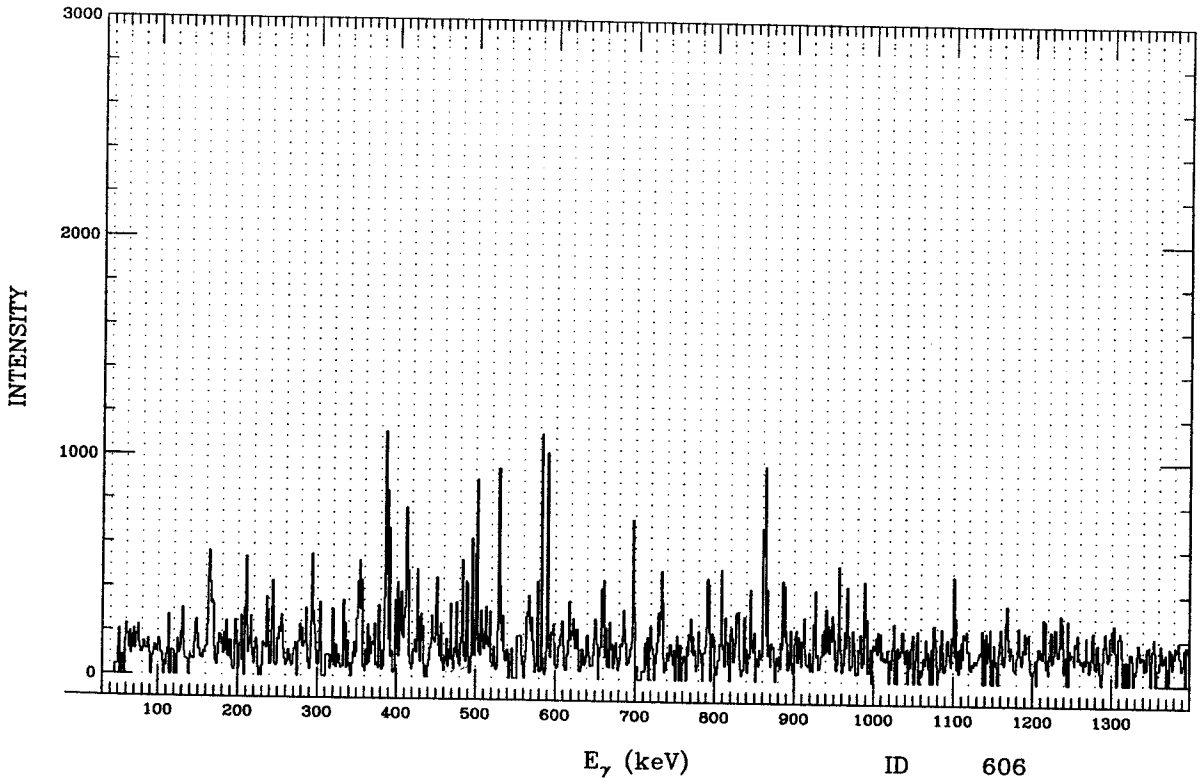

Figure F.58: ID 606. Multiple gate from ^{133}Pr, band 1.

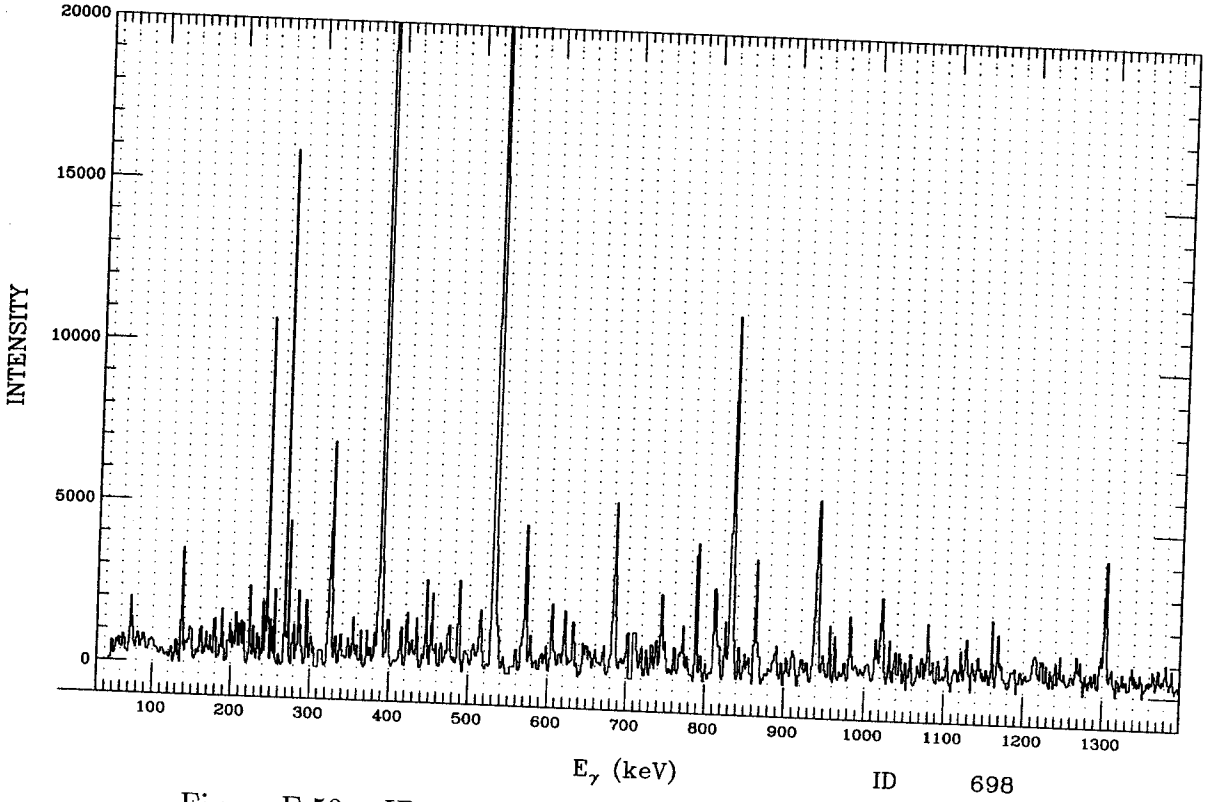

Figure F.59: ID 698. Multiple gate from ^{133}Pr, band 1.

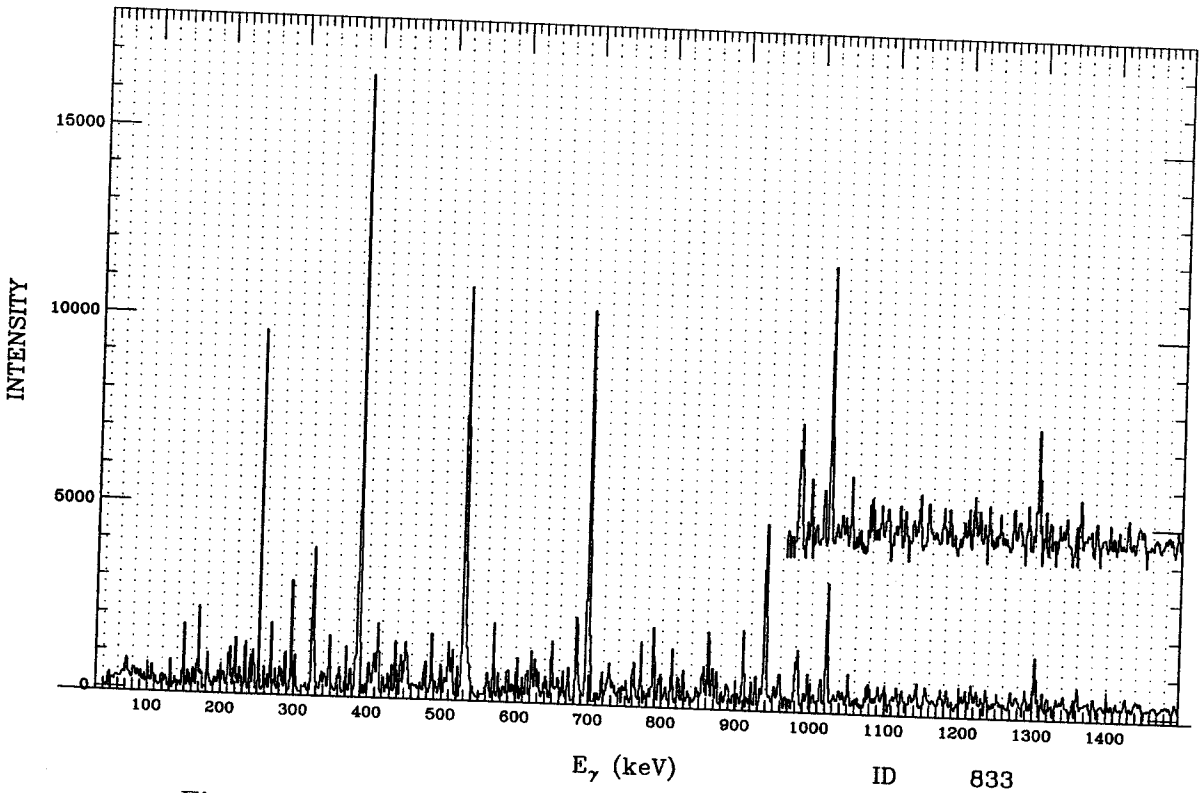

Figure F.60: ID 833. Multiple gate from ^{133}Pr, band 1.

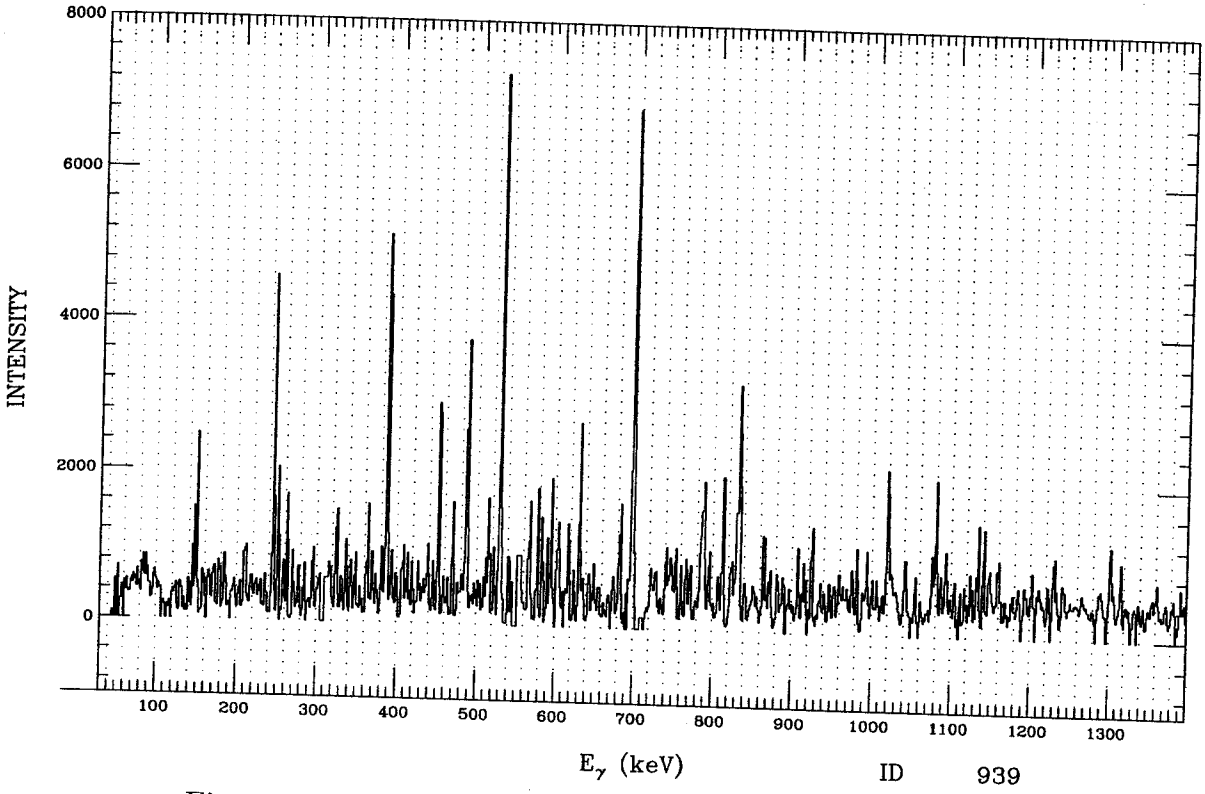

Figure F.61: ID 939. Multiple gate from ^{133}Pr, band 1.

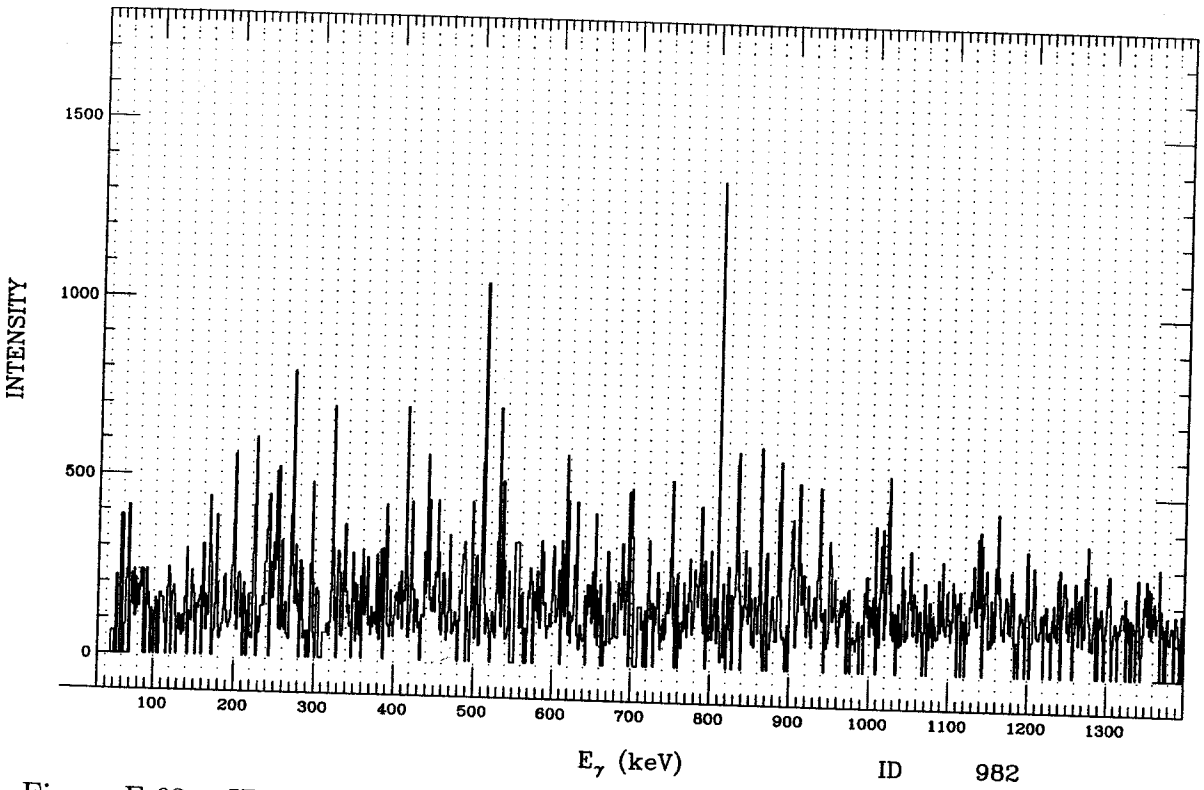

Figure F.62: ID 982. Multiple gate from ^{133}Pr, a link between bands 1 and 3.

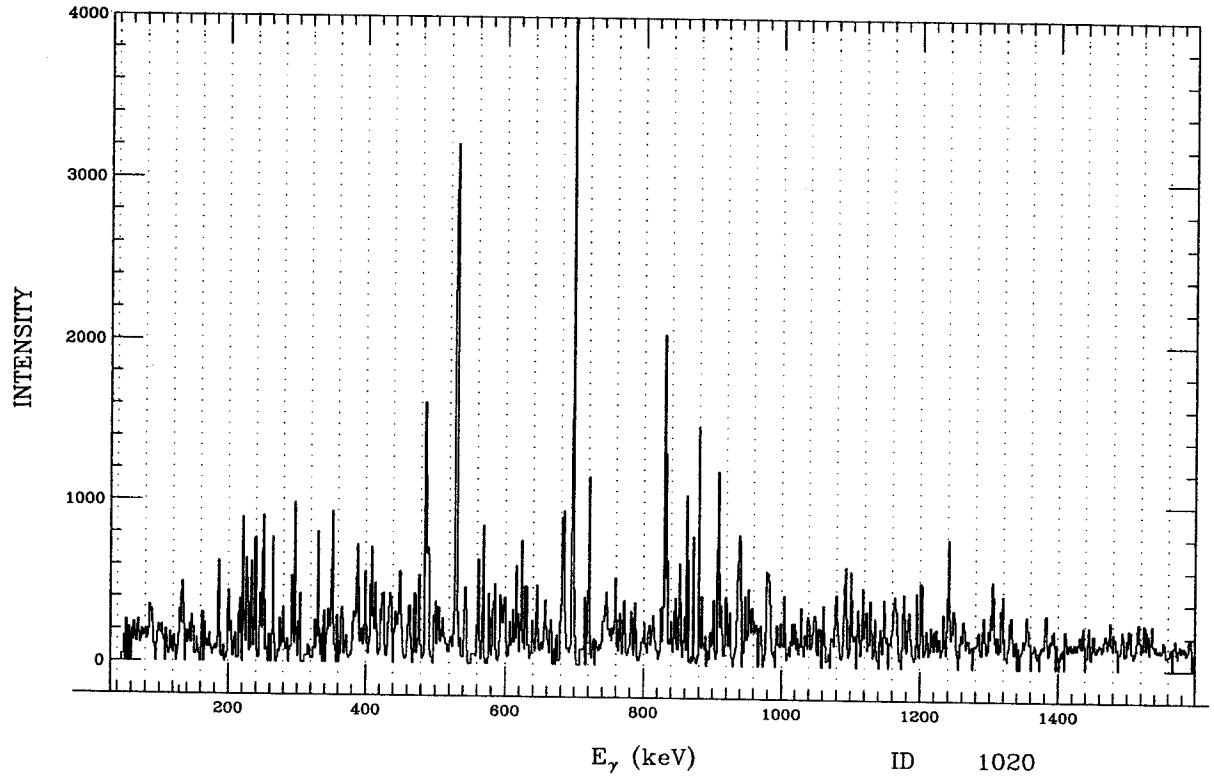

Figure F.63: ID 1020. Multiple gate from ^{133}Pr, band 1.

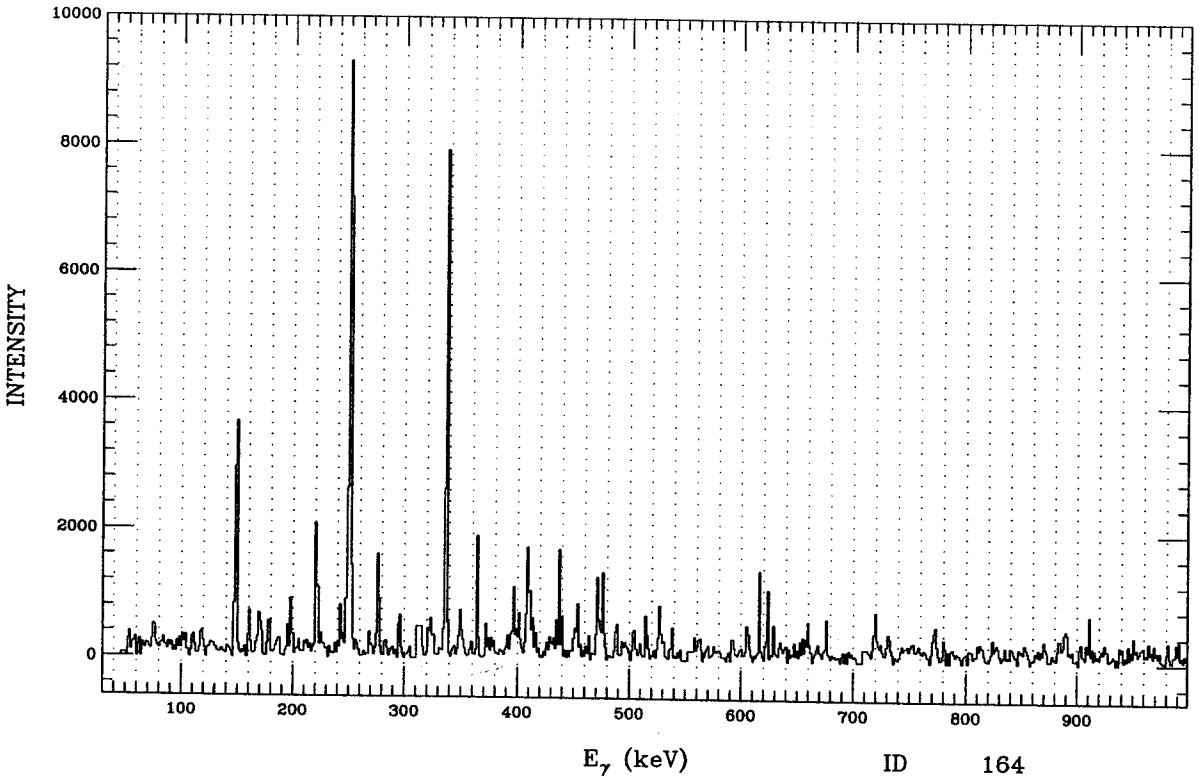

Figure F.64: ID 164. Multiple gate from ^{133}Pr, band 2 (or 5).

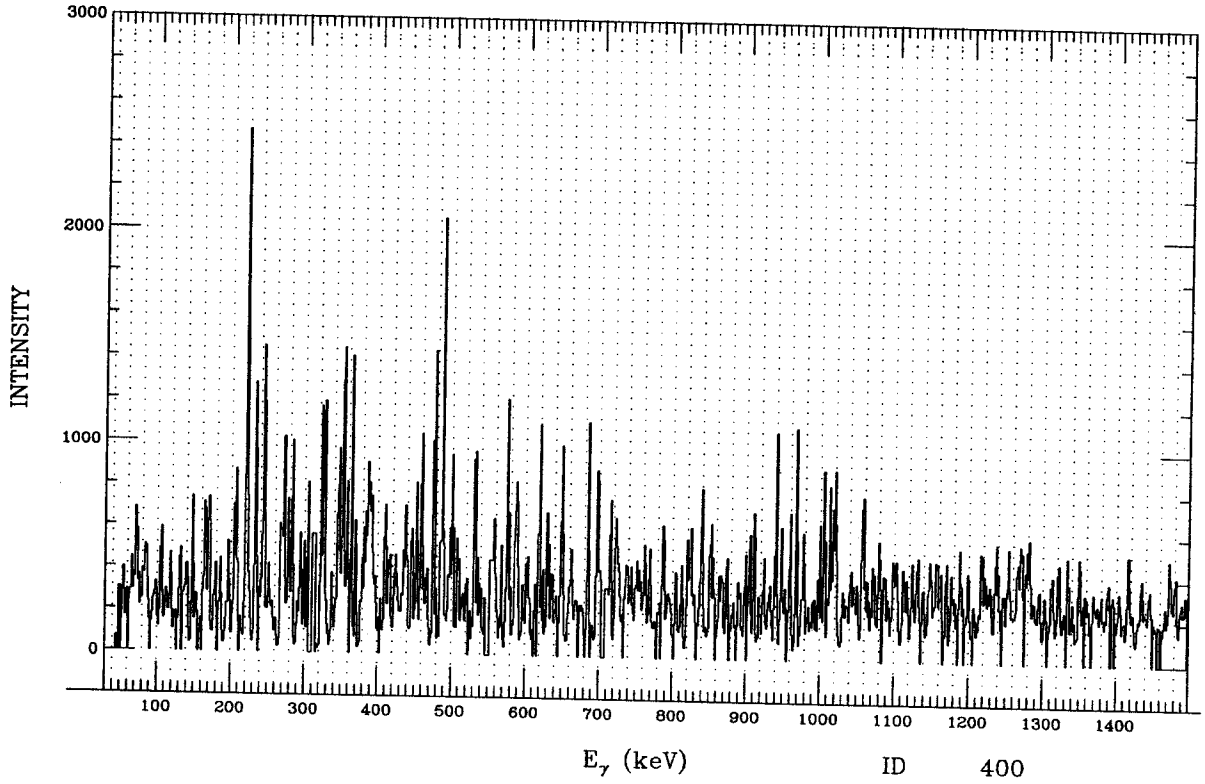

Figure F.65: ID 400. Multiple gate from ^{133}Pr, band 2.

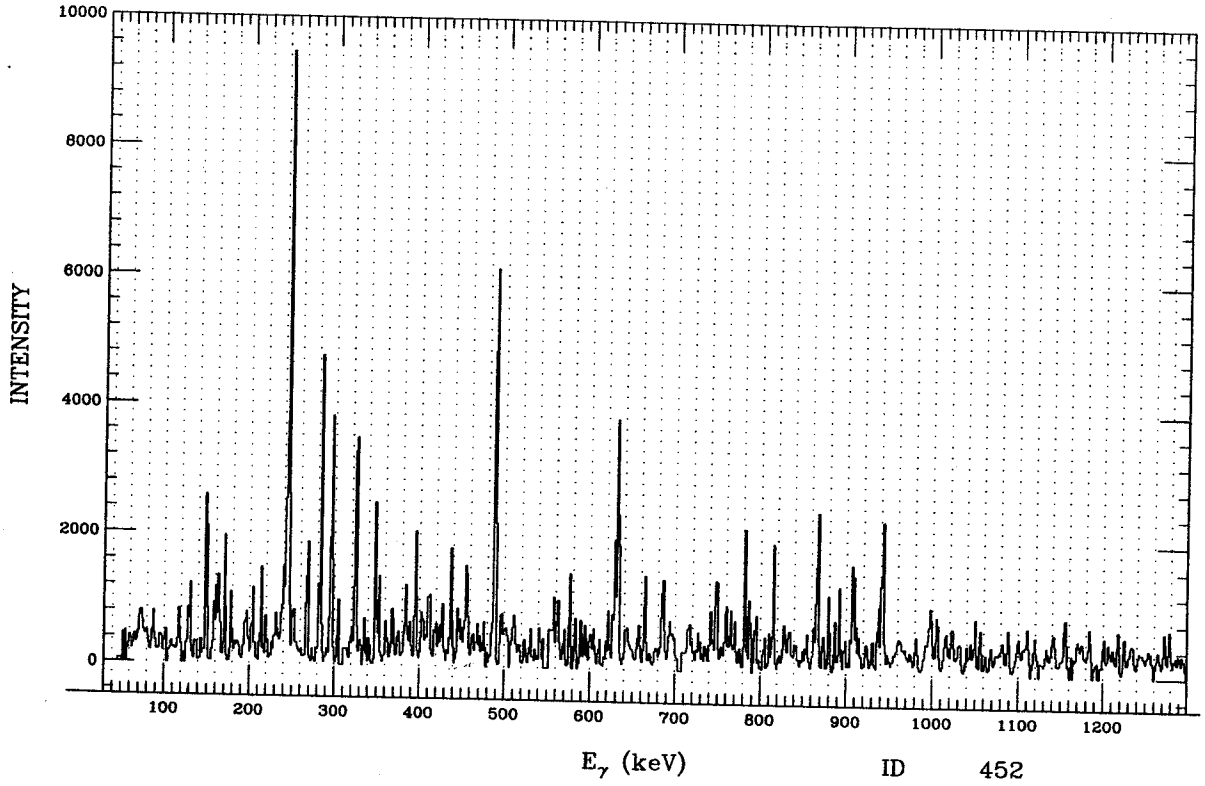

Figure F.66: ID 452. Multiple gate from ^{133}Pr, band 2.

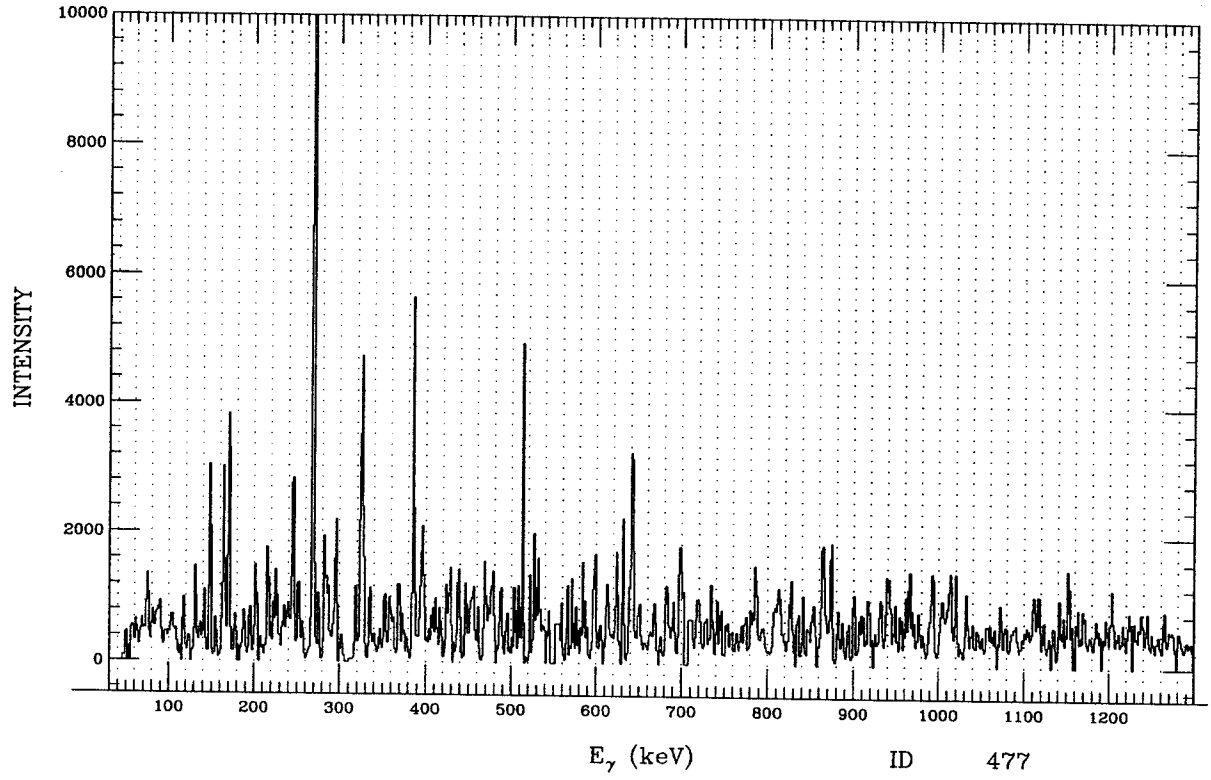

Figure F.67: ID 477. Multiple gate from ^{133}Pr, band 2.

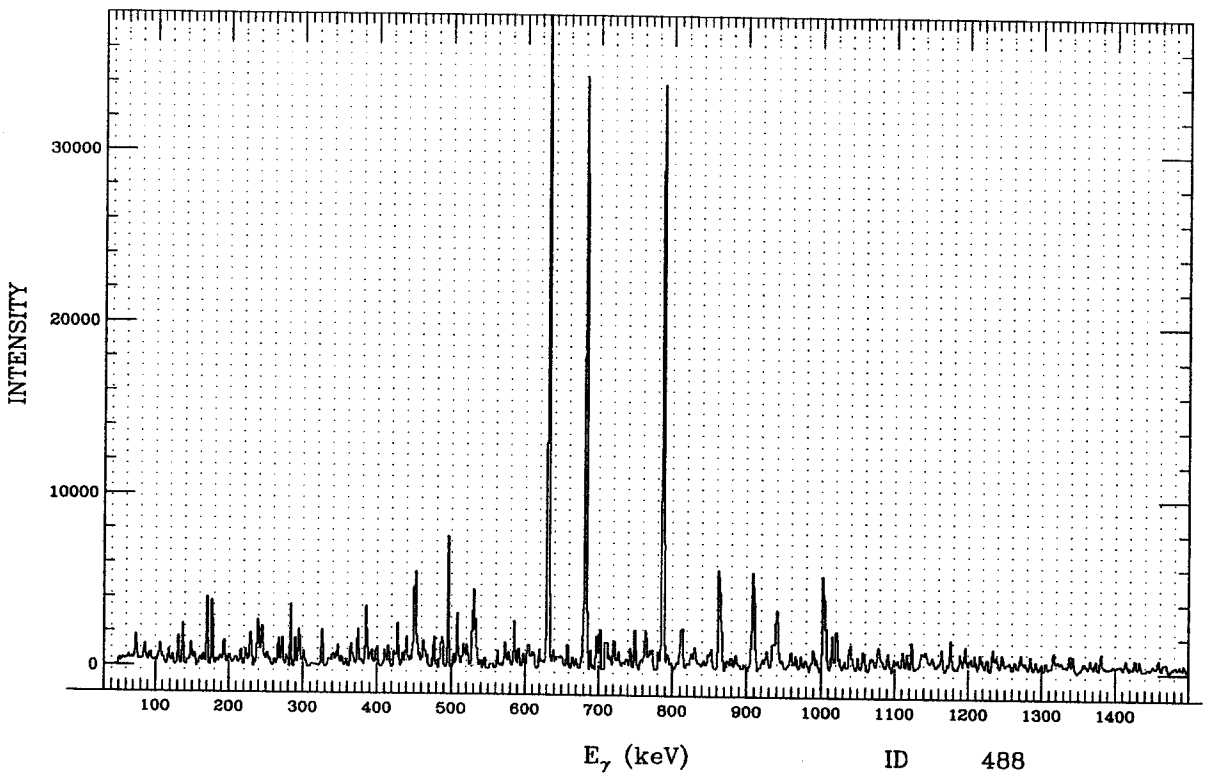

Figure F.68: ID 488. Multiple gate from ^{133}Pr, band 2.

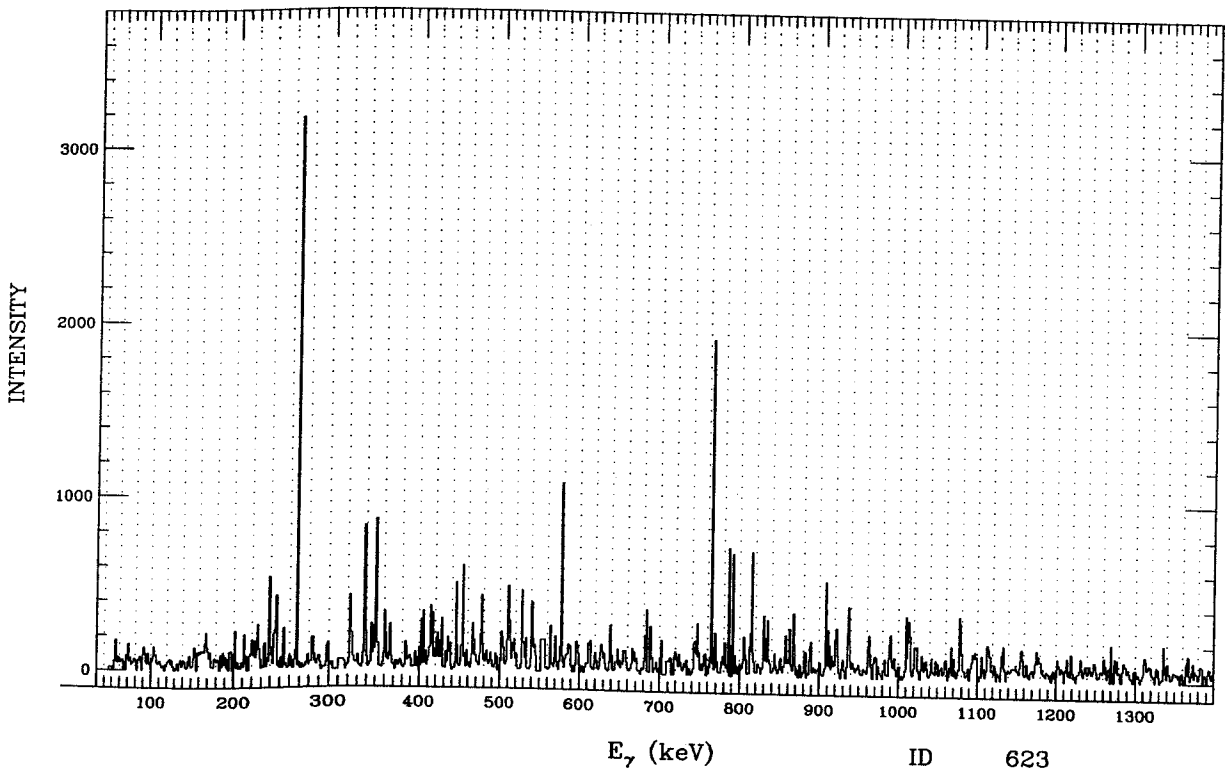

Figure F.69: ID 623. Multiple gate from ^{133}Pr, band 2.

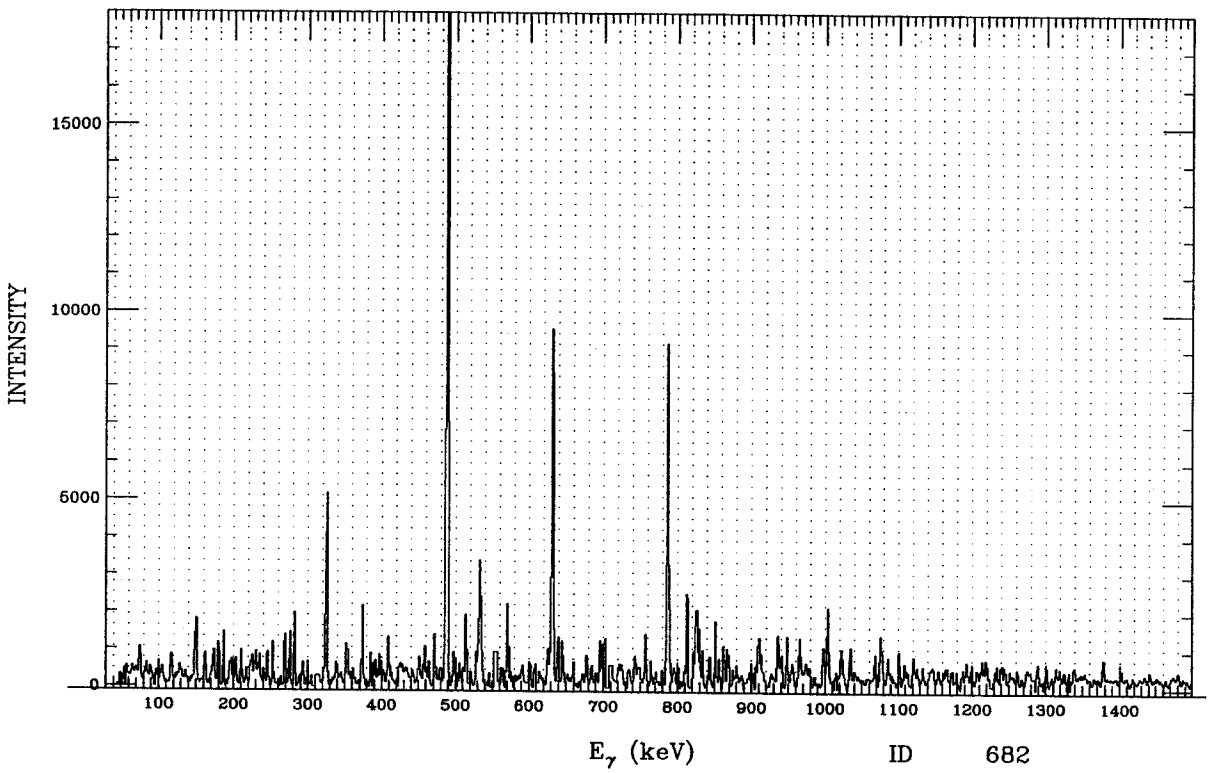

Figure F.70: ID 682. Multiple gate from ^{133}Pr, a link between bands 2 and 3.

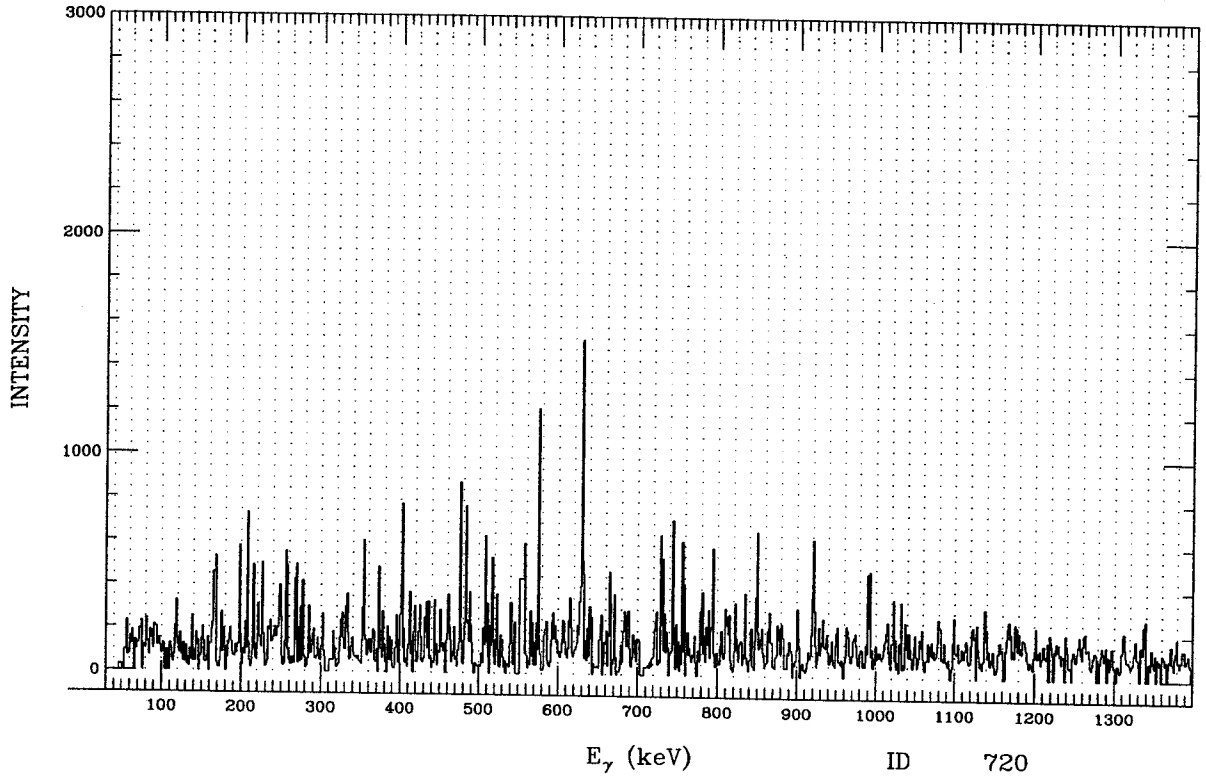

Figure F.71: ID 720. Multiple gate from ^{133}Pr, band 2.

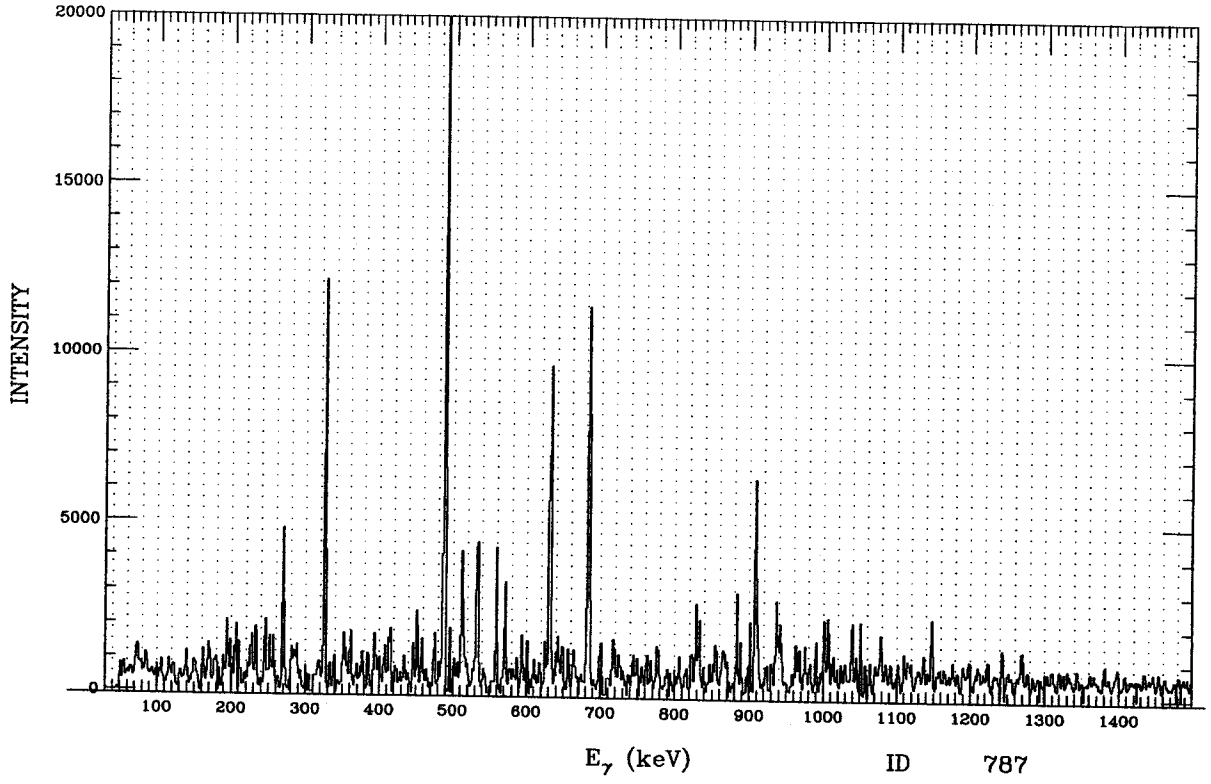

Figure F.72: ID 787. Multiple gate from ^{133}Pr, band 2.

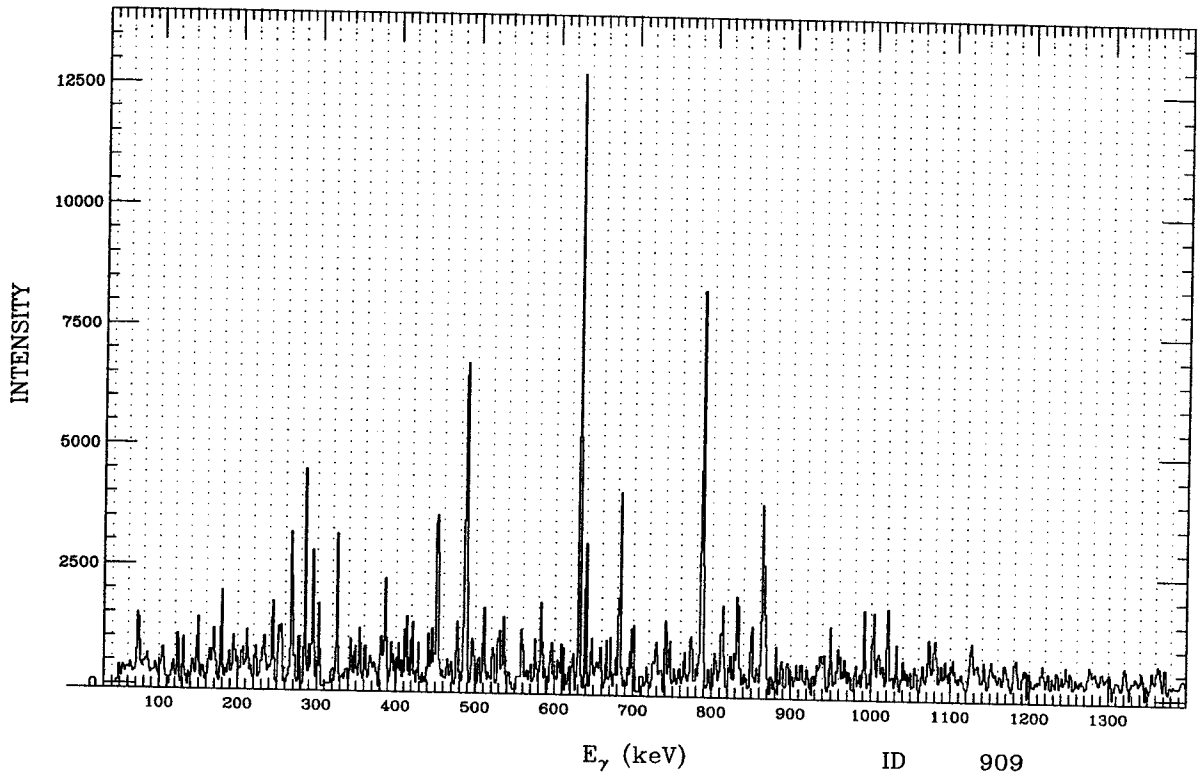

Figure F.73: ID 909. Multiple gate from ^{133}Pr, band 2.

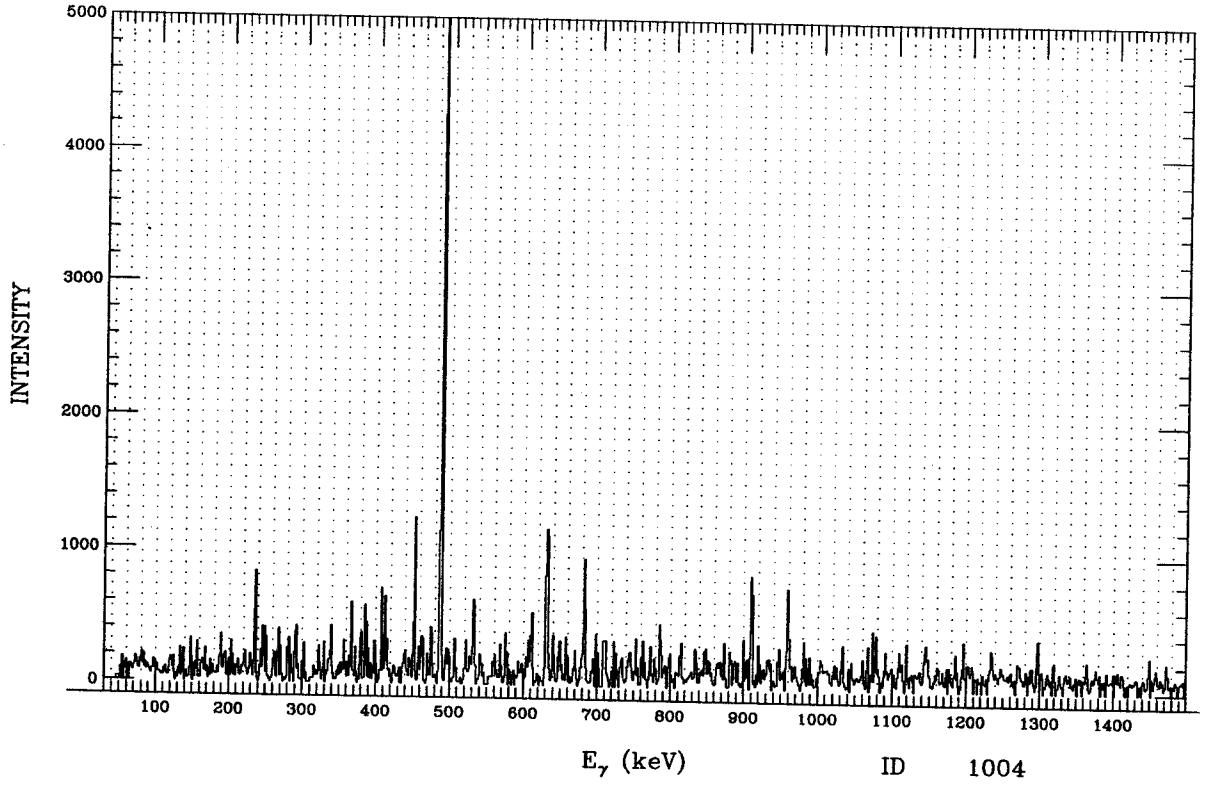

Figure F.74: ID 1004. Multiple gate from ^{133}Pr, band 2.

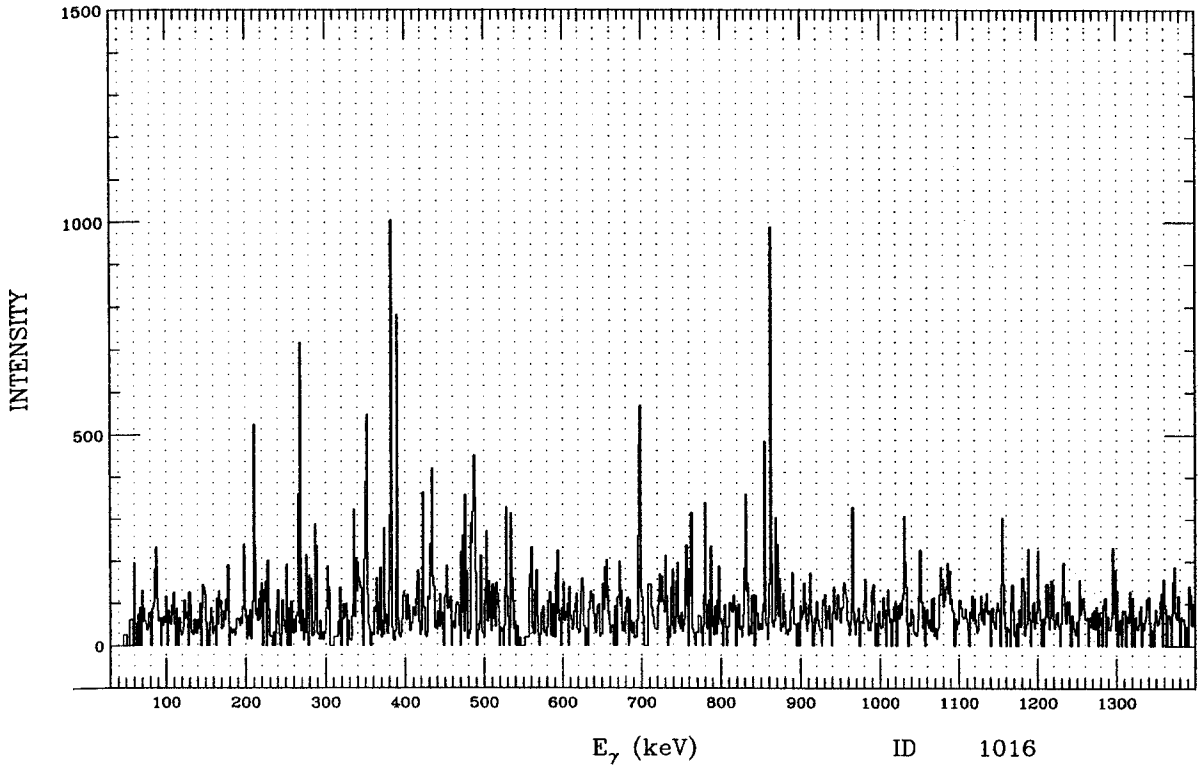

Figure F.75: ID 1016. Multiple gate from ^{133}Pr, band 2.

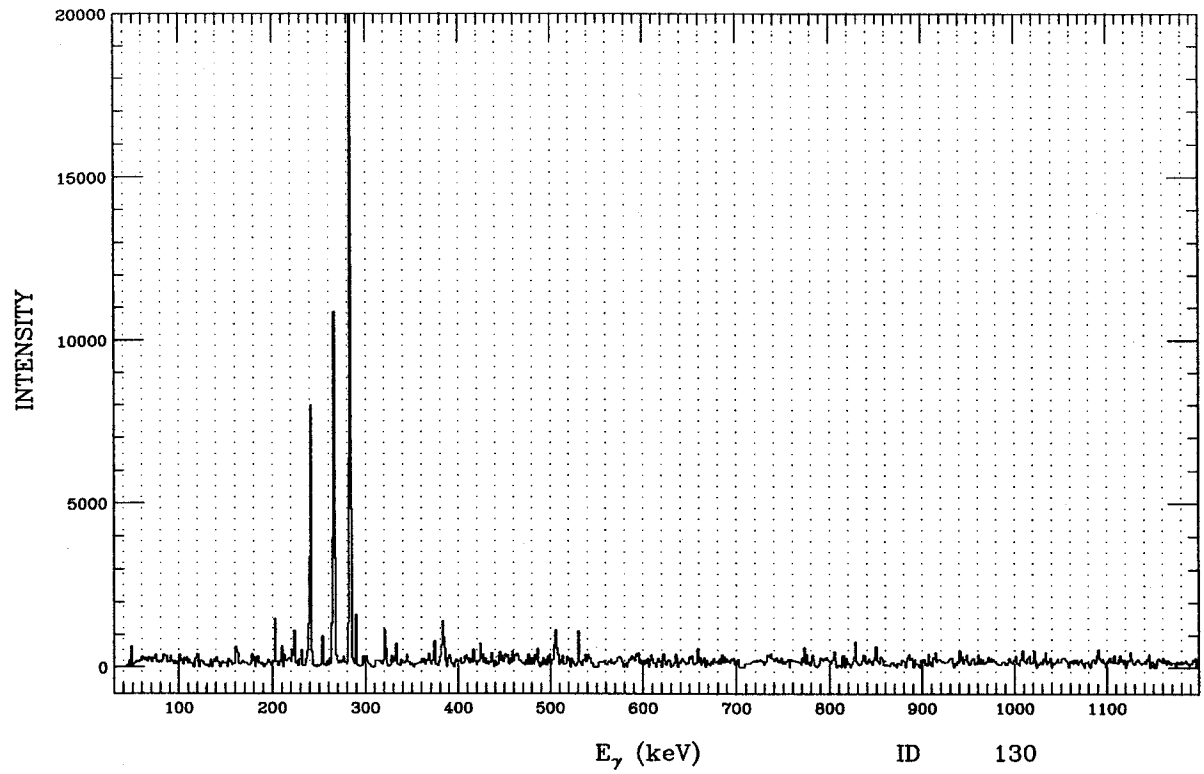

Figure F.76: ID 130. Multiple gate from ^{133}Pr array, for the ^{132}Pr nucleus.

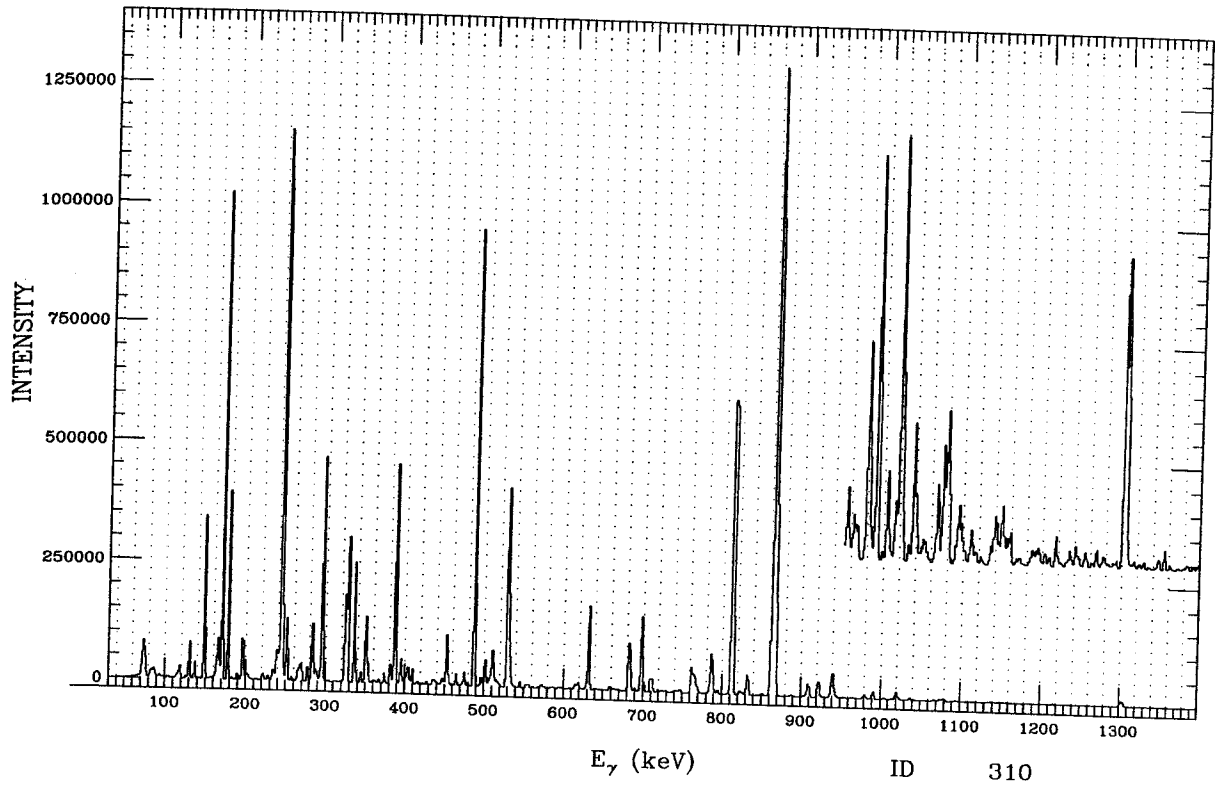

Figure F.77: ID 310. Multiple gate from ^{133}Pr, band 3.

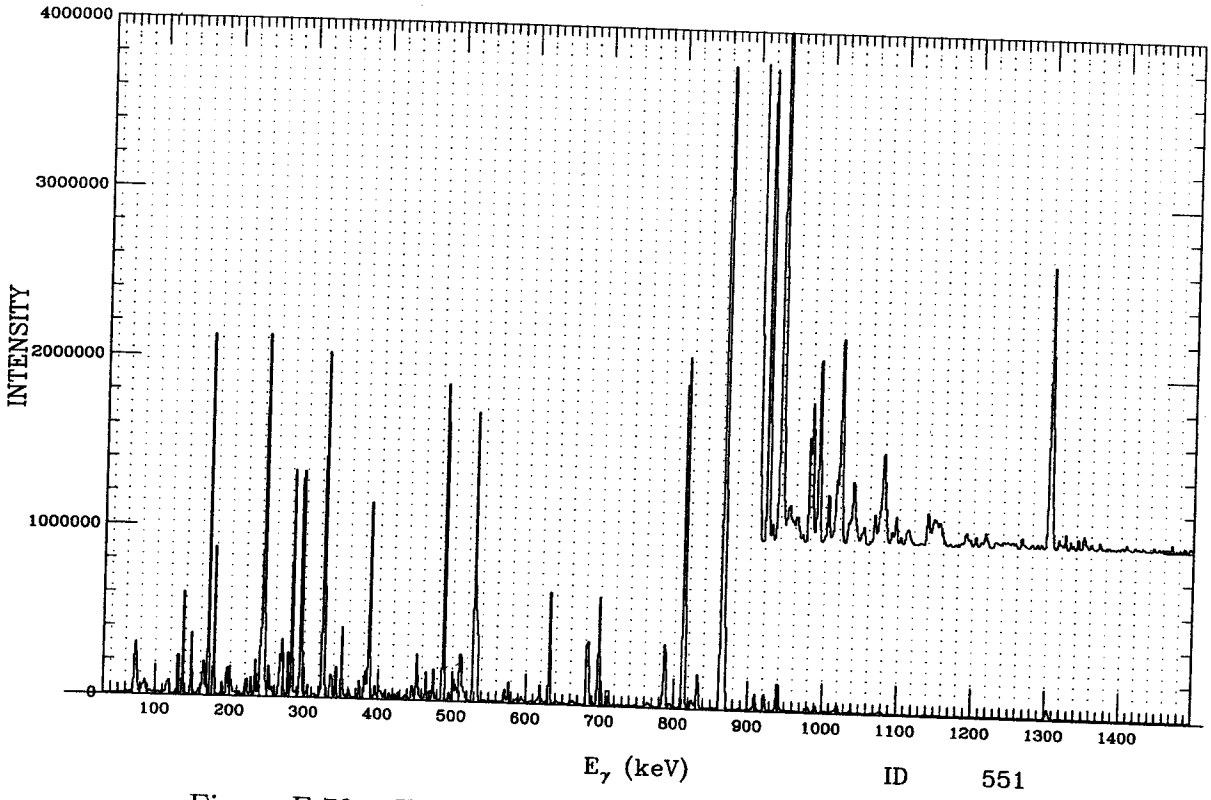

Figure F.78: ID 551. Multiple gate from ^{133}Pr, band 3.

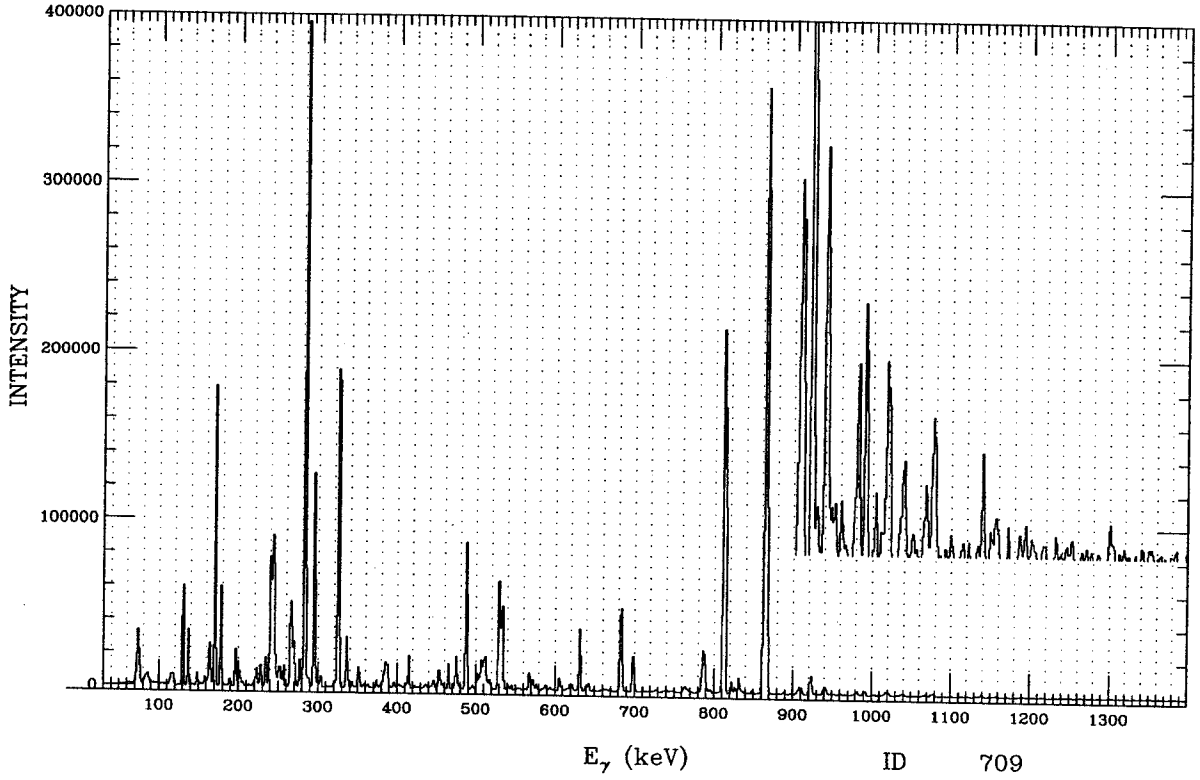

Figure F.79: ID 709. Multiple gate from ^{133}Pr, band 3.

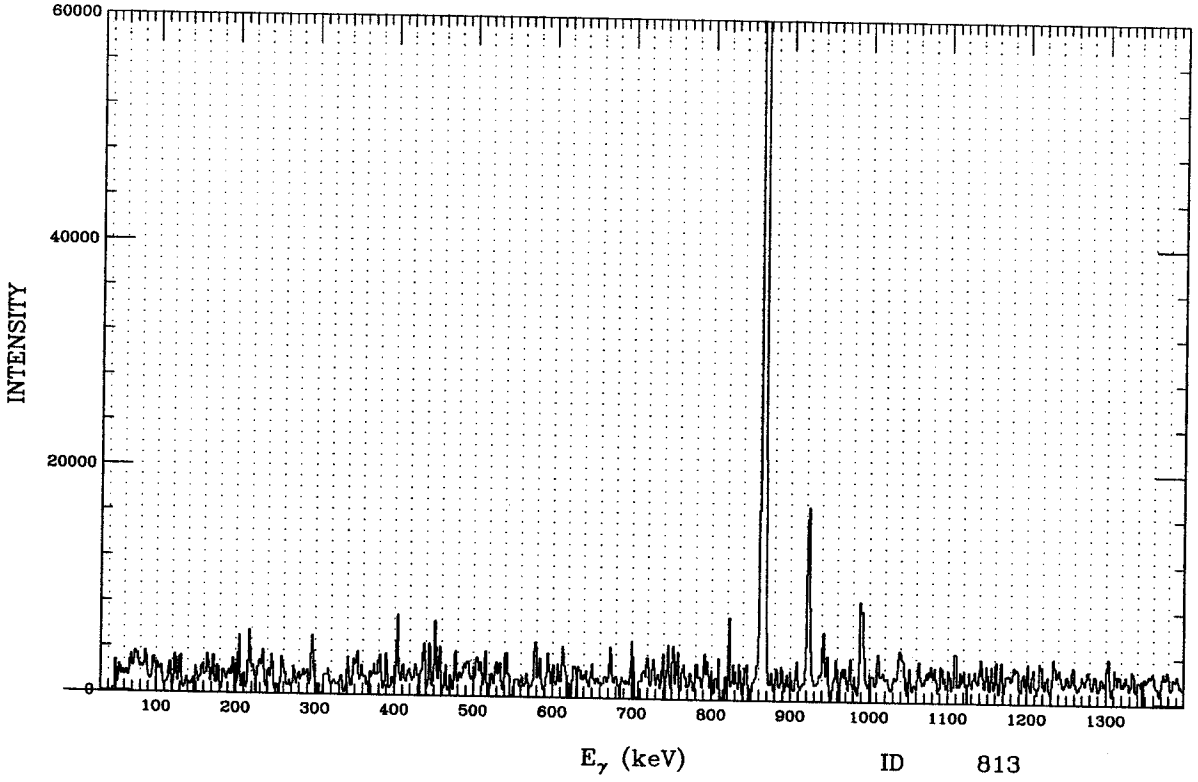

Figure F.80: ID 812. Multiple gate from ^{133}Pr, band 3.

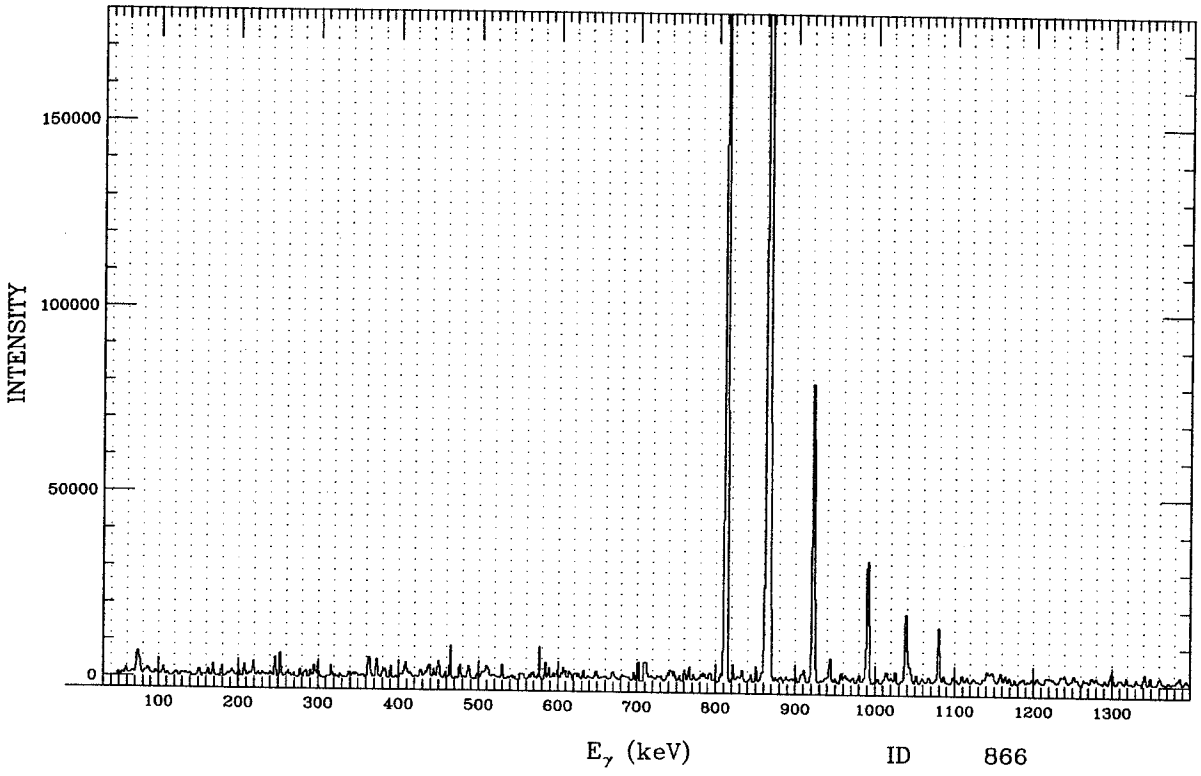

Figure F.81: ID 864-868 triplet. Multiple gate from ^{133}Pr, band 3.

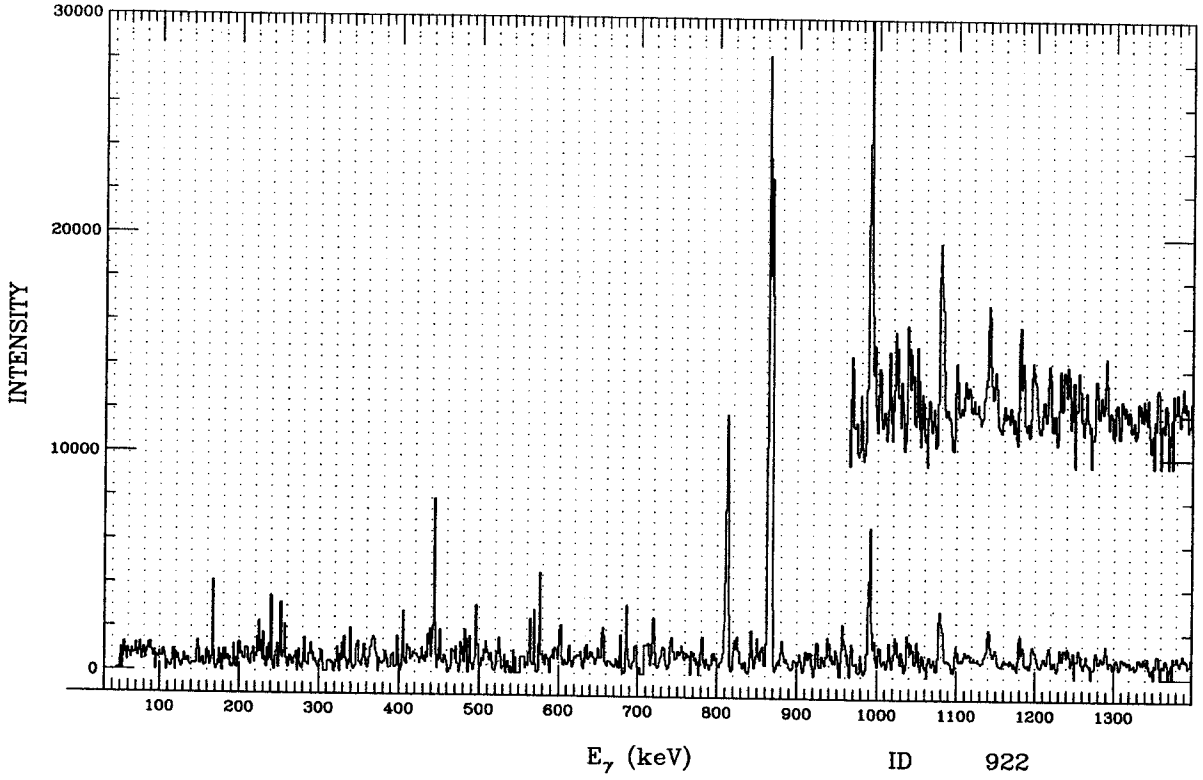

Figure F.82: ID 922. Multiple gate from ^{133}Pr, band 3.

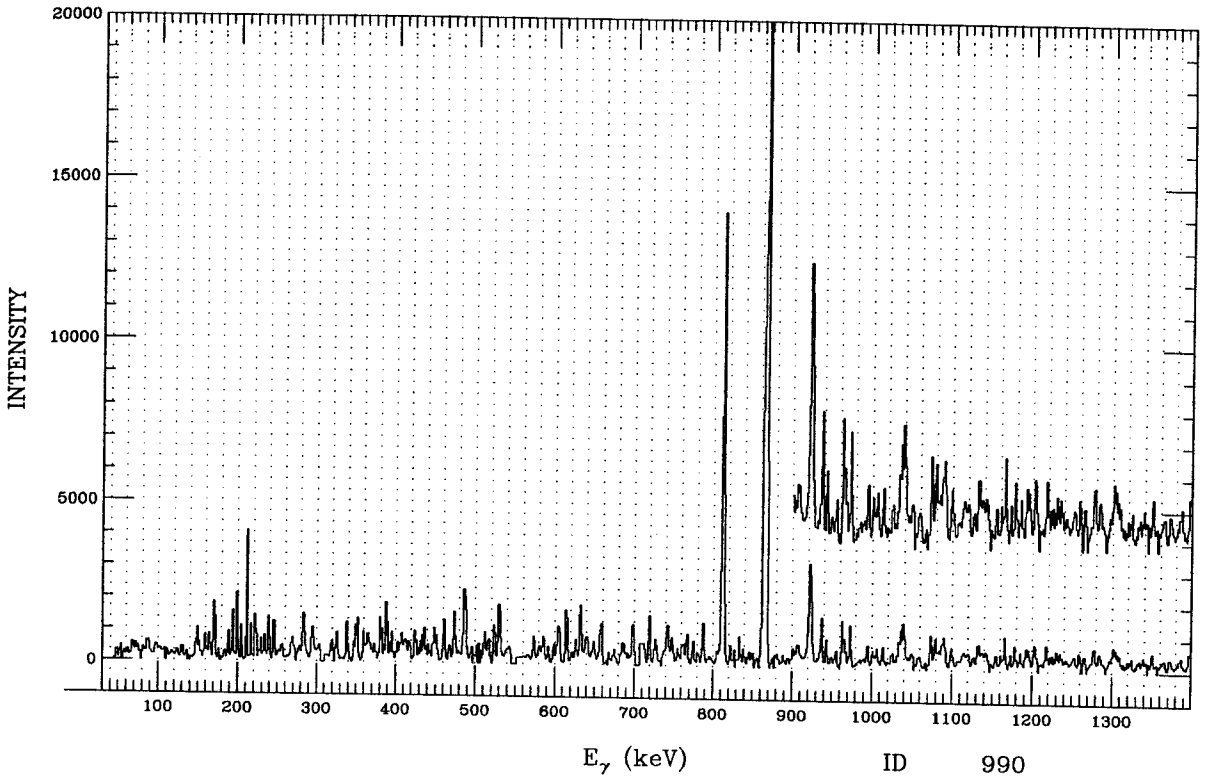

Figure F.83: ID 990. Multiple gate from ^{133}Pr, band 3.

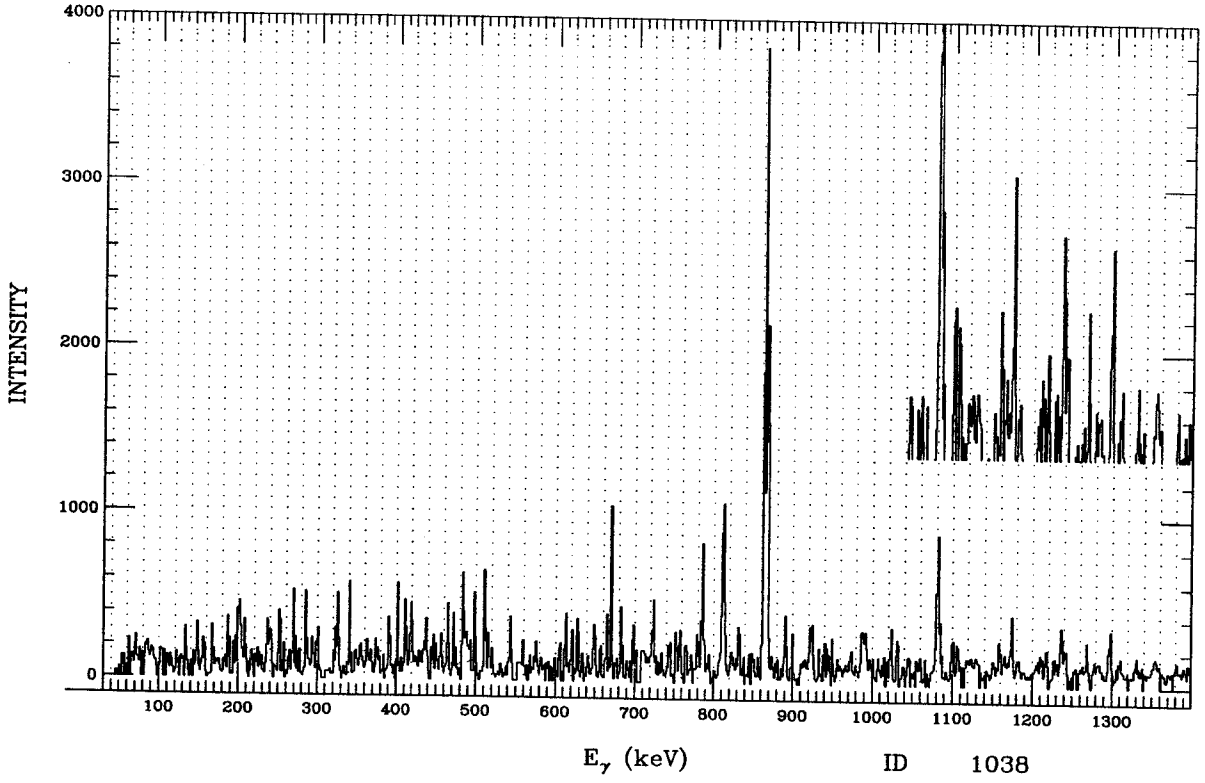

Figure F.84: ID 1037. Multiple gate from ^{133}Pr, band 3.

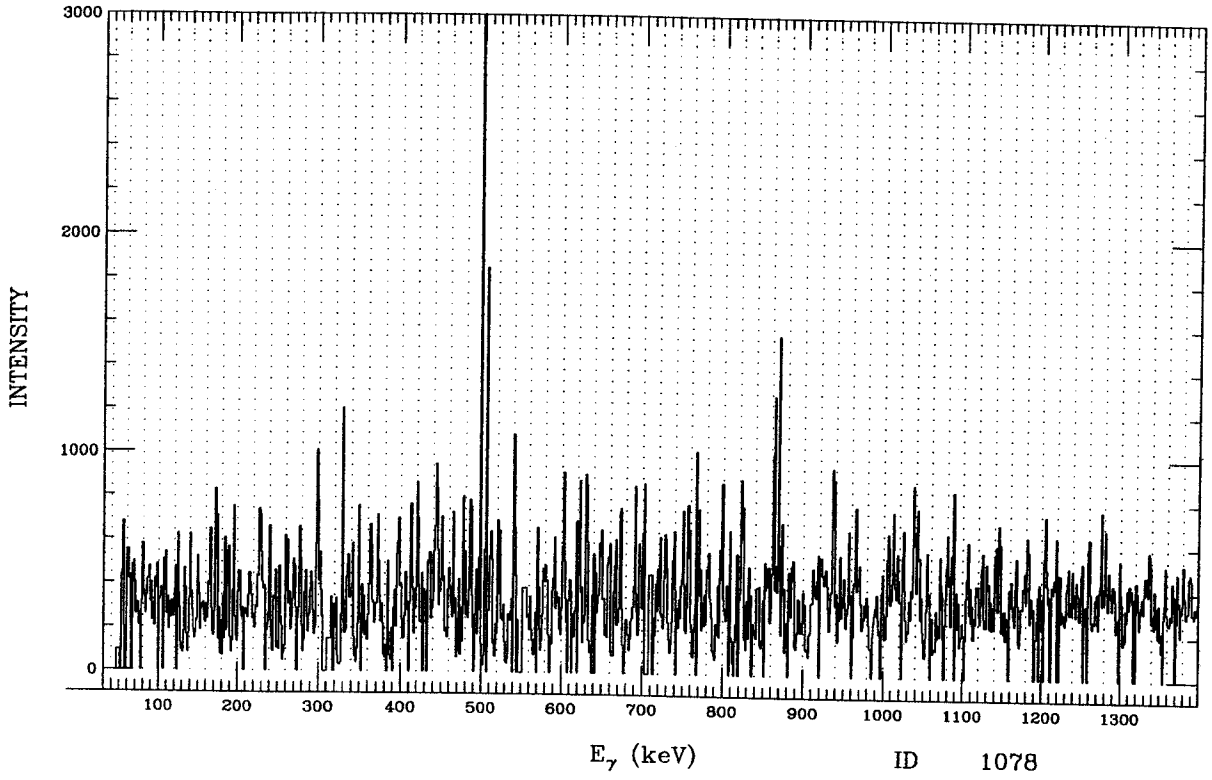

Figure F.85: ID 1078. Multiple gate from ^{133}Pr, band 3.

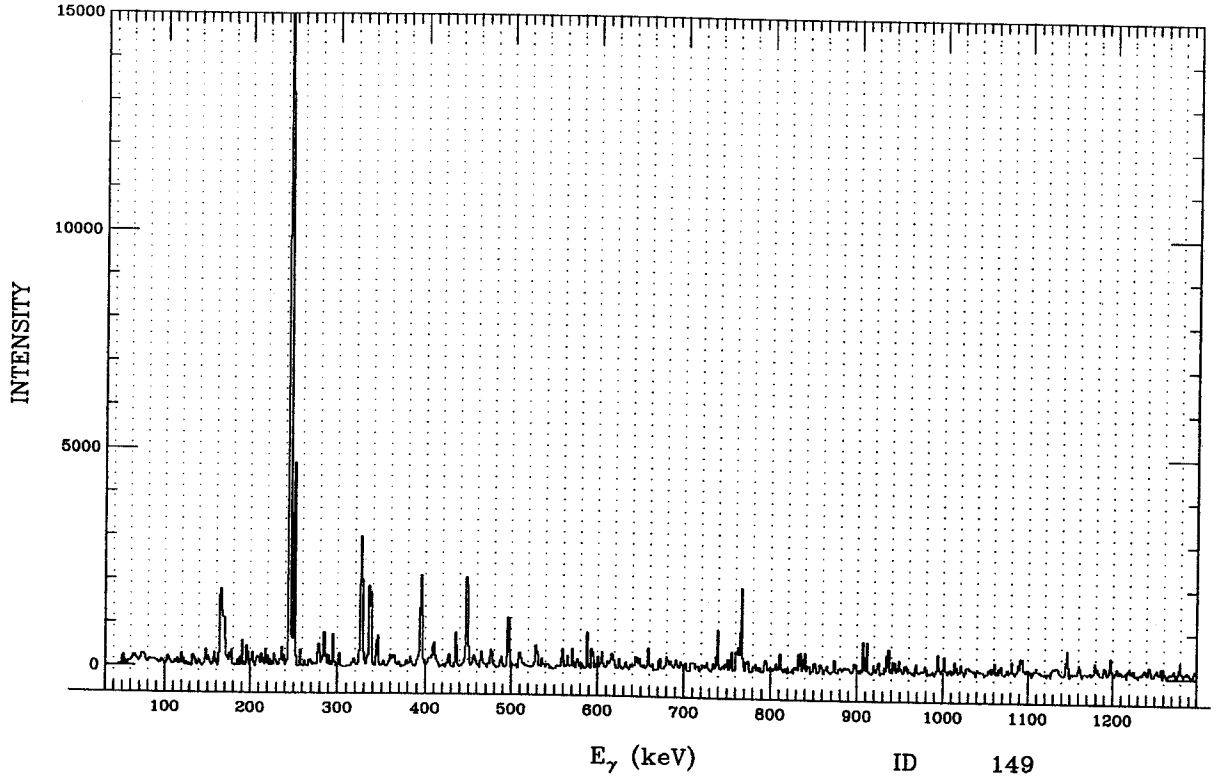

Figure F.86: ID 149. Multiple gate from ^{133}Pr, band 4.

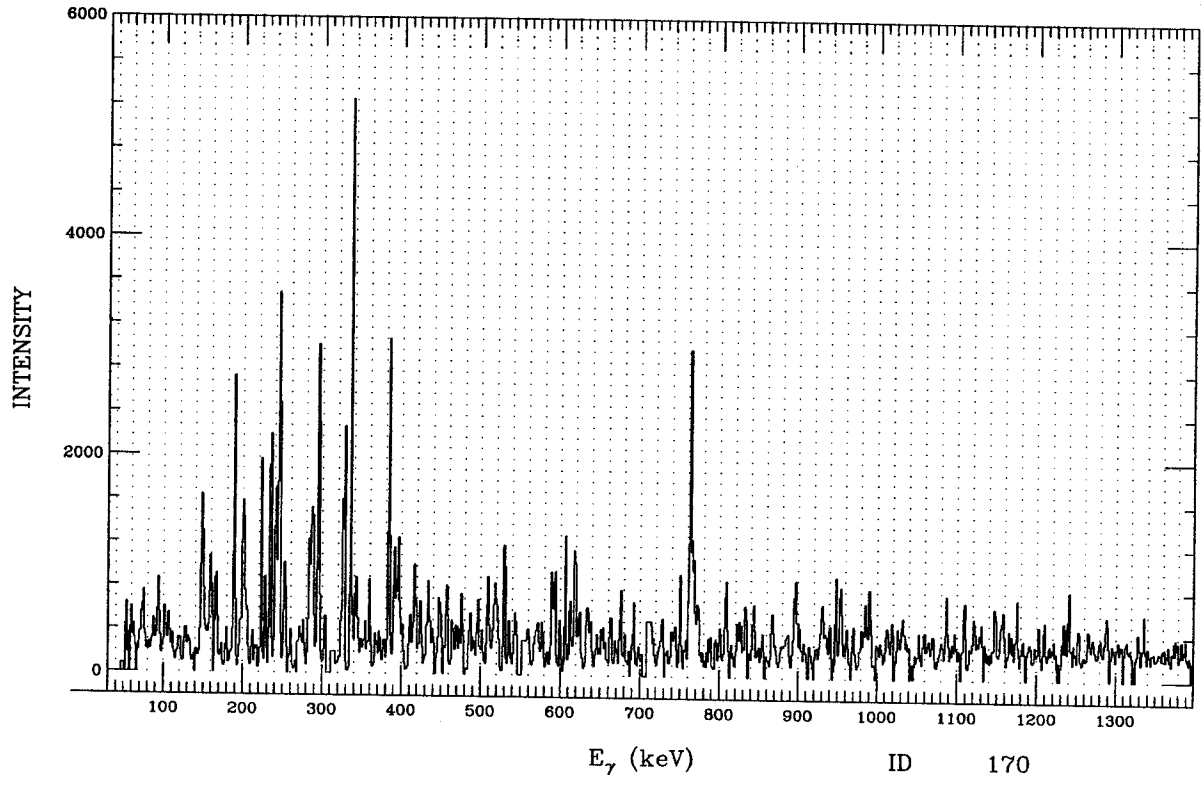

Figure F.87: ID 170. Multiple gate from ^{133}Pr, band 4.

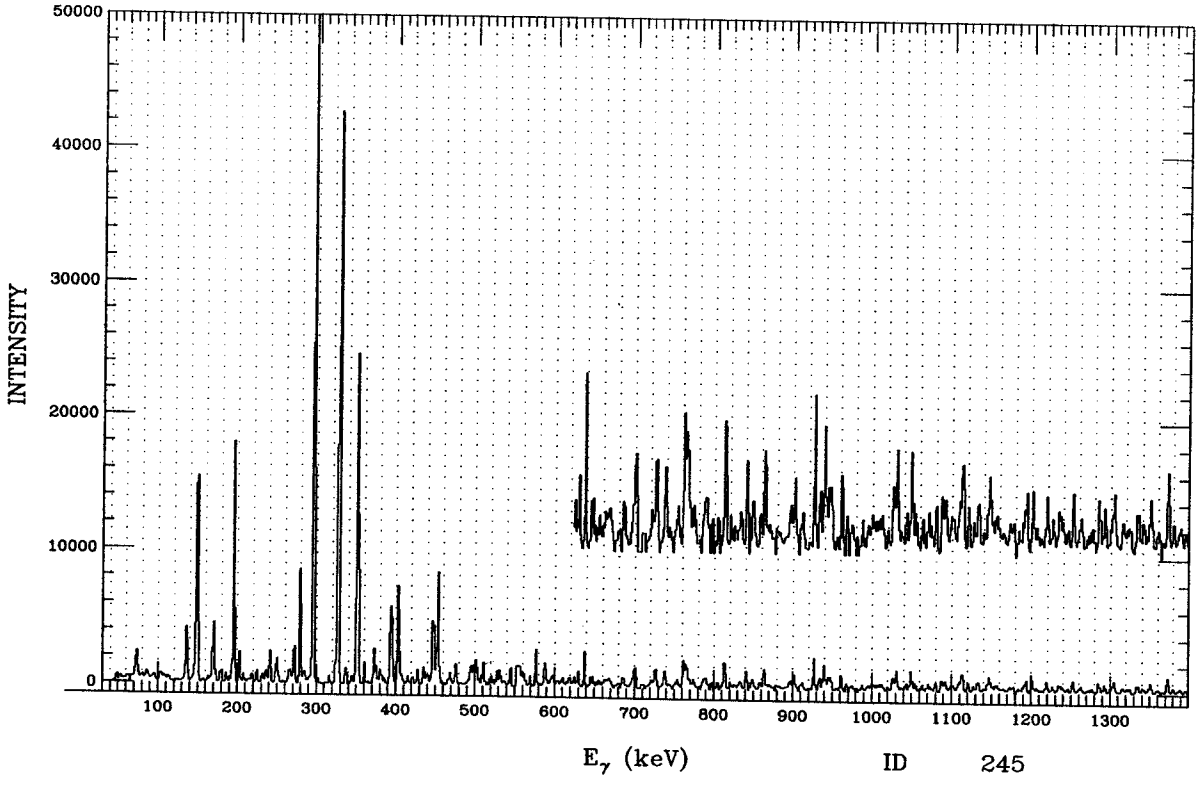

Figure F.88: ID 245. Multiple gate from ^{133}Pr, band 4.

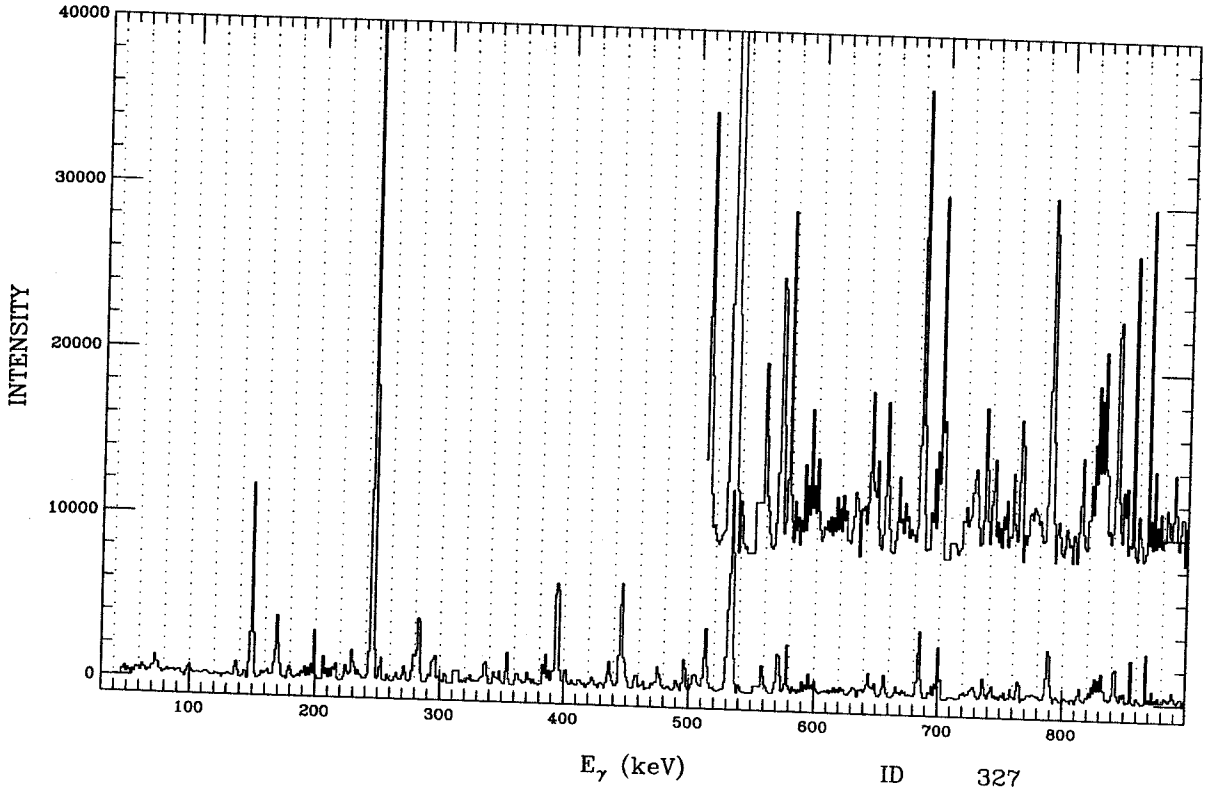

Figure F.89: ID 327. Multiple gate from ^{133}Pr, band 4.

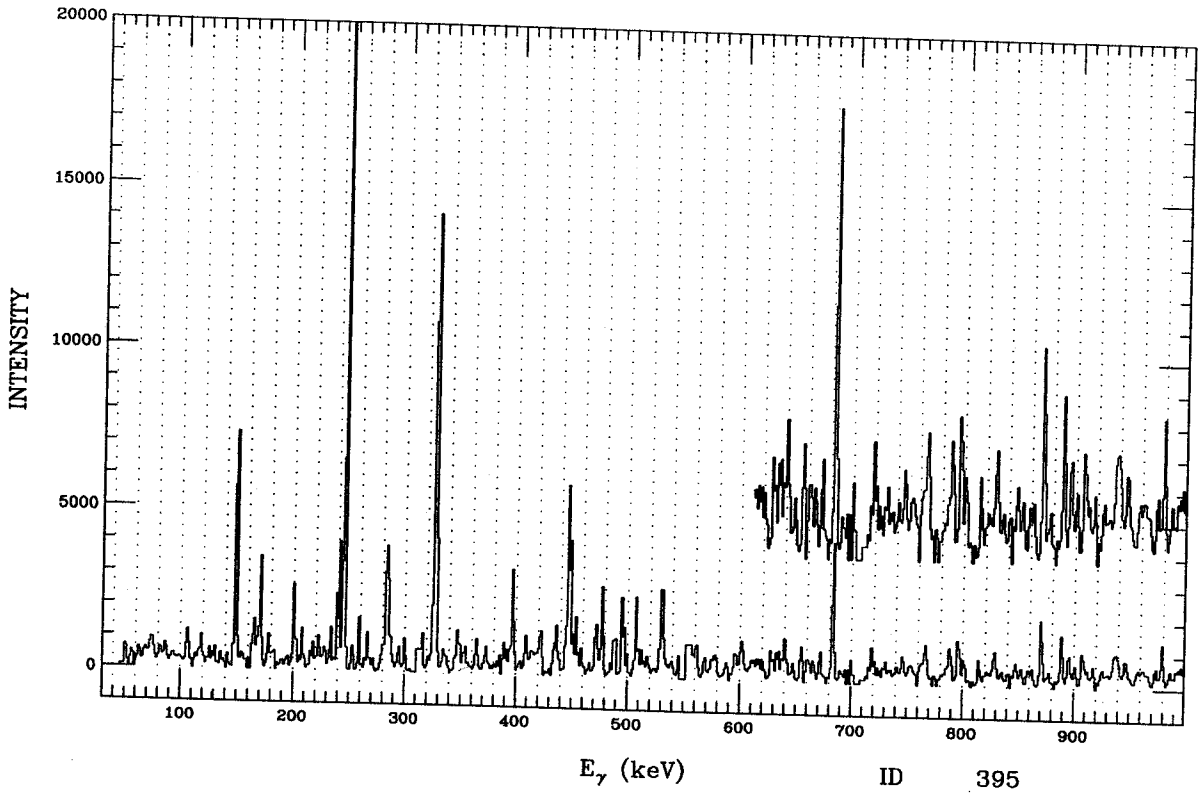

Figure F.90: ID 395. Multiple gate from ^{133}Pr, band 4.

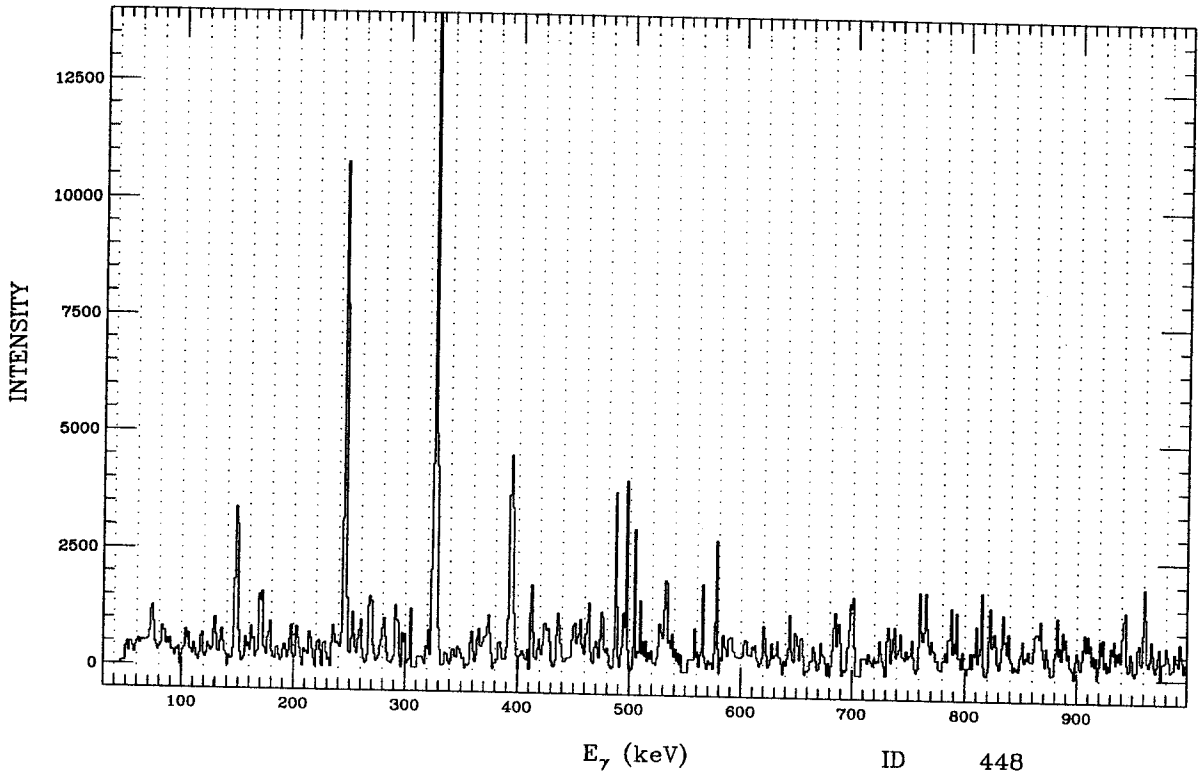

Figure F.91: ID 448. Multiple gate from ^{133}Pr, band 4.

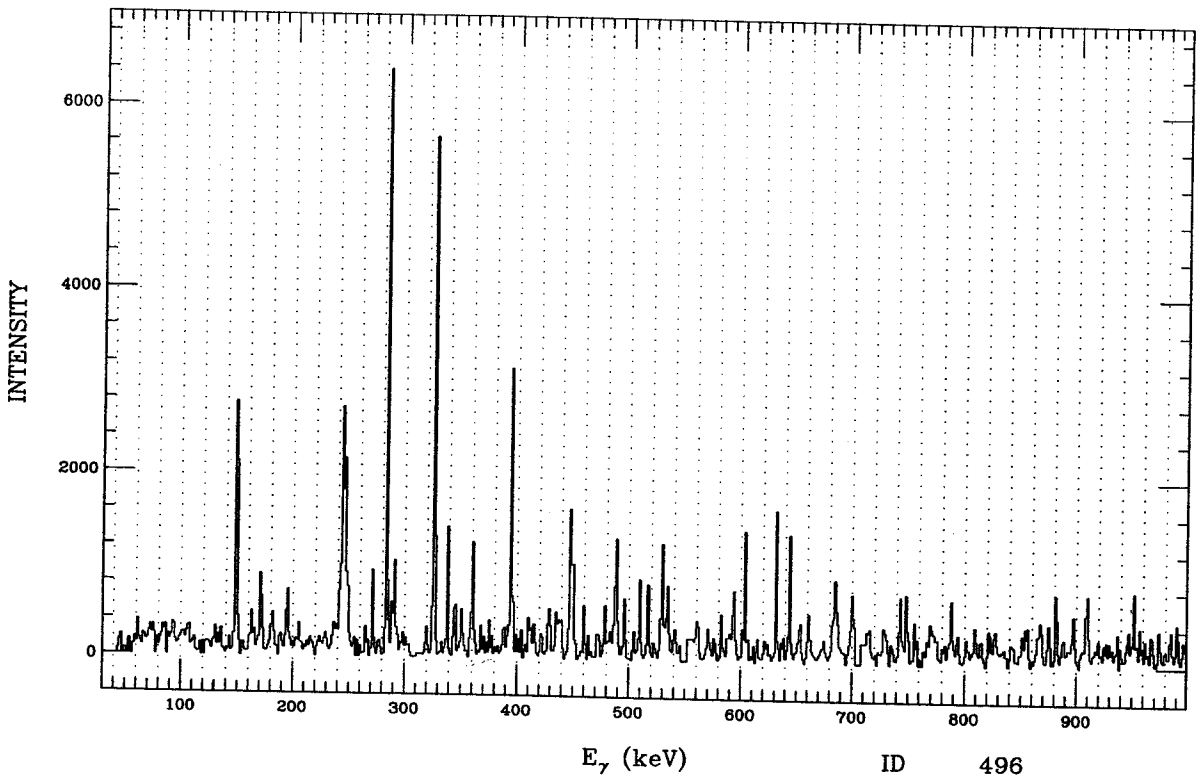

Figure F.92: ID 496. Multiple gate from ^{133}Pr, band 4.

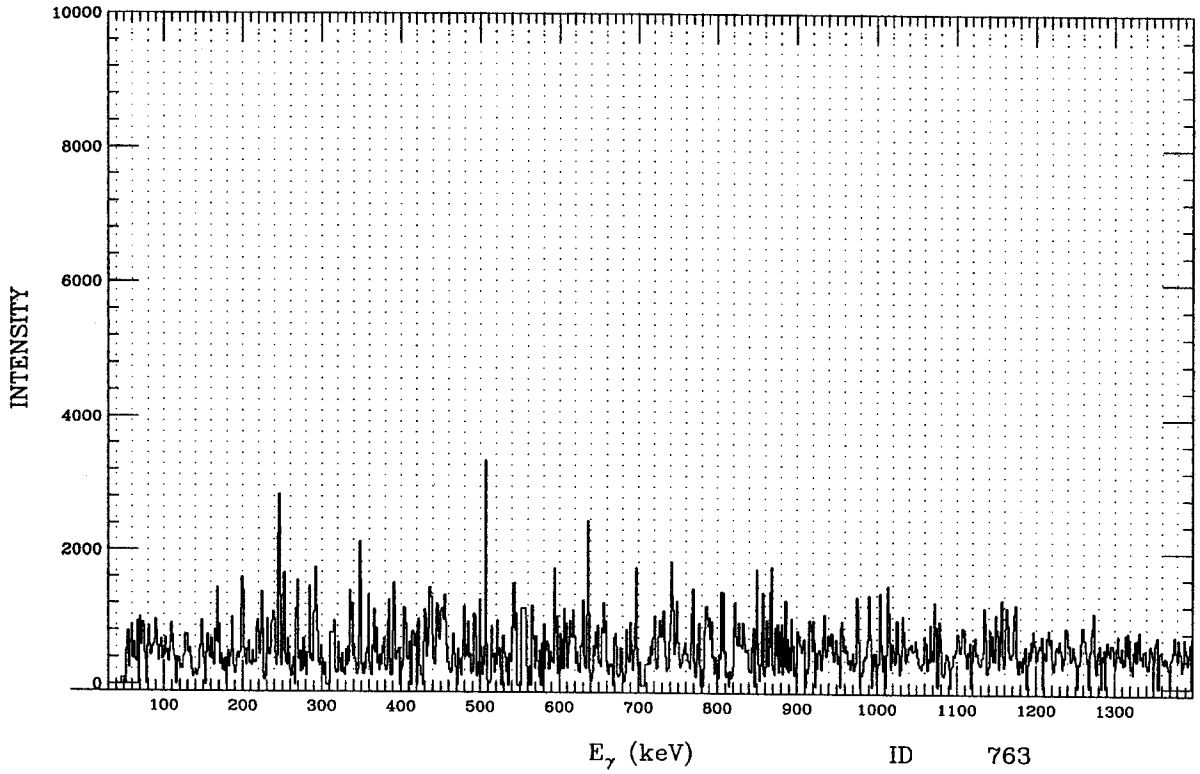

Figure F.93: ID 763. Multiple gate from ^{133}Pr, band 4.

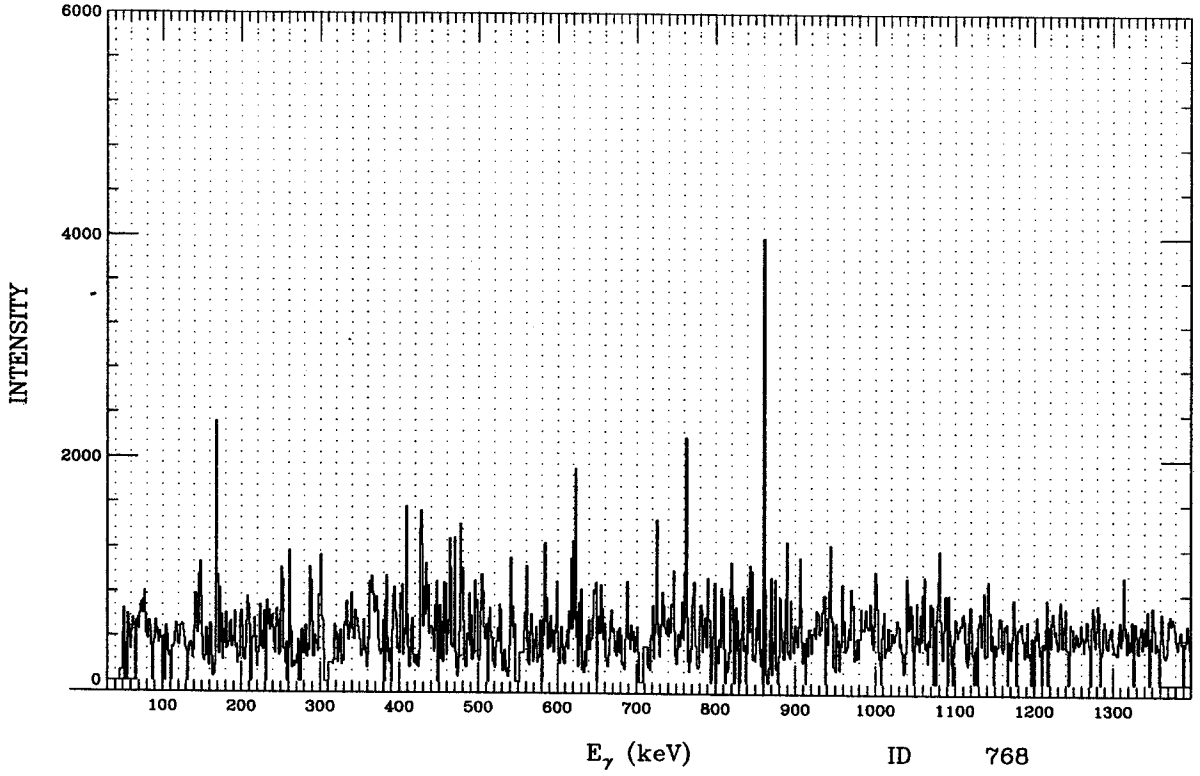

Figure F.94: ID 768. Multiple gate from ^{133}Pr, band 4.

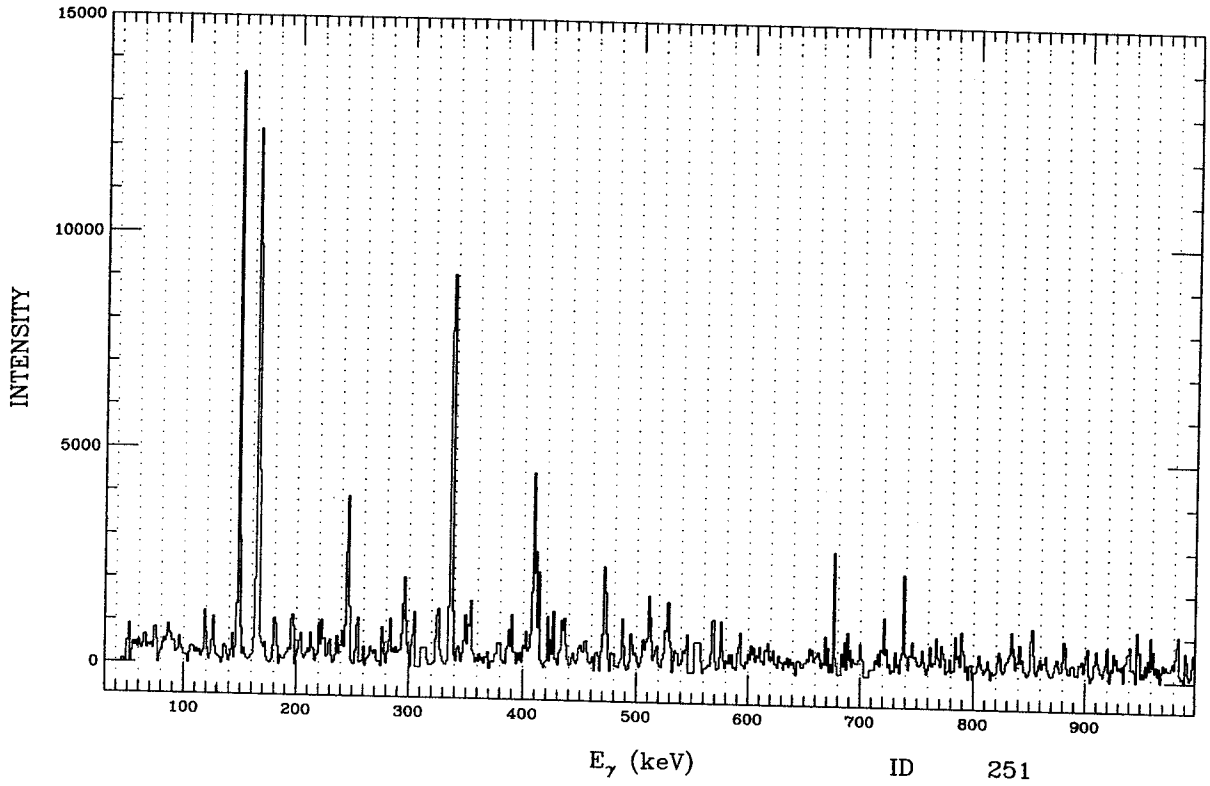

Figure F.95: ID 251. Multiple gate from ^{133}Pr, band 5.

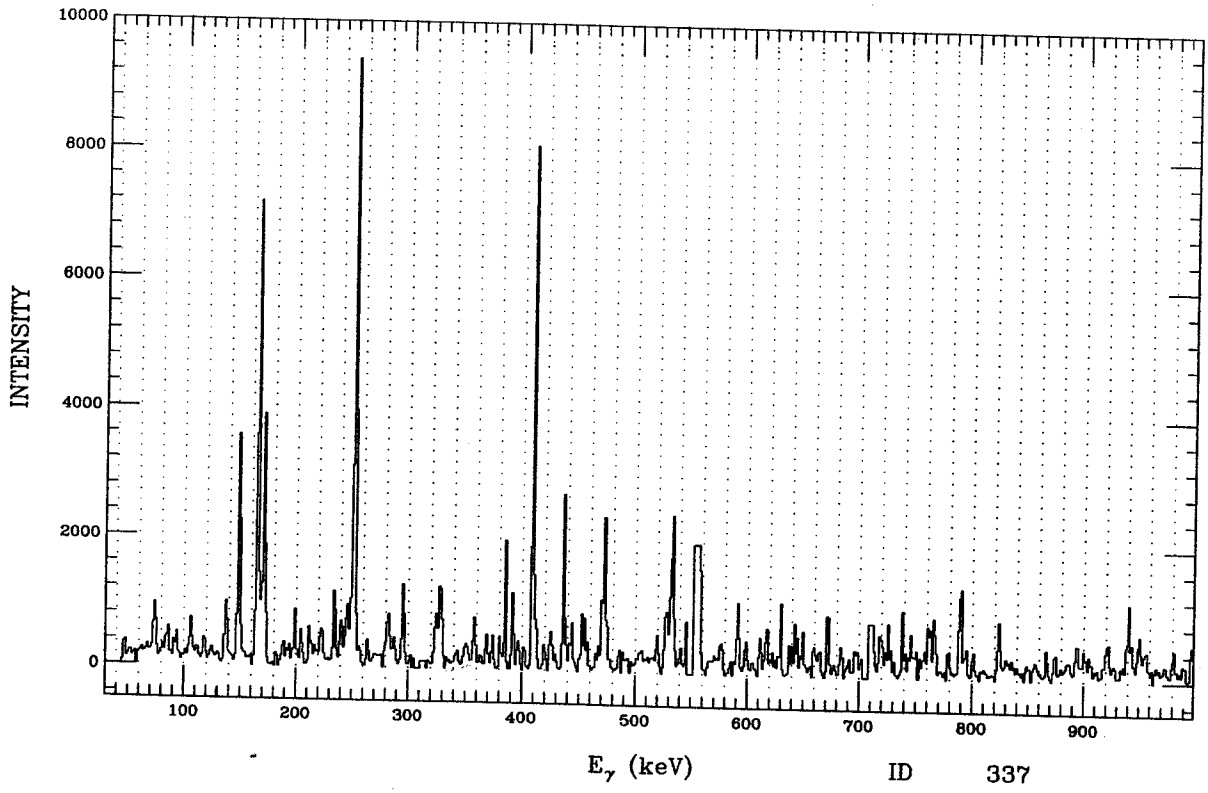

Figure F.96: ID 337. Multiple gate from ^{133}Pr, band 5.

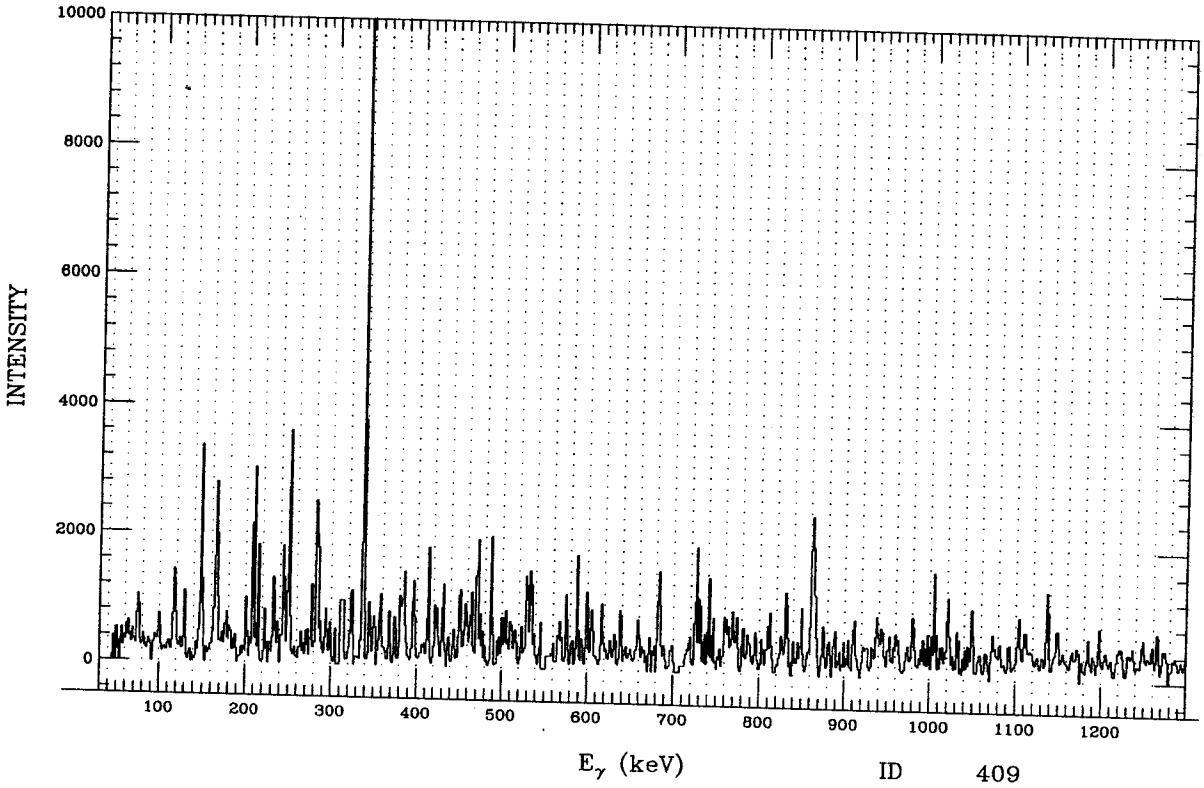

Figure F.97: ID 409. Multiple gate from ^{133}Pr, band 5.

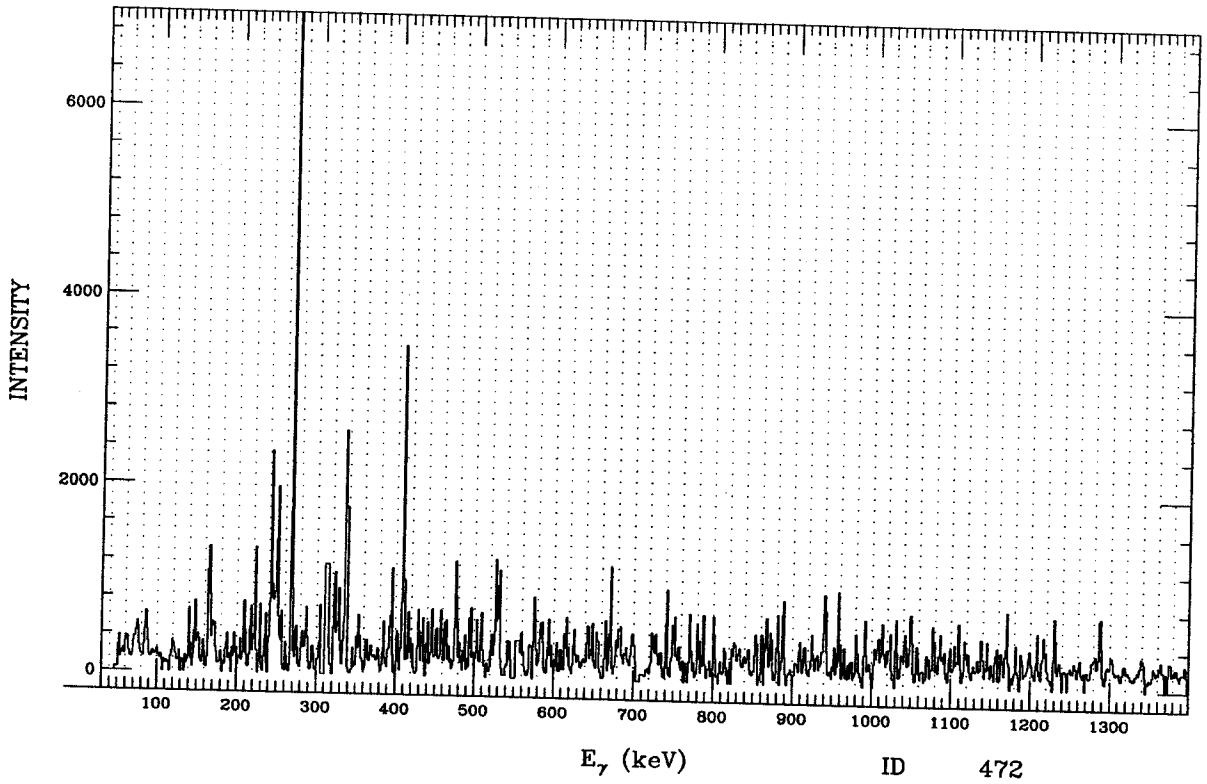

Figure F.98: ID 472. Multiple gate from ^{133}Pr, band 5.

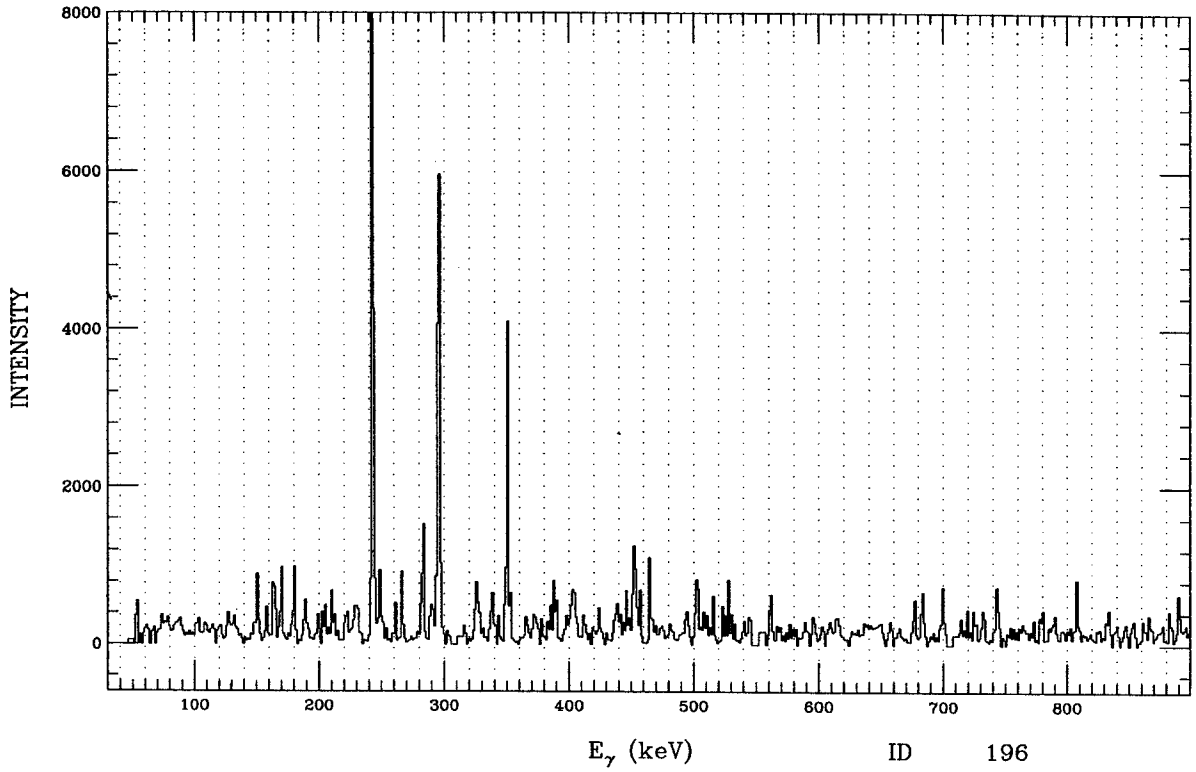

Figure F.99: ID 196. Multiple gate from ^{133}Pr, band 6.

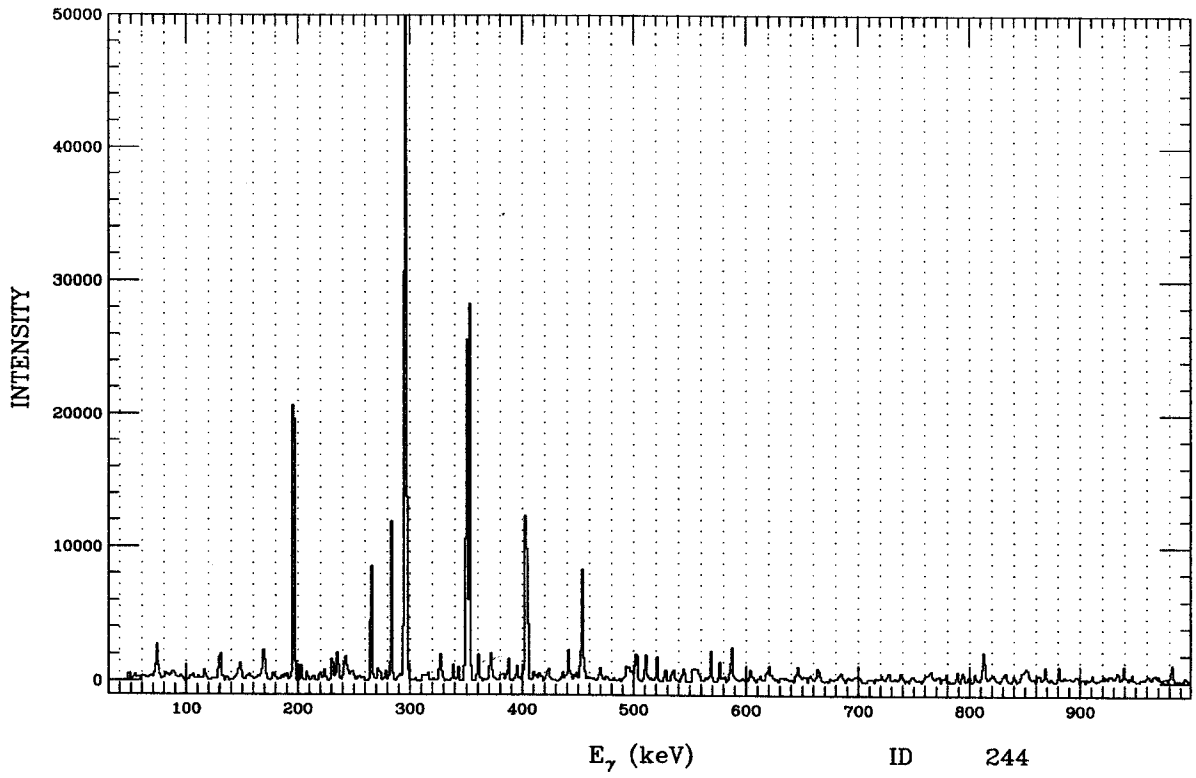

Figure F.100: ID 244. Multiple gate from ^{133}Pr, band 6.

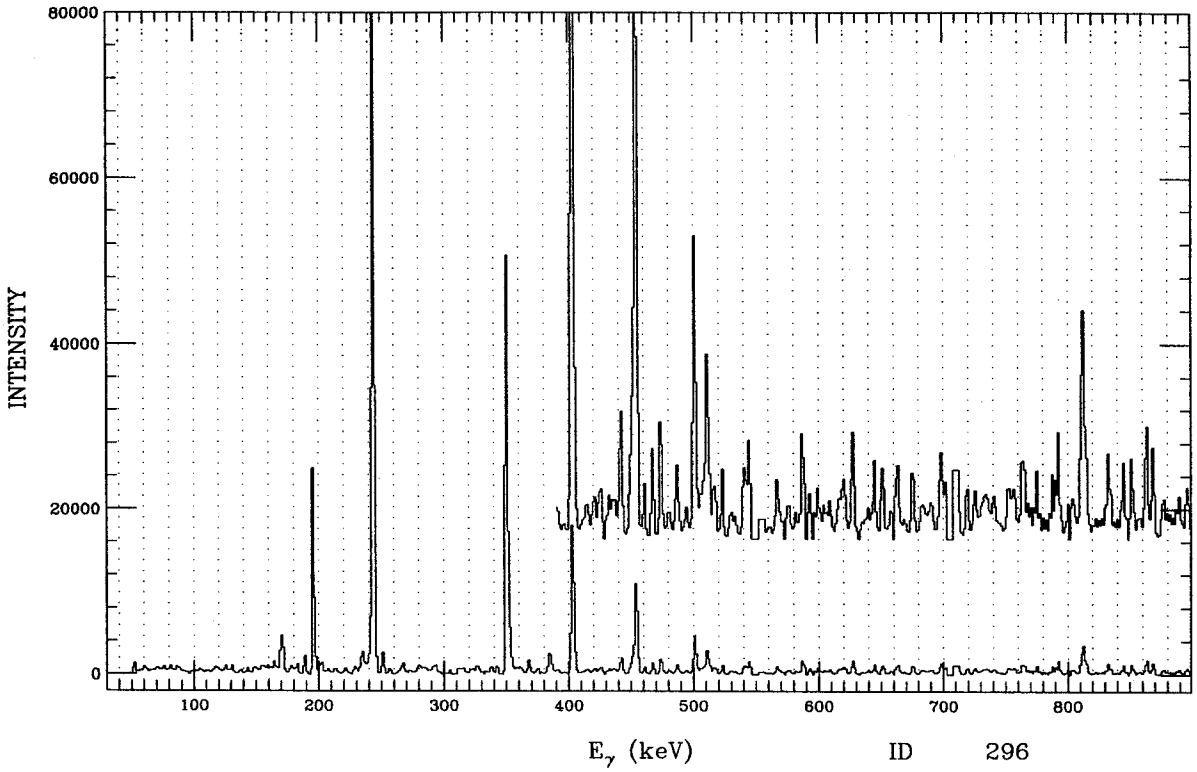

Figure F.101: ID 296. Multiple gate from ^{133}Pr, band 6.

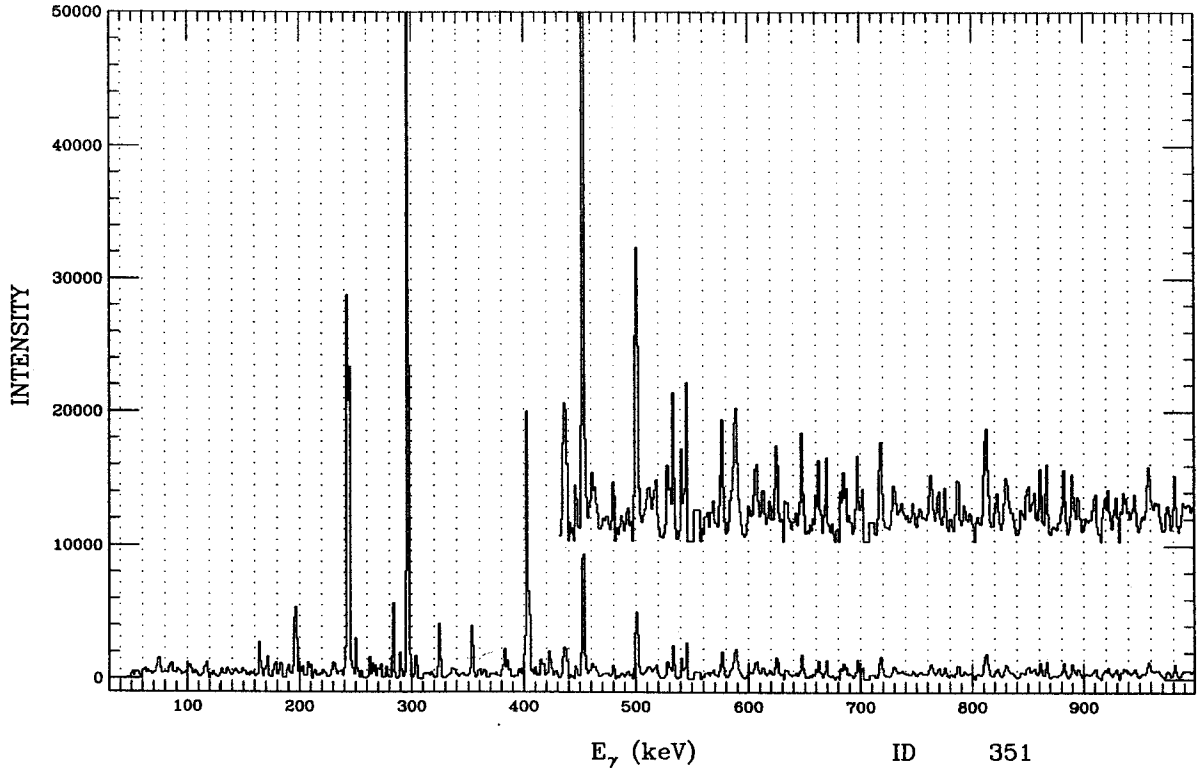

Figure F.102: ID 351. Multiple gate from ^{133}Pr, band 6.

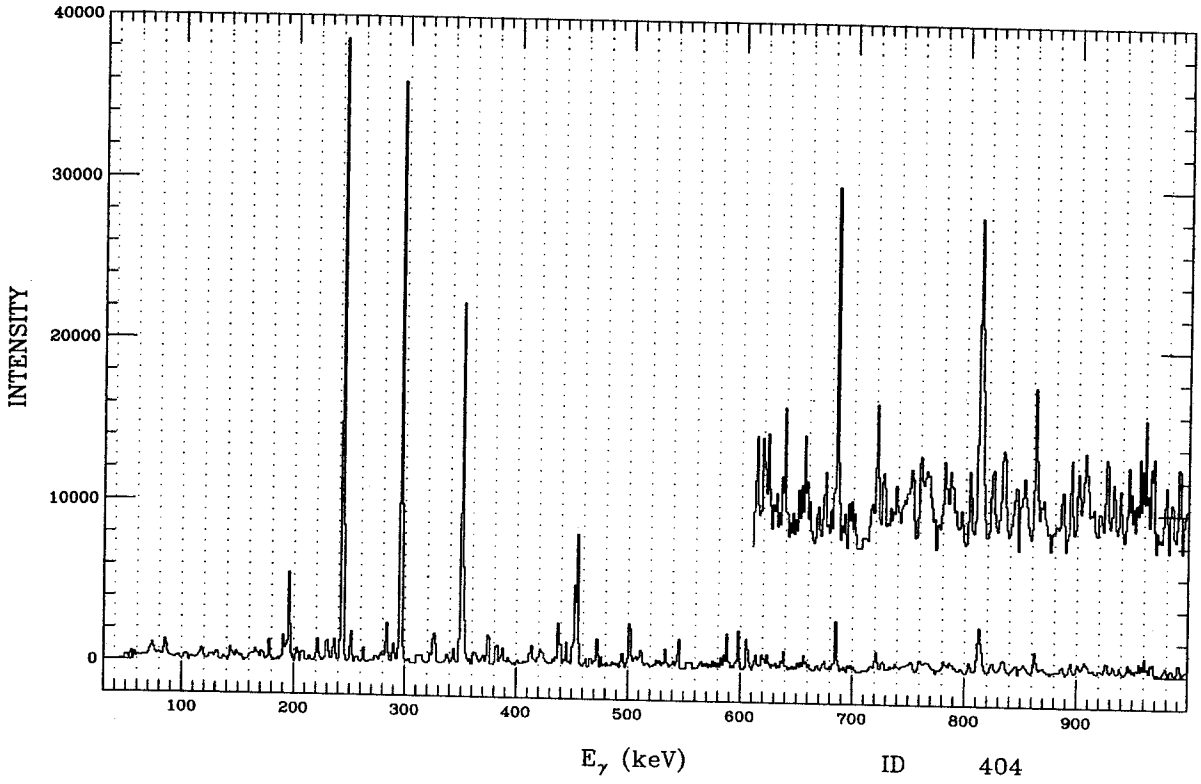

Figure F.103: ID 404. Multiple gate from ^{133}Pr, band 6.

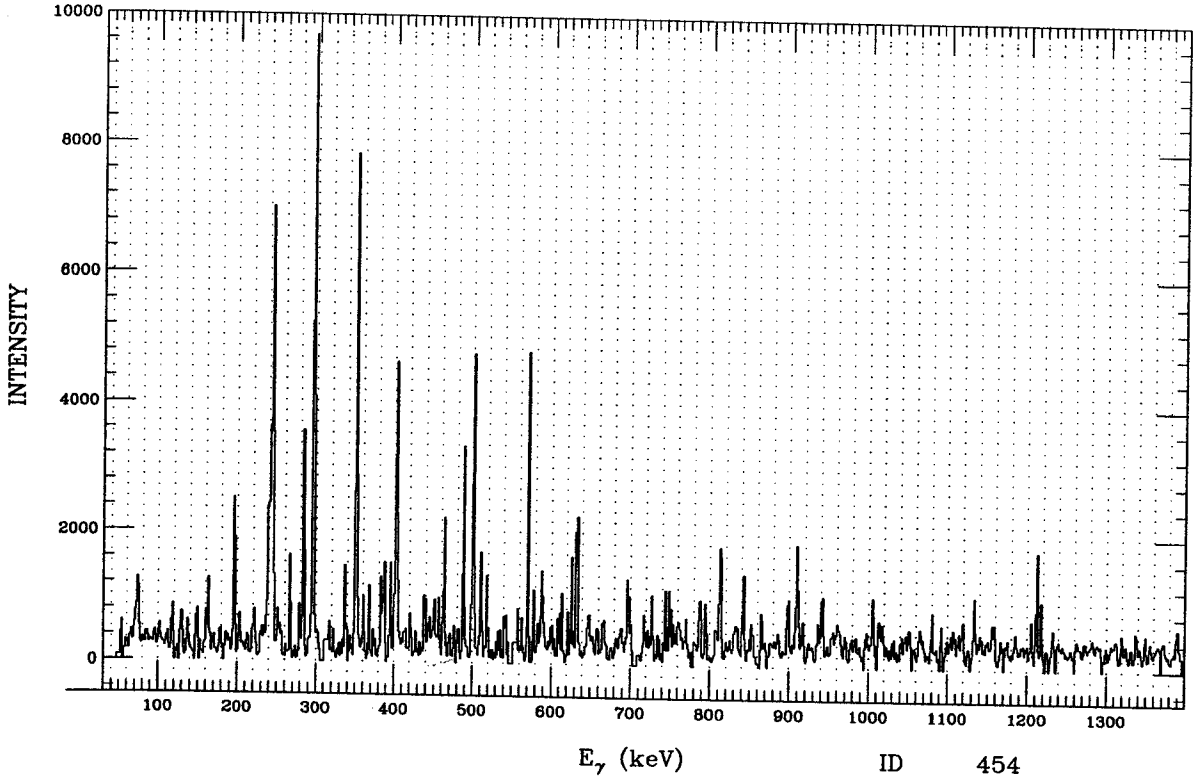

Figure F.104: ID 454. Multiple gate from ^{133}Pr, band 6.

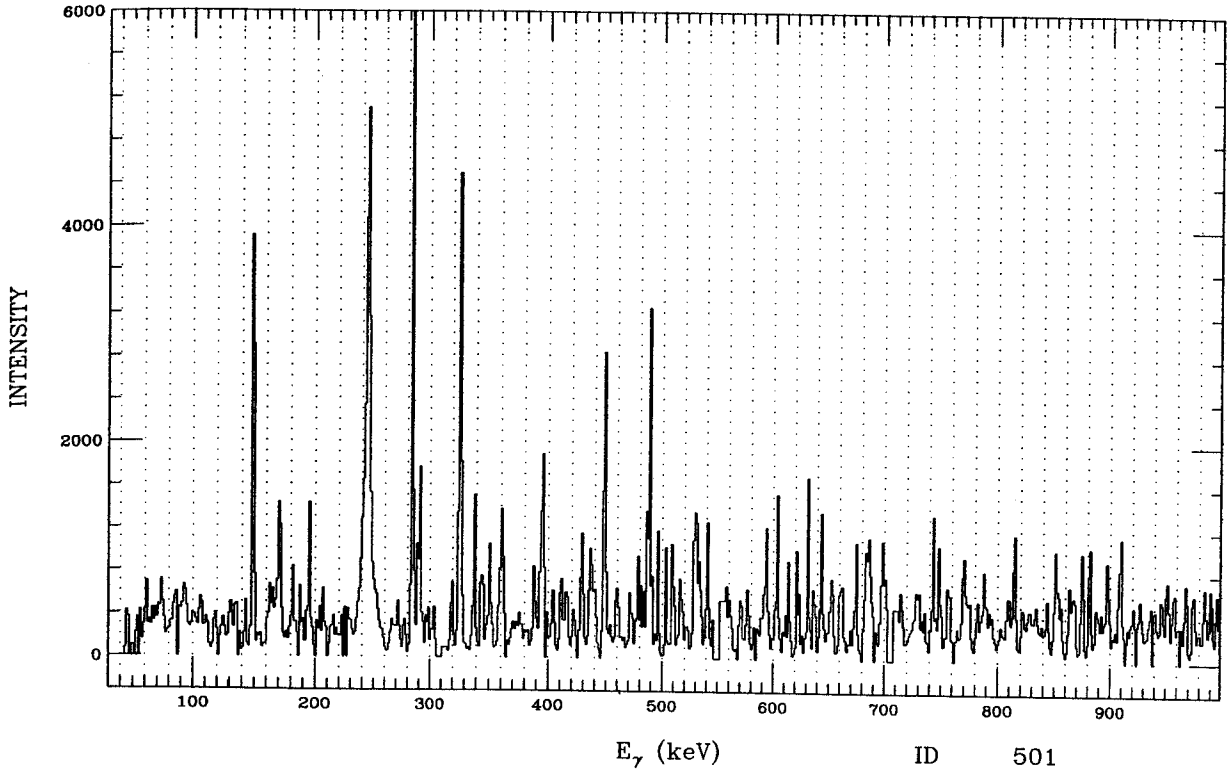

Figure F.105: ID 501. Multiple gate from ^{133}Pr, band 6.

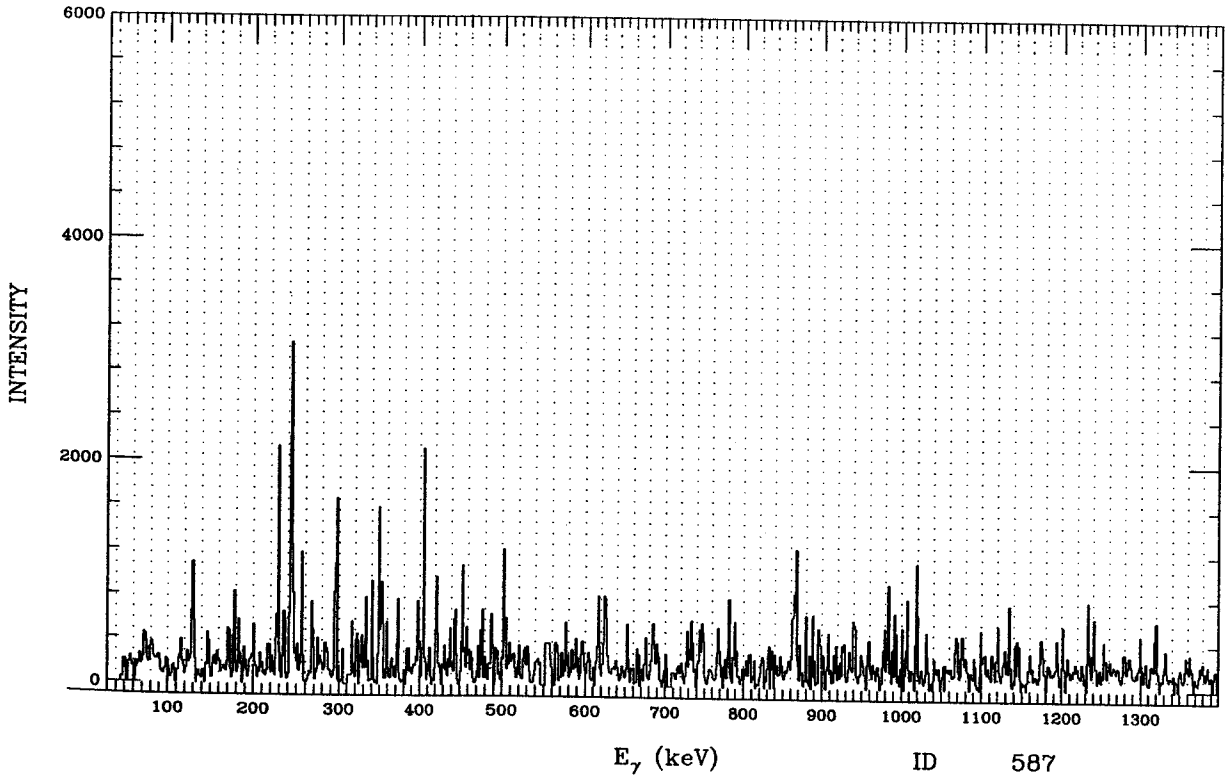

Figure F.106: ID 587. Multiple gate from ^{133}Pr, band 6.

F.3 Rotational Bands ^{133}Pr.

Spectra for the rotational bands in ^{133}Pr are listed in this Appendix. They were constructed by summing gates that fit the coincidence requirements. (See F.2 and F.1.) Each channel number gate, defining an energy peak, was subjected to the FFT noise reduction routine and summed over the peak. Local background was subtracted where indicated and a general background spectrum was also subtracted. The band numbers reflect individual rotational bands described in Figure 10.18.

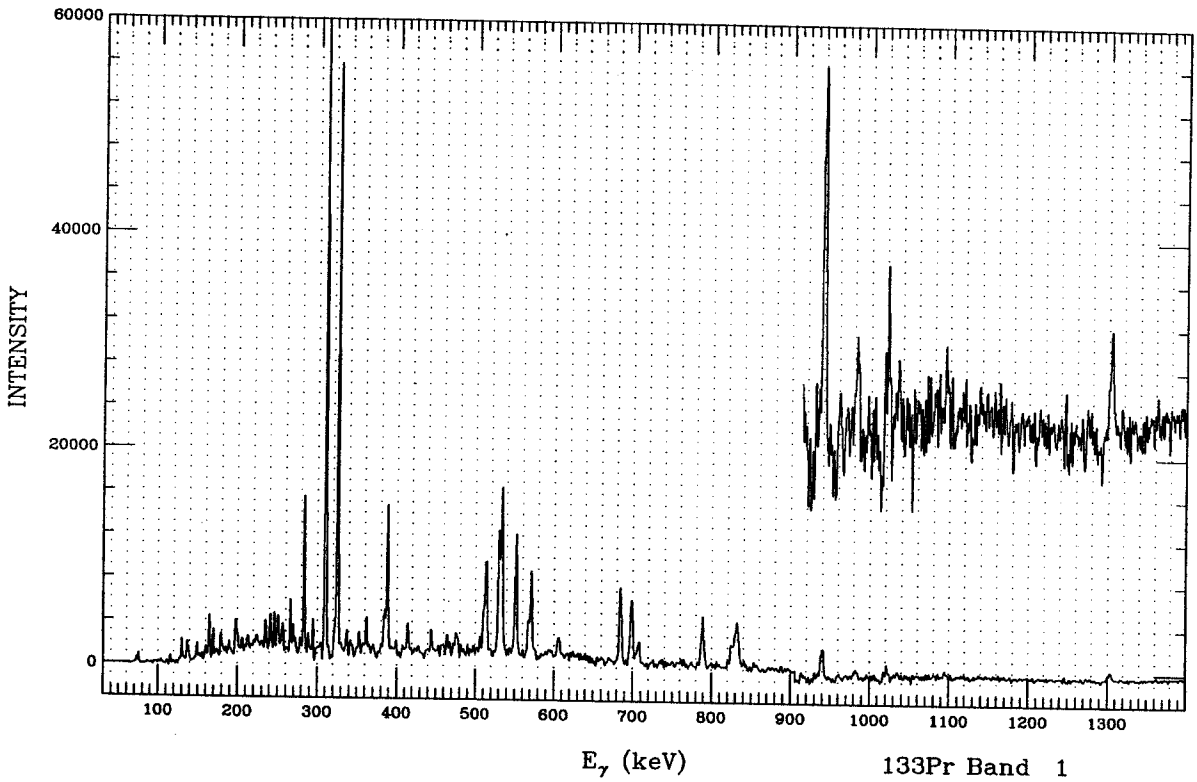

Figure F.107: Sum of gates at 414, 606, 567, 388, 530, 698, 833, 939, 1020, 1092 keV. for band 1 in ^{133}Pr, Simple gate.

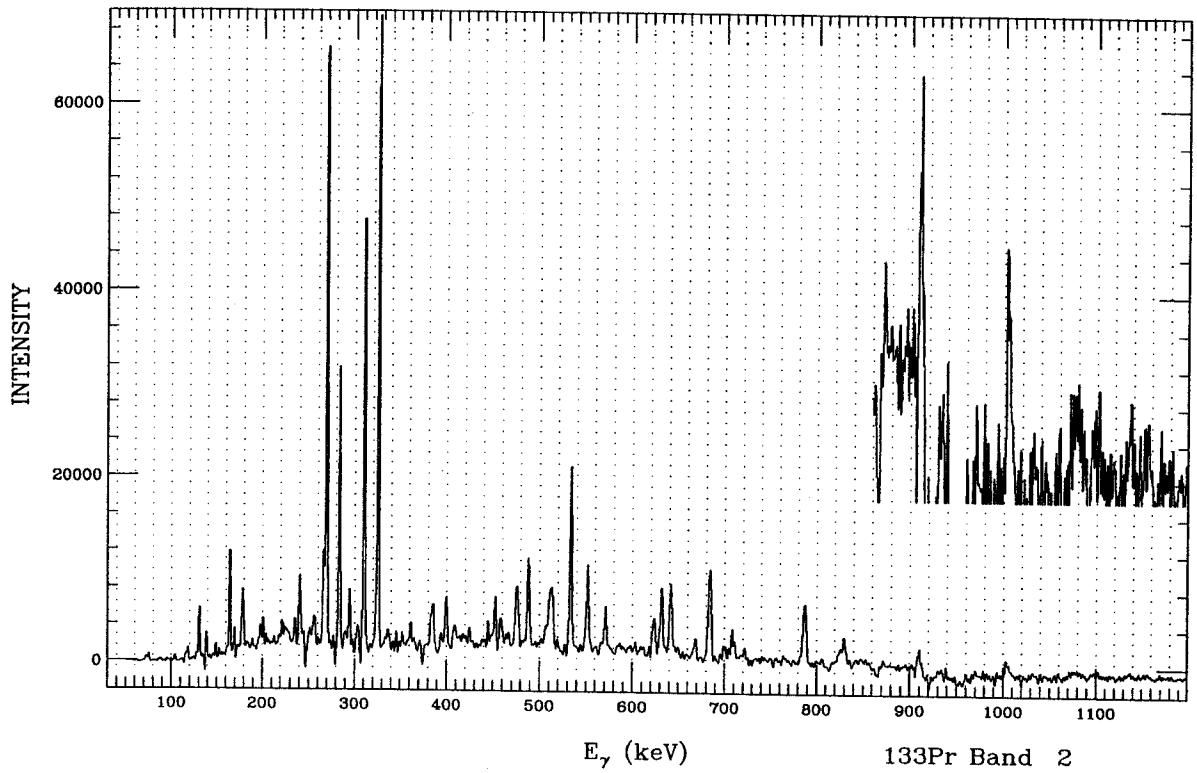

Figure F.108: Sum of gates at 477, 623, 667, 452, 488, 632, 787, 909, 1004 keV. for band 2 in ^{133}Pr, Simple gate.

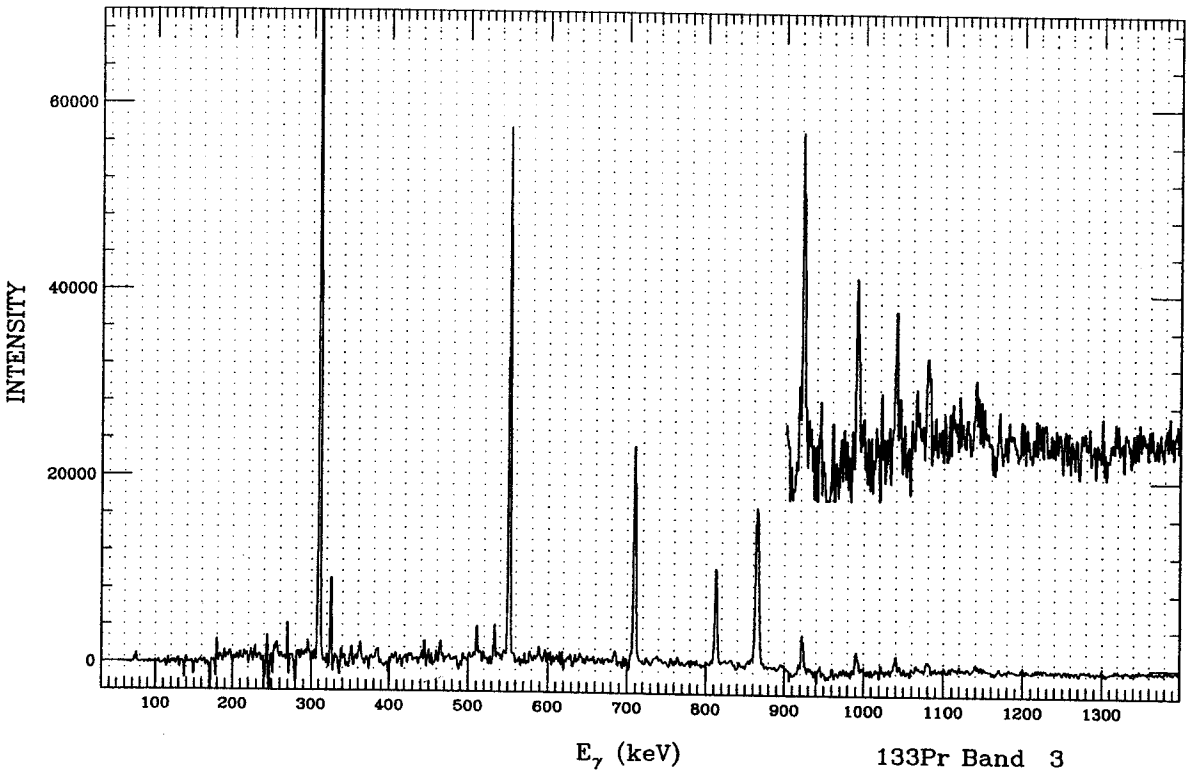

Figure F.109: Sum of gates at 813, 866, 922, 990, 1038, 1078, 1140 keV. for band 3 in ^{133}Pr, Simple gate.

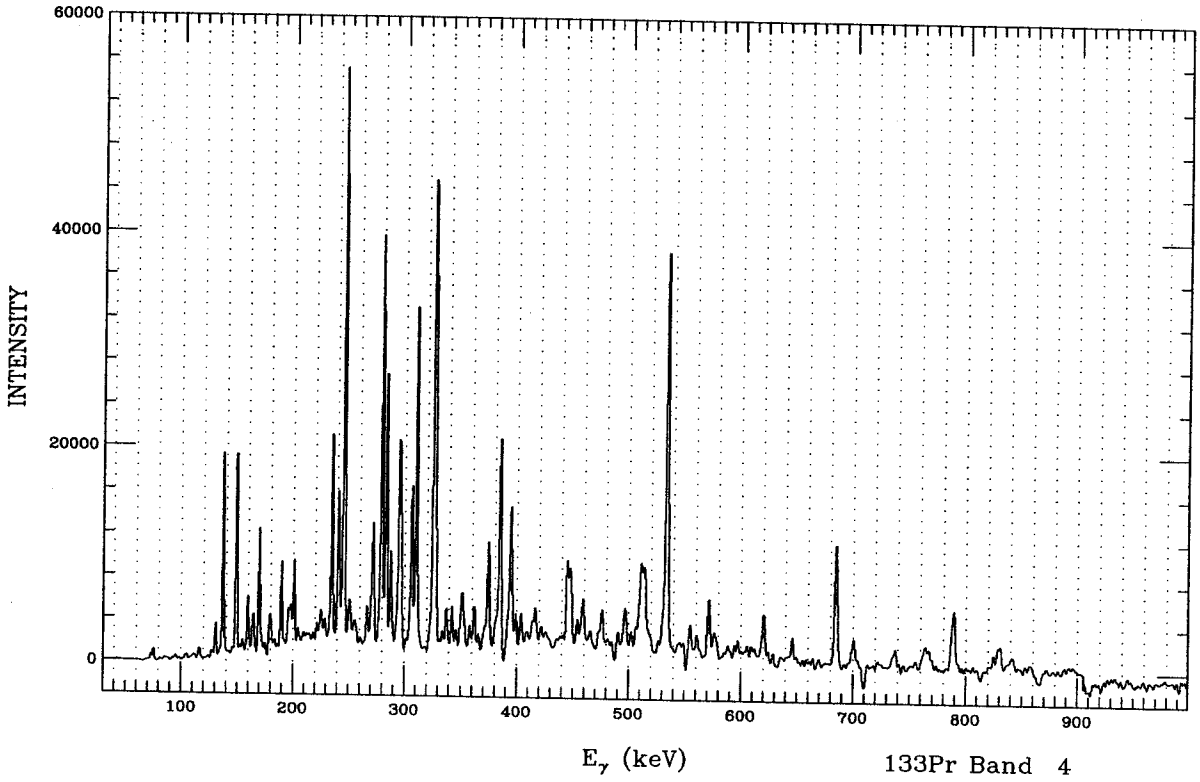

Figure F.110: Sum of gates at 763, 768, 170, 149, 245, 327, 395, 448, 496 keV. for band 4 in ^{133}Pr, Simple gate.

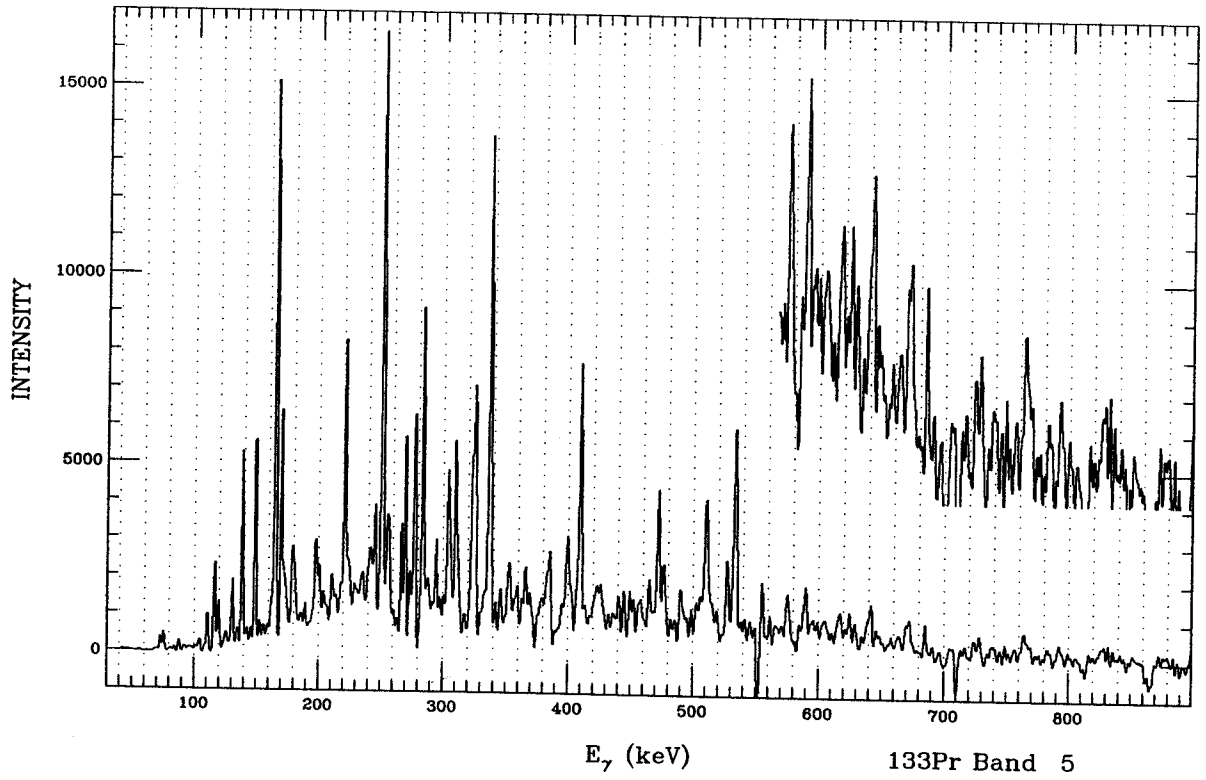

Figure F.111: Sum of gates at 164, 251, 337, 409, 472, keV. for band 5 in ^{133}Pr, Simple gate.

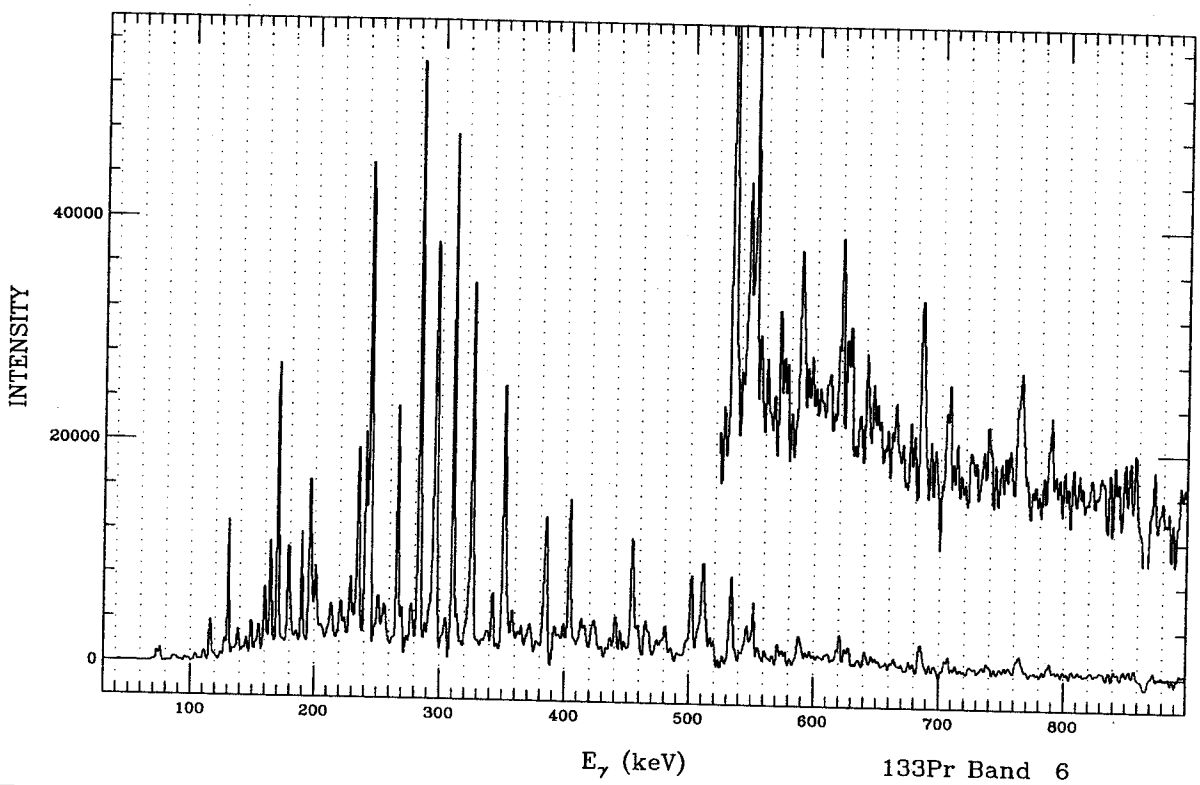

Figure F.112: Sum of gates at 197, 244, 296, 351, 404, 454, 501, 587 keV. for band 6 in ^{133}Pr, Simple gate.

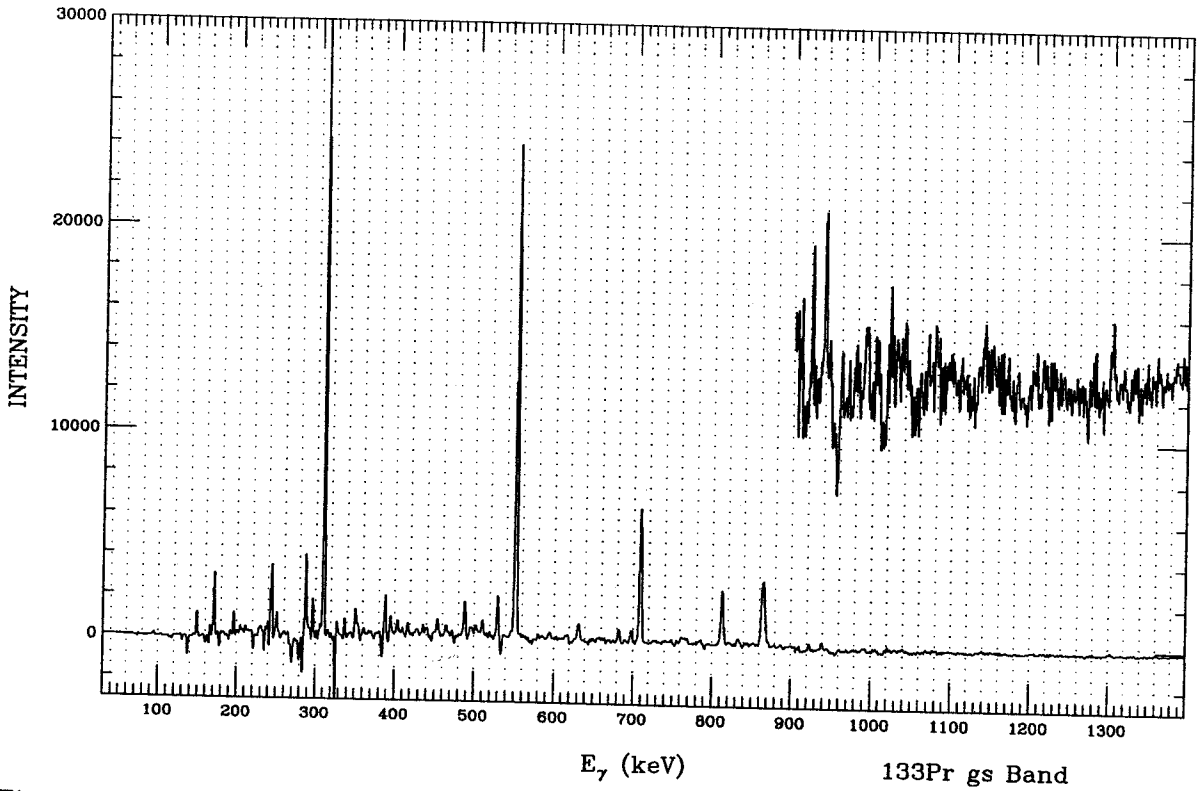

Figure F.113: Sum of gates at 310, 551, 709 keV. for gs band in ^{133}Pr, Simple gate.

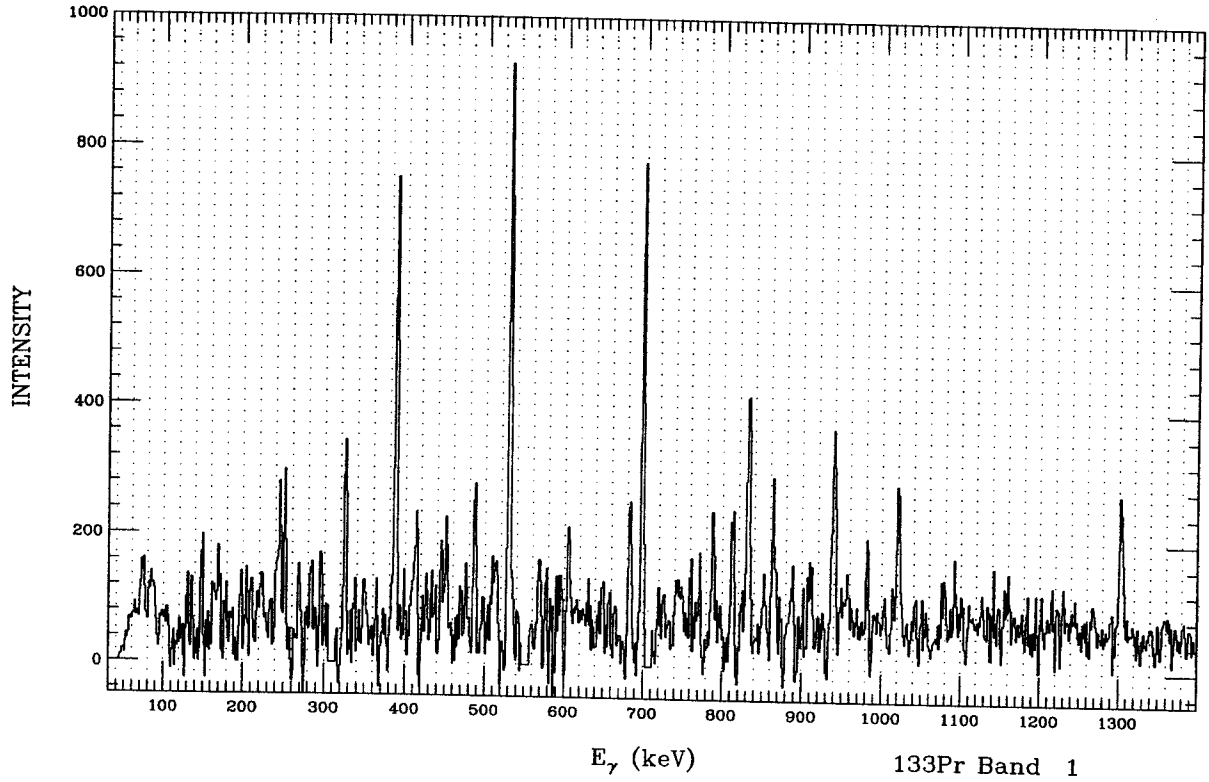

Figure F.114: Sum of gates at 414, 606, 567, 388, 530, 698, 833, 939, 1020, 1092 keV. for band 1 in ^{133}Pr, Multiple gate.

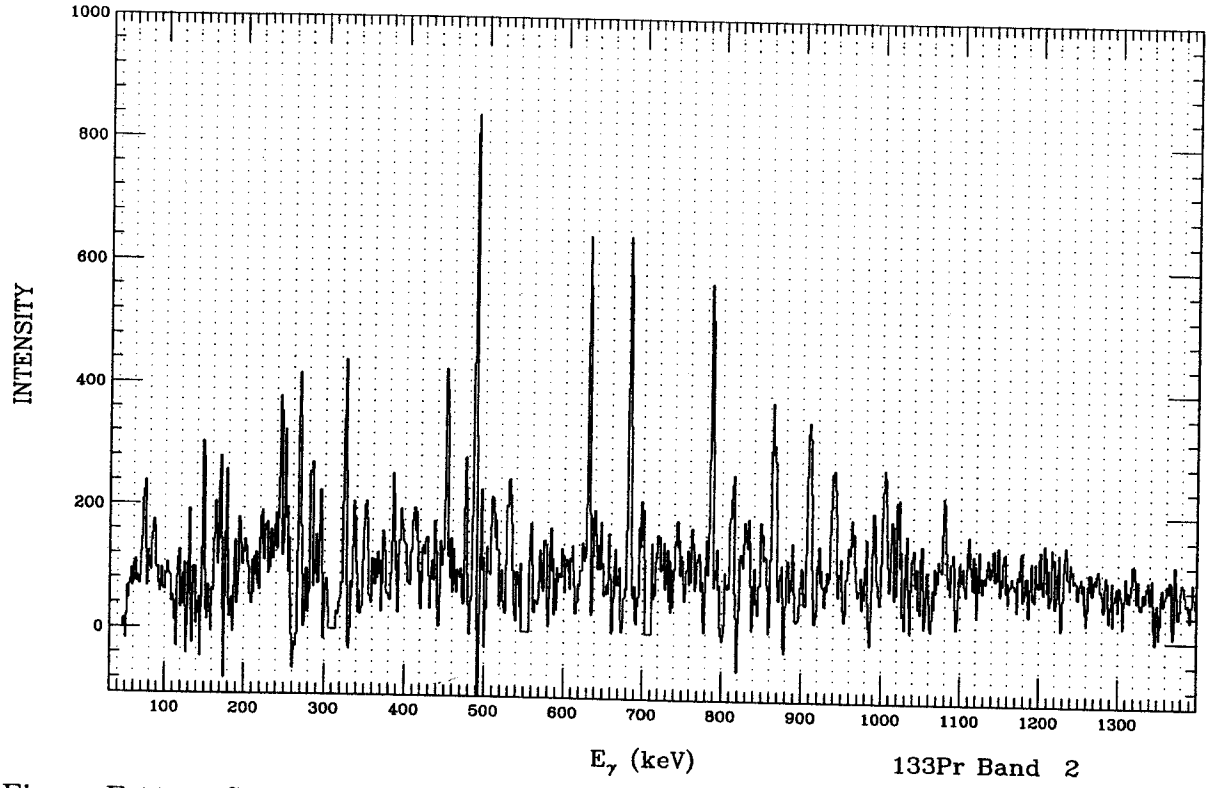

Figure F.115: Sum of gates at 477, 623, 667, 452, 488, 632, 787, 909, 1004 keV. for band 2 in ^{133}Pr, Multiple gate.

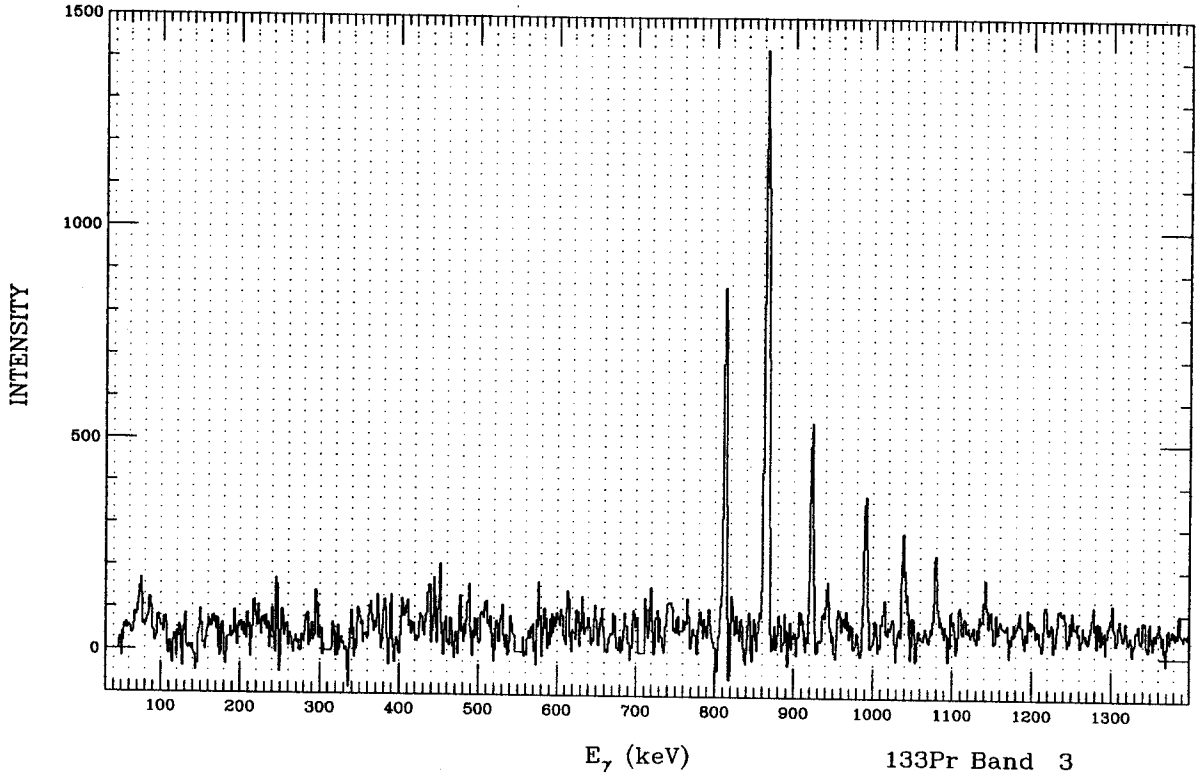

Figure F.116: Sum of gates at 813, 866, 922, 990, 1038, 1078, 1140 keV. for band 3 in ^{133}Pr, Multiple gate.

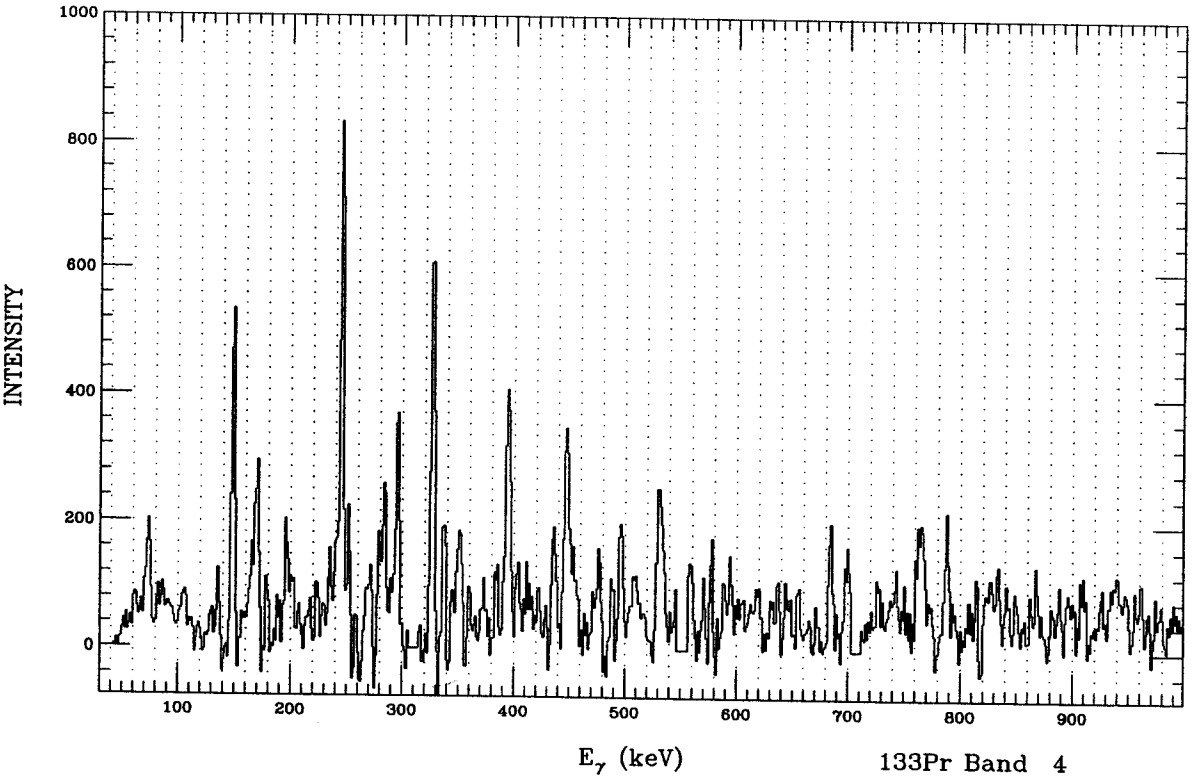

Figure F.117: Sum of gates at 763, 768, 170, 149, 245, 327, 395, 448, 496 keV. for band 4 in ^{133}Pr, Multiple gate.

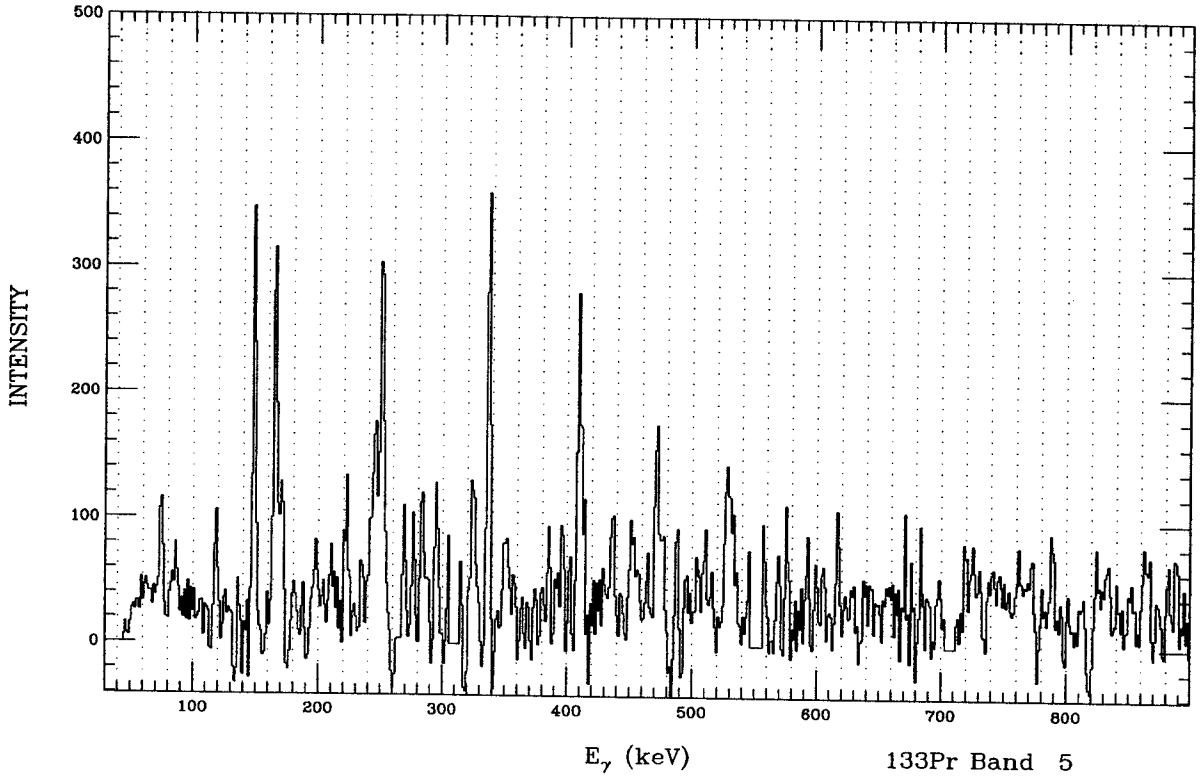

Figure F.118: Sum of gates at 164, 251, 337, 409, 472, keV. for band 5 in ^{133}Pr, Multiple gate.

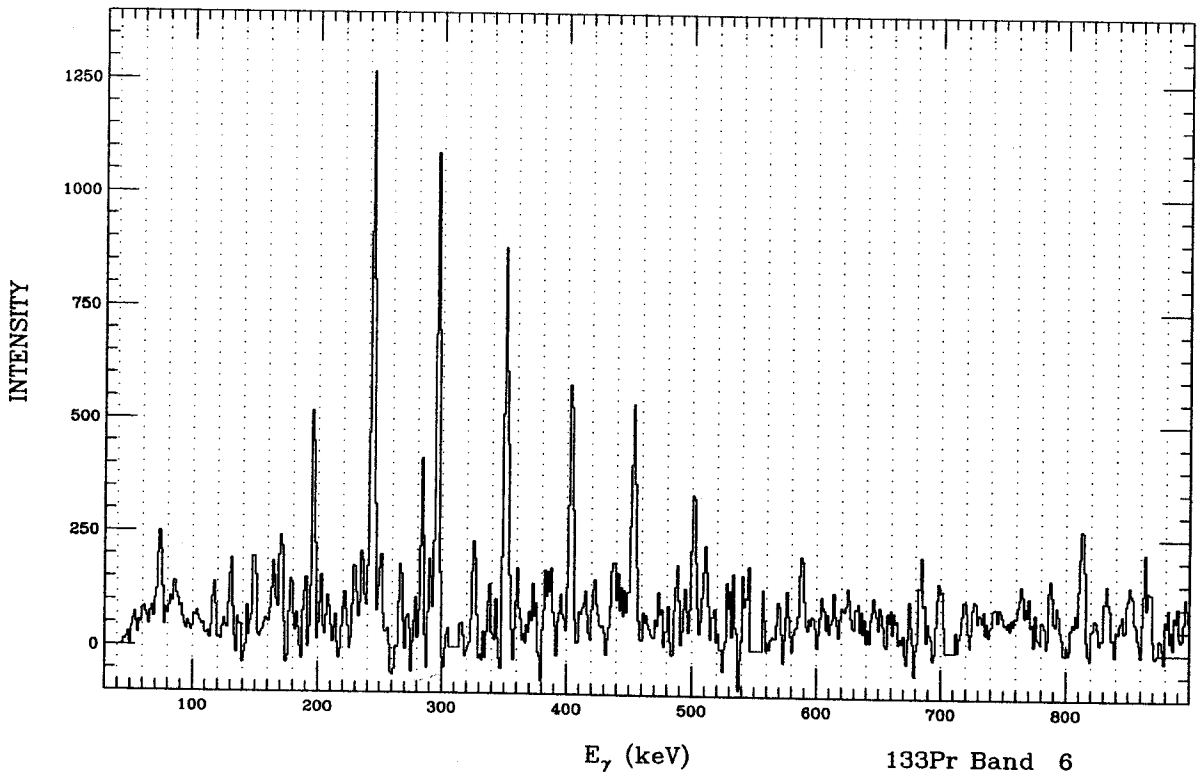

Figure F.119: Sum of gates at 197, 244, 296, 351, 404, 454, 501, 587 keV. for band 6 in ^{133}Pr, Multiple gate.

F.4 TAC Spectra ^{133}Pr

γ-γ-t (TAC) spectra were made for a few energies from the Energy versus Time arrays. By plotting the *log* of the TAC profile for an individual energy peak, the slope of the trailing edge of the prompt peak should yield a half-life value for the transition. The TAC profiles were obtained by summing the TAC counts across an energy peak. Many of the energy peaks contain a mixture of γ rays, therefore, their TAC peaks contain a mixture of activities. TAC profiles for transitions in ^{133}Pr are presented in this Appendix. Tables 5.11 and 5.12 list their probable half lives.

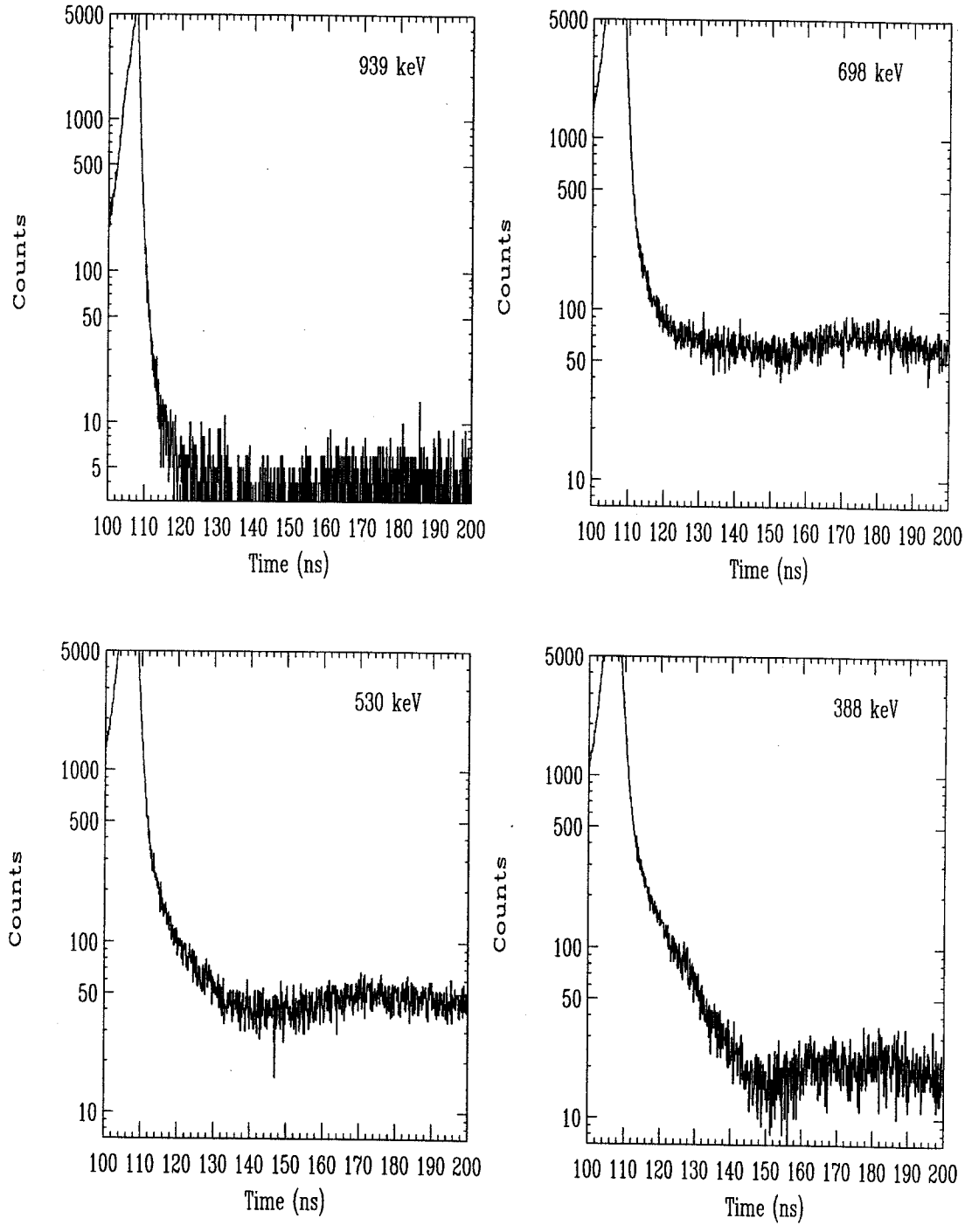

Figure F.120: Energy gated TAC spectra for 388, 530, 698, 939 keV.

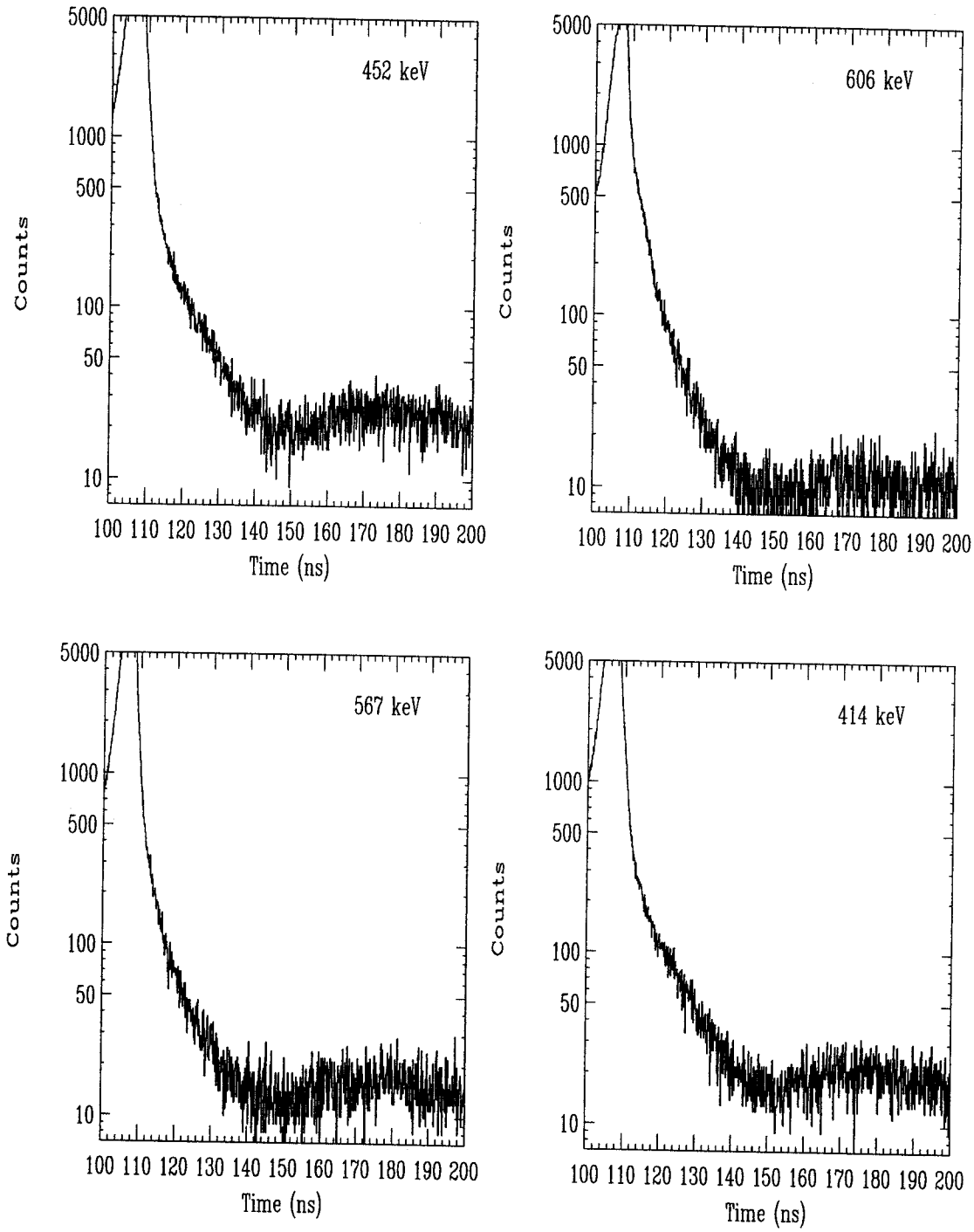

Figure F.121: Energy gated TAC spectra for 414, 567, 606, 452 keV.

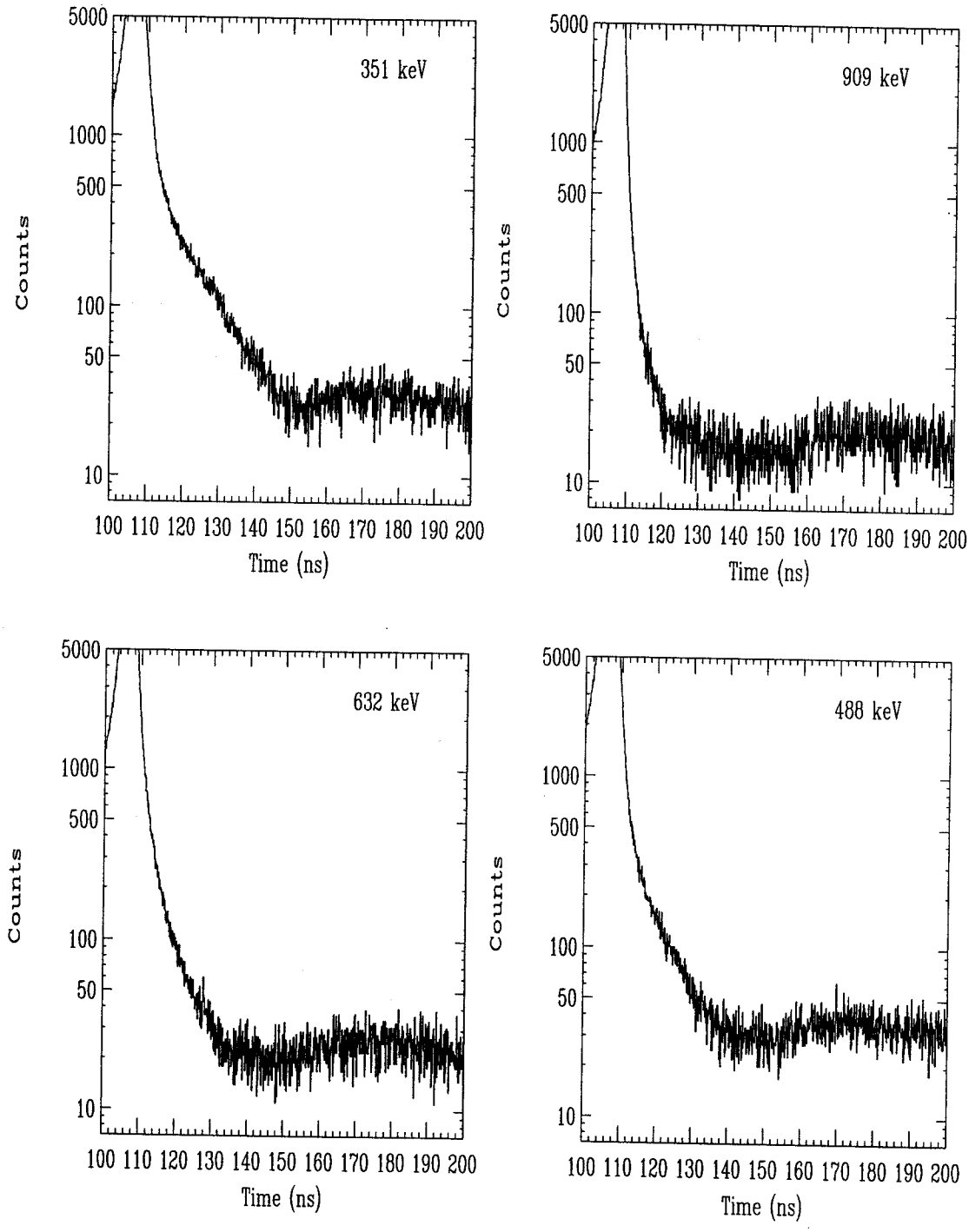

Figure F.122: Energy gated TAC spectra for 488, 632, 909, 351 keV.

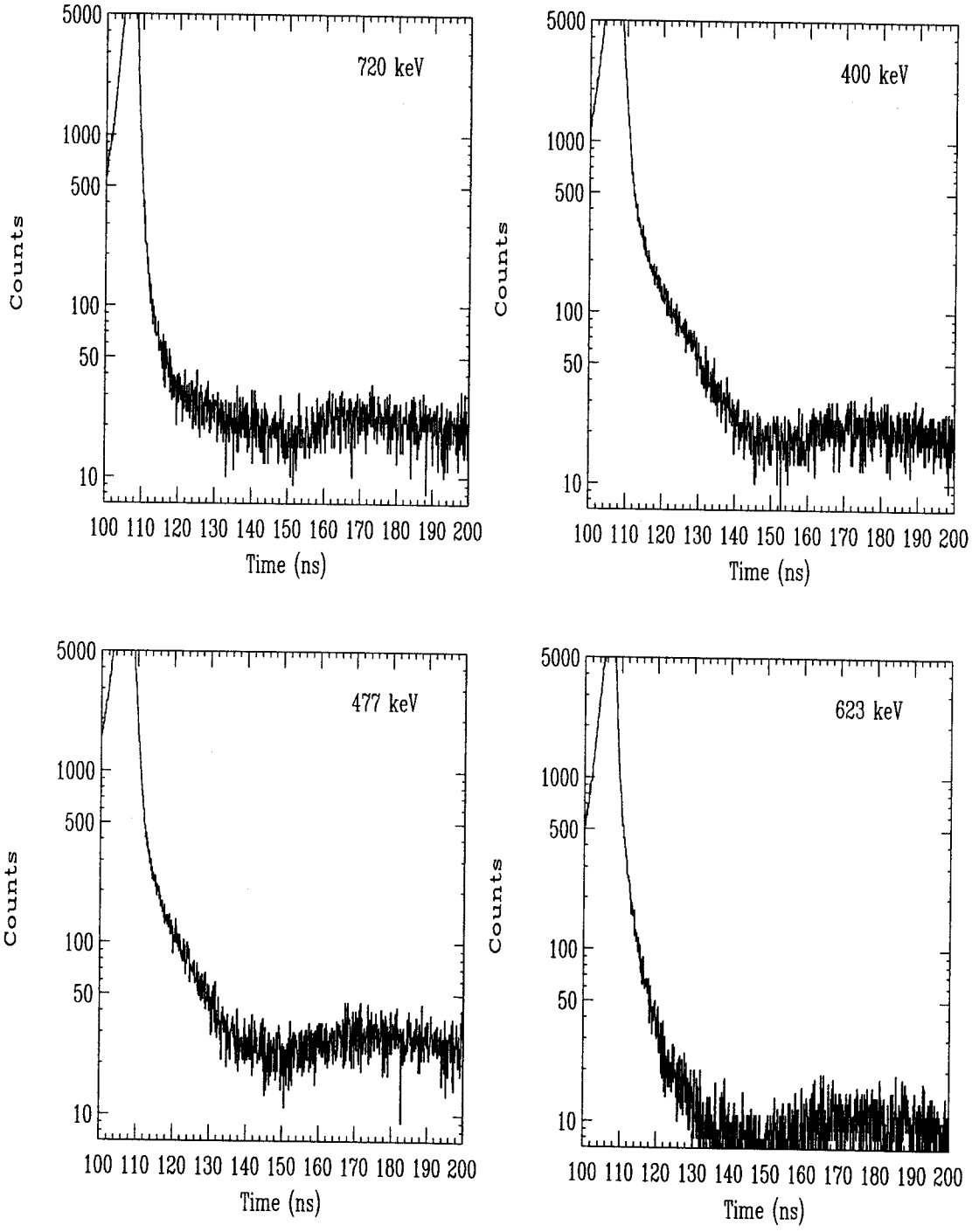

Figure F.123: Energy gated TAC spectra for 623, 477, 400, 720 keV.

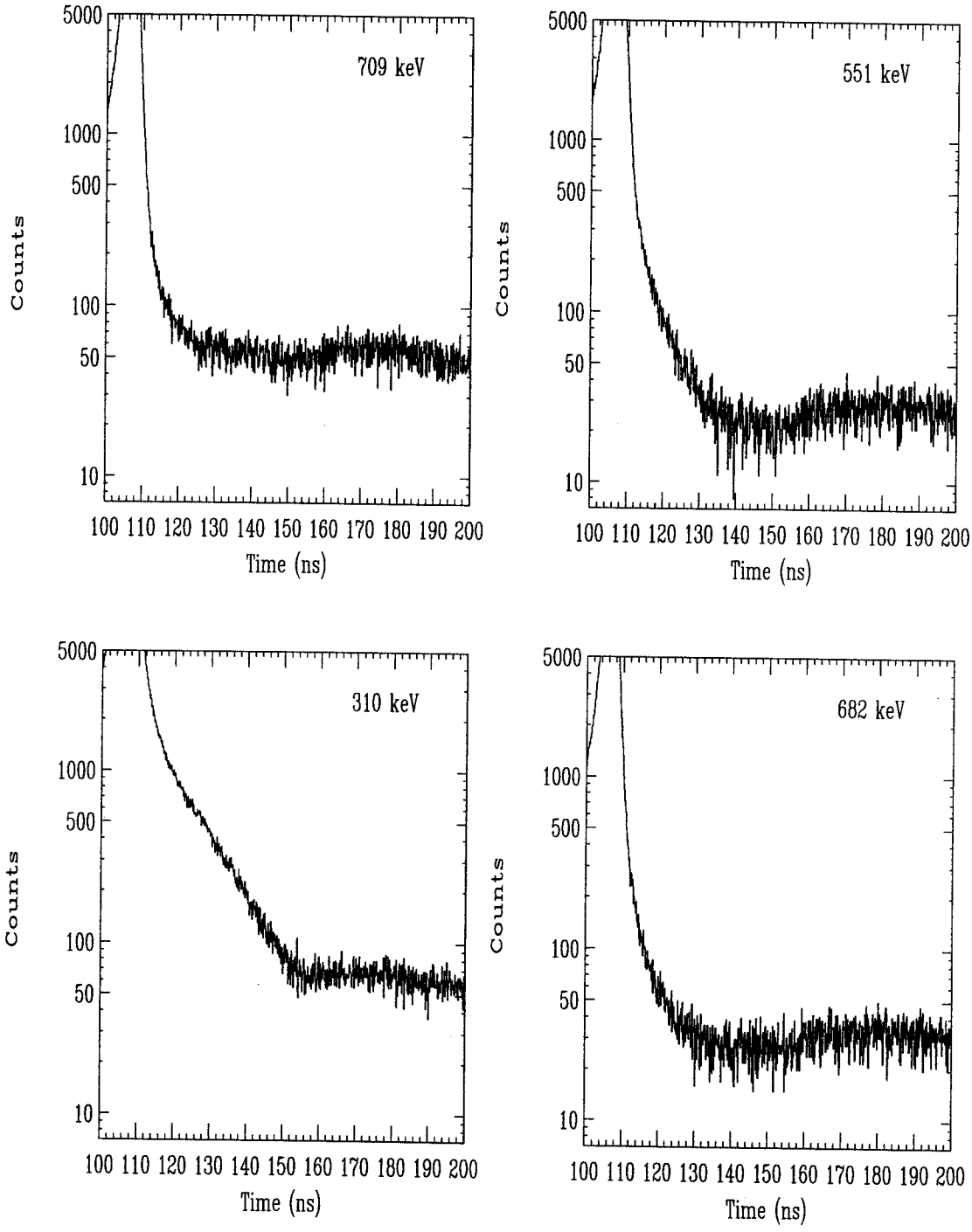

Figure F.124: Energy gated TAC spectra for 682, 310, 551, 709 keV.

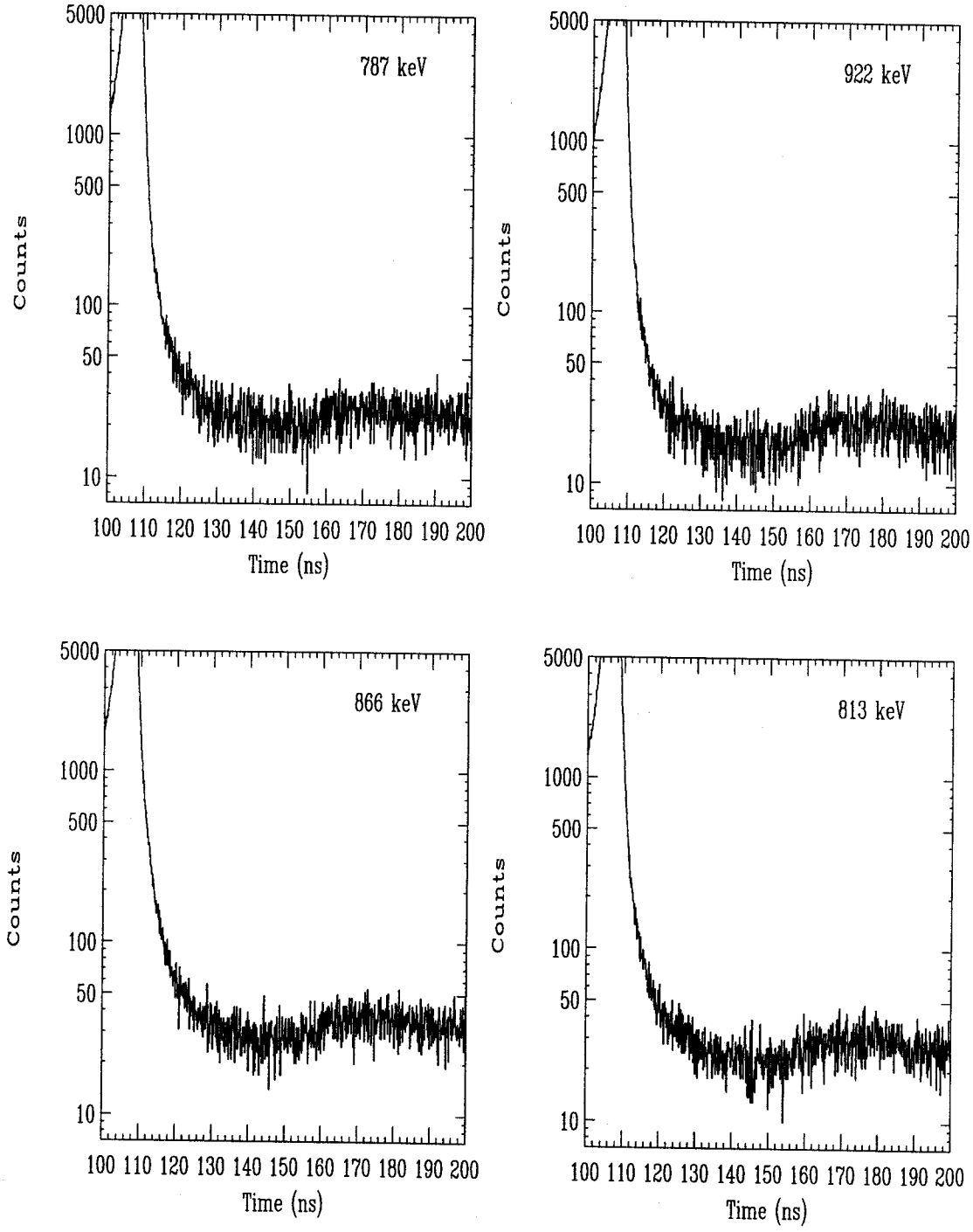

Figure F.125: Energy gated TAC spectra for 813, 866, 922, 787 keV.

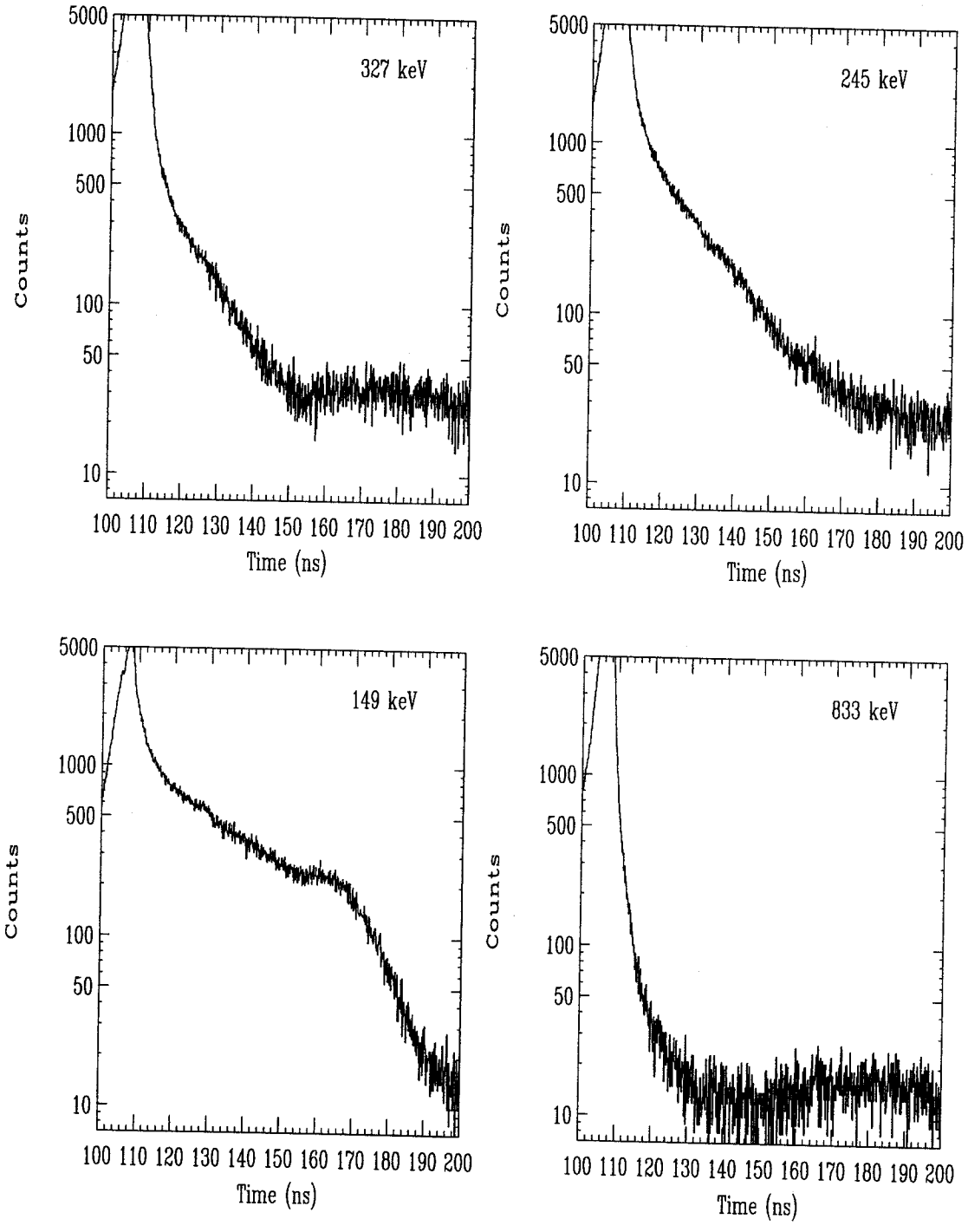

Figure F.126: Energy gated TAC spectra for 833, 149, 245, 327 keV.

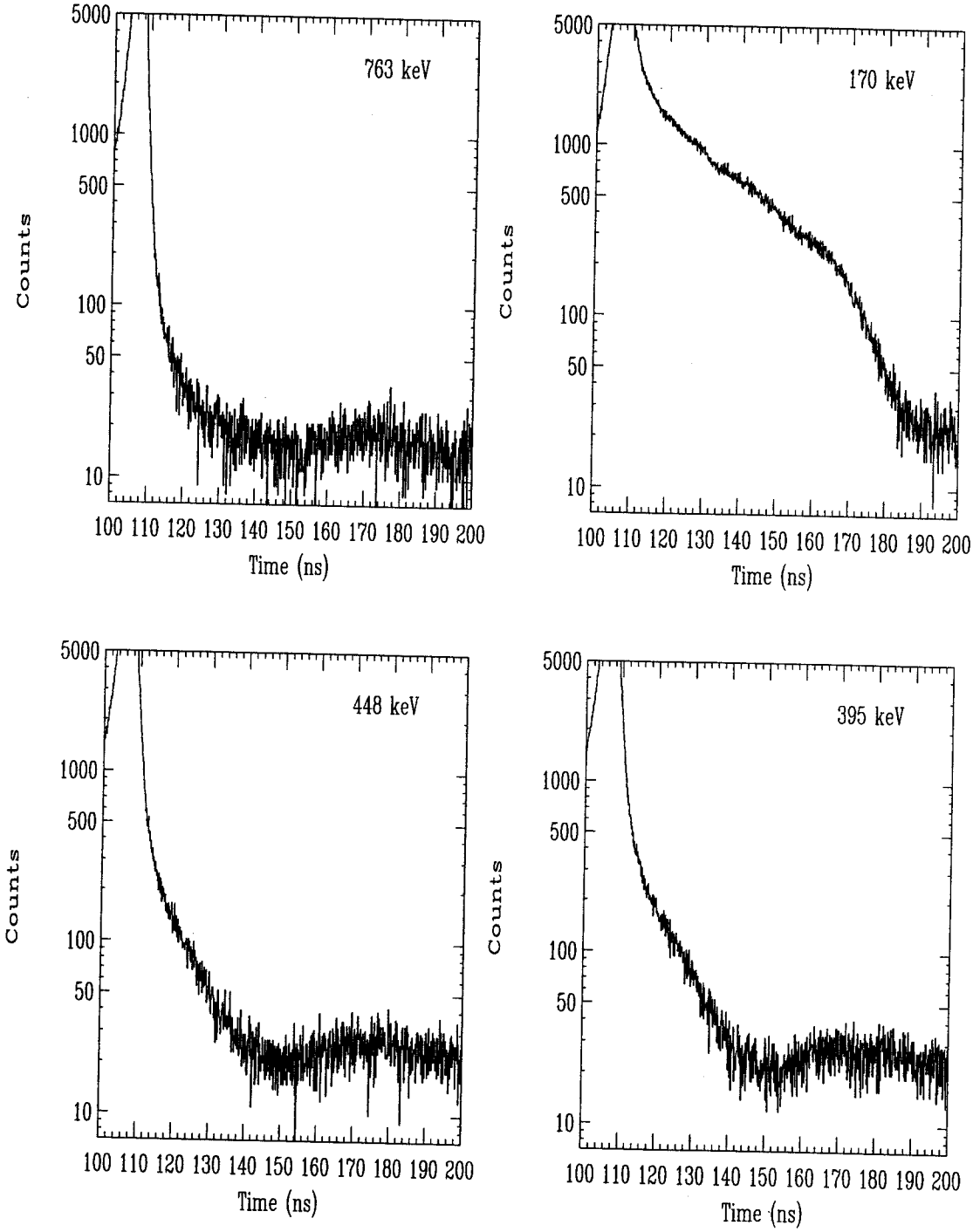

Figure F.127: Energy gated TAC spectra for 395, 448, 170, 763 keV.

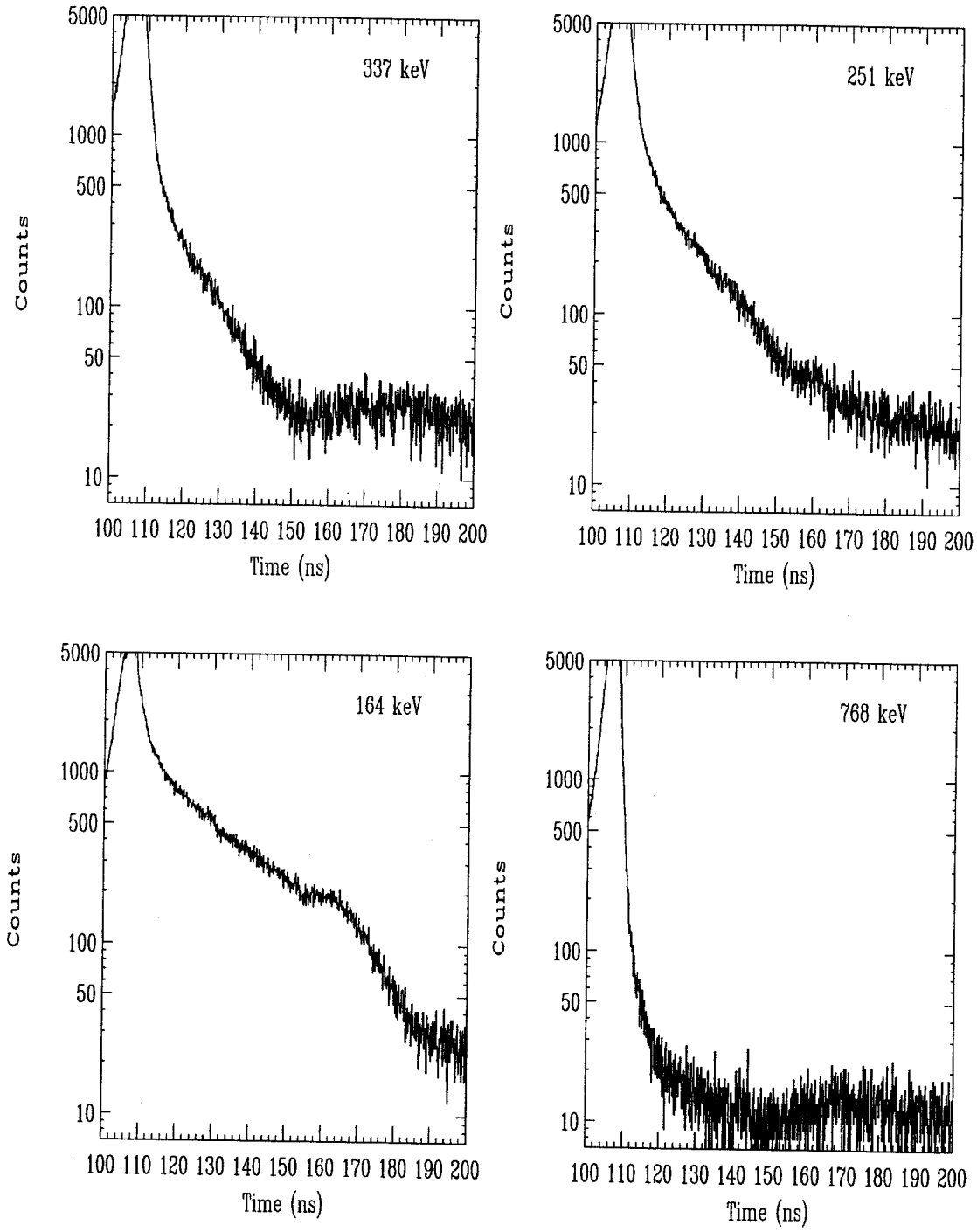

Figure F.128: Energy gated TAC spectra for 768, 164, 251, 337 keV.

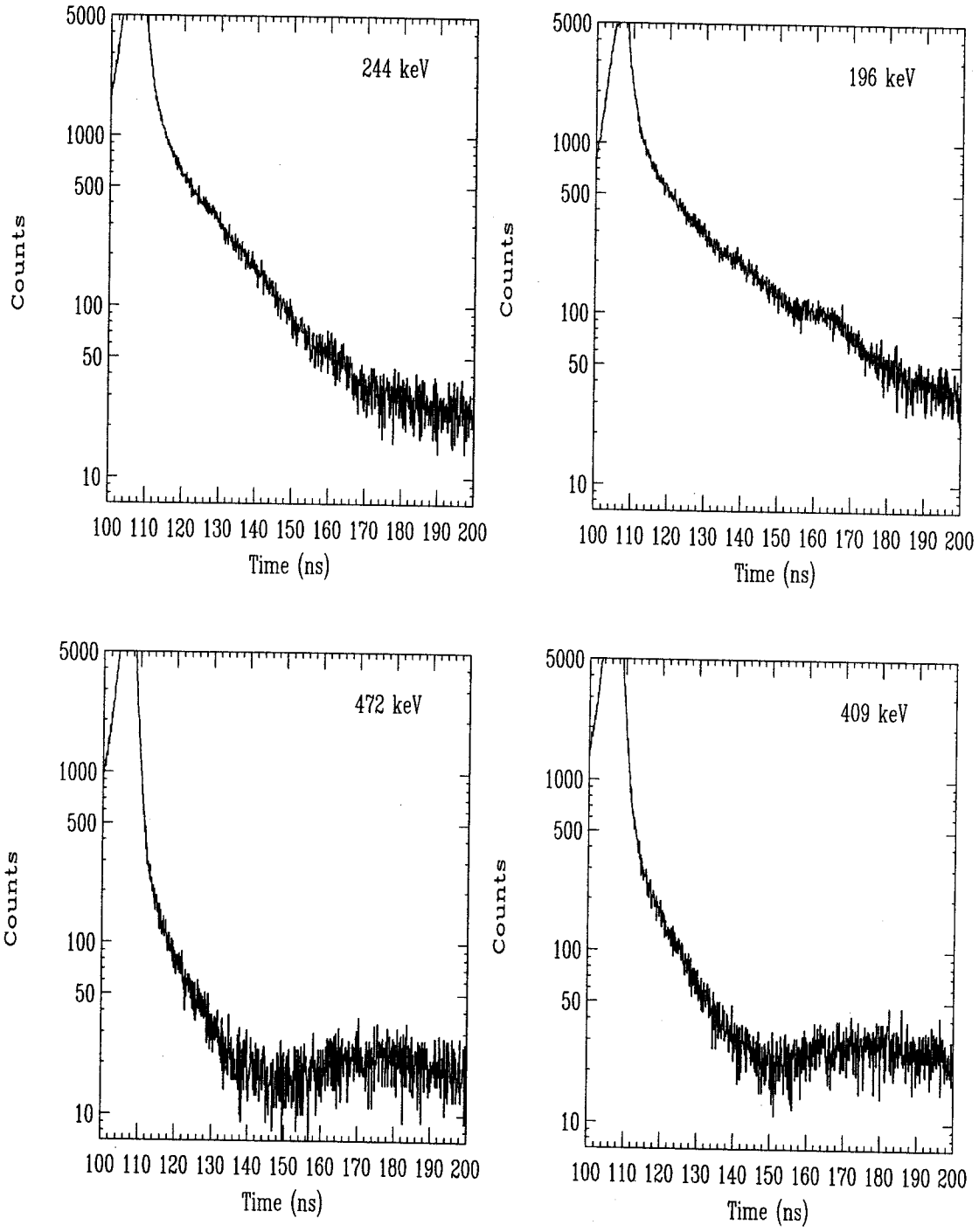

Figure F.129: Energy gated TAC spectra for 409, 472, 196, 244 keV.

Appendix G

Computer Routines

G.1 Usersubroutine Source Code

In order to convert the raw data events into gain and doppler-shifted events a user-subroutine was written in Fortran for the Oak Ridge software *LEMO*. *LEMO* processes one data stream into another data stream on tape. However it cannot be used for construction of data arrays. The usersubroutine is presented in this Appendix.

With a few logic unit changes, the same code can be used for the Oak Ridge software *SCAN* which processes a data stream into a 1-D or 2-D data array. For the sake of paper conservation, the *SCAN* usersubroutine was not duplicated here.

```
C       THIS PROGRAM EVTSCAN.FOR IS A SCAN ROUTINE TO BUILD
C       2-D SPECTRA, ENERGY VS. ENERGY. THE FOLLOWING LOGIC
C       UNITS ARE USED: LU0- TAC LIMITS
C                       1- GAIN SHIFT PARAMETERS
C                       2- RANDOM# SEEDS
C                       3- RANDOM#S
C                       4,5,6,10,14- USED BY SCAN
C                       7- .LOG FILE
C                       8- TAC SHIFT PARAMETERS
C        SEE ESCAN3.COM FOR OPEN COMMANDS
C       ------------------------------------------------------------
        SUBROUTINE USERCMP(IWD)
        INTEGER*4 IWD(20),LWD(2,40),ITYP(40),ISEED(1001)
        INTEGER*2 LLT,LHT,T(2)
        integer irndseed(1001),J,K
        REAL*4 E0G(100),E1G(100),E2G(100),E3G(100),E4G(100),E5G(100)
        REAL*4 TACN(100)
        EQUIVALENCE (KMD,LWD(1,1))
        COMMON/ABC/E0G,E1G,E2G,E3G,E4G,E5G,LLT,LHT,TACN
        COMMON/BCD/RN(4001)
        data J/97/
C       ------------------------------------------------------------
        CALL GREAD(IWD,LWD,ITYP,NF,1,80,NTER)
        IF(NTER.NE.0) GOTO 800
C
        IF(KMD.EQ.'SEED') GOTO 100
        IF(KMD.EQ.'RAND') GOTO 200
        IF(KMD.EQ.'SHFT') GOTO 300
        IF(KMD.EQ.'TACL') GOTO 400
        IF(KMD.EQ.'TACN') GOTO 500
C
        GOTO 800
C       ************************************************************
C       RANDOM NUMBER GENERATOR - initial seed
c       Seed generator function (VAX/VMS parallel Processing manual)---
c   --- This is extremely cpu intensive.-----
C       ************************************************************
 100    UNT=3
        READ(UNT,103) J
 103    FORMAT(I)
c
        call init_seeds(irndseed,1001,J)
c
        RETURN
c
C       ************************************************************
C       RANDOM NUMBER GENERATOR - kmd= RAND
C       ************************************************************
 200    DO 204 I=1,1001
        ISEED(I)=irndseed(I)
 204    continue
        K=ISEED(J+1)
        DO 209 I=1,4001
        RN(I)=RAN(K)
 209    CONTINUE
        NDV=7
        WRITE(NDV,240) J,K
 240    FORMAT(1X,'RANDOM NUMBERS',1X,'J=',I3,1X,'SEED=',I16)
        WRITE(NDV,250) (RN(I), I=1,10)
 250    FORMAT(5(F8.6,2X))
        RETURN
c
C       ************************************************************
C       GAIN & DOPPLER SHIFT PARAMETERS
C        E0G= OFFSET  E1G= SLOPE
C       ************************************************************
 300    NRD=1
        READ(NRD,*) (E0G(I),E1G(I),E2G(I),E3G(I),E4G(I),E5G(I), I=1,39,2)
C        READ(NRD,302) (E0G(I),E1G(I),E2G(I),E3G(I),E4G(I),E5G(I), I=1,39,2)
C 302   FORMAT(2X,6(D,1X))
```

```
C
    5   CONTINUE
        NDV=7
        WRITE(NDV,305)
  305   FORMAT(6X,'E0G',5X,'E1G',5X,'E2G',5X,'E3G',5X,'E4G',5X,'E5G')
        WRITE(NDV,310) (E0G(I),E1G(I),E2G(I),E3G(I),E4G(I),E5G(I), I=1,39,2)
C 310  FORMAT(2X,F,1X,F,1X,F,1X,F,1X,F,1X,F)
  310   FORMAT(2X,6(D,1X))
C
        RETURN
C       ***************************************************************
C       SET TAC THRESHOLD LIMITS
C       ***************************************************************
  400   TLU=0
        READ(TLU,401) (T(L), L=1,2)
  401   FORMAT(I4)
        LLT=T(1)
        LHT=T(2)
        WRITE(7,402)  T(1), T(2)
  402   FORMAT(5X,'TAC LIMITS',1X,I4,1X,'TO',1X,I4)
        RETURN
C       ***************************************************************
C       TAC SHIFT PARAMETERS
C       ***************************************************************
  500   NDV=7
        LUT=8
        READ(LUT,502) (TACN(N), N=2,40,2)
  502   FORMAT(1X,F)
        WRITE(NDV,505)
  505   FORMAT(2X,'TAC SHIFT PARAMETERS')
        WRITE(NDV,506) (TACN(N), N=2,40,2)
  506   FORMAT(2X,F)
  800   RETURN
        END
C       ---------------------------------------------------------------
        BLOCK DATA
        REAL*4 E0G(100),E1G(100),E2G(100),E3G(100),E4G(100),E5G(100)
        REAL*4 TACN(100)
        INTEGER*2 LLT,LHT
        COMMON/ABC/E0G,E1G,E2G,E3G,E4G,E5G,LLT,LHT,TACN
        COMMON/BCD/RN(4001)
        END
C       ---------------------------------------------------------------
c --Canned seed generator function (VAX/VMS parallel Processing manual)---

          subroutine init_seeds (seeds, n, iseed)
          integer n, iseed, seeds(n)
          real*16 rspace
          real*16 magic, cur_seed
          integer mplr, addend
          parameter (mplr=69069, addend=1)
          ispace=(2.0D0**32-1)/n
          magic=rspace(ispace)
          seeds(1)=iseed
          cur_seed=iseed
          if(cur_seed.lt.0) cur_seed=cur_seed+2.0q0**32
          do i=2,n
            cur_seed= ((mplr-1)*cur_seed+addend)*magic+cur_seed
            cur_seed=mod(cur_seed,2.0q0**32)
            if (cur_seed.ge.2.0q0**31) then
             seeds(i)=cur_seed-2.0q0**32
            else
             seeds(i)=cur_seed
            endif
          enddo

          end

          function rspace(space)
          real*16 rspace
```

```
141           integer space
142           integer mplr, addend
143           parameter (mplr=69069, addend=1)
144           real*16 pown,sum,binom,mod_15
145           mod_15=2.0q0**32
146           do i=3,15
147             mod_15=mod_15*i
148           enddo
149           pown=1.0q0
150           sum=0.0q0
151           binom=1.0q0
152           do i=1,16
153             binom= mod(binom*(space-i+1)/i, mod_15)
154             sum=mod(sum+binom+pown, 2.0q0**32)
155             pown=mod(pown*(mplr-1), 2.0q0**32)
156           enddo
157           rspace=mod(sum*addend, 2.0q0**32)
158
159   c------ End of canned routine ---------------------------------
160           end
161
162
163   C       ------------------------------------------------------------
164           SUBROUTINE USERSUB1(IBUF)
165           INTEGER*2 IBUF(512),LLT,LHT
166           REAL*4 TACN(100),MBUF(512)
167           REAL*4 E0G(100),E1G(100),E2G(100),E3G(100),E4G(100),E5G(100)
168           REAL*4 AI,BI,CI,DI,SI
169           COMMON/ABC/E0G,E1G,E2G,E3G,E4G,E5G,LLT,LHT,TACN
170           COMMON/BCD/RN(4001)
171           DATA NR/1/
172   C       ------------------------------------------------------------
173   C
174           DO 900 I=1,39,2
175           IF (IBUF(I).EQ.-1) GOTO 900
176           IF (IBUF(I).EQ.0)  GOTO 3
177           IF(IBUF(I+1).LE.LLT .OR. IBUF(I+1).GT.LHT) GOTO 3
178           MBUF(I)=FLOATI(IBUF(I))
179           NR=NR+1
180           IF(NR.GE.4000) NR=1
181
182           AI= E2G(I)*(MBUF(I)**2)
183           BI= E3G(I)*(MBUF(I)**3)
184           CI= E4G(I)*(MBUF(I)**4)
185           DI= E5G(I)*(MBUF(I)**5)
186           SI= AI + BI + CI +DI + E0G(I)
187           IBUF(I)=ININT((E1G(I)*(MBUF(I)+RN(NR))+SI)*1.6)
188
189           IF(MBUF(I).LE.0) GOTO 3
190           MBUF(I+1)=FLOATI(IBUF(I+1))
191           NR=NR+1
192           IF(NR.GE.4000) NR=1
193           IBUF(I+1)=ININT(TACN(I+1)*(MBUF(I+1) + RN(NR)) )
194           IF(MBUF(I+1).LE.0) GOTO 3
195           GOTO 900
196       3   IBUF(I)=-1
197           IBUF(I+1)=-1
198     900   CONTINUE
199           RETURN
200           END
end
```

G.2 FFT/SNIP source code

This is the FFT source code written as a modification for the HHIRF user-software, *DAMS*. There were a few versions constructed in order to accomodate changes in the versions of *DAMS* and the VAX/VMS X-windows software. What is presented here, contains the necessary modifications to *DAMS* to create the FFT and SNIP spectral enhancement techniques from Chapter 6.

```
C THIS WORK  CONTAINS
C FAST FOURIER TRANSFORM ROUTINES THAT MAY BE LINKED TO THE LARGER
C PROGRAM -DAMS (OR DAMM) IF THE IMSL, INC. MATH LIBRARY IS PRESENT.
C
C   BEN LIAN & CHRISTINE V.HAMPTON AT NSCL -11/25/92 initial work
C   C.V. HAMPTON /93    -COMPRESSION OF ZERO POINTS
C   C.V. HAMPTON /93    -SNIP
C   C.V. HAMPTON 1/14/96 -SEGMENTED FFT
C   WADE A. OLIVIER 10/95 -GEN_SPEC SUBROUTINE TO GENERATE TEST SPECTRA
C
C  THIS HAS BEEN WRITTEN TO MATCH THE STRUCTURE OF THE SUBROUTINE MILDO
C  FOR USE IN THE OAK RIDGE ROUTINE, DAMS, CREATED BY WT MILNER AT HHIRF
C  DURING 07/17/89
C  THIS WORK DOES NOT CONTAIN THE MILDO PROGRAMS
C*********************************************************************
C
      SUBROUTINE DFFT(IDONE,IERR)
C
      INTEGER*4 KBUF(33024)
      INTEGER*4 LIST(78),NDX(4)
C
      COMMON/DML0/ IWD(20),LWD(2,40),ITYP(40),NF,NTER
C
      COMMON/DML1/ NAMFIL(20,20),KFIL(20),LUC(20),LIN,LCM,LCI
C
      COMMON/LLL/  MSSG(28),NAMPROG(2),LOGUT,LOGUP,LISFLG,MSGF
C
      COMMON/MD00/ XBUF(33024),IOFF(2,2),KRUN,NUID
C
      DIMENSION XGS(4)
      DIMENSION ADAT(16384),BDAT(16384)
C
      INTEGER*4 IDATF(16384),JDATF(16384),IHEDF(128),JHEDF(128)
      INTEGER*2 IDATH(16384),JDATH(16384),IHEDH(256),JHEDH(256)

      INTEGER NREG
C      PARAMETER (NREG=4095)

      REAL SEQ(16384),COEF(16384),YTMP(16384),YVAL(16384)
      REAL OFFS,OFFS2
      REAL SCA1,SCA2,WFFTR(8205),REB,MMX,  YT,  MP
        INTEGER NSCALE1,NSCALE2,ZS,CH(16384),ZP(16384)
        INTEGER NF1,NF2,NB1,NB2
        INTEGER NI,CN,CT,NCT
C
      EQUIVALENCE (IHEDF(1),XBUF(1)),(IHEDH(1),XBUF(1))
      EQUIVALENCE (IDATF(1),XBUF(129)),(ADAT(1),XBUF(129))
      EQUIVALENCE (IDATH(1),XBUF(8321))
      EQUIVALENCE (JHEDF(1),XBUF(16513)),(JHEDH(1),XBUF(16513))
      EQUIVALENCE (JDATF(1),XBUF(16641)),(BDAT(1),XBUF(16641))
      EQUIVALENCE (JDATH(1),XBUF(24833))
      EQUIVALENCE (IDI,IHEDF(1)),(IDJ,JHEDF(1))
      EQUIVALENCE (NCHI,IHEDF(12)),(NCHJ,JHEDF(12))
      EQUIVALENCE (KMD,LWD(1,1))
      EQUIVALENCE (LIST(1),LWD(1,2))
      EQUIVALENCE (KBUF(1),XBUF(1))

        EXTERNAL FFTRF,FFTRB,FFTRI,F2TRF,F2TRB
        EXTERNAL HEDZOT,MILV,HEDCOP,IVALUE,MESSLOG
C
      DATA NCALL,NUID/0,0/
C
C     ****************************************************************
C     XBUF STRUCTURE
C
C     --FULL-WORD--
C         1 -   128  -- IHED  -   128 FULL-WORDS
```

```
C       129 - 16512  -- IDATF - 16384 FULL-WDS
C      8321 - 16512  -- IDATH -  8192 FULL-WORDS
C     16513 - 16640  -- JHED  -   128 FULL-WORDS
C     16641 - 32024  -- JDATA - 16384 FULL-WORDS
C     24833 - 32024  -- JDATH -  8192 FULL-WORDS
C     ****************************************************************
C
      IF(NCALL.NE.0) GO TO 20
      NCALL=1
C
      CALL HEDZOT(IHEDF)
      CALL HEDZOT(JHEDF)
C
      IOFF(1,1)=0              !FULL-WD OFFSET OF HEADER-1 IN XBUF
      IOFF(2,1)=128            !FULL-WD OFFSET OF DATA-1   IN XBUF
      IOFF(1,2)=16512          !FULL-WD OFFSET OF HEADER-2 IN XBUF
      IOFF(2,2)=16640          !FULL-WD OFFSET OF DATA-2   IN XBUF
C
      DO 10 I=1,4
      NDX(I)=1
      XGS(I)=0.0
   10 CONTINUE
C
   20 IERR=0
      IDONE='    '
C
C     ****************************************************************
C     PROCESS COMMAND
C     ****************************************************************
C
      IF(KMD.EQ.'FFT1') GO TO 444
      IF(KMD.EQ.'SNIP') GO TO 444
      IF(KMD.EQ.'PW  ') GO TO 492
      IF(KMD.EQ.'IPW ') GO TO 492
C      IF(KMD.EQ.'PLN ') GO TO 1652
      IF(KMD.EQ.'FFL ') GO TO 1930
      IF(KMD.EQ.'EFF ') GO TO 1930
      IF(KMD.EQ.'FBL ') GO TO 1940
      IF(KMD.EQ.'SNL ') GO TO 1960
      IF(KMD.EQ.'LLSI') GO TO 1970
      IF(KMD.EQ.'FLGI') GO TO 1971
      IF(KMD.EQ.'FLNI') GO TO 1972
      IF(KMD.EQ.'FSRI') GO TO 1973
      IF(KMD.EQ.'FPRI') GO TO 1974
      IF(KMD.EQ.'FSRO') GO TO 1975
      IF(KMD.EQ.'FLGO') GO TO 1976
      IF(KMD.EQ.'FEXO') GO TO 1977
      IF(KMD.EQ.'FPRO') GO TO 1978
      IF(KMD.EQ.'LLSO') GO TO 1979

C
      RETURN
C
C FFT PROGRAM
C     INITIALIZE TEMPORARY BUFFERS
444     DO 442 I=1,16384
        SEQ(I)=0.0
        COEF(I)=0.0
C       WFFTR(I)=0.0
        CH(I)=0
        ZP(I)=0
442     CONTINUE
        DO 445 I=1,16384
        YVAL(I)= 0.0
        YTMP(I)= 0.0
445     CONTINUE

C     ----------------------------------------------------------------
C     THIS IS THE ZERO POINT SUPPRESSION PART- TO REMOVE Y=0 VALUES AND
C     MAKE A RECORD OF WHERE THE ZERO POINTS ARE.
```

```
142
143           ZS=NF1
144           DO 447 N=NF1,NF2
145           IF (ADAT(N).EQ.0) GO TO 446
146                   ZP(N)=1
147                   YVAL(ZS)= ADAT(N)
148                   IF(KMD.EQ.'EFF ') YTMP(ZS)=BDAT(N)
149                   CH(ZS)= N
150                   ZS= ZS +1
151                   GO TO 447
152  446      ZP(N)=N
153  447      CONTINUE
154           IF(KMD.EQ.'EFF ') GO TO 1980
155  C     ------------------------------------------------------------------
156  C     FIND THE MINIMUM Y-VALUE, FOR THE OFFSET1, OFFS
157  C     ------------------------------------------------------------------
158           OFFS=0.0
159           MMX=0.0
160           DO 448 N=NF1,ZS
161           OFFS= AMIN1(YVAL(N),YVAL(N+1),OFFS)
162           MMX= AMAX1(YVAL(N),YVAL(N+1),MMX)
163  448      CONTINUE
164
165  C     ------------------------------------------------------------------
166  C     RESCALE THE Y-AXIS VALUE SO THAT NO VALUE IS BELOW 0.0, USE A MATH
167  C     OPERATOR ON THE RESULT AND NUMBER THEM SEQUENTIALLY FROM 1.0, FOR
168  C     THE FFT PROGRAM.
169  C     ------------------------------------------------------------------
170           IF (KMD.EQ.'SNIP') THEN
171                   NSCALE1=5
172  C                IF (MMX.LE.300) NB2=500
173           END IF
174
175           IF (NSCALE1.EQ.5) THEN
176                   DO 450 I=NF1,ZS
177                   SEQ(I-NF1+1)=LOG(LOG(SQRT(YVAL(I)-OFFS+1)+1)+1)
178  450              CONTINUE
179           ELSE IF (NSCALE1.EQ.2) THEN
180                   DO 451 I=NF1,ZS
181                   SEQ(I-NF1+1)=LOG(YVAL(I)-OFFS+1)
182  451              CONTINUE
183           ELSE IF (NSCALE1.EQ.3) THEN
184                   DO 452 I=NF1,ZS
185                   SEQ(I-NF1+1)=LOG10(YVAL(I)-OFFS+1)
186  452              CONTINUE
187           ELSE IF (NSCALE1.EQ.4) THEN
188                   DO 453 I=NF1,ZS
189                   SEQ(I-NF1+1)=SQRT(YVAL(I)-OFFS+1)
190  453              CONTINUE
191           ELSE
192                   DO 454 I=NF1,ZS
193                   SEQ(I-NF1+1)=YVAL(I)-OFFS+1
194  454              CONTINUE
195           END IF
196
197  C     ------------------------------------------------------------------
198  C     NREG, THE NUMBER OF CHANNEL NUMBERS TO BE TRANSFORMED, MUST BE
199  C     THE PRODUCT OF SMALL PRIME NUMBERS. EX.,1470=2*5*3*7*7.
200  C     NB. NREG MUST BE SET IMMEDIATELY PRIOR TO CALL FFTRF-- CANNOT
201  C     BE SET IN A KMD VARIABLE.
202  C     ------------------------------------------------------------------
203  C     DO THE FORWARD TRANSFORM
204
205           IF ((NF2-NF1).LE.1500) THEN
206                           NREG=1450
207           ELSE
208                           NREG=2840
209           END IF
```

```
211           CALL FFTRI(NREG,WFFTR)
212           CALL F2TRF(NREG,SEQ,COEF,WFFTR)
213
214 C       ADJUST THE RANGE FOR THE REVERSE TRANSFORM
215 C       ------------------------------------------------------------------
216           DO 222 I=1,NB1-NF1-1
217           COEF(I)=0.0
218 222       CONTINUE
219
220           DO 333 I=NB2-NF1+1,ZS-NF1
221           COEF(I)=0.0
222 333       CONTINUE
223 C       ------------------------------------------------------------------
224 C       DO THE REVERSE TRANSFORM
225           CALL F2TRB(NREG,COEF,SEQ,WFFTR)
226
227 C       ------------------------------------------------------------------
228 C       FIND THE OFFSET TO REBASELINE THE RESULT
229 C       ------------------------------------------------------------------
230           OFFS2= 0.0
231           DO 337 I=NF1,ZS
232           OFFS2= AMIN1(SEQ(I-NF1+1),SEQ(I-NF1+2),OFFS2)
233 337       CONTINUE
234           DO 338 I=NF1,ZS
235           YTMP(I-NF1+1)= SEQ(I-NF1+1)-OFFS2
236 338       CONTINUE
237
238 C       ------------------------------------------------------------------
239 C       THIS PART IS EQUIVALENT TO THE SNIP ROUTINE TO GENERATE A BASELINE
240 C       SPECTRUM. SEE NIM B34(1988)396 BY C.G.RYAN ET AL.
241 C       ------------------------------------------------------------------
242           NCT=1
243 C         IF (MMX.LE.500) NCT=3
244           IF (KMD.EQ.'SNIP') THEN
245           CT=0
246 345       PWID=1
247           DO 340 K=1,9
248           DO 339 I=NF1+PWID,ZS-PWID
249           L=I-NF1+1
250           IF (K.EQ.7) PWID=1
251           YTMP(L)=AMIN1(YTMP(L),(YTMP(L-PWID)+YTMP(L+PWID))/2)
252           IF(MMX.GE.500) GO TO 339
253           IF (PWID.GE.3) GO TO 346
254           YTMP(L)=AMax1(YTMP(L),(YTMP(L-PWID)+YTMP(L+PWID))/2)
255 346       IF(K.EQ.8) THEN
256           PWID=1
257           YTMP(L)=AMIN1(YTMP(L),(YTMP(L-PWID)+YTMP(L+PWID))/2)
258           END IF
259 339       CONTINUE
260           pwid=pwid+1
261 340       CONTINUE
262           IF(CT.EQ.NCT) GO TO 344
263           CT=CT+1
264           GO TO 345
265 344       CONTINUE
266 349       NSCALE2= 5
267
268           END IF
269 C     ------------------------------------------------------------------
270
271           DO 343 I=1,16384
272           YVAL(I)=0.0
273 343       CONTINUE
274 CC      ------------------------------------------------------------------
275 CC      USE AN INVERSE MATH OPERATOR ON THE RESULT
276 CC      ------------------------------------------------------------------
277           IF (NSCALE2.EQ.2) THEN
278                 DO 455 I=NF1,ZS
279                 YVAL(I)=((YTMP(I-NF1+1)/1443)**2)*0.1
280 455             CONTINUE
```

```
281           ELSE IF (NSCALE2.EQ.3) THEN
282                   DO 456 I=NF1,ZS
283                   YVAL(I)=(10**(YTMP(I-NF1+1)/1443))*0.1
284  456             CONTINUE
285           ELSE IF (NSCALE2.EQ.4) THEN
286                   DO 457 I=NF1,ZS
287                   YVAL(I)=(EXP(YTMP(I-NF1+1)/1443))*0.1
288  457             CONTINUE
289           ELSE IF (NSCALE2.EQ.5) THEN
290                   SCA1=0.000693147
291                   SCA2=0.1353352832
292                   DO 458 I=NF1,ZS
293                   YVAL(I)=SCA2 *EXP(2* EXP(YTMP(I-NF1+1)*SCA1))
294  458             CONTINUE
295           ELSE IF (NSCALE2.EQ.1)THEN
296                   DO 459 I=NF1,ZS
297                   YVAL(I)=(YTMP(I-NF1+1))/1443
298  459             CONTINUE
299           END IF
300  C     ---------------------------------------------------------------
301  C     REBASELINE AND REPLACE THE ZERO POINTS
302  C     ---------------------------------------------------------------
303           REB=0.01
304           DO 466 I=NF1,ZS
305           IF (REB.LE.1.0) GO TO 466
306           REB=AMIN1(YVAL(I),YVAL(I+1),REB)
307  466      CONTINUE
308  C THIS PROB. SHOULD BE: I= NF1,ZS
309  C        DO 467 I=NFI,ZS
310           DO 467 I=NF1,ZS
311           YVAL(I)=YVAL(I)-REB
312  467      CONTINUE
313
314  C THIS IS AN ATTEMPT TO ENCODE CHANNEL# 10 WITH A CODE FOR SNIP
315           DO 460 I= 1,16384
316           ADAT(I)=0.0
317           IF(I.EQ.10) THEN
318           IF(KMD.EQ.'SNIP') THEN
319           IF(MMX.LE.500) ADAT(10)=10.0
320           END IF
321           END IF
322  460      CONTINUE
323
324  461      CN=0
325           ADAT(29)= 0.0
326           DO 465 I=NF1,NF2
327           NI= I
328           IF(ZP(I).EQ.NI) GO TO 464
329           IF(KMD.EQ.'EFF ') OFFS=0.0
330           ADAT(I)=YVAL(I-CN)-OFFS
331           GO TO 465
332  464      ADAT(I)=0.0
333           CN=CN+1
334  465      CONTINUE
335
336         CALL HEDCOP(IHEDF,IHEDF)
337         GO TO 2500
338
339  C  ***************************************************************
340  C  RAISE THE DATA IN ADAT TO A POWER
341  C
342    492 CALL MILV(LIST,IDUM,PWR,KIND,IERR)
343         IF(IERR.NE.0) GO TO 2000
344         IF(KMD.EQ.'IPW ') GO TO 495
345         NDO=NCHI
346         DO 493 I=1,NDO
347         ADAT(I)=ADAT(I)**PWR
348    493 CONTINUE
349         CALL HEDCOP(IHEDF,IHEDF)
```

```
C
  495 NDO=NCHI
      DO 496 I=1,NDO
      ADAT(I)=ADAT(I)**(1/PWR)
  496 CONTINUE
      CALL HEDCOP(IHEDF,IHEDF)
      GO TO 2500


 1930  CALL IVALU (LIST(1),NF1,IERR)
      IF(IERR.NE.0) GO TO 2000
      CALL IVALU (LIST(3),NF2,IERR)
      IF(IERR.NE.0) GO TO 2000
        IF(KMD.EQ.'EFF ') GO TO 444
        GO TO 2500
 1940  CALL IVALU (LIST(1),NB1,IERR)
      IF(IERR.NE.0) GO TO 2000
      CALL IVALU(LIST(3),NB2,IERR)
      IF(IERR.NE.0) GO TO 2000
        GO TO 2500
 1960   CALL MILV(LIST,IDUM,NCT,KIND,IERR)
        IF(IERR.NE.0) GO TO 2000
        GO TO 2500
 1970   NSCALE1=5
        GO TO 2500
 1971   NSCALE1=2
        GO TO 2500
 1972   NSCALE1=3
        GO TO 2500
 1973   NSCALE1=4
        GO TO 2500
 1974   NSCALE1=1
        GO TO 2500
 1975   NSCALE2=2
        GO TO 2500
 1976   NSCALE2=3
        GO TO 2500
 1977   NSCALE2=4
        GO TO 2500
 1978   NSCALE2=1
        GO TO 2500
 1979   NSCALE2=5
        GO TO 2500
C ------------------------------------------------------------------------
C EFFICIENCY CALIBRATION ADJUSTMENT
C ------------------------------------------------------------------------
 1980   YT=0.0001
        DO 1983 I=NF1,ZS
        MP=YTMP(I)* YT
        IF(MP.LT.1.0E-8) MP=1.0E-8
        YVAL(I)=YVAL(I)/MP
 1983   CONTINUE
        GO TO 461
C ---------------------------------------------------------------
C
 2000 ENCODE(112,2010,MSSG)
      CALL MESSLOG(LOGUT,LOGUP)
 2010 FORMAT('ILLEGAL COMMAND OR SYNTAX ERROR')
C
 2500 IDONE='YES '
      RETURN
      END
end
```

G.3 Segmented-FFT code

This Appendix contains the programming for the Segmented-FFT search routine. The code is written in DCL for a VAX/VMS computer system. The second entry is the fortran software routine that calls the FFT software from IMSL, Inc.

```
$ set noverify
$ setup topdrawer
$ set default user_loan4:[hamptona.mo100.fft]
$! define yd user_loan4:[hamptona.mo100.fft]
$ define name 'P1'
$ as/us 'P1' 'name'
$ name:='P1'
$ define nma 'P2'
$ as/us 'P2' 'nma'
$ nma:='P2'
$ define nmb 'P3'
$ as/us 'P3' 'nmb'
$ nmb:='P3'
$! assign 'P1'.dat for020 ! input + (output file -summed spectrum)
$! assign 'P1'_ft.dat for040 ! fft output
$ assign/us 'P1'.list for030 ! list of back transform ch # ranges
$ assign/us 'P1'.lim for050  ! ymx y-limit from fft1000.for
$ assign/us 'P2'.dat for021  ! 1st data file -summed spectrum
$ assign/us 'P3'.dat for022  ! 2nd data file -summed spectrum
$ assign/us mltp.list for032 ! list of multiplication factors for spectrum 1
$ purge fft:fft_tmp.top
$ purge fft:fft_tmp.com
$ purge fft:add_seg.com
$ purge fft:mltp.list
$ purge *_ft.dat
$ purge fft:*.lim
$ purge 'P1'.list
$ purge *.dat
$! purge 'P1'add.dat
$!-------------------------------------------------
$! Initialize things
$!-------------------------------------------------
$ lst=0
$ lch=0
$ cut=0
$ cut2=0
$ c1=1
$ vmul=1
$ c2=1
$ l1=1
$ h1=1
$ stp=1
$ ymx=0
$ mcnt=0
$ addv=0
$ addv=F$INTEGER(addv)
$ seg=0
$ mcnt=F$INTEGER(mcnt)
$ ccnt=0
$ ccnt=F$INTEGER(ccnt)
$ scnt=0
$ scnt=F$INTEGER(scnt)
$ gcnt=0
$ gcnt=F$INTEGER(gcnt)
$ INQUIRE rng "Ch# range 1)70-1540 2)1300-2770 4)1200-2670 5)2625-4095 6)1-3000
  7)1-4095 8)Other"
$! If rng.EQ.8 then INQUIRE lo "Lo channel #"
$! If rng.EQ.8 then INQUIRE hi "High channel #"
$ INQUIRE freq "Forward transform only? y(1) n(2)"
$ If freq.EQ.2 then INQUIRE lst "External backtransform list? y(1)  n(2)"
$ if (freq.EQ.2).AND.(lst.EQ.1) then goto cont_ques
$ if freq.EQ.1 then goto cont_ques
$ If freq.EQ.2 then INQUIRE l1 "Beginning ch# for backtransform segment"
$ If freq.EQ.2 then INQUIRE h1 "End ch# for backtransform segment"
$ If freq.EQ.2 then INQUIRE stp "# of channels in step function "
$ If freq.EQ.2 then INQUIRE lch "Lo channel # constant(1). or variable(2)?"
$ cont_ques:
$ IF (freq.EQ.2).AND.(lst.EQ.1) then INQUIRE seg "Add Segments? y(1) n(2)"
$ If seg.EQ.1 then INQUIRE dis "Display Sum of segments only? y(1) n(2)"
$ IF (lst.EQ.1).AND.(seg.EQ.1) then INQUIRE lnam "Name of external list?"
```

```
$ IF (lst.EQ.1).AND.(seg.EQ.1) then INQUIRE gcnt "Number of segments in list?"
$ IF (lst.EQ.1).AND.(seg.EQ.1) then INQUIRE addv "Add valley segments to the sum
? y(1) n(2)"
$ If addv.EQ.1 then Inquire vnam "Name of valley .dat file to add"
$ If addv.EQ.1 then Inquire vmul "Multiplier for valley .dat file"
$!
$ INQUIRE vop "View spectrum (1) or plot (2) or make .PS (3)"
$ INQUIRE cut "Any peaks to remove? y(1) n(2) "
$ If (cut.EQ.1) then INQUIRE xl1 " peak cut: lo ch# "
$ If (cut.EQ.1) then INQUIRE xl2 " peak cut: high ch# "
$ INQUIRE man "Manual(1) or automatic(2) Y-axis limits?
$ If man.EQ.1 then INQUIRE ylo "Y-axis lo limit"
$ If man.EQ.1 then INQUIRE yhi "Y-axis high limit"
$ INQUIRE sm "Are you adding two spectra before fft? y(1) n(2) "
$ file:='mfile'
$ open/write mfile mltp.list
$ If sm.NE.1 then write mfile " 1 "
$ If sm.NE.1 then goto end_mfile
$ make_mltp:
$ INQUIRE c1 "Multiplier on spectrum 1 "
$ write mfile c1
$ mcnt=mcnt+1
$ If c1.EQ. " "  then goto end_mfile
$ goto make_mltp
$ end_mfile:
$ close mfile
$ If sm.NE.1 then mcnt=2
$ mcnt=mcnt-1    ! remove blank due to carriage return
$ If sm.EQ.1 then INQUIRE c2 "Multiplier on spectrum 2 "
$ If sm.EQ.1 then INQUIRE cut2 "Any spectrum 2 peaks to remove? y(1) n(2) "
$ If (sm.EQ.1).AND.(cut2.EQ.1) then INQUIRE xl11 "2nd spectrum peak lo ch# "
$ If (sm.EQ.1).AND.(cut2.EQ.1) then INQUIRE xl12 "2nd spectrum peak high ch# "
$ If (cut.EQ.2) then xl1=0
$ If (cut.EQ.2) then xl2=0
$ If (cut2.EQ.2) then xl11=0
$ If (cut2.EQ.2) then xl12=0
$ If rng.EQ.1 then lo=70
$ If rng.EQ.1 then hi=1540
$ If rng.EQ.2 then lo=1300
$ If rng.EQ.2 then hi=2770
$ If rng.EQ.3 then lo=500
$ If rng.EQ.3 then hi=1970
$ If rng.EQ.4 then lo=1200
$ If rng.EQ.4 then hi=2670
$ If rng.EQ.5 then lo=2625
$ If rng.EQ.5 then hi=4095
$ If rng.EQ.6 then lo=1
$ If rng.EQ.6 then hi=3000
$ If rng.EQ.7 then lo=1
$ If rng.EQ.7 then hi=4095
$ l1=F$INTEGER(l1)     !recognize l1,h1,hi,stp,h2,cnt,ttl as integers
$ h1=F$INTEGER(h1)
$ hi=F$INTEGER(hi)
$ stp=F$INTEGER(stp)
$ h2=0                 !initialize variable
$ h2=F$INTEGER(h2)
$ cnt=0
$ cnt=F$INTEGER(cnt)
$ lo1=0
$ lo1=F$INTEGER(lo1)
$ ttl=0
$ ttl=F$INTEGER(ttl)
$ ttl=(h1 - l1)/ stp
$ sp= "  "             !define two spaces as a parameter
$! ---------------------------------------------------------------------
$! Create a file to contain a list of back transform ranges
$!---------------------------------------------------------------------
$ If lst.EQ.1 then goto mlist
$ file:='pfile'
$ open/write pfile 'P1'.list
```

```
$ If freq.EQ.1 then write pfile lo,sp,hi
$ If freq.EQ.1 then goto stop
$ If lch.EQ.1 then lo1=l1
$ list:
$ h2=l1 + stp
$ If lch.EQ.1 then write pfile  lo1,sp,h2
$ If lch.EQ.2 then write pfile  l1,sp,h2
$ l1=l1 + stp
$ if h2.EQ.h1 then goto stop
$ cnt=cnt+1
$ if cnt.GT.ttl then goto stop
$ goto list
$ stop:
$ close pfile
$! ---------------------------------------------------------------
$! Open the multiplication list and read c1.
$! Create a temporary file to run add_spec.for to add two spectra
$!---------------------------------------------------------------
$ mlist:
$ file:='mfile'
$ open/read mfile mltp.list
$ read_mltp:
$ read/end=end_multp mfile c1
$ If sm.EQ.2 then goto dofft
$ add:
$ acnt=0
$ purge add_spec.com
$ file:='afile'
$ open/write afile add_spec.com
$ write afile "$ Assign 'P1'.dat for020 " ! output file -summed spectrum
$ write afile "$ Assign 'P2'.dat for021"  ! 1st data file
$ write afile "$ Assign 'P3'.dat for022"  ! 2nd data file
$ write afile "$ RUN add_spec "
$ write afile  sp,lo,sp,hi
$ write afile  sp,xl1,sp,xl2
$ write afile  sp,xll1,sp,xll2
$ write afile  sp,c1,sp,c2
$ close afile
$ acnt=1
$ @add_spec 'P1' 'P2' 'P3'
$!---------------------------------------------------------------
$! This part opens the list and reads each backtransform range.
$! For every range, temporary .com and .top files are created to
$! run the fft and print the results.
$! ---------------------------------------------------------------
$ dofft:
$! ---------------------------------------------------------------
$! Create temporary .com file to run the fft routine
$! ---------------------------------------------------------------
$ scnt=0
$ IF seg.EQ.1 then open/read pfile 'lnam'.list
$ IF (freq.EQ.1).OR.(seg.EQ.2).OR.(lst.EQ.2) then open/read pfile 'P1'.list
$ read_input:
$ read/end=end_input pfile bktr
$ sp= "    "
$ file:='ffile'
$ open/write ffile fft_tmp.com
$ write ffile " $ assign 'P1'.dat for020 "
$ write ffile " $ assign 'P1'_ft.dat for040 "
$ write ffile " $ assign 'P1'.lim for050 "
$ If hi.EQ.1540 then  write ffile " $ RUN fft1000"
$ If hi.EQ.2770 then  write ffile " $ RUN fft2000"
$ If hi.EQ.2670 then  write ffile " $ RUN fft4000"
$ If hi.EQ.1970 then  write ffile " $ RUN fft3000"
$ If (hi.EQ.4095).AND.(lo.NE.1) then  write ffile " $ RUN fft5000"
$ If hi.EQ.3000 then  write ffile " $ RUN fft10000"
$ If (hi.EQ.4095).AND.(lo.EQ.1) then  write ffile " $ RUN fft15000"
$ write ffile  sp,freq          ! 1=forward transform only, 2=back transform
$ write ffile  sp,lo            ! beginning channel # forward transform
$ write ffile  sp,hi            ! end channel # forward transform
```

```
$ write ffile "    1          "   ! Y input operator
$ write ffile "    1          "   ! Y output operator
$ write ffile "    0          "   ! Y linear scale factor
$ write ffile    sp,bktr       ! back transform channel # range
$ close ffile
$ @fft_tmp 'P1'
$! ------------------------------------------------
$ If (seg.EQ.2).OR.(lst.EQ.2).OR.(freq.EQ.1) then goto s_cont
$ add_seg:
$ purge add_seg.com
$ IF (rng.EQ.1).AND.(scnt.EQ.0) then copy/lo fft:blank70_1540.dat 'P1'add.dat
$ IF (rng.EQ.2).AND.(scnt.EQ.0) then copy fft:blank1300_2770.dat 'P1'add.dat
$! IF (rng.EQ.4).AND.(scnt.EQ.0) then copy fft:blank1200_2670.dat 'P1'add.dat
$! IF (rng.EQ.5).AND.(scnt.EQ.0) then copy fft:blank2625_4095.dat 'P1'add.dat
$! IF (rng.EQ.6).AND.(scnt.EQ.0) then copy fft:blank1_3000.dat 'P1'add.dat
$ IF (rng.EQ.7).AND.(scnt.EQ.0) then copy fft:blank1_4095.dat 'P1'add.dat
$ add_s:
$ file:='sfile'
$ open/write sfile add_seg.com
$ write sfile "$ Assign 'P1'.dat for020 " ! output file -summed spectrum
$ write sfile "$ Assign 'P2'.dat for021"  ! 1st data file
$ write sfile "$ Assign 'P3'.dat for022"  ! 2nd data file
$ write sfile "$ RUN add_spec "
$ write sfile  sp,lo,sp,hi
$ write sfile  sp,"0",sp,"0"
$ write sfile  sp,"0",sp,"0"
$ scnt=scnt+1
$ If (sm.EQ.1).AND.(scnt.GT.gcnt) then write sfile  sp,vmul,sp,"1"
$ If (sm.EQ.1).AND.(scnt.LE.gcnt) then write sfile  sp,"1",sp,"1"
$ If sm.EQ.2 then write sfile  sp,"1",sp,"1"
$ close sfile
$ If (addv.EQ.1).AND.(scnt.GT.gcnt) then @add_seg 'P1'addv 'vnam' 'P1'add
$ If (addv.NE.1).OR.(scnt.LE.gcnt) then @add_seg 'P1'add 'P1'add 'P1'_ft
$!
$ s_cont:
$! Read 'P1'.lim for y-axis limits
$! ------------------------------------------------
$ cnt=0
$ file:='lfile'
$ open/read lfile 'P1'.lim
$ read_lim:
$ read/end=end_lim lfile ymx
$ cnt=cnt+1
$ if cnt.GE.2 then goto end_lim
$ goto read_lim
$ end_lim:
$ close lfile
$! ------------------------------------------------
$! Create temporary .top file to produce a hardcopy
$! ------------------------------------------------
$ top_file:
$ sp=" "
$ file:='tfile'
$ open/write tfile fft_tmp.top
$! If vop.EQ.1 then write tfile "set device retro "
$ If vop.EQ.2 then write tfile "set device postscript "
$ If vop.EQ.3 then write tfile "set device postscript "
$ write tfile "set font duplex   "
$ write tfile "set label size 1.2   "
$ write tfile "set texture solid   "
$ write tfile "set size 13 by 10  "
$ write tfile "set window x from 1.5 to 12.6 y from 2 to 9    "
$ write tfile "set limits x from ",lo," to ",hi,"
$ If man.EQ. 1 then write tfile "set limits y from ",ylo," to ",yhi,"
$ If freq.EQ.1 then write tfile "title 0.8 4.9 angle 90 size 1.8 'Magnitude' "
$ If freq.EQ.1 then write tfile "title 5.6 1.6 size 1.8 'Ch #(frequency) ' "
$ If freq.EQ.2 then write tfile "title 0.8 4.9 angle 90 size 1.8 'Counts' "
$ If freq.EQ.2 then write tfile "title 5.6 1.6 size 1.8 'Channel Number' "
$! If vop.EQ.1 then write tfile "title top size 1.8 ' ",name,"'"
$! If vop.EQ.2 then write tfile "title top size 1.8 ' ",name,"'"
```

```
$ If sm.EQ.1 then write tfile "title 8 1.6 size 1.5 '",c1,nma,"+",c2,nmb,"'"
$ If cut.EQ.1 then write tfile "title 8 1.2 size 1.5 '",xl1,sp,xl2,sp,nma,"cut'"
$ If cut2.EQ.1 then write tfile "title 8 .8 size 1.5 '",xll1,sp,xll2,sp,nmb,"cut
'"
$ If seg.EQ.1 then write tfile "title 1 1.2 size 1.5 'Add segments from ",lnam,"
.list'"
$ If (addv.EQ.1).AND.(scnt.GT.gcnt) then write tfile "title 1 .8 size 1.5 'Add v
alley from ",vnam,".dat'"
$ write tfile "title 8.5 9.2 size 1.5 'y maximum",sp,ymx,"'"
$ If freq.EQ.2 then write tfile "title top size 1.8 'reverse transform ",bktr,sp
,name,"_ft.dat'"
$ If freq.EQ.1 then write tfile "title top size 1.8 'Frequency Spectrum ",name,"
'"
$ write tfile "set order x y "
$! write name_ft.dat input file
$ If seg.NE.1 then write tfile "set file input",sp,"'",name,"_ft.dat'"
$! write nameadd.dat input file after summing each segment
$ If ((addv.NE.1).OR.(scnt.LE.gcnt)).AND.(lst.EQ.1) then write tfile "set file i
nput",sp,"'",name,"add.dat'"
$! write nameaddv.dat input file after valley peaks have been added
$ If (addv.EQ.1).AND.(scnt.GT.gcnt) then write tfile "set file input",sp,"'",nam
e,"addv.dat'"
$ write tfile "histogram "
$! If vop.EQ.1 then write tfile "pause "
$ close tfile
$! If the sum of segments is to be displayed only then jump to the next input.
$ If (dis.EQ.1).AND.(scnt.LT.gcnt) then goto read_input
$ topdrawer fft_tmp.top
$!
$ If (vop.EQ.2) then print/delete/que=west_print fft_tmp.ps
$ If (vop.EQ.3) then copy/lo fft_tmp.ps 'P1'.ps
$ If (vop.EQ.3) then delete/lo fft_tmp.ps;*
$ If (addv.EQ.1).AND.(scnt.GT.gcnt) then goto In_vop
$ goto read_input
$ end_input:
$ close pfile
$ ccnt=ccnt+1
$ If ccnt.EQ.mcnt then goto end_multp
$ goto read_mltp
$ end_multp:
$ close mfile
$!
$ In_vop:
$ Inquire vop2 "Print last frame? y(1) n(2)"
$ If vop2.EQ.1 then goto print_sum
$ Goto e_print
$ print_sum:
$ sp=" "
$ file:='hfile'
$ open/write hfile fft_tmp.top
$ write hfile "set device postscript "
$ write hfile "set font duplex   "
$ write hfile "set label size 1.2   "
$ write hfile "set texture solid   "
$ write hfile "set size 13 by 10  "
$ write hfile "set window x from 1.5 to 12.6 y from 2 to 9    "
$ write hfile "set limits x from ",lo," to ",hi,"
$ If man.EQ. 1 then write hfile "set limits y from ",ylo," to ",yhi,"
$ If freq.EQ.1 then write hfile "title 0.8 4.9 angle 90 size 1.8 'Magnitude' "
$ If freq.EQ.1 then write hfile "title 5.6 1.6 size 1.8 'Ch #(frequency) ' "
$ If freq.EQ.2 then write hfile "title 0.8 4.9 angle 90 size 1.8 'Counts' "
$ If freq.EQ.2 then write hfile "title 5.6 1.6 size 1.8 'Channel Number' "
$ If sm.EQ.1 then write hfile "title 8 1.6 size 1.5 '",c1,nma,"+",c2,nmb,"'"
$ If cut.EQ.1 then write hfile "title 8 1.2 size 1.5 '",xl1,sp,xl2,sp,nma,"cut'"
$ If cut2.EQ.1 then write hfile "title 8 .8 size 1.5 '",xll1,sp,xll2,sp,nmb,"cut
'"
$ If seg.EQ.1 then write hfile "title 1 1.2 size 1.5 'Add segments from ",lnam,"
.list'"
$ If (addv.EQ.1).AND.(scnt.GT.gcnt) then write hfile "title 1 .8 size 1.5 'Add v
alley from ",vnam,".dat'"
```

```
339 $ write hfile "title 8.5 9.2 size 1.5 'y maximum",sp,ymx,"'"
340 $ If freq.EQ.2 then write hfile "title top size 1.8 'reverse transform ",bktr,sp
    ,name,"_ft.dat'"
341 $ If freq.EQ.1 then write hfile "title top size 1.8 'Frequency Spectrum ",name,"
    '"
342 $ write hfile "set order x y "
343 $! write name_ft.dat input file
344 $ If seg.NE.1 then write hfile "set file input",sp,"'",name,"_ft.dat'"
345 $! write nameadd.dat input file after summing each segment
346 $! If (addv.NE.1).OR.(scnt.LE.gcnt) then write hfile "set file input",sp,"'",nam
    e,"add.dat'"
347 $ If ((addv.NE.1).OR.(scnt.LE.gcnt)).AND.(lst.EQ.1) then write hfile "set file i
    nput",sp,"'",name,"add.dat'"
348 $! If ((addv.NE.1).OR.(scnt.LE.gcnt).OR.(seg.EQ.1)).AND.(lst.EQ.1) then write hf
    ile "set file input",sp,"'",name,"add.dat'"
349 $!
350 $! write nameaddv.dat input file after valley peaks have been added
351 $ If (addv.EQ.1).AND.(scnt.GT.gcnt) then write hfile "set file input",sp,"'",nam
    e,"addv.dat'"
352 $ write hfile "histogram "
353 $ close hfile
354 $!
355 $ topdrawer fft_tmp.top
356 $ print/delete/que=west_print fft_tmp.ps
357 $ e_print:
358 $! if the last segment has been added and you want to add valleys
359 $! then goto add_s
360 $ If (addv.EQ.1).AND.(scnt.EQ.gcnt) then goto add_s
361 $ End:
362 $ exit
end
```

```
      INTEGER  N
      PARAMETER (N=4095)
C     PARAMETER (N=1470)
      INTEGER I,L1,L2,HI,LO,YOP,YAX,CH(1:4095),forw,ax
      REAL COEF1(1:4095),SEQ(1:4095),WFFTR(16410)
      REAL x1,y1,offs,SCY,ymax,MY1,MY2,OUT(1:4095)
c     EXTERNAL FFTRB,FFTRF,DF2TRF,DF2TRB,DFFTRI
      EXTERNAL F2TRF,F2TRB,FFTRI
      INTRINSIC AMAX1
C
C SELECT Y-AXIS OFFSET
      offs=10
C OPEN ORIGINAL DATA FILE --NOTE THIS HAS BEEN OPENED IN DCL--
C     open(unit=20,status='old')

C     PRINT*,' Forward transform only? y(1) n(2) "
      READ(5,*)forw
C     PRINT*,'**ENTER FIRST CHANNEL#**'
      READ(5,*)LO
C     PRINT*,'**ENTER LAST CHANNEL#**'
      READ(5,*)HI
C
C SELECT Y-AXIS OPERATOR
C     PRINT*,'** PLEASE TYPE THE NUMBER FOR THE DESIRED Y-AXIS OPERATOR:
C     PRINT*,'** LINEAR        1
C     PRINT*,'** LN            2
C     PRINT*,'** LOG10         3
C     PRINT*,'** SQUARE ROOT   4
      READ(5,*)YOP
      IF (YOP.EQ.1) GO TO 01
      IF (YOP.EQ.2) GO TO 02
      IF (YOP.EQ.3) GO TO 03
      IF (YOP.EQ.4) GO TO 04
      IF (YOP.LT.1 .OR. YOP.GT.4)  GO TO 01

C READ IN THE DATA
01    do 21 I=LO,HI
      read(20,*)x1,y1
      SEQ(I)=y1+offs
      CH(I)=x1
21    continue
      GO TO 25
02    do 22 I=LO,HI
      read(20,*)x1,y1
      SEQ(I)=LOG(y1+offs)
      CH(I)=x1
22    continue
      GO TO 25
03    do 23 I=LO,HI
      read(20,*)x1,y1
      SEQ(I)=LOG10(y1+offs)
      CH(I)=x1
23    continue
      GO TO 25
04    do 24 I=LO,HI
      read(20,*)x1,y1
      SEQ(I)=SQRT(y1+offs)
      CH(I)=x1
24    continue
      GO TO 25

C  SET THE FFT WORKSPACE ARRAY = TO LENGTH (2*N +15)
C25   CALL FFTRI (N,WFFTR)
C25   CLOSE(UNIT=20) --NOTE THIS HAS BEEN ACCESSED IN DCL---
C     CALL F2TRF (N,SEQ,COEF1,WFFTR)

C   FOR DOUBLE PRECISION, WORKSPACE 4*N+30
25    CALL DFFTRI (N,WFFTR)

C  DO THE FOURIER TRANSFORM
```

```
71          CALL DF2TRF (N,SEQ,COEF1,WFFTR)
72
73  C SELECT Y-AXIS OUTPUT DISPLAY
74  C       PRINT*,'****  PLEASE ENTER Y-AXIS OUTPUT DISPLAY:
75  C       PRINT*,'****  LINEAR 1
76  C       PRINT*,'****  SQRT   2
77  C       PRINT*,'****  SQUARE 3
78  C       PRINT*,'****  LOG    4
79  C       PRINT*,'****  EXP    5
80  C       PRINT*,'****  INV.LOG 6
81          READ(5,*)YAX
82
83
84  C SELECT Y-AXIS SCALE FACTOR FOR OUTPUT DISPLAY
85  C       PRINT*,'****  ENTER Y-AXIS SCALE FACTOR FOR DISPLAY
86          READ(5,*)SCY
87
88  C SELECT REGION WHICH WILL BE BACKWARD TRANSFORMED
89  C       print*,'****   Please enter the selected spectrum region:
90  C       print*,'       [min:30  max:1500]'
91          read(5,*)L1,L2
92
93          IF (YOP.EQ.1) GO TO 150
94          IF (YOP.EQ.2) GO TO 10
95          IF (YOP.EQ.3) GO TO 12
96          IF (YOP.EQ.4) GO TO 14
97          IF (YOP.LT.1 .OR. YOP.GT.4)  GO TO 150
98
99  10      DO 11 I=L1,L2
100         COEF1(I)=EXP(COEF1(I))
101 11      CONTINUE
102         GO TO 150
103 12      DO 13 I=L1,L2
104         COEF1(I)=10**(COEF1(I))
105 13      CONTINUE
106         GO TO 150
107 14      DO 15 I=L1,L2
108         COEF1(I)=(COEF1(I))**2
109 15      CONTINUE
110 C
111 150     DO 16 I=LO,L1
112         COEF1(I)=0.0
113 16      CONTINUE
114
115         DO 17 I=L2,HI
116         COEF1(I)=0.0
117 17      CONTINUE
118
119         If (forw.EQ.1) then
120          DO I=LO,HI
121           OUT(I)=COEF1(I)
122          ENDDO
123          IF (YAX.EQ.1) GO TO 881
124          IF (YAX.EQ.2) GO TO 882
125          IF (YAX.EQ.3) GO TO 883
126          IF (YAX.EQ.4) GO TO 884
127          IF (YAX.EQ.5) GO TO 885
128          IF (YAX.EQ.6) GO TO 886
129
130  881     ymax=0.0
131          do 81 I=LO,HI
132          MY1=(OUT(I)/100+SCY)
133          MY2=(OUT(I+1)/100+SCY)
134          ymax= AMAX1(MY1,MY2,ymax)
135   81     continue
136          WRITE(40,999)(CH(I),((OUT(I)/100)+SCY),I=LO,HI)
137          go to 1000
138  882     ymax=0.0
139          do 82 I=LO,HI
140          MY1=(SQRT(OUT(I))+SCY)
```

```
141           MY2=(SQRT(OUT(I+1))+SCY)
142           ymax=AMAX1(MY1,MY2,ymax)
143    82     continue
144           WRITE(40,999)(CH(I),(SQRT(OUT(I))+SCY),I=LO,HI)
145           go to 1000
146    883    ymax=0.0
147           ax=100000
148           do 83 I=LO,HI
149           MY1=( (OUT(I)+SCY)**2)/ax
150           MY2=( (OUT(I+1)+SCY)**2)/ax
151           ymax=AMAX1(MY1,MY2,ymax)
152    83     continue
153           WRITE(40,999)(CH(I),((OUT(I)+SCY)**2)/100000,I=LO,HI)
154           go to 1000
155    884    ymax=0.0
156           ax=10000
157           do 84 I=LO,HI
158           MY1=(LOG10(OUT(I))/ax)+SCY
159           MY2=(LOG10(OUT(I+1))/ax)+SCY
160           ymax=AMAX1(MY1,MY2,ymax)
161    84     continue
162           WRITE(40,999)(CH(I),((LOG10(OUT(I))/ax)+SCY),I=LO,HI)
163           go to 1000
164    885    ymax=0.0
165           do 85 I=LO,HI
166           MY1=(EXP(OUT(I))/1000)+SCY
167           MY2=(EXP(OUT(I+1))/1000)+SCY
168           ymax=AMAX1(MY1,MY2,ymax)
169    85     continue
170           WRITE(40,999)(CH(I),((EXP(OUT(I))/1000)+SCY),I=LO,HI)
171           go to 1000
172    886    ymax=0.0
173           do 86 I=LO,HI
174           MY1=(10**(OUT(I))/1000)+SCY
175           MY2=(10**(OUT(I+1))/1000)+SCY
176           ymax=AMAX1(MY1,MY2,ymax)
177    86     continue
178           WRITE(40,999)(CH(I),((10**(OUT(I))/1000)+SCY),I=LO,HI)
179           go to 1000
180          END IF
181
182
183  C  DO THE BACKWARD TRANSFORM
184           CALL DF2TRB (N,COEF1,SEQ,WFFTR)
185
186  C  RESCALE AND WRITE TO OUTPUT
187           IF (YAX.EQ.1) GO TO 991
188           IF (YAX.EQ.2) GO TO 992
189           IF (YAX.EQ.3) GO TO 993
190           IF (YAX.EQ.4) GO TO 994
191           IF (YAX.EQ.5) GO TO 995
192           IF (YAX.EQ.6) GO TO 996
193
194    991    ymax=0.0
195           do 91 I=LO,HI
196           ymax=AMAX1((SEQ(I)/1000+SCY),(SEQ(I+1)/1000+SCY),ymax)
197    91     continue
198           WRITE(40,999)(CH(I),((SEQ(I)/1000)+SCY),I=LO,HI)
199           go to 1000
200    992    ymax=0.0
201           do 92 I=LO,HI
202           ymax=AMAX1((SQRT(SEQ(I))+SCY),(SQRT(SEQ(I+1))+SCY),ymax)
203    92     continue
204           WRITE(40,999)(CH(I),(SQRT(SEQ(I))+SCY),I=LO,HI)
205           go to 1000
206    993    ymax=0.0
207           ax=100000
208           do 93 I=LO,HI
209           ymax=AMAX1( ((SEQ(I)+SCY)**2)/ax,((SEQ(I+1)+SCY)**2)/ax,ymax)
210    93     continue
```

```
211           WRITE(40,999)(CH(I),((SEQ(I)+SCY)**2)/100000,I=LO,HI)
212           go to 1000
213    994    ymax=0.0
214           ax=1000
215           do 94 I=LO,HI
216           ymax=AMAX1( ((LOG10(SEQ(I))/ax)+SCY),((LOG10(SEQ(I+1))/ax)+SCY),ymax)
217     94    continue
218           WRITE(40,999)(CH(I),((LOG10(SEQ(I))/1000)+SCY),I=LO,HI)
219           go to 1000
220    995    ymax=0.0
221           do 95 I=LO,HI
222           ymax=AMAX1(((EXP(SEQ(I))/1000)+SCY),((EXP(SEQ(I+1))/1000)+SCY),ymax)
223     95    continue
224           WRITE(40,999)(CH(I),((EXP(SEQ(I))/1000)+SCY),I=LO,HI)
225           go to 1000
226    996    ymax=0.0
227           do 96 I=LO,HI
228           ymax=AMAX1(((10**(SEQ(I))/1000)+SCY),((10**(SEQ(I+1))/1000)+SCY),ymax)
229     96    continue
230           WRITE(40,999)(CH(I),((10**(SEQ(I))/1000)+SCY),I=LO,HI)
231           go to 1000
232    999    FORMAT(I11,5X,F15.5)
233   1000    WRITE(50,1001)ymax
234   1001    FORMAT(F15.5)
235           print*,'**** Job done.  ****'
236           END
end
```

Bibliography

Bibliography

[ada70] Adams, F., R. Dams, *Applied Gamma-Ray Spectroscopy*, second edition, revised, (1970, Pergamon Press, Oxford).

[ahm91] I. Ahmad, M. P. Carpenter, R. R. Chasman, R. V. F. Janssens, T. L. Khoo, "Rotational bands with identical transition energies in actinide nuclei ", Phys. Rev. C, *44* (1991) 1204.

[ale71] Alexander, T.K., J.S. Forster, "The Doppler Effect ", in *Excited N ?* (19).

[and79] Anderson, O., J. D. Garrett, G. B. Hagemann, B. Herskind, D. L. Hillis, L. L. Riedinger, "Transition-Energy Correlations in the γ-Ray Continuum —A New Approach", Phys. Rev. Lett., *43* (1979) 687.

[arf85] Arfken, G., *Mathematical Meth. for Physicists*, 3rd ed., (1985, Academic Press, Inc. Harcourt, Brace, Jovanovich).

[ar83a] Arya,A.P., " Nuclear Detectors", Project Physnet M.S.U. MISN-0-544, 18.

[ar83b] Arya,A.P., " Radioactive Decay", Project Physnet M.S.U. MISN-0-542, 1.

[ar83c] Arya,A.P., "Radioactivity and Successive Disintegration", Project Physnet M.S.U. MISN-0-543, 1.

[ar83d] Arya,A.P., "Energetics of Nuclear Reactions", Project Physnet M.S.U. MISN-0-546.

[ary84] Arya,A.P., " Interaction of Gamma Radiation with Matter", M.S.U. Project Physnet, MISN-0-557-6.

[aza91] F. Azaiez, W. H. Kelly, W. Korten, F. S. Stephens, M. A. Deleplanque, R. M. Diamond, A. O. Macchiavelli, J. E. Draper, E. C. Rubel, C. W. Beausang, J. Burde, J. A. Becker, E. A. Henry, S. W. Yates, M. J. Brinkman, A. Kuhnert, T. F. Wang, "Six 'Identical' Superdeformed Bands in ^{194}Tl ", Phys. Rev. Let., *66* (1991) 1030.

[bak92] C. Baktash, J. D. Garrett, D. F. Winchell, A. Smith, "Low-Spin Identical Bands in Neighboring Odd-A and Even-Even Nuclei: A Possible Challenge to Mean-Field Theories ", Phys. Rev. Let., *69* (1992) 1500.

[baz94] D. Bazzacco, F. Brandolini, R. Burch, S. Lunardi, E. Maglione, N. H. Medina, P. Pavan, C. Rossi-Alvarez, G. de Angelis, D. De Acuna, M. De Poli, J. Rico, D. Bucurescu, C. Ur, "Complete decay out of the superdeformed band in ^{133}Nd ", Phys. Rev. C, *49* (1994) R2281.

[bea95] C.W. Beausang, D. Prevost, M.H. Bergstrom, G. deFrance, B. Haas, J. C. Lisle, Ch. Theisen, J. Timár, P. J. Twin, J. N. Wilson, "Using high-fold data from the new generation of γ-ray detector arrays", Nucl. Instr. and Meth. in Phys. Res.A *364*, (1995) 560.

[bec87] Beck, E. M., F. S. Stephens, J. C. Bacelar, M. A. Deleplanque, R. M. Diamond, J. E. Draper, C. Duyar, R. J. McDonald, "Superdeformed Band in ^{135}Nd", Phys. Rev. Lett. *58* (1987) 2182.

[ben79] Bengtsson,T., S. Frauendorf, Nuc. Phys. A, *327* (1979) 139.

[ben85] T. Bengtsson, I. Ragnarsson, Nuc. Phys. A *436*, (1985) 14.

[ben88] T. Bengtsson, I. Ragnarsson, S. Åberg, "The role of high-N orbits in superdeformed states ", Phys. Let. B *208* (1988) 39.

[bet61] Bethe, H.A., Morrison, P., *Elementary Nuclear Theory*, second edition, (1961 John Wiley and Sons, In., N.Y.).

[ber72] Bertsch, G.F., *The Practitioner's Shell Model* (1972, American Elsevier Publishing Co., N.Y.)

[bla69] Blanpied, W. A., *Physics: It's Structure and Evolution*, (1969, Blaisdell Publishing Company, Waltham, MA.)

[bli74] Blinowska, K.J., E.F. Wessner, "A Method of On-Line Spectra Evaluation by Means of a Small Computer Employing Fourier Transforms", Nucl. Instr. Meth., *118* (1974) 597.

[boh75] A. Bohr and B. R. Mottelson, *Nuclear Structure*, Vol. II, (1975, W. A. Benjamin, Inc.).

[bri74] Brigham, E. Oran *The Fast Fourier Transform*, (1974, Prentice-Hall, Englewood Cliffs, N.J.).

[bro86] Browne, E., Firestone, R.B., *Table of Radioactive Isotopes*, ed. V.S. Shirley (1986, John Wiley and Sons, N.Y.).

[bur63] Burcham, W.E., *Nuclear Physics An Introduction* (1963, McGraw Hill Book Co., N.Y.).

[byr90] T. Byrski, F. A. Beck, D. Curien, C. Schuck, P. Fallon, A. Alderson, I. Ali, M. A. Bentley, A. M. Bruce, P. D. Forsyth, D. Howe, J. W. Roberts, J. F. Sharpey-Schafer, G. Smith, P. J. Twin, "Observation of Identical Superdeformed Bands in $N = 86$ Nuclei ", Phys. Rev. Let., *64* (1990) 1650.

[cab91] Cabral-Prieto, H. Jimenez-Dominguez, M. Torres-Valderrama, "A deconvolution method for use in small computers", Nucl. Instr. Meth., *B54* (1991) 532.

[cam69] Camp, D.C., Van Lehn, A.L., "Finite Solid-Angle Corrections for Ge(Li) Detectors ", Nucl. Instr. Meth., *76* (1969) 192.

[cas90] Casten, R.F., *Nuclear Structure from a Simple Perspective*, (1990, Oxford University Press, N.Y.)

[cas93] R. F. Casten, P. O. Lipas, D. D. Warner, T. Otsuka, K. Hyde, J. P. Draayer, *Algebraic Approaches to Nuclear Structure: Interacting Boson and Fermion Models*, Contempory Concepts in Physics Series, Vol. 6, Harwood Academic Publishers, Langhorne, PA (1993).

[ced94] B. Cederwall, R. V. F. Janssens, M. J. Brinkman, I. Y. Lee, I. Ahmad, J. A. Becker, M. P. Carpenter, B. Crowell, M. A. Deleplanque, R. M. Diamond, J. E. Draper, C. Duyar, P. Fallon, L. P. Farris, E. A. Henry, R. G. Henry, J. R. Hughes, T. L. Khoo, T. Lauritsen, A. O. Macchiavelli, E. Rubel, F. S. Stephens, M. A. Stoyer, W. Satula, I. Wiedenhoever, R. Wyss, "New Features of Superdeformed bands in ^{194}Hg", Phys. Rev. Let. *72* (1994) 3150.

[cho89] Chou, Wen-Tsae, PhD. Dissertation, Michigan State Univ., (1989).

[cla95] R. M. Clark, M. A. Deleplanque, B. Cederwall, R. M. Diamond, P. Fallonn, I. Y. Lee, A. O. Macchiavelli, F. S. Stephens, J. A. Becker, M. J. Brinkman, L. P. Farris, E. A. Henry, J. R. Hughes, M. A. Stoyer, J. E. Draper, C. Duyar, E. Rubel, H. Hübel, W. Korten, P. Willsau, "A pair of identical superdeformend bands in ^{136}Nd ", Phys. Let. B *343* (1995) 59.

[coo65] Cooley, J.W., and J.W. Tukey, "An algorithm for the machine computation of complex Fourier Series", *Mathematics of Computation, 19*, (1965), 297.

[cro95] B. Crowell, M. P. Carpenter, R. V. F. Janssens, D. J. Blumenthal, J. Timar, A. N. Wilson, J. F. Sharpey-Schafer,T. Nakatsukasa, I. Ahmad, A. Astier, F. Azaiez, L. du Croux, B. J. P. Gall, F. Hannachi, T. L. Khoo, A. Korichi, T. Lauritsen, A. Lopez-Martens, M. Meyer, D. Nisius, E. S. Paul, M. G. Porquet, N. Redon, "Relative spins and excitation energies of superdeformed bands in ^{190}Hg: Further evidence for octupole vibration ", Phys. Rev. C, *51* (1995) R1599.

[dag94] P. J. Dagnall, C. W. Beausang, P. J. Twin, M. A. Bentley, F. A. Beck, Th. Byrski, S. Clarke, D. Curien, G. Duchene, G. de France, P. D. Forsyth, B. Haas, J. C. Lisle, E. S. Paul, J. Simpson, J. Styczen, J. P. Vivien, J. N. Wilson, K. Zuber, "Excited bands in the doubly-magic superdeformed ^{152}Dy nucleus: evidence for the first $N = 7$ proton hyper-intruder orbital ", Phys. Let. B, *335* (1994) 313.

[deb64] DeBenedetti, S., *Nuclear Interactions* (1964, John Wiley and Sons, N.Y.).

[dia84] Diamond, R. M.,"High-Spin Gamma-Ray Spectroscopy", p.9 in *Nuclear Spectroscopy and Nuclear Interactions*, ed. by H. Ejiri and T. Fukuda, (1984, World Scientific, Singapore).

[dir58] Dirac, P.A.M., *The Principles of Quantum Mechanics*, 4th ed. revised, (1958, Clarendon Press Oxford, N.Y.)

[don67] Donnelly, D.P., Baer, H.W., Reidy, J.J., Wiedenbeck, M.L., "The Calibration of a Ge(Li) Gamma-Ray Spectrometer for Energy and Relative Intensity Measurements", Nucl. Instr. Meth., *57* (1967) 219.

[dra87] Dragulescu, E., Ivascu, M., Ionescubujor, M., Iordachescu, A, Petrache, C., Popescu, D., Pascovici, G., Semenescu, G., Gurgu, I., Baciu, F., Paar, V., Brant, S., Vretenar, D., "Rapid Shape Transition in Praseodymium Nuclei", in *Symmetries and Nuclear Structure*, Meyer, R.A., Paar, V., editors, (1987, Harwood Academic Publishers).

[eis87] Eisenberg,J.M., Griener,W.,*Nuclear Theory, I Nuclear Models Collective and Single Particle Phenomena*, 3rd ed. revised, (1987, North-Holland).

[eis58] Eisenbud,L., Wigner, E.P., *Nuclear Structure*, (1958, Princeton University Press, Princeton, N.J.).

[egg79] EG & G Ortec Gamma-X^{TM} Coaxial HPGe Detector Technical Data Sheet, 3135 1279.

[eks72] Ekstrom, C., S. Ingleman, M. Olsmats, B. Wannberg, G. Andersson, and A. Rosen, Nuc. Phys. A, *196* (1972), 178.

[els34] Elsasser, W., Jour. Phys. Rad., *5* (1934) 389,635.

[fal93] Fallon,P.,J.Burde, B. Cederwall, M.A. Deleplanque, R.M. Diamond, I.Y. Lee, J.R.B. Oliveira, F.S. Stevens, J.A. Becker, M.J. Brinkman, E.A. Henry, A. Kuhnert, M. A. Stoyer, J. E. Draper, C. Durjar, E. Rubel, "Evidence for M1 Transitions between Superdeformed States in 193Hg", Phys. Rev. Lett., *70*, (1993) 2690.

[fli93] Flibotte, S., et al., Phys. Rev. Lett., *71* (1993) 4299.

[flo92] Flores-Llamas, H., H. Yee-Madeira, "A correction to the power series expansion of Fourier transforms for deconvolution", Nucl. Instr. Meth., *B71* (1992) 103.

[fir94] Firestone, Richard B. and Balraj Singh, *Table of Superdeformed Nuclear Bands and Fission Isomers* , LBL report 35916, UC-413, (1994).

[fos90] D.B. Fossan et.al, Nuc. Phys. A, *520*, (1990) 241c.

[fri81] Friedlander, G., J.W. Kennedy, E.S. Macias, J.M.Miller, *Nuclear and Radiochemistry*, third edition. (1981, John Wiley and Sons).

[fre66] Freeman, J.M., Jenkin, J.G., " — Of Ge(Li) Gamma-Ray Detectors in the Energy Range 500 to 1500", Nucl. Instr. Meth., *43* (1966) 269.

[gal58] Gallagher, C. J., S.A. Moszkowski, Phys. Rev., *111*, (1958) 1282.

[gar69] Garvy, G.T., et al., Rev. Mod. Phys., *41* (1969) 51.

[gie71] Giesler, G.C., McHarris, Wm.C., Warner,R.A., Nucl. Instr. and Meth., *91*, (1971) 313.

[god89] Godfrey, M.J., Y. He, I. Jenkins, A. Kirwan, P. J. Nolan, R. Wadsworth, S. M. Mullins, J.Phys. G. *15* (1989) L163.

[gou74] Goulding, F.S., Pehl, R. H., "Semiconductor Radiation Detectors", chapter IIIA in *Nuclear Spectroscopy and Reactions*, ed., J. Cerny (1974, Academic Press, N.Y.).

[gro65] Grove, N.B. and R. L. Robinson, editors, *Nuclear Spin-Parity Assignments*, proceedings of the Conference on Bases for Nuclear Spin-Parity Assignments, Tennessee, 1965, (1966, Academic Press).

[gro76] v. Groote, H., Hilf, E.R., Takahashi, K., "A New Semiempirical Shell Correction to the Droplet Model – Gross Theory of Nuclear Magics ", Atomic Data Nuc. Data Tabls. *17* (1976) 418.

[gro94] C. J. Gross, C. Baktash, D. M. Cullen, R. A. Cunningham, J. D. Garrett, W. Gelletly, F. Hannachi, A. Harder, M. K. Kabadiyski, K. P. Lieb, C. J. Lister, W. Nazarewicz, H. A Roth, D. Rudolph, D. G. Sarantites, J. A. Sheikh, J. Simpson, Ö. Skeppstedt, B. J. Varley, D. D. Warner, "Identical bands in ^{77}Sr, ^{78}Sr, and ^{78}Rb: Evidence for a very good spectator orbital ", Phys. Rev. C, *49* (1994) R580.

[gui87] Guidry, M.W.,"A Q-Window with a View ", in *Workshop on Relations between Structure and Reactions in Nuclear Physics*, eds., D.H. Feng, M. Vallieres, B. H. Wildenthal (1987, World Scientific, Singapore).

[ham75] Hamilton, W.D.,ed., *The Electromagnetic Interaction in Nuclear Spectroscopy*, (1975, North-Holland Publishing Co.)

[ham90] C.V. Hampton, J. Johnson, Aracelys Rios, W.A. Olivier, R. M. Ronningen, Wm.C. McHarris, and ORNL Nuclear Structure Group, "Rotational Bands and Superdeformation in ^{132}Pr", 1990 NSCL Annual Report.

[ham94a] C.V. Hampton, R. Aryaeinejad, W.A. Olivier, R. Ronningen, Wm.C. McHarris, and ORNL Nuclear Structure Research Group, NSCL/MSU Annual Report, 99 (1994)

[ham94] C.V. Hampton, B. Lian, Wm.C. McHarris, Nucl. Instr. and Meth. in Phys. Res.A *353*, (1994) 280.

[ham96] C.V. Hampton, W.A. Olivier, Wm.C. McHarris, National Superconducting Cyclotron Laboratory Annual Report (1995) p.274 . Also, "A Search Technique for γ -ray Bands Using Segmented Fourier Analysis", presented at the Workshop on Data Analysis, HRIBF, ORNL, February 7-10, 1996 and Bull. Am. Phys. Soc.,Vol.41, p.861, A8.07 (1996).

[har65] Harris, S. M., Phys. Rev., *138* (1965) B509.

[hec69] K. T. Hecht and A. Adler, "Generalized Seniority for Favored $J \neq 0$ Pairs in mixed configurations", Nuc. Phys. A, *137* (1969) 129.

[har69] Harvey, B.G., *Introduction to Nuclear Physics and Chemistry*, 2nd ed., (1969, Prentice-Hall, Inc., N.J.)

[has94] D.S. Haslip, et al., Nucl. Instr. and Meth. in Phys. Res.A *345*, 534 (1994).

[hau94] K. Hauschild, R. Wadsworth, R. M. Clark, I. M. Hibbert, C. W. Beausang, S. A. Forbes, P. J. Nolan, E. S. Paul, A. T. Semple, J. N. Wilson, A. Gizon, J. Gizon, D. Santos, J. Simpson, "Deformed rotational bands in the doubly odd nuclei ^{134}Pr and ^{132}Pr ", Phys. Rev. C, *50* (1994) 707.

[hau95] K. Hauschild, R. Wadsworth, R.M. Clark, P. Fallon, D.B. Fossan, I.M. Hibbert, A.O. Macchiavelli, P.J. Nolan, H. Schnare, A.T. Semple, I. Thorslund, L. Walker, W. Satula, R. Wyss, Phys. Lett. *353B*, (1995) 438.

[hax50] Haxel, O., Jensen, J.H.D., Suess, H.E., Zeits. f. Physik *128* (1950) 295.

[hil86] Hildingsson, L.,C.W.Beausang, D.B. Fossan, W.F. Piel, Phys. Rev. C *33* (1986) 2200.

[hil88] Hildingsson, L.,C.W.Beausang, D.B. Fossan, W.F. Piel, Phys. Rev. C *37* (1988) 985.

[hol87] Holifield Heavy Ion Research Facility, User's Handbook, Oak Ridge National Laboratory, 1987.

[hor60] Hornyak, W. F., "The Interaction of γ rays with Matter", in *Nuclear Spectroscopy*, Part A, ed., F.Ajzenberg-Selove, (1960, Academic Press, N.Y.).

[hyd64] Hyde, E.K.,I. Perlman, G.T. Seaborg, *The Nuclear Properties of the Heavy Elements I. Systematics of Nuclear Structure and Radioactivity*, (1964, Prentice-Hall, Inc., N.J.)

[hey94] Heyde, Kris. L. G., *The Nuclear Shell Model*, 2nd edition, (1994, Springer-Verlag, N.Y.)

[imsl] IMSL, Inc., Math/Library Software, the algorithm used is based on the real, trignometric FFT developed by Paul Swarztrauber at the National Center for Atmospheric Research, Boulder, Colorado.

[ino69] Inouye, T., T.Harper, N.C. Rasmussen, "Application of Fourier Transforms to the Analysis of Spectral Data", Nucl. Instr. Meth., *67* (1969) 125.

[irv72] Irvine, J.M., *Nuclear Structure Theory*,Vol.49 in *International Series of Monographs in Natural Philosophy*, ed. D. terHaar, (1972, Pergamon Press, N.Y.).

[jai92] Jain, K., A. Kumar Jain,Atomic and Nuclear Data Tables, *50*, (1992) 269.

[jin92] H. -Q. Jin, L. L. Riedinger, C. -H. Yu, W. Nazarewicz, R. Wyss, J. -Y. Zhang, C. Baktash, J. D. Garrett, N. R. Johnson, I. Y. Lee, F. K. McGowan, "Electromagnetic properties of the $[3\tilde{0}3]5/2, 7/2$ pseudo-spin doublet in ^{175}Re ", Phys. Let. B, *277* (1992) 387.

[joh89] Johansson, J.K., H. R. Andrews, T. Bengtsson, A. Djaafri, T. E. Drake, S. Flibotte, A. Galindo-Uribarri, D. Horn, V. P. Janzen, J. A. Kuehner, S. Monaro, N. Nadon, S. Pilotte, D. Prévost, D. C. Radford, I. Ragnarsson, P. Taras, A. Tehami, J. C. Waddington, D. Ward, and A. Åberg, "Multiple Superdeformed Bands in ^{153}Dy", Phys. Rev. Lett., *63* (1989) 2200.

[kek86] Kekre, H.B., V.K.Madan, "Frequency Domain and Sequency Domain Filtering of Nuclear Spectral Data", Nucl. Instr. Meth., *A245* (1986) 542.

[kek89] Kekre, H.B., V.K.Madan, B.R.Bairi, "A Fourier Transform Method for the Selection of a Smoothing Interval", Nucl. Instr. Meth., *A279* (1989) 596.

[kik68] Kikuchi, K., Mitsuji Kawai, *Nuclear Matter and Nuclear Reactions*, a North-Holland Research Monograph in the Field of Nuclear Physics, ed., J.B. Marion, (1968, John Wiley and Sons, N.Y.).

[kir87] A. J. Kirwan, G. C. Ball, P. J. Bishop, M. J. Godfrey, P. J. Nolan, D. J. Thornley, D. J. G. Love, and A. H. Nelson, Phys. Rev. Lett. *58*, (1987) 467.

[kra71] Krane, K.S., "Solid-Angle Correction Factors for Coaxial Ge(Li) Detectors ", Nucl. Instr. Meth., *98* (1971) 205.

[kra88] Krane, K.S., *Introductory Nuclear Physics* (1988,John Wiley and Sons)

[kre90] A. J. Kreiner and A. O. Macchiavelli, " Coupling schemes in doubly odd nuclei and identical superdeformed bands", Phys. Rev. C, *42* (1990) R1822.

[kre94] A. J. Kreiner, M. A. Cardona, H. Somacal, M. E. Debray, D. Hojman, J. Davidson, M. Davidson, D. DeAcuna, D. R. Napoli, J. Rico, D. Bazzacco, R. Burch, S. M. Lenzi, C. Rossi Alvarez, N. Blasi, G. Lo Bianco, "Pseudospin flip in doubly decoupled structures and identical bands ", *50* (1994) R530.

[lee90] Lee, T.-S.H., R.B. Wiringa, *The Nuclear Shell Model*, Proceedings of a Symposium on the occasion of the 40th Anniversary of the Nuclear Shell Model, Argonne, (1990, North-Holland Elsevier Science Publications)

[ler91] Perlow, G.J., in *Encyclopedia of Physics*, Lerner,R.G., Trigg, G.L.,editors, (1991, VCH Publishers, Inc., N.Y.).

[liu96] Yunzuo Liu, Jingbin Lu, Yingjun Ma, Shangui Zhou, and Hua Zheng, "Systematic study of spin assignments and signature inversion of $\pi h_{11/2} \otimes \nu h_{11/2}$ bands in doubly odd nuclei around $A \approx 130$ ", Phys. Rev. C, *54* (1996) 719.

[mac95] A.O. Macchiavelli, B. Cederwall, R. M. Clark, M. A. Deleplanque, R. M. Diamond, P. Fallon, I. Y. Lee, F. S. Stephens, S. Asztalos, "C_4 symmetry effects in nuclear rotational motion ", Phys. Rev. C, *51* (1995) R1.

[mal81] Malmstadt,H.V., Enke, C.G., Crouch,S.R., *Electronics and Instrumentation for Scientists*, (1981, The Benjamin Cummings Publishing Co., Inc, Ca.).

[may49] Mayer, M.G., Phys. Rev., *75* (1949) 1969.

[may55] Mayer, M.G., J. Hans D. Jensen, *Elementary Theory Of Nuclear Shell Structure* (1955, John Wiley and Sons, N.Y.).

[may68] Mayer, M.G., J. H. D. Jensen, D. Kurath, "The Shell Model", Chapter IX in *Alpha-, Beta-, and Gamma- Ray Spectroscopy*, Vol. 1, Siegbahn, K., editor, (1968, North Holland Publishing Co.).

[mch65] McHarris, Wm. C, PhD. Dissertation, Univ. of California, Berkeley, (1965).

[mch86] McHarris, Wm. C, W.-T. Chou, J. Kupstas-Guido, W. A. Olivier, in "Nuclei Off the Line of Stability", ed R. A. Meyer and D. S. Brenner, American Chemical Society Symposium Series 324, (1986), 329.

[mch90] McHarris, Wm. C, editor, *Exotic Nuclear Spectroscopy* (1990, Plenum Press, N.Y.).

[mer70] Merzbacher, E., *Quantum Mechanics*, 2nd ed., (1970, John Wiley and Sons, N.Y.).

[mor76] Morinaga, H., T. Yamazki, *In-Beam Gamma-Ray Spectroscopy*, (1976, North-Holland Publishing Co.).

[mye74] Myers, W.D., Swiatecki, W.J., "The Nuclear Droplet Model for Arbitrary Shapes ", Ann. Phys. *84* (1974) 186.

[mye76] Myers, W.D., "Development of the Semiempirical Droplet Model ", Atomic Data and Nucl. Data Tabls, *17* (1976) 411.

[nat68] O. Nathan, S. G. Nilsson, "Collective Nuclear Motion and the Unified Model", Chapter X in *Alpha-, Beta-, and Gamma- Ray Spectroscopy*, Vol. 1, Siegbahn, K., editor, (1968, North Holland Publishing Co.).

[naz85] W. Nazarewicz, J. Dudek, R. Bengtsson, and I. Ragnarsson, Nucl. Phys. *A435*, 397 (1985)

[naz89] W. Nazarewicz, R. Wyss, A. Johnson, "Structure of Superdeformed bands in the $A \approx 150$ region ", Nuc. Phys. A *503* (1989) 285.

[naz90] W. Nazarewicz, P. J. Twin, P. Fallon, J. D. Garrett, "Natural-Parity States in Superdeformed Bands and Pseudo SU(3) Symmetry at Extreme Conditions ", Phys. Rev. Let., *64* (1990) 1654.

[nil69] S. G. Nilsson, C. F. Tsang, A. Sobiczewski, Z. Szymanski, S. Wycech, C. Gustafson, I. -L. Lamm, P. Möller, B. Nilsson, "On the nuclear structure and stability of heavy and superheavy elements ", Nuc. Phys. A, *131* (1969) 1.

[nis95] D. Nidius, R. V. F. Janssens, P. Fallon, B. Crowell, I. Ahmad, C. W. Beausang, M. P. Carpenter, B. Cederwall, P. J. Daly, M. A. Deleplanque, R. M. Diamond, D. Gassmann, Z. W. Grabowski, R. G. Henry, T. L. Khoo, T. Lauritsen, I. Y. Lee, A. O. Macchiavelli, R. H. Mayer, F. S. Stephens, P. J. Twin, "'Identical' superdeformed band in ^{151}Dy: further evidence for the pseudospin coupling scheme ", Phys. Let. B *346* (1995) 15.

[nol85] Nolan,P.J., Gifford, D.W., Nucl. Instr. and Meth., *A236* (1985) 95.

[nya84] Nyakó, B. M., J. R. Cresswell, P. D. Forsyth, D. Howe, P. J. Nolan, M. A. Riley, J. F. Sharpey-Schafer, J. Simpson, and N. J. Ward, "Observation of Superdeformation in ^{152}Dy", Phys. Rev. Let., *52* (1984) 507.

[par69] Paradellis, T., Hontzeas, S., "A Semi-Empirical Efficiency Equation for Ge(Li) Detectors ", Nucl. Instr. Meth., *73* (1969) 210.

[pau87] Paul, E.S., C.W. Beausang, D.B. Fossan, R. Ma, W.F. Piel, Jr., N. Xu, L. Hildingsson, Phys. Rev. C, *36* (1987) 1853.

[pau88] Paul, E.S., et al., Phys. Rev. C, *37* (1988) 1478.

[pol62] Polikanov, S. M. et al., Zh. Eksp. Teor. Fiz., *42* (1962) 1464.

[pau90] Paul, E.S., C.W. Beausang, D.B. Fossan, Y. Liang, R. Ma, W.F. Piel, Jr., S. Shi, N. Xu, "High-Spin Properties of Doubly-Odd Nuclei of Mass $\approx$130", in *Nuclei Far From Stability*, Ch. 24, edited by Wm. C. McHarris, (1990).

[puh77] "On the Interpretation of Evaporation Residue Mass Distributions in Heavy-Ion Induced Fusion Reactions ", Pühlhofer, F., Nucl. Phys. A, *280* (1977) 267.

[rai50] J. Rainwater, Phys. Rev., *79*,432, (1950).

[ras75] Rasmussen, J.O, "Models of Heavy Nuclei", Chapter IX.B in *Nuclear Spectroscopy and Reactions, Part D*, ed. J. Cerny, Academic Press, N. Y., (1975).

[rei80] Reitz, J.R., F.J. Milford, R.W. Christy, *Foundations of Electromagnetic Theory*, 3rd ed., (1980, Addison Wesley Publishing Co.)

[ril88] Riley,M.A., Virtanen, A.,"Shield Setup on the CSS", Holifield Heavy Ion Research Facility Report, Oak Ridge National Laboratory, May 29, 1988.

[ros78] Rösel, F., H.M. Fries, K. Alder, H.C. Pauli, "Internal Conversion Coefficients for all Atomic Shells", Atomic Data and Nuclear Data Tables, *21* (1978) 91.

[rya88] Ryan,C.G., E.Clayton, W.L.Griffin, S.H.Sie, D.R.Cousens, Nucl. Instr. and Meth., *B34* (1988) 396.

[see76] Seeger, P.A., Howard, W.M., "A Semiempirical Liquid-Drop Plus Shell-Correction Formula ", Atomic Data Nucl. Data Tabls. *17* (1976) 428.

[she76] Shera, E.B., et al., Phys. Rev. C *14* (1976) 731.

[shi88] Shi, S., C.W. Beausang, D.B. Fossan, R. Ma, E.S. Paul, N. Xu, A.J. Kriener, "Weak and Strong Signature Splitting in doubly odd ^{132}Pr", Phys. Rev. C, *37* (1988) 1478.

[shi90] Shimizu, Y. R., E. Vigezzi, R. A. Broglia, "Inertias of superdeformed bands" , Phys. Rev. C *41* (1990) 1861.

[sin96] Singh, B., R.B. Firestone, S.Y. Frank Chu, "Table of Superdeformed Nuclear Bands and Fission Isomers", 2nd Edition, LBL-38004 UC-413, May 1996.

[sla84] Slaughter, M.F., R.A. Warner, T.L. Khoo, W.H. Kelly, Wm. C. McHarris, "Rotational Bands in Odd-Odd 182Re", Phys. Rev. C, *29*, (1984), 114.

[srs96] "About Lock-in Amplifiers Application Note 3", Stanford Research Systems Scientific and Engineering Instruments Catalog, (1996) 169.

[ste71] F. S. Stephens and R. S. Simon, "Coriolis Effects in the Yrast States", Nuc. Phys. , *A183* (1972) 257.

[ste90] F. S. Stephens, et al., "Spin Alignment in Superdeformed Rotational Bands ", Nuc. Phys. A, *520* (1990) 91c.

[ste90a] F.S. Stephens *et al.*, Phys. Rev. Lett. *65*, 301 (1990).

[ste90b] F. S. Stephens, M. A. Deleplanque, J. E. Draper, R. M. Diamond, A. O. Macchiavelli, C. W. Beausang, W. Korten, W. H. Kelly, F. Azaiez, J. E. Becker, E. A. Henry, S. W. Yates, M. J. Brinkman, A. Kuhnert, J. A. Cizewski, "Pseudospin Symmetry and Quantized Alignment in Nuclei ", Phys. Rev. Let., *65* (1990) 301.

[ste91] Steffen, R.M., "Angular Correlation of Nuclear Radiation", in *Encyclopedia of Physics*, 2nd edition, R.G. Lerner and G.L. Trigg, editors, (1991, VCH Publishers, NY) p39.

[sug93a] K. Sugawara-Tanabe and A. Arima, "Quantization of Alignment and different Parity Pair Levels with $\Omega = 1/2$ ", Nuc. Phys. A, *557* (1993) 157c.

[sug93b] K. Sugawara-Tanabe and A. Arima, "Parity doublet levels in superdeformation ", Phys. Let. B, *317* (1993) 1.

[sug95] K. Sugawara-Tanabe, A. Arima, N. Yoshida, "Resurrection of the L-S coupling scheme in superdeformation ", Phys. Rev. C, *51* (1995) 1809.

[tre81] Trenn, T.J., *Transmutation: natural and artificial*, A Series of Historical Monographs on Fundamentals of Chemistry, Nobel Prize Topics in Chemistry, ed., J. W. Van Sprousen (1981, Heyden and Son).

[twi86] Twin, P. J., B. M. Nyakó, A. H. Nelson, J. Simpson, M. A. Bentley, H. W. Cranmer-Gordon, P. D. Forsyth, D. Howe, A. R. Mokhtar, J. D. Morrison, J. F. Sharpey-Schafer, G. Sletten, " Observation of a Discrete-Line Superdeformed Band up to $60\hbar$ in ^{152}Dy", Phys. Rev. Lett., *57* (1986) 811.

[ver83] Verma, R.,"Profile Deconvolution Method for Small Computers", Nucl. Instr. Meth., *212* (1983) 323.

[wad87] Wadsworth, R., A. Kirwan, D. J. G. Love, Y-X Luo, J-Q Zhong, P. J. Nolan, P. J. Bishop, M. J. Godfrey, R. Hughes, A. N. James, I. Jenkins, S. M. Mullins, J. Simpson, D. J. Thornley, K. L. Ying, J.Phys.G.,*13* (1987) L207.

[wad91] R. Wadsworth, S.M. Mullins, P.J. Bishop, A. Kirwan, M.J. Godfrey, P.J. Nolan, and P.H. Regan, Nucl. Phys. *A526*, 188 (1991)

[wap68] A. H. Wapstra, "The Coincidence Method ", Chapter VIIIc in *Alpha-, Beta-, and Gamma- Ray Spectroscopy*, Vol. 1, Siegbahn, K., editor, (1968, North Holland Publishing Co.).

[wap85] Wapstra, A.H. and G. Audi, "The 1983 Atomic Mass Evaluation (I), Atomic Mass Table ", Nucl. Phys. A *432* (1985).

[wil86] Wilhelmi, Z. and Szeflińska,"Coherent effects in highly excited nuclei", Proceedings of the XVIII Mikołajki Summer School on Nuclear Physics, Mikołajki, Poland, (1986).

[wil93] "Multiple, Excited Superdeformed Bands in ^{133}Pr", Wilson, J.N., P.J. Nolen, E.S.Paul, A.T.Semple, C.W. Beusang, S.A, Forbes, R. Wadsworth, K. Hauschild, I. M. Hibbert, R. M. Clark, J. Gizon, A. Gizon, D. Santos, B. Nyako, J. Simpson, Daresbury Lab 1992-1993 Annual Report, Appendix p.17 (1993).

[wil95] J. N. Wilson, *Ph.D. Thesis, University of Liverpool* (1995).

[wu93] Wu,C.-L., D.H. Feng, M. Guidry, "The Fermion Dynamical Symmetry Model", to be published in Adv. in Nucl. Phys, (revised June 7, 1993)

[wu95] C. S. Wu, "Decoupling and anomalous bandcrossings in odd-proton nuclei ", Phys. Rev. C, *51* (1995) 1819.

[wys88] R. Wyss, J. Nyberg, A. Johnson, R. Bengtsson, and W. Nazarewicz, Phys. Lett. B. *215*, 211 (1988)

[yan93] J. Yan, O. Vogel, P. von Brentano, A. Gelberg, "Systematics of triaxial deformation in Xe, Ba, and Ce nuclei ", Phys. Rev. C, *48* (1993) 1046.

[zha92] J.-Y. Zhang, R. F. Casten, W. -T. Chou, D. S. Brenner, N. V. Zamfir, P. von Brentano, "Identical Bands and the Varieties of Rotational Behavior ", Phys. Rev. Let., *69* (1992) 1160.

[zie80] J. F. Ziegler, "The stopping and ranges of ions in matter", Vols. 3 & 5, Pergamon Press (1980) .